NIST SPECIAL PUBLICATION 752

U.S. DEPARTMENT OF COMMERCE/National Institute of Standards and Technology

Laser Induced Damage in Optical Materials: 1986

BOULDER DAMAGE SYMPOSIUM

ASTM

STP 1028

Laser Induced Damage in Optical Materials: 1986

Proceedings of a Symposium Sponsored by:

National Institute of Standards and Technology
(formerly National Bureau of Standards)
American Society for Testing and Materials
Office of Naval Research
Department of Energy
Defense Advanced Research Project Agency
Air Force Office of Scientific Research

November 3–5, 1986

NIST (formerly NBS), Boulder, Colorado 80303

Edited by:

Harold E. Bennett
Naval Weapons Center
China Lake, California 93555

Arthur H. Guenther
Air Force Weapons Laboratory
Kirtland Air Force Base, New Mexico 87117

David Milam
Lawrence Livermore National Laboratory
Livermore, California 94550

Brian E. Newnam
Los Alamos National Laboratory
Los Alamos, New Mexico 87545

NOTE: As of 23 August 1988, the National Bureau of Standards (NBS) became the National Institute of Standards and Technology (NIST) when President Reagan signed into law the Omnibus Trade and Competitiveness Act.

BOULDER DAMAGE SYMPOSIUM

U.S. DEPARTMENT OF COMMERCE, C. William Verity, Secretary

NATIONAL INSTITUTE OF STANDARDS AND TECHNOLOGY, Ernest Ambler, Director
(formerly National Bureau of Standards)

Issued September 1988

Library of Congress Catalog Card Number: 88–600571

National Institute of Standards and Technology
Special Publication 752, 724 pages (Sept. 1988)
CODEN: XNBSAV

U.S. GOVERNMENT PRINTING OFFICE
WASHINGTON: 1988

For sale by the Superintendent of Documents, U.S. Government Printing Office, Washington, DC 20402–9325

Foreword

The Proceedings contain the papers presented at the Eighteenth Symposium on Optical Materials for High Power Lasers held at the National Bureau of Standards in Boulder, Colorado, on November 3-5, 1986. The Symposium was jointly sponsored by the National Bureau of Standards, the American Society for Testing and Materials, the Office of Naval Research, the Defense Advanced Research Projects Agency, the Department of Energy, and the Air Force Office of Scientific Research. The Symposium was attended by almost 200 scientists from the United States, the United Kingdom, Japan, France, and the Federal Republic of Germany. It was divided into sessions devoted to the following topics: Materials and Measurements, Mirrors and Surfaces, Thin Films, and finally Fundamental Mechanisms. The Symposium Co-Chairmen were Dr. Harold E. Bennett of the Naval Weapons Center, Dr. Arthur H. Guenther of the Air Force Weapons Laboratory, Dr. David Milam of the Lawrence Livermore National Laboratory, and Dr. Brian E. Newnam of the Los Alamos National Laboratory. They also served as editors of this report.

The editors assume full responsibility for the summary, conclusions, and recommendations contained in the report, and for the summaries of discussion found at the end of each paper. The manuscripts of the papers presented at the Symposium have been prepared by the designated authors, and questions pertaining to their content should be addressed to those authors. The interested reader is referred to the bibliography at the end of the summary article for general references to the literature of laser damage studies. The Nineteenth Annual Symposium on this topic will be held in Boulder, Colorado, October 26-28, 1987. A concerted effort will be made to ensure closer liaison between the practitioners of high peak power and the high average power community.

The principal topics to be considered as contributed papers in 1987 do not differ drastically from those enumerated above. We expect to hear more about improved scaling relations as a function of pulse duration, area, and wavelength, and to see a continuing transfer of information from research activities to industrial practice. New sources at shorter wavelengths continue to be developed, and a corresponding shift in emphasis to short wavelength and repetitively pulsed damage problems is anticipated. Fabrication and test procedures will continue to be developed, particularly in the diamond-turned optics and thin film areas.

The purpose of these symposia is to exchange information about optical materials for high power lasers. The editors will welcome comment and criticism from all interested readers relevant to this purpose, and particularly relative to our plans for the Nineteenth Annual Symposium.

H. E. Bennett, A. H. Guenther,
D. Milam, and B. E. Newnam
Co-Chairmen

Disclaimer

Certain papers contributed to this publication have been prepared by non-NBS authors. These papers have not been reviewed or edited by NBS; therefore, the National Bureau of Standards accepts no responsibility for their accuracy, nor for their comments or recommendations.

Certain commercial equipment, instruments, and materials are identified in this publication in order to explain the experimental procedure adequately. Such identification in no way implies approval, recommendation, or endorsement by the National Bureau of Standards, nor does it imply that the equipment, instruments, or materials identified are necessarily the best available for the purpose.

CONTENTS

Materials and Measurements

Thin Films

Surfaces and Mirrors

Fundamental Mechanisms

WELCOME TO THE EIGHTEENTH ANNUAL SYMPOSIUM ON OPTICAL MATERIALS FOR HIGH POWER LASERS

Arthur H. Guenther
Air Force Weapons Laboratory
Kirtland Air Force Base, New Mexico

On behalf of my three co-chairmen, Hal Bennett, Dave Milam and Brian Newnam, we would like to welcome you to this, the eighteenth in this continuing series of symposia. Unfortunately, Hal Bennett is not able to be with us this year. He was here until yesterday, but he had to appear in court to settle some legal matters in California and he wishes to express his regrets that he is not going to be present. He'll be here in spirit certainly. As you just heard from Dr. Kamper, we are welcome back next year. I'm sure Hal will be with us at that time.

As the first viewgraph shows, the conference continues its steady growth. Last year we had 67 papers and about 225 attendees. This year we have 75 papers and I don't know what we will have in attendance but the 145 or so pre-registered was the largest number so recorded through any of these meetings, and there were at least another 40 to 50 who signed in last night.

I think it is important to note that the symposium continues to reflect the recent interest in thin films at this particular meeting. This year there are still twice as many papers in that category as in any of the others that we normally separate our papers into: materials and measurements, surfaces and mirrors, and fundamental mechanisms. In fact, we have moved thin films up in the sequence to follow materials and measurements since it encompasses a very large part of the meeting.

We hope that the proceedings from the 1984 meeting will be available for you to pick up tomorrow afternoon if the printing office delivers as promised. (They were.) This meeting has been the most dynamic in scheduling and I would ask that each of you please check your program and the short, late-change sheet to ensure that you know where we are and that if you have a paper, you know where it occurs. If you can't find it, please let us know right away. We do have a couple of slots open because we have had some extra poster boards made and one cancellation has given us an additional oral position.

The '85 proceedings are progressing but at last count there are 16 manuscripts that have not been received. Some wanted me to read the delinquent authors' names and ask them to stand up so that you could look and see who they were, but even I didn't want to start off the meeting in that manner. Rather, I would like to ask those of you

who are here who have manuscripts that are still among the missing, they are listed on the bulletin board outside, to please check off the status and give an indication when we might expect them. I will say we are progressing very rapidly to sending the proceedings to the publisher. In fact, three manuscripts were delivered this morning from last year's meeting, so they made it within a year, but we do have 16 that are still delinquent.

This is an opportunity to say a few words to you on a subject I think is most important. Without a doubt, these symposium proceedings, in my opinion, form the best and most comprehensive chronology of power optics problems and solutions from 1969 on. I think they continue to form the framework of the most significant work in the field. They have led not only to an efficiency in our progress in advancing optical materials for high power lasers but a recognition and recording of previous work resulting in avoidance of duplication. In fact, they have formed the basis of a tutorial in an educational sense for others entering or working in the field. I can't emphasize enough the investment we've all made and the need to continue to document results as we solve problems and proceed to new areas. In fact, the very format of this meeting, to wit, no parallel sessions, lots of discussion opportunities, and unlimited documentation, has engendered the technical world a cadre of mature well-informed specialists who are frequently called upon to overcome a major constraint in laser development, applications, or to improve designs.

Let me now add a few words about the state of affairs concerning the topics of today's interests as relates to this meeting. We continue to see new materials coming on the scene, primarily driven by applications such as short wavelength operation. For example, there is a lot of attention being given in the transparent case to calcium fluoride and some to lithium fluoride or metallics or inter-metallics in the case of substrates or reflectors both at short wavelengths and in the infrared. Just as applicable, however, I don't know why polymers have not really caught on more and it is unfortunate that we just heard last week that Professor Manenkov will not be with us to share his latest results in this field. Certainly polymers is an area that has caught on quite heavily in the Soviet Union. On the other hand, we do continue to see continued improvements and opportunities in sol-gel and related material technologies.

However, as I indicated, coatings still dominate the meeting and there is no question as to why that is; there is considerable leverage because of the multitude of applications. There is, as well, an inherent belief that there is a lot of room for improvement. The focus this year comes in several categories. First, and perhaps foremost, is the attention that is being given to the issue of thermal conductivity in thin films. Thermal conductivity is a very structure-dependent property of the material. This quality has a great impact upon the modeling that we have heard so much about in the last few years. In the past, if people used the thermal conductivity of bulk material, to come up with an estimate to compare with experimental measurements of

damaged threshold, they had to evoke an extremely high and fictitious absorption level, too high in fact to be credible. People were starting to look for other explanations to explain the high absorption levels. Recent reports of thermal conductivity measurements, where we see decreases ranging from 50 to 500, and in some cases maybe even to 1000, greatly alleviates this apparent inconsistency in that it limits the amount of heat that can be conducted away from an absorbing site. This in fact will, I am sure, bring better agreement between the modeling estimates and the quality experimental measurements of the damage threshold that we obtain in the laboratory.

Another area that has received a lot of attention is certainly the application driven area. Free-electron lasers certainly come to mind immediately. Brian Newnam pointed out a few years ago that there is going to be a problem with high fluences and there's going to be a problem with the diverse duty cycles of rf and inductive driven accelerators; which give you entirely different pulse train considerations. Add to this the wavelength agility which others see as an advantage in FELs. It becomes nothing but a problem for the people who wish to design FELs to have all the advances that they inherently offer.

We do see continued advances in instrumentation, and you will hear some interesting papers this year on spectroscopic ellipsometry. There has been a lot of attention given to this work over the last two or three years at the Naval Weapons Center, at Bell Laboratories, and at the Materials Research Laboratory at Penn State. It appears now that this technique is starting to give us some information about the structure inside films and as was pointed out earlier this year by Hal Bennett and others, one can actually determine surface roughness by this technique. There has been excellent agreement between that predicted from the ellipsometric measurements and that determined from surface profilometry. But, of course, on the same issue of instrumentation, we still are seeking that illusive and what we hope eventually to be a widely accepted facile pre-catastrophic damage indicator. It still seems that a lot of people are working on the issue of desorption as one possible solution to their problem, and there are several papers on that subject at the meeting today. Finally, from the instrumentation standpoint, it is gratifying to note the increase in the automated damage testing facilities throughout the world and I think this can only help advance coating technologies in allowing more rapid and economical assessment of perhaps the last active coating area, and that is process improvement. Which is leading in its own way to better coatings, and I mean better in terms of the eventual application, which may not be the one that you went out to solve.

There is no question that the hallmark of this meeting has been its flexibility to go where the action is and to consider and conquer new problems in both a systematic and synergistic manner.

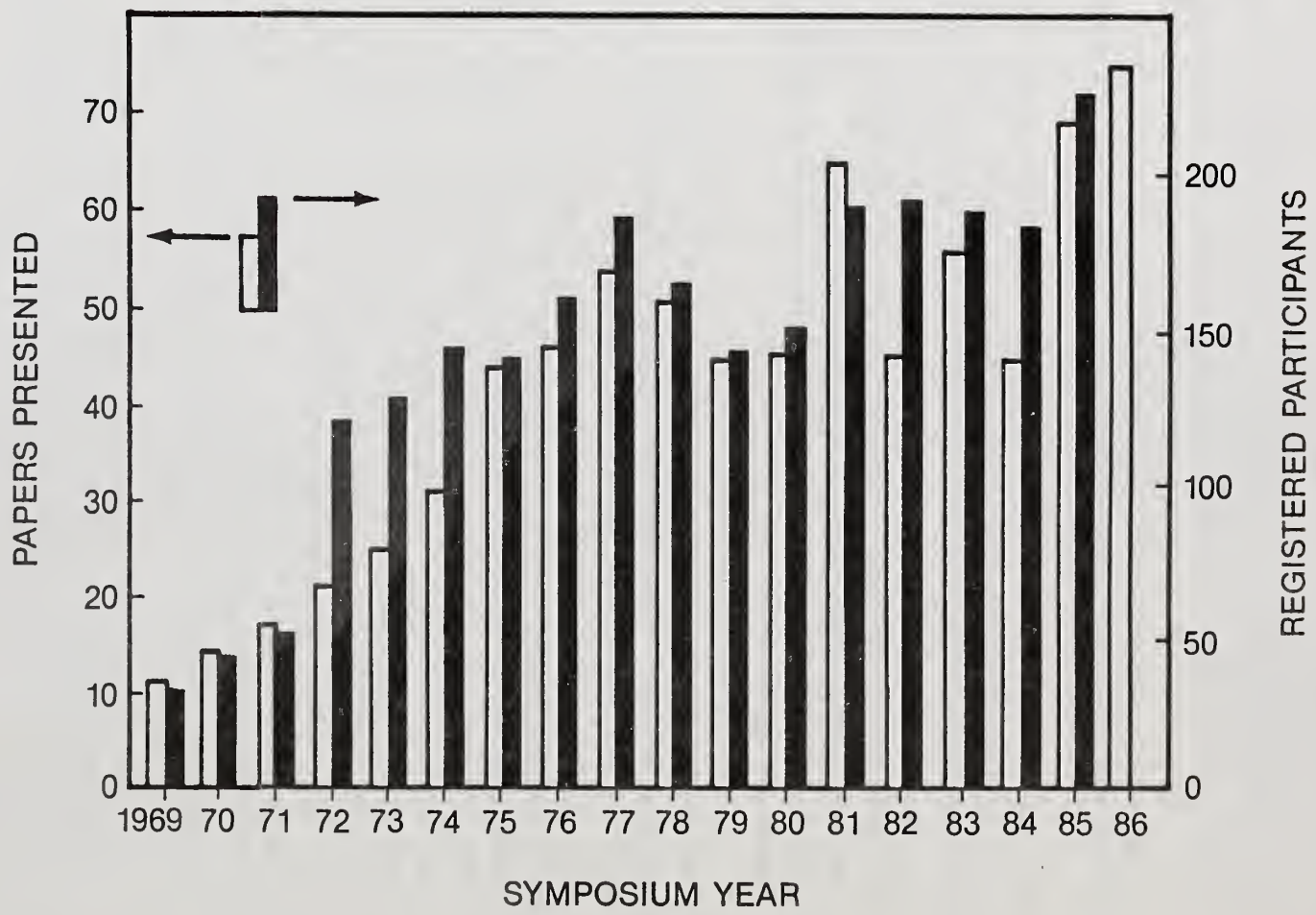
PAPERS PRESENTED
REGISTERED PARTICIPANTS
SYMPOSIUM YEAR
0
10
20
30
40
50
60
70
0
50
100
150
200
1969 70 71 72 73 74 75 76 77 78 79 80 81 82 83 84 85 86

Laser-Induced Damage in Optical Materials

Eighteenth ASTM Symposium

November 3-5, 1986

The Eighteenth Annual Symposium on Optical Materials for High Power Lasers (Boulder Damage Symposium) was held at the National Bureau of Standards in Boulder, Colorado, November 3-5, 1986. The Symposium was held under the auspices of ASTM Committee F-1, Subcommittee on Laser Standards, with the joint sponsorship of NBS, the Defense Advanced Research Project Agency, the Department of Energy, the Office of Naval Research, and the Air Force Office of Scientific Research. Approximately 200 scientists attended the Symposium, including representatives from the United Kingdom, Japan, France, and the Federal Republic of Germany. The Symposium was divided into sessions concerning Materials and Measurements, Mirrors and Surfaces, Thin Films, and Fundamental Mechanisms. As in previous years, the emphasis of the papers presented at the Symposium was directed toward new frontiers and new developments. Particular emphasis was given to materials for high power apparatus. The wavelength range of the prime interest was from 10.6 μm to the uv region. Highlights included surface characterization, thin film-substrate boundaries, and advances in fundamental laser-matter threshold interactions and mechanisms. Harold E. Bennett of the Naval Weapons Center, Arthur H. Guenther of the Air Force Weapons Laboratory, David Milam of the Lawrence Livermore National Laboratory, and Brian E. Newnam of the Los Alamos National Laboratory were co-chairmen of the Symposium. The Nineteenth Annual Symposium is scheduled for October 26-28, 1987 at the National Bureau of Standards, Boulder, Colorado.

Key words: laser damage; laser interaction; optical components; optical fabrication; optical materials and properties; thin film coatings.

1. Introduction

The Eighteenth Annual Symposium on Optical Materials for High Power Lasers (Boulder Damage Symposium) was held as in previous years at the National Bureau of Standards in Boulder, Colorado, November 3-5, 1986. The Symposium was held under the auspices of the ASTM Committee F-1, Subcommittee on Laser Standards, with the joint sponsorship of NBS, the Defense Advanced Research Projects Agency, the Department of Energy, the Office of Naval Research, and the Air Force Office of Scientific Research. Approximately 200 scientists attended the Symposium, including representatives from the United States, United Kingdom, Japan, France, and the Federal Republic of Germany. The Symposium was divided into sessions concerning Materials and Measurements, Mirrors and Surfaces, Thin Films, and finally, Fundamental Mechanisms. Of the 74 papers presented, this Proceedings contains 67 manuscripts plus abstracts only for the remaining 7 papers. We sincerely hope in future years to return to our tradition of publishing all papers which are presented at the Symposium. Harold E. Bennett of the Naval Weapons Center, Arthur H. Guenther of the Air Force Weapons Laboratory, David Milam of the Lawrence Livermore National Laboratory, and Brian E. Newnam of the Los Alamos National Laboratory were co-chairmen of the Symposium. Alexander J. Glass of KMS Fusion is Conference Treasurer and Aaron A. Sanders of the National Bureau of Standards acts as Conference Coordinator.

The purpose of these symposia is to exchange information about optical materials for high power lasers. The authors welcome comments and criticism from all interested readers relevant to this purpose and particularly relative to our plans for the Nineteenth Annual Symposium, scheduled for October 26-28, 1987, at the National Bureau of Standards, Boulder, Colorado.

2. Overview and Recommendations

Our objective in this section is to afford the reader a sense of the emphasis and general concerns of this year's symposium and recommendations of areas where additional work is clearly needed. There is much excellent work which cannot be mentioned because of space limitations, only a few of the highlights are presented herein.

Materials and Measurements

As in recent years a variety of sophisticated laser damage facilities and techniques were described. There was a continued emphasis on damage processes in the ultraviolet region of the spectrum. A change in the mechanism for laser damage and other effects occur in the ultraviolet as compared to the infrared region. Interactions are driven almost entirely by electronic excitations, which may be extremely complicated. For example, one paper reported that the damage threshold of CaF_2 decreased by over an order of magnitude when a few ppm of the rare earth impurity cerium was present. However, when in addition to the Ce, the crystal also contained 3 ppm of Ba, Pr, and nd, 10 ppm of La and 30 ppm of Y plus small amounts of various other impurities, the damage threshold became so high that it could not be measured with their equipment. The impurity level in this case was about $10^{18}/cm^3$ and the crystal was colored. They speculate that the avalanche ionization and catastrophic damage, thought to result from F-center formation when a small amount of impurity is present, is inhibited by the large number of traps present in a heavily doped sample. There is a question, however, of how important F-center formation is under any circumstances in laser damage.

A paper was presented specifically, concentrating on optical generation of defect centers in quartz during multiple pulse irradiation and its effect on laser damage. The authors measured the multiple pulse damage properties at wavelengths of 532 nm and 1064 nm of "wet" and "dry" fused silica, which they found to be nearly identical, in spite of the difference in defect generation between high-OH and low-OH concentration fused silica. In addition they irradiated BK-7 glass with x-rays and found that the damage threshold of the heavily irradiated glass differed only slightly from that found before irradiation. They concluded that the generation of color centers is not the primary mechanism for multiple pulse damage in these materials. Much more work clearly needs to be done to understand the solid state physics underlying this phenomenon. Another paper suggested that we may be dealing with a more macroscopic-microscopic phenomenon, such as submicroscopic inclusions or dislocation bundles. The density of

initiation sites implied by the frequency of occurrence and average spacing of damage bubbles at 532 nm were found to be comparable to the density of defects revealed by scattered light analysis should help to sort this question out. The details of the dopant is one we would expect to be important. However, the authors found no correlation with aluminum concentration in fused silica. Aluminum impurities are fairly common, and when nearby alkali ion sites acting as charge compensators are replaced by holes they become F-center sites. In another paper giving preliminary results on damage to titanium doped sapphire in the visible region at 532 nm, the observed threshold varied from 3 to 14 J/cm^2 but again depended only weakly on the dopant type. The highest observed threshold, 14 J/cm^2, was for the most heavily doped sample, the next, 13 J/cm^2, for the cleanest sample, and the worst as a function of dopant, 10 J/cm^2, for an intermediate doping. A strong dependence (factor of 4) was found on sample orientation but no clear relation to crystalline axis was found for these short pulse irradiations. A weaker dependence was found on surface finish, with the best finishes giving the highest damage threshold.

The condition of the surface becomes much more important in the ultraviolet than at longer wavelengths. A study on the effect of cleaning on the optical absorption of calcium fluoride and fused silica at 351 nm concluded that absorption in polished calcium fluoride could vary from over 500 ppm when a "conventional" cleaning method was used (cotton ball scrub in trichloroethylene, then acetone, then methanol followed by rinse in deionized water or isopropyl alcohol and drying in a vapor degreasing system) to 150 to 200 ppm when the same parts were soaked in 49% hydrofluoric acid followed by isopropyl alcohol and the degreaser. The HF rinse was not effective for SiO_2; there the best results were obtained by a hot (110°C) immersion in a sulfuric acid-ammonium persulfate bath. The absorption as measured calorimetrically at 351 nm was reduced by this treatment to about 100 ppm. Optimum cleaning details may vary; the point to be made is that much more care will have to be taken with both initial surface cleanliness and subsequent contamination when working in the ultraviolet than is necessary at longer wavelengths.

New techniques were suggested at this conference to study laser damage in the ultraviolet region. Second harmonic generation and sum frequency generation were two, provided the fluorescence problem can be overcome. UV photon-induced desorption was a third. Laser Induced Mass Analysis (LIMA) using 266 nm wavelength was described in one paper, giving us another mnemonic to remember when evaluating the extent of coating disruption near laser damage sites. Two other papers suggested a similar approach and two others described the mapping of coating defects using laser illumination and video microscopy. The latter technique was suggested as a possible way of scanning a part to identify potential damage sites before the damage occurs, although more work needs to be done to demonstrate the usefulness of this approach.

Bulk calcium fluoride was studied extensively, perhaps because of its possible use as a window material with KrF and other far ultraviolet lasers. A new silicophosphate glass having a thermal shock resistance 2.7 times higher than LHG-8 was reported and

the mechanism for photodegradation of bisphenol-A polycarbonate under ultraviolet irradiation was discussed. Quantum yields of laser irradiated and broadband irradiated samples were similar, leading to the conclusion that nonlinear photochemistry was not a factor. Damage in cross-linked epoxies was also studied and the threshold for 0.5 ms pulse length was shown to increase from 20 J/cm^2 in the ultraviolet to 40 J/cm^2 at a wavelength of 1 μm. The need to understand the behavior of polymers exposed to ultraviolet radiation was illustrated by a report on the use of polymers as a low cost cladding for amplifier discs in the Livermore NOVA laser.

Surfaces and Mirrors

The surface roughness of components used in the ultraviolet region is much more demanding than that at longer wavelengths (a factor of 4, for example, when going from a wavelength of 0.25 μm to one of 1 μm). An important advance in the state of the art bearing on this problem was reported at the conference. A non-contact polishing technique was reported to have produced surface roughnesses on sapphire of well under 1 Å rms. Scatter from such a surface in the ultraviolet will be over 100 times less than that of a very good conventional (10 Å rms) surface, and it is also possible, as suggested by the results on sapphire described above and those reported in previous conferences, that the laser damage threshold will be increased. More work is needed to establish this possibility.

A technique for producing superpolished single crystal molybdenum mirrors with surface roughness less than 5 Å rms was also reported. A key to this advance was the development of large single crystal blanks using a secondary recrystallization method. Final polishing was done using 0.1 μm Al_2O_3 powder in water.

Laser polishing of fused silica substrates was also investigated. To avoid the ridging effects commonly found when a laser beam is swept across the surface the entire surface of the mirror was floodloaded. Power densities ranged from 150 to 350 W/cm^2. Light scattering tests revealed that the surface roughness of the fused silica was reduced by this treatment. As expected the internal stress was increased and changes in microstructure were observed. Under some conditions the laser damage threshold appeared to increase, but more work will be required to optimize the processing parameters.

Diamond turning has been suggested to be the optimum method for producing optical surfaces with low subsurface damage. One would expect such surfaces to have very high damage thresholds, and indeed such expectations are often borne out by experiment. However, a study of the surface and subsurface damage in germanium produced by diamond turning demonstrates that the subsurface damage, which appears to correlate with the damage threshold, can be much more extensive for diamond turned surfaces than for conventionally polished surfaces. Single crystal germanium samples machined under

optimum conditions in the investigator's laboratory have demonstrated thresholds at 10.6 μm wavelength as high as 55 J/cm^2. Optically polished surfaces have thresholds of about 25 J/cm^2 and surface damage as detected using cross-sectional transmission electron microscopy extends about 60 Å below the surface of the material. Diamond machined single crystal surfaces produced using both stiff and less stiff machines have subsurface damage which can extend much deeper into the surface than is true for typical conventionally polished samples and produce damage thresholds as low as 8 J/cm^2. The damage threshold appears to correlate with crystallite pull-out associated with excessive cutting rates and with the depth and severity of subsurface damage. The damage threshold does not appear to correlate with ridging produced by the diamond tool on the sample surface.

Our understanding of the damage threshold of ideal metallic surfaces has reached a level where the experimentally observed values can be correlated remarkably well with theoretical predictions. This year's symposium enjoyed an excellent report on this subject for copper and aluminum. The single crystal copper samples were chemically polished; those of aluminum were electropolished to minimize surface damage. The resulting surfaces were checked using an x-ray diffractometer and by observing the electron channelling patterns (Kikiuchi lines) to ensure that the surface was undamaged. A Q-switched Nd:YAG laser was used for the damage measurements. Damage morphologies observed were, in order of increasing energy, (1) slip line formation, (2) ripple pattern formation, (3) flat melting and (4) boiling. Each was in excellent agreement with theoretical calculations involving the metallurgical properties of the material except the formation of slip lines, whose measured threshold was too high. The investigators believe that the cause of this discrepancy is the difficulty in observing very small slip lines experimentally. The thresholds for different crystal faces were determined and found to be slightly different and in agreement with theory. Finally, multipulse damage was considered and related to fatigue damage in metals. From the theoretical results it is possible to predict the storage cycle of thermal stress-strain energy induced by a laser beam reflected from the metal surface.

Thin Films

Properties of materials continue to be of great interest, and a fundamental contribution on the thermal properties of optical materials and how they may differ in thin film form from those in bulk material was reported. Preliminary results by another investigator for measuring thermal transport properties of thin films using thermal diffusion wave interferometry were reported. The low damage threshold of antireflection coatings in transmissive optics such as those in the NOVA laser is of continuing concern. An analysis of the damage threshold of 5 layer SiO_2/ZrO_2 anti-reflection coatings deposited on very smooth (5-9 Å rms) and rather rough (30-35 Å) BK-7 substrates by a Japanese group resulted in some very interesting results. They found that the damage morphology of the coating when irradiated by a Q-switched 1.06 μm Nd:YAG laser having a 1.5 ns pulse width consisted of wide shallow damage areas

probably only as thick as the top coating layer and narrow deep damage areas extending down to the substrate. The damage threshold of the deep areas is about 4 to 9 J/cm^2 according to their results and about 20 J/cm^2 for the shallow areas. The density of the deep damage sites is related to the laser intensity and to the roughness of the underlying substrate. The number of samples is very limited but the smoother samples have a higher damage threshold, which they attribute to higher damage resistance areas at the glass/coating interface for the smoother substrate. They were not able to identify the origin of the increased absorption sites but inferred them from their data. The possible existence of nodules in their coatings was not discussed, but the formation of coating nodules on substrate defect sites and their relation to laser damage threshold has been discussed in previous symposia and may help to explain their results. In any event their results reemphasize the importance of smooth substrates for high power ultraviolet applications.

Several papers reported that the columnar structure found in many thin films could be modified by additives. ZrO_2, for example, was reported to grow with columnar diameter proportional to the square root of film thickness. When the films become thicker than 250 nm and the column diameters have reached 39 nm there is evidence for a change in phase from cubic to monoclinic. When SiO_2 was added, the column diameters decreased. For concentrations more than 25 mole percent of SiO_2 the films became amorphous and the surfaces became smoother.

A similar result was reported for BaF_2 and PbF_2 films. In this study, which was performed under ultrahigh vacuum conditions in an MBE system, it was found that BaF_2 deposited as a rough layer at substrate temperatures below 350°C. However, smooth films were obtained at substrate temperatures of 40°C when PbF_2 was coevaporated even though the resulting film was 77% BaF_2. A solid solution of BaPbF may have been formed. Another way of controlling columnar growth was to deposit a thin BaF_2 layer between thin ZnS layers. Thicknesses of 75 Å of BaF_2 between 115 Å ZnS layers was tried successfully. Thicknesses were then varied from 2 Å to 240 Å and as many as 240 separate and discrete layers were laid down, giving effective indices between 1.45 to 1.76. Using a similar technique with PbF_2/ZnS films, an index range between 1.7 and 2.4 was achieved. The composite films were completely dense in thicknesses up to 2 μm. Most encouraging was the observation that no interface absorption was detected in these composite films. The total absorption of 120 layer films was comparable to that of a homogeneously alloyed film of the same thickness. Damage thresholds at a wavelength of 10.6 μm were over 40 J/cm^2 in small spot tests and some sites survived fluencies as high as 120 J/cm^2. The damage threshold values were not extrapolated to large sample sizes as suggested by Porteus or Foltyn, however, and should not be depended on as system design parameters without further study. However, the minifilm technique is promising and could become quite important.

Sol-gel films have a high damage threshold and single layer films have been used successfully as antireflective coatings. At wavelengths of 350 nm damage thresholds of 15-20 J/cm^2 were reported in this conference for SiO_2 in colloidal suspensions in ethanol or methanol. However, thicker coatings made by repeated applications had thresholds in the 7-9 J/cm^2 range. The investigators believed that the low thresholds resulted from incomplete evaporation of the carrier so that organic residue remained in the thicker films. By vacuum treatment, application of ozone or oxygen plus ultraviolet light, which produced ozone, they were able to bring the threshold values of the thicker films back to the single film values. In contrast, methyl radicals were intentionally introduced into a SiO_2 sol-gel coating used at 1,054 nm. Their presence reduced pinholes and thereby increased chemical durability and mechanical strength, increased film adhesion, and lowered the index of refraction from the 1.40 found for the untreated SiO_2 film to 1.3756, which better matches the square root criterion for antireflection. The output energy of a glass slab laser was increased by a factor of 1.85 by this coating.

Antireflection coatings can also be used to increase the surface damage threshold of bulk materials. Alexandrite lasers, for example, have a multipulse damage threshold of about 17 J/cm^2 at a pulse length of 200 ns and a repetition rate of 30 Hz. Thresholds of coated rods measured in this study were reported to be as high as 80 J/cm^2, an increase of almost a factor of 5.

The void fraction of films is difficult to measure and in many cases strongly affects the film performance. By measuring the ellipsometric parameters as a function of wavelength and assuming a physically reasonable model in reducing this data one group of investigators showed that the probable void fraction of a film on fused quartz could be determined as a function of depth. They concluded that the bottom 106 nm of the film tested had about 0.6% voids, the center 43 nm was free from voids, and the top 23 nm had an 8% void structure attributable to surface roughness. They call this technique Spectroscopic Ellipsometry or SE. It appears promising but tho credibility of the results would be strengthened by an independent measure of void fraction.

In recent years it has become necessary to introduce a phase retarder stack on top of a high reflectance (HR) multilayer stack designed for use at nonnormal incidence to adjust the relative phases of the s and p components of the reflected light. The best damage resistance of the four retarder designs tested at a wavelength of 1.064 nm by one group this year was 32 J/cm^2 for 45° retarders and 27 J/cm^2 for 90° retarders. In all cases where the initial HR stack had a high damage threshold the retarder layer reduced it. The order of the thresholds fit the internal field calculations on the retarder stack.

The damage threshold for a multilayer coating should depend strongly on the damage thresholds of the individual materials making up the stack. This year a comprehensive analysis of the one-on-one and N-on-one damage thresholds of films made from 27

different materials each deposited using electron beam deposition on three different substrates was reported. All films were 1/2 wavelength in optical thickness to minimize surface field effects and were tested in a 10^{-8} Torr vacuum at a wavelength of 1.06 μm using a Q-switched Nd:YAG laser with a 5 ns (FWHM) pulsewidth and a 500 μm $1/e^2$ diameter on target. Even at these short pulse lengths the damage threshold appears to increase with increasing substrate thermal conductivity. Damage thresholds from 1.4 J/cm^2 to 27.9 J/cm^2 were found. Charge emission was also monitored. No relationship of charge emission to imminent laser damage was found.

Typical high reflectance multilayer stacks for use in the infrared are quarter wave pairs of ThF_2 and either ZnS of ZnSe on Ag. Amorphous Si has a higher index of refraction than either ZnS or ZnSe and is harder and less susceptible to chemical attack. The complex index of refraction of amorphous Si at a wavelength of 10.6 μm was measured to be $(3.13 \pm 0.02) - j(0.011 \pm 0.004)$. The relatively high absorption coefficient, 140 cm^{-1}, should result in a peak reflectance lower than can be achieved using ZnS or ZnSe. However, if Si were used as part of the outer layer the reflectance should be slightly higher than in the conventional coating and the coating's resistance to chemical attack should be increased. Such films were deposited as double layer stacks on silicon and molybdenum substrates. Conventional films, which differed only in having an all ZnS of ZnSe outer layer, were also deposited. Their reflectances were 0.9954 for films containing ZnS and 0.9967 for those containing ZnSe. The damage threshold was tested using a ten sec exposure of a CO_2 laser yielding a spot size of 1.5 mm and a peak power of 80 kW/cm^2. The sample having a mixed Si and Se outer layer damaged at 60 kW/cm^2, all others had a damage threshold in excess of 80 kW/cm^2. All ZnSe coatings failed the humidity test including those containing Si, so the Si did not provide an adequate protection against humidity for ZnSe. All coatings containing ZnS survived the humidity test. The mixed Si:ZnS or ZnSe outer layer coatings appeared to have a slightly higher reflectance, 0.0004 in the case of ZnS and 0.0008 for ZnSe, than the conventional coatings, but the measurement uncertainty was $\pm$ 0.0010. It will take further work to demonstrate that the introduction of amorphous Si into the outer layer of these conventional coatings is of significant benefit to coating performance.

Light scattered from multilayer coatings is of considerable practical interest and the calculation of this scattered light presents a very difficult theoretical problem. At this symposium an analysis of this problem was presented using the vector theory of light scattering from slightly rough surfaces and taking into account how well correlated the irregularities at one film:film interface are with those of preceding or following interfaces. Both the microroughness of the initial substrate surface and the added microstructure of the multilayer films are considered, and either may be dominant. If there is very poor correlation between the irregularities in succeeding interfaces, it may be possible to design a multilayer stack of non-quarterwave layers so that the fraction of the reflected light which is scattered by the multilayer film may be significantly less than that of the uncoated substrate.

The scattered light problem will be greatly reduced by going to grazing incidence. Reflectances are readily calculated at large angles of incidence for either bare or coated surfaces using Fresnel's equations and impedance theory, but it is comforting to verify that the calculated reflectance values at 514.5 nm for a MgF_2 coated silver mirror agree with experiment for angles of incidence from 0° to 89°. Laser damage thresholds have been reported at previous conferences to not improve dramatically at large angles of incidence. In addition to the experimental reflectance values reported, a brief investigation of the options available to the designer of high-angle-of-incidence systems is given. Using a single dielectric film one can increase the reflectance in either s or p polarizations over that obtainable from a bare metal surface. In addition, it is theoretically possible to produce a mirror which has the same reflectance for both s and p polarized light over the entire angular range from 0° to 90°.

Fundamental Mechanisms

Normally we try to handle events in a solid by perturbation theory, which assumes that the equation of state of the solid in the absence of the excitation is not significantly different from that during the excitation. It is not clear that this approximation is valid when an intense laser beam interacts with a solid. For a CO_2 laser the intensity at which the perturbation approach will be invalid is of the order of 10^{10} W/cm^2. By analogy with the relativistic case of electron-poritron creation an attempt is made to develop a non-perturbation analysis using Green's functions. An expression is obtained which when expanded gives as its first term the summation of integrals found in perturbation theory. It is difficult to carry this expansion further, however, and the problem is still unresolved.

The problem of the effect of intense laser radiation on solids can also be approached via multiphoton excitation. If the radiation is sufficiently intense, there is the possibility that a wide bandgap in NaCl using 532 nm light and what the authors believe to be the first reliable measurements of four-photon absorption cross-section in any wide-gap ionic solid are given.

Another approach is to consider single or two photon excitation and attempt to calculate what effect the formation of defect clusters would have on optical absorption leading to avalanche breakdown. That approach has been used for Si and GaAs with the objective of determining if increases in defect density as a result of multipulse laser irradiation can account for the experimentally observed decrease in damage threshold. If damage is assumed to occur when the charge density exceed 10^{20} cm^{-3} by the end of the laser pulse, the results predicted by the model are in agreement with single shot damage experiments on both materials. It could also explain the decrease in damage threshold observed for N-on-one measurements in Si but not in GaAs. A more refined model is needed in this case.

The increase in absorption during the laser pulse is usually inferred in these models from the results. A possible method for measuring it directly was suggested. It involved using the phenomenon of thermal lensing to investigate the temperature changes in the space where the Q-switched laser beam focuses. The idea was modelled analytically but not demonstrated experimentally. It should provide experimentalists with an interesting new tool if it works.

For further information on these or other topics reported at this Symposium the interested reader should consult the individual manuscripts contained in this Proceedings.

3. Acknowledgements

The editors would like to acknowledge the invaluable assistance of Mr. Aaron A. Sanders and the other involved staff members of the National Bureau of Standards in Boulder, Colorado, for their interest, support, and untiring efforts in the professional operation of the symposium. Particular thanks to Ms. Susie Rivera for her lead in the preparation and publication of the proceedings as well as to Ms. Edit Haakinson and to Ms. Pat Whited of the Air Force Weapons Laboratory for conference coordination. This year we were pleased to have the able assistance of Ms. Sharon Chesnut of the Naval Weapons Center as well.

4. References

[1] Glass, A.J.; Guenther, A.H., eds. Damage in Laser Glass, ASTM Spec. Tech. Pub;. 469, ASTM, Philadelphia. PA; 1969.

[2] Glass, A.J.; Guenther, A.H., eds. Damage in Laser Materials, Nat. Bur. Stand. (U.S.) Spec. Publ. 341; 1970.

[3] Bloembergen, N. Fundamentals of Damage in Laser Glass, National Materials Advisory Board Publ. NMAB-271, National Academy of Sciences; 1970.

[4] Glass, A.J.; Guenther, A.H., eds. Damage in Laser Materials: 1971, Nat. Bur. Stand. (U.S.) Spec. Publ. 356; 1971.

[5] Bloembergen, N. High Power Infrared Laser Windows. National Materials Advisory Board Publ. NMAB-356; 1971.

[6] Glass, A.J.; Guenther, A.H., eds. Laser Induced Damage in Optical Materials: 1972, Nat. Bur. Stand. (U.S.) Spec. Publ. 372; 1972.

[7] Glass, A.J.; Guenther, A.H., eds. Laser Induced Damage in Optical Materials: 1973, Nat. Bur. Stand. (U.S.) Spec. Publ. 387; 1973.

[8] Glass, A.J.; Guenther, A. H. Laser Induced Damage in Optical Materials: A Conference Report. Appl. Opt. 13 (1): 74-88; 1974.

[9] Glass, A.J.; Guenther, A.H., eds. Laser Induced Damage in Optical Materials: 1974, Nat. Bur. Stand. (U.S.) Spec. Publ. 414; 1974.

[10] Glass, A.J.; Guenther, A.H. Laser Induced Damage in Optical Materials: 6th ASTM Symposium. Appl. Opt. 14 (3): 698-715; 1975.

[11] Glass, A.J.; Guenther, A.H., eds. Laser Induced Damage in Optical Materials: 1975, Nat. Bur. Stand. (U.S.) Spec. PUbl. 435; 1975.

[12] Glass, A.J.; Guenther, A.H. Laser Induced Damage in Optical Materials: 7th ASTM Symposium. Appl. Opt. 15 (6): 1510-1529; 1976.

[13] Glass, A.J.; Guenther, A.H., eds. Laser Induced Damage in Optical Materials: 1976. Nat. Bur. Stand. (U.S.) Spec. Publ. 462; 1976.

[14] Glass, A.J.; Guenther, A.H. Laser Induced Damage in Optical Materials: 8th ASTM Symposium, Appl. Opt. 16 (5): 1214-1231; 1977.

[15] Glass, A.J.; Guenther, A.H., eds. Laser Induced Damage in Optical materials: 1977, Nat. Bur. Stand. (U.S.) Spec. Publ. 509; 1977.

[16] Glass, A.J.; Guenther, A.H. Laser Induced Damage in Optical Materials: 9th ASTM Symposium, Appl. Opt. 17 (15): 2386-2411; 1978.

[17] Glass, A.J.; Guenther, A.H. Laser Induced Damage in Optical Materials: 1978, Nat. Bur. Stand. (U.S.) Spec. Publ. 541; 1978.

[18] Glass, A.J.; Guenther, A.H., eds. Laser Induced Damage in Optical Materials: 10th ASTM Symposium, Appl. Opt. 18 (13): 2212-2229; 1979.

[19] Bennett, H.E.; Glass, A.J.; Guenther, A.H.; Newnam, B.E. Laser Induced Damage in Optical Materials: 1979, Nat. Bur. Stand. (U.S.) Spec. Publ. 568; 1979.

[20] Bennett, H.E.; Glass, A.J.; Guenther, A.H.; Newnam, B.E. Laser Induced Damage in Optical Materials: 11th ASTM Symposium, Appl. Opt. 19 (14): 23375-2397; 1980.

[21] Bennett, H. E.; Glass. A.J.; Guenther, A. H.; Newnam, B.E. Laser Induced Damage in Optical Materials: 1980, Nat. Bur. Stand. (U.S.) Spec. Publ. 620; 1981.

[22] Bennett, H.E.; Glass, A.J.; Guenther, A.H.; Newnam, B.E. Laser Induced Damage in Optical Materials: 12th ASTM Symposium, Appl. Opt. 20 (17): 3003-3019; 1981.

[23] Bennett, H.E.; Guenther, A.H.; Milam, D.; Newnam, B.E. Laser Induced Damage in Optical Materials: 1981, Nat. Bur. Stand. (U.S.) Spec. Publ. 638; 1983.

[24] Bennett, H.E.; Guenther, A.H.; Milam, D.; Newnam, B.E. Laser Induced Damage in Optical Materials: 13th ASTM Symposium, Appl. Opt. 22 (20): 3276-3296; 1983.

[25] Bennett, H.E.; Guenther, A.H.; Milam, D.; Newnam, B.E. Laser Induced Damage in Optical Materials: 1982, Nat. Bur. Stand. (U.S.) Spec. Publ. 669; 1984.

[26] Bennett, H.E.; Guenther, A.H.; Milam, D.; Newnam, B.E. Laser Induced Damage in Optical Materials: 14th ASTM Symposium, Appl. Opt. 23 (21): 3782-3795; 1984.

[27] Bennett, H.E.; Guenther, A.H.; Milam, D.; Newnam, B.E. Laser Induced Damage in Optical Materials: 1983, Nat. Bur. Stand. (U.S.) Spec. Publ. 688; 1985.

[28] Bennett, H.E.; Guenther, A.H.; Milam, D.; Newnam, B.E. Laser Induced Damage in Optical Materials: 15th ASTM Symposium, Appl. Opt. 25 (2): 258-275; 1986.

[29] Bennett, H.E.; Guenther, A.H.; Milam, D.; Newnam, B.E. Laser Induced Damage in Optical Materials: 1984, Nat. Bur. Stand. (U.S.) Spec. Publ. 727; 1986.

[30] Bennett, H.E.; Guenther, A.H.; Milam, D.; Newnam, B.E. Laser Induced Damage in Optical Materials: 16th ASTM Symposium, Appl. Opt. 26 (5): 813-827; 1987.

[31] Bennett, H.E.; Guenther, A.H.; Milam, D.; Newnam, B.E. Laser Induced Damage in Optical Materials: 1985, Nat. Bur. Stand. (U.S.) Spec. Publ. 746; 1987.

Development of silicophosphate glass HAP-3

Manuscript Received
11-13-86

T. Izumitani, M. Matsukawa, C. Hata, K. Tanaka, and H. Toratani

HOYA CORPORATION
Tokyo, Japan

Silicophosphate glass HAP with high thermal shock resistance was developed. As the thermal conductivity of glass can not be increased, thermal expansion coefficient was tried to make smaller and mechanical strength to make higher. P_2O_5-SiO_2-Li_2O system was investigated. In P_2O_5-SiO_2-Li_2O system, thermal expansion coefficient decreases and mechanical strength increases with SiO_2 content, but chemical durability becomes worse. The weak chemical durability was improved by introducing Al_2O_3 in the system. HAP-3 selected from P_2O_5-SiO_2-Li_2O has higher thermal shock resistance, as 2.7 times as LHG-8, as 1.6 times high as LHG-5, low content of water and low concentration quenching.

Key words: HAP-3; nigh power; silicophosphate glass; concentration quenching; chemical durability; thermal shock resistance; fracture toughness; high repetition rate.

1. Introduction

Output energy of slab laser for high power or high repetition rate is limited by the thermal shock resistance of laser glass. Thermal shock resistance is given by the following equation:

$$R = \frac{S(1-\mu)\kappa}{\alpha E}$$

where S is mechanical strength, μ is Poisson ratio, κ is thermal conductivity, α is thermal expansion coefficient and E is Young's modulus.

In order to get high thermal shock resistance, the thermal expansion coefficient should be small and the mechanical strength should be high, because the thermal conductivity of glass is so low.

Lasing properties of phosphate laser glass are excellent but the thermal expansion is high and chemical durability is not so good. Therefore, silica was introduced into phsophate glass because silica used to give lower expansion coefficient and high chemical durability.

2. Experimental and Results

2.1 Abnormal behaviour of silicophosphate glass

Fig.1 shows the glass formation range of P_2O_5-SiO_2-Li_2O system. The chemical durability was expected to decrease with increasing SiO_2 content. On the contrary the chemical durability decreased with increasing SiO_2 content as shown in Fig. 2(A). As shown in Fig.3(B), the evaporation tendency of P_2O_5 in P_2O_5-SiO_2-Li_2O glass increased with higher SiO_2 content in spite that evaporation tendency of SiO_2 is quite small. The water content dissolved in glass increased with SiO_2 content. As shown in Fig. 3(A), the transmittance at 2.7μ decreases with higher SiO_2 content.

These phenomena were unexpected, because SiO_2 used to give higher chemical durability, lower evaporation tendency and lower dissolved water content than phosphate glasses.

2.2 Inprovement of chemical durability of P_2O_5-SiO_2-Li_2O glasses by introducing Al_2O_3.

As shown in Fig. 2(B), and 2(C), the chemical durability was improved very much by introducing Al_2O_3 into P_2O_5-SiO_2-Li_2O glasses. The evaporation tendency was also suppressed by introducing Al_2O_3 into P_2O_5-SiO_2-Li_2O system(Fig. 4). High water content in silicophosphate glass was reduced by dehydration procedure using drying gas[1,2](Fig. 5)

2.3 The thermal, mechenical properties of P_2O_5-SiO_2-Li_2O glasses

Fig. 6 shows the thermal expansion coefficient of P_2O_5-SiO_2-Li_2O glasses. Thermal expansion

---

Work supported partially by the Lawrence Livermore National Laboratory under Purchase Order Number 489105.

coefficient decreases with SiO_2 content as we expected.

As mechanical strength can only be measured with considerable scatter of the data, fracrure toughness, K_{IC} was measured instead. K_{IC} was measured by giving a flaw with a Vicher's indenter to the glass and then loading in a three points loading apparatus.

$$K_{IC} = \frac{\sigma (\pi a)^{1/2}}{\Phi}$$

where σ is the maximum stress for fracture, 2a is the flaw size generated by the Vicker's indenter and Φ is a factor relating to flaw shape.

Fig. 7 shows the toughness K_{IC} of P_2O_5-SiO_2-Li_2O glasses. Fig. 8 shows the thermal shock resistance for P_2O_5-SiO_2-Li_2O system.

Thermal shock resistance (R) and toughness (K_{IC}) increases with SiO_2 content.

2.4 Lasing properties of P_2O_5-SiO_2-Li_2O-Al_2O_3-Nd_2O_3 glasses

Fig. 9 shows stimulated emission cross section σ of P_2O_5-SiO_2-Li_2O glasses doped 3 wt % Nd_2O_3, with Al_2O_3 content of 0, 5 and 10 mol %. σ increases with P_2O_5 content.

Fig. 10 shows fluorescent life time of P_2O_5-SiO_2-Li_2O glasses doped 3 wt % Nd_2O_3, with Al_2O_3 content of 0, 5 and 10 mol %. τ decreases with P_2O_5 content.

Fig.11 shows concentration quenching in P_2O_5-SiO_2-Li_2O glasses. Concentration quenching tendency increases with SiO_2 content. (Glass No.8 and 3)

2.5 Properties of HAP-3

Z-35 in the P_2O_5-SiO_2-Li_2O-Al_2O_3-Nd_2O_3 system was choosed as HAP-3, as shown in Fig.12. Table 1 shows the properties of HAP-3 comparing to LHG-5 and LHG-8 phosphate glasses.

Fig. 13 shows the concentration quenching tendency of LSG-91H(silicate), LHG-5, LHG-8 (phosphate) and HAP-3(silicophosphate) glasses. HAP-3 shows lower concentration tendency.

2.6 Structure of silicophosphate glasses

It is interesting why introducing of SiO_2 into phosphate glasses causes the poor chemical durability, high evaporation tendency and high water content. There are two regions which have different properties and different structures, region A and region B in silicophosphate glasses (Fig. 14). IR spectrum was used to clarify this problem.

Fig. 15 shows the IR spectra of SiO_2 glass and phosphate glass.

Fig. 16 shows the IR spectra of the silicophosphate glasses. No. 8 and No. 11 glasses in low SiO_2 content region A show all the absorption peaks assigned to P-O bond and the network is shown to be consisted of P-O-P bonds. While, modified No. 3 glasses in high SiO_2 content region B shows 772 cm^{-1} peak indicating of the existing SiO_2 bond besides the peaks assigned to P-O bonds.

Therefore the network is considered to be consisted of Si-O-Si and P-O-P bonds.

Fig. 17 shows the IR spectra of low SiO_2 content silicophosphate glass and aluminophosphate glass. Their spectrum are quite similar. As the Al^{3+} is 6-coordinated and modifier ion, the Si^{4+} is also considered to be modifier ion in low silica content silicophosphate glass.

Fig. 18 shows the schematic structure of two types of silicophosphate glasses. A-type glass is low content of silica is considered to be built up of continuous phosphate network. Si ions like Li^+, Nd^{3+} and ions are modifier ions and combines phosphate chains. Each phosphate molecule is hardly eliminated from the network and the glass turns out to be chemically stable.

B-type glass with high content of SiO_2, the phsophate chain is broken in a few unites by Si-O bond, therefore each phosphate molecule is easily extracted with water and easily evaporated.

3. Conclusions

1) There are two regions in silicophosphate glasses. The glasses in low content SiO_2 region are essentialy phosphate glasses and have strong chemical durability, low water content and low evaporation tendency and give good laser glass. While, the glasses in high content SiO_2 region are consisted of O-Si-O and O-P-O networks and show the reverse properties.

2) HAP-3 laser glass with higher thermal shock resistance and low concentration quenching was developed for high power and high repetition rate slab lasers.

REFERENCES

1) T. Izumitani, M. Matsukawa, K. Takeuchi: Japanese Patent Application No. 60-174024
2) T. Izumitani, M. Matsukawa, K. Takeuchi: Japanese Patent Application No. 60-120955

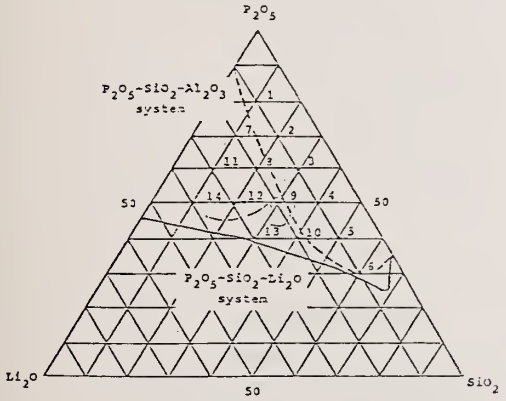

Fig.1 Glass formation range and glass melt number of P_2O_5-SiO_2-Li_2O system.

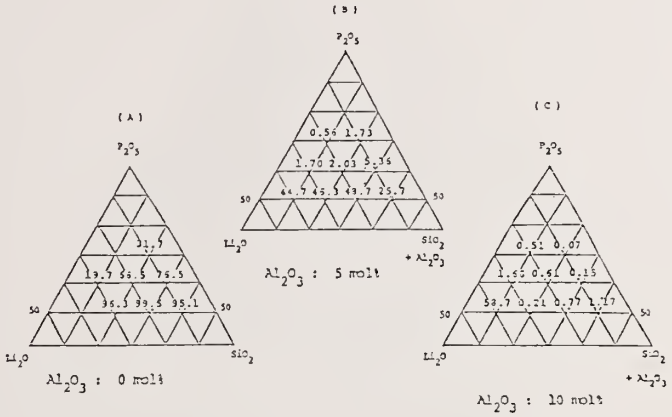

Fig.2 Weight loss percent (Dw) by water attack of P_2O_5-SiO_2-Li_2O system with Al_2O_3 content of 0, 5 and 10 mol%.

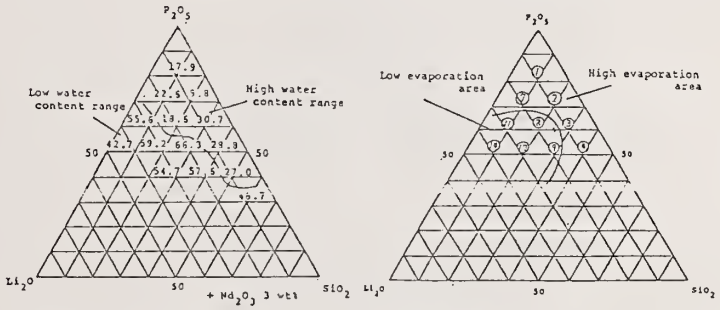

(A) Compositional area of low and high water content (Transmission at 2.7 μm)

(B) Compositional Area of low and high evaporation

Fig.3 Abnormal behaviour of P_2O_5-SiO_2-Li_2O glasses.

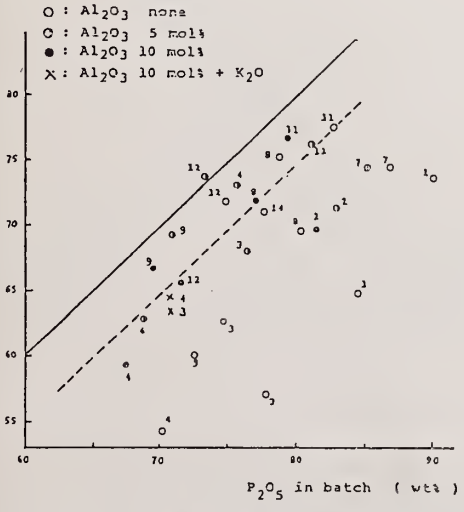

Fig.4 Suppress of evaporation tendency in P_2O_5-SiO_2-Li_2O glasses by adding Al_2O_3.

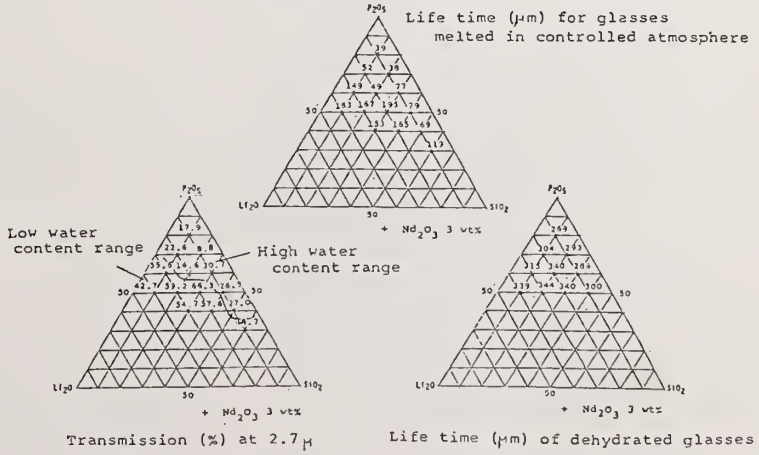

Fig. 5 Decrease of dissolved water content by dehydration

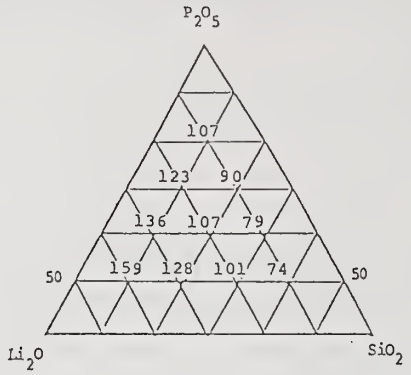

Fig.6 Thermal expansion coeffisient(10^{-7}/°c) of P_2O_5-SiO_2- Li_2O system

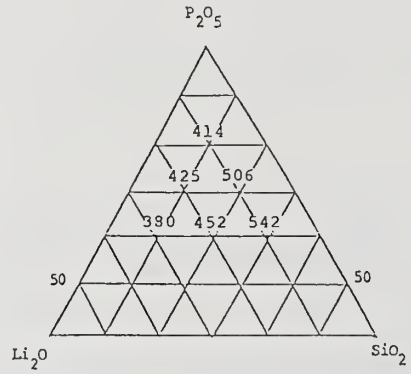

Fig.7 Toughness strength K_{IC}(10^{-3}MN/m$^{3/2}$) of P_2O_5-SiO_2-Li_2O system
(LHG-5 : 400X10^{-3})

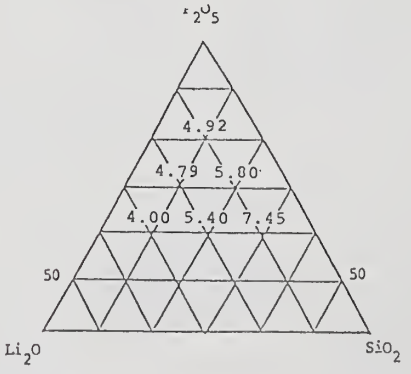

Fig.8 Thermal shock resistance R(10^5m$^{1/2}$deg.) of P_2O_5-SiO_2-Li_2O system
(LHG-5 : 4.57X10^5)

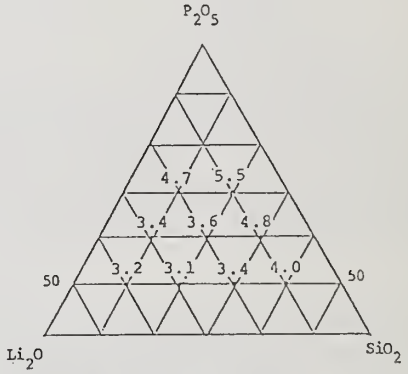

Fig.9 Stimulated emission cross section of P_2O_5-SiO_2-Li_2O system

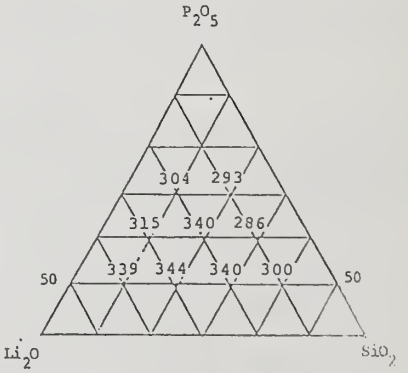

Fig.10 Fluorescent life time of P_2O_5-SiO_2-Li_2O system

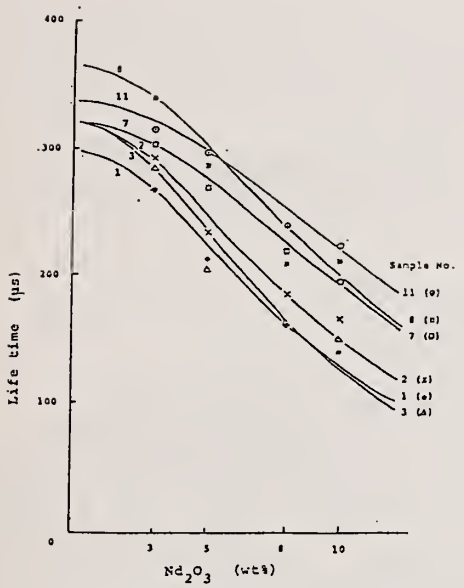

Fig.11 Concentration quenching in P_2O_5-SiO_2-Li_2O glasses.

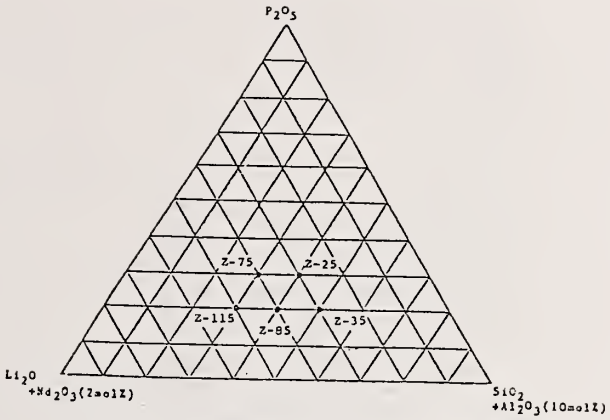

Fig.12 Glass composition of HAP candidate glasses.

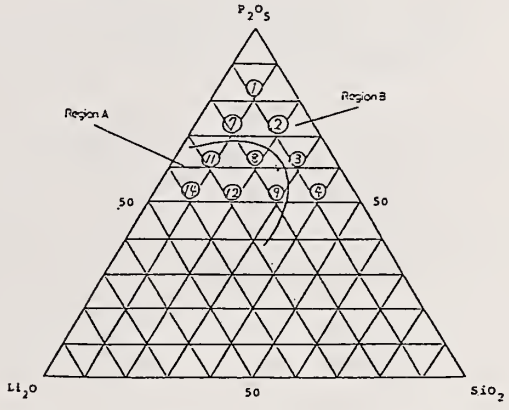

Fig.14 Two regions in silicophosphate glass with different properties and structure

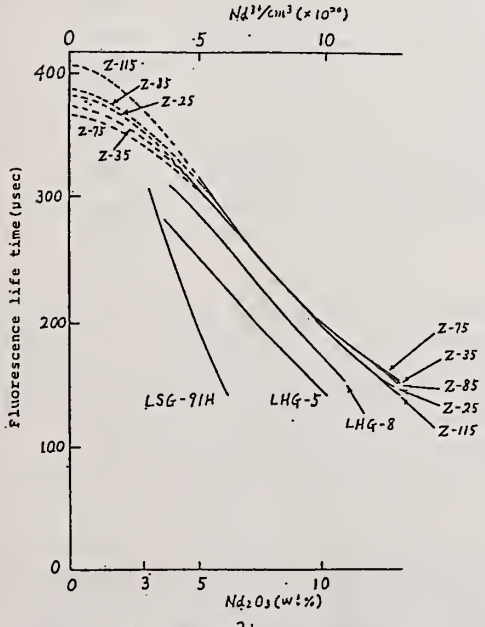

Fig.13 Life time-Nd^{3+} concentration relation(concentration quenching)

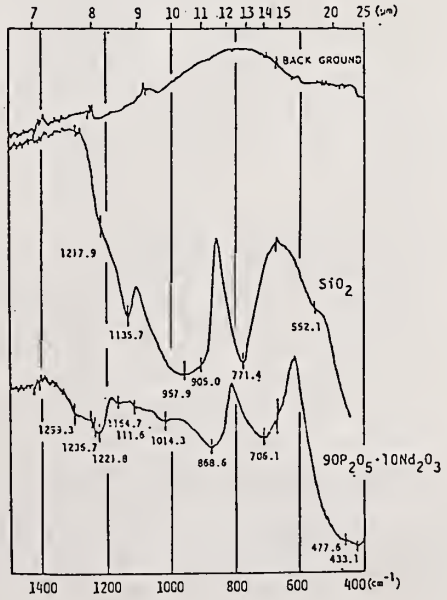

Fig. 15 IR spectra (reflection) of fused SiO_2 and phosphate glasses.

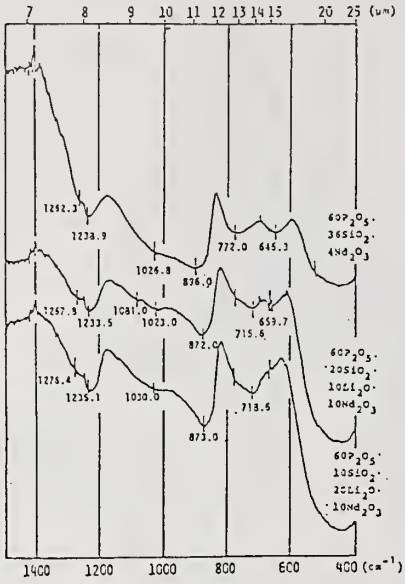

Fig.16 IR spectra of high silicophosphate and low silicophosphate glass.

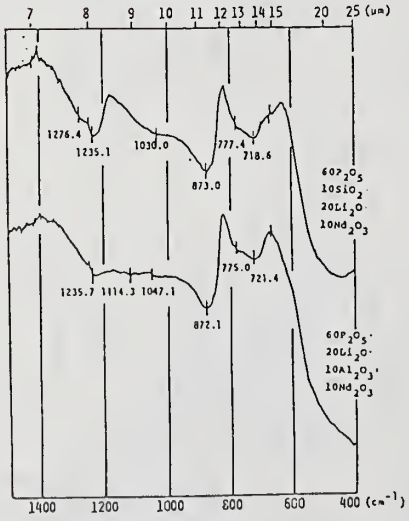

Fig.17 IR spectra of SiO_2 and Al_2O_3 containing phosphate glasses.

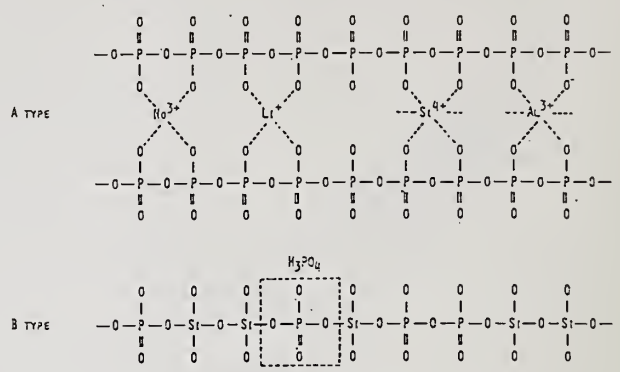

Fig.18 Schematic representation of glass structure in silicophosphate system.

TABLE 1

HIGH AVERAGE POWER LASER GLASS "HAP-3"

		HAP-3	LHG5	LHG8
Fracture Toughness	K_{Ic}	478 x 10^{-3} $MN/m^{1.5}$	390	290
Young's Modulus	E	7.19 x 10^{10} N/m^2	6.83	4.96
Poisson's Ratio	μ	0.225	0.243	0.266
Thermal Exponsion Coefficient	α	83 x 10^{-7} /°C	98	127
Thermal Conductivity	κ	3.25 KJ/m.h.deg	2.64	2.05
Thermal shock Resistance	R'	2.02 $KJ/m^{1/2}h$	1.16	0.69
R'/R'_{LHG8}		2.93	1.68	1
R'/R'_{LHG5}		1.74	1	0.59
Stimulated Emission Cross Section	σ	3.59 x 10^{-20} cm^2	4.1	4.2
Fluoresence Life Time	$\tau_{1/e}$	292 μs (2mol%)	290 (3.3wt%)	315 (3.0wt%)
Chemical Durability	D_w	0.09 wt loss%	0.08	0.13
	D_a	1.60 x 10^{-3} $mg/cm^2.h$	0.83	
	n_d	1.52993	1.54096	1.52962
	ν_d	67.25	63.49	66.49
	n_c	1.52755	1.53834	1.52718
	n_F	1.53543	1.54686	1.53515
	n_g	1.53956		
	n_2	1.1151	1.23	1.13

$R' = \kappa \cdot K_{Ic} \cdot (1-\mu) / E\alpha$

Manuscript Received
10-14-87

Development of Composite Polymer-Glass Edge Claddings for Nova Laser Disks*

J. H. Campbell, G. Edwards, F. A. Frick, D. S. Gemmell, B. M. Gim, K. S. Jancaitis, E. S. Jessop, M. K. Kong, R. E. Lyon, J. E. Murray, H. G. Patton, J. H. Pitts, H. T. Powell, M. O. Riley, E. P. Wallerstein, C. R. Wolfe, B. W. Woods

Lawrence Livermore National Laboratory
University of California
P.O. Box 5508, L-490
Livermore, California 94550

Large Nd:glass laser disks for disk amplifiers require an edge cladding which absorbs at 1 μm. This cladding prevents edge reflections from causing parasitic oscillations that would otherwise deplete the gain. We have developed a composite polymer-glass edge cladding that consists of absorbing glass strips bonded to the edges of laser glass disks using an epoxy adhesive. The edge cladding must survive a fluence of approximately 20 J/cm^2 in a 0.5-ms pulse. Failure can occur either by decomposition of the polymer or by mechanical failure from thermal stresses which leads to bond delamination. An epoxy has been developed that gives the required damage resistance, refractive index match and processing characteristics. A slight tilt of the disk edges greatly reduces the threat from parasitic oscillations and a glass surface treatment is used to promote bond adhesion. Laser disks fabricated with this new cladding show identical gain performance to disks using conventional fused-glass cladding and have been tested for over 2000 shots (equivalent to about a 4-year lifetime on Nova) without degradation.

Key Words: epoxy-glass bonding; laser glass edge cladding; Nova laser; optical epoxy; polymer damage.

1. Introduction

The architecture of most short-pulse, high-peak-power Nd:glass laser systems consists of a master oscillator followed by a series of power amplifiers [1,2]. An example of one such system is the 100 kJ Nova laser at LLNL [3]. In these systems the large power amplifiers contain disks of Nd-doped glass that are optically pumped by a series of Xe flashlamps. If not properly designed, the stored energy density in laser glass disks decreases as the product of the disk size (L) and small-signal-gain coefficient (α) (i.e. $\alpha \bullet L$) increases. This performance reduction is caused by the the complementary effects of amplified spontaneous emission (ASE) and parasitic oscillations that can occur in the Nd:glass disks [4-6].

Edge claddings are used on laser disks to absorb the ASE and suppress the onset of parasitic oscillations that would otherwise reduce the stored energy. In general these claddings consist of a material that is refractive index matched to the laser glass and which contains a dopant that absorbs at the laser (ASE) frequency. A number of different materials have been used for cladding, varying from sprayed-on glass frits [6] to liquids [7] to castings of monolithic glass [8,9]. In the 100-kJ Nova laser system at LLNL, we have used castings of monolithic glass doped with ionic copper that absorbs at 1 μm [8]. Although the performance of this latter cladding is excellent, it is expensive to apply; also, it is known to induce some degree of residual stress near the disk edges that can potentially affect beam quality.

When the Nova laser was commissioned in 1985 we found the phosphate laser glass contained a large number of microscopic Pt inclusions [9]. These inclusions produced fractures within the glass of the power amplifiers when subjected to the high fluence Nova beam. Consequently we are in the process of replacing this glass with a newly developed Pt-inclusion-free glass. As a part of this process we have developed a new cladding design that offers the same excellent performance as the old design but at greatly reduced cost.

*Work performed under the auspices of the U.S. Department of Energy by Lawrence Livermore National Laboratory under Contract No. W-7405-ENG-48.

The new cladding design consists of flat strips of Cu-doped glass that are bonded to the outside of the laser disks using an epoxy structural adhesive (fig. 1). The laser glass disks, rather than being cut in an elliptical shape as in the past, are cut into 6 or 8-sided polygons to provide flat surfaces to which the cladding is bonded. Also, the disk edges are machined with a slight tilt; as will be shown, this strategy greatly reduces the risk of bond failure and significantly reduces the need for an exact refractive index match of various cladding components.

This paper describes the technical requirements and development of this cladding. In the next section we present a brief physical description of ASE and the modes of parasitic oscillation that exist in a flashlamp-pumped laser disk. This is followed by a discussion of the major system requirements and the basis for our decision to use the epoxy-bonded glass cladding design. The remainder of the report summarizes the major technical results from this development effort. In a companion paper [10], we address the mechanism of optical damage in epoxy polymers caused by the radiation environment in the amplifier.

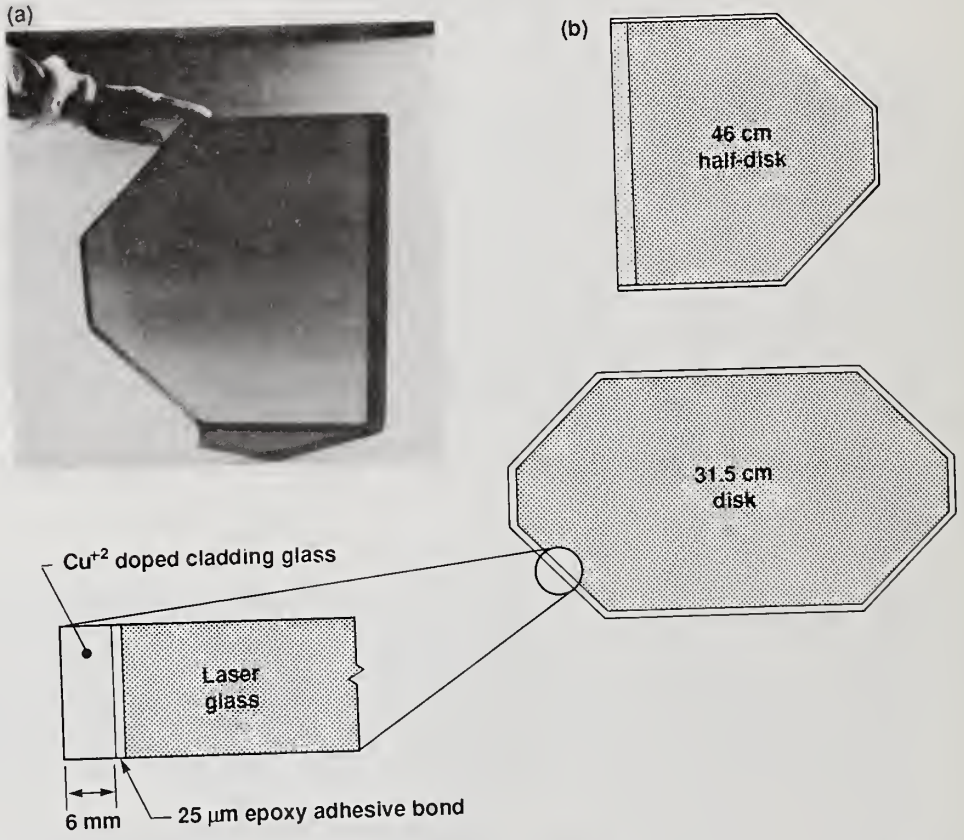

Figure 1. (a) One of the new, polygonally shaped Nova 46-cm half-disks with adhesively bonded edge cladding. (b) The Cu-doped cladding glass is bonded to the disks using a transparent epoxy structural adhesive.

2. ASE and Parasitic Oscillations in Disk Amplifiers

A number of authors [4-6, 11-14] have examined the effects of ASE and parasitic oscillations on energy storage in large aperture amplifiers. Thus, below we give only a brief physical explanation of the process as it relates to our development of the edge cladding.

During optical pumping, some of the excited Nd-atoms spontaneously decay, emitting photons at the frequency of the laser transition. These photons will subsequently be amplified as they travel through the disk. The signal gain (G) is given simply by:

$$G = \frac{I}{I_o} = \exp(\alpha \bullet \ell) \qquad (1)$$

where I_o (watts) is the initial intensity and I (watts) is the intensity after traveling a distance ℓ (cm) through a medium having a positive gain coefficient, α (cm^{-1}).

In a disk amplifier, approximately 75% of the decay photons are emitted at angles greater than the critical angle for total internal reflection (TIR). Thus these photons become "trapped" between the disk faces and travel through the disk by TIR until reaching the edge. Upon reaching the disk edge, the ASE can be totally or partially reflected back into the disk (fig. 2). If the gain in traversing the disk exceeds the edge reflection losses then the process can proceed indefinitely. This effect is referred to as a parasitic oscillation. In other words, parasitic oscillations are suppressed as long as $R \bullet G < 1$, where R is the reflectivity from the edge and G is the gain as described above.

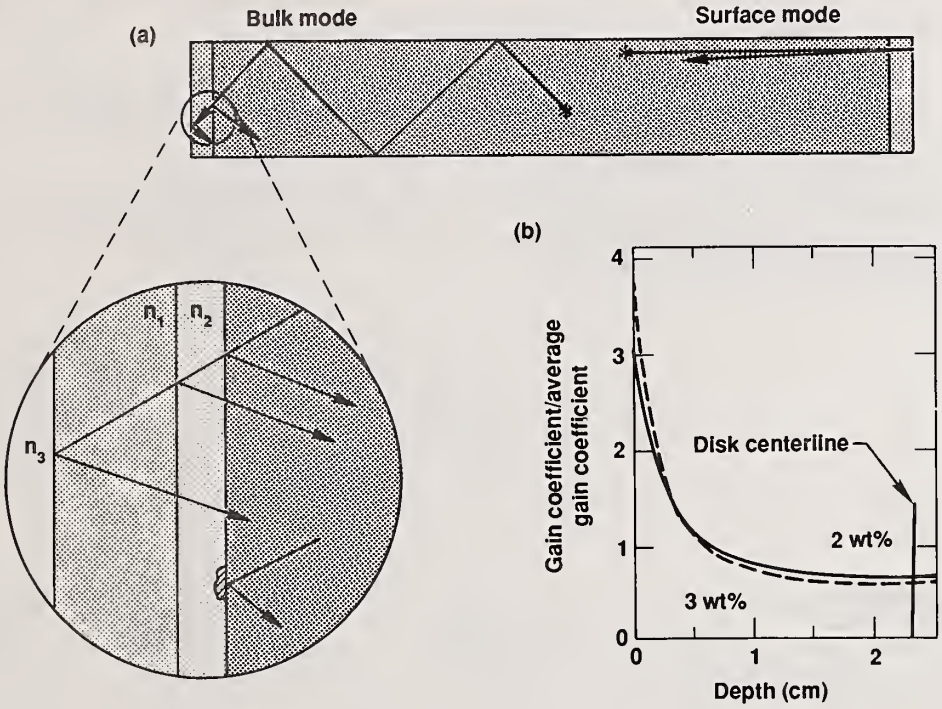

Figure 2. (a) Schematic view of laser disk in cross-section showing amplified spontaneous emission (ASE) and resulting parasitic oscillations due to reflection at the disk boundary. Surface parasitics are difficult to suppress because of the greater gain coefficient near the disk surface as shown (b) in this calculated gain profile for 4.3 cm thick, 2 x 10^{20} cm^{-3} Nd-doped laser disk.

It is important to note that two general modes of parasitic oscillations may occur within a disk [13,1]. One is a bulk-mode parasitic and refers to rays undergoing lossless reflections at the disk faces (fig. 2a). The threshold condition for this mode is:

$$G \bullet R_\theta = \exp(\bar{\alpha} n L) \bullet R_\theta = 1 \qquad (2)$$

where n is the refractive index of the disk at the ASE wavelength, $\bar{\alpha}$ (cm^{-1}) is the thickness-averaged gain coefficient and L is the length of the major axis of the disk (cm). R_θ is the reflectivity at an angle of incidence of $90° - \theta_{TIR}$ which for our case is about 49°.

The second major parasitic mode is the so-called surface mode and refers to rays traveling just beneath and parallel to the disk surface (see figure 2a). These undergo normal reflection at the disk edge (if the edge is perpendicular to the disk face) and have the characteristic threshold condition:

$$R_N G_s = \exp(\alpha_s L) \cdot R_N = 1 \qquad (3)$$

where α_s (cm^{-1}) is the gain just below the disk surface and R_N is the reflectivity normal to the cladding interface.

For large aperture disks with high Nd-doping levels, the gain profile through the disk is not constant (see fig. 2b). The gain is greatest at the disk faces and decreases to a minimum at disk center [15]. For example, for the Nova 31.5 cm aperture disks, the ratio of the surface-to-bulk gain coefficient is about 3 for a 2% Nd doping level [16]. Thus in large disk amplifiers the gains associated with surface parasitics are far greater than for the corresponding bulk modes.

Table 1 summarizes the expected gains for parasitic modes in the largest Nova laser disks. From these, the maximum edge reflectivity that can be tolerated is calculated using the above threshold criteria.

Table 1. Calculated surface and bulk-mode gains and the required edge-cladding index match needed to suppress bulk and surface mode parasitics in Nova 31.5-cm and 46-cm disks. The Nd-dopings are 2 and 3 x 10^{20} ions/cm^3. The cladding interface is assumed to be normal to the disk surface.

	31.5 cm Disk		46 cm disk	
	[Nd-doping(cm^{-3})]		[Nd-doping(cm^{-3}]	
	$2x10^{20}$	$3x10^{20}$	$2x10^{20}$	$3x10^{20}$
I. Disk characteristics				
Refractive index	1.520	1.520	1.520	1.520
Average gain coeff. $\bar{\alpha}$ (cm^{-1})	0.057	0.058	0.053	0.057
Ratio surface-to-avg. gain, $\alpha_s/\bar{\alpha}$	3.0	3.8	3.0	3.8
Longest gain path (cm)	61.5	61.5	47.8	47.8
II. Bulk-mode parasitics				
Bulk gain, exp ($\bar{\alpha}$nD)	205	226	47	63
Required cladding index match	0.049	0.046	0.108	0.091
III. Surface-mode parasitics				
Surface gain, exp (α_sD)	$3.4x10^4$	$9.2x10^5$	$1.9x10^3$	$3.6x10^4$
Required cladding index match	0.0082	0.0016	0.0035	0.0080

The primary sources for reflections are the refractive index mismatch and imperfections at the glass/polymer/cladding boundary (fig. 2a). Assuming for the moment that imperfections can be eliminated with the use of proper assembly methods then the polymer-to-glass index match becomes the limiting element. In table 1 we show the calculated index match needed to keep the reflectivity below threshold for both parasitic modes. In the calculations we assume the "worst-case" of in-phase addition of the two reflections. This is because the adhesive bond is thin ($\leq$ 25 μm) and the ASE has enough coherence that the two reflections from the glass boundaries interfere in-phase. It is clear from Table 1 that the surface parasitic modes place the most severe restriction on the refractive index match of the polymer.

Although we have not discussed the problem of imperfections, it is obvious that even small delaminations at the cladding-to-glass bond can lead to parasitic oscillations. As will be discussed later, we have adopted a strategy of slightly tilting the disk edges to reduce the threat from small bond delaminations near the disk face. This strategy has an added benefit in that it also reduces the index match required for preventing the surface mode parasitic.

3. Technical Requirements of a Polymer-Based Cladding

There are five key performance requirements that a polymer-based cladding must meet. First, the polymer must be able to tolerate the high radiation fluence inside the amplifier without damage. The incident light on the polymer originates from the combined broadband radiation from the Xe-flashlamps and the 1060 nm ASE in the disk (fig. 3). Jancaitis et al [16] have calculated the total fluence incident on the polymer to be about 20 J/cm^2; this consists of approximately 11 and 9 J/cm^2 contributions of flashlamp light and ASE, respectively. The duration of this fluence is about 0.5 ms. Note that the flashlamp emission below 350 nm is strongly absorbed by the Ce-doped glass envelopes of the flashlamps and the silicate glass blast shields. Also, the laser glass attenuates the 14 J/cm^2 of flashlamp light incident on the disk surface to about 11 J/cm^2 at the cladding interface. This is due to the intrinsic absorption of the Nd-ions in the glass.

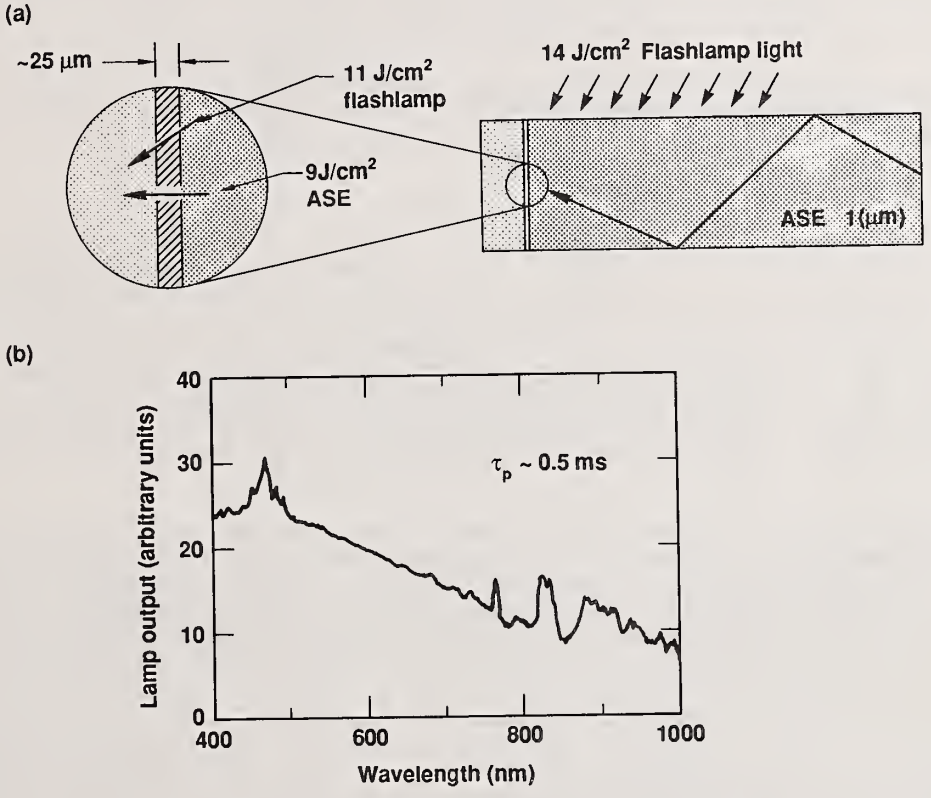

Figure 3. (a) The combined 1.06 μm ASE and broadband flashlamp fluence at the polymer bond is about 20 J/cm^2 with about 9 J/cm^2 originating from ASE [16]. The fluence of the flashlamp light reaching the disk surface is approximately 14 J/cm^2 but this is attenuated by nearly 20% upon passage through the disk. (b) Typical instantaneous spectral distribution of the flashlamp light after passing through the CeO_2-doped flashlamp envelop and blast-shields. Below 400 nm it rapidly drops to zero due to the absorption by the CeO_2 dopant [16].

The second requirement the cladding must meet is to absorb the ASE and suppress the onset of parasitic oscillations. The ASE can be adequately absorbed by choosing a cladding glass with the proper doping level and thickness. We have calculated that for our application the product of the cladding absorption coefficient and thickness should be greater than 1.8. Since we are constrained to a cladding thickness of no more than 0.6 cm then the cladding absorption at 1060 nm needs to be at least 3.0 cm^{-1}. Assuming that a properly doped cladding is used, then the suppression of parasitics depends on the refractive index match at the glass-to-polymer interfaces and the lack of imperfections that may cause Fresnel reflections. This requirement was discussed in the previous section and is summarized in table 1.

The third major performance requirement is a strong adhesive bond. The bond must be strong enough to withstand (a) the mechanical stresses in grinding and final polishing of the disk faces and (b) the repeated thermal stresses due to ASE absorption in the cladding. The bond must be able to repeatedly endure both the peak stresses and high strain rates associated with this interface heating.

The fourth requirement is that the cladding be relatively easy and inexpensive to apply. This is primarily a processing issue rather than a technical constraint. It is of major importance however since the primary reason for developing a new cladding process is to reduce the overall laser disk cost.

Finally, the cladding must be able to withstand, without degradation, a large number of amplifier firings. We have chosen a minimum value of 2000 shots. This is roughly the number of laser shots occurring over a period of about 4 years on the Nova system. Our expectation is that the cladding will withstand many more shots than this minimum requirement.

In the remaining sections of this report we discuss first the selection of cladding configuration and associated polymer followed by results showing that this design meets the above 5 requirements.

4. Choice of a Cladding Configuration

The use of a polymer to bond edge cladding to laser disks was first reported by Murray et al [17,18] in their work on the experimental, single-segment amplifier (SSA). The SSA used rectangular-shaped disks of a non-standard glass; without significant development it was not possible to use the conventional fused-glass cladding process with these disks. Therefore, adhesively bonding the cladding to the disk provided a successful alternative to the conventional cladding method. The polymer used by Murray et al was a silicone rubber index-matched to the laser glass. Although successful in this experimental application, the process was not developed to the point where it could be used in full production. Nevertheless, the relative ease with which disks could be clad by this new process led us to consider it for use with the new Pt-inclusion-free Nova disks.

We examined three variations on the polymer-cladding concept (fig. 4) before finally settling on the thin-bond design. The first idea was to eliminate the cladding glass altogether and use a doped-polymer instead (fig. 4c). The polymer would serve as both the adhesive and the absorber matrix. The absorber could be a dye homogeneously distributed in the polymer matrix or a heterogeneous mixture of absorbing (i.e. opaque) particles suspended in the polymer. Conceptually, this is a simple design using a single component that, in principle, could be easily and cheaply applied. The disadvantage with this design is that the volume of polymer used is large. This increases the chance for failure due to optical damage at a contaminating inclusion site. Also, an absorber or dye must be found that does not bleach or otherwise fail when exposed to the high fluences in the amplifier. Finally, differences in modulus between the glass and polymer would make optical finishing (i.e. grinding and polishing) difficult or even require post-finishing application of the cladding. The latter would be a difficult task.

The other two cladding configurations we considered are variations of the same concept. Both designs use a copper-doped absorber that is bonded to the laser disk using a polymer adhesive. In one case the cladding is embedded in the polymer forming a relatively thick bond-line (fig. 4b). In this design, the polymer serves to bond the cladding to the disk as well as bond the disk assembly into the disk holder. This is similar to the design used by Murray et al for the SSA tests. The final design uses a very thin bond ($< 25\ \mu m$) to adhesively bond the cladding to the laser disk (fig. 4a). This bond is formed by applying adhesive to the adjoining faces of the disk and cladding glass and then lightly pressing them together until the adhesive cures.

The thin bond-line concept is the system of choice for several reasons. First it minimizes the amount of polymer used and therefore lessens the chance for damage due to absorbing contaminates. Second, we found that the the small bond-line eliminates optical damage sites at the polymer surface apparently caused by particulates that accumulate during grinding and polishing of the disks. It is also easier to clean. Third, the overall disk dimensions remain nearly the same and thus can be used in our present amplifier without extensive modification or reduction of clear aperture.

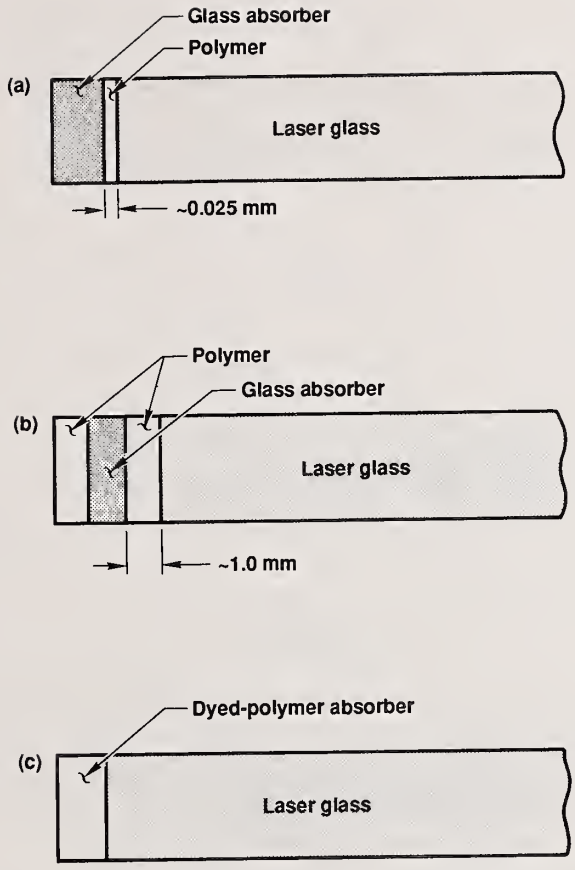

Figure 4. Three configurations of polymer-based edge claddings that were evaluated during development: (a) a glass absorber bonded with a thin line of adhesive, (b) a glass absorber embedded in a cast polymer and (c) a monolithic absorbing polymer. Design (a) is the cladding configuration that has been selected.

5. Adhesive Polymer Selection

The selection of a polymer for our cladding applications was based on both its optical/mechanical properties and its processing characteristics [19]. Optically the polymer had to be clear, colorless, non-scattering and a close index match to the laser and cladding glass (1.520 at 1053 nm). Mechanically the polymer must function as a structural adhesive with excellent mechanical and adhesive strengths and a high Young's modulus. Also, it must remain undamaged after several thousand shots in the high fluence amplifier environment.

From a processing viewpoint the polymer (or the reactants needed to form the polymer) must be readily available, have high purity and be easily filtered. Also during application the polymer must not release any volatile components, have a pot-life sufficient for the assembly time (approximately 1 hr.) and shrink little during cure (less than a few percent).

In our application it is also desirable to have a polymer with a glass transition temperature (T_g) above the maximum use temperature (about 35°C). Therefore, during the selection process we looked for polymers that would gel at room temperature and then fully cure to the desired T_g with only moderate heating.

We evaluated approximately twenty polymers from six major classes of adhesives. Epoxies were finally selected because they best satisfied the criteria outlined above. However, we could not find a commercially available epoxy with the required refractive index and processing characteristics. Consequently we formulated our own epoxies from commercially available resins and curing agents [19].

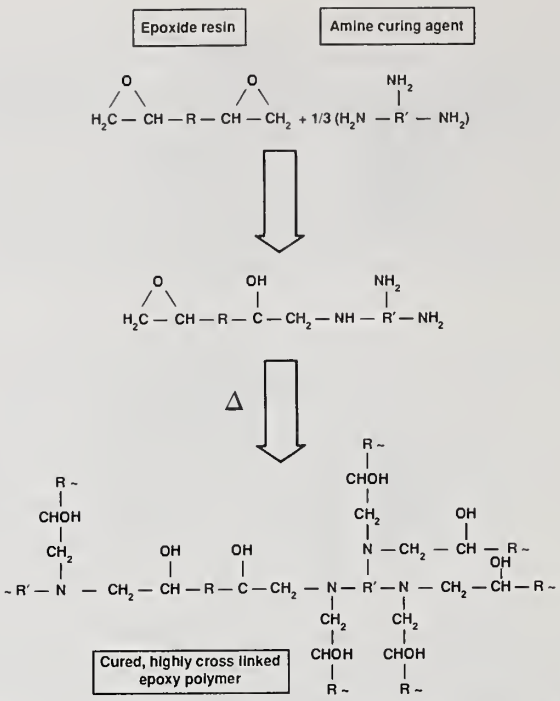

Figure 5. Reaction stoichiometry for amine-cured epoxies. Note that primary amines can undergo two epoxide reactions unless they become sterically hindered. Also in many epoxide systems the product alcohol group will further react with the epoxide particularly at elevated temperatures. This combination of reactions produces a highly cross-linked structure in epoxy polymers.

The final formulation is an amine-cured epoxy having the composition given in table 2; the epoxy curing reaction is shown schematically in figure 5. Note that epoxies are two-part adhesives. One part ("Part A") is a liquid resin that consists of molecular components that each contain two or more of the characteristic three-member cyclic ethers that are called epoxide groups. The second part ("Part B") consists of a material that will react with the epoxide groups ultimately forming a continuous polymer network (figure 5). Over 50 different functional groups are known to react with epoxides [20]. For our application we have chosen a mixture of amine-based compounds (table 2) since they react reasonably quickly near room temperature.

The composition of this adhesive is uniquely suited for our application for several reasons. First the resin is a mixture of an aliphatic (diglycidal ether of 1,4-butanediol) and aromatic (diglycidal ether of bisphenol-A) epoxides. As will be discussed later, by varying the ratio of these components we can adjust the refractive index to the value desired. Second, the amine has been specially formulated to meet our processing requirements. A small amount of a mixture of low-molecular-weight, primary amines is used as an accelerator to gel the epoxy in a few hours at room temperature. This allows sufficient time to complete the assembly operation yet also permits us to remove the disk from the gluing fixture in just a few hours. The remainder of the part B curing agent is a higher molecular weight polyether-triamine that upon full cure gives the desired T_g. To accomplish this, the clad laser disk is heated to a moderate temperature (80°C).

6. Damage Resistance

As discussed above, one of the most important properties of the cladding polymer is its optical damage resistance. In a separate paper [10] we present results from a study of flashlamp-induced optical damage in several amine-cured epoxies; this section summarizes the conclusions from that work.

There are two key mechanisms leading to optical damage in epoxy polymers. The first is pyrolysis caused by localized heating near absorbing inclusions and the second is photolysis by short-wavelength radiation (< 350 nm for epoxies of interest in this application). Both of these damage mechanisms are well known and were reported a number of years ago in a study by Lundberg et al [21] of flashlamp-induced damage in other types of polymers.

Table 2. Composition, Structure and Refractive Index of Epoxide Resins and Amine Curing Agents Used to Prepare the Cladding Adhesives.

Name	Structure	Refractive Index (n_D) Measured	Calculated	Wt.%
Part A: Epoxide Resins				
1. diglycidal ether of bisphenol A	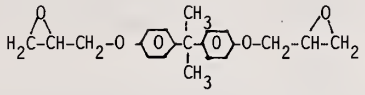	1.5704	1.5709	30.7
2. diglycidal ether of 1,4 butanediol	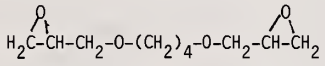	1.4626	1.4674	34.7
Part B: Amine Curing Agents				
1. Mixture of polyether triamines	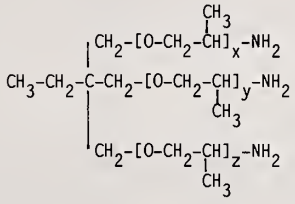 (x + y + z = 5.3)	1.4595	1.4570	31.3
2. Accelerator:				
- triethanolamine	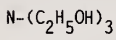			
- piperazine	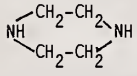	1.4951	1.4914	3.3
- aminoethylpiperazine	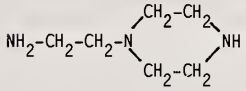			

In the case of pyrolysis, the extent of damage is governed by the thermal decomposition kinetics; thus the time-temperature history the polymer experiences is critical. For example, a polymer can be briefly heated to a temperature far in excess of its typical decomposition temperature without undergoing extensive pyrolysis. This is simply because there is insufficient time for significant polymer reaction. Of course there is some degree of decomposition but this may not be readily detected until the polymer is repeatedly heated under the same conditions.

Polymer pyrolysis products generally absorb strongly in the visible region of the spectrum. This is because they contain conjugated structures having low energy π-π^* or n-π^* transitions. Therefore the decomposition products themselves can cause either further localized heating or photolysis or both. The net result is that the extent of pyrolysis (i.e. damage) may rapidly grow with successive shots. We have seen this effect in several flashlamp-damage tests conducted on optical epoxies. What is initially observed as small black damage spots, widely distributed through the polymer, becomes massive regions of black decomposed polymer after just a few more shots.

The key feature in regard to the above mechanism is that once damage is initiated it will rapidly grow to the point where it causes catastrophic failure. As a consequence, extensive measures must be taken to remove all sources of absorbing inclusions from the polymer starting materials. This observation is not new and has been made by many others studying laser damage in polymers (for example see references 22-25). In fact, preparing clean starting materials has been the focus of much of the effort in making polymers with higher damage thresholds.

To eliminate possible damage due to absorbing inclusions we have used a filtration system capable of removing particles greater than 0.5 μm. Also all polymer preparations, glass surface treatment and cladding operations are carried out in a class-100 cleanroom. We have found that by using this technology we can increase the damage resistance of the amine-cured epoxy to the point where it can be safely used in our application.

The second mechanism for polymer damage is photolysis and is sensitive to the emission wavelength of the radiation. Many organic materials absorb strongly in the blue and near-UV and are particularly sensitive to photolytic damage by radiation in this region [26]. In fact photo-degradation and photo-oxidation is the reason for the poor environmental durability of most polymers.

Wolfe et al [10] have shown that epoxy polymers with the least absorption in the blue and near-UV region of the spectrum suffer the least damage when exposed to the broadband emission from a Xe-flashlamp. Similarly, removing the UV component of the flashlamp emission, while keeping the total fluence fixed, also significantly reduces the amount of damage [10].

The above observations suggest that the damage produced under these particular conditions is caused by a photolytic rather than pyrolytic mechanism. Unfortunately this conclusion is clouded by the fact that the damage initiates in spots rather than uniformly throughout the polymer. This latter observation suggests pyrolysis, due to absorbing inclusions, rather than photolysis. Of course it is probable that the two mechanisms are strongly linked and once decomposition starts they both proceed simultaneously. For example, it is well known that many products from polymer pyrolysis contain chromophoric groups (e.g. carbonyls, alkenes, etc.) that can cause further degradation by photolysis.

7. Suppression of Parasitic Oscillations.

Preventing parasitic oscillations in the laser disk requires (a) a proper refractive index match between the epoxy and the laser and cladding glasses and (b) elimination of any bubbles or other reflecting defects in or at the interface of the cladding. As mentioned above, the polymer refractive index is matched to that of the glass by varying the ratio of aliphatic to aromatic components in the epoxide resin.

7.1 Refractive Index Matching

The refractive index (n) of a dielectric material in the visible and near-visible region is directly related to its electronic polarizability by the well known Lorenz-Lorentz relationship:

$$\left(\frac{n^2 - 1}{n^2 + 2}\right) \frac{M}{\rho} = \frac{4}{3} \pi N \alpha_e \qquad (4)$$

where M is the molecule weight (g/mole), ρ the density (g/cm^3), N Avagadro's number (mole^{-1}) and α_e the electronic component of the polarizability (cm^{-3}). The term on the left hand side is known as the molar refraction, R, and to a good approximation consists additively of the electronic polarizability contributions of individual bonds in the molecule [27]. Therefore, in a polymer it is possible to adjust the refractive index by adding or subtracting functional groups with different polarizabilities; this is the approach we have used to index match the polymer to the glass.

Delocalization of the electrons in conjugated π-bonded systems dramatically increases the polarizability and hence the refractive index. Consequently aromatic compounds have higher indices of refraction than the corresponding aliphatic materials. This is clearly illustrated in figure 6 where the refractive indices are plotted for a series of compounds [28] having varying degrees of π-bond conjugation.

The refractive index region of interest can be bracketed by using diglycidal ether derivatives of bisphenol-A and 1,4-butanediol. The refractive indices of these materials are given in table 2. Also given are the calculated indices based on additivity of functional group contributions to the molar refraction, i.e.:

$$n = \left[\frac{1 + \frac{2\rho R_T}{M}}{1 - \frac{\rho R_T}{M}}\right]^{1/2} \qquad (5)$$

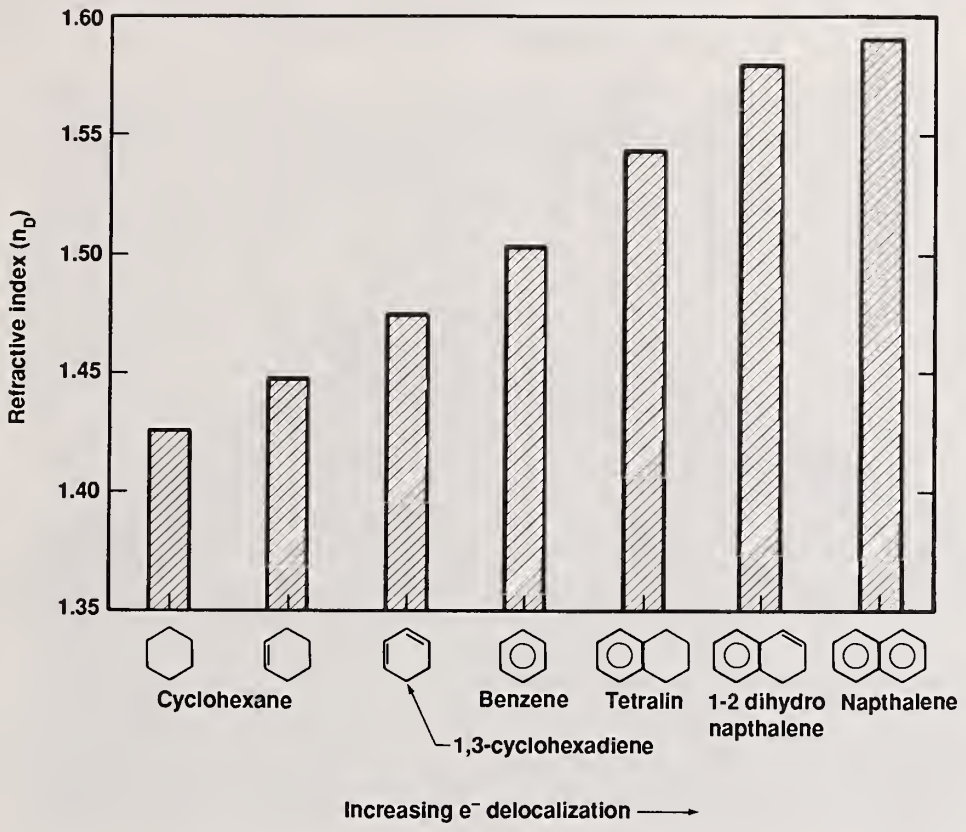

Figure 6. Refractive indices of a series of hydrocarbons with an increasing polarizability caused by electron delocalization in π-bonds.

where R_T is the sum of the molecular refraction contributions from the various functional groups in the polymer structure:

$$R_T = \sum_{i=1}^{n} R_i \qquad (6)$$

The group contributions (R_i) are based on the values compiled by Goedhart [29] as summarized by VanKrevelen [30].

Figure 7 compares the calculated and measured refractive indices for both cured and uncured mixtures of epoxy resin and amine curing agent. The cured polymer has a different index than the unreacted mixture because of both the change in molecular structure and the change in density that occurs during reaction. The change in structure is due to reaction between the amine and epoxide groupings and increases the index by about 0.007. The rest of the increase is due to the 6 to 7% densification that occurs upon complete curing. The generally good agreement between the calculated and measured index values demonstrates the usefulness of the additive relationship. By using the curves in figure 7, it is possible to pinpoint the composition that must be used to index match the glass.

The refractive index calculations are for 589 nm (Na-D) and must be corrected for dispersion since we require an index match at 1060 nm. The Δn change in the epoxy between 589 and 1052 nm is 0.0128 ± 0.0005.

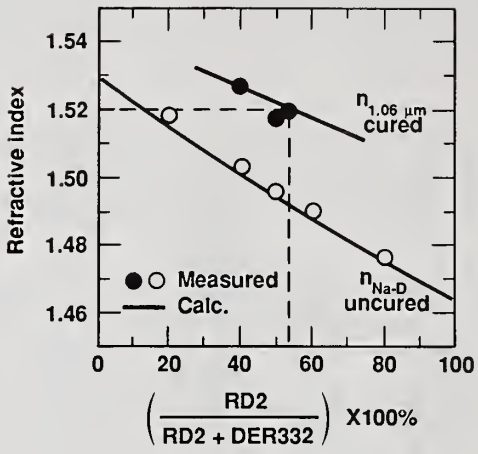

Figure 7. Measured (•) and calculated (-) refractive indices at 589 nm (Na-D) for uncured and at 1052 nm for cured epoxy mixtures. The dotted line is the composition of cured epoxy used to match the 1.520 index of the glass.

7.2 Parasitics Caused by Bond-Delaminations

As mentioned in Section 2, reflections from bubbles or other imperfections at the cladding interface can give rise to parasitic oscillations. The most serious threat is from imperfections that occur near the disk face since the gain for surface parasitics is much greater than for bulk modes.

One recurring problem we have faced is the presence of very small, almost microscopic, delaminations of the adhesive bond at the disk surface. The delaminations are apparently caused by stresses on the bond joint that occur during the final disk grinding and polishing.

In the case of a Nova 31.5-cm disk with parallel ends, Trenholme [31] has estimated that a long, thin delamination only a few microns in width could cause the onset of surface parasitic oscillations. Figure 8 shows the resultant cladding failure at the end of a 31.5-cm disk due to growth of small delaminations into large-scale bond separation. This failure is caused by surface parasitic oscillations initiated by the small (< 100 μm) delaminations at the disk surface. The parasitic oscillation extracts energy from the disk and, rather than distributing it uniformly over the entire area of the cladding, deposits it in a small region near the delamination. This in turn increases the thermal stresses causing the bond separation to grow. After only a few amplifier shots the delamination grows dramatically leading to a large scale bond failure as shown in figure 8.

Jancaitis et al [16] have developed a strategy for dealing with small bond delaminations on the Nova disks by slightly tilting the disk edges. This is shown schematically in figure 9a. The tilts prevent rays traveling near the surface from being Fresnel-reflected back along the same high-gain path. Instead they are reflected back into the lower gain interior of the disk and away from any possible surface separations on the opposing edge. The idea of slightly tilting the disk edges to prevent surface parasitics was also used by the Laboratory for Laser Energetics (University of Rochester) in the design of the active-mirror amplifier [32].

Using a Monte Carlo ray-tracing program, Powell et al [33] have shown that tilt angles of about 1.4° on the disk edges are sufficient to suppress parasitic oscillation from delaminations up to 1-2 mm in width. Based on the Monte Carlo calculations we determined effective tilt geometries for all edges of the 46-cm and 31.5-cm disks as shown in figure 9b; this is the final configuration chosen for the cladding application.

The significance of the edge-tilting strategy on relaxing requirements for other aspects of the cladding should not be overlooked. Note that by tilting the edges, potential surface parasitics are essentially diverted into bulk modes. From the results in table 1 it is clear that this strategy greatly relieves the index-matching requirement. In this case we were able to maximize the strength and processing characteristics without affecting our ability to match the

index of the glass. However, in some cladding applications it may not be possible to both match the index and meet the other polymer specifications. In those cases, the use of tilts gives the polymer chemist greater freedom in formulating the correct adhesive.

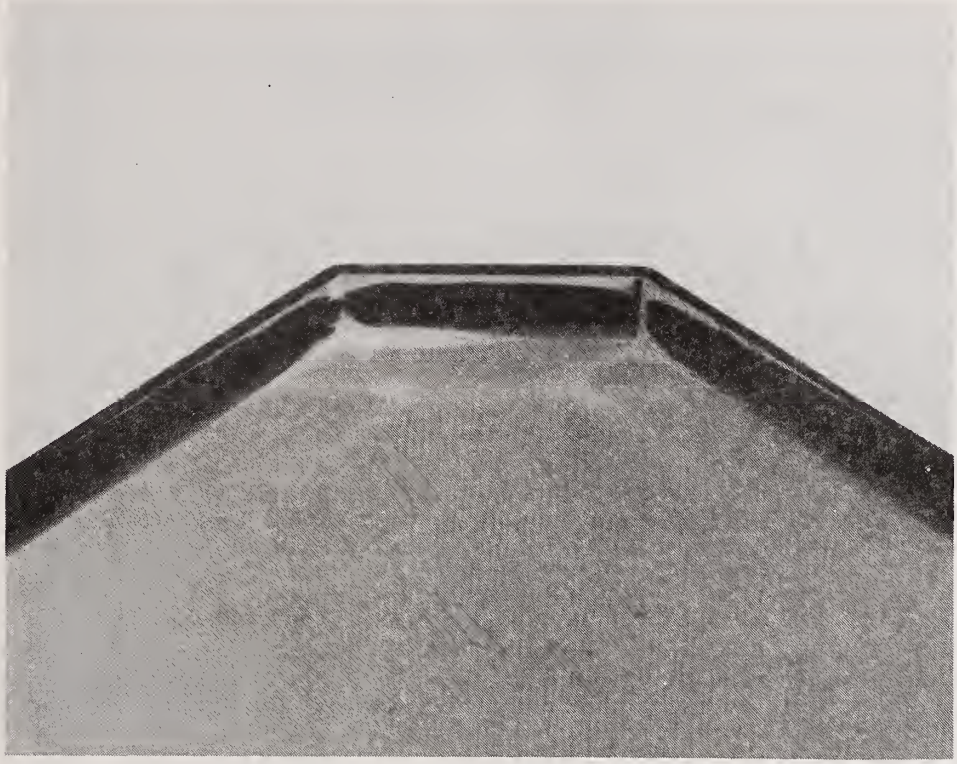

Figure 8. Photograph showing large-scale adhesion failure at the cladding interface of a 31.5-cm disk. The fracture is thought to have been caused by surface parasitic oscillations that started from small (< 100 μm) delaminations at the disk surface.

8. Improving Bond Strength and Durability

8.1 Estimates of Thermal Stresses

The absorption of the ASE energy in the cladding glass causes a corresponding increase in temperature and the resultant development of thermal stresses. The temperature rise, $\Delta T(x)$, through a uniform absorber receiving an instantaneous incident flux, I_o (J/cm^2), is simply given by:

$$\Delta T(x) = \frac{I_o \bullet \beta}{\rho \bullet C_p} \exp(-\beta x) \qquad (7)$$

where ρ_g is the glass density (2.83 g/cm^3), C_p the specific heat (0.72 J/g•K) and, β the absorption coefficient of the cladding glass at 1 μm. The cladding glass is designed to absorb strongly at 1 μm with relatively little absorption in the visible region. Consequently, there is a negligible contribution to the temperature rise from the flashlamp light. Figure 10a shows the expected temperature profiles through the cladding glass as calculated by eq. (7). The results are for three different values of cladding absorption with an incident ASE fluence of 10 J/cm^2. The peak temperature rise occurs at the cladding interface ($x = 0$) and is proportional to the cladding absorption coefficient; thus doubling the cladding absorption doubles the temperature rise at the interface.

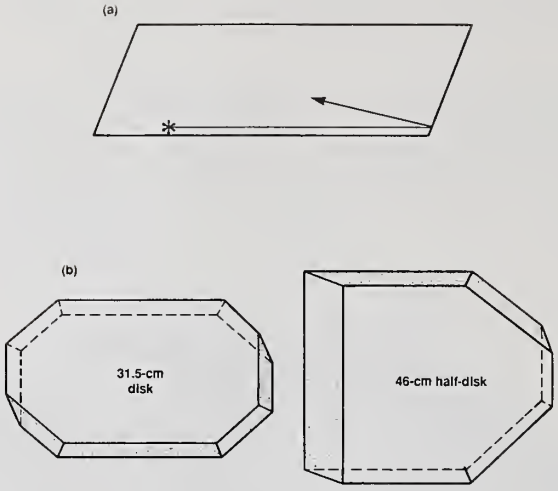

Figure 9. (a) Schematic drawing of disk edge tilt geometry in 2-D showing reflection of a hypothetical surface into the disk interior. (The size of the angle is exaggerated.) (b) The actual combination of tilts that will be used on the 46 and 31.5-cm Nova disks.

Pitts et al [34] have modeled the thermal stresses near the cladding interface using a two-dimensional finite-element stress analysis code. Their results for a 2-D cut through the Nova disk are shown in figure 10b-d; only a half-thickness of the disk was modeled since the problem is symmetric about the disk midplane. The temperature distribution assumed in the calculations corresponds to a cladding absorptivity of 7.5 cm^{-1} which gives a peak temperature rise at the interface of 36 K (see figure 10a). Figure 10b shows the predicted strains (magnified 1000x) and figures 10c and d the corresponding stress distributions perpendicular and parallel to the cladding interface. Table 3 summarizes the peak stresses (MPa) in the cladding, the laser disk and at the cladding/laser glass interface.

During heating, the expansion of the cladding is restricted by the adhesive bond to the laser disk causing lateral bending of the disk surface. This is clearly shown in the plot of the predicted material strains (figure 10b). The bending motion produces high tensile stress in the cladding that is perpendicular to the adhesive interface. This stress is particularly important since it can delaminate the adhesive bond and/or break the cladding glass.

We have measured shear and cleavage (perpendicular) bond strengths of 24 and 25 MPa, respectively, for phosphate glass bonded with the epoxy adhesive [35]. These would appear to be sufficiently strong bonds based on the predicted maximum stresses (8-10 MPa) given in Table 3. However there are several conditions that could either increase the stresses or reduce the overall strength of the bond. For example:

- Small delaminations of the bond near the disk surface can lead to the onset of parasitic oscillations producing significantly higher temperatures and stresses.
- Bond imperfections can produce stress concentrations.
- The bond may fatigue after several thousand cycles.
- Variability of the glass surface chemistry (e.g. by weathering) may reduce the bond strength.

During cladding testing we found that each of the above mechanisms could have been responsible for some of the observed bond failures. To increase the margin-of-safety against bond failure, we investigated ways to both reduce the thermal stresses and increase the bond strength.

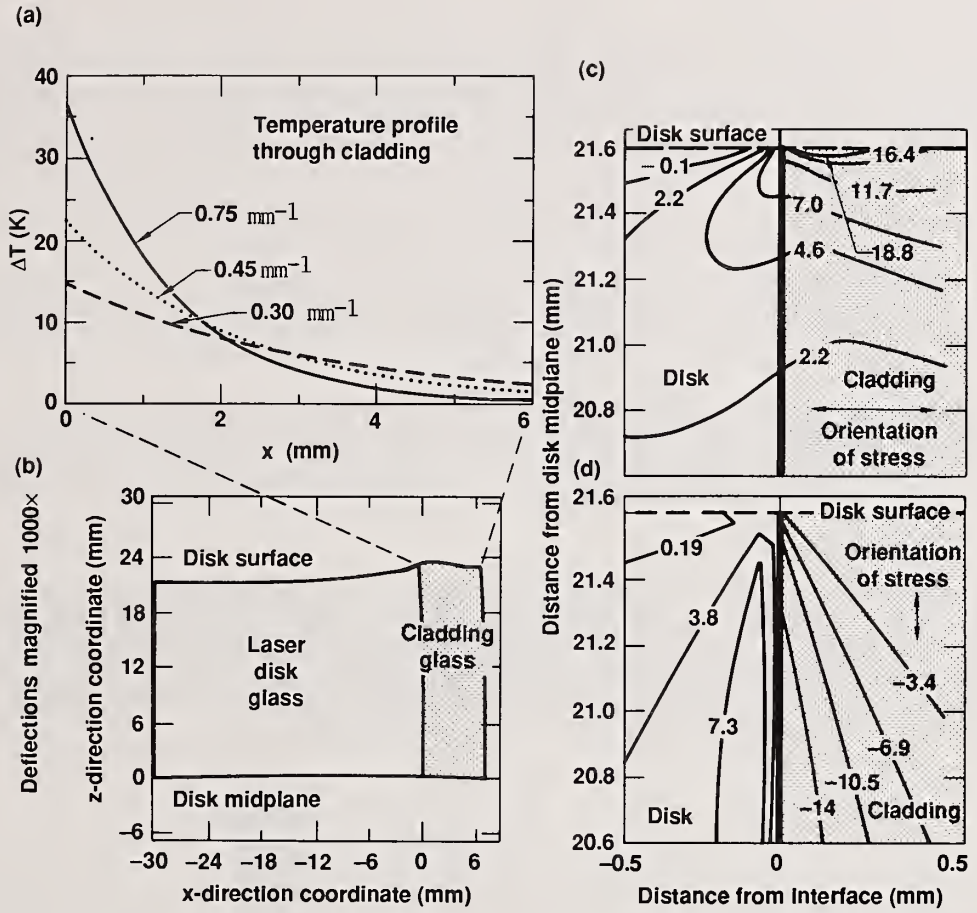

Figure 10. (a) Temperature profile through the cladding as computed with equation 7 for 3 different cladding absorption values and (b) the calculated deflection and stresses perpendicular (c) and parallel (d) to the cladding interface. These stress calculations correspond to the temperature rise produced by the 7.5 cm^{-1} absorption cladding.

Table 3. Peak thermally induced stresses from ASE absorption in a clad Nova laser disk as calculated with the 2-D finite-element, stress analysis code [34] (see figure 10). Compression is negative and tension positive. The cladding absorptivity is 7.5 cm^{-1}.

Stress Orientation	Calculated Peak Stress (MPa)
Cladding	
Parallel stress	- 21
Perpendicular stress	19
Disk	
Parallel stress	7.3
Perpendicular stress	7.0
Interface	
Shear stress	7.5
Perpendicular stress	9.5

8.2 Reducing Thermal Stresses

For a fixed disk geometry, the maximum stress at the cladding interface varies linearly with the temperature difference or, from eq. (7), with the cladding absorptivity. Therefore, reducing the cladding absorptivity by 50% will produce a corresponding 50% drop in the maximum stress. In most applications reducing the cladding absorptivity is not a problem because the cladding thickness (t) can be increased to give the doping-thickness product ($\beta \bullet t$) required for parasitic suppression. In the Nova application we are replacing disks on an already-built system. Thus we are constrained to the original amplifier dimensions and beam aperture and, accordingly, the cladding cannot be made thicker than the original 0.6 cm.

The original Nova disks used a cladding with a nominal doping-thickness product of 4.5 (i.e. 0.6 cm $\bullet$ 7.5 cm^{-1}) and we initially used a cladding having the same value. However, our calculations showed [33] that for the same thickness the cladding absorptivity could be as low as 3.0 cm^{-1} without affecting the amplifier performance.

Amplifier gain tests have been carried out on prototype disks with 0.6 cm thick claddings doped at 7.5, 4.5 and 3.0 cm^{-1} [33]. The results showed no appreciable loss in gain at lower cladding dopings. As a result, we have chosen a cladding doping of 4.5 cm^{-1}. This reduces the thermal stresses on the interface by 40% without any sacrifice in system performance.

8.3 Improving Bond Strength

The strength of adhesion of an organic polymer to an inorganic substrate depends on the sum of the forces acting across the interfacial boundary [36-38]. In general these forces can be broken into two parts: one associated with the long-range London dispersive forces and the other due to acid-base interactions (in the Lewis sense) between the two materials [38]. This observation is generally expressed in terms of the thermodynamic "work-of-adhesion", W_a, (the work needed to separate the two phases - i.e. the adhesive bond):

$$W_a = W_d + W_{a:b} \qquad (8)$$

where W_d and $W_{a:b}$ are work-of-adhesion contributions due to dispersion forces and acid-base interactions, respectively.

To increase W_d would require increasing the magnitude of the dispersion forces acting across the interface. For our case this is not practical since it would require changing either the polymer or the substrate or both. On the other hand it is possible to change the character of the glass surface to enhance the acid-base interaction. We have taken this approach to improve the bond adhesive strength.

The epoxy used to bond the cladding to the glass is an amine cured system (table 2) and is considered a Lewis base. The phosphate laser glass on the other hand is also normally a basic surface due to the migration of alkali and alkaline-earth ions to the glass surface. These ions can also readily react with water vapor and CO_2 in the air producing the corresponding basic hydroxide, carbonate and bicarbonate weathering products. By treating the glass surface with a dilute acid it is possible to remove the weathering products and temporarily replace the metal ions with protons (acidic sites) [39]. If bonding proceeds shortly after the acid treatment, then the amine can form acid-base bonds with the glass surface and increase the adhesive strength of the bond.

We have acid treated the surface of the phosphate glass (used to make the laser disks and cladding) and found that it significantly improves the epoxy adhesive strength (figure 11). The relative strength improvement was determined using a standard peel-test [40] that measures the force required to peel the polymer off the glass surface. The test is carried out using an Instron tensile-testing machine and is described in detail elsewhere [35].

A concentrated acid treatment produces no noticeable improvement in strength over that obtained with a dilute acid. Thus, we have adopted the dilute acid treatment in our cladding process.

The second method used to increase the bond strength is the application of a silane coupling agent to the glass surface. A silane coupling agent consists of an organofunctional group attached to an easily hydrolyzable alkoxysilane (fig. 12) [41]. In principle it works by bonding the siloxane portion of the molecule to the inorganic substrate and the organic portion to the polymer. The coupling agent is dissolved in an organic solvent and then hydrolyzed in water under either acidic or basic conditions. In our case we use a slightly acidic solution (pH = 4). The resulting silanol groups are thought to couple to the glass surface by either hydrogen-bonding (an acid-base interaction) or by direct formation of oxane bonds with the glass surface [41] (in this case Si-O-P, see figure 12).

The coupling agent we have chosen also has a diamine functional group that reacts with the epoxide rings in the adhesive. The reaction between the amine and epoxide is generically the same as outlined in figure 5. Note that in this case the coupling agent makes the glass surface basic (covered with amine groups) and the epoxide in the polymer acts as the Lewis acid. Therefore the application of a coupling agent can still be thought of as increasing the acid-base contribution to the work of adhesion.

Figure 11 shows the relative improvement in bond strength due to the application of the coupling agent. We have found that the use of an acid surface treatment followed by application of a silane coupling agent produces the highest bond strengths. Therefore we have adopted this procedure for use in cladding the new Nova disks.

9. Testing Prototype Disks

Back-to-back gain tests in a 46-cm amplifier were used to demonstrate that the epoxy-bonded cladding gives the same performance as fused-glass claddings [33,42]. These tests were carried out in the same amplifier using the nominal Nova phosphate laser glass (LG-750 and LHG-8) doped with 2 x 10^{20} Nd-ions/cm^3. The disks themselves had slightly different spontaneous emission lifetimes which were accounted for in making the performance comparison.

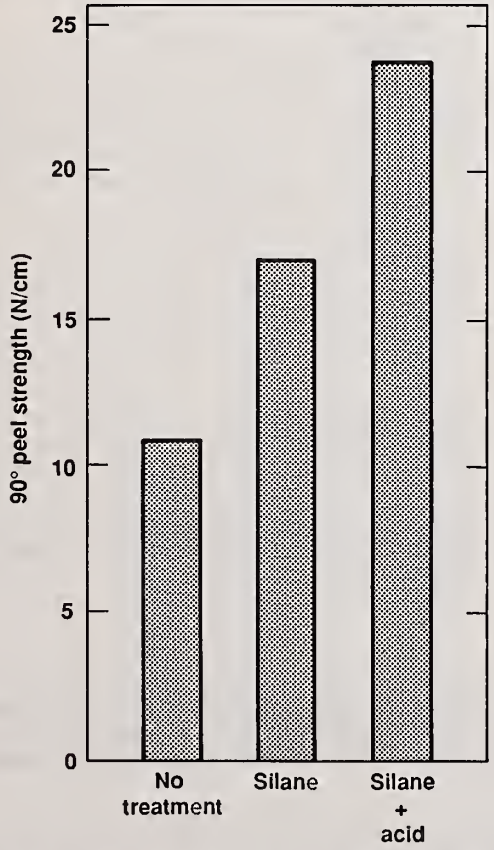

Figure 11. Effect of acid surface treatment and silane coupling agent on adhesive strength as measured by a standard 90° peel test.

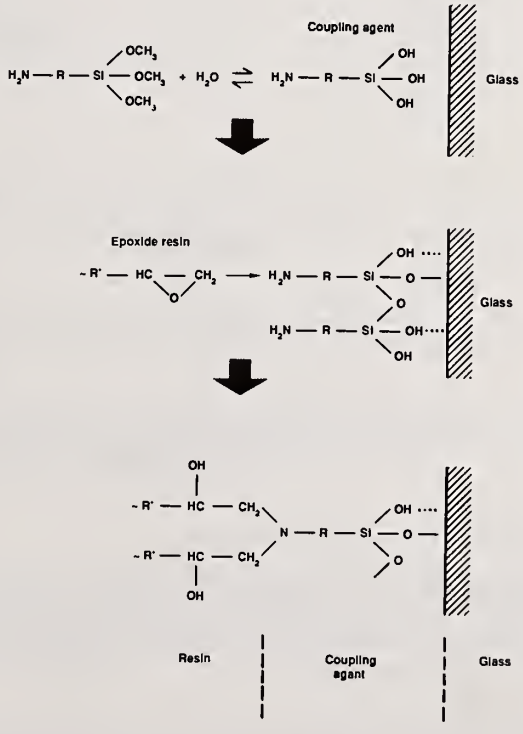

Figure 12. Structure and reaction of silane coupling agent.

Figure 13 shows the gain coefficients measured at the nominal Nova flashlamp operating voltage (20 kV) for five disks with epoxy bonded cladding and two disks with fused glass claddings. The data are plotted versus the measured spontaneous emission lifetimes for the disks.

Three of the disks were tested on the so-called "high-gain side" of the amplifier and the other four on the "low-gain side", thus the data in figure 13 are plotted in two subsets. The small difference in gain from one side of the amplifier to the other is a result of pumping differences in the 46-cm amplifier [43]. The lines through the two data subsets are based on model calculations [33,42] and show the expected slope the data should follow.

The results show that after accounting for the fluorescence-lifetime differences between the disks, the gain performance is about 3% higher for the fused glass cladding design. This remaining performance difference can be accounted for by the small area difference between the two types of disks. The polygonal-shaped disks with the polymer edge cladding exposes slightly more area to the flashlamp light than the original elliptical disks used with the fused-glass cladding. The additional disk area cannot be used by the Nova beam but it absorbs flashlamp light that might otherwise pump the useful aperture of the disk. After correcting for this area difference the gains for the two cladding types agree to better than 1% which is within the combined experimental error. We have therefore concluded that the gain performance achieved using the epoxy-bonded cladding is as good as that with fused-glass.

It should be added that in the final amplifier assemblies used on Nova we mask the unused area of the polygonal disk to avoid the pumping losses mentioned above.

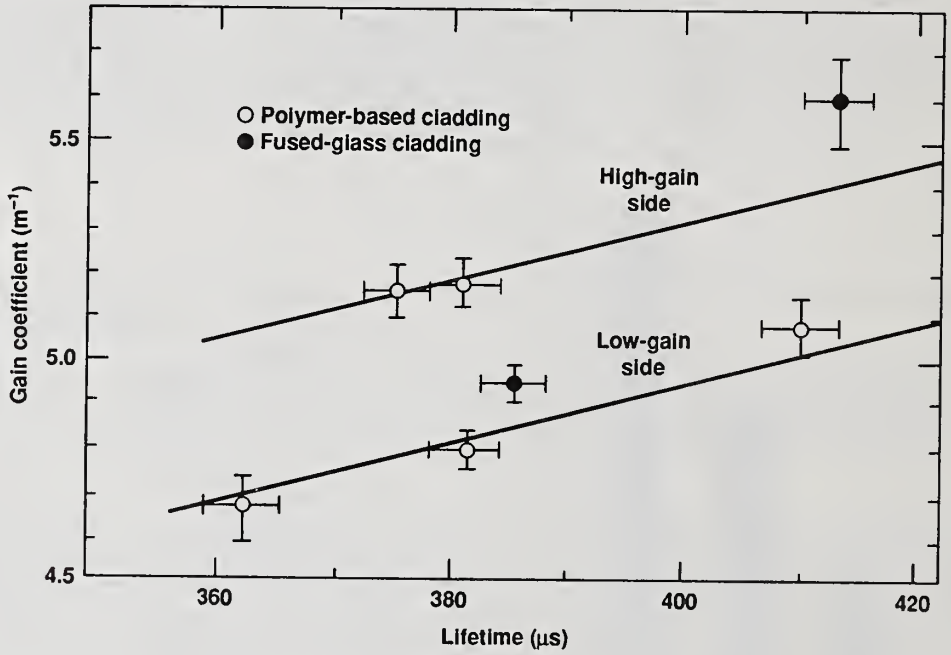

Figure 13. Gain performance comparison of epoxy-bonded and fused glass edge claddings on 2 wt% Nd-doped 46-cm amplifier disks.

9.1 Effect of Tilting Disk Edges

During the final disk fabrication we expect to be able to remove most but not all the small defects at the cladding interface. Consequently we developed a strategy for tilting the disk edges to protect against the onset of parasitic oscillations; this has been discussed in some detail in section 7.2.

The amplifier test results in figure 14 show the dramatic effect small angular tilts have on protecting against parasitic oscillations and extending the operating life of the disk. Two Nd-doped (2×10^{20} ions/cm^3), 31.5-cm disks with 7.5 cm^{-1} absorption cladding were individually tested in the same amplifier. The cladding on both disks had roughly the same number and distribution of flaws produced during fabrication. However in one case the disk had edges perpendicular to the faces whereas in the other case the edges at the long end of the disk

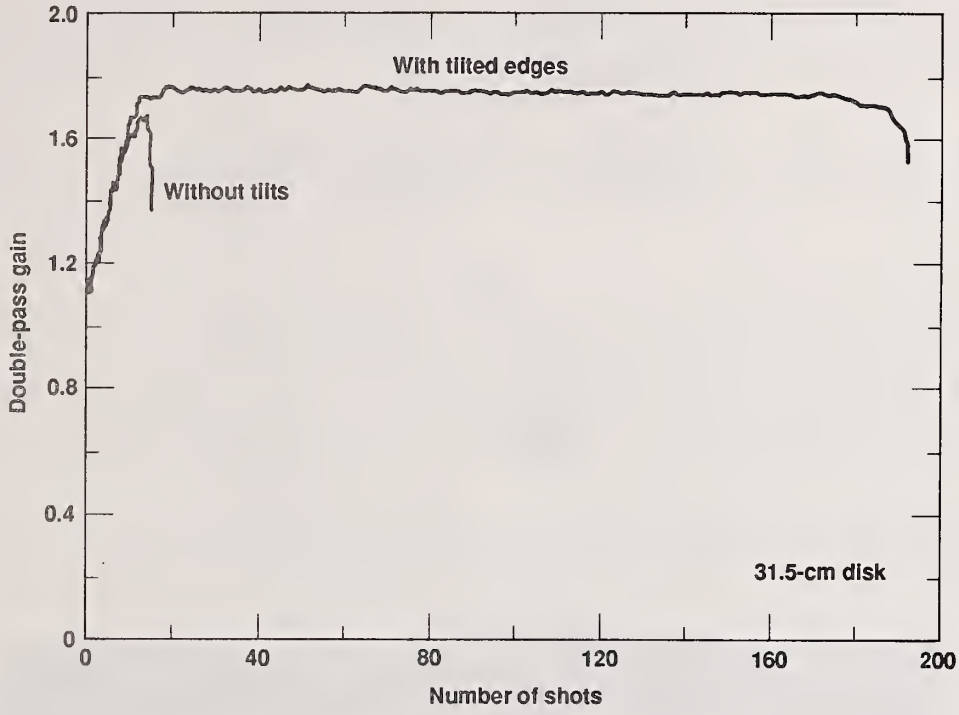

Figure 14. Gain vs. number of amplifier shots for two identically clad, 2 wt% Nd-doped, 31.5-cm disks with and without edge tilts.

were tilted by 0.8°. The disk without tilts failed during the first few shots as the gain was being increased to the nominal Nova operating conditions. The disk with the tilted edges, however, lasted for 174 shots before the gain began to rapidly fall off after the onset of parasitic oscillations. The parasitic oscillations occurred across the short dimension (i.e. width) of the disk between edges that were not tilted.

9.2 2000-shot Lifetime Test

Before proceeding with final production of the epoxy-bonded cladding we carried out a 2000-shot lifetime test on a prototype 31.5-cm disk. 2000-shots corresponds to about 4 to 5 years of Nova operation. The disk survived the 2000 shots without any visible degradation or change in gain.

The prototype disk used 6 mm thick edge cladding with an absorption of 4.5 cm^{-1}. The disk tilts were 0.8° and the cladding and disk bonding surfaces were treated with the silane coupling agent as discussed in the previous section.

Since this test we have adopted a slightly larger tilt angle (1.4°) and use the dilute acid surface treatment prior to adding the silane coupling agent. Both of these measures are designed to enhance the operating margin of safety for the final Nova disks.

10. The Cladding Process

The process of cladding the laser disks can be broken down into four major steps: (1) laser disk and cladding glass preparation, (2) glass surface treatment, (3) adhesive bonding and cure and (4) cladding finishing. These steps are shown schematically in figure 15 and discussed in further detail below.

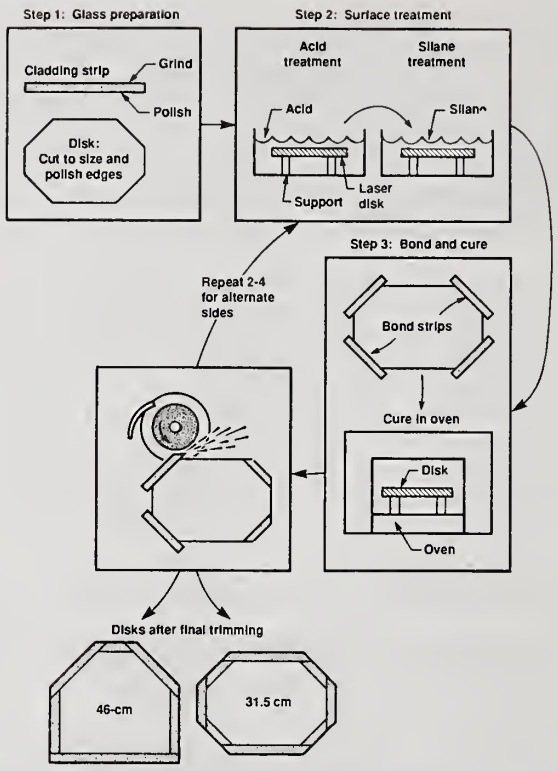

Figure 15. Schematic diagram of the cladding process.

In Step 1 the laser disks, as received from the glass companies, are shaped, edge polished, cleaned and inspected for foreign particles. In a similar fashion, the cladding glass strips are cut to size and then polished on one side and ground on the other. The polished side of the cladding later serves as the bonding surface while the ground side provides a diffuse reflecting surface for any ASE that is not absorbed on the first-pass through the cladding.

In Step 2 the bonding surfaces of both the cladding and laser disks are treated with a dilute acid followed by application of the silane coupling agent (figure 15). In the acid treatment, a 0.2 N solution of acetic acid is used to remove weathering products and acidify the glass surface; this is accomplished by simply submerging the disk into the acid bath for about 20 minutes. After removal, the disk is immediately transferred to a class-100, horizontal-flow clean room for application of the silane coupling agent and the subsequent bonding operations.

The silane coupling agent is also applied by submerging the disk in a tank. The solution consists of a mixture of 1% coupling agent (3-[2-aminoethylamino]-propyltrimethoxysilane; Z6020 made by Dow Corning Corp.) in 20% methanol and 79% distilled water. The pH of the coupling agent solution is adjusted to a value of about 4 using an acid. Again the disk is submerged for a few minutes, removed and thoroughly flushed with distilled water, then methanol and finally air dried.

The disks are temporarily stored in a dry environment until proceeding to step 3, the bonding operation. During bonding the disk is placed in a bonding fixture that is used to hold the disk and cladding strips in place. The adhesive reactants are filtered, mixed in the proper stoichiometric quantities and applied to the polished surface of the cladding glass. Each cladding strip is slowly pressed into place taking care to eliminate all bubbles. Once in place, it is lightly clamped with a pressure known to give the proper bond-line thickness (about 25 μm).

The disk remains in the bonding fixture for 24 hours at about 25°C. This is the time it takes the epoxy to set. The epoxy is then cured by heating at 3°C/h up to 80°C, holding at 80°C for 4 h and then cooling the disk at 3°C/h back to ambient. The slow heating rates are designed to minimize any thermal stresses in the disk. The temperature across the oven is uniform to within 1°C for the same reason.

The actual bonding process is accomplished in two phases. In phase-one cladding strips are applied to half the edges in an alternating pattern. The whole disk is then cured and machined to remove the excess length (figure 15). In phase 2 the process is repeated for the other edges. In this sequence, the longest strips remain unconstrained during the heating cycle. This minimizes potential problems due to thermal expansion differences between the disk glass and edge cladding.

Finally after all the cladding has been applied, the disk faces are ground and polished to the required $\lambda/8$ wave-front quality.

10.1 Technology Transfer

The edge cladding process has been fully developed and tested at LLNL on full-size prototypes of Nova disks. However, the actual cladding and polishing of the approximately 300 Nova disks will be carried out by two commercial glass finishing vendors selected by competitive bid (Eastman Kodak and Zygo Corp.). Over a period of about six to eight months the hardware and processing technology have been transferred to these companies. As part of that technology transfer process, a series of comprehensive QA/QC tests have also been developed and implemented to guarantee the final disk quality.

The cladding of the new platinum-inclusion-free Nova disks is nearing full production. Several new amplifiers have been assembled and placed into full operation on the Nova system (figure 16). We anticipate all 90 power amplifiers will have been retro-fitted with the new glass and edge cladding within 12 to 24 months (late 1988).

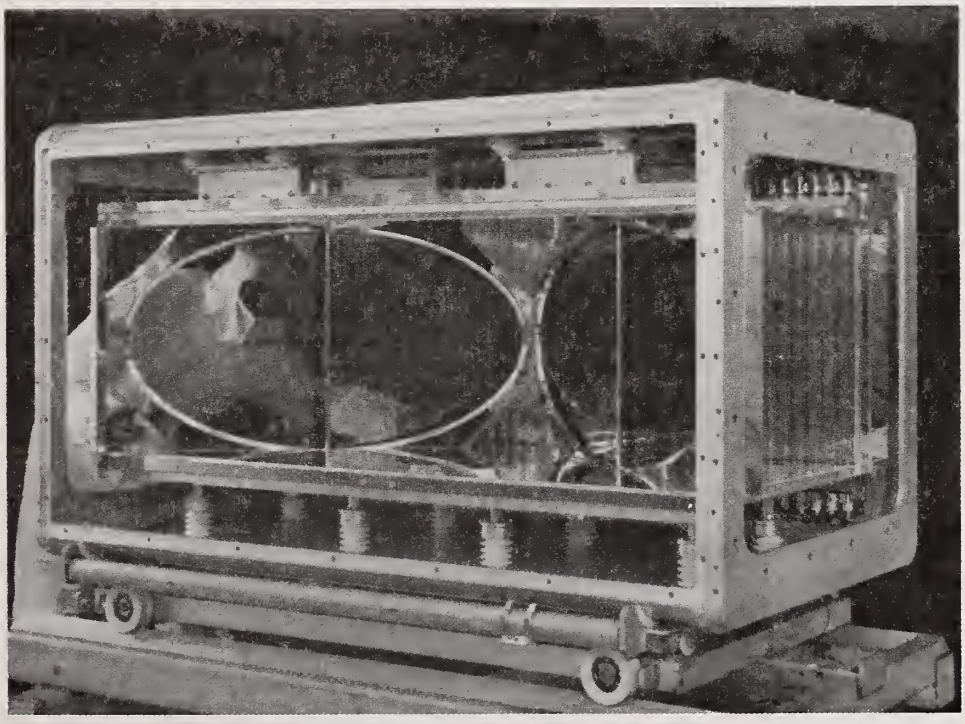

Figure 16. Final assembly of a Nova 46-cm amplifier showing the new polygonal-shaped, Pt-inclusion-free glass disks with epoxy-bonded edge cladding.

The authors gratefully acknowledge the assistance of Dr. J. Trenholme on several aspects of this project. The support of the LLNL clean room staff in preparing the test amplifiers and the contributions of Mr. C. Thompson, Ms. W. Sawvel and Mr. D. Larson and their associates in building and operating the 2000-shot lifetime test is appreciated. The efforts of Ms. A. Clasen in preparing this manuscript are also acknowledged.

11. References:

1. D. C. Brown, High-Peak-Power Nd:glass Laser Systems, Chapter 5, Springer-Verlag, New York, 1981.

2. W. Koechner, Solid State Laser Engineering, Chapter 4, Springer-Verlag, New York, 1976.

3. W. W. Simmons and R. O. Godwin, "Nova Laser Fusion Facility: Design, Engineering and Assembly Overview", Nuc. Tech./Fusion 4, 8 (1983).

4. J. B. Trenholme, "Fluorescence Amplification and Parasitic Oscillation Limitations in Disk Lasers", NRL Memorandum Rep. 2480, July 1972.

5. J. E. Swain, et al., J. Appl. Phys. 40, 3973 (1969).

6. J. M. McMahon, J. L. Emmett, J. F. Holzrichter, J. B. Trenholme, IEEE J. Quantum Electron. QE-9, 992 (1973).

7. (a) G. Dube' and N. L. Boling, Applied Optics 13, 699 (1974).
(b) S. Guch, Jr., Applied Optics 15, 1453 (1976).

8. 1980 Laser Program Annual Report, Lawrence Livermore National Laboratory, Report UCRL-50021-80, pg. 214-217, June 1981.

9. D. Milam, C. W. Hatcher and J. H. Campbell, "Platinum Particles in the Nd:doped Disks of Phosphate Glass in the Nova Laser", in Laser Induced Damage in Optical Materials: 1985; Proceedings of the Boulder Damage Symposium, Nov. 1985, Boulder, Colorado.

10. C. R. Wolfe, J. H. Campbell, R. E. Lyon, J. H. Pitts and H. T. Powell, "Optical Damage in Epoxy Polymers by Millisecond Light Pulses", in Laser Induced Damage in Optical Materials: 1986; Proceedings of the Boulder Damage Symposium, Nov. 1986; Boulder, CO.

11. L. Tonks, J. Appl. Phys. 35, 1134 (1963).

12. E. Sibert and F. Tittel; J. Appl. Phys. 40, 4434 (1969).

13. J. A. Glaze, S. Guch and J. B. Trenholme, Applied Optics 13, 2808 (1974).

14. D. C. Brown, S. D. Jacobs and N. Nee, Applied Optics 17, 211 (1978).

15. J. M. Soures, L. M. Goldman, M. J. Lubin, Applied Optics, 12, 927 (1973).

16. K. J. Jancaitis, H. T. Powell and J. B. Trenholme, "Design Considerations for Nova Edge Cladding", 1986 Laser Program Annual Report, UCRL-50021-86, Section 4.3.2, in press.

17. J. E. Murray, M. O. Riley, R. J. Poli, H. T. Powell and B. W. Woods, "Silicone Edge Claddings", 1983 Laser Program Annual Report, UCRL-50021-83, June 1984, Section 6-8.

18. J. E. Murray, M. O. Riley, R. J. Poli and H. T. Powell, "Silicone Rubber Edge Claddings for Laser Disk Amplifiers", CLEO 84, paper THF-2 (June, 1984).

19. M. O. Riley, E. Jessop and J. E. Murray, "Polymer Formulations and Properties", 1986 Laser Program Annual Report, UCRL-50021-86, Section 4.3.5, in press.

20. H. Lee and K. Neville, Handbook of Epoxy Resins, McGraw-Hill Book Co., New York, 1967, Chapter 4.

21. J. L. Lundberg, L. S. Nelson and M. Y. Hellmann, "Carbon Formation by Flash Illumination of Polymers", in the Proceedings of the Third Conference on Carbon, p. 411, Pergamon Press, 1957.

22. R. M. O'Connell and T. Saito, "Plastics for High-Power Laser Applications: A Review", Optical Engineering, 22, 393 (1983) and references cited therein.

23. A. A. Manenkov and V. S. Nechitailo, "Role of absorbing defects in Laser Damage to Transparent Polymers", Sov. J. Quantum Electron., 10, 347 (1980).

24. R. M. O'Connell, T. T. Saito, T. F. Deaton, K. E. Siegenthaler, J. J. McNally, A. A. Shaffer, "Laser Damage in Plastics at FJSRL", in Laser Induced Damage in Optical Materials: 1983; Proceedings of the Boulder Damage Symposium, No. 1983; Boulder, Colorado, p. 59.

25. A. V. Butenin and B. Ya. Kogan, "Mechanism of Damage of Transparent Polymer Materials due to Multiple Exposure to Laser Radiation Pulses", Sov. J. Quant. Electron, 6, 611 (1976).

26. B. Ranby and J. F. Rabek, Photo-degradation, Photo-oxidation and Photo Stabilization of Polymers, Principles and Applications, John Wiley and Sons, London, 1975.

27. N. E. Hill, W. E. Vaughan, A. H. Price and M. Davies, Dielectric Properties and Molecular Behavior, Van Nostrand Reinhold Company Ltd., London, 1969, Chapter 4.

28. CRC Handbook of Chemistry and Physics, R. C. Weast Editor, 67th Edition, CRC Press Inc., 1986.

29. D. J. Goedhart, Communication from Gel Permeation Chromatography International Seminar, Monaco, Oct. 12-15, 1969.

30. D. W. VanKrevelen, Properties of Polymers, Their Estimation and Correlation with Chemical Structure, Elsevier Scientific Pub. Co., New York, 1976, Chapter 10.

31. J. Trenholme, Lawrence Livermore National Laboratory, Private Communication, August 6, 1986.

32. D. C. Brown, High-Peak-Power Nd:glass Laser Systems, Springer-Verlag, New York, 1981, p. 156-157.

33. H. T. Powell, J. E. Murray and K. S. Jancaitis, "Optical Design and Performance of Edge Claddings for Nova Disk Amplifiers", Lawrence Livermore National Laboratory, Report UCRL (to be published).

34. J. H. Pitts, M. K. Kong and M. A. Gerhard, "Thermal Stress in the Edge Cladding of Nova Glass Laser Disks", in the Proceedings of the 12th Symposium on Fusion Engineering, Oct. 12-16, 1987, Monterey, California (in press).

35. R. E. Lyon, "Testing of Polymer Joints", 1986 Laser Program Annual Report, Lawrence Livermore National Laboratory, Livermore, CA, UCRL-50021-86, Section 4.3, in press.

36. D. H. Kaelble, Physical Chemistry of Adhesion, Wiley Interscience, New York, 1971, pp. 139-189.

37. F. M. Fowkes, "Attractive Forces at Interfaces", in Chemistry and Physics of Interfaces, American Chemical Society, Washington, D.C., D.E. Gushee, Ed., 1965, pp. 1-12.

38. F. M. Fowkes, "Role of Acid-Base Interfacial Bonding in Adhesion", J. Adhes. Sci. and Tech. 1, 7 (1987).

39. D. E. Clark, C. G. Pantano, and L. L. Hench, Corrosion of Glass, The Glass Industry, Inc., New York, 1979.

40. J. J. Bikerman, The Science of Adhesive Joints, Academic Press, New York, 1968, 2nd Edition, pp. 242-258.

41. E. P. Plueddemann, Silane Coupling Agents, Plenum Press, New York, 1982.

42. J. E. Murray, "Prototype Disk Testing", 1986 Laser Program Annual Report, Lawrence Livermore National Laboratory, Livermore, CA, UCRL-50021-86, pp. 4-24 to 4-30 (in press).

43. 1983 Laser Program Annual Report, Lawrence Livermore National Laboratory, Livermore, CA, UCRL-50021-83 (1984), pp. 6-2 to 6-8.

Manuscript Received
11-19-86

Mass Spectrometric Studies of Laser Damage in Calcium Fluoride

N. S. Nogar, E. C. Apel and R. C. Estler*

Chemical and Laser Sciences Division
Los Alamos National Laboratory
Los Alamos, New Mexico 87545

*Permanent Adress: Department of Chemistry
Fort Lewis College
Durango, Colorado 81301

Both electron impact- and laser ionization-mass spectrometry have been used to probe the material spalled from CaF_2 surfaces by the fundamental(1.06μ) and harmonic (355 nm and 266 nm) outputs from a Q-switched Nd:YAG laser. We have identified a number of gas phase products, including Ca, CaF and tentatively, CaF_2, and have measured their translational and internal energy distributions.

Our results suggest that while the 1.06μ experiments can be adequately modeled in terms of a single damage mechanism (likely avalanche breakdown), the short-wavelength results suggest the onset of second mechanism, perhaps multiphoton absorption. This is consistent with both the observed bimodal velocity distribution following short-wavelength damage, and with the decrease in CaF vibrational and rotational excitation.

Key words: CaF_2; damage; Nd:YAG; mass spectroscopy

1. Introduction

Experimental studies of laser induced damage in optical materials have traditionally concentrated[1] on phenomenology of the process: damage thresholds, and physical and bulk material properties effecting these thresholds. More recently, considerable attention[2,3] has been given to the mechanisms responsible for damage, and to the molecular phenomenae associated with the damage process.

In this work we describe a study of the interaction of relatively high-fluence laser pulses ($\phi \geq 10$ J/cm^2) with a (nominally) transparent optical medium. We have used both conventional electron impact ionization (with quadrupole mass discrimination) and RIMS (Resonance Ionization Mass Spectrometry) with time-of-flight detection as diagnostics for investigating the sputtered material produced from laser-solid interactions. RIMS[4] is a form of laser-ionization mass spectrometry which takes advantage of available laser-based multiphoton ionization schemes for the selective detection of atoms and small molecules. CaF_2 was chosen

for this study since it is a common dielectric used in UV and some vis-IR optics, and may be treated as a prototype system for these studies. The objective of this work was to obtain information about the laser-solid interaction through measurement of the chemical and velocity distributions of the particles ejected from the surface during damage.

2. Experimental.

All damage experiments were monitored by mass spectrometry, using one of two mass spectrometer/ionization systems: a quadrupole apparatus equipped with electron impact ionization, and a time-of-flight apparatus in which multiphoton photoionization was used. The source region of the quadrupole mass spectrometer (Extrel, C-50) was equipped with an axial ionizer modified[5] to allow the high intensity laser beam to pass through, Fig. 1. Primary ions produced by the damaging laser were detected by turning off the electron impact ionizer, while survey electron impact mass spectra were typically acquired at an energy of 75 eV. A base pressure of $\leq 1 \times 10^{-8}$ Torr was maintained by an ion pump. The time-of-flight mass spectrometer was modified[6,7] to permit optical access by both the damaging and interrogation laser beams. This latter apparatus was used to measure velocity distributions, and to provide optical spectroscopic identification of the ion precursors. Details have been presented elsewhere[6,7]. A base pressure of $\leq 1 \times 10^{-7}$ Torr was maintained by a L-N_2 trapped oil diffusion pump.

The CaF_2 substrates were polished flats (Janos Optical or Harshaw), 1.9 cm in diameter and 3 mm thick. Each sample was cemented to a 15-cm stainless steel rod for mounting within the mass spectrometer vacuum can. The substrates were placed near (1.5-3 cm) the axis of the mass spectrometer flight tube, and were manipulated by mounting the rods on a rotation-push/pull vacuum feedthrough (Varian Model 1371). The samples were rotated at rates of 1 revolution/15 minutes to 1 revolution/60 minutes, so that a fresh surface was continualy exposed to the laser beam.

Optical damage was initiated by either the fundamental (1.06μ), or frequency tripled (355 nm) or quadrupled (266 nm) output of a Nd^{+3}:YAG laser (Quanta Ray/Spectra Physics Model DCR 1A). The laser was equipped with filled-beam optics, and produced a beam whose spatial profile is somewhat more sharply peaked than for a gaussian beam. The Q-switched output was 10 nsec FWHM in duration, and smooth within the resolution of our electronics ($\approx$2 nsec).

The timing sequence was initiated by the Q-switch synch-out from the YAG laser. When using the quadrupole mass spectrometer, this signal triggered a boxcar averager (PARC 162/164) gated to accept signal from 10-100 μsec after the laser pulse. In experiments using the time-of-flight mass spectrometer, the YAG laser synch-out was passed through a variable delay (Tektronix 7904/7B85), a pulse generator (BNC 8010) and then to the trigger of a XeCl excimer laser (Lambda Physics EMG 101). The UV output from this laser was used to pump a tunable dye laser (Lambda Physics FL 2002) which could then probe, via multiphoton ionization, the material spalled by the laser damage event. The identity of the spalled material could be determined by varying the ionization wavelength, while the velocity distribution could be measured

by changing the delay between the damage and interrogation lasers. The boxcar gatewidth for these experiments was 500 nsec, which provides a mass resolution of ≈3 au.

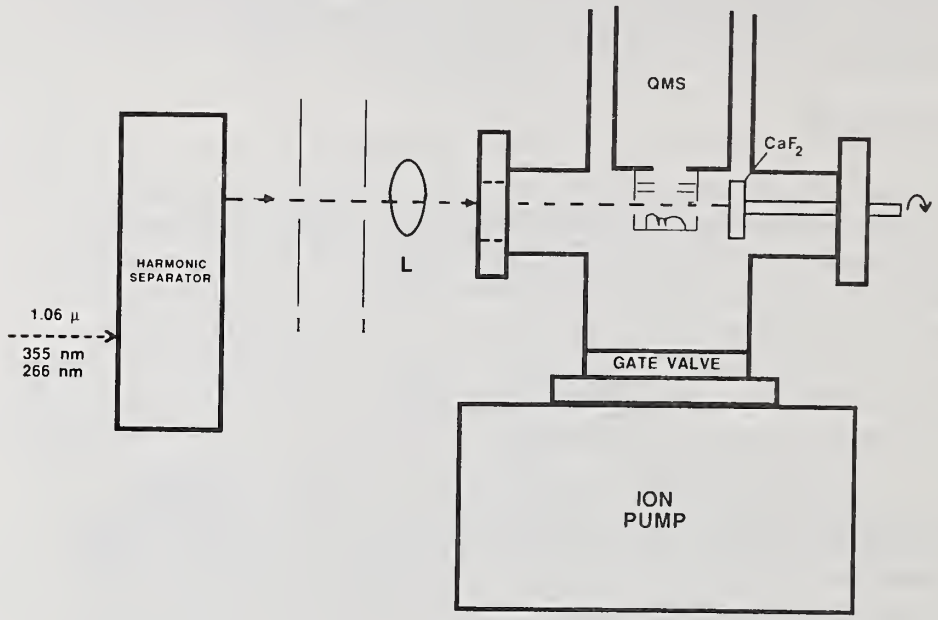

Figure1. Schematic of the experimental apparatus used for survey mass spectrometry. For details on time-of-flight apparatus, see ref. 7.

3. Results

Survey mass spectra were taken with the quadrupole mass spectrometer. Fig. 2 shows the spectrum generated with the electron ionizer turned off. It is dominated by the Ca^+ peak (40 au), with satellites observed at 42 and 44 due to isotopic variants, and very small contributions due to CaF^+ (59 au) and F^+ (19 au). With the electron impact ionizer turned on (75 eV energy), we generated the mass spectrum shown in Fig. 3. This spectrum is the result of a manual background (no laser) subtraction from the observed (laser damage) spectrum. Note the scale change on these figures, which reflects an obvious propensity for the desorption/ablation of neutral species in preference to ions. Even allowing for a reduced detection efficiency for ions formed outside the normal ionization region, we estimate the ratio M/M^+ to be ≥100.

The signals observed in Fig 3 can be divided into two types: those originating from the substrate material, and those likely associated with surface contaminants. For the former, a large 40 au peak is again observed, indicative of Ca^+. In this case we also observe a substantial peak at 59 au, and a large peak at 19 au. The latter suggests that F atom removal is a high probability process, in agreement with other observation[8]. Although we see no evidence of CaF_2^+, this does not mean the CaF_2 is not being sputtered from the surface. Indeed, a large body of evidence[9-10] suggests that CaF_2 is the dominant thermal evaporant. The reason for our non-observation of

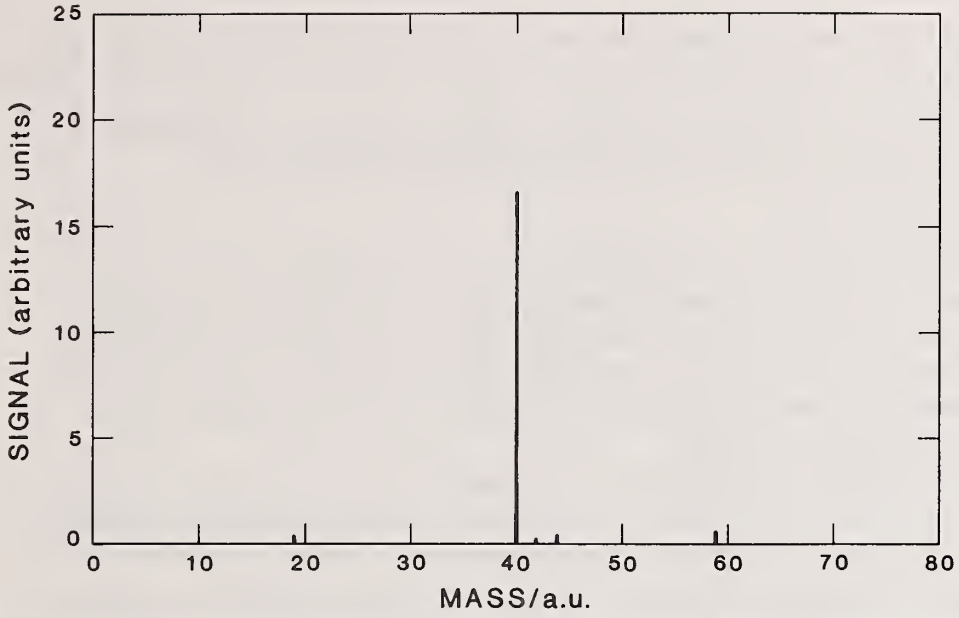

Figure 2. Survey mass spectrum of primary ions (no electron impact ionizer) produced by 266 nm damage on CaF_2 at 15 J/cm^2 (10 nsec pulse).

CaF_2^+ is that electron impact ionization[11,12] produces predominately CaF^+, and, at higher energies, Ca^+ from the parent molecule. The observed CaF^+ and Ca^+ signals are thus likely due to both direct ionization of Ca and CaF (see below), and to combined ionization/fragmentation of CaF_2. A number of other minority species (≤0.1%) can be observed at higher sensitivity, and are largely consistent with previous observations[13].

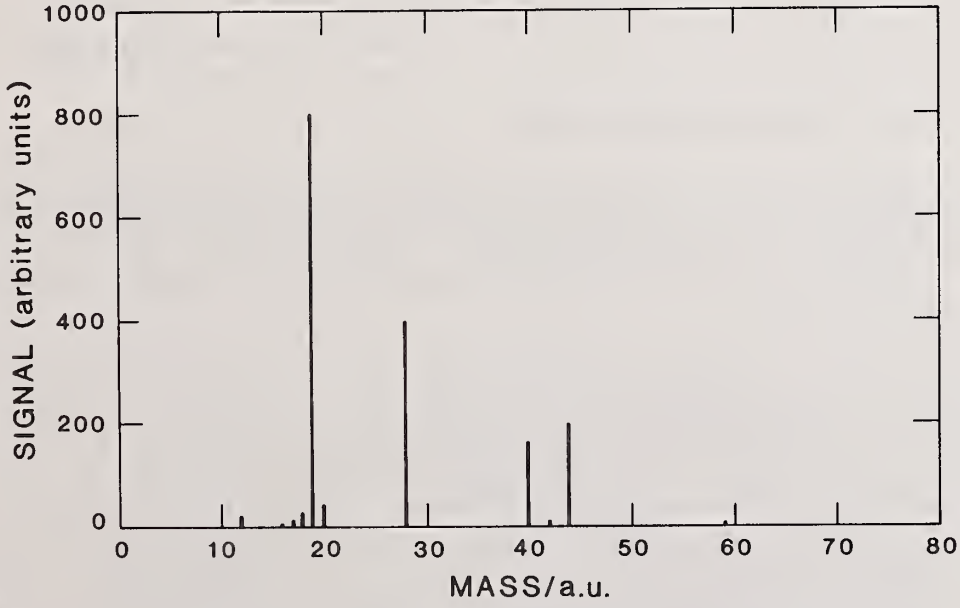

Figure 3. Survey mass spectrum of neutral species (ionized by electron impact) spalled from the CaF_2 surface. Conditions identical to Fig. 2.

Among the impurities routinely observed in the electron impact mass spectra are a large peak at 44 au, presumably CO_2, a peak at 28 due to CO (or N_2), the water group at 16,17 and 18 au, and a very weak signal at 12 au. We have not determined the identity of this last constituent, but it is a frequently observed signal in this apparatus. These results are consistent with the known[14,15] tendency of water to adsorb on CaF_2 surfaces.

Results from the laser damage/laser ionization experiments in the ToF mass spectrometer yield significant additional information. First, since the multiphoton ionization process is resonantly enhanced, the excitation (ionization) spectrum can be used to determine the precursor for a particular ion. And second, by varying the time delay between the damage and interrogation pulses, the velocity distribution of the spalled material can be obtained.

The Ca^+ observed in the laser ionization experiments is produced from atomic Ca by a "2+1" (photons to resonance + photons to ionize) process[7] through the enhancing $^1P_0^0$ state at 37298 cm^{-1}. Similarly, the CaF^+ observed in this set of experiments is derived from CaF by a 2+1 ionization process through the $F^2\Pi$ state (T_0=37550 cm^{-1}). These particular ionization paths were chosen so that both species could be detected with the same laser dye. While these results indicate that at least some of the ablated material is directly spalled as Ca and CaF, we have no direct evidence as to what fraction spalls as fragments, and what fraction as CaF_2 molecules. Neither the previously mentioned electron impact spectra, nor the optical ionization currently under discussion is sensitive to CaF_2. We can only infer from thermal vaporization studies[9,10] that a substantial fraction is likely to evaporate as molecules.

Additional information was obtained by measuring both the internal and translational energy distribution of the the spalled Ca and CaF. Velocity distributions were measured by varying the time delay between the damage and ionization (probe) lasers. The internal energy content of the CaF radicals was probed by varying the wavelength of the ionization (dye) laser, so that an excitation spectrum was obtained. Damage was initiated at the fundamental (1.06μ), and frequency tripled (355 nm) and quadrupled (266 nm) wavelengths. The results were found to be dependent on wavelength and may be summarized[7] as follows:

a. For 1.06μ irradiation, we observed thermal (850 K) velocity distributions for both Ca and CaF. In addition, the CaF radical exhibited significant amounts of internal (rotational and translational) excitation, consistent with an internal "temperature" of $\approx 10^3$K.

b. For both 355nm and 266nm irradiation, the velocity distributions were bimodal, Fig. 4, with a fraction ($\leq$50%) of the spalled material exhibiting very high (4000 K) kinetic temperatures, while the remainder exhibited a temperature similar (800-1000 K) to that observed for the 1.06μ experiments. Note that the flight times exhibited in Fig. 4 are for optical time-of-flight (from CaF_2 surface to interrogation zone) and <u>not</u> the flight time in the mass spectrometer flight tube. In addition, both the vibrational and rotational temperatures of the CaF radicals decreased with decreasing damage wavelength.

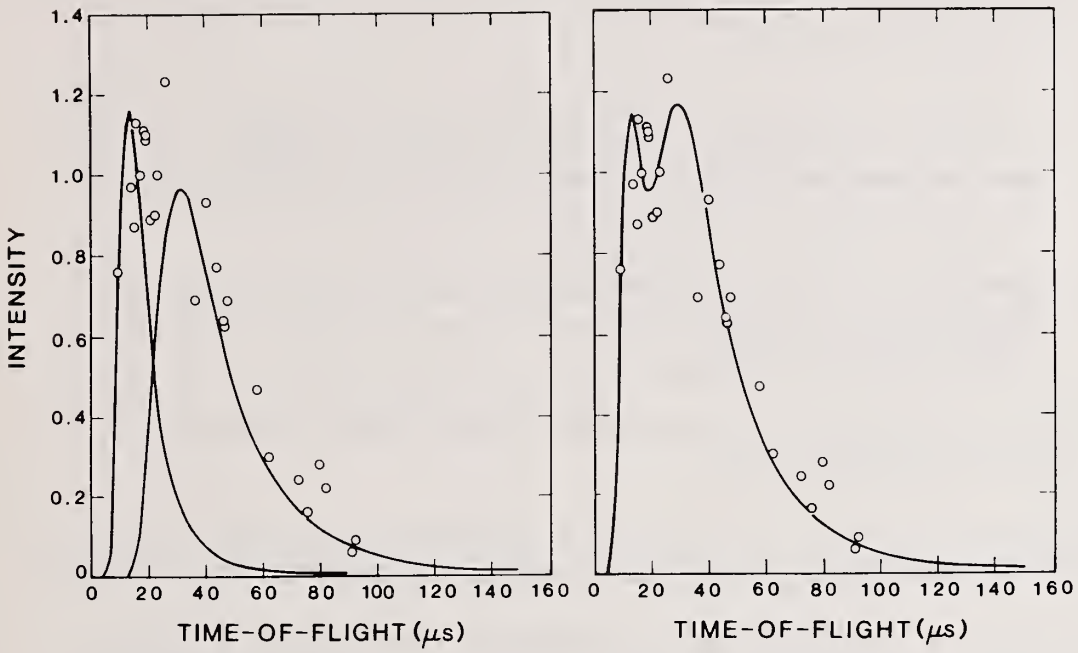

Figure 4. Optical time-of-flight distribution (o) for Ca spalled from CaF_2 surface at 266 nm, 15 J/cm^2: a) shows individual fast (4000K) and slow (850K) components for comparison with data, b) shows overall composite fit of fast (33%) and slow (67%) components.

4. Discussion

In regard to the characterization of the process of laser sputtering, or laser damage, the terms "thermal" and "electronic" have been used to describe different mechanisms of particle ejection from substrate surfaces in the hope of categorizing the numerous possible processes[16]. Thermal normally implies vaporization from a transiently heated surface, while electronic sputtering refers to a collection of processes commonly associated with the creation of electronic defects eventually leading to particle ejection. Such defects might include those resulting from direct interaction of the incident light with a surface atom or diffusing defects such as hole pairs. Such processes often lead to sudden bond rupture, and may lead to highly nonthermal velocity distributions in the ejected particles[17]. Indeed, the observation of nonthermal energy distributions have been used to infer the existence of a number of laser-material interactions[18], including direct photodissociation and ejection of surface material[19]. It is important to note, however, that some electronic sputtering mechanisms do lead to ejected particles with thermal velocity distributions[20].

[10] Blue, G. D.; Green, J. W.; Bautista, R. G.; Margrave, J. L. The Sublimation Pressure o Calcium(II) Fluoride and the Dissociation Energy of Calcium(I) Fluoride. J. Phys. Chem. 67; 877-882; 1963.

[11] Hildebrand, D. L.; Murad, E. The Dissociation Energy of Boron Monofluoride from Mass-Spectrtometric Studies. J. Chem. Phys. 43; 1400-1403; 1965; Mass-Spectrometric Determination of the Dissociation Energy of Beryllium Monofluoride. ibid, 44; 1524-1529; 1966.

[12] Farrow, R. F. C.; Sullivan, P. W.; Williams, G. M.; Jones, G. R.; Cameron, D. C. MBE-Grown Fluoride Films: A New Class of Epitaxial Dielectrics. J. Vac. Sci. Technol.; 19; 415-420; 1981.

[13] Buhl, R.; Preisinger, A. Crystal Structures and their Secondary Ion Mass Spectra. Surf. Sci. 47; 344-357; 1975.

[14] Palik, E. D.; Gibson, J. W.; Holm, R. T. Internal-Reflection -Spectroscopy Study of Adsorption of Water on CaF_2 Surfaces. Surf. Sci. 84; 164 -178; 1979.

[15] Allen, S. D.; Porteus, J. O.; Faith, W. N. ; Franck, J. B. Contaminant and Defect Analysis of Optical Surfaces by Infrared Laser Induced Desorption. Appl. Phys. Lett. 45; 997-999; 1984.

[16] Rothenburg, J. E.; Kelley, R. Laser Sputtering Part II: The Mechanism of the Sputtering of Al_2O_3. Nucl. Instr. Meth. B1; 291-300; 1984.

[17] Madey, T. E. Electron- and Photon-Stimulated Desorption: Probes of Structure and Bonding and Surfaces. Science 234; 316-322; 1986.

[18] Levine, L. P.; Ready, J. F.; Bernal, E. G. Production of High-Energy Neutral Molecules in the Laser-Surface Interaction. IEEE J. Quant. Elec. QE-4; 18-23; (1968).

[19] Bjourdon, E. B. D.; Cowin, J. P.; Harrison, I.; Polanyi, J. C.; Segner, J.; Stanners, C. D.; Young, P. A. UV Photodissociation and Photodesorption of Adsorbed Molecules. 1. CH_3Br on LiF(001). J. Phys. Chem. 88; 6100-6103; 1984.

[20] Stoffel, N. G.; Riedel, R.; Colavits, E.; Margaritondo, G.; Haglund, R. F.; Taglaner, E.; Tolk, N. H. Photon-Stimulated Desorption of Neutral Sodium from Alkali Halides Observed by Laser-Indueced Fluorescence. Phys. Rev. B32; 6805-6808; 1985.

[21] Jost, B.; Schueler, B.; Krueger, F. R. Ion Formation from Alkali Halide Solids by High Power Pulsed Laser Irradiation. Z. Natur-Forsch. 37a;18-27; 1982.

Our results do not necessarily point to a single mechanism in the initiation of the breakdown event, but are significant from the standpoint that a change in mechanism, i.e., an opening of a second channel at high photon energy, is indicated. The kinetic temperatures and qualitatively similar estimates of the CaF internal energies observed at 1.06μ argue for a thermal or sonic mechanism, possibly initiated by avalanche breakdown. In addition, it is tempting to speculate that absorption at this long wavelength is due to a physical or chemical defect in the substrate, since direct excitation of the crystal would imply simultaneous absorption of a large number of photons. The results at shorter wavelengths suggest a more direct photophysical interaction, where rapid energy deposition is followed by non-adiabatic transitions of the fragments to antibonding states[19,21]. Such a mechanism can lead to the nonequilibrium of the various degrees of freedom observed here and also to a nonisotropic angular distribution of products.

5. References

[1] Ready, J. F. Effects of High-Power Laser Radiation, New York, Academic, 1971.

[2] Smith, W. L. Laser-Induced Breakdown in Optical Materials. Opt. Engin. 17; 489-503; (1978).

[3] Kelly, R.; Cuomo, J. T.; Leary, P. A.; Rothenberg, J. E.; Braren, B. E.; Aliotta, C. F. Laser Sputtering Part I. On the Existence of Rapid Laser Heating at 193 nm. Nucl. Instr. and Meth. B9; 329-340; 1985.

[4] Nogar, N. S.; Estler, R. C.; and Miller, C. M. Pulsed Laser Desorption for Resonance Ionization Mass Spectrometry. Anal. Chem. 57; 2441-2444; 1985.

[5] Estler, R. C.; and Nogar, N. S. Mass Spectrometric Identification of Wavelength Dependent UV-Laser Photoablation Fragments from Polymethylmethacrylate. Appl. Phys. Lett.; in press.

[6] Estler, R. C.; Nogar, N. S. Investigation of Optical Damage via Resonance Ionization Mass Spectrometry. Proceedings of the Symposium Laser Induced Damage in Optical Materials: 1985, in press.

[7] Estler, R. C.; Apel, E. C.; Nogar, N. S. Laser Mass Spectrometric Studies of Optical Damage in CaF_2. J. Opt. Soc. Am. B., in press (1987).

[8] Hayes, W.; Lambourn, R. F. Production of F and F-Aggregate Centres in CaF_2 and SrF_2 by Irradiation. Phys. Stat. Sol.; 57, 693-699; 1973.

[9] Himpsel, F. J.; Karlsson, U. O.; Morar, J. F.; Rieger, D.; Yarmoff, J. A. Determination of Interface States for CaF_2/Si(111) from Near-Edge X-Ray-Absorption Measurements. Phys. Rev. Lett. 56; 1497-1500; 1986; Karlsson, U. O.; Morar, J. F.; McFeely, F. R.; Rieger, D.; Yarmoff, J. A. Formation of a New Ordered Structure of CaF_2/Si(111) by Ultraviolet Irradiation. ibid. 57; 1247-1250; 1986.

Manuscript Received
3-20-87

CaF_2: An ESCA Study

T. Raj and Marilyn Law

Martin Marietta Aerospace, Laser Systems Technology
P.O. Box 9316, International Airport
Albuquerque, NM 87119

This paper describes two observations made on CaF_2 during electron spectroscopy for chemical analysis (ESCA) studies. The first observation is that an ion-etched CaF_2 surface adsorbs several layers of water even in an ultrahigh vacuum (UHV) chamber ($P \sim 2 \times 10^{-10}$ torr). This water at the sputter-etched surface is responsible for the presence of oxygen peaks in the ESCA data. The presence of oxygen in the ESCA data can easily be misinterpreted as an impurity in the CaF_2 bulk. This observation is detailed in Part I of the paper.

The second observation is that CaF_2 (whether substrate, source material or coating) in a UHV environment releases a small amount of fluorine-containing gas. This is discussed in Part II of the paper.

Key words: ESCA; ESCA sputter-depth profile; fluorine; ultrahigh vacuum.

1. Part I

The adsorption of water on CaF_2 has been studied extensively (Ref. 1). Several monolayers of water can be chemisorbed and physisorbed when CaF_2 is exposed to water vapor. In addition, in a detailed study of CaF_2 substrates (Ref. 2), 6-12 atomic percent of oxygen was detected in all ESCA data on CaF_2. It was concluded that either oxygen was present in the bulk CaF_2 or that it was coming from the vacuum environment. The base pressure in the vacuum chamber was $\sim 10^{-8}$ torr. Though the sputter-etching pressure was not reported, it is assumed that the sputter-etching was performed with a conventional ion gun with a high background pressure ($\sim 10^{-5}$ torr). The present work reports that sputter-etched CaF_2 can adsorb water even at very low pressures ($\sim 2 \times 10^{-10}$ torr) in a vacuum chamber. This water at the surface is principally responsible for the presence of oxygen in the ESCA data of CaF_2.

The ESCA measurements were performed in an ion-pumped Φ-548 spectrometer. This ESCA system is a part of the multitechnique surface analysis system (Φ SAM 590/ESCA 548/SIMS 2500) at the Air Force Weapons Laboratory's Developmental Optics Facility (DOF), Kirtland AFB, NM. The ESCA spectrometer is equipped with a differentially pumped, sputter ion gun. A typical base pressure in the analysis chamber is 2×10^{-10} torr. The argon pressure in the chamber is less than 2×10^{-7} torr during the time that the sample is being sputter-etched for depth profiling. The x-ray source is equipped with a magnesium anode.

The original samples for the study were single-crystal (random orientation), 2.5 cm by 0.3 cm substrates as received from Optovac, and these Optovac substrates polished with diamond after grinding with Al_2O_3. The substrates were cut into smaller pieces ($\sim 1 \times 1$ cm) to fit into the ESCA sample carrousel. The parts were cleaned by an acetone/methanol sequence and dried with N_2 before introduction into the chamber.

*This effort was sponsored by the Air Force Weapons Laboratory, Air Force Systems Command, United States Air Force, Kirtland AFB, New Mexico 87117.

A complete chemical analysis of the sample surface was performed by ESCA surveys, time-averaged over intervals ranging from one-half hour to several hours. This signal-averaging time is denoted by DAT (data acquisition time) in this paper. This time-averaging of ESCA data is required (from the Φ-548) to increase the detection sensitivity to better than 0.5 atomic percent. In addition, the samples were analyzed by the ESCA depth profiling technique. In this technique, the sample is sputter-etched for a short period of time, followed by data collection for a few selected ESCA peaks; and this alternating process of etching and data collection is repeated. Typically, no signal averaging is performed for the ESCA data in the depth profiling. Consequently, the detection sensitivity is rather poor: 2-3 atomic percent for most elements.

ESCA surveys taken at the surface of a CaF_2 substrate indicated the presence of four principal components: calcium, fluorine, carbon and oxygen. The carbon and oxygen are due to the usual surface contamination. Small amounts of other materials detected at the CaF_2 surface were any or all of the following: aluminum, barium, magnesium, silicon and sodium. The materials involved in polishing (grinding compounds, polishing compounds, etc.) and cleaning and handling procedures could be responsible for the presence of these elements. These small contaminants will not be discussed here and will be reported in a future publication.

As an example, an ESCA survey (DAT = 120 minutes) taken at the surface of an Optovac CaF_2 substrate is illustrated in figure 1. The atomic percent concentrations of the contaminants are: carbon = 17.0, oxygen = 8.6, aluminum = 1.7 and barium = 0.3.

An ESCA sputter-depth-profile was taken for all of the detectable elements. The sputter-profile was continued for several minutes after the removal of the surface contaminants carbon and oxygen. Figure 2 illustrates a profile for the Optovac substrate. Table 1 indicates the atomic percent of carbon and oxygen as a function of the sputter time. Clearly, the surface was free of carbon and oxygen after sputter-etching for one-half minute.

Table 1. Oxygen and Carbon Contaminants in CaF_2 as a Function of Sputter Time

Sputter Time (minutes)	Oxygen (atomic percent)	Carbon (atomic percent)
0.0	8.6	17.0
0.5	1.2	2.6
1.6	0.8	2.1
2.6	1.8	0.5

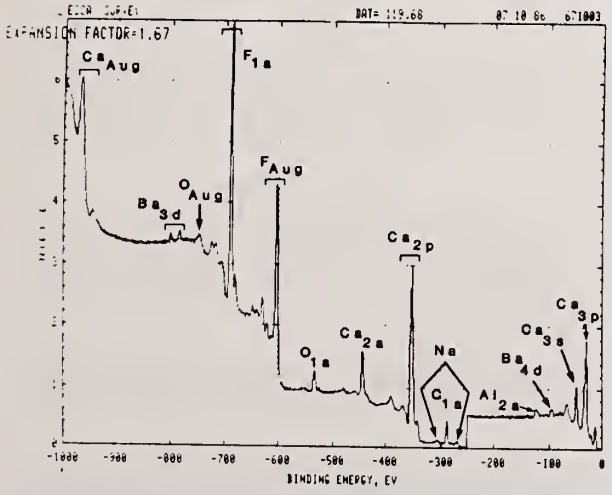

Figure 1. ESCA Survey taken at the Surface of a CaF_2 Substrate.

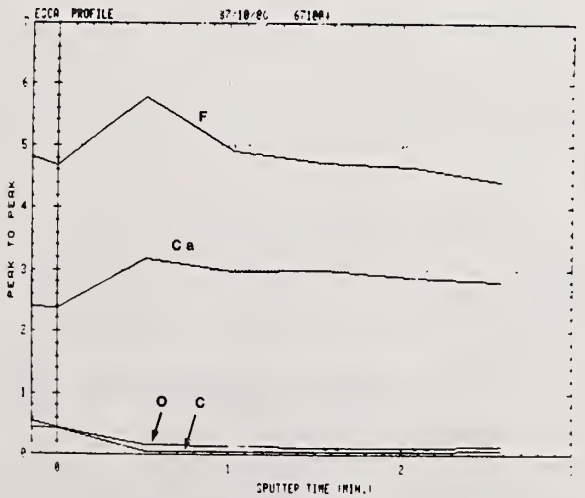

Figure 2. ESCA Sputter Depth Profile started at the Surface of the above CaF_2 Substrate.

However, an ESCA survey (DAT = 62 min) taken at the end of the sputter-depth-profile, shown in figure 3, indicates that the oxygen peak reappeared while the carbon peak was absent. Subsequently, this procedure of sputterprofiling until the oxygen disappears from the surface, followed by an ESCA survey, was repeated several times. Each time, oxygen reappeared in the survey. This implies that an oxygen-containing material deposits on the CaF_2 surface as soon as the ion etching is stopped. Since carbon does not reappear along with oxygen, the contaminant is not a carbonaceous material.

A residual gas analysis of the ESCA vacuum chamber ($P \sim 2 \times 10^{-10}$ torr) indicated the following main components (fig. 4):

$$H_2 > H_2O > N_2 \text{ (or CO)} > CO_2 > C$$

As is evident from figure 4, very little oxygen was present in the chamber. The source of oxygen at the CaF_2 surface must be the water in the chamber. It appears that the CaF_2 substrate became very reactive after the ion etching and formed a "water-containing layer" at the top surface. The existence of such a layer in a UHV environment implies that the water is chemically bound at the CaF_2 surface.

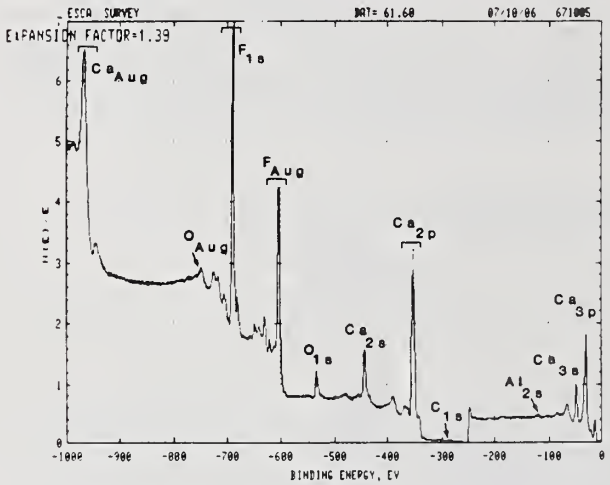

Figure 3. ESCA Survey taken at the End of the Sputter Depth Profile in Figure 2.

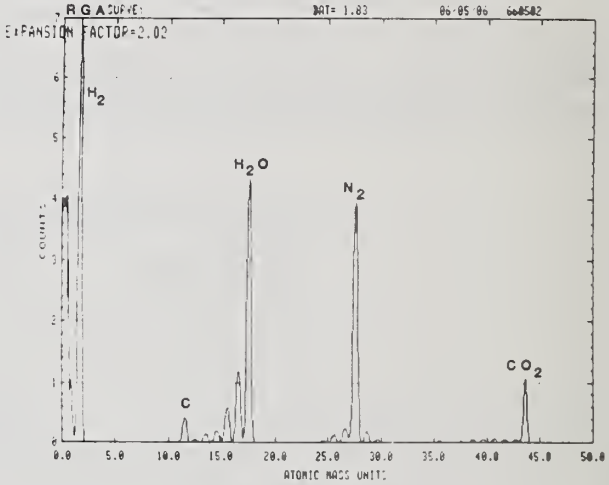

Figure 4. Residual Gas Analysis Survey of the ESCA Vacuum Chamber. ($P \sim 2 \times 10^{-10}$ torr.)

Since a time-averaged ESCA survey can take from one-half hour to several hours, the above ESCA profile/survey procedure does not provide any information on the rate of formation of the water-containing layer on the CaF_2 substrate. A modified sputter-profile procedure was used to determine the time required for the deposition of the water-containing layer. The substrate surface was profiled by ion sputter-etching until the oxygen signal disappeared. Etching was then stopped, and the elemental ESCA peaks were measured as a function of time. Table 2 shows the growth of the oxygen peak as a function of time.

It appears that the oxygen concentration at the CaF_2 surface increases monotonically up to about 30 minutes and stays constant after that time. Comparing the base pressure of the ESCA chamber ($\sim 2 \times 10^{-10}$ torr) to the pressure usually found in a standard coating chamber ($\sim 10^{-6}$ torr), it is evident that a CaF_2 surface will be covered with water within a few seconds of being ion etched in a conventional HV chamber.

It is not possible to determine the thickness of "water-containing layers" without knowing their exact chemical composition. A rough estimate from the sputter-etch rate of CaF_2 indicates that the thickness is less than 20 Å.

In summary, the top surface of a CaF_2 substrate has a chemical composition quite different from that of the bulk substrate. When ion etched, the surface becomes very reactive and combines readily with water present in the vacuum chamber. This water is principally responsible for the presence of oxygen observed at the CaF_2 surface in the ESCA survey data.

Table 2. Oxygen and Carbon Contaminants in CaF_2 as a Function of Time since the end of Sputtering

Elapsed Time (minutes)	Oxygen (atomic percent)	Carbon (atomic percent)
0.0	1.8	1.0
2.3	2.2	0.8
10.1	5.1	0.5
14.0	4.3	0.5
30.2	14.0	1.2
33.9	11.5	1.2
37.7	12.6	1.8
120.0	13.0	0.4
1200.0	13.8	1.7

2. Part II

An ESCA survey (DAT = 120 min) performed at the surface of a ZrO_2 coating produced by ion-beam-sputter-deposition (IBD) detected small (~ 0.5 atomic percent) fluorine peaks along with the common surface contaminant of carbon. The fluorine peaks were still present in an ESCA survey (DAT = 120 min) taken after sputter-etching the coating surface to remove the surface contaminants. This implied that a fluorine-containing component was present throughout the coating. Similar observations were made for another IBD ZrO_2 coating as well as for an electron beam (E-beam) evaporated ZrO_2 coating deposited in a UHV chamber. There did not appear to be a reasonable explanation for fluorine to be present in these films. We began to suspect that two CaF_2 parts (one Optovac CaF_2 substrate and one chunk of CaF_2 source material) which had been placed on the sample carrousel of the ESCA chamber might be the source of a fluorine-containing gas. The CaF_2 pieces were removed from the analysis chamber, and another set of IBD ZrO_2 coatings which had been on the sample carrousel was analyzed by ESCA. Figure 5 illustrates the ESCA survey taken at the surface of one of these IBD coatings. Small fluorine peaks (685 eV and 600 eV) can be observed along with zirconium, oxygen and surface-contaminant carbon. However, the fluorine peaks were absent from the ESCA surveys taken after sputter-etching the surface (fig. 6).

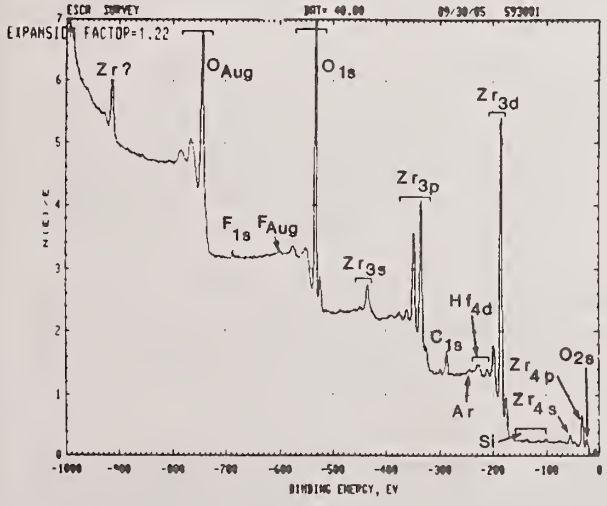

Figure 5. ESCA Survey taken at the Surface of an IBD Coating, Showing Fluorine Peaks (685 eV and 600 eV).

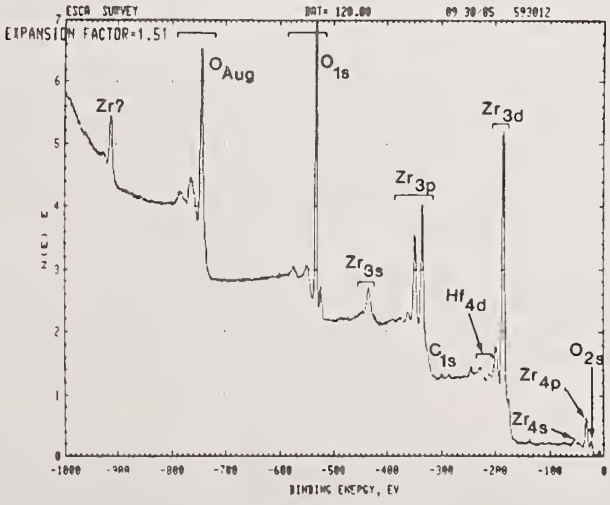

Figure 6. ESCA Survey taken at the Surface of the IBD Coating after Sputter Etching. [Fluorine peaks (685 eV and 600 eV) are absent from the survey.]

Fluorine contamination of the coatings in the ESCA vacuum chamber can be explained as follows. A fluorine-containing gas was released by the CaF_2 samples on the carrousel and adhered by chemisorption to the surface of the ZrO_2 coatings in the chamber; it was observed at the outer surface of each ZrO_2 film. After a ZrO_2 coating had been sputter-etched, the surface became more reactive. The fluorine-containing gas continued to accumulate at the clean surface during the lengthy time it took to collect the ESCA data. When the CaF_2 samples were taken out of the chamber, the ZrO_2 coating samples in the ESCA chamber had already gathered the fluorine component at the surface. The fluorine peaks were absent from the ESCA data taken after sputter-etching the coating surface because of the lack of any fluorine source in the chamber.

The exact chemical composition of the fluorine-containing gas released by CaF_2 cannot be determined by ESCA. However, the most probable guess would be hydrofluoric gas formed by a reaction between the "surface" water and CaF_2. It is recommended that all CaF_2 samples (substrates, source materials, coatings, etc.) be kept in well-maintained desiccators used exclusively for fluorides. Also, ESCA analysis of parts containing CaF_2 should be performed separately from other samples.

We would like to express our appreciation to Dr. C. K. Carniglia for his helpful discussions.

3. References

[1] Gibson, J. W.; Holm, R. T.; Palik, E. D. Internal-Reflection-Spectroscopy Study of Water Adsorbed on CaF_2. Nat. Bur. Stand. (U.S.) Spec. Publ. 509; 1977. 112-115 pp.

[2] Wittberg, T. N.; Hoenigman, J. R.; Moddeman, W. E.; Strecker, C. L. Detection of Oxygen in Calcium Fluoride Laser Window Materials by XPS. Nat. Bur. Stand. (U.S.) Spec. Publ. 509; 1977. 105-110 pp.

Manuscript Received
7-6-87

LIMA in Damage Diagnostics

Ian Laidler, Graham J. Edge and David C. Emmony

Loughborough University of Technology,
Loughborough, Leics. LE11 3TU.
United Kingdom

And

Paul A. Temple
Michelson Laboratory, Physics Division,
Naval Weapons Center,
China Lake, California.

LIMA (laser induced mass analysis) has been used as a damage testing facility incorporating damage detection and analysis of all ionic species generated by laser breakdown and plasma formation on a surface.

The laser radiation is frequency quadrupled Nd-YAG at 266 nm, enabling studies in the UV near to the most important KrF emission.

Preliminary qualitative results give an insight into damage mechanisms and coating weaknesses.

Two prototype coatings, an A.R. and an H.R., have been studied above and below the 50% damage fluence. The state of coating cleanliness is immediately obvious and it is possible to conclude the sources of sub-threshold damage and the extent of coating disruption. The ready availability of this information should led to forthcoming improvements from coating manufacturers.

Key Words: U.V. Damage, surface contamination, threshold.

1. Introduction

LIMA (laser-induced ion mass analyser) was primarily developed for surface analysis. In LIMA a pulsed laser is used to vapourise the surface of a solid, and a time-of-flight mass spectrometer then gives the masses of the ionised fragments in the laser plume.

A commercial instrument (Cambridge Mass Spectrometry Ltd.) was available for damage studies, but, as the machine is part of a contracting surface-analysis facility run by Loughborough Consultants Ltd., no modifications or alterations to the equipment could be contemplated. The basis of the laser-damage tests to be described centered around mass analysis of materials ejected from individual irradiation sites. Here, measurements were made in an attempt to distinguish between mass spectra associated with events that occurred at laser energies well below the 50% threshold energy and spectra associated with laser energies well above the 50% threshold.

Previous damage frequency work by Porteus, et. al., has developed a model where damage is initiated at individual sites. These sites exhibit their own unique "damage threshold" and surface density. The hypothesis we have tested in the work reported here is that at least some of the low-threshold sites might be sites of film contamination and that the contaminant would be revealed by the mass spectra of these sites.

It was anticipated that damage that occurs above the 50% level should show different characteristics from those below in terms of mass spectra if impurities are the cause of below-threshold damage. This paper explores qualitatively the differences between above- and below-damage threshold mass spectra in an attempt to identify the sources of damage in a number of thin-film-coated components.

2. System Description

The principal components of the LIMA instrument are shown in figure 1. A Nd:YAG laser is Q-switched and frequency quadrupled to 266 nm. The laser pulse is focused by a Cassegrain optical system to a spot size of 1 to 3 μm on the target surface. This allows the ions to be extracted along the axis of the exciting laser beam. The target is enclosed in a UHV chamber that is coupled to the time-of-flight mass spectrometer. In principle, the instrument is an integrated damage test facility; however, the spatial profile of the laser beam at the target surface has not been measured, and the laser pulse energy is not known absolutely. A beam splitter and photodiode allow the relative pulse energy to be determined. The small (≈1 μm) interaction area is ideal for laser damage measurements of this type, as it allows us to search the sample surface for individual defect sites. By contrast, with large spot damage measurements, one would choose a spot large enough that many sites of all types would be included in the spot.

The mass spectrometer employs a folded flight path with an electrostatic mirror to compensate for the different energies of ions with the same mass. Ions are accelerated by a potential V of ≈ 1.5kV before entering the flight tube of the spectrometer. A singly ionised ion will acquire an energy $eV = \frac{1}{2}mv^2$. Thus the velocity of the ion $v = \sqrt{2eV/M}$ or $v \propto M^{-\frac{1}{2}}$. Therefore, the time of flight is $\propto M^{\frac{1}{2}}$. The electrostatic mirror essentially removes velocity dispersion, and a 17-stage electron multiplier detects the ions. The multiplied ion current is recorded on a high dynamic range (10-bit) transient recorder and is subsequently processed by a microcomputer.

Only those ejected particles that are ionised by the laser are detected. A useful addition to the LIMA device would be a plume ioniser. In the series of measurements reported below, each site was irradiated once and then the sample was translated to a new site. Measurements were made on a 100 x 100 μm grid.

3. Data Interpretation

The instrument has a claimed sensitivity of 1 ppm for atoms in the vapour plume. However, the relative abundance of different ions is not directly given by the ion current because of different ionisation potentials of different atoms and how they are chemically bound. Figure 2 is the mass spectra of an AR coating of alumina (Al_2O_3) and cryolite (Na_3AlF_6) on a fused silica (Spectrosil B) substrate.

The spectra have three main features: (1) the presence of doubly-ionised atoms. These appear as ion peaks at one-fourth the flight time of singly-ionised atoms; thus, M is their apparent mass (e.g. C^{++}, O^{++} and F^{++}); (2) isotopes that are easily resolved and their relative abundance preserved; and (3) a negative shift in the DC level that follows a large ion current for a particular ion, e.g. figure 2. The large O signal saturates the multiplier and the H_2O peak is only just visible. This last feature can pose a problem in detecting ions that are present in small quantities and that possess masses larger than those ions that are abundant.

An aid to spectra recognition is the ability to resolve isotopes, for example, Si has peaks at M = 28, 29 and 30. The peak heights are in good agreement with the abundance ratios of 92.2, 4.2 and 3.1% respectively, for these isotopes.

Figure 3 represents the same sample (different site) and same incident laser energy. The spectrum is much weaker. The difference is associated with water seen in figure 2. No H or H_2O ions are visible in the second spectrum. The ion with mass 65 AMU might be interpreted as an isotope (30.9% abundance) of copper. However, the mass of the most abundant isotope is 63, which is absent. It is likely that the peak at 65 is due to a fragment Na-NaF.

4. LIMA Diagnostics on an HR Coating at 266 μm

An HR coating designed for 45-deg incidence at 266 μm was the first to be investigated. The mirror comprised $\lambda/4$-thick alternate layers of ZrO_2 and SiO_2 with a $\lambda/2$-SiO_2 overcoat. The damage threshold was determined by monitoring the photodetector voltage and ion current. In this way, the relative laser pulse energy needed to damage the coating with a 50% probability was determined. Convenient laser energies corresponding to 75% and 17% damage probability were used to carry out a sytematic survey of the coatings, corresponding to above- and below-threshold laser fluences, respectively. A series of sites were irradiated above and below threshold, and the data were recorded at each damage occurrence.

The table represents the occurrence of different ions for the two damage regimes. Zirconium dominates the data despite the $\lambda/2$-SiO_2 overcoat, which must have been destroyed to expose the ZrO_2 layers. Hydrogen and oxygen imply the presence of water in the coating, and LIMA experience with a variety of samples has shown that the detection of sodium and potassium in similar proportions is characteristic of human contamination.

Figure 4 shows the below-damage-threshold spectra of a site where water is present, and figure 5 shows another site where damage was initiated by human 'debris'. For comparison, figure 6 is a site exposed above the damage threshold and shows only zirconium-based ions. Note that the ion current (approximately given by the area under the curve) is smaller than in the two previous figures. This indicates that the plasma plume and therefore the damage event is weak. This is surprising considering that the above-damage fluence is about an order of magnitude higher than in the below-damage cases.

The presence of silicon in figure 4 (that is, where water is associated with damage) is in contrast to the other two spectra. The difference may be due to damage penetrating the silica substrate or indeed being initiated there; whereas the damage in the other two cases may be associated only with the outer layers where the low ionization rate of the silicon does not lead to an ion peak. Water may be present locally in the substrate following polishing procedures.

Haffnium was found in many of the damage sites, though only in small quantities. The size of the haffnium signal was generally proportional to the zirconium signal. This element is thought to be a common impurity of zirconia and may have been introduced at the source stage. The raw material was 99.99% pure.

In the table it can be seen that aluminium and aluminium oxide occurred at four sites. In three of these, no zirconium was observed. Two of these sites were above the threshold for the material. These damage sites are believed to be associated either with Al_2O_3 flakes on the coating - the flakes attributed to previous coating runs or to Al_2O_3 polishing residue. It was later confirmed by the manufacturer that this chamber is also used for Al_2O_3 coating depositions. Furthermore, it seems that the Al_2O_3 initiated plasma shielded the coating from further damage.

The initial substrate preparation had involved diamond paste, Al_2O_3 polish and SrO_2 final polish - the latter as a progressively watered barnsite slurry. No evidence of barnsite was found, although the slurry may have been the source of the water seen in figure 4.

5. Lima Diagnostics on a 248 nm AR Coating

The second coating to be investigated was a multilayer Al_2O_3/Na_3AlF_6 (cryolite) stack on a Spectrosil B substrate designed for normal incidence. The preliminary threshold determination and subsequent above and below-threshold measurements were as previously described. Figure 7 is a typical above-damage-threshold spectrum for this coating.

The following additional points could be noted:

(1) the coating contained a greater number of metallic impurities than the previous high reflector. They included Ti, Ca, Fe, Mo and Ce. Cerium also appeared as the oxide. Potassium was present, as well as sodium, which was associated with the cryolite, and masked any human contamination. These impurities were probably grown into the coating. Two consecutive sites gave large Ti signals, indicating a fairly large particle, possibly a TiO_2 flake from a previous coating run. Mo was found in many of the spectra and probably came from the source boat;

(2) K and Ca always occurred together, though generally in small quantitites so that any semi-quantitative assessments could not be made;

(3) the size of the Si signal is, as mentioned earlier, related to substrate damage; it was found to be higher whenever (a) water (H_2O) or (b) Ce and its oxide were present;

(4) Ce was observed in a larger proportion of the above-threshold spectra than in the below-threshold breakdowns. It is therefore concluded that Ce/CeO is localised deep in the coating and, in view of (3), in the substrate surface. Cerium oxide was used in polishing and its presence at the substrate surface is probably due to its use in the preparation of the substrate. Whenever Ce was observed without the oxide, the ion signal was very weak, possibly indicating that the substrate did not damage. It was possible to test this hypothesis by repeated irradiation

of the same site. In figure 8 (corresponding to the first shot) the total ion current is very small - no other ions being recorded other than Na, Al and Si. However, by the third shot on the same site (figure 9) damage progressed to the substrate, and a large Ce signal as well as a much higher total ion signal are evident.

A further series of experiments on areas near the edge, centre and the other edge on the common diameter was carried out to investigte the reproducibility of the LIMA technique. The main findings were as follows:

(1) the relative heights of the Na, Al and F approached constant levels as the laser fluence increased. This is in agreement with the idea that the relative abundances of these atoms is constant for the complete coating structure;

(2) all above-threshold spectra showed Si, indicating substrate damage. However, below-threshold events were consistently free - this element indicating that damage was initiated in or on the coating;

(3) water was associated with very large above-threshold events and was present across the sample;

(4) no new information was obtained concerning Ce. It would seem that a series of precoating tests would be worthwhile.

(5) the below-threshold events generally were associated with small ion currents, except in one instance when Ti was detected;

(6) the probability of damage at below-threshold levels was less at the centre than at the edge.

6. Conclusions

The systematic scanning of an optical surface at below-threshold fluences has allowed the identification of damage sources. In particular, polishing residues and water were seen to be associated with damage on a number of occasions. Human contamination can be detected by the observation of K and Na ions. Surface contamination of coatings by small flakes of material from previous coating runs has been observed.

Although the LIMA (laser-induced ion mass analyser) scans are quite qualitative, they do allow the determination of defect sites, a large area of irradiation at the same fluence may indicate impurities, using only a few shots necessary routinely to test components.

Acknowledgments

One of the authors (IL) would like to acknowledge the award of a research studentship by SERC in collaboration with BDH (Chemicals) Ltd. The work was carried out with the support of the Science and Engineering Research Council, UK, US Office of Naval Research and the US Air Force. This work was carried out while PAT was a visiting scientist at LUT. He would like to acknowledge the support of NWC and Dr.Arthur Guenther of AFWL, Kirtland AFB in this project.

7. References

[1] Porteus, J.O.; Franck, J.B.; Seitel, S.C.; Allen, S.D. Defect characterisation of Optical Surfaces using pulsed laser damage methods. Opt. Eng. 25: 1171-1176, 1986.

SITE	Zr/ZrO	Si	Na	K	Hf	O	H	Al/AlO
			ABOVE THRESHOLD IRRADIATION					
1	XXX	XX	X			X	X	
2								X
3	XX							
4	XXX	X	X					
6	XXX	X	X	X				
8								X
9	XX							X
10	XXX	X	X	X	X			
11	XX							
12	XXX	XXX	X		X	XX	XX	
13	XX				X			
14	XXX	XXX	X	X	X	XX	XX	
15	XXX	XX	X		X	XX	X	
16	XX	XX	X		X	XX	X	
			BELOW THRESHOLD IRRADIATION					
28	XXX	XX	XXX	XXX			X	
34	XXX	X	XXX	XXX	X			
46	XX							
47								X
52	X		X	X				
64	XXX	X	XXX	XXX	X			
73	XXX		XX	XX	X			
76	X							
81	XXX	XXX	XXX	XXX			X	
85	X							
86	XXX	XX	XXX	XXX		X	X	
87	XX		XX	XX	X			
93	X							

X = WEAK SIGNAL XX = MEDIUM SIGNAL XXX = STRONG SIGNAL

Table Breakdown of the Spectra for the ZrO_2/SiO_2 H.R. Coating.

Schematic diagram of LIMA 3

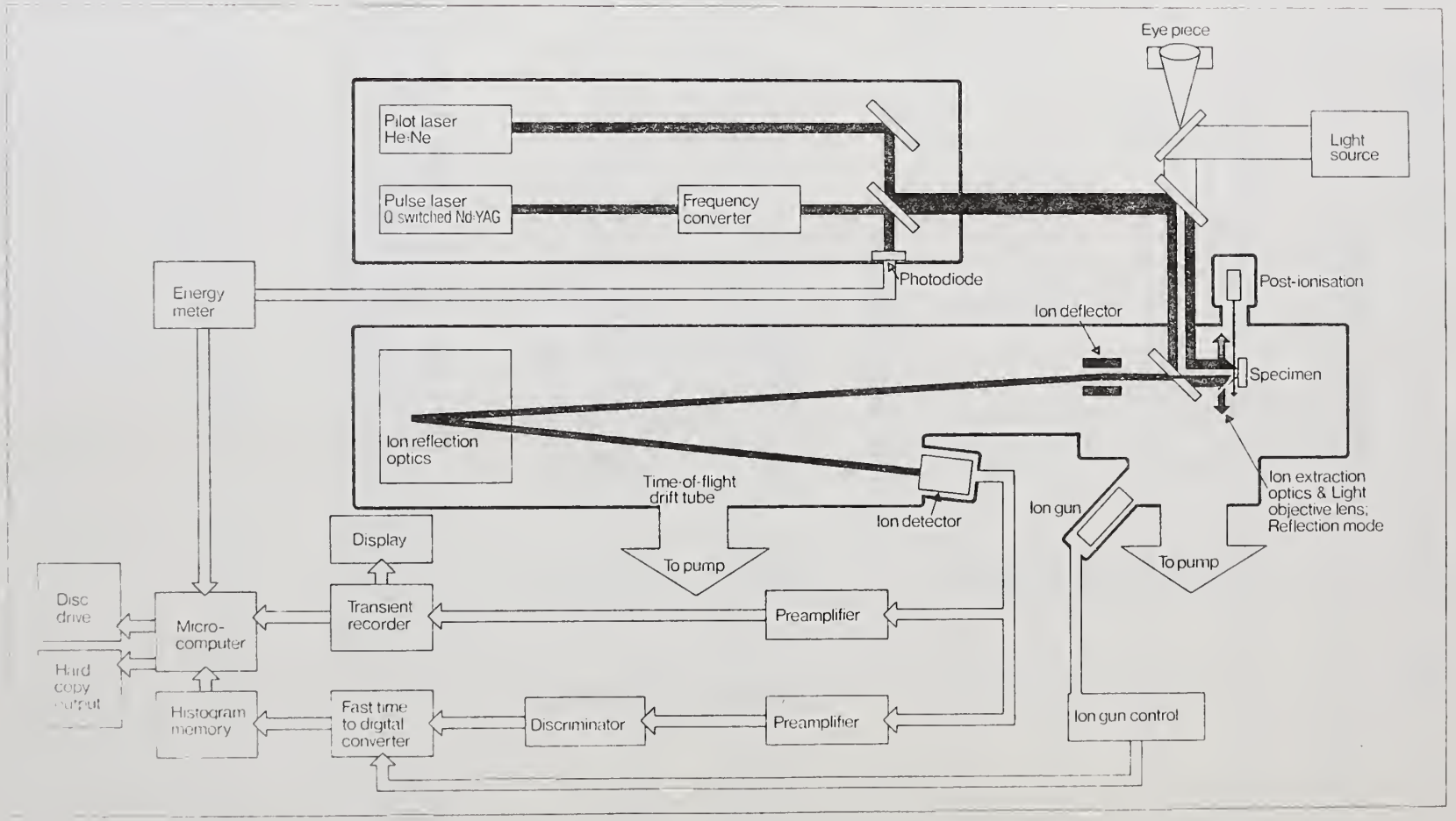

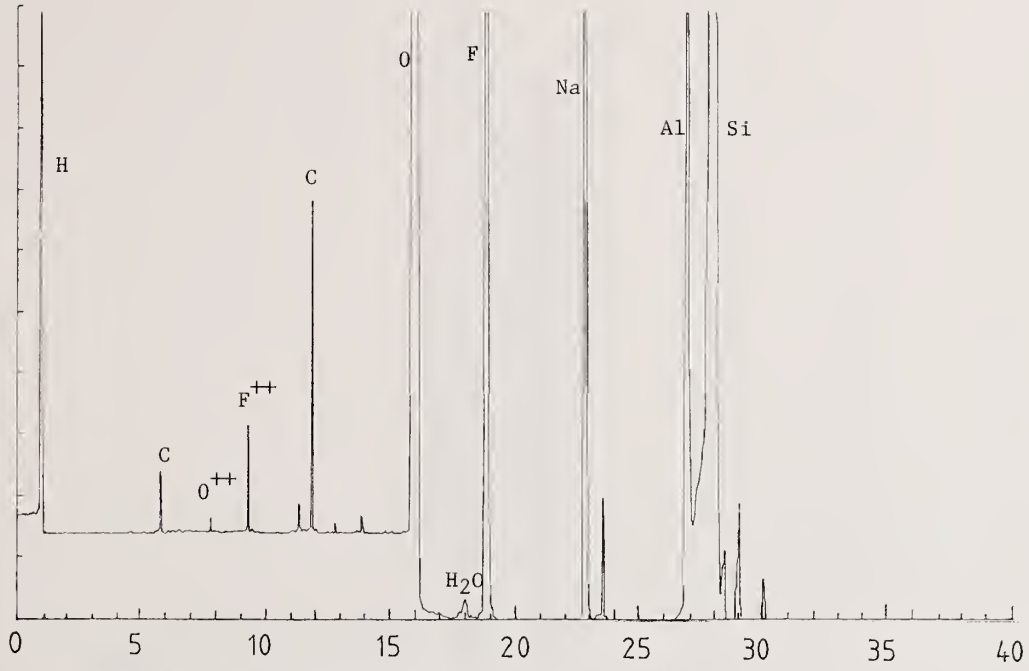

Figure 2 A.R. at 248nm Na_3AlF_6 - Al_2O_3

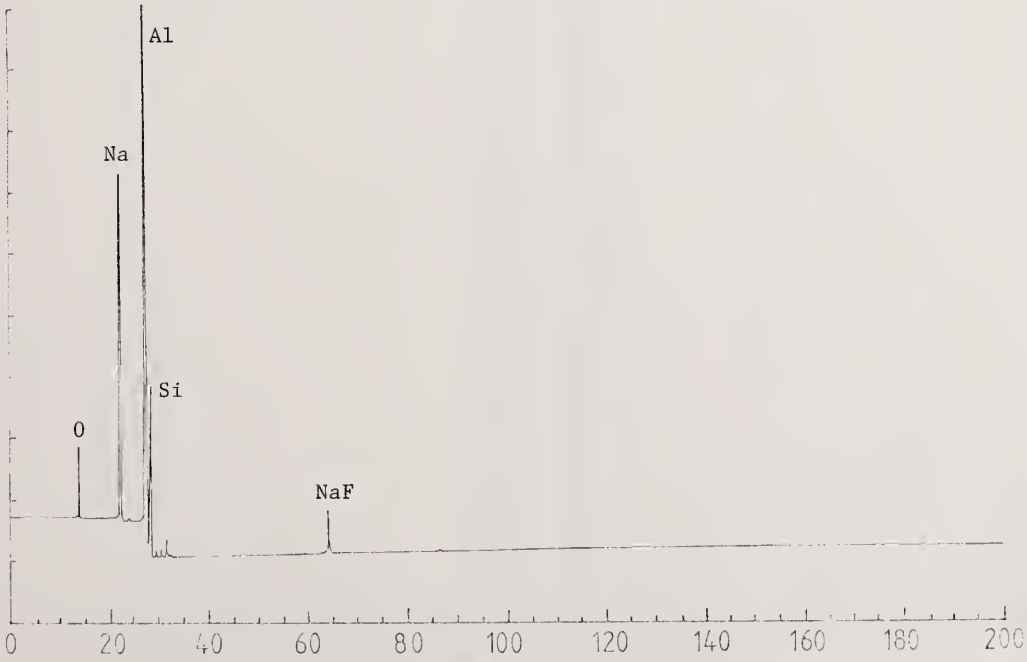

Figure 3 A.R. at 248nm Na_3AlF_6 - Al_2O_3 multilayer on silica

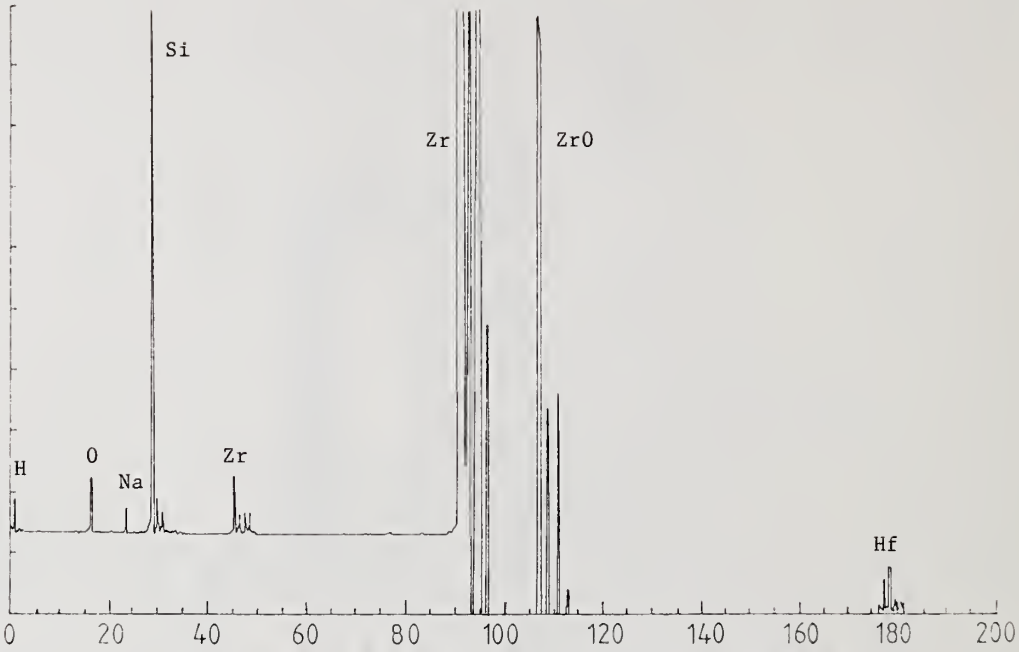

Figure 4 H.R. at 266nm ZrO_2 - SiO_2 low fluence

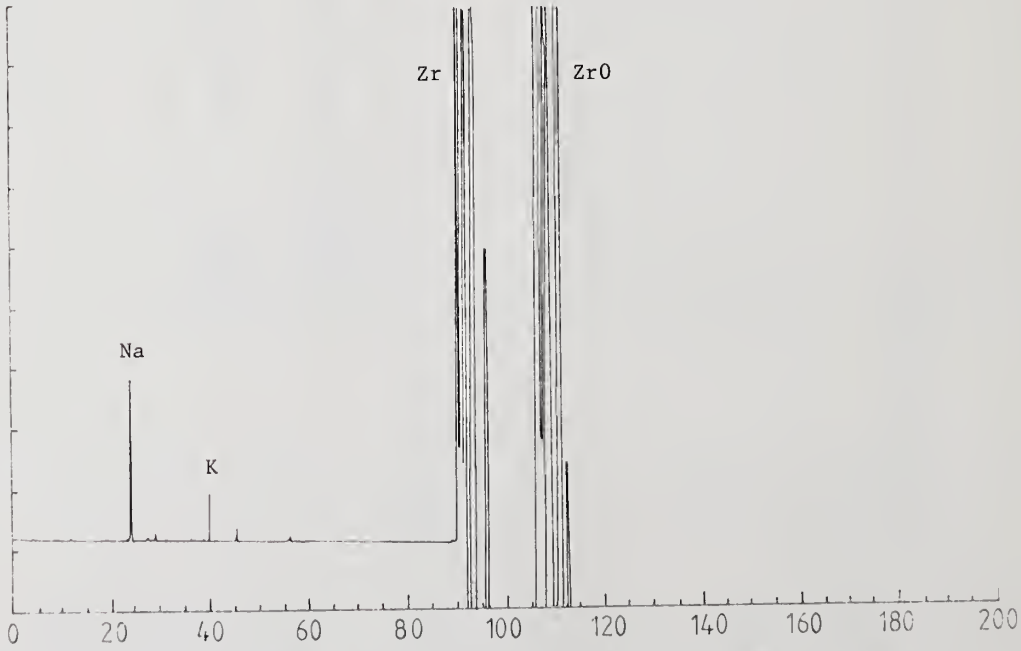

Figure 5 H.R. at 266nm ZrO_2 - SiO_2 low fluence : Human contamination

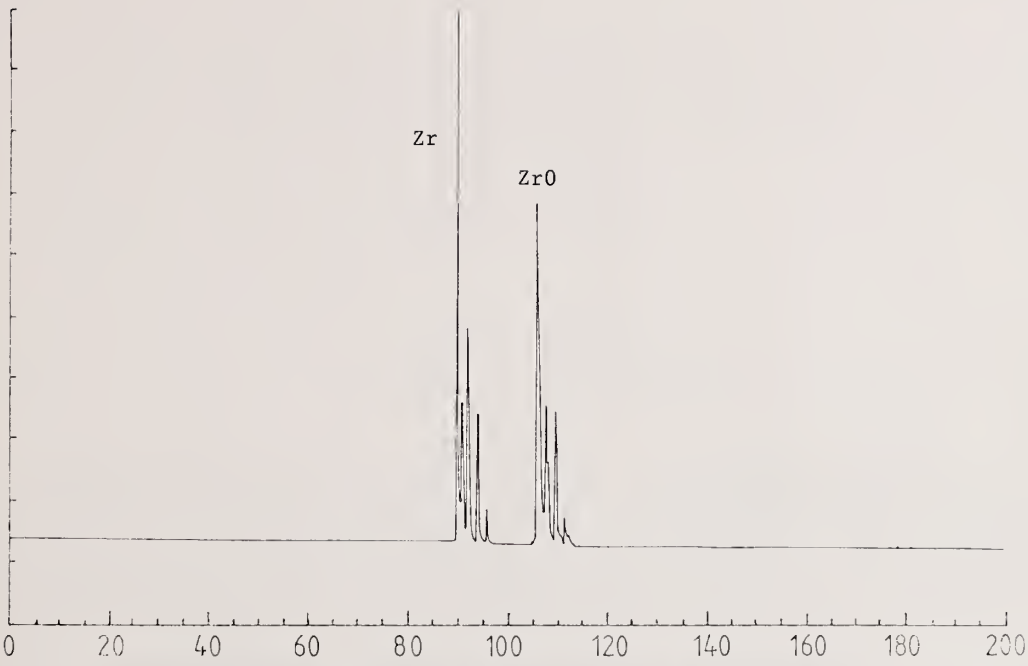

Figure 6 H.R. at 266nm ZrO_2 - SiO_2 high fluence

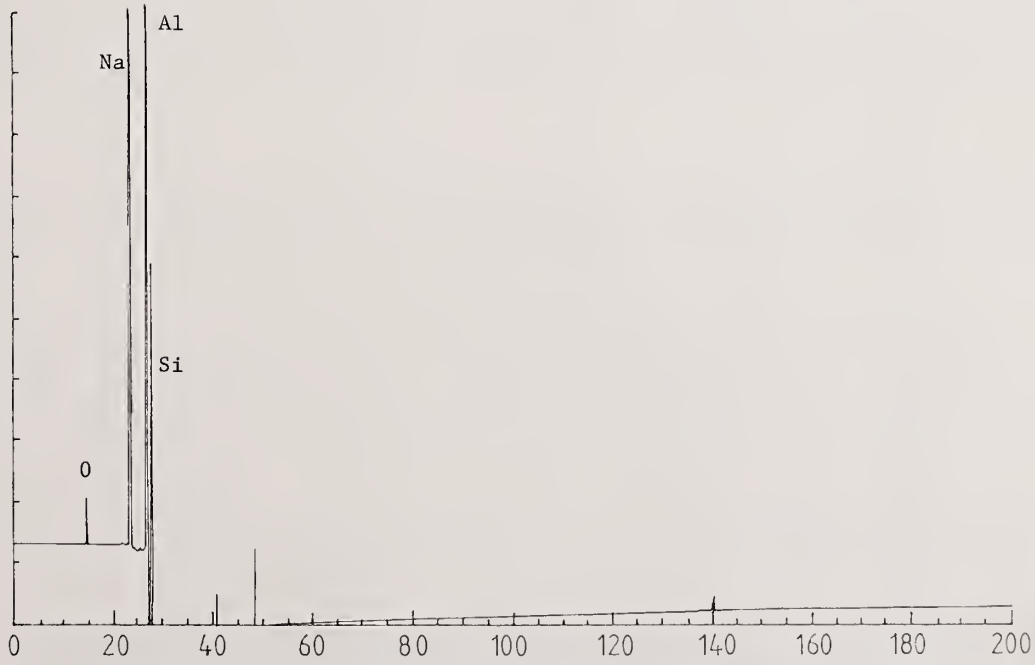

Figure 7 A.R. 248 nm Na_3AlF_6 - Al_2O_3 high fluence

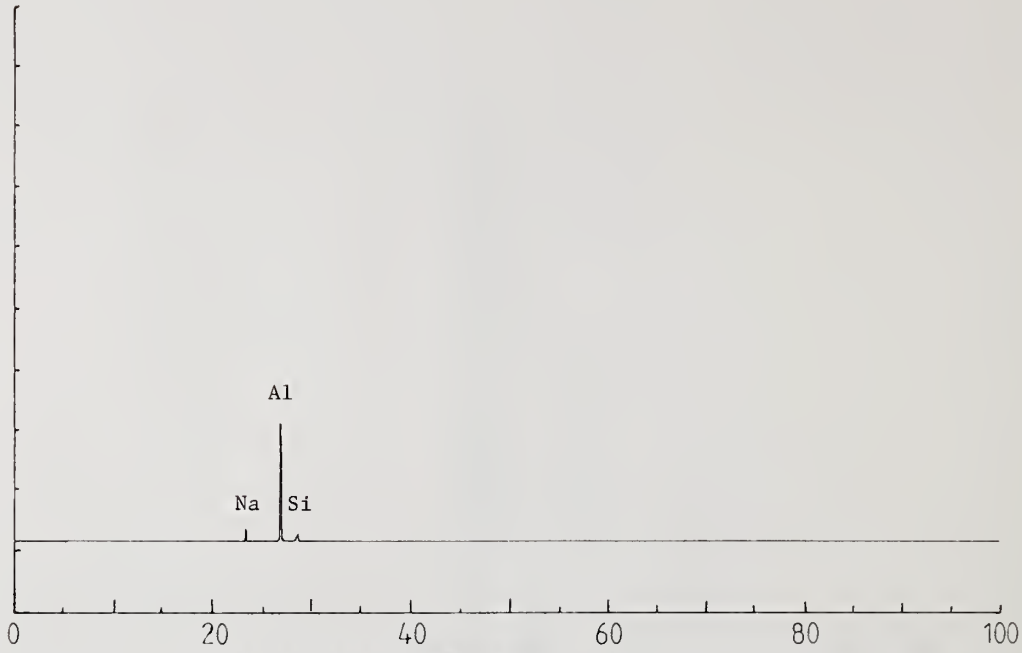

Figure 8 A.R. 248nm Na_3AlF_6 - Al_2O_3 first shot spectrum

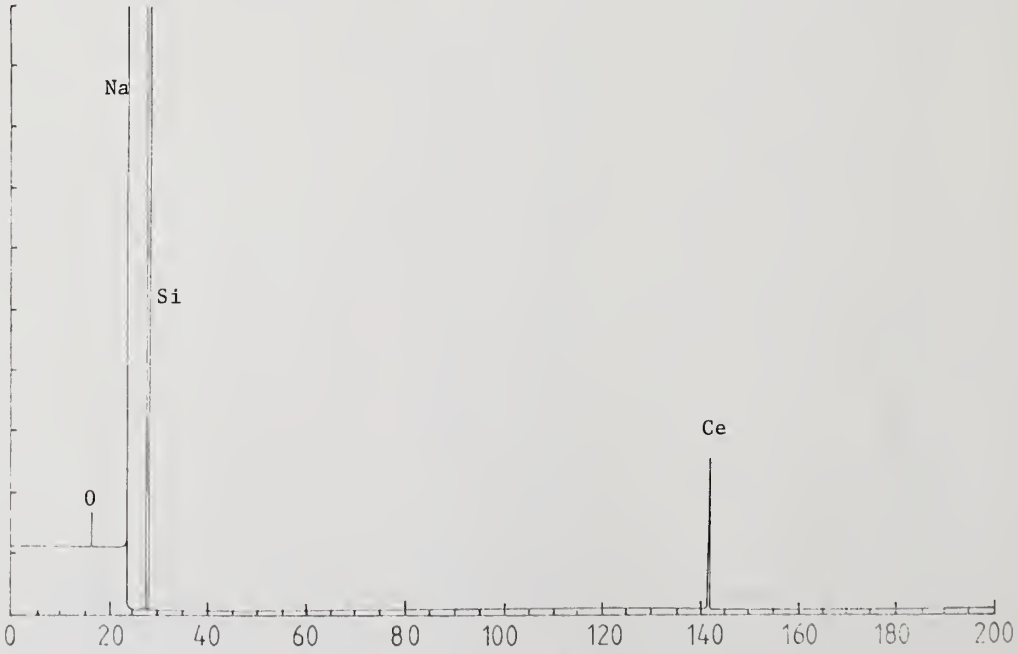

Figure 9 as Fig. 8 third shot spectrum

Manuscript Received
6-5-87

Laser-Induced Damage to Titanium-Doped Sapphire Using 532 nm Wavelength Pulses of 10 ns Duration

S. C. Seitel
Montana Laser Optics, Inc.
Bozeman, Montana 59715

and

L. G. DeShazer*
Spectra Technology
Bellevue, Washington 98004

Abstract

Preliminary laser exposure tests of uncoated, polished titanium-doped sapphire from Union Carbide Corporation are reported. The measured surface damage thresholds varied from ~3 to ~14 J/cm^2, depending on surface finish and sample orientation. The dependence on orientation is not correlated with crystallographic direction. A strong dependence on doping level was not observed. Well polished samples failed by pitting of the surface. On one sample, internal damage was also observed at fluences as low as 7 J/cm^2.

Key words: crystallographic orientation; doping level; laser damage; surface finish; Ti:sapphire; titanium-doped sapphire

1. Introduction

In the course of a materials development program at Spectra Technology, different titanium-doped sapphire (Ti:sapphire) laser crystals from Union Carbide Corporation were found to vary in damage resistance while lasing. As a first step in isolating the causes of this variability, Spectra Technology tasked Montana Laser Optics to determine the laser-induced damage threshold of selected crystals with different growth and fabrication histories. The goal was to determine whether any of the following factors strongly affected the measured damage thresholds: surface finish, doping level, or crystallographic orientation. This information would then be used to plan a more detailed investigation.

2. Samples

Three samples were selected for testing. Some growth and treatment data are summarized in table 1. Sample 2 was used previously in the Ti:sapphire laser studies of Albrecht, et. al. [1].

Table 1. Titanium-doped sapphire samples

Sample	Boule no.[a] (date grown)	Size (mm)	Abs. Coeff. (cm^{-1}) (532 nm)	(800 nm)	Polish	Annealed
2	R37-329-2 (11/84)	7x7x20	1.025	0.125	CORI[b]	Yes
6	R37-515-1 (6/85)	10(dia.)x15	0.97	0.055	Virgo[c]	No
11	R11-556-2	8x10x23	0.335	0.02	UCC[a]	Yes

[a]Union Carbide Corporation, Washougal, WA 98671; [b]Crystal Optics Research, Inc., Escondido, CA 92025; [c]Virgo Optics, Port Richey, FL 33568

*Presently with Solid State Laser Associates, 16150 NE 85th. St., Redmond, WA 98052

3. Experimental Arrangement

The laser damage test system, shown schematically in figure 1, has been described previously, along with the threshold measurement procedure [2]. The experimental parameters used in this study are summarized in table 2. The polarization of the laser beam was always set parallel to the optic axis (c axis) of the sapphire samples, except for the case of propagation along the c axis. This is the polarization direction used in pumping Ti:sapphire lasers.

Table 2. Test parameters

Wavelength:	532 nm
Pulse duration (FWHM):	10 ns
Repetition frequency:	10 Hz
Temporal modes:	SPO
Spatial modes:	TEM_{oo}
Spot size (FWI/e^2):	500 μm
Incidence angle:	0°
Polarization:	Linear

4. Surface Damage Morphology

On well polished surfaces, damage at threshold was one or more small pits at the point of maximum intensity in the beam footprint. At higher fluences, these pits were accompanied by visible light emission and noise. On successive pulses, they grew in size, leading to catastrophic cratering of the surface. Figure 2 shows the evolution from small damage pits to larger craters.

5. Damage Thresholds

The measured surface damage thresholds appear in table 3. Here "damage" refers to any permanent surface change observable at 150X in Nomarski or darkfield. "Threshold" refers to the least fluence which caused damage. The "spread" is the width of the damage/no damage overlap region, divided by the threshold fluence. Crystal orientation and finish are discussed in section 6.

Table 3. Surface damage thresholds

Sample	Absorption (cm^{-1})	Finish (rank)	Crystal orientation	Threshold (J/cm^2)	Spread
2	1.025	1	m	13	0.5
6	0.97	2	c	12	1.2
		5	a (15°)	11	- 0.1
			m (45°)	< 3	> 1.
			a (75°)	3	- 0.3
			m (105°)	8	0.3
11	0.335	3	m	14	0.3
		4		10	~ 1.

Although the experiments reported here were intended only to determine surface damage thresholds, bulk failures occasionally were observed. Table 4 contains the lowest fluence (measured at the entrance face) for which bulk failure was observed anywhere within a sample. The fluence in the interior was less, due to Fresnel reflection and beam divergence. Thus the "true" bulk thresholds cannot be less than the tabulated values.

Table 4. Bulk failures

Sample	Orientation	Failure obs. at (J/cm^2)
2	m	21
6	c	13
	a	7
	m	9
11	m	11

6. Factors Affecting Threshold

The absorption coefficient at 532 nm is a direct measure of titanium dopant concentration (1 $cm^{-1} \approx 0.7$ wt. %). From table 3, comparison of samples 2 and 11, which had similar surface finishes and crystal orientations, suggests that "low" concentration crystals are not markedly different in damage resistance from "high" concentration crystals.

Before testing, the surfaces were examined microscopically for quality of surface finish in the areas to be tested. A subjective ranking from 1 ("best") through 5 ("worst") was assigned, based on the presence and severity of residual polishing marks and handling marks. Sample 2 exhibited an essentially featureless surface, and was ranked 1 (fig. 2). The cylindrical surface of sample 6 was least well polished, with embedded polishing compound observable (fig. 3). Sample 11 had two distinctly different regions on one face (figs. 4,5), which were assigned different rankings. From the regular, repeated occurrence of the rectangular blemishes in figure 5, it appears that the surface degradation is associated with the crystal itself. One possibility is that the imperfections are due to local precipitation of TiO_2 from the melt [3]. From table 3, there is a general trend toward lower threshold with "poorer" surface quality. This is especially evident in the two regions of sample 11.

As shown in figure 6, sample 6 was cut with its cylindrical axis parallel to the crystal c axis. The a and m crystallographic directions were are perpendicular to the c axis and coincided with particular radial directions (established by X-ray diffraction) which were separated by 30°. By rotating the sample appropriately, the crystal could be exposed alternately along an a or m direction, in steps of 30°. The electric vector was always parallel to the c axis in these tests. From table 3, the damage threshold varied from ~3-11 J/cm^2 as the sample was rotated. This variation did not coincide with the crystal a,m directions. This behavior was unexpected because the crystal hardness does have a large variation correlated with the a,m directions [4].

7. Conclusions

For the particular irradiation conditions of this study, titanium-doped sapphire surface damage thresholds can range from as low as ~3 J/cm^2 to as high as ~14 J/cm^2, depending on surface finish and sample orientation.

The surface damage threshold does not appear to depend strongly on doping level. The surface damage threshold does depend strongly on the quality of the surface finish, with subjectively "poorer" surfaces having lower thresholds. The surface damage threshold also varies with angular orientation, but the variation apparently does not coincide with the a and m crystal axes.

8. References

1. L. G. DeShazer, G. F. Albrecht, and J. F. Seamans, "Tuneable Titanium Sapphire Lasers", in High Power and Solid State Lasers, ed. W. W. Simmons, Proc. SPIE 622, pp 133-141 (1986)

2. S. C. Seitel and E. A. Teppo, "Damage Testing in Optics Production and Procurement", Seventeenth Annual Symposium on Optical Materials for High Power Lasers (Boulder Damage Symposium), Boulder, CO, 28-30 Oct 1985 (proceedings in press)

3. K. Nassau, "Heat Treating Ruby and Sapphire", Gems and Gemology, pp. 121-131 (Fall 1981)

4. L. G. DeShazer and G. F. Albrecht, to be published

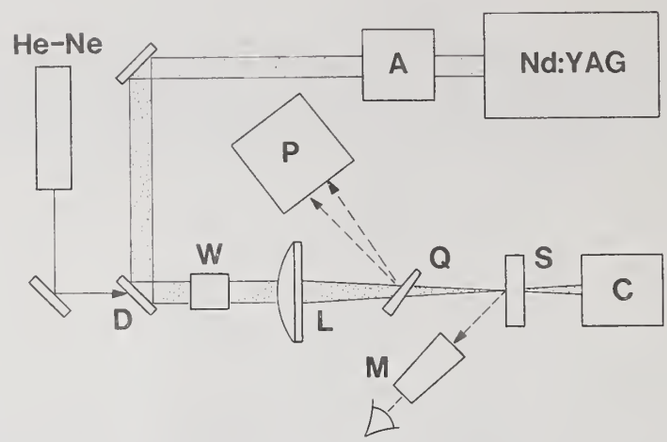

Figure 1. Laser Damage Test System. A, variable attenuator; D, dichroic; W, polarization rotator; L, focusing lens; Q, wedged beam splitter; P, spatial and temporal diagnostic package; S, test sample; M, observation microscope; C, calorimeter.

Figure 2. Typical Damage Site Above Threshold. 250X Nomarski micrograph of Sample 2 showing evolution from small damage pits through larger damage pits to crater. Large crater is approximately 100 μm in diameter. Note the high quality surface finish.

Figure 3. Sample 6 Surface (cylinder wall). 250X Nomarski micrograph, showing poor surface finish.

Figure 4. Sample 11 Surface, "Good" Region. 250X Nomarski micrograph showing residual polishing marks. Note fine structure approximately parallel to c axis.

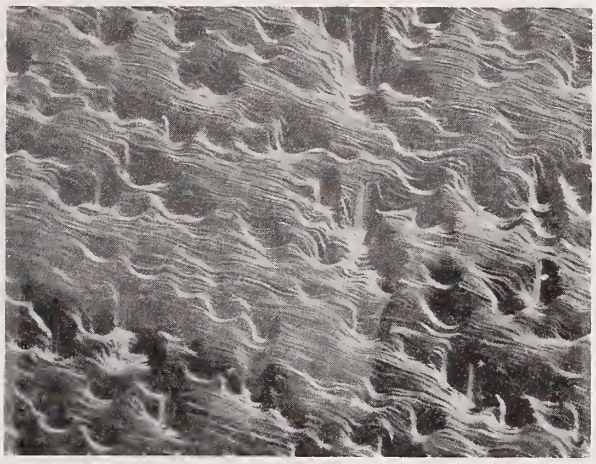

Figure 5. Sample 11 Surface, "Bad" Region. 250X Nomarski micrograph showing distortion of fine structure.

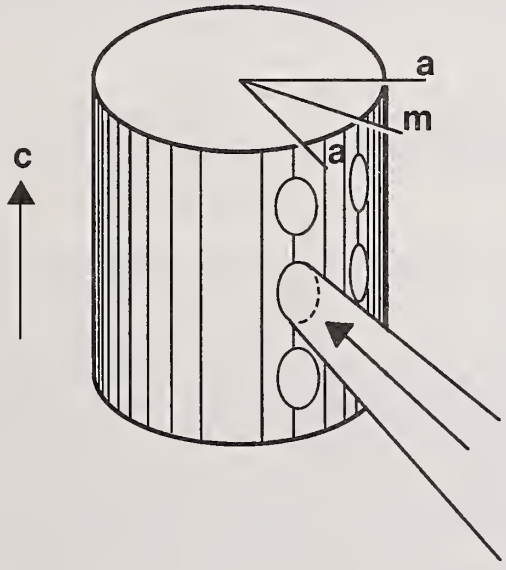

Figure 6. Crystallographic Orientation Test Geometry.

Manuscript Received
3-14-88

High-Energy Pulsed Laser Beam Profiling System

D. B. Nichols and P. D. Texeira

Boeing Aerospace
Seattle, WA 98124

and

T. M. Donovan
Naval Weapons Center
China Lake, CA 93555

Recent high-energy laser beam profile data have shown the need for complete shot-by-shot spatial information in the quantitative assessment of repetitively-pulsed optics damage results. A system designed for spatial profiling of repetitively-pulsed beams is described here. The configuration provides for data processing from a 16 x 16 pyroelectric array (Spiricon), through analog-to-digital conversion (Datel), frame grabbing, and computer storage and display (Hewlett-Packard). Design solutions are illustrated for the electromagnetic noise problems associated with high-energy laser environments. The system has been demonstrated in the high-current environment of a large flashlamp-initiated pulsed chemical laser. The system is designed for use in the measurement of both the spatial profile incident on an optical component, and the transmissive wavefront distortion introduced by the component, under high power loading.

Key words: electromagnetic noise; fiber optics; profile data processing; pyroelectric array; repetitively-pulsed diagnostics; two-dimensional array; wavefront distortion.

1. Introduction

In the measurement of damage thresholds for pulsed laser optics, two critical factors govern the accuracy of the result. One is the absolute energy per pulse; the other is the spatial distribution of that energy on the sample.

Good definition of the spatial profile is always a major concern, because threshold fluences depend on the square of the effective spot diameter. But a particular effort is required with large lasers because their beam profiles often lack convenient spatial symmetries, and, in the case of repetitive pulsed testing, may even change significantly from shot to shot. A further difficulty is the severe electrical-noise environment of high-power laser laboratories. Typical sources are the high-voltage switching and high-current pulses associated with electron guns or high-energy flashlamps.

The instrumentation described here was designed to address these problems, and provide shot-by-shot spatial profile data in two dimensions, at rates to 100 Hz, in a severe electromagnetic environment. The system provides 16 by 16 spatial resolution, and is usable over a very large range of laser wavelengths. The immediate application is with pulsed lasers having pulse lengths in the microsecond range. Other applications will include the measurement, in real time, of both transient and permanent Strehl ratios for pulse-loaded optical components.

This work was supported by SPAWARS SYSCOM PMW-145, through the Naval Weapons Center, China Lake, CA.

2. Components and Configuration

The detector element of this system is a 16 x 16 pyroelectric array made by Spiricon, Inc. The active area is 1.28 cm on each side, and it operates at room temperature. The spectral response is shown in figure 1.

Data rate requirements are illustrated in figure 2 for a 50-Hz example. The first two pulses of a burst are indicated at time = 0 and 20 ms. Pyroelectric detector temperature, observed as voltage response, is shown; cooling occurs between each incident pulse. This 20-ms interval sets the overall rate requirement on data-collection and processing for the whole system.

The lower curve of figure 2 shows the output of the array unit. Each pixel is read out in analog serial form at 4 μs per pixel, giving one full frame readout of 256 elements in 1 ms (nominal). One-millisecond readouts are indicated in figure 2 by R (Reset), P (Prepulse), and D (Datapulse). The Reset serves to clear initial resident values to zero, and Datapulse minus Prepulse is the increment due to the main laser-pulse event. The shortness of the 1 ms readout time interval, relative to the 20 ms interpulse time, assures good incremental temperature sampling on the recursive cooling curve of figure 2.

A Datel Intersil ADC-817MR analog-to-digital converter provides both the required rates and 12-bit resolution. Subsequent parallel data processing then requires two 8-bit bytes per element, or 512 bytes per frame. During each frame readout, then, 8-bit parallel data must be stored somewhere at the rate of one-half megabyte per second. Commercial frame grabbers were considered, but we eventually incorporated this function into the system computer, which is a Hewlett Packard 236 (formerly designated as the HP 9836). These rates require Direct Memory Access.

Figure 3 also shows a separation, typical in large laser facilities, between the laser area and the control area. Drivers are provided for these long cables. The EMI problem is addressed by inserting an 8-bit parallel optic-fiber isolation station between the computer and the primary expected sources of EMI--the laser itself and the long connecting cables.

Electromagnetic noise can still access the test-area elements of this system via the pretrigger cable from the high power laser, or by coming back along the transmission cables which go to the control room. These two paths are eliminated in the revised configuration of figure 4, by the introduction of a second fiber optic isolation station. In this arrangement the long transmission lines are isolated from the data processing functions at both ends.

A software package was developed for data handling within the HP-236. This package began with a Spiricon program, "Graphics 3D." This program provided for two- and three-dimensional screen displays, with variable scaling, 90-degree rotations of the perspective plots, hardcopy printouts, and some disk storage capability. Further custom software for this application has been developed by Boeing, and provides for extended 2-dimensional displays, fluence integration for total-pulse energy, contour plots of the profiles, and several printout options. Strehl ratios can also be computed. Pulse-by-pulse analysis of key profile parameters is given, for multiple-pulse laser runs.

The system has been demonstrated at repetitive pulsed rates near 50 Hz. It has passed electromagnetic noise tests in the Boeing PHOCL-10 DF laser laboratories, operating in close proximity to multiple flashlamp circuits which carry tens of kiloamps in microsecond pulses.

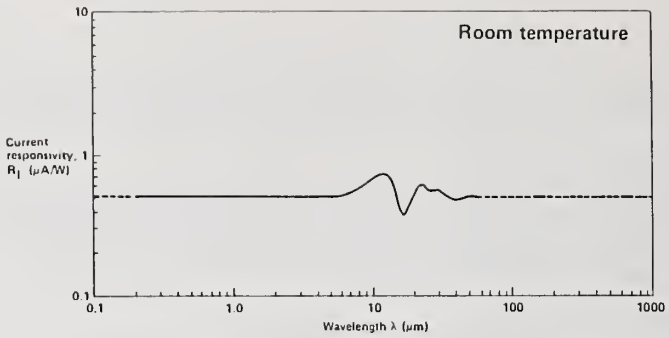

Figure 1. Spectral response curve of pyroelectric array. (Courtesy of Spiricon, Inc.)

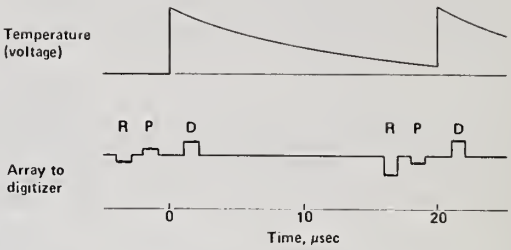

Figure 2. Array readout sequence (lower curve) related to detector temperature curve due to 50 Hz pulsed laser energy deposition.

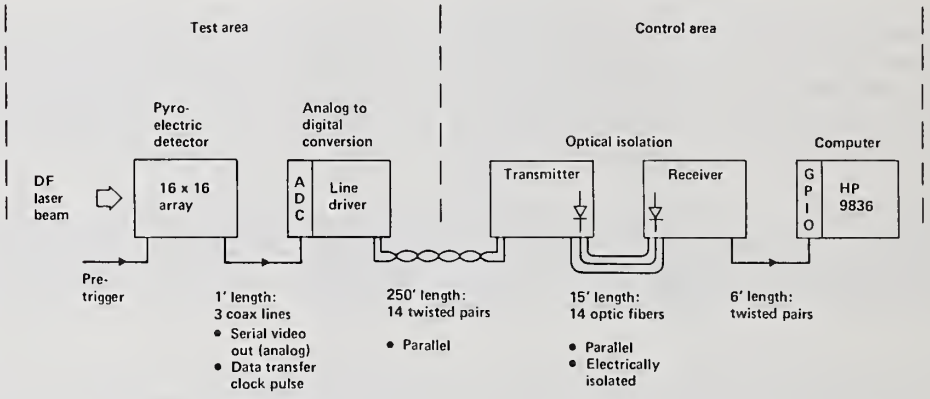

Figure 3. Beam profiling system with initial fiber optic electrical isolation.

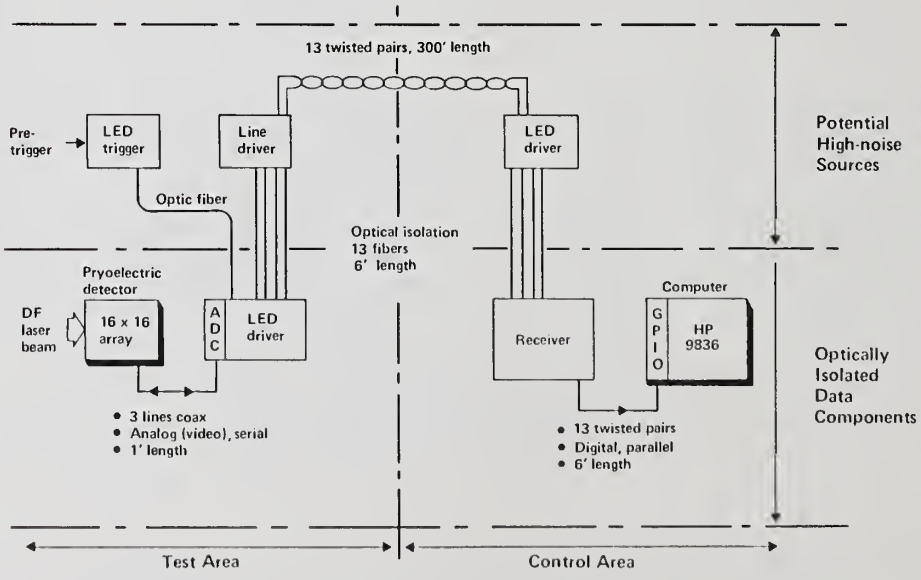

Figure 4. Beam profiling system with extended fiber optic electrical isolation.

Manuscript Received
5-13-87

Performance Characteristics of a Beam Profiling System Consisting of Various Solid State Imaging Devices and an 8-Bit Image Processor

Robert M. O'Connell*

Electrical and Computer Engineering Department
University of Missouri-Columbia
Columbia, MO 65211

Alan F. Stewart

AFWL/ARBD
Kirtland, AFB, NM 87117-6008

A beam profiling system that interfaces an 8-bit image processor to either of two self-scanned solid state area array cameras is described. Results of measurements to characterize the performance of the camera sensors, a frame transfer charge coupled device (CCD) and a charge injection device (CID), are presented and discussed. The CCD camera is shown to have the advantages of simpler interfacing requirements, greater access to the image processor software, better dark current pattern noise, and wider spatial frequency bandwidth. The CID camera may have wider dynamic range and better photosensitivity pattern noise, but further measurements of these properties are warranted.

Key Words: beam profiling; charge coupled device; charge injection device; dynamic range; fixed pattern noise; modulation transfer function.

1. Introduction

This paper presents recent progress in the development of a real time beam profiling system to be used in the Air Force Weapons Laboratory (AFWL) Laser Damage Laboratory [1]. The objectives of this development effort are real time operation with adequate spatial resolution and wide dynamic range. In this report we present the results of measurements made to evaluate the use of two solid state imaging devices (SSID) in the system. SSID's are attractive for beam profiling because they do not incorporate a photocathode and scanning electron beam. Thus many problems associated with conventional camera tubes, such as geometric distortion, image burn-in, and capacitive lag are eliminated or minimized [2]. The SSID's used in the present study included a frame transfer charge coupled device (CCD) camera [3] and a charge injection device (CID) camera [4].

A brief description of the beam profiling system is presented along with the specific interfacing requirements of the SSID's used in the study. Performance of each SSID was determined by measurements of fixed pattern noise, dynamic range, and modulation transfer function. The measurements are described and their results presented and discussed. Finally, images of a CW diode laser beam, obtained with each SSID, are presented.

2. System Description

A block diagram of the beam profiling system, as it was configured for this study, is shown in figure 1. The spatial distribution of light (the image) incident on the sensor under test varied depending on the specific measurements being made, but in all cases it consisted of the coherent output of a 633 nm helium-neon laser. The camera video output is digitized in the computer (an RCI Trapix 5500 image processing system) to a maximum of 256 grey levels (8 bits) and displayed on the 512 pixel X 512 pixel monitor. An external and versatile set of software programs, some of which will be described later, enable a wide variety of interactive and batch mode image analysis/processing operations. Selected images may optionally be stored in the hard disk memory.

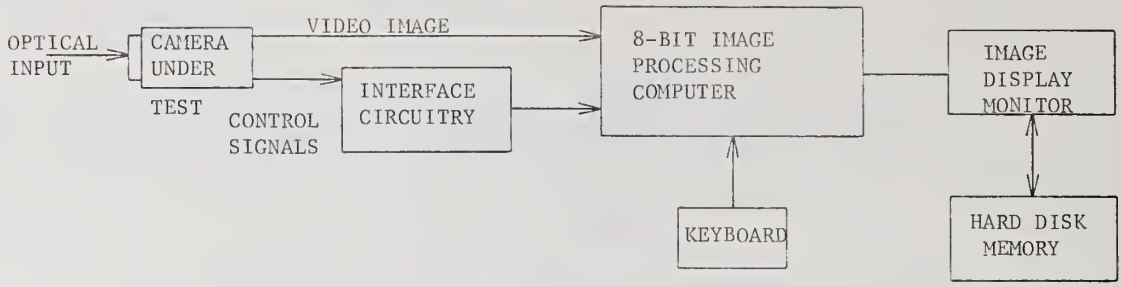

Figure 1. Block diagram of the SSID/8-bit image processor beam profiling system.

The 8-bit image processor can accept camera data in either RS 170/NTSC standard video, non-standard video, or even digital format. The CID camera used in this study (GE model TN 2509) outputs a non-standard video signal. For the image processor to properly receive such a signal, it must be accompanied by a pixel clock plus horizontal and vertical reset signals, all in TTL compatible, differential form. The CID camera provides these control signals in single-ended form; thus, the interface circuitry for it (see figure 1) consists of a simple differential line driver [5]. The CCD camera (VSP Labs model SC 505) outputs standard video, which the image processor can format to 512 X 512 with a 1:1 aspect ratio without additional control signals. Thus no interface circuitry is needed with that camera.

The fact that it outputs standard video gives the CCD camera a significant advantage when used in the AFWL beam profiling system. This is because many of the system's image analysis/processing software programs can be used only with standard video images. For example, whereas both the gain and offset of the digitizer voltage window can be adjusted to improve the grey level range of digitized standard video images, only the offset can be adjusted with non-standard video images.

3. Fixed Pattern Noise

Also called spatial uniformity of sensor responsivity, fixed pattern noise is the non-random pixel-to-pixel variation of sensor output, both for dark current (no illumination) and uniform illumination of the sensor. To obtain data, the grey level offset of each camera was first adjusted (using system software) for optimal suppression of background noise. Then, dark current frames were obtained and stored (in the hard disk memory) with the sensors covered, and frames for two levels of uniform illumination were obtained and stored using the optical arrangement illustrated in figure 2. Neutral density filters were used to adjust the intensity of the laser

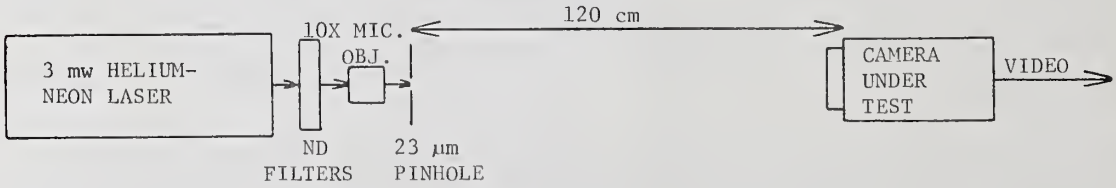

Figure 2. Optical arrangement used to measure fixed pattern noise of the SSID sensors.

light, which was focused with a 10X microscope objective and used to illuminate the 23 μm diameter pinhole of a spatial filter. The central lobe of the resulting Airy diffraction pattern expanded to a diameter of approximately 8 cm at the plane of the camera sensors, whose positions were adjusted so as to be optimally centered in the beam. The dimensions of the CCD and CID camera sensors, 6.0 x 4.5 mm and 7.3 x 7.1 mm, respectively, were much smaller than that of the diffraction pattern, thereby assuring reasonably uniform illumination.

Typical data frames are shown in figure 3 for the CCD camera and in figures 4 and 5 for the CID camera. The unenlarged images in figures 4a and 5a show that the CID images do not use the full 512 X 512 monitor frame. This is because of the non-standard video nature of the CID camera

output. The camera sensor has a 260 horizontal by 253 vertical square pixel format which is transmitted to the image processor one pixel at a time via the above-mentioned control signals. Thus, only the central 260 X 253 pixels of the 512 X 512 image processor (and its monitor) are used. System software also permits image enlargement up to 8X. For example, figure 4b and figures 5b and 5c are 2X enlargements of figures 4a and 5a, respectively. The fringes evident in figures 3b and 3c are due to coherent interference effects caused by a protective glass faceplate provided with the CCD camera, which could not be easily removed. The CID camera was provided with a protective faceplate also, but it was easily removed. Thus, fringing was not a problem with that camera as evidenced in figures 5b and 5c.

Analysis of the stored data frames was performed using a series of system software programs that calculate grey level statistics of any portion of an image. Thus, the superimposed histograms in figures 3, 4, and 5 indicate the distribution of pixel grey levels (from 0-255) throughout each frame. System software can also compute grey level means and standard deviations; thus, for example, in figures 3b and 5b the means/standard deviations are, respectively, 96.3/6.2 and 102.6/2.8. The profiles superimposed in the figures indicate the variation of grey levels along the line of pixels directly beneath the straight-line cursor. Except for the effects of the interference-induced fringes in figure 4, the profiles are quite flat, indicating the absence of geometric distortion, which is a problem with electron-beam scanned devices such as the silicon vidicon [1,6]. The integers 96 and 98 in figure 3c illustrate the magnitude of the interference effect caused by the faceplate on the CCD camera.

To quantify the spatial variation of sensor responsivity, the percent pattern noise, defined as the ratio of grey level standard deviation to grey level mean, was calculated for both the full sensor and the central 2.5 X 2.4 mm portion thereof for each camera using system software and the image frames shown in figures 3, 4, and 5. The results are given in table 1, from which three observations can be made. First, note that for each camera taken separately, pattern

Table 1. Percent Pattern Noise (grey level standard deviation/grey level mean) of the two SSID sensors.

CAMERA	PORTION OF SENSOR	DARK CURRENT	UNIFORM ILLUMINATION
CCD	Full 6.0 x 4.5 mm	12.1	6.5
	Central 2.5 x 2.4 mm	11.7	6.1
CID	Full 7.5 x 7.1 mm	17.4	2.7
	Central 2.5 x 2.4 mm	17.1	2.3

noise values for the central 2.5 x 2.4 mm portion of the sensor are very similar to those for the full sensor. This further illustrates the absence of any serious geometric distortion with these SSID cameras. Next, the dark current pattern noise of the CCD camera is significantly lower (better) than that of the CID camera. Finally, the photosensitivity pattern noise (responsivity to uniform illumination) of the CID camera appears to be better than that of the CCD camera, an apparent contradiction since the CID camera has a higher dark current pattern noise figure. This can probably be explained in terms of the faceplate-induced interference problem observed with the CCD camera (see figure 3) but not with the CID camera. With its faceplate removed, the CCD camera's photosensitivity pattern noise may be comparable to that of the CID camera.

4. System Dynamic Range

In this study, dynamic range was defined in terms of the range of input optical intensities producing a linear variation of video voltage in one image frame. Since the beam profiling system involves two voltage windows, i.e., that of the SSID camera and that of the 8-bit digitizer, the dynamic range of the system is set by the component with the smaller voltage window. Furthermore, since the camera video signal can easily be amplified or attenuated before it enters the computer (see figure 1), the voltage window of the camera can always be made smaller than that of the digitizer, making the dynamic range of the system identical with that of the camera.

To measure camera dynamic range, a suitable lens was added to the arrangement of figure 2 such that the pinhole was imaged onto the device sensor. The resulting video signal was moni-

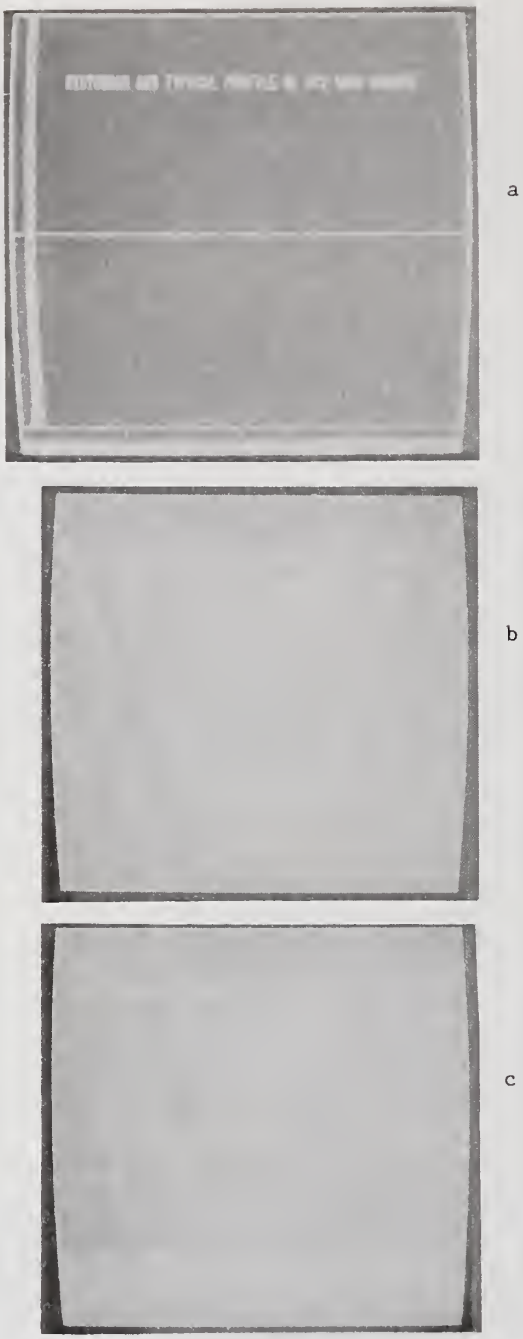

Figure 3. CCD camera sensor dark current (a) and response to uniform illumination (b and c).

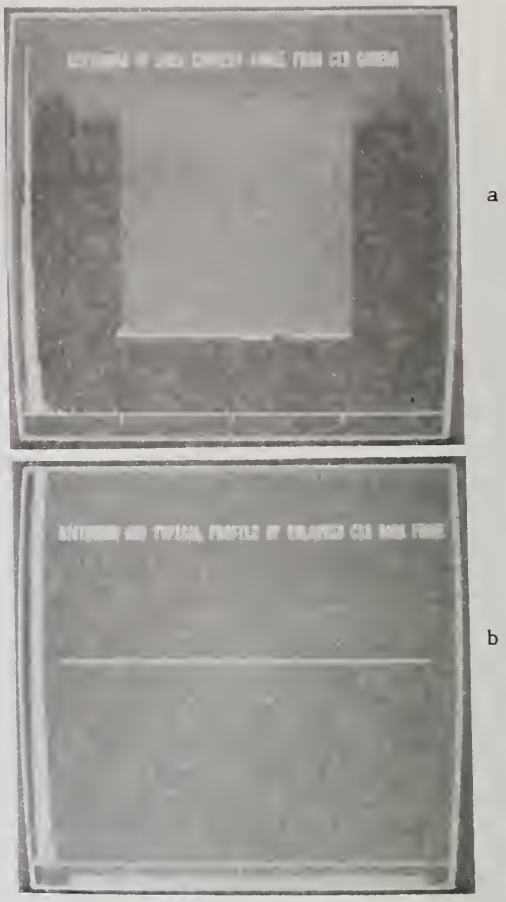

Figure 4. CID camera sensor dark current. Frame b) is a 2X software enlargement of the image in frame a).

tored with an oscilloscope. Starting with the illumination level at which sensor saturation became barely evident on the oscilloscope (defined as the 100% transmittance level), the laser was attenuated with neutral density filters of various transmittances and the amplitude of the resulting video signal recorded at each transmittance level. The results were then normalized to their respective maximum values and least-squares-fitted with straight lines, as shown in figure 6. The noise level line shown in the figure represents that of both cameras because their normalized noise values were virtually identical. Note that this result is based on the assumption that the data in figure 6 continues its linear dependence from the lowest measured transmittance level (8.4%) to the noise level. To verify this assumption, more data near the noise level would be needed.

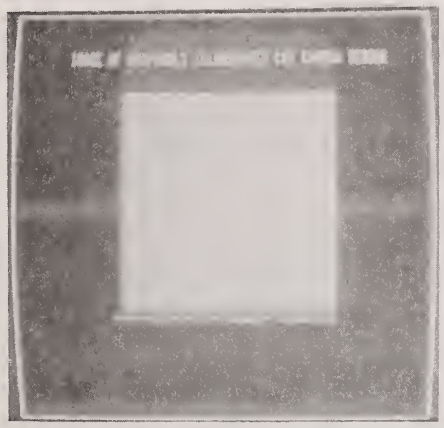

a

b

c

Figure 5. Response of CID camera sensor to uniform illumination. Frames b) and c) are 2X software enlargements of the image in frame a).

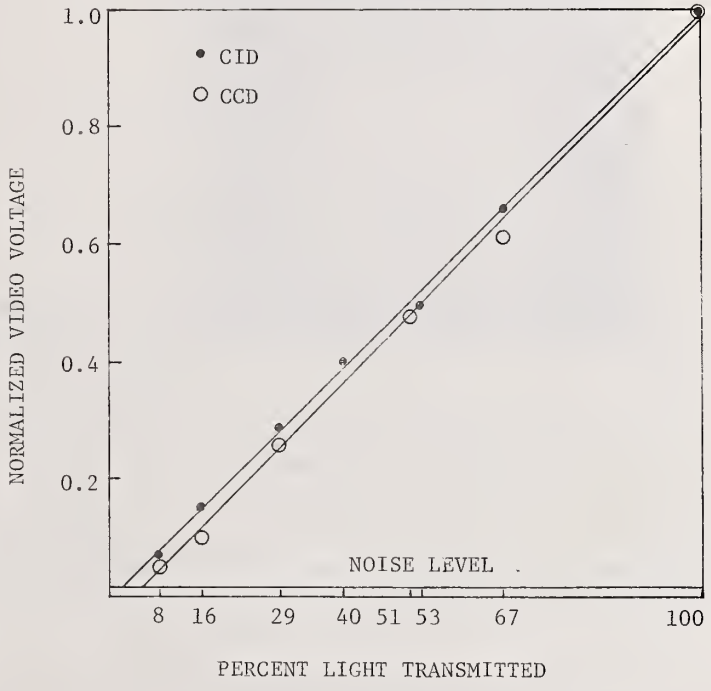

Figure 6. Results of the dynamic range measurements

Assuming that the data in figure 6 is linear from the saturation level (100% light transmittance) to the noise level, the dynamic range is the ratio of the maximum and minimum optical intensities above the noise level, i.e., 100% divided by the percent light transmitted at which the least-squares-fit and noise lines intersect. In figure 6, the intersections are at 5.9% and 2.1%, respectively, for the CCD and CID cameras. Therefore, their dynamic ranges are approximately 17 and 47, respectively.

5. Modulation Transfer Function (MTF)

The MTF of an optical sensor is the rolloff of sensor response with increasing spatial frequency. It characterizes the ability of the sensor to resolve fine detail within the object. In beam profiling, the detection of fluctuations such as hot spots would depend on this property of the sensor.

To measure the MTF's of the two subject SSID's, the optical system of figure 2 was modified as shown in figure 7. The Airy diffraction pattern produced by the pinhole was collimated with

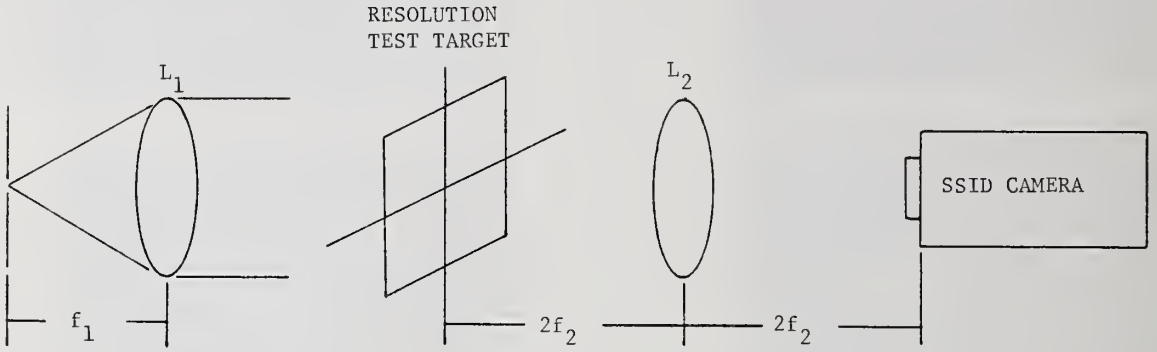

Figure 7. Optical arrangement used to measure sensor modulation transfer functions.

the first lens in the figure and used to uniformly illuminate a chromium USAF 1951 resolution test target, which uses pairs of orthogonal 3-bar patterns to synthesize a wide range of spatial frequencies. Portions of the illuminated test target were then imaged onto the camera sensor with the second lens, which was positioned for unity magnification. Typical images are shown in figures 8 and 9 for the CID and CCD cameras, respectively. Figures 8a and 9a show that the CID camera produces a much smaller image of the test target than the CCD camera. This is a result of the relative sizes of the active pixel elements in the two sensors. The pixels in the CID sensor are approximately 3 times as large on a side as those in the CCD sensor. Thus, the amount of light that illuminates one CID pixel and is transmitted to one image processor pixel will illuminate approximately 9 CCD pixels and occupy 9 image processor pixels. This point is further illustrated by figure 8b, a 3X software enlargement of figure 8a, which shows approximately the same portion of the test target as the 1X image in figure 9a. Figures 8c and 9b illustrate the relative resolution of the two cameras at spatial frequencies above 16 mm^{-1} (test target group 4 and above). The CCD camera is clearly better.

To obtain MTF curves, enlarged images of various portions (spatial frequencies) of the test target were then analyzed using system software. At each spatial frequency, the digitizer grey levels representing maximum and minimum image irradiance (g_{max} and g_{min}, respectively) were obtained from appropriate profiles and used to calculate the relative modulation M using the expression $M = (g_{max} - g_{min})/(g_{max} + g_{min})$. This was done for both vertical and horizontal spatial frequencies. For example, the images used to measure the vertical frequency responses of the CID and CCD cameras are shown in figures 10 and 11, respectively. The decreasing minimum/maximum excursion of the profiles shown in the two figures illustrate the rolloff of the vertical frequency responses of the two cameras. The results of analyzing these and similar images with horizontal profiles are plotted in figures 12 and 13, respectively, for the CID and CCD cameras.

As shown in figures 12 and 13, both the vertical and horizontal frequency responses of the CID sensor cut off at approximately 20 mm^{-1}, whereas those of the CCD sensor cut off at approximately 45 to 50 mm^{-1}. This difference can be explained primarily in terms of the pixel spacings (P) of the two sensors, because, depending on the interlacing format used [7], either 1/P or 1/(2P) represents the Nyquist or maximum spatial frequency resolvable by a sensor [8]. Based on pixel spacings and interlacing considerations, the horizontal/vertical Nyquist frequencies of the CID and CCD cameras can be shown to be approximately 18/18 mm^{-1} and 51/54 mm^{-1}, respectively, which largely explains the observed cutoff frequencies in figures 12 and 13. The CCD camera thus offers a significant advantage in its ability to resolve higher spatial frequencies.

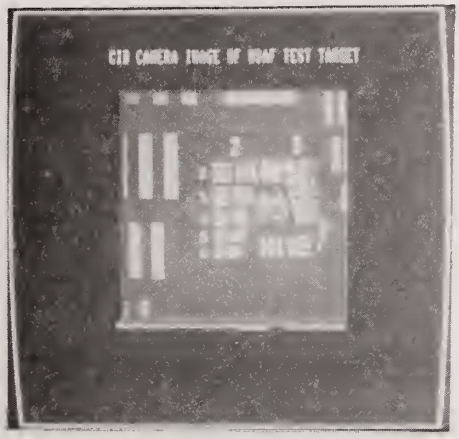

a

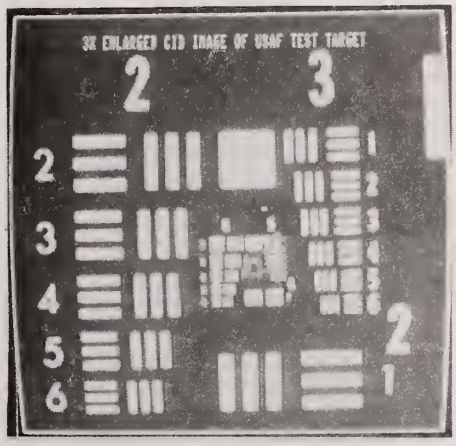

b

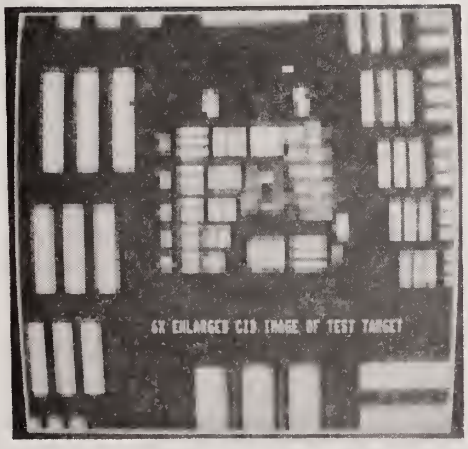

c

Figure 8. 1X, 3X, and 6X software enlargements of CID camera image of USAF resolution test target.

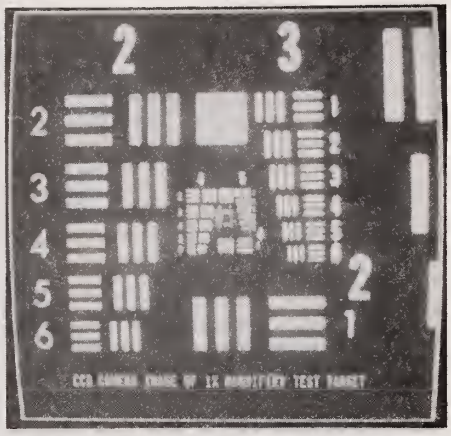

a

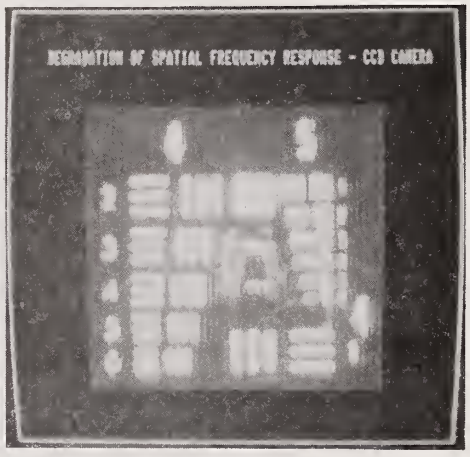

b

Figure 9. CCD camera image of USAF resolution test target. Frame b) is a 3X software enlargement of the image in frame a).

6. CW Diode Laser Beam Images

Finally, to demonstrate the system's beam profiling capability, unity magnification images of the identical output of a 1.06 μm CW diode laser were recorded with each camera. The results, along with histograms and typical profiles, are shown in figures 14 and 15, respectively, for the CID and CCD cameras. As explained above, the two cameras produce different size images on the monitor because their sensor pixels are of different sizes.

a

b

Figure 10. Images and profiles used to measure vertical frequency response of the CID camera from 4.5 to 14.3 mm^{-1}.

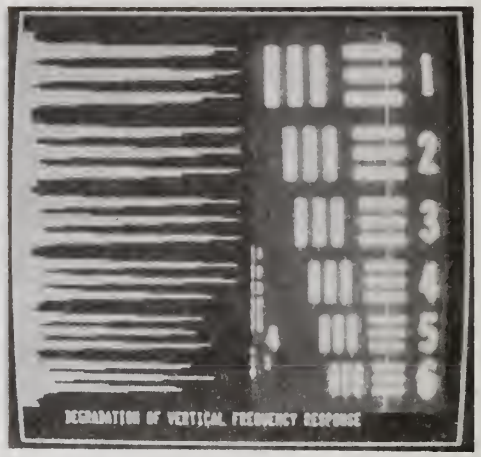

a

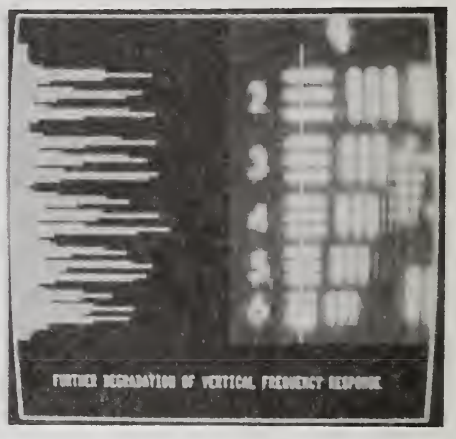

b

Figure 11. Images and profiles used to measure vertical frequency response of the CCD camera from 8.0 to 28.5 mm^{-1}.

From the superimposed histograms in each figure it can be seen that the intensity of the laser diode was well below the sensor saturation level and that the haziness surrounding the circular diode image is due to scattered diode light and not to some saturation-induced blooming effect. This latter point is supported by both the upper end of the histograms, which are well below saturation (the right edge of the image border) and the gradual decay of the distribution peak at the low end of the histogram. The component of this distribution representing dark current drops off much more rapidly, as shown in figures 3a and 4.

7. Summary and Conclusions

The AFWL beam profiling system, configured for the use of two SSID cameras and an 8-bit image processor, has been described and evaluated. The versatility of the system permits the use of a suitable video amplifier or attenuator to ensure full use of both the dynamic range of the sensor and the 256 grey levels of the digitizer.

The CID camera requires a differential line driver in order to interface with the image processor. Because the CCD camera outputs standard RS 170/NTSC video, it needs no interface circuitry. Furthermore, because of the CCD camera's standard video format, more of the system's image analysis/processing software programs can be used with it than with the CID camera.

The performance measurements showed that the CCD camera has better dark current pattern noise and wider spatial frequency bandwidth (resolution) than the CID camera. On the other hand, the CID camera appears to have a slightly wider dynamic range than the CCD device, but further measurements are needed to confirm this result. A fair comparison of the photosensitivity pattern noise of the two devices could not be made because the permanent protective faceplate on the CCD camera caused interference fringes that were not present with the CID camera.

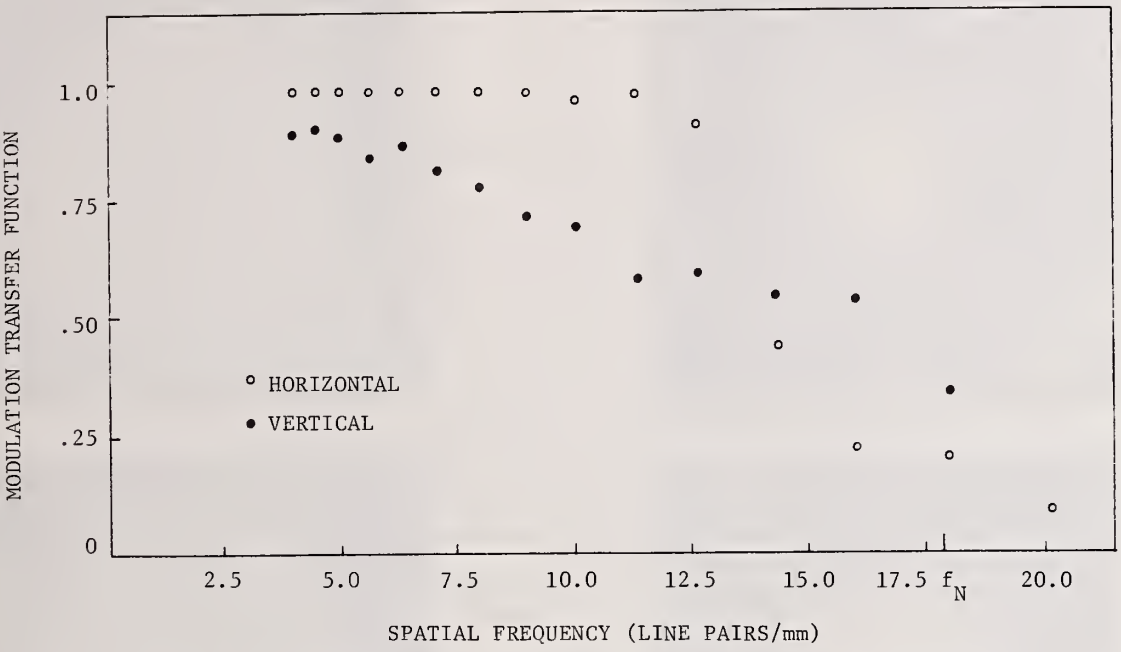

Figure 12. Measured spatial frequency response of the CID camera.

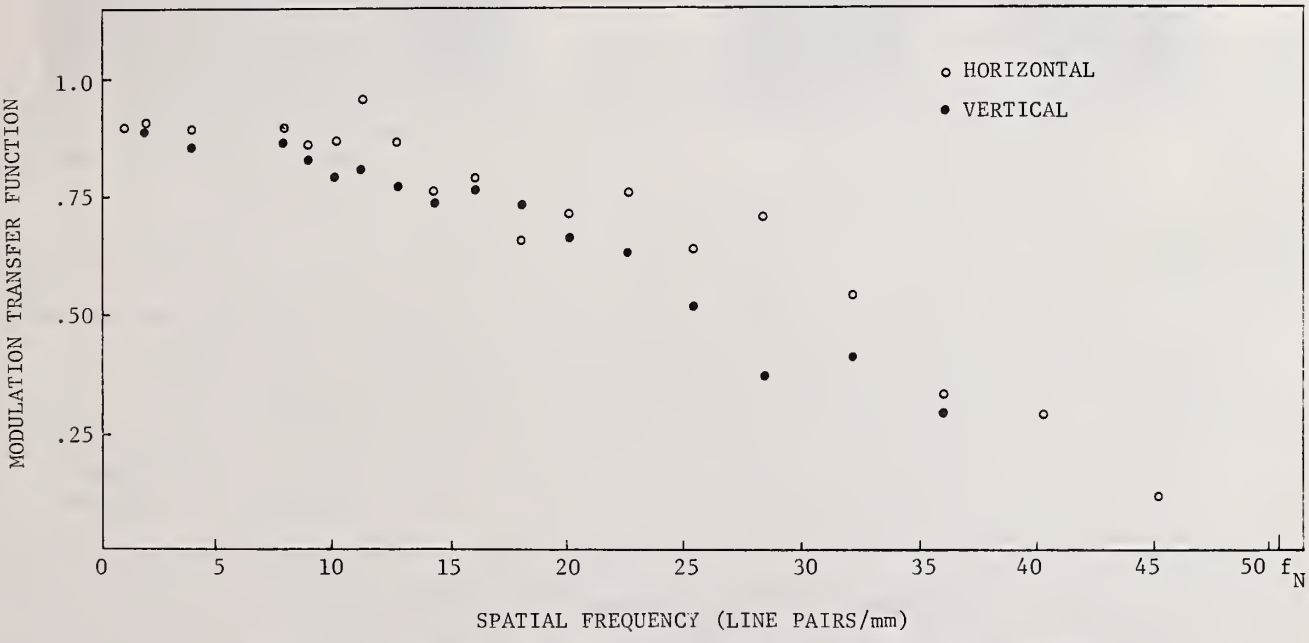

Figure 13. Measured spatial frequency response of the CCD camera.

---

*Research sponsored by the Air Force Office of Scientific Research/AFSC, United States Air Force, under Contract F49620-85-0013. The United States Government is authorized to reproduce and distribute reprints for governmental purposes notwithstanding any copyright notation hereon.

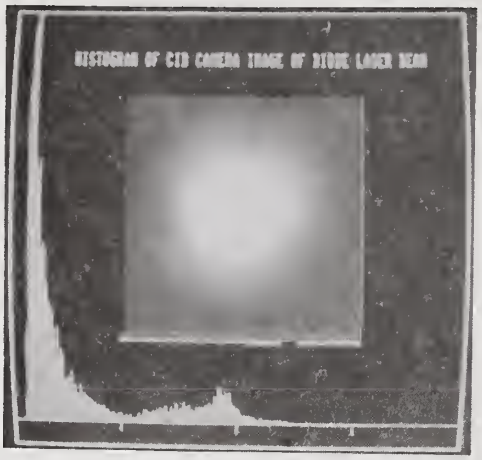

a

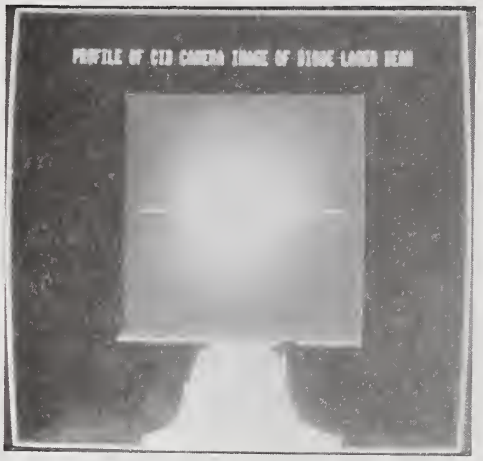

b

Figure 14. Histogram (a) and profile (b) of CID camera image of a 1.06 μm CW diode laser beam.

a

b

Figure 15. Histogram (a) and profile (b) of CCD camera image of a 1.06 μm CW diode laser beam.

8. REFERENCES

[1] O'Connell, R. M.; Vogel, R. A.; Stewart, A. F.; Smith, D. A. Beam Profiling Characteristics of a Sensitivity-Enhanced Silicon Vidicon System at 1.06 Microns. Proceedings of the 17th Annual Symposium on Optical Materials for High Power Lasers, Boulder, Co., 1985.

[2] Talmi, Y. TV-Type Multichannel Detectors. Anal. Chem. 47(7): 699A; 1975.

[3] Tompsett, M. F.; Amelio, G. F.; Bertram, W. J.; Buckley, R. R.; McNamara, W. J; Mikkelsen, J. C.; Sealer, D. A. Charge-Coupled Imaging Devices: Experimental Results. IEEE Trans. Electron Devices ED-18(11): 992; 1971.

[4] Burke, H. K.; Michon, G. J. Charge-Injection Imaging: Operating Techniques and Performance Characteristics. IEEE Trans. Electron Devices ED:23(2): 189; 1976.

[5] A camera controller for the GE model TN 2509 that converts the camera output to RS170/NTSC standard video is manufactured by Poynting Products, P.O. Box 1227, Oak Park, IL.

[6] Smith W. L.; DeGroot, A. J.; Weber, M. J. Silicon Vidicon System for Measuring Laser Intensity Profiles. Appl. Opt. 17(24): 3938; 1978.

[7] Sèquin, C. H. Interlacing in Charge-Coupled Imaging Devices. IEEE Trans. Electron Devices ED-70(6): 535; 1973.

[8] Barbe, D. F. Imaging Devices Using the Charge-Coupled Concept. Proc. IEEE 63(1): 38; 1975.

Manuscript Received
6-5-87

Laser-Induced Damage Detection and Assessment by Enhanced Surface Scattering

S. C. Seitel and Mark T. Babb

Montana Laser Optics, Inc.
Bozeman, Montana 59715

Abstract

A photoelectric damage detection and assessment system based on laser-induced changes in surface scattering is reported. The system is similar to one reported by Franck, et. al., with improved operating flexibility. It is integrated with a 1064/532 nm damage test facility used for routine testing of production optics. For some types of coated samples, a plot of scatter change vs. applied fluence can be extrapolated to the threshold fluence for surface pitting, eliminating the need for tedious microscopic assessment of near-threshold test sites. The system permits quantitative assessment of surface quality (by forward scatter) at a test site just prior to exposure by the damaging beam. thus, correlations between surface scatter and damage susceptibility may be investigated directly.

Key words: damage assessment; damage detection; damage evolution; experiment automation; intrinsic scatter; laser-induced damage; laser-induced scatter; surface blemishes; threshold extraction.

1. Introduction

Visual observation of increased scattering has long been used to detect laser-induced damage to optical surfaces [1]. A quantitative scatter measurement system integrated with an automated damage test system has been reported by the Naval Weapons Center (NWC) [2]. This system has been used to investigate damage susceptibility at infrared wavelengths as a function of initial scatter, with some success [3].

We have developed an automated quantitative scatter measurement system based on the NWC design, integrated it with the existing commercial laser damage tester, and have begun routine compiliation of scatter vs. damage data on selected samples. The ultimate intent of the initial measurements is to evaluate scatter as a measure of surface quality and cleanliness, as a damage detection and quantifying method, and possibly as a non-destructive damage predictor.

This paper reports the MLO scatter system concept, design, and calibration procedure. Applications to automated measurement functions are illustrated, including characterization of intrinsic surface scatter; monitoring of surface quality and cleanliness; laser-induced damage detection; damage threshold extraction; and cumulative damage assessment.

2. Scatter Probe Description

A general optical schematic of the MLO system is shown in figure 1. Damaging laser radiation is incident on a target site on the sample from the left. Chopped, continuous wave visible probe laser radiation is focused by means of a telescope onto the target site. Spot size is adjusted with the telescope to match the spot size of the damaging beam. The specular reflection is blocked with a beam stop. A collecting lens images radiation scattered from the sample surface past the beam stop onto a detector (B channel). The field of view is restricted with an aperture to accept only radiation from the target site. The output of the detector is measured with a computer-controlled lock-in amplifier to provide a quantitative measure of surface scatter into a small solid angle about the specular reflection direction.

As an option, a beam splitting plate directs a portion of the unchopped probe laser beam to a second detector (A channel) which serves as an incident power monitor. This detector is connected to an auxiliary "denominator" input on the lock-in for signal normalization.

The scatter probe system is sensitive primarily to radiation scattered from the illuminated portion of the front surface. Figure 2 shows that the specular reflection from the front surface of the test sample is blocked by the central obscuration at the collecting lens, while the specular reflection from the back surface is blocked at the image plane aperture. Similarly, radiation scattered from the back surface into the collecting lens does not reach the detector.

Figure 3 identifies those dimensions which are controlled in the MLO system, while the corresponding values appear in table 1.

Table 1. MLO scatter probe dimensions

Symbol	Dimension	Value
D_T	Illuminated spot diameter	1 mm
θ_s	Sample tilt[a]	1.5°
θ_i	Incidence direction[a]	10°
θ_r	Specular direction[a]	13°
f	Image lens focal length	118 mm
D_L	Lens clear aperture diameter	19 mm
D_o	Central obscuration diameter	9.8 mm
i	Image plane distance	325 mm
o	Object plane distance	185 mm
D_i	Image plane aperture diameter	3.25 mm

[a]Measured from damage tester centerline.

3. Calibration

Scattering signals often are expressed as a fraction of the power incident on the sample, divided by the collecting solid angle; units are parts per million per steradian (ppm/sr). This convention permits comparing results between instruments with different collection geometries. To convert scatter levels measured in microvolts (μV) to ppm/sr, it was necessary to determine 1) the collecting solid angle and 2) the incident power signal (in μV). the solid angle dS was calculated from quantities in table 1:

$$dS = \frac{\pi \times (D_L^2 - D_o^2)}{4 \times o^2} = 0.0062 \text{ sr.}$$

The incident power signal was determined indirectly. A planar, diffusely reflecting surface was prepared with Kodak White Reflectance Coating (Chemical no. 6080) [4] and installed in the target plane, normal to the incident beam. The scatter signal P_s was measured in μV as usual. From the known angular distribution function for a diffuse scatterer, the incident power signal P_i was inferred:

$$P_i = \frac{P_s}{R_D \times \text{Cos}\theta \times dS/\pi} = 5.52 \times 10^7 \ \mu\text{V}.$$

Here $\theta = \theta_i + \theta_r = 23°$. The total diffuse reflectance of the Kodak coating has the value $R_D = 0.985$. The units conversion follows from

$$P_s(\text{ppm/sr}) = \frac{P_s(\mu\text{V}) \times 10^6}{P_i(\mu\text{V}) \times dS} = 2.93 \times P_s(\mu\text{V}).$$

4. Intrinsic Scatter

To determine whether basic sensitivity was adequate, several samples, both coated and uncoated were tested. The smallest scatter signals were observed on $LiNbO_3$ surfaces; the "quietest" test sites scattered ~30-60 ppm/sr. Thus the minimum signal-to-noise ratio was ~100-200. Figure 4 shows a typical histogram. A total of 51 sites were tested. Of these, half scattered ~20 μV (~60 ppm/sr) or less. Higher scatter sites occurred less often.

5. Surface Blemishes

Cosmetic imperfections such as pits, scratches, particulates, etc. appear as locally bright scatter sources in the illuminated spot when viewed by eye. Different types of imperfections were targeted to evaluate system sensitivity to local blemishes. With the exception of hairline fractures, scatter signals from local imperfections were very large, often many times the signal from nearby unblemished surface. In the reverse experiment, observation of high scatter signal regions with the on-line microscope invariably revealed a corresponding imperfection. Thus, the presence of a blemish could be inferred from scatter level alone. The types of imperfections targeted are listed in table 2, along with a subjective assessment of detection efficiency.

Table 2. Sensitivity to imperfections

Imperfection type	Relative sensitivity
Small pit	High
Large pit	Very high
Small particulate	High
Large particulate	Very high
Scratch (vertical)	High
Scratch (horizontal)	High
Hairline fracture (vertical)	low
Hairline fracture (horizontal)	low
120° fracture (no apex pit)	low
120° fracture (apex pit)	High
Drag wipe residue	High

6. Threshold extraction

When the extent or severity of damage increases with applied fluence, the magnitude of the scatter change likely will increase also. Extrapolation to zero change thus provides an estimate of the damage threshold. Figure 5 compares a conventional damage frequency measurement to a simple linear extrapolation of the scatter signal. The sample was AR-coated BK-7 glass, which failed by pitting. In this case, the extrapolated scatter signal overestimates the pitting threshold by ~20 percent.

The conventional approach involved tedious darkfield examination of ~100 sites, requiring more than an hour of effort by a skilled microscopist. In contrast, the scatter data were acquired as the sample was exposed, saving this effort. The scatter approach lends itself to experiment automation, while microscopy does not.

7. Damage evolution

Laser induced surface scatter changes can be used to study surface changes under continued laser irradiation. Some sample types (e.g., AR-coated glass) characteristically damage to full extent in a single pulse, showing little or no change on successive pulses. With other sample types (e.g. multilayer dielectric reflectors), multiple pulse damage evolution can be quite complex. Figure 6 compares the cumulative damage behavior of an AR-coated BK-7 glass sample to a laser mirror, also on BK-7.

The AR-coating was exposed well above threshold, and pitted over much of the beam footprint on the first pulse. A few additional pits formed on the pulses immediately following. No new pits formed after ~10 pulses. The HR-coating was exposed below the single pulse threshold. No damage (scatter change) occurred for 10 pulses. On pulse 11, a single pit appeared centered in the footprint. On successive pulses, the pit grew by erosion at its perimeter, and the scatter signal increased dramatically. By ~30 pulses, the BK-7 substrate was exposed at the center. The substrate scattered less than the eroded coating. As more substrate was exposed, the scatter signal decreased, eventually stabilizing as the damaged area filled the beam footprint.

The number of pulses before damage is observed and the rate at which damage increases, once initiated, both depend on applied fluence. This is shown in Figure 7 for AR-coated Homosil.

8. Conclusions

The system is sufficiently sensitive to characterize the intrinsic surface scatter and scatter variations of typical coated and uncoated optical samples. The presence, but not the nature, of a cosmetic imperfection or surface contaminant can be inferred reliably from scatter values much larger than intrinsic. This allows automated monitoring of surface quality and cleanliness during a damage test.

Laser-induced surface changes are readily detected in scatter. Damage assessments made on the basis of scatter changes agree with conventional methods. This permits near-real-time damage evaluation without tedious microscopy. For some samples (e.g., AR-coated glass) the magnitude of the laser-induced scatter change depends on the applied fluence. Extrapolation to zero scatter change determines the threshold. Assessment of questionable (near threshold) damage sites is not forced.

Cumulative damage effects are readily observed in scatter.

We wish to acknowledge the generous financial and technical support provided by Crystal Technology, Inc., of Palo Alto, CA 93404. In particular, the technical reviews and evaluations of Mr. Ron Blachman were most helpful.

9. References

[1] For an early example, see Newnam, B. E. Damage resistance of dielectric reflectors for picosecond pulses. Glass, A. J.; Guenther, A. H., ed. Proceedings of the sixth annual symposium on optical materials for high power lasers; 1974, Boulder, CO. Nat. Bur. Stand. (U.S.) Spec. Publ. 414; 1974.

[2] J. B. Franck, et. al. Automated pulsed testing using a scatter-probe damage monitor. Bennett, H. E., et. al., ed. Proceedings of the sixteenth annual symposium on optical materials for high power lasers; 1984 Oct 15-17; Boulder, CO. Nat. Bur. Stand. (U.S.) Spec. Publ. 727; 1986 October. 71-76.

[3] J. O. Porteus, et. al. Correlation between local He-Ne scatter and defect-initiated laser damage at 2.7 um. Bennett, H. E., et. al., ed. Proceedings of the seventeenth annual symposium on optical materials for high power lasers; 1985 Oct 28-30; Boulder, CO. Nat. Bur. Stand. (U.S.) Spec. Publ. (in press).

[4] Eastman Kodak Company, "Kodak white reflectance products", Kodak publication no. JJ-31 (1984).

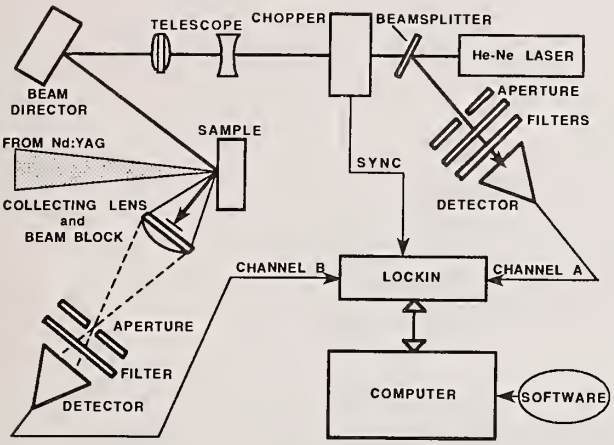

Figure 1. Optical schematic.

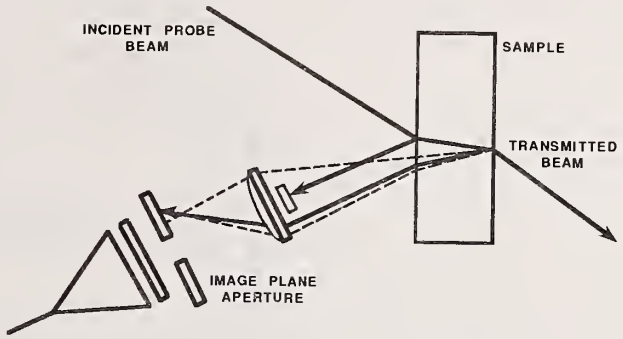

Figure 2. False signal rejection.

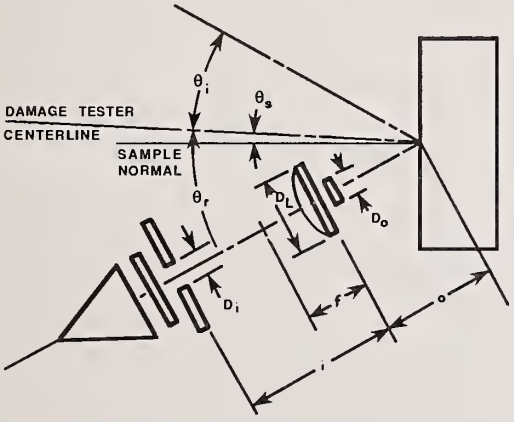

Figure 3. Controlled dimensions.

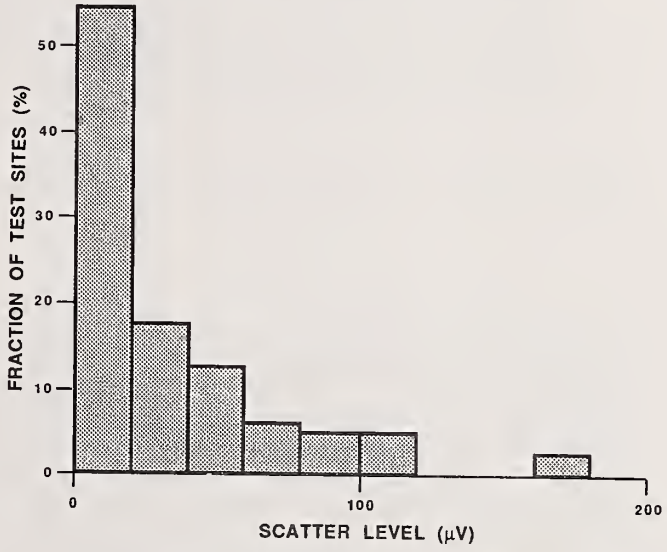

Figure 4. $LiNbO_3$ intrinsic scatter histogram.

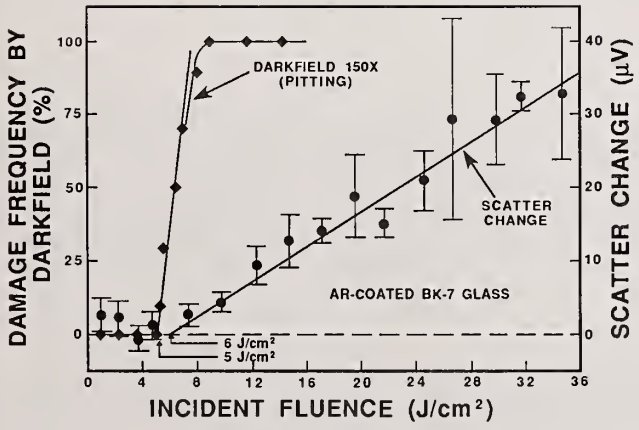

Figure 5. Damage threshold extraction.

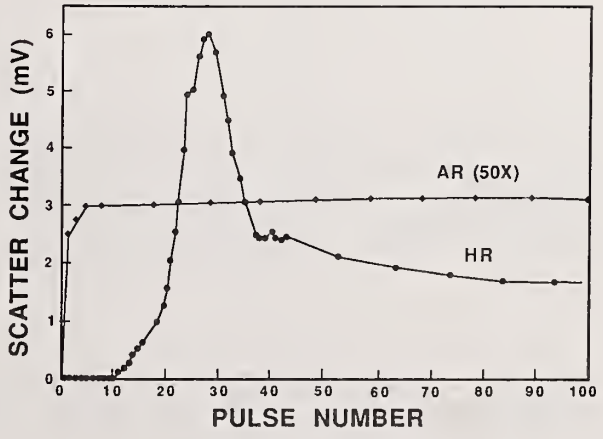

Figure 6. Cumulative damage for AR- and HR-coated BK-7 glass.

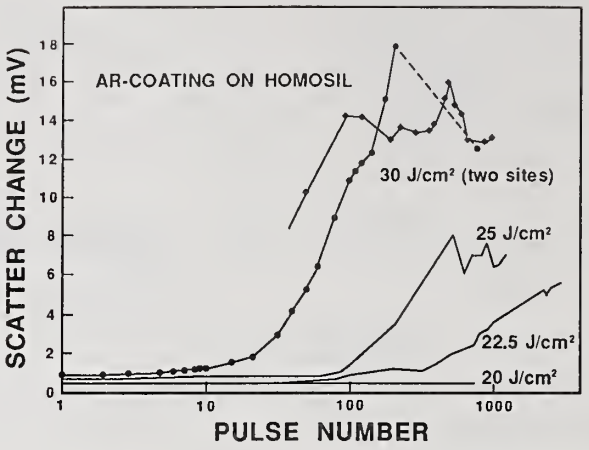

Figure 7. Dependence of cumulative damage on applied fluence.

Manuscript Received
4-1-88

Thermal Properties of Optical Materials*

D. L. Decker
Physics Division, Research Department
Naval Weapons Center, China Lake, California 93555

A knowledge of the thermal properties of optical materials is essential to an understanding of laser-induced damage for long-pulse or continuous-wave irradiation. This area has been long neglected partly because of the difficulty of reliable measurement. An extension of the thin film measurement technique described at the Boulder Laser Damage Conference in 1984 for the measurement of thermal conductivity is presented in this paper. Data are given for bulk Si, SiC, Si/SiC, and SiO_2. These results are interpreted using simple theories of inhomogeneous or locally disordered materials. Also indicated are the relationships between local material stress and thermal conductivity, and the temperature dependence of the thermal conductivity for several models of local disorder. Recommendations for further work are also indicated.

Key words: dielectric materials; disorder; stress; temperature dependence; thermal conductivity.

Introduction

Thermal transport is fundamental to an understanding of the laser damage process and the heat load and thermal distortion engineering of laser components for long-pulse (t > 1 nsec) and continuous-wave (CW) irradiation. Thermal conductivity is strongly dependent upon crystallographic perfection and direction [1,2].[1] It has been pointed out previously that thin films have remarkably lower thermal conductivity as a consequence of disorder [3-5]. In this paper, the bulk material SiC was chosen for examination because of its practical use as a mirror substrate and because of its intrinsically defected structure. SiC is the classic example of a crystalline material displaying the phenomena of polytypism that is caused by the presence of a superlattice-like structure due to screw dislocation steps [6]. This structure is pervasive in cubic SiC. The interesting and highly disordered bulk materials polycrystalline Si and fused SiO_2 were also included. Large reduction in thermal conductivity in bulk materials due to disorder has been observed in work elsewhere [7,8] and in this paper. For one-dimensional heat flow, the temperature is given by

$$\alpha \nabla^2 T = \partial T / \partial T \quad , \tag{1}$$

where the diffusivity α is simply the ratio of thermal conductivity K to the heat capacity C, $\alpha = K/C$ [9]. This paper describes the measurement of thermal conductivity by steady-state methods [10]. The diffusivity is then calculated as needed, since the heat capacity is nearly independent of material perfection. For nonequilibrium cases, nonlinear effects due to thermally induced stress (disorder) may be important. Application of steady-state results to pulsed irradiation problems should be made with caution.

Theory

Thermal conductivity is not an intrinsic property of a material but is dependent on crystallographic perfection; it may be influenced by purity, preparation methods, and thermal history.

*Work supported by Navy Independent Research Funds and the Strategic Defense Initiative Organization.
[1]Numbers in brackets indicate the literature references at the end of the paper.

Around the turn of the century, the importance of macroscopic irregularity was recognized in measurement and analysis of the properties of insulating materials such as kapok [11]. If two phases with conductivities K_1 and K_2 are present, then for parallel heat flow

$$K_{eff} = fK_1 + (1 - f)K_2 \quad , \tag{2}$$

where f is the volume fraction of phase 1. For series flow a similar expression can be derived:

$$K_{eff} = K_1K_2[fk_1 + (1 - f)K_2]^{-1} \quad . \tag{3}$$

In a real material, some combination of series and parallel flow will be present. In such a case (lacking detailed knowledge of the heat paths), an approximate expression derived from a random distribution of paths can be computed, which is given as the geometrical mean of K_1 and K_2:

$$K_{eff} = K_1^f K_2^{(1-f)} \quad . \tag{4}$$

Thermal conductivity is determined on a microscopic scale by lattice irregularity. From simple transport theory [2],

$$K = 1/3C\nu\ell \tag{5}$$

where ν is the transport velocity and ℓ is the mean free path. Conduction in metals is primarily by electron transport and in dielectrics by phonons. In dielectrics, ℓ can be decreased by 1 to 2 orders of magnitude from "perfect" single-crystal values by disorder in thin films and lattice defects in bulk materials. Primarily, this simple model was introduced to provide a basis for an intuitive physical link between the macroscopic average property K and the microscopic transport variable ℓ. Table 1 gives computed values of ℓ for the bulk materials considered in this work. Notice that for the amorphous material fused silica the computed value of ℓ is less than even the SiO_4 tetrahedra dimensions. Clearly, the value of ℓ computed for fused silica is so short that the simple continuum transport model does not apply, and this computed value is not accurate. For the other two crystalline materials, ℓ is two orders of magnitude larger, as is the thermal conductivity.

Table 1. Values of phonon mean free path ℓ are provided for materials of interest in this paper, as computed from typical values of thermal conductivity and an assumed value of ν of 5×10^5 cm/sec. Note that the computed value for fused silica is even smaller than the SiO tetrahedra dimensions, and in this case the model is undoubtedly not appropriate but is offered only for intuitive guidance.

Material	C(j/cm^3-°K)	K(w/cm-°K)	ℓ(Å)
Si	1.70	1.5	530
Si	2.1	1.12	320
SiO^2 (fused silica)	2.0	0.0069	2

In general ℓ is determined by more than one scattering process:

$$1/\ell = \sum_i 1/\ell_i \quad . \tag{6}$$

The temperature dependence of the thermal conductivity can provide valuable assistance in sorting out the scattering mechanisms [13]. At low temperature, ℓ is nearly constant (boundary scattering)

and since $C(T) \approx T^3$ for dielectrics, $K \approx T^3$. At high temperatures, the phonon concentration is $\approx T$; hence, $\ell \approx T^{-1}$, C(T) is constant, so $K(T) \approx T^{-1}$. It is important to realize that uniform stress (lattice dilation) does not in itself produce an increase in scattering. At low temperatures and for a concentration of N dislocation lines per unit area [12],

$$K \approx T^2/N \quad . \tag{7}$$

At high temperatures and in the limit of strong point-defect scattering,

$$K \approx (\varepsilon T)^{-1/2} \quad , \tag{8}$$

where ε is the defect concentration.

Experimental

The approach taken in the steady-state measurements reported in this paper is similar to that taken in earlier thin-film work [3]. The thermal potentiometric method has the advantage of providing results capable of absolute calibration and a means of simple assessment of systematic errors. Figure 1 is a schematic of the measurement assembly, which consists of an electrically heated source block, a potentiometric section, sample, another potentiometric section, an optional thermal resistance section, and, finally, a water-cooled sink block. The potentiometric and sample sections are 1.128 cm in diameter, which corresponds to a 1-cm cross-sectional area chosen for construction and computational convenience. In the potentiometric sections, 0.010-in.-diameter holes are drilled with a 1-cm spacing to the axis of these cylinders to provide suitable locations for fine wire chromel/alumel thermocouples. Thermocouples TC_3 and TC_4 are located only 0.005 in. from the sample interface surfaces and provide accurate measurement locations for sample surface temperature measurement. It is essential that the sample and interface surfaces of the potentiometric blocks be optically flat and smooth to prevent unknown thermal drops. These surfaces are wet with a microdrop of very light silicone oil, and the whole assembly is clamped with a force of approximately 1 kgm. Under these conditions, the measured thermal drop TC_3-TC_4 does not depend on clamping force. The geometry used is an attempt to establish one-dimensional heat flow, and this assumption can be verified by measurement of equal drops TC_1 to TC_2, TC_2 to TC_3, and so on. These drops are found to be equal to within experimental error, which is usually only a few percent except in those cases where very low heat flux (a few watts) is flowing and the drops themselves are small. By introducing a thermal resistance, conveniently provided by a fused quartz spacer stack, the average temperature of the sample can be raised to allow for elevated temperature measurement. The thermal conductivity of a sample of area A and length L, of course, is simply given:

$$K = \frac{Q}{A}\frac{\Delta L}{\Delta T} \quad , \tag{9}$$

where ΔT is the thermal drop across the sample, assumed to be TC_3-TC_4. The thermal flux Q is obtained by the thermal drop in the copper posts, with a check provided by the known Joule heat dissipated in the heater. The systematic errors are primarily due to unaccounted heat loss especially at high temperatures and thermometry errors. Thermal drops at the sample interfaces can be minimized as described above; they can be estimated directly by removal of the sample and a comparison of TC_3 and TC_4 with the potentiometric source and sink anvils in direct contact. Typically, a value less than 0.04°C/W is measured in this case. Figure 2 shows the thermal drops across 1, 2, and 3 identical sample sections stacked together. Note that there is no apparent sample interface drop, and that the extrapolated drop at zero sample thickness is of the same order as measured directly with no sample present.

A variety of materials were examined, including more or less homogeneous single-phase SiC as well as sintered two phase "siliconized" SiC. Two different types of fused silica were measured also. Table 1 summarizes the results obtained. The values of density were computed from the readily measured volume of the accurately shaped samples and their measured mass. It is interesting to note the difference in thermal conductivity and density of the two different CVD SiC sample types summarized, which were produced by different processes. The startling discovery that a two-phase inhomogeneous material could have a thermal conductivity 30% higher than the single-phase material is also documented. An analysis is presented in the next section that may explain this result.

Analysis

For the two-phase material, we can calculate the density of this material ρ_{ave} based on the density of phase 1, ρ_1(SiC) and of phase 2, ρ_2(Si).

$$\rho_{ave} = f\rho_1 + (1 - f)\rho_2 \text{ or } f = \frac{\rho_{ave} - \rho_2}{\rho_1 - \rho_2} \tag{10}$$

If we assume that $\rho_{sic} = 3.20$ gm/cm^3 and $\rho_{si} = 2.40$ gm/cm^3, $f = 0.67$. If we further assume $K_{sic} = 1.12$ W/cm-°K and $K_{si} = 1.5$ W/cm-°K, we can compute an effective thermal conductivity K_{eff} from eq. (4). The value of K assumed for Si is similar to that reported for single-crystal material.

$$K_{eff} = K_1^f K_2^{(1-f)} = 1.23 \text{ W/cm-°K} \quad . \tag{11}$$

If we assume series heat flow, the computed effective conductivity is 1.34 W/cm-°K; similarly, for parallel flow, the computed value is 1.24 W/cm-°K. From table 2, the measured value in this case was 1.30 W/cm-°K. This is reasonable agreement and suggests a simple explanation for the effect observed. Further examination of the origin of the relatively low values of thermal conductivity measured on Si and SiC in this study was undertaken with a series of temperature dependence measurements taken at slightly elevated temperature [13]. From figure 3 it can be seen that both the reaction-sintered SiC/Si and CVD Si thermal conductivities have similar temperature dependences and can be fit to a T^{-1} relationship quite well. This is, of course, exactly the predicted high-temperature dependence; however, since the Debye temperatures of Si and SiC are both on the order of 600°K, we are not really in the theoretical "high temperature" region, where this dependence would be valid. The temperature dependence of the CVD Si data is considerably weaker in the temperature range investigated and is well approximated by a $T^{-1/2}$ relationship.

Table 2. Results of density and thermal conductivity obtained on a variety of sample types measured in this work. Measurement details and sample characteristics are provided in the text. Note that average values are given. In some cases, a range of values is shown where significant spread occurred between several "identical" samples.

Sample materials	Process	Density, gm/cm$_3$	K, W/cm-°K	Comments
Si/SiC	Sintered/siliconized	2.76-2.79	0.91	Nonuniform hardness/ microstructure/porous
Si/SiC	Reaction sintered	2.92-2.95	1.30	Fully dense
SiC	CVD	3.12	0.85	Single phase
		3.23	0.93	
SiC	CVD	3.20	1.12	Single phase
Si	CVD	2.30	1.00	Microcrystalline
SiO_2	Fused glass	2.17	0.0069	GE 125
SiO_2	Fused glass	2.14	0.015	Suprasil
Si	Fusion cast	2.31	0.97	mm-size crystals

Conclusions

These data provide the basis for interesting speculation and for engineering calculation. Much more work, especially in direct investigation of microstructural details and measurement of the temperature dependence over a much broader range of temperature, would be required to understand the quantitative relationships involved. Even without such a detailed understanding, it is clear that macro- and microstructural inhomogeneity are important to the thermal conductivity of materials. The data presented in this paper provide validation of the experimental methods employed, and are in at least semiquantitative agreement with the theoretical models used. There is an obvious need to collect additional data for the materials investigated here and for additional samples prepared by different procedures. Significant improvement in thermal conductivity of both Si and SiC as fabricated by "practical" methods may be possible by further materials development. Nonlinear thermal transport effects due to high stress from large gradients await exploration.

References

[1] Sande, J. W. Vander. Diamond research; 1973 (Suppl. Ind. Diamond Rev.).

[2] Kittel, C. Solid state physics, 5th ed. New York; Wiley; 1976.

[3] Decker, D. L.; Koshigoe, L.; Ashley, E. J. "Thermal properties of optical thin-film materials," in Proceedings of the 16th annual symposium on optical materials for high power lasers, Bennett, H. E.; Guenther, A. H.; Milam, D.; Newnam, B. E. ed. 1984 October 15-17; Boulder, CO. Nat. Bur. Stand. (U.S.) Spec. Publ. 727; 1986 October. Pp. 291-297.

[4] McGuirk, M.; Poirier, R. D. "Thermal conductivity of enhanced high reflectors," presented at the 17th annual symposium on optical materials for high power lasers. 1985 October 28-30; Boulder, CO. (Proceedings in process.)

[5] Akhtar, S.H.J.; Ristau, D. "Thermal conductivity of dielectric films and correlation to damage threshold at 1064 nm," these proceedings.

[6] Verma, A. R.; Krishna, P., ed. Polymorphism and polytypism in crystals. New York; Wiley; 1966.

[7] Berman, R.; Martinez, M. Diamond research; 1976 (Suppl. Ind. Diamond Rev.).

[8] Zeller, R. C.; Pohl, R. O. Phys. Rev. B4; 2029; 1971.

[9] Carslaw, H. S.; Jaeger, J. C. Conduction of heat in solids, 2nd ed. Oxford; Clarendon Press; 1959.

[10] Lees, C. J. Phil. Trans. R. Soc. A20; 381; 1908.

[11] Baxter, S. Proc. Phys Soc. 48; 105; 1946.

[12] Klemens, P. G. Theory of thermal conductivity of solids in thermal conductivity, Vol. 1. R. D. Tye, ed. New York; Academic Press; 1969.

[13] "Values of K measured on pure highly ordered SiC single crystals can be as high as 15 w/cm-°C" (private communication from J. Choyke).

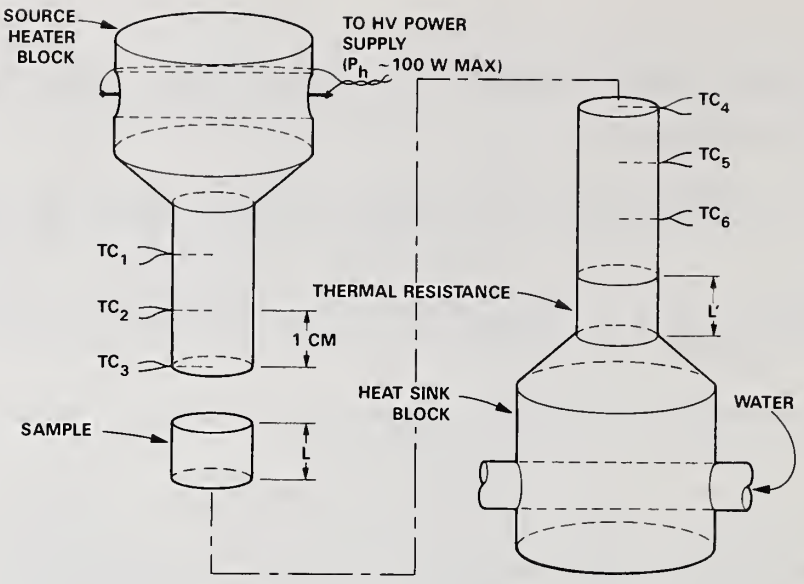

Figure 1. Exploded view of thermal potentiometric apparatus. One-dimensional heat flow between the source and sink blocks passes through a sample section. The sample temperature drop is inferred from the temperatures measured between TC_3 and TC_4. From the measured electrical power dissipated in the heater, the heat flux can be calculated knowing the cross-sectional area of the flow path. The thermal conductivity is simply calculated from these data. Additional details of operation are provided in the text.

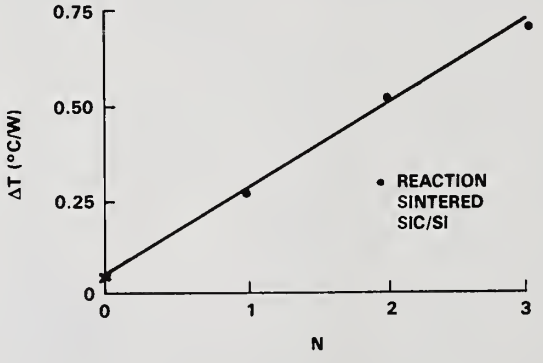

Figure 2. Sample temperature drop for a set of three identical SiC samples placed singly or stacked together. No apparent interface drop occurs, and the extrapolated offset for no sample present is very close to that directly measured, 0.04°C/W. This test is a valuable check on several potential sources of systematic error including interfacial effects, and provides direct indication of the linearity of the measurement itself.

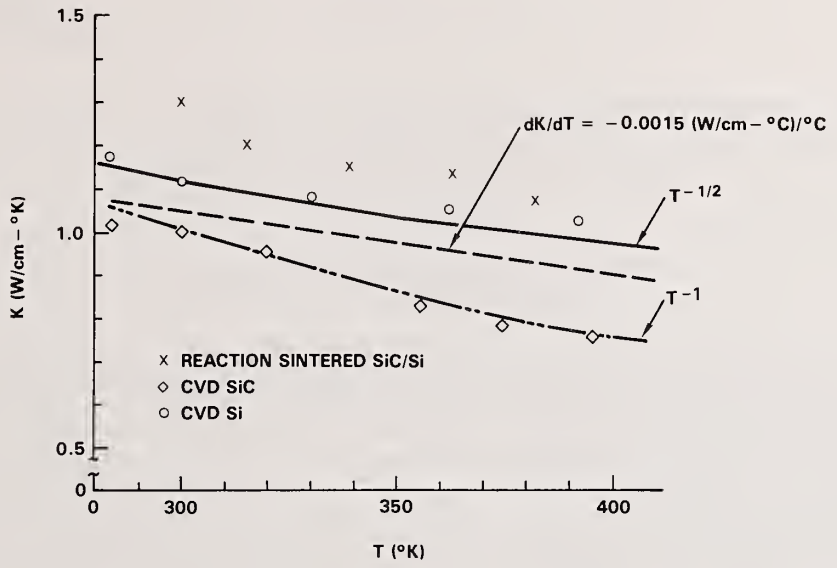

Figure 3. Temperature dependence of the thermal conductivity of reaction-sintered SiC/Si, CVD SiC, and CVD Si. The temperature range near room temperature for these disordered materials is especially valuable for elucidation of scattering mechanisms. For example, a T^{-1} dependence is expected in the high-temperature limit for phonon-phonon scattering. Additional details are provided in the text.

Manuscript Received
8-19-87

Beam-Induced Spherical Aberration in Cooled CW Laser Light Transmitting Components

Claude A. Klein

Raytheon Company, Research Division
Lexington, Massachusetts 02173

Thermally induced optical distortions severely degrade the quality of a laser beam thus reducing the irradiance on target. The objective of this paper is to formulate procedures for evaluating the impact of spherical aberrations generated by optically transparent cylindrical components subjected to CW laser radiation; specifically, the paper concerns edge- and face-cooled optical elements and assesses how beam shape and cooling strength affect the performance. The author first reviews the physics of thermal lensing and discusses how optical distortion coefficients relate the spatial temperature distribution to the wavefront error functions $\delta\phi_+$ and $\delta\phi_-$. For semiconductors with positive thermo-optic coefficients, the analysis can be carried out on a scalar diffraction basis, which implies that the degradation in focal irradiance associated with primary spherical aberrations originates from a single quartic term, $\delta\phi_4\rho^4$. On assuming that it is a good approximation to describe the beam-induced temperature rise by means of a fourth-order even polynomial, it is shown that the amplitude-weighted variance of $\delta\phi_4\rho^4$ provides a suitable measure of the degradation, which leads to the concept of a spherical aberration factor $S = \delta T_4\sqrt{\mathrm{var}[\rho^4]}$. The heat-flow equations for both edge- and face-cooled cylindrical components can be formulated non-dimensionally and solved exactly thus demonstrating that (a) temperature variations causing optical distortion scale with $\beta P/K$, *i.e.*, the total power deposited per unit length and the inverse thermal conductivity of the medium; (b) with the possible exception of high-truncation-parameter Gaussians, fourth-order polynomials yield reasonably accurate temperature profiles; and (c) apodization can be very useful in mitigating the deleterious effects of thermal lensing. For edge-cooled optical elements, the heat-transfer coefficient has no influence on the temperature profile, and the aperture diameter does not affect the performance. An appropriate materials figure of merit is $K/(\chi\beta_V)$, which includes the thermal conductivity K, the distortion coefficient χ, and the absorption coefficient β_V. The treatment of face cooling requires a more elaborate analysis and involves the Nusselt number $Nu = hL_c/K$, the sympol L_c referring to the characteristic length $(D/2)^2/L$. For weak cooling ($Nu \lesssim 1$), the spherical aberration factors are similar to those of edge cooling, but Nusselt numbers $Nu \gtrsim 10$ result in a significant reduction of the distortion, which has important implications for selecting proper operating conditions.

Key words: apodization parameter; cylindrical component; edge cooled; face cooled; laser beam; Nusselt number; optical distortion; spherical aberration; thermal lensing; truncation parameter.

1. Introduction

Optical systems that project laser radiation to a distant target are required to operate "close to the diffraction limit," which implies that the beam emerging from the exit aperture must be essentially aberration free. The optical train, however, always includes components such as windows, modulators, or isolators that absorb a fraction of the transmitted radiation thus giving rise to thermal loadings that may lead to phase distortions and, ultimately, to stress-induced fracture. At high average power levels, these components must be cooled in order to avoid "catastrophic failure"; in conjunction with nonuniform incident power distributions, this causes temperature gradients across the aperture and, by the same token, causes optical distortions [1-3].[1] These distortions, which encompass thermal focusing, wavefront errors, and stress-induced birefringence, severely degrade the quality of the laser beam thus reducing the irradiance on target. In effect, and considering the requirements of contemplated applications, beam-induced optical distortions are often the primary failure mode in the sense that they impose strict limits on the total power, or the total energy, that can be successfully handled by the system. For this reason, it should be of interest to review the physics of the "thermal lensing" process and to examine how the

[1] Numbers in brackets indicate the literature references at the end of the paper.

cooling scheme impacts the phase-aberration problem of high-power laser systems.

Earlier work on beam-induced optical distortions occurring in infra-red (IR) transmissive materials concerns primarily windows, in the thin-disc geometry, under operating conditions such that laser irradiation times remain small compared to thermal diffusion times [4-6]. Thermal lensing occurs because of radial variations in the optical pathlength caused by a combination of effects involving the expansion of the window in addition to temperature- and stress-induced changes of the refractive index; temperature differences of a few degrees only, between the center and the edge, are more than sufficient to destroy the diffraction-limited performance of the window. Components in the shape of long rods, or more generally, cylindrical components that transmit CW radiation and must be cooled have been given much less attention, albeit many applications now require detailed information on beam-induced aberrations. In this connection, we note that, of the various aberrations that may develop, the primary spherical aberration is the one of most significance in the operation of high-power lasers [7]. Consequently, it is the objective of this paper to formulate simple procedures for evaluating the potential impact of such aberrations in a CW regime and, following Gianino and Bendow [8], to assess the merits of edge- and face-cooling techniques. Furthermore, we are reporting on a systematic investigation of the effect of truncation and apodization, in other words, on how the beam shape affects the performance, keeping in mind that, for the purpose of a meaningful comparison, or for providing guidelines on selecting the most efficient operating conditions in terms of achievable focal intensities, the power passed through the component must be kept constant regardless of the irradiance distribution [9].

To accomplish these objectives, we are considering axially symmetric laser beams having Gaussian intensity distributions and traversing a cylindrical material medium normally to the end surfaces. These surfaces are assumed to be perfectly anti-reflection coated; in addition, we are postulating that (a) the media of interest exhibit sufficiently low absorption for the loss in intensity to the minimal, and (b) the thermal and elastic response to incident radiation are isotropic. At this point, and for the convenience of the reader, we will outline the major steps that the present investigation entails and, thus, provide an appropriate "roadmap."

1) The theoretical background required to properly describe laser-induced optical distortions is presented in Sec. 2. Starting with the Huyghens-Fresnel diffraction integral, we demonstrate that for materials such as semiconductors, which have large thermo-optic coefficients, the phase-aberration function effectively "maps" the radial temperature profile [10], *i.e.*,

$$\delta\phi(r) = k\ell\chi\delta T(r) \quad , \tag{1}$$

where χ represents the optical distortion coefficient; the other symbols are as identified in the Glossary. Regarding temperatures, we emphasize that δT measures the laser-induced temperature rise with respect to the coolant and is to be understood as an average over the thickness L,

$$\delta T(r) = \frac{1}{L}\int_{-L/2}^{+L/2} \delta T(r,z)\,dz \quad , \tag{2}$$

which must be obtained from the differential equation that controls the heat-flow pattern.

2) In Appendix A, we show that, for CW or quasi-CW loaded media, the equation to be solved reduces to

$$K\left[\frac{d^2(\delta T)}{dr^2} + \frac{1}{r}\bullet\frac{d(\delta T)}{dr}\right] - \frac{h_F \delta T}{L} + \beta I(r) = 0 \quad , \tag{3}$$

but proper solutions must also verify the boundary condition

$$-K\left.\frac{d(\delta T)}{dr}\right|_{D/2} = h_E \delta T(D/2) \quad , \tag{4}$$

which reflects the heat-transfer situation at the cylindrical edge. In Sec. 3, titled "edge-cooled components," we consider the limiting case of no heat transfer through the end faces ($h_F \equiv 0$), whereas Sec. 4, titled "face-cooled components," concerns the more complex case of an insulated edge ($h_E \equiv 0$) with active cooling of one or both end surfaces. Such cooling configurations are of considerable engineering significance [11], and we will demonstrate that they permit closed-form solutions; additional analytical results are presented in Appendices B and C.

3) Returning now to Eq. (1), it is seen that a fourth-order power-series approximation to the temperature profile leads to

$$\delta\phi(r) = k\ell\chi\left(\delta T_0 - \delta T_2 r^2 + \delta T_4 r^4\right) \quad , \tag{5}$$

which specifies the magnitude of thermal focusing and spherical aberration effects as in classical optical theory [12]. For small aberrations, the Strehl-ratio degradation then involves the variance across the amplitude-weighted aperture, which suggests to use the standard deviation of $\delta\phi_4 r^4$,

$$\left[\delta\phi_4 r^4\right]_{RMS} = (k\ell\chi)\delta T_4 \sqrt{\mathrm{var}\left[r^4\right]} \quad , \tag{6}$$

as a criterion for assessing failure through excessive generation of spherical aberration. The results of our analysis for edge-cooled and face-cooled components are given in Secs. 3 and 4, respectively; in this context, we demonstrate that beam-apodization techniques may indeed help to moderate the deleterious effects of thermal lensing.

2. Simple Theoretical Considerations

In a cylindrical geometry, the degradation in focal irradiance caused by thermal lensing is best described in terms of the two phase shifts $\delta\phi_\rho$ and $\delta\phi_\theta$ associated with radial and azimuthal polarizations; an evaluation of the Strehl ratio as carried out in Sec. 2.1 then yields the proper expressions for obtaining the optical distortion coefficients that relate the spatial temperature distribution to the wavefront error function. These distortion coefficients are discussed in some detail, and in Sec. 2.2 we derive explicit equations that relate the coefficients to intrinsic material properties and apply to thin-disc as well as long-rod configurations. In this light, and restricting now our attention to optically transmitting media with positive dn/dT's, we demonstrate that a scalar diffraction treatment as carried out in Sec. 2.3 should be quite acceptable thus providing a simple analytical base for "measuring" the impact of beam-induced spherical aberrations on the far-field irradiance.

2.1. Focal Irradiance Degradation

In the absence of aberration, the complex amplitude of an axially symmetric focused beam emerging from an aperture of diameter D is best described as follows [9]:

$$U(\rho) = \sqrt{I(\rho)}\ \exp\left[-\frac{ik(D/2)^2\rho^2}{2R_o}\right] \quad , \tag{7}$$

where ρ refers to the normalized radial distance in the aperture plane [$\rho = r/(D/2)$], whereas R_o measures the distance from the aperture to the intended focus thus defining the radius of curvature of the spherical wavefront. Assume now that the thermal lensing process gives rise to radially dependent wavefront distortions without altering the intensity distribution. In that case, the Strehl ratio, or ratio of focal irradiances with and without aberration, is simply [5]

$$S = \frac{\left|\int_0^1 (1/2)\left[\exp(i\delta\phi_\rho) + \exp(i\delta\phi_\theta)\right]\sqrt{I(\rho)}\rho d\rho\right|^2}{\left[\int_0^1 \sqrt{I(\rho)}\rho d\rho\right]^2} \tag{8}$$

if $\delta\phi_\rho$ and $\delta\phi_\theta$ are the phase distortions experienced by normally incident light polarized along the radial and azimuthal directions, respectively. For weak distortions, we may proceed by expanding the two multiplicative phase factors to second order in the manner originally suggested by Born and Wolf, *i.e.*, $\exp(i\delta\phi) \simeq 1 + i\delta\phi - \delta\phi^2/2$ [12]. On introducing symmetric and anti-symmetric combinations of the radial and azimuthal phase aberrations,

$$\delta\phi_+ = \frac{1}{2}\left(\delta\phi_\rho + \delta\phi_\theta\right) \tag{9a}$$

$$\delta\phi_- = \frac{1}{2}\left(\delta\phi_\rho - \delta\phi_\theta\right) \quad , \tag{9b}$$

this procedure then leads to a remarkably compact expression for the Strehl ratio,

$$S = 1 - \left\{\mathrm{var}\left[\delta\phi_+\right] + \langle\delta\phi_-^2\rangle\right\} \quad , \tag{10}$$

keeping in mind that the variance is defined in accord with

$$\mathrm{var}[X] = \langle X^2\rangle - \langle X\rangle^2 \quad , \tag{11}$$

and the symbol <> refers to amplitude-weighted averages over the entire aperture,

$$\langle Y\rangle = \int_0^1 Y\sqrt{I}\rho d\rho \ / \ \int_0^1 \sqrt{I}\rho d\rho \quad . \tag{12}$$

The advantage of this method is quite obvious: Since $\delta\phi_-$ exists only if $\delta\phi_\rho \neq \delta\phi_\theta$, Eq. (10) specifies the role of birefringence with regard to focal irradiances, compared to all other sources of distortion.[2]

2.2. Optical Distortion Coefficients

Prior to the onset of thermal loading, the distorting medium is assumed at uniform temperature and birefringence free; any normally incident light ray that traverses this medium without suffering significant deviation or loss in intensity then emerges with its phase shifted by an amount

$$\phi = k(n-1)\ell \quad , \tag{13}$$

where k designates the propagation constant, n is the unperturbed index of refraction, and l refers to the path length. The processing of laser power in the optical train gives rise to radially dependent aberrations as a result of the change in path length and the change in index caused by beam-induced temperature gradients:

[2]Note that issues relating to the depolarization associated with birefringence are not addressed in this paper.

$$\delta\phi = k\left[(n-1)\delta\ell + \ell\delta n\right] \quad . \tag{14}$$

The variation in path length reflects the magnitude of the tensor component of strain in the z direction, *i.e.*,

$$\delta\ell = \ell\varepsilon_{zz} \quad , \tag{15}$$

which relates to the temperature field and the stress tensor by means of Hooke's law,

$$\varepsilon_{zz} = \alpha\delta T + \sigma_{zz}/E - (\nu/E)(\sigma_{\rho\rho} + \sigma_{\theta\theta}) \quad . \tag{16}$$

Similarly, the change in index is caused by temperature variations and by thermal stresses:

$$\delta n = (\delta n)_{temp} + (\delta n)_{stress} \quad . \tag{17}$$

The effect of temperature can be easily formulated if the index of refraction varies more or less linearly over the temperature range of interest; in a first approximation, we may write

$$(\delta n)_{temp} = (\partial n/\partial T)_{\sigma=o}\delta T \tag{18}$$

and set $(\partial n/\partial T)_{\sigma=0}$ equal to the thermo-optic coefficient as measured at the fiducial temperature. An evaluation of index variations associated with thermal stresses involves considerations relating to the photo-elastic effect [13], which show that

$$(\delta n)_{stress} = \left(-n^3/2\right)\left(q_{||}\sigma_{\rho\rho} + q_{\perp}\sigma_{\theta\theta} + q_{\perp}\sigma_{zz}\right) \tag{19a}$$

for plane waves polarized along the radial direction and

$$(\delta n)_{stress} = \left(-n^3/2\right)\left(q_{\perp}\sigma_{\rho\rho} + q_{||}\sigma_{\theta\theta} + q_{\perp}\sigma_{zz}\right) \tag{19b}$$

for azimuthal polarizations, the symbols $q_{||}$ and $q_{\perp}$ referring to the stress-optic coefficients for stresses applied parallel and perpendicular to the polarization axis.

The stresses occurring in a solid cylinder that is not constrained by external forces, has an axially symmetric temperature distribution, and is made of elastically isotropic material can be described analytically for two simple model situations [14].

1) The plane-stress model, which applies to thin-disc geometries, and yields

$$\sigma_{\rho\rho} = \alpha E\left[\int_0^1 \delta T\rho'd\rho' - \left(1/\rho^2\right)\int_0^\rho \delta T\rho'd\rho'\right] \tag{20a}$$

$$\sigma_{\theta\theta} = \alpha E\left[\int_0^1 \delta T\rho'd\rho' + \left(1/\rho^2\right)\int_0^\rho \delta T\rho'd\rho' - \delta T\right] \tag{20b}$$

$$\sigma_{zz} = 0 \tag{20c}$$

for the principal stresses; note that for this approximation to be valid, the axial stress must vanish.

2) The plane-strain model, which yields

$$\sigma_{zz} = \sigma_{\rho\rho} + \sigma_{\theta\theta} \tag{21}$$

with planar stresses as in Eqs. (20a) and (20b) but for the factor αE that must be replaced by $\alpha E/(1-\nu)$; in principle, this "long-rod" approximation should be used when the path length becomes longer than the beam radius and axial stresses cannot be ignored.

Returning now to Eq. (9), it becomes a straightforward matter to establish that the two aberration-function combinations $\delta\phi_+$ and $\delta\phi_-$ relate to the temperature distribution in a fairly simple manner:

$$\delta\phi_+ = k\chi_+ \ell\, \delta T + \rho\text{-independent terms} \tag{22a}$$

$$\delta\phi_- = k\chi_- \ell \left[\left(2/\rho^2\right) \int_0^\rho \delta T \rho' d\rho' - \delta T \right] \quad , \tag{22b}$$

which takes into account that only radially-dependent phase shifts contribute to the variance of $\delta\phi_+$ and the degradation in focal intensity [see Eq. (10)]. Equations (22a) and (22b) define two optical distortion coefficients, χ_+ and χ_-, which characterize the medium's sensitivity to thermal lensing and properly "assemble" the material constants that control the thermal lensing process.[3] In a disc geometry, the calculation yields

$$\chi_+ = (\partial n/\partial T)_{\sigma=0} + (n-1)\alpha(1+\nu) + (n^3 \alpha E/4)(q_{||}+q_{\perp}) \tag{23a}$$

$$\chi_- = (n^3 \alpha E/4)(q_{||}-q_{\perp}) \quad , \tag{23b}$$

which demonstrates that χ_+ involves the temperature-induced change in index, the contribution due to bulging and the average photo-elastic effect for the two polarizations; the coefficient χ_- exists only if the medium is stress-birefringent. For long rods, we have

$$\chi_+ = (\partial n/\partial T)_{\sigma=0} + (n^3 \alpha E/4)(q_{||}+3q_{\perp})/(1-\nu) \tag{24a}$$

$$\chi_- = (n^3 \alpha E/4)(q_{||}-q_{\perp})/(1-\nu) \quad , \tag{24b}$$

which no longer includes a "bulging" term thus reflecting the well-known [14] observation that the thickness variation δl is ρ-independent in that geometry.

2.3. Spherical Aberration Evaluation

The most commonly used materials for laser transmissive optics are semiconductors such as Ge or ZnSe, which possess large thermo-optic coefficients that dominate the thermal lensing mechanism thus insuring that the birefringence contribution associated with $\delta\phi_-$ [see Eq. (10)] does not add significantly to the focal irradiance degradation [15]. From now on, we will restrict the analysis to situations that satisfy this condition, which implies that beam-induced aberrations can be treated in the context of a scalar theory with

$$\delta\phi(\rho) = k\chi\ell\, \delta T(\rho) \tag{25}$$

---

[3] Regarding stress-optic coefficients, we remind the reader that, for isotropic material, $q_{||}$ and $q_{\perp}$ are simply the piezo-optic constants q_{11} and q_{12} measured in the laboratory and tabulated in the handbooks. For cubic material, the theory holds only if the light propagates along the {111} direction; relevant elastic and photo-elastic coefficients must be obtained from the elastic compliance tensor in conjunction with the piezo-optic or the elasto-optic tensor [15].

and optical distortion coefficients as in Eq. (23a) or (24a).[4] The formula for the far-field irradiance on axis then reduces to a simple Fresnel integral [9],

$$I(R;0) = \frac{k^2(D/2)^4}{R^2}\left|\int_0^1 U(\rho)\exp\left[\frac{ik(D/2)^2\rho^2}{2R} + i\delta\phi(\rho)\right]\rho d\rho\right|^2 , \qquad (26)$$

where $\delta\phi(\rho)$ accounts for the deviation from the spherical reference wavefront and "maps" the temperature profile of the distorting medium; this integral expression provides a convenient starting point for the discussion that follows.

Assume now that it is a good approximation to describe the beam-induced temperature rise by means of a fourth-order even polynomial,

$$\delta T(\rho) = \delta T_0 - \delta T_2\rho^2 + \delta T_4\rho^4 . \qquad (27)$$

This allows us, through substitution into Eq. (25), to obtain a power-series expansion for the aberration function,

$$\delta\phi(\rho) = \delta\phi_0 - \delta\phi_2\rho^2 + \delta\phi_4\rho^4 , \qquad (28)$$

and, by the same token, to relate thermal defocusing as well as spherical aberration effects to the temperature profile [12]. With an aperture field as given earlier, Eq. (26) then suggests to compensate any thermally induced defocusing by "zooming" to a new focus, at a distance R_o' specified by the relation

$$\frac{1}{R_o'} = \frac{1}{R_o} - \frac{2\delta\phi_2}{k(D/2)^2} . \qquad (29)$$

The irradiance at the original focus (the target!) then amounts to

$$I(R_o;0) = \frac{k^2(D/2)^4}{R_o^2}\left|\int_0^1 \sqrt{I(\rho)}\,\exp\left(i\delta\phi_4\rho^4\right)\rho d\rho\right|^2 , \qquad (30)$$

which immediately tells us (see Sec. 2.1) that the Strehl ratio boils down to

$$s = 1 - \mathrm{var}\left[\delta\phi_4\rho^4\right] \qquad (31)$$

for small perturbations. In other words, after refocussing, the degradation in focal irradiance originates entirely from the quartic term $\delta\phi_4\rho^4$ associated with primary spherical aberrations. Keeping in mind that it is the purpose of this paper to assess the impact of spherical aberrations on the far-field performance, we conclude that the variance of $\delta\phi_4\rho^4$ represents a suitable "measure" since "failure" in the sense of Maréchal [12] reflects a Strehl of less than 0.8. Consequently, we take it that failure through excessive generation of spherical aberration reflects an RMS wavefront deformation $(1/k)[\delta\phi_4\rho^4]_{RMS} \gtrsim \lambda/14$. This definition disregards the potential benefit of "aberration balancing" techniques but conforms to our objective, which concerns thermally induced spherical aberrations and their dependence upon beam shape

[4] In effect, since the stress-optic and the expansion-related term are both much smaller than dn/dT, it should be acceptable to set χ equal to dn/dT for cylindrical components made of semiconducting material, irrespective of the aspect ratio L/D.

and cooling method. In this light, we will focus attention on the standard deviation

$$\left[\delta\phi_4\rho^4\right]_{RMS} = k\chi\ell S \tag{32}$$

and devote the rest of this paper to evaluating the spherical aberration factor

$$S = \delta T_4\sqrt{\text{var}\left[\rho^4\right]} = \delta T_4\sqrt{\langle\rho^8\rangle - \langle\rho^4\rangle^2} \tag{33}$$

for temperature distributions and intensity distributions that are believed pertinent in the context of operating cooled CW-laser optics.

The two weighted averages in Eq. (33) involve the aperture amplitude $\sqrt{I(\rho)}$; for our purposes, we write

$$I(\rho) = I_o G(\rho) \tag{34}$$

I_o referring to the peak intensity on axis and $G(\rho)$ describing the beam shape off axis. Since we wish to investigate how different intensity distributions may alter the response of a given component, the peak intensity must be adjusted so that the total power P transmitted through the aperture remains fixed,

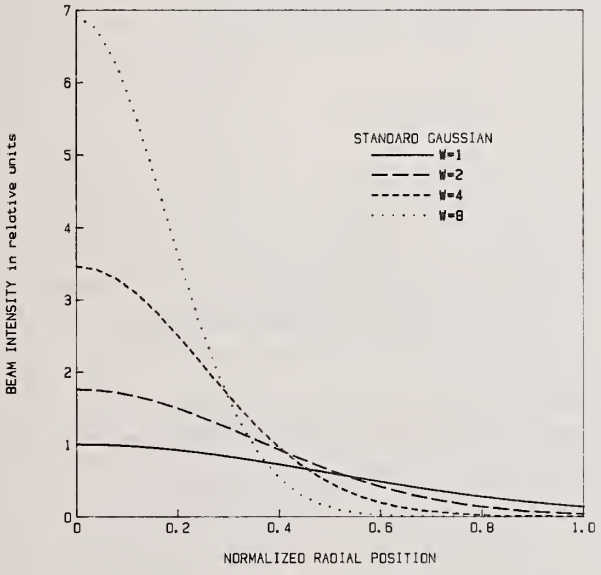

Figure 1a. Illustrates the radial dependence of Standard Gaussian beams, $I(\rho) = I_o\exp(-2W\rho^2)$, of identical total transmitted power $P = 2\pi(D/2)^2\int_0^1\exp(-2\rho^2)\rho\,d\rho$.

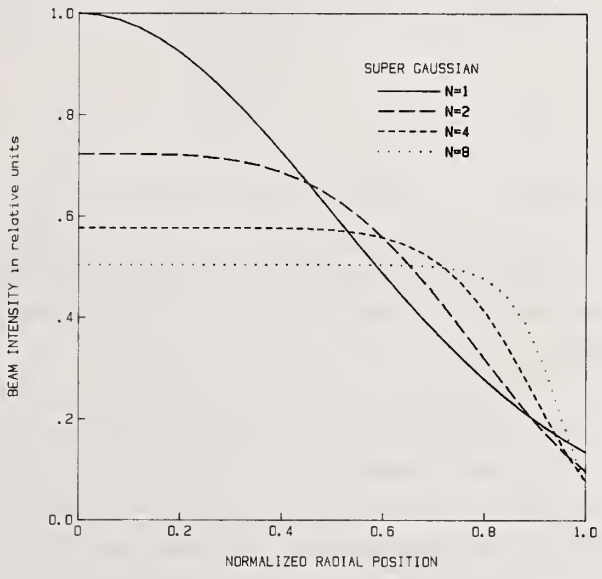

Figure 1b. Illustrates the radial dependence of Super Gaussian beams, $I(\rho) = I_o\exp(-2\rho^{2N})$, of identical total transmitted power $P = 2\pi(D/2)^2\int_0^1\exp(-2\rho^2)\rho\,d\rho$.

which suggests to express I_o in the following manner,

$$I_o = \frac{P}{2\pi(D/2)^2\int_0^1 G(\rho')\rho'd\rho'}\quad , \tag{35}$$

regardless of the shape function G. The shapes we propose to consider include Standard Gaussians,

$$G(\rho) = \exp(-2W\rho^2)\quad , \tag{36a}$$

the parameter W [$W = (D/2)^2/\omega^2$] characterizing the truncation, and Super Gaussians as defined in Ref. [16], *i.e.*,

$$G(\rho) = \exp(-2\rho^{2N}) \tag{36b}$$

with N > 1. For convenience, we may refer (perhaps incorrectly) to the parameter N as an "apodization" parameter considering that Eq. (36b) models quasi flat-topped beams, which are best created from conventional Gaussian inputs by means of an apodizer [17]. Figures 1a and 1b illustrate these shapes for

Table 1a. Amplitude-weighted RMS value of $\rho^4 (0 \lesssim \rho \lesssim 1)$ for Standard Gaussians; W is the truncation parameter.

W	$\sqrt{\text{var}[\rho^4]}$
1	0.27277
2	0.23746
3	0.19852
4	0.16135
5	0.12908
6	0.10268
7	0.08187
8	0.06578
9	0.05343
10	0.04396

Table 1b. Amplitude-weighted RMS value of $\rho^4 (0 \lesssim \rho \lesssim 1)$ for Super Gaussians; N is the apodization parameter.

N	$\sqrt{\text{var}[\rho^4]}$
1	0.27277
2	0.26437
3	0.26254
4	0.26294
5	0.26419
6	0.26572
7	0.26731
7	0.26888
9	0.27033
10	0.27120

peak intensities as given by Eq. (35) but normalized to $I_o = 1$ for conventional Gaussians (W = N = 1), thus emphasizing that larger truncation parameters point to narrower beams, whereas larger apodization parameters yield increasingly flat-topped profiles. For completeness, we are also providing (see Tables 1a and 1b) the results of evaluating $\sqrt{\text{var}[\rho^4]}$ for truncation/apodization parameter values ranging from 1 to 10; in this connection, we note that, if the beam covers the entire aperture ($1/e^2$-truncated Gaussian and the Super Gaussians), we have $\sqrt{\text{var}[\rho^4]} \simeq 0.27$, which shows that for a quarter-wave of spherical aberration at the edge ($\delta\phi_4 = \pi/2$), the Strehl ratio is close to 0.82 thus demonstrating the applicability of the Rayleigh criterion [18] to beam shapes as in Fig. 1b.

3. Edge-Cooled Components

The heat-flow equation for edge-cooled, CW-loaded cylindrical components can be formulated in a simple non-dimensional form that leads to a compact integral solution as demonstrated in Sec. 3.1; for Gaussian inputs, this solution yields an analytical expression that does not require computer processing for its evaluation (see Appendix B). Once the temperature distributions are available, and since a scalar treatment should be entirely adequate, we may derive the coefficients δT_4 of the power-series expansions (27) by means of non-linear regressions and obtain the spherical aberration factors as discussed in Sec. 3.2. The merits of this procedure are illustrated in Sec. 3.3, which concerns a germanium Faraday isolator and its power-handling capability for a variety of beam shapes.

3.1. Analytical Solution

For edge-cooled cylindrical components, the heat-flow equation (3) takes the form

$$K\left[\frac{d^2(\delta T)}{dr^2} + \frac{1}{r}\cdot\frac{d(\delta T)}{dr}\right] + \beta I_o G(r) = 0 \qquad (37)$$

if $I_o G(r)$ describes the incident beam, which we assume to propagate without divergence or attenuation. Note that Eq. (37) does not involve the heat-transfer coefficient, which implies that temperature variations within the optical medium reflect the transport of deposited heat towards the edge but are independent of the heat-transfer mechanism to the coolant. In terms of the dimensionless radial variable ρ, and taking Eq. (35) into account, we may rewrite the heat-flow equation as follows:

$$\frac{d^2(\delta T)}{d\rho^2} + \frac{1}{\rho}\cdot\frac{d(\delta T)}{d\rho} + G_o G(\rho) = 0 \qquad (38)$$

thus introducing the constant G_o,

$$G_o = \frac{\beta P/K}{2\pi\int_0^1 G(\rho')\rho' d\rho'} \quad , \qquad (39)$$

which combines relevant beam characteristics and material properties. Since the factor $\beta P/K$ has the dimension of a temperature, we may further simplify the analysis by expressing both δT and G_o in units of $\beta P/K$, which leads to

$$\frac{d^2(\delta T^*)}{d\rho^2} + \frac{1}{\rho}\cdot\frac{d(\delta T^*)}{d\rho} + G_o^* G(\rho) = 0 \quad , \qquad (40)$$

the symbols δT^* and G_o^* denoting that these are dimensionless quantities; in this connection, we should keep in mind that, for Standard as well as Super Gaussians, G_o^* depends exclusively upon the shape parameter W or N. Regarding boundary conditions, it is clear that, because of the azimuthal symmetry, the solution must satisfy the condition

$$d(\delta T^*)/d\rho\Big|_{\rho=0} = 0 \qquad (41)$$

on axis. At the edge, and following Horrigan [1], we may set the temperature equal to that of the coolant, *i.e.*,

$$\delta T^*(\rho=1) = 0 \quad , \qquad (42)$$

which amounts to postulating an infinitely large heat-transfer coefficient h_E [see Eq. (4)]; this is acceptable considering that, in the framework of our model, h_E controls the temperature discontinuity between the edge and the coolant but has no impact on temperature variations that cause thermal lensing.

The procedure that leads to a closed-form solution of the system (40-42) starts with an *Ansatz* such as

$$\delta T^*(\rho) = \int_\rho^1 \tau(\rho')d\rho' \quad , \qquad (43)$$

which satisfies the boundary condition at the edge and yields a first-order linear differential equation,

$$d\tau/d\rho + \tau/\rho - G_o^* G(\rho) = 0 \quad , \qquad (44)$$

after insertion into Eq. (40). This equation is of the type

$$y' + f(x)y = g(x) \qquad (45)$$

whose general solution [19] is well known and can be expressed in terms of integrals:

$$y(x) = \exp\left[-b(x)\right]\left\{C + \int^{x} g(\xi)\exp\left[b(\xi)\right]d\xi\right\} \quad , \tag{46}$$

where C is an integration constant and $b(x) = \int^{x} \bar{r}(\xi)d\xi$. Taking the on-axis boundary condition into consideration, the solution to Eq. (44) is therefore

$$\tau(\rho) = (G_o^*/\rho)\int_o^{\rho} G(\rho')\rho' d\rho' \quad , \tag{47}$$

which, in turn, provides a compact and aesthetically pleasing expression for the temperature distribution,

$$\delta T^*(\rho) = G_o^* \int_{\rho}^{1} d\rho'/\rho' \int_o^{\rho'} G(\rho'')\rho'' d\rho \quad . \tag{48}$$

In essence, the problem has been reduced to quadratures; for Standard Gaussian beam shapes, $G(\rho) = \exp(-2W\rho^2)$, both integrations can be carried out analytically, which leads to "exact" solutions as shown in Appendix B. But first, we wish to stress two important points that emerge from the analysis.

1) Since both δT^* and G_o^* are in units of $\beta P/K$, it is seen that temperature variations causing optical distortion "scale" with $\beta P/K$, *i.e.*, the total power deposited per unit path length and the inverse thermal conductivity of the medium.

2) In principle, the aperture diameter does not affect the performance, albeit there may be a "second-order" effect relating to the effective absorption coefficient β [see Eq. (A-4)] because the thickness L of passive components such as windows is indeed a function of the diameter D.

3.2. Numerical Evaluation

The steady-state temperature profiles of edge-cooled components subjected to incident beams as in Figs. 1a and 1b are displayed in Figs. 2a and 2b, respectively. These are solutions of the differential equation (40) that satisfy the boundary conditions and scale with $\beta P/K$, thus providing convenient "baseline numbers" for obtaining the true temperature distributions. As anticipated, at fixed beam-power levels, Standard Gaussians generate steeper profiles than Super Gaussians, which should be reflected in the magnitude of the quartic coefficient δT_4^* associated with primary spherical aberrations.

Taking the boundary conditions into account, a fourth-order polynomial approximation to the dimensionless temperature distribution $\delta T^*(\rho)$ has the form

$$\delta T^*(\rho) = \delta T_0^* - \delta T_2^* \rho^2 + \left(\delta T_2^* - \delta T_0^*\right)\rho^4 \tag{49a}$$

and involves two independent parameters only. The Marquardt-type regressions [20] that we performed for the purpose of fitting such polynomials to distributions as shown in Figs. 2a and 2b did not yield satisfactory results thus compelling us to proceed on a three-independent parameter basis, *i.e.*

$$\delta T^*(\rho) = \delta T_0^* - \delta T_2^* \rho^2 + \delta T_4^* \rho^4 \quad , \tag{49b}$$

which amounts to relaxing the edge-boundary condition. For Super Gaussians as well as relatively broadly-shaped Standard Gaussians, the residuals are minimal (see Fig. 3). In effect, if we characterize the quality of the fit by means of a relative standard deviation defined as follows,

$$\sigma(\%) = \frac{100}{\delta T_0^*}\sqrt{\frac{\Sigma(\text{residuals})^2}{N-P}} \quad , \tag{50}$$

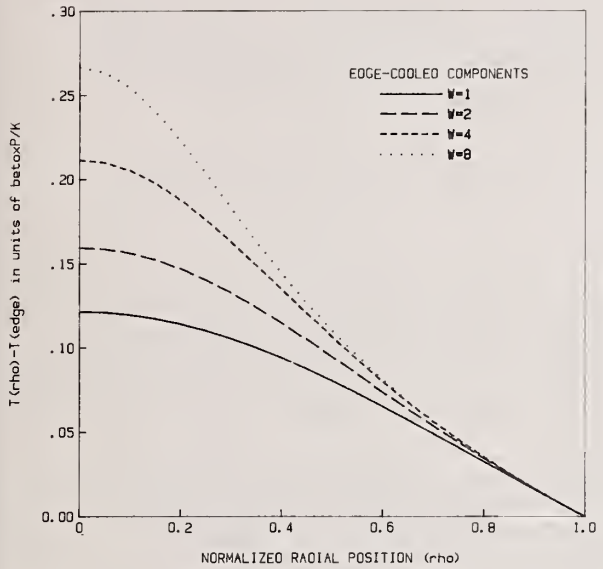

Figure 2a. Steady-state temperature profile of edge-cooled components subjected to Standard Gaussian beams as illustrated in Fig. 1a.

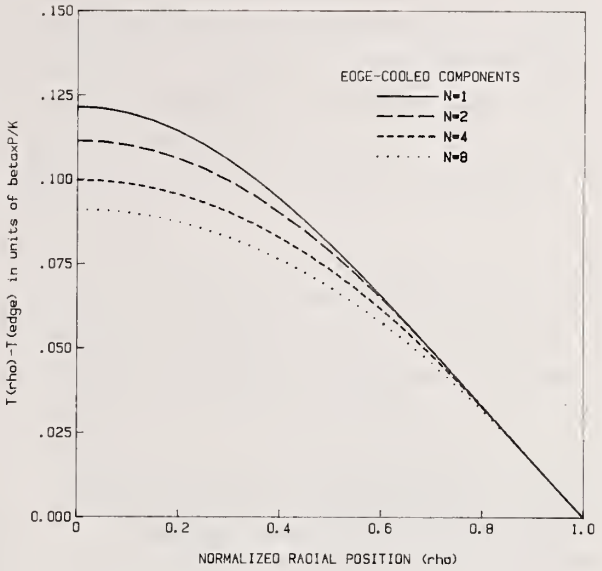

Figure 2b. Steady-state temperature profile of edge-cooled components subjected to Super Gaussian beams as illustrated in Fig. 1b.

where N is the number of data points and P is the number of independent parameters, it turns out that σ remains smaller than 1% for the Super Gaussians but may exceed 3% for Standard Gaussians having truncation parameters W > 3 (see Tables 2a and 2b). We conclude that, with the possible exception of

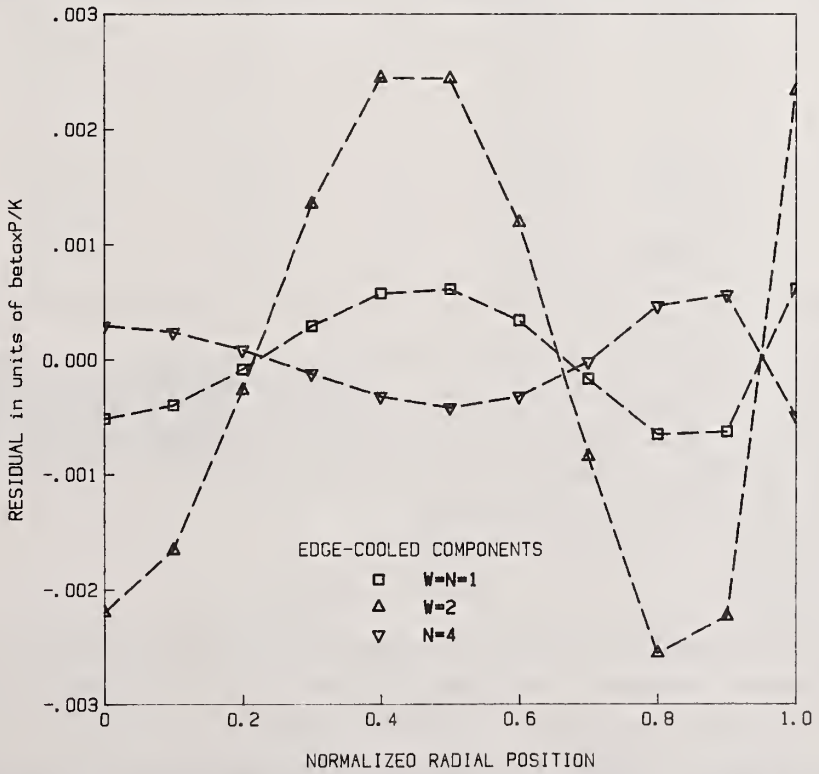

Figure 3. Residuals of three-parameter fits [see Eq. (49b)] to exact temperature distributions as displayed in Figs. 2a and 2b.

high-truncation-parameter Gaussians, the polynomial expansion (49b) yields reasonably accurate temperature profiles, thus implying that higher than Seidel aberrations should be inconsequential. The tables also provide a listing of the δT_4^*'s and $(\delta T_2^* - \delta T_0^*)$ differences for the three-parameter regressions, which demonstrates that our polynomials obey the edge-boundary condition surprisingly well.

Returning now to Eq. (33), we note that the spherical aberration factor in units of $\beta P/K$ is simply

$$S^* = \delta T_4^* \sqrt{\mathrm{var}[\rho^4]} \tag{51}$$

and can be easily obtained by referring to Tables 1 and 2; the results are displayed in Fig. 4 as a function of the truncation parameter (Standard Gaussians) or the apodization parameter (Super Gaussians). At a fixed incident power level, apodized beams generate much less aberration than Gaussians, which demonstrate that, indeed, apodization can be a viable method for suppressing deleterious effects induced by thermal

Table 2a. Lists the relative standard deviation [see Eq. (50)] and compares δT_4^* to $\delta T_2^* - \delta T_0^*$ [see Eq. (49b)] for edge-cooled components subjected to Standard Gaussian beams.

W	st. dev. (%)	δT_4^*	$\delta T_2^* - \delta T_0^*$
1	0.4690	0.05145	0.05084
2	1.4312	0.11308	0.11074
3	2.4854	0.16960	0.16505
4	3.4818	0.21669	0.20993
5	4.3792	0.25534	0.24655
6	5.1797	0.28743	0.27682
7	5.8922	0.31449	0.30228
8	6.5302	0.33769	0.32405
9	7.1052	0.35786	0.34295
10	7.6263	0.37562	0.35957

Table 2b. Lists the relative standard deviation [see Eq. (50)] and compares δT_4^* to $\delta T_2^* - \delta T_0^*$ [see Eq. (49b)] for edge-cooled components subjected to Super Gaussian beams.

N	st. dev. (%)	δT_4^*	$\delta T_2^* - \delta T_0^*$
1	0.46899	0.051453	0.050836
2	0.26776	0.029156	0.029432
3	0.41267	0.017510	0.017996
4	0.40794	0.011409	0.011900
5	0.36586	0.007928	0.008371
6	0.31787	0.005790	0.006175
7	0.27439	0.004396	0.004726
8	0.23807	0.003443	0.003726
9	0.20554	0.002765	0.003009
10	0.17964	0.002267	0.002478

lensing. With Standard Gaussians, on the contrary, the coefficient δT_4^* first increases with the truncation parameter thus giving rise to enhanced aberration effects for $W \lesssim 4$; beyond that point, gradual moderation sets in, in other words, the system becomes more aberration tolerant, which is understandable since the power is now concentrated in a small region near the center of the aperture, and outer-region aberrations do not contribute to the wavefront distortion process.

3.3. Practical Application

To illustrate how the results of our analysis can be applied to situations of engineering interest, we may consider the interband Faraday-rotator assembly displayed in Fig. 5, which was originally designed for a laser-fusion application at 10.6 μm [21]. The rotation medium consists of a near-intrinsic germanium rod (L = 12 cm, D = 2.67 cm) maintained at room temperature by means of a recirculating Freon coolant in thermal contact with the convex edge surface; the function of the evacuated chamber with its two

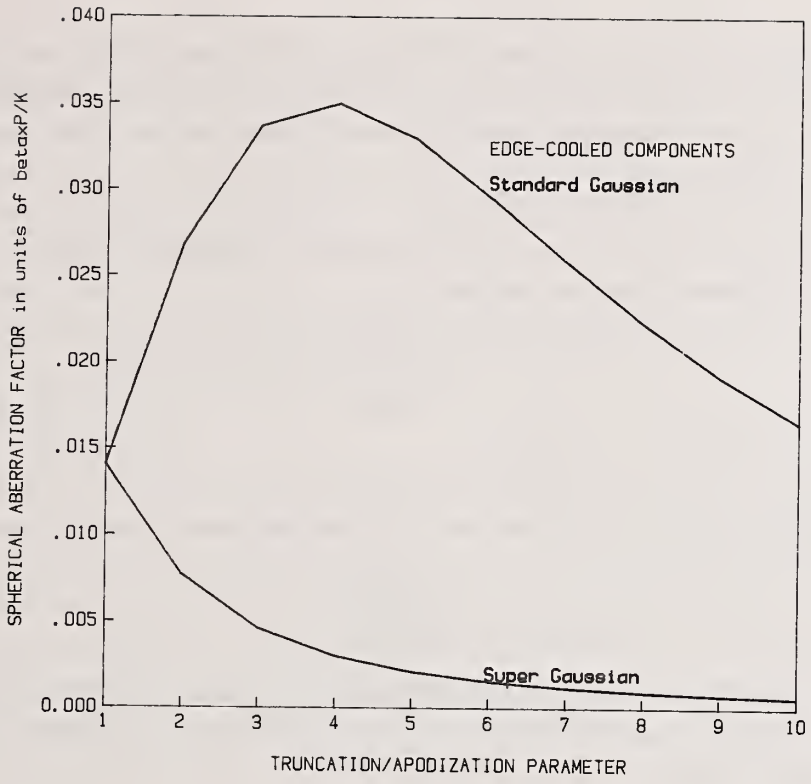

Figure 4. Non-dimensional spherical aberration factor of edge-cooled components subjected to Standard Gaussian or Super Gaussian laser beams.

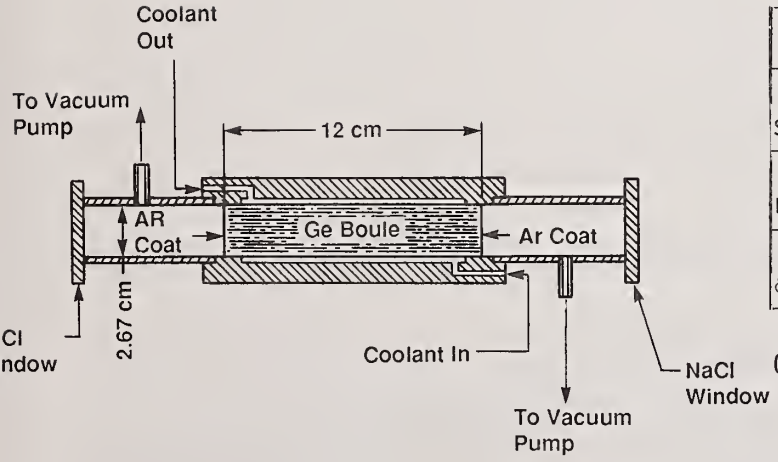

	W=N=1	W=2	N=4
$S^*(1)$	0.0140	0.0269	0.0030
$P_{lim}(W)$	59	31	277
$\delta T^{(a)}_{peak}(K)$	0.829	0.765	1.413

(a) Assumes $h_E = 1\ Wcm^{-2}K^{-1}$.

Figure 5. Interband germanium Faraday-rotator assembly for a CO_2-laser isolator application [21]; the table summarizes our evaluation of the performance characteristics in a CW mode of operation.

NaCl windows is to prevent condensation on the AR-coated end faces. Although not intended for high-average power operation, we may consider assessing the performance of this device in terms of thermal lensing as well as thermal runaway since both features ultimately control the power-handling capability in a CW or quasi-CW regime.

From a beam-quality point of view, we have seen (Sec. 2.3) that thermally induced spherical aberrations should be tolerable as long as the relation

$$\left[\delta\phi_4 \rho^4\right]_{RMS} \lesssim k(\lambda/14) \tag{52}$$

is satisfied. Since $\delta\phi_4 = (k\chi l)\,\delta T_4$ in the absence birefringence, and since $S = (\beta P/K)S^*$ for edge-cooled configurations, Eq. (52) can be rewritten as follows:

$$(k\chi\ell)(\beta P/K)S^* \lesssim k(\lambda/14) \quad , \tag{53}$$

which immediately tells us that the limiting total power, or power that can be passed without generating excessive distortion is

$$P_{lim} = \frac{(\lambda/14)K}{\chi\ell\beta S^*} \quad , \tag{54}$$

where S^* represents a spherical aberration factor as given in Fig. 4. In passing, we note that, for long rods or thick cylinders, the effective absorption coefficient β reduces to the bulk absorption coefficient β_V, and Eq. (54) then suggests an appropriate materials figure of merit,

$$FoM = K/(\chi\beta_V) \quad , \tag{55}$$

considering that S^* depends only upon the beam shape. In this connection, we may also reemphasize that, for such edge-cooled configurations, the power P_{lim} is completely independent of the aperture size. This, of course, does not hold for the peak temperature excursion since

$$\delta T_{peak} = (\beta P/K)\,\delta T^*(0) + (T_E - T_C) \quad , \tag{56}$$

where $(T_E - T_C)$ measures the temperature jump that occurs at the edge when the heat-transfer coefficient has a finite magnitude. In effect, since the deposited beam power amounts to $P\beta l$, and since the power removed via edge cooling is $\pi DLh_E(T_E - T_C)$, we have

$$T_E - T_C = \beta P/(\pi D h_E) \tag{57}$$

as long as $l = L$; all other factors remaining constant, the temperature discontinuity at the edge thus scales with 1/D, which could be significant if thermal runaway becomes an issue.

For the Faraday rotator of interest here, this analysis yields results as summarized in Fig. 5. The physical constants are as follows:

- Thermal conductivity $K = 0.67\ Wcm^{-1}K^{-1}$ at room temperature [22].
- Distortion coefficient $\chi \simeq dn/dT = 26.8 \times 10^{-5}K^{-1}$ at 10.6 μm [23].
- Absorption coefficient $\beta = 0.019\ cm^{-1}$ in the absence of free carriers [24].[5]

Note that, in germanium, the distortion occurs almost entirely as a result of the thermo-optic effect (see Sec. 2.2), which ensures that the beam induced stress-birefringence does not cause any depolarization

[5]For a 12-cm long rod, the beam-attenuation factor $e^{-\beta l}$ is therefore equal to 0.796, which implies that roughly 20% of the incident beam power will be dissipated in traversing the rod; our calculation does not take the intensity loss into account.

and, thus, does not interfere with the operation of the rotator. Regarding the tabulation in Fig. 5, three comments are in order:

1) The spherical aberration factors are as read-off the two curves plotted in Fig. 4 and apply to a $1/e^2$-truncated Gaussian (W=N=1), to a more strongly peaked beam (W=2), and a typical flat-topped shape (N=4).

2) Allowable average power levels turn out to be quite low, particularly for W=2 Gaussians, but apodization may improve the performance by almost an order of magnitude.

3) The predicted temperature excursions are based on a heat-transfer coefficient h_E of 1 $Wcm^{-2}K^{-1}$, which is representative of flowing liquid coolants [11], and suggest that thermal runaway situations can be avoided with a coolant at or slightly below room temperature.

4. Face-Cooled Components

The treatment of face cooling and its effect on beam quality requires a more elaborate analysis than the case of edge cooling. Following the pattern established in Sec. 3, we begin by formulating the heat-flow equation in a non-dimensional manner, which will give us an opportunity to define a suitable Nusselt number for describing the efficacy of the cooling process; an exact analytical solution will be derived in Sec. 4.1 and further discussed in Appendix C. Pertinent numerical evaluations are carried out in Sec. 4.2, primarily for the purpose of investigating how thermally induced spherical aberrations of face-cooled optical elements depend upon beam shape and cooling strength; a practical illustration is provided in Sec. 4.3, where we consider the surface cooling requirement of a double-pane ZnSe window for an industrial CO_2 laser.

4.1. Analytical Solution

As demonstrated in Appendix A, we can reasonably assume that the steady-state temperature profile of a face-cooled axisymmetric and optically transparent component obeys the following differential equation:

$$K\left[\frac{d^2(\delta T)}{dr^2} + \frac{1}{r}\cdot\frac{d(\delta T)}{dr}\right] - \frac{h_F \delta T}{L} + \beta I_o G(r) = 0 \quad , \tag{58}$$

where h_F represents the net heat-transfer coefficient, and δT refers to the thickness-averaged beam-induced temperature increase. Proceeding now as in Sec. 3.1, we may rewrite Eq. (58) in a manner such as

$$\frac{d^2(\delta T)}{d\rho^2} + \frac{1}{\rho}\cdot\frac{d(\delta T)}{d\rho} - \frac{h_F (D/2)^2}{KL} + G_o G(\rho) = 0 \quad , \tag{59}$$

which immediately suggests to make use of the Nusselt number [25]

$$Nu = h_F L_c / K \tag{60}$$

for characterizing the cooling process. Note that the symbol L_c refers to a characteristic length equal to $(D/2)^2/L$ and thus specifies how the geometry of the optical element, that is, aperture radius and aspect ratio, enter the definition of the Nusselt number. In this light, we may cast Eq. (59) in a completely non-dimensional form,

$$\frac{d^2(\delta T^*)}{d\rho^2} + \frac{1}{\rho}\cdot\frac{d(\delta T^*)}{d\rho} - Nu \times \delta T^* + G_o^* G(\rho) = 0 \quad , \tag{61}$$

if δT^* and G_o^* are both in units of $\beta P/K$; evidently, the two terms that originate from the Laplacian reflect lateral heat-transport contributions, the term $-Nux\delta T^*$ refers to heat losses via forced convection, and $G_o^* G(\rho)$ describes the heat source associated with fractional beam absorption. Regarding boundary conditions, we have

$$d(\delta T^*)/d\rho\Big|_{\rho=0} = 0 \tag{62}$$

on account of the azimuthal symmetry and

$$d(\delta T^*)/d\rho\Big|_{\rho=1} = 0 \tag{63}$$

on assuming that there is no heat loss at the edge [see Eq. (4)]. In the next paragraph, it will be shown that this system of equations admits an analytical solution and yields a closed-form expression for the temperature distribution.

For this purpose, we now introduce the variables $x = \sqrt{Nu}\,\rho$ and $y = \delta T^*(x/\sqrt{Nu})$. Equation (61) then reduces to a second-order, linear, and inhomogeneous differential equation of the type

$$\frac{d^2y}{dx^2} + \frac{1}{x}\cdot\frac{dy}{dx} - y = g(x) \tag{64}$$

with boundary conditions as follows:

$$dy/dx\Big|_{x=0} = dy/dx\Big|_{x=\sqrt{Nu}} = 0 \quad . \tag{65}$$

Since the modified Bessel functions $I_o(x)$ and $K_o(x)$ are non-trivial solutions of the homogeneous equation [26], the general solution is simply [19]

$$y(x) = A_1 I_o(x) + A_2 K_o(x) - I_o(x)\int^x \frac{g(\xi)}{W(\xi)} K_o(\xi)\,d\xi + K_o(x)\int^x \frac{g(\xi)}{W(\xi)} I_o(\xi)\,d\xi \tag{66a}$$

if $W(\xi)$ represents the Wronskian:

$$W(\xi) = \begin{vmatrix} I_o(\xi) & K_o(\xi) \\ I_o'(\xi) & K_o'(\xi) \end{vmatrix} = -1/\xi \quad . \tag{66b}$$

On taking the two boundary conditions into account, it then becomes a straightforward matter to generate an appropriate solution, *à savoir*,

$$y(x) = A_1 I_o(x) + \int_o^x \left[I_o(x)K_o(\xi) - K_o(x)I_o(\xi)\right] g(\xi)\,\xi\,d\xi \quad , \tag{66c}$$

where the constant A_1 is given by

$$A_1 = -\frac{1}{I_1(\sqrt{Nu})} \int_0^{\sqrt{Nu}} \left[I_1(\sqrt{Nu})K_o(\xi) + K_1(\sqrt{Nu})I_o(\xi)\right] g(\xi)\,\xi\,d\xi \tag{67}$$

and involves the four modified Bessel functions of order 0 and 1. Returning now to the original variables, and keeping in mind that the relation

$$g(x) = -\frac{G_o^* G(x/\sqrt{Nu})}{Nu} \tag{68}$$

applies, we find that, for face-cooled optical elements, the beam-induced temperature rise is best expressed as follows:

$$\delta T^*(\rho) = G_o^* I_o(\nu\rho)\left\{\int_0^1 \left[K_o(\nu\rho') + \frac{K_1(\nu)}{I_1(\nu)} I_o(\nu\rho')\right] G(\rho')\rho' d\rho' - \int_0^\rho \left[K_o(\nu\rho') - \frac{K_o(\nu\rho)}{I_o(\nu\rho)} I_o(\nu\rho')\right] G(\rho')\rho' d\rho'\right\}, \tag{69}$$

where ν stands for $\sqrt{Nu}$.[6] As in the case of edge cooling, the temperature scales with $\beta P/K$; the radial profile, however, now depends not only on the shape of the incident beam but also on the Nusselt number, which implies that, in addition to the heat-transfer coefficient, both the radius and the thickness of the optical element may have an impact on the solution.

4.2. Numerical Evaluation

Equation (69) involves integrals of Bessel functions that are not readily amenable to numerical evaluation, particularly in the context of an investigation as contemplated here, which covers a broad range of shape functions $G(\rho)$ and Nusselt numbers ν^2. A more convenient procedure consists in solving Eq. (61) by means of a fourth-order Runge-Kutta algorithm and relying on the "shooting method" in order to satisfy the edge-boundary condition [27]; some care is required because this condition refers to a slope [see Eq. (63)], hence the accuracy of the procedure must first be established. For this purpose, consider the case of a conventional Gaussian (W=1) in conjunction with relatively weak cooling (ν=1); on axis, the non-dimensional temperature rise,

$$\delta T^*(0) = G_o^* I_o(0) \int_0^1 \left[K_o(\rho') + \frac{K_1(1)}{I_1(1)} I_o(\rho')\right] G(\rho')\rho' d\rho' , \tag{70}$$

where

$$G_o^* = \left[2\pi \int_0^1 G(\rho')\rho' d\rho'\right]^{-1} \tag{71}$$

and

$$G(\rho') = \exp(-2\rho'^2) \tag{72}$$

then amounts to 0.34523, which confirms that the algorithm-based solution [$\delta T^*(0) = 0.34565$] is indeed acceptable.

Consider now the case of a fixed Nusselt number, say Nu=1, which should be representative of, or not too far from situations encountered in many design applications. Take, for instance, a high-power laser window of 10-cm radius and 1-cm thickness made of IR-transmissive material having a thermal

[6] To verify the validity of this equation, we are considering in Appendix C the limiting case of a flat incident beam [$G(\rho)\equiv 1$].

conductivity of 1 $Wcm^{-1}K^{-1}$; if the surface heat-transfer coefficient is of the order of $1x10^{-2}Wcm^{-2}K^{-1}$, as expected for face cooling by means of a flushing gas stream [28], we have indeed a situation characterized by a Nusselt number close to one. The steady-state temperature distributions associated with incident beams

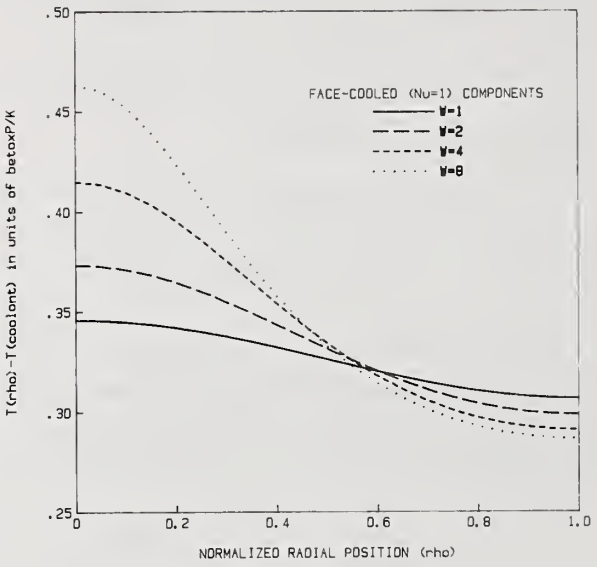

Figure 6a. Steady-state temperature profile of face-cooled components subjected to Standard Gaussian beams as illustrated in Fig. 1a; the Nusselt number is assumed equal to one.

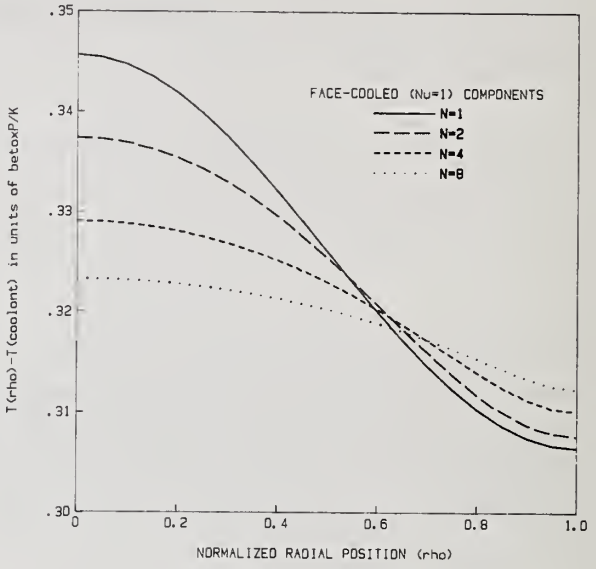

Figure 6b. Steady-state temperature profile of face-cooled components subjected to Super Gaussian beams as illustrated in Fig. 1b; the Nusselt number is assumed equal to one.

as in Figs. 1a and 1b then are as displayed in Figs. 6a and 6b, which the reader may compare to the distributions shown in Figs. 2a and 2b, keeping in mind that the reference temperature is now that of the coolant and not that of the edge. As in the case of edge cooling, the fourth-order polynomial approximation that satisfies the $\rho=1$ boundary condition,

$$\delta T(\rho) = \delta T_0^* - \delta T_2^* \rho^2 + (\delta T_2^*/2)\rho^4 \quad , \tag{73}$$

does not provide a suitable sub-routine for fitting the temperature distributions, thus forcing us to proceed on a three-independent parameter basis as in (49b) to derive "good" numbers for the quartic coefficient δT_4^*. These numbers are listed in Tables 3a and 3b (Standard and Super Gaussians, respectively) together with the $\delta T_2^*/2$ data derived from the regressions and standard deviations as defined in Eq. (50). Throughout the range of truncation and apodization parameter values, the regressions exhibit less deviation than recorded in Tables 2a and 2b for edge-cooled components and appear to be of consistently high quality but for $W \gtrsim 7$; in terms of obeying the boundary condition, however, there are serious discrepancies, particularly for $N \gtrsim 7$, but this should not impact our conclusions regarding the dependency of δT_4^* upon W and/or N. The dimensionless spherical aberration factors S^* [see Eq. (51)] derived from Tables 1 and 3 are displayed in Fig. 7 for both Standard and Super Gaussian beams. They are seen to be quite comparable to those presented in Fig. 4 and confirm that narrowing the beam degrades the performance, whereas apodization (in the sense of this paper) can be very useful in mitigating thermally induced aberrations; note that the discussion in Sec. 3.2 also applies. Actually, from the point of view of assessing the merits of face cooling, or providing guidelines on the selection of proper operating conditions, it should be more pertinent to investigate how the strength of the cooling as measured by the Nusselt number affects the emergence of aberrations.

Table 3a. Lists the relative standard deviation [see Eq. (50)] and compares δT_4^* to $\delta T_2^*/2$ [see Eq. (49b)] for face-cooled components subjected to Standard Gaussian beams.

W	st. dev. (%)	δT_4^*	$\delta T_2^*/2$
1	0.1521	0.04803	0.04309
2	0.5790	0.10641	0.08849
3	1.1274	0.16041	0.12710
4	1.6878	0.20564	0.15784
5	2.2164	0.24290	0.18238
6	2.7015	0.27391	0.20240
7	3.1433	0.30012	0.21910
8	3.5454	0.32263	0.23331
9	3.9124	0.34222	0.24560
10	4.2490	0.35949	0.25637

Table 3b. Lists the relative standard deviation [see Eq. (50)] and compares δT_4^* to $\delta T_2^*/2$ [see Eq. (49b)] for face-cooled components subjected to Super Gaussian beams.

N	st. dev. (%)	δT_4^*	$\delta T_2^*/2$
1	0.15210	0.048027	0.043088
2	0.09329	0.026652	0.028509
3	0.13200	0.015646	0.019857
4	0.12479	0.009946	0.014844
5	0.10882	0.006731	0.011707
6	0.09246	0.004779	0.009606
7	0.07862	0.003521	0.008121
8	0.06710	0.002671	0.007025
9	0.05734	0.002073	0.006188
10	0.04969	0.001640	0.005532

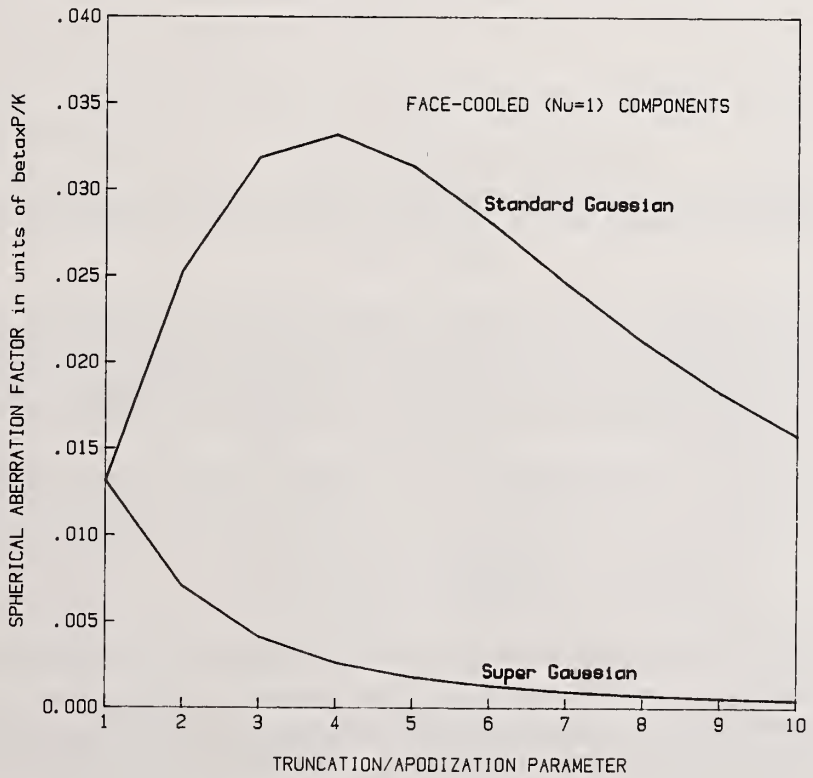

Figure 7. Non-dimensional spherical aberration factor of face-cooled components subjected to Standard Gaussian or Super Gaussian laser beams; the Nusselt number is assumed equal to one.

For this purpose, we may consider a conventionally $1/e^2$-truncated incident Gaussian beam, insert Nusselt numbers ranging from 10^{-3} to 10^3 into the heat-flow equation, and solve the system (61-63) by means of a Runge-Kutta algorithm as outlined earlier. Some of the results are displayed in Fig. 8,

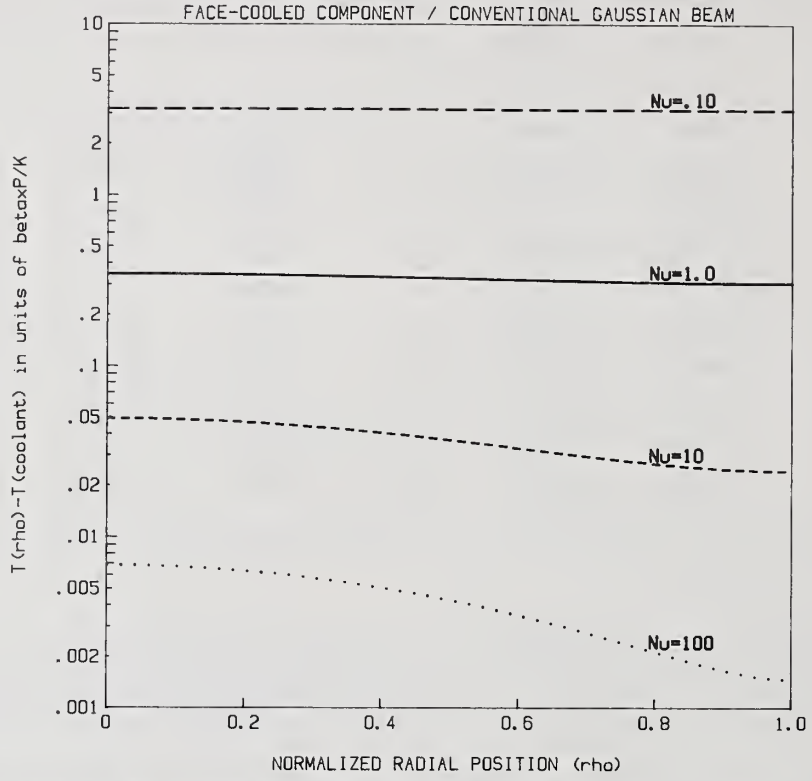

Figure 8. Steady-state temperature profiles of face-cooled cylindrical components for Nusselt numbers ranging from 0.1 to 100; the incident beam is a $1/e^2$-truncated Gaussian.

which illustrates how the temperature of face-cooled components and its radial distribution vary with cooling strength. In terms of spherical aberrations, such distributions lead to a Nusselt-number dependence as portrayed in Fig. 9, which also covers the case of a W=2 Standard Gaussian and, to some extent, the case of an N=4 Super Gaussian; three comments are called for:

1) For very weak cooling (Nu << 1), radial diffusion effects dominate, and the temperature distribution approaches that of a completely insulated component (see Fig. 3); the heat-flow equation then reduces to

$$\frac{d^2(\delta T^*)}{d\rho^2} + \frac{1}{\rho}\cdot\frac{d(\delta T^*)}{d\rho} + G_o^* G(\rho) = 0 \quad , \tag{74}$$

which is also the equation that governs the temperature profile of edge-cooled optical elements and, thus, may explain why the spherical aberration factors do not differ appreciably for Nu $\lesssim$ 1. In effect, such weak surface cooling simply prevents the temperature from increasing without limit, as would be the case for a truly insulated optical element.

2) For highly effective cooling (Nu >> 1), on the contrary, the diffusion of heat out of a unit-area volume through the thickness becomes negligible compared to the loss of heat that occurs at the surface; consequently, the steady-state temperature rise obeys the equation

$$- \mathrm{Nu} \times \delta T^{*} + G_{o}^{*} G(\rho) = 0 \qquad (75)$$

and "images" the incident beam shape as shown in Fig. 8 for Nu = 100. Furthermore, under these conditions the temperature rise should be proportional to 1/Nu, which has important implications for the distortion (see Fig. 9) because it demonstrates that a significant reduction of the aberration by means of face cooling requires Nusselt numbers of at least 10.

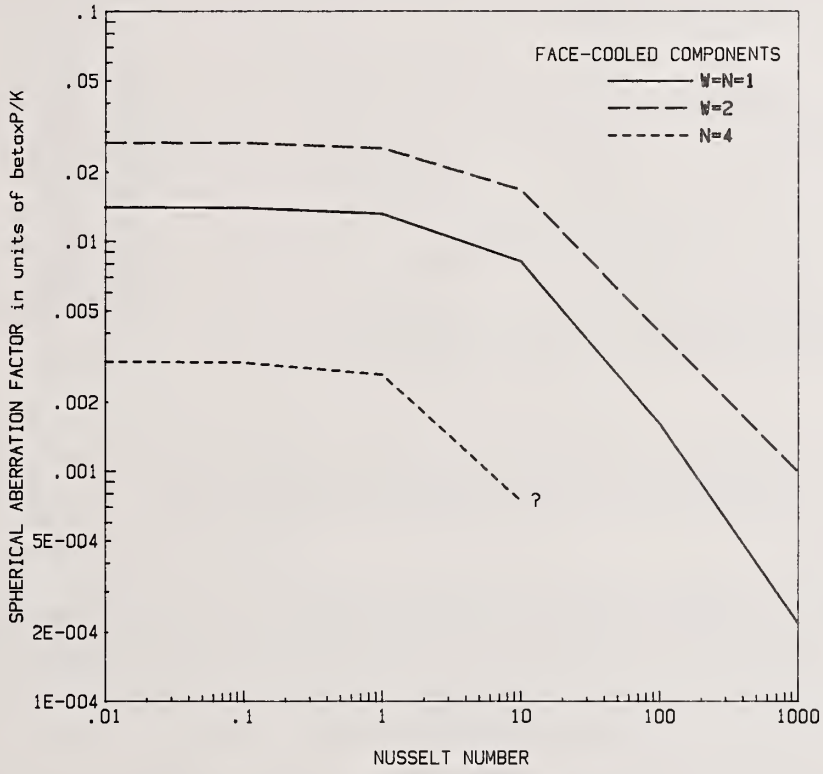

Figure 9. Non-dimensional spherical aberration factor of face-cooled components plotted as a function of the Nusselt number, for three representative beam shapes; fourth-order polynomial approximations to N=4/Nu $\gtrsim$ 10 temperature profiles do not yield acceptable results in terms of evaluating spherical aberrations.

3) At intermediate cooling strengths ($1 \lesssim \mathrm{Nu} \lesssim 10$), the diffusion of heat towards the edge "competes" with the loss of heat through one or both end surfaces, and a detailed analysis must be carried out for describing the steady state. In this context, we may emphasize that bigger apertures always improve the performance considering that the Nusselt number scales with the square of the radius; this assumes, of course, that the thickness L is either independent of or a weak function of the diameter D.

Returning now to Eq. (54) for the power-handling capability, we can take advantage of Fig. 9 for assessing the merits of face cooling and deriving appropriate figures of merit, albeit such considerations are beyond the scope of the present paper. For this purpose, and in light of the discussion that precedes, we may approximate the spherical aberration factor in a manner such as

$$S^{*} \simeq f(s)/[1 + g(s)\mathrm{Nu}] \quad , \qquad (76)$$

where f and g are functions of the beam-shape parameter only. For weak cooling, the allowable power then amounts to

$$P_{lim} \simeq \frac{(\lambda/14)K}{\chi \ell \beta f(s)} \quad , \quad Nu \lesssim 1 \tag{77a}$$

and is independent of the Nusselt number, thus suggesting that, if the heat-transfer coefficient remains low, say $h_F \lesssim 1 \times 10^{-3} Wcm^{-2}K^{-1}$, there is little to be gained in increasing the aperture size. In terms of a materials figure of merit, this leads to

$$FoM = K/(\chi\beta_V) \quad , \tag{78a}$$

which is identical to the figure of merit for edge cooling and assumes that bulk absorption dominates the beam-power dissipation process. For large Nusselt numbers, on the contrary, we have

$$P_{lim} \simeq \frac{(\lambda/14)K \times Nu}{\chi \ell \beta (f/g)} \quad , \quad Nu \gtrsim 10 \tag{77b}$$

which shows that the power-handling capability now depends upon the heat-transfer coefficient but no longer involves the thermal conductivity; in effect, the figure of merit then reduces to

$$FoM = 1/(\chi\beta_V) \tag{78b}$$

if $\beta \simeq \beta_V$. In the intermediate range, there is no such simple "response," as the entire parameter space now participates in setting a limit on the tolerable total beam power.

4.3. Practical Application

Figure 10 depicts a conceptual output-window design involving two ZnSe panes and configured for use in conjunction with an industrial CO_2-laser source operating at state-of-the-art CW power levels. The problem we wish to address concerns the surface cooling required to meet two key specifications: diffraction-limited performance in the sense of Maréchal and peak-temperature excursions of no more than 100 K. Since ZnSe windows do not experience stress-birefringence effects in passing CO_2-laser beams [29], our treatment of thermal lensing applies, and this model problem should give us an opportunity to exercise the theory in a realistic context.

Since both S^* and δT^* are in units of $\beta P/K$, it is immediately seen that the two specifications boil down to

$$S^* \lesssim \frac{(\lambda/14)K}{\chi \ell \beta P} = 2.96 \times 10^{-3} \tag{79}$$

and

$$\delta T^*(0) \lesssim 100\ K/(\beta P) = 0.145 \tag{80}$$

if $\lambda = 10.6\ \mu m$ (CO_2 laser), $K = 0.182\ Wcm^{-1}K^{-1}$ [29], $\chi = 7.3 \times 10^{-5}K^{-1}$ [29], $\ell = 2L = 0.588$ cm (see Fig. 10), $\beta = 8.37 \times 10^{-3}cm^{-1}$ (if $\beta_S = 0.1\%$ and $\beta_V = 5 \times 10^{-4}cm^{-1}$ as in [29]), and $P = 15$ kW [30]. Referring now to Fig. 9, we find that the relevant Nusselt numbers, in terms of Eq. (79), are as given in the tabulation of Fig. 10, which has the results for three "model" beam shapes; a similar procedure (but not illustrated here) can be applied with regard to the temperature on axis. These numbers clearly demonstrate the advantage of using apodized beams to enhance the aberration tolerance; in fact, our results suggest that, for

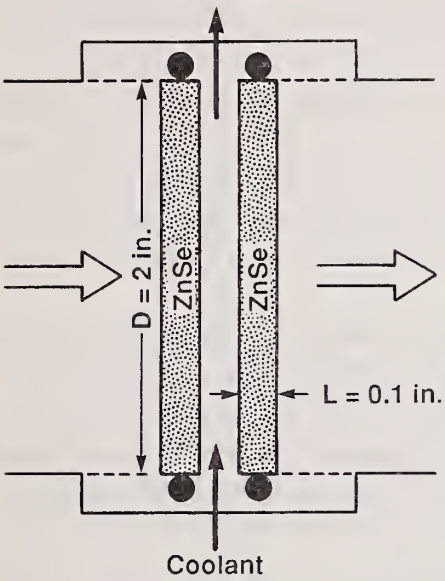

	W=N=1	W=2	N=4
Required Nu[a]	42.5 2.75	165 3.55	0.125 2.45
Required h_F ($Wcm^{-2}K^{-1}$)	0.305	1.18	0.0 176
Failure Mode	Distortion	Distortion	Temperature

(a) First line: distortion. Second line: temperature.

Figure 10. Double-pane ZnSe output-window for an industrial CO_2 laser; the table summarizes our evaluation of the cooling requirement in a CW mode of operation at the 15 kW power level.

apodized incident beams, the primary failure mode of ZnSe windows relates to the temperature excursion rather than the optical distortion. Regarding potential cooling schemes, we can take advantage of the relation

$$h_F = \frac{Nu \times KL}{(D/2)^2} \tag{81}$$

to estimate the magnitude of the heat-transfer coefficients required to achieve satisfactory operation of the window assembly. The results listed in Fig. 10 assume a window diameter of 2 in. (5.08 cm), which should be compatible with thicknesses of 0.1 in. (0.254 cm) bearing in mind that an L/D aspect ratio of 0.05 insures adequate structural integrity for pressure differentials of up to 1 atm [29]. In principle, such heat-transfer coefficients can be implemented [28] with flat jets of liquid coolant ($h_S \simeq 1\ Wcm^{-2}K^{-1}$) or nitrogen gas ($h_S \simeq 0.01\ Wcm^{-2}K^{-1}$), which leads us to conclude that a double-pane ZnSe window configuration with forced convective cooling as prescribed in Fig. 10 can provide an effective solution to the window problem on hand.

5. Conclusions

In this paper, we have carried out a fairly general analysis of the phase aberration problem that occurs when CW laser light propagates through an optical component made of semiconducting material; much attention was devoted to assessing how beam shape and cooling technique affect the degradation in far-field intensity caused by thermal lensing. With very reasonable and realistic assumptions, we have shown that "exact" solutions can be obtained for the temperature distributions, which allows us to characterize the spherical aberration by means of the factor S defined in Eq. (33). The discussion and, in particular, the

applications presented in Secs. 3.3 and 4.3 are meant to be relevant to high-power CW or quasi-CW systems operating at the CO_2-laser wavelength (10.6 μm), but the procedure should be applicable to a wide variety of cases or situations that require an evaluation of beam-induced optical distortions. In this connection, we may state the following conclusions:

1) For most of the commonly used materials in laser optics, stress-birefringence effects are inconsequential, which implies that the wavefront aberration relates to the temperature distribution by means of a single optical distortion coefficient χ. In Sec. 2, we show how to express χ in terms of material properties, for thin-disc as well as long-rod configurations, and demonstrate that, in effect, we have $\chi \simeq dn/dT$ independently of the geometry; refractive index variations induced by temperature gradients thus control the thermal lensing process.

2) If it is a good approximation to describe the beam-induced temperature rise by means of a fourth-order even polynomial, the degradation in focal irradiance caused by aberration originates entirely from the quartic term $\delta\phi_4\rho^4$. Upon refocusing (but no aberration balancing), the variance of $\delta\phi_4\rho^4$, properly weighted with regard to the aperture amplitude, then provides an appropriate measure of the degradation; in this context, it is the spherical aberration factor $S = \delta T_4 \sqrt{\text{var}[\rho^4]}$ that best describes the combined impact of temperature profile and beam shape.

3) On assuming that the internal beam-power distribution resulting from multiple reflections off AR coatings matches that of the incident beam, the heat-flow equations for CW-loaded cylindrical components can be formulated in a simple non-dimensional manner that leads to closed-form integral solutions. A common feature of these solutions is that temperature variations causing optical distortion "scale" with $\beta P/K$; for edge-cooled as well as face-cooled components, the "normalized" temperature then yields reliable δT_4^* values but for situations involving large truncation parameters.

4) At a given incident power level, flat-topped beams generate substantially less distortion than Gaussians, which confirms that apodization can be a very useful method for improving the performance of coherent systems subjected to thermal lensing. With Standard Gaussian beams, truncation parameters larger than one always result in enhanced distortion but for essentially on-axis propagation.

5) For edge-cooled cylindrical components, the heat-flow equation does not explicitly involve the heat-transfer coefficient, which leads to the result that the dimensionless spherical aberration factor S^* depends only upon the beam shape. If bulk absorption dominates, the power-handling capability is therefore independent of the aperture diameter [see Eq. (54)]; in other words, increasing the size of thick components will not improve the performance.

6) The heat-flow equation of face-cooled cylindrical components suggests to make use of the Nusselt number $Nu = h_F (D/2)^2/(LK)$ for characterizing the cooling process; the spherical aberration thus depends not only upon the shape of the incident beam but also upon the heat-transfer coefficient and the geometry of the optical element. In this regard, we find that a significant reduction of the aberration by means of face cooling requires Nusselt numbers $Nu \gtrsim 10$, which has important implications (see Sec. 4) in terms of selecting suitable material candidates and/or proper operating conditions.

6. Acknowledgements

This work was supported in part by MIT Lincoln Laboratory under Subcontract No. BX-1366 (Prime Contract No. F19628-85-C-0002). Terry Dorschner suggested the investigation of apodization as a potential tool for mitigating the deleterious effects of beam-induced aberrations on the focal intensity. Finally, I wish to acknowledge that, in preparing this paper, I benefited from the pioneering work on laser windows that was carried out by Frank Horrigan in the early seventies.

Appendix A

Problems relating to heat flow in a cylindrical geometry are well understood, and pertinent discussions have been given elsewhere; the treatment presented here is patterned upon the analysis of Horrigan [1] and is included for completeness. In cylindrical coordinates, the Fourier heat-conduction law leads to the following equation,

$$C' \frac{\partial T(r,z,t)}{\partial t} = K\left[\frac{\partial^2 T(r,z,t)}{\partial r^2} + \frac{1}{r}\cdot\frac{\partial T(r,z,t)}{\partial r} + \frac{\partial^2 T(r,z,t)}{\partial z^2}\right] + \beta(z) I(r,z,t) \quad , \tag{A-1}$$

for the time-dependent temperature distribution of an optic that transmits high-intensity radiation and has an absorption coefficient that is independent of the radial position. As noted in the Introduction, temperature variations that cause optical distortion are quite small, which implies that any temperature dependence of the heat capacity, the thermal conductivity, or the absorption coefficient should have minimal impact on applicable solutions, thus suggesting that a "linear" formulation should be quite adequate. Furthermore, we are postulating that (a) from the point of view of thermal loadings (see Sec. 1), the depletion of the laser beam as it passes through the absorbing medium is in fact negligible, and (b) from the point of view of phase aberrations (see Sec. 2), it is the z-averaged temperature, or average temperature through the thickness of the component,

$$T(r,t) = \frac{1}{L}\int_{-L/2}^{+L/2} T(r,z,t)\,dz \quad , \tag{A-2}$$

that matters. The equation that governs the evolution of this average temperature may then be obtained simply by "averaging" Eq. (A-1), which yields

$$C' \frac{\partial T(r,t)}{\partial t} = K\left[\frac{\partial^2 T(r,t)}{\partial r^2} + \frac{1}{r}\cdot\frac{\partial T(r,t)}{\partial r}\right]$$

$$+ \frac{K}{L}\left[\frac{\partial T(r,z,t)}{\partial z}\bigg|_{+L/2} - \frac{\partial T(r,z,t)}{\partial z}\bigg|_{-L/2}\right] + \beta I(r,t) \tag{A-3}$$

if one makes use of the concept of an effective absorption coefficient,

$$\beta = \frac{1}{L}\int_{-L/2}^{+L/2} \beta(z)\,dz = \frac{2\beta_S}{L} + \beta_V \quad , \tag{A-4}$$

where β_S is the fraction of incident radiation absorbed per surface, and β_V is the conventional bulk absorption coefficient. Further simplification can be brought about if one takes into account the thermal boundary condition at the two z-surfaces,[7]

$$-K\ \partial T/\partial \bar{u}\big|_S = h(T_S - T_C) \quad , \tag{A-5}$$

and assumes that, for cooling purposes, z-direction temperature variations are of no consequence; the temperature difference $\delta T = T(r,t) - T_C$ introduced in Sec. 1 then obeys the equation

$$C' \frac{\partial(\delta T)}{\partial t} = K\left[\frac{\partial^2(\delta T)}{\partial r^2} + \frac{1}{r}\cdot\frac{\partial(\delta T)}{\partial r}\right] - \frac{h_F \delta T}{L} + \beta I(r,t) \quad , \tag{A-6}$$

[7]Equation (A-5) reflects Newton's law of heat transfer for a flowing coolant, the symbol $\bar{u}$ designating the outward normal to the surface S.

where h_F is understood to represent a net heat-transfer coefficient combining the effect of coolant flow on both faces of the absorbing medium. In a steady-state regime, that is, for CW beams or pulsed beams with an inverse repetition rate that is much smaller than the thermal relaxation time constant $(C'/K)(L/\pi)^2$, Eq. (A-6) reduces to the time-independent ordinary differential equation given in Sec. 1. The edge boundary condition, Eq. (4), implicitly assumes that the edge coolant is at the same temperature as the face coolant, but this does not apply here (Secs. 3 and 4) because we are not concerned with "mixed" cooling (h_F and h_E both different from zero). Equations (3) and (4) then provide a relatively simple and entirely adequate system for obtaining the temperature distribution $\delta T(r)$ and, thus, for deriving solutions to the thermal problem by means of straightforward analytical or numerical procedures.

Appendix B

An alternative way of solving the heat-diffusion equation for CW-loaded, edge-cooled cylindrical components consists in rewriting Eq. (37) as follows,

$$\frac{1}{\rho}\frac{d}{d\rho}\left[\rho\frac{d(\delta T^*)}{d\rho}\right] = -G_o^* G(\rho) \quad , \tag{B-1}$$

which leads immediately to a solution as given in Eq. (48), for boundary conditions as specified in Eqs. (41) and (42). In principle, this closed-form solution relies on a computer evaluation for its effectiveness in delivering numerical results. With Standard Gaussian beam shapes, however, we may easily generate a directly applicable analytical solution. In a first step, and for $G(\rho) = \exp(-2W\rho^2)$, Eq. (B-1) boils down to

$$\rho\frac{d(\delta T^*)}{d\rho} = -G_o^* \int_0^\rho \exp(-2W\rho'^2)\,\rho'\,d\rho' \quad , \tag{B-2a}$$

which satisfies the on-axis boundary condition and yields

$$\frac{d(\delta T^*)}{d\rho} = -\frac{G_o^*}{4W\rho}\left[1 - \exp(-2W\rho^2)\right] \tag{B-2b}$$

upon performing the integration. The second step then amounts to solving the following integral expression for the temperature distribution,

$$\delta T^*(\rho) = \frac{G_o^*}{4W}\int_\rho^1 \frac{1 - \exp(-2W\rho'^2)}{\rho'}\,d\rho' \quad , \tag{B-3a}$$

which requires some manipulation and yields

$$\delta T^*(\rho) = \frac{G_o^*}{4W}\left\{\frac{1}{2}\left[E_1(2W) - E_1(2W\rho^2)\right] - \ln(\rho)\right\} \quad , \tag{B-3b}$$

thus satisfying the edge-boundary condition. Note that the function $E_1(z)$ denotes an exponential integral as defined in Ref. [26].

At this point, we may also consider the case of a uniformly loaded edge-cooled element, which should be of interest here because a flat beam is equivalent to a Gaussian whose truncation parameter is close to zero. From Eq. (39) it follows that

$$\lim_{W\to 0}\left[\frac{G_o^*}{4W}\right] = \frac{1}{4\pi W} \quad , \tag{B-4}$$

and since

$$\lim_{W\to 0}[E_1(z)] = -\gamma - \ell n(z) + z \quad , \tag{B-5}$$

where γ represents Euler's constant [26], we find that

$$\lim_{W\to 0}[\delta T(\rho)] = \frac{\beta P}{4\pi K}(1-\rho^2) \quad , \tag{B-6}$$

which points to a parabolic temperature disbribution. The reader may verify that Eq. (B-6) duplicates the classic expression [11] for the steady-state temperature in a solid cylinder where energy is generated at a uniform rate while the boundary surface is kept at a constant temperature.

Appendix C

The case of a uniformly loaded face-cooled optical element is of interest because there are no lateral heat-diffusion effects; the beam raises the temperature by a uniform amount,

$$\delta T = \beta I_o \ell / h_F \quad , \tag{C-1}$$

which reflects the steady-state heat balance and involves only the deposited power density plus the heat-transfer coefficient. In this Appendix, we examine some implications of Eq. (C-1) with regard to the generalized solution derived in Sec. 4.1 for arbitrary axisymmetric beam profiles $G(\rho)$. On introducing the variable $x = \nu\rho'$ and setting $G(\rho') \equiv 1$, Eq. (69) without the "stars" takes the form

$$\delta T(\rho) = (G_o/Nu)F(\nu,\rho) \quad , \tag{C-2}$$

where $F(\nu,\rho)$ designates a function of the Nusselt number and the radial variable:

$$F(\nu,\rho) = I_o(\nu\rho)\left\{\int_0^{\nu}\left[K_o(x) + \frac{K_1(\nu)}{I_1(\nu)}I_o(x)\right]x\,dx - \int_0^{\nu\rho}\left[K_o(x) - \frac{K_o(\nu\rho)}{I_o(\nu\rho)}I_o(x)\right]x\,dx\right\} . \tag{C-3a}$$

Since the factor G_o/Nu boils down to

$$G_o/Nu = \beta I_o L/h_F \tag{C-4}$$

on account of Eqs. (35), (39), and (60), we conclude that the identity

$$F(\nu,\rho) = 1 \qquad \text{for} \qquad 0 \leq \nu \leq \infty,\ 0 \leq \rho \leq 1 \tag{C-3b}$$

always holds (note that l=L for pertinent configurations). For finite values of ν, numerical evaluations of $F(\nu,\rho)$ are cumbersome but fairly straightforward and yield results that are, indeed, very close to one. Take, for example, the case of $\nu=\rho=1$; relying now on the Bessel-function tabulation of Ref. [26] and performing the integrations on a personal technical computer (HP-series 80), we find that $F(1,1) = 0.99996$. For very small Nusselt numbers, however, a difficulty arises since $K_o(z)$ and $K_1(z)$ both tend toward infinity as $z\to 0$; in effect, for such small arguments we have [26]

$$I_o(z) \simeq 1 \qquad K_o(z) \simeq -\ell n(z/2) \tag{C-5a}$$

and

$$I_1(z) \simeq z/2 \qquad K_1(z) \simeq 1/z \tag{C-5b}$$

for modified Bessel functions of order zero and one, respectively. Inserting now these limiting approximations into Eq. (C-3a), we get

$$\lim_{\nu\to 0}[F(\nu,\rho)] \simeq \int_0^{\nu}\left[-\ell n(x/2) + 2/\nu^2\right]x\,dx + \int_0^{\nu\rho}\ell n\left[x/(\nu\rho)\right]x\,dx \quad , \tag{C-6}$$

which tells us immediately that $F(0,\rho)$ equals one (1) on analytical grounds. The "strange" integral relation (C-3b) thus confirms our solution of the face-cooling problem, but a truly satisfactory demonstration still remains to be worked out.

Glossary

C'	:	heat capacity	T_C	:	coolant temperature
D	:	diameter or aperture	T_E	:	edge temperature
E	:	elastic modulus	U	:	complex beam amplitude
$E_1(z)$	:	exponential integral	W	:	truncation parameter
G_o	:	beam-profile constant	z	:	axial variable
$G(r)$	:	beam-profile function			
h	:	heat-transfer coefficient	α	:	expansion coefficient
h_E	:	heat-transfer coefficient/edge	β	:	effective absorption coefficient
h_F	:	heat-transfer coefficient/face	β_S	:	surface absorption coefficient
I	:	beam intensity	β_V	:	volume absorption coefficient
I_o	:	peak intensity	γ	:	Euler's constant
$I_o(z)$	:	modified Bessel function	δl	:	path length variation
$I_1(z)$	:	modified Bessel function	δn_θ	:	index variation/azimuthal
k	:	propagation constant ($2\pi/\lambda$)	δn_ρ	:	index variation/radial
K	:	thermal conductivity	δT	:	temperature increase
$K_o(z)$	:	modified Bessel function	δT_i	:	polynomial expansion coefficient
$K_1(z)$	:	modified Bessel function	$\delta\phi$	:	phase aberration
l	:	path length	$\delta\phi_i$	:	polynomial expansion coefficient
L	:	component thickness	$\delta\phi_\theta$	:	phase aberration/azimuthal
L_c	:	characteristic length	$\delta\phi_\rho$	:	phase aberration/radial
n	:	refractive index	$\delta\phi_+$	:	phase aberration/symmetric
N	:	apodization parameter	$\delta\phi_-$	:	phase aberration/anti-symmetric
Nu	:	Nusselt number	ε_{ij}	:	strain tensor component
P	:	incident beam power	λ	:	laser wavelength
P_{lim}	:	allowable beam power	ν	:	Poisson's ratio (Sec. 2)
$q_{\parallel}$	:	stress-optic coefficient/parallel	ν	:	square root of Nu (Sec. 4)
$q_{\perp}$	:	stress-optic coefficient/perpendicular	ρ	:	dimensionless radial variable
r	:	radial variable	σ	:	stress magnitude (Sec. 2)
R	:	on-axis distance	σ	:	standard deviation (Sec. 3)
R_o	:	focal distance	σ_{ij}	:	stress tensor component
s	:	Strehl ratio (Sec. 2)	$\tau(\rho)$	:	dummy function
s	:	beam-shape parameter (Sec. 4)	ϕ	:	phase shift
S	:	spherical aberration factor	χ	:	optical distortion coefficient
t	:	time variable	χ_+	:	optical distortion coefficient/symmetric
T	:	absolute temperature	χ_-	:	optical distortion coefficient/anti-symmetric

References

[1] Horrigan, F., and Deutsch, T., "Research in optical materials and structures for high-power lasers," *Report No. S-1335* (Raytheon Research Division, Waltham/MA, 1971).

[2] Bennet, H., "Thermal distortion thresholds for optical trains handling high pulse powers," in *Laser-Induced Damage in Optical Materials: 1976* (NBS Special Publication 462, Washington/DC, 1976), pp. 11-24.

[3] Klein, C., "Thermally induced optical distortion in high-energy laser systems," *Optical Engineering*, Vol. 18 (1979), pp. 591-601.

[4] Sparks, M., "Optical distortion by heated windows in high-power laser systems," *Journal of Applied Physics*, Vol. 42 (1971), pp. 5029-46.

[5] Bendow, B., and Gianino, P., "Optics of thermal lensing in solids," *Applied Optics*, Vol. 12 (1973), pp. 710-8.

[6] Klein, C., "Concept of an effective optical distortion parameter: application to KCl laser windows," *Infrared Physics*, Vol. 17 (1977), pp. 343-57.

[7] Sherman, G., and Frazier, G., "Transmissive optics for high-power CO_2 lasers: practical considerations," *Optical Engineering*, Vol. 17 (1978), pp. 225-31.

[8] Gianino, P., and Bendow, B., "Thermal distortion calculations for cooled ZnSe laser windows," in *Proceedings of the Fifth Annual Conference on Infrared Laser Window Materials* (Air Force Material Laboratory, WPAFB/OH, 1976), pp. 664-77.

[9] Mahajan, V., "Uniform versus Gaussian beams: a comparison of the effects of diffraction, obscuration, and aberrations," *Journal of the Optical Society of America A*, Vol. 3 (1986), pp. 470-85.

[10] Holmes, O., and Avizonis, P., "Approximate optical system model," *Applied Optics*, Vol. 15 (1976), pp. 1075-82.

[11] Mikhailov, M., and Özizik, M., *Unified Analysis and Solutions of Heat and Mass Diffusion*, J. Wiley & Sons, New York/NY, 1984.

[12] Born, M., and Wolf, E., *Principles of Optics: Fifth Edition*, Pergamon Press, Oxford/UK, 1975.

[13] Nye, J., *Physical Properties of Crystals*, Oxford University Press, Oxford/UK, 1957.

[14] Boley, B., and Weiner, J., *Theory of Thermal Stresses*, J. Wiley & Sons, New York/NY, 1960.

[15] Klein, C., "Stress-induced birefringence, critical window orientation, and thermal lensing experiments," in *Laser-Induced Damage in Optical Materials: 1980* (NBS Special Publication 620, Washington/DC, 1981), pp. 117-28.

[16] Korobkin, V., Polonskii, L., Poponin, V., and Pyatnitskii, L., "Focusing of Gaussian and Super-Gaussian laser beams by axicons to obtain continuous laser sparks," *Soviet Journal of Quantum Electronics*, Vol. 16 (1986), pp. 178-82.

[17] Skupsky, S., ed., "Liquid crystal soft apertures," *LLE Review*, Vol. 24 (1985), pp. 188-95.

[18] Smith, W., "Optical design," in *The Infrared Handbook* (Research Institute of Michigan, Ann Arbor/MI, 1978), Chap. 8.

[19] Benton, E., "Ordinary differential and difference equations," in *Handbook of Applied Mathematics* (Van Nostrand Reinhold Company, New York/NY, 1974), Chap. 6.

[20] Marquardt, D., "An algorithm for least-squares estimation of non-linear parameters," *Journal of the Society for Industrial and Applied Mathematics*, Vol. 11 (1963), pp. 431-41.

[21] Phipps, C., and Thomas, S., "High-power isolator for the 10-μm region employing interband Faraday rotation in germanium," *Journal of Applied Physics*, Vol. 47 (1976), pp. 204-13.

[22] Powell, R., and Childs, G., "Thermal conductivity," in *American Institute of Physics Handbook* (McGraw-Hill Book Company, New York/NY, 1972), Sec. 4g.

[23] Sahagian, C., and Pitha, C., "Compendium on high-power infrared laser window materials," *Report No. AFCRL-72-0170* (Air Force Cambridge Research Laboratory, Bedford/MA, 1972).

[24] Horrigan, F., and Rudko, R., "Materials for high-power CO_2 lasers," *Report No. S-1170* (Raytheon Research Division, Waltham/MA, 1969).

[25] Roberts, R., "Laminar and turbulent flow of gases," in *American Institute of Physics Handbook* (McGraw-Hill Book Company, New York/NY, 1972), Sec. 2u.

[26] Olver, F., "Bessel functions of integer order," in *Handbook of Mathematical Functions with Formulas, Graphs, and Tables*(NBS Applied Mathematics Series 55, Washington/DC, 1964), Chap. 9.

[27] Douglass, B., *Numerical BASIC*, Howard W. Sams & Co., Indianapolis/IN, 1983.

[28] Sparks, M., and Duthler, C., "Theoretical studies of high-power ultraviolet and infrared materials," *Eighth Technical Report* (Xonics, Santa Monica/CA, 1976).

[29] Klein, C., "Methodology for designing high-energy laser windows," in *Proceedings of the International Conference on Lasers: 1978* (STS Press, McLean/VA, 1979), pp. 283-95.

[30] Dance, B., "European group studies applications for industrial lasers," *Laser Focus/Electro Optics*, Vol. 23 No. 4 (April '87), pp. 62-4.

Manuscript received 10/26/87

Sum-frequency generation on dye-coated surfaces using collinear and noncollinear excitation geometries

R. E. Muenchausen, D. C. Nguyen, R. A. Keller, and N. S. Nogar

Chemical and Laser Sciences Division,
Los Alamos National Laboratory,
Los Alamos, New Mexico 87545

Resonantly enhanced surface second-harmonic generation and sum- frequency generation has been demonstrated on rhodamine 6G coated glass substrates using different excitation geometries. The collinearly excited, doubly-resonant sum-frequency signal is enhanced by more than two orders of magnitude relative to resonantly enhanced second-harmonic generation. For noncollinear excitation, the relative efficiency of nonlinear generation as a function of the angular dependence of the input beams is calculated and compared with experiment.

Key Words: rhodamine 6G, second-harmonic, sum-frequency

1. INTRODUCTION

It is well established that the lack of inversion symmetry at interfaces allows the electric-dipole contribution to the second-order susceptibility, $\chi^{(2)}$, which is the predominant source of surface second-harmonic (SHG) and sum-frequency generation (SFG)[1]. The temporal and spatial coherence of the nonlinear output from smooth surfaces is well established on both theoretical and experimental grounds. Due to its surface specificity, SHG has become an important surface probe.[2,3] It has also been demonstrated that SFG can be a sensitive technique for surface vibrational spectroscopy.[4,5]

In the case of surface adsorbed dyes, the second harmonic signal is resonantly enhanced when 2ω matches the $S_o \rightarrow S_2$ electronic transition of the dye. Marowsky et al. reported a three order of magnitude increase in the SHG signal of nile blue A compared to rhodamine 6G.[6] This increase was attributed to the simultaneous resonance of ω with the $S_o \rightarrow S_1$ transition and 2ω with the $S_o \rightarrow S_2$ transition. Generally, this full double-resonance enhancement cannot be realized with SHG for any molecule. For doubly-resonant sum-frequency generation, we expect the output to be enhanced orders of magnitude as was SHG of nile blue A, because two different frequencies can be used to address both resonant transitions.

Previous experimental studies of SHG and SFG from surfaces have used a collinear or a coplanar[4,5] excitation geometry. For

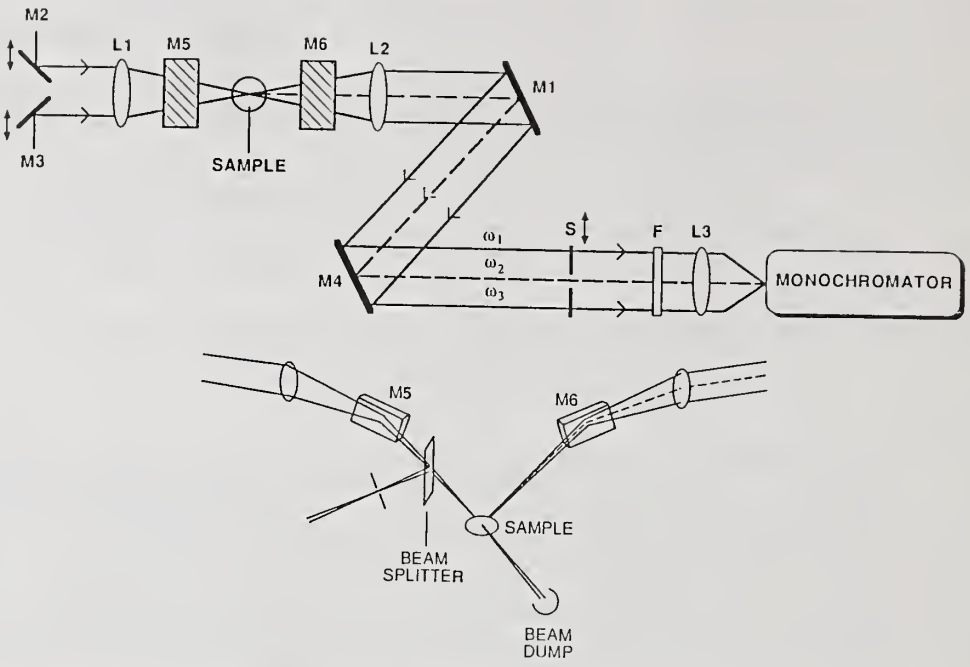

Figure 1. Schematic of SHG and SFG optical components for noncollinear excitation geometry. M1-M6, mirrors; F, color filter; L1, 18-cm. focal- length lens; L2, 15-cm. focal-length lens; L3, 7.5-cm focal-length lens; S, scannable slit.

surface generation the propagation distance of the fundamental beams through the nonlinear medium will be much less than their wavelength. The stringent phase-matching conditions for nonlinear generation in bulk media, which usually require collinear propagation of the input beams, can be relaxed for surface generation.[7]

These considerations suggest that it should be possible to use a noncollinear excitation geometry for the input beams to exploit the directional property of the output beam by spatially filtering the output. Spatial separation of the nonlinear output beam from the reflected fundamental beams will simplify the experimental setup and increase sensitivity relative to a collinear excitation geometry by reducing or eliminating the need for color filters or a monochromator.

2. EXPERIMENTAL

The experimental details of collinear SHG[8-10] and SFG[10] from rhodamine 6G coated substrates have been reported previously. The experimental setup used to accomodate a noncollinear excitation geometry is shown in Fig. 1.

For SHG a Nd:YAG pumped, tunable dye laser was operated at the peak of the SHG excitation curve at 695 nm. For SFG the tunable dye laser was used to provide ω_1 between 490 and 550 nm. The second laser beam at ω_2, 4% of the Nd:YAG IR fundamental, was delayed to synchronize the arrival times of both beams.

For collinear excitation the dye laser and IR beams were combined and directed onto the sample at an angle of incidence, $\theta \sim 60°$. For noncollinear excitation, the parallel input beams are focused onto the sample at $\theta \sim 60°$ using a f/1.8 focal-length lens. The angle between the projection of the input beams onto the surface, ϕ, could be varied between 3°- 15° by adjusting the separation of the input beams on the focusing lens by moving mirrors M2 and M3 conjointly. The reflected beams were collimated with a 15-cm focal-length lens. A slit was scanned across the collimated output beams in order to spatially resolve the nonlinear output and reflected pump beams.

The transmitted light, which passed through a color filter, was focused onto the slit of a monochromator and detected by a photomultiplier tube . The PMT output was amplified and detected by a gated integrator/boxcar. Spin coated samples[8] were prepared from a 3 x 10^{-3} M ethanolic rhodamine 6G solution deposited on microscope cover slides yielding coverages ranging from 0.2-30 monolayers. All observed signals were verified to be coherent SHG or SFG based on their monochromaticity at the sum frequency, laser power dependence and spatial profile as discussed previously.[9,10]

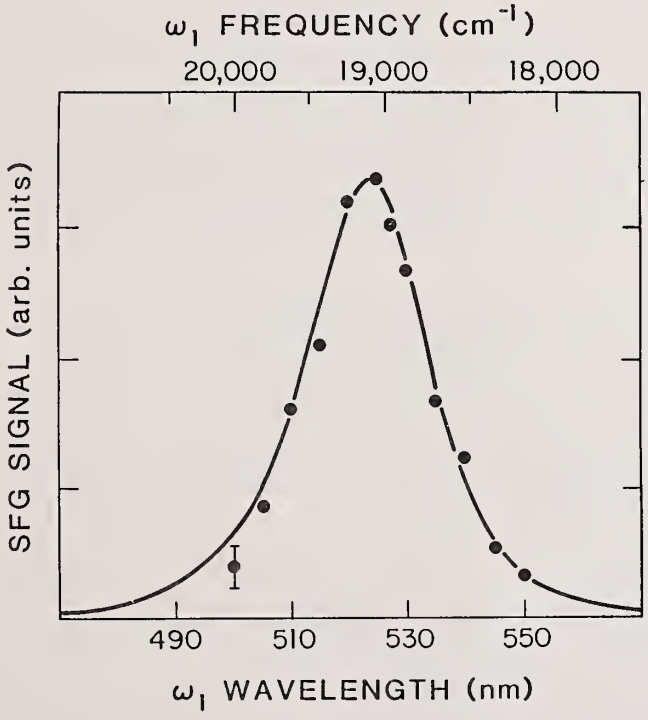

Figure 2. Sum-frequency excitation spectrum of rhodamine 6G with ω_2 = 9360 cm^{-1}. The calculated spectrum is shown as the solid curve and the points are experimental data.

3. RESULTS AND DISCUSSION

3.1 Collinear excitation

The magnitude of the SFG signal depends on the square of the complex second-order susceptibility, $|\chi^{(2)}|$, which can be expressed in terms denoting the resonant interactions between two input laser frequencies and a three-level system, summed over all excited states [11],

$$\chi^{(2)}(\omega_1, \omega_2, -\omega_{SF}) = \sum_{b,c} \frac{\mu_{ab}\,\mu_{bc}\,\mu_{ac}}{(\omega_{ba}-\omega_1+i\Gamma_{ab})(\omega_{ca}-(\omega_1+\omega_2)+i\Gamma_{ac})} \quad (1)$$

where
- $\omega_{1,2}$ = input laser frequencies
- ω_{SF} = $\omega_1 + \omega_2$ = output SFG frequency
- μ_{ab} = dipole moment of $a \rightarrow b$ transition
- ω_{ba} = frequency of $a \rightarrow b$ transition
- Γ_{ab} = homogeneous linewidth of $a \rightarrow b$ transition

and a, b, c denote the ground and excited energy levels.

To a first approximation, our model of rhodamine 6G energy levels consists of two excited singlet S_1 and S_2 levels as zero-vibration bands, overlapped with weaker vibronic bands. Equation (1) then reduces to four terms corresponding to the resonant pathways $S_o \rightarrow S_1 \rightarrow S_2$, $S_o \rightarrow S_{1*} \rightarrow S_2$, $S_o \rightarrow S_1 \rightarrow S_{2*}$, and $S_o \rightarrow S_{1*} \rightarrow S_{2*}$, where the asterisks denote the vibronic bands.

The theoretical excitation spectra of SFG and SHG were simulated by performing the summation in eq. (1) at constant $\omega_2 = 9360\ cm^{-1}$ (Nd:YAG 1.064 μ) for SFG, and $\omega_2 = \omega_1$ for SHG. Note that for SHG, eq. (1) must be multiplied by 1/2 to account for the fact that terms in the summation are counted twice because $\omega_2 = \omega_1$.[6] At the peaks of the excitation curves, the ratio of SFG to SHG is calculated to be 220. The peak of the calculated SFG excitation spectrum is shifted to the blue of the $S_o \rightarrow S_1$ absorption maximum by ca. 180 cm^{-1} because it is a convolution of the $S_o \rightarrow S_1$ and $S_o \rightarrow S_2$ profiles, and because our choice of $\omega_2 = 9360\ cm^{-1}$ results in a frequency detuning of 540 cm^{-1} between ω_2 and the peak of the $S_1 \rightarrow S_2$ transition. For rhodamine 6G, the maximum enhancement factor when $\omega_2 = \omega_{ca} - \omega_{ba} = 9900\ cm^{-1}$, corresponding to the fully resonant situation, is 320. The shape and peak intensity of the calculated SFG excitation spectrum were found to be insensitive to the vibronic band contributions, i. e. the second, third and fourth terms in eq. (1), because the vibronic bands have large frequency offsets with respect to the zero-vibration bands and because the non-linearity of SFG suppresses contributions from weak transitions.

In Figure 2, a sum-frequency excitation spectrum of rhodamine 6G taken at low pulse energies (0.3mJ) is shown superimposed on the calculated SFG and $S_o \rightarrow S_1$ absorption curves. The error bar is larger on the red side of the excitation spectrum due to a higher

background from interferences such as 355 nm scatter from the Nd:YAG and incoherent molecular fluorescence.[12] The agreement between the observed data and the calculated excitation spectrum is well within experimental errors. The blue shift of the observed excitation spectrum with respect to the $S_o \rightarrow S_1$ absorption spectrum and the observed lineshape are in good agreement with the theoretical model.

From measurements of the SFG output referenced to the strongly attenuated Nd:YAG 355 nm output, we estimated the number of SFG photons generated from a monolayer sample at the peak of the excitation curve to be 50,000/pulse. A direct comparison of SFG and SHG signals from the same sample under similar experimental conditions showed an enhancement factor, after correcting for different laser powers and irradiated areas, of 170 ± 50, in agreement with the calculated value of 220.[9]

3.2. Noncollinear excitation

Consider two beams incident upon the surface at azimuthal angles θ_1 and θ_2 whose planes of incidence have a projection angle ϕ in the *xy* plane. Figure 3 defines the geometry for this situation and directly follows from Bloembergen and Pershan.[13] Their coordinate system is chosen so that k_s is in the *xz* plane; the projection angles between the reflected nonlinear output beam and the reflected fundamental beams are δ_1 and δ_2 respectively, as measured from the *x* axis in the *xy* plane. Noting that $k_{sy} = 0$, and from conservation of momentum, we find that

$$\tan\delta_1 = \frac{k_2 \sin\theta_2 \sin\phi}{k_1 \sin\theta_1 + k_2 \sin\theta_2 \cos\phi}. \qquad (2)$$

For input beams with the same azimuthal angle, i.e. $\theta_1=\theta_2$, this expression reduces to

$$\tan\delta_1 = \frac{k_2 \sin\phi}{k_1 + k_2 \cos\phi}, \qquad (3)$$

where now the angular dependence of δ_1 is solely given by the projection angle ϕ. For SHG we have $k_1=k_2$ and hence Eq. (3) is satified for $\delta_1 = {}^1/_2\phi$, which fulfills our expectation that the nonlinear output beam simply bisects the reflected fundamental beams.

The angular dependence of surface sum and difference frequency generation for collinear input beams has been given by Dick et. al.[14], who determined the efficiency of nonlinear generation as a

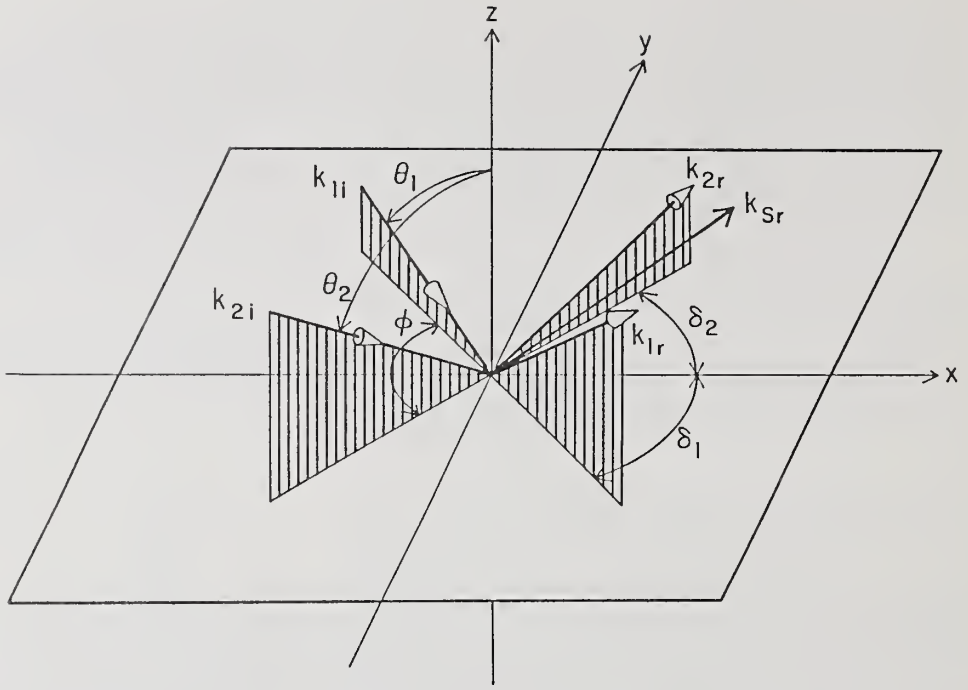

Figure 3. Simplified coordinate system that defines the noncollinear excitation geometry. The projection angle, ϕ, is the angle between the input beams in the *xy* plane. The reflected nonlinear output lies in the *xz* plane. The transmitted beams have been omitted for clarity.

function of the azimuthal angular dependence (θ) of the linear and nonlinear Fresnel factors. This model may be readily extended to include the projection angle dependence (ϕ) by using the nonlinear law of refraction as given by[13]

$$n_s^2\omega_s^2\sin^2\theta_s = n_{i1}^2\omega_1^2\sin^2\theta_1 + n_{i2}^2\omega_2^2\sin^2\theta_2 + 2\, n_{i1}\, n_{i2}\omega_1\omega_2\sin\theta_1\sin\theta_2\cos\phi \qquad (4)$$

For input beams where ϕ=0 and $\theta_1 = \pm\theta_2$, Eq. (4) reduces to Snell's law.[13]

Figure 4 presents the results for noncollinear SHG of rhodamine 6G for a projection angle of ϕ-8°. When the input beams are not overlapped, as shown in Fig. 4b), the two observed SHG peaks are seen to be collinear with the reflected fundamental peaks, which are shown in Fig. 4a). When the input beams are spatially overlapped , as shown in Fig 4c), the middle peak, corresponding to noncollinear SHG, is clearly evident. From the relative intensities of the three SHG peaks we calculate -75% overlap . This imperfect overlap explains the narrower spatial width of the middle SHG peak relative to the collinear SHG peaks, which have the same width as the input laser beams.

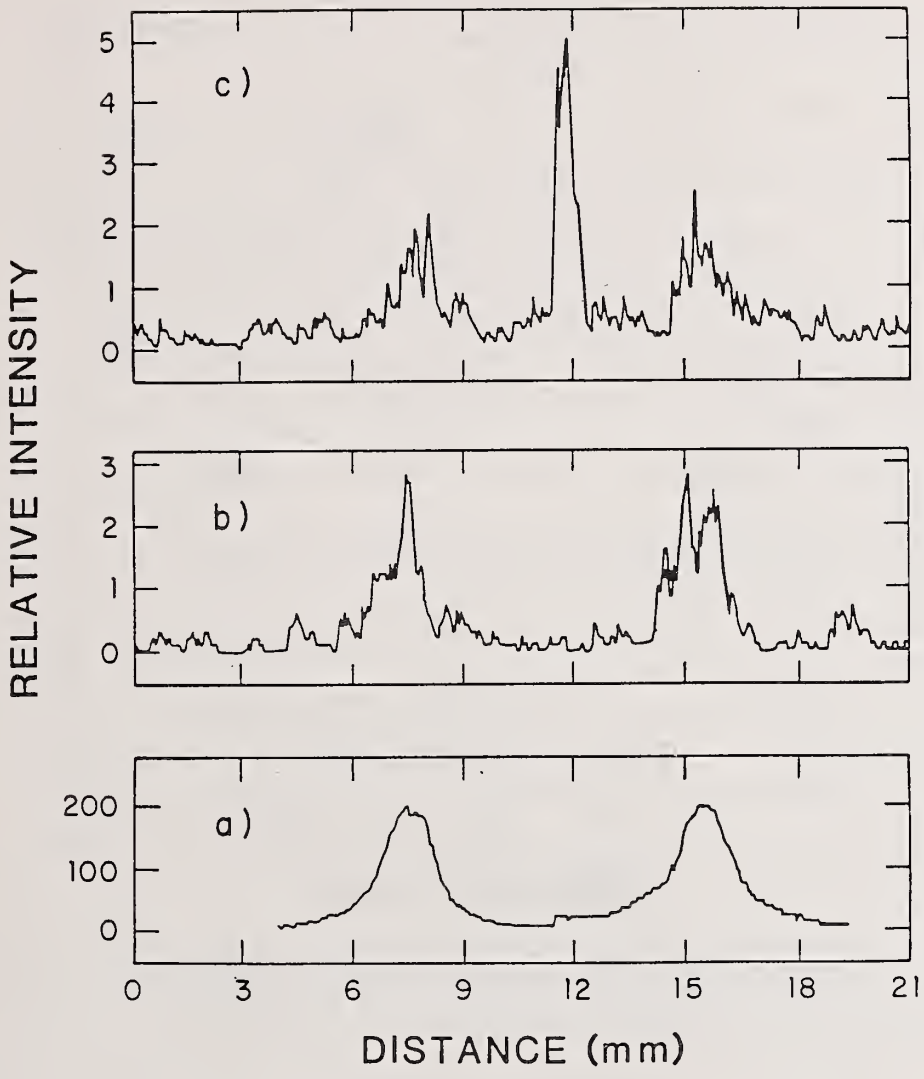

Figure 4. a) Spatial scan of the reflected 695 nm pump beams for noncollinear SHG excitation. b) Spatial scan of SHG with no pump beam overlap. c) Same as b) except for overlapped pump beams. Monochromator set at 347 nm.

Figure 5 shows the results for noncollinear SFG for a projection angle of ϕ-6° that represents the minimum projection angle necessary to achieve good spatial separation under our conditions. Note that the distance between the SFG peak and the 525 nm reflected light peak is about half the distance between the SFG and IR reflected light peaks. This is consistent with the small-angle limit of Eq. (3). From the measured distance between the output beam and the visible beam the output angle δ_1 was measured to be 1.8° ± 0.3° , in agreement with the calculated angle of 2°. There was no measureable variation in the noncollinear SHG or SFG intensity over the range in which the projection angle could be varied (3°- 15°), within our 15% experimental error. Furthermore, the measured conversion efficiencies for SHG and SFG agreed to within 30% of those previously obtained using collinear input beams.[10]

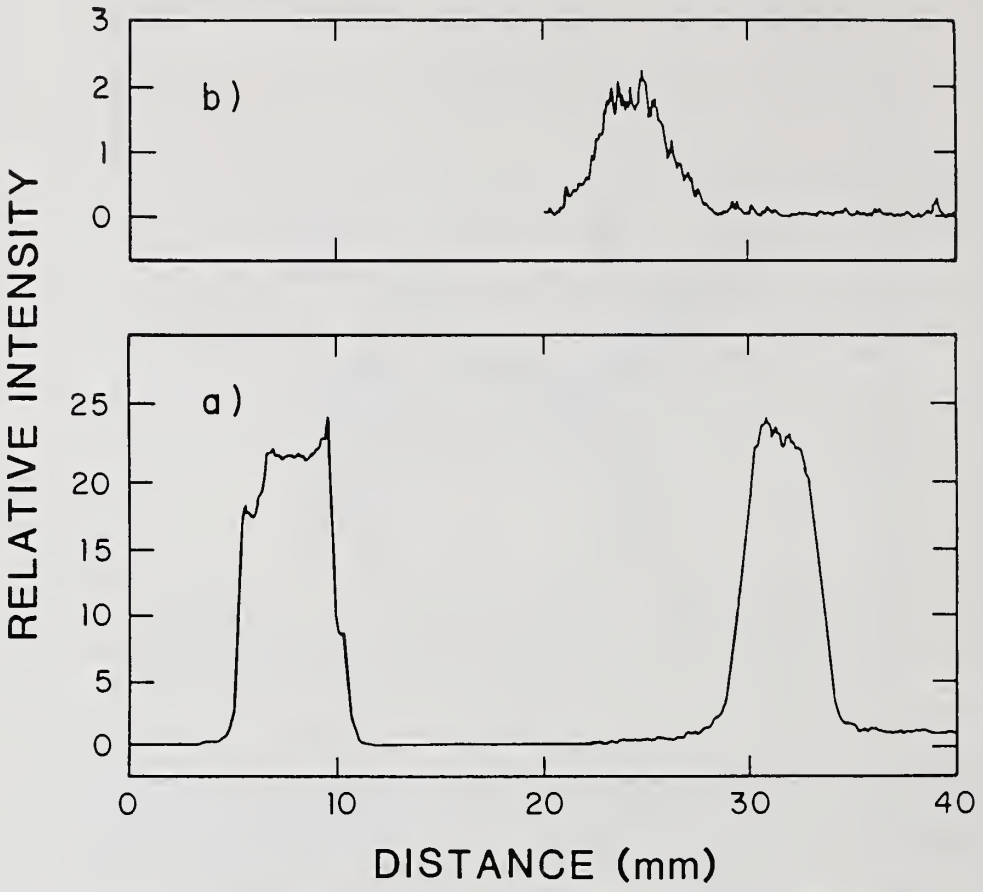

Figure 5. a) Spatial scan of IR (left) and 525 nm reflected light (right) for noncollinear SFG with no input-beam overlap. b) Spatial scan of noncollinear SFG with input beams overlapped and the color filter inserted. Monochromator set at 351 nm.

4. CONCLUSIONS

In conclusion, we have demonstrated doubly-resonant enhanced sum frequency generation from monolayers of dye. The SFG excitation spectrum is a convolution of both $S_o \rightarrow S_1$ and $S_o \rightarrow S_2$ absorption bands. The use of two input lasers allows the double resonance to be satisfied, resulting in a higher overall signal. Under the same experimental conditions, SFG was enhanced by about 170 over the SHG process.

Additionally, resonantly enhanced surface SHG and SFG using a noncollinear excitation geometry shows that for small projection angles, $\phi \leq 15^\circ$, effective separation of the nonlinear output beam from the reflected fundamental beams is achieved without significantly reducing the efficiency of nonlinear generation. Furthermore, the large reductions of detectable scattered light and fluorescence attainable by this technique should increase the sensitivity and versatility of surface SHG and SFG.

5. REFERENCES

[1.] N. Bloembergen, R. K. Chang, S. S. Jha and C. H. Lee, Phys. Rev. **174**, 813 (1968).

[2.] Y. R. Shen, J. Vac. Sci. Technol. B, **3**, 1464 (1985).

[3.] Y. R. Shen, Ann. Rev. Mat. Sci. **16**, 69 (1986).

[4.] H. W. K. Tom, Lawrence Berkeley Laboratory Report No. LBL-17820, 1984.

[5.] J. H. Hunt, P. Guyot-Sionnest and Y. R. Shen, Chem. Phys. Lett. **133**, 189 (1987).

[6.] G. Marowsky, A. Gierulski and B. Dick, Optics Commun., **52**, 339 (1985)
.

[7.] Y. R. Shen, The Principles of Nonlinear Optics, Wiley (New York; 1984).

[8.] T. F. Heinz, C. K. Chen, D. Ricard and Y. R. Shen, Phys. Rev. Lett., **48**, 478 (1982).

[9.] D. C. Nguyen, R. E. Muenchausen, R. A. Keller and N. S. Nogar, Opt. Commun., **60**, 111 (1986).

[10.]R. E. Muenchausen, R. A. Keller and N. S. Nogar, J. Opt. Soc. Am. B, **4**, 237 (1987).

[11.]B. Dick, A. Gierulski and G. Marowsky, Ber. Bunsenges. Phys. Chem., **89**, 346 (1985).

[12.]G. C. Orner and M. R. Topp, Chem. Phys. Lett., **36**, 295 (1975); H. Lin and M. R. Topp, Chem. Phys. Lett., **47**, 442 (1977).

[13.]N. Bloembergen and P. S. Pershan, Phys. Rev. **128**, 606 (1962).

[14.]B. Dick, A. Gierulski, G. Marowsky and G. A. Reider, Appl. Phys. B, **38**, 107 (1985).

- Manuscript Not Received -

Thresholds for and Time Dependence of UV-Photon-Induced Desorption of Lithium Atoms from Lithium-Fluoride Single Crystals

Richard F. Haglund, Jr. and Norman H. Tolk
Center for Atomic and Molecular Physics at Surfaces
Department of Physics and Astronomy
Vanderbilt University
Nashville, TN 37235

ABSTRACT

The rapid pace of development in short-wavelength light sources -- ranging from available excimer lasers to projected vuv and xuv free-electron lasers -- is stimulating investigations of the electronic photon-materials interactions which may be the rate-limiting processes in catastrophic optical damage.

We have measured photon-energy thresholds for ground-state neutral Li desorption from single-crystal LiF under ultrahigh vacuum conditions using laser-induced fluorescence, and found that as much as one-fourth of the total yield is traceable to photons with energies less than the LiF band gap. Moreover, time-resolved measurements of the desorption process have enabled us to identify the specific excitonic channels which lead to diffusion-driven, defect-induced desorption in this material. Excitonic energy-transfer mechanisms of this type are characteristic features not only of the alkali halides, but also of alkaline-earth halides, fused silica and many metal oxides.

Our results demonstrate that mobile surface and near-surface defects can be produced even by low-energy photons, and that the diffusion of these defects drives the formation of metal-rich overlayers in LiF and probably in many other short-wavelength optical dielectrics.

Key Words: electronic transitions; LiF; time resolved measurement; ultrahigh vacuum; uv laser damage

---

This research was supported in part by the Los Alamos National Laboratory, under Subcontract 9-X35-Y0131-1; by the Sandia National Laboratories, under Contract 65-2377; and by the Air Force Office of Scientific Research, under Contract AFOSR-86-0150.

Radiation Hardness of Nd:YAG and Nd:Cr:GSGG Laser Rods

Manuscript Received
11-13-86

by

M.A. Acharekar, M.M. Kaplan, D.P. McCarthy
Litton Systems, Inc.
Laser Systems Division
2787 So. Orange Blossom Tr.
Apopka, FL 32703

ABSTRACT

Gadolinium scandium gallium garnett (GSGG) co-doped with neodymium (Nd) and chromium (Cr), shows higher efficiency and optical damage threshold than commonly used neodymium doped yttrium aluminum garnet (Nd:YAG) laser rod. Nd:YAG and Nd:Cr:GSGG laser rods were irradiated with gamma radiation from Cobalt-60 source. Passive electronic and vibrational spectra of the laser materials were obtained before and after radiation. The near ultraviolet (NUV), visible (VIS) and near infrared (NIR) spectra were obtained using a Varian Model 2300 spectrophotometer. The infrared (IR) spectra were obtained using a Perkin-Elmer Model 783 Infrared Spectrophotometer and Model 7500 Infrared Data System. The active laser tests were conducted to study the effects of irradiation on the efficiency of the laser materials.

The data collected indicates that the Nd:YAG laser rod had transient radiation effects while the Nd:Cr:GSGG laser rod appeared to be resistant to the effects of the radiation dose in terms of the laser's output energy.

Key Words: Electronic and Vibrational Spectra; Gamma Radiation Effects; Laser Crystals; Nd:Cr:GSGG; Nd:YAG; Radiation Durability.

1. INTRODUCTION

Neodymium doped yttrium aluminum garnet (Nd:YAG) crystal is the most commonly used solid-state material for lasers at the present time[1]. The typical overall efficiency of Nd:YAG is limited to 2-3 percent. Gadolinium scandium gallium garnet crystal co-doped with nedoymium and chromium (Nd:Cr:GSGG) shows higher efficiency than the Nd:YAG crystal[2]. We previously reported[3],[4] the bulk and surface damage thresholds of Nd:Cr:GSGG crystal.

The complete characterization and performance comparison of Nd:YAG and Nd:Cr:GSGG crystals are necessary to evaluate the advantages and disadvantages of these crystals. In this paper, the radiation durability of Nd:YAG and Nd:Cr:GSGG crystals is reported using a Cobalt-60 gamma radiation source. The laser rods were fabricated using stress-free locations from crystal boules of Nd:YAG and Nd:Cr:GSGG.

The effects of Gamma radiation on the Nd:YAG and Nd:Cr:GSGG lasers' output energy performance is reported by Zharikov et.al.[5]. The change in laser output energy due to Gamma irradiation observed for the materials is shown in Figure 1-1. The work reported in this paper was undertaken to examine the changes in the materials due to Gamma radiation using active and passive tests before and after Gamma irradiation.

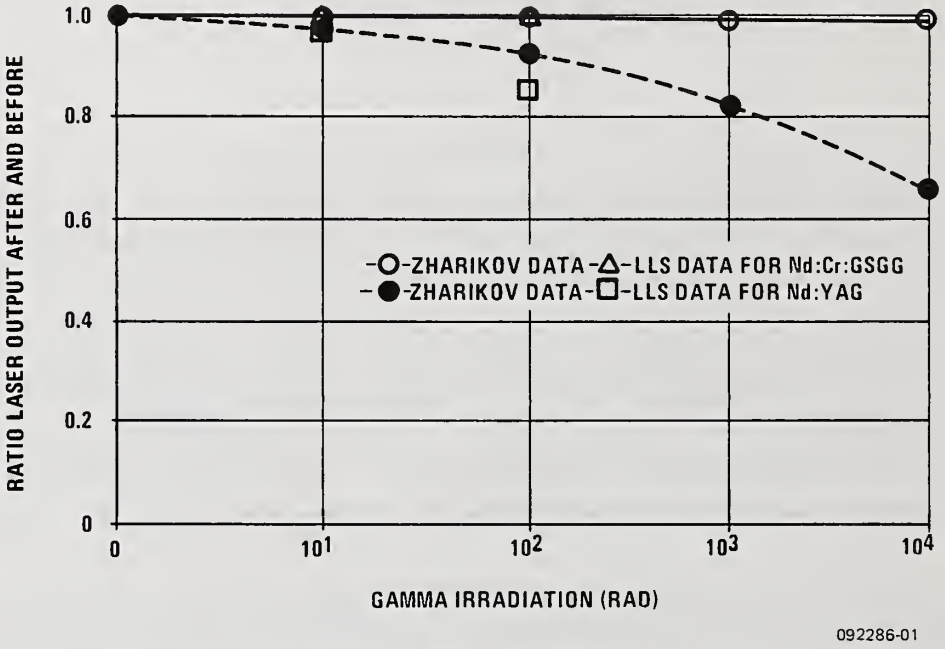

Figure 1-1. Effects of Gamma Irradiation on Laser Ouput.

The passive testing, performed before and after irradiation, included the measurement of the electronic and vibrational spectra of the laser rods. The active testing, also performed before and after irradiation, included the measurement of the lasing threshold and input/output characteristics of the laser rods.

2. PASSIVE TESTS

Nd:YAG and Nd:Cr:GSGG laser rods, 0.63 cm diameter by 7.5 cm long, were passively tested using the following types of spectrophotometric measurements:

- o Infrared Transmission Spectrum
- o UV-VIS-NIR Transmission Spectrum.

2.1 Infrared Transmission Spectrum

LLS has developed a technique to obtain and characterize the infrared spectrum of a laser crystal using the Perkin-Elmer Model 783 IR spectrometer and a rod holding fixture[6]. The data collected for 0.63 cm diameter by 7.5 cm long Nd:Cr:GSGG and Nd:YAG laser rods using the technique is shown in Figures 2-1 and 2-2 respectively.

The laser rods were irradiated with 100 rads radiation dose from a cobalt-60 gamma radiation source. The infrared spectrum obtained before and after irradiation shows a slight change. It may be noted that the infrared spectrum was obtained approximately 10 hours after the rods were irradiated. In Table 2-I, the effect of radiation on the infrared spectrum of the Nd:YAG laser is tabulated. As seen in the table, maximum negative change in the ratio of absorbance at 3203 cm^{-1} and 2517 cm^{-1} is observed, while maximum positive change in the ratio of absorbance at 3806 cm^{-1} and 2517 cm^{-1} is observed. Therefore, we plan to provide a high dose up to 1000 rads and carefully monitor the change in the infrared spectrum, particularly at 3203 cm^{-1} and 3806 cm^{-1}.

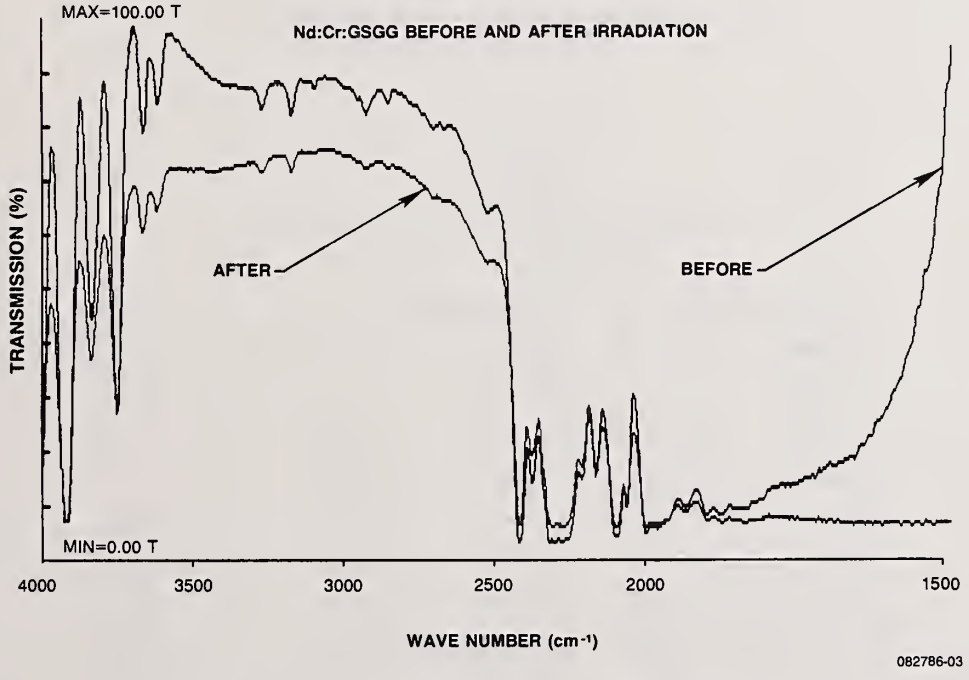

Figure 2-1. Infrared Spectrum for Nd:Cr:GSGG Laser Rod.

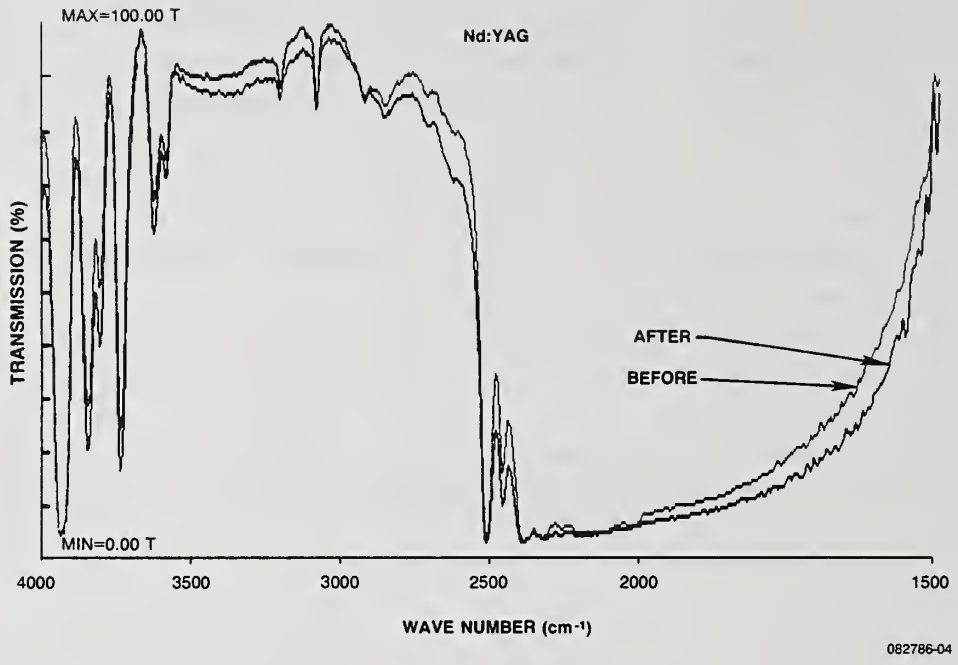

Figure 2-2. Infrared Spectrum for Nd:YAG Laser Rod.

TABLE 2-I

γ-RAY RADIATION EFFECTS ON Nd:YAG LASER ROD

Radiation Dose = 100 rads

WAVE NUMBER IN cm^{-1}	BEFORE RADIATION		AFTER RADIATION		% CHANGE DUE TO RADIATION
	ABSORBANCE	RATIO OF ABS*	ABSORBANCE	RATIO OF ABS*	
2517	1.4060	-	1.4767	-	-
3933	1.4960	1.0641	1.4996	1.0155	- 4.8
3847	0.5453	0.3879	0.6965	0.4717	+17.7
3806	0.2914	0.2072	0.3938	0.2667	+22.3
3737	0.6155	0.4378	0.7799	0.5281	+17.1
3624	0.1735	0.1234	0.2145	0.1453	+15.0
3585	0.1257	0.0894	0.1459	0.0988	+ 9.5
3203	0.0637	0.0453	0.0532	0.0360	-25.8
3083	0.0726	0.0516	0.0738	0.0500	- 3.2
2463	0.7906	0.5623	1.0003	0.6774	+16.9

*Ratio is the absorbance at the wave numbers in Column #1 and the absorbance at the reference wave number 2517 cm^{-1}.

2.2 UV-VIS-NIR Transmission Spectrum

LLS has developed a method to obtain near ultraviolet (NUV), visible (VIS), and near infrared (NIR) spectrum of laser rods[7] using the Varian Model 2300 spectrophotometer and a rod holding fixture. The fixture holds the rod in the sample beam of the spectrophotometer parallel with the optic axis. The sample beam of the spectrophotometer, thus, goes through the length of the laser rod.

In Figures 2-3, 2-4, and 2-5, low VIS, high VIS, and NIR spectra obtained for Nd:YAG and Nd:Cr:GSGG laser rods using the technique are shown. It may be noted that for a Nd:Cr:GSGG laser rod longer than 1 cm, it is not possible to obtain good UV and visible spectra due to strong broad chromium absorbance bands. In Figures 2-6, 2-7,

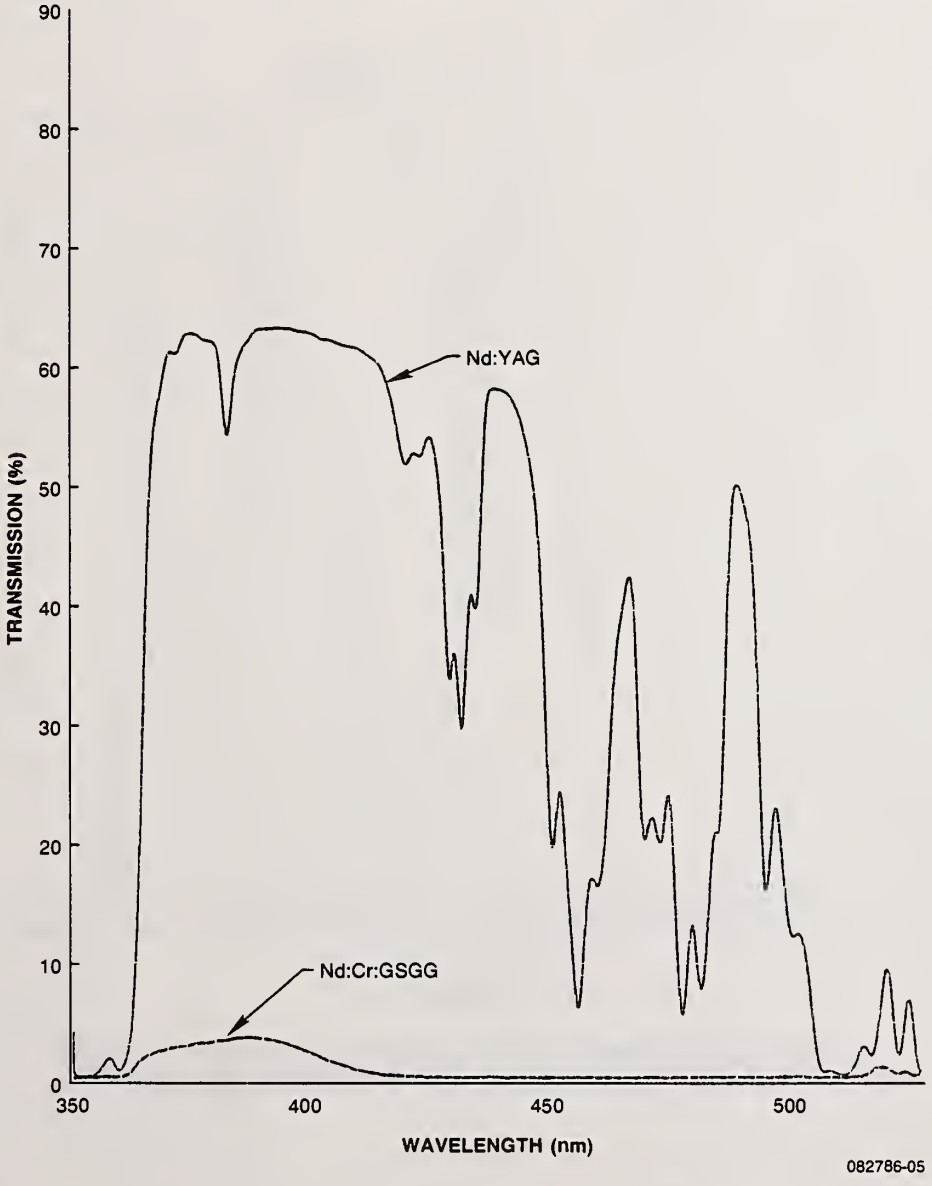

Figure 2-3. Low Vis Spectra for Nd:YAG and Nd:Cr:GSGG Before Irradiation.

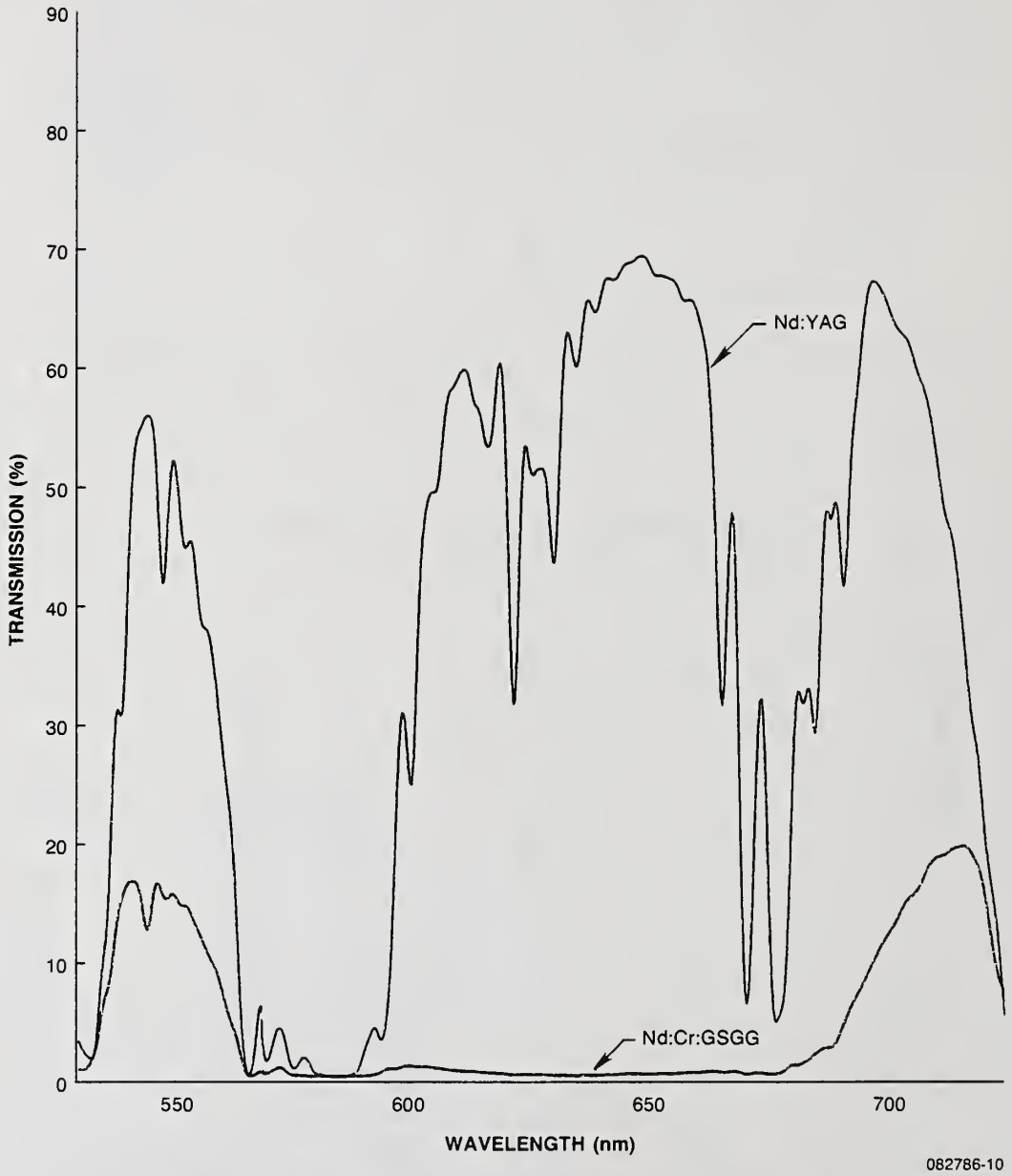

Figure 2-4. High Vis Spectra for Nd:YAG and Nd:Cr:GSGG Before Irradiation.

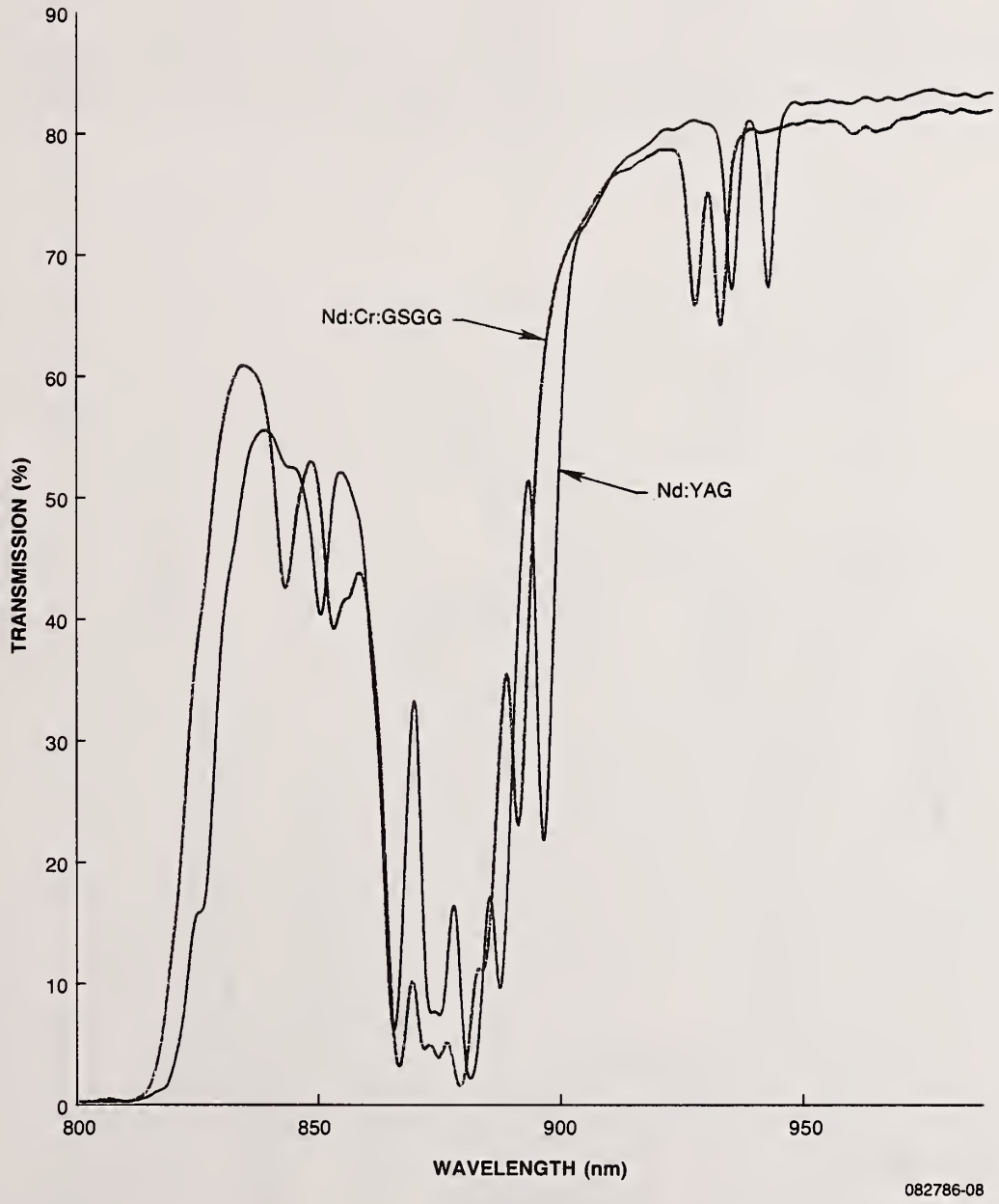

Figure 2-5. Near IR Spectra for Nd:YAG and Nd:Cr:GSGG Before Irradiation.

and 2-8, low VIS, high VIS, and NIR spectra obtained for the same laser rods after 100 rad dose from γ-ray radiation from a cobalt-60 source are shown. The data collected show that either there were no changes in the range of 500-750 nm due to radiation in Nd:YAG or Nd:Cr:GSGG materials or the materials were completely recovered when the data were collected (within 1 hour after irradiation). However, in the low visible range 350-450 nm, a significant change in transmittance is observed after irradiation. The dose of 100 rads changes the transmittance at 400 nm from 63 percent to 60 percent; also, a slight change in transmittance is observed at 940 nm, after the gamma irradiation in Nd:YAG laser rod.

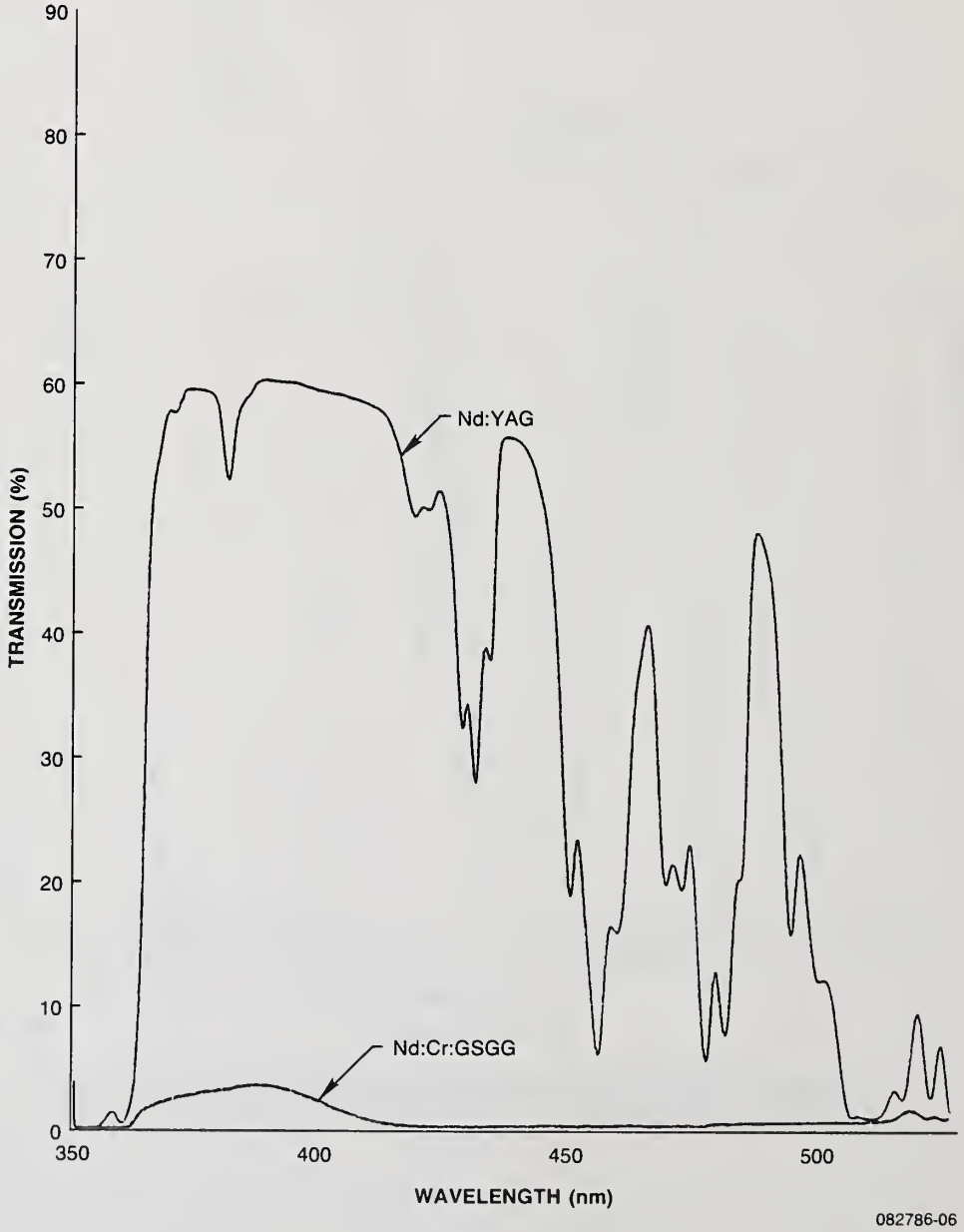

Figure 2-6. Low Vis Spectra for Nd:YAG and Nd:Cr:GSGG After Irradiation.

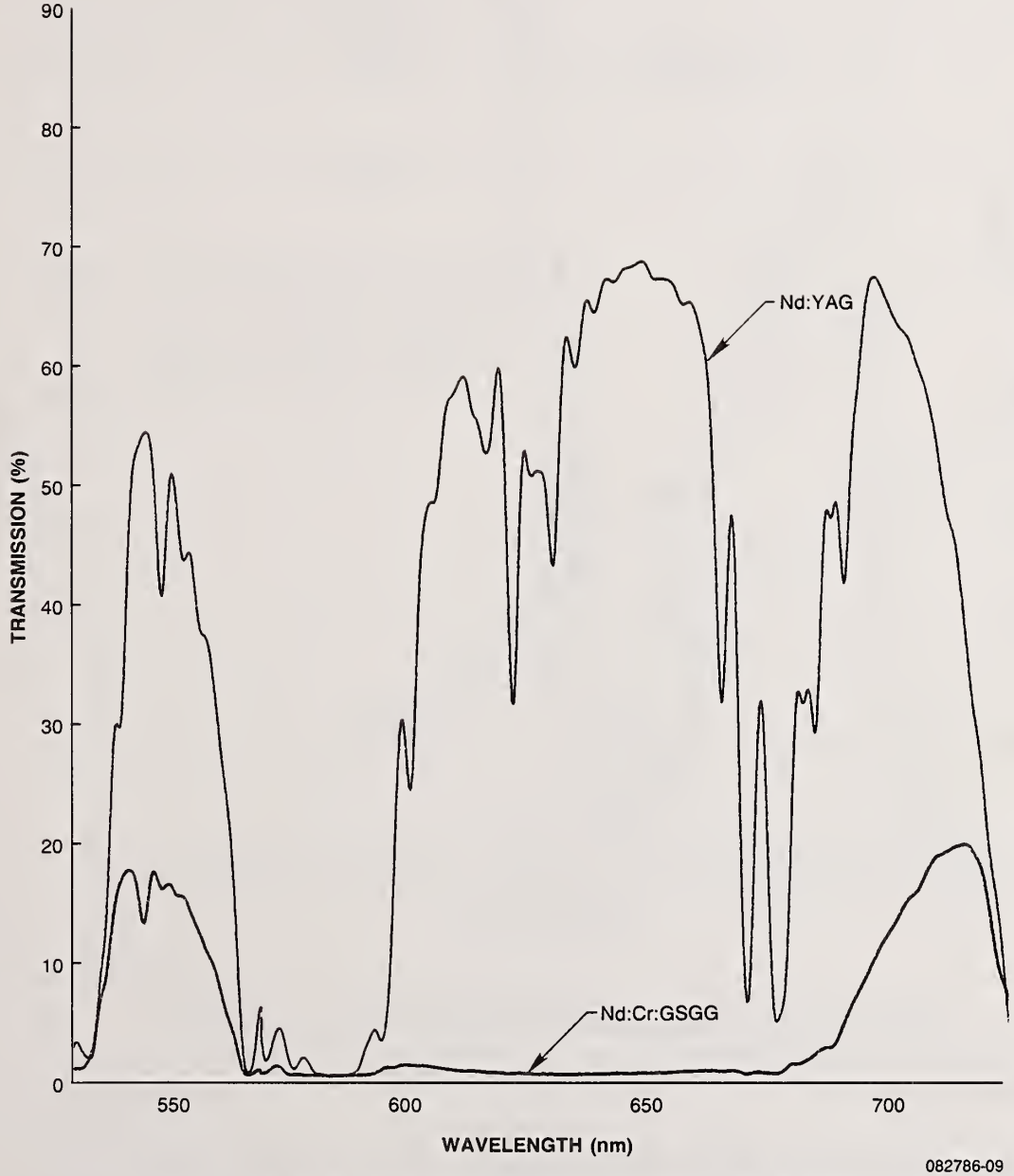

Figure 2-7. High Vis Spectra for Nd:YAG and Nd:Cr:GSGG After Irradiation.

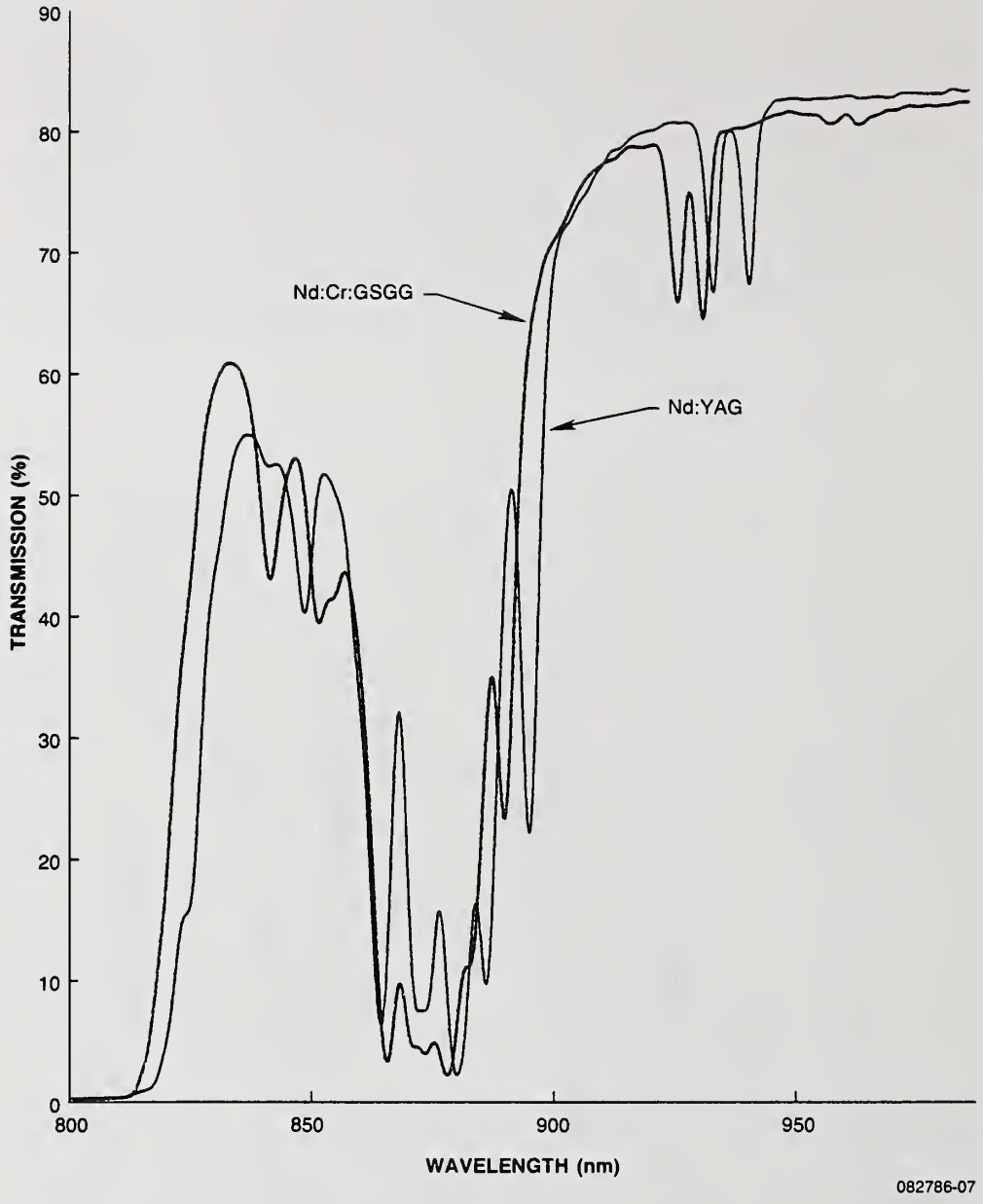

Figure 2-8. Near IR Spectra for Nd:YAG and Nd:Cr:GSGG After Irradiation.

3. Active Tests

The performance of the Nd:YAG laser rod shows a number of effects due to γ-ray radiation from Cobalt-60 source. These effects include change in laser threshold, change in slope efficiency, and lower output efficiency. Therefore, active tests for the irradiated rods included following measurements:

- o Threshold Measurements
- o Normal mode Input-Output characteristics.

The data obtained for 0.63 cm diameter by 7.5 cm long Nd:YAG and Nd:Cr:GSGG laser rods are shown in Figure 2-9. It may be noted that the laser rods were irradiated with 100 rads dose and the active tests were conducted within 1 hour after the irradiation. The data collected showed a negligible change in Nd:Cr:GSGG laser characteristics, while the Nd:YAG laser rod showed an increase of threshold energy from 4 J/P to 4.7 J/P and an overall 15 percent reduction in output energy.

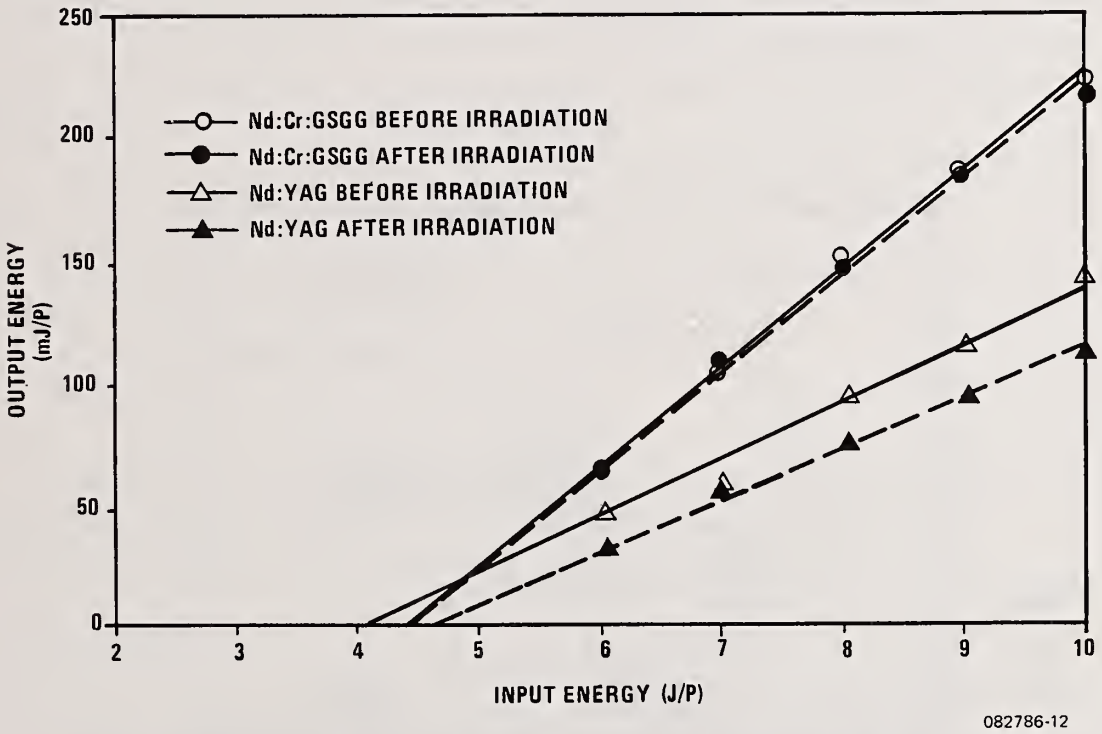

Figure 2-9. Nd:YAG and Nd:Cr:GSGG Laser Characteristics Before and After γ-Ray Irradiation.

The other effects observed in the laser materials are:

- o Recovery of the material as the rods are exposed to the UV-VIS-NIR light from the flashlamp
- o Recovery of the material with the time lapse.

The Nd:YAG laser rod which was exposed to 100 rads dose level was completely recovered within 12 hours after the exposure in terms of its laser threshold and input-output characteristics.

4. GAMMA RAY IRRADIATION

Nd:YAG and Nd:Cr:GSGG laser rods were irradiated using gamma rays from a Cobalt-60 radiation source. The experimental set up used for the test is shown in Figure 2-10. A brief description of the experimental set up is given here. The Cobalt-60 radioactive source is housed in a heavily shielded container supplied by the Radiation Products Division of Tech/Ops, Inc., Burlington, MA. The container is provided with a remote turn off/on control and grazing incidence gamma ray pipe. The gamma ray pipe is terminated with a collimater assembly. The collimater provides a uniform 3" diameter spot of gamma rays, 12" from the collimator. Therefore, the collimator is supported on a 12" long aluminum tube of 4" diameter. The entire set up is enclosed in a cement block laboratory of 15' x 15' in size and the leaked radiation is monitored at the perimeter of the lab.

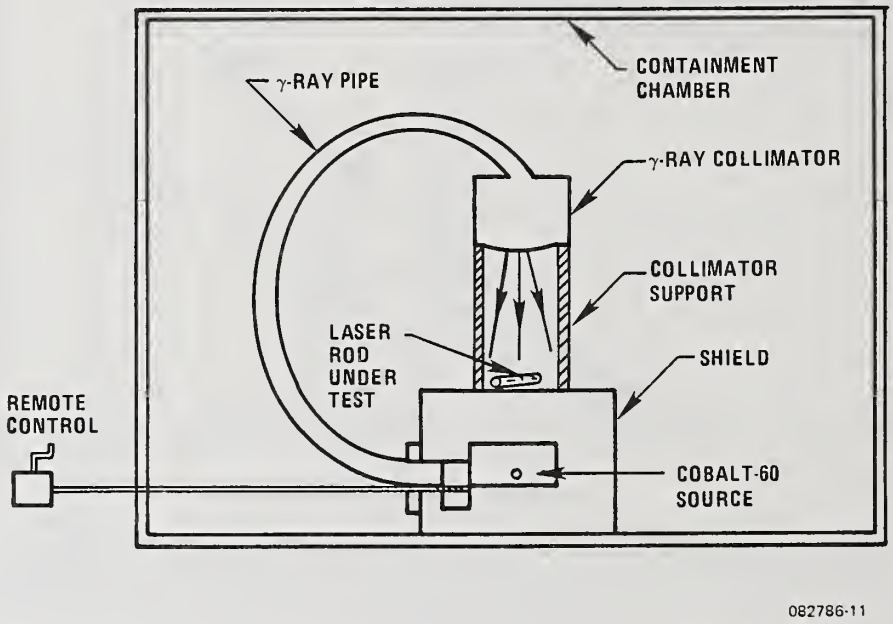

Figure 2-10. Experimental Set-Up for Laser Rod Irradiation.

5. CONCLUSIONS

a. The infrared spectrum of Nd:Cr:GSGG revealed that the hydroxyl-related lattice perturbation apparently was markedly reduced after exposure to gamma irradiation.

b. The infrared transmittance at 1500 cm^{-1} was significantly reduced after gamma irradiation indicating a possible matrix change; however, the exact molecular reorientation is not precisely known at this time.

c. The infrared spectrum of Nd:YAG revealed a similar observation noted in paragraph (a) of the conclusions; namely, reduction of hydroxyl-related lattice perturbation after gamma irradiation.

d. The infrared transmittance at 3806 cm^{-1} was decreased significantly after gamma irradiation showing possible transmission changes at the lasing wavelength of 1.06 microns.

e. The low and high regions of the visible spectra of Nd:Cr:GSGG shows poor transmittance before and after irradiation because of the dopant Cr absorbing in the visible spectral range. In the case of Nd:YAG, however, the 400 nm region had a decrease in transmittance after gamma irradiation. This region of the spectrum is normally associated with the laser rod solarization.

f. No changes were observed in Nd:Cr:GSGG in the near infrared spectrum after gamma irradiation. Nd:YAG, however, had a small decrease in transmittance at 940 nm, after gamma irradiation.

g. The data presented in this paper is at the threshold of the gamma irradiation effects. High gamma irradiation dose data is being collected.

6. ACKNOWLEDGEMENTS

This work is a part of an internal R&D program conducted at and supported by Litton Laser Systems, Orlando, FL. Thanks are due to Julie Trudell, Phyllis Milligan, and Jacqueline Gibson for preparation of this manuscript.

7. REFERENCES

[1] Koechner, W.; "Solid-State Laser Engineering," Springer-Verlag, New York, Chapter 2, (1976).

[2] Zarikov, N.N.; Laptev, V.V.; et.al., Sov. J. Quantum Electron. 13 (1), 82-85, 1983 Jan.

[3] Acharekar, M.A., McCarthy, D.P.; Blackman, R.; Pulsed laser induced optical damage threshold in Nd:Cr:GSGG crystal, Laser Induced damage in optical material, Boulder Damage Symposium, 1984 Sept., (Proceedings to be published).

[4] Acharekar, M.A.; Infrared absorption spectroscopy of Nd:YAG and Nd:Cr:GSGG Surface contaminants, Laser Induced damage in optical material, Boulder Damage Symposium, 1985 Nov. (Proceedings to be published).

[5] Zharikov, E.V., at.al.; Bull. Acad. Sc. USSR, Phys. Ser. (USA), 48 (7), 95-97, 1984.

[6] Acharekar, M.A., Infrared spectra and characteristic frequencies of Nd:YAG crystal. Spectrochemica Acta, Part A, (To be published).

[7] Acharekar, M.A., Laser Focus 18 (11), 63-66, 1983.

Manuscript Received
6-25-87

The Effect of Impurities on U.V. Damage in CaF_2

Ian Laidler & David C. Emmony

Department of Physics, Loughborough Unversity of Tehnology
Loughborough, Leics. LE11 3TU. United Kingdom

The paper discusses the role of impurities in bulk laser breakdown. Crystals of CaF_2 have been grown with different impurity content. The introduced impurities are mainly rare earths, these being the most common contaminent species found in CaF_2. Crystals selectively doped with Ce as well as very pure, strain annealed specimens were also grown. The generation of defect centres as a function of incident 248 nm laser fluence was monitored by transient absorption measurements. Bulk damage measurements indicated that the Ce doped crystals had the lowest thresholds followed by the pure strain annealed crystals, despite a complete absence of excited state absorbing centres produced during laser irradiation. Those crystals which showed a significant production of transient defects and fluorescent levels had very high damage thresholds.

Key words: colour centres; excimer damage; effect of impurities; surface and bulk effects; transient absorption; 248nm

1. Introduction

Most workers in the field of laser induced damage are familiar with the formation of colour centres within certain materials and particularly when working in the ultraviolet region of the spectrum. Intuitively the bulk damage threshold is thought to be correlated with the formation of those colour centres. The nature of the correlation, however, has remained unknown. Kabler and Williams [1] pointed out two possible effects resulting from the formation of primary defects:

(i) new channels of energy deposition to the lattice are created by the presence of primary defects. These could drastically lower the theoretical damage threshold predicted by either the electron avalanche or multiphoton model;

(ii) the efficient removal of electron-hole pairs by the rapid process of primary defect formation hinders the generation or build up of conduction band electrons and hence affects the free carrier absorption mechanism of Joule-lattice heating. This would oppose the effect mentioned in (i).

The question as to which of these two processes would dominate the damage threshold is studied in this paper.

2. Defect Types and Processes

Colour centre formation in relatively pure single crystal material, ie, CaF_2, MgF_2 may be regarded as a photochemical phenomena. This is no new area of research, though the production of vacancies and interstitials by band gap excitation alone was not common until the advent of U.V. lasers. There are a number of reasons for this. The energy supplied by the photon must exceed the sum of the formation energy of the defect and any intermediate state en-route. There is then needed some reaction after excitation to prevent total recombination occurring. Colour centres are seen in the alkali-earth halides because the reaction $X^- + X \rightarrow X^-_2$ is exothermic. Often when vacancies and interstitials are formed they exist for such brief periods they are considered inconsequential. With respect to a 30 ns duration laser pulse, however, they are relatively long-lived and need to be considered. There is general agreement throughout the literature that the primary products of radiolysis in the alkali and alkali-earth halides are the F centre and complimentary H centre. The ionizing radiation produces 'free electrons' and holes. The 'free electrons' may actually be trapped at impurities and lie within a band gap.

These would require further photon absorption before being lifted to the conduction band. The electrons in the conduction band thermalize rapidly, injecting energy into the lattice. The holes in the halide lattices quickly self trap (in 0.1 to 1 psec) and fast pulse optical studies by Williams, Bradford and Faust [2] indicate that F centres may be formed within the ground state 10 psec after the band gap excitation. This is short compared with the radiative lifetime of the F centre which is around 600 μ sec.

Figure 1 is a schematic representation of the V_k centre, the H centre and the self-trapped exciton in the fluorite structure. The self-trapped exciton can be thought of as a close F-H pair. The V_k centre is a 'molecular type' defect, a hole localized between two halide ions. To a good approximation it can be regarded as an X^-_2 molecule. The F centre (the most widely studied colour centre in ionic crystals) consists of an electron localised at a halide ion vacancy. It has frequently been modelled along the lines of a hydrogen atom, being given the same molecular orbitals. The final defect to be considered, the H centre, is a neutral anion interstitial, and similar to the V_k centre resembles an X^-_2 molecule. In CaF_2 the V_k centre has a (100) molecular axis whilst the H centre has a (111) molecular axis with one of the fluorine atoms near the centre of the normally empty cube of the fluorite structure.

Figure 2 shows the F and H centre formation mechanism in CaF_2. (a) is the perfect lattice and (b) the V_k centre. This centre appears unstable in the presence of an electron and moves to the (111) orientation associated with an H centre. The electron is thus trapped at an anion vacancy forming a close F-H pair, (c). Radiative recombination may occur from this position in times of 5 to 10 ms restoring the perfect lattice. Also possible is the physical separation of the pair via thermal migration, resulting in a set of stable defects capable of colouring the crystal.

Direct band gap excitation is unlikely to cause defects as the band gap for CaF_2 is 10.6 eV. At 248 nm we are seeing colouration and luminescence, produced by 5 eV photons. It is suggested that impurity atoms acting as electron acceptors initiate the sequence detailed above. The impurities allow electrons to be trapped within the band gap by photon excitation from the valance band. The impurity then becomes a donor lying below the conduction band, and through further photon absorption can yield its electron to the conduction band. This system provides the necessary source of free electrons and holes for intrinsic defect formation to occur.

Once the close F-H pair has been created, a number of routes are open to it regarding its decay. These are shown in figure 3.

3. Experimental Procedure

The experiment is designed to monitor the defect population in CaF_2 as it is irradiated by 248 nm KrF excimer radiation. The concentration of close F-H pairs is monitored by measuring the relative absorption at 339 nm. the experimental arrangement, shown in figure 4, has been described previously [3]. Briefly, it consists of:

(i) a Lambda Physik EMG 200 laser operating at 248 nm;

(ii) a Laser Damage facility including an absolute energy calorimeter and the Image III beam profiling system [4];

(iii) a synchronously pumped dye laser (Lambda Physik FL 2000) operating at 339 nm to monitor the absorption of the close F-H pairs.

The samples were in the form of 2 cm cubes of CaF_2, single crystal and the excimer beam and dye laser probe beam were arranged to interrogate the same portion of the crystal, the dye beam arriving 4 ns after the onset of the 30 ns excimer pulse. The probe beam and a reference beam, derived by beam splitting the dye laser light upstream of the target, are terminated on a vacuum photodiode connected to an oscilloscope capable of resolving the dye laser's temporal profile. The reference beam is optically delayed by about 35 ns before detection. Direct comparisons can be made between probe and reference beams to monitor the extent of transient absorption due to centres created in the crystal by the excimer beam. The system is designed such that thermal lensing effects are avoided. The system therefore enables measurement of the defect population as a function of time and incident energy.

4. Sample Preparation

Seven samples were investigated, grown from two sources of raw material. One source, referred to as Mexican, was the 'as mined' material. The other, Optipur, is a synthetic CaF_2 of high purity. Mass spectrographic analysis was performed on both sources. The results are summarized in table 1. The main family of impurities were the rare earth series of lanthanides and actinides. These are a common substitutional impurity of the fluorites and enter the lattice in place of the calcium ion. They enter, however, in the trivalent excitation state and are thus ideal electron acceptors, enabling the initiation of a defect sequence. In the Optipur material, when detected these impurities were below the calibration limit of the machine. The Mexican material, however, had ppm levels of Ce, Pr, Nd, Ba, Gd, 30 ppm of Y and 10 ppm of La. Samples were grown using differing proportions of these two source materials, as well as one sample of Optipur material doped with 10 ppm Ce. A further sample of Optipur was strain annealed. The measured bulk damage thresholds, composition, and nomenclature of the samples is shown in table 2.

Sample B, we believe was poisoned during growth as its absorption spectra was very similar to the cerium doped sample (sample F). Cerium in CaF_2 is well-known as an easily excited electron source, hence the low damage threshold of these two samples (samples B and F).

5. Results

The ratio of the reference to probe dye laser intensities, and hence relative absorption, is shown plotted as a function of excimer fluence. The graphs correspond to a time 12 ns after the onset of excimer excitation, figure 5.

It can be seen that there is no transient absorption for the pure CaF_2. Those samples with impurities present had a peak defect concentration at 10 Jcm^{-2}. Figure 6 shows the peak relative absorption against the percentage increase in impurities (viz. from sample A to E). This graph is linear. Transient absorption would therefore appear to be linearly dependent upon the rare-earth impurity concentration. The graphs indicate that a level of saturation is reached, after which the defect concentration falls. It is suggested that a certain fluence is required to establish the maximum attainable, impurity limited, defect population. Once this level has been reached, defect depleting mechanisms such as further photon absorption, dissociation, or defect separation, takes place, thereby reducing the absorption strength. The damage thresholds indicate that the impure materials have a higher damage threshold than the pure. It is suggested that the impurities, acting as electron acceptors, or the holes that are generated via the impurities, are continually trapping the conduction band electrons, thereby hindering the formation of an efficient electron avalanche process. Samples C, D and E showed visible colouration, sample A showed none. Thus the presence of defects, F and H centres within a crystal, would not appear to be sufficient justification for assuming a low damage threshold. The density of impurities is in the order of $10^{18}cm^{-3}$ and this excess level of electron traps over and above conduction band electrons will be maintained in the crystal throughout, regardless of the processes taking place. This imbalance on the side of electron acceptors would appear to strengthen the crystal against laser induced damage.

6. Summary

The concentration of rare earth impurities is shown to be linearly related to the transient absorption in CaF_2 crystals due to the close F-H pair (self-trapped exciton). The absorption saturates and is limited by the impurity concentration. Crystals that showed visible colouration due to F-H centre generation had a greater resistance to laser induced damage. This would indicate that impurities, or holes generated by impurities trapping excited valence electrons, are acting as efficient depleters of the conduction band electrons, thereby hindering the build-up of an electron avalanche.

Acknowledgments

This work was carried out with a CASE award in collaboration with BDH (Chemicals) Limited and a grant from the Science and Engineering Research Council. The support of both these organisations is gratefully acknowledged.

7. References

[1] Kabler, M.N.; Williams, R.T. Vacancy-interstitial pair production via electron hole recombination in halide crystals. Phys.Rev.B. 18: 1948-1960, 1978.

[2] Williams, R.T.; Bradford, J.N.; Faust, W.L. Short pulse optical studies of exciton relaxation and F-center formation in NaCl, KCl and NaBr. Phys.Rev.B. 18: 7038-7057, 1978.

[3] Laidler, I.; Emmony, D.C. Excimer colouration processes and surface damage to single crystal CaF_2 substrates. Proceedings of the XVIIth Symposium on Optical Materials for high power Lasers, Boulder (1985).

[4] Clark, S.E.; Laidler, I.; Emmony, D.C.; Omar, B.A.; Shaw, M.J. U.V. laser beam diagnostics using a computer controlled video frame store system. Proceedings of the XVIIth Symposium on Optical Materials for High Power Lasers, Boulder (1985).

Table 1

Lanthanides/Source Material			Actinides/Source Material		
Element	Mexican	Optipur	Element	Mexican	Optipur
Ce	3.0	<0.1	Th	<0.1	-
Pr	3.0	<0.1	Pa	-	-
Nd	3.0	<0.4	U	<0.1	-
Pm	-	-	Np	-	-
Sm	<0.6	<0.4	Pu	-	-
Eu	0.6	<0.2	Am	-	-
Gd	2.0	<0.3	Cm	-	-
Tb	0.3	<0.1	Bk	-	-
Dy	1.0	<0.3	Cf	-	-
Ho	0.3	<0.1	Es	-	-
Er	1.0	<0.3	Fm	-	-
Tm	<0.1	<0.1	Md	-	-
Yb	<0.6	<0.3	No	-	-
Lu	<0.1	<0.1	Lw	-	-
La	10.0	<0.1			
Ba	3.0	<0.1			
Y	30.0	<0.1			

Table 1 Main impurities and their concentrations in ppm found by mass spectrographic analysis.

Sample	A	B	C	D	E	F	Optovac
Mexican	0	25	50	75	100	0	0
Optipur	100	75	50	25	0	100 10ppm Ce	100
Damage Threshold Jcm^{-2}	72	6.8	couldn't damage			4.2	66

Table 2 Crystal composition and measured bulk damage threshold.

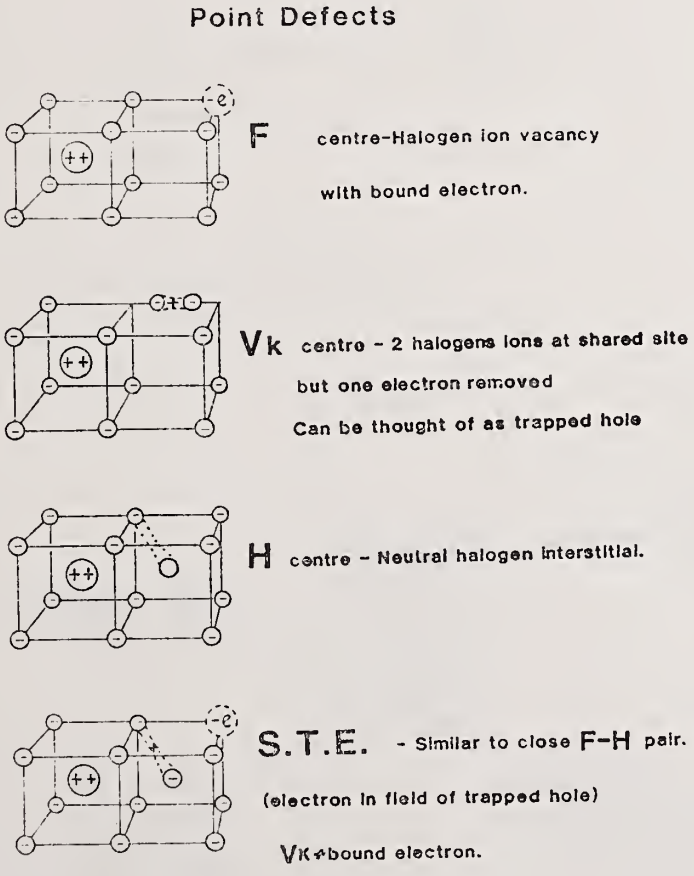

Figure 1

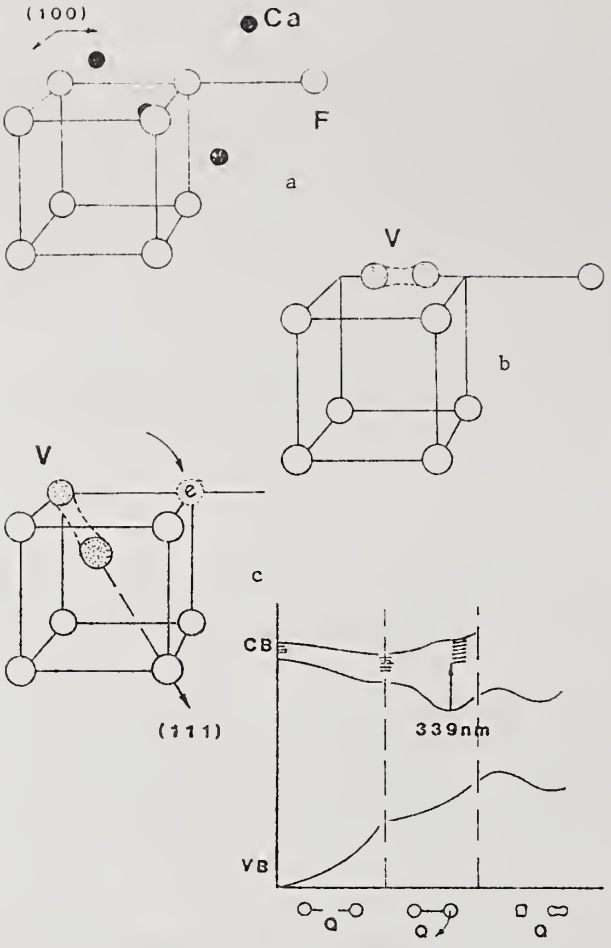

Figure 2

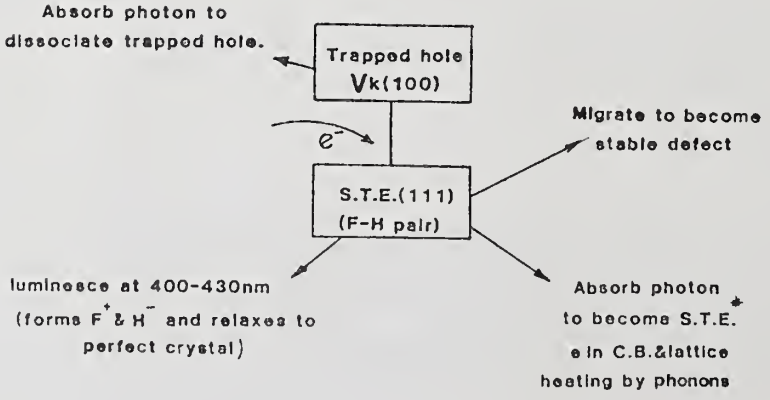

Figure 3

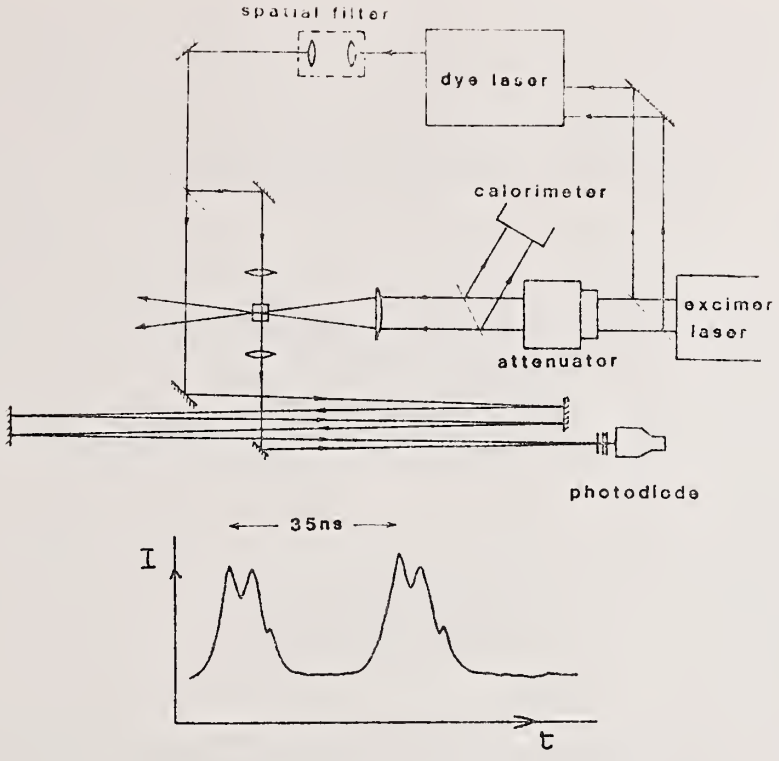

Figure 4

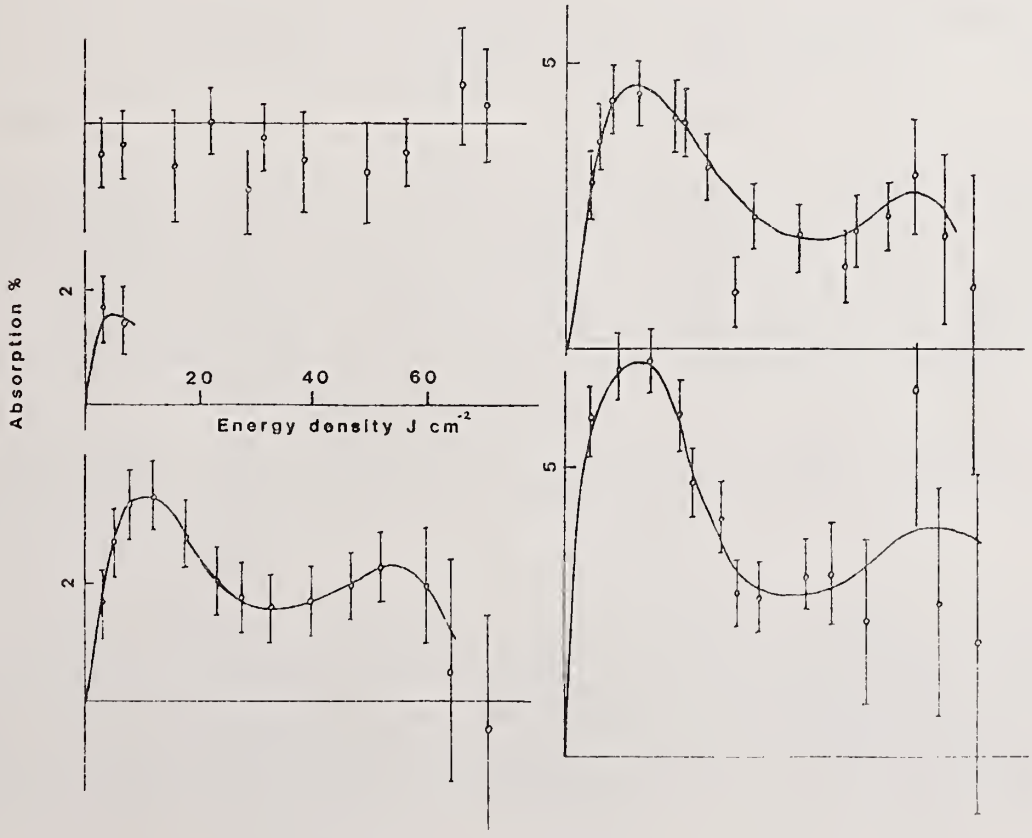

Figure 5

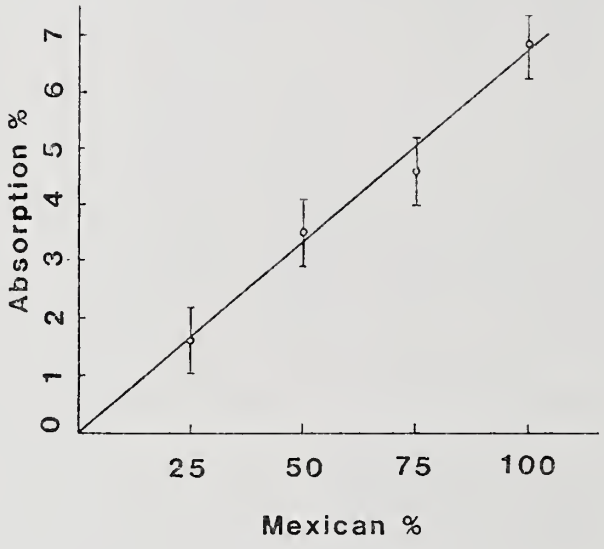

Figure 6

Manuscript Received
3-12-87

Effect of Cleaning on the Optical Absorption of Calcium Fluoride and Fused Silica at 351 nm

D. J. Gallant

Rockwell International
Rocketdyne Division
P.O. Box 5670
KAFB, New Mexico 87185

and

Marilyn Law and Brad Pond

Martin Marietta Corporation
P. O. Box 9316
KAFB, New Mexico 87119

Optical absorption values of uncoated calcium fluoride and fused silica substrates were measured at 351 nm using the 3-slope laser calorimetry technique. In addition, various substrate cleaning techniques were tried in order to lower the absorption, and to assess the contribution of surface contaminants to the total absorption.

Key Words: Calcium fluoride; cleaning; fused silica, laser calorimetry; optical absorption

1. Introduction

The optical absorption of high power laser components is an important quantity to consider when developing a laser system. If the absorption is too high thermal problems can lead to optical distortion and catastrophic laser damage of the component. In the ultraviolet region of the spectrum two candidate materials for optical use are fused silica and calcium fluoride. Fused silica is one of the most well understood materials available and exhibits low optical absorption but relatively poor thermal properties. Calcium fluoride has desirable properties such as a higher thermal conductivity, low thermal stress and low birefringence. However, this material is difficult to polish and typically has a higher optical absorption than expected, possibly due to contamination during the polishing procedure.

In this paper the measured optical absorption values of calcium fluoride and fused silica are reported, and the question of surface contamination is addressed. Various surface cleaning procedures were tried and the effect on the optical absorption measured at 351 nm using a precision laser calorimeter.

2. Experimental Procedure

The optical absorption was measured in a vacuum calorimeter as shown in figure 1. The design of this calorimeter is based on a similar system developed at Optical Coating Laboratory Inc. [1], with significant modification to allow measurement of up to ten parts during a single vacuum pump down. The laser source used in these experiments was an argon ion laser operated with UV cavity optics. Single line output at 351 nm was obtained by using a dispersing prism external to the laser cavity and blocking unwanted wavelengths. An uncoated fused silica beamsplitter reflected part of the laser beam to a thermopile powermeter used to monitor the laser power incident upon the test sample.

The vacuum box was evacuated by a clean pumping system consisting of a Venturi pump and LN_2 sorption pumps. Tests were conducted at a vacuum of 200 mtorr. Up to ten samples were loaded into a carrousel at a time and placed in the vacuum chamber. Remotely controlled stepper motors were used to rotate the carrousel and lower each sample into the correct position to be tested. In the measurement position, the sample rested on top of two thermistors mounted on thin glass rods and a third glass rod with no thermistor attached. A reference optic, supported in the same manner, was located nearby. The four thermistors were connected together in an AC bridge network driven by a 700 Hz oscillator. The differential output from the sensor bridge was fed into a lock-in amplifier, and the amplified signal from the lock-in was fed into an A to D board controlled by a DEC LSI1 II computer. The computer controlled the experiment by opening and closing an electronic shutter, recorded the sample temperature versus time data, and analyzed the data. Care was taken to prevent direct laser scatter from hitting the glass posts or any of the thermistors. Vacuum chamber entrance and exit windows were AR coated on both surfaces and copper shields were set next to the glass rods and thermistors to block any laser scatter.

Data analysis was based upon the 3-slope method where the absorption is proportional to the initial sample temperature slope before the laser is "turned on", the sample heating slope during laser irradiation and the sample cooling slope after the laser is "turned off".

Calibration of the calorimeter instrument was done by an electrical substitution technique, and also using samples whose absorption was determined independently. The calibration factor for the thermistor bridge was measured to be 3.1mv/°C.

The fused silica samples, made of Corning 7940 material, were stress wafers obtained from Hibshman Corporation. These samples were 1.0 inch in diameter and 0.015 inch thick. The UV grade calcium fluoride was obtained from Optovac. Calcium fluoride samples were 1.0 inch in diameter and 0.060 inch thick. No particular crystal orientation was specified for the calcium fluoride, and the vendor's standard polish using diamond powder was used to finish the parts. Each fused silica and calcium fluoride sample was measured uncleaned as received from the manufacturer, and after various cleaning processes.

The first cleaning procedure, used for both calcium fluoride and fused silica, consisted of a light scrubbing of the optic with a cotton ball in a bath of trichloroethylene (TCE), immersion and scrubbing in a bath of acetone and then immersion and scrubbing in a bath of methanol. These steps were performed with the chemical baths at room temperature. The final step was a deionized (DI) water or isopropyl alcohol rinse and a 15 minute immersion in a vapor degreasing system using "Genesolve" drying fluid. This drying method insured that all alcohol residues were completely removed.

The second cleaning procedure, used for the calcium fluoride samples, began with the same procedure described above. After the samples were dried in the vapor degreaser they were then immersed in concentrated (49%) hydrofluoric acid (HF) at room temperature for 10 minutes. The samples were then rinsed in isopropyl alcohol and dried in the vapor degreaser. Care was taken to remove all residue left on the calcium fluoride samples, and in practice it was found that a short pre-soak in HF was needed before the 10 minute soak in a clean HF bath, as well as using three separate clean isopropyl alcohol rinse baths.

Atomic absorption analysis of the used HF solution showed the presence of calcium indicating that the calcium fluoride or other calcium compounds were being etched from the surface. Using an ion selective electrode placed in the solution, it was determined that the equivalent of several hundred angstroms of surface had been removed. Scanning electron microscope pictures taken of the surface of a calcium fluoride sample are shown in figure 2. Figure 2a shows the surface of an unetched, as received part, while figure 2b shows the same surface after etching in HF acid as described above. Note that numerous polishing scratches became evident after etching.

The third cleaning procedure, used for the fused silica substrates, started with a light scrubbing in TCE followed by another scrubbing in acetone. The parts were then scrubbed in a solution of soap and water containing calcium carbonate and rinsed separately in DI water, methanol, and isopropyl alcohol, and then placed in the vapor degreaser. The fused silica parts were then immersed in a hot (110°C) sulfuric acid-ammonium persulfate mix for a 10 minute period. The samples were then rinsed with DI water, isopropyl alcohol and dried in the vapor degreaser. Ammonium persulfate was used because it is a strong oxidizing agent and a sulfuric acid-oxidizing agent mixture is commonly used in the semiconductor industry for removal of organic surface contaminants. This mixture does not etch fused silica.

The fourth cleaning procedure, again used for the fused silica substrates, started with the same routine as in the third cleaning procedure. In this case however, in place of the sulfuric acid mixture, the parts were immersed in 2.5% hydrofluoric acid at room temperature for a 10 minute period. This was followed by a rinse in isopropyl alcohol and drying in the vapor dryer. Fused silica is etched in hydrofluoric acid, however, no determination was made as to the depth of etching that was achieved.

3. Experimental Results

Absorption values measured at 351 nm on calcium fluoride and fused silica substrates are shown in figures 3-5. Each figure shows the results for four different test samples. A total of four calcium fluoride samples and eight fused silica samples were used during these tests. In all cases the absorption values represent total absorption i.e., the sum of the sample's bulk absorption and the absorption from both surfaces. Each absorption value represents a single measurement on each part, under each test condition. A control sample of Corning 7940 material was measured before and after each test sequence to insure the continuity of all measurements and calibration stability. This control sample was carefully cleaned using Cleaning Procedure 1 as described earlier, and after repeated measurements the absorption of the control sample was determined to be 148 ppm ± 11 ppm.

The absorption values for the calcium fluoride samples are presented in figure 3. The average absorption for the uncleaned (as received) parts was measured to be 490 ppm ± 54 ppm with one part measuring as high as 570 ppm. In most cases cleaning the samples using procedure 1, a "conventional" cleaning technique reduced the absorption by 10-100 ppm. In one case the absorption increased, possibly due to residue from the cleaning fluids or polishing compound that was moved from the edge of the sample to the center region during the cleaning process. Using cleaning procedure 2, which actually etched the surface, the absorption decreased dramatically. This decrease ranged from 260 ppm to 370 ppm from the uncleaned values. The average final absorption value was found to be 175 ppm ± 37 ppm. Such a decrease supports the theory that surface contamination was contributing substantially to the absorption. The decrease in the standard deviation of the absorption values could indicate that the etched surfaces were much more uniform than the uncleaned surfaces as received from the vendor. While the etching of the calcium fluoride surfaces led to a lower absorption, it was evident that the surface "quality" of the samples had degraded. The shape of the calorimeter absorption curves showed the presence of increased laser scatter levels. Faint polishing scratches could be observed on the samples under bright light illumination before etching but after etching scratches were much more pronounced.

In figure 4 are shown the calorimetry measurement values for the fused silica samples that were measured as received from the vendor, after "conventional" cleaning, and after cleaning with the sulfuric acid mixture. The average absorption of the as received samples was measured to be 150 ppm ± 10 ppm, reflecting a higher quality and more uniform surface than was measured for the calcium fluoride substrates. This result is not surprising considering the difficulty of polishing calcium fluoride which is a soft and chemically active material. "Conventional" cleaning of the fused silica, as per cleaning procedure 1, did not decrease the absorption as much as it did with the calcium fluoride, and again, one of the samples increased in absorption, presumably due to cleaning residue. In all cases, cleaning the fused silica samples with the sulfuric acid mixture as per cleaning procedure 3, resulted in a decrease in absorption compared with the uncleaned measurements. In one case the absorption increased compared to the "conventionally" cleaned measurement again possibly due to polishing and/or cleaning residue. The final average absorption value of the acid cleaned fused silica was measured to be 116 ppm ± 20 ppm. Unlike the etched calcium fluoride, the sulfuric acid mixture cleaned fused silica did not show any evidence of increased laser scattering and no polishing scratches were evident.

Presented in figure 5 are calorimetry measurement values for fused silica samples that were "conventionally" cleaned using cleaning procedure 1. Measurement values for these parts after cleaning in HF acid per cleaning procedure 4 are also shown for comparison. From figure 4, it can be seen that the uncleaned fused silica parts had an absorption of approximately 150 ppm. If this is taken as a base line, then figure 5 shows that the absorption was reduced in some cases by conventional cleaning, but that HF acid cleaning did not decrease the absorption further. In other cases the conventional cleaning did not have much effect, and the HF acid cleaning, while decreasing the absorption slightly, did not have a dramatic impact. Under bright light illumination polishing scratches were evident due to the etching, however, no increase in laser scattering was observed while measuring the samples.

4. Discussion

Measurements on calcium fluoride and fused silica reported here have shown that with proper surface treatment the optical absorption of these materials can be reduced, and in some cases the reduction can be quite significant. Other work at Lawrence Livermore National Laboratory has shown that cleaning of calcium fluoride in HF acid or Nitric acid will increase the surface laser damage threshold of calcium fluoride [2]. These results indicate that the present commercial surface finish of calcium fluoride is inadequate for high power laser use. Continued effort is required to optimize the polishing of this optical material.

In this study, the exact interaction between the HF acid, used as a cleaning agent, and the calcium fluoride surface is not known. Various contaminants introduced during the manufacturing or polishing process could be present on the calcium fluoride surface, as well as a layer of water vapor or calcium oxide compounds. If such layers exist the HF may be changing the stoichiometry of the calcium fluoride surface. Since dissolved calcium was present in the used HF bath it is clear that etching of the calcium fluoride had taken place. It is not clear, however, how deep an etch is required in order to change the optical properties of calcium fluoride. Further work is needed to establish if organic and other contaminants, or a calcium oxide layer, is responsible for the observed optical absorption values.

Measurements on fused silica have shown that a hot mixture of sulfuric acid and ammonium persulfate acts as a thorough cleaning agent on fused silica. The acid mixture oxidizes and removes organic contaminants from the surface, but does not etch the fused silica or cause degradation of the surface quality.

5. Summary

The optical absorption of calcium fluoride and fused silica wafers was measured by laser calorimetry. The as received, "conventionally" cleaned, and acid cleaned absorption values were reported. A "conventional" cleaning of the calcium fluoride parts had mixed results, however, the absorption of some parts was reduced 75 - 100 ppm. In all cases, acid cleaning of the calcium fluoride in concentrated hydrofluoric acid reduced the absorption substantially. It is believed that contamination from the polishing procedure or the presence of calcium oxides on the sample's surface was responsible for the high absorption values measured. Clearly, more work is needed to optimize the polishing of calcium fluoride to make this material more suitable for high power laser optics.

Three different cleaning techniques were tried on fused silica. The best cleaning procedure was found to be an immersion in a hot sulfuric acid-ammonium persulfate mixture. Using this technique, the measured absorption values decreased by an amount ranging from 6 ppm to 63 ppm, presumably due to a thorough cleaning of organic contaminants from the surface of the fused silica. An immersion of the fused silica in dilute hydrofluoric acid did not produce a significant reduction in absorption values when compared to a "conventional" cleaning technique.

The authors would like to acknowledge R. Manning for performing the absorption measurements, and thank Dr. A. F. Stewart for his suggestions on this paper. This work was supported by the Air Force Weapons Laboratory, JON No. GBL12311, Supported by SDI WPD 2.311

6. References

[1] Allen, Thomas H.; Apfel, Joseph P.; Carniglia, C. K., in Laser Induced Damage in Optical Materials: 1978, Bennett, H. E.; Glass, A. J.; Guenther, A. H.; Newman, B. E., Eds., NBS Special Publication 541; 1978, pp. 33-36

[2] Private communication with Ian Thomas, Lawrence Livermore National Laboratory, Livermore, CA.

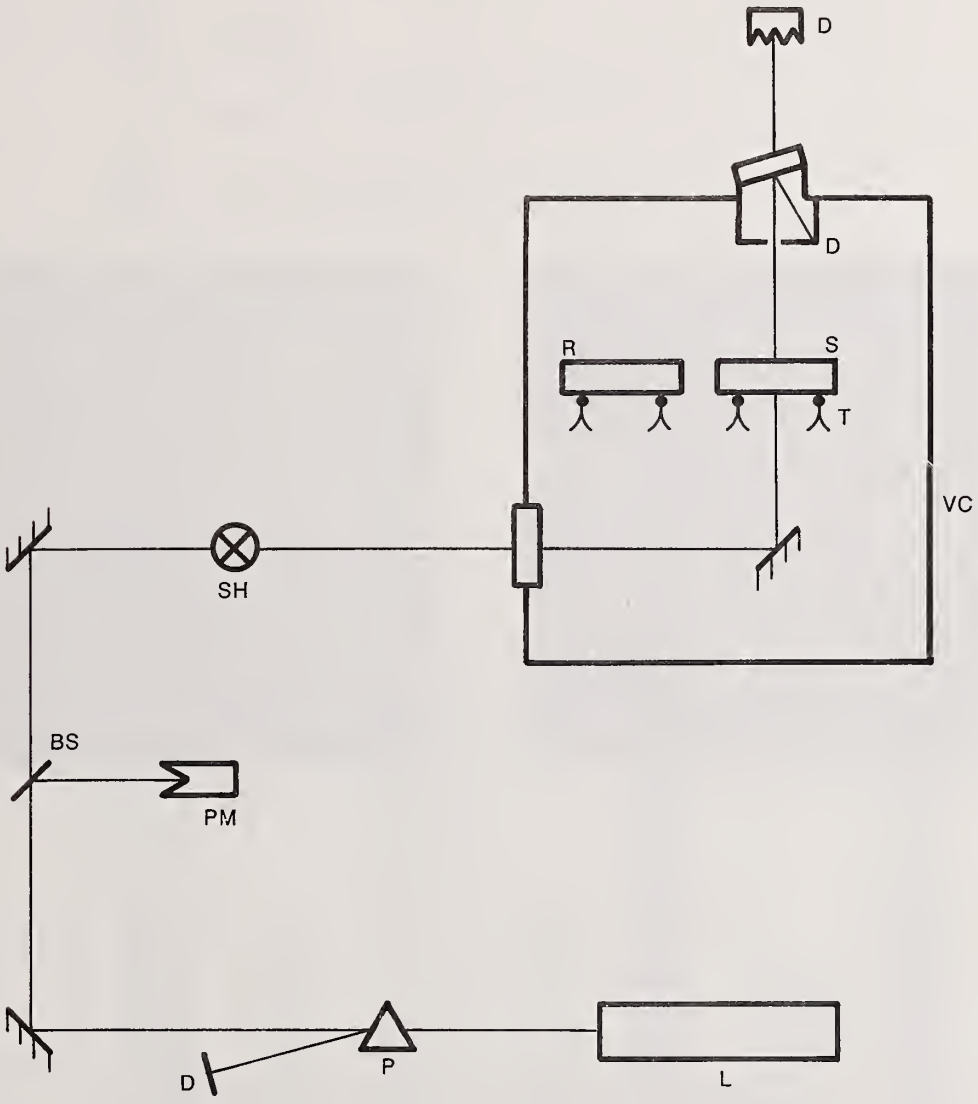

Figure 1. Optical layout of the laser calorimeter:

(L) Argon ion laser, (P) Prism, (BS) Beamsplitter,
(PM) Power Meter, (SH) Shutter, (VC) Vacuum Chamber
(T) Thermistor, (S) Sample, (R) Reference,
(D) Beam Dump

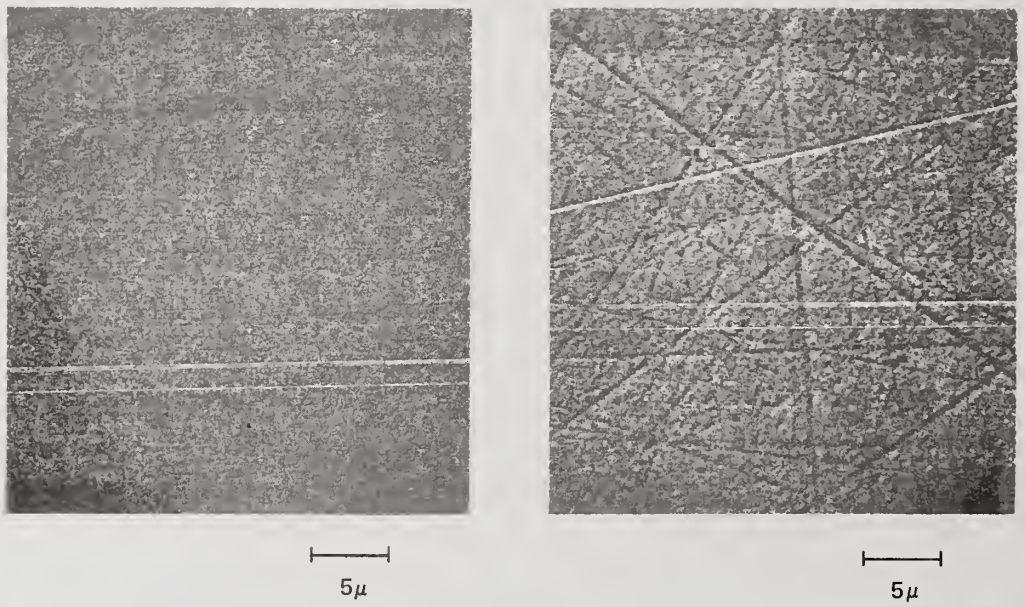

Figure 2. SEM photographs of a commercially polished calcium fluoride surface; A. unetched and B. etched in HF acid as described in the text.

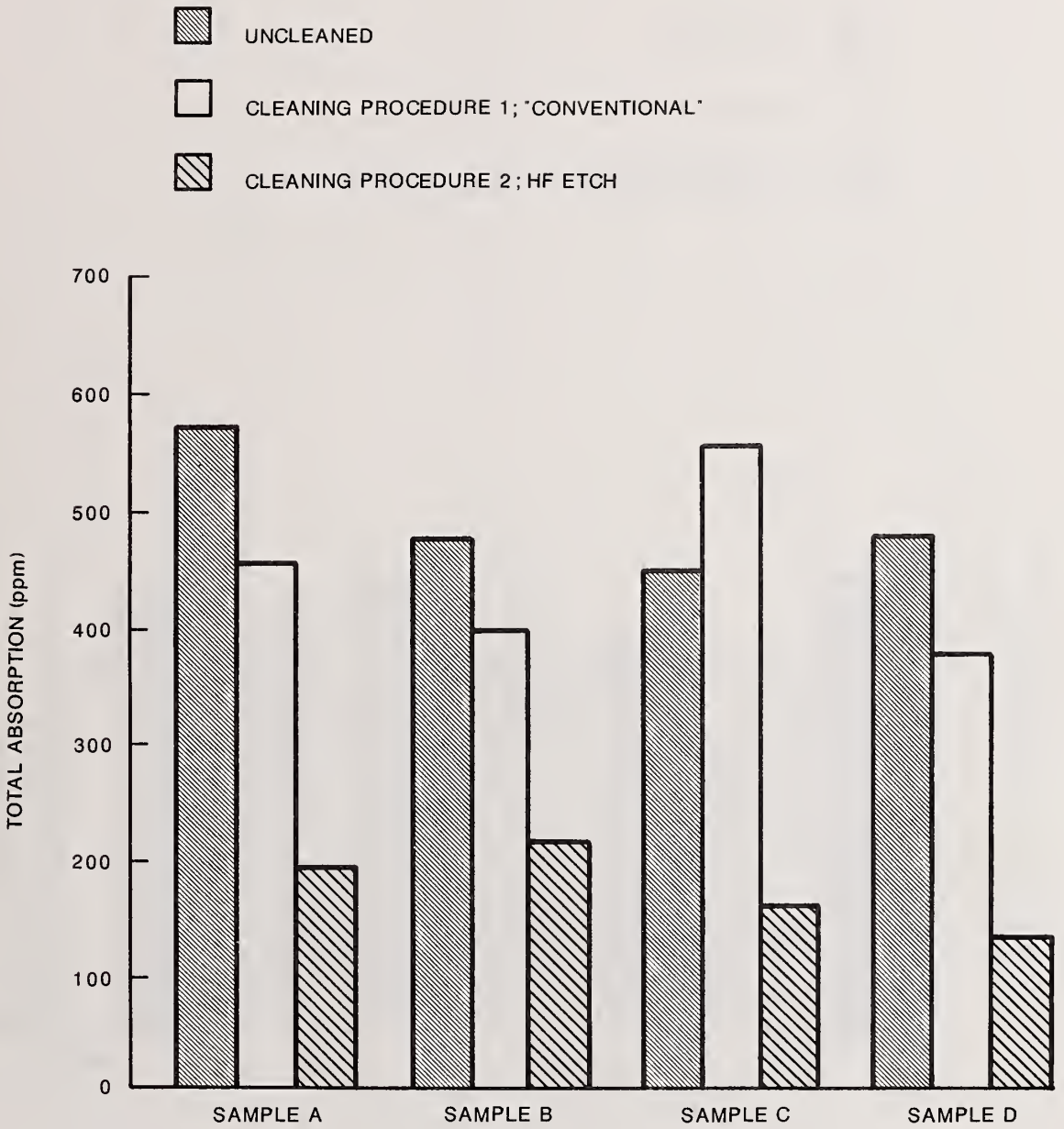

Figure 3. Optical absorption values for calcium fluoride samples cleaned by various methods as described in the text.

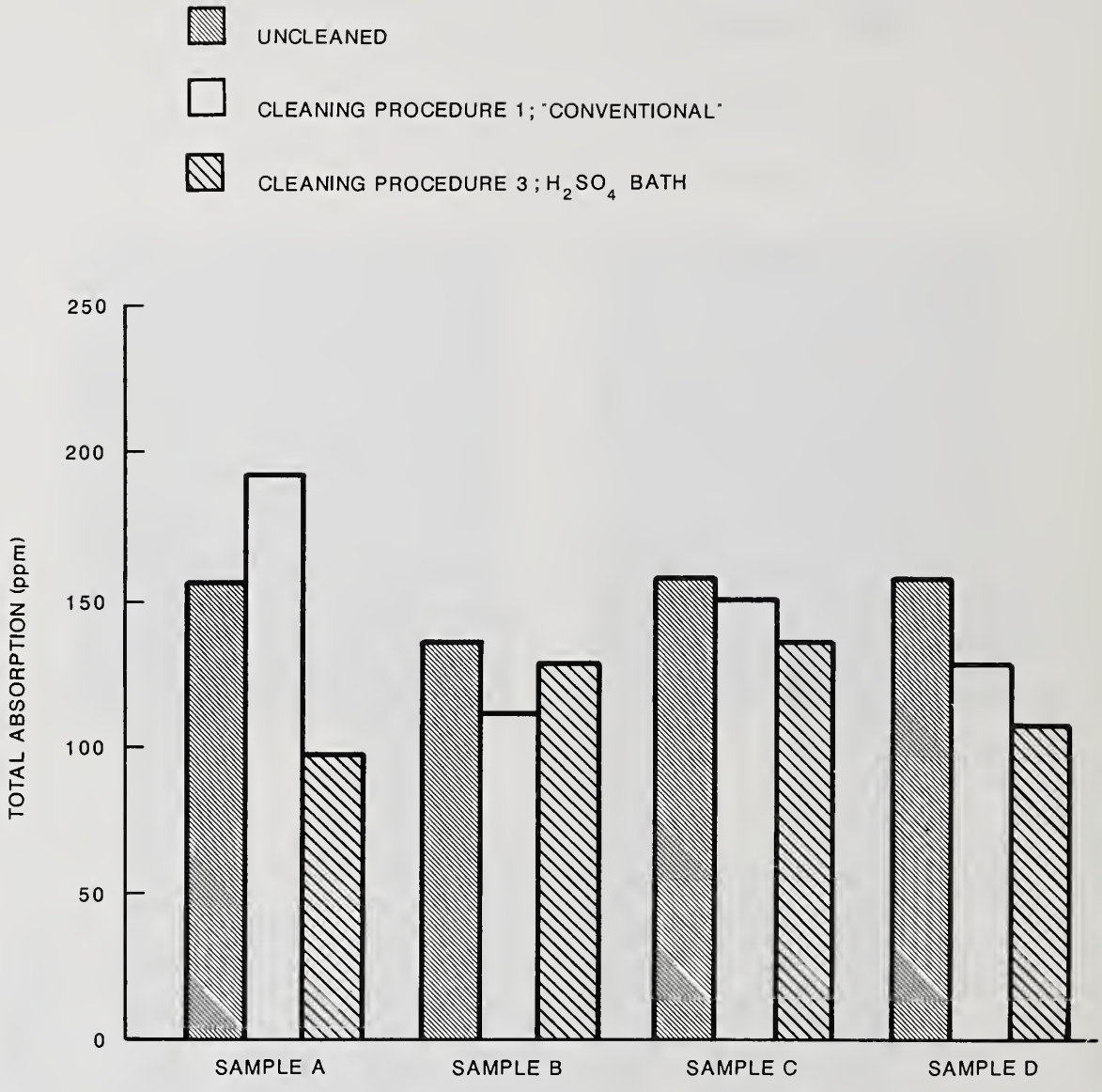

Figure 4. Optical absorption values for fused silica samples cleaned by various methods as described in the text.

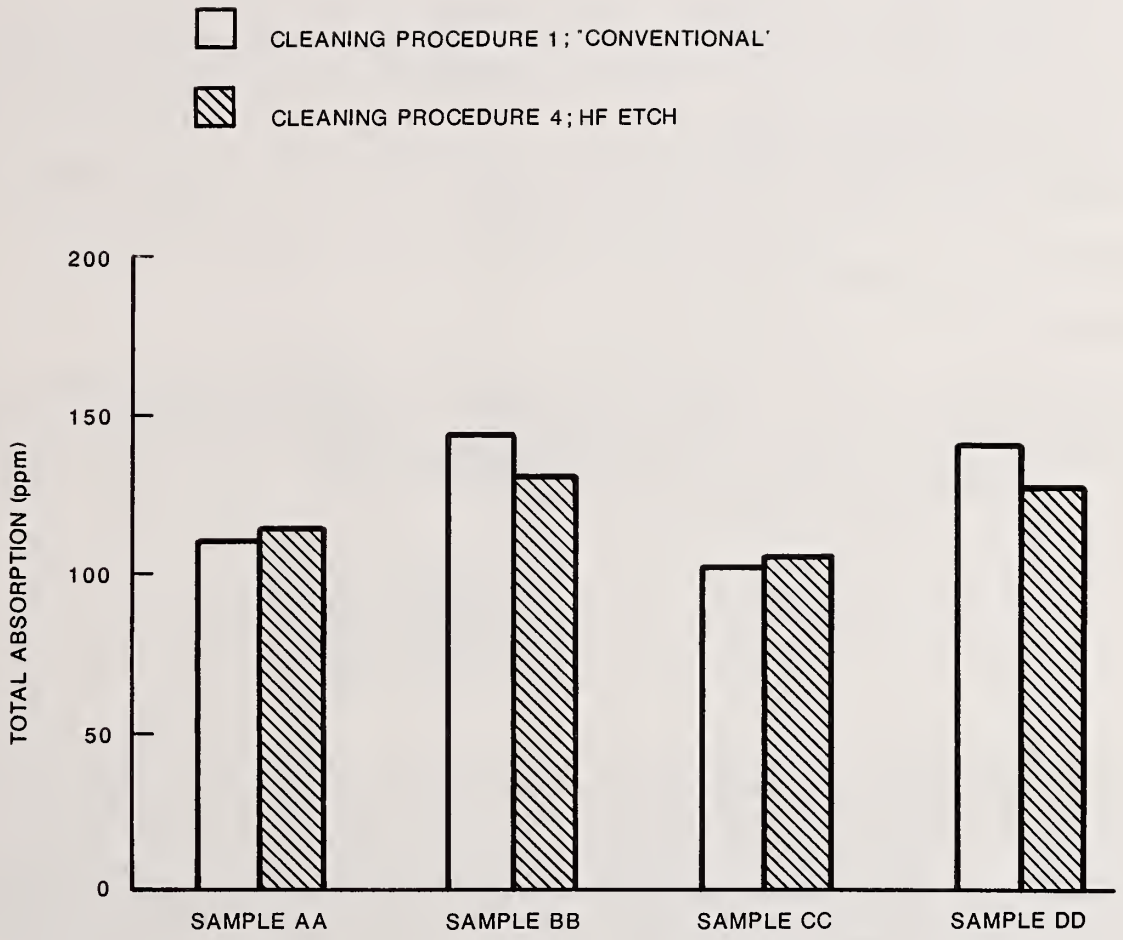

Figure 5. Optical absorption values for fused silica samples cleaned by various methods as described in the text.

Manuscript Received
11-6-86

Chemically strengthened slab laser glass with optical surface quality

C. Hata, T. Inazumi and T. Izumitani

HOYA CORPORATION
Tokyo Japan

Slab laser glass was chemically etched to remove microcracks on the polished surface and increase the fracture strength. Xe lamp irradiation test showed dramatically high fracture strength for chemically etched surface compared to polished surface. However, the chemically etched surface is optically neither flat nor smooth. The new fabrication method, chemical polishing, was developed to get simultaneously both chemically strengthened and optically smooth surface.

The slab laser glass fabricated by the new method showed 2.5 times high bending strength as well as optical flat and smooth surface.

Key words; chemical etching; chemical polishing; fracture resistance; HAP laser; strengthening; thermal shock resistance.

1. Introduction

Slab laser glass is expected to be available for KW high average power (HAP) laser system. The slab laser glass needs to be strengthened, because the output power of zig-zag optical path slab laser is limited by fracture owing to thermal stress. The fracture resistance under the Xe lamp pumping can be characterized by thermal shock resistance. The thermal shock resistance factor, R, is represented by the follow equation [1].

$$R = \frac{S\,(1-\mu)\,\kappa}{\alpha\ E}$$

S : mechanical strength
κ : thermal conductivity
α : thermal expansion coefficient
E : Young's modulus
μ : Poisson's ratio

The thermal shock resistance is increased by increasing mechanical strength S and mechanical strength can be increased by surface strengthening.

The surface strengthening methods of laser glass for HAP have recently been investigated by several workers. J. Marion, LLNL [2], has reported the mechanical strength of laser glass was improved about 10 times stronger by chemical etching than conventional polishing. K.A. Cerqua et al. [3], Rochester univ., have investigated strengthening by ion exchange method.

By the chemical etching, surface damages such as microcracks formed in the mechanical fabrication process are removed. In spite of increasing of the bending strength, optical surface quality of the laser glass is degradiated extremely.

In the ion exchange strengthening, compressive surface layer is formed to suppress propagation of microcracks. It is difficult to make clear ion exchanged layer optically. Especially in phosphate laser glass, glass network is easily broken by ion exchange reaction to make white deposits and/or stained layer.

We have studied to strengthen phosphate laser glass by means of chemical etching and new chemical polishing methods. Our purpose of this work is to get strengthened slab laser glass with having high optical surface quality.

2. Experimental

Nd doped laser glasses, LHG5 and HAP-3, which are candidates for HAP laser materials were used in this work.

2.1 Strengthening of laser glass

(1) Chemical etching

Glass specimens were ground preliminary in a shape of slab in a roughness of #1000 - #1500. The specimens were treated in the alkaline solution consisted from a mixture of NaOH 5 - 30wt% and KOH 5 - 30wt% at a temperature of 40 - 100°C and after that they were immersed in H_3PO_4 conc. solution at a temperature of 80 - 100°C in order to remove deposits on the surface [4]. As a result,surface layer in which microcracks have been formed in the mechanical fabrication process, was removed 50 - 300 μm in thickness.

In these treated specimens, three type of fracture strength were measured. Measurement methods are described later in this section.

(2) Chemical polishing [5]

The chemical polishing process of this work was designed to polish the slab surface with no microcracks and no fabrication stress. FIG.1 shows schematic presentation of polishing apparatus.

Specimens in the shape of 4 x 10 x 40 mm were fixed on the holder disk and they were ground in #1500 roughness in order to generate flatness of the disk. After that surface layer of the specimens were removed 50 - 200 μm in thickness by the chemical etching. The specimen disk was attached on the polisher's disk.

Chemical polishing were carried out under the condition of small loading and mild etching at a temperature of 30 - 60 °C. During polishing the specimens were immersed in the polishing solution. The kinds of polishing powder used in this experiment were fumed SiO_2-I, fumed SiO_2-II, fumed Al_2O_3, powdered Al_2O_3 and powdered CeO_2. Polishing powder was dispersed 2 - 20 wt% in the distrilled water or diluted alkaline solution by means of ultra-sonic vibration.

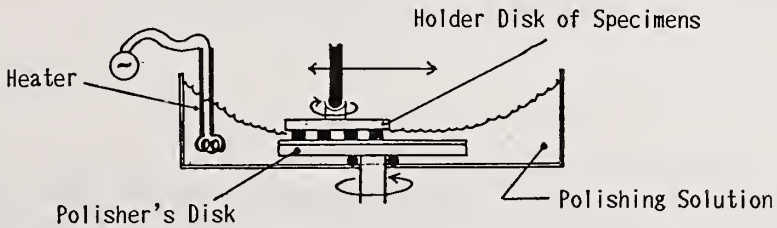

FIG.1 Schematic Presentation of Polishing Apparatus

2.2 Measurements of fracture strength and optical quality of surface.

(1) Three point bending test

Mechanical strength was measured by three point bending method shown in FIG.2. Size of the specimens was 3 x 10 x 40 mm, bottom span was 20 mm and speed of load increasing was 0.5 mm/min. The data of strength is the mean value of 10 pieces.

(2) Thermal shock test

Specimens, their dimension was 3 x 10 x 40 mm, heated in the oven at a temperature of T (oven) °C were quenched in the ice-water (T (ice-water) °C). Critical temperature difference at which fracture occur in the specimen is ΔTc (ΔTc = T(oven) - T(ice-water)). Thermal shock resistance can be defined by the ΔTc.

(3) Xe lamp irradiation test

Large size slab, its dimension was 186 x 60 x 6 mm, was placed in the lamp house shown in FIG.3. It was thermally loaded by Xe lamp irradiation until it was fractured by the thermal stress.

Xe lamp irradiation was carried out practically as follows:

(Power Supply: 1.69 kv, 575 J/pulse)

IRRADIATED AT THE RATE OF 1PPS FOR 2 MIN → STOPPED FOR 1 MIN →
→ THE RATE OF 2PPS FOR 2 MIN → STOPPED FOR 1 MIN →
→ THE RATE OF 3PPS FOR 2 MIN → STOPPED FOR 1 MIN →
→ .....
→ The repitition rate, PPS, is increased until fracture occur.

Surface temperature distribution was observed by thermal image scope in a few minutes.

Fracture resistance to Xe lamp irradiation is measured by total input power and maximum temperature of fractured slab surface.

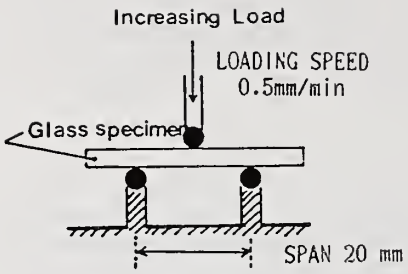

FIG.2 3-POINT
BENDING APPARATUS

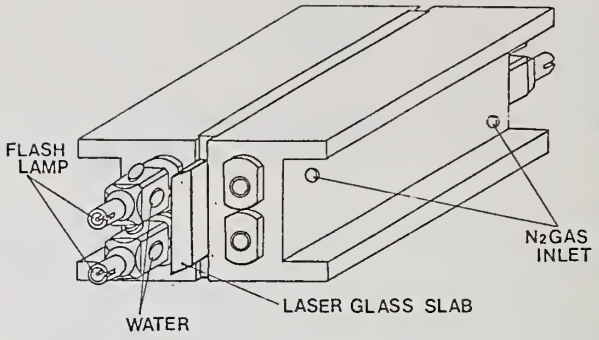

FIG.3 LAMP HOUSE for
Xe lamp irradiation test

2.3 Observation of finished surface profile

Surface profile of slab was observed by the differential interfero-microscope(Nomarski interference contrast).

Surface roughness of slab was measured by Talystep to an accuracy of a few angstrom. The mean roughness Rz is average value of the three highest data.

3. Results and discussion

3.1 Strengthening by chemical etching

Surface profile of laser slab was getting rough with duration of chemical etching. Photographs of changing surface are shown in FIG.4. The upper photo shows initial surface profile and middle and lower photos show the profile after etching. In laser glass LHG5, #1000 ground, initial surface roughness Rz was 2.7 μm and after etching for 1 hour the Rz increased up to 7.0 μm.

FIG.5 shows ΔTc vs thickness of removal layer. ΔTc was increased with increasing of thickness of the removal layer in which there were microcracks formed during mechanical fabrication process. The depth of damaged layer by conventional processing seems to be 50 - 200 μm, since the ΔTc became constant in the region of removal thickness more than 50 - 150 μm.

FIG.4 SURFACE PROFILE CHANGE
WITH CHEMICAL ETCHING

Pictures of Glass Surface

Surface profile was getting rough with duration of etching.

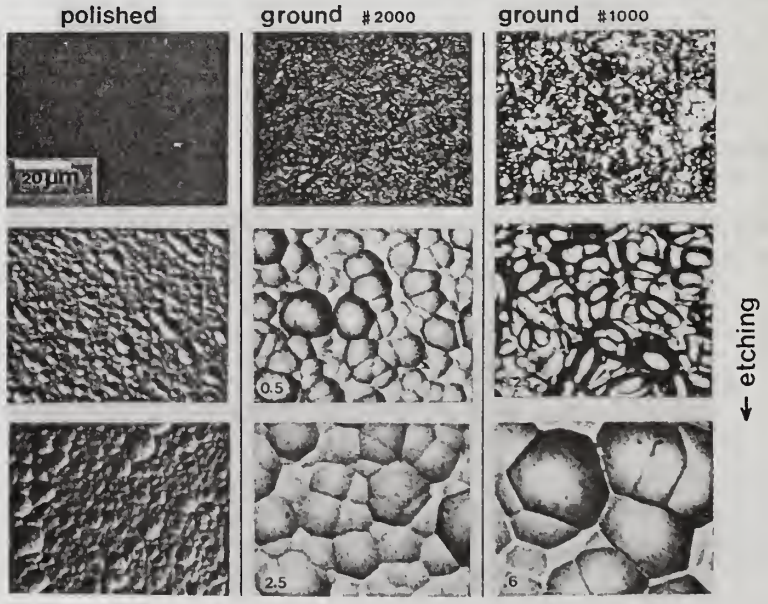

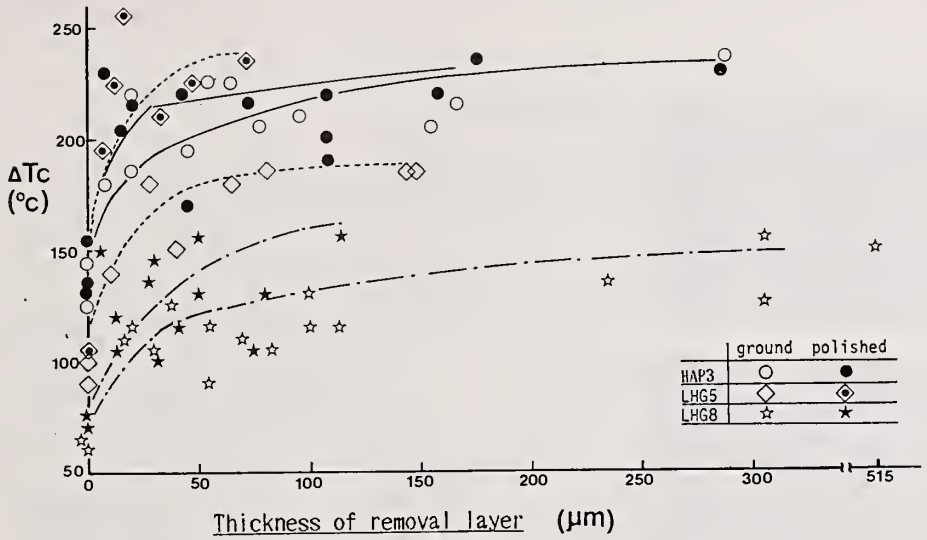

FIG.5 △Tc vs THICKNESS OF REMOVAL LAYER

TABLE 1 DATA OF △Tc AND BENDING STRENGTH

	Final Fabrication	LHG5	HAP3
Thermal shock △Tc (℃)	Ground (#1500)	95	120
	Conventional Optical polishing	110	130
	Chemical Etching	235	235
Three point bending strength (kg/cm²)	Ground (#1200)	660	720
	Conventional Optical polishing	2000	2200
	Chemical Etching	3000～8000	5000～10000
	The new chemical polishing	3500～7000	–
Fracture toughness K_{Ic} ($10^{-3}MN/m^{1.5}$)	Optic1 polishing (Vicker's stylus)	485	675

The data of ΔTc and bending strength are summarized in Table 1. Thermal shock resistance after chemical etching was improved by about 2 times higher than that of conventional polishing and mechanical strength was increased up to 2.5 - 5 times higher than conventional process.

TABLE 2 RESULT OF XE LAMP IRRADIATION TEST

Repitition Rate(PPS) and Total Number of Shots until laser glass was fractured by thermal stress.

Final Fabrication	LHG5		HAP3	
	Nd_2O_3 6wt%	8wt%	6wt%	8wt%
Conventional Optical polishing	7 PPS 3332 shots Tmax~300 ℃	——	10 PPS 6320 shots Tmax~340 ℃	7 PPS 3346 shots Tmax~340 ℃
Chemical Etching	11 PPS 7920 shots Tmax~400 ℃	7 PPS 3360 shots Tmax~ - ℃	——	10 PPS 6270 shots Tmax>400 ℃

Power supply; 1.69 kv, 575 J/pulse
Cooling ; dry air, > 300 L/min

Table 2 shows the results of Xe lamp irradiation test. Repitition rate(PPS) and total number of shots until laser glass slab was fractured by thermal stress are summarized. In this measurement, total number of shots were also increased by about 2 times by means of chemical etching. Fracture pattern by Xe lamp irradiation is shown in FIG.6 and typical surface temperature distribution of fractured slab is shown in FIG.7.

FIG.6 FRACTURE BY XE LAMP IRRADIATION

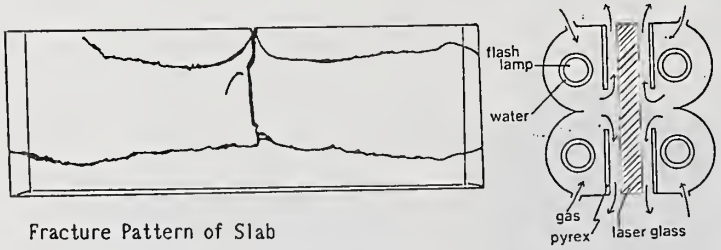

Fracture Pattern of Slab

Photograph of Propagation of Fracture Surface

FIG.7 SURFACE TEMPERATURE DISTRIBUTION OF FRACTURED SLAB

Typical pattern of temperature distribution(polished LGH5, 6% dope) 3332 shots, Tmax = 300°C

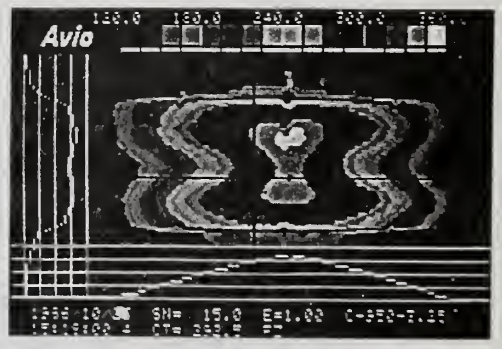

Fracture strength of slab was improved by the chemical etching, however its surface profile was extremely degradiated. The strengthened slab can not be available in the laser glass except for further improvement.

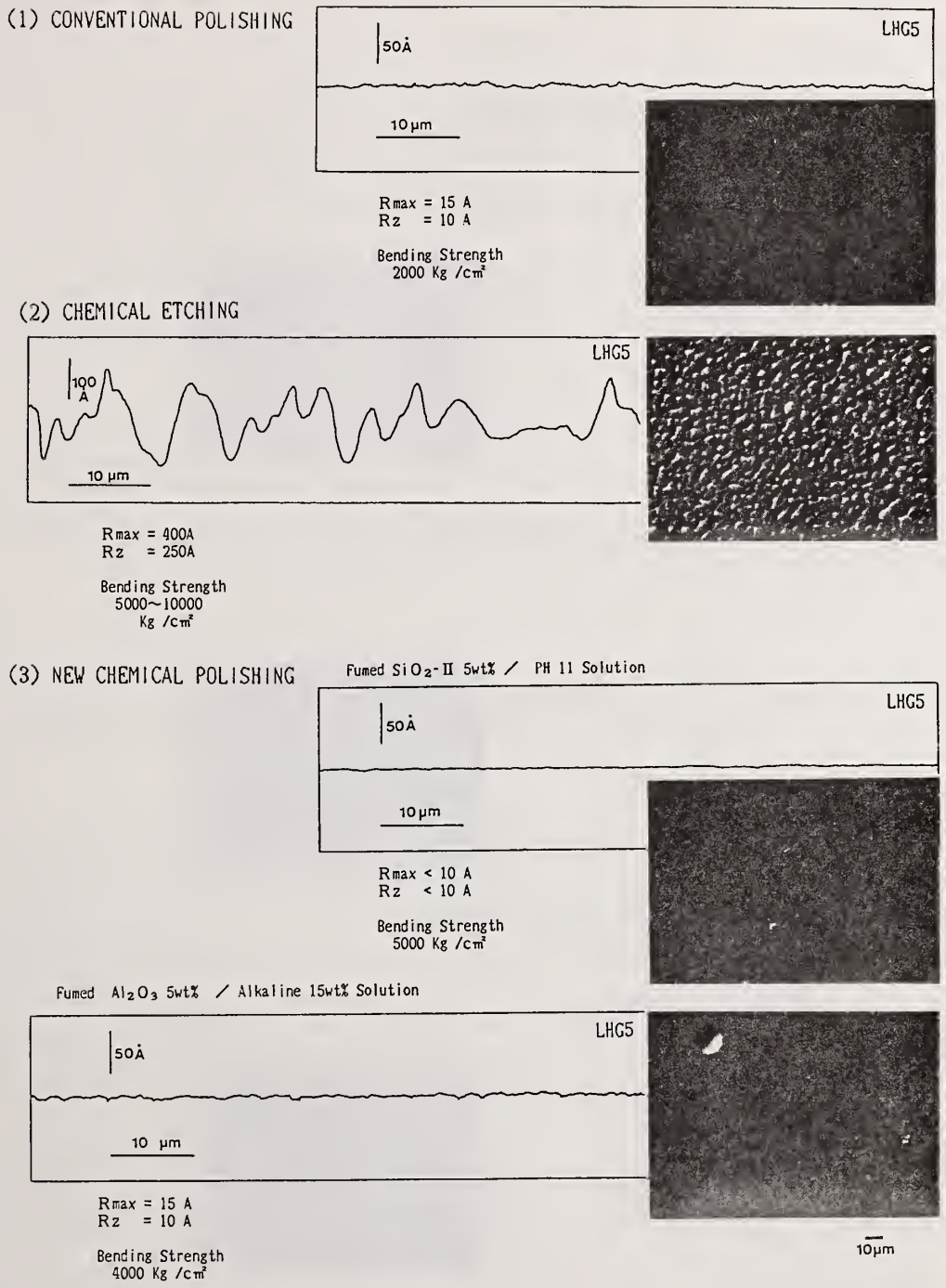

FIG.8 SURFACE ROUGHNESS of Finished Surface

(1) In the conventional polishing, finished slab surface profile was optically smooth, however its bending strength was not high.

(2) Mechanical strength was improved with the chemical etching, although the quality of surface smoothness was extremely degradiated.

(3) In the chemical polishing, especially used fumed silica as polishing powder the roughness of finished surface showed accuracy of Rz<<10 A and the bending strength was 2.5 times as strong as conventional optically polished surface.

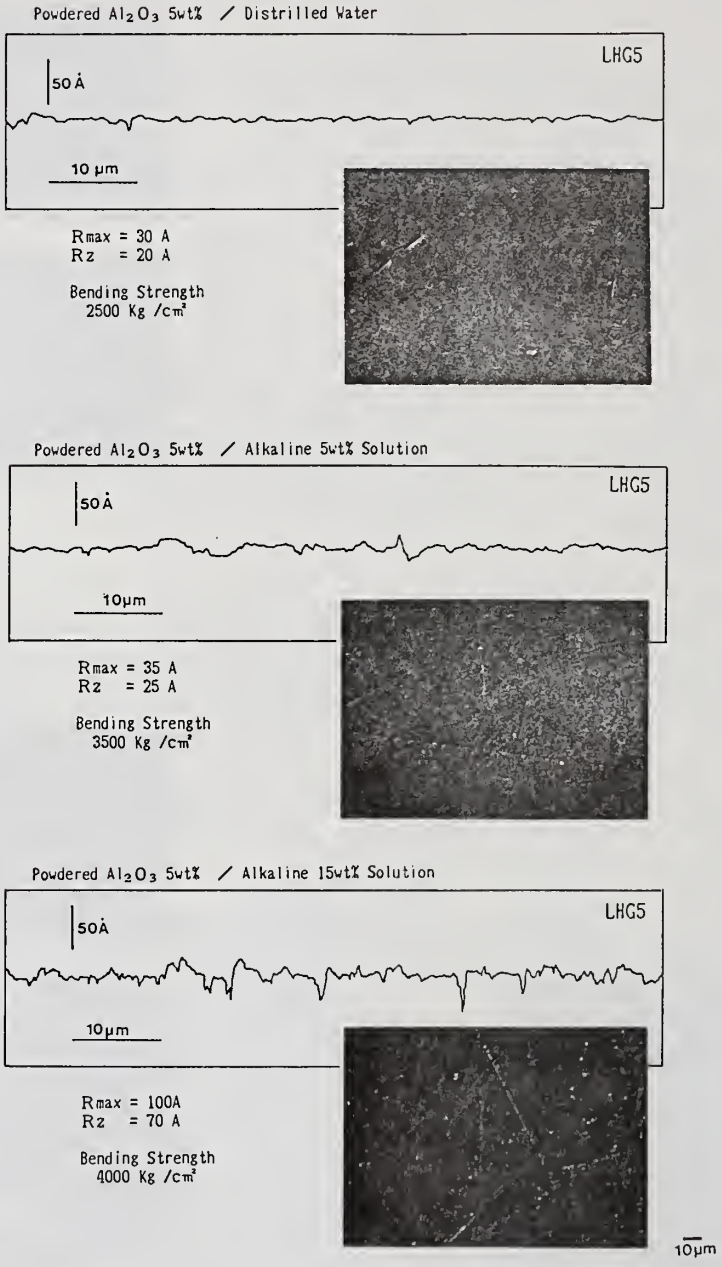

FIG.9 CHEMICAL POLISHING

SURFACE ROUGHNESS of Finished Surface

When powderd Al_2O_3 was used as polishing powder, scratches on the surface were increasing with alkaline concentration of polishing solution, although its bending strength became stronger. This tendency was observed similarly in powdered CeO_2 polishing.

3.2 Strengthening by chemical polishing

FIG.8 and FIG.9 show surface roughness, surface profile and bending strength of finished slab fabricated by the new chemical polishing.

In the conventional polishing, finished slab surface profile was optically smooth, Rz = 10 A, however its bending strength was 2000 kg/cm^2 and it is not strong enough. Mechanical strength was improved with the chemical etching up to 5000 - 10000 kg/cm^2, although the quality of surface smoothness was extremely degradiated(Rz = 250 A).

In the chemical polishing, especially used fumed silica as polishing powder, the roughness of finished surface showed accuracy of Rz << 10 A and the bending strength was 2.5 times as strong as conventional optically polished surface.

In this polishing process, powdered Al_2O_3 and powdered CeO_2 were used as polishing powder. In such a case, as shown in FIG.9, scratches on the surface were increasing with alkaline concentration of polishing solution, although its bending strength became stronger (Rz; 20→25→70A, Bending strength; 2500→3500→4000 kg/cm^2).

It is considered that the etching proceeded faster than the polishing. Glass surface became soft under the etching condition, so that scratches was formed easily by harder polishing powder.

In our polishing process, both the degree of etching effect and polishing effect can be balanced by means of controlling experimental condition, such as kinds of polishing powder, temperature and concentration of polishing solution, polishing speed and loading weight. The best condition is determined for kinds of laser glass. As a result of polishing used fumed SiO_2-II suspended in alkaline solution PH 11 at a temperature of 45 - 55 °C, it is obtained finished laser glass LHG5 with optical quality of surface and high bending strength as shown in FIG.8-(3).

The conditions of this chemical polishing are described details in the Japanese patent which is applied.

4. Conclusion

Slab laser glass with optical quality of surface(Rz<<10 A) and high mechanical strength (2.5 times higher compared with conventional polishing) is fabricated by the method of chemical polishing in which both etching and polishing are proceeded simultaneously.

5. References

[1] Kingery, W. D.;Symposium On Thermal Fracture. J. American Ceramic Soc.38; 1955. 1p.

[2] Marion, J. E.; Strengthened Solid-State Laser Materials. App. Phys. Lett. 47; 1985 Oct. 694p.
Marion, J. E.; Fracture Of Solid State Laser Slabs. LLNL Report UCRL-93543; 1985 Oct.

[3] Cerqua, K. A.; Jacob, S.; Ion Exchange Strengthening of Nd Doped Phosphate Laser Glass. LLE REVIEW Volume 25; 1985 Oct-Dec. 33p.

[4] Japanese patent applied No. 60-152312.(HOYA CORP.; C. HATA, K. HARA AND T. IZUMITANI)

[5] This Japanese Patent is applied.(HOYA CORP.; C. HATA, K. HARA AND T. IZUMITANI)

Manuscript Received
3-5-87

Comparison of Frequency Response Characteristics of an Optical Scatterometer and a Mechanical Profilometer

S.R. Wilson, G.A. Al-Jumaily, and J.R. McNeil

Department of Electrical Engineering
Center for High Technology Materials
The University of New Mexico
Albuquerque, NM 87131

The frequency response characteristics of an angle-resolved optical scatterometer and a mechanical profilometer are examined. The transfer function for the scatterometer is found to be constant within the spatial frequency bandwidth of the system. The mechanical profilometer is found to have a nonlinear, lowpass-like response. A computational model is used to examine the effects of the nonlinear stylus response on realistic surfaces.

Key words: optical; profilometer; scatter; scatterometer; spatial frequency response; stylus.

1.0 Introduction

Many systems have been devised to characterize the microstructure of optical surfaces. These systems can be divided into two general types: (1) systems that yield a profile of the surface, and (2) systems that produce statistical parameters of an optical surface. Instruments that measure surface profiles, usually referred to as profilometers, may be mechanical devices that employ a diamond stylus to traverse the surface, or noncontact optical devices that make use of interference effects. Instruments that yield surface statistics involve the measurement of optical scatter, and include total integrated scatter (TIS) systems and angle-resolved scatterometer (ARS) systems.

For an instrument to be useful for surface microstructure measurements, the frequency response and spatial frequency bandwidth of the instrument should be known. This information specifies those regions of parameter space over which the instrument will produce accurate measurements.

In this paper we examine the frequency response characteristics of an ARS and a stylus profilometer. Using a computational model for the stylus motion of a mechanical profilometer, we have examined the spatial frequency bandwidth and transfer function characteristics of this type of instrument.

2.0 Angle-Resolved Scatterometer

2.1 Decomposition of Surface Roughness

The scatter of light from a surface has been treated by Church [1] and other investigators. The structure of a surface with isotropic microroughness can be considered as a superposition of randomly oriented sinusoidal components, each having a specific spatial frequency, f, and amplitude, a. To illustrate this principle, consider a shallow one-dimensional sinusoid on a perfectly reflecting surface. The surface profile is given by:

$$z(x) = a\sin(\frac{2\pi x}{d}) \qquad 2\text{-}1$$

where a is the vertical amplitude and d is the spatial wavelength. In order to satisfy the smooth surface limit, the amplitude a must be sufficiently small such that

$$(ka)^2 << 1 \qquad 2\text{-}2$$

where $k = \frac{2\pi}{\lambda}$ and λ is the wavelength of light. A beam of light incident on this surface is diffracted into different orders on both sides of the specular beam. The intensity of the light reflected in the n-th order is given by [1]

$$I_n \approx (ka\cos\theta_i)^{2n} \qquad 2\text{-}3$$

where θ_i is the angle of incidence from the normal. In the smooth surface limit, the intensity in the higher orders will be very small, and therefore, only the first order ($n = \pm 1$) and specular beam ($n = 0$) contributions are considered. The angle between the first order beam and the specular beam is given by the grating equation as

$$\sin\theta_s = \sin\theta_i \mp \frac{\lambda}{d} \qquad 2\text{-}4$$

Equations (2-3) and (2-4) illustrate important points which are the basis for scatterometer measurements: the intensity of scattered light is proportional to the square of the vertical amplitude of the surface roughness, and the angular spread of the scattered light is proportional to the spatial frequency of the surface roughness [1]. When the smooth surface condition is satisfied, a simple mapping is obtained in which the intensity of the light scattered at a given angle is mapped to the power spectral density (PSD) at the corresponding spatial frequency.

Data obtained using an optical scatterometer pertains only to the limited band of spatial frequencies which contribute to the measurement. The lower spatial frequency limit is defined by that component which diffracts at an angle close to the specular beam but remains resolvable. The upper spatial frequency limit, f_{max}, is defined by that spatial frequency component which diffracts at an angle of 90° from the normal to the surface. The value of f_{max} is determined by the laser wavelength and the measurement geometry. For the case of normal incidence, f_{max} is equal to λ^{-1}.

2.2 Optical Scatterometer

The arrangement of the UNM optical scatterometer is illustrated in figure 1. This configuration has been reviewed by Church [1,2], Stover [3], and McNeil [4]. The light source is a linearly polarized HeNe laser. S-polarized light is normally used. The spatially filtered laser output is focused ~40cm from the sample. The photomultiplier tube (PMT) detector rotates about the scatter point at this same radius. Hence, measurements are performed in the far field. Neutral density filters are used to attenuate the incident light observed by the PMT, providing a dynamic range of over ten orders of magnitude in the measurement of light intensity.

The spatial frequency bandwidth of the UNM scatterometer is 0.014 to 1.56 μm^{-1} and is determined by the experimental geometry and the laser wavelength through eq (2-4). Thus, scattering caused by surface structures of approximately 0.64 to 70 μm spatial wavelength can be examined. System background noise is measured as a function of spatial frequency before measurements are made on the sample and is accounted for in the PSD and rms roughness calculations.

2-3 Optical Transfer Function of the Optical Scatterometer

A most effective way of describing an optical system is by specification of its transfer function $H(f)$. The transfer function describes the effect of the system in the frequency domain. The transfer function is given as

$$H(f) = M(f)e^{j\theta(f)} \qquad 2\text{-}5$$

where $M(f)$ and $\theta(f)$ are known as the Modulation Transfer Function (MTF) and the Phase Transfer Function (PTF), respectively. The MTF specifies the relative attenuation of various spectral components [5]. The MTF is obtained either directly or indirectly by Fourier transformation of the impulse response of the optical system.

The output of the scatterometer is expressed as the power spectral density (PSD) of the surface roughness as a function of spatial frequency. The PSD varies linearly with scattered light intensity [1]. The intensity varies with the square of the surface roughness amplitude eq (2-4) and the intensity of the incident beam. The MTF of the optical scatterometer is therefore constant

between the limits on spatial frequency given above. Figure 2 illustrates the MTF of an ARS.

3.0 Mechanical Profilometers

3.1 Introduction

Mechanical profilometers use a diamond stylus of radius typically in the range of 1 μm (or smaller) to 12 μm. Stylus loading, typically a few milligrams, determines whether the surface is marked by the stylus. Bennett and Dancy [6] reported that loading as small as 2 milligrams can produce permanent marks on the surface of single-crystal KC*l*. The height sensitivity of the instrument can be as small as a few angstroms. The height sensitivity depends on the sensitivity of the electromechanical transducer, the signal to noise level of the electronic signal, the noise of the system [7], and, as we show below, the lateral dimension (i.e. spatial wavelength) of the surface structure of the sample. The lateral resolution of the system depends on the heights and slopes of the sample surface structure as well as the stylus radius. Elson [8] has suggested a simple relation to estimate the minimum spatial wavelength that can be resolved by a stylus instrument. If the surface height variation is a single sinusoid of amplitude a and wavelength d, then the smallest spatial wavelength which can be resolved by a stylus of radius r is

$$d_{\min} = 2\pi\sqrt{ar}. \tag{3-1}$$

To illustrate the significance of the relation between the amplitude a and $d_{\min} = \frac{1}{f_{\max}}$, consider the following examples. If $a = 100$ A and $r = 1\mu m$, then $d_{\min} = 0.63\mu m$. As another example, consider a spatial wavelength of 500 A. To resolve a 500 A sinusoidal structure using a stylus of $r=1.0\mu m$, the amplitude of the sinusoid must be less than 0.6 A. Similarly, for $r = 12\mu m$, the amplitude must be less than 0.05 A. Clearly these amplitudes are not realistic. If the amplitude of the structure is larger than the values specified by eq (3-1), the curvature of the surface exceeds that of the stylus, and the surface will not be accurately profiled. The situation becomes very complicated when one considers more realistic surfaces which consist of many spatial wavelengths.

Describing a system by its frequency response implies that the system is linear. Linearity in turn implies that the principle of superposition can be applied to the system [5]. Consider, for example, a system having a response represented by the operator S. For two input signals $f_1(x)$ and $f_2(x)$, the responses of the system $g_1(x)$ and $g_2(x)$ are given by

$$g_1(x)=S[f_1(x)] \tag{3-2a}$$

and

$$g_2(x)=S[f_2(x)]. \tag{3-2b}$$

Then, for two arbitrary constants α_1 and α_2, the system is said to be linear if for an input equal to the sum $[\alpha_1 f_1(x)+\alpha_2 f_2(x)]$, the output is given by

$$S[\alpha_1 f_1(x)+\alpha_2 f_2(x)] = \alpha_1 g_1(x)+\alpha_2 g_2(x) \tag{3-3}$$

This is simply another statement of the principle of superposition. The linearity of the mechanical profilometer will be discussed below.

3.2 Computational model for the stylus profilometer

To examine the properties of a mechanical surface profilometer, the path taken by the stylus must be calculated as it traverses a mathematically defined surface. The path calculation (tracking calculation) is performed using a computational model which approximates the properties of a physical stylus.

For the spherical stylus, a surface with continuous first partial derivatives, and in the absence of external forces, it is apparent that the center of the stylus must lie along a line normal to the surface at the point of contact. This is shown in figure 3. The center of the stylus is at a distance r from the point of contact along the normal. The equation of the tangent plane at the point of contact is given as

$$Ax+By+Cz+D=0. \tag{3-5}$$

Here A, B, C, and D are constants at each point on the surface $z=f(x,y)$ being profiled. The normal to the tangent plane is given by

$$\vec{N} = A\vec{i}+B\vec{j}+C\vec{k}, \tag{3-6}$$

where $\vec{i}$, $\vec{j}$, and $\vec{k}$ are the Cartesian unit vectors. The normal, $\vec{N}$, can be found by evaluating the gradient at the point of contact,

$$\vec{N} = \frac{\nabla f}{|\nabla f|}\Bigg|_{x=x_c, y=y_c, z=z_c,} \tag{3-7}$$

where (x_c, y_c, z_c) is the point on the surface being considered for profiling. Under most conditions, the point of consideration will also be the point of contact. The gradient is defined as

$$\nabla f = \frac{\partial f}{\partial x}\vec{i}+\frac{\partial f}{\partial y}\vec{j}+\frac{\partial f}{\partial z}\vec{k} \tag{3-8}$$

and exists only when the surface f is differentiable. The parametric equation of a line which originated at the point of contact and extends in the direction of the normal is given as

$$\begin{aligned} x(t) &= x_c+tA \\ y(t) &= y_c+tB. \\ z(t) &= z_c+tC \end{aligned} \tag{3-9}$$

The location of the center of the stylus is computed by finding t_{cp} such that

$$[x(t_{cp})-x_c]^2+[y(t_{cp})-y_c]^2+[z(t_{cp})-z_c]^2 = r^2. \tag{3-10}$$

After choosing the appropriate root, the coordinates of the center of the stylus are found by inserting t_{cp} into eq (3-9).

A physical problem with stylus profilometers occurs when the local surface curvature exceeds the radius of curvature of the stylus. The local surface curvature is defined as the surface curvature that exists in the neighborhood of the point of consideration. The excess curvature causes the stylus to contact the surface simultaneously in more than one point. Furthermore, it is possible that the point of consideration is *not* a point of contact. This effect causes the computed path in our model to contain loops, as shown in figure 4. Loops may be multiply nested. The loops arise from the fact that the tracking calculation is done on a point by point basis; no consideration is given to the nonlocal shape of the surface. The loops can be removed using numerical techniques, yielding the profile of the surface as traced by the stylus.

The constraints placed upon differentiability of the surface are necessary to guarantee that a unique normal exists for each point along the path taken by the stylus. If the surface is not differentiable, then the position of the center of the stylus cannot be computed. This is particularly troublesome, for example, when one attempts to compute the stylus profile for the edge of a square ruling, the apex of a cone, or any other object of impulsive nature. In a physical profilometer, the stylus suspension supplies enough force to either round off the points of non-differentiability, or stabilize the stylus in a otherwise nonequilibrium position.

The implementation of the computational model was accomplished using vector algebra in the parametric representation. Care was taken to insure numerical stability. Since the resulting profile would likely be subjected to discrete Fourier analysis, further care was taken to insure adequate sampling to satisfy the Nyquist criteria [5]. For simplicity, the model was implemented for one dimensional surfaces only. The implementation of a two dimensional model is straight forward, although costly in terms of computation time.

3.3 Results of computational modeling

3.3.1 Linearity of the Surface Profilometer

The stylus profilometer was found to possess a nonlinear response. The nonlinear properties of the stylus profilometer can be illustrated by considering a surface which consists of two rectangular features of the same width. The height of one feature is twice that of the other, as shown in figure 5. The response of the stylus is also plotted in figure 5, assuming a spherical stylus of radius r. The response is found by calculating the variation in height of the center of the stylus as it traverses the surface. From figure 5 it can be first seen that the width of the response of the stylus to one feature is not the same as that of the other feature, indicating that the principle of

superposition does not apply to the mechanical profilometer. The cause of this nonlinearity is the gradual rise of the stylus as its center approaches the feature. It can be easily shown that the extent of the gradual rise, b is given by

$$b = \sqrt{2ar - r^2}, \tag{3-11}$$

where a is the height of the feature and r is the stylus radius.

3.3.2 Transfer function of the Stylus Profilometer

Regardless of the nonlinearity described above, it is advantageous to calculate an approximate transfer function for the mechanical profilometer. To calculate the approximate transfer function, the tracking calculation was used to trace the height of the center of the stylus as it contacts a surface composed of a single sinusoid of variable frequency. The amplitude of the output signal is plotted as a function of spatial frequency in figure 6. Note that this is a general plot, in which the horizontal scale is spatial frequency in units of r^{-1}. The two curves correspond to two different amplitudes of surface roughness, expressed as a fraction of the stylus radius r. Note that this transfer function is derived assuming *only* a single-spatial-frequency surface. It can be seen in figure 6 that the MTF of a stylus profilometer decreases with increasing spatial frequency. In addition, figure 6 illustrates the dependence of spatial frequency bandwidth on the stylus radius and the amplitude of the surface roughness. Also illustrated in figure 6 is the maximum spatial frequency, f_{max}, calculated from eq (3-1).

Case I: Harmonic Distortion

Harmonic distortion is a consequence of the nonlinearity and is a special case of nonlinear mixing. It manifests itself by the introduction of frequency components in the output which are not present in the input. Only in considering a single-spatial-frequency surface is the effect of nonlinear mixing easy to quantify. For more realistic surfaces which may have many spatial frequencies present, the nonlinear mixing is still present but is much more difficult to analyze. To illustrate the harmonic distortion effect, a single frequency surface is profiled using the tracking calculation. The output signal is Fourier analyzed using a Fast Fourier Transform (FFT) code. Figure 7 illustrates the initial surface, its profile, and the magnitude spectrum of the profile. The output spectrum clearly indicates that the surface profile is composed of the fundamental frequency as well as higher order harmonics. Total harmonic distortion (THD) is used to quantify this type of frequency distortion. THD is defined as the ratio of power in the higher harmonics to that in the fundamental component of the output and can be expressed as [9]

$$THD = \frac{\sum_{n=2}^{\infty} a_n^2}{a_1^2} \tag{3-12}$$

where a_n is the amplitude of the nth harmonic. Figure 8 illustrates the THD in percent calculated as a function of spatial frequency in units of r^{-1}. Single frequency surfaces having the same amplitude were profiled using the tracking procedure, with a stylus of fixed radius. Data is shown corresponding to surfaces of two amplitudes, $0.01r$ and $0.001r$. Also indicated in figure 8 are the values of $f_{max} = d_{min}^{-1}$ calculated for each surface using eq (3-1). It can be seen that at frequencies approaching f_{max}, the THD can be as large as 5 percent for the surfaces illustrated. For surfaces of larger amplitude, the THD is more significant. In addition, at frequencies larger than f_{max} where the system response is reduced, a higher percentage of the response is in the harmonics (i.e. larger THD). Figure 5 illustrates that although an input signal may appear to be accurately represented by the output, the frequency characteristics may not be identical.

Case II: Multicomponent surfaces

When two or more spatial frequency components are present in the surface to be profiled, the output spectrum includes the fundamental components, their harmonics, and the sum and difference frequency components along with other components. This is shown in figure 9, which illustrates the output spectrum corresponding to an input signal composed of just two sinusoidal frequency components, f_1 and f_2. Note that in this example both f_1 and f_2 are less than f_{max}, and both components have the same amplitude.

For a surface composed of many spectral components, the situation is less clear. A typical surface will have a nearly continuous spectrum, generally with an energy distribution that falls off somewhat exponentially with frequency. To see the effect of the nonlinear response on a "realistic" surface, the tracking calculation was performed on two one-dimensional mathematically defined surfaces constructed from a large number of sinusoidal components with random phase. Surface A was formed from components following an exponential decay in amplitude for increasing spatial frequency. Surface B was formed identically to surface A with the exception that beyond a certain spatial frequency the component amplitudes were set to a constant. These surfaces were profiled using the computational model with a 1 μm stylus radius. The output was subjected to Fast Fourier Transform analysis. The input and output spectra are shown in figures 10 and 11 respectively.

The input spectra depict the distribution of energy as a function of spatial frequency for the input surfaces. Curve A displays the spectrum for surface A, and shows the expected exponentially decaying envelope. Curve B shows the spectrum for surface B, and is identical to curve A except for the constant amplitude for spatial frequencies greater than 2.5 μm^{-1} .

The output spectra in figure 11 illustrate several interesting effects. The output spectrum for surface A has been modified in a low-pass filter-like manner. Some energy has been redistributed from higher frequencies into lower frequency bands. The output spectrum from surface B shows the same effect, with additional complex behavior. A particularly interesting outcome is that the areas under curves A and B are nearly identical. This indicates that the RMS roughness of surfaces A and B will be found by the stylus to be nearly equal, i.e. the stylus is unable to differentiate between the two surfaces in spite of the large differences in spectral content.

4.0 Discussion

The transfer function for the ARS, as mentioned above, is constant within the spatial frequency bandwidth of the system. However, the "transfer function" for the stylus profilometer presented in figure 4 is not. Although approximate in meaning, the transfer function is still useful in understanding some of the properties of the stylus profilometer. A cutoff spatial frequency is defined for a given amplitude. The cutoff frequency changes for varying surface roughness amplitude, as described by eq (3-1). This indicates that in reporting a value for the spatial bandwidth of a stylus profilometer, the amplitude for which the bandwidth is calculated should be reported. It should be noted here that the cutoff frequency is derived *only* for single-sinusoid surfaces.

Results indicate that the stylus profilometer is a nonlinear device. The source of the nonlinearity is the finite size of the stylus. As a consequence of this nonlinearity, no real transfer function for a stylus profilometer can be defined. A profilometer measurement may also exhibit nonlinear mixing effects. The magnitude of the THD depends on the amplitude of the surface roughness, the stylus radius, and the spatial frequency. The presence of nonlinear mixing in the profilometer response provides an additional source of error making the output an inaccurate representation of the input. Because the relation between input and output is nonlinear, surface statistics (such as correlation functions) calculated from stylus profiles may not be accurate. The effect of the stylus properties on the measurement of surfaces with realistic spectral content is found to be quite complex.

5.0 Summary

We have developed a model for the stylus motion of a mechanical profiling instrument. The model was used to examine the frequency response characteristics of the instrument and was demonstrated to be a nonlinear system. This nonlinearity causes the frequency response of the system (MTF) to be amplitude dependent, and introduces nonlinear mixing into the spectrum of the profile. Extreme care should be taken when a stylus system is used to profile surface, especially a surface consisting of many spatial frequency components.

REFERENCES

[1] E.L. Church, H.A. Junkinson, and J.M. Zavada, Opt. Eng. 16, 360 (1977).

[2] E.L. Church and J.M. Zavada, Appl. Opt. 14, 1788 (1975).

[3] J.C. Stover, S.A. Serati, and C.H. Gilespie, Opt. Eng. 23, 406 (1984).

[4] J.R. McNeil, L.J. Wei, G.A. Al-Jumaily, S. Shakir, and J.K. McIver, Appl. Opt. 24, 480 (1984).

[5] J.D. Gaskill, *Linear Systems, Fourier Transforms & Optics*, Wiley, New York (1978).
[6] J.M. Bennett and J.H. Dancy, Appl. Opt. 20, 1785 (1981).
[7] J.M. Bennett, Opt. News 11, 17 (1985).
[8] J.M. Elson and J.M. Bennett, J. Opt. Soc. Am. 69, 31 (1974).
[9] F.G Stremler, *Introduction to Communication Systems*, Addison, Reading (1982).

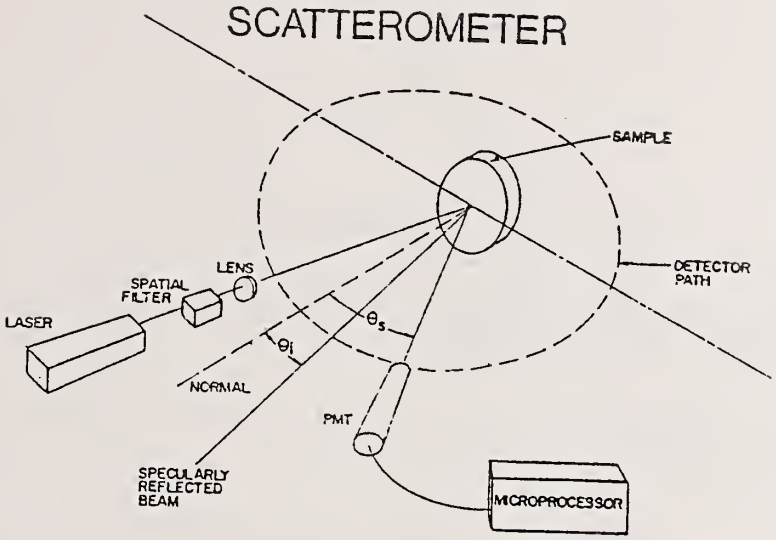

Figure 1. Schematic of the optical scatterometer.

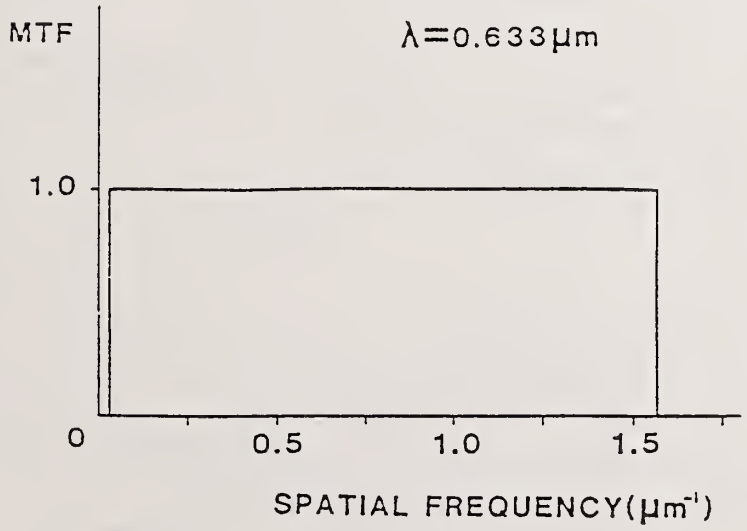

Figure 2. MTF of an optical scatterometer.

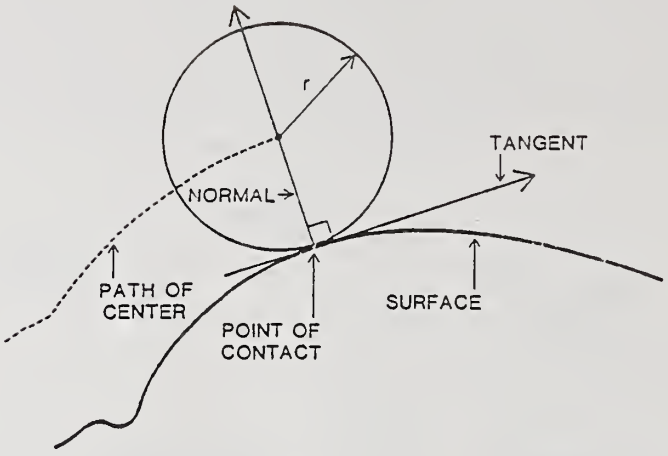

Figure 3. Schematic of the tracking model.

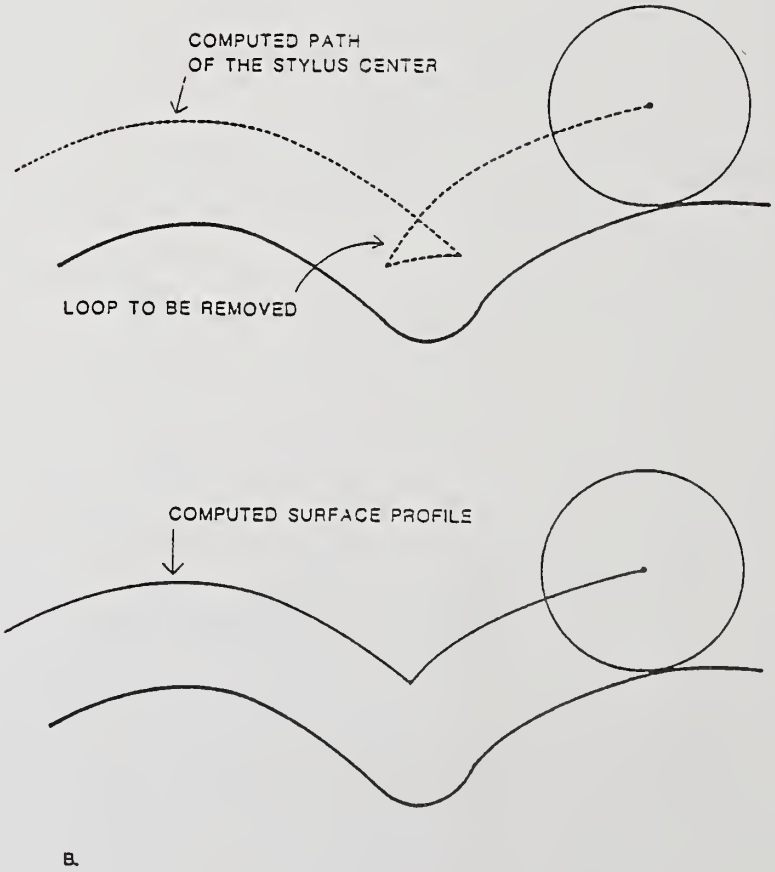

Figure 4. Computed path of the center of a spherical stylus (a) with the loop and (b) with the loop removed.

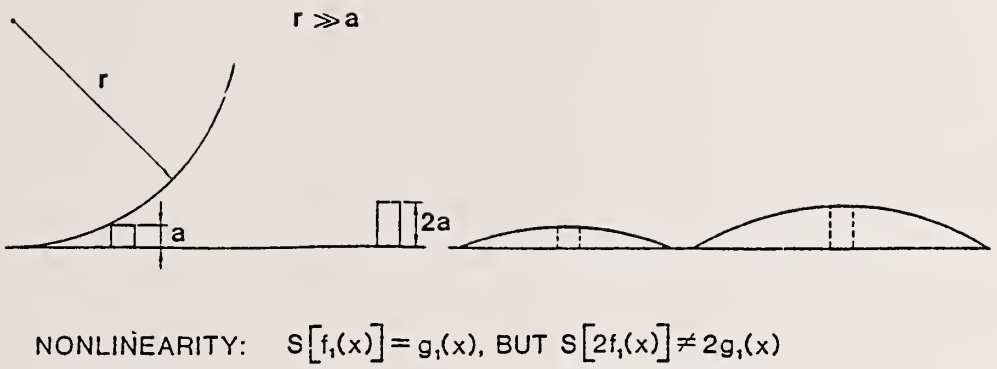

Figure 5. Schematic illustration of the superposition principle as applied to the surface profilometer.

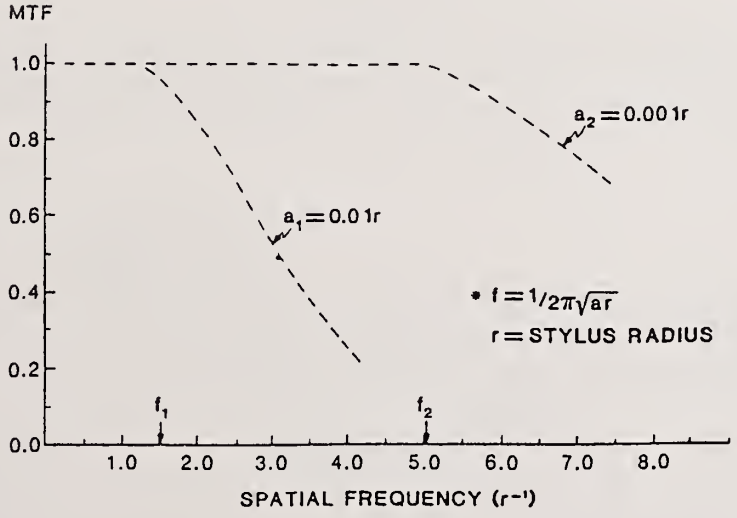

Figure 6. Approximate MTF of a surface profilometer calculated using single-sinusoidal surfaces.

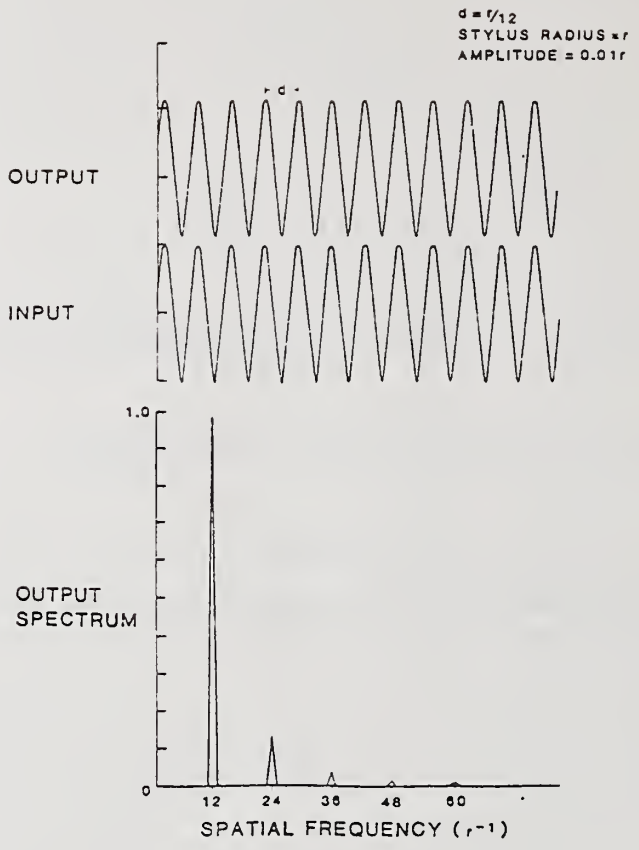

Figure 7. Harmonic distortion in the output of a profilometer. The top curve represents the surface profile, the middle curve representst the true surface, and the lower curve represents the normalized spectrum of the surface profile.

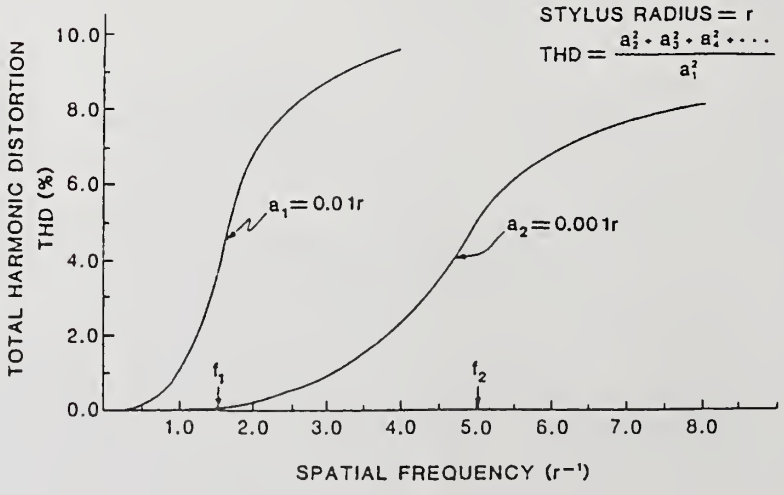

Figure 8. The THD calculated as a function of spatial frequency for two values of sinusoid amplitude.

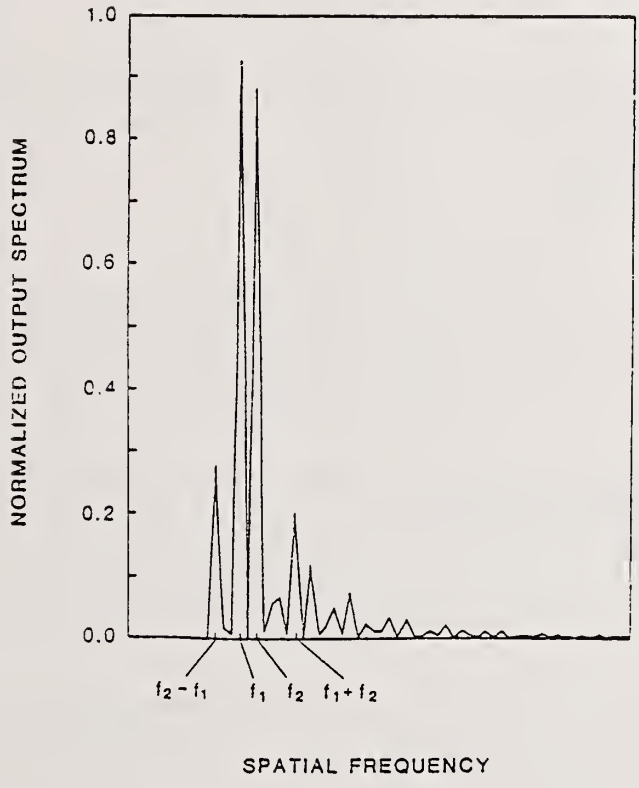

Figure 9. The normalized spectrum of the profile of a surface composed of two sinusoids. Note the presence of the sum and difference components, as well as other harmonics generated by the nonlinear interaction.

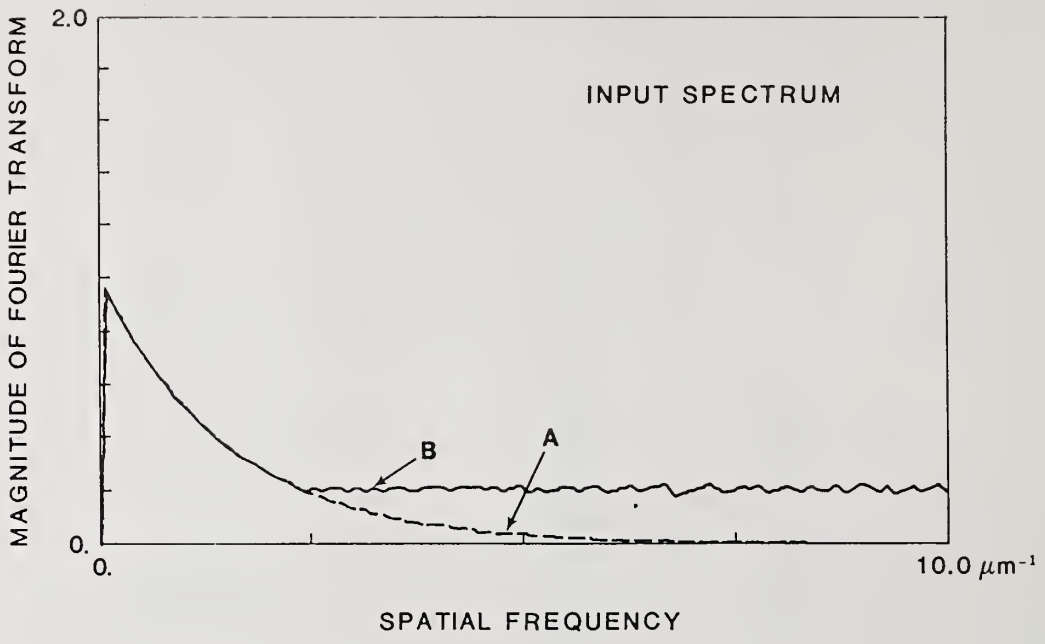

Figure 10. Input spectra for two surfaces: A) exponential spectrum, B) exponential spectrum with floor.

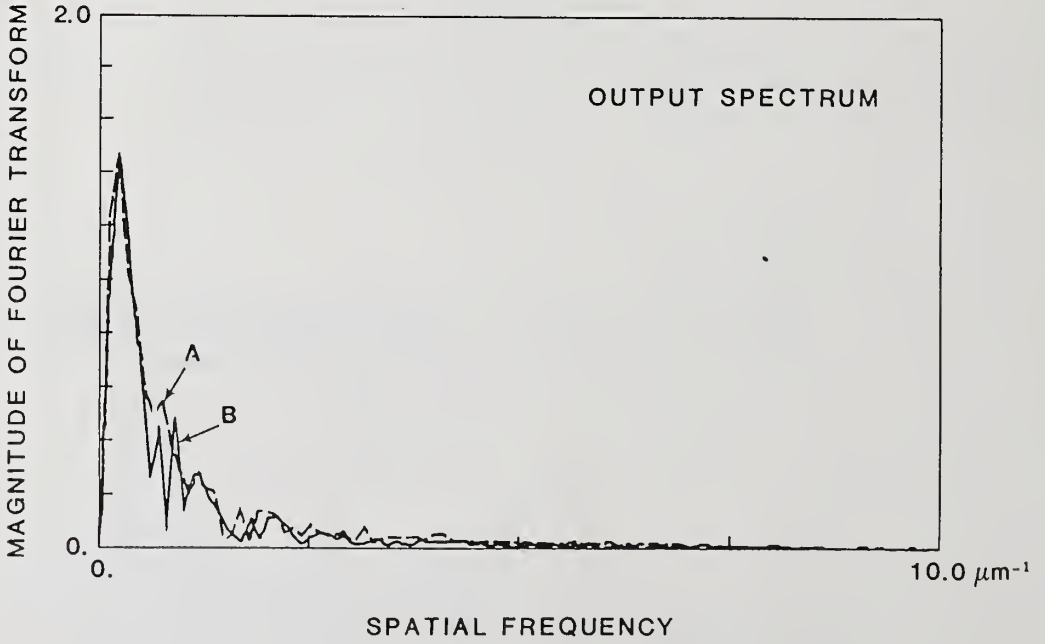

Figure 11. Output spectra computed from the profiles of surfaces A and B. Note that the area under the two curves is nearly the same.

Manuscript Received
4-1-88

Ultrasmooth Sapphire Produced by Noncontact Polishing*

J. J. Shaffer and J. M. Bennett

Physics Division, Research Department
Naval Weapons Center, China Lake, California 93555-6001

The history and theory of noncontact polishing is discussed, along with a simple machine that will perform noncontact polishing including lap speeds and polishing pressure. Research using this machine is described. An extended polishing experiment produced the smoothest surface ever measured at the Naval Weapons Center.

Key words: aquaplaning; noncontact polish; sapphire surface roughness; tin lap.

Introduction

Within the last decade, a relatively new method of polishing has made its way into the optical world. This technique was pioneered by Dr. Yoshiharu Namba of Osaka University in Japan [1].[1] Using this technique, it is possible to polish some substrates to less than the noise level on most surface roughness measuring devices [2]. Sapphire can be polished to less than one-half of an angstrom unit, rms roughness [3].

The substrates being polished ride on a thin film of slurry similar to a car aquaplaning across a puddle of water. Dr. Namba's theory is that the work is accomplished when the particles of abrasive strike the substrate at extreme grazing angles. The energy exchange on impact exceeds the molecular bond, and one or more molecules are torn loose from the substrate. Because of the extreme grazing angle, this action is preferential; the high spots are affected more than the low spots. Also, it appears that a chemical action may be taking place.

Machine Parameters

The machine used for noncontact polishing is very similar to a ring polisher. It has an annular lap running on a vertical spindle with a power-driven work spindle situated over this lap. In order to achieve a flatness of less than one or two wavelengths, the machine must be very rigid and have some form of temperature control. Just to prove the concept, however, these parameters are not mandatory. The speeds of both spindles are infinitely adjustable from 0 to 100 rpm. The lap is made of tin with 2-mm-wide lands and 1-mm-wide grooves (fig. 1).

Dr. Namba's machine was made by the Toyoda Company of Japan. The lap used on this machine was fabricated using a stainless steel disk with a layer of tin cast on the top side. The lap used at the Naval Weapons Center (NWC) was made from solid tin. Though it must be handled very carefully, it has less tendency to warp during temperature changes. The machine fabricated and used at NWC is very crude compared to the Toyoda machine. It operates in a temperature-controlled room, but it has no temperature control of its own. It is powered by a fractional horsepower dc motor whose speed is adjustable from 0 to 100%. The pulley sizes were selected so that 100% corresponds to 100 rpm. The upper spindle is driven with an o-ring belt from a pulley that is attached to the lower spindle (fig. 2).

Polishing Lap

Pure tin was used for the polishing lap; however, a tin-lead mixture might be a good candidate (other materials have been tried in Japan). Plastics have been used with some success on soft substrates. It was decided, however, to stay with a tin lap for these experiments in order to

*Work supported by Navy Independent Research Funds.

[1]Numbers in brackets indicate the literature references at the end of the paper.

limit the variables. The lap was cast in one piece as contrasted with the Toyoda Company's lap. It was cut using a simple but effective unit that bolts onto the baseplate and holds a regular lathe tool that has been sharpened to a square point (fig. 3). The lap used in Japan was cut in such a manner to produce 2-mm-wide lands and 1-mm-wide grooves. Because the lead screw in the cutting device was not in metric units, it was decided to cut the lap to produce lands measuring 0.100 in. wide and grooves 0.050 in. wide.

Theory

When discussing a new theory it is sometimes useful to compare it to an older theory that has withstood the test of time. It would be desirable, for instance, to compare noncontact polishing with conventional polishing [4]. Unfortunately, very little is known about what is actually taking place during conventional polishing. There are three prevalent schools of thought. One holds that the process is mechanical and particles of substrate are scraped off of the workpiece, much as in a machining operation. Particles of substrate can be found in the slurry. Another theory has it that a chemical action is taking place, which can be just the simple dissolving and redepositing of the material or a more complex process wherein a third, and possibly softer, compound is formed. When standard polishing practices are employed on glass substrates, silica can be detected in solution in the slurry. In the case of sapphire polishing, andalusite can be identified in the slurry. Andalusite is an aluminum silicate (Al_2SiO_5) that is softer than sapphire. A third theory holds that sufficient heat is produced when the polishing compound breaks down to actually melt the topmost layer of the substrate and is smeared around on the surface. A scratch on the surface of a glass substrate can be polished out without reducing the thickness of the substrate by the depth of the scratch. This would tend to support the idea that a filling-in process was taking place, either by solution and redeposition or by smearing. These two hypotheses can be supported by the fact that in some cases the scratch can be redisclosed by etching or cleaning.

Noncontact polishing does not appear to suffer from subsurface damage. It would seem, therefore, that the smearing or solution theories will not hold up. The theory that is espoused by Dr. Namba, who originated the idea of noncontact polishing, is as follows. The workpiece is held off of the lap by a film of slurry that forms hydrodynamically. The gap between part and lap (although never measured) must be quite small. The slurry rushing through this gap does the work. Each particle of abrasive in the slurry must sooner or later strike the substrate. Because the gap is very small, the abrasive particles strike at extreme grazing angles. The energy exchange on impact exceeds the molecular bond; therefore, a small bit is literally knocked off of the substrate. Since it is an extreme grazing angle, the action is preferential and the high spots are affected more than the low spots. Obviously, the part will get smoother. Because the action is produced by impact, the hardness of the "polishing" compound is not important. A chemical action cannot be ruled out, however, and the andalusite intermediate compound may be aiding the process. It seems that a hard substrate such as sapphire could not be scraped or chipped away by a soft polishing compound such as is used in the process described. The polishing compound used is amorphous fumed silica of 70 Å units particle size. It is much softer than sapphire; therefore, it would seem that the mechanical scraping/abrading theory alone could not be applicable.

Experiment

Using the exploratory machine described above, it was decided to work with sapphire substrates and ascertain whether or not the concept could be proven. Three pieces of 14-mm-diameter by 2-mm-thick, single-crystal, c-axis cut sapphire were chosen for the trial runs. The loading pressure was controlled by the weight of the blocking plate to which the samples were attached. In the final form, this loading worked out to be 500 gm/cm^2. The rotational speed of the lap was set at 80%. The pulleys that drive the upper spindle were selected so that the rotational speed of this spindle was about 60 rpm. Upon checking these parameters later, it was found that the lap was turning 82 rpm and the upper spindle was turning 61 rpm.

The samples were polished on the machine for a total of 40 hr. The final profiles on one of the samples were so smooth that the roughness could not be distinguished from the noise level of the Talystep. This sample was subsequently measured on a newer machine located at the University of Alabama at Huntsville. The signal was digitized by a Hewlett-Packard (HP) Model 3478A multimeter used as a voltmeter and interfaced to a HP 320 computer. The overall instrument gain was 2,000,000. An output filter removed frequencies higher than about 25 Hz, which reduced the noise level to an equivalent roughness of 0.4 Å units rms. Profiles of the sample are shown figure 4. The sample shows a slight long-term waviness, but no scratches or other small defects. The 0.5 rms surface roughness shown on the figure includes the noise level of the machine.

Polishing Cycle

For the purpose of this discussion, the polishing cycle is referred to as a "run." At the start of a series of runs, the lap is freshly cut. As this is a relatively straightforward process, it will not be covered here. The freshly cut lap is very shiny and dulls somewhat after a run or two. A pronounced dulling and/or darkening of the slurry indicates that the parts are not riding on the slurry film and are, in fact, contacting the lap. If this occurs, it is best to begin the series again using a freshly cut lap. The first step with a new setup is to establish a set of parameters that will assure that the lap is covered with slurry. This is especially important immediately in front of the samples. The machine is started with the slurry in the bowl -- but without the samples in place. In the event that the slurry does not behave as desired, a stir stick or two can be inserted in the flow of slurry to better direct it. When the slurry flow is satisfactory, the parts are put in position and the machine is started. The slurry consists of water with 2 or 3 wt% of the silica added. At startup and after shutdown, the parts are setting in the lap -- of course in contact with it. They rise up on the film of slurry almost immediately after startup and continue to "float" on this film until shortly after shutdown. As might be expected, the lap will exhibit two areas of scuffing or darkening corresponding to the contact made at startup and shutdown. Sometimes the samples will grab at startup. If this happens, the run must be aborted and begun again. Once a successful startup is achieved, the run can be continued indefinitely or until the slurry darkens. An average run is about 1 hr. Some of the sapphire runs were overnight. If the darkening of the slurry is gradual rather than abrupt, the run can be continued for 24 hr or more.

Conclusions

It seems beyond cavil that the system known as "noncontact" polishing does work. To our knowledge, the surfaces produced and described here are the smoothest ever measured. There is little or no subsurface damage resultant from this procedure. Under magnification, examination of the surfaces reveals entirely different characteristics from those produced by conventional polish. The concept can be proven with relatively inexpensive equipment. If high production and/or very flat work are required, the machine must be temperature controlled and be quite rigid. The Toyoda machine, although quite expensive, meets these requirements.

Areas needing further study include the importance of the polishing pressure, the adaptation of the principles to spherical work, the possibility of using the technique on massive optics, the importance of the size of the gap between part and lap, and the relationship of this work to other schemes such as elastic emission machining [5].

References

[1] Namba, Y; Tsura, H. Ann. CIRP 28; 325; 1977.

[2] Bennett, J. M.; Dancy, J. H. Appl. Opt. 20; 1785; 1981.

[3] Bennett, J. M.; Shaffer, J. J.; Shibano, Y.; Namba, Y. Appl. Opt. 26; 696; 1987.

[4] Preston, F. W. Trans. Opt. Soc., London 27; 1926.

[5] Mori, Y.; Ikawa, N.; Sugiyama, K.; Okuda, T.; Yamauchi, K. Japan J. Soc. of Precision Engr. 51; 1985. (In Japanese.)

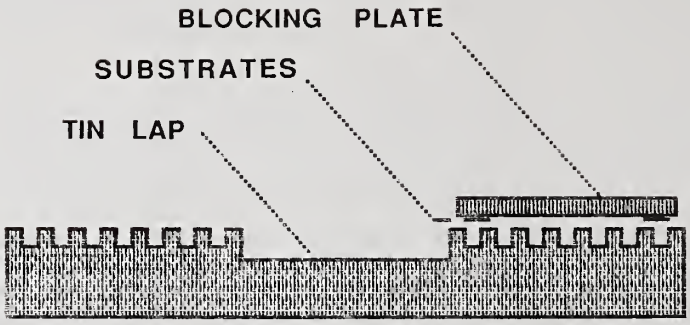

Figure 1. Cross section of polishing lap and components being polished showing groove and land structure. The lands are 0.100 in. wide and the grooves 0.050 in. wide.

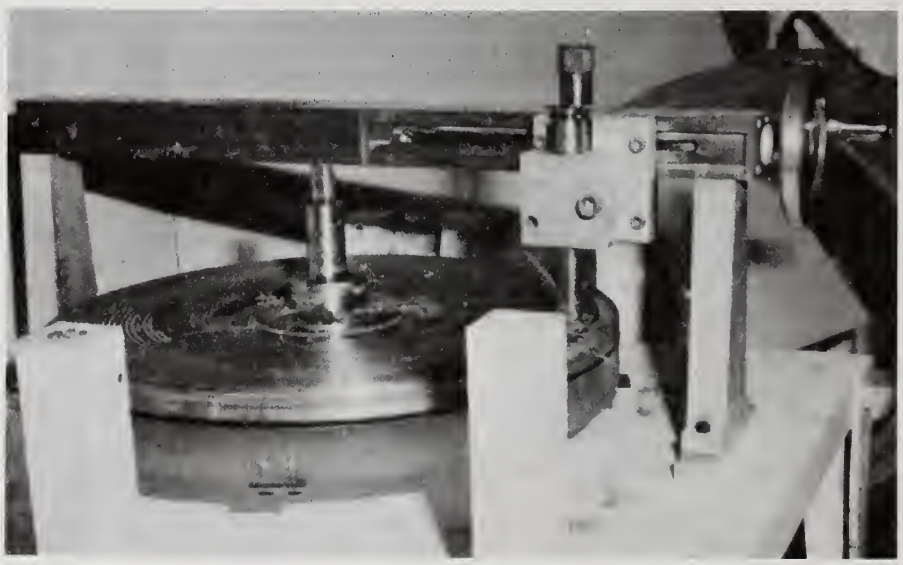

Figure 2. Overall photo of noncontact polishing machine showing lucite bowl to contain polishing slurry and the rotating cage to drive the polishing block on the lap.

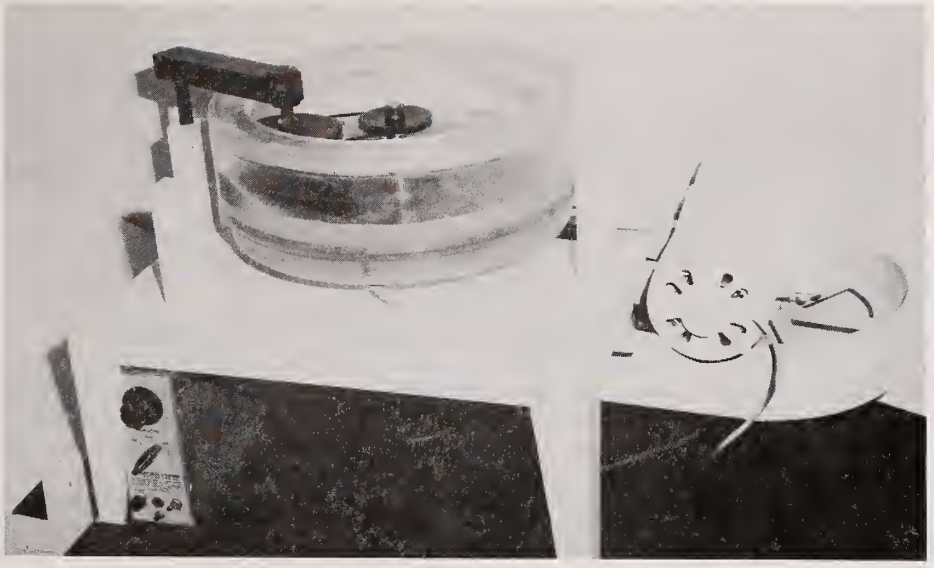

Figure 3. Photo of the lap-machining mechanism. Note that this operation is manual both for in-feed adjustment and for transverse motion.

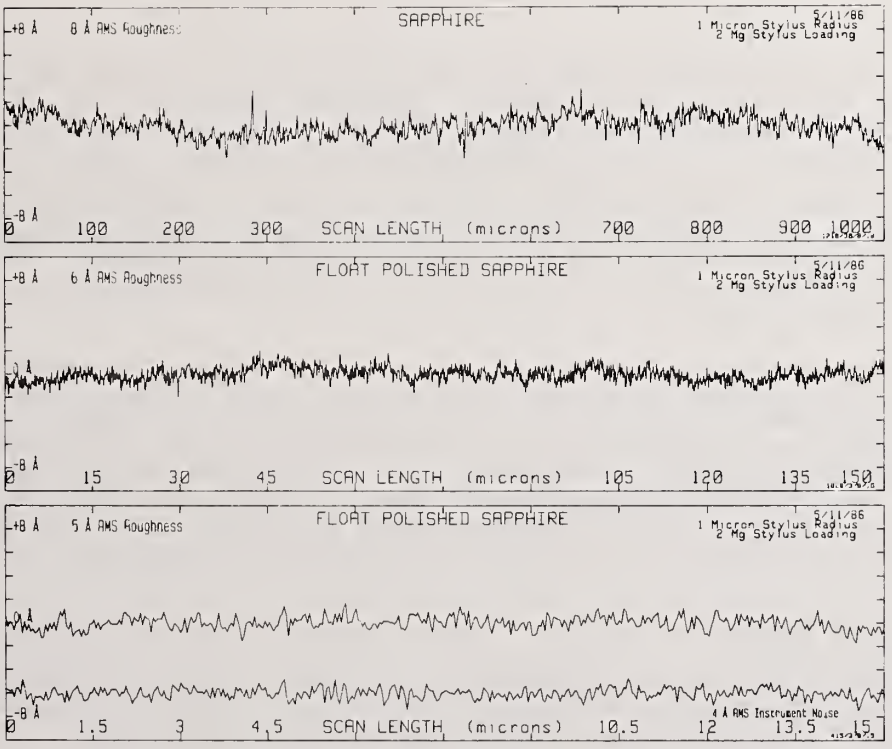

Figure 4. Talystep data for noncontact polished sapphire sample. Included in bottom trace is a scan that shows the "noise equivalent roughness" of the Talystep instrument. The rms roughness of the scan made on an actual sample is only slightly larger than the instrumental noise of 0.4 Å.

Manuscript Received
10/19/87/sar

Optical Damage in Epoxy Polymers by Millisecond Light Pulses*

C. R. Wolfe, J. H. Campbell, R. E. Lyon,
J. H. Pitts, and H. T. Powell

Lawrence Livermore National Laboratory
University of California
P. O. Box 5508, L-482
Livermore, Ca. 94550

We have studied optical damage in epoxy based polymers used to attach absorbing cladding onto the edge of laser disks of the Nova laser. Damage was produced by exposing the polymers to a 20-40 J/cm^2 fluence of broad band Xe-flashlamp light having a pulselength of approximately 0.5 ms. This simulates the pump environment of Nd:glass laser amplifiers. The predominant damage mechanisms appear to be pyrolysis, associated with absorbing inclusions and photolysis, associated with intrinsic absorption of the polymer. The amount of damage can be minimized by: (1) careful filtering of the polymer to reduce the presence of foreign material, (2) minimizing the near UV absorption of the polymer and (3) reducing the UV emission of the flashlamps.

Key Words: epoxy; flashlamp light; laser glass edge cladding; optical damage; photolysis; pyrolysis.

1. Introduction

A composite polymer/glass edge cladding has been developed for use on the Nd:glass disks in the Nova laser at the Lawrence Livermore National Laboratory. A companion paper [1] describes the laser amplifier system of which the cladding is a part and gives an overview of the cladding development and production. As part of the development of the cladding, we have studied the optical damage of amine cross-linked epoxies that occur in the harsh environment of high power laser amplifiers. This environment includes high fluences of 1-μm amplified spontaneous emission and broad-band flashlamp light. Localized light absorption in laser components can cause localized heating and thermal stress. To utilize epoxies as components of laser amplifiers, the conditions encountered by the polymer and the material's response to those conditions must be understood.

Laser damage in polymers has been studied in the Soviet Union [2-5], in the U.S., and elsewhere [6-9]. Most of these studies have been concerned with vinyl-based polymers, in particular poly-methylmethacrylate (PMMA). In this paper we consider the damage of amine cross-linked epoxies, and we believe this is the first attempt to do so. It is generally agreed that one mechanism of laser damage to polymers arises from radiation absorption by foreign bodies (inclusions). These sites of high absorption can reach high temperatures and the surrounding polymer decomposes via pyrolysis. The Soviet literature also describes damage in terms of the mechanical response of the polymer to the shock and high temperature produced at these absorbing sites.

In this paper we discuss the results of flashlamp damage testing of amine cross-linked epoxies and numerical modeling of the thermal history of absorbing sites. First we describe the environment inside the amplifiers of the Nova laser. Second, we propose two mechanisms we believe to be most responsible for the damage we observe. These are pyrolysis, mentioned above, and photolysis. Third, we present experimental evidence for these mechanisms.

---

*This work was performed under the auspices of the U. S. Department of Energy by the Lawrence Livermore National Laboratory under Contract No. W-7405-ENG-48.2892R.

2. The Radiation Environment

There are two components of the radiation environment in the Nova amplifiers that the edge cladding epoxy must survive without damage. The first is broad band Xe-flashlamp light that is used to pump the Nd:doped phosphate glass laser disks. The approximate pulse length is 0.5 ms. The typical time-integrated flashlamp output in a Nova laser amplifier has the spectral distribution shown in figure 1. It is suppressed below approximately 350 nm due to absorption by the Ce-doped fused quartz lamp envelopes and the silicate glass amplifier blast shields. In addition, Nd^{3+} absorption in the visible and near-IR further attenuates the radiation that reaches the polymer. As a result, the UV component of the flashlamp output that reaches the polymer is mostly between 350-400 nm. The expected flashlamp fluence is approximately 11 J/cm^2 measured at the disk edge [10]. The second component of the amplifier radiation environment is amplified spontaneous emission with a wavelength of 1 μm. Approximately 75% of this 1-μm fluorescence is retained in the laser disk due to total internal reflection at the surfaces. The expected energy loading on the cladding from this source has been calculated to be approximately 9 J/cm^2 for the operating conditions of the Nova laser.

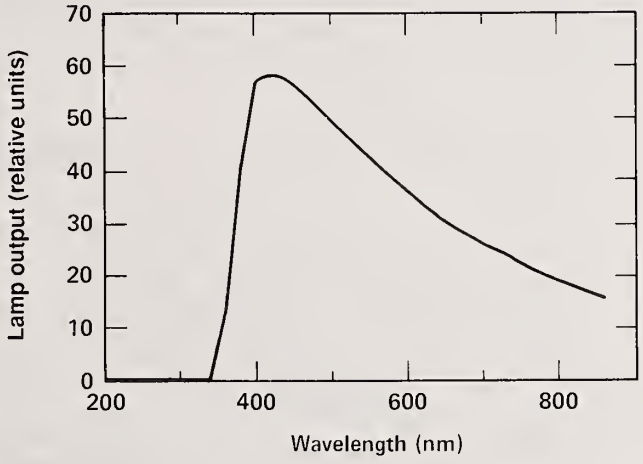

Figure 1. Schematic drawing of Xenon flashlamp output showing the suppression of emission below 350 nm due to the flashlamp envelop and blast shield absorption.

3. Sample Preparation/Apparatus

We studied the degradation of the optical epoxy used in the edge cladding by producing and measuring damage in 25-50 μm thick layers of the polymer. All studies were conducted on fully cured two-part epoxies that were cast between two pieces of borosilicate glass like that used in our blast shields (fig. 2a). All samples were prepared in a class 100 cleanroom to minimize particulate contamination. The two-part epoxies were thoroughly mixed and vacuum de-aired to remove air bubbles introduced during mixing. For reasons described below, the mixed liquid epoxy was filtered to remove inclusions having diameters greater than 0.5 μm. The few bubbles introduced during this final filtration were then forced out of the glass/epoxy interface and the assembly was allowed to fully cure.

The flashlamp system used to simulate the amplifier environment is shown in figure 2b. The fluence experienced by the polymer in these tests was controlled by variation of the charging voltage of the flashlamp capacitor bank. The single pass energy incident at the sample position was up to 20 J/cm^2 as measured by a carbon calorimeter. The amount of damage produced was determined by measuring the size and counting the number of damage spots produced in the polymer layer.

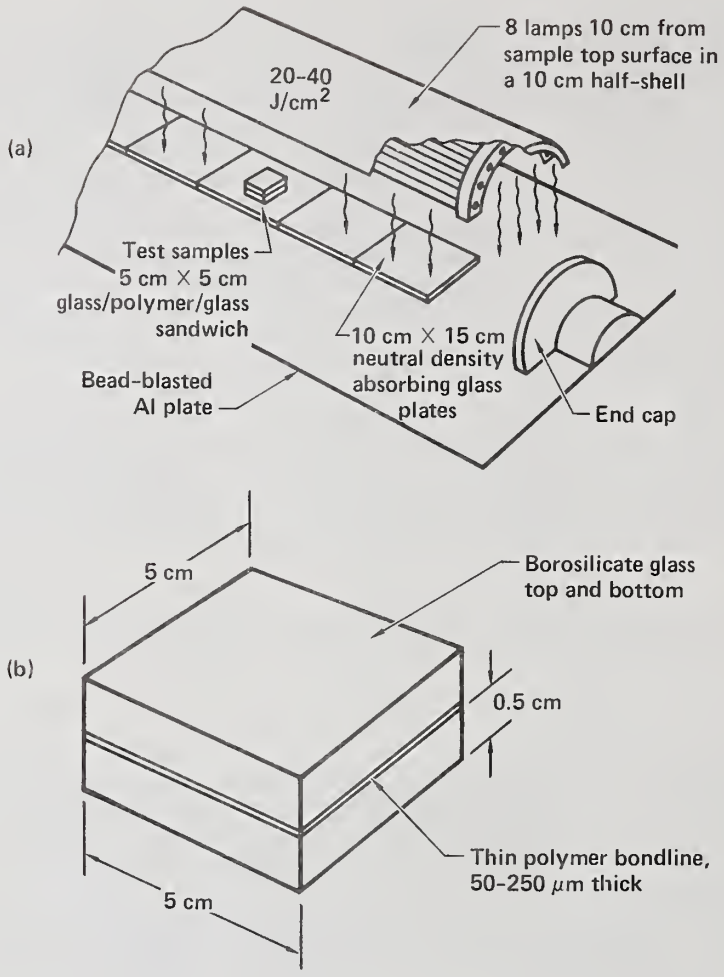

Figure 2 (a) Flashlamp test sample consists of a glass/epoxy/glass sandwich and (b) the flashlamp test exposure system using a 10 cm laser amplifier half-shell.

4. Damage Mechanisms

4.1 Thermal Decomposition

Polymers may contain contaminants in the form of inclusions that are wholly or partially absorbing. They are the natural result of manufacture and handling. Polymer degradation by pyrolysis at high temperature can occur when light energy is absorbed by these inclusions [2,3,6]. Energy deposited in this way heats the particles and locally surrounding material for short periods of time. Repeated thermal excursions further decompose the surrounding polymer, which in turn adds to the size of the absorbing site, thus amplifying the damage growth. The magnitude of the temperature excursion experienced is primarily dependent upon the physical size of the inclusion, its optical absorptivity, and the thermal diffusivity of the surrounding polymer. We have modeled the temperature rise of absorbing inclusions in organic polymers to calculate the amount of decomposition.

For simplicity, consider first the case of a small particle whose thermal diffusion length during the flashlamp pulse, αt, is large compared to its radius (here α denotes the thermal diffusivity of the particle, m^2/s). In this case the particle can be considered internally isothermal. In thermal steady state the temperature rise of the particle upon irradiation is given by:

$$\Delta T_{max} = Pa/\kappa \qquad (1)$$

where: P = surface flux absorbed (W/m^2),
a = particle radius (m),
κ = polymer thermal conductivity ($Wm^{-1}K^{-1}$).

We have also analyzed the more realistic case that models the behavior of large inclusions where transient heat conduction within the particle and into the surrounding polymer is significant. This situation was solved by numerical calculation using a 2-dimensional finite element heat transport code [11]. We selected a carbon inclusion as a reference case and assumed a heating pulse in the form of a half-sine wave with a maximum flux of 10 kW/cm^2 and extending over a time span of 0.5 ms (fig. 3). This results in an integrated absorbed energy of 3.2 J/cm^2. The results of these calculations are shown in figure 3. This figure shows that only for inclusions of diameter greater than 3-4 μm does the transient solution vary significantly from the simple steady-state case described above. Notice also that the maximum temperature rise occurs for particles whose diameter approximates the thermal diffusion distance during the flashlamp pulse. Both models indicate that very high temperatures can be reached near absorbing
sites.

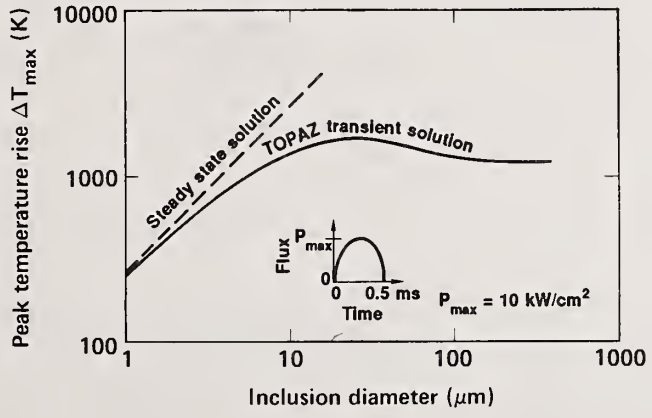

Figure 3. Calculated peak temperature rise vs. absorbing inclusion diameter. High temperatures can be reached near inclusions having diameters greater than several microns.

The heating pulse occurs within the time scale of the flashlamp pulse, on the order of 0.5 ms. The above calculations show that heating to temperatures exceeding 300°C can occur. We must determine at what temperature the polymer near an inclusion will begin to undergo significant pyrolysis. Pyrolysis is complicated by the fact that the inclusion and surrounding polymer is heated and cooled very rapidly due to the short duration of the flashlamp pulse. We measured the decomposition kinetics of the epoxy at slow heating rates. We then used a simple first order decomposition model to extend the kinetic analysis to the rapid heating and cooling regime that occurs near an inclusion.

Thermal gravimetric analysis of a typical optical epoxy showed that the peak decomposition occurs in the region of 300-325°C at modest heating rates (fig. 4). Further non-isothermal kinetic analysis [12] of the data showed that the mass loss due to decomposition can be accurately modeled by the simple first order rate expression,

$$dP/dt = -kP \quad (2)$$

where:

dP/dt = rate of polymer decomposition (mole$\cdot$m$^{-3}\cdot$s^{-1}),
P = concentration of polymer (mole$\cdot$m^{-3}),
k = first order rate constant, (s^{-1}), obtained from an Arrhenius fit to the temperature dependence of the reaction rate;

$$k = A \exp [-E/RT(t)] \quad (3)$$

and:

A = a pre-exponential coefficient (s^{-1}),
E = activation energy (J$\cdot$mole^{-1}),
T = time dependent temperature (K),
t = time (s),
R = gas constant (J$\cdot$mole$^{-1}\cdot$K^{-1}).

The values of the activation energy and pre-exponential coefficient determined from this analysis are:

A = 1.6 x 10^{12} (s^{-1}) , and
E = 1.65 x 10^{5} (J$\cdot$mole^{-1}).

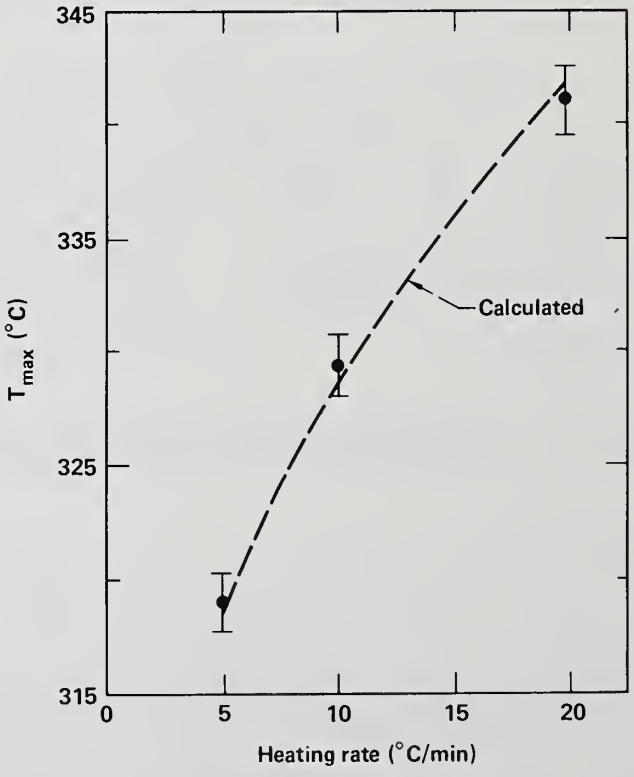

Figure 4. Dependence of peak decomposition temperature on heating rate. The dashed line was determined by fitting data from thermal gravimetric analysis.

Although these values accurately model the thermal decomposition that occurs at modest heating rates, one cannot be certain that this model will apply at the high temperatures and heating rate of the amplifier pulse. It is clear that this simple kinetic analysis is only a crude model of the complex reaction chemistry that occurs during pyrolysis. Nevertheless it provides a measure of the approximate amount of decomposition that may occur near an absorbing inclusion. Similar analysis of pyrolysis of fossil fuels under rapid heating has been found to be accurate [12,13].

Using the above model for pyrolysis, we have calculated the fraction of the polymer that will decompose when subjected to various temperature excursions during a flashlamp pulse. We again used a 0.5 ms half sine heating pulse and various peak temperature rises corresponding to different particle sizes. The results shown in figure 5 indicate that if during a flashlamp pulse the surface of an absorbing inclusion were heated to 400°C, then the fraction of polymer in contact with the surface that will decompose will be approximately 10^{-4}. If the effect is additive, 100 shots will locally decompose approximately 1% of the polymer.

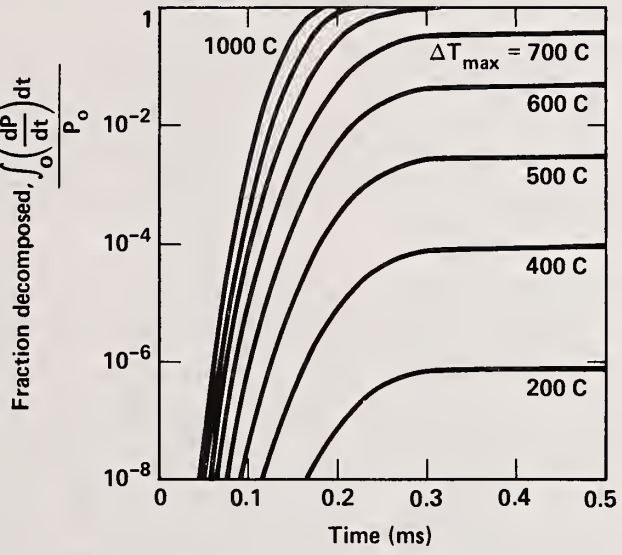

Figure 5. The fractional polymer decomposed vs. time for a given peak temperature rise at the inclusion.

Two additional characteristics of this damage mechanism are worth noting. First, due to the very short time interval spent at the high temperature, the polymer can be heated to rather high temperatures (e.g.400°C) without significant decomposition. Secondly (and of particular importance considering the pulsed operation of the laser), damage produced in this way will accumulate around absorbing sites and will grow significantly with repeated laser operation. In general, most polymers produce volatile components and black carbonaceous residue during decomposition [6,12,13]. Thus, pyrolysis at the surface of an absorbing inclusion has the effect of increasing its size. The absorbing site becomes the original inclusion plus the thickness of the surrounding pyrolyzed region. The result summarized in figure 3 indicates that as site size grows so does the peak temperature rise. Consequently, as pyrolytic deposits accumulate around absorbing inclusions, they amplify the damaging absorption, producing greater absorption and higher temperatures. This process is clearly catastrophic. Finally, we have observed such catastrophic failure of epoxy bonds; once damage sites are initiated, they grow until mechanical failure occurs.

4.2 Photochemical Decomposition

In addition to the decomposition via the pyrolytic pathway described above another mechanism for energy transfer to, and subsequent damage of, the polymer is absorption of light by the polymer itself. The presence of a photolytic (photochemical) damage mechanism should reveal itself if the damage is sensitive to changes in the lamp emission spectrum and the polymer adsorption spectrum. However, conclusions based solely on the spectral dependence of damage must be tempered by the fact that inclusions may also have absorptions which increase in the UV, contributing more strongly to the pyrolytic mechanism. The most damaging component of the radiation environment is the short wavelength, the blue and near-UV, regions of the lamp output spectrum. Organic materials absorb strongly in the blue and near-UV and photon energy in excess of that required for bond cleavage is readily available [14-17]. The absorption of complex polymer networks can be predicted because simple functional groups always absorb in the same region of the spectrum [15,18].

5. Experimental Results

Polymer samples described in figure 2a were repeatedly exposed to our flashlamp tester in 0.5-ms pulses at 20 J/cm^2. When samples were prepared from unfiltered epoxy materials we observed massive damage in only a few shots using the complete flashlamp spectrum. The amount of damage appeared to correlate with the number of inclusions that were observed microscopically. The general damage morphology was similar in all cases. We observed millimeter size spots with black carbonaceous residue surrounded by a region of polymer/glass delamination presumably caused by a localized high pressure pulse. Upon repeated exposure the damage sites grew in size.

When the glass surfaces of the epoxy samples were cleaned in a cleanroom and the epoxy precursors were filtered to remove inclusions with diameter greater than 0.5 μm, the amount of damage decreased dramatically. Using the full lamp spectrum and a fluence of 20 J/cm^2, we were unable to significantly damage the epoxy in hundreds of shots. To accelerate the production of damage for further study, we removed the black absorbing glass under the samples, allowing the flashlamp light to reflect from an aluminum backing plate. This roughly doubled the fluence the epoxy experienced. With these double pass conditions, even the filtered polymers damaged in a few shots.

We then investigated the difference in damage produced by using the full lamp spectrum and the lamp spectrum filtered to remove the near-UV component [21]. The optical absorption of two candidate optical epoxies [19,20] are shown in figure 6. Those spectra were obtained from uncured epoxy samples using a Cary 14 spectrometer, the optical path length was 1 cm. Optical damage testing of samples of these epoxies prepared as described above indicate that the polymer that exhibits least absorption in the blue and near-UV regions of the spectrum, damages least. In addition, the amount of damage produced in both of these materials could be reduced by preventing the UV component of the flashlamp emission spectrum from reaching the epoxies. In one experiment a band-pass filter (L-39, Hoya Corp., Tokyo, Japan) was placed between the flashlamp and the sample to prevent transmission of wavelengths less than 390 nm. The lamp capacitor bank voltage was increased to keep the total fluence fixed. The amounts of damage produced by 9 shots (double pass) is shown in figure 7.

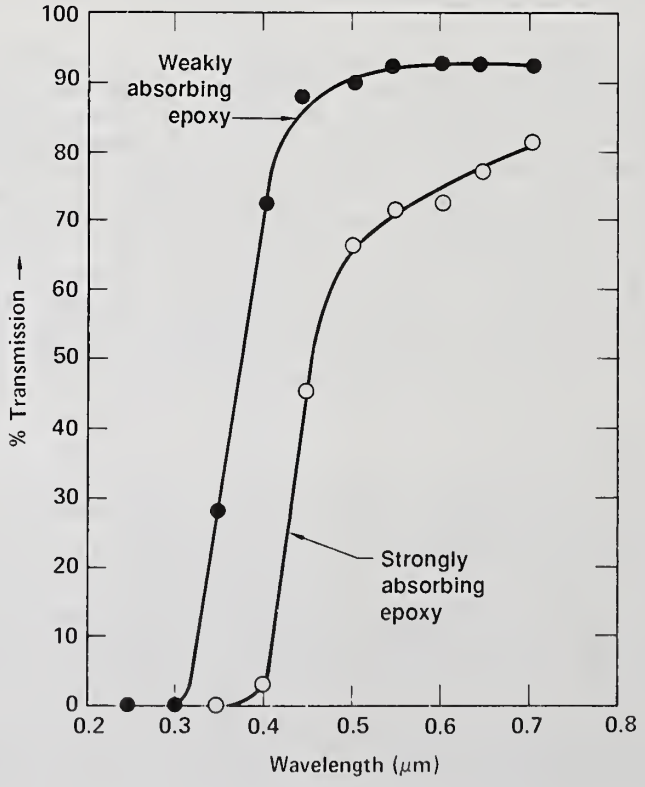

Figure 6. Spectral transmission of two uncured epoxies showing differences in the near-UV and visible regions.

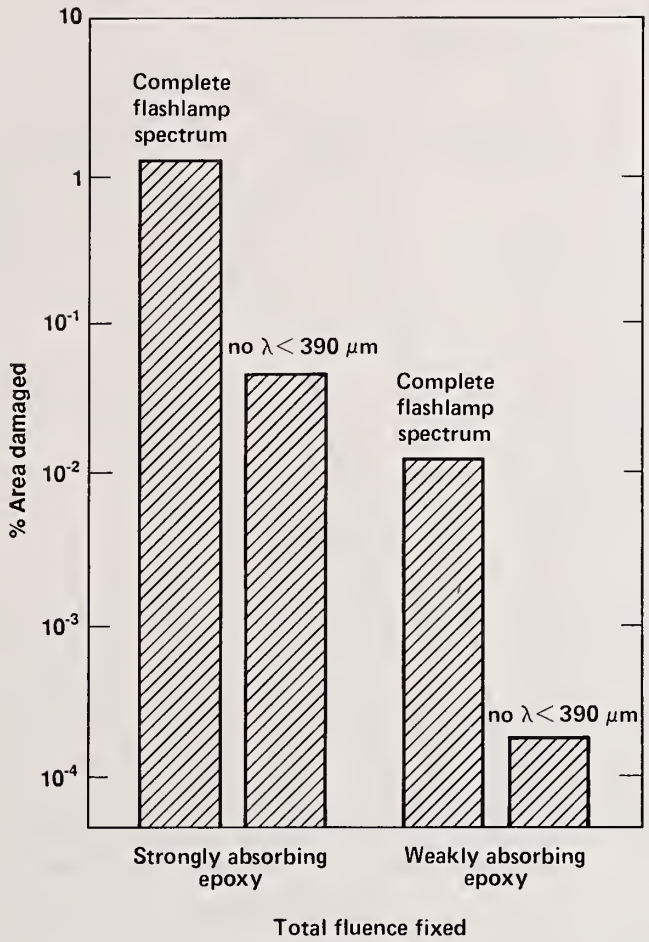

Figure 7. Bar graph showing percentage area damage in weakly and strongly absorbing epoxies that have been exposed to flashlamp light with and without the UV component.

In another experiment a UV absorbing dye [22] was dissolved in the epoxy. The amount of damage was reduced in samples containing the dye that were exposed to the entire lamp spectrum compared to samples without the dye.

The weakly absorbing epoxy shown in figure 6 is formulated from a blend of two resins and an amine curing agent. One of these resins is aliphatic [23], the other is primarily aromatic [24]. The spectral transmission of each of these epoxide resins is shown in figure 8. We formulated and tested eight amine-cured epoxies made from blends of these resins ranging in composition from 100% aliphatic to approximately 50% aromatic. The samples were made under identical cleanroom conditions, and were filtered to remove inclusions having diameters > 0.5 μm. The spectral transmission of these blended epoxies all lie within the "envelope" of the two pure resins shown in figure 8. The amount of damage produced as a function of epoxy composition is shown in figure 9. Comparison of figures 8 and 9 again suggests a connection between optical damage and near-UV absorption. The least damage occurred in the epoxy made from the resin that is 100% aliphatic, which has the least near-UV absorption.

It is important to note that the damage produced in these epoxies always occurs in spots. This leads us to suspect the existence of "favored sites" for damage. In addition, no significant variation in average size of individual damage spots was observed in these samples. The increase in damage that was observed as aromatic functionality is increased is primarily the result of more initiation sites.

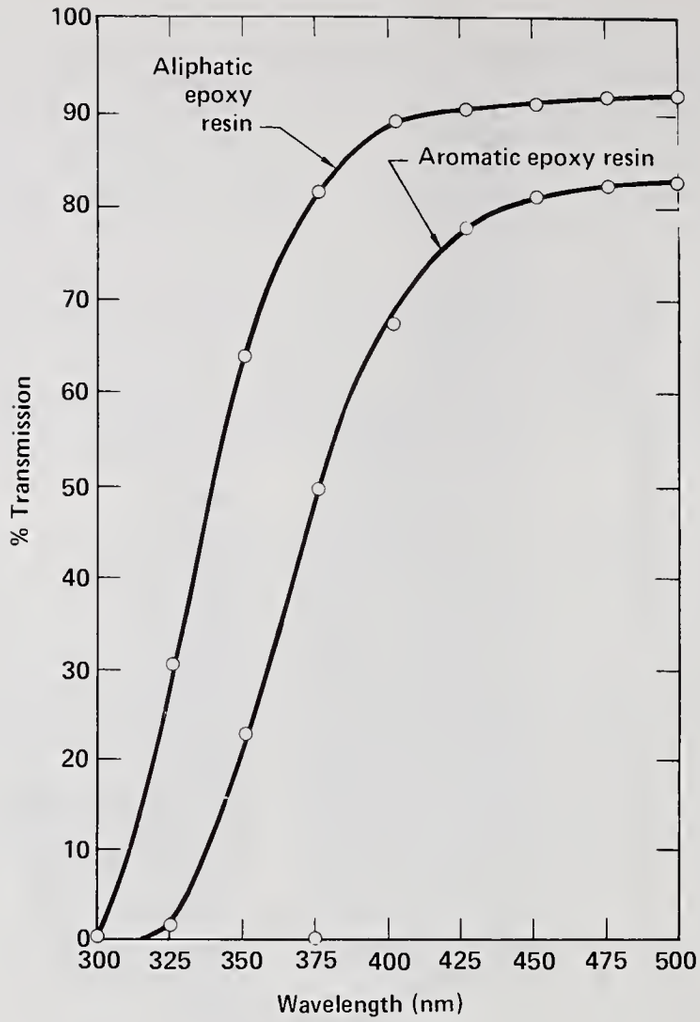

Figure 8. Spectral transmission of an aliphatic[23] and aromatic[24] epoxide resin.

6. Discussion

The mechanisms of polymer degradation by photolysis and pyrolysis in the harsh environment of the laser amplifier are closely interrelated.

Photo-initiated degradation of polymers begins with the production of radicals via the absorption of a sufficiently energetic photon. The energy required to accomplish this depends upon the absorption characteristics of the polymer. Radicals produced by photoionization are unstable and in the presence of oxygen can react through a chain that can propagate the initial dissociation many times [14,25]. The oxygen required for these reactions is provided at a free surface or is dissolved in the polymer. In this propagating free radical chain reaction [25,26] as chromophores are produced, the polymer becomes photosensitized at longer wavelengths and the photochemical process is accelerated. At some point photo-initiated damage becomes large enough and sufficiently absorbing that pyrolysis begins.

On the other hand, pyrolysis of polymers initiated by inclusions leads to the production of a highly absorbing organic residue [6,13]. If oxygen is present in the polymer network, it can also participate in the early stages of the degradation process by oxidizing the polymer, forming carbonyl groups. Due to their longer wavelength absorption than the unoxidized polymer, the carbonyl groups will photosensitize the polymer. The pyrolytic elimination of oxygen from ether linkages [27] is an example. Thus high temperature pyrolysis of the epoxy network near inclusions accelerates the process of photolysis.

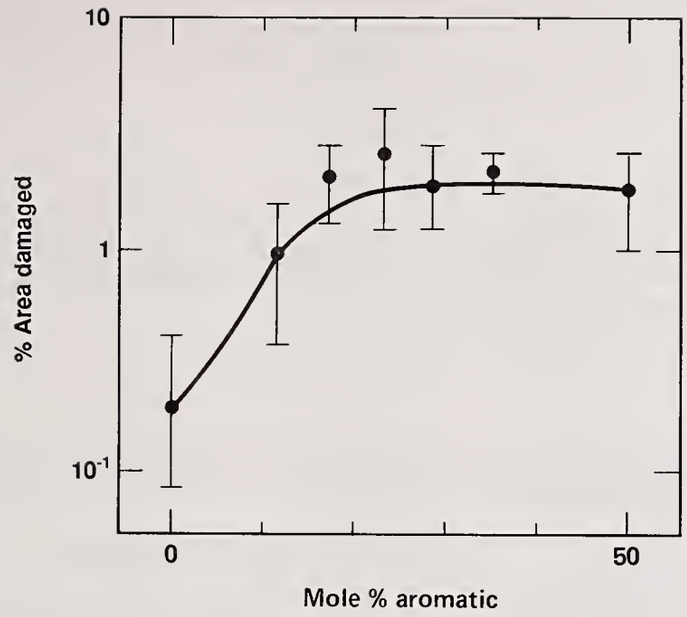

Figure 9. Percent area damage vs. mole-% aromatic resin used in the epoxy. Note that the degree of optical damage correlates with increasing aromaticity.

We have also observed that the accumulation of chromophores in the epoxy is accelerated by slow heating. The resultant "yellowing" of the epoxy is obvious to the eye. It is also significant that while many examples of pyrolysis accelerating photolysis are known, the reverse has also been observed. Partial photo-degradation has been shown to accelerate the process of pyrolysis [14]. The explanation given is that low molecular weight polymer chains created by photo-degradation are more easily pyrolyzed than the initial high molecular weight three dimensional cross-linked network.

Finally, the morphology of optical damage (spots) in the epoxy polymers studied indicates that favored sites, which easily damage, are present. The pyrolytic damage originating from absorbing inclusions obviously provides for these sites. The data suggest that favored damage sites for photochemical degradation are also present in the polymer. These sites are chromophores unevenly distributed in the polymer when it is cast and cured. That such chromophores reside in polymers is apparent from the fact that free radicals are produced in polymers by the absorption of light where the pure polymer should have no intrinsic absorption [28]. The exact structure of chromophores responsible for this absorption and subsequent decomposition are not known.

That the polymer is not homogeneous is no surprise. Inclusions and crystalized resins reside even in filtered polymers and can result in areas of enhanced reactivity. Contamination [29] can only be reduced, not eliminated by careful cleanroom procedures. These sites can become nucleation centers for crystallite formation causing mechanical stress. Such regions have been found to enhance the reactivity of polymers in general [30] and epoxies in particular [25].

7. Summary and Conclusions

Our observations of optical damage in epoxies suggest the importance of both pyrolytic and photolytic damage mechanisms. Calculations show that absorbing inclusions as small as a few microns in diameter can cause temperature rises large enough to produce significant epoxy decomposition. Evidence for a pyrolytic damage mechanism caused by foreign inclusions is shown by the reduction in damage by filtering the epoxy precursors, and by the fact that damage always occurs in spots rather than uniformly. The presence of a photolytic damage mechanism is shown by strong dependence of the amount of damage on the UV content of the light and the UV absorption of the epoxy. The data show that the photolytically-initiated damage also occurs in spots.

We hypothesize that the temperature rise around absorbing inclusions can produce decomposition products that photosensitize the polymer further, thus linking the two mechanisms. Furthermore, photolysis can produce absorbing regions that initiate pyrolysis.

Given the interconnected nature of the damage mechanisms described above, any attempt to improve the performance of optical epoxies as laser materials must address both sources of damage. This has been the focus of our epoxy development effort. We have found that the removal of intrinsic near-UV absorption and particulate contamination is key to the use of these materials in laser amplifier components.

The authors wish to thank Mike Riley and Ted Jessop for epoxy absorption measurements, Gary Edwards for assistance in preparing the polymer samples and characterization of damage morphology, Wanda Sawvel for assistance in operating the flashlamp apparatus, and Ken Kulander for assistance with computer modeling of pyrolysis.

8. References

[1] Campbell, J. H., et al; "Composite polymer/glass edge cladding for new nova laser disks", in Laser Induced Damage in Laser Optical Materials: 1986; Proceedings of the Boulder Damage Symposium, Nov. 1986; Boulder, CO, in press.

[2] Butenin, A. V., Kogan, B. Ya.; "Mechanism of optical breakdown in transparent dielectrics", Soviet Journal of Quantum Electronics 1,5, 1972.

[3] Manenkov, A. A., et al; "Role of absorbing defects in laser damage to transparent polymers", Sov. Jour. of Quan. Elec. 10,3,1980.

[4] Manenkov, A. A., Nechitallo, V. S., Tsaprilov, A. S.; "Analysis of a mechanism of laser damage to transparent polymers associated with their visco-elastic properties", Sov. Jour. of Quan. Elec. 11,4,1981.

[5] Dyumaev, K. M., et al; "Influence of visco-elastic properties of the matrix and of the type of plasticizer on the optical strength of transparent polymers", Sov. Jour. of Quan. Elec. 12,7,1982.

[6] (a) Lundberg, J. L., et al; "Carbon formation by the flashlamp illumination of polymers", Proceedings of the Third Conference on Carbon, Symposium Publications Div., Pergamon Press, 1957.

(b) Lundberg, J. L. and Nelson, L. S., "Initiation of thermal reaction by illumination of absorbing bodies", Nature, 153, 1959, pp. 1560-1562.

[7] Parts, L., Hardy, E. E., et al; "Laser induced , residue free localized decomposition of some plastics", Ind. Eng. Chem. Prod. Dev. 9,1,1970.

[8] O' Connell, R. M., Saito, T. T.; "Plastics for high power laser applications: a review", Opt. Eng. 22,4,1983.

[9] O' Connell, R. M., et al; "Laser damage in plastics at the Frank J. Seiler Laboratory (FJSRL)", NBS Special Publication 688, 1983.

[10] Jancaitis, K. J., et al; "Design considerations for Nova edge cladding", 1986 Laser Program Annual Report, Lawrence Livermore National Laboratory report, UCRL-50021-86, Section 4.3.2, in press.

[11] Shapiro, A. B.; "TOPAZ - A finite element heat conduction code for analyzing 2-d solids", Lawrence Livermore National Laboratory Report UCID- 20045 March, 1984.

[12] Koch, E.; "Non-isothermal reaction kinetics of elementary processes. Chapter 3 in Non-Isothermal Reaction Analysis, Academic Press (London) 1977, pp. 90-126.

[13] (a) Jüntgen, K. and VanHeek, K. H.; "Gas release from coal as a function of the rate of heating", Fuel, 47, 1968, pp. 103-117.

(b) Jüntgen, H. and VanHeek, K. H.; "An Update of German Non-isothermal Coal Pyrolysis Work", Fuel Processing Tech., 2, 1979, pp. 261-293.

[14] Roylance, D., Roylance, M.; Weathering in fiber-reinforced epoxy composites. Polymer Engineering and Science 18, 1978, p. 249.

[15] Calvert, J. C., Pitts, J. N.; "Photochemistry of the polyatomic molecules", chapter 5 in Photochemistry, John Wiley and Sons Inc. (New York) 1966, pp. 368-579.

[16] Turro, N. J.; "The nature of electronically excited states", Chapter 4 in Molecular Photochemistry, W. A. Benjamin Inc. (Reading Mass.) 1965, pp. 44-91.

[17] Wayne, R. P.; "Reactions of excited species", Chapter 6 in Photochemistry, American Elsevier Pub. Co. (New York) 1970 pp. 167-192.

[18] March, J.; "Instrumental methods for the determination of structure", Chapter 6 in Advanced Organic Chemistry: Reactions Mechanisms, and Structure, McGraw-Hill (New York) 1968, pp. 167-198.

[19] Kodak Optical Cement Hel04-2, manufactured by the Eastman Kodak Co., Rochester NY., 14617.

[20] Epo-Tek 301, manufactured by Epoxy Technology Inc., Billerica Mass., 01821.

[21] Bryce-Smith, D., Senior Reporter; A specialist periodical report - photochemistry 4 938; 1972 (July 1971-June 1972), The Chemical Society, Burlington House London.

[22] Tinuvin 328 ,substituted 2-(2'-hydroxyphenyl)- benoxitriazole manufactured by Ciba-Geigy Corp.

[23] DER-332; diglycidal ether of bisphenol-A.

[24] RD-2; diglycidal ether of 1,4-butanediol.

[25] Bellenger, V., Verdu, J.; Oxidative skeleton breaking in epoxy-amine networks. Jour. Appl. Poly. Sci. 30 1985 pp. 363-379.

[26] Grassie, N., Guy, M. I., Tennent, N. H.; "Degradation of epoxy polymers: 3-photo-degradation of bisphenol-a diglycidal ether", Polymer Degradation and Stability, 13, 1985, pp. 249-259.

[27] March, J.; "Mechanisms and orientations in pyrolytic eliminations", in Advanced Organic Chemistry : Reactions Mechanisms and Structure, Mcgraw-Hill (New York) 1968 p747.

[28] Ranby, B., Rabek, R. A.; "General mechanism in polymer degradation", in Photo-Degradation, Photo-Oxidation and Photostabilization of Polymers, John Wiley and Sons (New York) 1975 p42.

[29] Graft, D.; Microelectronics 3,14 (1970).

[30] Popov, A. A., Krisyuk, B. E., Blinov,N. N., Zaikow, G. E.; European Polymer Journal 17, 1981, pp. 167-173,.

- Manuscript Not Received -

Variations with Laser Pulse Duration of the Thresholds at 350-nm and 1064-nm for Bulk Damage in Crystals of KDP

R.P. Gonzales, M.C. Staggs, M.F. Singleton, D. George
C.L. Weinzapfel and S. Weinzapfel
Lawrence Livermore National Laboratory
University of California
P.O. Box 5508, L-490
Livermore, California 94550

ABSTRACT

Five separate laser facilities were used to measure 350-nm and 1064-nm thresholds for bulk damage in crystals of KDP. At 1064-nm, tests were made with single laser pulses having durations of 1, 9 and 25 ns and with 9-ns pulses incident at 10 Hz. At 350-nm test were made with single pulses having durations of 0.6, 5.0 and 25 ns and with 25-nm pulses incident at rates up to 50 Hz. Over the range from 0.6 to 25 ns, 350-nm thresholds increased by a factor of approximately 2, and 350-nm thresholds were almost independent of laser repetition rate. The 1064-nm thresholds increased by a factor > 3 as pulse duration increased from 1 to 25 ns. Laser hardening of thresholds was observed at both 350-nm and 1064-nm.

Key Words: damage threshold; KDP; Laser hardening; pulse length dependence

---

Work performed under the auspices of the U.S. Department of Energy by Lawrence Livermore National Laboratory under Contract No. W-7405-ENG-48.

2927R

Manuscript Received 12/21/87/sar

Production Oriented Laser Damage Testing at Hughes Aircraft Company

David W. Mordaunt, Jonathan W. Arenberg, and Mark E. Frink

Hughes Aircraft Company
Electro-Optical and Data Systems Group
P.O. Box 902
El Segundo, CA 90245

This paper describes the laser damage test station used by Hughes Aircraft Company for production support and incoming inspection of optics. It is emphasized that this is a high volume production station which is utilized almost full time for lot sample testing and related production support activities.

The evolution of damage testing at Hughes over a 15 year period is described from early efforts with ruby lasers to the current facility used in support of our Nd:YAG laser programs. The test station and procedures are described in detail including the use of a reference optic as a standard of comparison. Also discussed is the long term success of this test in providing usable components which are acceptable in actual hardware. Plans are presented for the development of the next generation of production related damage test station which incorporates more sophisticated diagnostics and the potential for almost complete automation of the actual damage test.

Keywords: conditioned damage threshold; laser damage reference samples; laser damage testing; production support damage test; unconditioned damage threshold.

1. Introduction

Laser induced damage is a serious problem for the laser manufacturer. A laser damage test station used heavily to support a production line has a number of requirements which are neither necessary nor desirable for a low volume test station concerned mainly with fundamental mechanisms or basic damage research. A production oriented laser damage test station needs to be fixed and stable, highly reliable, operator independent, straightforward to operate, and capable of rapid, high volume testing. This paper describes the development of such a laser damage tester at Hughes Aircraft Company with its emphasis on supporting laser production lines and preventing laser damage related failures either in production or after delivery to our customers. The first portion of this paper will describe the historical development of damage testing at Hughes and the differing methodologies developed for our ruby and Nd:YAG laser systems. The development and a detailed description of our current test station and test procedures will be presented along with the philosophy of testing which guided this development. The final portion of this paper will describe the applications of laser damage testing to the manufacture of rugged, reliable laser hardware and the plans we have for improving and increasing the sophistication of our test station and procedures.

2. History and Development of Laser Damage Testing at Hughes

Hughes Aircraft has been damage testing optics for our ruby laser production programs since 1977. This test was developed strictly as a means of screening our incoming optics to avoid laser damage either during assembly, test or while used in the field. The test procedure developed was designed strictly as a functional test where the optic is exposed to test conditions which simulate the actual use environment as closely as possible. The optics tested are certified to the minimum level required to survive in the laser system using a test laser similar to our production units. Since this is a certification test only, no quantitative determination of the damage threshold is made. This type of certification procedure has been very successful in acceptance screening of optics and results in few production line failures due to laser induced damage.

The actual test procedures used for the ruby laser optics screening are straightforward. Anti-reflection coatings designed for use inside the resonator are tested by operating the test laser at a higher than normal fluence level and placing the parts to be tested inside the resonator. The required production margin is obtained because of the elevated fluence level in the test laser. Any optics which pass this test without damage are considered acceptable for use in production. Optics intended for use outside the resonator are tested by partially focusing the output beam from the test laser, thus providing a higher fluence than the optic would be exposed to in the final system. Because a production type laser is used in both cases, the operating parameters such as pulsewidth, mode structure, and spatial profile are approximately the same as the conditions under which the optics will be used. For both types of optics, those parts which pass the damage certification test are used directly on the production line.

A somewhat different test methodology was developed in support of our Nd:YAG laser production lines. Hughes originally started damage testing in response to problems encountered during the development phase of our early YAG systems (ca. 1971). Testing since 1971 has been on an occasional basis for laser development with continuous testing since 1979 in support of our YAG production lines. The basic test station and test procedures developed in 1979 have continued since then with some minor instrumental improvements but with no changes in the basic test design or methodology. In order to provide design information and to track vendor performance, an actual determination of the threshold is made. This is necessarily a destructive test and acceptance of optics is based on testing of lot witness samples which are coated on the same substrate and in the same coating run as the production lot being evaluated.

The Hughes damage test is designed as a functional test: its purpose is to provide a steady flow of acceptable parts to the laser production lines. The damage threshold is measured relative to a reference optic consisting of AR-coated BK-7 glass, a technique similar to methods previously used in the industry and documented in the scientific literature [1]. These reference optics are typically ordered in batches and each batch is checked against the previous group before using. In addition, the individual pieces within each batch are checked against each other whenever a new reference is used. Because the test is designed to be a functional measure of the survivability of optics in our laser systems, it was decided to define damage as catastrophic surface damage or cratering, often accompanied by a visual spark at the surface of the optics. Although many types of optics display small amounts of surface pitting or increased scatter prior to catastrophic failure, these phenomena will not necessarily cause a functional failure of the laser system. However, a large surface crater typically leads to propagating damage on successive pulses followed by a decrease in the laser output energy and beam quality, thereby causing the system to fail to meet its specifications.

The test laser used is a generic production type laser which approximates the operating characteristics of our different production laser systems. It is repetitively pulsed at rates on the order of tens of Hz rather than being a single shot test, as this more closely approximates the end use of the optics. The laser runs with multiple transverse and also multiple longitudinal modes and the output consists of Q-switched pulses with pulsewidths on the order of tens of nanoseconds.

The test procedure uses a conditioned test in which the laser is focused on a single point on the surface of the test piece and the fluence slowly increased from a low level up until damage is detected. Once damage is detected at this point, the beam is blocked and the optic moved until a new position on the surface is ready to be irradiated. The test spots on the surface are separated by a distance large enough to ensure that no debris from previously tested spots interferes with the current measurement. The damage threshold of a particular surface is defined as the average of at least 5 test spots which are typically 0.5 mm or less in diameter. In some materials there is a tendency for bulk damage due to self focusing to occur prior to observation of surface damage. Our test is only concerned with damage that occurs at the surface of the optics and in order to avoid bulk damage, the optics are tested just behind the focal plane of the lens. For the test procedure defined here, no significant differences were observed between the relative damage thresholds measured in the focal plane and the thresholds measured just behind the focus.

The substrates and coating designs of the AR-coated BK-7 reference optics have been carefully tracked and documented over the years. The relative damage thresholds have been found to be stable typically to 10-15% from batch to batch and also from part to part within a single coating run. Some specific improvements have been made including the addition of a laminar flow bench and enclosure to aid in keeping the test station and optics as clean as possible. Another important improvement increased the sensitivity of damage detection by using a video camera and display to provide image magnification of the test spot. A He-Ne laser has been incorporated into the test station to illuminate the test part and allow visual observation of surface scattering prior to testing. The current configuration of the damage test station used for production support is shown in figure 1.

3. Applications of Damage Testing to Laser Manufacturing

The test station described above is used full time for lot sample screening of incoming optics with a typical test activity of 80-100 parts per month. An equally important application is the use of damage testing for support of our current vendors and for qualification of new vendors. Before accepting a new vendor for a critical optical component, a high degree of confidence is needed in the capability of that supplier to produce quality parts on a consistent basis. One way of demonstrating this capability is for the vendor to have a record of providing high damage threshold parts on a development or qualification basis. Support of our current suppliers is another area of importance for laser damage testing. By keeping a record of trends and actual threshold values rather than just pass-fail records, a vendor's performance can be tracked on an ongoing basis. This enables us to help our suppliers avoid process related problems which can lead to a decrease in damage threshold and the eventual failure of lot samples, an occurence which is expensive for both the supplier and the laser manufacturer. When a previously qualified vendor has problems in passing our damage specifications, this sort of interaction between the vendor and a damage test facility can speed the resolution of the problem.

The volume of parts to be tested emphasizes the requirement for a test station and test procedures which are fast, reliable and capable of handling a high throughput of parts. Our production screening test has been very successful in avoiding production line failures or stoppages for damage or durability related problems. Typically, less than 1% of the optics accepted for use in production have damage related failures.

A number of changes and improvements in our damage test procedure are planned in order to provide a more standardized and well characterized test. A major change would be a shift to a damage test that is calibrated on an absolute basis. This would allow easier comparison between different test stations and would eliminate the dependence on reference optics. An unconditioned test is probably more appropriate for our laser systems and is closer to the standard procedure for most of the damage industry. The effect of conditioning is sufficiently variable in both its exact magnitude and degree of permanency [2] that it would be preferable to remove this as a variable in the test. Another desirable change would be to use a test spot on the order of 2 mm diameter to ensure that the area under test is larger than the defect spacing of the optic in question. In some cases a certification test similar to that performed for our ruby laser programs may be desirable for the YAG programs also. However, the ability to accurately measure the damage threshold will always be a useful development and problem solving tool.

The increased use of damage testing by optics vendors and laser manufacturers will have a number of desirable effects. We hope to implement a calibrated damage test which is suitable for production support activities and capable of a high throughput. If developed into an industry standard, this type of test will allow the straightforward comparison of test results from different facilities. Optics and coating manufacturers will be able to do independent testing of their products and have reasonable confidence that these products will be acceptable to their customers. Having a common language and procedure for damage testing would increase the interaction between laser manufacturers and optics vendors. This would prove beneficial to both parties and indeed to the industry as a whole. Finally a standard test format would greatly simplify the incorporation of laser damage specifications into the optics procurement process.

References

[1] Milam, D; Willis, J.B.; Rainer, F.; and Wirtenson, G.R. Determination of laser damage thresholds by comparison with an absolute laser damage standard. Appl. Phys. Lett. 38 (6): 402-404; March 15, 1981.

[2] Frink, M.E.; Arenberg, J.W.; Mordaunt, D.W. Temporary laser damage threshold enhancement by laser conditioning of antireflection coated glass. Presented at the Eighteenth Annual Sumposium on Optical Materials for high power lasers, Boulder, CO, November 1986 (proceedings to be published).

Figure 1. Schematic of laser damage test station.

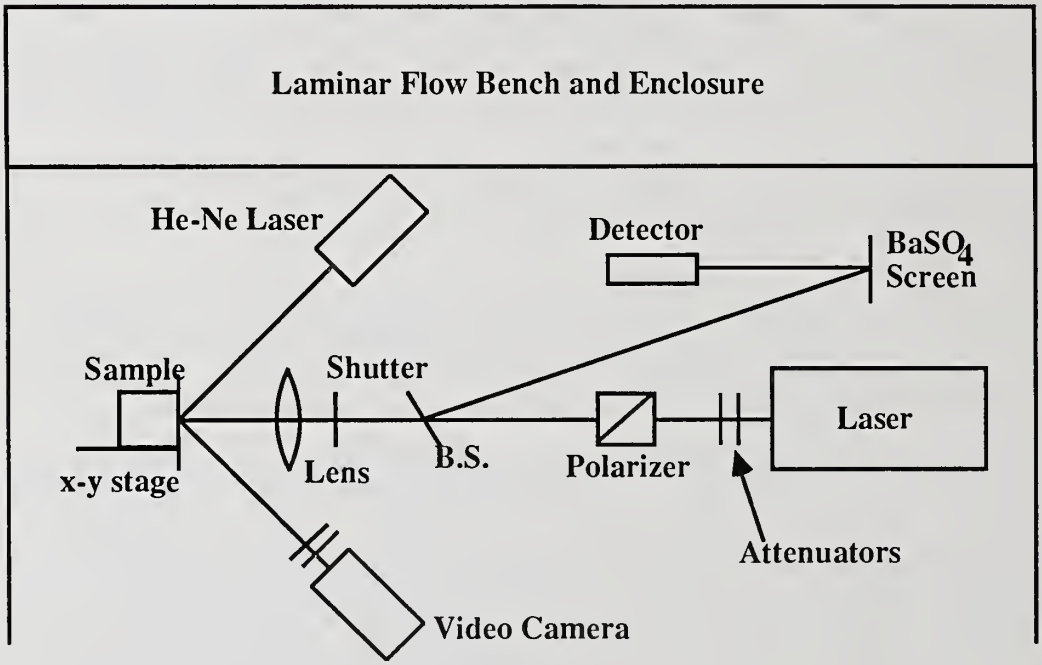

Manuscript Received
11-3-86

Laser Damage Testing at the Atomic Weapons Research Establishment (AWRE)

C J Norman

Atomic Weapons Research Establishment
Aldermaston Berkshire England

The damage testing facility at AWRE was established to support the manufacture and procurement of optical materials and coatings for the HELEN Nd glass laser system. The damage testing facility uses two laser systems both operating at 1064 nm with pulse lengths of 330 ps and 10 ns respectively. This paper describes the facility, its operation and methods of beam diagnostics. The results of damage tests are given on a variety of coatings manufactured at AWRE, from traditional multilayer dielectrics to high damage level chemically processed AR coatings. Also discussed are methods of examining and testing laser glass discs for inclusions.

Key words: Laser damage; optical coating; inclusions; beam diagnostics.

1. INTRODUCTION

The damage laser systems at AWRE are operated by the Applied Optics Group whose primary task is to support the HELEN high power laser system[1] used to investigate laser plasma phenomena relevant to weapons physics studies. The HELEN system is run at high fluence and hence requires advanced types of coatings and materials. The Optics Group is involved in the production, procurement and testing of these items.

The production capabilities of the group include facilities for grinding, polishing and optically coating a wide variety of optical components. Coatings include anti-reflection, high reflectors and filters. Although the main technique for producing anti-reflection coatings is the vacuum deposition of single and multilayer dielectric films, new techniques, which produce higher damage levels are being investigated. These include graded index processes using chemical etching (eg the neutral solution process) and a collodial silica (Sol-Gel) process.

The measurement facilities include 18" ZYGO or 16" LUPI interferometers for testing the optical quality of substrates. Also accurate measurements of coating reflectivities are made at laser wavelengths and for more detailed analysis spectrophotometer scans are performed. All coated optical components in the HELEN system have their damage threshold levels measured to reduce the chance of interruption to the shot programme due to component damage. The "short pulse" damage laser facility is used for this purpose.

LLNL have reported internal damage at high fluences in laser glass from microscopic platinum inclusions[2]. Significant improvements have now to be made to the manufacturing process. To check the new glass specification all laser glass discs will be damage tested for inclusions using a dedicated facility, a longer pulsed (10 ns) Q-switched system.

2. LASER DAMAGE SYSTEMS

2.1 Short Pulse System

The short pulse damage laser system (fig. 1) consists of a Nd-Yag oscillator producing a 300 ps Q-switched pulse which is amplified by a pair of rod amplifiers. The pulse repetition rate is 1 pps. Energy levels are varied by a combination of amplifier selection or adjustment of crossed polarizers. Following the polarizers multiple beams are produced by a pair of

angled mirrors, one high reflector and one 80% reflector. This is adjusted to produce a horizontal row of four beams for each shot, decreasing in output energy by 20% between each successive beam with a maximum energy of 6 mJ in the first beam. The beams are focussed by a 1 metre focal length lens on to the sample. By adjusting the sample vertically between shots it is possible, with variation of the laser output level, to cover a 2 mm square area of the sample with a matrix of spots 500 μm apart bracketing the damage level.

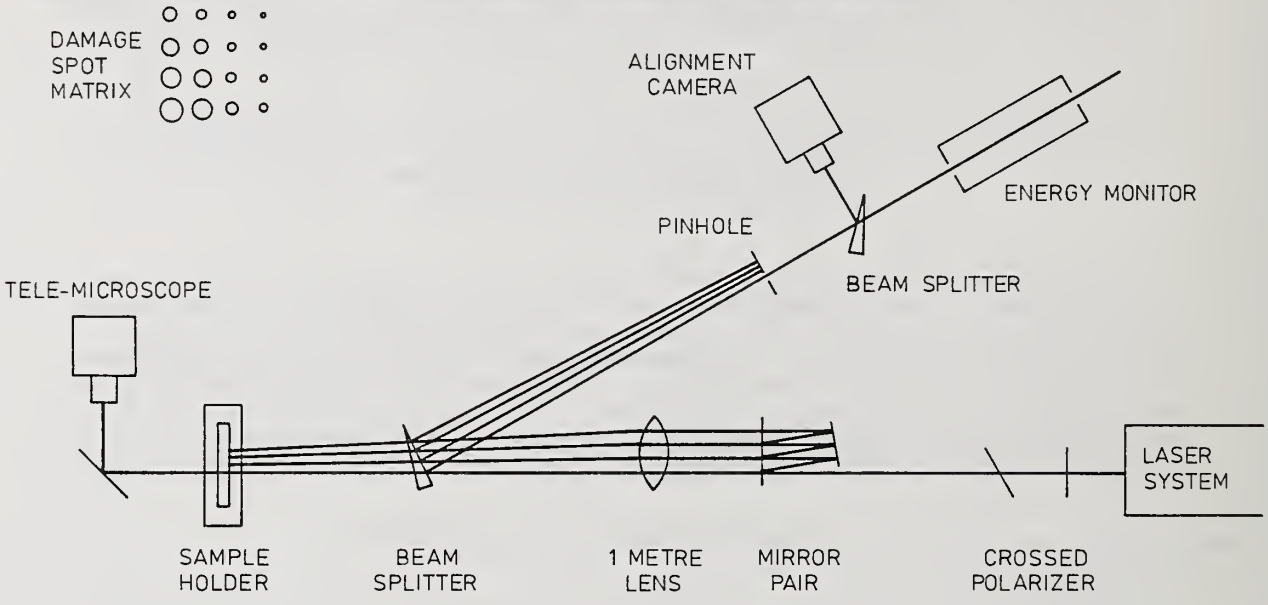

Figure 1. Short pulse damage system

The beam intensity is measured by reflecting a second series of converging spots, at an equivalent focal plane to the damage sample, using an uncoated BK7 glass wedge. The peak intensity spot is centered on a pinhole approximately 50 μ in diameter and the transmitted energy through the pinhole measured with a calibrated energy monitor. A further BK7 wedge is positioned at 45 degrees after the pinhole to illuminate a vidicon TV Camera. This has a frame store to record the transmitted beam and acts as a alignment aid for the pinhole. An additional alignment check is a measurement of the ratio between the transmitted beam and the energy level at the input to the mirror pair.

The damage surfaces are examined after each shot with a microscope mounted in-situ with dark field illumination. Precise damage levels are established subsequently to a group of shots, when the samples are removed for examination on a Zeiss microscope. This is equipped to make measurements with dark field illumination or Nomarski interference contrast.

2.1 Glass Inclusion Testing System

This system is being developed to test laser glass discs for platinum inclusions (fig. 2). The Nd-Yag laser is a Spectron type SL283 with an output of 800 mJ, a nominal beam diameter of 8 mm and a repetition rate of 10 pps. The beam is reduced with a lens and focussed on to the discs held in the scanning mount. A glass beam splitter reflects part of the focussed beam on to a pinhole and energy monitor. As with the short pulse system the pinhole is at an equivalent focus position to measure the flux distribution in the beam. Part of this reflected beam is also directed to a streak camera (measuring pulse length), and a video camera with a frame store. This records beam profiles and acts as an alignment aid.

The mount is microprocessor controlled and scans the discs at a rate of 10 mm per second horizontally and 1 mm per second vertically to produce a raster pattern. The laser beam will be shut off during the vertical movements. The mount has been designed to hold elliptical discs with a major axis up to 400 mm. Brewsters angle incidence is used to avoid Fresnel reflections and interference peaks.

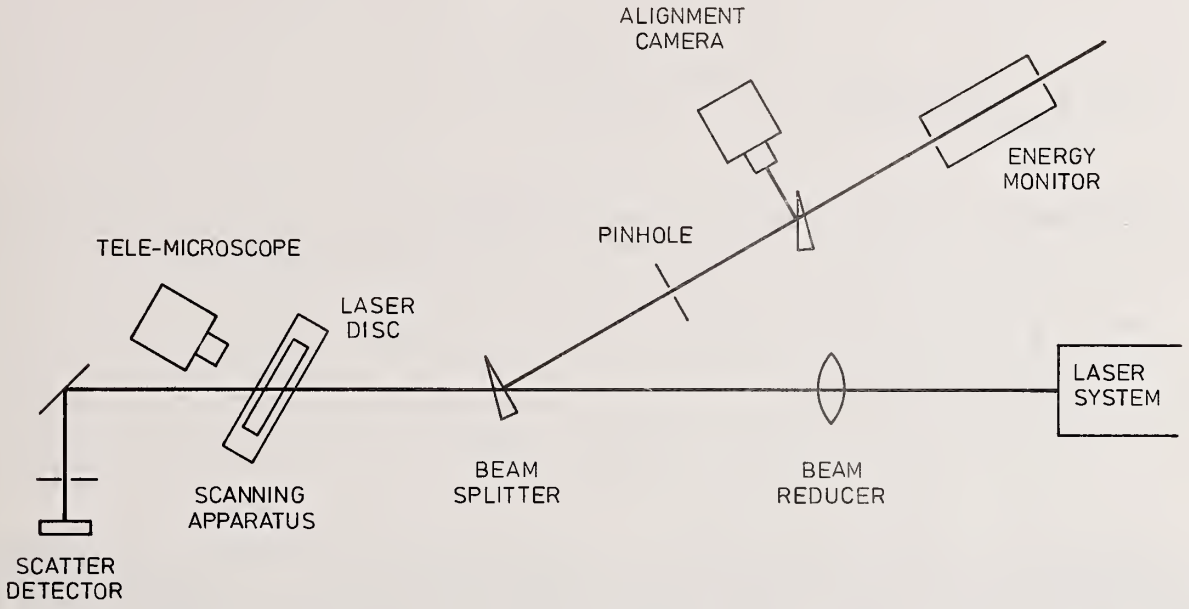

Figure 2. Glass inclusion testing system

The focussed beam has a Gaussian distribution with a peak fluence level of 11 J/cm^2 and a beam diameter of 4.3 mm at the 1/e^2 intensity level. The average fluence level over a 90% peak intensity beam diameter of .94 mm would be 10 J/cm^2. Scanning will overlap to give complete coverage of disc. Single pulses will be used at each location at the 10 J/cm^2 fluence level, however, due to the beam size and scan rate, each .94 mm site will receive 3 shots at a fluence level of 5 J/cm^2 or above along a central line of 2.7 mm diameter. The lowest damage level reported for platinum inclusions has been 2.5 J/cm^2 and the entire surface will receive 4 shots at or above this level. It has been estimated that to scan a 400 mm ellipitical disc will take four hours.

It is intended to inspect the discs visually for inclusions using scattered light. However, for the inclusion sizes of importance (between 5 and 25 microns) visual detection is difficult and time consuming so that damage laser scanning will be the primary method of detection. The discs will be examined for damage immediately after scanning with a tele-microscope mounted behind the disc. Illumination is by forward scattered light in dark ground from a HeNe or white-light fibre optic. Detectors to measure the scattered light will also be placed in this position to measure changes in intensity level due to obscuration and scattering by inclusions.

2.3 Laser Flux Density Measurement

The flux density in the damage spot is calculated from the energy transmitted by a pinhole small in diameter compared with the beam diameter. The profile can be approximated to a Gaussian and the energy distribution in a Gaussian is represented by:-

$$E = E_o \, e^{-2r^2/w^2} \qquad \ldots (1)$$

The transmitted fraction of a Gaussian through a centrally disposed pinhole is:-

$$\%T = 1 - e^{-2a^2/W^2} \qquad \ldots (2)$$

where a = aperture radius
W = $1/e^2$ radius.

Measurements on the short pulse beam gave a transmission "T" through a 53 μm pinhole of 7%. This gives a spot size of 266 μm measured to the $1/e^2$ intensity points.

The transmitted energy E(Tr) through the pinhole is given by:

$$E(Tr) = \frac{\pi w^2 E_o}{2} \left[1 - e^{-2a^2/w^2}\right] \qquad \ldots (3)$$

The pinhole diameter can be obtained to .5 μm by measurements on the Airy disc pattern. Energy moniters are used (calibrated over a range from 1 μJ to 1 J) to record the energy through the pinhole. Hence a measurement of the energy transmitted through a pinhole can yield peak intensity, average intensity and a nominal beam diameter with only small potential errors. For a small transmission the average value measured is very close to the peak. Even if the beam is distorted and not circularly symmetrical this method yields good estimates of the damage flux with errors that cannot exceed a small part of the fractional transmission.

The total energy in each of the four beams is known for each shot. Given this data and the energy density over the pinhole area, the Gaussian beam profile can be computed for each damage spot. Damage spots usually have a well defined diameter. It should be possible to measure this diameter and relate it to a corresponding width on the Gaussian intensity profile and hence calculate an accurate damage level at the edge of a damage spot. In practice this method was correct for damage spots which have diameters within 20% of the peak beam intensity and was useful in confirming results, beyond this the spots correspond to a beam with a narrower profile. Researchers at Berne University have reported similar beam profiles after measuring damage spots[3]. They concluded that the beam resembles a modified Lorentzian profile and confusing the two profiles can lead to an over-estimation of mean beam intensities by 20%. The methods used at AWRE, of measuring the beam intensity with pinholes at small diameters compared to the beam diameter, eliminates the problem of the beam being non-Gaussian below 20% of the peak.

3. LASER DAMAGE MEASUREMENTS

A wide variety of coatings have been measured on the short pulse damage system. The results are illustrated below (fig. 3).

The results given as manufacturer's coatings summarises a coating survey. Ten different suppliers were represented, they produced HR and AR coatings to a test specification but with no design or material control. There were eight high reflectors which gave results between 2.5 and 20 J/cm^2, thirteen anti-reflection coatings giving damage levels between 3 and 12 J/cm^2 and two samples of polarizers giving 6 and 12 J/cm^2.

Within AWRE anti-reflection coating techniques five between 7 and 10 J/cm^2 for cryolite, depending which plant is used and between 12 to 20 J/cm^2 for both chemically processed Sol-Gel and neutral solution coatings. A sample of a cryolite coating has been kept for 12 months, tested at regular intervals and shown constant damage levels to within a measurement capability of ± 10%.

The group have recently commissioned an electron beam plant to extend the range of materials that can be produced and preliminary results shown below on silicon dioxide and titanium dioxide are encouraging.

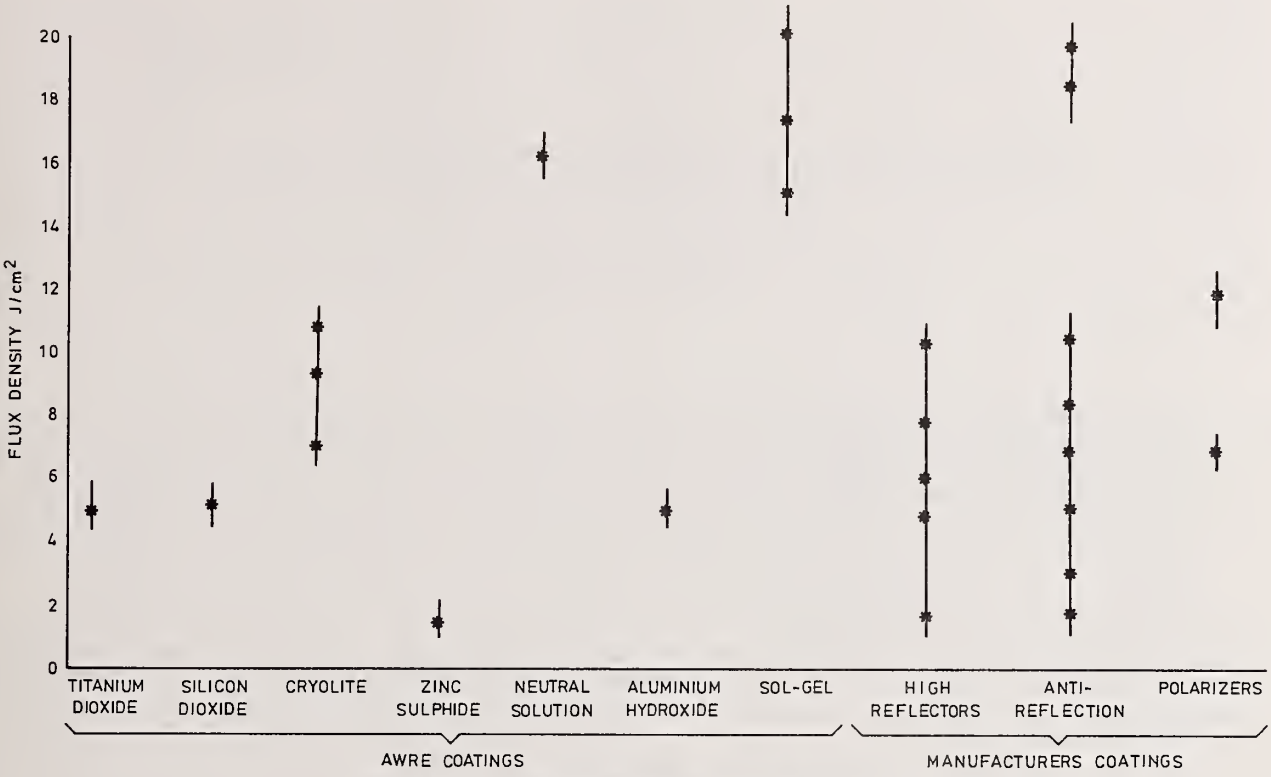

Figure 3. Damage measurements at 300 ps

4. CONCLUSION

The purpose of this paper was to describe the damage laser systems at AWRE, the methods of testing and give examples of the results. A consistant damage measurement capability has been shown with a reliable calibration technique. The work of the Optical Group at AWRE has also been mentioned since this is closely linked to the damage testing systems and promising improvements have been demonstrated in coating capability.

The HELEN system is being enlarged with the addition of two 208 amplifiers plus a separate backlighter beam. The present system is now exclusively operated at 533 nm with attendant higher 1064 nm fluence levels. This has increased the work of the group in coating production and testing. The emphasis on 533 nm reinforces the need for damage measurements at this wavelength and plans to implement a system are being considered.

The Author wishes to thank Mr D J Hunt and Mr M R Wall for their invaluable help in preparing this manuscript and to Mr M R Wall for the original method of flux density calibration. Thanks also to; Mr D Henson and Mr T Rodwell and their work with the Sol-Gel and neutral solution coatings; Mr A Smith and Mr I Odell for the evaporated coatings.

5. REFERENCES

[1] Cooke, R L; Norman, C J; Danson, C N. Beam diagnostics on the HELEN laser system at the Atomic Weapons Research Establishment (AWRE). SPIE Vol 343 Laser Diagnostics (1982).

[2] Milam, D; Hatcher, C W and Campbell, J H. "Platinum particles in the Nd:doped disks of phosphate glass in the NOVA laser". Proceedings of the Boulder Damage Conference, October 1985.

[3] Schwarzenback, A P; Weber, H P. Laser damage on Balzers thin film coatings. Applied Optics Vol 23 No. 21 P3764.

Manuscript Received
10-24-87 sar

Temperature Effects on Laser Induced Damage and Accumulation in Silicon

John R. Platenak*, Rodger M. Walser, and Michael F. Becker

The University of Texas at Austin
Department of Electrical and Computer Engineering
Austin, TX 78712

*E-Systems, Dallas, Texas

In this paper we describe an investigation of the accumulation effect in N-on-1 laser damage to silicon at 1.06 microns. Experiments were conducted on thermally annealed samples and on samples at elevated temperatures at various pulse repetition rates. Experiments on thermally annealed samples suggest accumulation is not due to any extrinsic structural defect that could be annealed at 1000°C. Experiments involving accumulation at elevated temperatures as a function fo pulse repetition rate indicate that any defect responsible for accumulation must have a lifetime of at least 1 second at 500°C. This suggests that an extended structural defect may be involved in accumulation. Results of these experiments also support a thermal melting model for laser damage to silicon at 1.06 microns.

Keywords: accumulation, silicon, temperature effects, rep rate effects

1. Introduction

If a silicon surface is not damaged by a single laser pulse, it might be expected that repeated pulse irradiation at the same fluence will also result in no damage. The reason for this would be the deterministic nature of damage to silicon by a melting mechanism. If pulsed irradiation resulted in no changes in the optical or transport properties of the silicon, then each pulse would induce the same spatial and temporal profile of temperature in the material. Thus a pulse of insufficient energy to damage could be repeated indefinitely without damaging the material. The above behavior is not found experimentally to be the case for silicon or many other materials [1-7]. In fact, laser pulses of fluence sufficiently near but below the one pulse damage fluence will initiate damage after a finite number of pulses. This effect, known as accumulation, implies that a single laser pulse in this fluence range results in a change in the optical absorption and/or the energy transport characteristics of silicon.

It has not been previously established whether the accumulation effect, in laser damage to silicon, is due to an intrinsic property of the material such as laser induced structural defects, extrinsic defects already present in the material, or a combination such as laser induced changes in defects already present. Although a precise characterization of the accumulation effect is difficult due to the wide variety of defects possible in a crystalline material, we have obtained some information about the effect through temperature dependent damage experiments. Laser damage studies of thermally annealed samples identify the contribution of any defects already present in the material. Studies of the pulse repetition frequency dependence of the accumulation effect, especially at elevated temperatures, establish the time scale over which the accumulated specie exists and help to narrow the possible explanations of the effect.

2. Samples and Experimental Setup

The silicon samples used in these experiments were n-type, <111> orientation wafers with a resistivity of 10 to 40Ω -cm. The wafers were cut from Czochralski grown boules, polished on one side, and had a finished thickness of 10 to 18 mils and a diameter of two inches. The samples were cleaned before experiments by boiling for five minutes followed by ultrasonic cleaning for two minutes successively in the solvents trichloroethelyne, acetone, and methanol. The wafer was then rinsed in de-ionized water and air-dried.

The experimental arrangement is shown in figure 1. All the experiments were conducted at a wavelength of 1.064 microns using a Quantel Model YG-580-10 Q-switched Nd:YAG laser with a

full width half maximum (FWHM) pulse length of 10 nanoseconds. The repetition rate of the pulses was 10 Hz in most cases, but could be changed to 5 or 2 Hz by interrupting the Q-switch trigger signal. The repetition rate could also be computer controlled to any integral divisor of 10 Hz using the computer controlled data aquisition system to shutter off any number of pulses between the applied pulses. The incident beam was focused using a 460 millimeter focal length lens. By using a computer controlled knife edge scan, the spot size at the sample plane was determined to be 340 microns in diameter. The spot size was measured three to five times before any series of experiments in one day. The measured size had a standard deviation of about 6% for individual measurements. The day to day variation of spot sizes, determined by averaging three to five daily measurements, was only 2%; about what would be expected for the standard deviation of the mean. Although the laser output energy fluctuated from pulse to pulse, the standard deviation for a train of pulses was typically less than 2%. The incident energy of a pulse could be adjusted by the rotation of a half-wave plate located in front of a thin film polarizer. The polarization selected for transmission was with the electric field vector horizontal.

An IBM PC-XT with Metrabyte data acquisition and control interfaces was used for computer controlled data acquisition. Trigger signals for experimental timing were generated from a silicon photodiode sampling part of the laser output energy. The computer controlled an electromechanical shutter through a digital I/O port. A portion of the incident beam was split off and measured by a reference energy meter. This reference meter was calibrated several times daily against an energy meter in the direct line of the incident beam. Energy data for each shot incident on the sample were saved in data files for future analysis.

Damage at an irradiated site was established by post-experiment observation of the sample under a Nomarski microscope. In virtually all experiments, energy fluence was varied for a fixed number of pulses to determine the damage threshold at that pulse number. Depending on the fluence and number of pulses applied to a particular site the damage could be observed without magnification or at 50, 100, 200 or 500 power magnification. In almost all cases damage not observable at 200X was also not observable at 500X and thus for practical purposes the presence or absence of damage for a particular site could be established at 200 power magnification.

Experiments at elevated temperatures were conducted using a laboratory-built heat stage. The heat stage held the silicon sample to a quartz plate which was in direct contact with a heating element composed of a total of 20 ohms of 24 gauge nichrome wire wrapped in 20 turns around another quartz plate. The entire assembly was mounted to an aluminum frame which was attached to a translation stage. The actual sample temperature was monitored with a thermocouple and controlled by switching the power applied to the stage on and off with a digital temperature controller. The on power level applied to the heating element was manually adjusted using a variac and was normally fixed for experiments at any given temperature. The rise time to the experiment temperature was typically in the range of 3 to 5 minutes. Temperatures were controlled to ± 1C.

3. Experimental Results and Discussion

The accumulation effect, a reduction in the damage threshold for multiple pulses, has been observed before for laser irradiation of silicon at 1.064 microns with pulse lengths in the picosecond regime [5]. The effect has also been observed for pulses 5 nanoseconds in length [6] and now for pulses of 10 nanoseconds in length. These latest results are shown in figure 2 which shows a plot of the fluence necessary to cause a 50% probability for damage in a specified number of pulses versus that number of pulses. It is seen that the multiple pulse damage threshold reaches a lower limit of about 70% of the one shot threshold; this limit is effectively reached at around 30 pulses. The same data is plotted in a different manner in figure 3. A plot of the logarithm of accumulated fluence versus the logarithm of number of pulses has been used previously to investigate the accumulation effect in several materials [5,7]. For both metal mirrors and the picosecond irradiation of silicon two separate slopes were needed to fit the data in the single and multiple pulse limits. As can be seen in figure 3, the current data falls on a single line.

It can readily be shown that the accumulation effect is not due to any extrinsic defects in the silicon sample. Figure 4 demonstrates the results of laser damage experiments on thermally annealed samples. Shown on the bar graph are the ratio of thirty shot to one shot damage thresholds for annealed samples. This ratio is used as a measure of the amount of accumulation since the individual one and thirty shot thresholds vary by as much as 10% from wafer to wafer. Determined thresholds also vary from day to day by as much as 3% even for identical experiments since there are errors due to pulse to pulse energy variations, spot size determinations and energy calibrations. In all cases, for any given sample the one and thirty shot damage thresholds in

these experiments are determined in the same period of time. This minimizes any errors in determining the amount of accumulation effect in a sample; and then by taking a ratio of thirty and one shot thresholds, comparisons between different samples may be done most effectively. The thirty shot threshold for damage relative to the one shot threshold is used as a convenient measure for accumulation since it requires experiments with not too large a number of pulses, and yet the thirty shot threshold appears to be very close to the minimum multiple pulse damage threshold in these experiments.

The ratio of thirty shot to one shot damage thresholds at room temperature for four different samples at various stages of annealing are plotted in figure 4. The native sample value appears as the leftmost member of a series and the annealing temperature in degrees centigrade and time in hours are given for the other members of the series. The letter identifies a series of samples from the same wafer. In general the accumulation for a sample seems relatively independent of the annealing conditions. This is supported by several facts. Any variations in the thirty to one shot thresholds over a series of annealings are no larger than random variations in this value found in repeated experiments on a single sample which has not undergone any annealing treatment. The range over which the ratio varies for different experiments on identical samples is approximately ± 5%. Although in the series of annealed samples for wafers E and N there seems to be a general trend for the ratio to increase, wafer S annealed for one hour at 1000C in a nitrogen atmosphere shows no increase in the ratio. If any annealing of extrinsic defects responsible for accumulation were taking place at a temperature below 1000C they should be annealed even more completely at the higher temperature. This is supported by extensive data available for defect annealing in silicon where more complete annealing at higher temperatures is the general trend [8]. It should be noted that annealing at temperatures below 1000C was not conducted in an inert atmosphere, but at the temperatures investigated this should not present any problems due to lack of growth of significant amounts of oxide at these temperatures over short times. Therefore it can be concluded that the accumulation effect in silicon is not due to any extrinsic defect, at least not one that can be thermally annealed. This covers a broad range of defects in silicon and thus the accumulation effect seems to be a fundamental property of the material and not a relic of sample preparation.

Other experiments were conducted to help identify the nature of the defect responsible for accumulation in silicon. The central objective of these experiments was to observe a change in the amount of accumulation as a function of temperature or as a function of pulse repetition frequency (PRF). As mentioned previously, no PRF dependence was found for laser damage studies of silicon with 60 picosecond pulses, [7] even though it had been observed in other materials [1,4,9]. The lack of a PRF dependence of accumulation in silicon suggests a long-lived defect responsible for the effect. In an attempt to observe PRF dependence, laser damage studies of silicon samples at elevated temperatures were undertaken. It was hoped that by elevating the temperature the lifetime of the defect responsible for the accumulation would be reduced sufficiently to bring about a PRF dependence, and eventually at high enough temperatures (short enough lifetimes) to reduce the magnitude of the accumulation effect. If the lifetime of accumulation at several temperatures could be determined through PRF dependent experiments, then annealing kinetics of the defect responsible for accumulation could be established. This could then serve to identify the defect.

Figure 5 shows a plot of damage threshold fluence for one and thirty shots as a function of temperature. The line on the graph is a curve representing the threshold fluence to induce melting in silicon as a function of temperature calculated from theory presented by Meyer, et al. [10]. The theory will be discussed more completely in section 4 of this paper, but it is important to note that the theory applies to uniform irradiation. For a Gaussian beam the irradiation intensity varies over the beam. The line in figure 5 gives the average beam fluence (corresponding to the use of average fluence for experimental points $F_{av} = E/\pi w_o^2$) for a beam which has a fluence above the uniform melting threshold over a diameter of 116 microns. This is for a beam with $1/e^2$ diameter of 340 microns. The placement of the calculated curve can be adjusted by selecting different values for the diameter of the beam which is above melt threshold. A diameter of 116 microns shows a good fit to the data at high temperatures. This value also agrees well with the observation of melt rings with diameter approximately 120 microns for spots irradiated near threshold at these temperatures. It is not known why smaller melt rings are not observed with a correspondingly lower threshold fluence.

It is also seen in figure 5 that the shape of the calculated curve fits the experimental data quite well except for some small deviation at the lower temperatures. This suggests a damage by melting mechanism with the possible exception of the lower temperatures. There are other mechanisms that could be contributing at the lower temperatures. One possibility is that thermally

induced stress beyond the yield point could occur due to the laser pulsing and cause damage before the melt threshold can be reached. This would be consistent with the larger thermal excursions and larger stresses involved in going from a lower initial temperature towards the melt onset. It is also consistent with some observations of damage morphology as a function of temperature.

The photographs in figures 6-11 show damage spots at different temperatures all at 500X magnification. The magnification is slightly less than 500X as printed, and the ripples visible in most of the figures have a 1.06 micron period. In each photograph the damage spot is caused by 30 shots at a fluence near the 1 shot damage threshold at that particular temperature. Table 1 gives the temperatures, the one shot damage threshold at that temperature, the average fluence of the thirty shots causing the damage spot shown and the corresponding figure number. The application of 30 shots at the one shot damage threshold at an given temperature results in a decreasing amount of damage as temperature increases. At room temperature, 30 shots applied at the one shot damage threshold caused the ejection of significant amounts of silicon, creating a large crater. At 100C, 30 shots applied at the 100C one shot damage threshold resulted in ripple patterns as well as some areas of more severe surface disruption. However, no material appears to be ejected in this case. Between 200C and 400C, damage from 30 shots at the one shot threshold consisted primarily of a ripple pattern. A melt boundary ring may also be observed in some cases. Figure 9 is particularly interesting in that the ripple pattern seems to end at the edge of the melt ring. This suggests that ripple formation occurred only in melted areas.

TABLE 1

T(°C)	$F_1(J/cm^2)$	$\langle F \rangle (J/cm^2)$	Figure
20	1.73	1.74	6
100	1.27	1.27	7
200	0.99	1.02	8
300	0.82	0.84	9
400	0.62	0.64	10
500	0.48	0.51	11

<F> is the average fluence applied at a given temperature to give the damage spot shown in the indicated figure. Also given is the one shot damage threshold at that temperature for comparison. <F> is about 120% of the damage threshold for N = 30.

It should be noted that when ripple patterns are observed, they consist of ridges running perpendicular to the incident electric field. These features have been widely observed in laser damaged silicon. One damage spot with a nicely developed pattern of ridges was used to measure the spacing of the ridges. The number of ridges over a length of 35 millimeters was counted to be 66, giving a ridge spacing of 1.06 microns in excellent agreement with the free space wavelength of the incident radiation. This spot was not unique in any other way and is not shown here.

Figure 11 shows the damage pattern resulting from 30 shots at the 500C one shot damage threshold. At 500C the damage morphology consists of a melt ring and a faint indication of ripple formation. Figures 6 through 11 demonstrate a clear trend. The continued application of pulses at the 1 shot damage threshold at any given temperature results in less damage for increasing temperatures. At the higher temperatures the surface is merely melted and deformed by the incident damaging pulses while at room temperature the pulses violently boil material from the surface. This implies a greater ability to resist damage propagation at the higher initial temperatures. Whatever mechanism is responsible for the tendency to catastrophic damage propagation at room temperature could also be responsible for sub-melt threshold damage at room temperature. One possibility is sub-melt threshold damage at room temperature due to thermally induced stress. Another possibility is an apparently greater tendency to inhomogenous damage at the lower temperatures. While damage by melting produces a melt ring and relatively little surface disruption, a more intense surface disruption is evident in figure 7 at 100C. This could be due to a local superheating or even boiling of the material. This tendency to heterogeneous nucleation is observed only at 100C and below, and it could explain sub-melt threshold damage.

The initial objective of these temperature dependent experiments was to reduce the magnitude of the accumulation effect by reducing the lifetime of the accumulated specie to the order of the dwell time between laser pulses. If the lifetime of the accumulation were sufficiently short

it would completely anneal between laser pulses and thus the thirty shot threshold would approach the one shot threshold. Figure 12 shows the ratio of the thirty to one shot thresholds as a function of temperature. No significant trend for the increase of this ratio with temperature was found. In fact, the smallest value of this ratio other than the room temperature value was found at 500C. In no case did the ratio approach one, the limiting value for complete annealing of accumulation between pulses. As before, the variability of the ratio does not appear significantly larger than the uncertainty in its determination.

Some caveat must be made about the possibility of the thirty shot threshold approaching the one shot threshold. In determining the thirty shot threshold, the individual pulses in the train of thirty had a standard deviation in energy < 2%. Thus even if the one and actual thirty shot thresholds were the same, a thirty shot sequence of average energy equal to the threshold would have some shots above threshold. These shots would have a greater probability to damage. Therefore the determined thirty shot threshold would be slightly below the determined one shot threshold. This effect does not seem to present a problem or contradict the conclusions derived from figure 12. In table 2 the one and thirty shot thresholds as a function of temperature are given. Also given are the average and maximum fluence of a thirty shot sequence with average fluence close to the thirty shot threshold. In no case does any one shot for a sequence with average fluence near the thirty shot threshold approach the one shot threshold. Thus the data of figure 12 are a significant indication of accumulation and are not just a result of the statistical distribution of the incident pulse fluences.

TABLE 2

T(°C)	F_1	F_{30}	$\bar{F}$	$F_{x,max}$
20	1.73	1.45	1.47	1.52
100	1.27	1.17	1.17	1.20
200	0.99	0.86	0.87	0.90
300	0.82	0.71	0.70	0.73
400	0.62	0.55	0.55	0.57
500	0.48	0.41	0.42	0.43

All fluences are in units of J/cm^2.

Although the independence of the ratio of thirty to one shot damage thresholds with respect to temperature indicates a lack of reduced accumulation lifetime, independent means of verification were conducted. Specifically, the PRF dependence of this ratio was investigated at 300C and compared to similar experiments at room temperature. Figure 13 shows the results of the room temperature experiment. The thirty shot damage threshold is determined to be independent of dwell time between laser pulses (the inverse of the pulse repetition frequency) over a range of one tenth to one second. If the lifetime of the accumulation were anywhere in this range there should have been a dependence. This result agrees with that of Jhee [7] for similar experiments on silicon with pulses 60 picoseconds in length. Rather than decrease the PRF to inconveniently low values (long experiment times), a similar experiment was performed at a higher temperature, 300C. Figure 14 shows the results of that experiment. Here, the thirty shot damage threshold seems to have a small dependence on pulse repetition frequency. But once again it must be noted that the variation in the thirty shot damage threshold is not much larger than random variations in its determination.

The independence of the thirty shot threshold on PRF at room temperature sets a lower limit on the lifetime at that temperature of about 3 seconds. Additionally, if there actually is dependence on PRF at 300C then the upper limit on the lifetime at that temperature is about 1 second. These two limiting values may be used to establish a minimum activation energy for any defect responsible for accumulation. Assuming first order kinetics, the dependence of the rate of annealing on temperature should follow the equation:

$$\text{rate} = A \exp[-E_a/kT] \quad . \tag{1}$$

Using the inverse of the limiting values of the lifetime at the two temperatures as an estimate of the limiting values of the rate at those temperatures, the equation may be solved for E_a and A. The result is a minimum activation energy (E_a) for the accumulation defect of 0.13 eV and

a minimum value of the pre-exponential factor (A) of 56 inverse seconds. These are absolute minimum values derived from the PRF dependent data. The value for A may be unrealistically low; and longer values of the defect lifetime at room temperature would give a larger value for the pre-exponential factor and a larger activation energy. Even for the minimum value of activation energy, an extrapolation of the lifetime to 500C would give a maximum value of 0.12 seconds. A lifetime this short would certainly affect the ratio of the thirty to one shot damage thresholds at that temperature.

The PRF dependence experiment was repeated at 500C and the results are shown in figure 15. Since no PRF dependence was observed, it must be concluded that the data for the thirty shot threshold at 300C is not actually PRF dependent. The variation in the thirty shot threshold at 300C must be explained by uncertainties in its determination. The data at 500C suggests that the lifetime of the accumulated specie is greater than 1.0 seconds at this temperature. Thus the defect responsible for accumulation is not only long-lived at room temperature, but difficult to anneal even at 500C.

The lack of ability to anneal the accumulation effect on a short time scale at any of the temperatures investigated prevents determining its annealing kinetics, thus eliminating the possibility of firmly identifying the defect responsible for accumulation. However, the persistence of accumulation over a lifetime of at least one second even at 500C eliminates the possibility of any simple low energy defect being responsible for the effect. More likely, any mechanical defect responsible for accumulation must be rather complex and difficult to anneal. It is interesting to note that even though silicon seems to have a greater ability to resist damage propagation at high temperatures, as judged from damage morphology; accumulation still exists in heated samples. Apparently, the mechanism by which damage increases for multiple pulses above the one shot damage threshold is at least partially independent of the mechanism by which accumulation is induced below the one shot threshold.

4. Theory

The theory used to calculate the melting fluence of silicon as a function of the initial temperature was presented by Meyer, et al. [10]. The problem is one of solving the heat and excess carrier diffusion equations self-consistently. An exact solution can only be ahcieved numerically, but some approximations allow for considerably simplified calculations. The approximations are to initially exclude thermal diffusion and surface recombination and then to reincorporate them phenomenologically after the coupled diffusion equations have been solved. However, for silicon, surface recombination is negligible [11]. Incorporating thermal diffusion phenomenologically could present problems, especially at low initial temperatures. The carrier density is assumed to be in steady state since at high carrier densities the free-carrier lifetimes are shorter than the laser pulse duration. This approximation should be valid in this case since free-carrier lifetimes are calculated to be at least a factor of 2 shorter that the 10 nanosecond pulse duration. The last significant approximation is to let the temperature as a function of depth be approximated by its value at the surface. This should be good for silicon where surface recombination is negligible.

The above approximations lead to the following closed form expression for the power necessary to melt a semiconductor [10]:

$$P_o = \frac{\rho\, c(T_o)\, \Delta T L_h}{[1-R(T_o)]\, t_p} \qquad (2)$$

where P_o is the power density required to heat the semiconductor from initial temperature T_o to final temperature T_f, Δ is the mass density, c is the gram specific heat, ΔT is $T_f - T_o$, R is the reflectivity and t_p is the length of the laser pulse. The quantity L_h is given by the following equation:

$$L_h = \frac{1-R(T_o)}{c(T_o)\, \Delta T} \int_{To}^{Tf} \frac{c(T)\, dT}{(1-R)\, \alpha} \left[\frac{X_T}{L_t \alpha + 1} + X_o^{NR} / (L_t \alpha + Ld \alpha + 1) \right] \qquad (3)$$

where α is the total optical absorption coefficient including one photon and free carrier absorption, L_d is the free-carrier diffusion length and L_t is the thermal diffusion length. χ_T and χ_S are the fraction of laser energy which go into thermalization of excess carriers and non-radiative bulk recombination respectively. For silicon it is assumed that there is no surface recombination and the reflectivity is independent of temperature. The temperature independence of the reflectivity has been confirmed indirectly, but conclusively, by the irradiation fluence dependence of silicon reflectivity [12]. The temperature dependence of all other material parameters are taken from theoretical and empirical equations presented in [11]. These equations are used to numerically evaluate the integral for L_h.

A computer program was written to utilize the above theory in a calculation of the power density required to melt silicon as a function of initial temperature. Then energy fluence damage threshold is the power denisty damage threshold multiplied by the pulse length. Since the power density enters into the calculation for L_h through free carrier generation and absorption, eq (2) for the power density to melt must be solved iteratively.

A correction factor was alluded to when the this calculation was discussed previously in section 3. A factor of 1.5846 is divided into the calculated fluence to melt for uniform irradiation. This gives the average fluence for a Gaussian beam of waist diameter 340 microns in which a fraction of the beam of diameter 116 microns has fluence greater than the uniform fluence threshold. This factor may be calculated as follows. The intensity profile of a beam of average intensity A is:

$$I = 2A \exp[-2(r/w_0^2] \ . \tag{4}$$

To have a beam of radius r with power above the uniform threshold intensity B requires:

$$2A \exp[-2(r/w_0)^2] > B \ . \tag{5}$$

This results in the equation for the correction factor:

$$\text{correction factor} = 2 \exp[-2(r/w_0)^2] \ . \tag{6}$$

Substituting r = 116/2 and w_0 = 340/2 gives the correction factor 1.5846.

5. Conclusions

The experiments described in this paper have firmly established several aspects of the accumulation effect in laser damage to silicon which were previously not known. Accumulation is a fundamental property of laser interactions with silicon and not a product of sample preparation. This is indicated by the presence of accumulation even in samples annealed up to 1000C prior to damage experiments. This level of annealing removes virtually all defects that would be generated in the silicon as a result of sample preparation. Although some defects such as impurities cannot be removed by annealing, if these are involved in the accumulation effect it is only through pulse-by-pulse changes that this is brought out. There is some indication that an extrinsic defect may be involved in the accumulation effect. This is because the ratio of thirty shot to one shot damage thresholds is found to vary from sample to sample. This in turn requires that the samples in some way be distinct from one another. Possible differences from sample to sample include doping and other impurity levels. Structural defects are not a likely explanation for sample to sample variations since these variations are not affected by the high temperature annealing.

The defect responsible for accumulation was found to have a long lifetime, even at high temperature. The pulse repetition frequency independence at 500C indicates a lifetime of at least 1 second at that temperature. The actual lifetime at this temperature could be considerably longer, this is only an absolute lower limit.

Another result of our experiments is temperature dependent data which supports a melting model for laser damage to silicon with 10 nanosecond pulses. This temperature dependent data is also important in that damage morphologies at high temperatures suggest a greater ability to resist damage propagation at these temperatures. This is in sharp contrast to the independence of accumulation from 20C to 500C. It requires that the mechanism for growth of damage have a temperature dependence different from that of accumulation. This suggests completely different mechanisms for accumulation and the growth of visible damage.

Accumulation in silicon almost necessarily involves some change in the optical absorption or energy transport properties of the material through the action of sub-damage laser pulses. This is required to explain the reduced multiple pulse damage thresholds observed. Alternative explanations of the effect are contradicted by observed damage morphology. In these experiments, near threshold damage morphologies almost always appeared as homogeneous melt rings. This is in contrast to the heterogeneity observed for damage growth at temperatures below 100C.

Since impurities or dopants have been suggested as possible contributors to accumulation, a systematic study of the amount of accumulation present in a sample as a function of these species concentrations would be useful. Such a study would complement this one either by completely eliminating extrinsic defects from the mechanism for accumulation or firmly establishing the importance of compositional defects. It would be instructive to sensitively measure the optical properties of silicon which has undergone sub-damage threshold irradiation. This could help identify one possible mechanism by which accumulation could lower the damage threshold. The related mechanism of accumulation dependent energy transport could be investigated also. Thermal transport is not likely to be affected greatly by any non-visible defect in the silicon. However, carrier transport could be greatly affected by even small defects in the material. Therefore, sensitive measurement of the carrier transport properties of sub-damage threshold irradiated silicon would help identify the mechanism for lower damage thresholds in laser irradiated silicon. It is now clear that such experiments should be possible, since the lifetime of accumulation must be very long at room temperature. Using a minimum value for the lifetime at 500C of 1 second and a reasonable activation energy of 1 eV, the lifetime of accumulation is estimated to be at least 10^{10} seconds at room temperature.

This research was supported by the Texas Advanced Technology Research Program.

6. References

[1] E.K. Maldutis, S.K. Balickas, and R.K. Kraujalis, "Accumulation and laser damage in optical glasses," NBS Spec. Pub'l. 638, 96 (1981).

[2] S.N.Zhurkov, S.B. Eron'ko, and A. Chmel', "Thermal fluctuation origin of the optical strength of transparent insulators," Sov. Phys. Solid State 24, 414 (1983).

[3] R.M. O'Connell, T.F. Deaton, and T.T. Saito, "Single- and multiple-shot laser-damage properties of commercial grade PMMA," Appl. Opt. 23, 682 (1984).

[4] L.D. Merkle, "Multiple pulse bulk laser damage of transparent materials," Int'l. Conf. on Lasers '84, (1984).

[5] Y.K Jhee, M.F. Becker, and R.M. Walser, "Charge emission and precursor accumulation in the multiple-pulse damage regime of silicon," J. Opt. Soc. Am. B 2, 1626 (1985).

[6] M.F. Becker, F.E. Domann, A.F. Stewart, and A.H. Guenther, "Charge Emission and Related Precursor Events Associated with Laser Damage," NBS Special Publication #688 p. 429 (1983).

[7] Y. Jee, M.F. Becker, F.E. Domann, A.F. Stewart, and A.H. Guenther, "Charge Emission and Related Precursor Events Associated with Laser Damage," NBS Special Publication (1983).

[8] S.K. Ghandi, VLSI Fabrication Principles, Wiley-Interscience, New York, 1983.

[9] R.M. Wood, S.K. Sharma, and P. Waite, "Variation of laser induced damage threshold with laser pulse repetition frequency," NBS Spec. Pub'l. #669, 44 (1982).

[10] J.R. Meyer, F.J. Bartoli, and M.R. Kruer, "Optical heating in semiconductors," Phys. Rev. B 21, 1559 (1980).

[11] J.R. Meyer, M.R. Kruer, and F.J. Bartoli, "Optical heating in semiconductors: laser damage in Ge, Si, InSb, and GaAs," J. Appl. Phys. 51, 5513 (1980).

[12] J.M. Liu, H. Kurz, and N. Bloembergen, "Picosecond time-resolved plasma and temperature-induced changes of reflectivity and transmission in silicon," Appl. Phys. Lett. 41, 643 (1982).

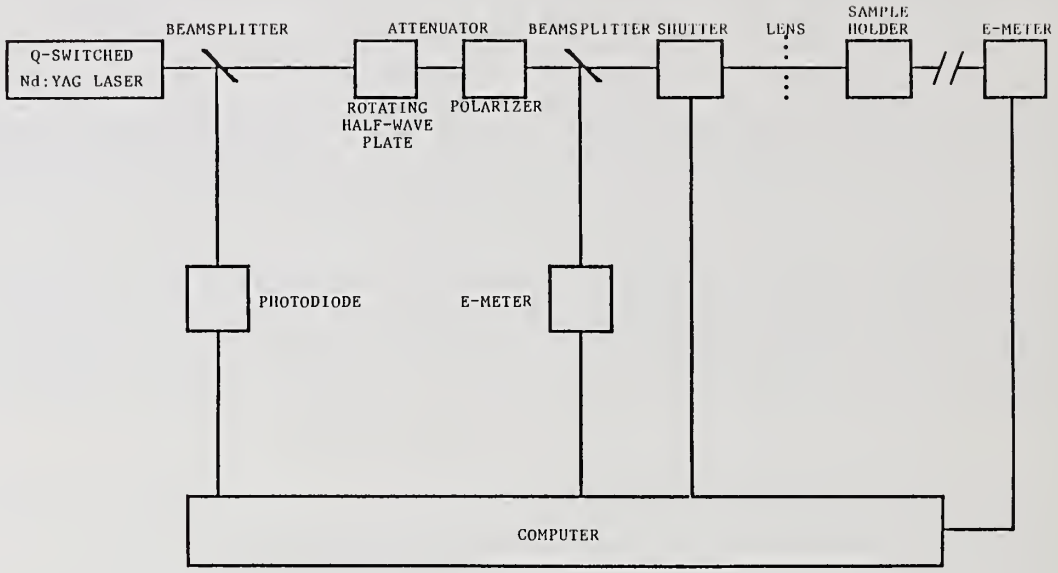

Fig. 1 Experimental set up.

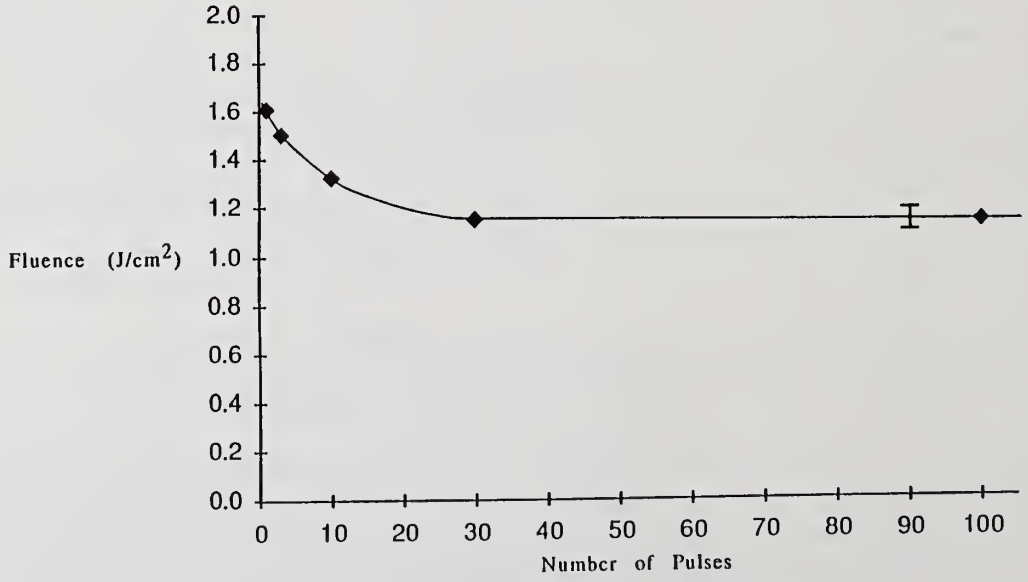

Fig. 2 50% damage probability fluence versus number of pulses.

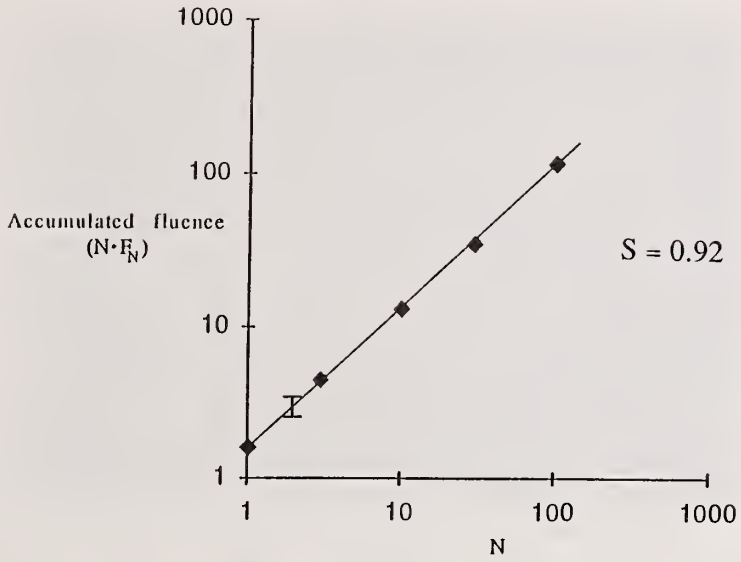

Fig. 3 Accumulated fluence versus number of pulses.

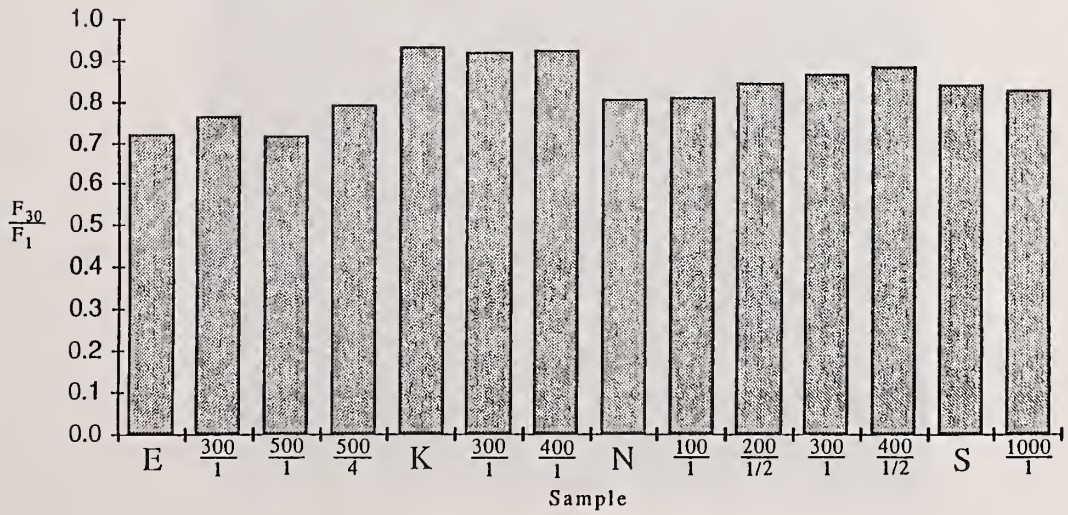

Fig. 4 Ratio of 30 shot to 1 shot damage thresholds for different samples and annealing cycles. Letters denote a series of samples from the same wafer, and numbers denote anneal temperature over anneal time in hours.

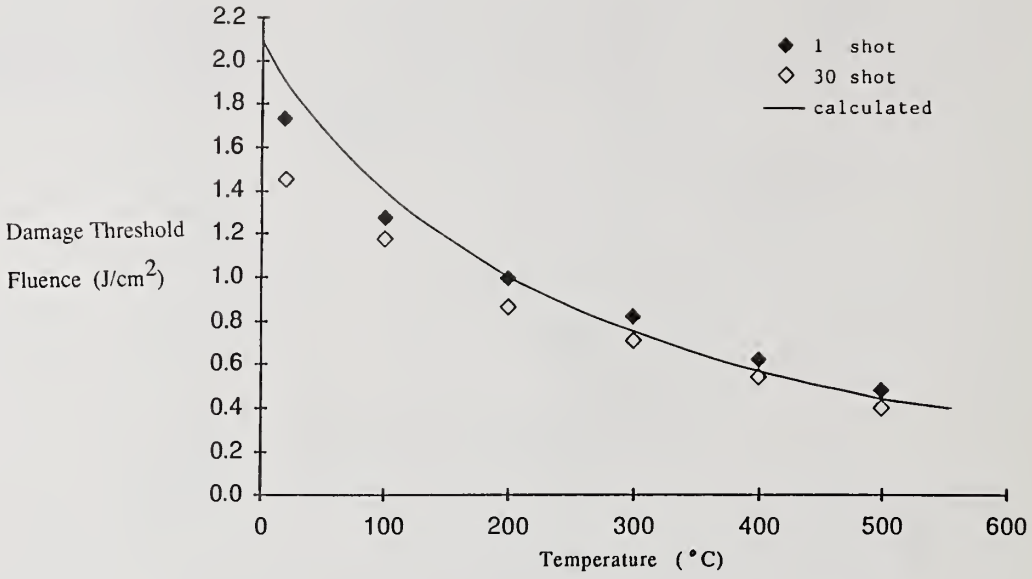

Fig. 5 Thirty and one shot damage thresholds versus temperature.

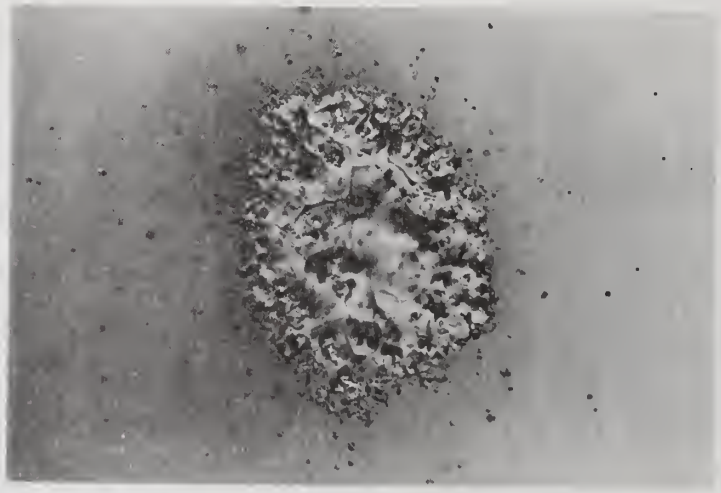

Fig. 6 Damage due to 30 shots of 1.74 J/cm^2 at 20C.

Fig. 7 Damage due to 30 shots of 1.27 J/cm^2 at 100C.

Fig. 8 Damage due to 30 shots of 1.02 J/cm^2 at 200C.

Fig. 9 Damage due to 30 shots of 0.84 J/cm^2 at 300C.

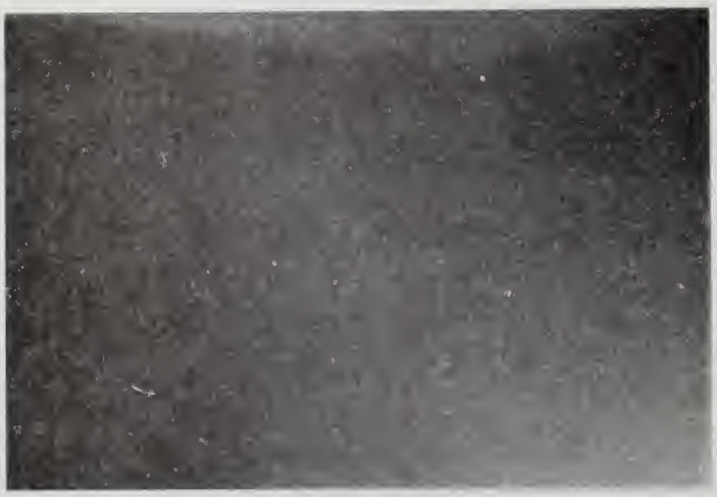

Fig. 10 Damage due to 30 shots of 0.64 J/cm^2 at 400C.

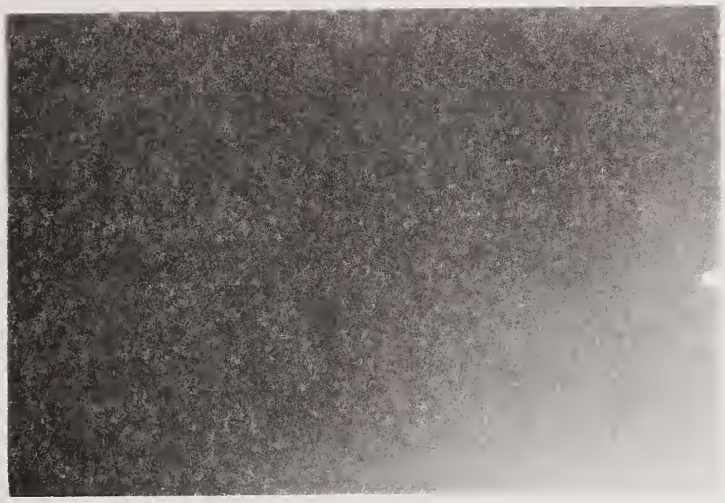

Fig. 11 Damage due to 30 shots of 0.51 J/cm^2 at 500C.

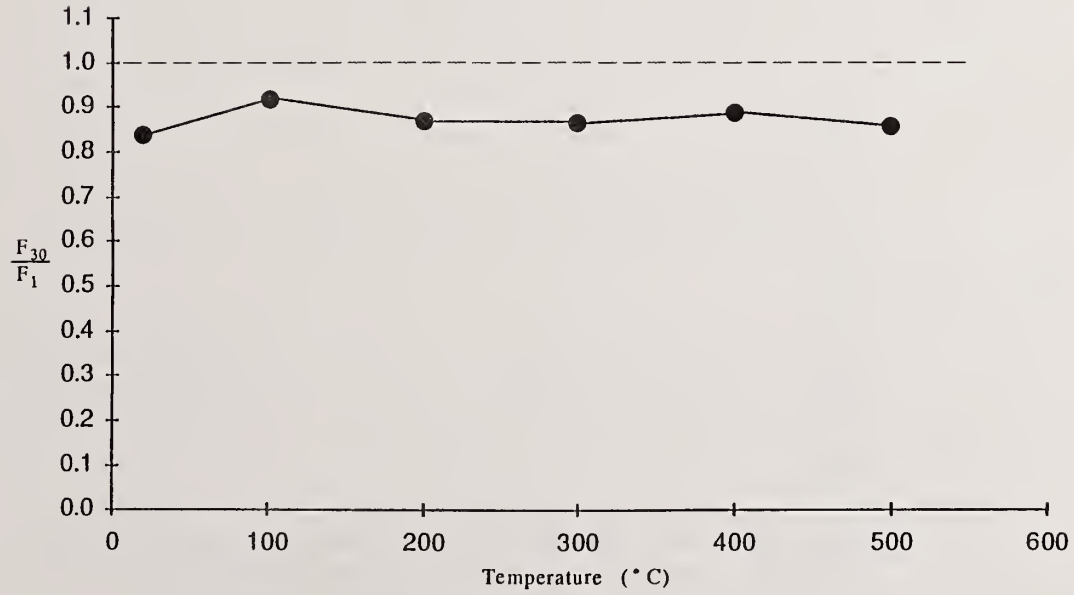

Fig. 12 Ratio of 30 shot to 1 shot damage thresholds versus temperature.

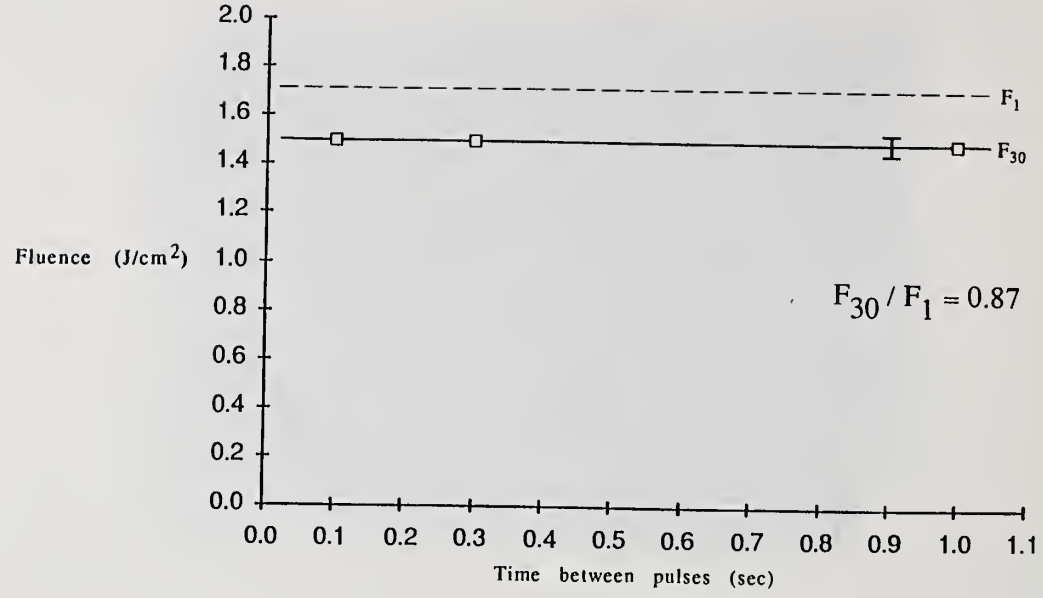

Fig. 13 Thirty shot damage threshold versus time between pulses at 20C.

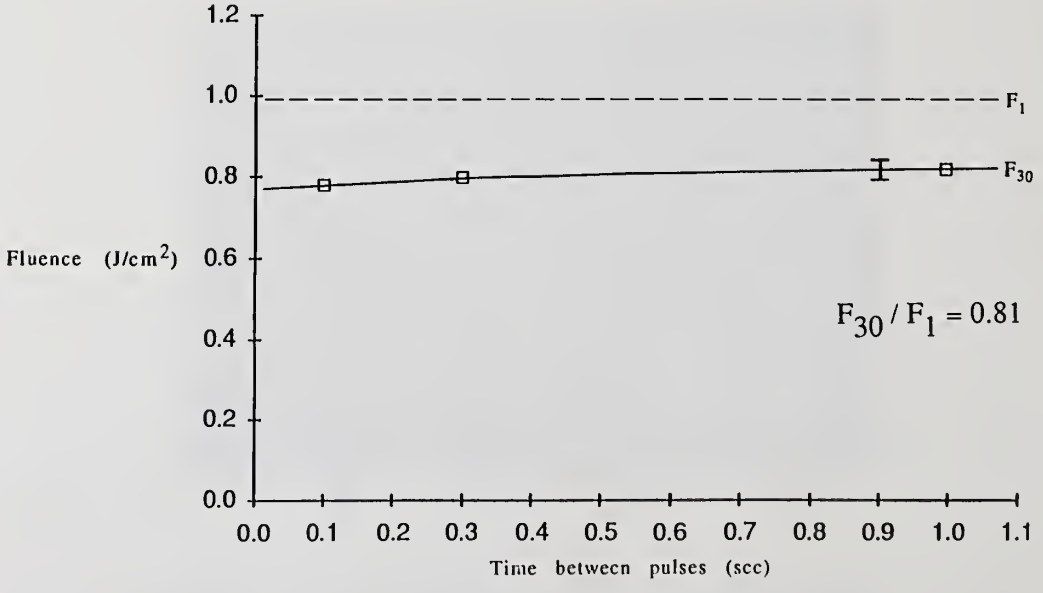

Fig. 14 Thirty shot damage threshold versus time between pulses at 300C.

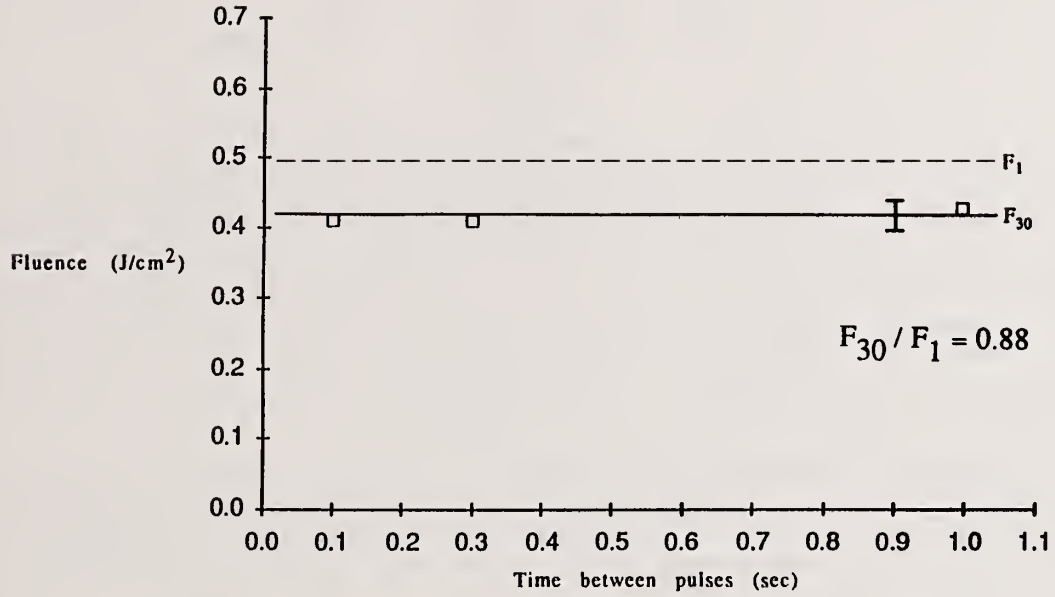

Fig. 15 Thirty shot damage threshold versus time between pulses at 500C.

End-Group Effects on the Wavelength Dependence of Laser-Induced Photodegradation in Bisphenol-A Polycarbonate

J. D. Webb and A. W. Czanderna

Solar Energy Research Institute, Golden, CO 80401

This is an extended summary of a complete paper published recently in Macromolecules. The photochemistry of bisphenol-A polycarbonate (BPA-PC) has been the subject of a number of investigations since losses of desirable properties such as transparency, tensile strength, impact resistance, and rigidity result from photodegradation when this well-known engineering polymer is used in outdoor applications [1-3]. Since many of these properties are adversely influenced by reactions at the surface of the solid polymer, where solar UV absorption and uptake of oxygen and water are highest, the addition of UV stabilizers and/or antioxidants to the bulk polymer has been generally unsuccessful in extending its outdoor service life to beyond 3 years [4]. Attempts to extend the outdoor service life of polycarbonates by incorporating them into laminates of weatherable, UV-absorbing acrylate and methacrylate polymers have also been unsuccessful, although efforts in this direction continue [5].

In this work, monochromatic laser UV radiation was used at 265, 272, 285, 287 and 308 ± 0.01 nm to investigate the wavelength dependence of photodegradation in thin films of capped and uncapped BPA-PC in dry, synthetic air. The technique of Fourier transform infrared reflection-absorption (FTIR-RA) spectroscopy was used to measure photochemically induced changes in the vibrational spectra of the BPA-PC film samples in situ. Changes in the molecular weight distribution of the UV-exposed films were determined by size-exclusion chromatography (SEC).

BPA-PC polymers I-IV (table 1) were obtained from Polysciences, Inc. and were purified by precipitation from unstabilized, distilled tetrahydrofuran (THF, Burdick and Jackson) into ether or methanol. A general formula for these polymers is given in table 1. Low molecular weight, uncapped BPA-PC polymers I-III were synthesized as described by Merrill [6]. BPA-PC IV is a commercial pelletized resin. Acetyl-capped BPA-PC (V) was prepared by refluxing I over Mg in a 50/50 (v/v) THF/acetyl chloride (Aldrich, 98%) blend while raising the reflux temperature from 35 to 50°C during a 4-h period, followed by precipitation into ether, filtration, redissolution in THF, filtration, and reprecipitation into methanol.

Table 1
BPA-PC Polymer Types Studied: $R_1(C_6H_4C(CH_3)_2C_6H_4OOCO)_nR_2$

BPA-PC Type	R_1	R_2	% Chain Ends with R_1 and R_2 attached (F)	$\bar{M}_n$
I	-OH	$-C_6H_4C(CH_3)_2C_6H_4OH$	100	2510
II	-OH	$-C_6H_4C(CH_3)_2C_6H_4OH$	88	2850
III	-OH	$-C_6H_4C(CH_3)_2C_6H_4OH$	94	3720
IV	$-OOCOC_6H_6$	$-C_6H_5$	88	18360
IV	-OH	$-C_6H_4C(CH_3)_2C_6H_4OH$	12	18360
V	$-OOCCH_3$	$-C_6H_4C(CH_3)_2OOCCH_3$	99	3120
V	-OH	$-C_6H_4C(CH_3)_2OH$	1	3120

Number-average molecular weights ($\bar{M}_n$) and polydispersities (D) for I-V were calculated from SEC data of ~ 0.1 g/L solutions of each material in pure THF. These data were obtained with a Varian Model 5030 HPLC system consisting of an isocratic pump operated at 1.2 mL of THF/min, high-resolution SEC columns, a Varian Model VUV-10 variable-wavelength UV detector, and a Hewlett-Packard Model 3388A integrator with SEC software.

Thin-film samples of I-V were prepared on IR-reflective, gold-coated glass substrates by casting from 2.5% solutions in THF and drying in nitrogen, followed by vacuum annealing at 103 ± 1°C for 1 h. The average thicknesses of the BPA-PC films, varied from 67 to 210 nm.

As a source of monochromatic UV radiation from 265 to 287 nm, a tuneable Lambda-Physik Model FL-2000 dye laser utilizing Coumarin 153 dye and a potassium hydrogen phthalate crystal for frequency doubling was used. The dye laser was pumped at 308 nm by a Lambda-Physik pulsed excimer laser (Model EMG-50E) operated at 3-15 Hz and utilizing xenon chloride as the excimer species. The pulse energy of the dye laser was 50-100 μJ/pulse for 10-ns pulses, as measured before and after sample exposure with a Scientech Model 38-0105 UV calorimeter with a quartz window and thermal insulation. The output energy of the dye laser was also monitored during sample exposure. The polymer/gold samples were mounted in a specular reflectance cell [7], which enables in-situ measurement of the IR-RA spectra of an 0.6 x 0.2 cm elliptical area at the center of each sample during exposure to UV radiation. In-plane p-polarized IR radiation was incident at a mean angle of 74° for all sample analyses. The cell is mounted in the front IR beam path of a Nicolet 7199 FTIR spectrophotometer with a cryogenic mercury cadmium telluride (MCT) detector. Before the sample spectra were collected, a reference spectrum of an uncoated Au reflector mounted in the cell was stored. IR-RA spectra of the samples were computed from the logarithmic ratios of the sample and reference spectra, for which 1000 interferometer scans at 2 cm^{-1} resolution, requiring about 12 min, were used. The samples were maintained at 25-29°C in a continuous flow of dry, CO_2-free air while being exposed to UV radiation in the cell.

For sample exposure, laser UV wavelengths of 265, 272, 285, and 287 nm were chosen to be close to the wavelengths of UV absorbance maxima in solid BPA-PC. Radiation at 308 nm, which is in the tail of the UV absorption edge in BPA-PC, was also utilized. Before exposure, an initial IR-RA spectrum of the sample was taken, and subsequent spectra were collected in situ after exposure of the sample to a series of laser pulses. Photodegradative changes in the IR-RA spectra were also followed by digital subtraction. This enabled the total number of laser UV pulses per sample to be limited to produce a change in the BPA-PC carbonyl band intensity (1776 cm^{-1}) of 1-10% so that only initial photodegradative changes would be measured.

After UV exposure, the supported polymer film samples were removed from the cell and the exposed area of the polymer films (about 1 cm^2) was dissolved in about 0.2 mL of THF. The samples were then injected into the appropriate SEC column for determining their molecular weight and their molecular weight distributions (MWD).

An absorbance at 1750 cm^{-1} is clearly visible in the IR-RA spectra of I-III and is much weaker in the spectra of IV and V. This absorbance is due to main-chain carbonyl groups in I, which are either inter- or intramolecularly hydrogen bonded to the terminal phenolic hydrogen or to other polar molecules such as BPA and H_2O, as proposed by Farenholtz [8] and Pryde [9]. The hydrogen-bonded carbonyl groups may form the periphery of the "polar clusters", containing phenolic end groups and small polar molecules, in the model proposed by Pryde [10].

To determine quantum yields of the various photoreactions observable with IR-RA spectroscopy, it is necessary to calculate the number of chemical bonds broken or created per sample during exposure. To address this problem, the single-frequency optical model [7] was enhanced (DELRI algorithm) to permit calculation of changes in k_2 from changes in IR-RA at the fundamental frequencies of up to ten different functional groups, which may exhibit nonlinear, overlapping IR-RA bands.

The relative changes in k_2 for the polymer and photoproduct absorption bands, as determined from the IR-RA spectral changes for each sample using the DELRI algorithm, were linear with UV dosage, although the IR-RA changes generally were not. This linearity indicates that competitive absorption and/or quenching by photoproducts [12] was not important in the thin BPA-PC films during the limited exposure sequences utilized. High signal-to-noise ratios and good base line stability are obtained with the in situ IR-RA technique; representative spectra showing the quality of our data have been published recently [13].

To estimate the fraction of incident UV radiation absorbed by the samples, the thin-film optical model [7] was also modified to calculate the absorptance (fractional UV absorption, in contrast to absorbance, which is the negative logarithm of transmittance) of the BPA-PC films on gold substrates at normal incidence.

The quantum yields for degradation processes affecting molecular size in I-V calculated from SEC data show a dramatic wavelength dependence. Cross-linking and chain scission reactions apparently occur simultaneously in the exposed samples, as shown by the increase in polydispersity index measured for all samples after exposure, in accordance with a study by Pryde [9].

However, the effect of the hydrogen-bonded phenolic end groups in I-III is to cause a cross-linking reaction to predominate over chain scission at 285-287 nm, within the UV absorption band of the phenolic end groups.

The quantum yield ratios, ϕ_{1515}/ϕ_{1507}, for depletion or accumulation of terminal phenolic groups (1515 cm^{-1}) relative to depletion of main-chain aromatic groups (1507 cm^{-1}) have been obtained as a function of laser irradiation wavelength [13]. These data show positive maxima for depletion of terminal phenolic groups relative to depletion of main-chain aromatic groups in I-III at 285-287 nm.

The quantum yield ratios for depletion or accumulation of hydrogen-bonded carbonyl groups (1750 cm^{-1}) relative to depletion of free carbonyl groups (1776 cm^{-1}) have also been obtained and published [13]. The yield ratios for I-III exceed $F/10^2n$ (table 1) at all wavelengths, indicating that hydrogen-bonded carbonyl groups are selectively degraded. Positive maxima for depletion of hydrogen-bonded carbonyl groups relative to free carbonyl groups occur in the plots for I and II at 285-287 nm. Although the maxima are less distinct than those for ϕ_{1515}/ϕ_{1507}, the influence of the phenolic end groups on the carbonyl groups to which they are hydrogen bonded is evident.

The data obtained in this study are consistent with a number of conclusions regarding the influence of various end groups on the wavelength dependence of photodegradation in BPA-PC. A complete summary of our conclusions and other aspects of this work are given in Ref. 13.

We thank R. Burrows (SERI) for thermal characterization of the polymers studied, C. A. Pryde and D. L. Allara (AT&T Bell Laboratories), and A. Factor (GE Corporate Research Laboratories) for helpful discussions. We are grateful to the Office of Energy Research, Division of Materials Sciences for operational support and to the DOE Office of Solar Thermal Technology for supporting acquisition of capital equipment utilized in this work.

Key Words:

Laser-induced photodegradation, bisphenol-A polycarbonate, polymer photodegradation, vibrational spectra, infrared reflection-absorption, phenolic end-groups, hydrogen-bonded carbonyl groups, polymer films, end-group effects, FT-IR, photo-Fries rearrangements, photochemistry.

References

[1] Schissel, P.; Czanderna, A. W. Solar Energy Mater., 1981, 3, 225.

[2] Blaga, A.; Yamasaki, R. S. J. Mater. Sci., 1976, 11, 1513.

[3] Davis, A.; Golden, J. H. J. Macromol. Sci., Rev. Macromol. Chem., 1969, C3(1), 49.

[4] Ram., A.; Zilber, O.; Kenig, S. Polym. Eng. Sci., 1981, 25, 535.

[5] Huyett, R. A.; Wintermute, G. E. Air Force Mater. Lab., Tech. Rep. AFML-TR (U.S.), 1976, AFML-TR 76-24, 129.

[6] Merrill, S. H. J.Polym. Sci., 1961, 55, 343.

[7] Webb, J.; Jorgensen, G.; Schissel, P.; Czanderna, A. W.; Chughtai, A. R.; and Smith, D. M. ACS Symp. Ser., 1983, No. 220, Chapter 9.

[8] Farenholtz, S. R. Macromolecules, 1982, 15, 937.

[9] Pryde, C. A. ACS Symp. Ser., 1985, No. 280, Chapter 23.

[10] Pryde, C. A.; Hellman, M.Y. J. Appl. Polym. Sci., 1980, 25, 2573.

[11] Gupta, A.; Renbaum, A.; Moacanin, J. Macromolecules, 1978, 11, 1285.

[12] Gupta, A.; Liang, R. Macromolecules, 1980, 13, 262.

[13] Webb, J. D.; Czanderna, A. W. Macromolecules, 1986, 19 (2810).

Manuscript Received
3-10-87

Scatter Intensity Mapping of Laser-Illuminated Coating Defects*

M. B. Moran, R. H. Kuo, and C. D. Marrs

Lauritsen Laboratory, Physics Division
Naval Weapons Center, China Lake, California 93555-6001

The ability to detect and locate defects nondestructively in multilayer optical coatings has been demonstrated using a video microscopy system. The system uses laser-excited scattering to illuminate defects responsible for laser-induced damage in multilayer dielectric mirrors. So far, attempts to predict the particular defect that will initiate damage have been unsuccessful. Presently, intensity maps and contours can be generated by digitizing the video images of scattering from individual defects. These can reveal characteristic defect scatter features possibly related to damage probability, and they offer a means to follow the development of these features from incipient to catastrophic damage. Examples of defect scatter maps and intensity contours for a dielectric mirror will be presented and discussed.

Key words: coating defects; defect scattering; dielectric mirrors; laser damage; light scatter; surface scatter; thin films; video-image processing.

Introduction

Experimental evidence suggests that laser-induced damage to coated optical components is initiated at defects introduced during coating deposition or substrate preparation [1].[1] The ability to detect and locate coating defects nondestructively has been demonstrated using a video microscopy system (VIMS) [2]. This paper describes qualitative scatter-intensity mapping that reveals characteristic laser-illuminated defect features as observed with the VIMS. The possible relationship of these features to a probability of laser-induced damage could provide a nondestructive means to predict individual laser-illuminated defect failure. Examples of laser-illuminated defect scatter intensity maps and contours for a dielectric coating will be presented.

Experimental

The laser-illumination studies were performed previously in the Naval Weapons Center's visible wavelength damage facility. This facility has been described in detail in the literature [3]. The video-image-processing system (VIPS) is a recent addition to the overall laser damage facility. The VIPS consists of an Eigen F-100 digital image processor and a Hewlett-Packard Model 216 computer controller.

The Eigen F-100 is designed to grab a single video field (256 × 512 pixels) or frame (512 × 512 pixels) and detail the image in its solid state memory. The video input can be any National Television Standard Code source (video camera or videotape). The digitized video data can then be stored in the F-100's integral 20-Mbyte Winchester disk or transferred to the computer for analysis or storage on floppy disks. The Winchester disk allows 100 video fields (50 frames) to be stored. Other important features include (1) dynamic resolution of 256 gray levels, (2) five levels of noise reduction, (3) simultaneous display of two fields, (4) contrast and level controls, and (5) burst mode (stores two frames per second to the Winchester disk). All functions are computer controlled by means of an IEEE 488 interface.

The Hewlett-Packard Model 216 computer was specially outfitted to handle the large matrices of digital video data. Internal RAM memory had to be 3.5 Mbytes or larger. This requirement is dictated by the number of pixels being analyzed. Other features include (1) floating point math coprocessor, (2) 1-Mbyte disk storage, and (3) Hewlett-Packard extended BASIC 3.0. A BASIC complier will soon be implemented to increase further the computational speed.

---

*Work supported by Navy Independent Research Funding.

[1]Numbers in brackets indicate the literature references at the end of the paper.

Display

The computer output can be displayed either as a contour map or a surface-scatter intensity map. Examples are given in figures 1 through 8. Contour maps represent the two-dimensional real surface array. The array need not be square. The minima and maxima can be specified and are the lowest and highest levels (gray scale), respectively, of the contour lines. They allow the user to specify the exact range within which contours are desired. Contour lines outside this range will not be plotted. The contour interval specifies how far apart the contour lines must be (in value, not distance). The smaller the interval, the denser the contour plot. A variable called EXTREMES may also be used. This is a logical variable that specifies whether or not to label local maxima and minima. A local maximum is a point whose value is larger than its eight neighbors immediately to the west, northwest, north, northeast, east, southeast, south, and southwest. A local minimum has a corresponding definition. The final variable that may be used is STATS. This is a logical variable that specifies whether or not to print the statistics of the data array. STATS includes (1) array size in terms of rows and columns, (2) minimum and maximum contour levels, and (3) contour interval.

The other type of graphical surface representation is a surface-scatter intensity map. The subprogram for this map receives the two-dimensional real surface array (the array used for contour maps) and plots the surface as a series of lines of constant row: One row in the surface array results in one line on the plot. This line indicates the height (intensity) of the surface array at any point along the line. Several variables may be used in this subprogram. OPAQUE is a logical variable that specifies if the surface is to look opaque, i.e., whether or not to remove hidden lines. If OPAQUE is true, hidden lines will be removed and the bottom may be a different color. This is used to help understand the data. If OPAQUE is false, the plot will be all one color and the whole surface will be visible. The FRONT- and BACK-EDGE variables specify the height. The front and back edges of the array are to be on the display surface. If FRONT EDGE is less than BACK EDGE, more of the top surface will be visible. If the FRONT EDGE is greater than the BACK EDGE, more of the bottom surface will be visible. If the FRONT EDGE = BACK EDGE, the surface will be plotted edge on. TRANSP is a logical variable that specifies array rotation. If TRANSP is true, the rows and columns are transposed so that a "side" view of the surface is seen. The final variable that can be selected is BACK-GRD. The BACK-GRD variable sets a discrimination value; that is, everything below a certain value is made zero. This feature can enhance details in a "noisy" surface array.

Results and Discussion

The illuminated defects were observed in a multilayer dielectric coating. The multilayer was an antireflection coating designed for 500 nm and was developed for protective use on laser windows. This coating consisted of alternating layers of aluminum nitride and aluminum oxide on a fused quartz substrate [4]. The coating was measured to be approximately 90% transmissive at the illumination laser wavelength of 515 nm. The laser-illuminated area was approximately 1 × 0.8 mm.

The progression from defect illumination to laser-induced damage as the laser intensity increases is shown in figure 9. These video fields were recorded immediately following a nondamaging [figure 9(a)] and subsequent damaging [figure 9(b)] pulse of higher intensity. Damage was initiated at defects A and C. Defect B did not damage at the higher intensity laser pulse. The areas digitized for analysis are enclosed by the solid white rectangles. The rectangles encompass approximately 50 × 50 pixels. Smaller subset arrays were analyzed from these large arrays to highlight details.

Contour maps of laser-illuminated defects A, B, and C during a nondamaging laser pulse are presented in figures 1 through 3. Smaller arrays were used to "magnify" the details in the video image. Arrays ranged from 29 × 29 pixels [figure 1(a)] to 5 × 5 pixels [figures 3(a) and (b)]. Unique illuminated defect features appeared for defects A (figure 1) and C (figure 3). These features consisted of two diamond-like patterns in close spatial proximity; whereas, contours shown by defect B (figure 2) show no discernible unique features. It must be emphasized that any contour pattern is dictated not only by scatter intensity, but is an artifact of the video resolution and the computer algorithm. Correlation of these features to a probability of laser-induced damage is discussed.

Contour maps of laser-illuminated defect A during a damaging laser pulse are shown in figure 4. The level of scattered illumination saturated the camera system and thus prevented the use of VIPS for scatter-feature discrimination. This was true for all damaged laser-illuminated defects analyzed. It will be necessary to reduce the amount of scattered light into the camera system in future experiments.

Scatter-intensity maps are presented for laser-illuminated defects A, B, and C in figures 5 through 8. "Side" views (transposed rows and columns) are shown in figures 6(b) and 8(b). These "side" views aid in understanding the intensity of scatter from a different perspective. Details such as the two higher intensity peaks [figure 8(b)] are revealed; whereas, in the contour map [figure 4(b)] these are obscured. The extent to which the background suppression aids in resolving details is seen in figure 5(b). The higher intensity scatter sites are more readily perceived when a discrimination value of 40 was used. The scatter-intensity maps offer a means to view the scattered light in a more quantitative sense than the contour maps, i.e., ability to see relative peak intensity as compared to the background and changes in background noise levels.

Comparison of laser-illuminated-defect features to laser-induced damage has provided some correlation results. Laser-illuminated defects with the characteristics of defects A and C (i.e., two distinctly separated defects aggregate in close spatial proximity and with similar contour features) have shown laser-induced damage 100% of the time. However, illuminated defects with characteristics of defect B (i.e., a singular defect aggregate with no distinct contour features) produced laser-induced damage only approximately 50% of the time. It is possible that some of the damaged defects may have had similar features to defects A and C, but those features were obscured due to the limited resolution of the video image and the image processor.

Conclusions

We have shown that the video-image-processing system (VIPS) holds promise for discriminating between nondamaging and damage-initiating laser-illuminated defects. VIPS has demonstrated that it is possible to correlate the laser-illuminated-defect features to a probability of laser-induced damage.

Future plans for VIPS will emphasize two areas: (1) continuation of laser-illuminated-defect feature characterization and (2) correlation of laser characteristics and profile-to-scatter-intensity distribution on the sample surface.

The application of VIPS to determine a correlation of sample response with the laser characteristics will include (1) polarization effects, (2) wavelength and pulse-width effects, and (3) spatial-intensity-profile distribution and surface scatter. The analysis of this type of information will aid in the understanding of laser-induced damage to optical surfaces.

References

[1] Johnson, L. F.; Ashley, E. J.; Donovan, T. M.; Franck, J. B.; Woolever, R. W.; Dalbey, R. Z. "Scanning electron microscopy studies of laser damage initiating defects in ZnSe/ThF_4 and SiH/SiO_2 multilayer coatings," in Laser induced damage in optical materials: 1984, Bennett, H. E.; Guenther, A. H.; Milam, D,; Newnam, B. E., ed. 1984 October 15-17; Boulder, CO. Nat. Bur. Stand. (U.S.) Spec. Publ. 727; 1986 October. Pp. 356-370.

[2] Marrs, C. D.; Porteus, J. O.; Palmer, J. R. "Nondestructive defect detection in laser optical coatings," J. Appl. Phys. 57; 1719; 1985.

[3] Marrs, C. D.; Faith, W. N.; Dancy, J. H.; Porteus, J. O. "Pulsed laser-induced damage of metals at 492 nm," Appl. Opt. 21; 4063; 1982.

[4] Koshigoe, L. G.; Johnson, L. F.; Donovan, T. M.; Marrs, C. D. Characterization of aluminum nitride/aluminum oxide reactively sputtered antireflection coatings. Naval Weapons Center technical publication, TP 6651 (1985).

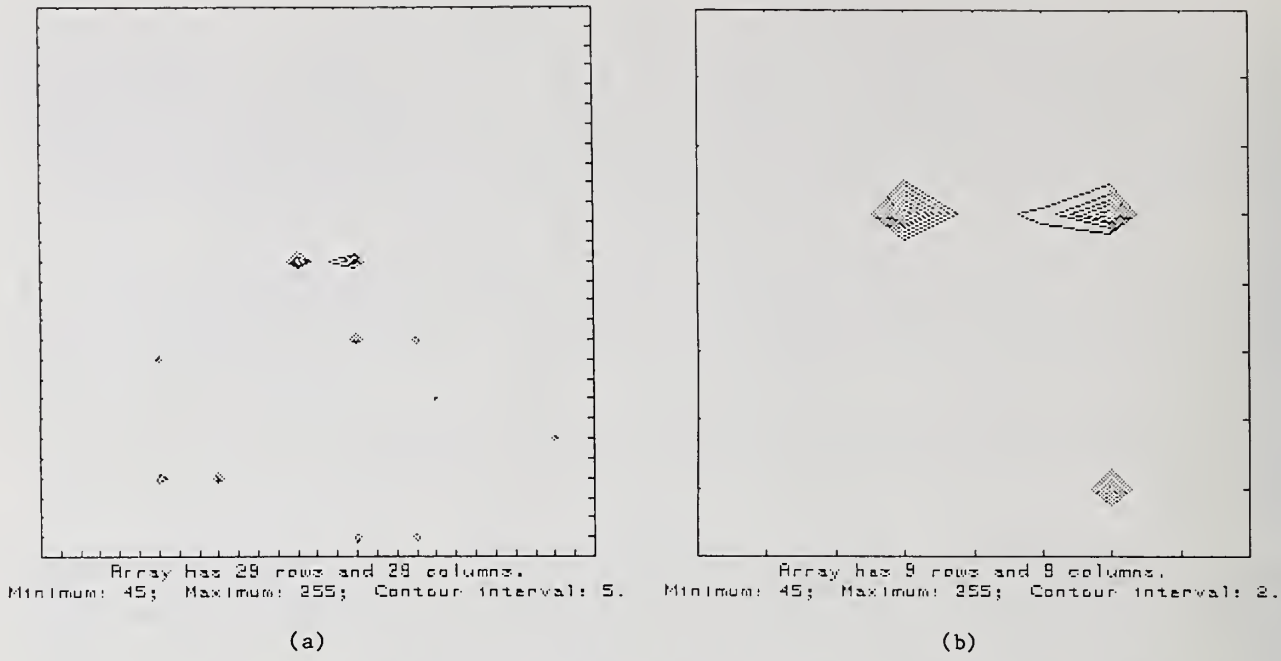

Figure 1. Intensity contour maps of illuminated defect A during nondamaging laser pulse at (a) 1X and (b) 3X magnification. Size of illuminated defect is 5 to 7 μm. Note similar distinctive contour features of illuminated defects.

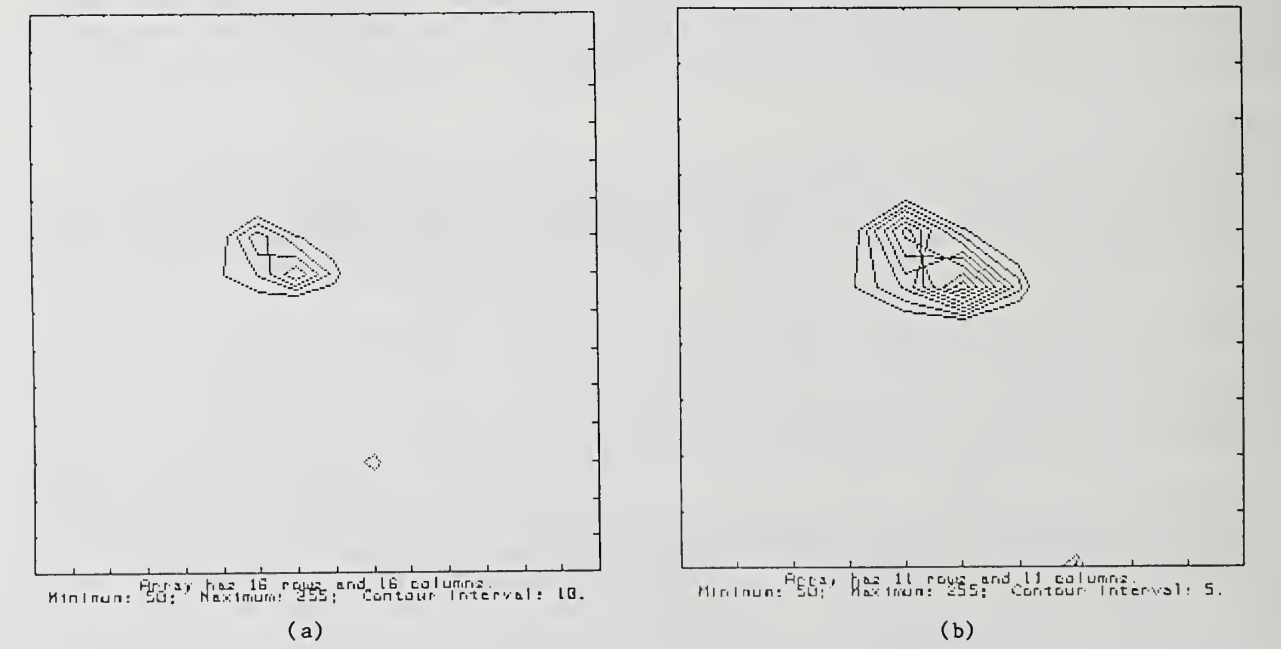

Figure 2. Intensity contour maps of illuminated defect B during nondamaging laser pulse at (a) 2X and (b) 2.5X magnification. Size of illuminated defect is 7 μm.

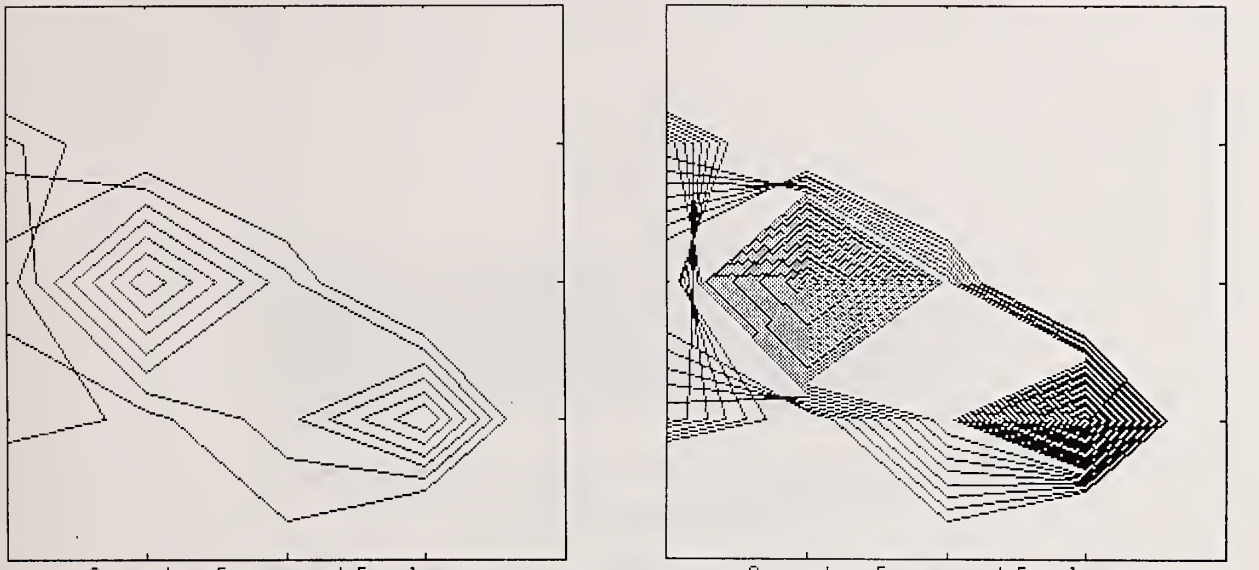

(a) (b)

Figure 3. Intensity contour maps of illuminated defect C during nondamaging laser pulse; (a) and (b) 6X magnification. Size of illuminated defect is 25 μm. Note similar distinctive characteristic features of illuminated defects.

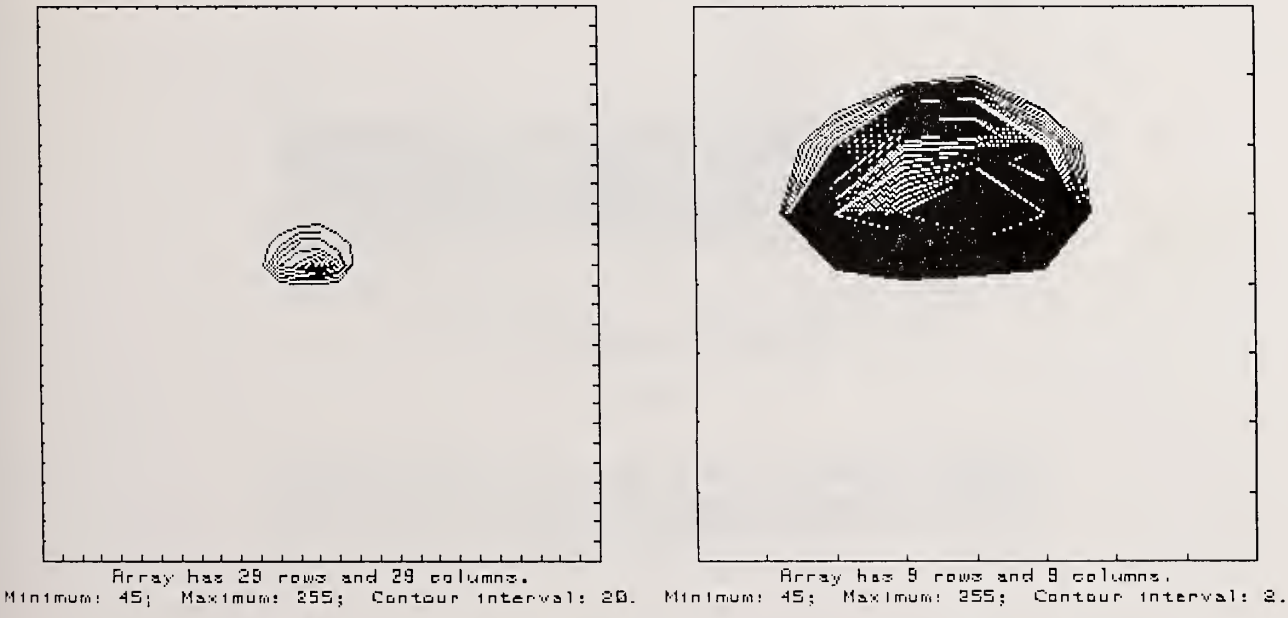

(a) (b)

Figure 4. Intensity contour maps of illuminated defect A during damaging laser pulse at (a) 1X and (b) 3X magnification. Size of illuminated defect is 15 μm.

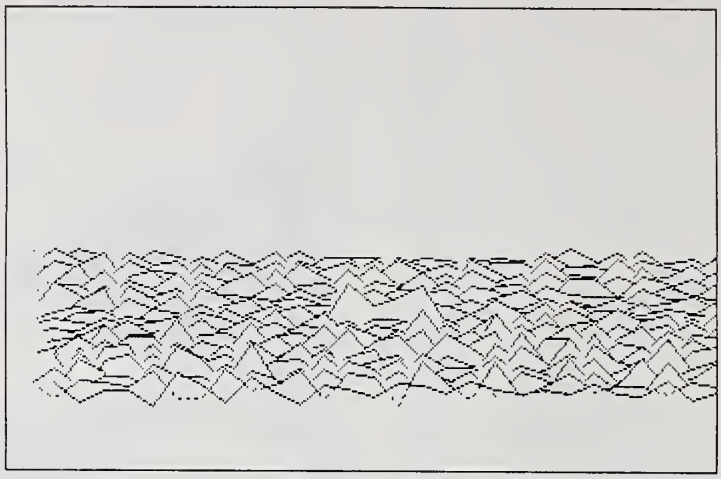

FRONT EDGE = 10 BACK EDGE = 40
BACKGROUND SUBTRACTED = 0

(a)

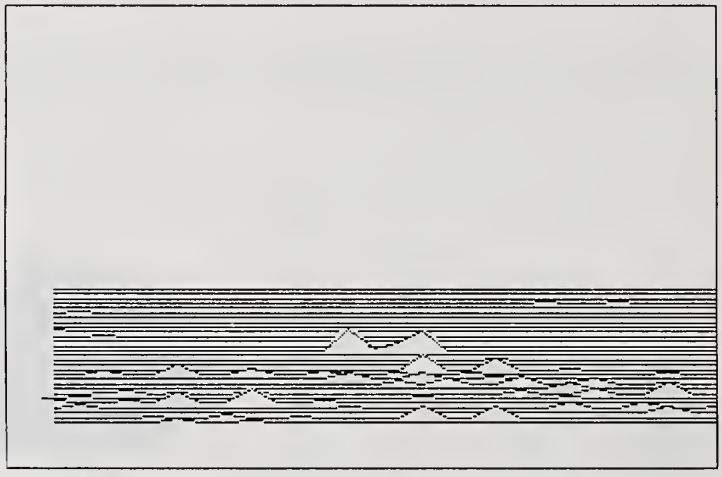

FRONT EDGE = 10 BACK EDGE = 40
BACKGROUND SUBTRACTED = 40

(b)

Figure 5. Scatter-intensity maps of illuminated defect A during nondamaging laser pulse; (a) and (b) "front" views. Size of illuminated defect is 5 to 7 μm.

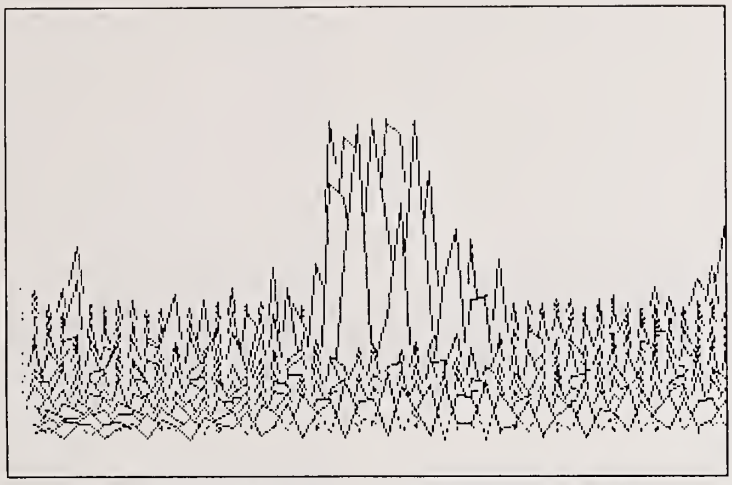

(a)

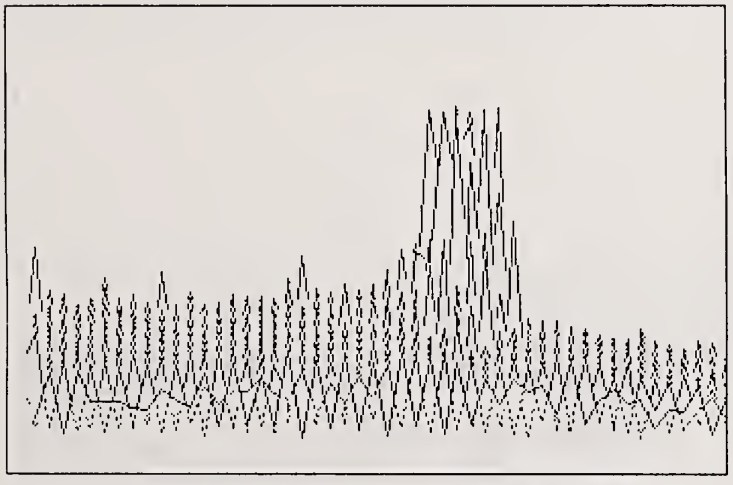

(b)

Figure 6. Scatter-intensity maps of illuminated defect B during nondamaging laser pulse; (a) "front" and (b) "side" views. Size of illuminated defect is 7 μm.

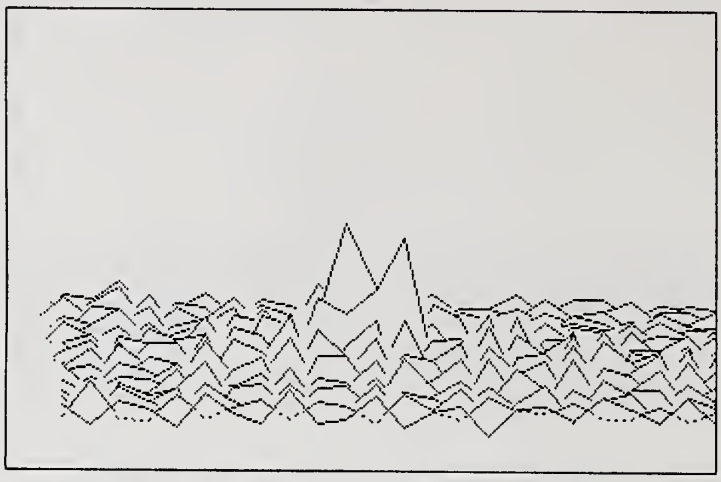

(a)

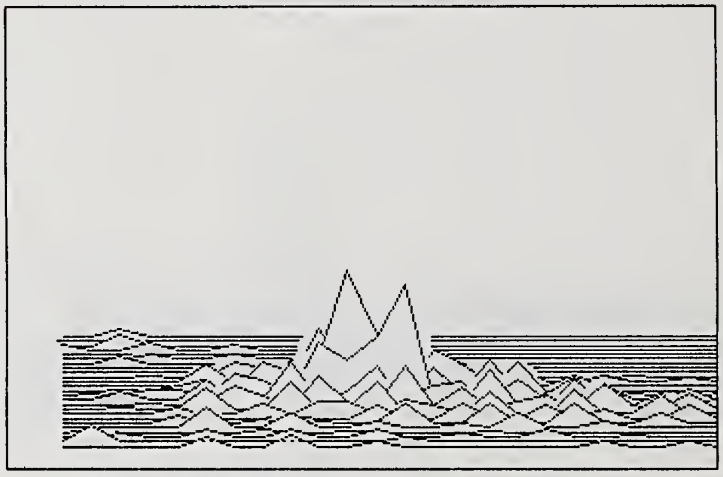

(b)

Figure 7. Scatter-intensity maps of illuminated defect C during nondamaging laser pulse; (a) and (b) "front" views. Size of illuminated defect is 25 μm.

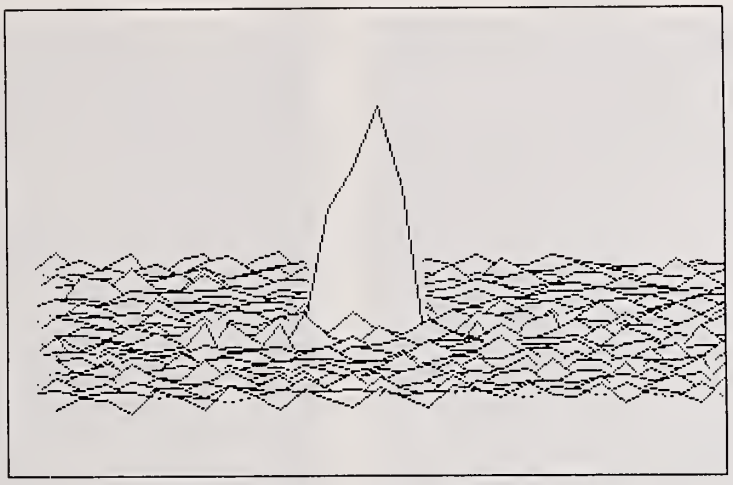

(a)

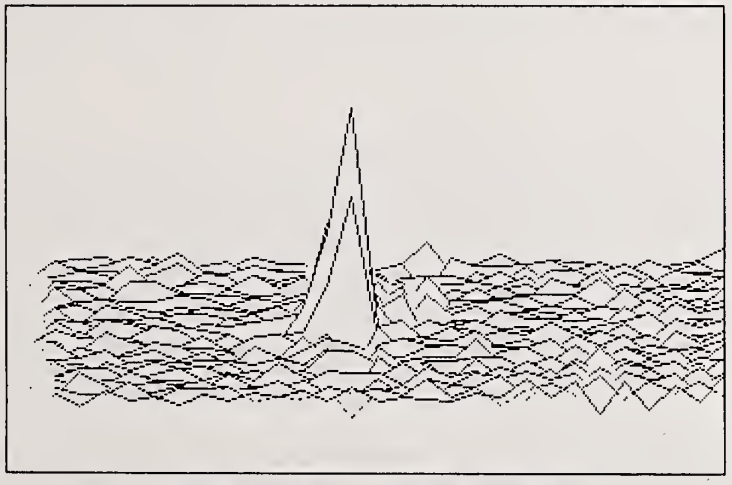

(b)

Figure 8. Scatter-intensity maps of illuminated defect C during damaging laser pulse; (a) "front" and (b) "side" views. Size of illuminated defect is 15 μm.

(a) (b)

Figure 9. Illuminated defects of $AlN/Al_2O_3/AlN$ multilayer antireflection coating for 500 nm during (a) predamage laser pulse and (b) damaging laser pulse; 1-mm FOV. Note illuminated defects A, B, and C.

Manuscript Received
3-10-87

Spectral Emission Studies of Optical Coating Defects*

C. D. Marrs, S. J. Walker, M. B. Moran and J. O. Porteus

Lauritsen Laboratory, Physics Division
Naval Weapons Center, China Lake, California 93555-6001

Video monitoring of pulsed visible-wavelength mirror damage led to the previously reported observation of illuminated coating defects as precursors to microscopic damage. Typically, many defects are observed in the laser interaction area, but only a few act as damage initiators. The present study seeks to identify the latter defects via any special characteristic of their laser-excited emission spectra that may serve as a recognizable signature. The ability to make such recognition nondestructively is crucial to producing optical coatings that perform at intrinsic damage levels. The video microscopy apparatus and methodology for measuring emission spectra of individual defects will be described. Results from various dielectric mirrors will be presented, including conclusive evidence that defect illumination is primarily the result of defect scattering. The dependence of defect image intensity on laser wavelength is examined more closely.

Key words: coating defects; dielectric mirrors; laser damage; nondestructive test.

Introduction

The ability to identify material defects responsible for laser-induced damage to optical coating would significantly advance coating technology, as well as provide a more efficient and economical means of quality control than damage testing. A defect illumination method that uses a video microscope for observing defects illuminated by a repetitively pulsed, visible-wavelength dye laser was reported at this conference in 1983 [1,2].[1] While this method has been proven effective for defect detection, it does not specifically identify damage-initiating defects, nor does it provide information on defect characteristics that may be related to damage. Furthermore, while circumstantial evidence indicated that defect scattering was the physical mechanism of the illumination, this was not conclusively demonstrated. The work reported here was designed to develop further the method of defect illumination in order to address these issues.

Specifically, the objectives of this work have been to design and implement an optical system capable of (1) imaging individual illuminated coating defects and (2) analyzing the light from individual defects for spectral characteristics and for variations in intensity with laser wavelength. Additionally, the relationship of unique defect characteristics to laser-damage initiation will be explored within the confines of these objectives.

Experimental

A schematic configuration of the experimental apparatus is shown in figure 1. Light from the repetitively pulsed dye laser passes through an intensity-controlling attenuator and is focused on the coated sample. A small part of this incident light is diverted for pulse-energy monitoring. A magnified image of the illuminated defects at the sample surface is provided by a QM1 Questar telescope whose axis lies at an angle of 15 deg to the incident laser beam. The image is formed on the back surface of an optical interface box (figure 2), which is apertured to a fiber-optic data link. A pellicle inside the box provides external viewing of the illuminated defects in relationship to the aperture by a low-light-level video camera. Using the video camera, the sample can be translated to position the image of an individual defect within the aperture. A video recorder provides a record of the defect-image pattern.

The light from the selected defect, after traversing the data link, enters a diode array rapid scanning spectrograph (DARSS) where it is analyzed; the spectrum is displayed as an oscillograph

*Work supported by the Navy Independent Research Funds and SDIO Short Wavelength Laser Coating Program.

[1]Numbers in brackets indicate the literature references at the end of the paper.

trace. Specifications of the laser source and computer-controlled sample-manipulation stage are given in table 1. Specifications of the optical system used for viewing and analyzing the defect illumination are given in table 2.

Table 1. Systems specifications

Laser source: TFDL-10 dye laser, Candela Corp.
Lasing bandwidth: 490 to 514 nm
Linewidth: 0.05 nm
PRF: 1 to 100 Hz
Energy/pulse: >0.8 J
Pulse width: 1.2 μs
Sample manipulator: PC-series, Daedal, Inc.
x, y, z linear translation stages
50-mm travel
Resolution: 2 μm

Table 2. Optical system specifications

Telescope: QM1 Questar
3-in. aperture
Focus from 22 to 77 in.
Fiber optic data link: ST-U series Diaguide, Inc.
1-mm core diameter, 4-ft single SiO_2 fiber
Transmission: >98%/meter for 0.4 to 1.9 μm
10-and 20-mm focal length collimators
f number matching optics for DARSS
DARSS: TN-series, Tracor Northern
f/4.0, 275-mm focal length spectrometer; gatable 1024-element array
Entrance slit: 250 μm
300-g/mm grating: 300-nm spectral range/scan
1200-g/mm grating: 75-nm spectral range/scan
time/scan: 10 ms to 500 s
scans/run: 1 to 4096

The samples used in this study were multilayer dielectric mirror coatings deposited on fused silica substrates. These were of two types: (1) broadband coatings tuned for maximum reflectance at 500-nm wavelength and (2) edge coatings designed to produce a reflectance maximum near 500 nm and a minimum at approximately 530 nm. Other sample characteristics, including coating materials and reflectances, are given in table 3.

Table 3. Sample characteristics

Design	R(%) 500 nm
Dielectric broadband mirror coatings[a]	
Ta_2O_3/SiO_2	99.5
HfO_2/SiO_2	99.0
ZrO_2/SiO_2	99.7
Al_2O_3/Na_3AlF_2	99.6
Wavelength (nm)	**R(%)**
Dielectric edge mirror coatings[a]	
491.6	99.1
504.1	83.7

[a] SiO_2 substrates for all coatings.

Observations

An example of an illuminated defect-image pattern obtained with the video system is given in figure 3. The field of view is 360 μm. The larger bright area, labeled A near the center of the figure, is produced by scattered laser light reflected from the fiber-optic entrance optics into the low-light-level camera. Bright spots B through E are images of coating defects illuminated directly by the laser and range from 10 to 40 μm in diameter. A typical spectrum obtained from one of these spots when centered on the apertured area A is shown in figure 4. Only the spectral line, which is characteristic of the laser source, has been observed from any of the defects examined thus far, indicating conclusively that defect illumination results primarily from defect scattering rather than a luminescence mechanism. While the laser line measured by DARSS is significantly broader than that measured directly from the laser source, the difference can be accounted for by the higher resolution characteristics of the spectrometer used for the latter measurement. Although spectral characteristics originally believed to be defect signatures were observed at various times in the course of this work, further careful investigation invariably showed that these were attributable to spurious spectrographic effects.

Another aspect of our previous work that was examined more closely is the dependence of individual defect-image intensities on laser wavelength. Figure 5(a) shows the adjacent images of two defects labeled A and B in the edge mirror as viewed with 491.6-nm laser light. When the wavelength was changed to 504.1 nm [figure 5(b)], the intensity of the defect A image is essentially the same; the defect B image decreased by 78%, based on video-image processing [3]. To obtain a spectral evaluation, the spectra were measured at the two laser wavelengths, with both defect images positioned simultaneously with the probe aperture. The results from DARSS scaled to equivalent photon number are shown in figure 6. The intensity of the 504.1-nm spectrum (spectrum B in the figure) is only 45% of the 491.6-nm spectral intensity (spectrum A). The half-maximum widths of the two scattered spectra are identical.

Discussion

The wavelength dependence of the defect-image intensities can be explained qualitatively in terms of the defect depths within the multilayer dielectric coating. Figure 7 shows the electric field distribution within the edge mirror (which determines the field strength available for scattering) for the two wavelengths used in the experiment. Presumably, defect A, whose image shows negligible wavelength response, is either (1) extended substantially in depth so as to average out the field variations or (2) localized near a point corresponding to an intersection of the two curves in the figure. Defect B, on the other hand, is evidently located at a position where the field strength for scattering is less at 504.1 nm than at 491.6 nm. The only positions where this occurs are at the low/high (L/H) index intefaces.

Summary

In summary, we have built and demonstrated a system that has the following combined capabilities: (1) imaging of laser-illuminated coating defects previously shown to be related to visible-wavelength laser damage [1,2] and (2) spectral analysis of light scattered from, or emitted by, individual illuminated defects. Using this system, we have demonstrated conclusively that the light from illuminated defect images is primarily scattered light that has the same wavelength characteristics as the laser source. Closer investigation of the previously reported dependence of defect-image intensity on wavelength indicates that closely adjacent defects can show substantially different dependences. Aside from the intensity variation, no other wavelength dependence was evident. These results can be explained qualitatively on the basis of scattering by defects located at specific depths or range of depths within the multilayer dielectric coating.

Future Work

We propose to increase the sensitivity of the DARSS using an intensified diode array, with the prospect of detecting weak defect signatures that are inaccessible with the present sensitivity. If found, special features of these spectral signatures would be correlated with the frequency of damage initiation. Also, the increased sensitivity would allow the study of Raman scattering from individual defects. A related study that might prove fruitful with the present apparatus is the investigation of the infrared spectral characteristics of the laser-illuminated defects.

References

[1] Marrs, C. D.; Porteus, J. O.; Palmer, J. R. "Nondestructive defect detection in laser optical coatings." J. Appl. Phys. 57; 1719; 1985.

[2] Marrs, C. D.; Porteus, J. O.; Palmer, J. R. "Defect damage precursors in visible-wavelength mirrors," in Laser induced damage in optical materials: 1983, Bennett, H. E.; Guenther, A. H.; Milam, D.; Newnam, B. E., ed. 1983 November 14-16; Boulder, CO. Nat. Bur. Stand. (U.S.) Spec. Publ. 688; 1985 November. Pp. 378-384.

[3] Moran, M. B.; Kuo, R.; Marrs, C. D. "Scatter intensity mapping of laser-illuminated coating defects," these proceedings.

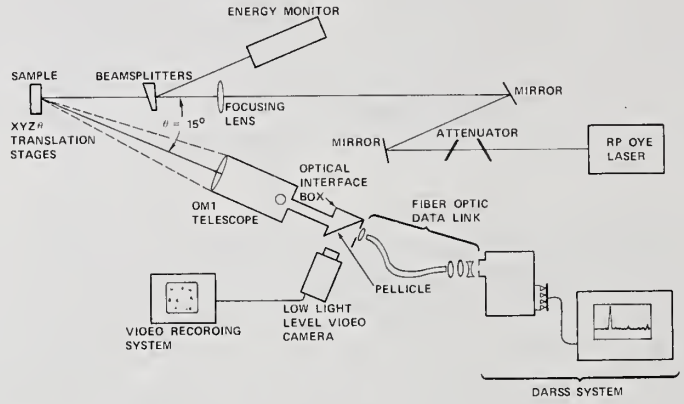

Figure 1. Experimental apparatus for spectral emission studies.

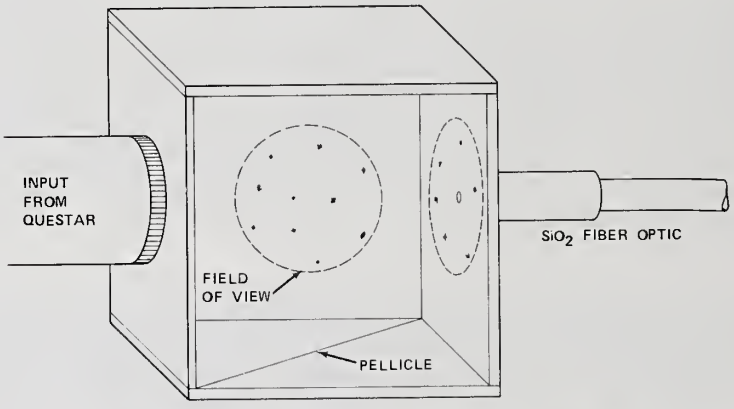

Figure 2. Optical interface box.

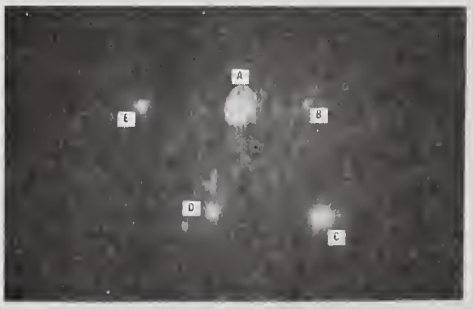

Figure 3. Defect-illuminated area seen by low-level-video camera; field of view (FOV) is 360 μm. The bright area in the middle of the FOV is the fiber-optic collimating lens A. Illuminated defects are B, C, D, and E.

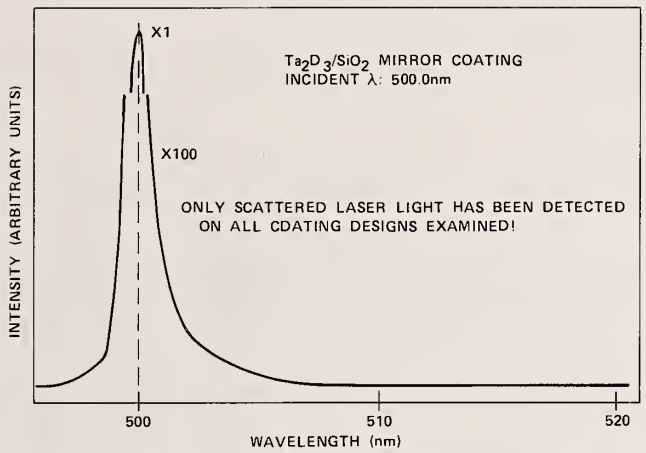

Figure 4. Spectrum measured from illuminated defect on Ta_2O_3/SiO_2 mirror coating. Incident wavelength was 500 nm. Spectral range of spectrum shown is 496 to 520 nm, but measurements extended from 490 to 565 nm with integration time = 60 s. Although the 0.05-nm FWHM laser line is broader (1.5 nm), only scattered laser light was detected. All coating designs examined show same result.

(a) (b)

Figure 5. Defect-illuminated area in edge mirror with (a) 491.6- and (b) 504.1-nm laser light: note illuminated defects A and B. Their intensities are approximately equal in (a), while defect B is barely visible compared to A in (b).

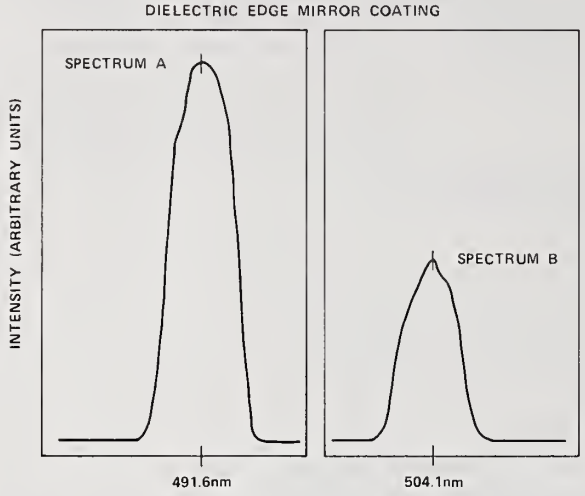

Figure 6. Defect intensity versus wavelength from defects A and B in dielectric edge mirror. The incident laser wavelengths are 491.6 nm for spectrum A and 504.1 nm for spectrum B; integration time = 0.3 s. The energy/pulse was scaled to equivalent incident photon number.

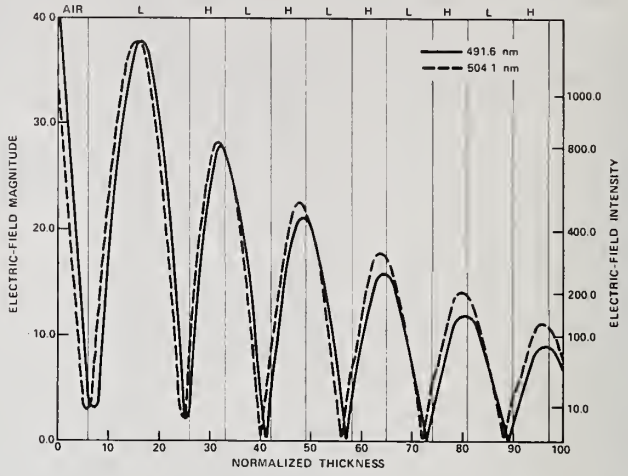

Figure 7. Electric field distributions in outer ten layers of the dielectric edge mirror stack for 491.6 and 504.1 nm.

Manuscript Received
5-22-87

PHOTOTHERMAL MEASUREMENT OF OPTICAL COATING THERMAL TRANSPORT PROPERTIES

Randall T. Swimm and Lisa J. Hou

Electrical Engineering-Electrophysics and Center for Laser Studies
University of Southern California, Los Angeles, CA 90089-1112

We report the present status of a project to measure the thermal transport properties of optical coating materials in thin-film format. The measurement technique employs a noncontact nondestructive method based on thermal diffusion-wave interferometry. Initial results confirm the feasibility of the method. Data on nickel coatings show thin film transport parameters slightly smaller than corresponding bulk values. and in addition clearly display the effects of a nonideal thermal bond between the coating and the substrate.

key words: laser-induced damage; nondestructive evaluation; optical coatings; thermal conductivity; thermal contact resistance; thermal diffusivity; thermal properties; thermal transport, thin films.

In this paper we describe a noncontact, nondestructive method of measuring the thermal transport properties of coatings, surfaces and interfaces. We will describe the method of performing the measurements, will present recent results on nickel coatings, and finally will discuss our planned work for the immediate future.

The measurements that we will describe were performed by means of interferometry. However, the wave field used was not light; instead it was heat. The waves used are thermal diffusion waves [1,2,3], and the coating sample operates as a Fabry Perot interferometer for these diffusion waves.

Since thermal diffusion waves (also called thermal waves) are not widely discussed outside the photothermal measurement community, their properties will be summarized here. Consider a solid whose surface temperature is modulated sinusoidally by an external heating source. The temperature history of this surface heating will diffuse into the bulk, and there will be a time delay for the instantaneous surface heating signal to diffuse to a given depth. Because of the way in which the diffusion equation differs from the wave equation, there exist no propagating solutions. Instead, the waves are evanescent: the temperature modulation of the bulk due to sinusoidal surface-temperature modulation is a critically-damped sine wave:

$$T(x,t) = T_o\, e^{-kx} \cos\,(kx-\omega t + \phi)\,. \qquad (1)$$

Here, k is the reciprocal of the thermal diffusion length, and also the wave number of the diffusion wave:

$$k = \sqrt{\frac{\omega}{2\kappa}} \quad \text{where } \kappa = \text{thermal diffusivity.}$$

This wave nature makes interference possible, even though temperature is a scalar field. Note that the thermal diffusion wave is not to be confused with an acoustic wave or with a phonon.

The thermal diffusion wave serves as a probe that can be used to study thermal transport in a coating-substrate system. The first mechanism to note is that a discontinuity in the appropriate thermal transport parameter (thermal effusivity) of the sample at the coating-substrate interface will cause the thermal diffusion wave to be partially reflected. When the reflected component returns to the surface. it will interfere with the instantaneous term due to

surface heating. (Multiple reflections are taken in to account in a complete analysis.) The relative phase of the return wave at the surface depends on the propagation delay in comparison with the modulation period, and the magnitude of the return wave depends on the mismatch of the thermal effusivity between the coating and the substrate. The larger mismatch, the larger the reflection at the interface. By varying the wavelength of the diffusion wave via the modulation frequency, one generates the range of possible interference patterns of a Fabry-Perot interferometer, except that instead of a bright or dark spot at the center of the pattern, one has a hot or cold spot.

In practice, this effect is achieved using the apparatus shown schematically in figure 1. The system may be subdivided into two parts; one part generates the diffusion waves, and the other part detects them. The generation is accomplished by heating the sample surface using a sinusoidally modulated argon ion laser beam. The resulting temperature response at the surface is monitored using a helium neon laser beam. In these measurements the outermost coating is metallic, and the dependence of the coating reflectivity upon temperature provides the means of measuring the temperature variation [3]. The HeNe beam is initially unmodulated, but after it reflects from the coating surface, an intensity modulation is induced. Thus, the surface temperature dependence upon diffusion wave interference effects can be measured.

The main strength of this work is that the experimental results can be analyzed using a tractable theoretical model. The analysis involves solving the boundary value problem associated with heat flow through the coating. The key to simple modelling is to force the physical operating regime into a sufficiently simple asymptotic limit. This is done as follows. First, the pump spot size is sufficiently large that the problem may be treated within a one dimensional approximation. Second, source heating and temperature sensing occur only at the surface of the sample because the outermost coating is metallic. (Corrections due to the nonzero penetration depth of the pump and probe beams in the metal coating may be required.) In the present work, a 1000 Å Ni coating is used for this purpose. This thin nickel coating therefore serves a dual role, providing a nearly delta-function heating source, and acting as a temperature transducer to be read by the HeNe probe beam.

With these simplifying choices, the theoretical analysis becomes straight forward. It is sufficient to model the surface temperature and its first derivative using a matrix transport equation [4]. Within a piecewise-constant approximation, this is:

$$\begin{pmatrix} T \\ f \end{pmatrix}_{\text{surface}} = \begin{bmatrix} C_1 & \frac{S_1}{\xi_1} \\ \xi_1 S_1 & C_1 \end{bmatrix} \begin{bmatrix} \cdots \end{bmatrix} \begin{pmatrix} T \\ f \end{pmatrix}_{\text{substrate interface}} \qquad (2)$$

where each coating layer is represented by one square matrix. The definition of terms is as follows:

Temperature = T

Heat flux = $f = -K \vec{\nabla} T$

$= -K \frac{\partial T}{\partial x}$, here

where K = thermal conductivity

$$\xi_j \equiv K_j k_j (1+i)$$
$$= e_j (1+i) \sqrt{\frac{\omega}{2}}$$

where e = thermal effusivity

ω = angular modulation frequency

$i = \sqrt{-1}$

Matrix component $C_j = \cosh [k_j l_j (1+i)]$

Matrix component $S_j = \sinh [k_j l_j (1+i)]$

where l_j = thickness of layer j

$k_j = \sqrt{\frac{\omega}{2\kappa_j}}$

where κ = thermal diffusivity

Note $f_{surface} = (1-R)\ I_o$

= the absorbed fraction of the incident intensity of the pump laser

Also note $f_{interface} \propto T_{interface}$

since there is no reflected wave in the substrate.

For the case of a single-layer coating, this equation is easily solved analytically to obtain the time-dependent surface temperature as a function of the modulated incident intensity of the pump laser. All of the necessary information for the thermal transport parameter determiniation is contained in the complex phase of the solution. The problem has been treated in the literature by Bennett and Patty [1] and by Swimm [2]. As shown in figure 2, the phase solutions as a function of the wavenumber of the diffusion wave (or as a function of the square root of the modulation frequency) form a family of curves that oscillate smoothly about $-\pi/4$ with diminished excursions at higher modulation frequencies.

This phase signature is verified in data taken on a single coating of nickel 1.8 μm thick, deposited on an SiO_2 substrate, as shown in figure 3. The data show the first quarter cycle of the phase oscillation. For reasonable coating thickness, the first high frequency zero crossing occurs at an inaccessibly high modulation frequency. These data are consistent with values for the thermal conductivity and thermal diffusivity that are smaller than bulk values by a factor of about five. However, measurements over a wider frequency range (both high and lower) are necessary before a well defined value for the thermal transport parameters can be determined. Higher frequencies are needed to obtain data beyond the first phase extremum in order that its location can be accurately identified. The need for data at lower frequencies will be evident shortly, from data taken on a thinner nickel coating.

Consider the possibility of an imperfect bond between the coating and the substrate. This case may be analyzed by treating the interface as a separate layer [4]. The resulting matrix equation describing the system is as follows:

$$\begin{pmatrix} T \\ f \end{pmatrix}_{Surface} = \begin{bmatrix} C & \frac{S}{\xi} \\ \xi S & C \end{bmatrix} \begin{bmatrix} 1 & R \\ 0 & 1 \end{bmatrix} \begin{pmatrix} T \\ f \end{pmatrix}_{Substrate} \qquad (3)$$

Here, R is the thermal contact resistance (unit area) of the interface. R may be viewed as the effective interface thickness divided by the effective interface thermal conductivity. However, these factors cannot be separately resolved. This equation can also be solved analytically. The solution for the complex phase is

$$\phi = \phi_N - \phi_D - \frac{\pi}{4} \qquad (4)$$

where

$$\phi_N = \tan^{-1}\frac{[\sinh x + g\cosh x]\sin x + h\,[\sinh x \sin x + \cosh x \cos x]/\sqrt{\pi}}{[\cosh x + g\sinh x]\cos x + h\,[\cosh x \cos x - \sinh x \sin x]/\sqrt{\pi}}$$

$$\phi_D = \tan^{-1}\frac{[\cosh x + g\sinh x]\sin x + h\,[\cosh x \sin x + \sinh x \cos x]/\sqrt{\pi}}{[\sinh x + g\cosh x]\cos x + h\,[\sinh x \cos x - \cosh x \sin x]/\sqrt{\pi}}$$

where $x = \sqrt{\pi f/f_c}$ (Note: x^2 = dimensionless modulation frequency)

critical frequency $f_c = \kappa/\ell^2$ where ℓ = coating thickness

(Note: At modulation frequencies higher than a few times f_c, interference effects are negligible.)

and where $g = e_{coating}/e_{substrate}$

(Note: This is the thermal diffusion wave analog of the ratio of refractive indices for reflection of light at an interface.)

and where $h = R/R_3$ where R is the thermal resistance of the interface, and R_3 is the thermal resistance of a substrate layer of thickness equal to the thermal diffusion length at a modulation frequency equal to the critical frequency f_c of the coating. $R_3 = (\ell/K_{ss})\sqrt{\kappa_{ss}/\pi\kappa}$ where ss = substrate

The phase signatures for a relatively large value of thermal contact resistance R (h = 100) are plotted in figure 4 for various effusivity ratios g. The g = 1 curve corresponds to coating and substrate being thermally matched. Values of g greater than 1 correspond to thermally insulating coatings on thermally conducting substrates. The converse applies for g values less than 1. If the thermal contact resistance were zero (h = 0) then the g = 1 line (thermally matched case) would be constant, with $\phi + \pi/4$ equal to zero. This is because in the thermally matched case, there would be no reflected wave, and no interference. However, if the bonding of the coating to the substrate is not ideal, then there is a reflection at the interface even if the coating and substrate effusivities are matched. Phase signatures for g values greater or less than 1 form a family of curves about the g = 1 curve.

The high frequency zero crossing found in the ideal bonding case is also found in the nonideal bonding case. This crossing is off the figure. The most significant new feature of the non-ideal phase signature is the low frequency zero crossing. This crossing never occurs for sufficiently low thermal contact resistance, and always occurs for sufficiently large thermal contact resistance.

Figure 5 shows data obtained for a 1000 Å Ni coating on an SiO_2 substrate. Because the coating is about 20X thinner than the coating described earlier, all of the structure is shifted to modulation frequencies about 400X higher than before. Now a zero crossing of the phase is seen, clearly implying a nonideal bond between coating and substrate. This is the justification for the earlier statement that lower-frequency data are needed for the 1.8 μm thick nickel coating; the effects of coating adhesion must be included.

Since there now exist three parameters to be obtained from the data (f_c, g, h), it is not yet possible to evaluate the data. (The data in figure 5 effectively provide only a slope and an intercept.) Additional data can be obtained either by extending the dynamic range of the measurement system or by measuring an independent system variable, preferably the temperature response of the interface. Both extensions are planned, and the latter method has already been reported in an earlier study by Swimm [2].

Plans for the immediate future are as follows. We will continue to refine and upgrade the measurement systems. We intend to complete the characterization of nickel coatings in preparation for the study of dielectric coatings with nickel overlayers. We have obtained an extensive set of such two-layer coating samples with SiO_2, Al_2O_3, and TiO_2 dielectric coatings overcoated with Ni and deposited on SiO_2 and Si substrates. Completing the characterization of these samples is our primary objective. Finally, we are exploring long-range options for the application of diffusion-wave interferometry to other surface, coating, and interface systems.

CONCLUSION

Thermal diffusion-wave interferometry has been demonstrated as a sensitive tool for measuring the thermal transport parameters of coatings, as well as providing a remote quantitative probe of the thermal bond between a coating and its substrate. Initial data have been presented on nickel coatings 2 μm and 0.1 μm thick. Short-range objectives for future work have been summarized.

ACKNOWLEDGEMENTS

These results would have been impossible to obtain without the interest and support of Alan Stewart. Valuable contributions to the project by Susan Allen, Laurie Fathe, Mark Innocenzi and Jason Machan are gratefully acknowledged. LJH acknowledges funding by the Muses and the Southern California Academy of Sciences, and thanks Duane Nichols for his many efforts. This project was funded by the Air Force Weapons Laboratory.

REFERENCES

[1] Bennett, Jr., C.A. and Patty, R.R., Appl. Optics, 21, 49 (1982)

[2] Swimm, Randall T., Appl. Phys. Lett., 42, 955 (1983)

[3] Rosencwaig, Allan, Opsal, Jon, Smith, W. L., and Willenborg, D. L., Appl. Phys. Lett. 46, 1013 (1985)

[4] Carlslaw, H. S., and Jaeger, J. C., Conduction of Heat in Solids, 2nd ed. (1986), §3.7.

Other reported coating thermal transport measurements include the following:

Decker, D. L., Koshigoe, L. G., and Ashley, E. J., 1984 Boulder Damage Symposium, NBS Special Publication 727

McGuirk, M., and Poirier, R. D., 1985 Boulder Damage Symposium

Akhtar, S.M.J., Ristau, D., and Ebert, J., 1986 Boulder Damage Symposium.

Jacobs, Stephen D., LLE Review Quarterly Report 29, 30 (1986)

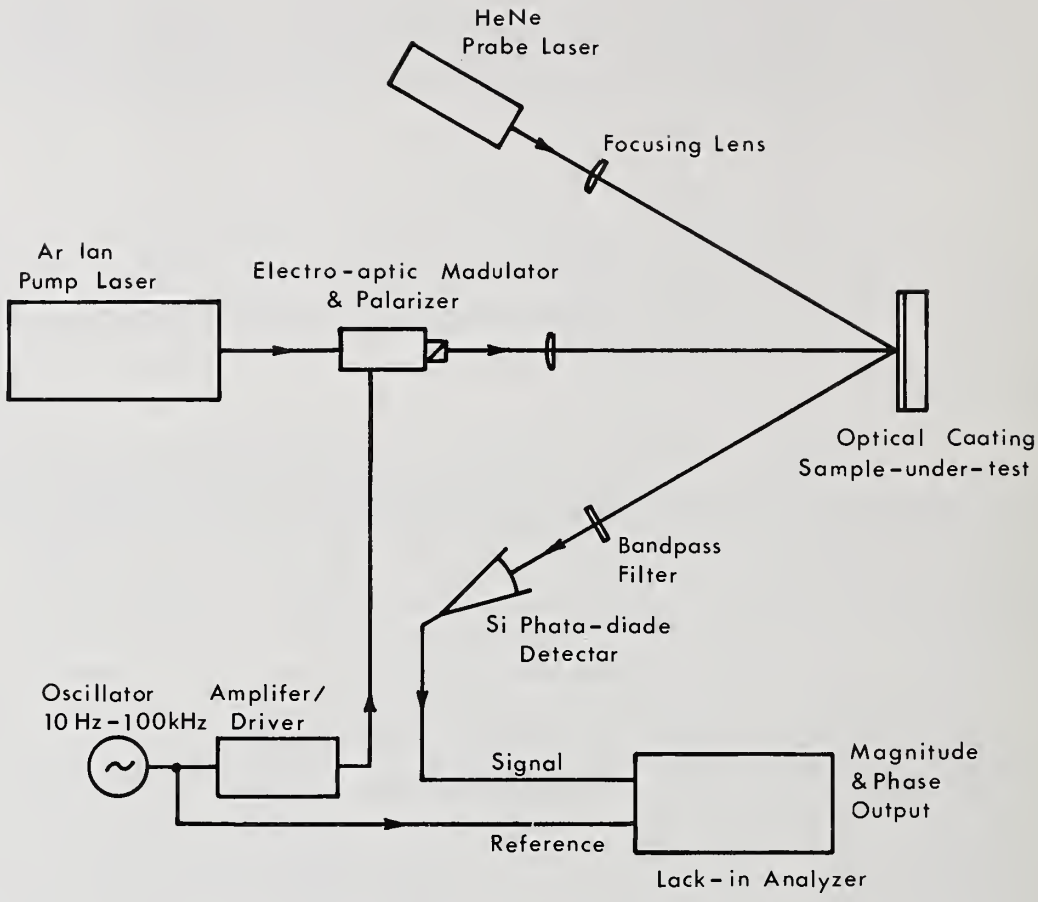

Figure 1

Experimental Configuration: Optical Coating Thermal Properties Measurement

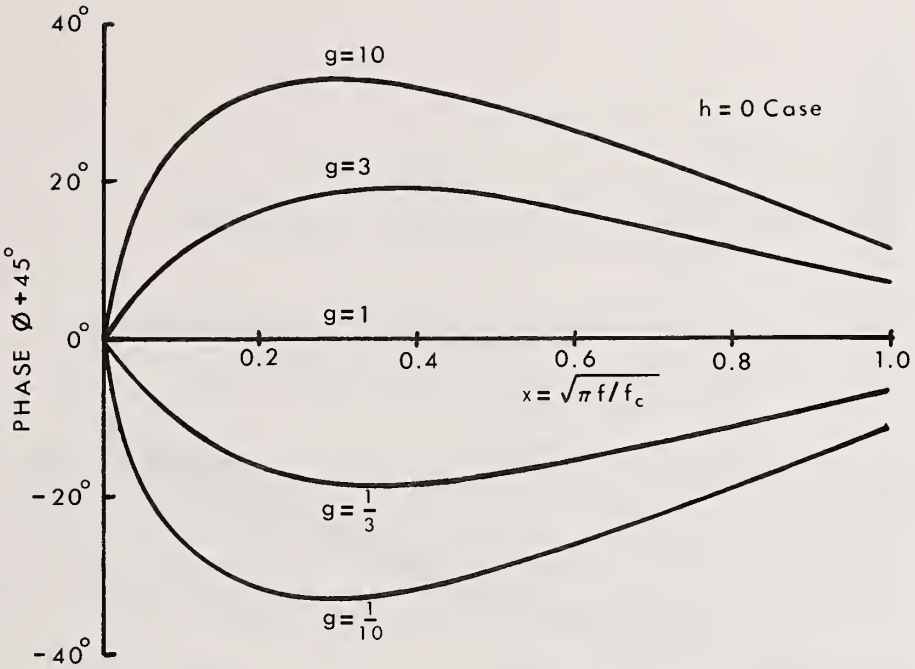

Figure 2 Predicted phase versus square root of modulation frequency for zero contact resistance case. Values of g<1 correspond to thermally conducting film deposited on thermally insulating substrate. Conversely for g>1. Curves cross axis at x = π/2.

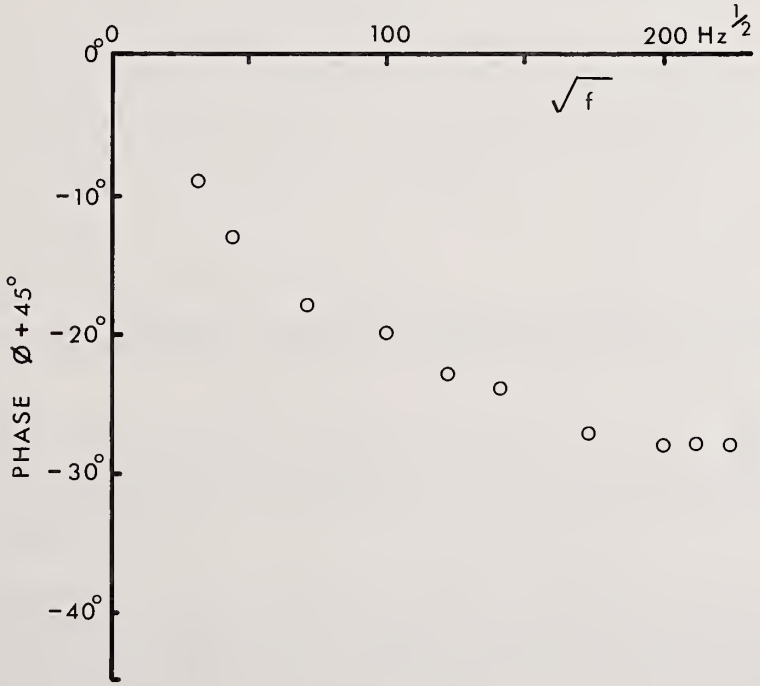

Figure 3 Measured phase versus square root of modulation frequency for 1.8 μm Ni coating deposited on SiO_2 substrate. In a two-parameter model with parameters g and f_c, the phase at the first phase extremum determines g, and the frequency of the first phase extremum determines f_c. The thermal diffusivity and thermal conductivity are determined in terms of these parameters. (See reference [2]).

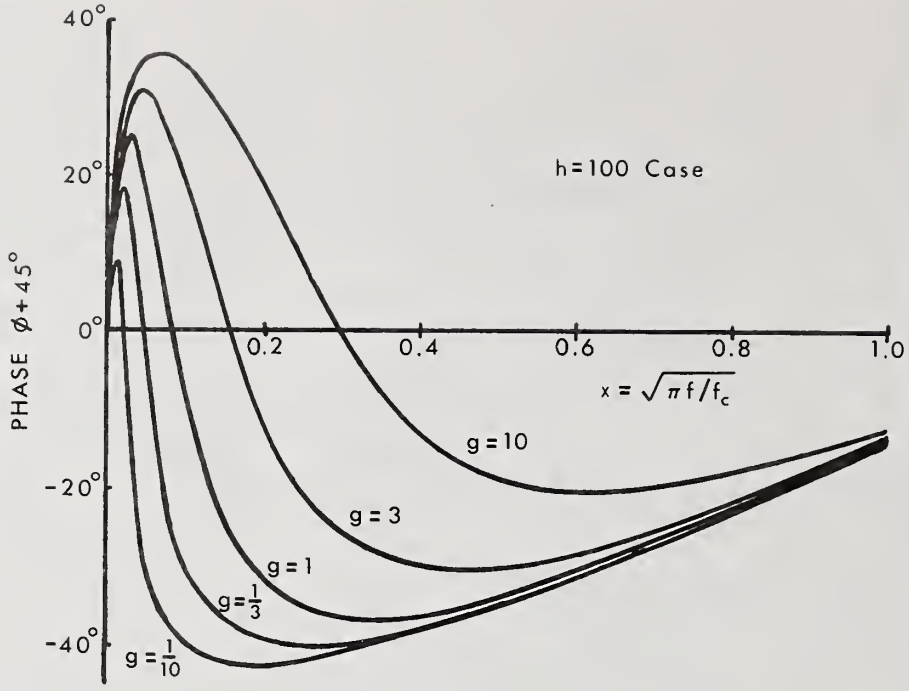

Figure 4 Predicted phase versus square root of modulation frequency for large h value. The parameter h depends linearly on the thermal contact resistance, and inversely on coating thickness. Therefore, thin coatings show stronger interface effects than thick coatings, other things being equal.

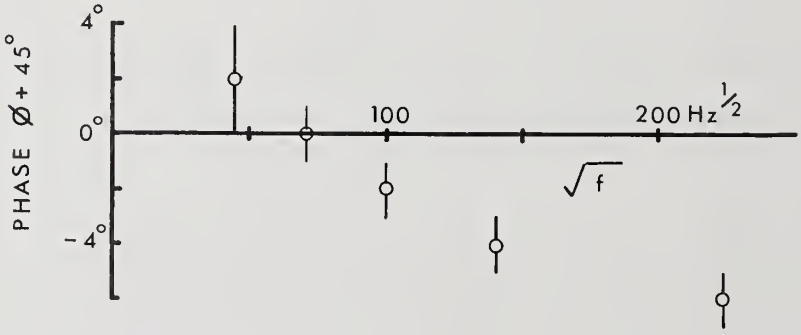

Figure 5 Measured phase versus square root of modulation frequency for 0.1 μm Ni coating deposited on SiO_2. The zero crossing implies relatively large thermal contact resistance.

Manuscript Received
11-3-86

Dependence of Damage Threshold of Anti-Reflection Coatings on Substrate Surface Roughness

Y. Nose, Y. Kato, K. Yoshida
and C. Yamanaka

Institute of Laser Engineering, Osaka University
Suita, Osaka 565, Japan

Geometrical shapes of the damage sites in the 5-layer SiO_2/ZrO_2 anti-reflection (AR) coatings generated by 1μm laser irradiation have been accurately determined. The damages can be classified into two types; deep damage and shallow damage, the former having the lower threshold. Dependence of the damage threshold of the deep damages on substrate surface roughness is given. It is suggested that presence of absorption centers embedded in the substrate is responsible for determining the damage threshold. Possible approaches that will lead to stronger AR coatings are proposed.

Key words: Anti-reflection coating; laser-induced damage; polishing process; surface roughness.

1. Introduction

Previous observations show that transmitting coatings such as anti-reflection (AR) coatings and polarizing beam splitters have lower damage threshold than high-reflectance (HR) coatings [1]. The damage to AR coatings originate at the interface between the first coating layer and the substrate [2]. However the exact process which leads to the laser-induced damage in the AR coating has not been clarified so far.

We report here the results of the detailed observations of the laser-induced damages in the AR coatings. In particular we have studied the correlation between the damages and the surface roughness of the substrate. Based on these observations the most probable mechanism for damage formation in the AR coatings is discussed. Proposals are made which will lead to the improvement of the damage threshold of the AR coatings.

2. Experimental Conditions

2-1.Preparations of the substrates

In order to obtain consistent results in the damage properties of the AR coatings, careful attentions were paid to fabrication of the substrates and the coatings used in the following experiments.

The substrates were high optical quality BK-7 glasses of 30 mm in diameter and 10 mm in thickness. They were polished either by conventional polish or by bowl-feed polish process, respectively [3]. In the latter the substrates were immersed during polishing in the liquid containing the polishing compounds, resulting in smooth surfaces. Ceria compounds were used as the polishing material.

The surface roughness of the polished substrates were measured with a Wyko NCP-1000M optical profilometer. The typical rms (peak-to-valley) surface roughness was 30-35 Å (∿200 Å) for conventional polish and 5-9 Å (30-60 Å) for bowl-feed polish, respectively. Figure 1 shows the surface profiles of the substrates #1 and #2 which were prepared by conventional and bowl-feed polishes, respectively. As shown in Figure 1, we define two parameters which characterize the lateral scale length of the surface profile: the average distance between the peaks (Δd) whose height exceed the rms roughness and the typical width of these peaks (Δw). Table 1 shows these parameters for the samples #1 and #2. We note that deep and wide rough peaks produced by conventional polish (#1) are smoothed by bowl-feed polish (#2) resulting in smaller value of Δw.

2-2. Coating

Five layer SiO_2/ZrO_2 AR coatings of quarter-wave design were vacuum deposited on the substrates, with the first SiO_2 layer as the undercoat to increase the damage threshold [4]. The substrates after polish and before coating (typically ∿1 week) were kept in dry atmosphere to prevent chemical changes on the fresh surface. All the substrates with different surface roughnesses were coated at the same time in order not to introduce uncertainty due to the coating process.

2-3. Laser irradiation

Each sample was irradiated with a laser pulse of 1.064 μm wavelength from a Q-switched Nd:YAG laser. The pulse width was 1.5 ns, generated by slicing a Q-switched pulse with a fast Pockels cell switch. After two-stage amplification with Nd: glass amplifiers of 15 mm diameter, the laser pulse was focused with a 500 mm focal length lens. The laser beam on the sample had a smooth Gaussian spatial distribution with the spot diameter of 400 μm at $1/e^2$ point. The laser energy was measured with a calibrated photodiode.

The irradiation site was observed in site with a Nomarski microscope before and after each laser irradiation to detect the laser-induced damage. The sample was moved after each laser shot irrespective of the presence or absence of the damage.

2-4. Characterization of the laser-induced damages

The following techniques were used in order to definitely determine the geometrical shapes of the damage sites generated at different experimental conditions.

1) Optical microscopy: A Nomarski microscope was used to inspect and record the morphology of the damages.
2) Electron microscopy: Enlarged views of the damages were obtained with a scanning electron microscope.
3) Surface profilometry: A Talystep surface profilometer was used to determine the surface profile and the depths of the damage sites, since these parameters are difficult to determine with the optical and electron microscopes.
4) Material analysis: An electron-probe x-ray microanalyzer (XMA) was used to identify the materials at the damage sites.

3. Experimental results

We have studied the dependences of the laser-induced damages on the surface roughness of the substrates. First we show the results regarding the geometrical shapes of the damage sites generated at typical experimental conditions. Then more quantitative relations between the damages and the surface roughness of the substrates are presented.

3-1. Geometrical shapes of the damage sites

1) Optical microscopy

Morphology of the damages obtained with a Nomarski microscope are shown in Figure 2. The two samples are AR coatings fabricated using the subrates #1 and #2 which have different roughness as shown in Table 1. The damages were produced at the laser fluences (E_L) near the damage threshold ($E_L \sim E_C$) and far above the threshold ($E_L \sim 3E_C$). Note that the damage threshold depends on the surface roughness as will be described later; therefore E_C and E_L are quite different in Figure 2 for the two samples.

Near the threshold, damages which have small diameter (which we call "deep damages" hereafter) are distributed over the irradiated area. When the laser fluence is increased, the number density of the deep damages increases significantly, but the size changes very little. Futhermore when the fluence exceeds approximately twice the threshold of the deep damages, damages covering the large area (which we call "shallow damages" hereafter) are generated.

2) Electron microscopy

Magnified views of the damages obtained with an electron scanning microscope are shown in Figure 3. The deep damages are mostly circular with the diameters of 3-4 μm. The microscope picture for #2 near $E_L \sim E_{CT}$, which was taken at a tilted angle of 15°, reveals each coating layer at the wall of the crater. It shows that the damage wall has two steps: SiO_2, ZrO_2/SiO_2 and ZrO_2/SiO_2 counted from the outer surface to the substrate. The deep damages have the depth which probably reaches to the substrate, although it is difficult to definitely conclude only with the electron microscopy.

At the higher fluence of $E_L \sim 3E_{CT}$, shallow damages are produced over the wide area covering the deep damages. In the shallow damages, the top coating layer (SiO_2) is removed from the ZrO_2 layer. However it appears that the top layer remains around the deep damages with the diameter of 20-30 μm even with high fluence irradiation.

3) Surface profilometry

A Talystep was used to measure the depths of the damages. Figure 4 shows the Talystep scans of the samples having the shallow damages. It shows that the depth of the shallow damage corresponds approximately to the thickness of the top coating layer, and the depth of the deep damage is close to the total thickness of the 5 coating layers. However the latter is not accurate since the stylus is not small enough to reach to the bottom of the deep damage which has ∿1 μm diameter at the bottom. Also this measurement confirms that the top coating layer remains around the deep damage within the shallow damage.

4) Material analysis

Figure 5 shows the results of the XMA analysis at four different sites outside and within the damages. Although XMA does not provide good depth resolution since the probe electrons (25 kV) have 1∿2 μm peneration depths, the result supports the above observations regarding the profiles of the damage sites.

Figure 6 gives the schematic picture of the damage sites based on our experimental observations. At $E_L \sim E_c$, deep damages which extend to the substrate are generated. At far above threshold like $E_L \sim 3E_c$, the top coating layer is blown-off resulting in the shallow damage, whereas the top layer remains around the deep damages.

3-2. Dependence of the deep damages on the laser fluence and the surface roughness

Since the deep damage has a lower threshold than the shallow damage, we study here dependences of the deep damage on the two parameters; laser fluence and surface roughness.

1) Dependence on the laser fluence

Here we determine the exact damage threshold of the deep damage using the sample #2 whose substrate has been bowl-feed polished.

The laser beam has the Gaussian spatial distribution on the sample given by

$$E(r) = E_p e^{-2r^2/a^2} \quad , \qquad (1)$$

where a=200 μm and E_p is the peak fluence at r=0. The damage occurs within the area of radius r_c where E(r) exceeds the threshold fluence E_c; $E(r_c)=E_c$. We have examined the laser damages with the Nomarski microscope, and determined the critical radius r_c and derived the threshold fluence E_c. For the damages generated at different laser energies up to the peak fluence on the sample of 30 J/cm^2, the value of E_c thus determined was approximately constant having the value of 7.5 J/cm^2. Therefore we may conclude that the actual threshold for the deep damages is 7.5 J/cm^2 for the particular sample that we have studied.

The area within r_c is given by

$$S = \pi r_c^2 = (\pi a^2/2) \ln (E_p/E_c) \quad , \qquad (2)$$

If all the deep damages have the same threshold of E_c, then the number of the deep damages within the area S should increase logarithmically with E_p. Figure 7 shows the experimental results of the total number of the damages and the average distance between the damages plotted against the peak fluence E_p. Since the number of the damages increases with E_p more strongly than logarithmic, this shows that the deep damages have variation of the thresholds whose lowest value is 7.5 J/cm^2.

2) Dependence on the surface roughness

It is reasonably well established [1] and our present results support that the damages in the AR coating are caused by some imperfections at or near the boundary between the coating and the substrate. Also there is a set of experimental data that higher damage threshold is obtained with the bowl-feed polish compared with the conventional polish [2].

Figure 8 shows our experimental data of the damage threshold plotted against the rms surface roughness and the peak-to-valley surface roughness. Three bowl-feed polished and one conventional polished samples were used. The damage threshold was determined as the peak fluence at which the damage was detected in situ with the Nomarski microscope. The error bars in the damage threshold show the range of data obtained from many shots on each sample. These data clearly show that the AR coating deposition on the smooth substrate results in higher damage threshold. However it should be noted that the threshold of $E_c \sim 9$J/cm^2 is lower than that obtained with good HR coatings in which the value of $E_c \gtrsim 12$ J/cm^2 has been achieved [1,5].

We have measured the diameters and the average distances of the deep damages produced at high laser fluence of $E_l \sim 3E_c$, and compared them with the lateral scale lengths of the surface roughness of the substrates that we have defined in Figure 1. The result is shown in Table 2. Here we find close correlation between the diameter of the deep damage and the width of the surface roughness (Δw), and also between the average distance between the damages and the average distance between the peaks of the surface roughness (Δd). The implications of this results are discussed in the next section.

4. Discussion

First we discuss on the deep damages that give the lower bound of the damage threshold of the AR coating. Lowdermilk and Milam suggested [1] that the damage begins with the generation of very hot spot near the interface with the substrate. The intense heat melts the glass and generates high pressure which lift the coating layers. When the crack reaches to the surface, molten glass is ejected from the center and solidifies quickly.

Our observation of the geometrical shape of the deep damages shows that the damage is extending to the substrate. The damage threshold is related to the surface roughness of the substrate. Also we found close correlation between the geometrical size of the damage and the typical width of the surface roughness, and the correlation between the distance between the damages and the distance between the peaks of the surface roughness. In addition we have other data with the AR coating on a conventional-polished substrate in which deep damages are aligned on a straight line. Close examination of the substrate before coating with the Nomarski microscope reveals the presence of sharp straight scratches on the surface.

Considering these observations, we may propose that the deep damages are generated due to the presence of absorption centers in the substrate. With the bowl-feed polish compared with the conventional polish, the size and also the number density of these absorption centers become less, resulting in higher damage threshold. The nature of the absorption centers is not clear; however they may well be the polishing compounds that are embedded in the valley of the scratches or in the subsurface structure.

It is an intriguing question that how much we can improve the damage threshold when we keep reducing the surface roughness using special techniques. If these new techniques could reduce the absorption centers in the substrate during polishing, then they will result in higher damage threshold. Otherwise it will be difficult to attain significantly better result. We may chemically remove the absorption centers, however it might result in rough surface with high scattering level. Laser annealing of AR coating by repetitive irradiation with low power laser is known to be an effective process to increase the damage threshold [6]. In this case, absorption centers probably spread due to laser heating, resulting in less absorption and thus

higher threshold.

We have another viewpoint which we have derived from our recent work on porous dielectric coating [7]. In this coating, SiO_2 and NaF are coated at the same time on the substrate and NaF is dissolved after coating, leaving porous layer of SiO_2. This coating has very high damage threshold of 12-13 J/cm^2 at 1 μm even when we use rough substrate. According to our interpretation, the reason for the high damage threshold of the porous coating is that the pressure generated at the absorption centers is not accumulated under the coating layer, but it is quickly released due to the porous nature of the coating [8].

The shallow damages have higher threshold than the deep damages. Although we have not tried to accurately determine the threshold of the shallow damage, it is 20∿25 J/cm^2 for the 5-layer SiO_2/ZrO_2 AR coating on the bowl-feed polished substrate. Therefore if we could completely eliminate the deep damages, there is a possibility that the AR coating could have the damage threshold exceeding 20 J/cm^2.

It is an interesting observation that the top layer remains around the deep damages located within the shallow damage. One of the possible interpretations is that the plasma ejected from the deep damage refracts and absorbs the laser beam, reducing the laser fluence and thus preventing the damage around the deep damage. There may be interference of the refracted beam with the direct beam near the damage affecting the damage threshold of the shallow damage. Further study will be necessary to clarify various aspects related to the shallow damages.

5. Conclusion

Based on our experimental observations, we have suggested that the presence of absorption centers in the substrate is responsible for determining the damage threshold of the deep damages which give lower bound of the threshold of the AR coating. If this interpretation is correct, then there are two possibilities that we could take to improve the threshold to above 10 J/cm^2 and possibly to 20 J/cm^2. The first is to reduce the size (and the number) of the absorption centers. Smaller absorption center will result in the reduction of pressure caused by the heating of the absorption center and thus increase in the damage threshold. Further quantitative experimental and theoretical studies are necessary to clarify these relationship. Another possibility is to develop porous coatings which releases the pressure generated at the substrate. The porous AR coatings have already been developed [7,9,10]. However this concept could be extended to other transmitting coatings such as the polarizing beam splitter.

The above discussions are pertinent to the AR coating at 1 μm where the damage is determined by the substrate property. At shorter wavelengths such as in the ultraviolet, the damage is mostly determined by the absorption within the coating layer. In this case selection of the coating materials becomes more important. However porous nature of the coating might help improving the damage threshold also in this wavelength region.

6. Acknowledgement

We appreciate T. Izawa of Showa Optical Company for preparation of the samples used in this study.

7. References

[1] W.H. Lowdermilk and D. Milam, IEEE J. Quant. Electr. QE-17, 1888 (1981), and references sited therein.

[2] C.K. Carniglia, J.H. Apfel, G.B. Carrier and D. Milam, NBS Special Pub. 541, 218 (1978).

[3] R.W. Dietz and J.M. Bennett, Appl. Opt. 5, 881 (1966).

[4] J.H. Apfel, E.A. Enemark, D. Milam, W.L. Smith and M.J. Weber, NBS Special Pub. 509, 255 (1977).

[5] T. Izawa, I. Hashimoto and H. Shikakura, Rev. Laser Eng. 11, 662 (1983) (in Japanese).

[6] J.E. Swain, W.H. Lowdermilk and D. Milam, Appl. Phys. Lett. 41, 782 (1982).

[7] K. Yoshida, H. Yoshida, Y. Kato and C. Yamanaka, Appl. Phys. Lett. 47, 911 (1985).

[8] K. Yoshida, T. Yabe, H. Yoshida and C. Yamanaka, J. Appl. Phys. 60, 1545 (1986).

[9] L.M. Cook, W.H. Lowdermilk, D. Milam and J.W. Swain, Appl. Opt. 21, 1482 (1982).

[10] I.M. Thomas, Appl. Opt. 25, 1481 (1986).

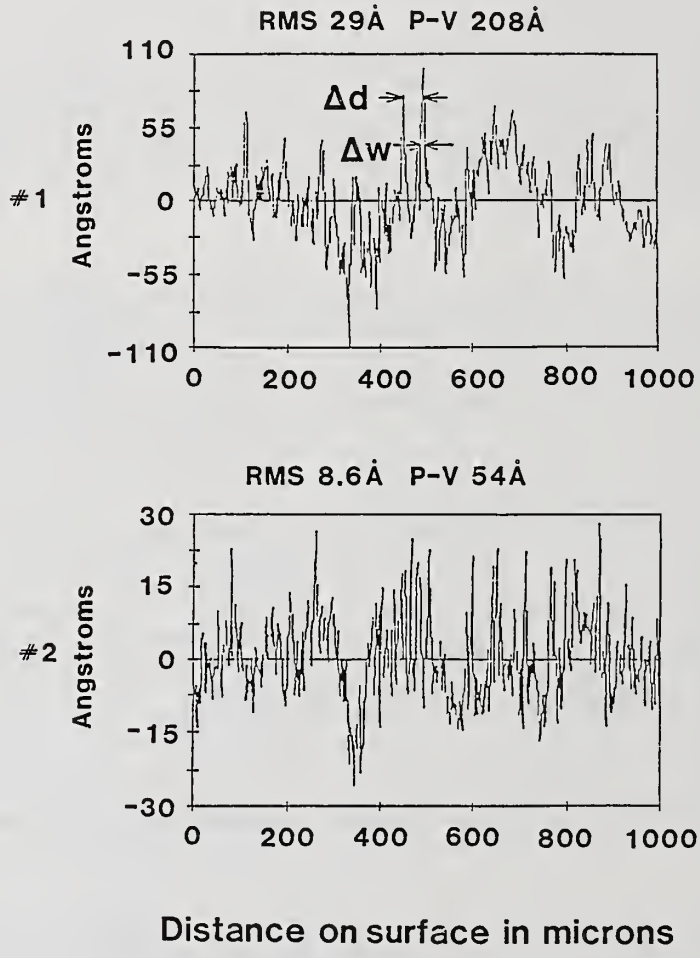

Figure 1 Surface profiles of the substrates prepared with different polishing techniques; conventional polish (#1) and bowl-feed polish (#2). Shown in the figure are definitions of Δw and Δd which characterize lateral scale-lengths of the surface roughness.

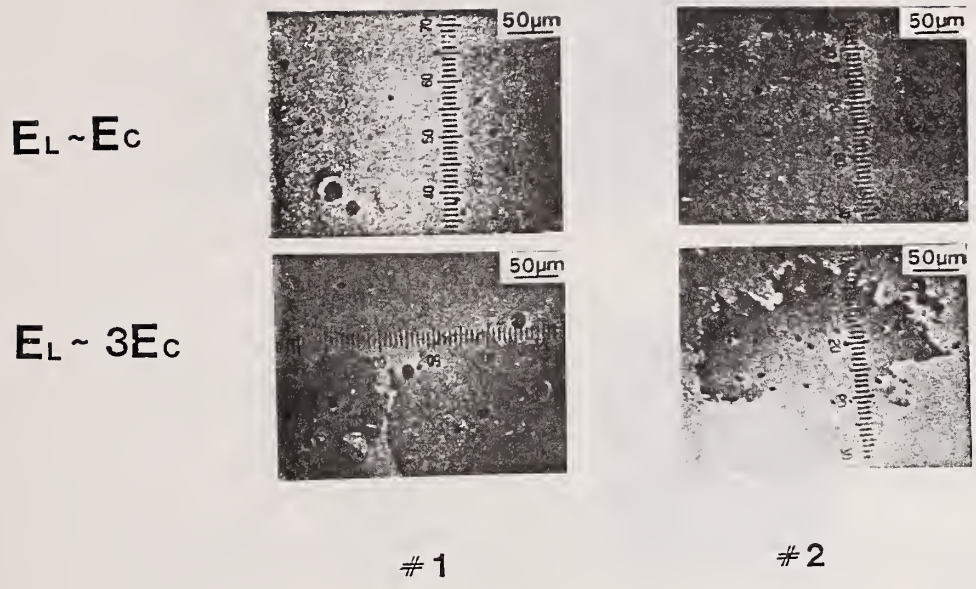

Figure 2 Morphology of the damages of the AR coatings on the substrates #1 and #2 having different surface roughness. Damages near the threshold ($E_L \sim E_C$) and far above the threshold ($E_1 \sim 3E_C$) are shown.

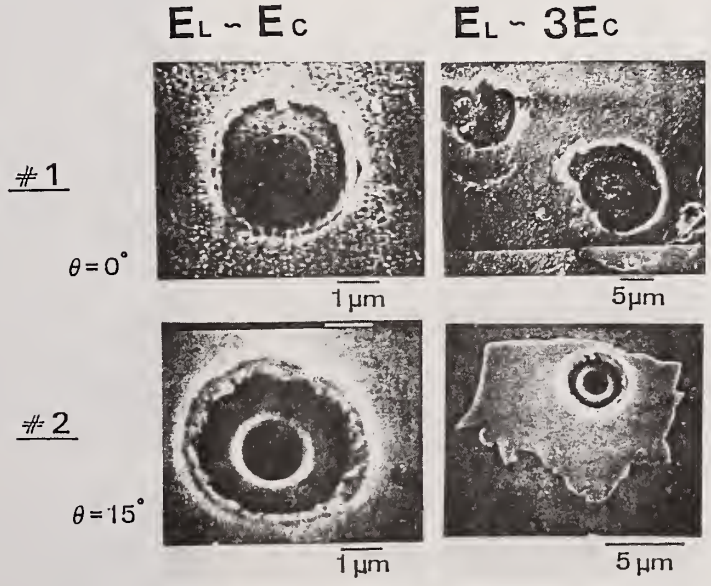

Figure 3 Scanning electron microscope pictures of the deep damages of the AR coatings on the substrates #1 and #2 having different surface roughness. Damages near the threshold ($E_L \sim E_C$) and far above the threshold ($E_L \sim 3E_C$) are shown. For #2 the substrates were tileted at 15° for better observation of the crater walls.

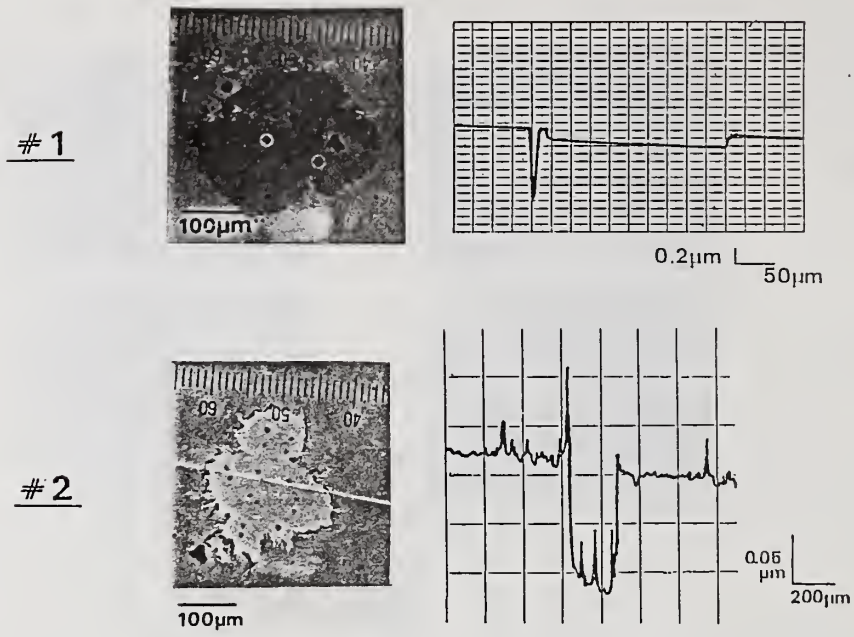

Figure 4 Talystep scans of the damages of the AR coatings on the substrates #1 and #2 having different surface roughness. The scales of the deep damage and the shallow damage are shown in the scan for #1 and #2, respectively.

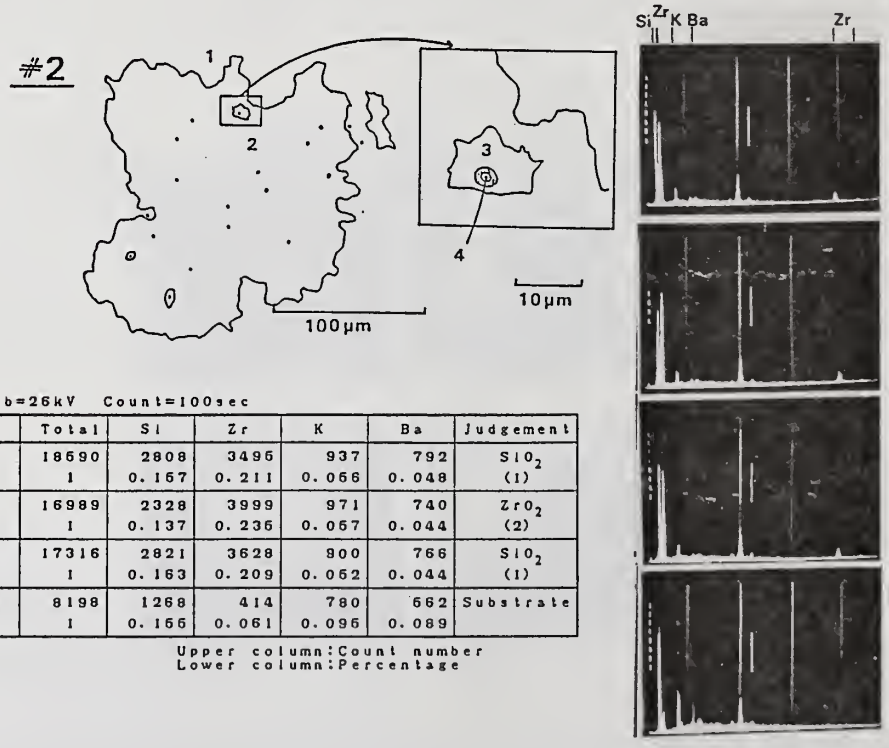

Prob=26kV Count=100sec

	Total	Si	Zr	K	Ba	Judgement
1	18690	2808	3495	937	792	SiO_2
	1	0.157	0.211	0.066	0.048	(1)
2	16989	2328	3999	971	740	ZrO_2
	1	0.137	0.236	0.057	0.044	(2)
3	17316	2821	3628	900	766	SiO_2
	1	0.163	0.209	0.052	0.044	(1)
4	8198	1268	414	780	662	Substrate
	1	0.155	0.051	0.095	0.081	

Upper column:Count number
Lower column:Percentage

Figure 5 XMA analysis of the sample #2 at four different sites; 1: undamages site, 2: in the shallow damage, 3: near the deep damage, and 4: in the deep damage.

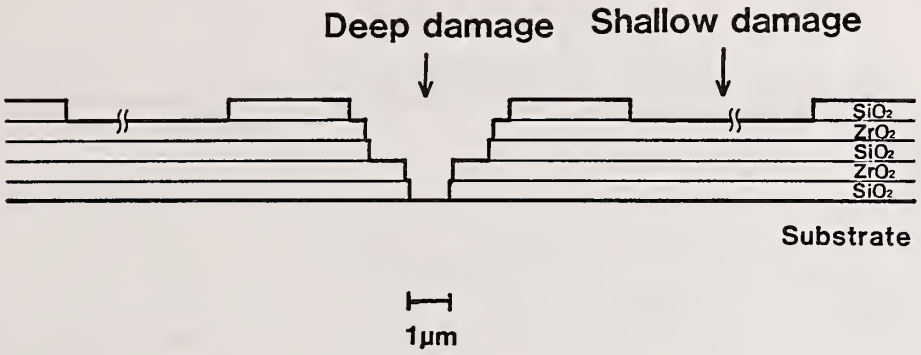

Figure 6 Schematic picture of the damage site of the 5-layer SiO_2/ZrO_2 AR coating.

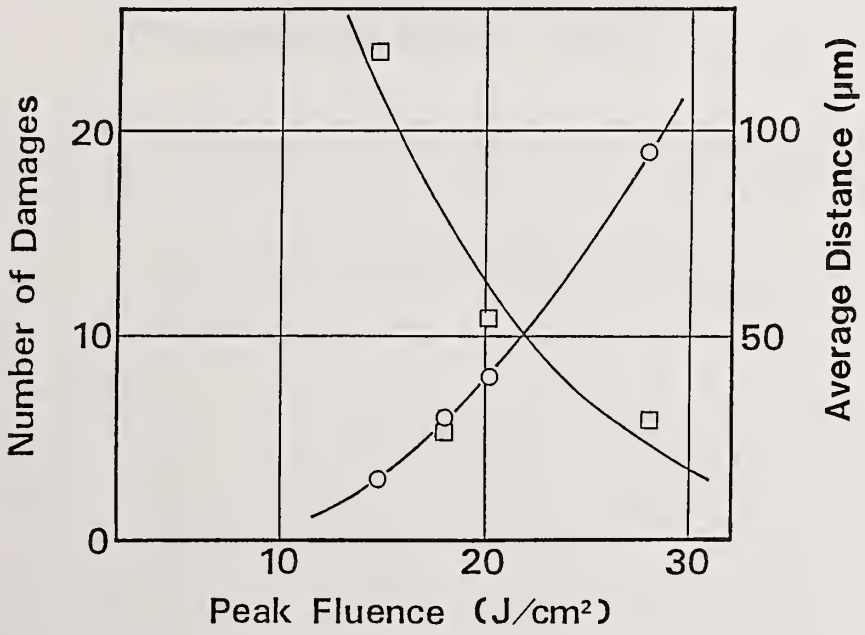

Figure 7 Total number of the deep damages (o) and the average distance between them (□) generated within the laser-irradiated area at different laser fluences.

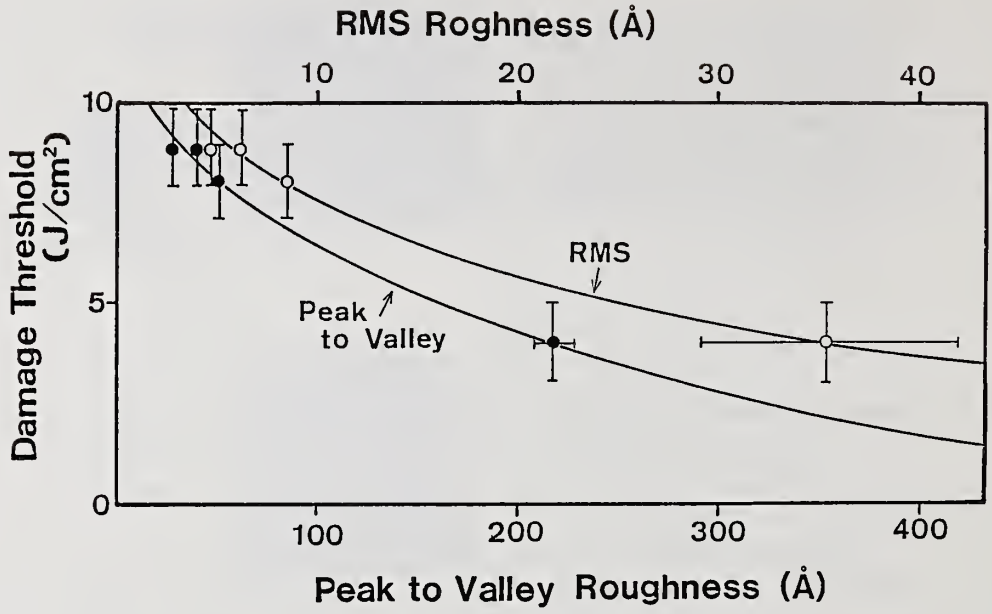

Figure 8 Dependence of the damage threshold of the AR coating on the surface roughness of the substrate.

Table 1. Surface roughness and lateral scale lengths of the two samples prepared by different polishing processes.

Sample	Polish	Surface roughness		Scale length	
		rms	peak-to-valley	Δw	Δd
#1	Conventional	29A	208A	11μm	39μm
#2	Bowl-feed	8.6A	54A	4μm	25μm

Table 2. Diameters of and average distances between the deep damages produced at $E_l \sim 3E_c$. Also shown are lateral scale lengths of the surface roughness of the substrates.

Sample	Polish	Deep damage		Scale length	
		Diameter	Distance	Δw	Δd
#1	Conventional	4-15μm	32μm	11μm	39μm
#2	Bowl-feed	3-5μm	26μm	4μm	25μm

- Manuscript Not Received -

Mechanical Stability and Absorptance of Metal Films

Michael McGuirk
Perkin-Elmer

ABSTRACT

The absorptance of gold films deposited under a variety of conditions was measured to an accuracy of .0002 with an HF Laser Calorimeter. The absorptance was observed to vary from .0107 to .0091, which is an 18% change.

The specimens were analyzed with a Perkin-Elmer PHI Auger spectrometer and the absorptance was found to be directly correlated with the impurity content.

The impurities were determined to originate in the residual gas in the chamber. A Dycor residual gas analyzer was used to locate and eliminate the sources of the impurities.

Films deposited at the same rates and temperatures, but with essentially no impurities were found to have absorptance ten times greater than the original films. These films have a dramatically different structure. They have been commonly observed, and are generally described as "recrystallized."

Impurities were intentionally added to produce an absorptance of approximately .0095. The doped films were observed to be substantially more stable than un-doped films under thermal cycling between room temperature and 225°C. The dopant atoms are believed to pin the grain boundaries. While no quantitative hardness measurements were made. The doped films are also expected to be harder.

Similar results were observed for silver. Partial recrystallization is hypothosized to explain the reflectance degradation of siver based EHR coatings reported by Dr. Don Decker in 1982.

Key Words: contaminant related absorptance; gold films; recrystallization; silver films; thermal cycling.

- Manuscript Not Received -

Highly Damage Resistant Anti-reflection Coating on the Chemically Etched Surface for High Power Lasers

K. Yoshida, H. Yoshida, Y. Kato and C. Yamanaka
Institute of Laser Engineering
Osaka University
Suita, Osaka 565, Japan

and

M. Ohtani
Physical & Chemical Technology Dept. 1
Canon Inc.
Ohta-ku, Tokyo 146, Japan

ABSTRACT

When the surface of BK-7 glass is conventionally polished by CeO_2 as polishing compound, the polishing compound is buried into the substrate. The buried compound can not be removed by standard optical cleaning techniques. Therefore, when the polished surface is anti-reflection (AR) coated and exposed to the focussed laser beam, the surface ionization occurs due to absorption at the isolated sites, leading to laser induced damages in the AR coating.

In order to improve the damage threshold, we have prepared the BK-7 substrate which was chemically etched after polishing. The damage threshold of the AR coating on the etched surface showed 1.5～2 times improvement compared with that of un-etched surface, at the laser wavelength of 1.06 μm and 1 ns pulse width. Due to the special etching technique, the surface roughness of the etched surface was 10～15 Årms, which was close to the surface roughness before etching (7～12 Årms).

Key Words: antireflection coatings; CeO_2 contamination; optical polishing; surface etching; surface roughness.

Manuscript Received
1-8-87

Influence of Solution Chemistry on the Microstructure of Sol-Gel Derived Films

Kim F. Ferris, Gregory J. Exarhos, and Clark Nguyen

Pacific Northwest Laboratory
Richland, Washington 99352

Recent work in this laboratory has demonstrated that the crystalline phase of titania deposited onto silica fibers by sol-gel techniques can be altered through changes in solution chemical equilibria brought about by variations in pH or chloride ion concentration. Molecular characterization of the solution microstructure and identification of the crystalline phase for deposited films is accomplished by Raman spectroscopic methods. The rutile phase of TiO_2 has been identified in films deposited from solutions prepared with $TiCl_4$ and HCl after a low-temperature densification (ca. 250°C) step. The more commonly observed anatase phase was formed without the addition of acid. Increased concentration of HCl in an alcoholic ethyl titanate solution results in increased stress in the anatase phase. A mixture of rutile and stressed anatase phases is found upon addition of LiCl to the acidic titaniumn alkoxide solution. These results suggest that the gel microstructure, which is a function of the solution chemistry, directly affects the crystal structure of the dehydrated, densified gel.

Key words: phase identification; Raman spectroscopy; sol-gel coatings; thin films

1. Introduction

The terms "sol-gel" or "sol-derived" materials arise from the fact that precursor materials are prepared in solution prior to a gelation stage by which the final product is isolated [1]. In the formation of metal oxide films, a number of potential starting compounds may be used for the preparation of the sol. These include, but are by no means limited to, metal alkoxides, chlorides, or nitrates [2, 3]. Early work in this area led to the fabrication of anti-reflective coatings for optical elements [4] and stimulated recent applied work regarding the development of interference coatings [5, 6]. However, fundamental work concerning the relationships between solution microstructure, solution chemistry, and the structure of sol-gel deposited films is lacking. This article attempts to address some of the more fundamental issues which govern the properties of deposited films.

Formation of an extended inorganic network in solution is dependent upon competing chemical equilibria in the solution and the rates by which overall chemical equilibrium is attained. Factors that control these processes include: solution pH, presence of competing ions in solution, steric hinderance caused by bulky organic groups bound to the metal cation, and solution temperature. Films deposited from solution as a function of time are expected to correlate structurally with the transient microstructure of the solution that exists at that particular time. Thus, both chemical equilibria and relative reaction rates will influence the structure of a deposited film.

Three important chemical reactions that control the solution microstructure are identified below and in figure 1.

(i) complexation $MCl_4 + 2Cl^- = MCl_6^{-2}$

(ii) hydrolysis $M(OR)_x + xH_2O = M(OH)_x + xROH$

(iii) condensation $2M(OH)_x = M_2O_x + xH_2O$

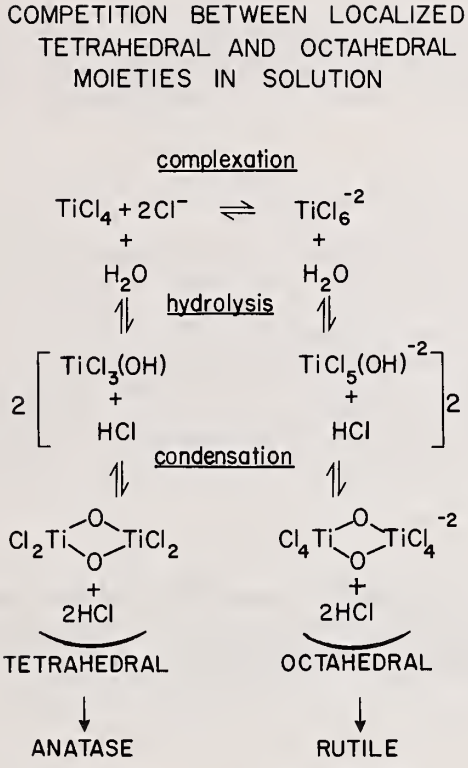

Figure 1. Generalized chemical reactions showing competition between localized tetrahedral and octahedral moieties in sol-gel solutions.

With the notable exception of the silicon and phosphorus systems, metal alkoxides, $M(OR)_x$, are readily hydrolyzed to the corresponding hydroxide [7].

In the case of TiO_2-deposited thin films, exposure of the alkoxide precursor to atmospheric moisture is sufficient to promote hydrolysis, forming the alcohol, ROH, and a polycondensed Ti compound. This step is usually followed by a heat treatment to eliminate the volatile reaction products and to achieve densification of the film. Studies on alkali-free silica substrates have shown that the anatase structure is formed when the material is heat-treated at temperatures below ca. 500°C [4, 8]. A rutile phase component has been found in films obtained from ethyl titanate solutions doped with $BiCl_3$ heated in excess of 500°C [9].

However, these methods do not fully exploit titanium sol-gel chemistry. In the case of silicon alkoxide, water may be added to the precursor compound since its hydrolysis is relatively slow unless catalyzed by the addition of acid. On the other hand, the condensation process is relatively slow under acidic conditions and is accelerated by the addition of base. Sol-gel materials derived under these conditions are not fully hydrolyzed and do not achieve full condensation unless heat-treated to near the glass transition temperatures [10]. A common technique for preparing a highly cross-linked material involves pre-hydrolysis of the metal alkoxide under acidic conditions prior to base-catalyzed condensation [8].

Such behavior is not readily observed in the titanium alkoxide system. The addition of water to the metal alkoxide results in the formation of an amorphous TiO_2 phase which rapidly precipitates from solution. An alternate strategy for the introduction of water to this system requires the addition of an aqueous mineral acid such as HCl. Ethyl titanate sols prepared under acidic conditions will be usable over longer periods of time since the condensation kinetics should be considerably slower and $(TiO_2)_n$ is soluble in HCl. As a result, the range of coordination chemistry for titanium is considerably expanded, allowing the preparation of novel precursors for titania films.

Molecular bonding in sol-gel solutions containing titanium alkoxides and in titania films deposited on silica substrates from these solutions has been evaluated using laser Raman

spectroscopy. Time-dependent changes observed in the vibrational spectra of these solutions suggest a kinetic influence on solution microstructure, which controls the resulting phase of the deposited film. The interrelationship among solution pH, chloride ion concentration, and alkoxide chain length on the phase of deposited films comprises the focus of reported work.

2. Experimental

Alcoholic solutions of $TiCl_4$, $Ti(OC_2H_5)_4$, and $Ti(OC_4H_9)_4$ were prepared with a range of metal alkoxide/acid/lithium chloride ratios as shown in table 1. Thin film coatings on silica fibers were prepared using the dip-coating method. These fibers were allowed to hydrolyze overnight in a controlled humidity environment (92% relative) prior to heat treatment at 250°C for four hours. Raman spectra were acquired from solutions as a function of time and from fibers both prior to and following heat treatment. Unambiguous identification of crystallite phase and phase composition were inferred from measured spectra. Furthermore, observed shifts in band frequencies were correlated with inherent film stress [11]. Measurements were performed using a 90° scattering geometry and conventional instrumentation. Slitwidths were maintained at 200 micrometers.

Table 1 - Composition of Alcoholic Titanate Sol-Gel Solutions Used to Deposit TiO_2 Films on 1000 μm Diameter Silica Fibers. Phase Composition of Thin Films Following Heat Treatment was Discerned From Raman Spectra

System	Composition (M/ℓ) Ti	H_2O	HCl	LiCl	Anatase E_g mode (cm^{-1})	Phase
Ethanol + $TiCl_4$						
1. No acid addition	0.50	0.0	0.0	0.0	146	80% stressed anatase + rutile
2. HCl added	0.50	2.8	0.6	0.0	-	Pure rutile
Ethanol + $Ti(OC_2H_5)_4$						
1. No additions	0.54	0.0	0.0	0.0	143	Anatase
2. HCl added	0.54	11.0	1.2	0.0	144	Stressed anatase
3. 2xHCl added	0.54	11.0	2.4	0.0	146	Stressed anatase
4. HCl + LiCl added	0.54	11.0	1.2	1.08	147	Stressed anatase, tr. rutile
5. 2xHCl + LiCl added	0.54	11.0	2.4	1.08	148	60% stressed anatase + 40% rutile
Butanol + $Ti(OC_4H_9)_4$						
1. No additions	0.54	0.0	0.0	0.0	-	Amorphous
2. HCl added	0.54	11.0	2.4	0.0	144	Anatase
3. LiCl added	0.54	11.0	0.0	1.08	-	Amorphous
4. HCl + LiCl added	0.54	11.0	2.4	1.08	149	50% stressed anatase + rutile

3. Results and Discussion

Titania thin films are usually prepared using an in situ hydrolysis of a thin film obtained from a metal alkoxide or metal chloride precursor. As such, the microstructure of the thin film formed from the metal precursor solution is controlled by the ligand groups to the titanium atom, possibly altered by the addition of dopants. The crystal phase of titania prepared from such materials is typically anatase and can be characterized by Raman bands at 143, 395, 515, and 636 cm^{-1} [12].

The effect of hydrolysis prior to film deposition is shown in figure 2. The addition of 5% hydrochloric acid to the ethanolic titanium tetrachloride sol results in a completely rutile phase [2a] after a low-temperature thermal densification. The anatase phase [2b] was found without the addition of acid. Referring to figure 1, the addition of acid, which shifts the equilibrium of the complexation reaction towards the formation of localized octahedral groups, results in the formation of the rutile phase.

The metal complexation equilibrium can be further perturbed by variations in the acid and chloride ion concentrations. The addition of hydrochloric acid and lithium chloride alone and in combination to a butyl titanate sol results in dramatic changes in the Ti-O stretching region (600-800 cm^{-1}) of the Raman spectrum as shown in figure 3. The solvent bands are relatively unperturbed by the salt and acid additions.

The effect of these additions on the thin film coatings were determined from Raman spectra of deposited films. Table 1 indicates the composition of the sols and the physical characteristics of the deposited films. A single-phase anatase material results from the thermal densification of amorphous titania prepared without the addition of LiCl or acid. The presence of hydrochloric acid in the processing sol induces considerable stress in the densified coating as indicated by the shift in the 143 cm^{-1} band to higher frequency. LiCl has a similar effect on the resulting thin film. The addition of both HCl and LiCl leads to a highly stressed phase of anatase plus the appearance of rutile. Figure 4 shows the relative frequency shift in the 143 cm^{-1} mode for films deposited from the butyl titanate sol and a sol containing HCl and LiCl additions. The measured band shift corresponds to an applied pressure of 10 kbars, based upon previous studies of the pressure dependence of the vibrational modes in bulk anatase [11].

The time-dependent evolution of sol structure is a well-known characteristic of silicon alkoxide sol-gel chemistry. The continual condensation of hydrolyzed precursor results in the eventual gelation of the sol. It has been shown that the ratio of linear-to-branched oligomeric materials, which generate this gel, is controlled by the pH of the sol.

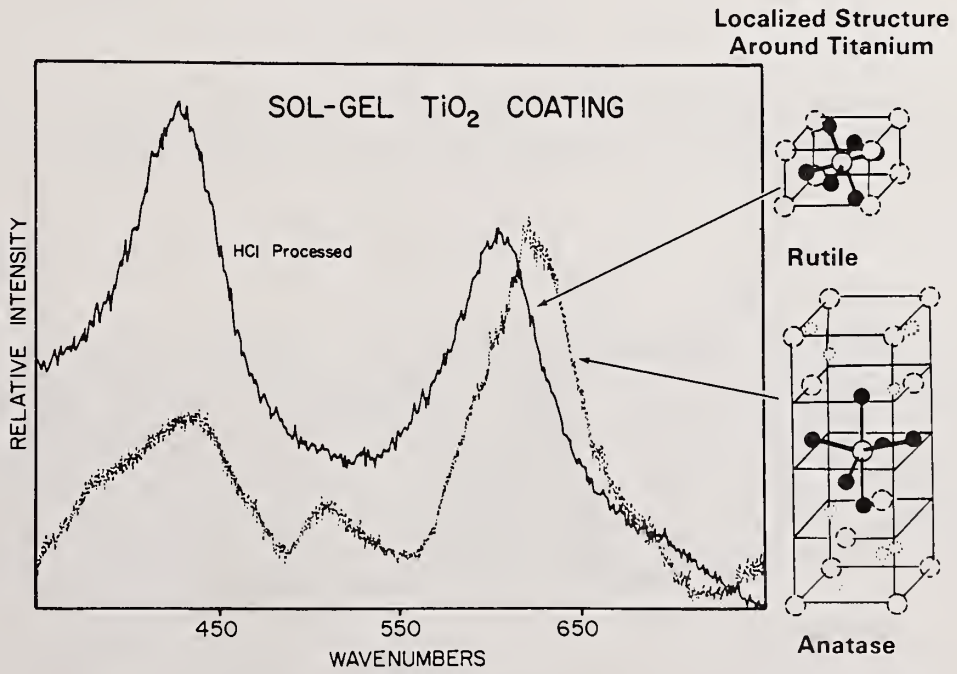

Figure 2. HCl addition to $TiCl_4$ in ethanol leads to stabilization of the rutile phase in sol-gel deposited films.

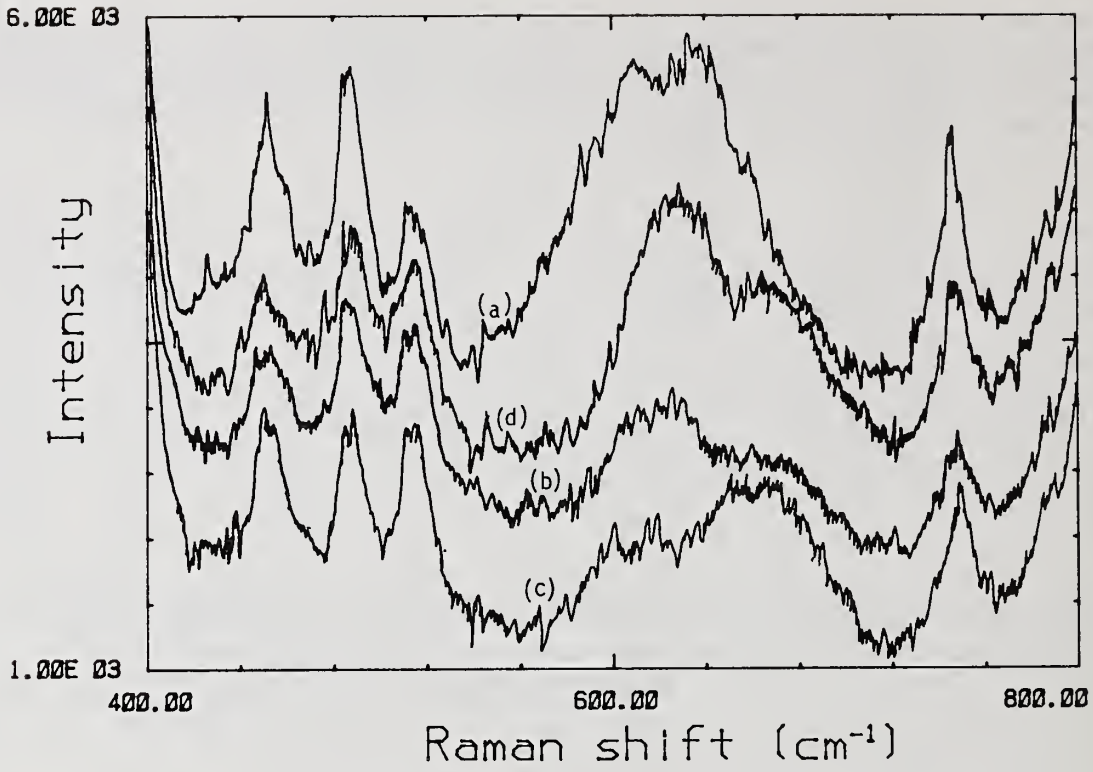

Figure 3. Effect of solution chemistry on the localized vibrational modes in the titanium-oxygen stretching region for alcoholic solutions of titanium butoxide; (a) titanium butoxide in butanol; (b) HCl added; (c) LiCl added; (d) both HCl and LiCl additions.

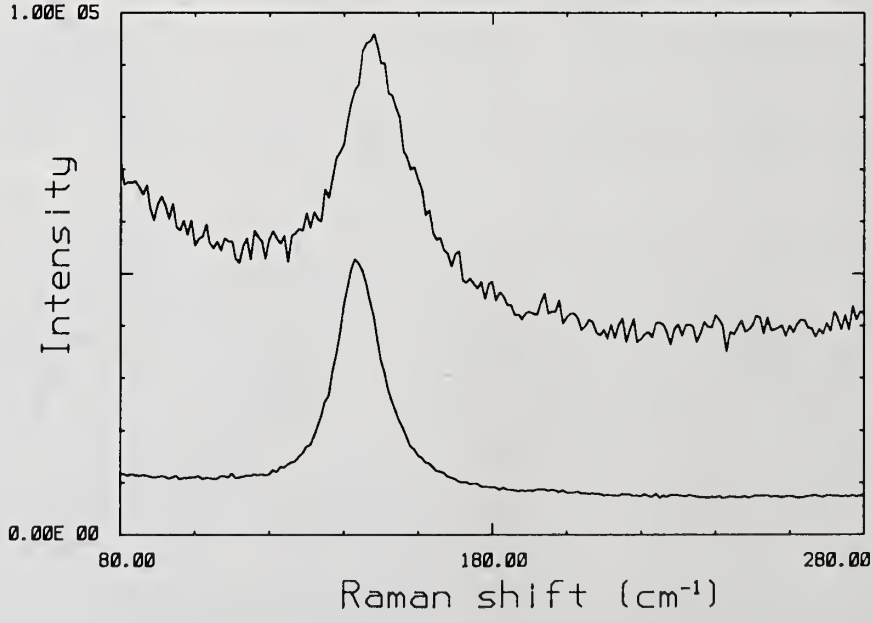

Figure 4. Localized stress in sol-gel deposited anatase films manifested by shifts in the 143 cm^{-1} E_g mode; bottom spectrum is of unstressed anatase.

Likewise, the structural evolution of the butyl titanate sol is observable using Raman spectroscopy. Figure 5 illustrates the Raman spectra of a 0.54 M ethyl titanate plus 2.4 M HCl sol over a two-day time period. There are dramatic changes in the low frequency region indicative of structural differences of this time period. In addition, the broad fluorescence feature observed in this spectrum underwent an initial rise and later decreased to a negligible level. The exact assignments of the structural bands in the 500-600 cm^{-1} region and the fluorescence feature are still unclear but may be related to oxygen or peroxo containing species identified in earlier work [13, 14]. Further work is being pursued to unambiguously assign these features.

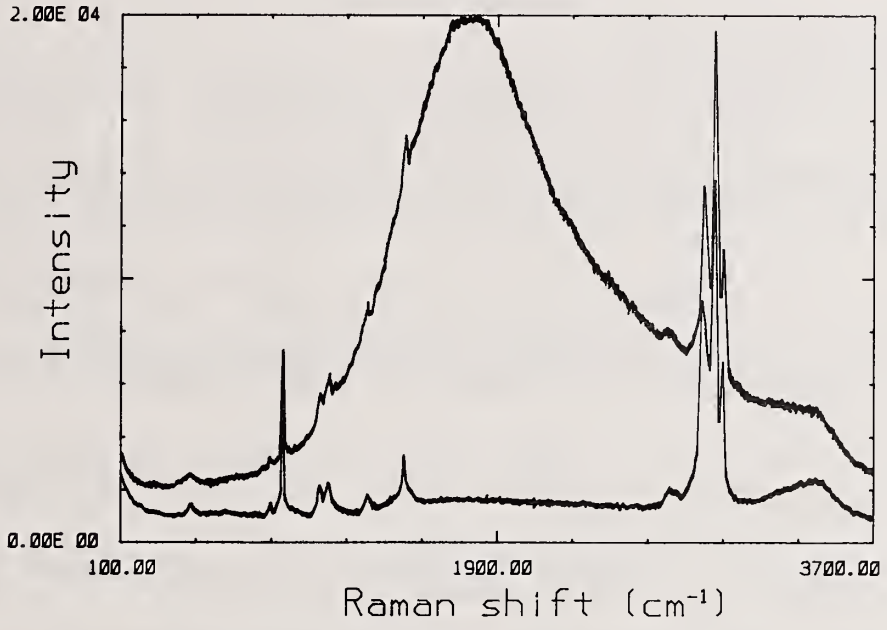

Figure 5. Transient changes in measured Raman spectra of titanium ethoxide in ethanol containing HCl. Top curve recorded 30 minutes following mixing; bottom curve was recorded 30 hours later.

4. Conclusions

The phase of sol-gel deposited films is determined by localized chemical bonding in solutions from which the film is formed. Several factors that control solution equilibria were shown to be pH and chloride ion concentration. Recent studies on zirconia-forming sol-gel solutions also indicate a marked pH dependence on the phase of the deposited material [15]. Low solution pH apparently acts to retard the condensation or network-forming reaction, allowing localized complexation equilibria to govern the solution structure. These studies have shown that sol-gel solutions prepared under conditions that minimize the condensation reaction deposit titania films rich in the rutile phase. Knowledge of conventional acid-base chemistry for metal cation-containing sol-gel solutions can be utilized to control localized solution structure that will, in turn, influence the crystalline phase of deposited films.

This work has been supported by the U. S. Department of Energy, Office of Basic Energy Sciences, under Contract DE-AC06-76 RLO 1830. Clark Nguyen also acknowledges partial support from the Department of Energy under NORCUS contract DE-AM06-76-2225.

5. References

[1] Thomas, I. M. "Optical Coatings by the Sol-Gel Process," Optics News 18-22; 1986.

[2] Sakka, S. "Sol-Gel Synthesis of Glasses: Present and Future," Am. Ceram. Soc. Bull. 674(11); 1463-1466; 1985.

[3] Mukherjee, S. P. "Sol-Gel Processes in Glass Science and Technology," J. Non-Cryst. Solids 42(1-3); 477-488; 1980.

[4] Bach, H.; Schroeder, H. "Kristallstruktur und Optische Eigenschaften von Dunnen Organogenen Titanoxyd Schichten auf Glasunterlagen," Thin Solid Films 1; 245-254; 1967.

[5] Phillips, R. W.; Dodds, J. W. "Optical Interference Coatings Prepared from Solution," Applied Optics 20(1); 40-47; 1981.

[6] Yoldas, B. E; O'Keeffe, T. W. "Anti-reflective Coatings Applied from Metal-Organic Derived Liquid Precursors," Applied Optics 18(18); 3133-3138; 1979.

[7] Dislich, H; Hussmann, E. "Amorphous and Crystalline Dip Coatings Obtained from Organometallic Solutions: Procedures, Chemical Processes, and Products;" Thin Solid Films 77: 129-139; 1981.

[8] Schroeder, H. "Oxide Layers Deposited from Organic Solutions," in Physics of Thin Films, Hass, G; Thun, R. E., ed. Academic Press, New York and London; 1969. Pp. 86-141.

[9] Schroeder, H. "Properties and Applications of Oxide Layers Deposited on Glass from Organic Solutions," in Proceedings of the Collogue sur les Materiaux Optiques, 1961 July 7; Paris, France. Pp. 249-254.

[10] Strawbridge, I; Craierich, A. F.; James, P. F. "The Effect of the H_2O/TEOS Ratio on the Structure of Gels Derived by the Acid Catalyzed Hydrolysis of Tetraethoxysilane," J. Non-Cryst. Solids 72; 139-147; 1985.

[11] Ohsaka, T.; Yamaoka, S.; Shimomura, O. "Effect of Hydrostatic Pressure on the Raman Spectrum of Anatase (TiO_2)," Solid State Commun. 30; 345-347; 1979.

[12] Beattrie, I. R.; Gilson, T.R. "Single Crystal Laser Raman Spectroscopy," in Proceedings Royal Soc. London, Sec. A, 307; 1972. Pp. 537-539.

[13] Muhlebach, J.; Muller, K.; Schwarzenbach, G. "The Peroxo Complexes of Titanium," Inorg. Chem. 9 (11); 2381-2390; 1970.

[14] Davies, J. E. D.; Long, D. A. "The Vibrational Spectra of Titanium Tetrachloride-Hydrochloric Acid and Titanium Tetrachloride-Tri-n-butyl Phosphate Systems and the Hexachloro-anions of Zirconium (IV), Hafnium (IV), Niobium (V), and Tantalum (V)," J. Chem. Soc. A; 2560-2566; 1968.

[15] Srinivasan, R.; DeAngelis, R. "Factors Influencing the Stability of the Tetragonal Form of Zirconia," J. Mat. Res. 1 (4); 583-588; 1986.

Manuscript Received
3-19-87

Quantification of the Magnitude and Duration of the Preconditioning Effect in AR Coated BK-7 Glass

M.E. Frink, J.W. Arenberg and D.W. Mordaunt

Hughes Aircraft Company*
El Segundo, California 90245

S.C. Seitel and E.A. Teppo

Montana Laser Optics*, Inc.**
Bozeman, Montana 59772

This paper presents the difference observed in laser damage thresholds between a ramped preconditioned type test and an unconditioned test method. The enhancement of the laser induced damage threshold observed by the preconditioned test was found to be on the order of 40%. We investigated the amount of preconditioning required to induce the threshold enhancement as well as the duration of the preconditioning effect. Our studies demonstrate that the test procedure used to induce catastrophic coating damage on AR coated BK-7 glass is critical in defining the absolute laser induced damage threshold level. Furthermore, preliminary measurements indicate that the observed preconditioning enhancement is not a permanent effect.

Keywords: antireflection coating; conditioning; damage threshold enhancement; preconditioned; thin films; unconditioned; 1.06μm.

* Electro-Optical & Data Systems Group
P.O. Box 902, E1/B129

** MLO*, P.O. Box 4151

1. Introduction

During a collaborative effort between Hughes Aircraft Company (HAC) and Montana Laser Optics*, Inc. (MLO*) it became apparent that our lack of correlation on round robin 1.06μm testing was due to testing procedure differences [1]. For the HAC standard test a sample site was selected and laser energy was slowly ramped up until catastrophic coating failure was induced (N on 1 type test) [2]. For the MLO* standard test the conventional (1 energy on 1 site) testing method was used. It was concluded that the difference in irradiance history on the same part, with the different tests, was somehow "conditioning" the coated surface. In all cases the preconditioning (irradiation at sub-threshold fluences) of the surface significantly increased the laser-induced failure level of AR coated BK-7 glass. A similar phenomenon has been reported in the literature for neutral solution processed BK-7 [3].

The important question pursued in our investigations was whether this observed increase in threshold was a permanent feature. If a permanent effect, then preconditioning may provide a means for enhancing resonator component performance in system hardware. If the effect is temporary, then the question of the appropriate damage test exposure procedure arises.

2. Experimental

The experimental procedure (N energies on 1 site, to insure correlation) used for measuring catastrophic damage thresholds at both the HAC and MLO* laboratories has been described [1]. The occurence of damage is identified by flash, damage, noise (FDN) accompanying the damaging laser pulse. All reported damage thresholds are front surface coating failure thresholds due to our method of testing behind focus. All parts were tested at 0° incidence at 1.06 μm and at 10 Hz. Laser parameters for both testing facilities are listed in table 1. All samples were prepared with an acetone and then an ethanol drag wipe. It should be emphasized that these are all single 'V' AR coated (1.06 μm) BK-7 glass samples.

Table 1. Laser Parameters

Parameter	HAC	MLO*
Wavelength (μm)	1.06	1.06
Repetition Rate (Hz)	10	10
Pulse Width (FWHM)	15-25 nsec	11 nsec
Modal Content	multimode	TEM_{oo}
Spot Size (FW @ $1/e^2$)	180 μm	500 μm

3. Results

MLO* (Experiment #1)

Preliminary scanning of samples revealed unconditioned catastrophic surface failures (FDN) consistently occurring at 44 J/cm^2, rarely at 35 J/cm^2. This was done with a spot size of 1 mm (FW @ $1/e^2$), larger than the standard testing size of 500 μm. When the surface was exposed at 33 J/cm^2, non-catastrophic pitting of the AR-coating definitely occurred, but flashes were not observed. This was taken as the maximum safe preconditioning level. Test sites which had been preconditioned at this level for even a few seconds (tens of shots) did not fail when exposed at 58 J/cm^2 (the maximum available fluence at this spot size) immediately afterwards. The apparent durability improvement was from 44 J/cm^2 to at least 58 J/cm^2, or at least 40% (~1.5 dB), a worthwhile gain. In addition, this experiment indicates preconditioning endures beyond the actual moments of testing.

Four samples were systematically preconditioned at 33 J/cm^2. On each sample, 100 test sites on a square 10 x 10 grid were irradiated for 5-10 seconds each. Site separation was 2 mm, as shown in figure 1. Pitting of the AR coating definitely occurred at all sites. In addition, a few sites failed on the surface or internally. These sites are noted on the preconditioning maps for each sample (example fig. 1).

Immediately after the preconditioning, the four sites at the corners of the grid were subjected to slowly increasing fluence until catastrophic failure "FDN" occured. The resulting damage craters are shown on the maps and serve to establish the coordinate system on the sample surface for future tests. The grand mean for the four samples was 73 J/cm^2, in satisfactory agreement with the 74 J/cm^2 value reported previously for the mean of 20 identically coated AR coated BK-7 optics [4]. These four samples were then sent to the HAC laboratories for further testing.

HAC: (Experiment #1)

The four preconditioned optics from MLO* were tested at the HAC laboratories 10 days later. Although the HAC damage test is not absolutely calibrated, the values (mV) are proportional to fluence levels. The preconditioned threshold off the preconditioned grid was 18 mV. The unconditioned threshold off the preconditioned grid was 15 mV. The observed unconditioned threshold on the preconditioned grid was 14 mV (±1 mV). (See table 2).

Table 2. Preconditioned vs. Unconditioned Thresholds

Sample		Threshold
3	preconditioned off the grid	17 mV
	unconditioned off the grid	15 mV
	unconditioned on the grid	14 mV
---	---	---
2	preconditioned off the grid	19 mV
	unconditioned off the grid	15 mV
	unconditioned on the grid	14 mV

Samples preconditioned 7-9-86; tested on 7-19-86
Threshold is lowest value of sites tested.

Most, if not all, of the preconditioning effect appeared to have been lost after 10 days. Additional results support these findings, as shown in table 2 and in figure 2.

Further testing at the HAC laboratories used a single preconditioned line across the optic face. These tests confirmed that the preconditioning was permanent at 1 hour and at 20 hours after initiation. (See fig. 3).

Table 3. Preconditioned vs. Unconditioned Thresholds

Sample		Threshold
2	preconditioned off the grid	21 mV
	unconditioned off the grid	16 mV
	unconditioned on the grid	18 mV
3	preconditioned off the grid	19.5 mV
	unconditioned off the grid	16 mV
	unconditioned on the grid	17 mV
4	preconditioned off the grid	17 mV
	unconditioned off the grid	15 mV
	unconditioned on the grid	16 mV
5	preconditioned off the grid	18.5 mV
	unconditioned off the grid	17 mV
	unconditioned on the grid	17 mV

Samples preconditioned on 7-9-86; tested on 7-21-86
Threshold is lowest value of sites tested.

To insure that the testing results were not biased by testing method or spot size effects, further testing used the same amount of surface area and the same number of test sites. In addition, the lowest value (instead of the mean) was used in each test method. In every case, the lowest value on the preconditioned test was higher than the lowest point on the unconditioned test. After further testing, it appears that the preconditioning effect fades over a period of 4 to 10 days, as illustrated in figure 3.

MLO*: (Experiment #2)

An experiment was conducted to determine the minimum fluence required to produce preconditioning enhancement of the damage threshold. The unconditioned threshold of a sample was determined. This value was termed the 100% value. Then selected areas of the surface were irradiated at fractional fluences below this 100% (threshold) value. These "conditioned" surfaces were then tested at an unconditioned level slightly higher than threshold (100%). Four sites were tested at each level and the results are shown in figure 4. It can be seen that except for the one weak site at 80% the cutoff is quite distinct. As little as 50% of the unconditioned threshold fluence is sufficient to precondition the surface and enhance the damage threshold.

(Experiment #3)

An experiment was conducted to determine the effect of water exposure on the preconditioning enhancement. A sample was tested and found to have an unconditioned threshold of 39 J/cm^2 and a preconditioned threshold of 53 J/cm^2, (35% increase with conditioning). A large area of the surface was preconditioned at 38 J/cm^2, just below the unconditioned threshold. Immediately after conditioning the area, 12 sites were tested at 46 J/cm^2 (between the two threshold levels). Only one of the 12 sites failed. The sample was then soaked in distilled water for 10 hours. The sample was removed from the water and dried with nitrogen. Seven sites were tested at 46 J/cm^2 and all seven sites failed. The sample was then flooded with acetone and drag wiped. Five sites were tested at 46 J/cm^2 with no failures. This indicates that water has a principal role in deactivating the preconditioning enhancement.

HAC: (Experiment #4)

Four samples were preconditioned and then set aside. Two samples were left exposed on the lab bench and two were placed inside a dessicater. After 10 days the parts were all tested. All four samples had lost any preconditioning effect. Although preliminary, these results indicate that there may be other mechanisms at work. However, it may be that brief exposure of the optic to water vapor and not continuous exposure is all that is needed for the threshold enhancement deactivation mechanism.

4. Conclusion

It has been shown that the testing procedure and the irradiance history of AR coated BK-7 glass samples significantly affect the laser induced damage threshold value. Sub-threshold laser irradiation of the surface can increase the observed threshold by as much as 40%. It has also been shown that this effect, a preconditioning effect, is not permanent over long periods (days). The exact mechanism for the initial preconditioning increase in the threshold value and the mechanism(s) of its apparent loss are yet to be determined. The absorption of water is apparently one mechanism contributing to the decline of the threshold enhancement. However, it appears other mechanisms may also be contributing to the threshold deactivation. This emphasizes the need for continued study of this phenomenon along with the expansion to other coatings and substrates.

Acknowledgement: The authors thank Mark Babb (MLO*) for his contributions.

References

[1] Arenberg, J.W., Frink, M.E., Mordaunt, D.W. Lee, G., Seitel, S.C., Teppo. E.A. Correlation of Damage Levels at 1.06 μm Varying Modal Content and Irradiance History on Representative Coated Laser Optics, presented at the Nat. Bur. Stand. (U.S.) Damage Symposium 1986.

[2] Mordaunt, D.W., Frink, M.E., Arenberg, J.W. Production Oriented Laser Damage Testing at Hughes Aircraft Company, presented at the Nat. Bur. Stand. (U.S.) Damage Symposium 1986.

[3] Swain, J.E., Lowdermilk, W.H., Milan, D. Raising the Surface Damage Threshold of Neutral Solution Processed BK-7 by Pulse Laser Irradiation, Nat. Bur. Stand. (U.S.) Spec. Publ. 669; 1982. 292-295.

[4] Seitel, S.C. and Teppo, E.A. private communication.

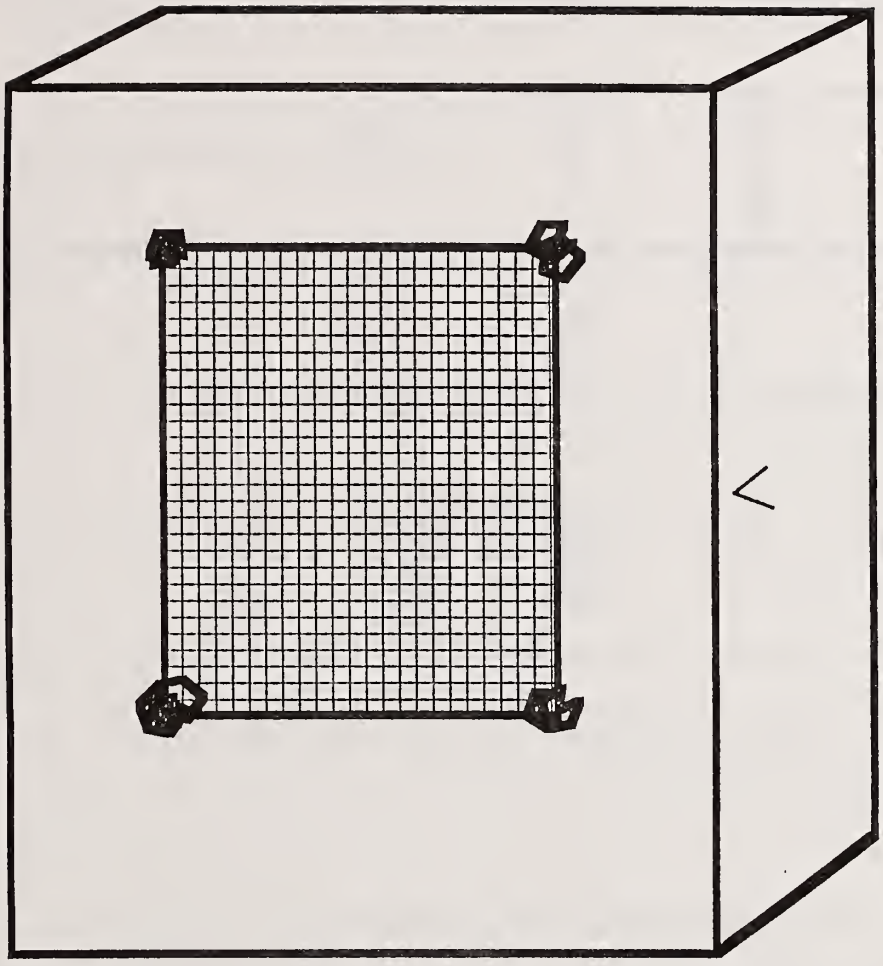

Grid Spacing 2 mm x 2 mm
"X" Surface Damage
"B" Internal or Rear Damage

Figure 1. Preconditioned grid on optic surface

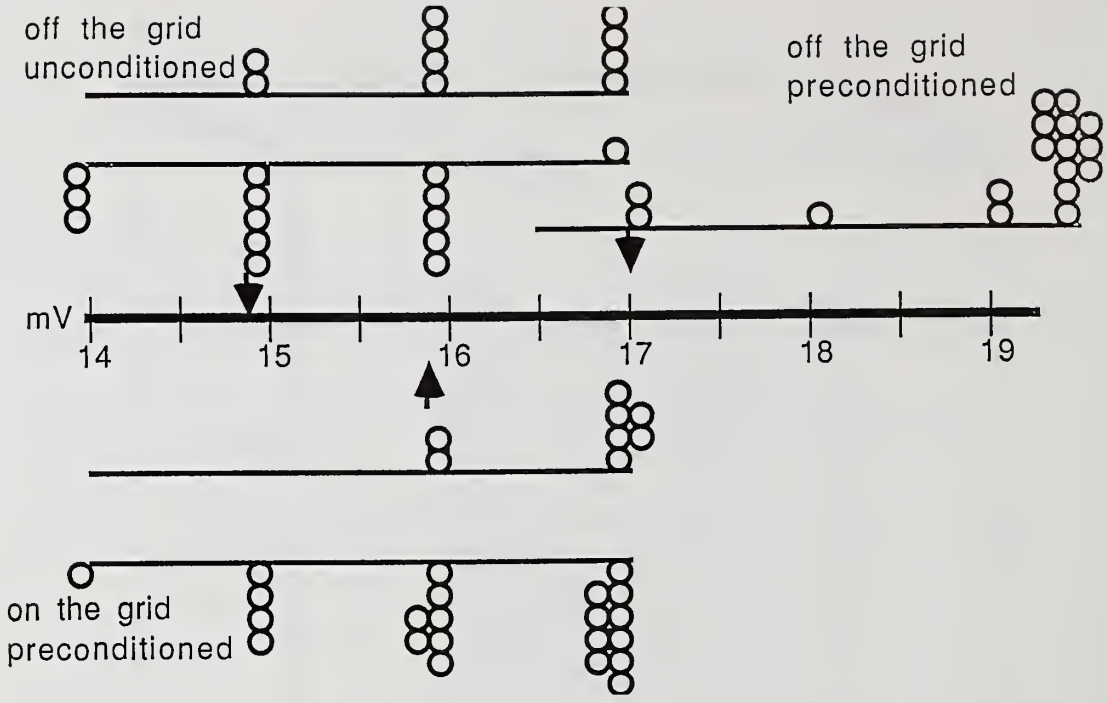

Figure 2. Tested sites on and off the preconditioned grid

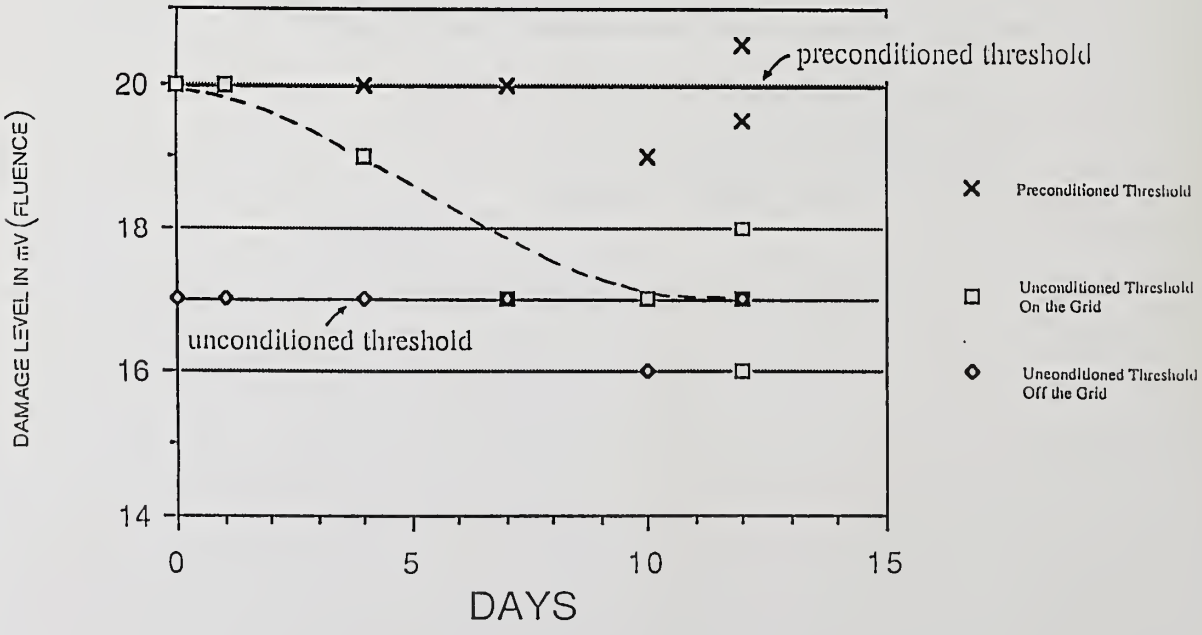

Figure 3. Decline of the preconditioning effect

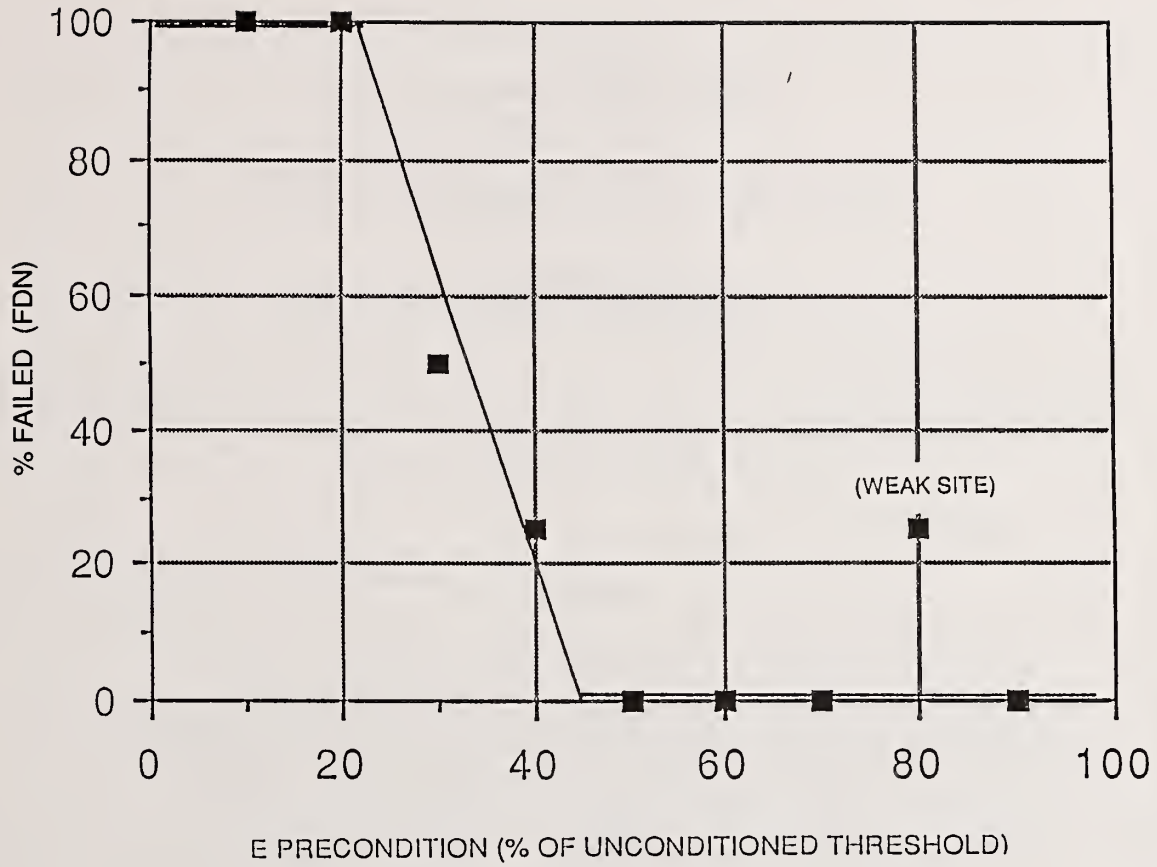

Figure 4. Minimum fluence required to produce preconditioning

- Manuscript Not Received -

MICROSTRUCTURAL AND PHYSICO-CHEMICAL INVESTIGATIONS OF DIELECTRIC MULTILAYERS

Karl H. Guenther
Center for Applied Optics, University of Alabama
Huntsville, AL 35899

and

Walter T. Pawlewicz
Battelle Pacific Northwest Laboratory
Richland, WA 99352

ABSTRACT

Dielectric multilayer coatings of SiO_2 and Si_3N_4 prepared by RF diode sputtering show very good environmental stability which surpasses that of conventional vapor deposited coatings. It is generally assumed that sputtered films have a higher packing density which makes them less susceptible to water penetration. Transmission electron micrographs of cross-section replicas of these multilayer structures show a columnar microstructure of the individual Si_3N_4 films which is qualitatively denser than that of other high index films made by electron beam deposition. Hence, some porosity may be still assumed for the sputtered films, and therefore other mechanisms to make them less humidity susceptible than just desiccation. For instance, it has been found that the wetting properties of dielectric thin films not only depend on their material but also, to a minor extent though, on the method of how they were deposited. Another possible explanation for improved humidity stability is that the plasma discharge in the sputtering process may polymerize residual hydrocarbons or silicone in the vacuum chamber to form hydrophobic thin films in between the dielectric layers and also on their inner surfaces, so that the voids between the columns in the films become less able to absorb water. First results on both contact angle measurements to assess the wettability of coating surfaces and on electron spectroscopic imaging for detecting presumed hydrocarbon contamination are presented.

Manuscript Received
4-10-87

An Investigation of Laser Processing of Thin Film Coatings

Annetta J. Weber and Alan F. Stewart

Air Force Weapons Laboratory
Kirtland Air Force Base, New Mexico 87117

Gregory J. Exarhos

Battelle Pacific Northwest Laboratories
Richland, Washington 99352

An initial set of experiments has been conducted to determine the practicality of laser processing of thin film coatings. A high average power CO_2 laser was used to flood load the entire surface of each test sample. Thin film coatings of HfO_2 and MgF_2 on fused silica substrates were irradiated with power densities between 25 and 125 W/cm^2.

Extensive pre- and post-test characterization revealed that some changes in the microstructure were observed, the coating optical thickness was reduced and short wavelength transmission was improved.

Key words: HfO_2; MgF_2; Raman spectroscopy; surfaces; thin films; total integrated scattering

1. Introduction

Materials processing has proven to be an extremely important application of the laser [1,2]. Techniques have been developed which extensively modify material surface properties so as to better fit their intended use. Dramatically increased hardening and the formation of alloys and metastable phases on metallic surfaces have been observed in experiments with pulsed and continuous irradiation. Extensive work has dealt with laser annealing of silicon wafers to repair structural damage caused by ion implantation. In addition, lasers have been used to fire polish the surfaces of fused silica and pyrex for optical applications and produce phase transformations and alloying in thin film structures [3-5].

A preliminary set of experiments designed to determine the practicality of laser processing of thin film coatings is described in this paper. A high average power CO_2 laser was used in these experiments. In contrast to earlier work in this field, the entire surface of each test sample was flood loaded with a uniform beam intensity distribution.

Before and after irradiation, samples were characterized to carefully determine changes in the optical and material properties. Analysis methods utilized included spectrophotometry, total integrated scatter, and Raman spectroscopy.

Our data indicates that laser irradiation of thin film coatings will require extensive additional study. The optical thickness of selected coatings was reduced and these samples showed improved short wavelength transmission for carefully chosen irradiation conditions.

2. Experiment

A continuous wave, 15 kilowatt CO_2 laser system shown in figure 1 was used in these experiments [6]. Multimode operation at 10.6 microns with stable resonator optics results in a uniform annular beam profile. However, annular rings appear in the beam with a 5% modulation depth due to diffraction from the output coupler aperture.

The experimental arrangement used in these experiments is shown in figure 2. Beam power levels were monitored in real time using a sodium chloride beamsplitter and a thermopile calorimeter. Output power during a 10 second run was stable to within 5%. The beam was reflected unfocussed towards the coated samples with a diameter of 9.4 cm in the test plane as determined by Plexiglas burn patterns. Samples were translated across the beam in order to average out the effects of beam nonuniformity. The translation stage platform moved at a constant speed of 1.5 cm/second resulting in a beam dwell time on the surface of 6.3 seconds.

Thin film coatings of HfO_2 and MgF_2 on superpolished Suprasil 1 fused silica substrates were irradiated in this study. The coatings were fabricated using commercial electron beam deposition with an optical thickness of $\lambda/2$ at 1.06 microns. A centered sputtered molybdenum dot 12mm in diameter and 1000 angstroms thick was deposited on the substrate prior to the application of the dielectric coating to facilitate measurements of total integrated scatter (TIS). Coated substrates were cleaned prior to irradiation using a spin cleaning system with spectroscopic grade methanol and collodion. Relatively low incident intensities were required to effect significant changes in the coatings. Intensities used ranged from 25 to 125 W/cm^2 intervals.

3. Analysis and Discussion

3.1 Spectrophotometry

A Varian 2320 spectrophotometer was used to measure the transmission of samples from 1900 to 8000 angstroms. Transmission curves obtained on thin film coatings of HfO_2 and MgF_2 films appear in figures 3-6. It is most clearly illustrated in figures 3 and 4 that laser irradiation results in a shift in the transmission maxima and minima to shorter wavelengths. This means that the optical coating thickness is reduced. This could occur if material was ablated from the surface, water was driven out of a porous coating, or if the coating microstructure was physically altered through densification or a phase transformation. This phenomenon is apparent also in the data obtained on MgF_2 films, although the similarity in refractive indices of coating and substrate makes it more difficult to observe.

For both types of films, transmission at wavelengths shorter than 4000 angstroms is significantly enhanced for samples irradiated at 50 W/cm^2. Samples irradiated at intensities both at 25 W/cm^2 and at higher levels show reduced transmission. Increased transmission could be the result of a phase transformation in the coating and hence reduced absorption. The irradiation could also lead to the desorption of absorbing impurities or the annealing of defects such as dangling bonds on the surface and in the interior of the coating. At higher power levels, transmission is reduced due to changes in the crystalline structure, stoichiometry and chemical bonding in the film. It was visually obvious that MgF_2 films became MgO films at higher intensity levels.

3.2 Total Integrated Scatter

Total integrated scatter (TIS) measurements were performed on thin film coated samples before and after irradiation. Measurements were performed at 633 nm. The molybdenum dot on the coated substrates provided a suitable reference surface. The instrument has been described in detail elsewhere [7]. Repeatability and precision of the instrument is 0.5 angstroms RMS. TIS data is summarized in table 1, with the surprising result that the surface roughness increases only slightly for moderate irradiation levels.

3.3 Raman Spectroscopic Analysis

Raman spectroscopy was used at Battelle Pacific Northwest Laboratories to study the structure of CO_2 laser processed thin film coatings. As in all Raman spectra, the observed features correlate to vibrational and rotational transitions in the material. Poor scattering efficiency in the MgF_2 films prevented us from obtaining useful spectra. Raman spectra were obtained on laser irradiated thin film coatings of HfO_2. As shown in figure 7, spectra from thin film coatings of HfO_2 irradiated at 0-125 W/cm^2 are compared with that obtained on a monoclinic structure powder sample. At incident intensities of 100 W/cm^2 and higher, HfO_2 films begin to crystallize with the emergence of peaks at ~490, ~590, ~650 and ~680 cm^{-1}. The spectrum of the film irradiated at 75 W/cm^2 also shows the formation of small peaks at ~590 cm^{-1} and 600 cm^{-1}. Spectra recorded on the control sample and on films irradiated at 25 and 50 W/cm^2 are relatively smooth with a single small peak at ~600 cm^{-1}. This peak does not match up with any of the features in the HfO_2 reference spectrum but does correlate to a well known feature of the silica substrate spectrum. However, the 600 cm^{-1} peak in the fused silica spectrum should not be observable using the z(xy)z scattering geometry used in this work. The fact that this peak is seen in these spectra is probably due to depolarization of the probe beam from birefringence in the film possibly caused by stress. It is difficult to determine the correlation between the improved optical properties of HfO_2 films irradiated at 50 and 75 W/cm^2 with changes in microstructure observed in the Raman spectra.

4. Discussion and Conclusions

This preliminary study of CO_2 laser irradiation of optical thin film coatings has demonstrated that exposure of films to a specific range of intensities may result in increased short wavelength transmission. These observations may indicate that coatings can be "repaired" by laser processing so that their properties approach those of the bulk material. However, improved transmission of coatings below 400 nm occurs without measurable changes in film microstructure.

The mechanisms responsible for changes in the optical properties of thin film coatings may in fact correlate to those responsible for improvements in electrical properties of semiconductors as observed following laser or rapid thermal annealing procedures. The removal of a high density of bandgap states by an annealing process would also significantly affect the optical transmission of the material. Raman spectra obtained on the films used in this study indicated a largely amorphous structure which is synonymous with dangling bonds and a high density of bandgap states. The fact that optical transmission near the bandgap improved in certain samples without accompanying changes in the film microstructure may indicate that a single type of defect or impurity is responsible for the observed phenomena. Future work will attempt to correlate deposition conditions and hence preexisting microstructure with changes in optical properties.

Table I: TIS Data (on Molybdenum Dot)

Laser Annealed HfO_2 and MgF_2 Coatings*

	HfO_2			MgF_2		
	Before	After	Δ	Before	After	Δ
Control	6.2	6.2	0	18.6	17.5	-5.9%
25 W/cm^2	6.5	6.5	0	17.8	16.9	-5.1%
50 W/cm^2	7.2	7.4	-2.8%	23.5	22.6	-3.8%
75 W/cm^2	9.0	7.4	-18%	20.5	40.2	+96%
100 W/cm^2	7.7	8.3	+7.8%	18.8	∞**	+ ∞
125 W/CM^2	7.5	8.6	+15%	18.4	∞	∞

* λ/2 Optical thickness at 1.06 microns
** Formation of MgO

List of Figures

6) Transmission curves obtained on MgF_2 thin film coatings- Control, 75, 100 and 125 W/cm^2.

7) Raman spectra obtained on HfO_2 thin film coatings for various incident power levels compared to a standard.

4. References

[1] See for example:

"Laser and Electron-Beam Solid Interaction and Materials Processing", Gibbons, J.F., Hess, L.D. and Sigmon, T.W. (editors).
Proceedings of the Materials Research Soc. Ann. Meeting, Boston MA, Nov 1980
"Laser and Electron-Beam Interactions with Solids", Appleton, B.R. and Celler, G.K. (editors).
Proc. of the MRC Soc. Ann. Meeting, Boston MA, Nov. 1981.
"Laser-Solid Interactions and Transient Thermal Processing of Materials", Narayan, J., Brown, W.L. and Lemons, R.A. (editors).
Proc. of the MRC Soc. Ann. Meeting, Boston MA, Nov. 1982.

[2] Gnanamuthu, D.S., "Laser Surface Treatment," Opt. Engr Vol. 19.5 pp 783-792 (1980).

[3] Temple, P.A., Lowdermilk, W.H., and Milam, D. "Carbon Dioxide Laser Polishing of Fused Silica Surfaces for Increased Laser-damage Resistance at 1064 nm, Appl. Opt. 21, 3249-3255, (1982).

[4] Xiao, Y.M. and Bass, M., "Thermal Stress Limitations to Laser Fire Polishing of Glasses," Appl. Opt. 22, 2922-2936 (1983).

[5] Baufrey, L., Andrew, R., Pigeolet, A. and Laude, L.D., "Preparation of AlSb films by Laser Annealing," Thin Solid Films, 90, pp 69-74 (1982).

[6] "A 15kW Electric Discharge Coaxial Laser" Air Force Weapons Laboratory Technical Report pp 76-115, (August 1976).

[7] Bennett, J.M. and Stowell, W.K., "Round-Robin Testing of Low Scatter Optics," Nat. Bur. Stand. (U.S.) Spec. Publ. 688; pp 183-190 (1983).

EXPERIMENTAL ARRANGEMENT FOR LASER POLISHING/ANNEALING STUDIES

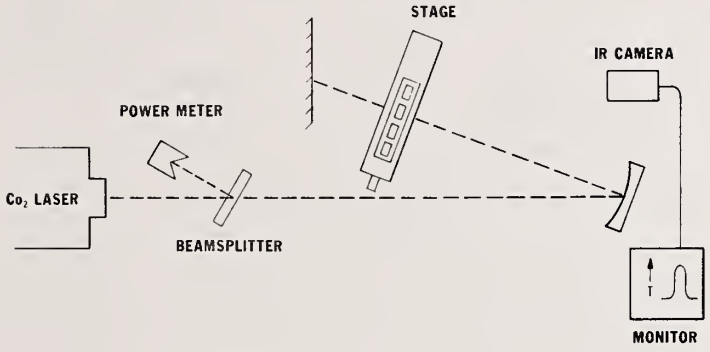

Figure 1.

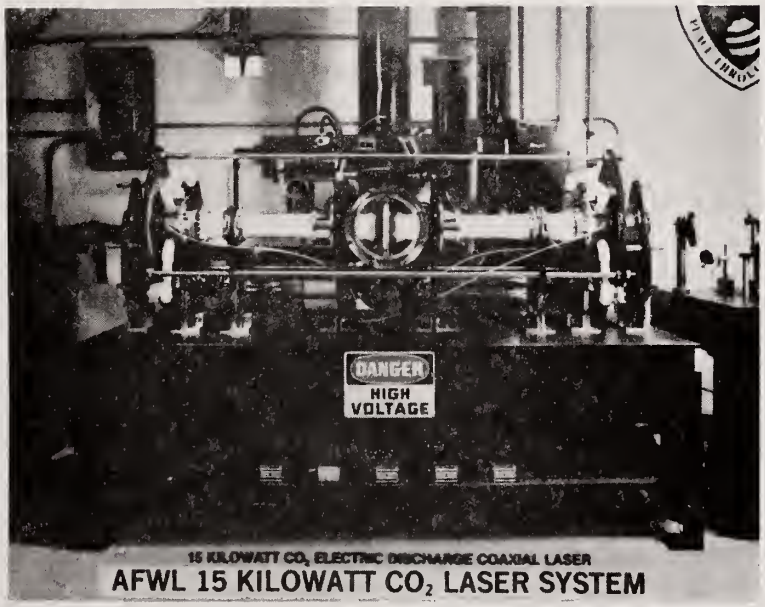

Figure 2.

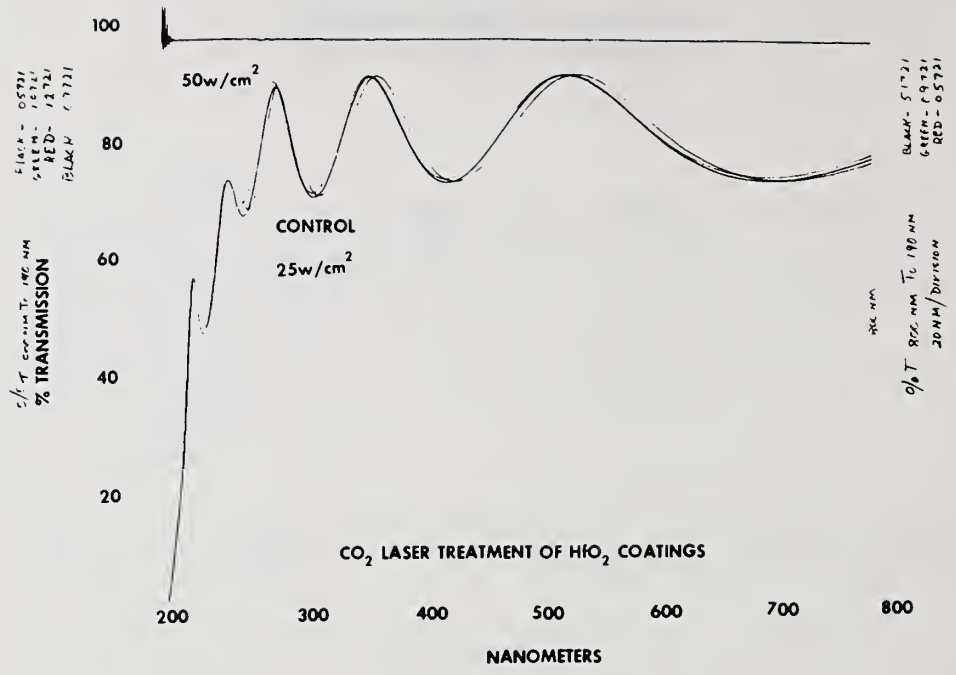

Figure 3.

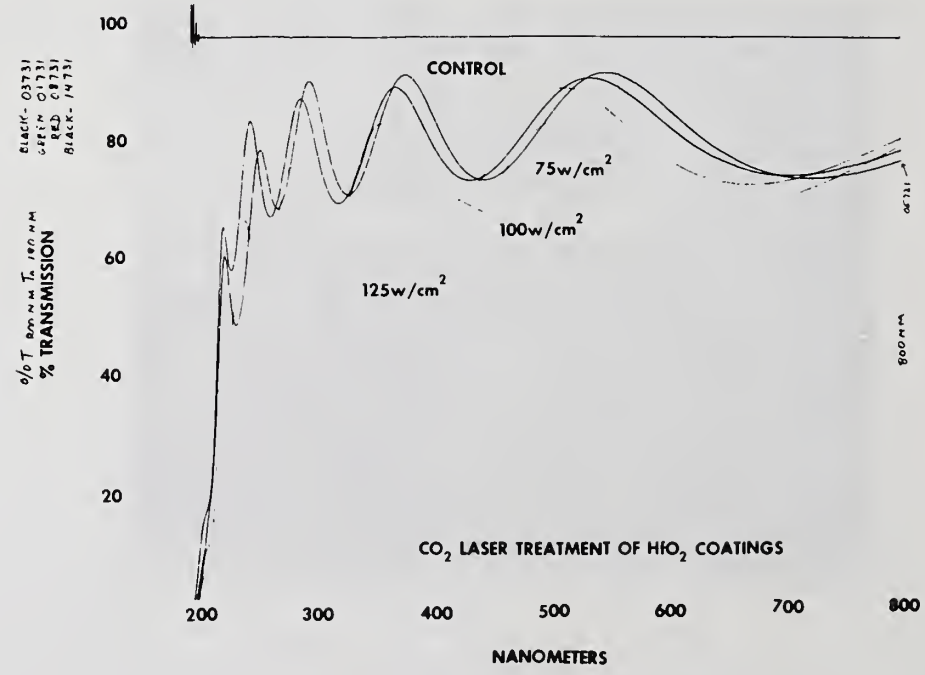

Figure 4.

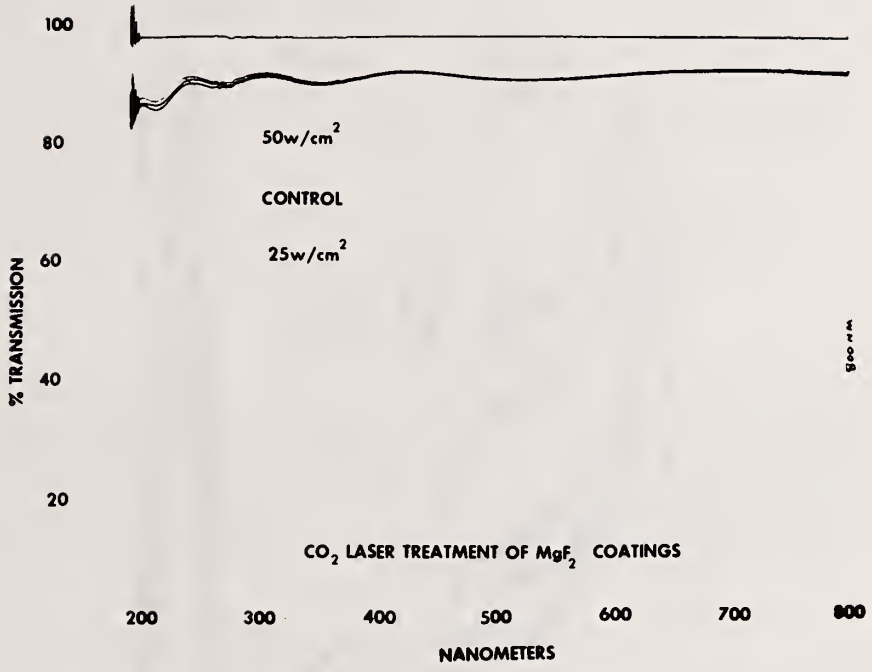

Figure 5.

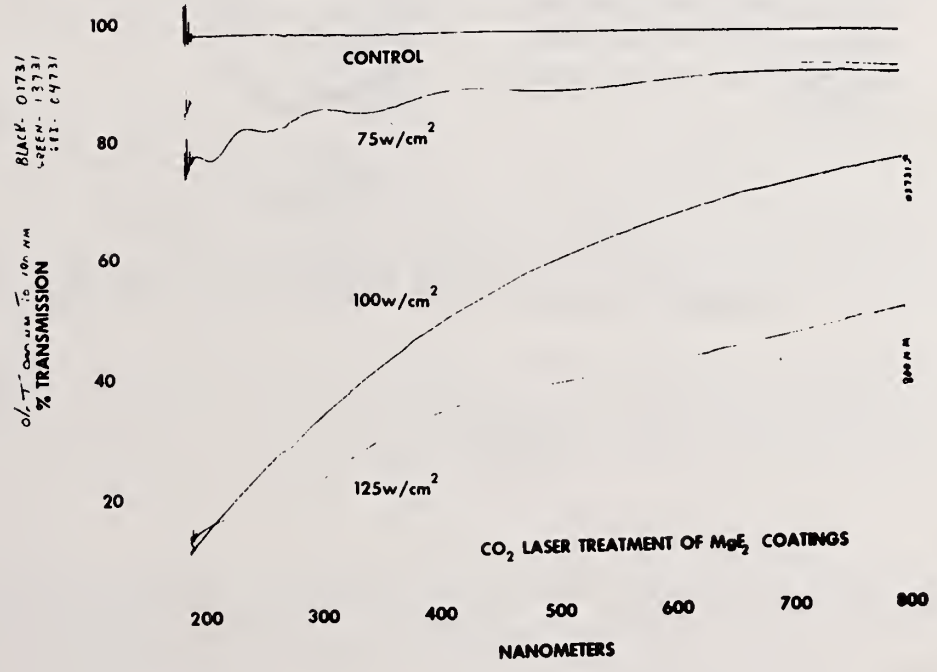

Figure 6.

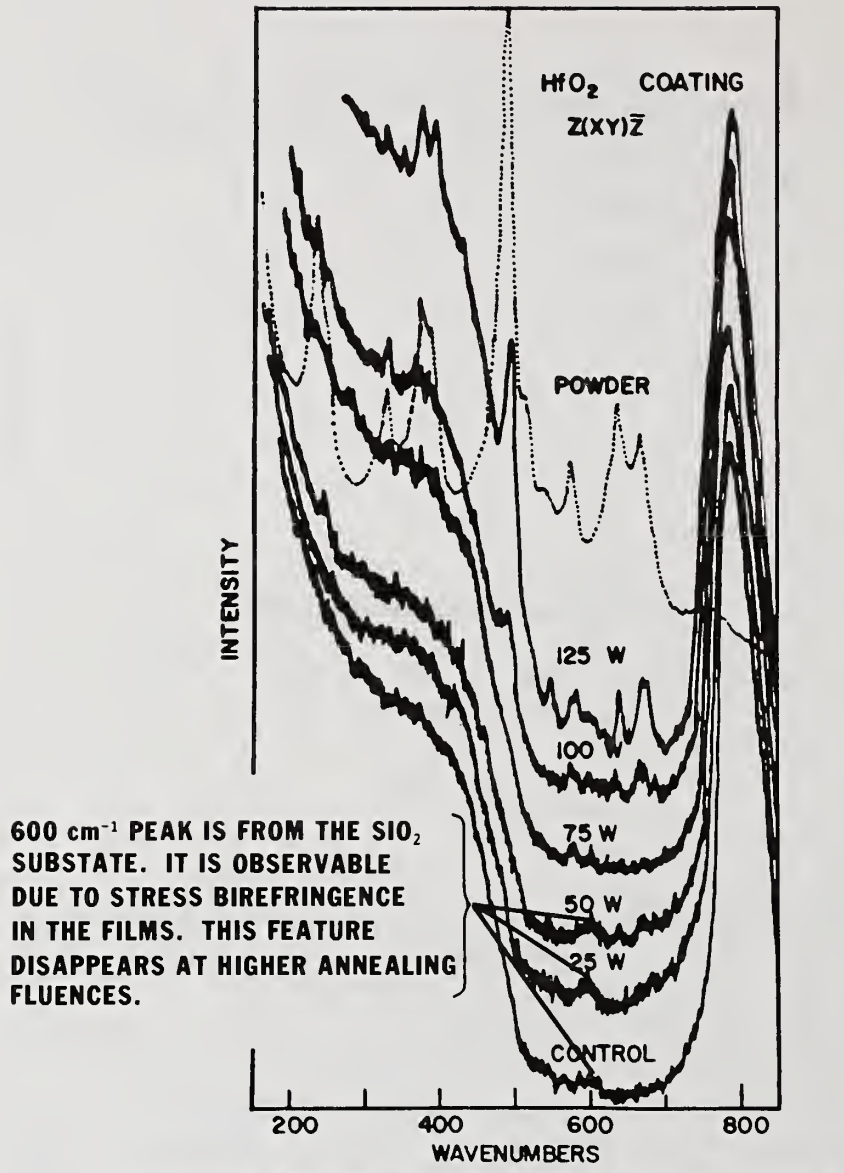
HfO_2 COATING
Z(XY)$\bar{Z}$
POWDER
INTENSITY
125 W
100 W
75 W
50 W
25 W
CONTROL
200
400
600
800
WAVENUMBERS
600 cm^{-1} PEAK IS FROM THE SiO_2 SUBSTATE. IT IS OBSERVABLE DUE TO STRESS BIREFRINGENCE IN THE FILMS. THIS FEATURE DISAPPEARS AT HIGHER ANNEALING FLUENCES.
RAMAN SPECTRA FROM ANNEALED HfO_2 FILMS

Figure 7.

Manuscript Received
7-9-87

Influence of Post-deposition Treatment by UV Light and Oxygen (ozone) on 350 nm Damage Thresholds of SiO_2 Films Deposited From Sols*

I. Thomas, J. Wilder, A. Lee and D. George

Lawrence Livermore National Laboratory
University of California
P.O. Box 5508, L-490
Livermore, California 94550

Certain multilayer porous silica AR coatings on fused silica substrates prepared by the sol-gel process have been found to have a much lower laser damage threshold than single layer coatings prepared by the same method. Treatment with UV light in the presence of oxygen (which gives ozone) at low temperature was found to restore damage thresholds to the levels found in single layers. Damage thresholds were measured at 350 nm with a 25 ns pulse for 1000 shots at 25 Hz. The effect of exposure time and other factors such as replacement of oxygen with nitrogen and vacuum are described.

Key words: laser damage, SiO_2, sol-gel, AR coatings.

1. Introduction

We have previously reported the preparation of high damage threshold, single layer, porous silica AR coatings on fused silica and KDP optical components.[1] We these coatings prepared by applying a colloidal suspension of silica in methanol or ethanol to a substrate at room temperature with no further processing required after the alcohol has evaporated. The wavelength of minimum reflectivity is controlled by varying the coating thickness.

We have now extended our coating investigation to multicoated optical systems, such as mirrors and polarizers, which consist of alternating layers of high and low index oxides. We hoped to prepare these from colloidal oxide suspensions, in like manner to the silica AR materials, and intended to use the silica suspension for the preparation of the low index components. Preliminary to this work, we decided to investigate a simple multicoat system of silica prepared by successive application to a fused silica substrate of our colloidal silica suspension in alcohol. We would thus be making thick, porous silica coatings to compare with the thinner ones used for AR applications to see whether any unexpected difficulties would arise because of the multicoats.

Our spectrographic measurements on thick layers indicated that the coating index remained constant at about 1.22 and therefore the uniformity of the multilayers with respect to porosity remained constant. However, we found a drastic reduction in laser damage threshold at 350 nm. One possible explanation for this result was that absorptive species were possibly being trapped in the lower layers. As this process was rather rapid, with only 60 seconds drying time between coats, there was a distinct possibility that

---

*Work performed by the Lawrence Livermore National Laboratory under the joint auspices of the Air Force Weapons Laboratory, Kirtland AFB, New Mexico 87117-6008, under P.O. #85-060, and the U.S. Department of Energy under Contract No. W-7405-ENG-48.

absorptive organic entities did not have time to evaporate from the initial coats and were being trapped by the later coats. Based on this premise, we undertook a short research program aimed at removal of these absorptive species. We tried two types of treatment after coating, one using ozone to remove undesirable material by oxidation and the other using heat or vacuum or both to remove this material by volatilization. Both methods proved to be successful and the results are described in the following sections.

2. Experimental

Coatings were prepared on 5 cm diameter by 1 cm thick fused silica substrates by spinning on a colloidal suspension of 1% silica in ethanol-n-propanol. This suspension was prepared as a 3% silica in ethanol by a method previously described[1] and then diluted with twice its weight of n-propanol. A spin speed of 1800 r.p.m. was used, the apparatus being contained in a 0.2 micron filtered forced air clean hood. One minute drying time was allowed between successive coats. A total of five coats was applied which gave a total thickness of about 0.36 microns.

The apparatus for the UV treatments is shown in Fig. 1. The sample was contained in a borosilicate glass container with a gas inlet at the bottom. A fused silica plate rested unattached on the top and allowed the gas to bleed out through the gap between the plate and container. A 3000 watt mercury vapor UV source was used to irradiate the sample through the silica plate. Oxygen or nitrogen was passed in the gas inlet as required. For the UV/vacuum experiment the silica plate was sealed and vacuum applied through the gas inlet.

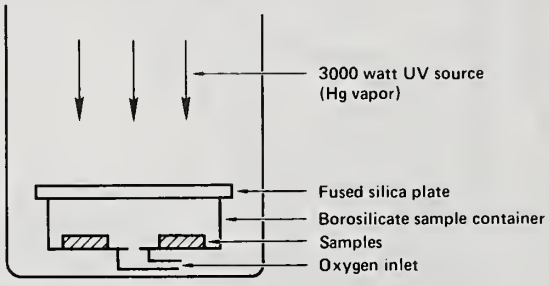

Figure 1. Apparatus for UV treatment

For experiments requiring ozone only, the apparatus was modified and is shown in Fig. 2. Oxygen was passed through a silica tube which was exposed to the UV source and the gas then passed over the sample in a borosilicate glass container external and unexposed to the UV source.

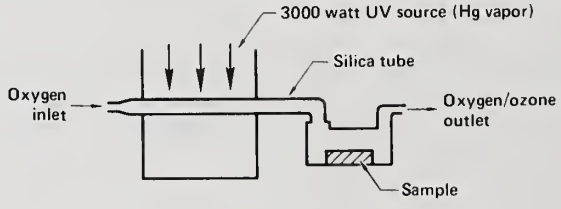

Figure 2. Apparatus for ozone treatment

Damage thresholds were measured at 350 nm using a 25 ns pulse for 1000 shots at 25 Hz. Samples were measured before and after treatment.

3. Discussion of Results

The average damage thresholds of all samples before and after treatment are shown in Table I. Considering the UV/O_2 samples first, it can be seen that, for treatment times of 15 minutes, 30 minutes and 60 minutes, improvements were obtained in all cases. The final damage thresholds are comparable to those normally obtained for single layer SiO_2 coatings (15 - 20 J/cm^2). The thresholds obtained for treatment times of 90 minutes are anomalous. It is unfortunate that these samples had the lowest initial thresholds but the improvements were not up to the level of the others. This series also had the only sample that did not change after treatment. The different treatment times were carried out to determine whether threshold increase was dependent on treatment time. One might deduce from the results that 15 minute treatment time is insufficient and 90 minutes too long. However, we do not have an explanation for why excess time appears to be detrimental.

Treatment	Time	Average damage Before	Average damage After	Number of samples
UV/O_2	15 mins	12.1 J/cm^2	14.0 J/cm^2	5
UV/O_2	30 mins	8.5 J/cm^2	17.7 J/cm^2	6
UV/O_2	60 mins	8.4 J/cm^2	16.7 J/cm^2	4
UV/O_2	90 mins	6.6 J/cm^2	10.7 J/cm^2	6
UV/N_2	60 mins	7.3 J/cm^2	7.6 J/cm^2	2
UV/vacuum	60 mins	7.6 J/cm^2	21.0 J/cm^2	1
Vacuum/80°C	60 mins	9.0 J/cm^2	19.0 J/cm^2	2
O_3/room temp.	30 mins	13.3 J/cm^2	19.3 J/cm^2	2

Table 1. Damage thresholds before and after treatment

The threshold results from the other treatments are significant. UV irradiation in the presence of nitrogen has no effect. This result shows that ozone, not UV light, is the effective reagent for the damage improvement. This conclusion is confirmed by the results from ozone treatment alone in the absence of UV.

Vacuum treatment either at 80°C or with UV light also appeared to be effective. It is probable, based on the other results, that the UV light here is of no significance.

4. Conclusions

1. Organic residues trapped in multilayer coatings are the probable cause of the low damage thresholds of these coatings.

2. These residues can be removed either by oxidation with ozone or by volatilization under high vacuum.

3. After treatment the damage thresholds of multicoated samples are the same as those for single coats.

References

1. I. M. Thomas, App. Opt. 25, 1481 (1986).

Manuscript Received
4-6-87

LASER INDUCED DAMAGE OF DIELECTRIC PHASE RETARDATION MIRRORS AT 1.064 MICRONS

D. Ristau, S. M. J. Akhtar*

Institut für Quantenoptik, Universität Hannover
Welfengarten 1, 3000 Hannover, Germany-West

and

J. Ebert

Laseroptik GmbH, 3008 Garbsen 8, Germany-West

Dielectric phase retarders are frequently used in high power laser systems for cutting and welding. The phase shift is commonly achieved by total reflection or optical tunneling.

In this paper laser induced damage thresholds of plane phase retardation mirrors are measured using single 14 ns Nd-YAG laser pulses. The results are compared to the properties of the corresponding nonshifting deflectors. We investigated in stacks of Titania, Tantala, Hafnia and Zirconia in conjunction with Silica designed for retardation angles of 45° and 90°. Laser induced damage thresholds are related to the field strength distribution in the layers.

Key words: Phase retarding mirrors, standing wave field, oxide materials, Titania, Tantala, Silica, laser damage

1. Introduction

Phase retardation techniques are commonly applied in modern optics. In particular a phase shift of 90° is often required for optical isolation, for the optical disk and for laser material processing. Crystalline quarterwave plates are well suited to all these applications. But they are expensive and can not be produced with a large aperture. Therefore attempts were made to design dielectric structures that are able to replace the crystalline quarterwave plates.

The phase retardation between s and p component induced by a periodic multilayer reflector was investigated by APFEL [1]. One important statement of this paper is that the maximum obtainable phase change induced by a periodic structure is less than 30°. This results in the need of multiple reflections for achieving a sufficient retardation by periodic reflectors. SOUTHWELL [2] designed aperiodic multilayer structures with 90° phase retardation for the infrared. His designs consist of a high reflecting

---

* S.M.J. Akhtar is a DAAD fellow from the Pakistan Institute for Nuclear Science and Technology, P.O. Nilare, Islamabad

metal film and a subsequent dielectric stack which has different optical penetration depths for the s and p component. Thus the phase retardation is due to the polarizing action of the dielectric structure. The approach by SPILLER [3] is based on total reflection at the boundaries in the coating. Those designs must be coated on a prism because an incident medium of higher refractive index than air is required. Compared to phase retarding mirrors totally reflecting retarders have some advantages. The phase retardation is insensitive to a variation of the wavelength or the angle of incidence and only four layers are sufficient for most of the applications.

From the standpoint of laser damage resistance phase retarders based on a dielectric high reflecting stack are of special interest. No antireflection coating is necessary as in the case of total reflecting retarders. Unfortunately a large number of layers is required to produce all dielectric retarders with high reflectivity and 90° phase shift for s and p component of the incident light.

In this paper we will discuss designs and damage thresholds of dielectric phase retarding mirrors. Aperiodic multilayer stacks of Titania, Tantala, Hafnia and Zirconia were designed for 45° phase retardation. In order to determine the materials suitable for high power phase retardation mirrors, damage thresholds of the 45° phase retarders were measured and compared to thresholds of the corresponding periodic stacks. Designs for Tantala as the best material were optimized for 90° phase retardation, minimum internal field strength, broadest range of operation and simplicity of production. Laser induced damage thresholds of the phase retarders were measured and related to the calculated field strength distributions in the active layers.

2. Design

The fundamental design of the produced phase retarding mirrors is shown in figure 1. It consists of a periodic high reflecting $\lambda/4$-stack and an additional polarizing layer system. For the fixed light incidence of 45° the polarizing stack introduces the phase shift due to a longer optical path of the p component in this structure. The advantage of this fundamental design is that only the outer layers have to be optimized meanwhile the high reflecting stack is uneffected. In order to achieve the desired phase shifts a computer program with a least squares fit algorithm is used. The startpoint is an arbitrary design. Film thicknesses can be varied by a Monte Carlo method or by a method based on the selection of the layers with the largest effect on the merit function. The merit function is defined by the sum of the squared deviation of the actual calculated dependence from the demanded wavelength dependence of the phase shift and reflection coefficients. The optimization program is terminated if there is no further decrease from one variation step to the other.

Start designs for the phase retarding mirrors are $\lambda/4$-stacks. The number of fixed layers forming the reflecting section is choosen according to a residual transmission of approximately 0.1%. Optimization runs were carried out for numbers of outer layers between five and twenty-seven. Depending on the material a 45° phase shift is possible with a polarizing stack consisting of four to six layers. The designs with a minimum number of outer layers are given in table 1 for Zirconia, Hafnia, Tantala and Titania. As an example the calculated wavelength dependence of the phase shift for the Zirconia system is shown in figure 2. For this simple design the phase shift is nearly constant in a range of 30 nm. Especially for the materials with an index of refraction higher than two, much broader ranges can be achieved with more outer layers. However, since the main purpose of the 45° phase retarders was to study the laser induced damage thresholds, we restricted ourselves to the listed designs.

Due to their low index of refraction the performance of Zirconia and Hafnia for 90° phase retarding mirrors is not satisfactory. Optimized systems are built up of a large number of layers and have narrow wavelength ranges which are very sensitive to thickness errors. From the standpoint of designing 90° phase retarders, Titania is best suited. Only six active layers are sufficient for a usable 90° phase retarding mirror. In contrast

to this Titania has a high absorption and a low damage threshold. Therefore we choose Tantala as the basic material for the investigations in the 90° phase retarding mirrors.

The designs for the five best mirrors are given in table 2. They are selected from the huge number of possible designs for lowest sensitivity to thickness errors. The sensitivity S to thickness errors is defined by the sum of the squared deviations of the performance $f(\lambda_0, d_i)$ due to a thickness error Δd_i for each layer.

$$S = \frac{1}{N} \sum_{i=1}^{N} \{(f(\lambda_0, d_i) - f(\lambda_0, d_i + \Delta d_i))^2 + (f(\lambda_0, d_i) - f(\lambda_0, d_i - \Delta d_i))^2\}$$

Where N is the number of active layers. The properties of the designs are shown in table 3: Design number 2 has the lowest number of active layers meanwhile design number 3 is usable for a broad wavelength range as depicted in figure 3. Unfortunately design number 4 with the lowest sensitivity to thickness errors is built up of 18 layers.

Table 3: Properties of 90° phase retarding mirrors

Design number	Number of active layers	Range of retardation wavelength [nm]	angle [°]	Sensitivity [rel.units]
2	9	15	1	0.615
3	12	40	1	0.643
4	18	30	1	0.196
5	10	20	1	0.923
6	10	20	7	0.785

The internal intensity distribution of design 5 is depicted in figure 4 for unpolarized light. It has the typical behavior as in all phase retarding mirrors disussed here. An exponentially increasing intensity in the $\lambda/4$-stack is followed by a standing wave field pattern with high amplitudes in the outer layers. This is due to the constructive superposition of the incoming and the reflected light in the active layers. Considering the intensity distributions for the s and p component seperately, the patterns and the amplitudes are different. The maximum internal intensity of the s component is always higher than that of the p component.

For most of the applications a phase retarding mirror with a broad range of operation in terms of angles of incidence is desirable. Therefore we included an algorithm in our optimization program which takes into account the angle of incidence. Design number 6 is the result of this optimization procedure. It is most comparable to the performance of the other designs.

3. Experimental

All phase retarding mirrors were produced by e-beam evaporation at a reactive oxygen pressure of 1.5 to $3*10^{-4}$ mbar. The $\lambda/4$-stack as well as the active layers can be built up in one run with the aid of an optical monitoring system including a monochromator and two test glasses. The glasses are changed after the deposition of the stack and some of the following layers. The second test glass is used for completion of the layer system. This technique can only be applied in conjunction with a computer program which simulates the evaporation process and predicts the transmission of the test glass. However it allows for coating every layer to an extremum of transmission by choosing the appropriate wavelengths.

The phase retarding action of the designs was tested with the aid of a linearly polarized cw Nd-YAG laser and an analyser. The polarization of

the laser is oriented in an angle of 45° with respect to the plane of incidence. The light reflected by the component under test is analysed for its state of polarization by registrating the intensity as a function of the angle of rotation. By evaluating the recorded polar diagram, the phase shift between s and p component can be determined. As an example the measured phase shift as a function of angle of incidence for design number 6 is shown in figure 5.

The damage tests were carried out with a two stage Nd-YAG laser described elsewhere [4]. For all measurements the pulsewidth of 14 ns was controlled by a TECTRONICS R 7912 transient digitizer. The spot size is adjusted to 300 microns with the aid of a diode array. During experiments a scatterometer is utilized for damage detection. In order to control the results of the scatterometer the samples are inspected by Nomarski microscopy after the test. The reliability of the scatterometer is better than 95% in these experiments.

4. Results and Discussion

The damage threshold data of the 45 ° phase retarding systems and the corresponding deflection mirrors are presented in a histogram (fig.6). With the exception of Titania, phase retarding mirrors have lower damage thresholds than their corresponding mirrors without overcoating. This is due to the fact that the standing wave field pattern has higher amplitudes in the polarizing stack than at the last interface of a high reflecting mirror. But there is no quantitative agreement between the maximum intensity in the active layers and the damage thresholds. This may be due to a stress stabilizing action of the polarizing layers on the stacks. By comparing properties like melting point, damage thresholds, thermal conductivities and absorption of the constituent single materials to the performance of the layer systems, no correlation can be seen. As expected from the single films, systems with Titania have low damage thresholds. Although damage spot morphology yields evidence of different mechanisms, thresholds of all the other systems are only slightly differing in the range from 26 J/cm² to 32 J/cm². Therefore the choice of materials for phase retarding mirrors is mainly determined by design problems. Fortunately Tantala systems meet the design requirements and have the highest damage thresholds at the same time. Accordingly, all investigations on 90° phase retarding mirrors are based on Tantala designs.

The damage characteristics of the 90° phase retarding mirrors are depicted in figure 7. For the purpose of comparison the column for the 45° retarder is also added to the histogram. In addition damage thresholds and other parameters are given in table 4. Whereby the average of the highest intensities for the s and p component at the interfaces in the active layer systems is termed maximum intensity. An intensity of 1 corresponds to the incoming intensity level.

Table 4: Damage thresholds of phase retarders with Tantala

Design number	Phase shift [°] theor.	exp.	Maximum intensity [rel. units]	Damage thresholds [J/cm²] exp.	theor.
1	45	43.7	5.20	32 ±6	33.5
2	90	87.5	7.00	21 ±7	20.2
3	90	88.0	6.65	22 ±4	22.1
4	90	66.5	7.80	15 ±1	16.8
5	90	87.2	4.45	20 ±7	43.7
6	90	88.5	6.15	27 ±1	25.2

With the exception of design number 4 the phase shift errors are below 3.5%. Number 4 is the design with most active layers but the lowest sensitivity to thickness errors. Nevertheless it has an intolerable deviation of phase shift. This is probably due to limitations of the technique for coating layers with arbitrary thicknesses as described above. Since thickness errors add up with the layers, this method becomes more and more inaccurate with increasing number of layers coated on one test glass. With the optical monitor system applied for the production of the phase retarding mirrors, a maximum of 7 active layers per test glass could be coated without exceeding the error limits.

As expected the damage thresholds of the 90° phase retarding mirrors are lower but in the same fluence range as those of the nonretarding mirrors. According to its internal intensity, design number 4 has the lowest damage threshold. The plot of damage thresholds versus internal intensity shows evidence of a correlation between these two parameters (fig.8). A least squares fit reveals that there is almost a square root dependence i.e. the damage thresholds are nearly proportional to the reciprocal value of the highest electric field at an interface. No meaningful result is obtainable by relating the highest intensity in the bulk of an active layer to the damage thresholds. Therefore the damage resistance of phase retarding mirrors with high standing wave fields are mainly influenced by the quality of the interfaces between the active layers and by the field pattern. But there are also other parameters like stress, impurity density and surface roughness that may have an effect on damage thresholds and accordingly, the power resistance of a mirror can not be raised to any level just by designing for lowest internal intensity. An example is design number 5 with the lowest intensity and a moderate laser induced damage threshold. Instead of a stabilizing Silica layer it has an outer Tantala layer. This may be the reason for the low damage threshold. In practice the highest damage threshold should be obtained from a 90° phase retarding mirror with a maximum internal intensity around 5 because for that value the rule still holds.

Design number 6 is a good compromise. It has the highest damage threshold, only ten active layers and a moderate wavelength range. The operation range for the angle of incidence is maximum. For that reason this design should be optimized further for mass production.

5. Summary

Laser induced damage thresholds of all dielectric phase retarding mirrors have been investigated. In order to find the material best suited, 45° phase retarders have been designed with the aid of a computer program and tested. Tantala is found to be most applicable for the production of 90° phase retarding mirrors. Systems have been designed for a low number of active layers, broad range of operation, low sensitivity to thickness errors and low internal intensity. Designs with high standing wave fields result in a correlation between damage thresholds and maximum field strength at the interfaces. Highest damage thresholds for 45° and 90° phase retarding mirrors are 32 J/cm² and 27 J/cm² respectively.

6. References

1 J. H. Apfel; Phase retardance of periodic multilayer mirrors. Appl. Opt. 21(4): 733-738; 1982 February

2 W. H. Southwell; Multilayer coatings producing 90° Phase change. Appl. Opt. 18(11): 1875; 1979 June

3 E. Spiller; Totally reflecting thin film phase retarders. Appl. Opt. 23(20): 3544-3549; 1984 October

4 Ristau, D.; Dang, X.C.; Ebert, J.; Laser induced damage in optical materials. Nat. Bur. Stand. (U.S.) Spec. Publ. 727; 1984. 298p

Table 1: Designs of the 45° phase retarding mirrors

45°-Phaseretarder Zirconia

Layer Number 1 to Number 35 : 1Qwot HR-Stack

Layer Number	Index of Refraction	Optical Thickness
36	1.46	0.201
37	1.88	1.445
38	1.46	0.837
39	1.88	0.646

45°-Phaseretarder Hafnia

Layer Number 1 to Number 32 : 1Qwot HR-Stack

Layer Number	Index of Refraction	Optical Thickness
33	1.95	2.483
34	1.46	1.100
35	1.95	0.527
36	1.46	0.372

45°-Phaseretarder Tantala

Layer Number 1 to Number 23 : 1Qwot HR-Stack

Layer Number	Index of Refraction	Optical Thickness
24	1.46	0.885
25	2.05	0.415
26	1.46	3.033
27	2.05	0.295
28	1.46	0.396
29	2.05	0.547

45°-Phaseretarder Titania

Layer Number 1 to Number 23 : 1Qwot HR-Stack

Layer Number	Index of Refraction	Optical Thickness
24	1.46	0.524
25	2.28	1.399
26	1.46	0.468
27	2.28	0.701
28	1.46	1.990

Table 2: Designs of the 90° phase retarding mirrors

All polarizing layers are deposited on a stack of 24 layers Tantala/Silica.

Design Number 2

Tantala		Silica	
Layer Number	Thickness	Layer Number	Thickness
25	1.100	26	0.594
27	1.118	28	0.693
29	1.107	30	0.977
31	0.460	32	1.218
33	1.117	34	1.691

Design Number 3

Tantala		Silica	
Layer Number	Thickness	Layer Number	Thickness
25	0.577	26	0.964
27	1.221	28	1.054
29	0.445	30	1.083
31	0.724	32	1.197
33	1.147	34	0.303
35	1.402	36	5.946

Design Number 4

Tantala		Silica	
Layer Number	Thickness	Layer Number	Thickness
25	0.632	26	0.993
27	0.532	28	1.140
29	0.949	30	1.050
31	1.029	32	0.224
33	0.326	34	0.932
35	0.765	36	0.435
37	1.204	38	0.672
39	0.229	40	0.777

Design Number 5

Tantala		Silica	
Layer Number	Thickness	Layer Number	Thickness
25	1.100	26	0.938
27	0.968	28	1.182
29	2.744	30	1.126
31	0.841	32	1.084
33	1.050	34	0.364
35	1.035		

Design Number 6

Tantala		Silica	
Layer Number	Thickness	Layer Number	Thickness
25	0.994	26	0.309
27	1.288	28	0.915
29	1.190	30	0.729
31	2.842	32	0.948
33	1.267	34	1.568

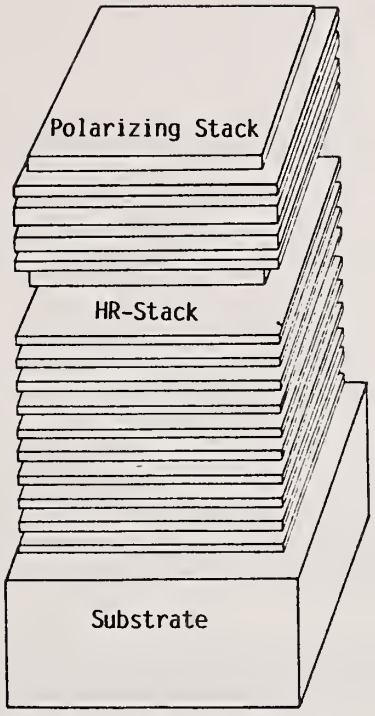

Fig. 1. Fundamental design for the phase retarding mirrors. A high reflecting stack is coated on the substrate. The phase shift is induced by the additional polarizing stack.

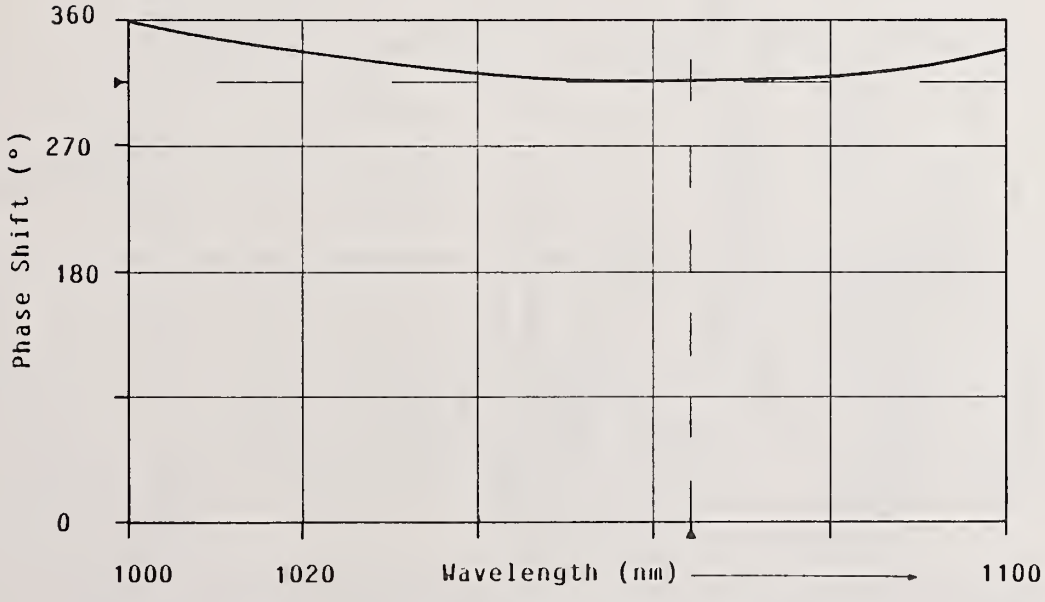

Fig. 2. Phase shift as a function of wavelength for the phase retarding mirror of Zirconia. The usable wavelength range is broader than 20 nm.

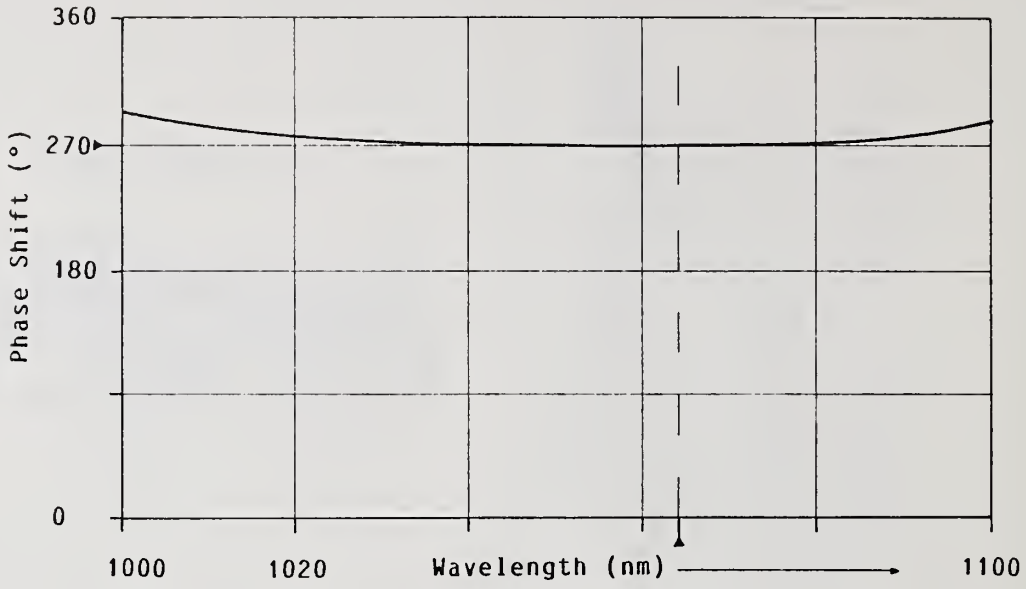

Fig. 3. Phase shift as a function of wavelength for design number 3. The usable wavelength range is approximately 40 nm.

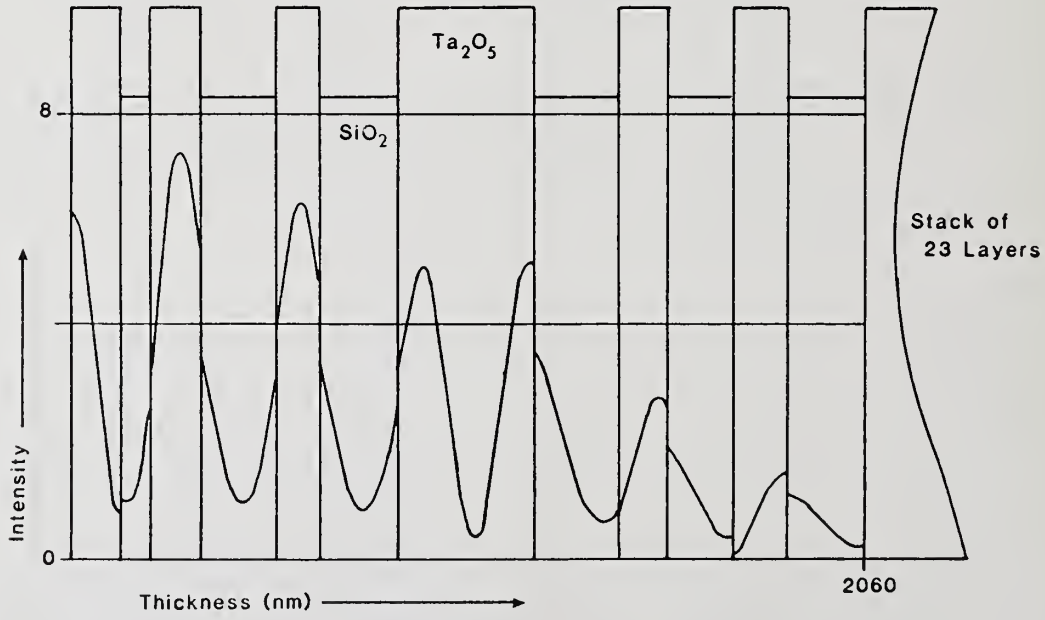

Fig. 4. Internal intensity distribution for design number 5. The maximum intensity is located at the third interface.

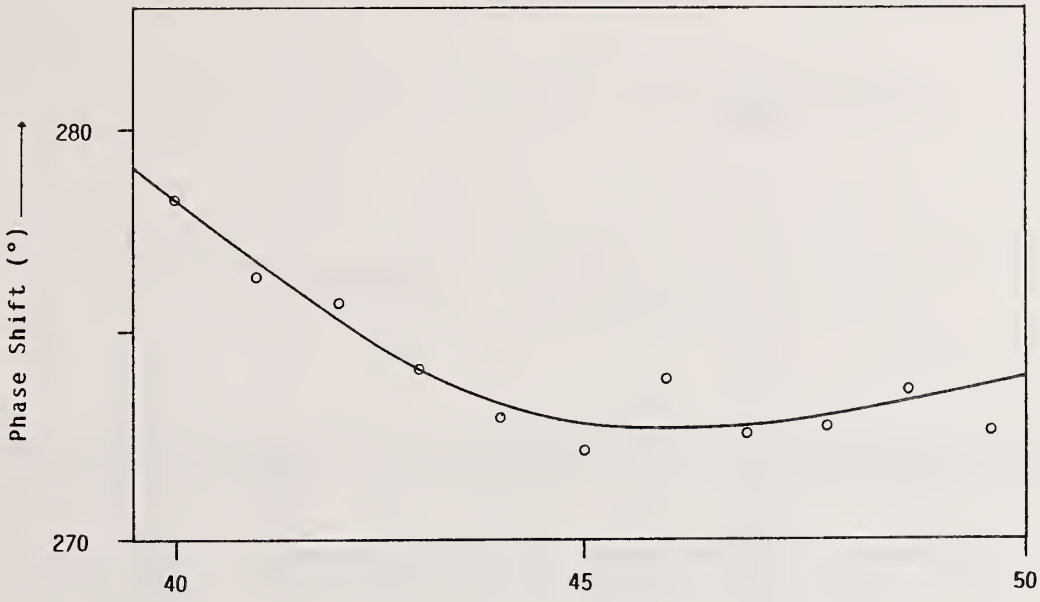

Fig. 5. Measured variation of the phase shift due to the angle of incidence for design number 6.

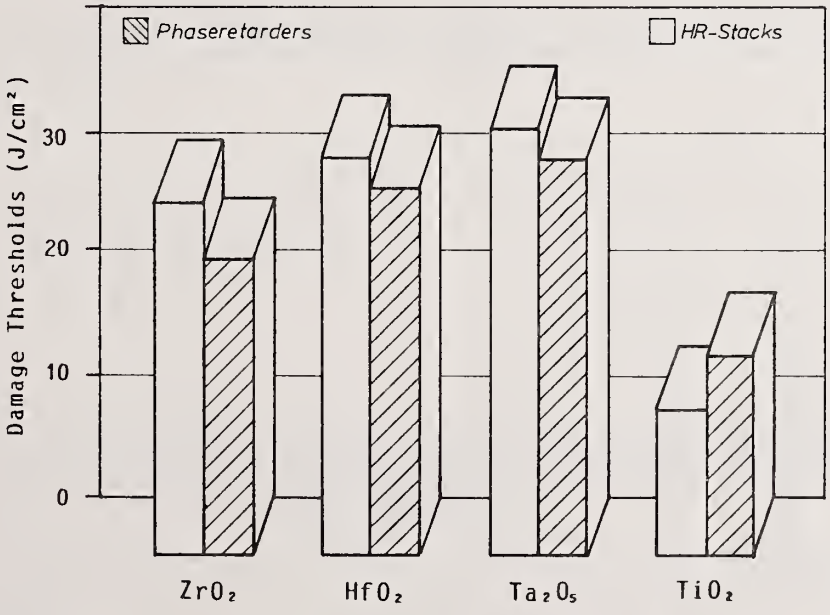

Fig. 6. Damage thresholds of the 45° phase retarding mirrors and the corresponding deflection mirrors without overcoating. The spotsize is 300 microns and the pulse width is 14 ns at a wavelength of 1.064 microns.

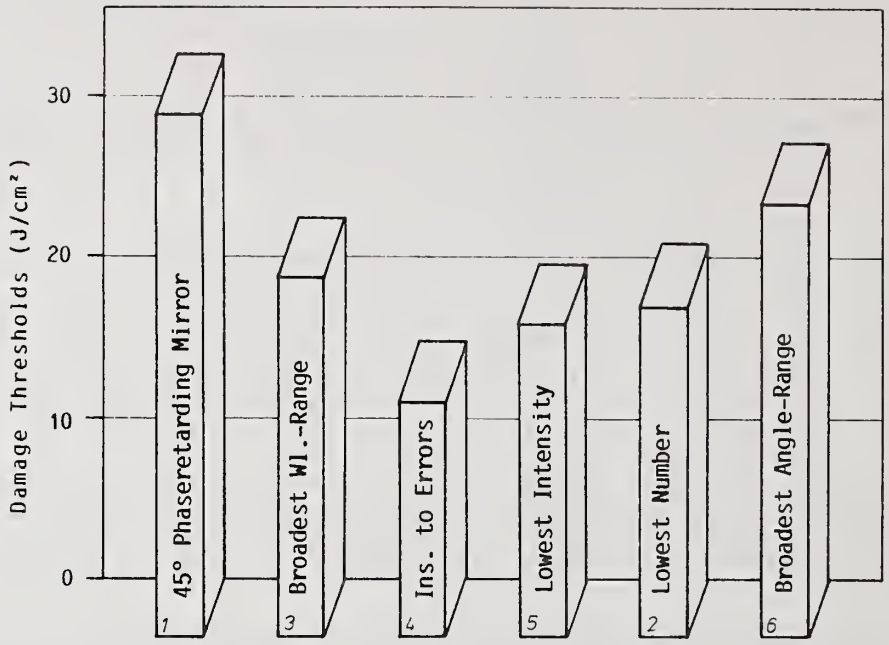

Fig. 7. Damage thresholds of the 90° phase retarding mirrors.

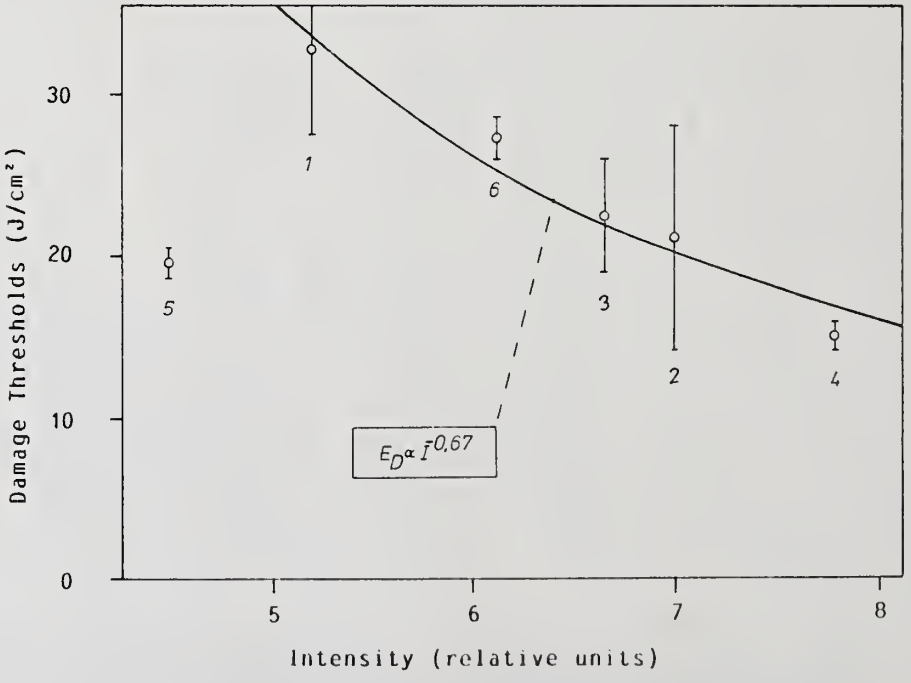

Fig. 8. Damage thresholds for the phase retarding mirrors of Tantala as a function of the internal intensity. The solid line indicates the dependence expressed by the formula.

Manuscript Received
11-3-86

AMORPHOUS SILICON FOR CO_2 LASER MIRROR COATINGS

F. DUTOIS, J. MOUCHART, B. POINTU and G. VILLELA

LABORATOIRES DE MARCOUSSIS - Centre de Recherches de la C.G.E.
DIVISION OPTRONIQUE - 91460 MARCOUSSIS - FRANCE

High power CO_2 laser require mirrors with high reflectivity, high laser damage threshold and efficient mechanical and chemical protection. Enhanced metallic coatings are generally used.

Amorphous silicon thin films are hard, with low porosity and have a high refractive index ; unfortunately the low absorption at 10.6 μm is however too high for quarterwave layer at that wavelength.

When associated with a classical transparent but softer high index material such as ZnSe or ZnS, amorphous silicon can nevertheless be used in order to design the last composite high index quaterwave. Theoretical calculations predict an optimum reflectance for a fixed a : Si : H thickness.

The amorphous silicon thickness is thin enough to obtain a high reflectivity coating although its absorption, but thick enough to provide a good chemical and mechanical protection. Besides, experimentally determined that such enhanced coatings have a high laser damage threshold level.

Key words : amorphous silicon ; CO_2 laser mirrors ; humidity test ; laser damage threshold ; optical coating ; reflectivity.

INTRODUCTION

Amorphous silicon is a well known material [1]. its structure is a tetraedral bonded silicon with dangling bonds. These dangling bonds are responsable of energy states in the gap and the material presents poor optical and semiconductor properties. if they are passivated by hydrogen, the density of gap states is lowered and the material has better properties.

The hydrogen can be bonded by Si-H or $Si-H_2$, ... $Si-H_n$ bonds, and the quality of the materials depends on the hydrogen concentration and on the nature of the bonds : the $Si-H_2$... $Si-H_n$ bonds have to be minimized.

When the gap state density is low, smaller than 5.10^{16} eV^{-1} cm^{-3}, the hydrogenated amorphous silicon can be doped with phosphorus (n type semiconductor) or boron (p type semiconductor). With such properties, the material can be used as a semiconductor device for several applications when large surfaces are needed [2] :

- photovoltaïc solar energy conversion
- electrophotographic receptor for copying machines and laser printers
- linear and matricial image sensors with 1/1 magnification
- thin film transistors for liquid crystals displays.

Hydrogenated amorphous silicon presents several other interesting properties such as :

- good infrared transmission
- high refractive index
- hardness
- amorphous structure without grain boundary
- inertia to chemical etching

so it can be used as an optical and protective layer for infrared CO_2 laser mirror coatings.

EXPERIMENTAL DETAILS

Hydrogenated amorphous silicon can be prepared by several different methods such as glow discharges, sputtering, ion beam deposition, etc...

One of the most attractive methods is to use glow discharges. The deposition is obtained by decomposition of silane SiH_4 mixed with hydrogen H_2 in a radiofrequency excited plasma. The apparatus used, supplied by Alcatel (France) is shown on fig. 1. It is composed of three elements :

- vacuum facilities with mechanical and diffusion pumps
- gas supply and distribution
- radiofrequency power supply and matching network.

The cathode, 150 mm in diameter, is water cooled and the substrates are located on an anode which can be heated up to 450° C. The reactor can be evacuated down to 2.10^{-7} Torr before the process.

The properties of the deposits depend on a lot of parameters such as :

- RF power density
- negative bias of the cathode
- negative bias of the anode
- composition of the mixture of gases
- flowrate and pressure
- temperature of the substrate.

In our experiment, we have used classical parameters summarised on table I optimized for photoreceptor devices except for the temperature which has been lowered because of the materials deposited in previous processes. With further tests, it is probably possible to improve on the final result by a special optimization of these parameters for infrared coating (fig. 2).

INDICES MEASUREMENTS

A thin hydrogenated amorphous silicon film - 1 μm thick - is deposited on a ZnSe substrate. The refraction and extinction indices have been obtained by Abeles method [3] from measurements of front and back reflectance and transmittance on a 781 Perkin Elmer spectrophotometer with data station 3600.

At $\lambda = 10,6\ \mu m$, the calculated indices are :
$n = 3.13 \pm 0.02$
$k = 0.011 \pm 0.004$

The low substrate temperature is responsable for the low n index.

DESIGN COATING

Owing to its attractive mechanical and chemical properties, hydrogenated amorphous silicon can be used as a thin protective film for CO_2 laser mirror coatings. Generally, the reflective surface is made

of a metallic layer - silver or gold - and on the top of it alternate low L and high H index dielectric layers deposited in λ/4 configuration to improve the reflectivity. The most commonly used materials are ZnS or ZnSe for high index and ThF_4 for low index layers.

The maximum reflectance obtained in this way depends on the indices of the materials according to Koppelmann formula [4].

$$R_{max} = 1 - 2\pi \frac{(k_H + k_L)}{n_H^2 - n_L^2}$$

n_H, k_H and n_L, k_L being the indices of the H and L layers.

As a result, with a high refractive index n_{Si} and a fairly high extinction index k_{Si}, it is not suitable to use hydrogenated amorphous silicon :

- just above the metallic layer (n_{Si} and k_{Si} are then too high)
- as high index λ/4 layer in enhanced coating (k_{Si} is too high)

but the best way is in enhanced coating when creating the last high index layer as a composite one made of both classical high index material and a-Si:H on the top.

Provided the following conditions exist :

$$n_{Si} > n_H \quad \text{and} \quad k_{Si} > k_H$$

there is an optical thickness for a-Si:H - and for the high index material (their sum being around λ/4) - for which reflectivity is optimum, and slighty higher than that of λ/4 high index material alone. Figure 3 presents the theoretical variations of R with the a-Si:H thickness.

So, the hydrogenated amorphous silicon film has two different functions : first, to protect the coating and second, to boost the reflectivity. Such a design is shown on fig. 4.

RESULTS

We present here some characteristics obtained with coatings on molybdenum or silicon substrates. The design coatings are :

substrate-Ag-$(ThF_4 - ZnS)^2$
substrate-Ag-$(ThF_4 - ZnSe)^2$

The last layer (ZnS or ZnSe) being or not a a-Si:H composite layer.

1. *Reflectivity*

The reflectivity is measured with a 781 Perkin Elmer spectrophotometer by comparison with a standard (polished molybdenum substrate whose reflectivity is 0.982 at λ = 10.6 μm). The accuracy of the measurements is evaluated to be of ± 0.001. Results are summed up in table II.

2. *Laser damage threshold*

The visual laser damage threshold is measured with a cw 600 watts CO_2 laser ; the irradiation time is 10 seconds, with uncooled mirrors. The laser is focused on the mirrors with a ZnSe lens (f = 400 mm), and the spotsize is about 1.5 mm. The maximum of the average power density given by this laser (80 kW/cm^2) is obtained from the energy measured behind a 0.7 mm diameter pinhole.

All the above coatings have a laser damage threshold higher than the maximum deliverable power density except for the coating with a a-Si:H composite ZnSe layer deposited on silicium substrate. For the latter, the laser damage threshold is 60 kW/cm^2.

3. *Environment test*

The coatings were subjected to the humidity test following the S10-010 AFNOR norm (93 ± 3 % saturated vapour at 50° C during 24 hours). All the ZnS coatings with or without a-Si:H composite layer passed the test whereas all the ZnSe coatings with or without a-Si:H composite layer failed.

CONCLUSION

Thin a-Si:H film have been deposited on enhanced ZnS/ThF_4 and ZnSe/ThF_4 silver coatings on silicon and molybdenum. With a last a-Si:H and ZnS or ZnSe composite layer, hardness and reflectivity are improved. Measurements concerning laser damage thresholds and environment humidity tests show that there is no degradation when employing hydrogenated amorphous silicon associated with ZnS/ThF_4 enhanced coatings.

These results probably could be improved by a better optimisation of amorphous silicon deposition parameters for 10.6 μm application, especially by lowering the percentage of Si-H_{2n} bonds which are not favorable for the transmitivity at this wavelength.

REFERENCES

[1] Pankove, J.I. (volume editor), "Hydrogenated amorphous silicon - Preparation and structure", Semiconductors and semimetals, Vol. 21, Part A, Academic Press 1984.

[2] Pankove, J.I. (volume editor), "Hydrogenated amorphous silicon - device applications", Semiconductors and semimetals, Vol. 21, Part D, Academic Press 1984.

[3] Abeles, F. and Theye, M.L., Surface Science 5, p. 325 (1965).

[4] Koppelmann, Ann. Phys. (Leipzig), 5 ; p. 388 (1980).

DEPOSITION PARAMETERS	
GAS COMPOSITION	70% SiH 4 30% H 2
PRESSURE	3 10^{-2} mbar
R.F. POWER	60 W
CATHODE VOLTAGE	-560 V
TEMPERATURE DEPOSITION	150 °C (INSTEAD OF 300 , 350 °C IN CLASSICAL DEPOSITION)
DEPOSITION RATE	450 Å/mn

TABLE 1

Reflectivity at $\lambda = 10.6\ \mu m$

	Ag - $(ThF_4/ZnS)^2$		Ag - $(ThF_4$- ZnSe$)^2$	
	with a:Si:H	without a:Si:H	with a Si:H	without a:Si:H
Reflectivity	0.995_8	0.995_4	0.997_5	0.996_7

Laser damage threshold

Source : cw. CO_2 laser
Irradiation time : 10 seconds
Samples not water cooled

Threshold > 80 kW/cm² for all deposits on Si and Mo substrates except composite a:Si:H/ZnSe on Si (threshold 60 kW/cm²).

Environment test

(93 ± 3 % saturated vapour at 50° C during 24 hours)

all ZnS coatings passed the test
all ZnSe coatings failed the test

TABLE II

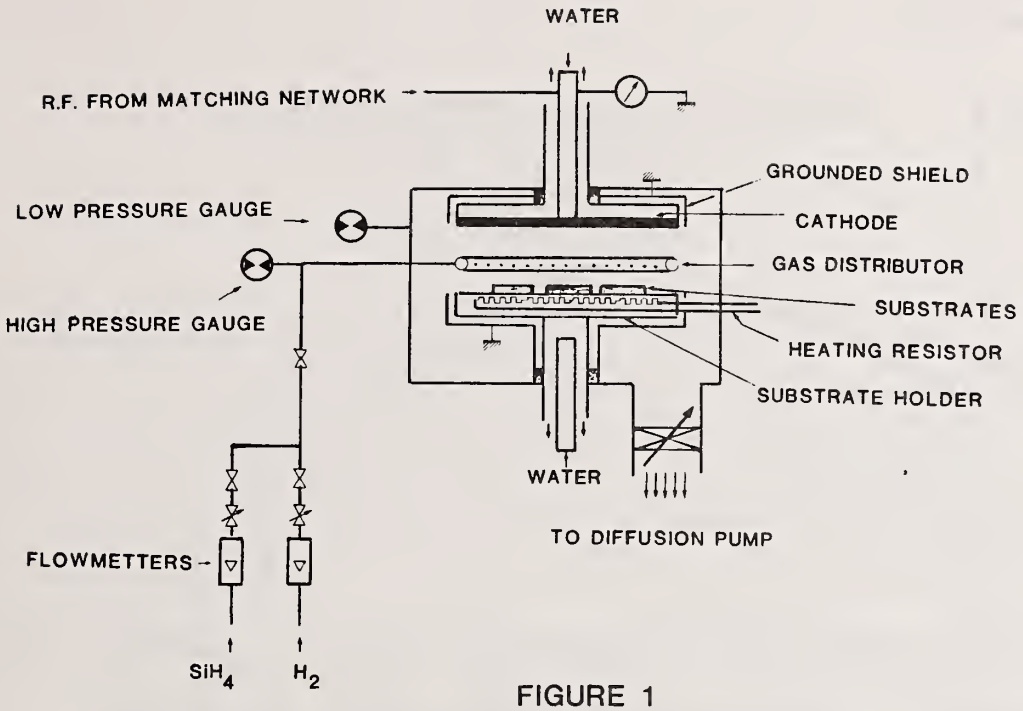

FIGURE 1

SCHEMATIC REPRESENTATION OF THE EXPERIMENTAL APPARATUS

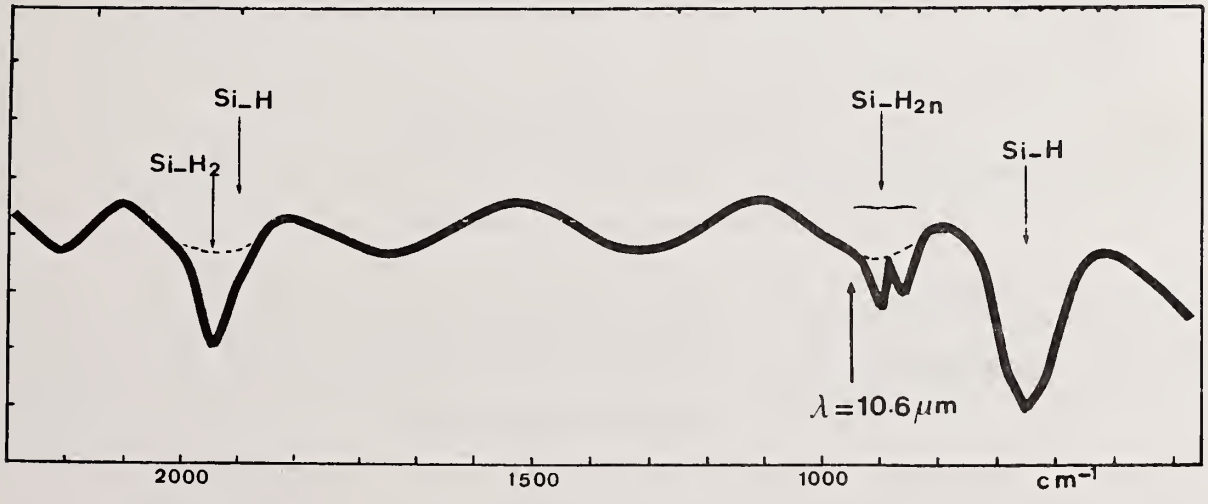

FIGURE 2 · INFRARED SPECTRUM OF a Si:H ON Ge SUBSTRATE

(DEPOSITION TEMPERATURE :150 °C , THICKNESS : 4 μm)

$$\left.\begin{array}{l} n = 3.13 \pm 0.02 \\ k = 0.011 \pm 0.004 \end{array}\right\} \lambda = 10.6\mu m$$

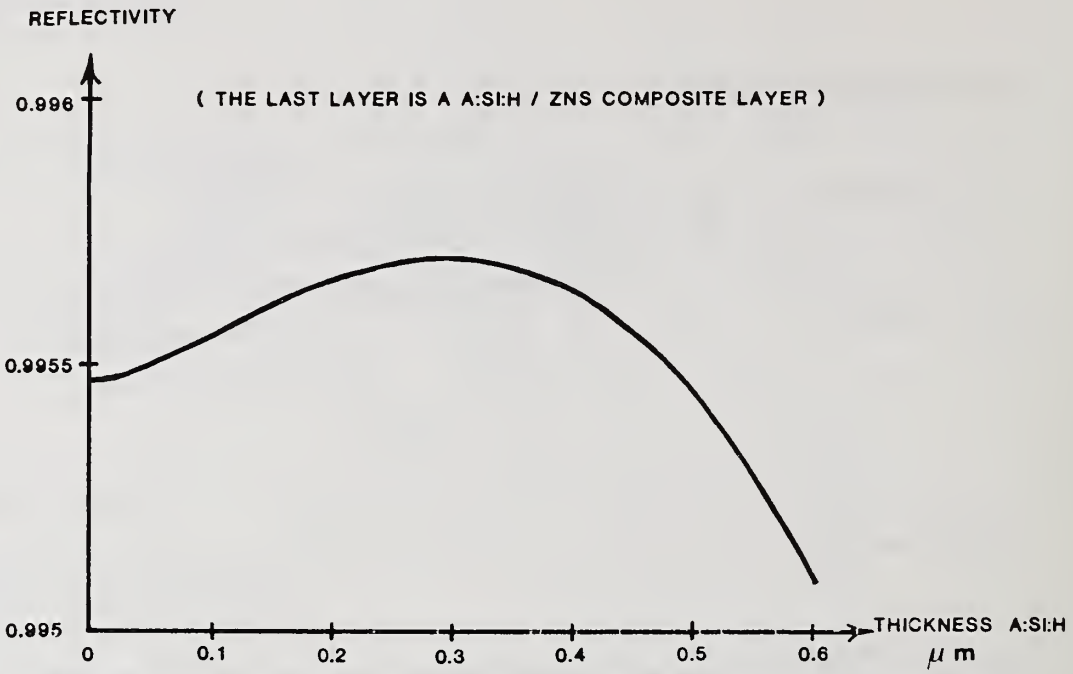

FIGURE 3 . REFLECTIVITY VERSUS A:SI:H THICKNESS

AG - $(THF_4 / ZNS)^2$ COATING

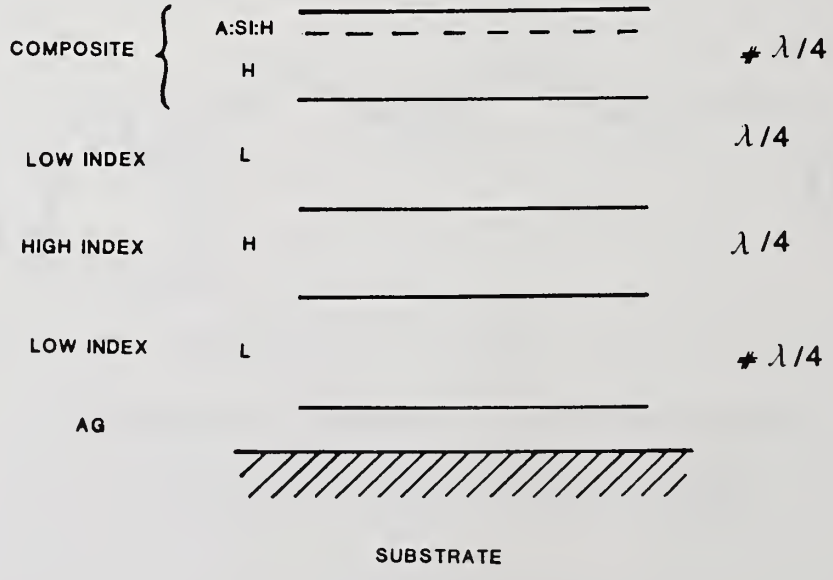

FIGURE 4 . COATING STRUCTURE

Manuscript Received
6-26-87

A Study of Thin Film Growth in the ZrO_2 - SiO_2 System

E. N. Farabaugh*, Y. N. Sun**, J. Sun***,
A. Feldman* and H.-H. Chen****

National Bureau of Standards
Gaithersburg, MD 20899

X-ray diffraction and transmission electron microscopy have been used to examine the microstructures of thin films of pure ZrO_2 - SiO_2 films formed by e-beam coevaporation. The results suggest that films composed of 100% ZrO_2 grow by the formation of tapered polycrystalline columns. Near the substrate the columns are small in diameter and consist of a single crystalline phase, but at increasing distances from the substrate the column diameters increase and material with two polycrystalline phases appears. At a given distance from the substrate, small additions of SiO_2 to the film composition result in a smaller column diameter. Films with 25 mole% SiO_2 show an amorphous electron diffraction pattern, a result consistent with previously observed x-ray diffraction patterns. The surfaces of the amorphous films appear nearly featureless and are significantly smoother than the surfaces of the pure ZrO_2 films.

Key Words: e-beam evaporation; microstructure; thin films; transmission electron microscopy; x-ray diffraction; ZrO_2 - SiO_2 system.

1. Introduction

In the past, x-ray diffraction investigations were made on a series of films formed by e-beam coevaporation in the ZrO_2 - SiO_2 system [1] to study the relationship between deposition parameters and the microstructure of the deposited films. The results of that work indicated that the microstructures of the films were dependent on the quantity of SiO_2 added to the ZrO_2 film. For pure ZrO_2, two crystalline phases were observed. With the addition of SiO_2 the films displayed an amorphous x-ray diffraction pattern. Because of the interest in the use of ZrO_2 in multilayer optical coatings in the ultraviolet portion of the spectrum, an investigation of the growth of similarly prepared films was undertaken using transmission electron microscopy (TEM) and x-ray diffraction (XRD) to characterize the early stages of film formation. The results of this study have shown that both pure ZrO_2 and films with small admixtures of SiO_2 display a tapered columnar structure, the mixed film possessing a more gradual increase in the diameter of the columns. With an addition of 25 mole% SiO_2 via coevaporation, films are produced which are amorphous to electron diffraction and have considerably smoother surfaces than the pure ZrO_2 films.

Previous investigations of ZrO_2 films include TEM work on ZrO_2 films formed anodically [2,3] and by thermally forming oxides on zirconium [4,5,6], optical and XRD analyses of e-beam deposited ZrO_2 [7], and XRD and RHEED examination of ZrO_2 films grown on Si substrates by e-beam evaporation [8]. The use of ion-assisted deposition to form high index ZrO_2 films and the characterization of these films have also been reported [9,10]. To the best of our knowledge no results have been published on TEM analyses of e-beam formed films in the ZrO_2 - SiO_2 system.

2. Experimental Considerations

The films in the ZrO_2 - SiO_2 system were prepared by e-beam coevaporation. Each source was individually controlled by a quartz crystal thickness monitor which was shielded from the vapors originating from the other source. The monitors were calibrated on the basis of stylus measurements of the thicknesses of pure films of each component. Substrates were mica for films to be

* This work supported in part by the Air Force Office of Scientific Research under contract #AFOSR-ISSA-85-0068.
** Guest Worker from Langhou Institute of Physics, Langhou, People's Republic of China
*** Guest Worker from Shanghai Institute of Ceramics, Shanghai, People's Republic of China
**** Guest Work from Precision Instrument Development Center, Hsinchu, Taiwan

examined by TEM, and microscope slides for films to be examined by XRD. Substrate temperatures of 300°C were maintained for all depositions using a quartz heater lamp. The base pressure in the deposition chamber was 5-7 x 10^{-8} torr with no backfilling of oxygen during the deposition. The deposition rate was 0.2 nm/s for all films.

For TEM the following films were prepared: 100% ZrO_2, 10, 25, 50, 100 and 150 nm thick; 96 mole% ZrO_2 - 4 mole% SiO_2, 25, 50 and 75 nm thick; 75 mole% ZrO_2 - 25 mole% SiO_2, 50 nm thick. All thicknesses are nominal, based on quartz thickness monitor readings.

To examine the changes in microstructure in thicker pure ZrO_2 films, a series of films were prepared on microscope slide substrates with thicknesses of 100 nm, 200 nm, 400 nm and 800 nm. These films were characterized by XRD techniques.

The films to be examined by TEM were deposited on mica substrates which had been previously lightly coated with carbon. After the film deposition was completed and the substrate removed from the deposition chamber, the film was floated off by slowly submerging the mica substrate in water. The film was then captured on a TEM grid by slowly lowering the water level until the film rested on the grid surface. The carbon coating adhered to the ceramic film, providing additional strength and also a conducting path that helps to minimize charging effects in the microscope.

3. Results - Discussion

In figure 1 are seen TEM micrographs taken from pure ZrO_2 films of different thicknesses. Examination of the selected area diffraction patterns shows that all films contain a single crystalline phase which we assume to be tetragonal, with the possibility of amorphous material being present as well. (The diffraction pattern of the 10 nm film shows one faint ring due to crystalline material which is difficult to see in the reproduction.) No evidence of the monoclinic phase was seen in any of the patterns. Because the small grain size in the film does not allow the resolution of the diffraction rings necessary for unequivocal phase identification, we have assumed the phase present to be tetragonal rather than cubic. This assumption is based on the stabilization of tetragonal ZrO_2 by small grain size [11]. It is noted that the tetragonal phase has been identified in ultrafine powders in the ZrO_2 - SiO_2 systems prepared by the inductively coupled plasma technique [12] using XRD to reveal the characteristic peaks (002) - (202) and (113) - (131).

Coarsening of the physical microstructure as shown in the micrographs of figure 1 is also evident as the films become thicker. Assuming that the microstructural entities represent the diameters of columns, a physical picture for film growth can be formed based on measurements of column diameter as a function of film thickness. Figure 2 shows such a plot for a series of thin films. Consider the pluses, the data for pure ZrO_2. A monotonic increase of column diameter with increasing film thickness is seen. The curve fitted to the data points is based on a square root dependence of column diameter on film thickness, a fit which is superior to a linear fit. It is assumed in all cases that at nucleation, the column diameter is zero. This picture of thin film formation supports the model of Yehoda and Messier [13].

In this series of pure ZrO_2 films, no column diameters of >30 nm were seen. It is expected, however, that thicker films of pure ZrO_2, known to contain the monoclinic phase, would have column diameters that exceed 30 nm, a condition that seems necessary for the formation of the monoclinic phase. Presently, charging effects have made it difficult to image the microstructure of the thicker films to demonstrate this effect.

Changes in the film's microstructure by adding SiO_2 to ZrO_2 by coevaporation are seen in the micrographs of figure 3. All films in this series were nominally 50 nm thick. Small microstructural features are seen in the pure ZrO_2 film and the film is of a single crystalline phase. As SiO_2 is added to the ZrO_2, the physical microstructures decrease in size as does the crystallinity of the film as revealed in the electron diffraction pattern. This is similar to the observations by Jacobson [14] in mixed ZnS - CeF_3 films and mixed CeO_2 - CeF_3 films. When 25 mole% SiO_2 is added, it is seen that the surface of the film is nearly featureless and that the diffraction pattern displays a completely amorphous character. Thus, on this scale, just as for the thicker film examined by XRD [1], the addition of >20 mole% SiO_2 produces a truly amorphous film whose surface appears to be much smoother than the surface of the pure ZrO_2 film.

The smoothing of the surface seen in figure 3 was confirmed by RMS surface roughness measurements made on a series of thicker films in the ZrO_2 - SiO_2 system deposited under nearly identical deposition conditions. Table 1 shows the results of these measurements. The volume fraction of SiO_2 has been calculated on the basis of thickness measurements obtained from the quartz crystal monitors. These data show that pure ZrO_2 film possesses the largest roughness value and pure SiO_2 the smallest, close to that of the well polished substrate (fused silica). The addition of SiO_2 to the ZrO_2 shows a significant smoothing effect.

The final series of films, a series of one composition but different thicknesses is shown in figure 4. These films have a composition of 96 mole% ZrO_2 - 4 mole% SiO_2 and thicknesses of 25, 50 and 75 nm. The 25 nm thick film is seen to have a small microstructure and an amorphous electron diffraction pattern. The 50 nm thick film has slightly larger microstructural features and contains slightly crystalline single phase material. The 75 nm film displays microstructure features which have increased in size when compared to the 50 nm and its electron diffraction pattern again shows single phase fine grained polycrystalline material. These results suggest that a tapered columnar structure is present. When data from these micrographs are plotted on figure 2 (diamonds), it is seen that the columns do not expand nearly as rapidly as the columns in pure ZrO_2. From previous work on thicker films (>300 nm) it is noted that only single crystalline phase is observed in mixed films of this composition. Thus, it is assumed that even at thicknesses of 350 nm the columns do not achieve a diameter large enough to allow the formation of mono-clinic phase.

Since results for this present work show that pure ZrO_2 films up to 150 nm are single phase and previously studied films 350 nm thick exhibited two phase material, a series of 100, 200, 400 and 800 nm thick films of pure ZrO_2 were formed and studied by XRD techniques using CuK_α radiation to determine at what thickness a second phase starts to form. Figure 5 shows the XRD patterns taken using a diffractometer from this series of specimens. It is seen that no monoclinic phase is observed in the 100 nm, 200 nm and 400 nm thick films. Only in the diffraction pattern taken from the 800 nm thick film do monoclinic peaks appear. Thus it is evident that there is a change in the crystal structure of pure ZrO_2 with thickness. Klinger and Carneglia [7] have previously noted a variation of crystallinity with thickness as determined by XRD studies of thin film ZrO_2 stacks. They reported that the transition region which the monoclinic phase developed lay around 100 nm. To characterize our films of this series more completely, a modified Debye-Sherrer wide film x-ray camera, a Read camera [15,16] was used. Figure 6 shows the x-ray diffraction patterns obtained using the Read camera. In the diffraction pattern for the 800 nm thick film five bright continuous rings are seen. These rings correspond to the five peaks seen in the diffractometer trace for the 800 nm film in figure 5. Note the discontinuity in the (002)T ring near the horizontal axis of symmetry of the pattern. This diffraction did not show up in the diffractometer trace and indicates that there are no (002)T planes oriented parallel to the film's surface. However, both x-ray techniques show that two phase material is present in the 800 nm thick ZrO_2 film. The wide film pattern for the 400 nm thick film shows both monoclinic and tetragonal diffraction; however, the monoclinic diffraction is much weaker, especially for diffraction from planes orientated parallel to the film's surface. Note here the preferred orientation of the (002)T planes giving rise to the relatively strong tetragonal peak in the diffractometer trace for the 400 nm film. For this thickness film we have different results, the Read camera showing two-phase and the diffractometer showing one-phase material. For the 200 nm thick ZrO_2 film, tetragonal diffraction is seen in the diffraction pattern of each technique. Some preferred orientation in the (111)T is seen, being brighter near the horizontal axis of the pattern. The Read camera pattern also shows faint monoclinic diffraction while the diffractometer trace shows no monoclinic diffraction. In the last 100 nm thick film only tetragonal diffraction is seen, the (111)T, (002)T and (207)T rings in the wide film pattern and only the (111)T peak in the diffractometer trace. Thus, it appears that one cannot use only diffractometer traces to characterize the microstructure of these thin films. Preferred orientations which are easily seen using the Read camera would be lost in the diffractometer trace. The results of the application of these two techniques suggest that somewhere in the region of 200 nm the pure ZrO_2 films start to grow the monoclinic phase.

4. Summary

Our TEM and XRD investigation have shown that 100% ZrO_2 films grow as tapered columns which are single phase material (tetragonal) up to about 200 nm when two phase material (tetragonal and monoclinic) starts to develop. The transition region was determined with a modified Debye-Scherrer wide film technique which compliments the powder diffraction XRD patterns. It has been shown that the addition of SiO_2 to ZrO_2 films produce films with smaller microstructure features and that when

25 mole% or more of SiO_2 is present, the resulting films are amorphous to both x-ray and electron diffraction and have smoother surfaces than pure ZrO_2. It was also demonstrated that fixed composition films 96 mole% ZrO_2 - 4 mole% SiO_2 grow in a fashion similar to pure ZrO_2 except that the taper of the columns is much less.

We thank T. Vorburger and C. Giauge of the Surface and Particle Metrology Group (NBS) for measurements of surface roughness and film thickness.

5. References

[1] Farabaugh, E. N.,; Sanders, D. M. Microstructure of dielectric thin films formed by e-beam coevaporation. J. Vac. Sci. Technol. A1(2): 356-359; 1983 Apr-June.

[2] Panagopoulus, C. Structural study of anodic ZrO_2 films. Mater. Letters 3(9,10): 393-395; 1985 July.

[3] Ploc, R. A.; Miller, M. A. Transmission and scanning electron microscopy of oxides anodically formed on zircaloy-2. J. Nuclear Materials 64: 71-85; 1977.

[4] Ploc, R. A. Transmission electron microscopy of αZrO_2 films formed in 573K oxygen. J. Nuclear Materials 61: 79-87; 1976.

[5] Bailey, J. E. On the oxidation of thin films of zirconium. J. Nuclear Materials 28: 48-60; 1968.

[6] Bailey, J. E. On the oxidation of thin films of zirconium. J. Nuclear Materials 8(2): 259-262; 1963.

[7] Klinger, R. E.; Carneglia, C. K. Optical and crystalline inhomogeneity in evaporated zirconia films. Appl. Optics 24(19): 3184-3187; 1985 October.

[8] Morita, M.; Fukumoto, H.; Imura, T.; Osaka, Y. Growth of crystalline zirconium dioxide films on silicon. J. Appl. Phy. 58(6): 2407-2409; 1985 September 15.

[9] Martin, P. J.; Netterfield, R. P.; Sainty, W. G. Modification of the optical and structural properties of dielectric ZrO_2 films by ion-assisted deposition. J. Appl. Phy. 55(1): 235-241; 1984 January 1.

[10] Martin, P. J.; Macleod, H. A.; Netterfield, R. P.; Pacey, C. G.; Sainty, W. G. Ion-beam-assisted deposition of thin films. Appl. Optics 22(1): 178-184; 1983 January 1.

[11] Garve, R. C. in Part II Oxides of Rare Earth, Titanium, Zirconium, Hafnium and Tantalum, edited by A. M. Alpher (Academic, New York): 117-124; 1970.

[12] Ono, T.; Kagawa, M.; Syono, Y. Ultrafine particles of the ZrO_2 - SiO_2 system prepared by the spray-ICP technique. J. Mater. Sci. 20: 2483-2487; 1985.

[13] Yehoda, J. E.; Messier, R. Are thin film physical structures fractals? Applications Sur. Sci. 22/23: 590-595; 1985.

[14] Jacobsson, R. in Optical Properties of Dielectric Films, edited by N. N. Axelrod (Electochemical Society, Inc., New York): 169-191; 1968.

[15] Read, M. H. 27th Ann. Pittsburgh Diff. Conf.; 1964 November.

[16] Read, M. H.; Hensler, D. H. X-ray analysis of sputtered films of beta-tantalum and body-centered cubic tantalum. Thin Solid Films 10: 123-135; 1972.

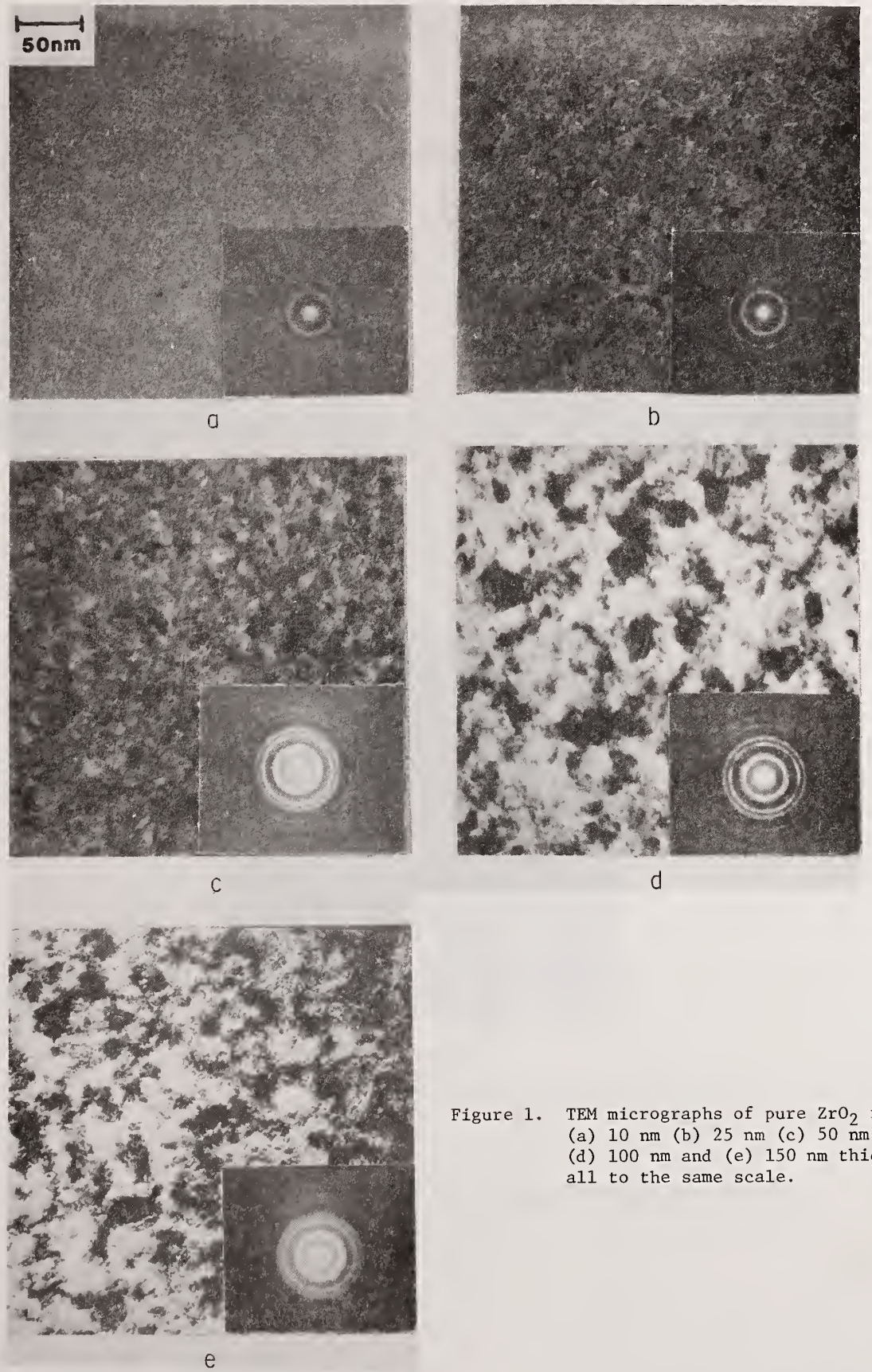

Figure 1. TEM micrographs of pure ZrO_2 films (a) 10 nm (b) 25 nm (c) 50 nm (d) 100 nm and (e) 150 nm thick, all to the same scale.

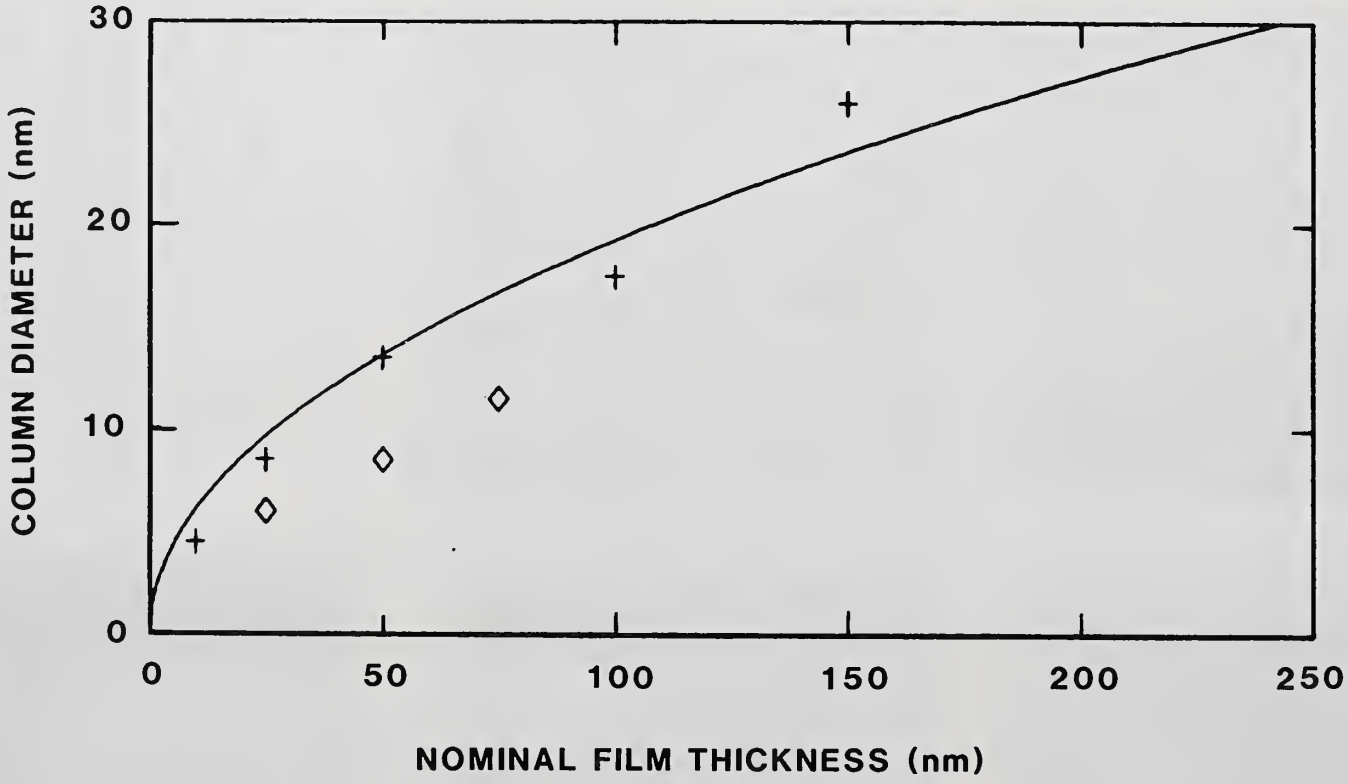

Figure 2. Column diameter as a function of film thickness for pure ZrO_2 (pluses) and ZrO_2 - SiO_2 (diamonds) films.

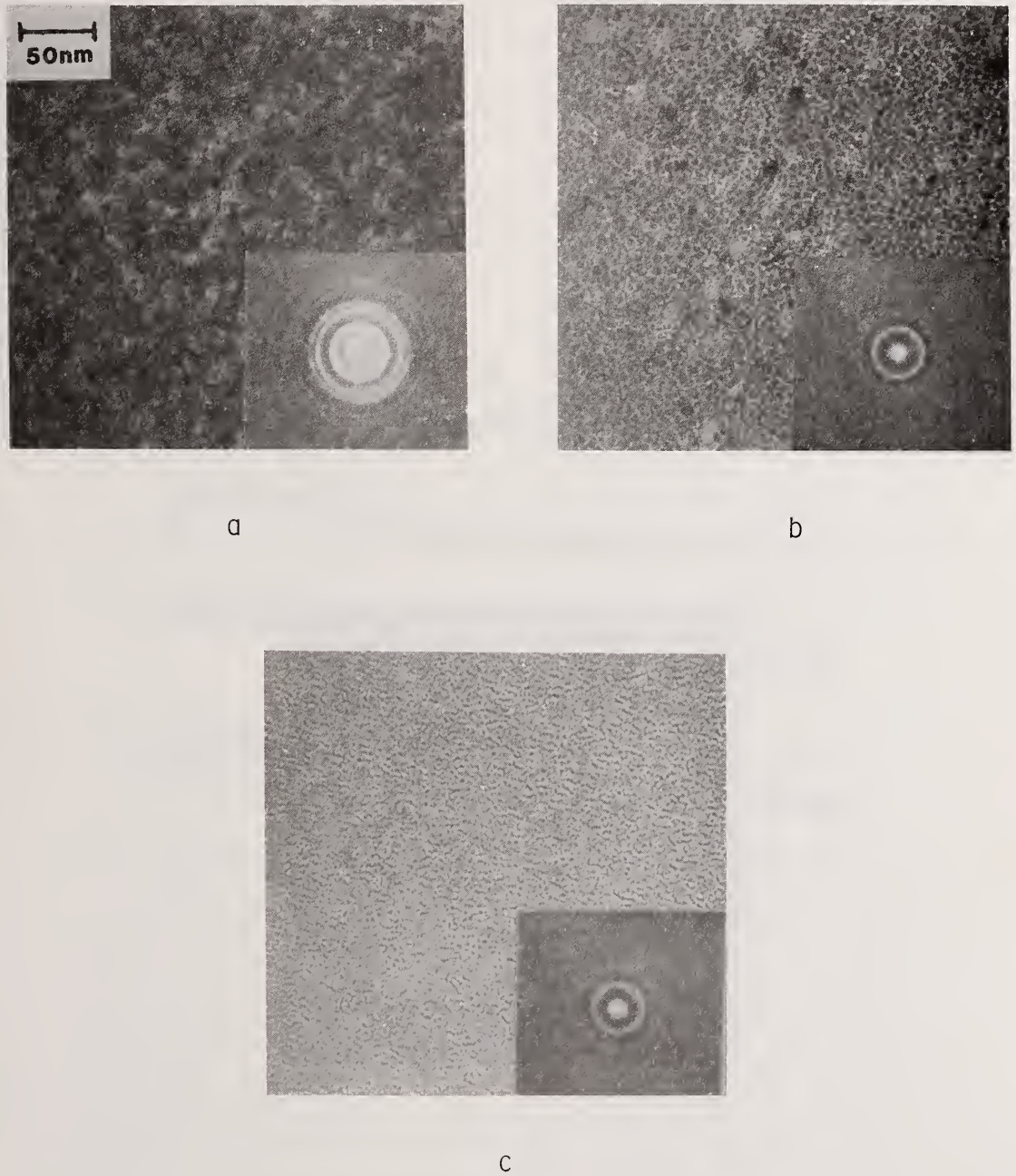

Figure 3. TEM micrographs of 50 nm thick film with composition (a) 100 mole % ZrO_2 (b) 96 mole % ZrO_2 - 4 mole % SiO_2 and (c) 75 mole % ZrO_2 - 25 mole % SiO_2, all to the same scale.

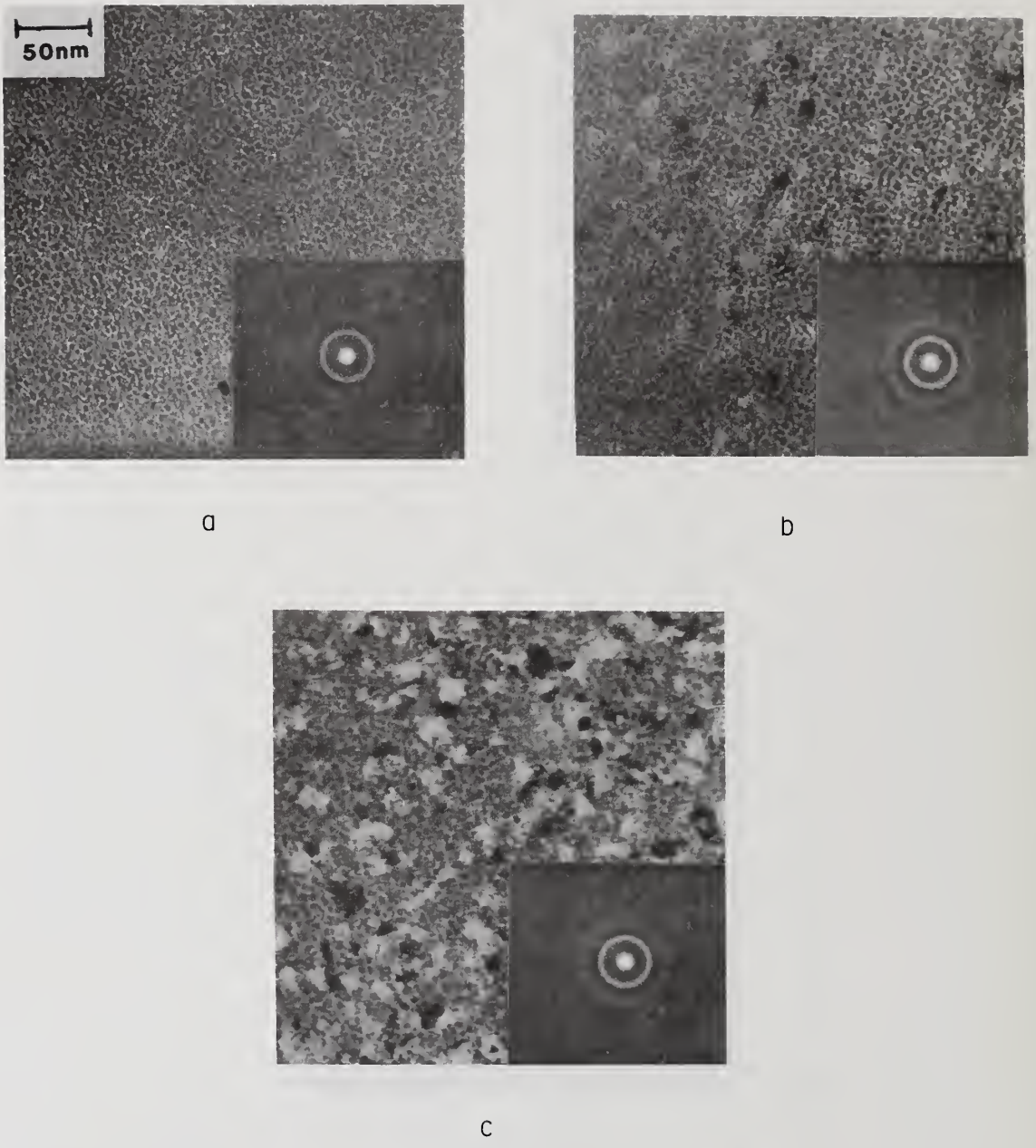

Figure 4. TEM micrograph 96 mole % ZrO_2 - 4 mole % SiO_2 films (a) 25 nm (b) 50 nm and (c) 75 nm thick, all to the same scale.

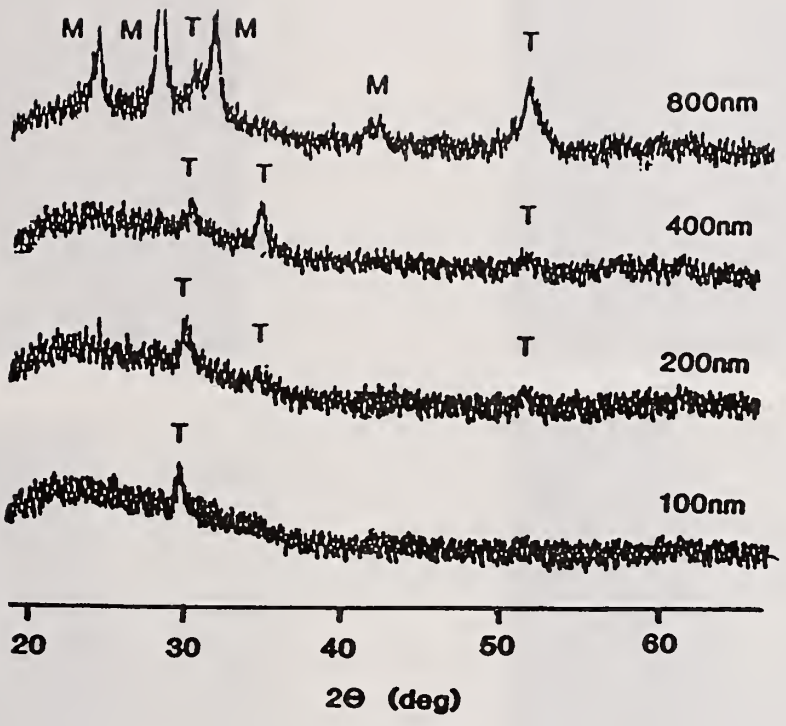

Figure 5. XRD pattern of different thicknesses of ZrO_2 films showing the development of the monoclinic phase. Tetragonal and monoclinic phases are identified by T and M respectively.

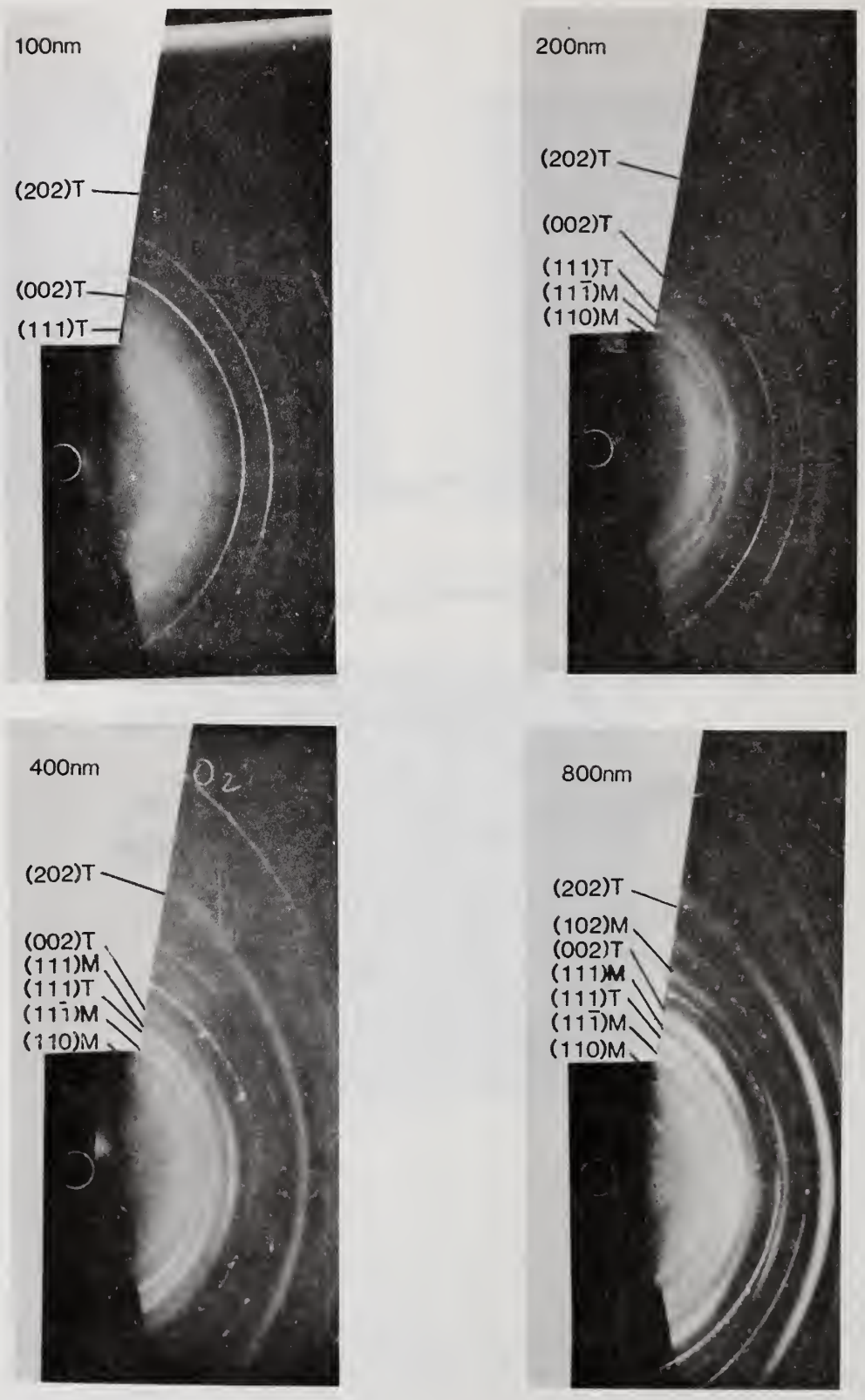

Figure 6. Read camera diffraction pattern of the same 100 nm, 200 nm, 400 nm, and 800 nm thick films whose diffractometer traces were shown in Figure 5.

Table 1. RMS Surface Roughness of ZrO_2 - SiO_2 Films

Nominal Vol. Fraction SiO_2	Surface Roughness (nm)
0	2.3
0.135	0.6
0.30	0.5
0.49	0.6
0.68	0.5
1.00	0.4
substrate	0.3

Manuscript Received
9/10/87/sar

Admixture of SiO_2 to Suppress TiO_2 Crystallization

J. R. Sites, J. S. Postek, R. S. Robinson, T. D. Schemmel, and C. Y. She

Physics Department, Colorado State University
Fort Collins, CO 80523

Crystallization of glassy TiO_2 films used in optical coatings can be a problem in high power applications and may be a major limitation to the laser damage threshold. An attempt to suppress such crystallization involved mixing small amounts of SiO_2 into TiO_2 during the ion-beam sputter deposition process. An admixture of 5% SiO_2 increased the crystallization onset temperature, determined by Raman spectroscopy, by approximately 150°C. The refractive index was relatively unaffected by the addition of 5% SiO_2, dropping from 2.42 to 2.38. Optical loss, which shows a sharp increase near 350°C for pure TiO_2, did not increase measurably for the films with SiO_2 admixture of 5% or greater.

Key words: optical coatings; TiO_2; SiO_2; Raman spectroscopy; refractive index.

1. Introduction

A coating consisting of alternate layers of high and low refractive index materials is a common technique for enhancing the reflectivity of an optical component at a selected wavelength or decreasing it to very nearly zero. Titania is often used as the high index material and almost always paired with SiO_2, because that combination has a large difference in refractive index, it can be fabricated with low visible and IR absorption, and it is relatively stable against environmental effects.

Typically TiO_2 films are fabricated by evaporation or by ion-beam sputter deposition [1,2]. They tend to be glassy with no measurable crystalline structure. Upon heating to approximately 350°C, however, glassy TiO_2 will begin to crystallize into the anatase or rutile structure, depending we believe on its original microstructure [3,4]. The crystallization process destroys the optical utility of a coating because the scattering loss and effective extinction coefficient are dramatically increased [4]. This problem is most serious in high power laser applications. Any defects in the coating will absorb extra energy, locally raising the temperature and locally crystallizing TiO_2. The absorption will increase and additional light will further raise the temperature in a runaway process.

The purpose of this paper is to report a relatively simple strategy, the addition of a small fraction of SiO_2 to a TiO_2 layer, to stabilize the glassy phase.

2. Experimental

Mixed TiO_2/SiO_2 films were fabricated by ion-beam sputter deposition. Overlapping targets of titanium and SiO_2 were bombarded by a mixed argon-oxygen sputter beam from a Kaufman ion source [1,2]. The composition of each film was measured by comparing the areas of x-ray photoelectron spectroscopy (XPS) peaks to those from pure TiO_2 and SiO_2 films [5]. Refractive index and effective extinction coefficient were deduced from transmission spectrophotometry. Finally, the degree of crystallization as each film was heated was determined with Raman spectroscopy techniques [6].

3. Results

The refractive indices of a series of TiO_2/SiO_2 films are shown in figure 1. The transition near 30%, also seen in bandgap vs. composition, is real, but not important here where only TiO_2-rich films are considered. For the TiO_2-rich films, the refractive index drops 0.04 for each 5% SiO_2 admixture. Thus 90% TiO_2 has an index of 2.34 and 95% has 2.38, compared to 2.42 for pure TiO_2. These values are still greater than most other high refractive index oxides. Furthermore, the optical absorption edge of the TiO_2-rich mixtures showed no measurable change from pure TiO_2, implying that the high index mixtures should be applicable to the same wavelength range as pure TiO_2.

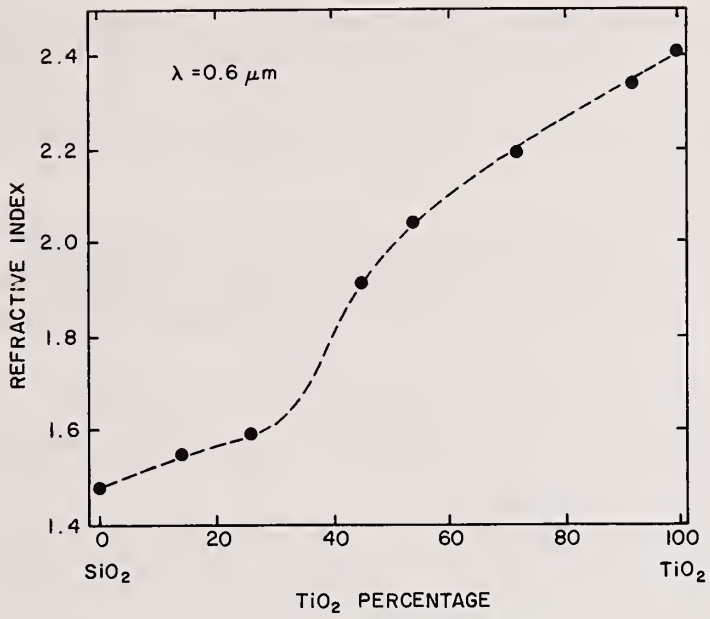

Figure 1. Refractive index of TiO_2/SiO_2 mixtures.

Typical Raman spectra from TiO_2-rich films on glass substrates are shown in figure 2. The films studied in this work were all deposited with the substrates held at room temperature, and all

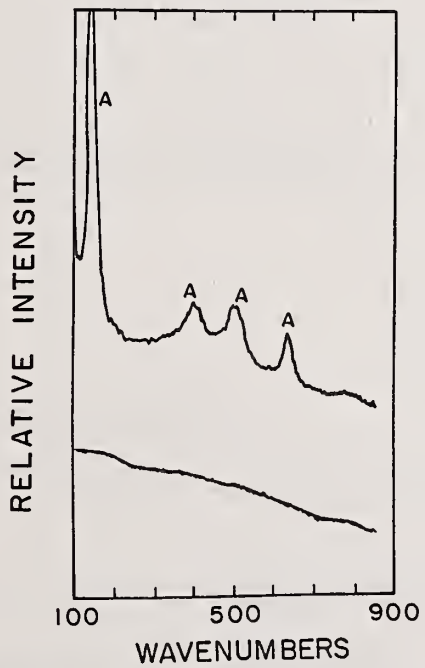

Figure 2. Raman spectra from an as-deposited (lower) and crystallized (upper) TiO_2-rich film on glass.

showed initial crystallization into the anatase phase during subsequent thermal cycles. At sufficiently high temperatures, however, the crystal structure would change from anatase to rutile. The lower spectrum in figure 2 is from an as-deposited glassy film and shows only the substrate background. The upper spectrum was taken after a nearly complete crystallization cycle, and the anatase peaks have become quite pronounced. Intermediate amounts of crystallization produce spectra with intermediate anatase magnitudes.

Figure 3a shows the amount of anatase crystallization as a function of annealing temperature. The samples were held at each annealing temperature for 20 minutes, returned to room temperature for

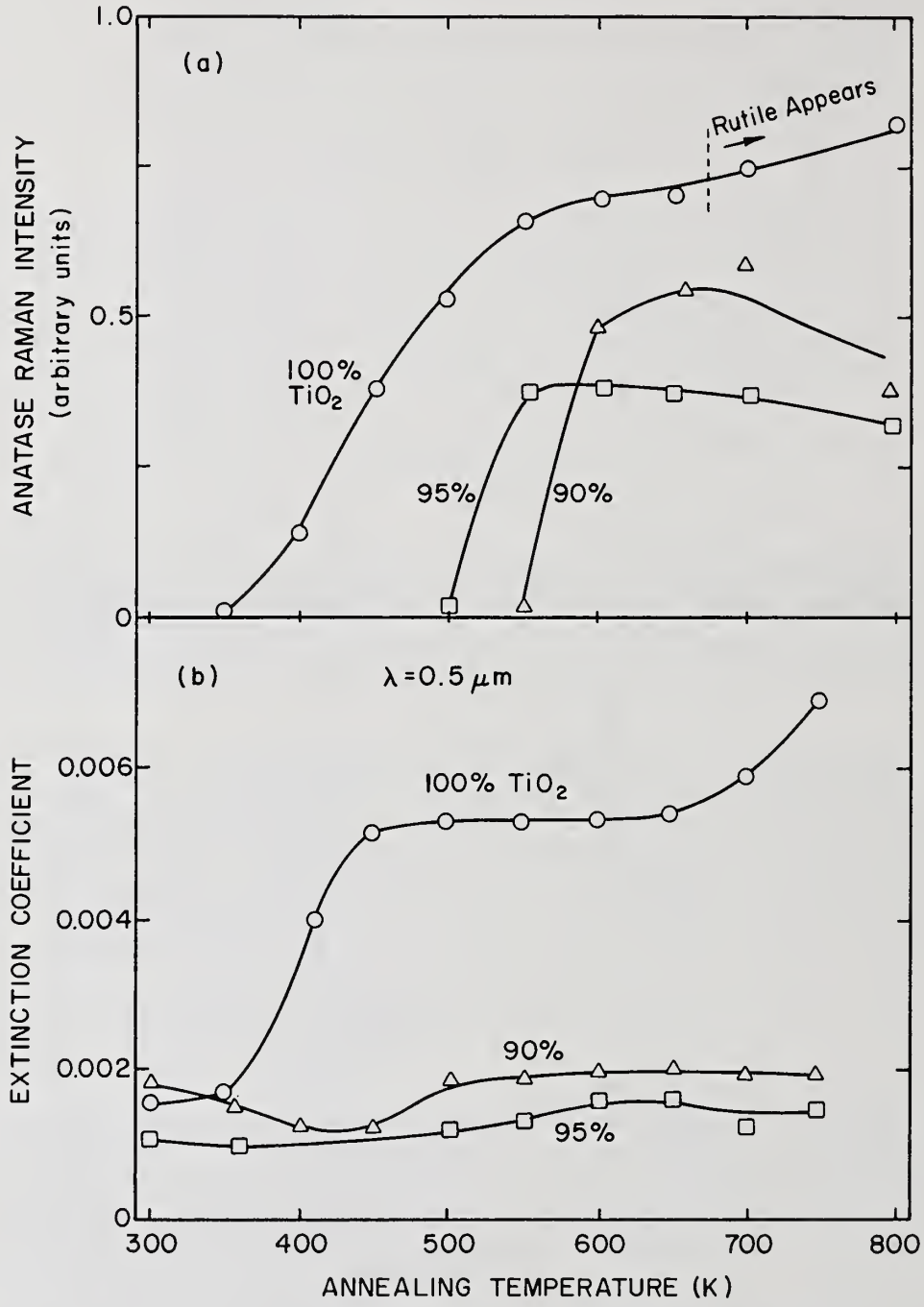

Figure 3. Suppression of TiO_2 crystallization seen in (a) Raman spectra and (b) effective extinction coefficient.

the Raman spectrum, then heated to the next temperature. The onset of measurable crystallization occurred just above 350°C for the pure TiO_2 film. At the same temperature, as seen in figure 3b, optical degradation begins. The quantity plotted is the extinction coefficient deduced from transmission spectrophotometry, which physically includes scattering as well as true absorption.

When small amounts of SiO_2 are incorporated in the TiO_2 film, the onset of crystallization is delayed to 500°C and above. When very large amounts, e.g., 50% SiO_2, are added, the films showed physical deterioration near 800°C before any crystallization was noted in the Raman spectra. When

TiO_2-rich films were deposited on crystalline silicon instead of glass, the suppression of crystallization was qualitatively similar to figure 3a. The extinction of coefficient of figure 3b showed no increase when SiO_2 was added. However, the initial spectrophotometric extinction was relatively high, and it may well be that a lower baseline in figure 3b would yield results that more obviously track the more sensitive Raman data.

4. Conclusions

The addition of small amounts of SiO_2 to TiO_2 films appears to be a successful technique for suppressing crystallization and hence for increasing the functional temperature range of TiO_2 optical coatings by the order of 150°C. The concept of mixing oxides during deposition may be generally useful in expanding the possibilities for layered optical coatings.

This work was supported by the Air Force Weapons Laboratory under contract F29602-83-K-0079.

5. References

[1] Sites, J. R.; Gilstrap, P.; Rujkorakarn, R. Ion beam sputter deposition of optical coatings. Optical Engr. 22(4): 447-449; 1983 July-August.

[2] Demiryont, H.; Sites, J. R. Oxygen threshold for ion-beam sputter deposited oxide coatings. NBS Special Publication 727: 180-186; October 1986.

[3] Rujkorakarn, R.; Hsu, L. S.; She, C. Y. Crystallization of titania films by thermal heating. NBS Special Publication 727: 253-261; October 1986.

[4] Hsu, L. S.; Rujkorakarn, R.; Sites, J. R.; and She, C. Y. Thermally induced crystallization of amorphous-titania films. J. Appl. Phys. 59(10): 3475-3480; 15 May 1986.

[5] Sites, J. R.; Demiryont, H. Interfacial structure of ion-beam sputter deposited SiO_2/TiO_2 coatings. NBS Special Publication, 1985. Boulder Damage Symposium, to be published.

[6] Hsu, L. S.; She, C. Y. Real-time monitoring of crystallization and structural transformation of titania films with Raman spectroscopy. Optics Letters 10(12): 638-640; December 1985.

Manuscript received
9-18-87/sar

Long-Range Pulselength Scaling of 351 nm Laser Damage Thresholds

S. R. Foltyn and L. John Jolin

Los Alamos National Laboratory
CLS-6 MS-J564
Los Alamos, NM 87545

In a series of experiments incorporating 351-nm pulselengths of 9, 26, 54, and 625 ns, it was found that laser damage thresholds increased as (pulselength)^x, and that the exponent averaged 0.36 and ranged, for different samples, from 0.23 to 0.48. Similar results were obtained when only catastrophic damage was considered. Samples included Al_2O_3/SiO_2 in both AR and HR multilayers, HR's of Sc_2O_3/SiO_2 and HfO_2/SiO_2, and an Al-on-pyrex mirror; 9-ns thresholds were between 0.2-5.6 J/cm^2.

When these data were compared with a wide range of other results – for wavelengths from 0.25 to 10.6 μm and pulselengths down to 4 ps – a remarkably consistent picture emerged. Damage thresholds, on average, increase approximately as the cube-root of pulselength from picoseconds to nearly a microsecond, and do so regardless of wavelength or material under test.

Key words: Al_2O_3; catastrophic damage; coating defects; damage thresholds; excimer lasers; HfO_2; multilayer dielectric coatings; pulselength scaling; Sc_2O_3; XeF lasers.

1. Introduction

Scaling of optical damage thresholds over a long pulselength range has become increasingly important with the continued development of electron-beam pumped excimer lasers. Pulselengths of e-beam devices (0.5 to 2 μs) are about two orders of magnitude longer than of avalanche discharge lasers typically used in the laboratory, yet the latter provide the only reliable means to obtain high quality, statistically significant optical damage data.

In order to develop a capability to predict microsecond thresholds from 10-ns data, a representative set of 351-nm optical coatings was tested at pulselengths from 9 to 625 ns. In addition to measurement of threshold scale factors, issues such as the functional form of pulselength scaling, scaling for catastrophic damage versus microscopic damage, and the influence of pulselength on defect density were studied.

A wealth of experimental pulselength scaling data has appeared in the literature over the past 15 years. Since the present results cover a previously unexplored region of long pulselength and short wavelength, a survey of past results was conducted to determine whether pulselength scaling under present conditions differs from that obtained previously.

2. Experimental Conditions

2.1. Laser Operating Conditions

Table 1. contains a listing of laser sources and relevant operating parameters for the four pulselengths employed in this work. The 9-ns measurements were made in a production test facility under standard conditions for excimer-based testing at Los Alamos. The longer pulselength work was conducted in an adjoining laboratory using a similar hardware configuration and methodology. The newer excimer laser in this facility was equipped with high-energy electrodes, producing a 26-ns pulselength and a more nearly square beam cross section. Increasing optical feedback from 4% to values between 50% and 90% more than doubled the pulselength and, in the case of 50% feedback, doubled the output energy to 350 mJ. For these tests, however, 90% was found to provide the smoothest temporal shape with sufficient energy (100 to 150 mJ).

Table 1. Sources and Test Conditions

Pulselength[a]	Laser	Spotsize[b]	Wavelength	PRF
9 ns	XeF excimer (Lumonics 861)	0.44 nm	351 nm	35 pps
26 ns	XeF excimer (Lumonics 861T-4)	0.71 mm	351 nm	35 pps
54 ns	XeF excimer (Lumonics 861T-4)[c]	0.72 mm	351 nm	35 pps
625 ns	Frequency-doubled dye (Candela UV-500)	0.44 mm	355 nm	0.5 pps

[a] FWHM.
[b] Mean diameter @ $1/e^2$ amplitude.
[c] With 10% output coupling.

The longest pulse was obtained with a commercial flashlamp-pumped dye laser and second-harmonic generator. LD-700 in methanol provided the fundamental frequency, which was doubled to 355 nm in an angle-tuned ADP crystal. Although the pulse repetition rate of this laser was substantially lower than that used for the other tests, previous results [1] at 308 nm have demonstrated that thresholds are unaffected by prf variations below 250 pps.

Temporal profiles for each pulselength are shown in figure 1.

2.2. Test Samples

Six coating types were chosen for these experiments to represent a realistic cross section of 351-nm optics. Multilayer dielectric reflectors included a narrow bandwidth design incorporating Al_2O_3 and SiO_2, plus Sc_2O_3/SiO_2, and two broadband examples of HfO_2/SiO_2. Designs were all-quarterwave with a halfwave overcoat, and employed a sufficient number of layers to achieve 99% reflectance at 351 nm. In addition, an Al_2O_3/SiO_2 AR coating was evaluated, as was a MgF_2-overcoated Al mirror. Substrates for the dielectric films were fused silica; the Al coating was deposited on pyrex.

2.3. Test Methodolgy

Each test involved the generation of a damage probability plot typically incorporating data from several samples; between 50 and 400 sites were tested on each coating type at each pulselength. Three methods were employed to scale results obtained at different pulselengths:

Method 1. Comparison of the 0% intercepts of linear regression fits to the probability data;

Method 2. Comparison of the lowest damaging fluence values;

Method 3. Comparison of the lowest fluence values producing catastrophic damage.

3. Results and Discussion

Short-pulse damage thresholds from 0.2 to 5.6 J/cm^2 were measured for the six sample types. Perhaps 95% of the 351-nm optics tested at Los Alamos fall within this range. Thresholds were typical for the antireflection coating and the Al mirror, while the Sc_2O_3 reflector was somewhat above average and the Al_2O_3 reflector was a very weak example of this coating type. One reflector using HfO_2 was near the top of its normal range, the other was at the bottom. Measured 9-ns thresholds and scale factors (ratios of 625- to 9-ns thresholds) appear in Table 2.

Scale factors are seen to vary somewhat with method of comparison. Since the variations are largest for coating types with shallow probability curves, they can likely be attributed to uncertainty in the determination of individual thresholds. In order to reduce the effect of these uncertainties and also to more accurately represent the process normally used to extract a threshold from probability data, scale factors in the discussion that follows are average values from Methods 1 and 2. These methods involve microscopic damage events; considering only catastrophic damage (Method 3) gives similar results.

Table 2. Damage Threshold Scale Factors: 9 to 625 ns

Coating Materials	9-ns Damage Threshold	Scale Factor for 625-ns Threshold		
		Method 1	Method 2	Method 3
Sc_2O_3/SiO_2 (HR)[a]	5.6 J/cm^2	5.0	7.5	6.7
HfO_2/SiO_2 (HR)[a]	3.7 J/cm^2	2.7	2.8	4.3
Al_2O_3/SiO_2 (AR)[b]	1.5 J/cm^2	4.2	5.4	---
HfO_2/SiO_2 (HR)[c]	0.7 J/cm^2	5.6	4.7	4.2
Al_2O_3/SiO_2 (HR)[b]	0.5 J/cm^2	6.6	9.0	3.7
Al on pyrex[d]	0.2 J/cm^2	2.4	2.9	2.9

Method 1. Intercept of linear regression fit.
Method 2. Lowest damaging fluence.
Method 3. Lowest fluence for catastrophic damage.

a. Interoptics, Ltd.
b. Broomer Research Corp.
c. Laser Optics, Inc.
d. Newport Corp.

Damage thresholds at all four pulselengths are summarized in figure 2. Power-law fits indicate that threshold improvement with pulselength ranges, for different sample types, from a fourth-root to a square-root dependence. There is no correlation between these scaling rates and any readily apparent or measureable property of the coatings such as index, threshold, bandgap [2], or reflectance. A particularly good illustration of this is the two examples of HfO_2/SiO_2, which are essentially identical designs produced by different vendors, and which have markedly different scaling behavior.

Another observed difference between coating types was a change in the density of damage-prone defects for 9-ns versus 625-ns pulses. Since the test spotsize for these two pulselengths was identical, slopes of the probability curves are directly related to defect density [3]. For the Al_2O_3/SiO_2 reflector of figure 3, slopes are nearly identical after fluence scaling; this implies that the defect density is the same for both pulselengths. For the antireflection coating of the same materials (figure 4) they are notably different, indicating a higher density for the shorter pulselength. Half of the six coating types exhibited no density variation with pulselength while, for the other half, short-pulse defect densities were 2-6x higher. Again, these variations in defect density were uncorrelated with scaling rates or other readily apparent coating properties.

4. Comparison with Other Data

Figure 5 is a compilation of published scaling results at 351 to 355 nm with thresholds normalized to 10 ns. In addition to the present work, three independent data sets are included:

1. A quarterwave single layer tested at 355 nm with 20 ps and 27 ns pulselengths [4];
2. Eight materials in various thickness single layers tested at 353 nm with 5 ns and 15 ns pulselengths [5];
3. Five HR and four AR coatings tested at 351 or 355 nm with pulselengths of 0.6, 1, 5, and 9 ns [6].

The results are remarkably consistent. From 0.6- to 625-ns average scaling is $\tau^{0.32}$. For the Walker, Rainer, and present results, both fast (0.5 to 0.8) and slow (0.0 to 0.2) scaling exponents were observed.

Extending this comparison further is a listing, in Table 3, of test data covering wavelengths from 248 nm to 10.6 μm and more than five decades in pulselength [4-14]. Again, the results are remarkably consistent. While scaling exponents for individual tests vary widely, the average scaling

Table 3. Pulselength Scaling Comparison

Reference		Wavelength (μm)	Pulselength Range (ns)	Scaling Exponent[a] Range	Average
Soileau	[7]	1.05	0.004 - 0.008	0.0 - 0.5	0.3
Bliss	[8]	0.69	0.020 - 23	0.4 - 0.5	0.4
Newnam	[4]	0.36	0.020 - 27		0.2
Soileau	[7]	0.53	0.03 - 0.15	0.1 - 0.9	0.7
Deaton	[9]	0.27	0.1 - 0.7	0.0 - 0.7	0.3
Milam	[10]	1.06	0.17 - 3.2	0.3 - 0.5	0.4
Lowdermilk	[11]	1.06	0.17 - 3.5	0.0 - 0.5	0.3
Rainer	6]	0.36	0.6 - 9	0.1 - 0.5	0.3
Milam	[12]	1.06	1 - 9	0.3 - 0.6	0.6
Newnam	[13]	10.6	1.7 - 65	0.2 - 0.3	0.3
Walker	[5]	0.27	5 - 15	0.0 - 1.0	0.5
		0.36	5 - 15	0.0 - 0.8	0.5
		0.53	5 - 15	0.0 - 0.8	0.5
		1.06	5 - 15	0.0 - 0.7	0.3
Boyer	[14]	0.25	10 - 38	0.2 - 0.5	0.3
This Work		0.35	9 - 625	0.2 - 0.5	0.4

[a] The value of x in the relationship: threshold fluence $\propto$ (pulselength)^x

rate has a nearly constant value from 4 ps to 625 ns. Thresholds improve as $\tau^{0.3\text{-}0.4}$ for picosecond pulses, and continue to do so for pulselengths up to a microsecond. It is apparent from this compilation that cube-root scaling – as opposed to square-root - is a more accurate rule of thumb for the effect of pulselength on damage threshold.

One final observation is illustrated by the 20–ps datum of Newnam in figure 5. Although this point falls within the error bars for an individual measurement, its position relative to the other data suggests an inflection at about 1 ns. Such inflections - as well as other forms of non-power law behavior - have been predicted in both inclusion [15-17] and avalanche [18] models of damage. Typically the inflection or curvature is invoked to reconcile τ^0 dependence for short pulselengths and τ^1 dependence for long ones. From picosecond to microsecond pulselengths, this transition from a constant fluence regime to one in which the damaging field is constant is experimentally unsupported: A simple power law relationship provides a good description of experimental results over the entire range.

5. Conclusions

In testing six 351–nm coating types, damage thresholds were found to increase - from 9 to 625 ns – at a rate varying from the fourth–root of pulselength to the square–root. The increase was the same for both catastrophic and microscopic damage, and was not correlated with any readily apparent optical or physical property of the coatings.

A review of published pulselength scaling data indicates that the present work is consistent with earlier findings: From the uv to the mid–ir, and from picoseconds to a microsecond, fluence thresholds improve on average as the cube-root of pulselength, while individual samples may scale quite differently.

This wide range of scaling rates severely limits the ability to accurately predict individual long–pulse thresholds from short–pulse data. As an example, the present results indicate that a 3 J/cm^2 coating at 9 ns can be expected to have a threshold anywhere between 9 and 29 J/cm^2 at 1 μs.

The authors wish to acknowledge the assistance of Bill Leamon who produced most of the 9-ns test results and also contributed to the testing at longer pulselengths.

6. References

[1] Foltyn, S.R. Optical damage research at Los Alamos. Los Alamos Report LA-UR-86-3446. 1986 November.

[2] Brawer, S.; Smith, W.L. Theory of laser damage in dielectric solids. Nat. Bur. Stand. (U.S.) Spec. Publ. 541; 1978. 303 p.

[3] Foltyn, S.R. Spotsize effects in laser damage testing. Nat. Bur. Stand. (U.S.) Spec. Publ. 669;

[4] Newnam, B.E.; Gill, D.H. Ultraviolet damage resistance of laser coatings. Nat. Bur. Stand. (U.S.) Spec. Publ. 541; 1978. 190 p.

[5] Walker, T.W.; Guenther, A.H.; Nielsen, P.E. Pulsed laser-induced damage to thin-film optical coatings -- Part I: Experimental. IEEE J. Quant. Elect. QE-17(10): 2041-2052; 1981 October.

[6] Rainer, F.; Vercimak, C.L.; Milam, D.; Carniglia, C.K.; Tuttle Hart, T. Measurements of the dependence of damage thresholds on laser wavelength, pulse duration and film thickness. Nat. Bur. Stand. (U.S.) Spec. Publ. 688; 1983. 268 p.

[7] Soileau, M.J.; Williams, W.E.; Van Stryland, E.W.; Boggess, T.F.; Smirl, A.L. Temporal dependence of laser-induced breakdown in NaCl and SiO_2. Nat. Bur. Stand. (U.S.) Spec.

[8] Bliss, E.S.; Milam, D. Laser induced damage to mirrors at two pulse durations. Nat. Bur. Stand. (U.S.) Spec. Publ. 372; 1972. 108 p.

[9] Deaton, T.F.; Smith, W.L. Laser-induced damage measurements with 266 nm pulses. Nat. Bur. Stand. (U.S.) Spec. Publ. 568; 1979. 417 p.

[10] Milam, D. 1064-nm laser damage thresholds of polished glass surfaces as a function of pulse duration and surface roughness. Nat. Bur. Stand. (U.S.) Spec. Publ. 541; 1978. 164 p.

[11] Lowdermilk, W.H.; Milam, D.;, Rainer, F. Damage to coatings and surfaces by 1.06 μm pulses. Nat. Bur. Stand. (U.S.) Spec. Publ. 568; 1979. 391 p.

[12] Milam, D.; Thomas, I.M.; Weinzapfel, C.; Wilder, J.G. Pulse duration dependence of 1064-nm laser damage thresholds of porous silica antireflection coatings on fused silica substrates. Nat. Bur. Stand. (U.S.) Spec. Publ. 727; 1984. 211 p.

[13] Newnam, B.E.; Nowak, A.V.; Gill, D.H. Short-pulse CO_2 Laser damage studies of NaCl and KCl windows. Nat. Bur. Stand. (U.S.) Spec. Publ. 568; 1979. 209 p.

[14] Boyer, J. (unpublished work in progress).

[15] Bliss, E.S. Pulse duration dependence of laser damage mechanisms. Nat. Bur. Stand. (U.S.) Spec. Publ. 341; 1970. 105 p.

[16] Danileiko, Yu. K.; Manenkov, A.A.; Nechitailo, V.S. The role of absorbing defects in the laser damage of transparent materials. Nat. Bur. Stand. (U.S.) Spec. Publ. 620; 1980. 369 p.

[17] Lange, M.R.; McIver, J.K. Laser induced damage of a thin film with an absorbing inclusion: thermal considerations of substrates and absorption profiles. Nat. Bur. Stand. (U.S.) Spec. Publ. 688; 1983. 448 p.

[18] Sparks, M.; Holstein, T.; Warren, R.; Mills, D.L.; Maradudin, A.A.; Sham, L.J.; Loh, E.; King, F. Theory of electron avalanche breakdown in solids. Nat. Bur. Stand. (U.S.) Spec. Publ. 568;

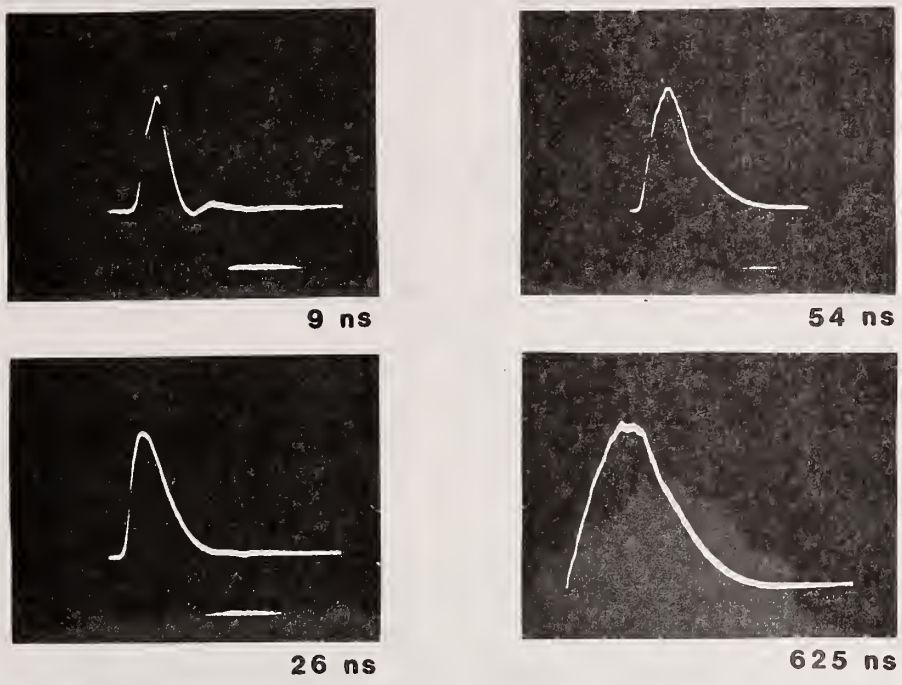

Figure 1. Oscilloscope traces and FWHM values for each of the pulselengths used in this work.

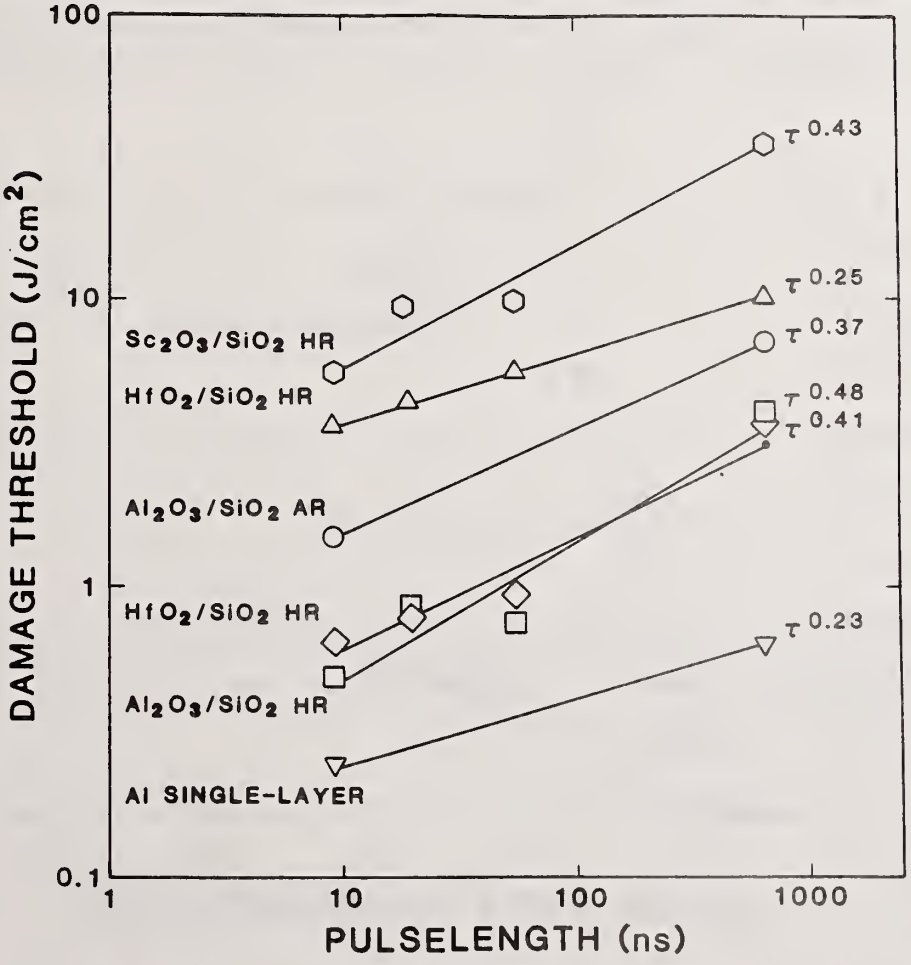

Figure 2. Damage thresholds at 9, 26, 54, and 625 ns pulselengths for six different 351-nm coating types. Slopes of the lines, which represent best linear regression fits to the data, indicate that thresholds scale at rates ranging from fourth-root to square-root of the pulselength.

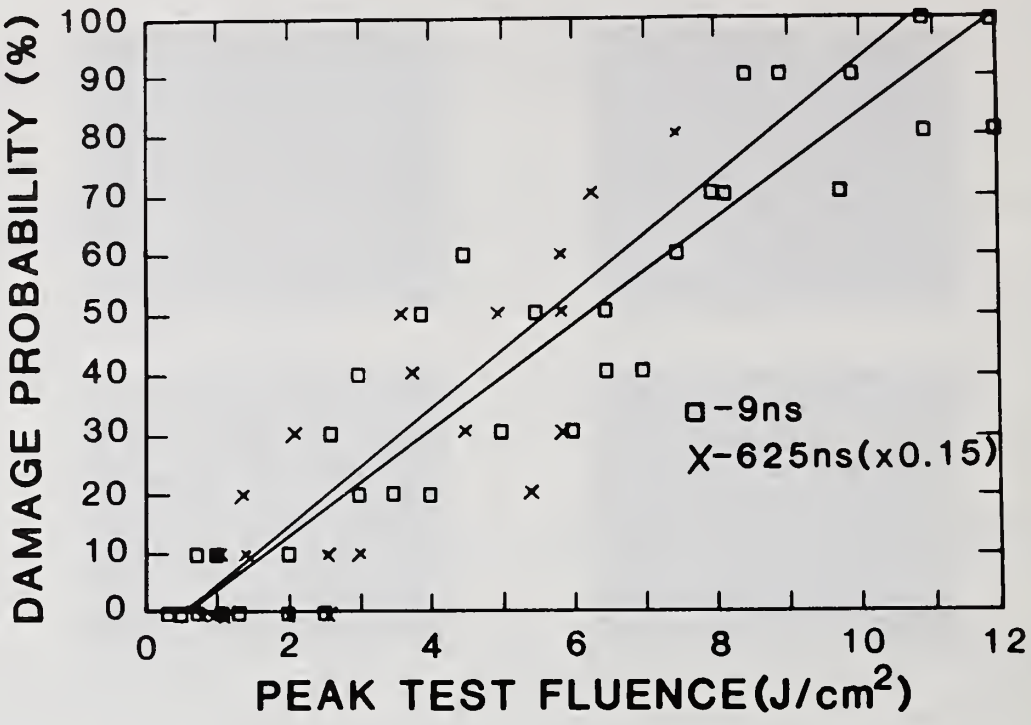

Figure 3. Damage probability plots for the Al_2O_3/SiO_2 reflectors at 9 ns and - with scaled fluence values - 625-ns pulselengths. After scaling, the slopes are nearly identical indicating equal defect densities at each pulselength.

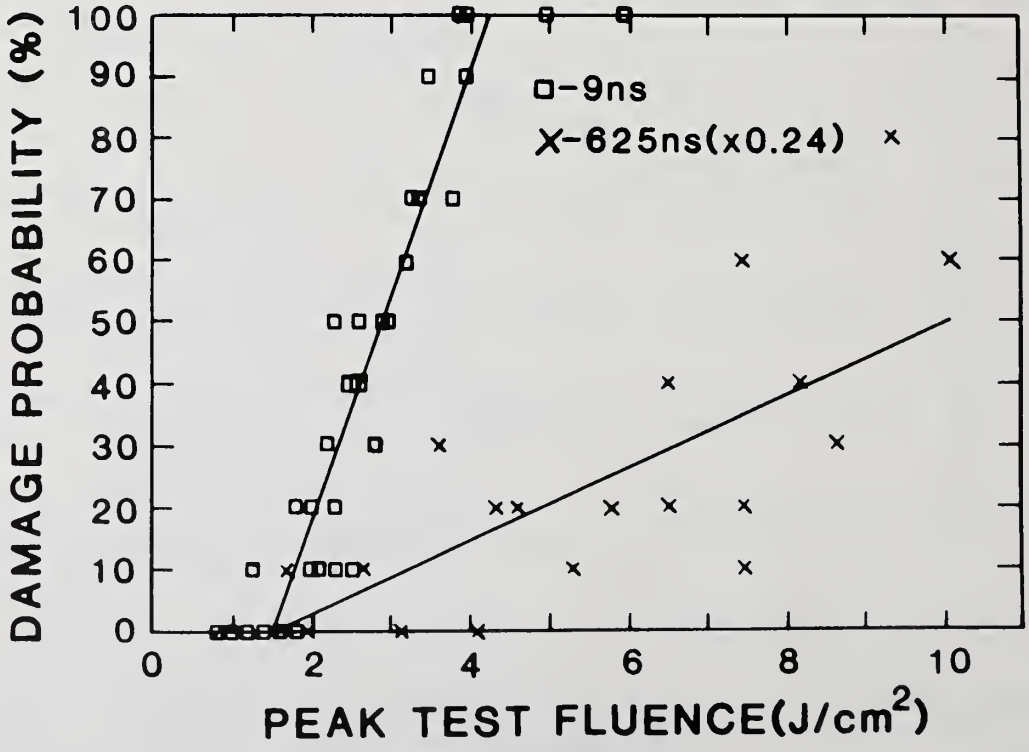

Figure 4. Probability plots for Al_2O_3/SiO_2 antireflection coatings. The steeper slope for 9 ns indicates a 6x higher density of defects for the shorter pulses.

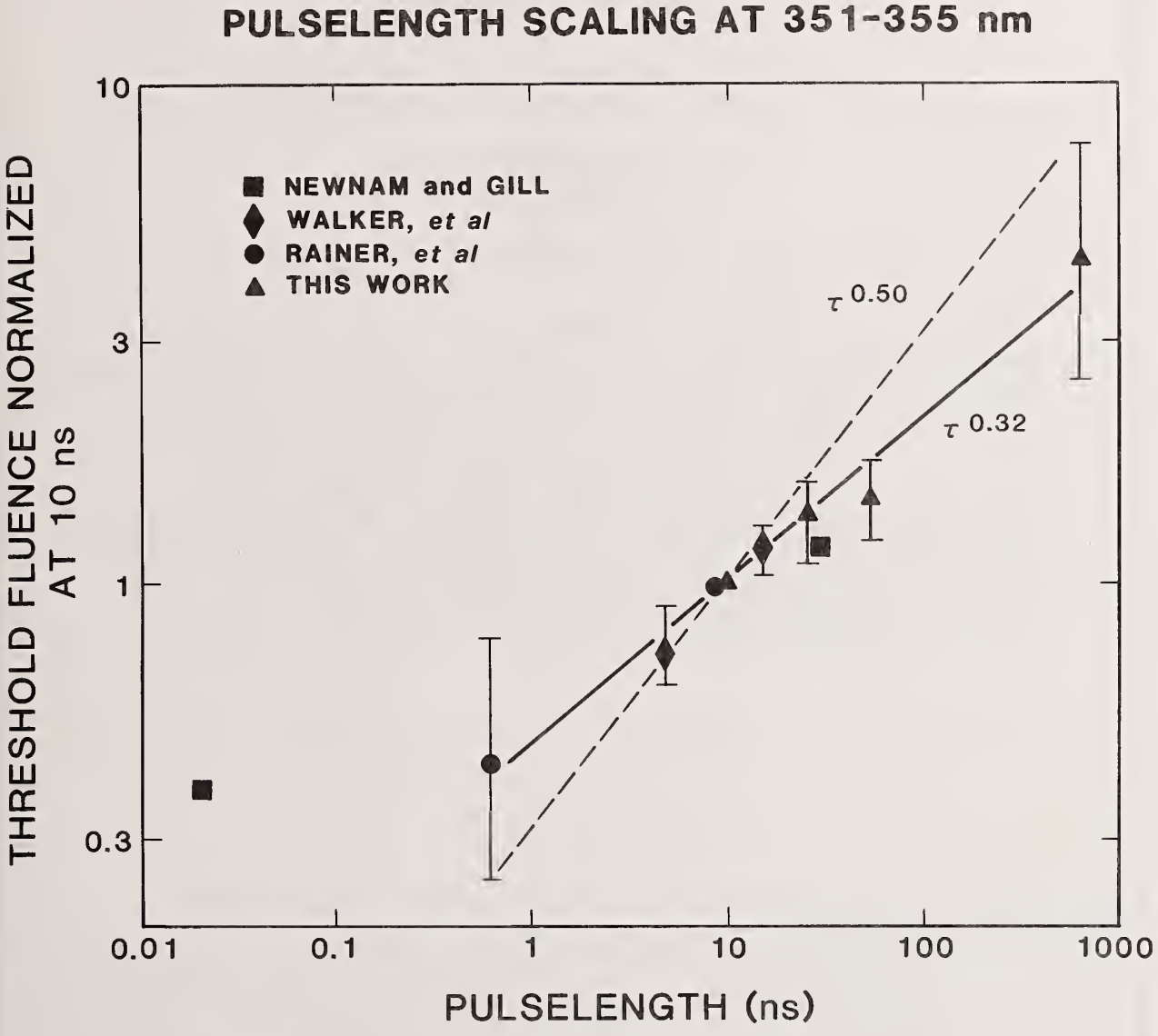

Figure 5. Results of this work plus three other 351- to 355-nm data sets (refs. 2–4). All thresholds are normalized to 10 ns. Symbols represent average scaling for each data set; error bars represent extreme scaling values for each set. Solid line indicates the weighted average scaling for the range 0.6 to 625 ns, which is $\tau^{0.32}$. The dashed line indicates the slope appropriate for square-root scaling.

- Manuscript Not Received -

TIME TO FAILURE IN SINGLE PULSE LASER INDUCED DAMAGE IN THIN FILM OPTICAL COATINGS

J. Boyer
Los Alamos National Laboratory
Los Alamos, NM 87545

ABSTRACT

Measurement of the time between the start of the laser pulse and the disruption of the irradiated surface provides information not available in traditional damage measurements. The importance of the rate of energy input versus the total energy deposited may be studied by varying the pulse energy and measuring the time at which damage is initiated. If the diagnostics are of adequate sensitivity, a damage threshold fluence can be assigned to each damage event and the fluence distribution of the defect population can be measured.

I will discuss the test configuration and diagnostics for both transmitting and reflecting coatings. Preliminary data at 248 nm with a 23 ns pulse length will be presented.

Key Words: defect population; diagnostics; optical coatings; time dependence of damage.

Manuscript Received
6-15-87

THERMAL CONDUCTIVITY OF DIELECTRIC FILMS AND CORRELATION TO DAMAGE THRESHOLD AT 1064nm

S. M. J. Akhtar*, D. Ristau

INSTITUT FÜR QUANTENOPTIK, Universität Hannover
Welfengarten 1, 3000 Hannover, Germany-W.

and

J. Ebert

LASEROPTIK GmbH, 3008 Garbsen 8, Germany-W.

ABSTRACT

An infrared line scanning technique has been used to measure thermal conductivities of TiO2, Ta2O5, ZrO2, HfO2, Al2O3 and SiO2 layers. Damage thresholds are determined using a two stage Nd:Yag laser with pulse length of 14ns and spot size of 300μ. A correlation between thermal conductivity, absorption coefficient, melting point and damage threshold is established. To explain the relation, theoretical models based on absorption and inclusion breakdown are analysed.

Key words: Thermal conductivity ; thin films ; oxide materials ; laser damage

1. INTRODUCTION

Since damage in thin films occurs mainly due to thermal processes it is necessary to investigate thermal properties of dielectric films. We have measured thermal conductivities of Hafnia, Zirconia, Tantala, Alumina, Silica and Titania films and correlated to damage thresholds. For the measurement of absorption coefficients and thermal conductivities,an infrared line scanning laser calorimeter has been developed by Ristau, D etal [1]. Same arrangement has been used for these measurements except one modification. A HgCdTe detector is installed instead of a PbSe detector. Considering damage mechanisms in such films,two theoretical models based on temperature generation due to absorption in film volume [1] and inclusion (Goldenberg and Tranter [2]) were analysed. Using measured values of absorption coefficient α and thermal conductivity K_1, damage thresholds have been calculated and compared with the measured data.

---

* DAAD Fellow from Pakistan Institute of Nuclear Science and Technology, P.O.Nilore, Islamabad, Pakistan and CSSP, Punjab University, Lahore.

2. ABSORPTION AND THERMAL CONDUCTIVITY MEASUREMENTS

Absorption and thermal conductivity were measured by the technique described by Ristau, D. and Ebert, J [3]. Experimental arrangement is depicted in figure 1. A high power cw Nd-Yag laser is focussed(500μ) on to the film sample which is placed inside a vacuum chamber. The incident radiation is absorbed by the film and its temperature rises. The temperature profile is recorded by a thermal imaging system which consists of a gold coated concave mirror, scanning mirror and HgCdTe detector. An AR-coated Ge window is put between detector and scanning mirror to suppress the scattered pump light. The recording system has two channels, one is used for recording temperature profiles by computer and the other one is connected to the lock-in-amplifier. If the lock in amplifier is synchronized to the scanning motion of the temperature recording system, the output voltage is directly related to the temperature in the beam centre of the laser heated sample. Therefore the absorption of the film can be calculated with the aid of a theoretical model that describes the situation and the boundary conditions of the experiment correctly (fig.2). A thin film on a disc-shaped substrate is placed in vacuum and heated by a laser with gaussian intensity profile. The steady state temperature profile for this problem can be calculated by solving the heat transport equation with the appropriate boundary conditions [3]. The result of this calculation is:

$$T(R) = \sum_{m=1}^{\infty} \frac{U(\mu_m R)}{W_1^2 - \mu_m^2} \left[1 + \frac{1}{N}\left\{\frac{h_1 + W_1}{\mu_m + h_1}\left[(K_2 - K_1)A(\mu_m) - (K_1 + K_2)F(\mu_m)\right] + D(\mu_m)\exp(-W_1 Z_1)(1+V_1)\right\}\right] \quad (1)$$

$$N = (K_2 - K_1)(V_1 V_2 e_1^- e_1^- e_2^+ - e_1^+ e_1^+ e_2^-) + (K_1 + K_2)(V_2 e_2^+ - V_1 e_2^-)$$

$$A(\mu_m) = V_2 e_1^- e_1^- e_2^+ + e_1^+ e_1^+ e_2^-$$

$$F(\mu_m) = V_2 e_2^+ + e_2^-$$

$$D(\mu_m) = \left[\frac{K_1 W_1}{\mu_m} + K_2\right] e_1^+ e_2^- + \left[\frac{K_1 W_1}{\mu_m} - K_2\right] e_1^- e_2^+ V_2$$

$$h_j = \frac{H_j}{K_j} \quad ; \quad V_j = \frac{K_j \mu_m - H_j}{K_j \mu_m + H_j} \quad ; \quad e_j^{\pm} = \exp(\pm \mu_m Z_j)$$

$$U(\mu_m) = \frac{\alpha P J_0(\mu_m R)}{\pi K_1 J_0(\mu_m)^2} \exp(-\omega_0^2 \mu_m^2 / 4 a^2)$$

Where P is the incoming laser power and α is the absorption

coefficient of the film. a is the substrate radius, $a*Z_1$ and $a*(Z_1-Z_2)$ are the thicknesses of the film and the substrate meanwhile K_1 and K_2 are the corresponding thermal conductivities. The radiation heat loss at the surfaces is taken into account by the parameters h_1 and h_2 which contain the emissivities of the surfaces and the Stephan Boltzman constant. The eigenvalues μ_m are the positive roots of the equation:

$$J_o'(\mu_m) = 0 \qquad (2)$$

The radial position is denoted by a*R. An ideal thermal contact is assumed at the film substrate interface by stating a continuos heat flux across the boundary. Thus, if the parameters are known the absorption can be calculated from the lock in amplifier output voltage. On the other hand it is possible now to calculate the thermal conductivities from the output voltages for identical films of different thicknesses. The thermal conductivity effects the increase in central temperature as a function of thickness. If the film conductivity is equal to that of the substrate, the temperature rise is proportional to the film thickness. But for a film with different thermal conductivity this increase will also depend on the ratio of K_1 /K_2 . Therefore the film thermal conductivity can be determined by the ratio of lock in amplifier output voltages of samples with similar films of different thicknesses. Neither the heat capacity nor the density of the film is necessary for this method because the case of thermal equilibrum is considered. Besides, the measured temperature profile is not disturbed by the recording system so that the experimental setup corresponds exactly to the situation described by the model.

However in contrast to the aforementioned advantages a number of specific sources of errors have to be considered. Inhomogenity and thickness errors may effect the measurements drastically. This has to be carefully considered during the production of samples and the subsequent analysis of their spectral performance. Therefore it is necessary to prepare several samples of identical films to test the reproducibility of the results. In order to produce films with identical properties, specimens of one material should be produced in one batch. As a consequence of the columnar structure an anisotropy in thermal conductivity might be expected for vapor deposited films. Such a film would presumeably have a higher conductivity in the direction of the columns than perpendicular to the growth orientation. The present model can be extended to take into consideration the anisotropy, with the result, that the temperature in the centre is almost perfectly determined by the component perpendicular to the surface. Therefore the measurements of thermal conductivity were based on the isotropic model. The errors induced by the standing wave field pattern are negligible because the thermal diffusion length is large compared to film thickness and wavelength of the incident light.

In order to measure the thermal conductivities, for each material, three samples of different thicknesses (λ,2λ,3λ) were prepared by e-beam evaporation in a reactive oxygen athmosphere. The film thickness was controlled during evaporation with the aid of an optical monitoring system. After deposition, homogenity of the films was examined by its spectral performance. Considering the errors induced by inhomogenity and experimental setup, the estimated uncertainty is found to be less than 30% for the conductivity values ranging from 5E-5 to 5E-4 W/cm°C.

3. THERMAL CONDUCTIVITY AND CORRELATION TO DAMAGE THRESHOLD

Results of absorption coefficient, film thermal conductivities and damage thresholds for six oxides have been listed in table 1. Comparing bulk and film conductivities, it is obvious that film values are much lower than the bulk ones, especially Hafnia show a very low value which could be due to the crackening in the film. Only the value of Alumina is compareable. In fact the problem of heat transport in films is complicated and could be influenced by columnar structure of most of the films. At the

column bounderies, heat transport is poor and could be a reason for such low values of thermal conductivity. Decker, D. L. [4] explains low values on the basis of phonon mean free path which is limited by scattering from other phonons, lattice bounderies and imperfections, resulting in poor conductivity. If anisotropy in thermal conductivity is taken into account, the perpendicular component should be higher than the parallel due to the columnar structure. Amorphous films of Alumina and Silica show relatively compareable values.

Table 1. Thermal parameters and damage threshold of oxide layers

Material	K(bulk) (W/cm°C)	K(film) (W/cm°C)	Abs.Coeff α(1/cm)	Melting Point (°C)	Damage Threshold (J/cm²) Calc.	Measured
HfO_2	1.7E-1	7.7E-6	0.3	2758	40	41 ± 3
Al_2O_3	2.7E-1	3.3E-1	2.3	2072	38	39 ± 1
ZrO_2	1.1E-1	1.4E-4	2.0	2700	36	34 ± 1
SiO_2	1.4E-2	1.0E-3	0.1	1723	35	34 ± 7
Ta_2O_5	---	2.6E-4	2.4	1918	27	28 ± 2
TiO_2	9.7E-2	1.8E-4	5.9	1775	15	13 ± 1

At a glance no correlation exists between thermal conductivity and damage threshold. In fact melting points of these oxides should be taken into consideration which contribute mainly in forming a correlation. A best fit has been obtained by the following formulation.

$$E_D \propto M_p * K_1^{0.04} / \alpha^{0.1} \qquad (3)$$

It is apparent from the formula that absorption coefficient and thermal conductivity have a very minor contribution but they cannot be neglected. Melting point has the main influence. HfO_2 has the highest melting point and exhibit the highest damage threshold. By the above formulation, the calculated values of damage threshold are found to be compareable with the measured data.

4. BREAKDOWN MECHANISMS

Generally, damage in thin films is recognised by two break down mechanisms : absorption by the film volume or by the impurities present in the film. In the first case, incident laser energy is absorbed in the film volume and its temperature rises, leading to a break down in the film. A theoretical expression has been derived by Ristau, D etal [1] for the temperature rise at the film surface due to volume absorption. The final expression is an approximation for the short laser pulses and is given by:

$$T(r,0,t) = F \int_0^t dt \, [\exp(r^2/p(t))\{(1+R1)I(d,0)+R2I(2d,d)\}] \qquad (4)$$

$$\text{where} \quad I(a,b) = \int_{b/2\sqrt{kt}}^{a/2\sqrt{kt}} dv \, \exp(-v^2) \quad ; \quad p(t) = 4kt + 2s^2$$

$F = 2\alpha Ios^2 / \Pi \rho c$; Io is incoming intensity, d is the film

thickness, α is absorption coefficient, s is the beam radius, R1 & R2 are the thermal reflection coefficients, c is heat capicity, ρ is the density and k is thermal diffusivity of the film material.

In the theoretical model for impurity dominated damage, it has been supposed that the absorbing particles in the host material are spherical in shape. Hopper and Ulhman [5] have solved the heat transport equations to calculate the temperature in host material,considering metallic impurities of spherical shape. In practice, inclusions in evaporated films are of dielectric in nature and have lower thermal diffusivities than the metallic impurities. Thermal equations for such a case have been developed by Walker, T. W [6]. Solution to these equations is given by Goldenberg & Tranter [2] in which temperature rise in a spherical impurity of radius a has been calculated and is given by:

$$T = 3QI/4K_p\, a * \{ K_p /3K_h + (1-r^2/a^2)/6 - 2ab/r\Pi \int_0^\infty dY$$

$$.\exp(-Y^2tp/\tau_1 * \frac{(\sin Y - Y\cos Y)\, \sin(rY/a)}{Y^2[(c\sin Y - Y\cos Y)^2 + b^2Y^2\sin^2 Y]} \} \qquad (5)$$

where $\tau_1 = a^2/Dp$; $c = 1-(K_h / K_p)$
$b = (K_h / K_p)\ \sqrt{D_p/D_h}$
Q--absorption cross-section and can be calculated by Mie scattering theory.
K_h--thermal conductivity of the host material
K_p--thermal conductivity of the impurity
a --impurity radius
r --radial distance from the impurity boundary
I --incident laser intensity
D_h--thermal diffusivity of host material
D_p--thermal diffusivity of impurity
tp--Laser pulse width

Using the measured values of absorption coefficient and thermal conductivity for the six oxides, temperature rise in the film volume has been calculated by equation 4 and listed in table 2. Similarly, considering T to be the melting temperature in equation 5, damage thresholds have been calculated and listed in table 2.

Table 2. shows calculated values of temperature rise in oxide films(Eq.4), damage thresholds by inclusion model(Eq.5), measured α & E_D.

MATERIAL	ABSORPTION COEFFICIENT α (1/cm)	TEMP.RISE IN FILM T(°C)	DAMAGE THRESHOLD (J/cm²) EXP	CAL(SPHERE)
HfO_2	0.3	207	41	36
Al_2O_3	2.3	3980	39	1955
ZrO_2	2.0	217	34	43
SiO_2	0.1	25	34	29
Ta_2O_5	2.4	86	28	29
TiO_2	5.9	745	12	32

Considering calculated and measured values of damage thresholds it can be realised that the values for Al_2O_3 and T_iO_2 are not comparable. This means that both materials are not damaged by inclusion but by absorption. This is also verified by very high values of temperature rise i.e 3980°C and 745°C respectively. This indicates that incident energy

produces high temperatures at the film surface which lead to breakdown. The other four materials are damaged by inclusion. Measured and calculated values are fairly comparable.

5. CONCLUSIONS

A study on single layer dielectric films of various oxides have been performed. Thermal and optical properties were measured. Following conclusions are deduced from the results:

1. Thermal conductivities of films of six oxides are found to be much lower than the bulk material.
2. A correlation between thermal conductivity, absorption coefficient, melting point and damage threshold is established.
3. Calculated values of temperature rise in Al_2O_3 and TiO_2 films show a tendecy of damage due to absorption. Other four oxides are likely to be damaged by inclusions.

REFERENCES

[1] Ristau, D. ; Dang, X. C. and Ebert, J. ; Laser induced damage in optical materials. Nat. Bur. Stand. (U.S) Spec. Ppubl. 727; 1984. 298p.

[2] Goldenberg, H. and Tranter, M. A. ; Heat flow in an infinite medium heated by a sphere; Brit. J. Appl. Phys. ; 1952. 296p.

[3] Ristau, D. and Ebert, J. ; Development of a thermographic laser calorimeter; Appl. Opt. ; Vol. 25, No. 24 ; 1986. 4571p.

[4] Decker, D. L. ; Koshigoe, L. G. and Ashley, E. J. ; Laser induced damage to optical materials. Nat. Bur. Stand. (U.S) Spec. Publ. 727; 1984. 291p.

[5] Hopper, R. W. and Ulhmann, D. R. ; Mechanism of inclusion damage in laser glass ; Appl. Phys. 41, No.10 ; 1970. 4023p.

[6] Walker, T. W. ; Guenther, A. R. and Nielsen, P. ; Pulsed laser induced damage to thin film optical coatings ; IEEE. J. Quantum Electronics ; vol. QE-17. No.10 ; 1981. 2053p.

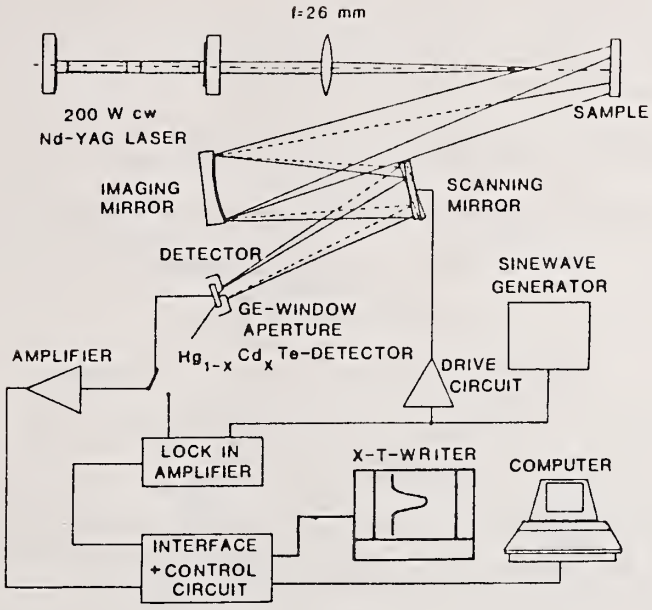

Figure 1 Experimental set up for thermographic laser calorimeter

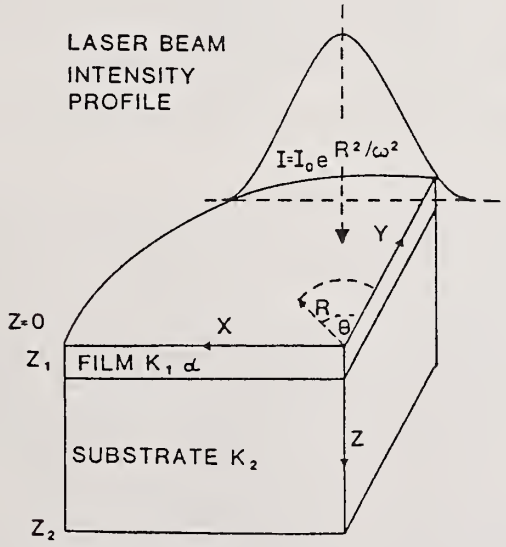

Figure 2 Beam profile at film sample: I, peak intensity; I(R), beam intensity at R; R=1, substrate radius; Z=0, film surface; $Z=Z_1$, substrate-film interface; $Z=Z_2$, substrate back plane.

Manuscript Received
8-7-87

Correlation of Damage Levels at 1.06μm Varying Modal Content and Irradiance History on Representative Coated Laser Optics

Jonathan W. Arenberg, Mark E. Frink, David W. Mordaunt and Gordon Lee

Hughes Aircraft Company
P.O. Box 902
El Segundo, CA 90245

Steven C. Seitel, Edward A. Teppo

Montana Laser Optics*
P.O. Box 4151
Bozeman, MT 59772

This paper reports on efforts to correlate two commercially oriented laser damage tests. The two test facilities are located at Hughes Aircraft Company and Montana Laser Optics*.

A variety of coated laser optics have been tested under different test conditions and the damage levels compared. The test parameters varied were transverse modal content, spot size, sample conditioning history and, to a lesser degree, pulsewidth. The accumulated results were correlated by ascertaining the existence of a high probability functional relationship (linear fit) between pairs of damage levels for the same optics under different test conditions. A strong correlation was found between samples tested with the same irradiance history, regardless of the modal content and pulsewidth. Comparison of the samples of different irradiance conditioning history were found not to correlate in general.

Key Words: conditioning; correlation; preconditioning correlation procedure; production laser damage tests

This paper discusses the methodology and results from a cooperative study of laser damage test correlations carried out between Hughes Aircraft Company (HAC) and Montana Laser Optics* (MLO*). Both laboratories have experience in the field of damage testing optics as a screen in the production of lasers.

The reasons for seeking a test correlation are several fold. The first is historical interest in the ability of various labs to reach similar conclusions on the laser damage resistance of optics [1]. This study represents an extension of previous correlation efforts using the same exact samples rather than nominally identical samples. Secondly, comparison of the two tests originally involved in the correlation effort allowed for the isolation of salient factors in considering any optimization of the damage test. Thirdly, a well defined correlation method is a necessary step in the definition and implementation of a standardizable test. Finally, from the point of view of a laser manufacturer, correlation among test labs allows for the use of damage measurements made at one lab to be compared to another for the purposes of vendor development, qualification and support.

A correlation is defined as a functional relationship between sets of data. In this usage, a function is defined in the sense of being a single valued relationship of one set of data to another. The correlation may be quantified by three numbers. First is the correlation coefficient, r^2. The second is a measure of the likelihood that the correlation value (r) is due to chance, and is quantified by P(N,r). The relative uncertainty, expressed in percent, of the parameters of the fit is the third figure of merit.

The correlation coefficient, r^2, is well known to anyone who has performed a regression. r^2 is a measure of the reciprocity of the choice of independent or dependent variables. r^2 varies from 0 to 1, with unity indicating a perfect correlation. P(N,r) is the probability that N random data points will yield a correlation coefficient of r or greater. [2] P(N,r) is given as,

$$P(N,r)=\left(\frac{2}{\sqrt{\pi}}\right)\int_{|r|}^{1}\frac{\Gamma(\nu+1)}{\Gamma(\nu+2)}(1-\rho^2)^{(\nu-2)/2}\,d\rho \qquad (1)$$

where ν=N-2. A parameterized plot of P(N,r) is given in figure 1 for various values of r and N. The value of P(N,r) varies from 0 to 1. The value zero indicates that there is no chance that an uncorrelated sample could give a value of |r| or greater. Further, all correlations of two points have a P(2,r) of 1. Since one can always draw a line between any two points, and this line has an |r| value of 1, the chance of any two uncorrelated points yielding an r value of less than 1 is zero. Therefore, the probability that two points have an r value of 1 is always unity. The relative uncertainties of the various parameters used in the formation of the functional relationship also indicate the quality and usefulness of the correlation. The more uncertain the parameters, the lower the quality of the usefulness of the fit. So in sum, the better the fit the higher the value of r^2, the lower the value of P(N,r) and the smaller the relative uncertainty of the parameters of the fit.

For the initial purposes of this study the two parameters being compared are the standard production damage tests, as performed routinely by both laboratories. In the case of the Hughes test, it is a conditioned average type test that is explained in detail elsewhere in these proceedings [3]. Conditioning is defined as the increase in damage level due to exposure to sub-lethal fluences. The MLO* test is closer to an archetypal test, being an unconditioned threshold determination [4]. Typical values for the test parameters are given in figure 2. It should be noted that the MLO* test interrogates more surface area and should be expected to yield lower results due to spot size effects [5].

The functional relationship chosen to match the two data sets being correlated is linear. The reasons for the choice are several fold. The first is an appeal to intuition. If the two measurements are actually measuring the same thing, the results should differ at most by a multiplicative constant. This multiplicative factor is introduced by calibration and measurement differences. Furthermore, a linear function is easy to remember and the computer routines are well defined and available. Finally, initial trials with higher order fits yielded unphysical results, mainly multivalued relationships upon interchange of dependent and independent variables.

It was desired to weight the regression so that well defined points, i.e., those with small error bars, were treated "with more respect" compared to less well defined points. This method used for treating uncertainty in regression calculations is given by Bevington [6]. Since both the dependent and independent variables have associated uncertainties, the uncertainty of a pair, σ_p, was assigned to the dependent variable via,

$$\sigma_p^2 = y^2\left(\frac{\sigma_x^2}{x}+\frac{\sigma_y^2}{y}\right) \qquad (2)$$

The use of the percent uncertainty, σ_x/x or σ_y/y, removes the need for common units between x and y. The size of the multiplicative constant relative to the units of x and y does not alter the existence or quality of the correlation.

Figure 3 represents the first attempt to correlate the damage data from the two laboratories. The data points on this and all subsequent graphs, plots the damage value of one test versus another test made on the same part on the same side of the optic under test. Figure 3 represents a very poor correlation or what may be called a discorrelation. There is a very low correlation coefficient $r^2 = 0.03$ and there is a high likelihood that this correlation is due to random chance, $P(13,0.18) \geq 0.47$. Next, an attempt to correlate the (HAC) lowest observed conditioned point damage and the (MLO*) unconditioned threshold was made. This correlation was posited to be stronger since both measurements were of the weakest sites. The results are shown in figure 4. The correlation of weakest sites is, however, not a good one even though it has an increased r^2 and decreased P(N,r) relative to the previous correlation. Indeed, even the sign of the slope relating the HAC and MLO* damage levels is of the wrong sign, a major counter intuitive flaw.

At this point, it should be reiterated that the two attempts at correlation shown above involve conditioned and unconditioned tests. Further experiments, attempting to correlate conditioned and unconditioned damage tests were performed on the HAC lasers LARRY and MOE. Since LARRY and MOE have the same spot size, these experiments removed spot size effects as the possible cause of the lack of correlation. The results were the same, discorrelation.

The major difference between the two tests that could affect the existence of the correlation is conditioning. The spot size effects are related to the total area interrogated in a monotonic fashion. The spot size effects are predicted to change the magnitude of the damage test results. The ordering of samples in terms of their thresholds is expected to remain the same regardless of spot size. Thus it is concluded that there is no useful one-to-one correlation among conditioned and unconditioned damage tests. Therefore, it was decided to correlate tests of similar irradiance history.

The initial attempt to correlate damage tests of similar irradiance history antedates the present study and was done between the HAC test lasers LARRY and MOE. The results are displayed in figure 5. The axes in figure 5 are in dB from reference, dBR, the damage levels are assigned by the ratio of failure level of the test part to the failure level of a coated reference optic. The r^2 value is 0.82, and P(41,0.9) is very much less than 0.01, indicative of a good correlation. Thus, it is seen that two damage tests of similar irradiance history are correlatable.

Using this historical data as a precedent, an attempt was made to correlate conditioned tests of various transverse modal contents at MLO* to the test measurements made at HAC. About 25 parts having about an order of magnitude difference in conditioned laser damage threshold were selected to be tested at MLO* and HAC on test laser MOE. All of the parts were tested at MLO* for conditioned average damage level using a TEM_{00} beam and a multimode beam. These same parts were tested at HAC following the same irradiation procedure using a multi transverse mode beam.

There are three correlations possible, namely MLO* TEM_{00} versus MOE, MLO* Multimode versus MOE and MLO* TEM_{00} versus MLO* Multimode. These combinations establish the effect of transverse modal content on the existence and quality of the correlation. The three possible correlations were analyzed using both the weighted and unweighted regression options. The scatter plots are shown in higher value of r^2. All of the correlations are of good quality with an r^2 value of 0.758 for the MLO* TEM_{00} vs MOE correlation, $r^2 > 0.95$ for the MLO* Multimode vs MOE and an r^2 value of 0.958 for with the MLO* TEM_{00} vs. MLO Multimode The P(N,r) in all cases much less than 0.01. Thus, given common irradiance history, it may be concluded that the transverse modal content affects the quality of the correlation but not the existence of a correlation.

Finally, a similar set of experiments was performed in attempting to correlate the unconditioned thresholds as measured at the two labs. The transverse modal content was fixed at MLO* allowing for only unconditioned single mode tests to be made at MLO*. These parts were tested at HAC on both LARRY and MOE, following the same binary search used at MLO* to determine the lowest damaging fluence in an unconditioned damage test. The identification of the lowest damaging fluence took about 20 exposures at each lab. This was a substantial increase in the area interrogated over the conditioned test (about a factor of 4-5), and should give a more certain estimation of the threshold fluence. The correlation scatter plots are shown in figures 9 and 10 and show good correlations in both the weighted and unweighted cases with the unweighted regressions resulting in higher r^2 values. This is probably due to a smaller sample size than in the conditioned correlation cases, about 15 for the unconditioned and about 23 samples for the conditioned test. Again the tests of similar irradiance history are found to correlate.

So, in conclusion it has been shown that similar irradiance histories are required to correlate damage tests. The transverse modal content of the test beam affects the quality of the correlation but not its essential existence in the cure of similar conditioning histories. Thus, with proper knowledge of two test procedures, correlations between test labs performing a similar test may be established using the present work as a paradigm.

References

[1] Guenther, K. G., et al, "1.06 Micron Laser Damage of Thin Film Optical Coatings - a Round Robin Experiment Involving Various Pulse lengths and Beam Diameters"; Laser Induced Damage in Optical Materials: 1983 " H. E. Bennett, A. H. Guenther, D. Milam and B. E. Newnam, Editors, Nat. Bur. Stand. (U.S.) Spec. Publ. 688; 1983.

[2] Bevington, P. R., Data Reduction and Error Analysis for the Physical Sciences, McGraw-Hill, 1969. Chapter 7.

[3] Mordaunt, D. W., Arenberg, J. W. and Frink, M. E., "Production Oriented Laser Damage Testing at Hughes Aircraft Company", These Proceedings.

[4] S. C. Seitel, "Planning A Laser Damage Test", Photonics Spectra, August 1985, p84.

[5] L. G. DeShazer, B. E. Newnam and K. M. Leung, "The Role of Coating Defects in Laser Induces Damage to Thin Films", "Laser Induced Damage in Optical Materials: 1973", A.J. Glass and A. H. Guenther, editors, Nat. Bur. Stand. Spec. Publ. 387, 1973.

[6] Bevington, op. cit., Chapter 6.

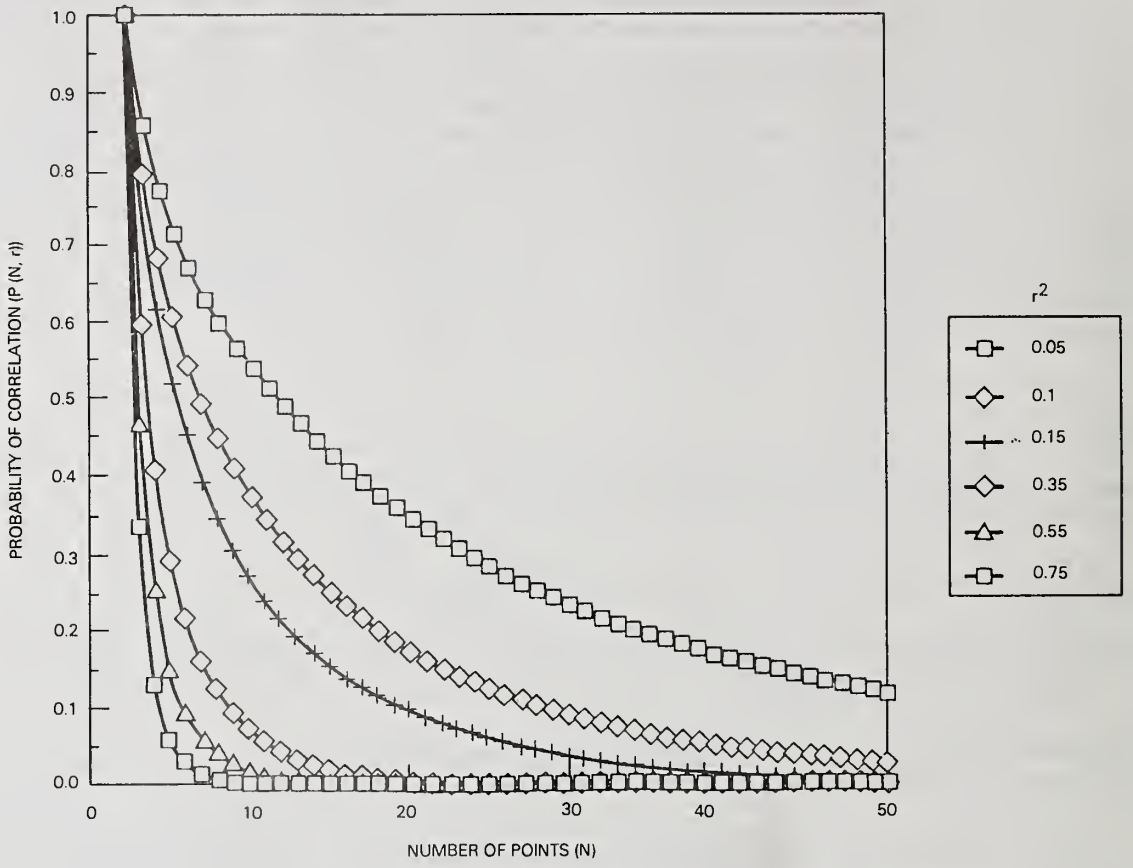

Figure 1. Parametric plot of P (N, r).

TEST PARAMETER \ TEST LAB	HAC	MLO*	
WAVELENGTH (NM)	1064	1064	
PRF (Hz)	10	10	
PULSEWIDTH (NS)	20 ± 4	11 ± 1	40 ± 4
TRANSVERSE MODAL CONTENT	MULTI	TEMoo	MULTI
SPOT SIZE (FW $1/e^2$)	180 μm	500 μm	μm
TEST PROCEDURE	CONDITIONED AVERAGE	UNCONDITIONED THRESHOLD (LOW PT)	
TYPICAL AREA OF INTERROGATION	1.3×10^{-3} CM^2	53×10^{-3} CM^2	
LASER NAME	LARRY, MOE	MLO* SM	MLO* MM

Figure 2. Typical test parameters.

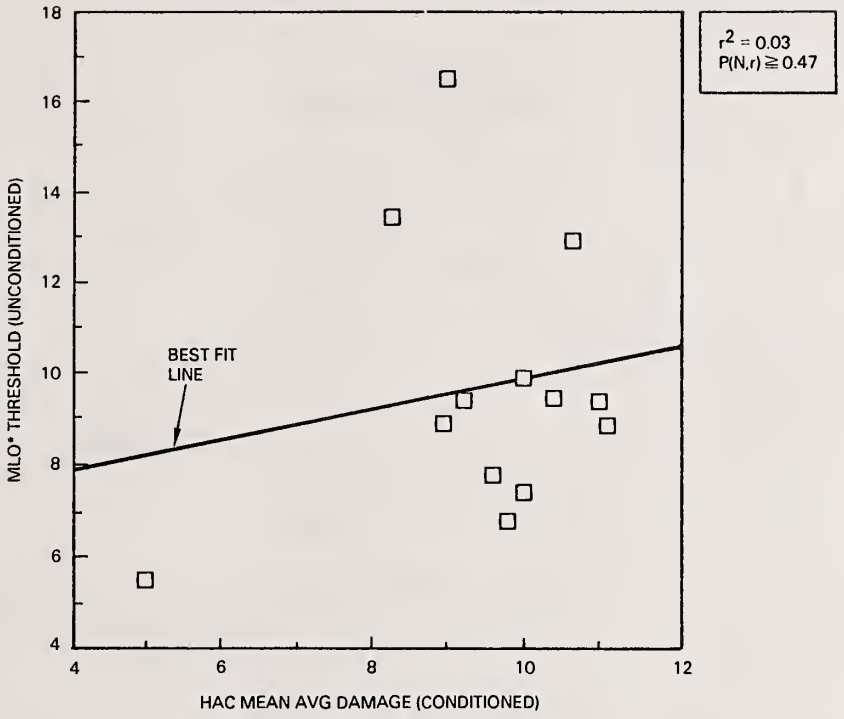

Figure 3. Conditioned-unconditioned correlation.

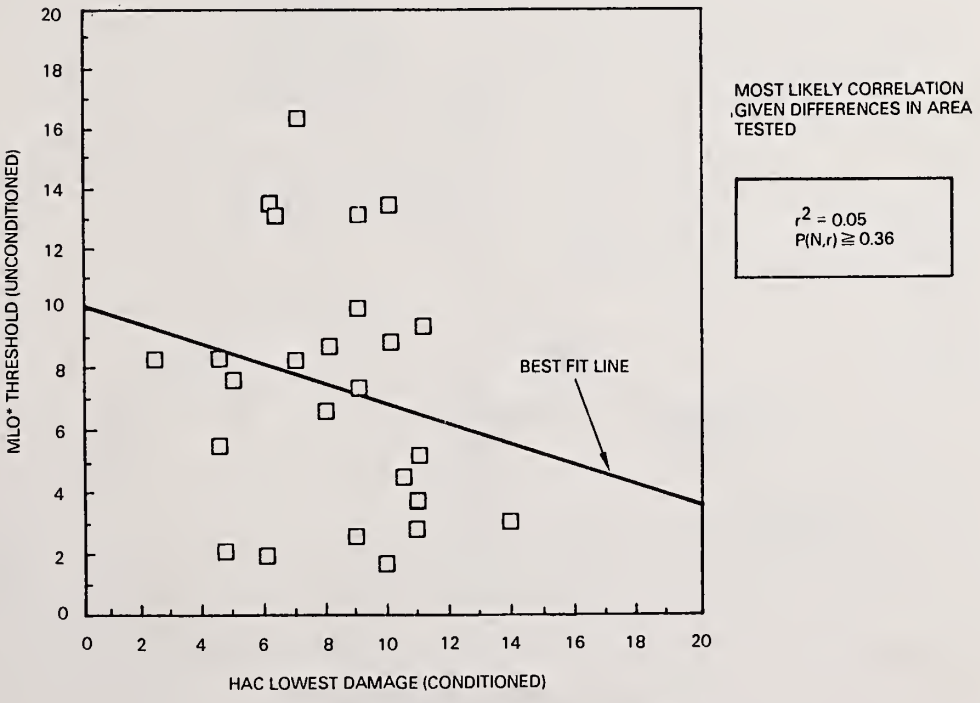

Figure 4. Conditioned-unconditioned correlation.

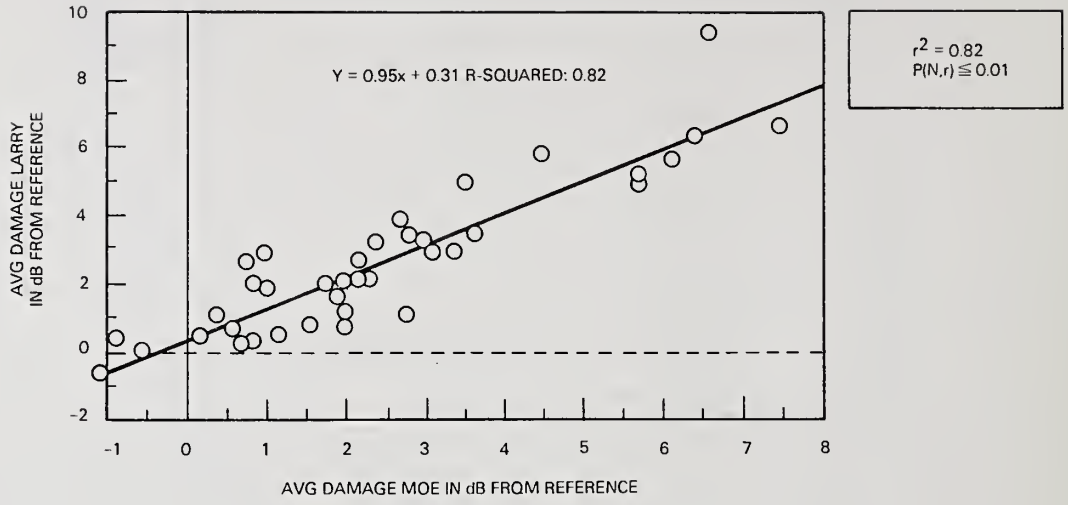

Figure 5. Conditioned correlation.

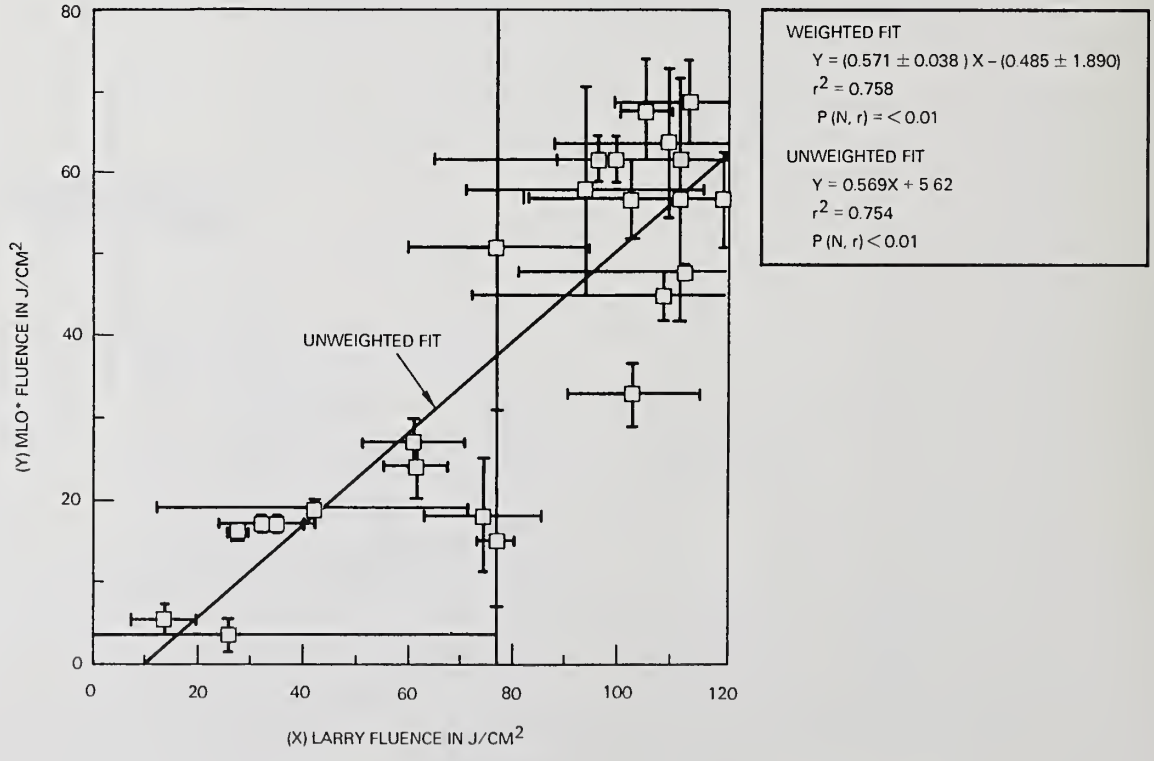

Figure 6. Conditioned correlations.

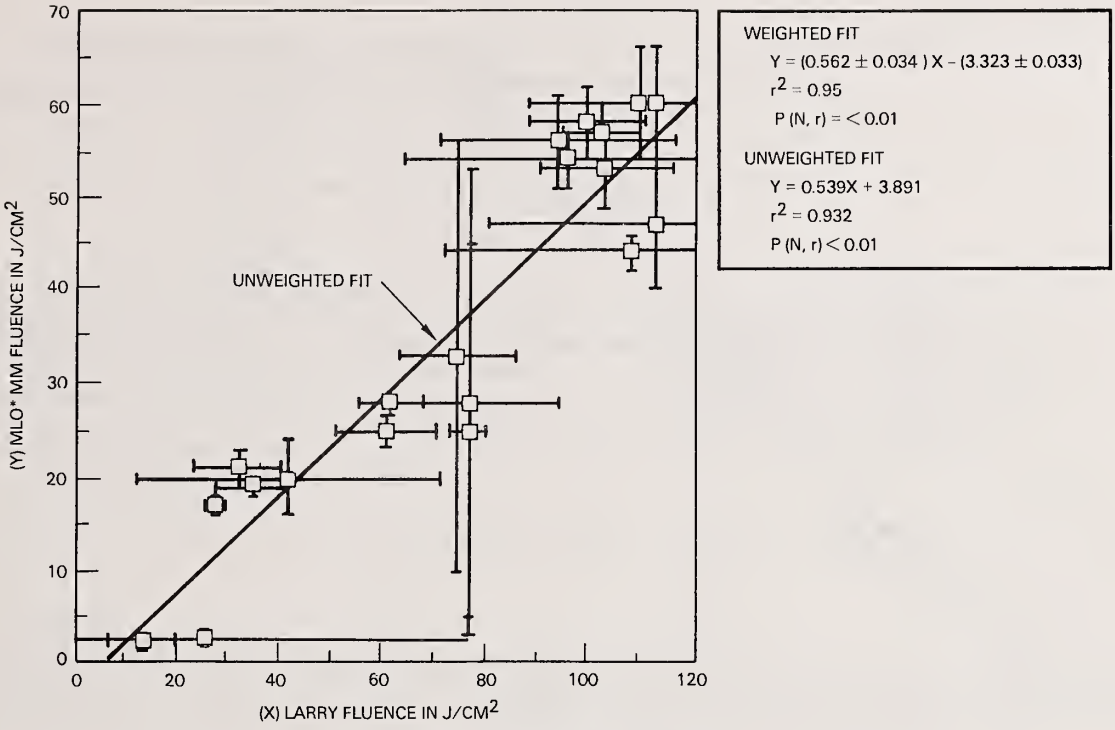

Figure 7. Conditioned correlation.

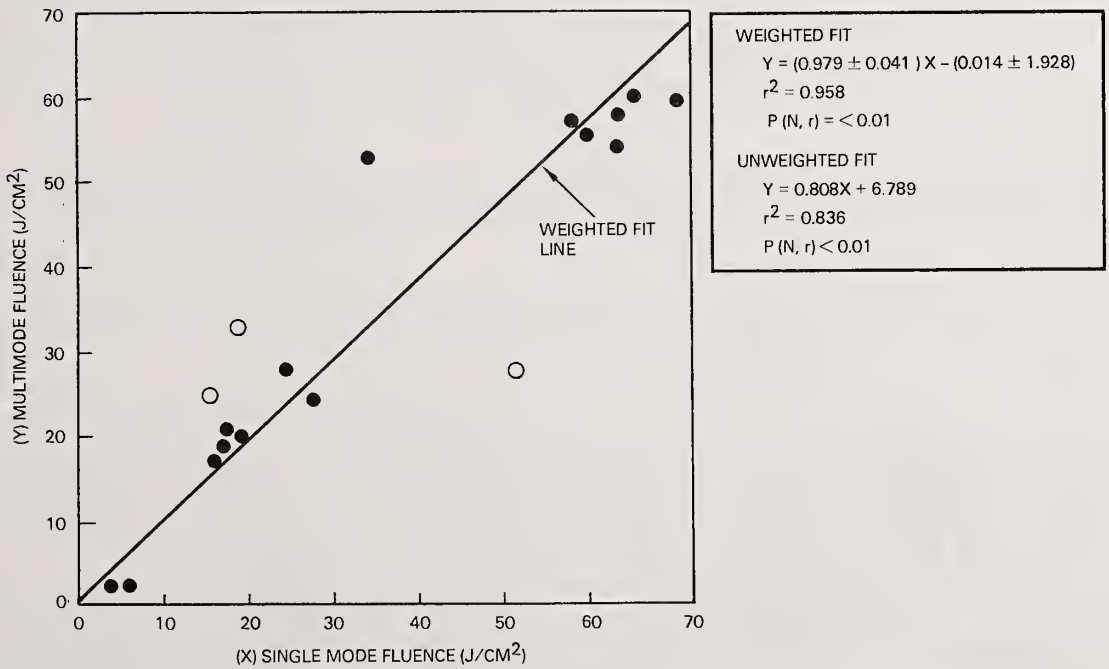

Figure 8. Conditioned correlation.

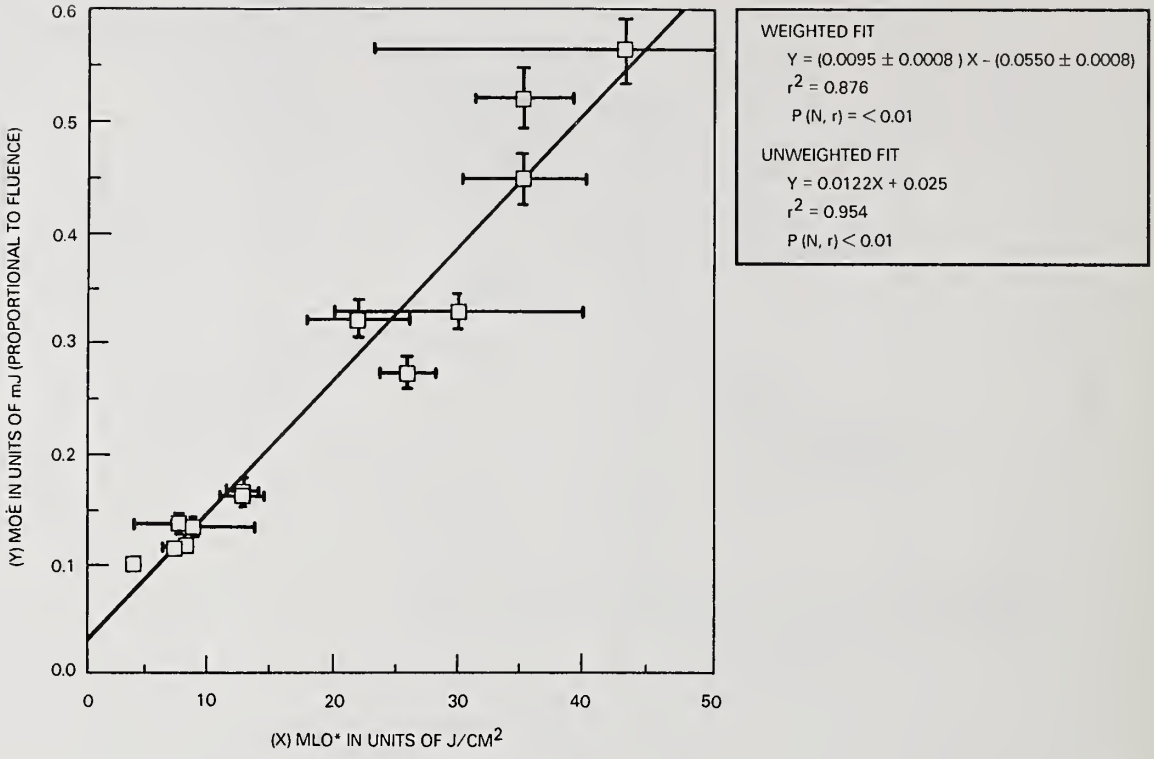

Figure 9. Unconditioned correlation.

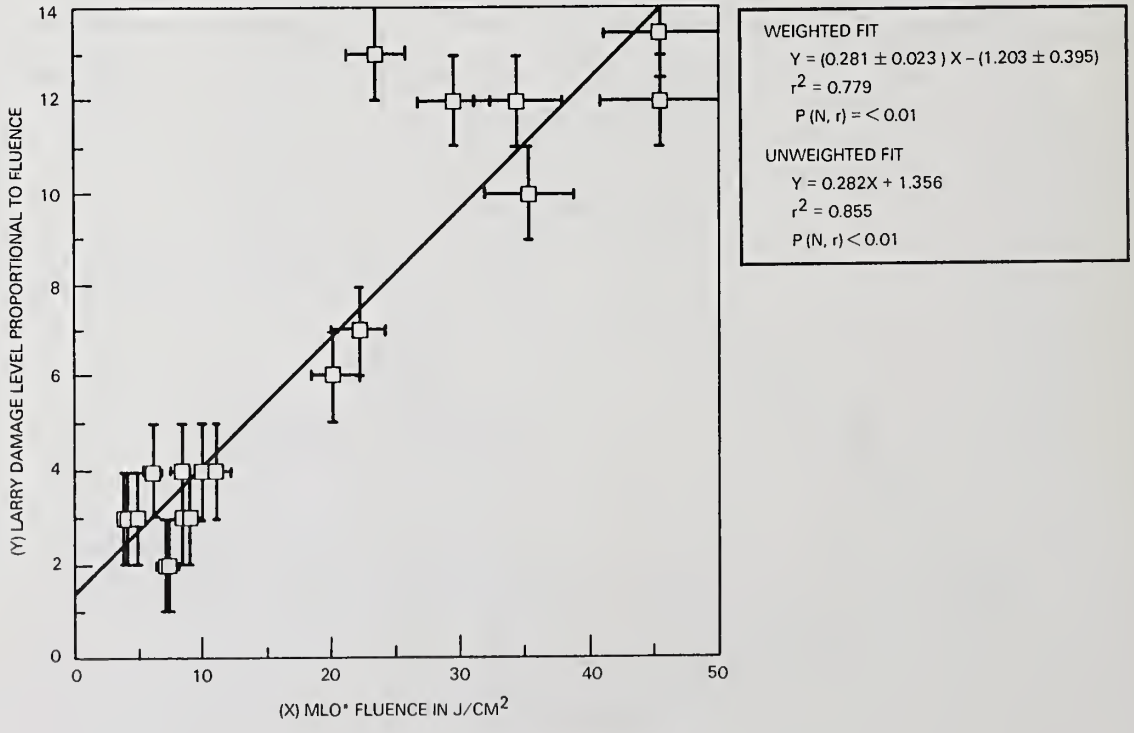

Figure 10. Unconditioned correlation.

Manuscript Received
7-9-87

1064 nm and 350 nm Laser Damage Thresholds of High Index Oxide Films Deposited from Organic Solutions and Sols*

I. Thomas, J. Wilder, R. Gonzales and D. George

Lawrence Livermore National Laboratory
P. O. Box 5508
Livermore, California 94550

High index optical coatings of the oxides TiO_2, Ta_2O_5, ZrO_2 and HfO_2 have been prepared from solutions of metal organic precursors and from colloidal oxide suspensions. Room temperature processing gives porous coatings of comparatively low refractive index (1.8-1.9). Heat treatments can, in some cases, increase the index. Laser damage threshold levels at 1064 nm with a single 1 ns pulse are in the range 6-10 J/cm^2, which is comparable with coatings of the same materials produced by electron beam evaporation. Lower figures are obtained at 350 nm with a 25 ns pulse under multishot (25 Hz) conditions.

Key words: Laser damage, TiO_2, Ta_2O_5, ZrO_2, HfO_2, HR coatings, sol gel.

1. Introduction

The preparation of high index optical coatings of oxide materials by a sol-gel process was first reported by Schroeder in 1959.[1] These were of titania and prepared by the application of a solution of a titanium alkoxide to a suitable substrate followed by air exposure and heat. The initial use was for heat control in architectural windows and was commercialized.

Later, in the USSR, an extensive effort was made on the preparation of a number of oxide coatings specifically for application in high power laser systems.[2-3] This was the first work in which high damage resistance was reported.[4] Several other non-laser applications have more recently been reported, one of particular significance being the use of TiO_2 and Ta_2O_5 as AR coatings for silicon solar cells. Multicoated systems consisting of high-low index stacks have also been investigated. AR coatings of TiO_2 and SiO_2 were prepared and commercialized by Schott Glass in 1959.[1] The investigators in the USSR also reported the preparation of HR mirrors and polarizers for laser systems and high damage thresholds were measured. A more detailed summary of all this work is reported in the brief review by Thomas.[5]

At LLNL high damage threshold coatings are of particular interest and our earlier success with sol-gel coatings has prompted us to further investigate sol-gel systems for high index coatings. There are two general methods for the preparation of optical coatings by the sol-gel process:

(a) Application of a precursor solution to a substrate with subsequent conversion of the precursor to an oxide on the substrate surface.

(b) Application of a colloidal suspension of an oxide to a substrate with only evaporation of the suspending medium required.

Most of the prior art describes coatings prepared by the first method. This method has both advantages and disadvantages. The application of the oxide precursor, for example a reactive metal organic compound, to a surface followed by conversion to oxide requires the removal of fairly large quantities of organic residues. This removal can cause shrinkage and stress in the coating and is not alleviated by the heat treatment that is normally required for complete conversion. It is therefore particularly difficult to prepare thick coatings in one step and better to apply a number of thin coatings with processing between applications. This stress and shrinkage problem becomes worse with multicoat systems. However, hard, dense coatings can be obtained if a heat treatment to 400-500° is applied.

---

*Work performed under the auspices of the U.S. Department of Energy by Lawrence Livermore National Laboratory under Contract No. W-7405-ENG-48.

The colloidal oxide method has been used much less frequently and has only been reported in optical applications for AR SiO_2 [6] and AR Al_2O_3 [7] coatings. It also has its advantages and disadvantages. The conversion of a suitable oxide precursor is completed prior to the application to a substrate and only the evaporation of the suspending medium is required. This leaves a substantially stress-free coating which normally requires little or no heat treatment after application. The coatings are porous and, have low index due to their microscopic porosity. They are also relatively easily abraded because only the point contact force between particles keeps the coating intact.

We have found that the laser damage thresholds of coatings we prepared by the colloidal method are higher than those prepared from solution. This result may be due to the difficulty in completely removing unwanted and potentially damaging organic residues from the oxide during the conversion process. We therefore prefer this method but have investigated both methods primarily because it has been difficult to prepare suitable coating suspensions of certain of the oxides.

2. Coating Preparation

We prepared four high index oxide coatings and made two types of laser damage measurements on them. TiO_2 and Ta_2O_5 coatings were investigated for damage at 1064 nm with a single pulse of 1 ns duration. Ta_2O_5, ZrO_2 and HfO_2 coatings were investigated for damage at 350 nm with multishots of pulse duration 25 ns at 25 Hz, 1000 shots normally being applied.

The typical reagents used as sol-gel precursors are metal alkoxides, chlorides or chloroalkoxides. We used all three types, depending on the metal. The equations below illustrate the reactions involved in the conversion of the different precursors to oxides:

1. $Ti(OC_3H_7)_4 + 2H_2O \rightarrow TiO_2 + 4C_3H_7OH$
2. $2TaCl_3(OC_2H_5)_2 + 5H_2O \rightarrow Ta_2O_5 + 4C_2H_5OH + 6HCl$
3. $ZrOCl_2 + H_2O \rightarrow ZrO_2 + 2HCl$
4. $HfOCl_2 + H_2O \rightarrow HfO_2 + 2HCl.$

We used the solution process for Ta_2O_5, ZrO_2 and HfO_2. This process involved the application of an alcohol solution of the precursor materials, shown above, to a substrate by spin or dip followed by atmospheric exposure to initiate hydrolysis from atmospheric moisture. Subsequent treatment involved exposure to ammonia to remove chlorine and finally heat to evaporate residues and compact the coating. In all cases there was considerable difference due to shrinkage between the initial film applied at room temperature, and the final, treated film.

In the colloidal method, which was only used for TiO_2, an alkoxide was hydrolysed in a large excess of water giving a precipitate of hydrated titania. This precipitate was then resuspended in the water by the addition of a small amount of organic base. Ultimately a colloidal suspension of crystalline anatase, approximately 20 nm in size, was obtained. After application of this suspension to a substrate, a thin layer of anatase resulted after evaporation of the water. The base stabilizer normally remains after a room temperature dry but can be removed with mild heat (50°C). There is little or no change in the TiO_2 film even after heat treatment to 500°C.

3. Damage Thresholds

The damage thresholds of TiO_2 and Ta_2O_5 coatings at 1064 nm are shown in Figs. 1 and 2. TiO_2 ranges from 3-13 J/cm^2 with an average of 7.2 J/cm^2 and Ta_2O_5 from 2-10 J/cm^2 with an average of 6.4 J/cm^2. Both of these are porous coatings of comparatively low index, about 1.8. These damage thresholds are about the same as those obtained for evaporated coatings of the same oxides.

There was a wide variation in the damage thresholds of Ta_2O_5, ZrO_2 and HfO_2 at 350 nm. The results for ZrO_2 and HfO_2 are shown in Figs. 3 and 4. Ta_2O_5 thresholds were very low, about 1 J/cm^2, and are not shown. With both ZrO_2 and HfO_2, the final processing temperatures were 100-150°C. There was definite evidence that further heating, to 300°C or higher, caused a reduction in the damage thresholds. This result is possibly due to carbonization of trace quantities of organic residues left in the coatings from the solvent leading to absorption.

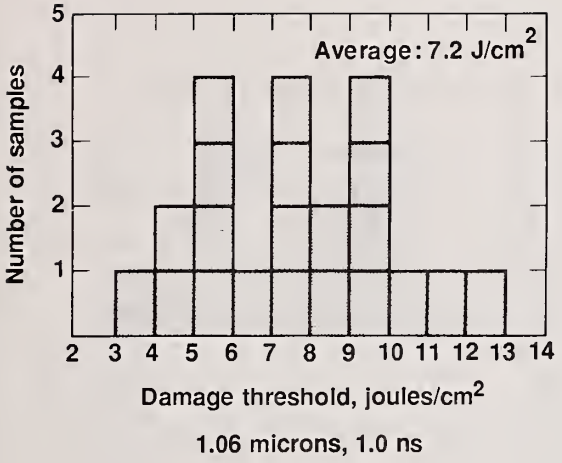

Figure 1. Damage thresholds of TiO_2 coatings from sols.

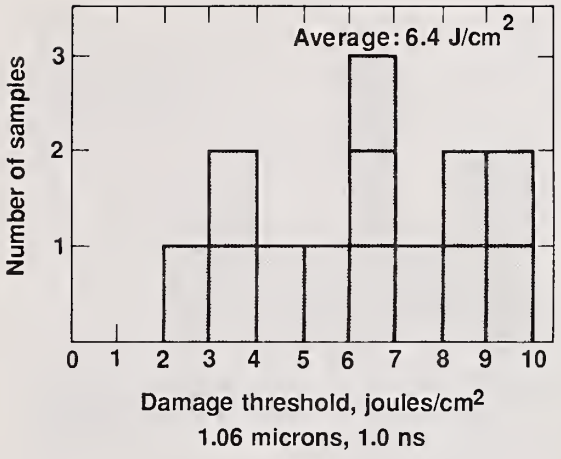

Figure 2. Damage thresholds of Ta_2O_5 coatings.

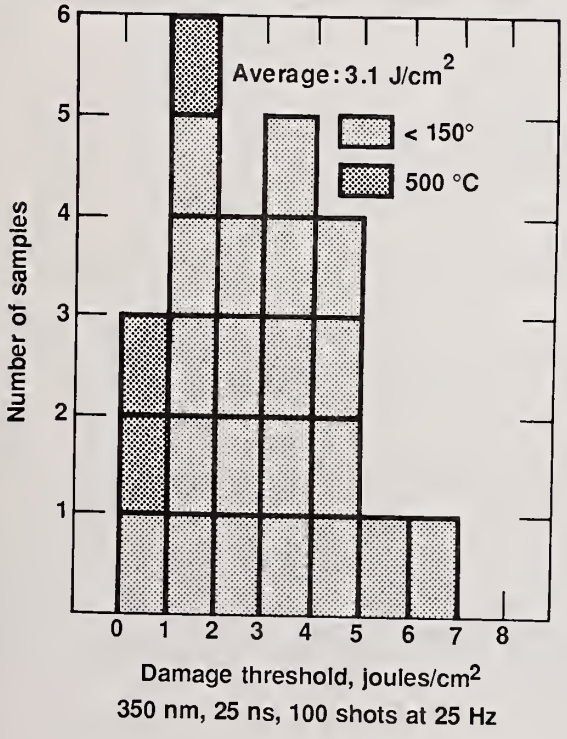

Figure 3. Damage thresholds of ZrO_2 coatings.

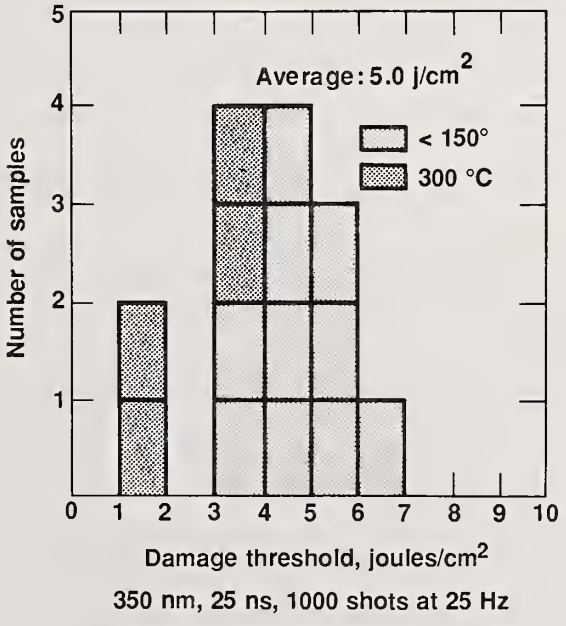

Figure 4. Damage thresholds of HfO_2 coatings.

Another factor of note was, that for all the oxides at some threshold level above the initial damage, all coatings showed total absorption. This is illustrated in Fig. 5, which shows damage on a rather substandard ZrO_2 coating at various fluence levels. The complete beam print is shown at 4.6 J/cm^2 with initial damage at 1.2 J/cm^2. This total absorption level might possibly be related to the nominal UV cut-off wavelengths and it may be significant that the best coatings have the lowest UV cut-offs. This is illustrated in Fig. 6 which shows some damage thresholds that we have measured on a variety of sol-gel type coatings compared with their UV cut-off wavelengths.

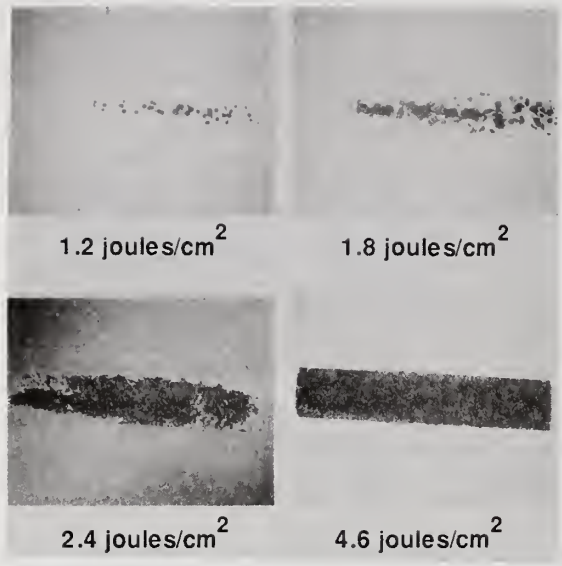

Figure 5. Typical damage of ZrO_2 coating at 350 nm.

Coating	Approximate damage	Massive damage	UV cut-off
Ta_2O_5	1 J/cm^2	3-4 J/cm^2	300 nm
ZrO_2	3	5-6	230
HfO_2	5	7-12	215
Y_2O_3	6	11	210
SiO_2	20	—	<200
MgF_2	20	—	<200
CaF_2	20	—	<200
YF_3	9	13	<200

350 nm, 25 ns, 1000 shots at 25 Hz

Figure 6. Coating materials for 350 nm.

Summary

1. TiO_2, Ta_2O_5, ZrO_2 and HfO_2 coatings have been prepared by deposition from a solution of a suitable precursor or from a colloidal oxide suspension.

2. All coatings are porous with indices between 1.8 and 1.9.

3. Single shot laser damage thresholds of TiO_2 and Ta_2O_5 coatings at 1064 nm and 1.0 ns pulse length have been in the range 6-10 J/cm^2.

4. Multishot laser damage thresholds of Ta_2O_5, ZrO_2 and HfO_2 coatings at 350 nm and 25 ns pulse length at 25 Hz are approximately 1, 3 and 5 J/cm^2 respectively.

References

1. H. Schroeder, "Oxide layers deposited from organic solutions", Phys. Thin Films, 5, 87 (1969).

2. T. N. Krylova, R. S. Sokolova and I. F. Bokhonskaya, "Interference coating with a large number of layers prepared by a chemical method", Sov. J. Opt. Technol. 34, 664 (1967).

3. R. S. Sokolova, "The production of thin oxide films from hydrolysable solutions under different atmospheric conditions", Sov. J. Opt. Technol. 40, 761 (1973).

4. M. B. Svechnikov, "Radiation strength of two layer chemical coating", Sov. J. Opt. Technol. 45, 665 (1978).

5. I. M. Thomas, "Optical coatings by the sol-gel process", Optics News, 12, 18 (1986).

6. I. M. Thomas, "High damage threshold porous silica antireflective coatings", Appl. Opt. 25, 1481 (1986).

7. B. Yoldas, "Investigations of porous oxides as an antireflective coating for glass surfaces", Appl. Optics, 19, 1425 (1980).

Manuscript Received
11-6-86

Fabrication Of Fluoride Thin Films Using Ultra-High Vacuum Techniques

K L Lewis, A M Pitt, N G Chew, A G Cullis, T J Wyatt-Davies, L Charlwood and O D Dosser and I T Muirhead*

Royal Signals and Radar Establishment
Malvern, Worcestershire, WR14 3PS England

Previous papers at this meeting have highlighted the potential afforded by molecular beam techniques in producing optical thin film structures with a high resistance to laser induced damage. These techniques have been recently applied to the growth of polycrystalline thin films of candidate fluoride materials suitable for use over a wide range of laser wavelengths. Here the chief materials of interest have been barium and lead fluoride. Despite sharing a common vaporisation process, significant differences exist in the behaviour of the two molecules on condensation. In the case of barium fluoride, the surface morphology is rough in films produced at room temperature and it is necessary to deposit at significantly elevated temperatures to obtain smooth films even in UHV. In comparison, lead fluoride films have an exceptionally smooth morphology, even when produced at ambient temperatures. Such factors have an important influence on the laser damage thresholds of the films.

In multilayer designs, some control of columnar microstructure is also possible by a stratification technique where two differing component materials are used to prevent microstructure propagation. The coating is built up by alternating the materials throughout the coating until the desired thickness is achieved. By continuously varying the relative thicknesses of the individual laminations, it is possible to produce graded index coating designs. These allow the exploration of interface effects, hitherto difficult using optical techniques.

Key words: fluoride films; laser damage; thin films; ultra-high vacuum

1. Introduction And General Survey

The family of fluoride materials is of interest to the optical coatings community because of their low indices of refraction, and their wide spectral bandwidths (see table 1). For example lead fluoride with its short wavelength transmission limit of $<0.2\mu m$ and its multiphonon absorption edge of $>15\mu m$ finds application for UV, visible and infrared applications. The fluorides are also stable in fluorine containing environments, thus becoming prime candidates for use in HF/DF or excimer laser systems. However, the major disadvantage of the fluorides is their solubility in water. This can vary over several orders of magnitude with some members of the class being relatively inert eg magnesium and calcium fluoride, allowing then to become standard materials for the optical industry. Even the "softer" members of the class eg lead fluoride are not particularly soluble and can be considered for a wide variety of uses. However the actual moisture resistance of a film will also be dependent on the techniques used for deposition and the presence of residual porosity can greatly affect the stability of the film.

---

*OCLI Optical Coatings, Dunfermline, Fife, KY11 5JE Scotland

Table 1 Properties of Fluoride Materials of Interest as Thin Films

Materials	Solubility in cold water	Expansion Coeff ppm	Spectral Bandwidth	Refractive Index
NaF	4.22	36	0.15 - 11	1.33
LiF	0.27	37	0.11 - 9	1.40
CaF_2	0.0016	18	0.13 - 12	1.4
SrF_2	0.011	18	0.13 - 14	1.4
BaF_2	0.12	18	0.14 - 15	1.45
Cryolite			0.2 - 14	1.35
AlF_3	0.56		0.2 - ?	1.35
MgF_2	0.0076	16	0.11 - 9.7	1.39
PbF_2	0.064	11	0.19 - 17	1.76
ThF_4	i		0.25 - 15	1.5

The range of materials presented in table 1 is reasonably large, but is considerably extended when account is taken of the engineering of properties possible by alloying two or more components together. For binary systems of one lattice type, a series of solid solutions is possible. Examples of those studied as thin films include the alkaline earth fluorides [1]. These find application as epitaxial insulating films in semiconductor/insulator/semiconductor and MIS heterostructures. Many of the simple binary fluorides crystallize in the cubic fluorite structure where all the tetrahedral sites between the metal atoms are occupied. This structure can also accept mixed crystals (eg calcium yttrium fluoride) in which the excess fluorine atoms occupy interstitial sites. Some of the materials also exhibit more than one stable form, for example lead fluoride can exist as both cubic and orthohombic variants, although it is the cubic β form that is typically found in thin films. The possibilities afforded by the family of ternary fluorides has hardly been explored and the only well recognised material is cryolite. For more complex mixtures a family of glassy materials are produced with an amorphous microstructure. These are of current interest as bulk materials both from the point of view of high energy laser optical components and for optical communication applications, and have been widely studied [2].

The vaporisation of simple binary fluorides has been studied by Farrow et al [3], who conclude that the dominant vapour species are the undissociated molecules. This may explain the ease with which it is possible to produce epitaxial films on clean, ordered surfaces of semiconductor materials at comparatively low deposition temperatures (200°C) despite poor lattice match. On the other hand it may also serve to explain the difficulty experienced in achieving fully dense polycrystalline films of such fluorides at room temperatures since there is no exothermic chemical reaction at the surface. The difficulties of producing fully dense films are well known in the case of magnesium fluoride where film packing densities when deposited at room temperature are only about 0.8 [4]. At substrate temperatures of 190, 280 and 340°C the packing densities were found to be 0.895, 0.935 and 0.955 respectively. Similar behaviour is found for calcium and barium fluorides. Although it is possible to utilise higher growth temperatures to achieve the desired surface mobility of adsorbing species during the molecular process of film growth, this poses problems when it is required to produce complex multilayers incorporating such films. An alternative technique, recently exploited for magnesium fluorides [5] is to provide the additional energy required for adatom mobility by low energy (< 250 eV) ion bombardment during film growth. However there is risk of introducing a deleterious shift of UV absorption edge towards longer wavelengths. Significant changes in film microstructures can also occur as a result of such ion assisted deposition (IAD) and may well be the major factor in determining the high durability of such films [5].

In previous work [6] on advanced thin film fabrication, we have highlighted the potential of molecular beam techniques for the production of coatings with a dense microstructure. The present work is concerned with an extension of this research to a study of candidate thin film fluoride materials, and to an assessment of their performance from a laser damage viewpoint in multilayer systems. The materials selected for detailed examination are barium and lead fluoride. It has been necessary to determine the separate influence of film microstructure and interface character in the ensuing multilayer designs. Both conventional and stratified (digital) designs have been assessed.

2. Experimental

The coatings were deposited in a dedicated Vacuum Generators load-locked UHV system fitted with 3 Knudsen sources and in-situ surface diagnostics (Auger and X-ray photoelectron spectroscopy) as previously described [6]. The source materials (BDH Optran) were contained within high purity graphite crucibles which were carefully outgassed following baking of the entire deposition chamber at 180°C. Source temperatures were adjusted to give deposition rates in the range 0.1 to 1 μm/hour, but were typically 1200-1300°C for barium fluoride and 600-700°C for lead fluoride. ZnSe and ZnS films were deposited from high purity source material previously prepared by chemical vapour deposition and contained within graphite and pyrolytic boron nitride crucibles respectively. Film deposition was studied at growth temperatures over the range 40-350°C.

The availability of in-situ XPS analysis techniques allowed the study of both surface pre-treatment procedures and the examination of transient species at film/film interfaces. These latter studies were carried out by following the deposition of a few monolayers of thin film material onto a previously assessed substrate and examining the shift in binding energies of the characteristicelectronic states. This is a powerful technique and can detect any change in the chemical environment of the constituent atoms as a result of the formation of any intermediate chemical species at the interface.

Film structure was determined ex-situ by X-ray diffractometry. Substrates used were silicon ZnSe, ZnS and glass. Cross sections were prepared for transmission electron microscopy by cleaving, epoxy mounting and abrasive thinning to 100μm in thickness. Final thinning was carried out by reactive ion beam bombardment using argon and/or iodine ions as appropriate [6]. Cross sections so prepared were examined on a JEOL 4000EX transmission electron microscope. Optical transmission and reflection spectra were determined using a Perkin Elmer 983G spectrometer for the infrared and Perkin Elmer Lambda 9 spectrometer for the UV/VIS/NIR. The detector system in the Lambda 9 was replaced with a 60mm diameter integrating sphere accessory which allowed the assessment of total integrated scatter as a function of wavelength. Spectra were acquired using an on-line computer and digitally processed to correct for the effects of baseline non-uniformity and specimen holder geometry.

Damage thresholds were determined at 10.6μm using a short cavity TEA laser of pulse length 33 nsec, with beam focussed to a spot size of 100μm $1/e^2$ diameter (determined by pinhole scanning techniques). Ten separate irradiations were carried out at each nominal value of incident energy at separate sites in a well defined matrix pattern. Damage was assessed by optical microscopy at x400. Simultaneous measurements of incident and transmitted energies allowed the determination of transmittance values for each irradiation pulse. Damage threshold were determined from statistical probability plots produced from up to 80 separate irradiations.

3. MIcrostructure Of Lead And Barium Fluoride Films

Significant differences were found between the morphology of barium fluoride films and that of lead fluoride films produced in UHV. In the case of barium fluoride, the surface morphology is rough, and of poor durability in films produced at room temperature, as shown in figure (1a). Optical scatter values determined as backscatter by the integrating sphere technique are high and vary approximately linearly with film thickness. As the deposition temperature is increased to 250°C, the film microstructure changes gradually to a more well defined crystalline habit as shown in figure (1b). Films produced at 350°C were exceptionally smooth and quite hard. Such differences are reflected in the values of optical scatter measured for such films, with a typical molecular flux dependence of the form shown in figure (2).

Here the scatter values measured at 250nm are normalised to a film thickness of 1μm to allow the comparison of a larger population of samples. Refractive indices of films produced at 350°C are close to 1.58 (measured at 400nm) suggesting that these films are theoretically dense. The room temperature deposited material has refractive indices in the range 1.45-1.49. On the basis of Maxwell-Garnett theory, the relative film density is estimated to be about 0.81 when produced at 40°C.

The general trend in the cross-sectional morphology of the film can be revealed by SEM examination of cleaved edges of the film (figure (3)). At room temperature, the films are a polycrystalline mass with no evidence of strong columnar growth habit. At higher temperatures, the average crystallite size increases until at 350°C the effect of increased adatom mobility is sufficient to produce a dense columnar film. The lower temperature films absorb moisture over a period of time giving rise to a broad absorption band centred at 3400 cm^{-1}. The SEM cross-section of figure (3a) is not sufficiently detailed to show the amount of porosity present in the film,

but this is easily revealed by the cross-sectional TEM techniques. Figure (4) shows a typical region and highlights the "chevron" texture of dendritic growth habit of this material. The dendrite features propagate from a central axis, at some angle to the direction of film growth, and are sometimes interspaced with amorphous material. Porosity is evident in the film, not just propagating from the surface, but also between the individual crystallites in the chevron arrays. Close examination of the film/substrates interface (figure (5)) reveals that the barium fluoride initially grows as an amorphous film, and that this gradually evolves into the dendritic growth habit.

Film growth rate is a function of temperature and molecular flux as shown in figure (6). An interesting anomaly occurs at the higher flux where the 40°C film growth is significantly reduced compared with that at 110°C. This may well be a consequence of the poor adatom mobility. X-ray diffraction studies show that the barium fluoride films are cubic, but with evidence of (111) texture on both Si and ZnSe substrates. Interestingly, at growth temperatures of 250°C, the films show strong (220) texture before reverting to (111) at higher temperatures. The lattice constant was determined to be 6.199Å in agreement with published values [9].

In comparison, it was possible to produce exceptionally smooth films of lead fluoride at ambient temperatures on well polished silicon substrates. No improvement was found in depositing the material at high temperatures and indeed at temperatures above 150°C, the quality of the film seriously degraded. On ZnSe substrates, the films were slightly rougher with definite evidence of a precipitation effect at the substrate/film interface. This may be caused by a surface reaction and is discussed in more detail in a later section. On glass and ZnS substrates, the films were colourless although reflectivity measurements indicated weak UV absorption in the film at energies above the band edge of the substrate. Variations were also found in refractive indices with values as high as 1.89 being measured at 5-10 m in films deposited at room temperature. Such values are higher than reported for bulk lead fluoride (1.76) and serve to indicate a degree of non-stiochiometry in the material Using the in-situ XPS analysis facility we have been able to study this in more detail, and we find that the high indices are indeed associated with a fluorine deficiency of the order of 8%. Similar deficiencies have been found in the case of magnesium fluoride where they were attributed to thermal decomposition of the evaporant in the source crucible [5] or to ion impact induced decomposition [7].

Cross sectional TEM examination of room temperature deposited lead fluoride films (figure (7)) reveals that the films have a composite microstructure, consisting of very large (3000-4000Å) columns interspaced with a large number of small crystallites and voids. The large columns are of good crystalline quality with clear evidence of low dislocation density. The small crystallites sometimes take on the form of a definite geometric form, suggesting perhaps a different structural phase of the material. X-ray diffraction studies show however that the films are of phase cubic lead fluoride with (111) texture, but the technique is unable to detect any difference in the structure of the small crystallites from that of the large columns, due to their relative dimension.

4. The Barium Fluoride-Lead Fluoride System

The barium-lead fluoride system is of some interest, not the least because of the variation in lattice constant over the composition range (5.94-6.2), but because of the potential of synthesising films of refractive index anywhere in the range 1.45 to 1.76 simply by choosing the correct composition. An intermediate compound BaPbFs is known in the X-ray literature [8], but no reference has been previously made to studies of the solid solutions as thin films. The molecular beam technique allows the deposition of such films with ease and in a well controlled manner. simply be combining incident beams of the constituent molecules. Compositions are varied by changing the source temperature of the barium fluoride or lead fluoride and are determined in our case by in-situ XPS analysis. It is only necessary to deposit a film some 10 monolayers thick to allow XPS analysis and such a procedure can be routinely used as part of a particular film deposition cycle.

Since significant differences exist in the morphology of films of the two pure components, it was also of interest to examine the effect of mixing the incident molecular species to see whether any change could be induced in adatom mobility. This was clearly revealed to be the case and even films containing 77% barium fluoride are quite smooth when deposited at 40C. The variation in lattice constant over the composition range is shown in figure (8). The dependence is monotonic within the range of experimental error, as would be expected for a well behaved solid solution system. However, it was notable that the alloy films exhibited (311) texture as compared to the (111) texture of the pure components. Some instances of film crazing were found when the alloy was deposited at room temperature on ion beam etched ZnSe or CdTe substrates. This could be avoided by depositing a thin buffer layer of ZnSe immediately before the alloy film, suggesting

that some chemical reaction may be taking place between the alloy and the highly reactive ion beam etched surface. This was investigated further in the simplified case of barium fluoride on ZnSe using XPS. Here an ion beam etched ZnSe surface was analysed before and after deposition of a monolayer or so of barium fluoride. Detailed examination of the 3d derived band for Se revealed small but definite changes in binding energy suggesting a change in its chemical environment. Such behaviour is discussed in more detail in a following section.

5. Control Of Microstructure In Fluoride Films

In many ways it is unfortunate that it is necessary to deposit fluorides such as those of barium, calcium and magnesium at elevated temperatures to ensure freedom from porosity and achievement of a fully dense microstructure. In previous work [6] we had suggested the possibility of controlling the columnar microstructure of thin films by a stratified approach in which alternate layers A and B (which are in themselves not lattice-matched to each other) are repeated throughout the thickness of the film. It was envisaged that new critical nuclei for film growth would be produced at each level of stratification. However in the ZnSe/ZnS system initially addressed, the mismatch between the two zinc blende lattices was too small (ca 5%), and the columnar structure propagated through the ZnSe/ZnS interfaces by producing a region of heavily microtwinned material in the thin ZnS layers.

In the case of a stratified heterostructure for example based on barium fluoride and zinc sulphide, the degree of lattice mismatch is considerably larger, of the order of 15%. Furthermore, the component materials, although basically cubic, crystallise in the fluorite and zinc blende structures respectively. Such a heterostructure thus should have the greatest potential for preventing the propagation of columnar morphology. The cross-sectional TEM image shown in figure (9) directly demonstrates that this can be done and is the first conclusive evidence for a synthetically engineered microstructure. Here, a composite built up from 75Å of barium fluoride interspaced between 115Å of ZnS produces crystallite blocks some 80Å in dimension. The transmission micrograph also reveals the dense character of the heterostructure and indicates the freedom from porosity found over the whole specimen area. Figure (10a) shows a high resolution lattice image of the film and highlights the random orientation of crystallite planes within each block. The electron diffraction pattern of such a structure (figure (10b)) confirms its pseudo-amorphous character.

It is a relatively simple extension of such technology to engineer a graded index antireflection coating simply by varying the relative contributions (ie the mark-space ratio) of barium fluoride and zinc sulphide to the stratified film as deposition proceeds. These designs can produce A/R coatings with exceptionally wide bandwidths as shown by the example in figure (11) which is that of a (PbF_2/ZnSe) structure with effective refractive index linearly graded from 1.7 to 2.4 in a 2μm total thickness. This contains 240 separate discrete layers with thicknesses varying from 2Å to 240Å. The A/R performance can be improved even further by utilising barium fluoride rather than lead fluoride. Ultimately, the minimum reflectivity actually achieved will be that produced by the lowest index material available. Further improvement can be made to such a coating as in figure (11) by deliberately profiling the surface of the coating by ion beam etching techniques to give a residual "moth's eye" structure.

6. Role Of Interface Absorption Effects

A factor of critical importance in such complex multilayer structures is the degree of optical absorption produced at the discrete interfaces within the heterostructure. In our initial studies on the (ZnSe/ZnS) system [6] we found that the presence of 120 or so separate interfaces had no effect on the 10.6 m laser damage threshold of the film, and that it was equivalent to a homogeneously alloyed film of the same average composition. When reactive materials such as the fluorides are are incorporated within such heterostructures, the possibility of inducing solid state reaction at the interface region is greatly enhanced. In the case of lead fluoride and zinc sulphide any such reaction would be likely to produce PbS which is a narrow bandgap material (0.29 eV) and would seriously degrade the optical transmission of the coating. Such effects can be explored by producing digital graded index films of the two materials, which would suppress the usual transmission maxima and minima found in resonant thin film systems. The UV/VIS/NIR tranmission spectrum of a lead fluoride/zinc sulphide graded heterostructure (figure (12), lower trace) shows that a significant absorption occurs, commencing at wavelengths as high as 1900 nm. This can be totally suppressed by interspacing a mere 20 to 30Å of barium fluoride between the lead fluoride and the ZnS as shown by the upper trace in figure (12). Unlike PbS, BaS is a relatively wide bandgap material and is not going to produce deleterious optical loss in the visible spectral region. The residual modulation in the upper trace in figure (12) is produced as a result of the non graded barium fluoride component in the coating. The production of such a multilayer is a fairly remarkable achievement. bearing in mind that it is made up of over 400

separate films each of controllably varying thickness. Such structures can only be reliably produced in UHV where the necessary degree of control is available and the incorporation of extrinsic impurities at the interfaces can be avoided.

7. Laser Damage Studies

Many of the issues discussed in the previous sections are fundamental to the development of improved optical coatings with enhanced laser damage thresholds, and the range of materials and film microstructure obtainable allow many of the separate effects achievable to be explored.

The effects of surface roughness have been examined by producing films of barium fluoride over a range of deposition temperatures and at varying incident molecular fluxes. Surface roughnesses were compared by means of integrated scatter measurements in the UV at 250 nm. Damage probabilities were determined using the statistical technique described above, giving typical dependence on energy density of the type shown in figure (13). This shows the experimental data plotted both on a yes/no and probability basis. In this case, that of a barium fluoride film produced at 40°C, there is a significant difference between the minimum energy LD_0 required just to produce damage, and the maximum energy LD_{100} required to produce damage on every shot. This shows that the coating is capable of surviving very high incident energies at times, at fluxes some 80% in excess of that of the uncoated substrate. The two LD values are listed in table (2) for a series of coatings produced at different temperatures, and with different degrees of optical scatter (surface roughness). It is readily apparent that the LD_0 value is approximately constant for the whole series, but the LD_{100} is indirectly related to the growth temperature, with specimens with rough surfaces having a higher LD_{100} value. This effect is not fully understood but may be associated with the ability of the rough surface to redistribute the electric field intensity over a greater volume of material.

It is possible to produce very smooth, dense barium fluoride films on eg ZnSe and Si substrates under more optimum conditions. These films have very high damage thresholds, certainly in excess of the uncoated substrate materials as shown in table (3). In comparison the thresholds for lead fluoride films on ZnSe and Si substrates can vary significantly but are not correlated with the refractive index of the film. The thresholds for the mixed alloy films are somewhat intermediate between lead fluoride and barium fluoride produced at room temperature, and identical to digital (PbF_2/BaF_2) heterostructures.

Table 2 Laser damage thresholds of barium fluoride films on ZnSe substrates at 10.6 m

Thickness m	Growth temperature C	Damage threshold J/cm^2		Normalised 250 nm scatter for 1 m film thickness ie %/ m
		LD(0)	LD(100)	
Uncoated	-	49	74	2.0
1.7	40	46	104	7.7
3.0	116	41	79	9.8
1.4	250	40	60	12.8
1.8	350	44	48	5.2

Digital heterostructures containing lead fluoride with ZnSe or ZnS whether graded or not have damage thresholds equivalent to lead fluoride and not intermediate between the lead fluoride and the chalcogenide. Thus the problem with such multilayers appears to be the lead fluoride component and presumably arises from the non-stoichiometric character of this material. The assessment of lead fluoride films produced under more optimum conditions is still underway. In contrast, the damage thresholds of digitally graded heterostructures containing BaF_2 are exceptionally high. On multispectral grade ZnS substrates, the LD_0 value is about 58 J/cm^2, whilst several sites survived fluences in excess of 120 J/cm^2 with no damage.

Table 3 Laser damage threshold of fluoride thin films and multilayers

Film	Substrate	Composition %(Ba)	Refractive	Damage threshold J/cm^2	
				LD(0)	LD(100)
	ZnSe			49	74
	Si			67	98
BaF_2	Si		1.52	68	83
BaF_2	ZnSe			68	89
PbF_2	ZnSe		1.64	22	32
PbF_2/ZnSe	ZnSe		1.73	24	74
PbF_2	ZnSe		1.85	4	35
PbF_2	ZnSe		1.89	6	46
PbF_2	ZnS		1.89	51	90
$(BaPb)F_2$	Si	19.4		31	46
$(BaPb)F_2$	ZnSe	56.0	1.59	33	60
$(BaPb)F_2$	Si	77.0	1.60	27	49
d-PbF_2/BaF_2	ZnSe		(1.84)	31	47
d-PbF_2/ZnSe	ZnSe		(2.02)	21	41
d-BaF_2/ZnSe	ZnSe		(1.63)	58	89
gd-BaF_2/ZnS	ZnS			58	120
gd-PbF_2/ZnS	ZnS			27	42
gd-PbF_2/ZnS	ZnS			26	33

NOTES Alloys denoted by eg $(BaPb)F_2$ d - digital coating
gd - graded digital coating gbd - graded, buffered digital

8. Conclusions

A study has been carried out of the deposition of some candidate fluoride materials for high energy laser optical components, and of the problems likely to be encountered in incorporating the materials into multilayers. Films of barium fluoride with excellent morphology and high laser damage threshold can be produced, but problems are met with lead fluoride with the effect of non-stoichiometry and with the control of microstructure. The solid solution system formed between barium and lead fluoride has been explored and has considerable potential for allowing the synthesis of coatings with refractive indices selectable in the range 1.5 to 1.75. A considerable advance has been made in controlling the microstructure of thin films using a stratification technique. The ultrastructures produced are pseudo amorphous with "crystallite" size determined by the selection of laminate thickness. The technology has been extended to the synthesis of graded index antireflection coatings with excellent broadband properties. Such coatings can have very high laser damage thresholds, with a (BaF_2/ZnS) example on ZnS having thresholds in excess of 58 J/cm^2, but with several sites irradiated surviving fluences in excess of 120 J/cm^2.

9. References

[1] Sullivan, P.W., Farrow, R.F.C. and Jones, G.R., J Crystal Growth 60 403 (1982).

[2] Bendow, B., Burge, D.K., Bennett, H.E., Johnston, L.H. and Mecholsky, J.J., Proc Boulder Laser Damage Symp. (1983), NBS Spec Pub 688 30 (1985).

[3] Farrow, R.F.C., Sullivan, P.W., Williams, G.M., Jones, G.R., and Cameron, D.C., J Vac Sci Technol, 19 415 (1981).

[4] Ritter, E. and Hoffman, R., J Vac Sci Technol 6 733 (1969).

[5] Kennemore III, C.M. and Gibson, V.J., Applied Optics 23 3608 (1984).

[6] Lewis, K.L., Pitt, A.M., Cullis, A.G., Chew, N.G., and Charlwood, L., Proc Boulder Laser Damage Symposium (1985), and preceding conference.

[7] Martinu, L., Biederman, H., and Holland, L., Vaccuum 35 531 (1985).

[8] Hoppe and Blinne., Z Anorg Allg Chem 293 251 (1958).

[9] Swanson and Tatge., JC Fel Reports, NBS (1949).

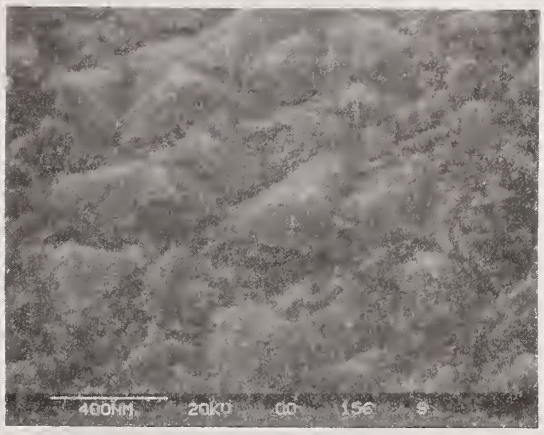

A

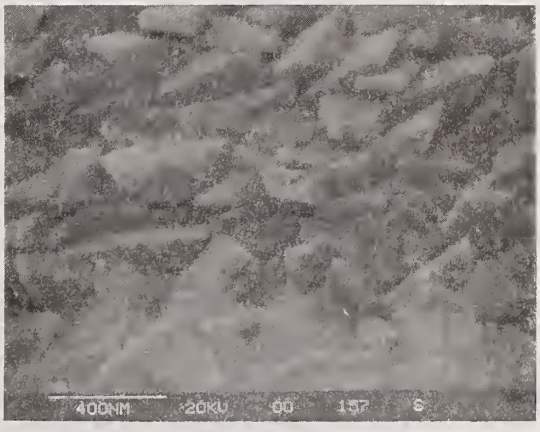

B

Figure 1 Scanning electron micrographs of surfaces of barium fluoride films produced at (a) 40°C and (b) 250°C.

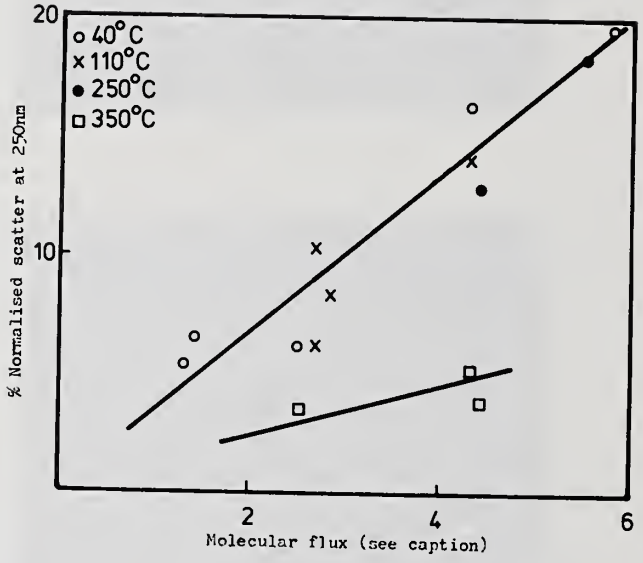

Figure 2 Dependence of optical scatter on molecular flux for barium fluoride films produced at different temperatures. The values of flux are determined on a cooled quartz crystal monitor situated immediately adjacent to the substrate. A flux unit of 5 is equivalent to a room temperature film growth rate of about 0.85μm/hour.

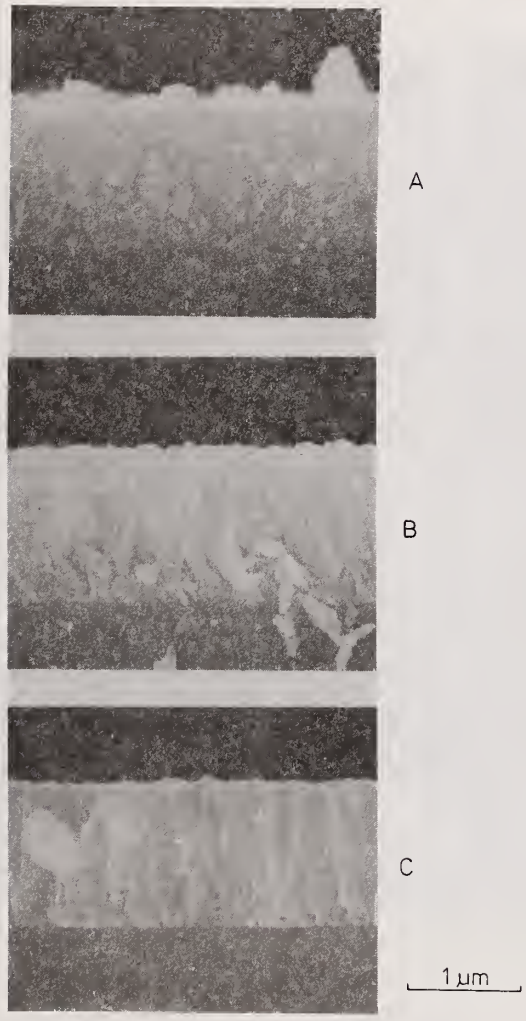

Figure 3 Scanning electron micrographs of cleaved edges of barium fluoride films deposited at (a) 40°C, (b) 250°C and (c) 350°C.

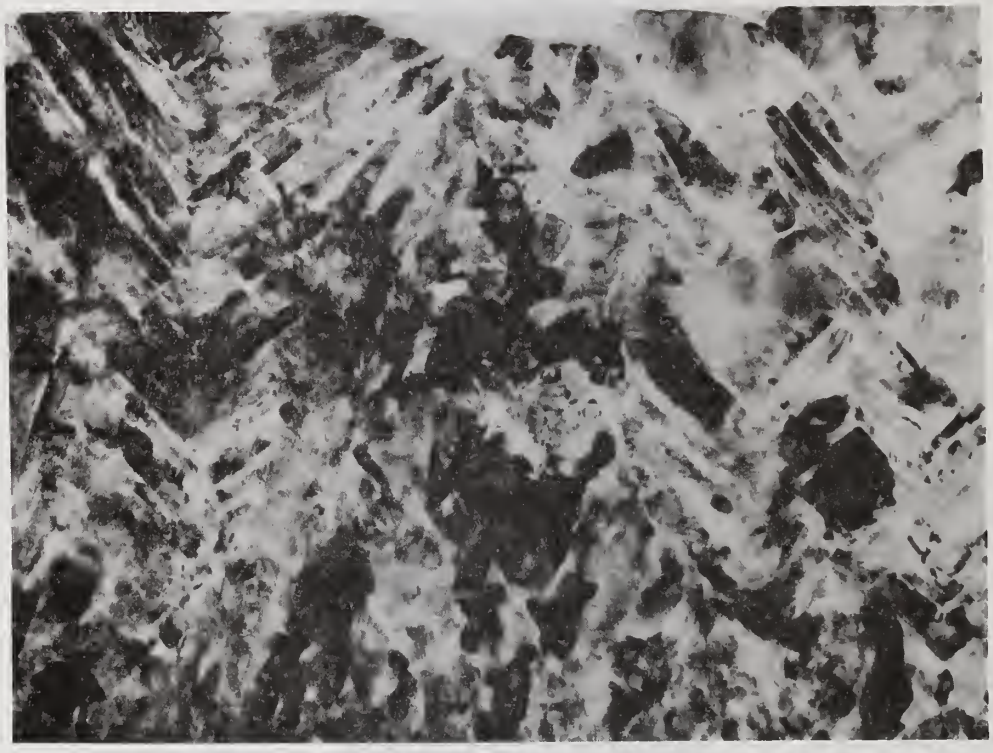

Figure 4 Cross sectional transmission electron micrograph of barium fluoride film produced at ambient temperatures showing dendritic growth habit.

Figure 5 Detail of barium fluoride film near substrate interface showing transitional amorphous structure.

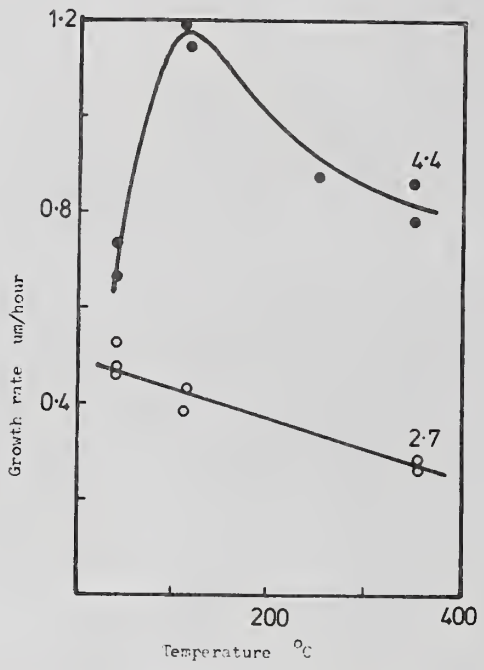

Figure 6 Relationship between the growth rate of barium fluoride and deposition temperature at different molecular fluxes.

Figure 7 Cross sectional transmission electron micrograph of lead fluoride film deposited at ambient temperatures showing its composite character, with residual porosity in intergranular regions.

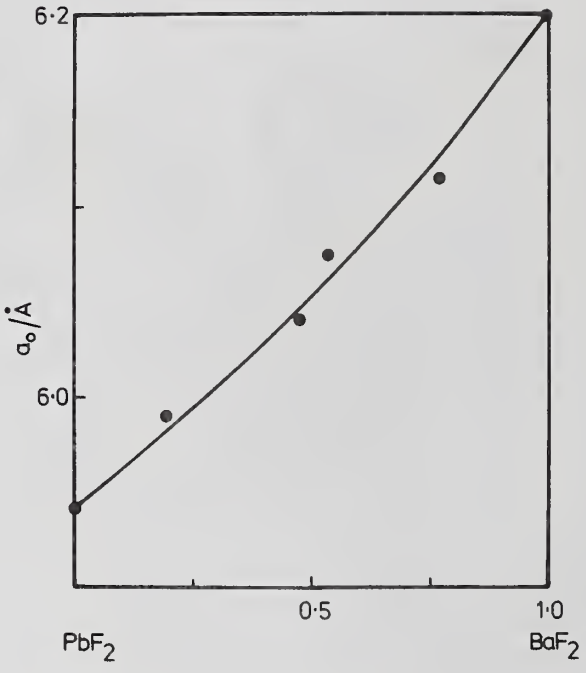

Figure 8 Variation of lattice constant of barium lead fluoride alloys over the composition range.

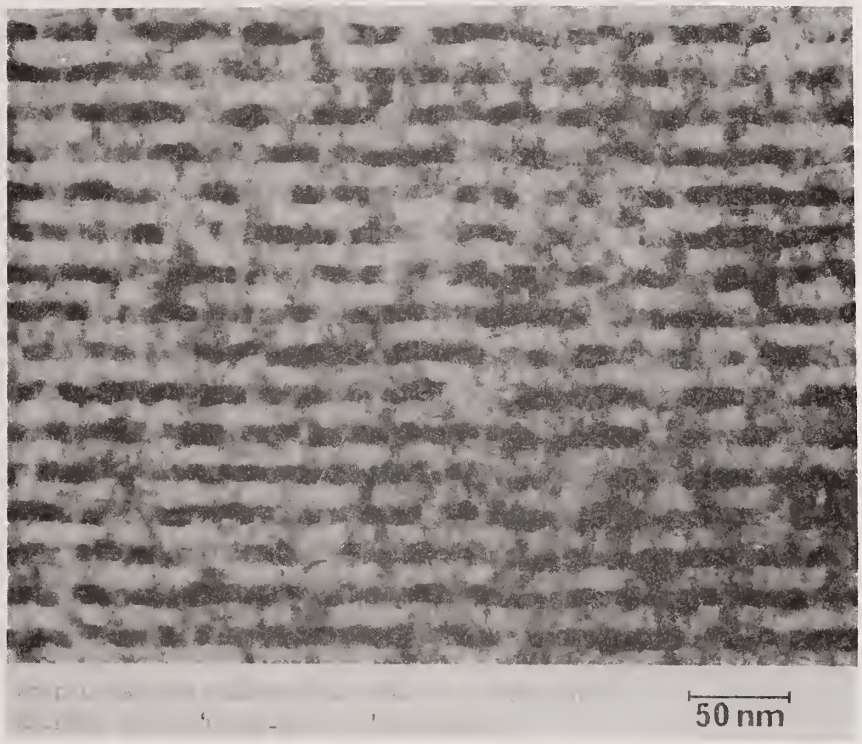

Figure 9 Detail of stratified barium fluoride/ZnS microstructure taken under bright field conditions showing "pseudo-amorphous" morphology.

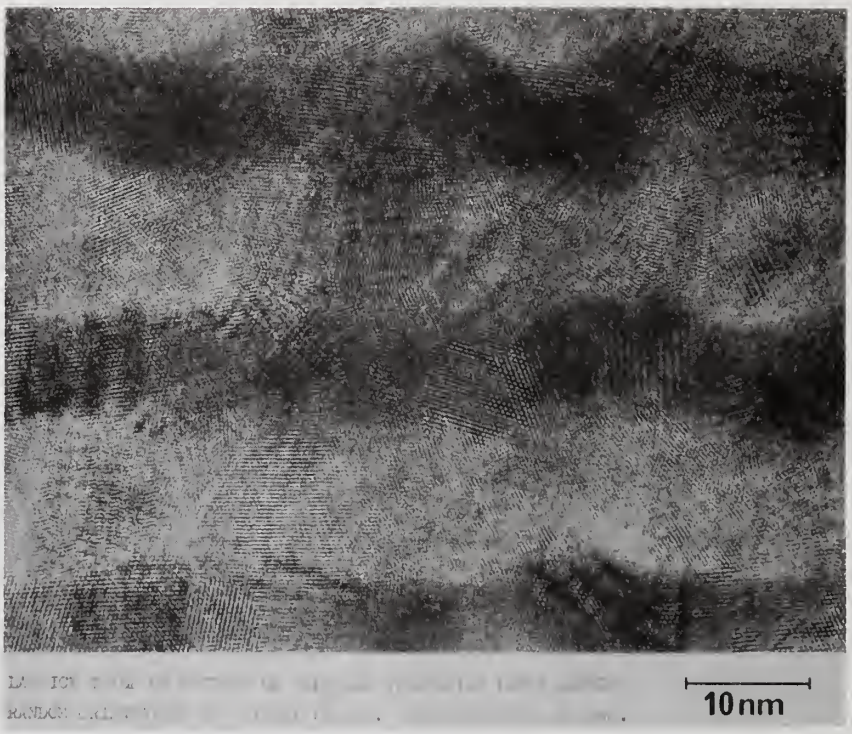

Figure 10a Lattice image of section of barium fluoride/ZnS stratified layer showing random orientation of crystal planes. Light regions are ZnS.

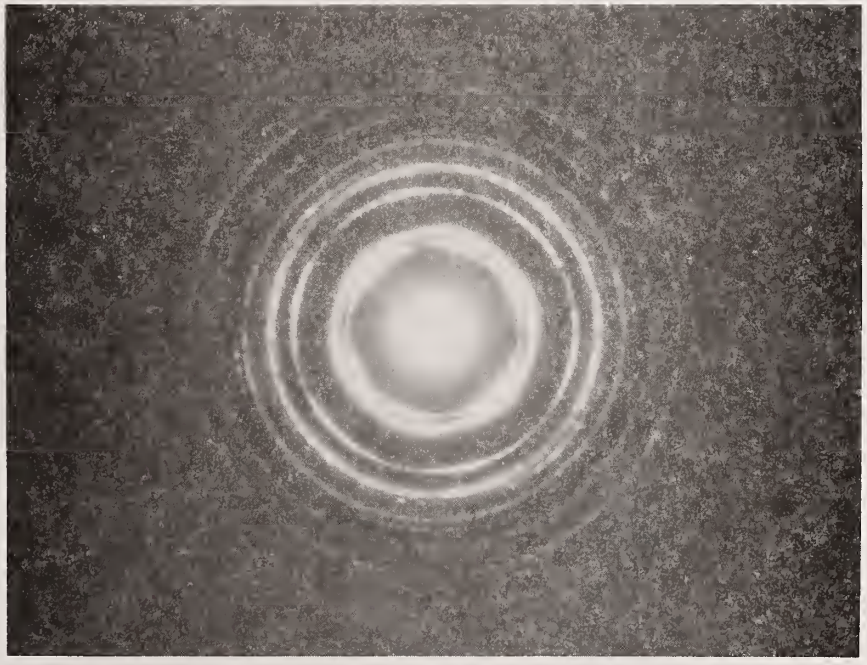

Figure 10b Electron diffraction pattern of barium fluoride/ZnS stratified structure taken through 0.5μm aperture.

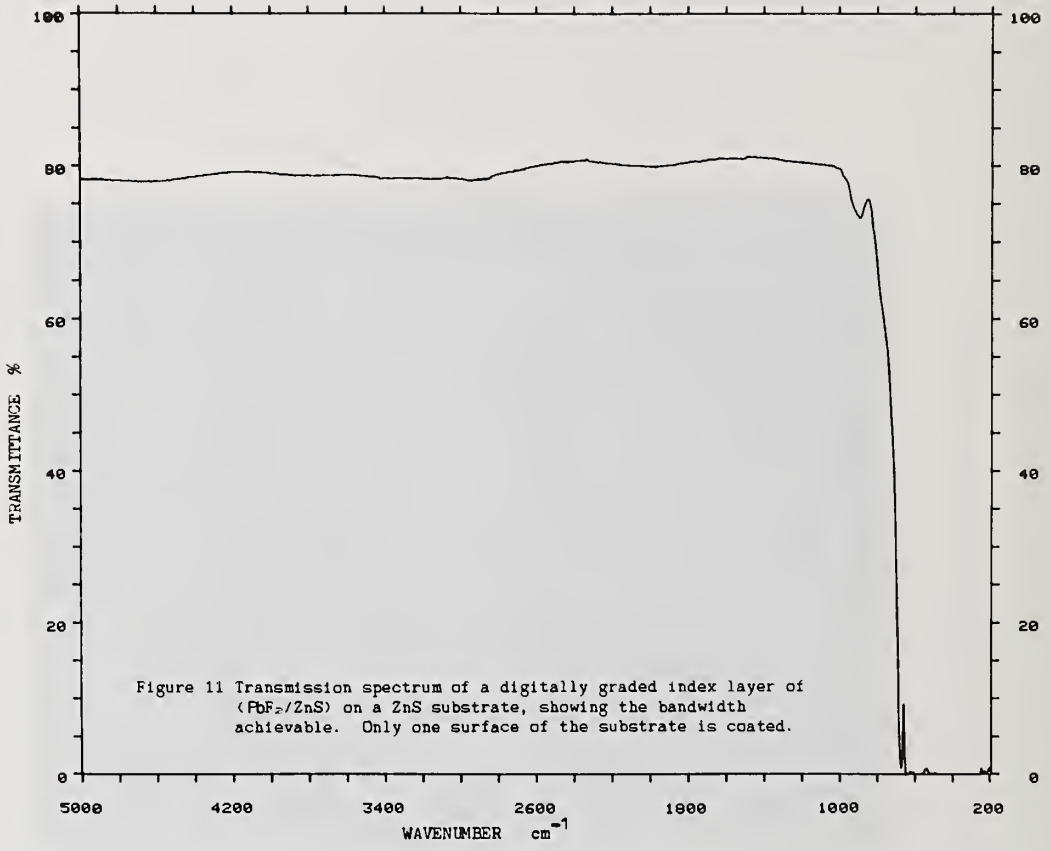

Figure 11 Transmission spectrum of a digitally graded index layer of (PbF_2/ZnS) on a ZnS substrate, showing the bandwidth achievable. Only one surface of the substrate is coated.

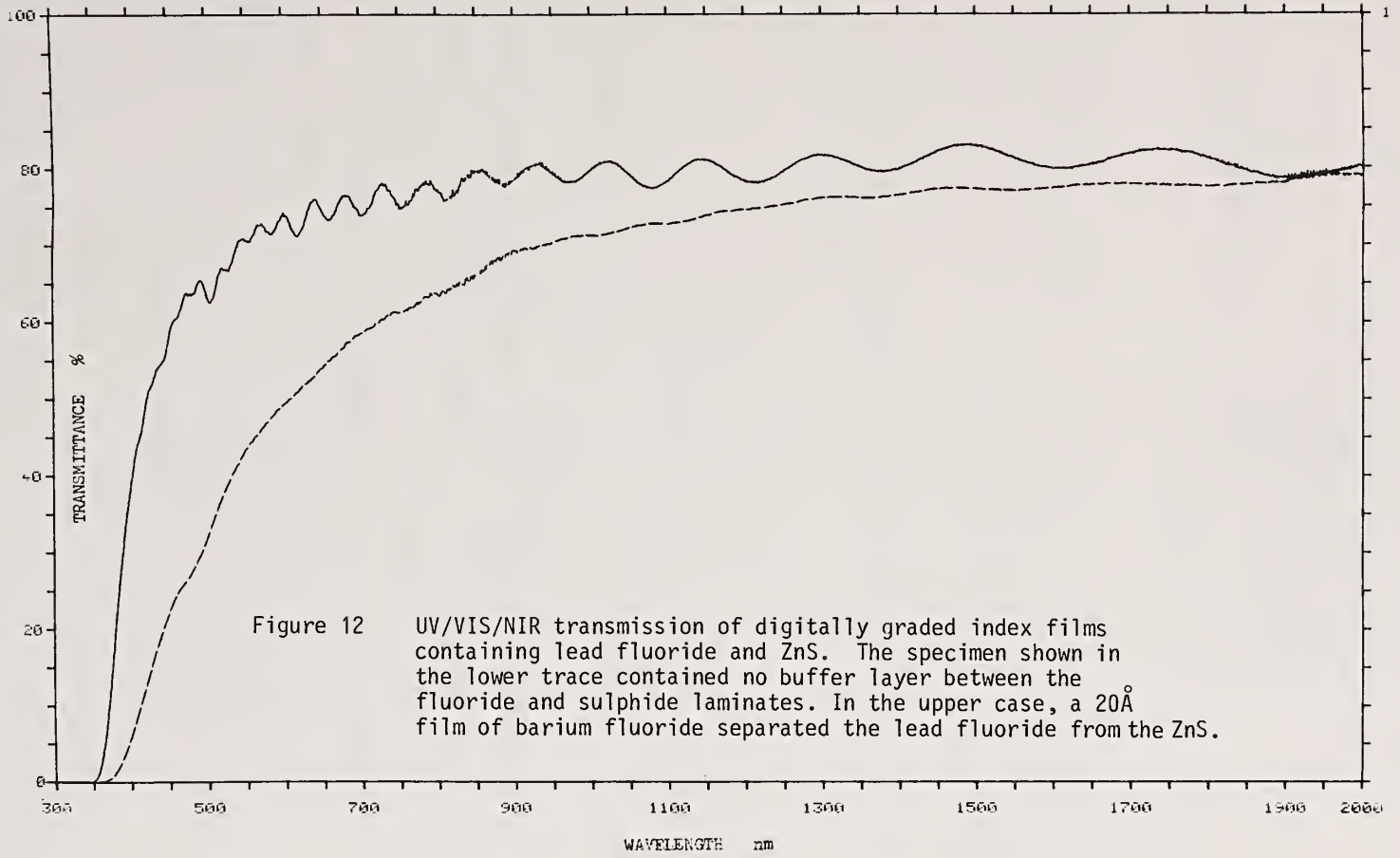

Figure 12 UV/VIS/NIR transmission of digitally graded index films containing lead fluoride and ZnS. The specimen shown in the lower trace contained no buffer layer between the fluoride and sulphide laminates. In the upper case, a 20Å film of barium fluoride separated the lead fluoride from the ZnS.

Figure 13 Typical damage probability plot determined for a film of barium fluoride deposited on ZnSe at ambient temperature.

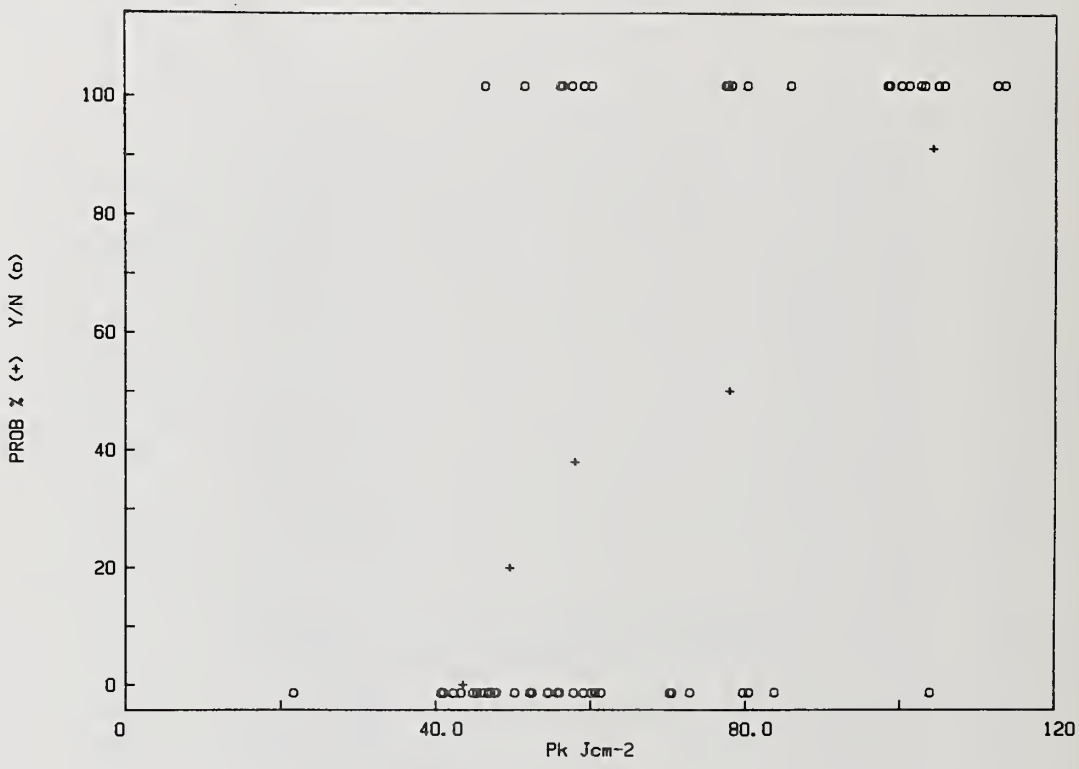

Chemical Vapor Deposition of TiO_2 Thin Films at Room Temperature*

J. Wilder and I. Thomas
Lawrence Livermore National Laboratory
University of California
P.O. Box 5508, L-490
Livermore, California 94550

ABSTRACT

Titania coatings were prepared using a chemical vapor deposition (CVD) apparatus at room temperature. Coating were deposited by the reaction of gaseous $TiCl_4$ and H_2O at the substrate surface. High refractive indices were obtained with damage thresholds to 12.9 J/cm^2, at 1.06 μm, 1 ns.

Key Words: thin films; chemical vapor deposition; titanium dioxide; laser damage

Introduction

TiO_2 thin films are attractive components in multilayer coatings used in antireflective (AR), high reflective (HR), and polarizer applications. Various evaporation techniques are well known and routinely used for the deposition of TiO_2 thin films for optical applications. The optical performance of these coatings is excellent and the highest laser damage thresholds are in the range of 7-10 J/cm^2 at 1.06 μm, 1 nsec.[1]

This damage threshold is sufficient for use in current high powered lasers such as the Nova at the Lawrence Livermore National Laboratory, but will probably be inadequate for future designs. Consequently, we decided to investigate potential alternative methods of forming TiO_2 films. A room temperature, atmospheric pressure, chemical vapor deposition (CVD) process from inorganic chemical precursors was selected for initial investigation. The advantages are an inexpensive apparatus, the exclusive formation of four valent titanium, the elimination of organic residues, and the elimination of solvents and catalysts. These conditions might contribute to a higher laser damage threshold.

*Work performed by the Lawrence Livermore National Laboratory under the joint auspices of the Air Force Weapons Laboratory, Kirtland AFB, New Mexico 87117-6008, under P.O. #85-060, and the U.S. Department of Energy under Contract No. W-7405-ENG-48.

We began by following the lead of previous workers who have produced TiO_2 films from various apparatuses.[2-10] Most of the published work is directed toward the semi-conductor industry. The remaining work does not specifically address optical applications especially high energy lasers.

Methods of Deposition

Gaseous chemical precursors, diluted in an inert gas, ideally react on contact with a surface (Fig. 1a) to give a smooth uniform coating. However, under certain conditions, premature reaction can occur (Fig. 1b) giving a gas phase precipitation which results in a rough, light scattering coating. This, of course, is undesirable. In this case, the reagents selected were titanium tetrachloride ($TiCl_4$) and water (H_2O) with nitrogen as the carrier gas. These reagents are liquid at standard conditions but are volatile and the reaction may be illustrated by the following equation:

$$TiCl_4 + 2H_2O \rightarrow TiO_2 + 4HCl \qquad (1)$$

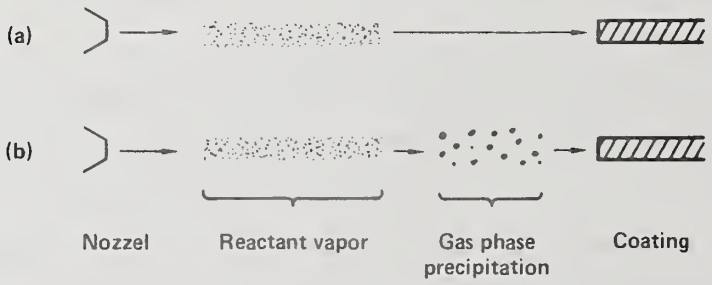

Figure 1. Chemical Vapor Deposition Schematic.

This system allows the substitution of $TiCl_4$ with silicon tetrachloride ($SiCl_4$). $SiCl_4$ is also a volatile liquid that reacts similarly:

$$SiCl_4 + 2H_2O \rightarrow SiO_2 + 4HCl \qquad (2)$$

This could easily be incorporated later on in a coating system to produce multilayer high-low index coatings. The coating apparatus is illustrated in Fig. 2. Polypropylene was the chosen apparatus material because it was available, easy to machine, and inert to both the coating reagents and cleaning chemicals. The slide was connected to a timed reversing pneumatic cylinder that moved the sample back and forth past the slits delivering the reactants. The speed, stroke, and cycle time was adjustable.

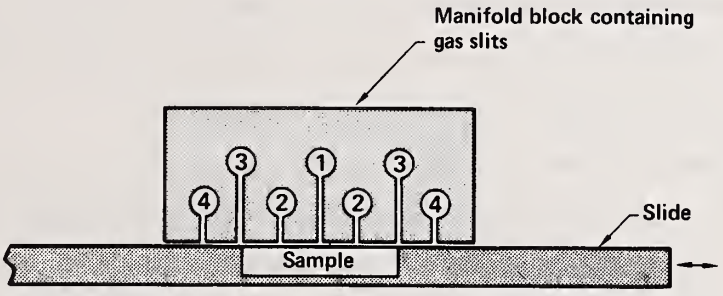

Figure 2. CVD Apparatus.

A number of coatings were made with the following gas configuration:

Slit 1 = N_2 + $TiCl_4$

Slit 2 = Vacuum

Slit 3 = Dry N_2

Slit 4 = N_2 + H_2O

The intent of this configuration was to keep the water separated from the $TiCl_4$ until after exposure to the substrate to avoid a gas phase precipitation. If the vacuum rate at slit two is greater than the $TiCl_4$ delivery at slit one but less than the sum of the $TiCl_4$ and N_2 at slit three, then the two reactant gases should not come in contact until after adhesion to the substrate.

Other combinations tried were:

Slit 1 = N_2 + $TiCl_4$

Slit 2 = Vacuum

Slit 3 = Dry N_2

Slit 4 = Vacuum

Outside = Humid air

and:

Slit 1 = N_2 + $TiCl_4$

Slit 2 = Vacuum

Slit 3 = N_2 + H_2O

These conditions represent a more extreme attempt to maintain the separation between $TiCl_4$ and H_2O in the former and to have the reactants combine just above the substrate in the latter. Heating the reactants was also tried in some cases.

Post treatments included exposure to liquid water, ammonia gas, and heat. The water and ammonia were used to drive the reaction to completion via hydrolysis or HCl removal. The post heat treatment was to drive off any remaining chlorine, hydroxyl, water, or HCl and increase the refractive index.

Discussion and Results

Twenty-two TiO_2 coatings were made. They had an optical thickness from 1000Å to 2500Å and refractive indices from 1.8 to 2.4. Two samples were three layer TiO_2-SiO_2-TiO_2 where $TiCl_4$ was substituted with $SiCl_4$ to form the low index SiO_2 layer. These coatings had a total optical thickness of approximately 5000Å. Deposition rates ranged from 45 min. to 4 hours per layer.

Most coatings exhibited some degree of scatter when examined under an intense light beam. We believe the scatter was due to gas phase reaction and precipitation. This was evident by a substantial amount of TiO_2 powder accumulation in the vacuum slit of the apparatus. It would appear that the gas streams were not as well separated as planned. All coatings lacked uniformity, indicating greater precision is required in apparatus construction. In general, the faster the coating was deposited, the more scatter it exhibited. The exception being when the delivery of H_2O became small in comparison to the $TiCl_4$ rate, the scatter would decline. These coatings were soluble in water, indicating that hydrolysis was not complete. In practice, this required the flow of $TiCl_4$ to be high resulting in a coating being deposited in 30 min. or less.

Damage testing was performed with a uniform three millimeter diameter beam of 1.06 μm light at 1-ns duration. Each sample was irradiated at various energy levels until a damage threshold, ± 15%, was determined. No test site was irradiated more than once. Each site was inspected under a microscope at 108x and photographed using Polaroid 667 (ASA 3000) film. Any observable change was considered to be damage. Energy levels 50% greater than the damage thresholds typically were below the resolution of the photographs.

The ten coatings with least scatter were damage tested. These included three multilayer ones which damaged at 3.4, 3.5 and 4.4 J/cm^2. The seven remaining single layer coatings damaged at 4.2, 5.3, 5.8, 7.8, 8.7, 9.0, and 12.9 J/cm^2.

Conclusion

This CVD process has demonstrated that it is possible to deposit TiO_2 thin films of high refractive index and good optical performance. Some of these coatings demonstrated a laser damage threshold that is superior to those made from conventional evaporation techniques.

References

1. W. T. Pawlewicz, R. Busch, D. D. Hays, P. M. Martin, and N. Laegreid; Laser Induced Damage in Optical Materials Processes, (1979).
2. G. Haas, Vacuum, 2, No. 4, p. 331 (1952).
3. K. S. Yeung, Y. W. Lam, Thin Solid Films, 109 (1983).
4. A. E. Feuersanger, IEEE Proceedings, pp. 1463-1465 (Dec. 1964).
5. J. M. Blocker, Jr., Thin Solid Films, 77, pp. 51-63 (1981).
6. E. T. Fitzgibbons, K. J. Sladek, W. H. Hartwig, J. Electrochem. Soc., 119, No. 6 (June 1972).
7. C. C. Wang, K. H. Zaininger, M. T. Duffy, RCA Review, pp. 728-741 (Dec. 1970).
8. H. J. Hovel, J. Electrochem. Soc., 125, No. 6 (June 1978).
9. S. Patai and M. Michman, J. Crystal Growth, 17, p. 298-301 (1972).
10. K. J. Sladek and H. M. Herron, I & EC, 11, p. 92 (March 1972).

3065R

Manuscript Received
11-3-86

Nondestructive Depth Profiling of Optically Transparent Films by Spectroscopic Ellipsometry

K. Vedam, S.Y. Kim, L. D'Aries
Materials Research Laboratory and Department of Physics
The Pennsylvania State University
University Park, PA 16802

and

A.H. Guenther
U.S. Air Force Weapons Laboratory
Kirtland Airforce Base, NM 87117

Spectroscopic ellipsometric (SE) measurements followed by linear regression analysis of the SE data obtained on optically transparent thin films of ZnS and MgO on vitreous silica substrates, reveal the distribution of voids (or low density regions) in these thin films.[A]

Key Words: Depth profile, thin films, voids, spectroscopic ellipsometry

1. Introduction

It is well known that the internal physical structure of vacuum deposited optical thin films are not homogeneous, but are actually composites of high density columnar structures (with their column running across the films in the direction of film growth) and low density regions or voids. The geometry of the network of voids or low density regions possesses essentially an infinite variability depending on the preparatory history of the film, and in general the percentage of voids fraction can and does vary with the thickness of the film. This inhomogeneity and its effect on the optical properties of the film has been the subject of a number of recent studies [1-12]. The most exhaustive study to date is that of Borgogno et al. [6,10] who have developed a metnod of determining the complex refractive index, the thickness and the magnitude of inhomogeneity from an analysis of normal incidence spectral reflectance and transmittance results with the assumption that the refractive index of the film decreases (or increases) linearly with thickness due to inhomogeneity. This assumption is not always valid, as will become evident from what follows.

Very recently Vedam et al. [13,14] have demonstrated that spectroscopic ellipsometry (SE) can be used to depth-profile multilayer structures of semiconductors yielding the thickness and composition of each layer and that such results are in excellent agreement with the direct results obtained by cross section transmission electron microscopy of the same specimens. The present article describes the results of similar depth profile study by SE on optically transparent thin films of ZnS and MgO on vitreous silica substrates. The technique of SE has in fact been used by Arwin and Aspnes [15] to determine the thickness and the dielectric function of thin films, but for the case when the substrate has a strong optical structure (i.e., a critical point as in crystalline Si or Ge etc.). When the substrate (like vitreous silica) does not have a structure, the technique of Arwin and Aspnes cannot be employed.

Thin films (~170nm thick) of ZnS and MgO were deposited on vitreous silica substrates by the standard technique of evaporation in high vacuum. The samples were exposed to normal atmospheric environment for a number of months before SE measurements were performed. The spectroscopic ellipsometer employed is a rotating polarizer type commercial unit manufactured by Sopra, Bois-Colombes, France. SE measurements were carried out at 50 wavelengths equally spaced in the spectral range 350-800nm. The SE data were then analyzed by linear regression analysis (LRA) technique of screening a number of appropriate models following the procedure

[A]Careful assessment of SE data can be used as well to address water infiltration by thin films by recourse to analysis of dispersion characteristics.

described elsewhere [14]. The selection of the final model was based on the simultaneous fulfillment of the following three criteria (i) lowest value of the unbiased estimate of standard error σ, (ii) reasonably low values of the 90% confidence limits of the variable parameters employed in the model and (iii) good agreement between the calculated and observed values of the complex dielectric constant $(\varepsilon_1+i\varepsilon_2)$ or of the ellipsometric parameters cos Δ and tan ψ as a function of wavelength.

Figure 1(a) shows the observed values of $\bar{\varepsilon}_2$ the imaginary part of the pseudo-dielectric constant of ZnS, along with the corresponding values calculated using the simplest model of a single homogeneous layer of pure ZnS on vitreous silica substrate. Czyzak et al.'s [16] data on the dispersion of the refractive index of β-ZnS was used as the reference data in these calculations. The LRA analysis technique yielded the thickness of the ZnS film to be 178.5$\pm$0.7nm. However it is seen that the value of σ is rather large and the agreement between the calculated and observed values of $\bar{\varepsilon}_2$ is not good. Further from this figure it is seen that the calculated and the observed $\bar{\varepsilon}_2$ peaks alternate as a function of the photon energy (or the wavelength) as in the interference pattern obtained with <u>two</u> film layers. Consequently a two layer model with varying percentages of voids was tried. The LRA analysis yielded the parameters of the variables employed as shown in Fig. 1(b). It is seen that the value of σ has improved slightly, but a marked improvement in the fit between the calculated and observed values of $\bar{\varepsilon}_2$ is observed particularly at longer wavelengths. This indicates that now the discrepency is confined to the shorter wavelength region, where again one notices the calculated and observed peaks in $\bar{\varepsilon}_2$ alternate as a function of wavelength. Using the same argument as before and the fact that the incident light with shorter wavelength samples only the surface layer due to its high absorption, indicates that the top most layer in Fig. 1(b) must be subdivided again into two layers with varying void contents.

Hence such a three layer model with voids in all the three layers was tested with LRA technique. As can be seen from Fig. 1(c) we now obtain a good low value of σ as 0.037 as well as an excellent agreement between the calculated and the observed values of $\bar{\varepsilon}_2$. The corresponding agreement in the values of $\bar{\varepsilon}_1$ is also excellent even though it is not presented here. Furthermore the low figures of the 90% confidence limits of the estimated values of the thickness of the different layers also support the validity of this model. Thus the present studies show that the ZnS film on vitreous silica substrate can be described as composed of three distinct layers: namely (i) a bottom layer of 115.8nm of ZnS with 3% voids, (ii) an intermediate layer of 47.6%nm of ZnS with 1$\pm$1% voids i.e., almost no voids and (iii) a topmost layer of 20.8nm of ZnS with 17% voids representing a micorough surface region [13-14,17-18].

There have been numerous reports in the literature [18-21] that many of the optical thin films, on exposure to normal ambient atmosphere adsorb water vapor to such an extent that the effective index of the films is noticeably altered. Since our present samples had been exposed to the normal atmosphere for a period of a few months, the three layer model shown in Fig. 1(c) was reexamined by the LRA technique with the voids replaced by water. The data of Tilton and Taylor [22] on the dispersion of the refractive index of water were used for this analysis. The results of the LRA analysis clearly ruled out the presence of water in this ZnS film as judged by the high value of σ (0.73) and negative values of the void fraction of water in the film. Since the dispersion of the refractive index of water is so different from that of air (or void), the SE technique would have detected even partial monoatomic layer of water if present in the film. Such a result is not surprising considering the fact that the middle section of the film is almost theoretically dense [See Fig. 1(c)] and hence any adsorption of water on the surface cannot migrate and be stored into the bulk of the film.

Figure 2 shows the final results of similar SE studies followed by LRA analysis of the SE data obtained on MgO film on a vitreous silica substrate. For the LRA of these data, Stephens and Malitson's [23] data on the dispersion of the refractive index of MgO were used. Here again the observed SE data could be explained satisfactorily only by a three layer model for the MgO film on vitreous silica substrate - i.e., (i) a bottom layer of 106.9nm of MgO with 0.6% voids, (ii) an intermediate layer of 43.3nm of pure MgO and (iii) a topmost layer of 22.9nm of MgO with 8% voids representing the microrough surface region. Here it must be mentioned that even though the intermediate region was scanned by LRA technique for the

[B]The LRA modeling procedure adopted treats the roughness (between the environment and the film) as void-like, i.e., a greater roughness will appear as a region of reduced density of higher void content and vice versa.

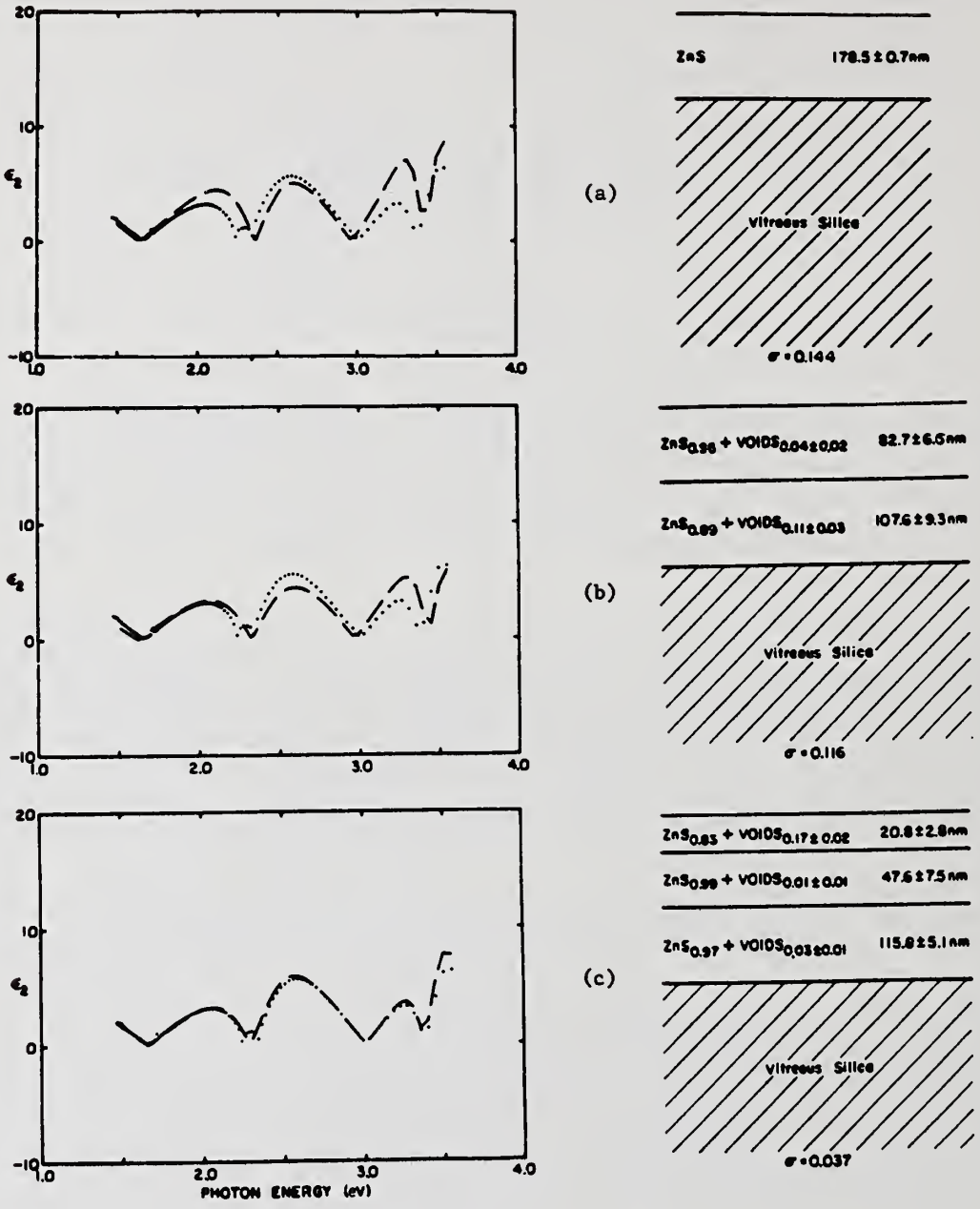

Figure 1. Imaginary ($\bar{\epsilon}_2$) part of the pseudo-dielectric function $\bar{\epsilon}$ as a function of photon energy of ZnS film on vitreous silica substrate .... observed data, xxxx calculated daa. (a) Single layer model, (b) 2 layer model, (c) three layer model.

presence of voids in the range of 0-10%, the final result yielded by the computer was 0.00 ± 0.00% thereby clearly indicating that the intermediate region is truly void-free.

The recent SE study of rf sputtered a-Ge films by McMarr et al. [24] also reveal very similar distribution of void structure in the a-Ge films. Thus the present work as well as the results on a-Ge film clearly support the model of film growth based on continual competition for random cone growth. The cones originate from the clustering which occurs due to random ballistic aggregation [25] and grow due to the atomic self shadowing [26] leading to

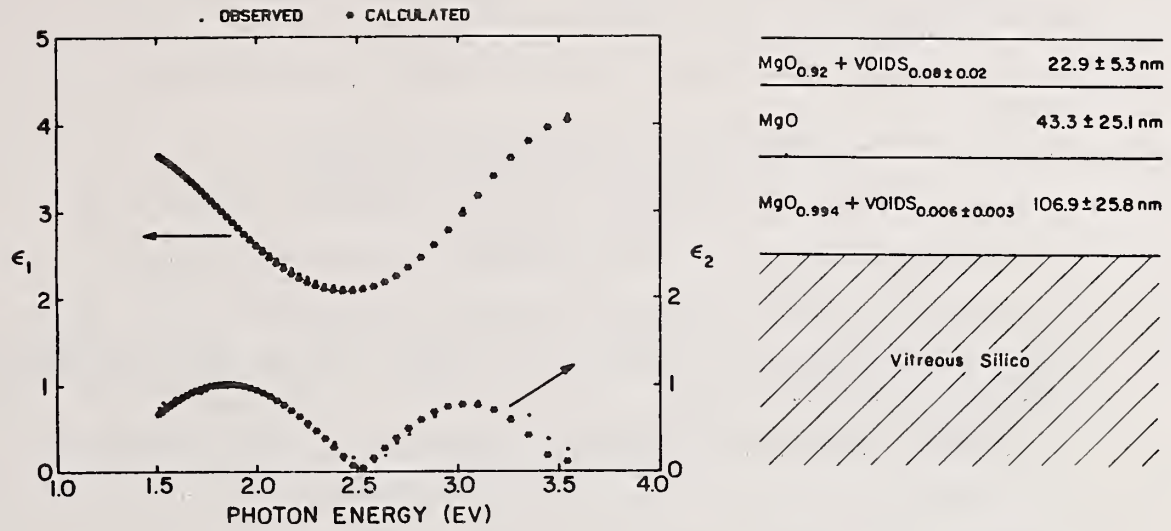

Figure 2. Real ($\bar{\epsilon}_1$) and imaginary ($\bar{\epsilon}_2$) parts of the pseudo-dielectric function $\bar{\epsilon}$ as a function of photon energy of MgO film in vitreous silicate substate .... observed data, xxx calculated data.

random fractal description of void network structure. Using such a model Messier and Yang [27,28] have recently simulated with the help of a computer the cross sectional growth evolution of films, in which the cones are initially distributed randomly, the growth cones shaped according to a power law [29,30], the competition for cone growth-death decision when two cones intersect as random, and the top surface curvature of each cone as an arc of a circle. Such a study reveal for a typical minimum cluster size (10-30Å) and associated nucleation (cluster) density, the cones become nearly vertical after about 500nm for a typical exponent of 2 (i.e., parabolic shaped cones) and ~100nm for exponent of ~3. The distribution of void structure in ZnS and MgO film indicate that the exponent of 3 is a more appropriate figure for the power law of growth function of these films.

The authors would like to express their gratitude to the National Science Foundation for the support of this work through grant No. CBT-85-04076 and to the U.S. Dept. of Energy for the equipment grant No. DE-FG05-84ER75158 to acquire the spectroscopic ellipsometer.

2. References

[1]. W.L. Bragg and A.B. Pippard, Acta. Cryst. 6, 865-867 (1953).

[2]. V.N. Yadava, S.K. Sharma and K.L. Chopra, Thin Solid Films 21, 279-312 (1974).

[3]. M. Harris, H.A. Macleod, S. Ogura, E. Pelletier and B. Vidal, Thin Solid Films 57, 173-178 (1979).

[4]. E. Ritter, Appl. Opt. 20, 21-25 (1981).

[5]. R.J. King and S.P. Talim, Optica Acta 28, 1107-1123 (1982).

[6]. J.P. Borgogno, B. Lazarides and E. Pelletier, Appl. Opt. 21, 4020-4029 (1982).

[7]. F. Horowitz and H.A. Macleod, Proc. SPIE 380, 83 (1983).

[8]. P.J. Martin, R.P. Netterfield and W.L. Sainty, Jour. Appl. Phys. 55, 235-241 (1984).

[9]. M. Harris, M. Bowden and H.A. Macleod, Opt. Commns. 51, 29-32 (1984).

[10]. J.P. Borgogno, F. Flory, P. Rouche, B. Schmitt, G. Albrand, E. Pelletier and H.A. Macleod, Appl. Opt. 23, 3567-3570 (1984).

[11]. R.P. Netterfield, W.G. Sainty, P.J. Martin and S.H. Sie, Appl. Opt. 24, 2267-2272 (1985).

[12]. H.A. Macleod, Jour. Vac. Sci. Tech. 4A, 418-422 (1986).

[13]. K. Vedam, P.J. McMarr and J. Narayan, Appl. Phys. Lettrs. 47, 339-341 (1985).

[14]. P.J. McMarr, K. Vedam and J. Narayan, Jour. Appl. Phys. 59, 694-701 (1986).

[15]. H. Arwin and D.W. Aspnes, Thin Solid Films 113, 101-113 (1984).

[16]. S.J. Czyzak, W.M. Baker, R.C. Crane, and J.B. Howe, Jour. Opt. Soc. Amer. 47, 240-243 (1957).

[17]. D.E. Aspnes, J.B. Theeten and F. Hottier, Phys. Rev. B20, 3292-3302 (1979).

[18]. D.E. Aspnes, Jour. Vac. Sci. Technol. 3A, 1018-1019 (1985).

[19]. S. Ogura and H.A. Macleod, Thin Solid Films 24, 371-375 (1976).

[19]. H.A. Macleod and D. Richmond, ibid 37, 163-169 (1976).

[20]. N.E. Holm and Christensen, ibid 67, 239-244 (1980).

[21]. S.G. Saxe, M.J. Messerly, B. Bovard, L. Desandre, F.J. VanMilligen and H.A. Macleod, Appl. Opt. 23, 3633-3637 (1984).

[22]. L.W. Tilton and J.K. Taylor, J. Res. Nat. Bur. Stds. 20, 419-477 (1938).

[23]. R.E. Stephens and I.H. Malitson, Jour. Res. Nat. Bur. Stand. 49, 249-252 (1952).

[24]. P.J. McMarr, J.R. Blanco, K. Vedam, R. Messier and L. Pilione, Appl. Phys. Letters 49, 328-332 (1986).

[25]. P. Ramanlal and L.M. Sander, Phys. Rev. Lett. 54, 1828-1831 (1985).

[26]. A.G. Dirks and H.J. Leamy, Thin Solid Films 47, 219-223 (1977).

[27]. Russell Messier, Jour. Vac. Sci. Technol. A4, 490-495 (1986).

[28]. B. Yang and R. Messier (to be published).

[29]. R.A. Roy and R. Messier, J. Vac. Sci. Technol. A2, 312-315 (1984).

[30]. R.A. Roy and R. Messier, Mat. Res. Soc. Symp. Proc. 38, 363-370 (1985).

Manuscript Received
2-9-87

Application of sol-gel coating to slab laser

T.Inazumi, K.Hara, and T.Izumitani

HOYA CORPORATION
Tokyo, Japan

The oscillation efficency of the slab laser has been improved with sol-gel coating film containing methyl radicals. Methyl radical in the silica coating film, effectively improves adherence and decreases refractive index(1.3756),removes pinholes and thereby improves chemical durability and mechanical strength. The sol-gel coating film was applied on the laser glass slab. The oscillation experiments showed the laser glass slab with the coating film has 1.85 times higher output energy and 2.3 times higher slope efficiency as the laser slab without the coating film.

Key words: bending strength; chemical durability; laser glass slab; pinholes; silica film including methyl radical; slope efficiency; sol-gel coating.

1. Introduction

The zig-zag slab geometry laser is very efficient in developing high average power. However, the maximum output energy of the laser glass LHG-5 or HAP-3 can not be extracted due to the scattering loss of the zig-zag laser beam on the slab surface.

Therefore we tried to improve the output laser energy of the laser slab by applying the sol-gel coating film on the slab surface to reduce the scattering loss. Simultaneously, we tried to improve the durability and mechanical strength of laser glass.

The requirements of sol-gel coating film are as follows:

(1)Refractive index of film is lower than 1.394 which meets the condition of total reflection.
(2)No pinholes.
(3)High chemical durability against coolant solutions.

To satisfy the above requirements, methyl radical was introduced into silica film because the conventional sol-gel silica film has many pinholes and the index of silica film is more than 1.40.

We expected that by introducing the methyl radical into silica film, the adhesion force between the film and glass will become stronger, and the pinholes and refractive index of silica film decrease. We found experimentally that the silica film including methyl radical has a refractive index of 1.3756, no pinholes and is very durable. The transmittance for the Xe lamp in the range of 400-1000nm is high. The laser output energy of LHG-5 with silica film including methyl radicals is 1.85 times higher than that without the film. The laser output energy of HAP-3 with the same film is 1.78 times higher than that without the film. Our experiment shows that the application of silica film including methyl radicals to laser glass slab increases the laser output energy dramatically.

2. Experiment procedure

2.1 Sol-gel coating process [1]

The raw materials are methyltriethoxysilane $CH_3Si(OC_2H_5)_3$ to introduce the methyl radical into the silica film, tetraethoxysilane $Si(OC_2H_5)_4$ to build the siloxane chain, water to hydrolyze the above mentioned silicone alchoxides, hydrochloric acid as catalyst for hydrolysis and ethanol as solvent. To prepare the coating solution a mixture of water, ethanol and hydrochloric acid were poured into solution of methyltriethoxysilane and tetraethoxysilane. The solution was stirred with a magnetic stirrer for 30 minutes.

Before dip coating, the coating solution was filtered through a 0.2μm membrane filter. The laser glass slab was dipped into the coating solution and pulled up at the speed of 3cm/min. After dipping, it must be dried at 120°C for 1 hour to vaporize water and ethanol. The film was heated at 320°C for 20 hours in an oxygen atmosphere to oxidize the ethoxy radicals, and then at 430°C for 20 hours in nitrogen atmosphere not to oxidize the methyl radical and to promote

dehydration.

Figure 1 shows the IR spectrum of the silica film including methyl radical. The dotted line shows transmittance of the film which had been dried at 120°C in air for 20 hours and the solid line is that of the film heated at 320°C in oxygen atmosphere for 20 hours and then at 430°C in nitrogen atmosphere for 20 hours.

The absorption of the ethoxy radical at 950cm^{-1}disappeared after heat treatment but that of the methyl radical at 1310cm^{-1}was not changed after heat treatment. According to the IR spectrum, the film prepared is consisted of silica film with methyl radicals.

The refractive index of the silica film including methyl radical at 1054nm is 1.3756 which meets the condition of total reflection. The thickness of the film was 2740Å.

The bending strengths of LHG-5 samples with silica film including methyl radicals, with the conventional sol-gel silica film and without the film were measured by using the three-point bending test. The test samples were of two types, one LHG-5 with polished surfaces,and the other LHG-5 with bottom surface ground(#1000)(and others surfaces polished) as shown in Table 1. The bending strength of the polished LHG-5 with the silica film including methyl radical was 1.34 times higher than that without the film. The bending strength of LHG-5 which has the bottom ground surface with coated the film was 1.98 times higher than that without the film.

This experimental result suggest that the strengthning mechanism of sol-gel coating is to fill microcracks due to grinding and prevent the propagation. The bending strength of the LHG-5 with the conventional sol-gel film was 1.75 times higher than that without the film. The bending strength of the LHG-5 with silica film including methyl radicals was higher than that with the conventional sol-gel silica film. It suggests that the adhesion forces between the silica film including methyl radicals and LHG-5 glass surface is stronger than that between the conventional sol-gel silica film and the LHG-5 glass surface.

Picture 1 shows the surface of conventional sol-gel silica film and that of silica film including methyl radicals after one week in water at 50°C. The conventional sol-gel silica has many defects in the film but the silica film including methyl radicals is not changed and has no defects. The silica film including methyl radicals is not changed for 11 days in water at 50°C and is not changed in a solution of ethylene glycol and water of a 1:0.95 molar ratio after 3 months. The silica film including methyl radicals has high transmittance in the range of 400-1000nm for Xe lamp irradiation.

2.2 Laser slab geometry

The laser glass slab used for experiment were LHG-5 with 6% Nd doping, 186mm x 60mm x 6mm in size and HAP-3 silicophosphate glass with 6% Nd doping of the same size. The number of zig-zag paths was 13 and the pumping light was provided by four 152.4mm long Xe flash lamps cooled by water and surrounded by gold reflectors. The pulse forming network(PFN) was a circuit against four lamps and the maximum voltage was 2.4KV. The maximum input energy to lamps was 1.1KJ. The cooling for the glass slab was made by air. The reflective ratio of flat output mirror was 60%. Figure 2 shows the structure of the laser head and figure 3 shows the cooling system of the laser glass slab and Xe lamps.

3. Oscillation experiment of sol-gel coated laser glass slab

We measured the output energy of HAP-3 and LHG-5 with silica film including the methyl radical and without film respectively.

The oscillation behaviors of HAP-3 with 6% Nd doping, with film and without film are shown in figure 4. The maximum output laser energy of HAP-3 with film was 37.6J, total efficiency was 3.5% and the slope efficiency was 3.9%. The maximum laser output energy of HAP-3 without film was 21.1J, the total efficiency was 2.0% and the slope efficiency was 2.8%. The total efficiency with film was 1.78 times higher than that without film, the slope efficiency with the film was 1.39 times higher than that without film.

The oscillation behavior of LHG-5 with 6% Nd doping with the film and without the film are shown in figure 5. The maximum laser output energy of LHG-5 with the film was 40.8J, the total efficiency was 3.8% and the slope efficiency was 4.2%, which the maximum output energy of LHG-5 without the film was 22.0J, the total efficiency was 2.1% and the slope efficiency was 1.8%. The total efficiency of LHG-5 with the film was 1.85 times higher than that without the film. The slope efficiency of LHG-5 with the film was 2.33 times higher than that without the film.

4. Conclusions

(1)A very good film (was obtained by a sol-gel process) consistng of silica film including methyl radicals. The properties are as follows:

No pinholes
High durability(stable for 3 months)
n=1.3756(λ =1054nm)

High transmittance for Xe lamp light

(2)By application of the film to LHG-5 slab, 4.2% slope efficiency was obtained and the maximum output energy was increased by a factor of two.

5. Reference

[1] T.Inazumi, K.Hara, C.Hata, and T.Izumitani: Japanese patent is applied

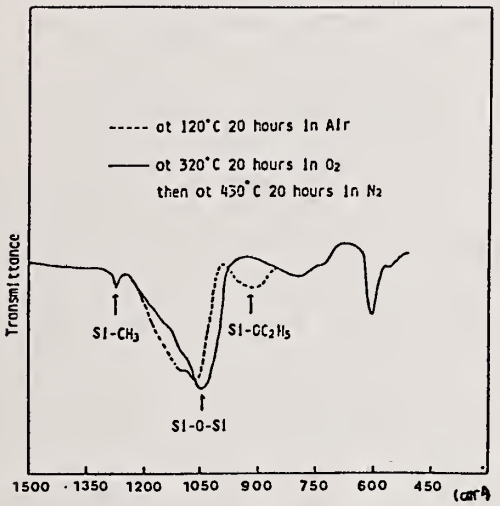

Fig.1 IR Spectra for SiO_2 including methyl radical

SiO_2 including methyl radical (After 1 week in 50°C water, x640)

Picture.1

TABLE 1

A) Bending Strength of Polished LHG-5

	SiO_2 Film Including Methyl Radical	No Film
Bending Strength (kg/cm²)	1800±300	1341±146
Ratio	1.34	1

B) Bending strength of LHG-5 Plate with Bottom Ground Surface and Other Polished

	SiO_2 Film Including Methyl Radical	SiO_2 Film	No Film
Bending Strength (kg/cm²)	1649±186	1489±58	833±130
Ratio	1.98	1.75	1

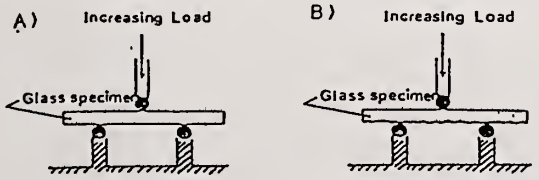

3-POINT BENDING

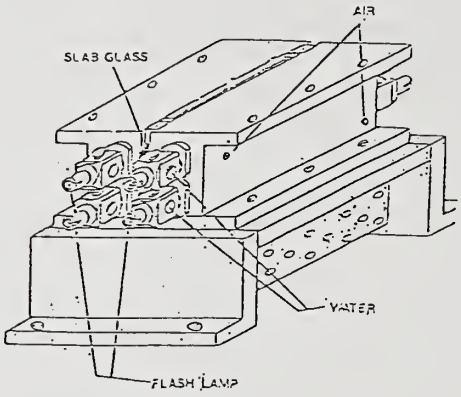

Fig.2 Slab Laser Head

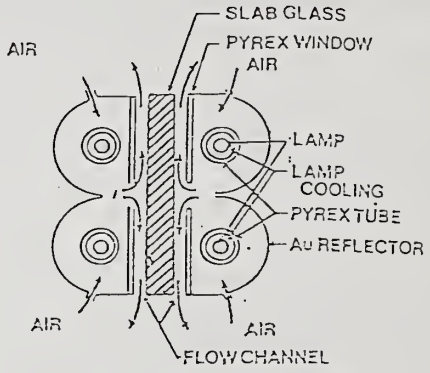

Fig.3 Cooling System

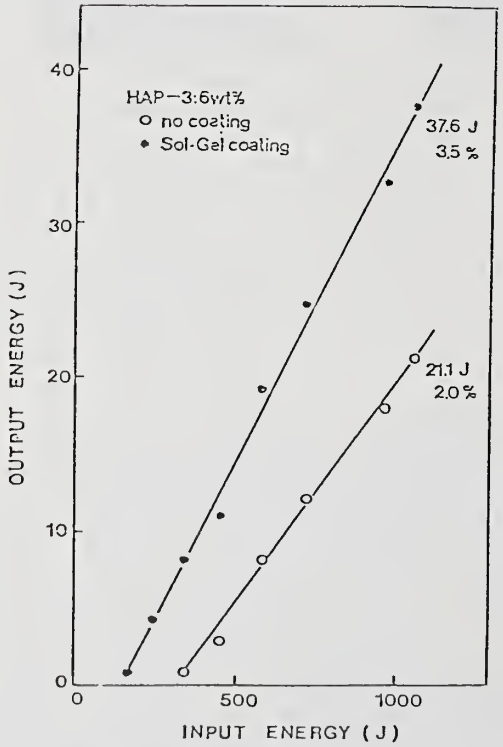

Fig.4 Oscillation behavior of HAP-3 laser glass

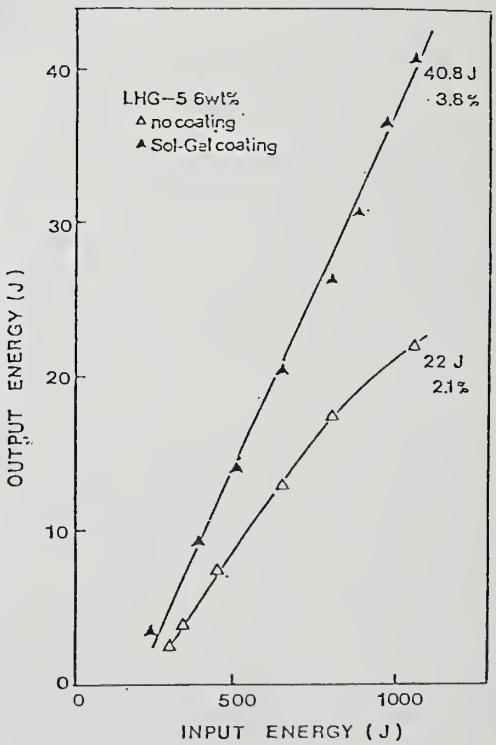

Fig.5 Oscillation behavior of LHG-5 laser glass

Manuscript Received
11-5-86

PROPERTIES OF IAD SINGLE- AND MULTI-LAYER OXIDE COATINGS

James J. McNally

Department of Physics
United States Air Force Academy, CO 80840-5701

F.L. Williams, S.R. Wilson and J.R. McNeil
University of New Mexico
Albuquerque, NM 87131

Properties of oxide thin films deposited using oxygen-ion assisted deposition (IAD) were studied. Previously,[1] we reported on the properties of Al_2O_3/SiO_2 and Ta_2O_5/SiO_2 anti-reflection coatings fabricated using IAD. In this report we present results illustrating the effects of ion bombardment during the deposition of single-layer films of Ta_2O_5, Al_2O_3 and SiO_2. The optical constants and stress measurements of these films are reported. Oxygen ion bombardment during deposition produced Ta_2O_5 and Al_2O_3 coatings with larger values of refractive index (n). No increase in n was observed for IAD SiO_2. Laser damage results at 351 nm for Al_2O_3/SiO_2 and Ta_2O_5/SiO_2 AR coatings are presented. It appears that the IAD coatings did not have higher damage threshold values than the coatings deposited with no ion bombardment. A number of coatings were exposed to fluorine gas tests. The results from these tests are reported.

Key Words: F_2 resistance; laser-damage; oxygen-ion assisted deposition

1. INTRODUCTION

The optical, physical and chemical properties of materials in thin film form can vary significantly from their bulk properties. These differences in properties are directly related to film microstructure which is predominantly columnar, containing voids and material inhomogeneities. Microstructure-related effects on coating performance can be observed in the following properties: increased optical scatter, degraded environmental durability, decreased optical stability and lower laser damage thresholds. A number of novel deposition techniques have been developed in attempts to improve the properties of thin films. One of these techniques is ion assisted deposition (IAD).

Ion assisted deposition employs a separate ion source to direct a beam of ions at the growing film during deposition. A separate ion source allows control of the ion energy, current density, arrival direction and species independent of the material deposition process. Thin films deposited using IAD have exhibited increased values of refractive index, improved stability and durability, and modifications in stress.[2-9] McNally et. al. reported the effects on the properties of Ta_2O_5 and Al_2O_3 films bombarded with O_2^+ during deposition.[2] They also deposited protective coatings at low temperature on heavy metal fluoride glass using IAD.[3] Martin et. al. have studied the effects of O_2^+ bombardment on the properties of ZrO_2 and CeO_2.[4,5] McNeil et. al. examined the effects of 30 and 500 eV O_2^+ bombardment on the properties of TiO_2 and SiO_2 films.[6,7]

This parametric study was an attempt to compare e-beam deposited Ta_2O_5 and Al_2O_3 coatings to ion assisted e-beam deposited coatings. The parameters varied were oxygen-ion energy and current density. The optical constants and stress measurements of single-layer coatings are reported. Single-layer coatings were tested for their resistance to fluorine gas attack. Anti-reflection (AR) coatings were laser damage tested at Los Alamos National Laboratory (LANL). The effects of

different filament materials in the ion source on laser-induced damage threshold (LIDT) values were studied. The results of these tests are presented.

2. EXPERIMENTAL ARRANGEMENT

The coatings were deposited in a cryogenic pumped vacuum system capable of routinely achieving a base pressure of 2.0×10^{-8} Torr. A schematic of the chamber is illustrated in Figure 1. A Kaufman ion source provided a monoenergetic, neutralized ion beam independent of the material evaporation process. It provided a beam of O_2 ions incident on the film during deposition at an angle of 45^{o}. The Ta_2O_5, Al_2O_3 and SiO_2 coatings were electron-beam evaporated at a rate of 0.30 - 0.40 nm sec^{-1} with oxygen backfill pressure of 1.0×10^{-4} Torr. The coatings were deposited onto substrates heated from the backside ($275^{o}C$). The gases used were Ultra High Purity grade (99.995+%) with a total hydrocarbon content less than 0.5 ppm.

The coating spectra were measured over the wavelength range 0.185 - 1.2 μm using a dual-beam spectrophotometer. These spectra were used to calculate the refractive index (n), the extinction coefficient (k) and the thickness (t) for each coating using a technique from Manifacier et. al.[8] The stress characteristics of a number of Ta_2O_5 coatings were measured using a ZYGO Mark III Interferometer System. The coatings were deposited onto 0.5 mm thick fused silica substrates. The interferometer used a phase measurement technique to perform optical wavefront measurements. The system modulated the interference pattern piezoelectrically and detected the varying light intensity with a diode array camera. The information was automatically evaluated by the processor module which performs a least-squares fit to calculate the fractional deviation of the interference pattern from a flat plane. The deviation (or deflection) from flatness is then analyzed following a technique given by Ennos.[9]

A few single-layer coatings were tested at LANL for their resistance to fluorine gas attack. The coated substrates were used as windows on one end of a gas filled cannister. The gas content was 0.5% F_2 in He at 3 atm. The transmittance at 351 nm was monitored at various time intervals to examine the durability of the coatings in the fluorine gas environment.

The AR coatings were laser damage tested at LANL by Stephen Foltyn and L. John Jolin.[10] (LIDT) values were measured with 9 nsec 351 nm pulses. The pulse repetition frequency was 35 pps. The laser beam was focused to give a beam spot diameter ($1/e^2$) of 0.46 mm at the sample. All the damage testing was n-on-m, where m=10 sites were irradiated at each laser fluence for a maximum of n=140 pulses. Damage was defined as any visible change in the coating observed under 60X microscope examination. The LIDT value was defined as the zero-probability intercept.[10] The AR coatings were deposited onto Corning 7940 fused silica substrates with bare surface LIDT values equal to 8 J cm^{-2}. The coating design was SLLHL where S was the substrate, L was quarter-wave thick SiO_2 and H was quarter-wave thick Al_2O_3 or Ta_2O_5.

3. RESULTS

The values of n (at λ = 400 nm) for Ta_2O_5 coatings bombarded with 200, 300 and 500 eV oxygen ions are plotted in Figure 2 as a function of O_2^+ current density. The error bars indicate the uncertainty in the index values introduced by the precision of the spectrophotometer. The values increased from 2.16 for coatings deposited without bombardment to maximum values of 2.25, 2.28 and 2.19 for films bombarded with 500, 300 and 200 eV O_2^+, respectively. The increase in the values of n with increasing O_2^+ current density indicated that ion bombardment during deposition

resulted in film densification. The results indicated that the coatings bombarded with 300 eV O_2^+ had larger values of n than those bombarded with 500 eV O_2^+. A similar dependence of refractive index on bombarding ion energy has been reported for other ion assisted films.[4,5]

The current density value (for a fixed ion energy) at which the maximum n occurs is often termed the critical value. The results in Figure 2 illustrate that film index values decreased for ion current densities larger than the critical values. The decrease in index may be explained as a result of degradation in film stoichiometry, creation of closed isolated voids or oxygen incorporation into the films. The decrease was largest for bombardment with 500 eV ions and least for 200 eV ions. Similar results for which the values of refractive index decreased for current densities larger than the critical values have been reported.[2,4,5]

The coatings bombarded during deposition at oxygen ion current densities up to approximately the critical values exhibited good optical characteristics. For higher levels of bombardment, the optical absorption of the coatings increased. In Figure 3, values of extinction coefficient (k) for Ta_2O_5 coatings (300 nm thick) bombarded with 500, 300 and 200 eV oxygen ions are plotted as a function of O_2^+ current density. The values of k were calculated at λ = 400 nm. The error bars indicate the uncertainty in the values of k introduced by the precision of the spectrophotometer. The dashed line across the bottom at $k = 2.0 \times 10^{-4}$ indicates the level below which the values of k were too small to be regarded as reliable because of the minimum absorption values measurable by the spectrophotometer (0.2%).

As illustrated in Figure 3, film optical absorption increased with higher levels of oxygen ion bombardment. The most probable mechanism for this is the preferential sputtering of oxygen in the Ta_2O_5 molecule. Preferential sputtering would result in oxygen-deficient layers continuously integrated into the coatings as deposition occurs. Values of k for coatings bombarded at a fixed current density were the lowest for 200 eV O_2^+, higher for 300 eV and highest for 500 eV O_2^+. This result is consistent with increasing preferential sputtering yields for higher energy ions. This mechanism has been observed in other IAD films.[4]

The values of n (at λ = 350 nm) for Al_2O_3 coatings bombarded with 300, 500 and 1000 eV oxygen ions are plotted in Figure 4 as a function of O_2^+ current density. The values increase from 1.64 for coatings deposited without bombardment to maximum values of 1.70, 1.68 and 1.68 for films bombarded with 1000, 500 and 300 eV O_2^+, respectively. The increase in the values of n for increasing levels of O_2^+ current density is similar to Ta_2O_5 results (Figure 2) and indicated that ion bombardment during deposition resulted in film densification. The results indicated that the Al_2O_3 coatings bombarded with 1000 eV O_2^+ had larger values of n than those bombarded with 500 and 300 eV O_2^+. These results illustrate that the effects of ion bombardment on the values of n are material dependent. The ion energy at which the largest value of n occurred for Ta_2O_5 was 300 eV, yet, for Al_2O_3 it was 1000 eV. The results in Figure 4 illustrate that values of n decreased for ion current densities larger than the critical values. The decrease was largest for bombardment with 1000 eV ions and least for 300 eV ions. This energy dependent decrease is consistent with the results for IAD Ta_2O_5 coatings (Figure 2).

Attempts to measure the values of extinction coefficient for the Al_2O_3 coatings (400 nm thick) were limited due to the minimum sensitivity of the measurement equipment. All computed values of k were less than 2.0×10^{-4}. The low values of k calculated for all the Al_2O_3 coatings indicate that for the conditions examined, preferential oxygen sputtering is not a dominant mechanism for Al_2O_3 as was the case for Ta_2O_5 (Figure 5). This result again illustrates that the

effects of ion bombardment on film properties are material dependent.

The values of n for SiO_2 coatings bombarded during deposition with 300 and 500 eV O_2^+ are listed in Table I. The values of refractive index for SiO_2 were measured using an ellipsometer at λ = 633 nm. The values of n in Table I do not vary by more than the precision of the measurement technique. Therefore, there was no significant effect on the refractive index of SiO_2 due to ion bombardment during deposition.

TABLE I

IAD Conditions and Refractive Index Values for SiO_2

E (eV)	J ($\mu A\ cm^{-2}$)	n (λ = 633 nm)
0	0	1.44
300	30	1.45
300	60	1.45
300	90	1.45
300	195	1.43
500	30	1.45
500	60	1.44
500	90	1.45
500	195	1.45

A number of Ta_2O_5 coatings were examined for intrinsic stress. The stress was measured interferometrically. The stress was computed from measured substrate bending, and because film thickness was much less (factor of 1000) than substrate thickness the elastic constants of the coating were not required. The stress was assumed uniform and isotropic in the coating. The stress induced a deflection of the substrate from an ideal optical flat. The deflection from flatness was defined as Δ in units of μm. The stress was computed using the equation[9]

$$S = \frac{4}{3} \frac{Y}{(1-\nu)} \frac{d^2}{D^2} \frac{\Delta}{t}$$

The values of Young's Modulus (Y) and Poisson's ratio (ν) for the fused silica stress substrates were 7.31×10^{10} N m^{-2} and 0.16, respectively. The substrate diameter (D) and thickness (d) were 25.4 mm and 0.51 mm, respectively. The film thickness (t), in units of μm, was calculated from transmittance spectra for each coating. Because the uncoated substrates deviated from ideal flats, each substrate was characterized before and after coating.

Figure 5 illustrates the values of film stress plotted versus oxygen ion current density. The triangles (Δ) and circles (o) represent stress values for coatings bombarded during deposition with 300 and 500 eV O_2^+, respectively. The results indicated film stress was compressive and increased for increasing levels of ion bombardment.

A number of coatings were studied for the effects of static exposure to F_2. To date the results from tests at LANL have shown degradation in optical performance of almost all coatings exposed to F_2. Three single-layer Al_2O_3 coatings were exposed to 0.5% dry F_2 in He gas mixture and their transmittance at 351 nm was measured at various time intervals. The three coatings were multiple half-wave in optical thickness at 351 nm. Figure 6 illustrates the results of the F_2 testing for Al_2O_3 coatings. The vertical axis is the decrease in transmittance at 351 nm

relative to the pretest value, in percent. The horizontal axis is the length of time the coating was exposed to F_2. The coating deposited with no ion bombardment (J=Ø) suffered no degradation in transmittance after 67Ø hours of exposure. Although not shown in the figure the transmittance for this coating dropped by 4% after 1ØØ3 hours. The Al_2O_3 coating bombarded during deposition with 5ØØ eV O_2^+ at a current density of 5Ø A cm^{-2} suffered 4.5% loss in transmittance after 47Ø hours of exposure. The coating bombarded with 5ØØ eV O_2^+ at 25 μA cm^{-2} suffered 1Ø% loss in transmittance after only 28 hours exposure. Figure 7 illustrates the results of F_2 testing for SiO_2 coatings. The J=Ø SiO_2 coating suffered Ø.5% loss after 698 hours. The coating bombarded during deposition with 5ØØ eV O_2^+ at J=21 μA cm^{-2} suffered 4.5% transmittance loss after 385 hours. The coating bombarded with 5ØØ eV O_2^+ at J=12 μA cm^{-2} suffered 7.5% loss after only 5Ø3 hours. Four Ta_2O_5 coatings were exposed to F_2. The four coatings all suffered a >5% loss in transmittance after only 3ØØ hours exposure. The performance of the Ta_2O_5 coatings was very poor relative to required performance criteria.

The zero-probability LIDT values for Al_2O_3/SiO_2 coatings bombarded with 3ØØ and 5ØØ eV oxygen ions are plotted versus O_2^+ current density in Figure 8. Tantalum (Ta) filaments were used in the ion source for all the results in Figure 8. The values plotted are the average LIDT values for coatings deposited under the same conditions. The error bars represent the range of LIDT values obtained for all the coatings deposited under the same conditions. With one exception, it appears that the IAD coatings did not have higher LIDT values than the coatings deposited with no ion bombardment (J=Ø). The coatings bombarded with 3ØØ eV O_2^+ at a current density of 1Ø μA cm^{-2} had an average LIDT value of 6.1 J cm^{-2} with a ±7% variation for the coatings tested. This represents a 65% increase in LIDT value over the J=Ø coatings.

Figure 9 illustrates the effects of different cathode filaments in the ion source on LIDT values. A contamination analysis of IAD coatings indicated that tungsten (W) filament material was incorporated into the coatings.[11] The amount of W present in the TiO_2 coatings ranged from 13Ø to 51Ø ppm and increased as J increased. As part of this study a number of IAD AR coatings were deposited using W filaments in the ion source ("W coatings"). Another set of coatings were deposited using identical IAD conditions except Ta filaments were used in the ion source ("Ta coatings"). The purpose of this comparison was to attempt to control one defect in IAD coatings and to measure LIDT values for coatings in which different filaments were used.

As observed in the figure the "Ta coatings" had LIDT values consistently higher than the "W coatings". The largest difference is for the higher energy (5ØØ eV), higher current density (4Ø μA cm^{-2}) case. The average value of the increase in LIDT for the "Ta coatings" was 4Ø%. This exceeded the run-to-run variations in LIDT values which was ±25%. The results appear to indicate an improvement in LIDT value for "Ta coatings" over "W coatings".

The laser damage results were analyzed for both sample-to-sample variations and run-to-run variations in LIDT values. Sample-to-sample variations were calculated for three sets of two coatings each deposited at the same time. Run-to-run variations were calculated for three sets of two coatings each deposited using identical IAD conditions but at different times. The average value of the sample-to-sample variations was ±14%. The average value of the run-to-run variations was ±25%. When the damage thresholds were measured several times for the same coating, the results agreed to within ±5%.

The zero-probability intercept fluence values for Ta_2O_5/SiO_2 AR coatings bombarded with 3ØØ and 5ØØ eV O_2^+ are plotted versus O_2^+ current density in Figure 1Ø. Only a limited number of

coatings (9) were tested which precluded examining laser damage for wide variations in the parameter set. This also limited the number of coatings which were deposited with similar IAD conditions but in different runs. For the conditions examined, it appears that the IAD coatings did not have higher LIDT values than the coatings deposited with no ion bombardment (J=Ø). The LIDT values for coatings bombarded during deposition with 5ØØ and 3ØØ eV O_2^+ at current densities of 4Ø and 6Ø μA cm^{-2}, respectively, were 32% lower than the J=Ø coatings. This decrease in LIDT values is consistent with the increase in optical absorption for single-layer Ta_2O_5 coatings deposited using identical IAD conditions (Figure 3).

4. DISCUSSION

The dynamics of fluorine gas attack in optical coatings are not well understood. One could speculate that less porous coatings would be more resistant to F_2 attack. The reason for this is that denser coatings would adsorb less water. When exposed to F_2 gas the tendency to form HF would be smaller because the hydrogen content in the coatings would be small. There is evidence which supports the contention that IAD coatings are dense. The evidence includes larger values of refractive index, decreased optical scatter and improved optical stability.[1,4] This would indicate that IAD coatings should be less susceptible to F_2 attack. However, the results obtained from the fluorine tests in this study do not support this contention.

The transmittance spectra for a few of the coatings exposed to F_2 were measured. The Al_2O_3 spectra neither shifted in wavelength nor did the differences in the transmittance extrema change significantly. These results indicated that material was not converting to AlF_3 nor eroding away during exposure. The coatings did become foggy during exposure. This characteristic plus the behavior of the spectra indicated that scattering was the most probable loss mechanism. For the Ta_2O_5 coatings there was a clear indication that film material was eroding. It is likely that the oxide material was converting to TaF_5, a volatile substance.

5. SUMMARY

Oxygen ion bombardment during deposition produced Ta_2O_5 and Al_2O_3 coatings with increased values of refractive index. The increase in n was dependent on ion energy and current density. An increase in optical absorption was observed for IAD Ta_2O_5 coatings. Increases in optical absorption were not observed for Al_2O_3 or SiO_2 coatings. The effects on the optical constants of IAD coatings were found to be material dependent.

A limited number of coatings were subjected to F_2 gas tests. It appeared that IAD did not improve the resistance of the coatings to fluorine gas attack. Further testing is required to better understand the degradation mechanism(s). A number of Al_2O_3/SiO_2 AR coatings were laser damage tested. Only one set of IAD conditions resulted in an increase in LIDT values for the AR coatings. Due to the limited number of coatings examined, further testing is warranted before any definite conclusions can be made. As part of the laser damage study a number of IAD Al_2O_3/SiO_2 AR coatings were deposited using different filament materials in the ion source. The results indicated the "Ta coatings" had LIDT values consistently larger than the "W coatings". It appears for the Ta_2O_5/SiO_2 AR coatings examined in this study that ion assisted deposition does not improve their laser damage resistance at 351 nm. However, the results for single-layer Ta_2O_5 and Al_2O_3 coatings indicated that IAD produced coatings with larger values of refractive index, reduced optical scatter and improved environmental stability.[1,2] Further exploration of

the mechanisms for laser damage in IAD coatings is warranted.

REFERENCES

1. J.J. McNally, F.L. Williams, S.R. Wilson, and J.R. McNeil, "Properties of IAD Al_2O_3/SiO_2 and Ta_2O_5/SiO_2 Thin Film AR Structures," Nat. Bur. Stand. (US), to be published.
2. J.J. McNally, G.A. Al-Jumaily and J.R. McNeil, "Ion Assisted Deposition of Ta_2O_5 and Al_2O_3 Thin Films," J. Vac. Sci. Technol. A4, 437 (1986).
3. J.J. McNally, G.A. Al-Jumaily, J.R. McNeil and B. Bendow, "Ion-Assisted Deposition of Optical and Protective Coatings for Heavy Metal Fluoride Glass," Appl. Opt. 25, 1973 (1986).
4. P.J. Martin, R.P. Netterfield and W.G. Sainty, "Modification of the Optical and Structural Properties of Dielectric ZrO_2 Films by Ion-Assisted Deposition," J. Appl. Phys. 55, 235 (1984).
5. R.P. Netterfield, W.G. Sainty, P.J. Martin and S.H. Sie, "Properties of CeO_2 Thin Films Prepared by Oxygen-Ion Assisted Deposition," Appl. Opt. 24, 2267 (1985).
6. J.R. McNeil, A.C. Barron, S.R. Wilson and W.C. Herrmann, Jr., "Ion-Assisted Deposition of Optical Thin Films: Low Energy vs High Energy Bombardment," Appl. Opt. 23, 552 (1984).
7. J.R. McNeil, G.A. Al-Jumaily, K.C. Jungling and A.C. Barron, "Properties of TiO_2 and SiO_2 Thin Films Deposited Using Ion-Assisted Deposition," Appl. Opt. 24, 486 (1985).
8. J.C. Manifacier, J. Gasiot and J.P. Fillard, "A Simple Method for the Determination of the Optical Constants n, k and the Thickness of a Weakly Absorbing Thin Film," J. Phys. E9, 1002 (1976).
9. A.E. Ennos, "Stresses Developed in Optical Film Coatings," Appl. Opt. 5, 51, (1966).
10. S.R. Foltyn and B.E. Newnam, "Ultraviolet Damage Resistance of Dielectric Reflectors Under Multiple-Shot Irradiation," IEEE J. Quant. Elect. QE-17, 2092 (1981).
11. G.A. Al-Jumaily, S.R. Wilson, A.C. Barron, J.R. McNeil and B.L. Doyle, "Contamination Analysis of TiO_2 Thin Films Deposited Using Ion Assisted Deposition," Nucl. Instr. and Meth. B7/8, 906 (1985).

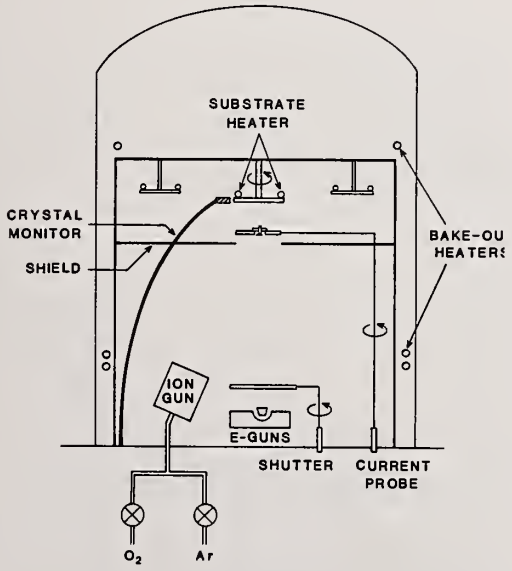

Figure 1. Schematic of deposition system.

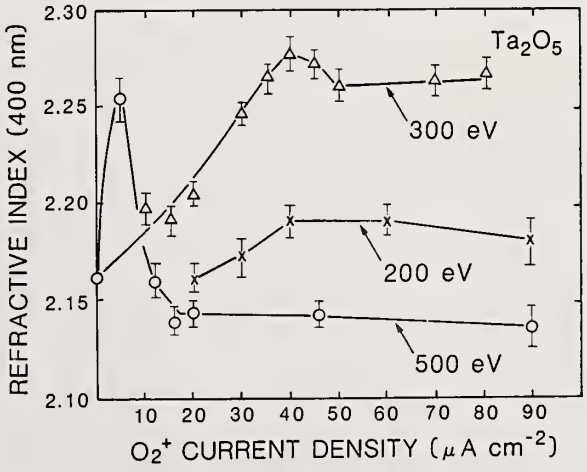

Figure 2. Values of refractive index for Ta_2O_5 coatings plotted as a function of O_2^+ current density.

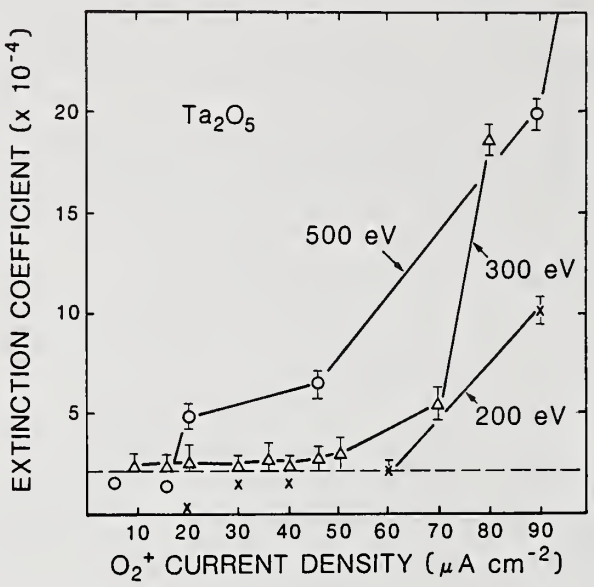

Figure 3. Values of k for Ta_2O_5 coatings plotted as a function of O_2^+ current density.

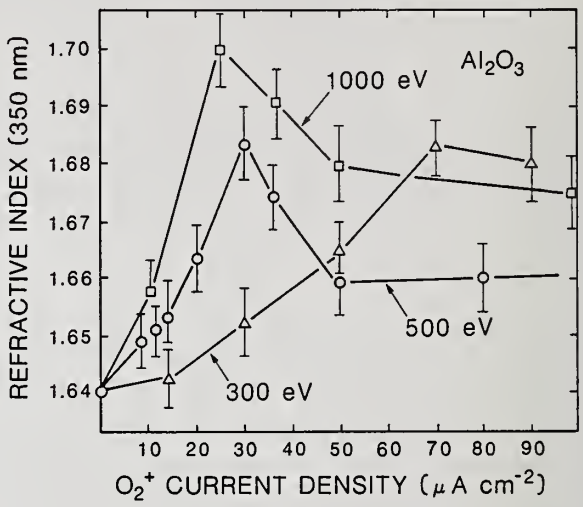

Figure 4. Values of refractive index for Al_2O_3 coatings plotted as a function of O_2^+ current density.

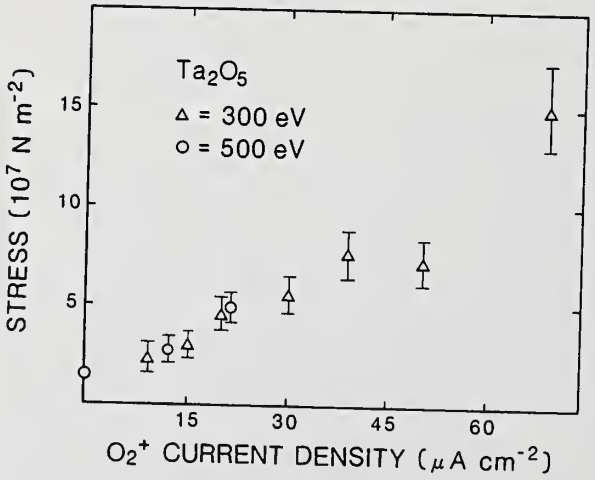

Figure 5. Values of stress for Ta_2O_5 coatings vs O_2^+ current density.

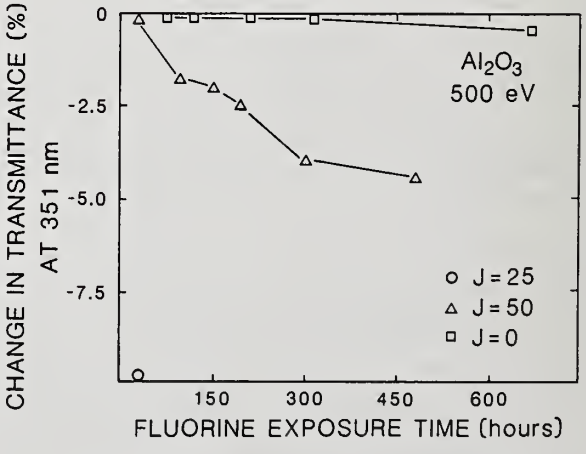

Figure 6. Decrease in transmittance at 351 nm for Al_2O_3 coatings vs F_2 exposure time.

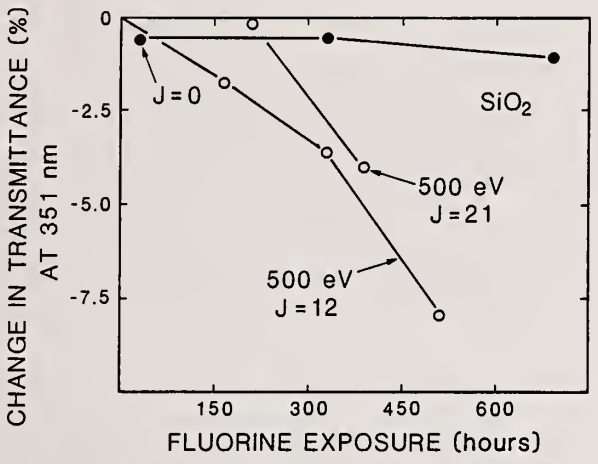

Figure 7. Decrease in transmittance at 351 nm for SiO_2 coatings vs F_2 exposure time.

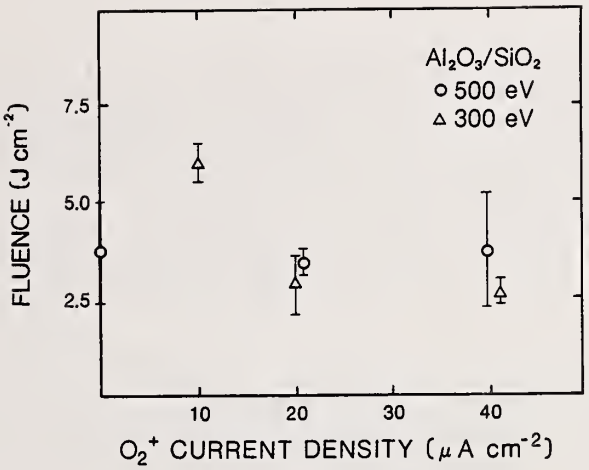

Figure 8. LIDT values for Al_2O_3/SiO_2 AR coatings vs O_2^+ current density.

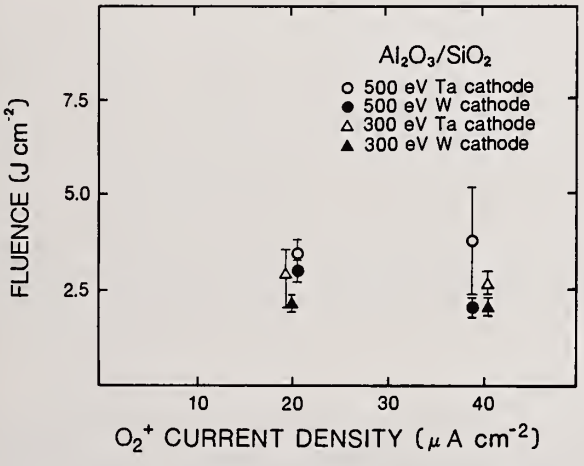

Figure 9. LIDT values for Al_2O_3/SiO_2 AR coatings deposited using W or Ta filaments in the ion source vs O_2^+ current density.

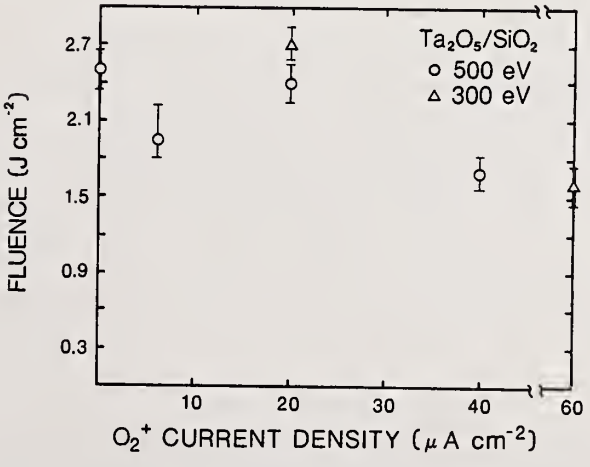

Figure 10. LIDT values for Ta_2O_5/SiO_2 AR coatings vs O_2^+ current density.

Manuscript Received
5-4-87

Comparison of the Optical Properties of some High-Index Oxide Films prepared by Ion Beam Sputter Deposition with those of Electron Beam Evaporated Films

Brad Pond, R. A. Schmell, C. K. Carniglia and T. Raj

Martin Marietta Aerospace, Laser Systems Technology
P. O. Box 9316, International Airport
Albuquerque, NM 87119

A typical thin film of a high-index oxide coating material deposited by electron-beam (E-beam) evaporation has a refractive index lower than the bulk value for the material. This indicates that the film is porous, having a density less than the bulk density. In addition, such films are often inhomogeneous, having a higher refractive index near the substrate surface. Thin films of the same materials deposited by ion beam sputter deposition (IBD) techniques tend to have higher and more uniform refractive indices, indicating that IBD films are denser and more homogeneous. We have measured the index of refraction n, the extinction coefficient k and the degree of inhomogeneity of several high-index oxide materials deposited by IBD and by standard E-beam evaporation. The materials investigated were the oxides of zirconium, tantalum, hafnium, niobium and aluminum. In all cases, the IBD films were found to have higher refractive indices than their evaporated counterparts. The IBD films, in general, exhibited an inhomogeneity which was the reverse of the inhomogeneity found in the E-beam films. This indicates a difference in the nucleation and growth of the films. Tantala films show an absorption band in the visible spectral region resulting from electron trapping sites. Thus, this material is probably not suitable for coatings for visible and UV laser systems.

Key Words: absorption; Al_2O_3; electron beam evaporation; HfO_2; inhomogeneity; ion beam sputter deposition; Nb_2O_5; refractive index; Ta_2O_5; ZrO_2.

1. Introduction

The process of formation of coatings by ion beam sputter deposition (IBS or IBD) involves directing an ion source at a target composed of a suitable coating material. The material sputtered from the target is directed towards the substrate being coated [1]. The sputtered particles have a significantly greater kinetic energy (tens of electron volts) than do conventionally evaporated species (approximately one-tenth of an electron volt) [2]. As a result of the higher energy of the particles condensing on the substrates, IBD coatings have several advantages over conventionally evaporated coatings. The films have a higher density, and thus a higher refractive index. The energetic sputtered particles dislodge adsorbed impurities from the substrate surface and from the coating as it is being deposited, thus leading to better adhesion and lower impurity levels. In addition, IBD coatings can be produced without applying external heat to the substrates. Two limitations of the IBD process are a low deposition rate (< 1 Å/s) and the high compressive stress of the films [3].

In the past several years, the IBD process has become more widely used for production of optical coatings; however, the published literature on these coatings is still limited [4 through 12]. A survey of these publications indicates that no systematic comparison has been made between the optical properties of IBD films and those of conventionally evaporated films. This paper presents such a comparison. In particular, single-layer films of five commonly used high-index oxide coating materials have been prepared using IBD and conventional electron-beam (E-beam) evaporation. The film materials are zirconia (ZrO_2), hafnia (HfO_2), tantala (Ta_2O_5), niobia (Nb_2O_5) and alumina (Al_2O_3). Each set of coatings (IBD and E-beam evaporated) was made under what might be considered a set of standard conditions for the particular process. The only parameter which was adjusted for particular materials was the oxygen pressure. The following section discusses the experimental procedures used in depositing and analyzing the films. This is followed by a section discussing the results.

2. Experiment

The IBD films were fabricated in a cryopumped, 20-in bell jar using a Kaufman-type ion source with a 3-cm aperture. A beam of argon ions with an ion energy of 1000 eV [5] was used to sputter material from a hot-pressed oxide target onto a rotating substrate. A partial pressure of oxygen was supplied directly into the chamber to achieve stoichiometric films [5]. The partial pressure of oxygen needed to achieve the desired stoichiometry was material dependent and varied between 2.0×10^{-5} torr and 1.0×10^{-4} torr. A total background pressure of 2.6×10^{-4} torr or 3.0×10^{-4} torr was used depending upon the material being deposited. The substrate temperature rose above ambient during deposition due to radiant heating from the ion source. The highest substrate temperatures varied from 40°C to 60°C. The deposition rates were in the range of 15-50 Å/min.

The E-beam films were deposited in an oil-diffusion-pumped, 18-in bell jar using E-beam evaporation. The vacuum system produced base pressures of 6.0×10^{-6} torr or lower. The partial pressure of oxygen was 1.4×10^{-4} torr for the tantala, 2.1×10^{-4} torr for the niobia and 3.5×10^{-5} torr for the alumina, hafnia and zirconia. The substrate temperature was maintained at approximately 225°C for all of the materials. The deposition rates varied depending upon the material and were in the range of 5-20 Å/s.

In both processes, the films were deposited on substrates held in racks which were rotated using single rotation. The substrates used for these coatings were 1-in diameter, 0.030-in thick, UV-grade fused silica. The film thicknesses were monitored using optical monitoring systems: the IBD films were monitored using front surface reflection monitoring, and the E-beam films, using transmission monitoring. In each case, an optical thickness of approximately five quarterwaves at 550 nm was deposited on the substrates.

The envelope method [13,14] was used for determining the optical constants and the physical thicknesses of the films. This method is based on the analysis of spectral scans of transmittance and reflectance of the samples. These scans were made on a Cary 2300 dual-beam spectrophotometer covering the visible, near-UV and near-IR wavelength range. The envelope method of analysis allows the determination of the refractive index n and the extinction coefficient k of the films. The method has been modified to allow for the determination of the degree of inhomogeneity $\Delta n/n$ of absorbing films [15]. This additional information provides useful insight into the growth process of the films.

Established procedures [13] were used for making the transmittance and reflectance measurements necessary for the determination of n, k and Δn. The transmittance measurements were made by first scanning an uncoated fused silica substrate and then scanning the coated part. The transmittance was determined by taking the ratio of the two scans. The reflectance was measured using a single-bounce reflectance attachment. The reflectance measurements were made at near-normal incidence, but the deviation from normal incidence was ignored. Only the reflectance from the first surface of the sample was measured. The reflectance from the second side was eliminated by using an index-matching fluid to attach a piece of fused silica to the back side of the sample being measured. The second surface of this piece of fused silica was frosted to diffuse the reflected light.

The necessary data were taken manually from the spectral scans and used to determine the optical constants and physical thicknesses of the films.

3. Results

The dispersive refractive index and absorption coefficient are presented for the five materials in figures 1 through 5. Each figure compares the n and k values of the IBD and E-beam films for that material. The refractive index curves are identified by either an "i" or an "e" to indicate whether the curve represents an IBD film or an E-beam film, respectively. The dispersive absorption coefficients are shown as solid curves for the IBD films and by broken curves for the E-beam films.

The precision in the determination of n is estimated to be 0.01, while the uncertainty in k ranges from about 0.0015 at the IR end of the spectrum to about 0.0003 at the UV end.

The major observation that can be made from the graphs presented in figures 1 through 5 is that, for each material, the refractive index is higher for the IBD film than it is for the

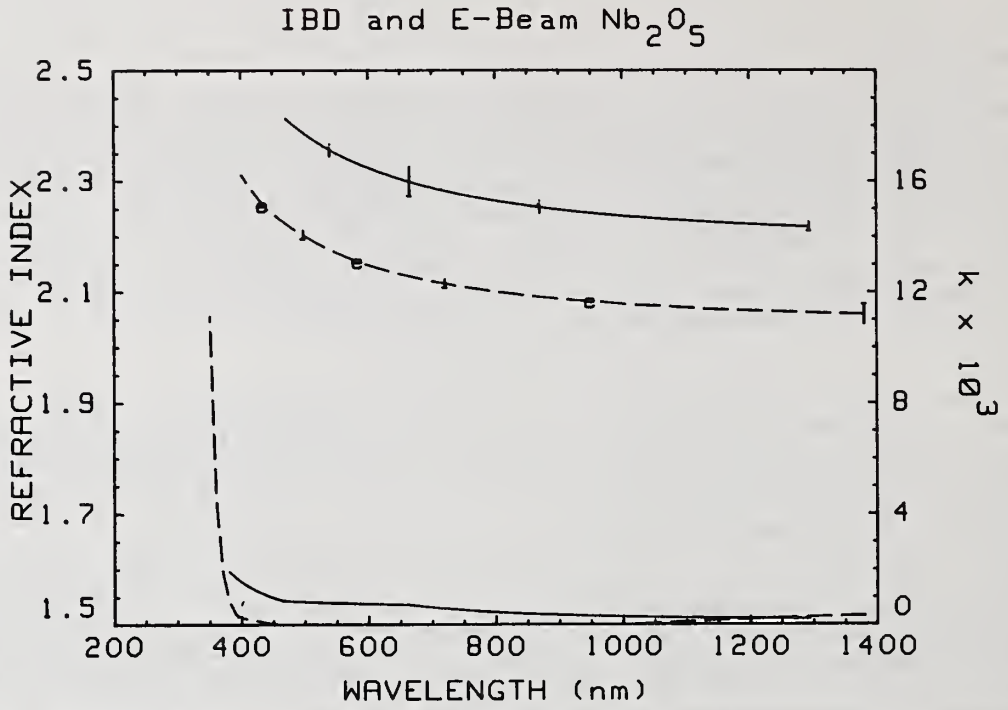

Figure 1. Dispersive Refractive Index and Extinction Coefficient for IBD and E-Beam Niobia.

NOTE: The refractive index curves are identified by an "i" for the IBD film and by an "e" for the E-beam film. The scale for the refractive index is given on the left-hand side of the graph. The vertical bars on the refractive index curves indicate the variation in index or inhomogeneity of the film. A more complete description of the interpretation of these bars is given in the text. The lower curves represent the extinction coefficient, plotted against the right-hand scale. The solid curve depicts the IBD film, and the broken curve, the E-beam film.

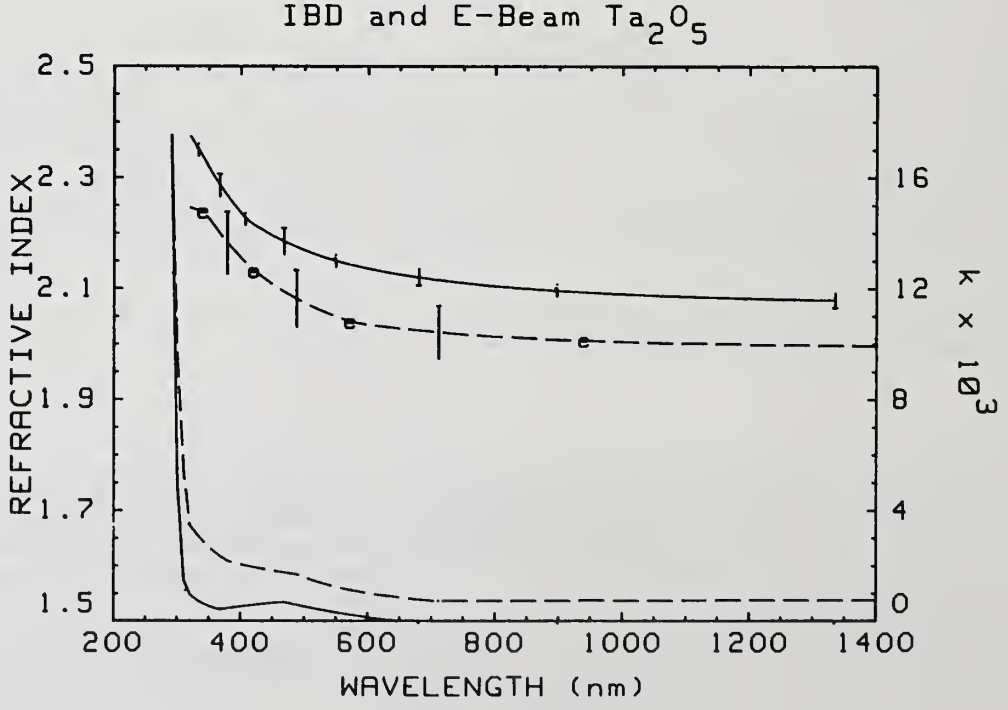

Figure 2. Dispersive Refractive Index and Extinction Coefficient for IBD and E-Beam Tantala. See Note, figure 1.

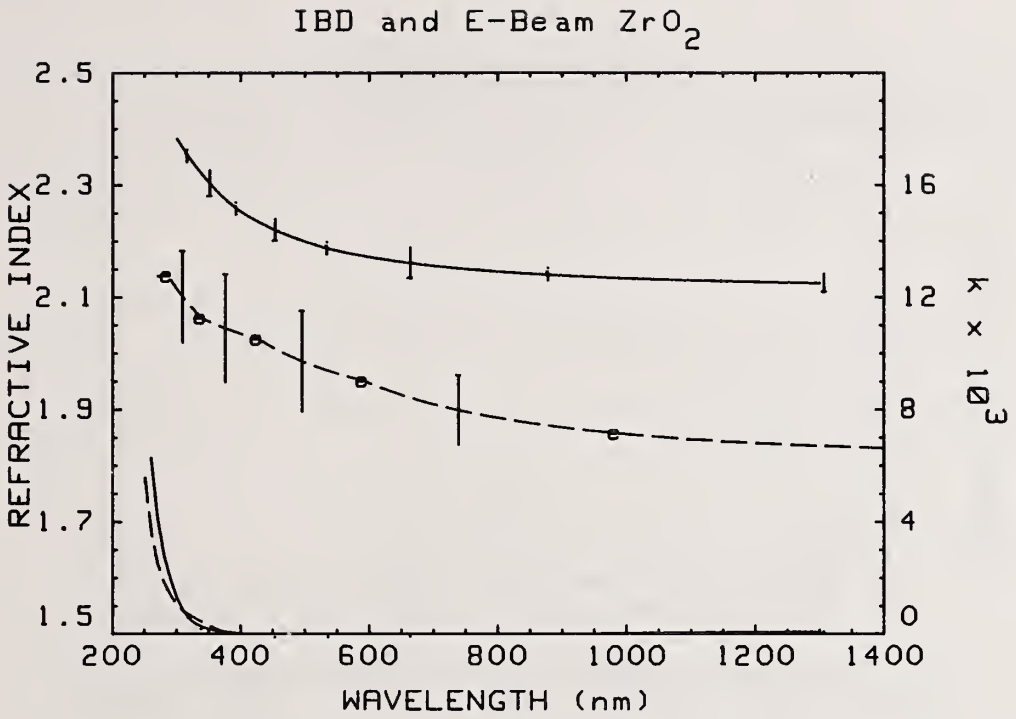

Figure 3. Dispersive Refractive Index and Extinction Coefficient for IBD and E-Beam Zirconia. See Note, figure 1.

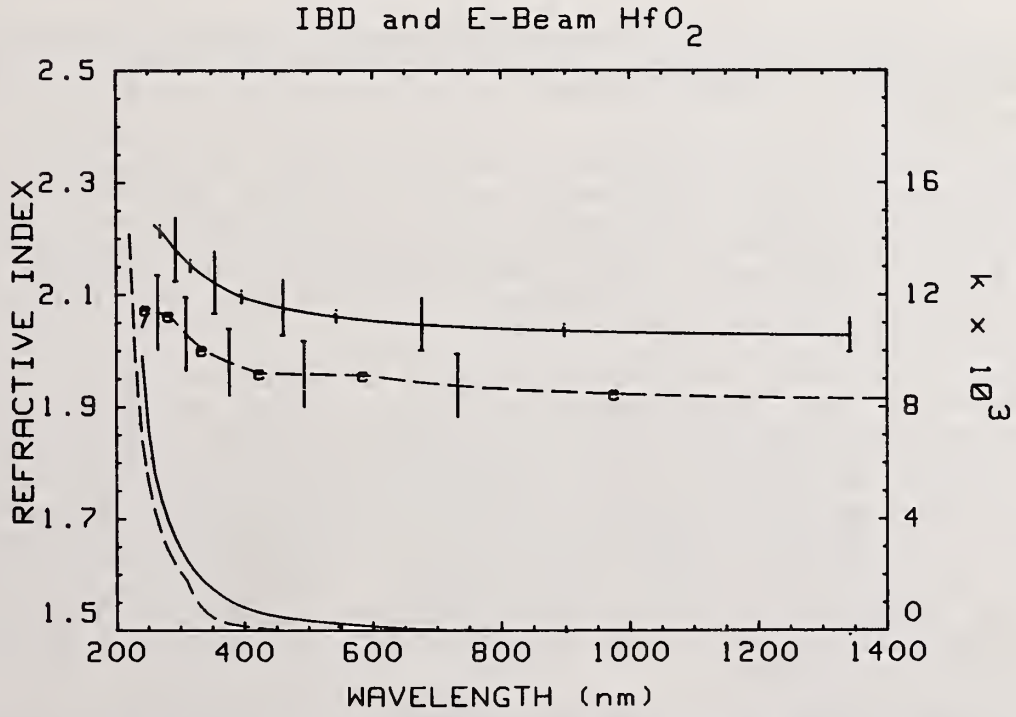

Figure 4. Dispersive Refractive Index and Extinction Coefficient for IBD and E-Beam Hafnia. See Note, figure 1.

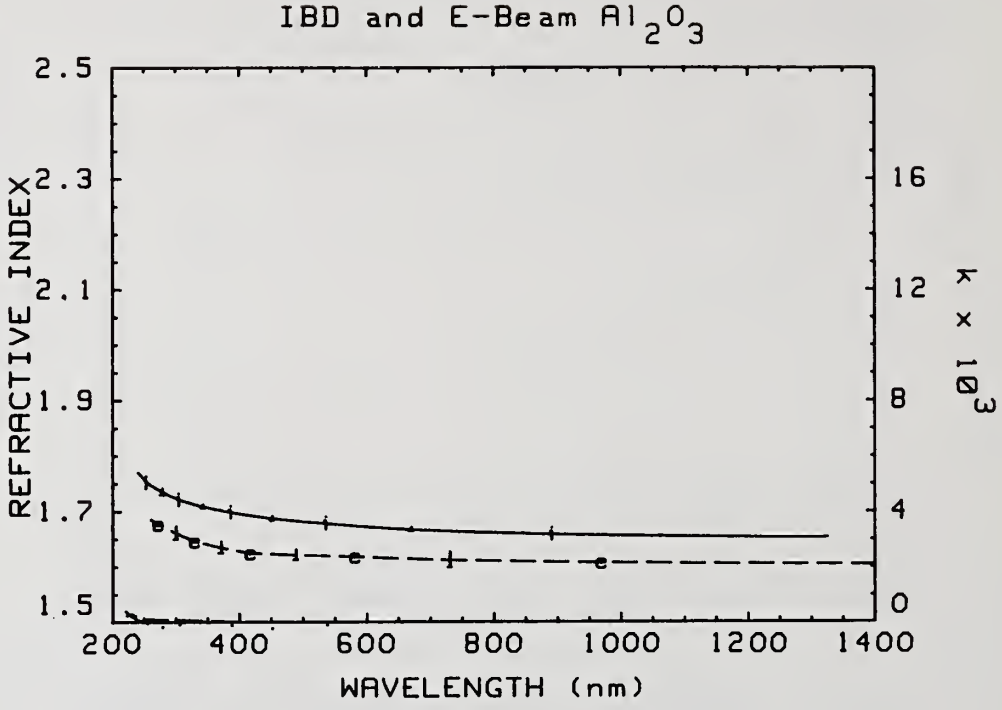

Figure 5. Dispersive Refractive Index and Extinction Coefficient for IBD and E-Beam Alumina. See Note, figure 1.

E-beam film. This is an expected result, as the sputtered films typically have a noncolumnar structure and a higher density, whereas the E-beam films tend to have a columnar structure and a larger void fraction. This result has been reported by others for titania [7,12], tantala [5] and zirconia [10] films.

The trends for the extinction coefficients are not so clear. The k values for the zirconia and alumina films are essentially the same whether one uses IBD or E-beam evaporation. The IBD hafnia films have a slightly higher absorptance than the E-beam hafnia films. The IBD niobia film has a significantly higher k value than the E-beam film through the visible range of the spectrum, while the E-beam tantala film is more absorbing than its IBD counterpart. We believe that the observed differences in the absorption of these films can be essentially eliminated by further optimization of the deposition processes.

An especially interesting feature is the absorption band observed in the range of 400-600 nm for the IBD tantala films. The absorptance at the peak of this band corresponds to about 1% loss in the film, which is sufficiently far above the estimated measurement error that the feature can be considered as valid. A similar, less well-defined feature may also be present in the niobia films. Note that the detection of this absorption band by spectrophotometric analysis of single-layer films requires the procedures used here; namely, analysis of both reflectance and transmittance scans, as well as a fairly thick film. This absorption band corresponds in energy to the levels reported for an electron trapping site found in sputtered tantala films [16]. It is possible that this absorption band could be reduced or eliminated by proper optimization of the deposition parameters. Even so, the fact that it can be induced by irradiation of the film with UV light means that IBD tantala may not be the best material for high-energy-laser applications below about 500 nm.

The inhomogeneity or variation in the index of the film is indicated by vertical lines on the index curves in figures 1 through 5. The tic mark located at either the top or bottom of the vertical line indicates the value of the refractive index at the substrate/film interface. The

opposite end of the vertical line indicates the value of the refractive index at the film/air interface. This variation in the refractive index represents the inhomogeneity of the film.

A summary of the average degree of inhomogeneity $\Delta n/n$, together with the calculated physical thickness of all the films, is presented in table 1. The material is listed in column one, and the average degree of inhomogeneity for the IBD films and the E-beam films is given in columns two and three. The measured values for the degree of inhomogeneity between 300 nm and 800 nm were averaged to obtain this value for each film. A positive sign is used to indicate that the refractive index decreases as the film grows, and a negative sign is used to indicate the refractive index increases as the film grows. The physical thicknesses of the IBD films and the E-beam films are presented in the fourth and fifth columns of table 1.

Table 1. Summary of Inhomogeneity and Physical Thickness of IBD and E-beam Films

Material	$(\Delta n/n)_{av}$* (x10-3)		Physical Thickness (nm)	
	IBD	E-Beam	IBD	E-Beam
Al_2O_3	- 4.9	- 14.0	401	452
HfO_2	- 49.9	+ 60.9	334	383
ZrO_2	- 21.4	+ 83.8	306	377
Ta_2O_5	+ 1.0	+ 50.0	321	350
Nb_2O_5	- 38.5	- 7.1	289	339

* Averaged from 300 nm to 800 nm.

There are several general trends which can be seen in the data presented in table 1. One of these is that most of the E-beam films have a positive inhomogeneity. This is typical of most E-beam evaporated films. The inhomogeneity observed in such films is believed to be caused by changes in the physical structure of the film [17]. The film becomes more porous as it grows, due to the columnar microstructure of the film, and consequently, the refractive index decreases from its initial value. In contrast, almost all of the IBD films have a negative inhomogeneity, which would imply that the density of the film is increasing as it grows. These results indicate that there are some definite differences in the manner in which the IBD films and the E-beam films grow. This is not suprising since the energy of the sputtered particles is much higher than that of the evaporated material [2], thus altering the growth process [18]. Another result which can be seen from table 1 is that, for most of the materials, the IBD films are more homogeneous than the evaporated films. This is due to the noncolumnar structure of the sputtered films. There are some films, such as the IBD alumina and the IBD tantala, in which the inhomogeneity is almost negligible.

An interesting observation can be made in regard to the inhomogeneity of the hafnia film. Note that the IBD and E-beam films appear to nucleate with about the same refractive index; i.e., the tic marks on the index bars which indicate the index at the substrate are nearly coincident for the two types of films. After nucleation, the films grow in different ways - the IBD film growing more dense and the E-beam film, less dense. For the other materials, the differences between the nucleation of the IBD films and the E-beam films is much larger.

4. Conclusions

The results presented here demonstrate that, in general, IBD produces a film with a higher refractive index than does E-beam evaporation. We attribute this difference to an increased density of the film resulting from the higher energy of the material forming the film.

In addition, the variation of the refractive index or inhomogeneity is different for IBD films than for E-beam films. In most cases, Δn is more negative for IBD films. This indicates a difference in the growth mechanism between the two types of films.

For the level of accuracy provided by spectrophotometric measurements, the observed differences in extinction coefficient between IBD and E-beam films are small. It is likely that these differences can be eliminated by proper optimization of the deposition parameters.

The authors wish to acknowledge that Thomas H. Allen of Optical Coating Laboratory, Inc. provided the reference to the electron trapping sites observed in sputtered tantala films.

The authors also acknowledge the assistance of Willy Kunzler, Wayne Wasson and Dan O'Shea of the AFWL/Technical Services Division, Metrology Laboratory, Kirtland AFB, NM, in making the spectral measurements of the films and Mike Hernandez for help with the data reduction and analysis.

This effort was sponsored by the Air Force Weapons Laboratory, Air Force Systems Command, United States Air Force, Kirtland AFB, New Mexico 87117.

5. References

[1] Harper, J. M. E. "Ion Beam Deposition," in Thin Film Processes, Vossen, J. L., and Kern, W. (eds), Academic Press, New York, 1978.

[2] Wehner, G. K.; and Anderson, G. S. "The Nature of Physical Sputtering," in Handbook of Thin Film Technology, Maissel, L. I., and Glang, R. (eds), McGraw-Hill Book Co., New York, 1970.

[3] Castellano, R. N. "Composition and Stress State of Thin Films Deposited by Ion Beam Sputtering," Vacuum 27; 109-117; 1977.

[4] Demiryont, H.; Kerwin, D. B.; Sites, J. R. "Optical Properties of Ion Beam Sputtered TiO_2 Films," NBS (U.S.) Spec. Publ. 688; 311-316; 1983.

[5] Sites, J. R.; Gilstrap, P.; and Rujkorakarn, R. "Ion-Beam Sputter Deposition of Optical Coatings," Opt. Engr. 22; 447-449; 1983 July-August.

[6] Rossnagel, S. M.; and Sites, J. R. "X-Ray Photoelectron Spectroscopy of Ion-Beam Sputter Deposited SiO_2, TiO_2 and Ta_2O_5," J. Vac. Sci. Technol. A2(2); 376-379; 1984 April-June.

[7] Demiryont, H.; Sites, J. R. "Effects of Oxygen in Ion-Beam Sputter Deposition of Titanium Oxide," J. Vac. Sci. Technol. A2(4); 1457-1460; 1984 October-December.

[8] Sites, J. R.; Demiryont, H.; Kerwin, D. B. "Ion-Beam Sputter Deposition of Oxide Films," J. Vac. Sci. Technol. A3(3); 656; 1985 May-June.

[9] Allen, T. H. "Optical Materials Deposited using Ion Beam Sputtering," OSA Tech. Dig.; 102; 1985.

[10] Raj, T.; Price, J. S.; Carniglia, C. K. "Ion Beam Deposited Oxide Coatings," NBS (U.S.) Spec. Publ., 1985, to be published.

[11] Kalb, A.; Mildebrath, M.; Sanders, V. "Neutral Ion Beam Deposition of High Reflectance Coatings for use in Ring Laser Gyroscopes," J. Vac. Sci. Tech. A4(3); 436-437; 1986 May-June.

[12] Kalb, A. "Neutral Ion Beam Sputter Deposition of High Quality Optical Films," Optics News 12 (8); 13-17; 1986 August.

[13] Arndt, D. P.; et al. "Multiple Determination of the Optical Constants of Thin-Film Coating Materials," Appl. Opt. 23(20); 3571-3596; 1984, October 15.

[14] Carniglia, C. K. "Effects of Dispersion on the Determination of Optical Constants of Thin Films." Jacobsson, J. Roland, ed. SPIE Proceedings Vol 652; 1986 April 15-17; Innsbruck, Austria. SPIE 652; 158-168.

[15] Carniglia, C. K. "Method for Measuring the Optical Properties of Slightly Absorbing, Inhomogeneous Dielectric Thin Films," J. Opt. Soc. Am. A3(13); 40; 1986.

[16] Seki, Shunji; Unagami, Takashi; Tsujiyama, Bunjiro "Electron Trapping Levels in rf-Sputtered Ta_2O_5 Films," J. Vac. Sci. Technol. A1(4); 1825-1830; 1983 October-December.

[17] Harris, M.; Macleod, H. A.; Ogura, S. "The Relationship between Optical Inhomogeneity and Film Structure," Thin Solid Films, 57; 173-178; 1979.

[18] Vook, Richard W. "Nucleation and Growth of Thin Films," Opt. Eng. 23(3); 343-348; 1984 May/June.

Manuscript Received
10/19/87/sar

An Analysis of Rugate Filter Behavior

Roger J. Becker

University of Dayton Research Institute
Dayton, Ohio 45469-0001

An analysis is made of the performance of a Bragg filter of arbitrary modulation profile in terms of solutions to the wave equation for a single repeat unit. This approach has advantages over the standard multiplication of matrices corresponding to very thin but flat steps in that it allows for rapid calculations and analytic studies. Special attention is given to filters with sinusoidal profiles. The transfer matrix for the filter is expressed in terms of the wavefunction and its first derivative. In the case of sinusoidal modulation, the wavefunctions are Mathieu functions. In all cases, simple relationships exist between centerband frequencies and linewidths, and the basic characteristics of the filter, such as the mean index and modulation depth. The results of computer simulations used in parametric studies of filter performance are presented and compared with analytic predictions, especially those of Coupled Mode Theory. It is found that corrections to the simplified theory must be made to account for the finite width of the filter. One benefit of the adopted approach is that it gives directly the strength of the optical electric field as a function of position in the filter.

Key words: coupled-mode theory; interference filter; Mathieu functions; multilayered films; thick films; transfer matrices.

1. Introduction

Bragg filters have long proven to be a useful means of enhancing peak reflectivity while simultaneously minimizing reflection (stop) band bandwidth. Bragg filters are based on the interference effects in wave propagation due to spatial variations in the susceptance of the medium. The traditional interference filter is based on a quarter-wave stack with only a few layers. Recent advances in materials processing technology have made possible a new class of Bragg filters known as rugate filters.

1.1 Background

A dielectric can be tailored to an arbitrary specification between the limiting value of the dielectric constants of a given set of materials by making an appropriate solution of these materials. In the following, the term rugate will be used to refer to any interference filter with a continuous or nearly continuous and smoothly varying graded index, in which the dielectric is made of a solution of two or more constituents. The filter design engineer is severely

hampered in not having the freedom to specify the susceptance (this implies the refractive index) of the medium at a given location. Hence the interest in rugate filters. The most immediate applications for continously graded index filters require designs in which the index profile undergoes only small excursions about a mean value. Therefore the filter is nearly homogeneous and is usually considered to be a single material, especially when contrasted with quarter-wave stacks of two dissimilar materials. This feature eliminates problems with defects at heterogeneous interfaces, and furnishes a means of fabricating filters with very small index excursions. Indeed, the narrowness of the modulation in the dielectric constant is limited only by the ability of a given film deposition process to control the film stoichiometry, and not by differences in the dielectric constants of standard optical materials. A third advantage of rugate filters is that they give the designer increased flexibility in the choice of modulation profile for the dielectric constant. Sinusoidal filters are of particular interest, and the term rugate is often associated only with sinusoidal modulation. The prominence of the sinusoidal profile in research on rugate theory and technology is partly due to early intuitive concepts of performance, particularly a belief that sinusoidal profiles would eliminate harmonic stop bands, and partly to its familiarity in conjunction with the need for a model continuously varying profile to compare with the familiar step-function, or flat index profile. Below we will show that while the elimination of harmonic stop bands is an oversimplification, a sinusoidal profile is a natural choice from a theoretical standpoint and is indeed useful in suppressing harmonic stop bands.

Current research on rugate filters is directed almost entirely toward the production of filters with ultranarrow linewidths and high pass-band transmission, especially filters which can withstand high optical intensities. The possibility of making multiline filters is also of interest. Doubtless many more applications will appear, especially in electrooptics, as interest increases.

This paper examines the factors affecting the performance of a filter from an analytical perspective. Although specifically directed at optical filters, most of the discussion is quite general, applying to the propagation of any wave in a medium with a spatially modulated response or susceptance. The intent of this work is to examine the factors affecting filter performance with a view toward perfecting filter design.

Below we present the results of a preliminary analysis of theoretical filter performance. The analysis is based upon a solution of the wave equation for the filter. Earlier work has relied mostly on computations of spectral performance using matrix multiplication. Graded-index profiles are simulated by a series of very thin constant-index steps. This method can be slow, especially when precise results are desired. A serious drawback for matrix multiplication is that it is an inappropriate method for use in conjunction with analytic calculations and does not lend itself to obtaining physical understanding. The wave-equation approach to obtaining filter transfer matrices adapted for this work overcomes these limitations. Moreover, it yields directly the electric field strength as a function of position in the filter, a quantity of importance

with regard to laser hardening, and gives a convenient means of obtaining comparisons with work in other fields in which similar physical principles are involved.[1,2]

1.2 Approach

There are two basic starting points for solving wave transmission problems. The first is a direct solution of the partial differential equation (PDE) for the wave amplitude and phase, Ψ. The second is a conversion from a PDE to a difference equation. The difference equation approach is most useful when the index modulation is large over short, well separated regions (tight-binding approximation) or when the modulation is small (nearly free case). In the latter case, the difference equation is obtained by a Fourier transformation of the PDE. Of course, the direct solution of the PDE is most useful when the index modulation over a given interval has a behavior close to that in which solutions are known. Perturbation theory may be used with either approach.

Each type of analysis is most useful when expressions for the dispersion/attenuation or reflection/transmission curves are given in terms of the functional form of the index modulation. However, a good qualitative understanding of a problem is often possible in terms of integrals which may be obtained numerically for specific instances. Figure 1 shows the relationships among various functions commonly used in different approaches to the problem.

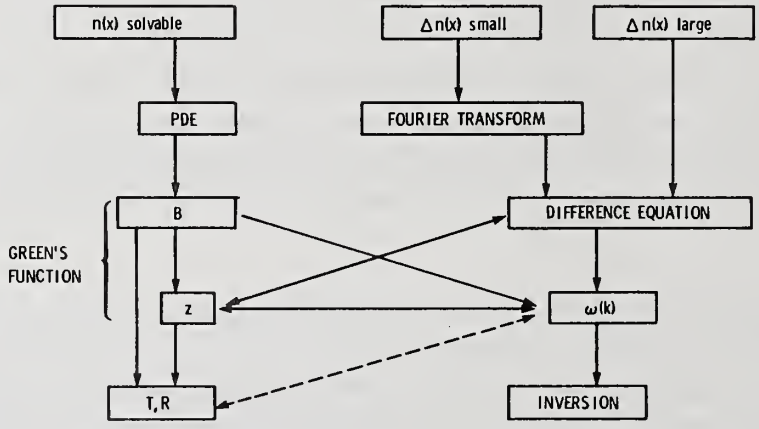

Figure 1. Relationships between various approaches to the solution of the wave equation.

The solution to the wave equation and its derivative may be thought of as a vector, so that the quantity relating the input and output values of this vector is a matrix. In an optics problem we actually need to know four functions to completely specify one of these vectors, (e.g., for propagation in the x direction we need to know E_x,E_y,H_x, and H_y), so that in general, we need a four-by-four matrix to describe the medium. However, we usually assume a scalar behavior for the dielectric, reducing our four-by-four matrix to two two-by-two matrices, one for TE waves, and one for TM waves. Once we have obtained the matrix coefficients for ψ and ψ', the problem is essentially solved.

Wave propagation in a periodic medium is governed primarily by fundamental considerations without regard to the details of the system in question (some of these fundamental features are discussed in the Appendix). In particular, it is universally found that a periodic modulation of the medium response will produce not just a single stop, or reflectance band, but a series of such bands with increasing frequency. The higher order band structure is related to the details of the modulation profile. In the event a filter is designed for a multi-octave frequency range, the details of the index contour will become important.

The analysis adopted in the following review of filter performance is analytic. The philosophy is that an analytic (in contrast to a numerical, e.g., matrix multiplication) approach has advantages for conferring insight on the essential physical parameters that determine filter performance. This allows filter behavior to be studied from a generic standpoint. It also results in very rapid calculations. A second goal is the application of analysis to optical design, especially the design of continous gradient filters. This paper begins to lay the goundwork for development of an optimum transfer function and a determination of appropriate values for the filter parameters. The author believes that this analysis will answer questions on the effect of discontinuities and of continuously varying susceptibilities on filter performance, and the degree to which an ideal notch filter can be approximated.

An analytic approach has special advantages when a problem becomes complex. An example is the extension of simple, one-dimensional filters with purely real refraction indices to three-dimensional filters with complex susceptibilities. This problem can be handled analytically by a resolvant, or Green's function approach. The Green's function method is a generalization of the concepts addressed in this paper.

Reflection and transmission spectra were calculated using a transfer matrix approach. The essential theory, reviewed below, is contained in Born and Wolf[1] and Yariv and Yeh[2] and is described in a technical report by the author.[3] Programs to calculate spectra were completed and streamlined, and special features, such as the inclusion of absorption or incomplete layers, were added. The approach taken was to predict filter behavior using analysis, simulate spectra as a function of certain filter parameters, store essential features of these spectra, such as line-width, in a file, plot the resulting functional dependence, and compare the results with the analytic predictions.

A quick review of terminology is in order. When discussing the sinusoidal dielectric filter (Mathieu case), we will often refer to the symbols in figure 2:

ε_0 = mean dielectric strength in filter
ε_1 = amplitude of dielectric modulation
n_1 = index of medium from which light is induced
n_2 = index of medium to which light exits
θ = angle of incidence to the filter for incoming light
N = number of unit cells comprising the filter
z_o = fraction of full layer at the end of the filter

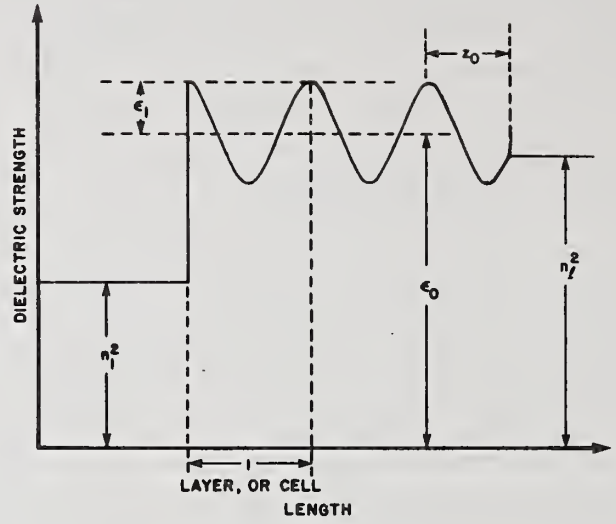

Figure 2. Sinusoidal profile and key parameters.

When discussing filters with piecewise constant, or square well, dielectric modulation we will use the notation from figure 3:

$\bar{n}$ = mean index of the filter

Δn = amplitude of index modulation

d = length of one modulation cycle

a = length of the high part of the modulation cycle.

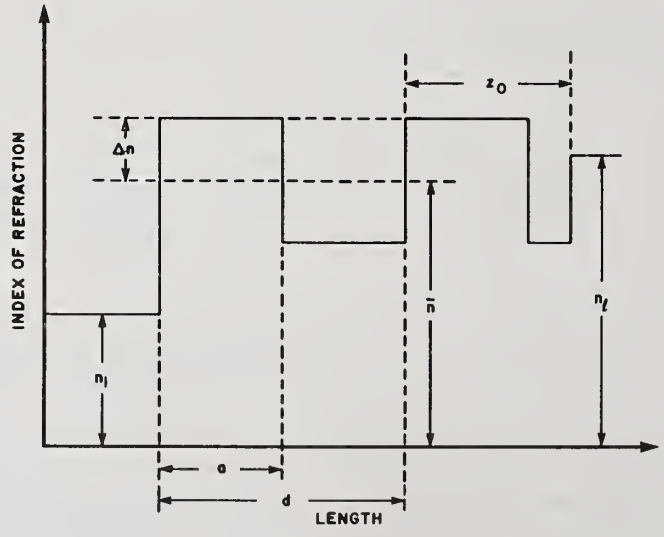

Figure 3. Step-function profile and key parameters.

The ratio of a over d is generally referred to as the ratio a/d. ϵ_1 and Δn are referred to as the modulation depth of the filter.

Other notation includes:

k_o = the wave number of the incident wave, normalized to the length of unit cell.
k = the complex wave number that the light wave assumes inside the filter. This is the Block wave number, and is referred to as kd where it appears in plots.
R = reflection coefficient
R_p = peak reflection of a spectrum
k_c = value of k_o at which the peak reflectance occurs
Δk = width of the main peak. This is taken as the distance between the k_o values at which $R = 1/2\ R_p$

The square-well case is discussed in terms of refraction indices, while the Mathieu case is defined in terms of dielectric constant. ε_o is comparable to $\bar{n}^2$, and since the relative modulation depth is usually small, $2\Delta n/\bar{n}$ is comparable to $\varepsilon_1/\varepsilon_o$. The reason for the difference in notation lies in the different approaches taken in making calculations for each case. Programs written to study square-well filters operated entirely in terms of transfer matrices whose standard forms are well known. Matrices for a single layer of the filter were evaluated and then raised to the Nth power using Chebyschev polynomials. Reflection and transmission coefficients were calculated directly from the completed transfer matrix. It was more convenient in this case to use indices of refraction rather than dielectric constants.

The main body of the Mathieu programs, however, contains routines to solve the wave equation. Here it is more convenient to use dielectric constants. Transfer matrices, though still included in the programs, play a lesser role and are themselves evaluated in terms of wave function solutions.

The input to programs was as follows:

SQUARE WELL	MATHIEU
1) $\bar{n}$	1) ε_o
2) Δn	2) ε_1
3) N	3) N
4) z_o	4) z_o
5) n_1 & n_ℓ	5) n_1 & n_ℓ
6) θ	6) θ
7) a/d ratio	7) imaginary parts of ε_1 and ε_o corresponding to absorption

Both sets of programs deal primarily with transverse electric (TE) components of light waves. The square well programs also have the capability of describing transverse magnetic (TM) waves, thus enabling the study of differences between TM and TE wave behavior at non-normal incidences.

Each program produces either reflection spectra (e.g., see fig. 4) or dispersion curves (an example is given in fig. 5). The Mathieu program is also capable of producing plots of the wave function inside the filter. The wave function is equivalent to the electric field strength. The

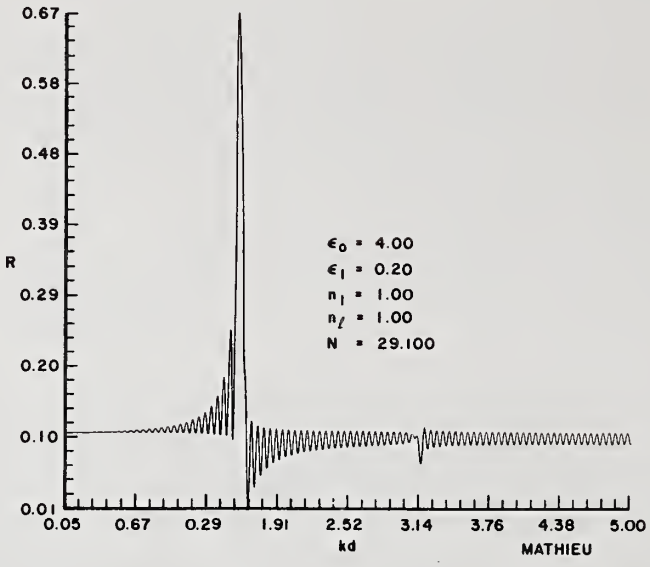

Figure 4. Typical rugate spectrum showing non-zero harmonic peak.

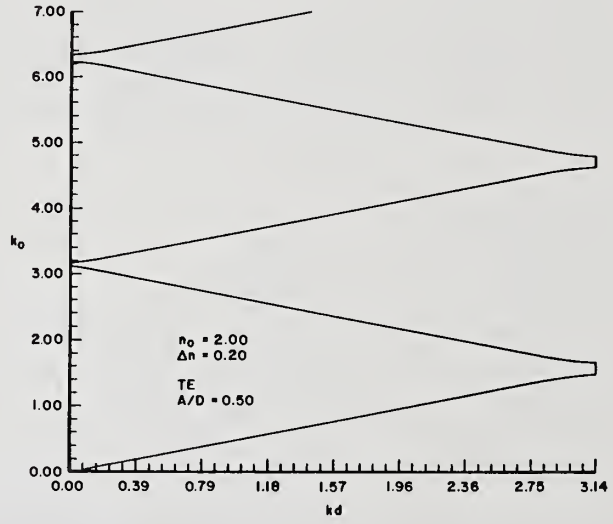

Figure 5. Typical dispersion curve. Curve shown is for step-function profile.

reflection spectra show the reflection coefficient, R, as a function of incident wave number. To illustrate the effects of absorption on filter performance, transmission curves can also be obtained (fig. 6). Dispersion curves plot the Block wave number (horizontal axis) as a function of incident wave number, k_o. The result is a very clear picture of the stop and pass locations for a filter. Places on the curves where the Block wave number suddenly remains constant for a short range of k_o values indicate the appearance of a stop band.

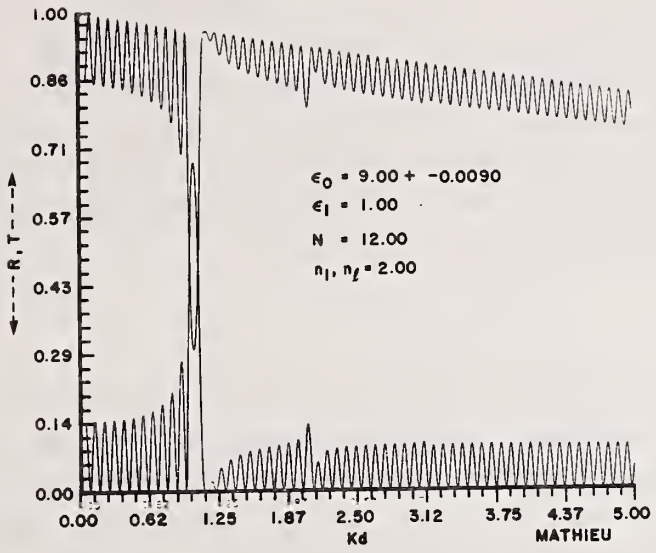

Figure 6. Transmission and reflection rugate spectra for filter with complex dielectric constant.

Figure 7 illustrates the differences between wave function behavior inside and outside of stop bands. While the passband waves oscillate at a fairly constant amplitude, the stop-band wave in figure 7 shows a characteristic decay for the oscillation due to reflection.

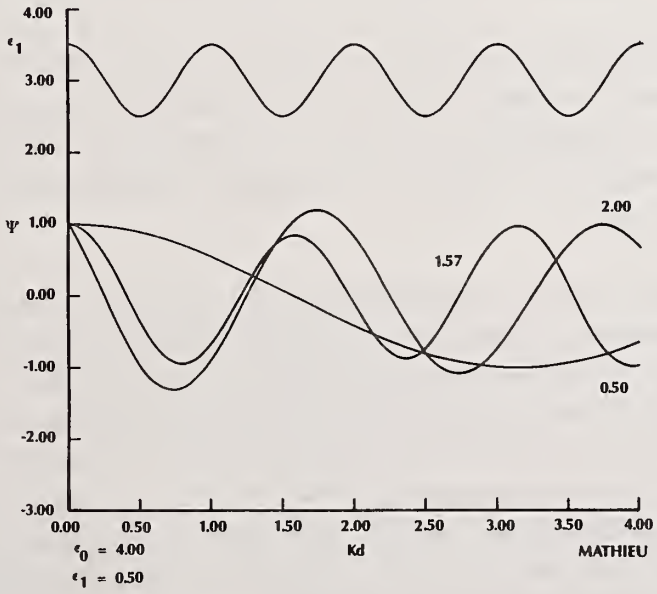

Figure 7. Electric field strenght as a function of position for light of various normalized wavelengths.

Routines were written to analyze spectra for the location of the peak reflectance, the value of the reflectance at the peak, and the width of the main stop band. Large files of these characteristics were accumulated and an analysis of their behavior was made with the aid of Chi-squared curve-fitting routines. Most of the initial attempts at finding analytic functions to describe the changes in filter behavior versus changes in filter parameters were made with the assumption that the indices of the media surrounding the filter were equal to the mean index of the filter (matched indices); that is,

$$\epsilon_o(\text{or } \bar{n}) = n_1 = n_\ell \qquad (1)$$

This case is easiest to treat, as the contribution to the reflectance comes solely from the filter's dielectric modulation. Effects on the spectrum due to the finite size of the filters are minimized, and predictions made for infinitely long filters are good for N as low as five layers. Coupled Mode Theory (CMT) as presented by Yariv and Yeh in Optical Waves in Crystals[2] is the inspiration for many of the analytic formulas studied. Predictions made by CMT assume a semi-infinite filter.

When the indices of the external media are allowed to be arbitrary, the analysis of filter behavior becomes more complicated. Contributions to reflectance now come from both the filter's dielectric modulation and the sudden changes in potential that occur at the filter surfaces. Though the result is predictably a combination of these effects, it cannot be assumed that the combination is merely linear or multiplicative. The approach adopted was to model the convolution of the spectral profile for an infinite filter with sinc function representing the Fourier transform of a finite filter by adding terms in $1/N$ and $1/N^2$ to the formulas for infinite filters. This ad hoc approach was taken to approximate the significant size effects that occur for small N.

The center frequency is also affected by changes in the dielectric modulation. When ϵ_1 is changed, the mean index also changes slightly inside the filter. The result is a different optical path length and a different set of parameters required for the satisfaction of the Bragg condition. For the extent of modulations represented in figure 7, the effect is less than 0.1% of the predicted peak location.

The relevant theory is given in Section 2, with essential results summarized in Paragraph 2.1. Paragraph 2.2 presents an overview of filters, of different means of describing their performance, and of the diverse subjects which share essential features. The critical conclusion of Paragraph 2.2 is that a complete description of the performance of a filter may be obtained once the wave equation is solved over the fundamental repeat region (unit cell) of the filter cascade. The solution of the wave equation is then discussed in Paragraph 2.3 with special emphasis on the two cases of special interest, step function and sinusoidal modulation. These two cases are compared, and some general observations are made about the behavior of the solutions, particularly the appearance of stop and pass bands.

Paragraphs 2.4 and 2.5 discuss various means by which the solution of the wave equation may be converted to an algebraic problem. Algebraic procedures are especially useful in describing multiple periodic filters, as well as terminations, junctions, and other local departures from the

periodic profile. They are a prime analytic tool. The mathematical basis for Paragraph 2.4 is given in Appendix A.

The results of a large number of computer simulations are summarized in Section 3. The dependence of the centerbond frequency, linewidth, and peak reflectance and the behavior of harmonies and sidebond spectra are studied as a function of the modulation depth, modulation profile, thickness of the filter, and certain departures of the filter from strict periodicity. Conclusions are given in Section 4.

2. Theory

This section covers the mathematical aspects of filter behavior from a fundamental standpoint, illustrating techniques that may be used to perform calculations in various circumstances. Before plunging into a long series of equations, let us summarize essential concepts.

2.1 Highlights

Any tractable treatment of filter performance must be expressed in terms of the transfer matrix. In the following discussion the transfer matrix is derived from the solution to the wave equation for a single repeat unit of the filter, a departure from the conventional approach. Theory show that the response of the filter (i.e., the reflectance, linewidth, etc.) can conveniently be expressed in terms of simple formulas, most of which involve a coupling coefficient, κ. The computer simulations reported in Section 3 were undertaken to determine the manner in which κ depends upon the filter parameters. Within the limit that the modulation depth is small and the filter is made up of a great many repeat units, the filter response can be conveniently formulated in terms of Fourier coefficients. This is the case described by Coupled Mode Theory (CMT), and the case of greatest interest at the present time. In the Coupled-Mode limit κ is simply a Fourier coefficient of the modulation profile. However, as the modulation depth increases and/or the thickness of the filter decreases, corrections for κ must be made to the Fourier approximation.

Since both the Kronig-Penney and the Mathieu problems are exactly solvable, comparisons have been made of the stop and pass bands created by these modulation profiles. The result depends on the relative size of the distances a and b in the Kronig-Penney profile. When a b, the two profiles give very similar results. The width of the pass bands relative to the stop bands increases with the ratio of b/a.[4]

As a wave propagates through the filter, it is partly reflected due to modulations in refractive index. If the wavelength is much greater that the periodicity in ($\bar{n}k_o d \ll 1$ for a mean index $\bar{n}$), the wave will not see the index modulation, and the wave will be passed. When the wavelength in the medium nearly matches d, the wave will interact strongly with the modulated profile; constructive interference will occur between reflections that occur at distances d apart.

This will also occur at wavelengths which are submultiples of this critical wavelength--a series of stop and pass bands will occur. The width of the stop bands is roughly proportional to the amplitude of the index modulation.

By our argument, we see that successive stop bands arise in part from the corresponding Fourier components of the modulation profile. Thus the second stop band is sensitive to the strength of the second Fourier component of the index modulation, etc. Consequently the widths and positions of the lowest bands are not very sensitive to changes in the modulation profile, only to its periodicity (length of the unit cell). Changes in the shape of the profile have their greatest effect on the higher-order bands. For example, if we approximate a sinusoidal index modulation by a series of thin steps, we may expect very little effect on the location of the edges of the lowest bands. At high bands corresponding to wavelengths on the order of the step thickness, we would anticipate relatively large changes. Of course, these higher order bands may well correspond to wavelengths that lie above the bandgap of the dielectric materials. If the step thickness is 100 nm, we would expect strong changes in the bands corresponding to energies of, say, 10eV. However, this region is not of particular interest. In other words, the modulation depth and overall periodicity d are the main parameters affecting the band edges of interest. Fine details of the shape of the modulation are not very important.

If the system is multiple, periodic higher-order bands at corresponding multiples will be affected. We will discuss this further in paragraph 2.4, but we can see from the argument given above that since a multiple periodicity implies that second and higher order Fourier components of the modulation profile will be large, the stop bands (band gaps) above the fundamental will be widened.

2.2 The Transfer Matrix

Once we have a solution for ψ, we may obtain the matrix elements of B immediately.[5] A second order PDE will have two independent solutions. Let these be ϕ_1 and ϕ_2, and let

$$\psi = c_1\phi_1 + c_2\phi_2 \quad . \tag{2}$$

Then

$$\psi' = c_1\phi' + c_2\phi'_2 \quad . \tag{3}$$

Solving for c_1 and c_2 we find we can write

$$\begin{bmatrix} \psi(x) \\ \psi'(x) \end{bmatrix} = [B] \begin{bmatrix} \psi(x') \\ \psi'(x') \end{bmatrix} \quad , \tag{4}$$

with

$$b_{11} = [\phi_1(x)\phi_2'(x') - \phi_2(x)\phi_1'(x')]/D \quad , \tag{5}$$

$$b_{12} = [\phi_2(x)\phi_2(x') - \phi_1(x)\phi_2(x')]/D \quad , \tag{6}$$

$$b_{21} = [\phi_1'(x)\phi_2'(x') - \phi_2'(x)\phi_1'(x')]/D \quad , \tag{7}$$

and

$$b_{22} = \phi_2'(x)\phi_1(x') - \phi_1'(x)\phi_2(x')]/D \quad , \tag{8}$$

where

$$D = \begin{vmatrix} \phi_1(x) & \phi_2(x) \\ \phi_1'(x) & \phi_2'(x) \end{vmatrix} . \tag{9}$$

We see that

$$b_{11} = -\partial b_{12}/\partial x' \tag{10}$$

$$b_{22} = \partial b_{12}/\partial x \quad , \tag{11}$$

$$b_{21} = \partial b_{11}/\partial x = \partial b_{22}/\partial x' = \partial^2 b_{12}/\partial x \partial x' \quad , \tag{12}$$

and

$$\partial b_{11}/\partial x = \partial b_{22}/\partial x' \quad . \tag{13}$$

Usually we have

$$b_{22} = b_{11}^* \quad . \tag{14}$$

We note that using eq. (2), we have

$$\cos kd = [\phi_1(x)\phi_2'(x') - \phi_2(x)\phi_1'(x') + \phi'_2(x)\phi_1(x') - \phi_i'(x)\phi_2(x')]/D^2. \tag{15}$$

The expression of the matrix elements in terms of x and x' highlights their connection with Green's functions. Often we can reduce these expressions to expressions in terms of one or more distances between x and x'.

For example, for a simple step function modulation with characteristic distances a and b,

$$a + b = d \quad , \tag{16}$$

we have[1,6,7]

$$B(x,x') = \begin{bmatrix} G(a,b) & H(a,b) \\ G'(a,b) & H'(a,b) \end{bmatrix} \quad . \tag{17}$$

We now illustrate how this may be done, using as an example the solution to the equations

$$d^2\psi/dx^2 + k^2\psi = 0 \quad . \tag{18}$$

The solutions are

$$\phi_1 = \cos kx \tag{19}$$

and

$$\phi_2 = \sin kx \tag{20}$$

We let

$$x' = x-a \quad , \tag{21}$$

and find

$$D = k[\cos^2 kx + \sin^2 kx] = k \quad , \tag{22}$$

$$b_{12} = [\sin kx \cos k(x-a) - \cos ka \sin k(x-a)]/k$$
$$= k^{-1} \sin ka \quad , \tag{23}$$

$$b_{11} = [k\cos kx \cos k(x-a) + k\sin kx \sin k(x-a)]/k$$
$$= \cos ka \tag{24}$$

$$b_{21} = [-k^2 \sin kx \cos k(x-a) + k^2 \cos kx \sin k(x-a)]/k$$
$$= -k\sin ka \tag{25}$$

$$b_{22} = [k\cos kx \cos k(x-a) + k\sin kx \sin k(x-a)]/k$$
$$= \cos ka \quad . \tag{26}$$

With the identifications

$$G(a) = \cos ka \quad , \tag{27}$$

$$H(a) = k^{-1} \sin ka \quad , \tag{28}$$

we obtain the form of eq. (17).

Expressions for the transfer matrix B in literature give the function G and H of equation (17) in terms of the unit cell distance d:

$$G(a,b) = G(a + b) = G(d) \quad , \tag{29}$$

$$H(a,b) = H(a + b) = H(d) \quad . \tag{30}$$

A comparison of eqs. (17) and (4) to (8) raises the question as to whether the matrix element in Equations (5) to (8) can expressed in terms of d. We are also interested in the connection, if any, between the G and H functions or equivalently, between b_{11} and b_{22}. If such a connection exists, we may solve for the B matrix elements, given the dispersion relation. This would be a great help, since we can often obtain the form for the dispersion relation directly, without first finding the form for B, as we will show in Paragraph 2.4. This could be one step in an inversion process.

Equations (10) to (14) suggest a means of answering both of these questions. We may rewrite the relations, eqs. (5) to (8) in terms of the difference between x and x':

$$x - x' = r \quad . \tag{31}$$

Usually we will choose r = d. From the definition, eq. (31), we obtain

$$\partial r/\partial x = 1 \quad , \; \partial r/\partial x' = -1 \quad . \tag{32}$$

We write

$$d\phi/dr = \phi' \quad , \tag{33}$$

and see that

$$\frac{\partial \phi}{\partial x} = \frac{d\phi}{dr}\frac{\partial r}{\partial x} = \phi' \tag{34}$$

and

$$\frac{\partial \phi}{\partial x'} = \frac{d\phi}{dr}\frac{\partial r}{\partial x'} = -\phi' \quad . \tag{35}$$

Also,

$$\frac{\partial^2 \phi}{\partial x \partial x'} = \frac{d^2\phi}{dr^2}\frac{\partial^2 r}{\partial x \partial x'} = -\phi'' \quad . \tag{36}$$

It seems then, that we may write

$$B = \begin{bmatrix} b' & b \\ -b'' & b' \end{bmatrix} \tag{37}$$

i.e., $G \sim H'$. (38)

From eq. (37), it appears that we may write eq. (2.) or eq. (28) as

$$2\,b' = \cos kd \quad . \tag{39}$$

Consequently, if we have a dispersion relation of the form

$$2\,g(d) = \cos kd \quad , \tag{40}$$

we may write

$$b = \int g \quad , \tag{41}$$

or

$$B = \begin{bmatrix} g & \int g \\ -g' & g \end{bmatrix} \quad . \tag{42}$$

We see then that the central problem is to solve the PDE equation for ψ. We now discuss means of obtaining this solution further, and give pertinent examples in which the solutions have been obtained.

2.3 Solution of the Wave Equation

We will make some simplifications in our discussion, mostly for the sake of clarity. We will confine most of our remarks to the one-dimensional problem. We will also deal in general with real refraction indices and infinitely long systems. All of these simplifications can easily be extended to treat a more general case. We will also confine our discussion to systems that are strictly periodic with period d. This is an important boundary condition. From the discussion that follows, we will see that it will not seriously limit the performance of our filter.

We seek to solve equations of the form[1]

$$\frac{d^2U}{dx^2} = k_o^2(n^2(x) - s^2)U = \frac{d\ell n\varepsilon}{dx}\frac{dU}{dx} \tag{43}$$

and

$$\frac{d^2V}{dx^2} + k_o^2(n^2(x) - s^2)V = \frac{d\ell n(\mu - s^2/\varepsilon)}{dx}\frac{dV}{dx} \tag{44}$$

for TM waves and

$$\frac{d^2U}{dx^2} + k_o^2 \, [n^2(x) - s^2]U = \frac{d\ell n\mu}{dx} \frac{dU}{dx} \tag{45}$$

and

$$\frac{d^2V}{dx^2} + k_o^2 \, [n^2(x) - s^2]V = \frac{d\ell n(\varepsilon - s^2/\mu)}{dx} \frac{dV}{dx} \tag{46}$$

for TE waves. Even if μ is a constant, ε will not be. If ε varies slowly, we may make a WBKB approximation[8,9] and set the right side of these equations equal to zero. In general, this approximation will not be valid. It can serve as a good starting point for perturbation theory, it makes contact with a large body of literature, and it is instructive. Therefore, we will consider solutions to the equation

$$\frac{d^2\psi}{dx^2} + k_o^2 \, [n^2(x) - s^2] \, \psi = 0 \quad . \tag{47}$$

Without loss of generality, we may simplify our discussion by setting $s^2 = 0$ (normal incidence).

In mechanics, we have[10]

$$n(x) \sim \sqrt{(E - V(x))/E} \tag{48}$$

where E is the energy and V(x) is the potential. In the particular case of quantum mechanics, we have

$$k = p/h \quad ,$$

and an equation of the form eq. (47) which is Schroedinger's equation. A great deal of work has been done on periodic systems using this equation in the band theory of solids; n corresponds to the impedance z in transmission line problems. In acoustics, we have $n \sim \rho v$, for velocity v and density ρ.[11]

2.3.1 Piecewise Constant Modulation

The step function modulation is one of the most thoroughly analyzed of any periodic response function.[4,12-26] It is easy to construct experimentally, can be solved exactly, and has cosines and sines for eigenfunctions, so that products of eigenfunctions can often be reduced to a compact form. Since the system is piecewise solvable, we may multiply matrices of the form

$$\begin{matrix} \cos k_o n_i \ell_i & n_i^{-1} \sin k_o n_i \ell_i \\ -n_1 \sin_o k_i n_i \ell & \cos k_o n_i \ell_i \end{matrix} \qquad (49)$$

for each layer of thickness ℓ_1 and index n_i. The most studied case is the double layer (one atom), with periods a and b and indices n_a and n_b. After multiplying matrices, we obtain the dispersion relation from eq. (21):

$$\cos kd = \cos k_o n_a a \cos k_o n_b b$$

$$- \frac{1}{2} \left(\frac{n_a}{n_b} + \frac{n_b}{n_a}\right) \sin k_o n_a a \sin k_o n_b b \quad . \qquad (50)$$

Here d = a + b. We see that when $n_a \to n_b = n$, we find

$$\cos kd = \cos k_o n (a + b) \quad , \qquad (51)$$

as we should. When $n_a << n_b$ and a b we find

$$\cos kd \approx \cos k_o n_b b - \frac{1}{2} k_o n_b a \sin k_o n_b b \quad . \qquad (52)$$

A problem of more widespread interest occurs when $n_b b << n_a a$, but $n_b >> n_a$. Then we have

$$\cos kd \approx \cos k_o n_a a - \frac{1}{2} (n_b/n_a) k_b b \sin k_o n_a a, \qquad (53)$$

where $k_b = k_o n_b$. This system was studied by Mason in regard to acoustic filters as early as 1927,[16] but is best known as the Kronig-Penney problem, after these authors published their independent derivation of the solution applied to a model of energy bands in solids in 1931.[17] Usually a variable n_e is defined in such a way that

$$n_e a = \frac{1}{2}(n_b/n_a)k_b b \quad . \qquad (54)$$

Using eq. (48), with V(x) = - U >> E over region b, V(x) = 0 over region a, and $E = k_o^2$ we have n_a = 1 and $n_b^2 \approx U/E$, so that $\frac{1}{2} n_b^2 k_o b/n_a \to \frac{1}{2} Ub/k_o$. This is commonly written as U'a.[13] This model is frequently used for energy band calculations.[19-21] If we make the association $n_a \sim z_a$, $\frac{1}{2}$ $k_o b n_b = n_b' = z_b$, we make contact with the problem of a transmission line with unloaded line impedance z_a that is loaded at distances a apart by discrete impedances z_b:

$$\cos kd \quad \cos k_o n_a a - (z_b/z_a) \sin k_o n_a a \quad . \qquad (55)$$

For a string or rod loaded by point masses, $z_b = m\omega$.[11] If we now consider only long wavelength waves, we may write:

$$1 - \cos kd \quad (n_b'/n_a) k_o n_a a \quad , \qquad (56)$$

or

$$2 \sin^2 \left(\tfrac{1}{2} kd\right) \quad k_o n_b' a \quad , \tag{57}$$

making contact with the literature on lattice dynamics.

The double periodic square well potential has been studied by Dubrovskii and Pogorelskii;[20] the resulting expression for the dispersion relation is complicated.

2.3.2 Sinusoidal Modulation

Another problem that can be solved exactly is that in which the potential is sinusoidal. This was first treated by Morse in 1930.[23] Morse solved the problem in three dimensions as well as in one dimension. We write $\varepsilon(x)$ as

$$\varepsilon(x) = \varepsilon_o - \varepsilon_1 \cos(2\pi x/a) \tag{58}$$

and letting

$$\alpha = k_o^2 \varepsilon_o, \; q = \tfrac{1}{2} k_o^2 \varepsilon_1, \text{ and } \varepsilon = n^2 \tag{59}$$

we may write eq. (47) (with s = 0) as

$$d^2\psi / dx^2 = [\alpha - 2q\cos(2\pi x/a)]\psi \quad . \tag{60}$$

This is the standard form of Mathieu's equation.[24] The solutions are circular elliptic functions. There are four basic types of these functions:

$$ce_{2n}(z,q) = \sum_r A_{2r} \cos 2rz \quad , \tag{61}$$

$$ce_{2n+1}(z,q) = \sum_r A_{2r+1} \cos(2r+1)z \quad , \tag{62}$$

$$se_{2n+1}(z,q) = \sum_r B_{2r+1} \sin(2r+1)z \quad , \tag{63}$$

and

$$se_{2n+2}(z,q) = \sum_r B_{2r+z} \sin(2r+2)z \quad , \tag{64}$$

where $z = \pi x/a$ and should not be confused with the impedance. The functions ce_m and se_m go over to cosine and sine functions when ε_1 is small compared to ε_o. The Mathieu functions may also be expanded in terms of cylindrical Bessel functions and Hankel functions, and in the case of large

q, may be approximated by parabolic cylinder functions.[25] We will discuss various expansions of the Mathieu functions in Section 2.5.

Levine has examined the effect of various terminations on the stop and pass bands pertaining to the Mathieu problem. Perturbations were studied by Slater,[26] who considered a dielectric of the form $\varepsilon_o + \varepsilon_1 \cos 2z + \varepsilon_2 \cos 2pz$, as well as $\varepsilon_o + \varepsilon_1 \cos 2z + \varepsilon_2 \cos z$. Slater considered two- and three-dimensional perturbation problems as well as the one-dimensional problem.

The regions of stop and pass bands are separated by characteristic curves on an α-q plot. As k_o is incremented, the corresponding value of k traces out a straight line on this plot (fig. 8). Hence the widths and locations of stop bands for thick filters can readily be found graphically, given ε_o and ε_1.

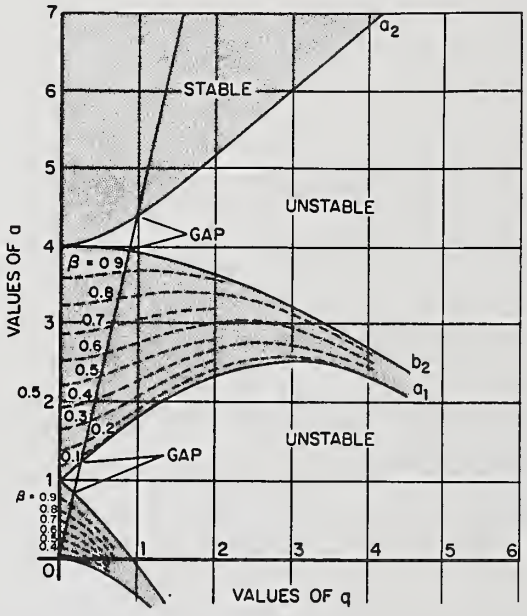

Figure 8. Stability chart for sinusoidal potential.

2.4 Difference Equation Calculations

Often we can convert a PDE into a difference equation by an appropriate series transformation or decomposition, followed by an approximation which allows us to limit the coupling that occurs between the basis states of the decomposition. We now give two examples of how this can be done. The first is a Fourier transformation; the second is known as the tight binding, or LCAO method. The approximation limiting the number of connected basis states appearing in the difference equation makes the difference equation method practical. Consequently, this approach is only useful when such an approximation can be made.

2.4.1 Fourier Transformation[27,28]

We wish to solve the PDE of the form in eq. (47). We make the decompositions

$$\psi_k(x) = \sum_j A_j(k)\, e^{ik_j x} \quad , \tag{65}$$

where

$$k_j = k + 2\pi j/d \quad , \tag{66}$$

and

$$n^2(x) = \sum_\ell g_\ell e^{iK_\ell x} \quad , \tag{67}$$

where

$$K_\ell = 2\pi\ell/d \quad .$$

Substituting eq. (66) and (67) in (47), we find

$$\sum_j [(k + k_j)^2 + k_o^2(s^2 - \sum_\ell g_\ell e^{iK_\ell x})]\, A_j(k) e^{ik_j x} = 0 \quad . \tag{68}$$

In principle, eq. (68) is exact, but involves an infinite sum over the Fourier components g_ℓ for the square of the index, n^2. We need to reduce drastically the number of these components. Fortunately, if $n_2(x)$ is a reasonably smooth function, we may terminate the series in ℓ after a few terms. As an example, we consider the Mathieu problem, in which we have

$$g_\ell = g\delta_{\ell\pm1} . \tag{69}$$

Substitution of eq. (69) into eq. (68) now gives

$$[(k + k_j)^2 + k_o^2 s^2]\, A_j = g[A_{j-1} + A_{j+1}] \quad . \tag{70}$$

This is a solvable equation. Rather than pursue it here, we go on to derive a similar equation by another means.

2.4.2 Tight-Binding Approximation[28]

A great deal of work has been done using difference equation calculations in the band theory of solids based on the tight binding approximation.[29-32] This corresponds to the case in which regions of large refractive index are sufficiently separated by regions of low refractive

index that they form optical wells which are only weakly coupled. Parallel calculations have been made in three dimensions as well as one dimension and include investigation of the effect of various terminations (surface states). Although they are most accurate in cases of very deep modulation of the index profile, they provide an instructive insight into band behavior, and serve as good points for comparison with more general calculations.

Let us assume that we have a complete set of known orthonormal solutions ϕ_n for the equation

$$\psi_n'' + k_o^2[n_o^2(x) - s_o^2]\,\psi_n = 0 \quad , \tag{71}$$

and that we wish to solve eq. (47):

$$\psi'' + k_o^2[n^2(x) - s^2]\psi = 0 \quad , \tag{72}$$

for some

$$n^2(x) = n_o^2(x) + \eta^2(x) \quad . \tag{73}$$

We may expand ψ in terms of some as yet unknown coefficients a_n as follows:

$$\psi = \sum_n a_n \phi_n \quad . \tag{74}$$

Upon substitution of eq. (74) into eq. (72), we obtain

$$\sum_n a_n k_o^2[s^2 - s_o^2]\phi_n = \sum_n a_n k_o^2 \eta^2 \phi_n \quad . \tag{75}$$

If we multiply this equation of ϕ_m and integrate, we will obtain the results

$$\sum_n a_n k_o^2[s^2 - s_o^2] = \sum_n a_n k_o^2 \int dx\ \phi_m(x)\phi_n(x)\eta^2(x) \quad . \tag{76}$$

Since the functions $\phi_n(x)$ are known, the integrals are obtainable in principle, and we may solve for the coefficients a_n in terms of them. The result will be a series of coupled equations. This can get very messy if a given initial solution ϕ_m is coupled by $\eta(x)$ to very many other solutions ϕ_n. The conversion to a difference equation is only practical if the coupling is only to a few other solutions. An example in which this can occur is when the ϕ_n are localized in a region smaller than the (unit cell) distance d. We consider the case in which we have

$$\begin{aligned} \int dx\ \phi_m(x)\phi_n(x)\eta^2(x) &= \alpha \quad , \quad m = n \\ &= \beta \quad , \quad m = n \pm 1 \quad , \\ &= 0 \quad , \quad (m - n) > 1 \quad . \end{aligned} \tag{77}$$

Then we will find

$$\beta(a_{n+1} + a_{n-1}) = (\bar{s} - \alpha)a_n \quad , \tag{78}$$

with $s^2 - s_o^2 = \bar{s}$. We see that we have greatly simplified the solution by our approximation. It has been found useful to assume that a_n is of the form

$$a_n = \lambda^n \quad . \tag{79}$$

Substitution of eq. (79) into eq. (78) yields

$$\lambda^{n-1} [\beta\lambda^2 - (\bar{s} - a)\lambda + \beta] = 0 \quad . \tag{80}$$

We now rewrite eq. (80) as

$$\lambda^2 - [\frac{s-\alpha}{\beta}]\lambda + 1 = 0 \quad . \tag{81}$$

We note that eq. (81) is of the same form as the eigenvalue equation for the transfer matrix, B. That is, if we wish to solve the equation,

$$\psi(x+d) = \lambda\psi(x) \quad , \tag{82}$$

we need to find the roots of the transfer matrix as given for example in eq. (79):

$$\begin{vmatrix} G(d) - \lambda & H(d) \\ G\neq(d) & H\neq(d) - \lambda \end{vmatrix} = 0 \quad . \tag{83}$$

This gives

$$\lambda^2 - [G(d) + H'(d)]\lambda + 1 = 0 \quad , \tag{84}$$

since det[B] = 1.

We know that the dispersion relation is

$$Tr[B] = G + H' = 2\cos kd \quad , \tag{85}$$

and take advantage of this insight to make the assumption

$$(\bar{s} - \alpha)/\beta = 2\cos kd \quad . \tag{86}$$

Now if we substitute eq. (86) into eq. (81), we will find

$$\lambda = \cos kd \pm i\sin kd = e^{\pm ikd} \quad . \tag{87}$$

In turn, substitution of eq. (87) into eq. (79) will bring

$$a_n = Pe^{iknd} + Qe^{-iknd} \quad . \tag{88}$$

Since the basis functions ϕ_n were assumed to be known, the problem has now been solved given the appropriate boundary conditions. We see from eq. (88) that we have shown that the assumption eq. (86) implies that the expansion eq. (74) is in terms of Block waves. Usually the equivalence is derived in the other direction: the Block expansion allowed due to the periodicity of the system implies the condition eq. (85).[32,33] We note that eqs. (70) and (78) are of similar form. This is in part due to our use of a Block expansion.

2.4.3 Termination Layers

We can investigate effects such as terminating the filter through the boundary conditions. We let the filter consist of N periods of length d, so that the filter has a length

$$L = Nd \quad . \tag{89}$$

We then impose the boundary condition that ψ be zero at L:

$$a_n = 0 \quad . \tag{90}$$

Together with eq. (88), eq. (90) implies that

$$a_n = A\sin(N - n)kd \;/\; \sin Nkd \quad . \tag{91}$$

Since A / sinNkd is simply a constant normalizing factor, we drop it in favor of

$$a_n = \sin(N - n)kd \quad . \tag{92}$$

We obtain our other boundary condition at the termination by making the substitution

$$\beta a_1 = (\bar{s} - \alpha')a_o \quad . \tag{93}$$

for eq. (78). Then eqs. (92) and (93) give

$$(\bar{s} - \alpha')\sin Nkd = \beta\sin(n - 1)kd \quad . \tag{94}$$

From eq. (94) and (86) we get

$$(\alpha - \alpha')/\beta + 2\cos kd = \cos kd - \cot Nkd \sin kd \quad , \tag{95}$$

or, with

$$\zeta = (\alpha - \alpha') / \beta \quad , \tag{96}$$

$$\zeta = -\sin(N = 1)kd / \sin Nkd \quad . \tag{97}$$

The intersection of this family of curves with the curves $\zeta(kd)$ = constant yield solutions for $\zeta > 1$. One solution, corresponding to a_o, the "surface state," will give a complex value of k. This wave will not propagate through the filter.

The edges of the pass band are given by the dispersion relation eq. (86). The density of states will be greatest at the band edges.

2.4.4 Extensions and Multiple Periodicity

The difference equation tack is a useful means of studying the effects of multiple periodicity. The conversion to a difference equation has been used extensively for this purpose in band theory and lattice dynamics. The published literature is a valuable guide for parallel calculations which we might wish to make. However, the results obtained in these fields are not readily used in optics, since energy band results seek to solve for the eigenvalues (or energy) of the Schroedinger equation, which is equivalent to solving for s in eq. (76) or $\bar{s}$ in eq. (78). We can easily take $\bar{s} = 0$, and wish to find the relation between k_o and k. We are also interested in an algorithm that is generally useful beyond the nearly free and tight binding approximations. It seems that this can be done. Let

$$\begin{bmatrix} \psi(x) \\ \\ \psi'(x) \end{bmatrix} = \vec{\psi}(x) \quad . \tag{98}$$

Then

$$\vec{\psi}(x+d) = B(d)\vec{\psi}(x) \quad . \tag{99}$$

and

$$\vec{\psi}(x-d) = B^{-1}(d)\vec{\psi}(x) \quad . \tag{100}$$

Hence

$$\vec{\psi}(x+d) + \vec{\psi}(x-d) = [B(d) + B^{-1}(d)]\vec{\psi}(x) \quad . \tag{101}$$

$$\vec{\psi}(x+d) = e^{kd}\vec{\psi}(x) \tag{102}$$

and

$$\vec{\psi}(x-d) = e^{-kd}\vec{\psi}(x) \quad , \tag{103}$$

we find

$$B(d) + B^{-1}(d) = 2\cosh(kd) \quad . \tag{104}$$

From eq. (17) (and the discussion following it in Paragraph 2.3) we have

$$B = \begin{bmatrix} G & H \\ G' & H' \end{bmatrix} \quad . \tag{105}$$

The inverse of B is

$$B^{-1} = \begin{bmatrix} H' & -H \\ -G' & G \end{bmatrix} \quad . \tag{106}$$

Therefore we may write eq. (104) as

$$\begin{bmatrix} G+H' & 0 \\ 0 & G+H' \end{bmatrix} = 2\cosh(kd) \quad , \tag{107}$$

or

$$(G+H') \begin{bmatrix} 1 & 0 \\ 0 & 1 \end{bmatrix} = 2\cosh(kd) \quad . \tag{108}$$

It seems that the difference method may be applied to a general problem, if the boundary conditions are suitably chosen with respect to the unit cell. This would be very useful for the analysis of a multiply periodic medium. Consider the system

$$\vec{\psi}_b = \left(\beta\vec{\chi}\right) \tag{109}$$

$$\vec{\psi}_a = \left(\alpha^{-1}\vec{\chi}\right) \quad , \tag{110}$$

where the subscripts refer to distances with respect to the argument of the r.h.s. We find

$$\vec{\psi}_b + \vec{\psi}_a \quad (\beta + \alpha^{-1})\vec{\chi} \quad . \tag{111}$$

Now

$$\vec{\chi}_a = \alpha\,\vec{\psi} \tag{112}$$

and

$$\vec{\psi}_{\bar{b}} = \beta^{-1}\vec{\psi} \quad . \tag{113}$$

Therefore

$$\vec{\chi}_a + \vec{\chi}_{\bar{b}} = (\alpha + \beta^{-1})\vec{\psi} \quad . \tag{114}$$

From eqs. (109) and (112) we get

$$\begin{aligned}(\beta + \alpha^{-1})\,(\alpha + \beta^{-1})\vec{\psi} &= (\beta + \alpha^{-1})\,(\vec{\chi}_a + \vec{\chi}_{\bar{b}}) \\ &= \vec{\psi}_{b+a} + \vec{\psi} + \vec{\psi} + \vec{\psi}_{\bar{a}+\bar{b}} \\ &= \vec{\psi}_d + 2\vec{\psi} + \vec{\psi}_{\bar{d}} \quad . \end{aligned} \tag{115}$$

We write eq. (113) as

$$[(\beta + \alpha^{-1})(\alpha + \beta^{-1}) - 2]\vec{\psi} = \vec{\psi}_d + \vec{\psi}_{\bar{d}} \quad . \tag{116}$$

With

$$\vec{\psi}_d = \lambda\vec{\psi} \tag{117}$$

and

$$\vec{\psi}_{\bar{d}} = \lambda^{-1}\vec{\psi} \tag{118}$$

we have

$$(\beta + \alpha^{-1})(\alpha + \beta^{-1}) - 2 = \lambda + \lambda^{-1} \quad , \tag{119}$$

or

$$\beta\alpha + \alpha^{-1}\beta^{-1} = \lambda + \lambda^{-1} \quad . \tag{120}$$

We let

$$M = \beta\alpha \tag{121}$$

and

$$\lambda = e^{kd} \quad . \tag{122}$$

Then we have

$$Tr[M] = \cos kd \quad . \tag{123}$$

2.5 Perturbation Expansions

We now look at some of the ways in which we can find approximate solutions for ψ and for the dispersion relation when the index modulation has a small departure about a profile for which we can solve.

2.5.1 Pedestrian Expansion

If we know that our modulation profile is similar to one for which we have a closed form solution we may make expansions about both the known solution and its corresponding modulation profile.[34] We let the known solution be ψ_1, and the unknown solution be ψ. We then write

$$\psi \approx \psi_1 + \delta_1\psi_2 + \delta_1^2\psi_3 \quad , \quad \delta_1 << 1 \quad . \tag{124}$$

As δ_1 increases, we will need to include more terms in the expansion for ψ. Similarly, if the dielectric constant for the known case goes like $n_1^2(x1)$, we write

$$n^2(x) = n_1^2(x) + \delta_2 n_2^2(x) + \delta_2^2 n_3^2(x) \tag{125}$$

for $n_2(x)$ in the unknown case. Then, upon substituting eqs. (131) and (132) into eq. (47) with $s^2 = 0$:

$$d^2\psi/dx^2 + k^2n^2(x)\psi = 0 \quad , \tag{126}$$

we obtain

$$d^2(\psi_1 + \delta_1\psi_2 + \delta_1^2\psi_3)/dx^2 +$$

$$k^2(n_1^2 + \delta_2 n_2^2 + \delta_2^2 n_3^2)(\psi_1 + \delta_1\psi_2 + \delta_2^2\psi_3) = 0 \quad . \tag{127}$$

We can separate terms of a given order and arrive at a series of equations:

$$\psi_1'' + k^2n_1^2\psi_1 = 0 \quad , \tag{128}$$

$$\psi_2'' + k^2n_1^2\psi_2 = -(\delta_2/\delta_1)n_2^2\psi_1 \quad , \tag{129}$$

and

$$\psi_3'' + k^2 n_1^2 \psi_3 = -(\delta_2/\delta_1) n_2^2 \psi_2 - (\delta_2/\delta_1)^2 n_3^2 \psi_1 \qquad (130)$$

Equation (135) is our solvable homogeneous equation with a known solution. Equations (136) and (137) are similar to eq. (135) but are inhomogeneous. We can think of eq. (136) as a problem in which the solution to eq. (135) drives an oscillator of the same form as that of eq. (135).

We can learn something about the dispersion relation (k_o versus k) if the amplitude of the index modulation is small by making another expansion, similar to that of eq. (65), We write

$$\psi_k(x) = \sum_j A_j(k) e^{ik_j x} \quad , \qquad (131)$$

with

$$k_j = k + 2\pi j/d \quad . \qquad (132)$$

2.5.2 Band Gap for Small Perturbations

We assume a small perturbation in the index modulation about a value for which we can solve. Then we have[26,27]

$$\psi_k(x) \approx A_m e^{ik_m x} + \delta_1 \sum_j A_j e^{ik_j x} \quad . \qquad (133)$$

We begin by letting m = 0. We write our equation for ψ as

$$\psi'' + k_o^2 (n_0^2 + \delta_2 n_1^2)\psi = 0, \qquad (134)$$

with.

$$n_1^2 = \sum_\ell g_\ell e^{iK_\ell x} \quad , \qquad (135)$$

and

$$K_\ell = 2\pi\ell/d \quad . \qquad (136)$$

Then we substitute eqs. (140) and (142) into eq. (141) and find

$$A_o(k_o^2 n_o^2 - k^2)e^{ikx} + \delta_1 \sum_j{}' (k_o^2 n_o^2 - k_j^2) A_j e^{ik_j x}$$

$$+ \delta_2 k_o^2 A_o \sum_\ell g_\ell e^{iK_\ell x}$$

$$+ \delta_1 \delta_2 k_o^2 \sum_j{}' \sum_\ell g_\ell A_j e^{i(k_j + K_\ell)x} = 0 \quad . \tag{137}$$

To first order we let

$$\delta_1 \approx \delta_2 = \delta \quad .$$

Then to first order we have approximately[27]

$$A_o(k_o^2 n_o^2 - k^2)e^{ikx}$$

$$+ \delta \sum_j [(k_o^2 n_o^2 - k_j^2) A_j + A_o k_o^2 g_\ell] e^{ik_j x} \approx 0 \quad . \tag{138}$$

We now operate on eq. (145) with

$$\int_o^d dx\, e^{-ik_j x} \quad .$$

We find

$$k \approx n_o k_o \quad , \; j = 0 \quad . \tag{139}$$

$$A_j = \frac{k_o^2}{k_j^2 - n_o^2 k_o^2} g_\ell A_o \quad , \quad j \neq 0 \quad . \tag{140}$$

We see that to first order in δ, k is unchanged, and the form for ψ is modified slightly. If we operate with

$$\int_o^{\;d} dx e^{-ikx}$$

we find to second order in δ (see Reference 27)

$$A_o(k_o^2 n_o^2 - k^2)d + \delta_1 \delta_2 \sum_j{}' \sum_\ell A_j g_\ell \int_o^d dx e^{i(k_j + K_\ell - k)x} \approx 0 \quad . \tag{141}$$

The integral vanishes, unless

$$\ell = -j \quad . \tag{142}$$

Hence

$$A_o(k_o^2 n_o^2 - k^2) + \delta_1\delta_2 \sum_j{}' A_j g_{-j} = 0 \quad . \tag{143}$$

From eq. (140), we find

$$k^2 = k_o^2 n_o^2 + \delta_1\delta_2 \sum_j{}' \frac{k_o^2}{k_j^2 - n_o^2 k^2} g_j g_{-j} \quad . \tag{144}$$

We see that a problem develops in eqs. (140) and (144) when $k \to k_j$. We can patch this up by increasing the contribution from the mth term:

$$\psi = A_o e^{ikx} + A_m e^{ik_m x} + \delta_1 \sum_j{}'' A_j e^{ik_j x} \quad . \tag{145}$$

Then proceeding as before, we find to first order

$$A_o(n_o^2 k_o^2 - k^2) + \delta k_o^2 A_m g_m = 0 \tag{146}$$

and

$$\delta k_o^2 A_o g_{-m} + (n_o^2 k_o^2 - k_{-m}^2) A_m = 0 \quad . \tag{147}$$

Hence

$$(n_o^2 k_o^2 - k^2)\,(n_o^2 k_o^2 - k_{-m}^2) = \delta^2 k_o^4 g_m^2 \quad . \tag{148}$$

For $k \approx k_{-m}$ we find approximately

$$k_o^2 \approx k_{\bar{m}}^2 / (n_o^2 + \delta g_m) \quad . \tag{149}$$

This creates a band gap with width

$$\Delta k = \frac{g_m}{2n_o^2} k_m = \frac{g_m}{2\varepsilon_o} k_m \quad . \tag{150}$$

This means that a stop band is formed whose width for the mth band is proportional to the mth component of n_1^2.

3. RESULTS

3.1 Centerband Frequency

The location of the jth order peak in a spectrum can be found by the Coupled Mode formula

$$k_c = \pi j/\sqrt{\varepsilon} = {}_o\pi j/\bar{n} \quad . \tag{151}$$

For matched index filters there is agreement within 1% with eq. (158) at N as low as 12. For N in regions of interest (~100) there is neglibible discrepancy (0.01%). The prediction of CMT for unmatched external indices is somewhat less accurate and may have 1% or better accuracy down to only N = 50. However, in regions of interest the size effect poses little problem.

An incident angle other than zero will cause an increase in the center frequency

$$k_c = \frac{k_n}{\cos[\sin^{-1}(n_1/\bar{n}\ \sin\theta)]} \quad . \tag{152}$$

where $k_n = k_c$ at $\theta = 0$. For $\cos\theta$ close to 1, the formula can be rewritten in the form shown on Table 1. This table also gives χ^2 values for fits to eq. (152) of simulated data. An example of such a fit is given in figure 9. The modulation depth plays a comparatively small role in the angular dependence of the center frequency. Because of Snell's Law the frequency shift can be lessened if the mean index of the filter is increased. For small angles

$$k_c(\theta) \sim 1/\bar{n}^2 \quad .$$

Figure 10 illustrates the dependence of the center frequency upon N. At the low end of the graph, the center frequency markedly departs from its predicted location. Figure 11 is similar to figure 10 although the filter length is not restricted to integer number of layers (partial cycles at the end of the filter are included). The oscillation evident here is generally increased when external indices are unmatched.

The effect of the shape of the modulation profile, length of the filter, modulation depth, and harmonic number was studied for Kronig-Penney profiles. In all cases the shift is quite small, being most pronounced for filters with only a few layers (fig. 12) or large modulation depth (fig. 13). The shift will be positive or negative depending on whether the harmonic is even or odd (fig. 14).

Allowing the indices of the external medium to be unmatched to the mean index of the filter increases the deviations from the CMT center frequency prediction. One way of negating this effect is to add index matching layers to the filter. Another is to increase the modulation depth. The result will be a greater relative contribution to the reflectance by the filter. Figure 15 illustrates the corrective effect of increasing the modulation depth in a filter with unmatched external indices.

Table 1. Angular dependence of peak location.

n_1	n_ℓ	ε_1	ε_0	θ range = 0 → 45° Cells	$n(\sqrt{\varepsilon_0})$ predicted	n	χ^2	% err.
1	2	0.1	4	100	2	1.9548	0.02	2.3
1	2	0.1	4	200	2	1.9537	0.02	2.3
1	2	0.2	4	100	2	1.9547	0.02	2.3
1	2	0.2	4	200	2	1.9518	0.02	2.3
1	3	0.09	9	100	3	2.9786	0.0004	0.7
1	3	0.9	9	100	3	2.9849	0.001	0.5
1	1.7321	0.03	3	100	1.7321	1.6879	0.03	2.5
1	1.7321	0.3	3	100	1.7321	1.6860	0.04	2.7
1	2.4495	0.06	6	100	2.4495	2.4203	0.002	1.2
1	2.449	0.06	6	100	2.4495	2.4216	0.002	1.1

$$\frac{\delta k_c}{k_n} = 1 - \cos\left|\sin^{-1}\left(1/n \sin\phi\right)\right|$$

$$\delta k_c = k_c - k_n \qquad k_n = k_\phi = 0 \quad .$$

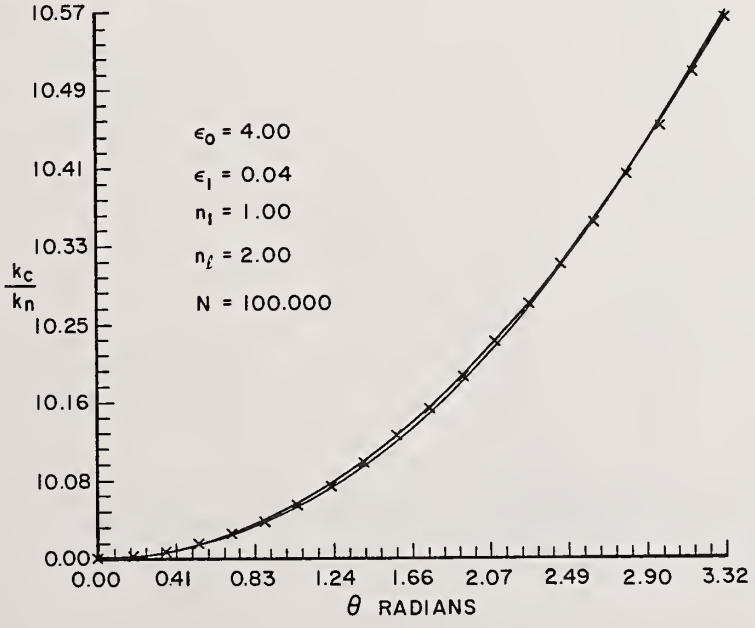

Figure 9. Comparison of simulated and predicted shift of peak frequency versus angle of incidence.

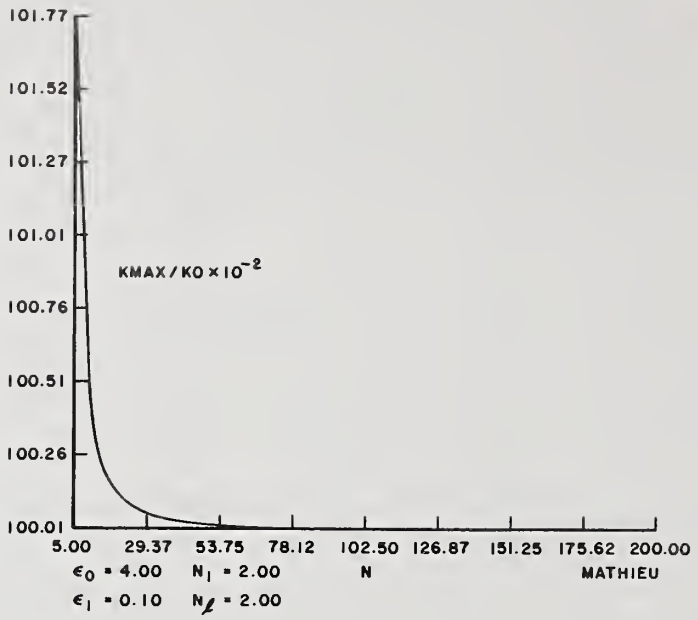

Figure 10. Shift in peak frequency as a function of filter length for sinusoidal profile.

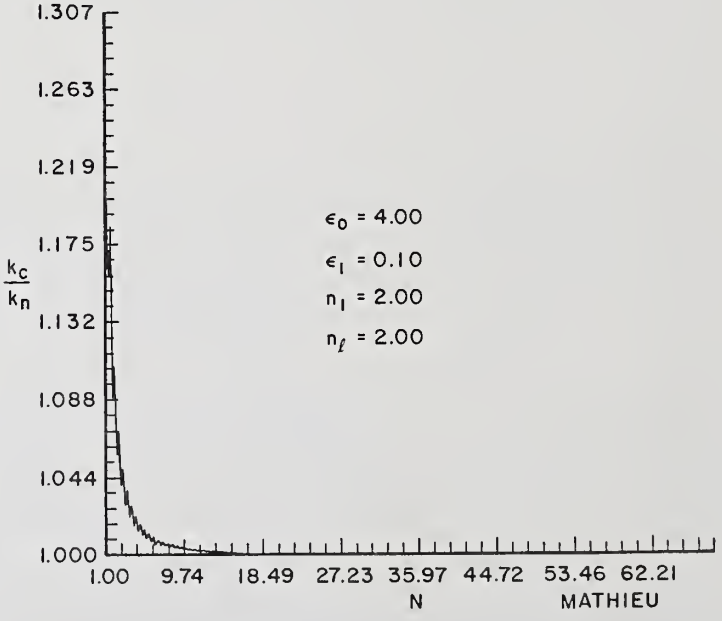

Figure 11. Shift in peak frequency as a function of modulation profile shape.

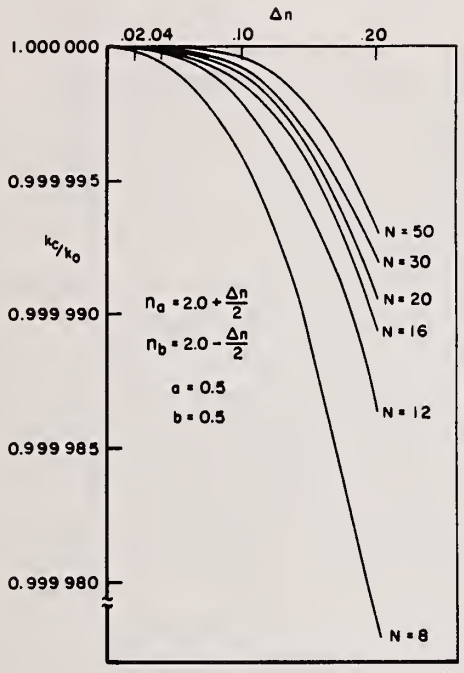

Figure 12. Shift in peak frequency as function of both modulation depth and filter length for step-function profile.

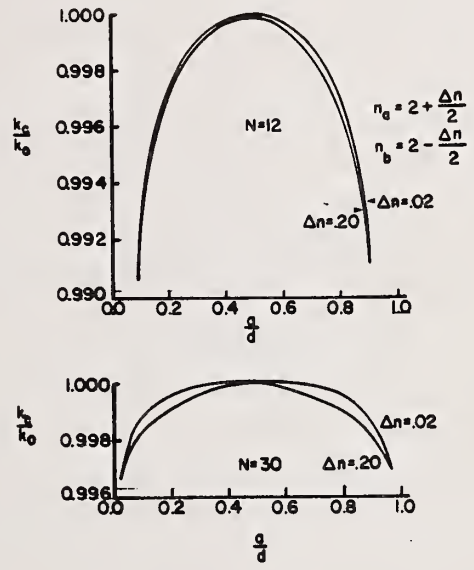

Figure 13. Shift in peak frequency as a function of modulation profile shape.

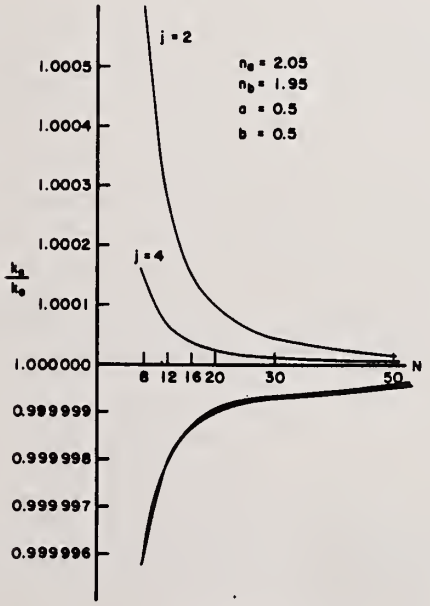

Figure 14. Mode dependence of peak frequency shift with filter length. Even harmonics shift up, while odd harmonics shift down.

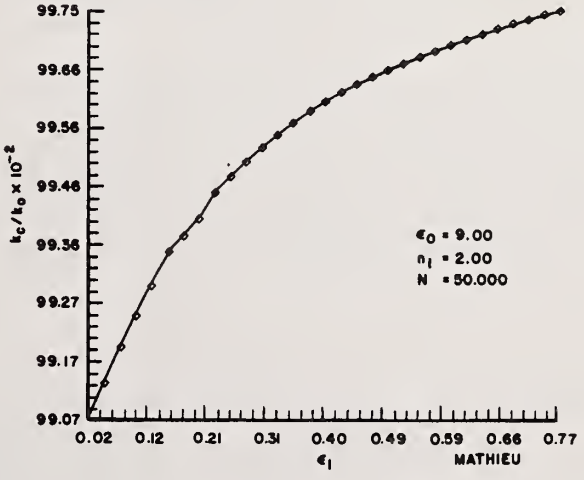

Figure 15. Shift in peak frequency versus modulation depth for sinusoidal profile.

3.2 Line Width

The stop-band line width was taken as the fill width at half maximum (FWHM) of the reflectance. This is not the same as the width of the band gap--the range of k_o values for which the resulting Block wave has an imaginary part. Though both criteria are good indicators of the width of the peak, they coincide only for very long filters. CMT predicts that the band gap in the dispersion curve scales linearly with $\varepsilon_1/\varepsilon_0$. It was found that the same behavior was true of the FWHM except that a size effect becomes noticeable for small modulations. Figure 16, depicting Kronig-Penney simulations, shows that whereas the normalized linewidth is linear with the normalized modulation depth out to quite large (→100%) values of modulation, the graph depicting this dependence has a nonzero intercept. This is due to the finite thickness of the filter, which is not taken into account in CMT. The effect is quite significant even at N = 50, and means that filters will have finite linewidths even if the modulation depth is arbitrarily small. This means that ultranarrow band filters must be made very thick. The slope of the Δk vs Δn dependence depends on the harmonic of the band in question and the shape of the modulation profile. Thus the relative widths of various harmonic stop bands will depend upon the modulation depth, as well as upon the shape of the modulation profile (fig. 17). Figure 18 illustrates how these two parameters are related for the fundamental band in a square-well filter. For small modulation depths the Δk vs Δn dependence is no longer linear. The curve bends so that the dependence on Δn becomes slight. An attempt was made to find a simple empirical formula for this curve, based on the concept that CMT should be corrected for finite filter thickness.

The analytic formula fitted to the reduced data, was:

$$\frac{\Delta k}{k_c} = \sqrt{\alpha(\varepsilon_1/\varepsilon_o)^2 + \beta^2} \quad . \tag{153}$$

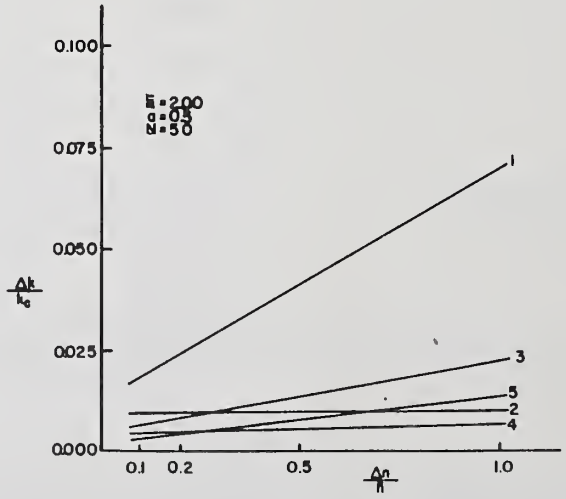

Figure 16. Scaling of line width as a function of modulation depth for first five harmonics of square-well profile. Non-zero intercept is due to filter length.

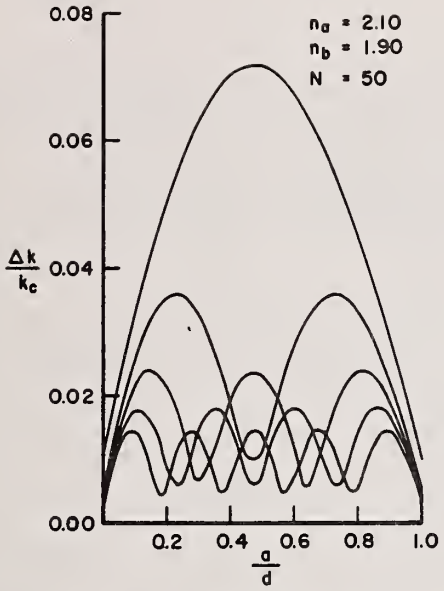

Figure 17. Seating of line width as a function of profile shape for first five harmonics of step-function profile. The dependence is given exactly by a Fourier-transform of the modulation profile. Non-zero pedestial is due to finite filter length.

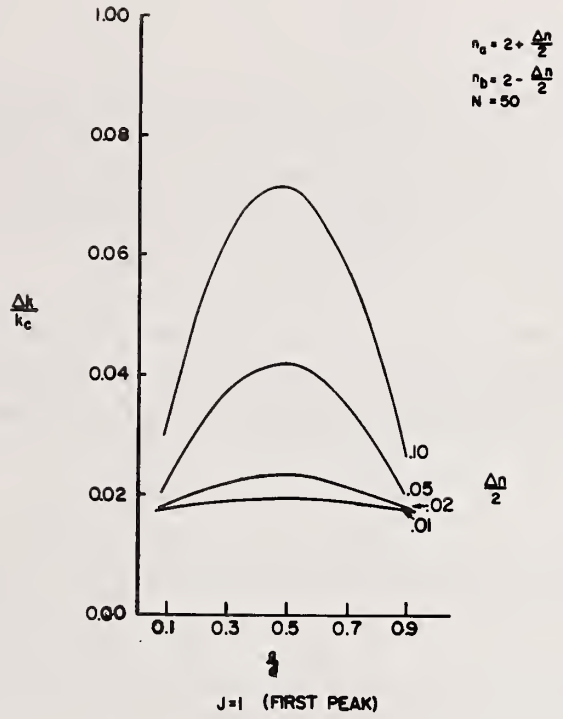

Figure 18. Scaling of line width for both modulation depth and profile shape for fundamental peak.

The parameter β is a function of N. First, a simple $1/N^2$ correction was made to eq. (153). The results from this are given in Tables 2 and 3. It was found that a power series in 1/N without the radical worked better. The formula and results for this model are given in table 4.

Figure 19 shows the line width plotted against the relative modulation depth for the Mathieu case. Figure 20 shows the fitted analytic function (marked by x's) as well. The curvature at the left end of the plots is less for large N. Figure 21 shows the N-dependence of the peak width. The figure shows a fit to a formula which corrects for finite filter thickness through a 1/N power series, along with the Chi-squared value and the values of the formula parameters obtained.

3.3 Peak Reflectance

When the mean index of the filter matches the indices of the adjoining media, the value for peak reflectance can be obtained with great accuracy using a very simple CMT prediction,

$$R_p = \tanh^2 \kappa N \qquad (154)$$

κ is called the coupling constant and is equal to the maximum imaginary part that the Block wave attains inside the band gap. According to CMT, this value scales linearly as $\varepsilon_1/\varepsilon_o$. It was found that in the Mathieu case

$$\kappa = \frac{\pi}{4}\frac{\varepsilon_1}{\varepsilon_o} \quad . \tag{155}$$

The same linear scaling factor was determined for a variety of square-well cases, each with a different a/d ratio. Table 5 gives the Mathieu results, and Table 6 gives the square-well results. The resulting dependence of κ on the relative modulation depth is plotted in fig. 22. A κ versus a/d plot is shown in fig. 23. The x's show the best attempted fit to this curve thus far. Agreement is only qualitative.

Two peak reflectance versus N curves with their fit to eq. (154) are shown in figs. 24 and 25. Chi-squared values for these fits often dropped below 10^{-8}, indicating an error as likely intrinsic to computer digitation as it is to the equation itself.

Table 2.

Δk vs. $(\varepsilon_1/\varepsilon_0)$ N

$n_1 = n_\ell = 2.0 \quad \varepsilon_o = 4.0$

N	α	β	χ^2
12	0.6027	0.8826	5×10^{-5}
30	0.6075	0.8889	2×10^{-2}
100	0.5579	0.9624	0.1

$n_1 = n_\ell = 3.0 \quad \varepsilon_0 = 4.0$

N	α	β	χ^2
12	0.6048	0.8803	2×10^{-4}
30	0.6157	0.8838	5×10^{-4}
50	0.5944	0.8947	4×10^{-2}
100	0.5481	0.9271	8×10^{-2}
200	0.5137	0.9302	3×10^{-2}

$$\frac{\Delta k}{k_c} = \sqrt{\left(\frac{\varepsilon_1}{\varepsilon_o}\right)^2 + \left(\frac{\beta}{N}\right)^2}$$

Table 3.

Δk vs. $(N)\varepsilon_1$

$n_1 = n_\ell = 2.0 \quad \varepsilon_o = 4.0$

ε_1	α	β	χ^2
0.10	0.5599	0.8702	0.04
0.25	0.5563	0.8802	0.3
0.50	0.5296	0.9058	10

$n_1 = n_\ell = 3.0 \quad = 9.0$

ε_1	α	β	χ^2
0.10	0.5999	0.8581	0.2
0.25	0.5974	0.8847	0.03
0.50	0.5819	0.8570	0.6

Table 4. Three parameter fit.

$n_1 = n_\ell = 2.0 \quad \varepsilon_0 = 4.0$

ε_1	α	β	γ	χ^2
0.01	0.2256	0.8718	-0.04642	0.008
0.10	0.4791	0.6576	0.7462	0.08
0.25	0.4919	0.5349	0.9320	0.1

$$\frac{\Delta k}{k_c} = \alpha \frac{\varepsilon_1}{\varepsilon_0} + \frac{\beta}{N} + \frac{\gamma}{N^2}$$

This form is an expansion of the square root. It cannot be used for $\varepsilon_1/\varepsilon_0$ versus γk, as it yields only a straight line in N.

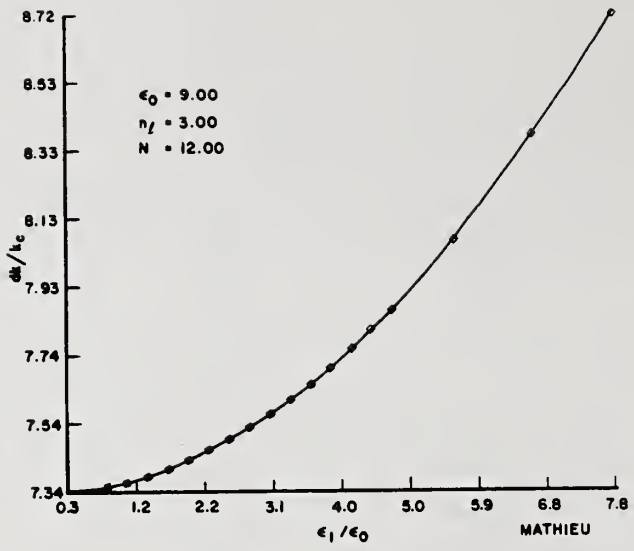

Figure 19. Comparison of computer simulations to predicted shift in peak frequency versus modulation depth for sinusoidal profile.

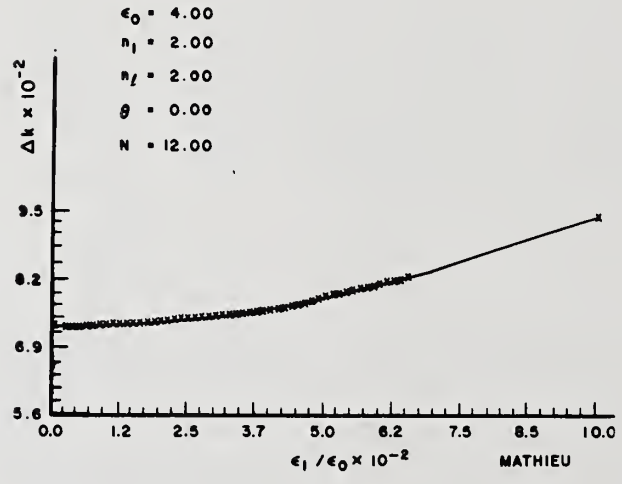

Figure 20. Fit of computer simulation to predicted increase in line width as a function of modulation depth.

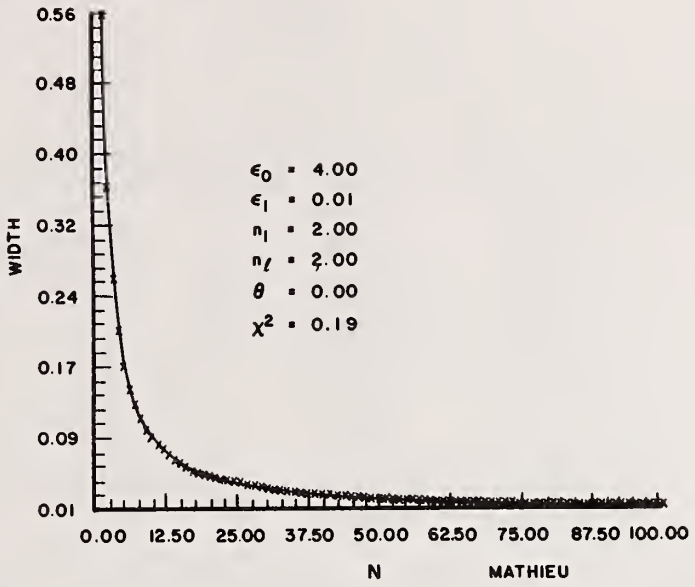

Figure 21. χ^2 fit of simulated data to predicted change in line width as a function of filter length.

Table 5. R_p versus N for matched indices

$n_1 = n_\ell = 2$

$\varepsilon_o = 4.0$

ε_1	κ	χ^2	$K\frac{\varepsilon_o}{\varepsilon_1}$ *
0.01	1.9635×10^{-3}	3×10^{-7}	0.7854
0.10	1.9638×10^{-2}	2×10^{-4}	0.78552
0.25	4.915×10^{-2}	6×10^{-3}	0.7864
0.40	7.875×10^{-2}	2×10^{-2}	0.7875
0.50	9.859×10^{-2}	3×10^{-2}	0.78872

$n_1 = n_\ell = 3$

$\varepsilon_o = 9$

0.10	8.727×10^{-3}	1×10^{-4}	0.78543
0.25	2.1821×10^{-2}	1×10^{-3}	0.78556
0.50	4.3681×10^{-2}	2×10^{-2}	0.78626

$R = \tanh^2 \kappa N$

* These numbers approach $\pi/4$.

Table 6.

κ vs. ε_1

$n = n_1 = n_\ell = 2.0$

a/d	b	c	$\chi^2 \times 10^{-5}$
0.1	0.3041	0.3443	6
0.2	0.5845	0.4592	2
0.3	0.8092	0.3835	0.3
0.4	0.9528	0.1960	0.6
0.5	1.0035	-0.0599	4
0.6	0.9524	-0.2639	0.3
0.7	0.8081	-0.3767	0.3
0.8	0.5843	-0.3515	3
0.9	0.3056	-0.2107	2

$\kappa = b\varepsilon_1/\varepsilon_0 + c(\varepsilon_1/\varepsilon_0)^2$

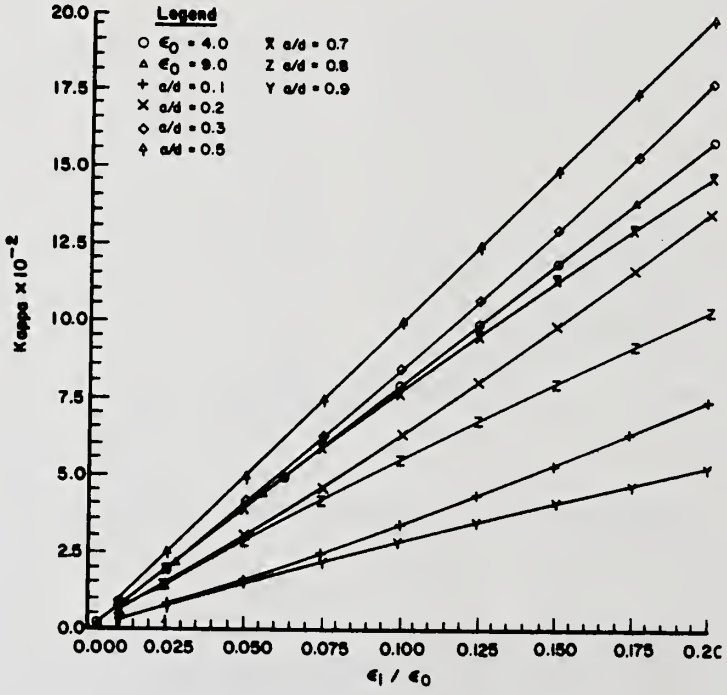

Figure 22. Dependence of coupling parameter κ on modulation profile shape and depth.

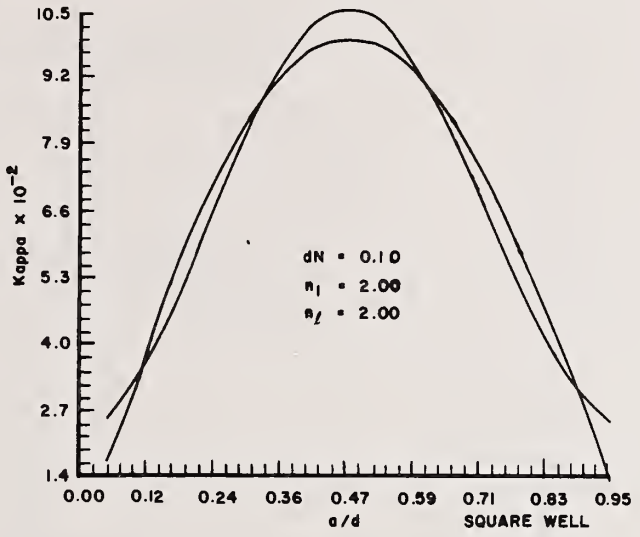

Figure 23. Breakdown of predictions of couple-mode theory of dependence of κ on profile shape.

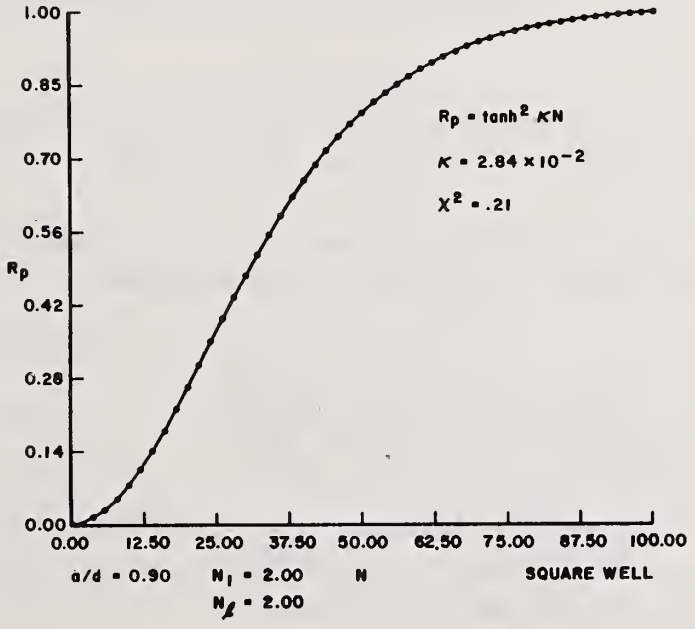

Figure 24. Agreement of computer simulations to analytic predictions of the scalling of peak reflectance versus filter length for square-well profile.

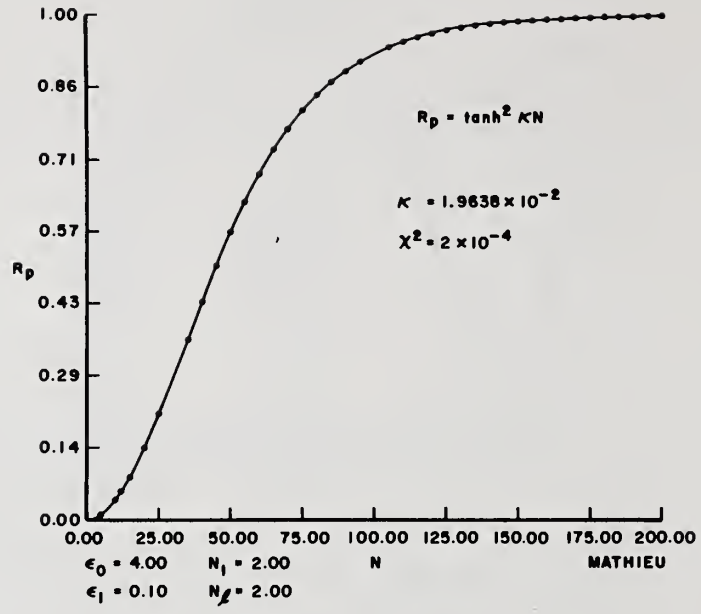

Figure 25. χ^2 fit of scaling of peak reflectance with filter length for sinusoidal profile with analytic predictions.

Figure 26 is a plot of peak reflectance versus the product of N and the modulation depth. It serves further to illustrate the validity of eqs. (154) and (155).

If the filter has unmatched external indices, eqs. (154) and (155) no longer give accurate predictions. Since the change in curve form was greatest for small N, a perturbation in eq. (154) was first tried:

$$R_p = \left(\frac{\sinh(\kappa N + A_2 + A_3/N + A_4/N^2)^2}{\cosh(\kappa N + A_5 + A_6/N + A_7/N^3)} \right) \quad . \tag{156}$$

Some of the resulting parameter values and Chi-squared values are given in table 7. Once good parameter values are established, the peak reflectance can be found to within 1% down to N = 3, but the equation is rather cumbersome to use.

A second formula was used that dealt with optical density rather than reflectance. The equation is an upward opening with an arbitrary center.

$$D = A_1 + (N + A_2)^2 + A_3^2 \quad . \tag{157}$$

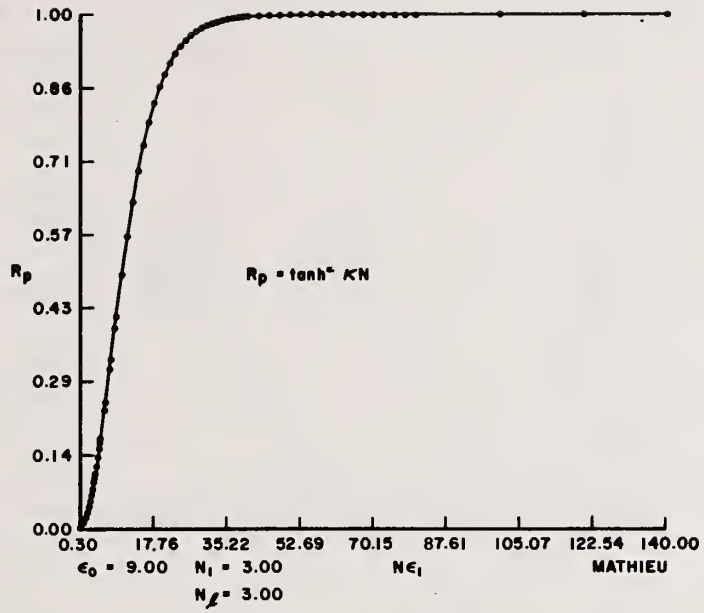

Figure 26. χ^2 fit to analytic predictions showing scaling of peak reflectance as a function of $N\epsilon_1$.

Table 7. R_p versus N

Unmatched Indices

$\epsilon_0 = 4$ $N_1 = 1$ $N_e = 2$ $\epsilon_0 = 9$ $N_1 = 1$ $N_\ell = 3$

1	0.10	0.25	0.10
κ	1.646×10^{-2}	1.784×10^{-2}	6.891×10^{3}
A_2	0.3063	0.6469	0.5241
A_3	8.952×10^{-2}	0.2487	4.832×10^{-2}
A_4	-4.872×10^{-2}	4.636×10^{-2}	5.015×10^{-2}
A_5	0.2924	0.6461	0.5088
A_6	-9.839×10^{-3}	4.496×10^{-2}	4.9613×10^{-2}
A_7	4.835×10^{-3}	3.657×10^{-3}	5.000×10^{-3}
χ^2	0.4	0.5	0 2

$$R_p = \left(\frac{\text{sink } (KN + A_2 + A_3/N + A_4/N^3)^{\,2}}{\cosh\,(KN + A_5 + A_5/N + A_7/N^3)} \right) .$$

Equation (157) produced chi-squared values comparable to those given by eq. (155) using only four parameters. The fit to the data is given in fig. 27. The curve is nearly linear for N ~ 60. Parameter values for this fit are $\kappa = 1.771 \times 10^{-2}$, $A_1 = -0.8053$, $A_2 = 4.6595$, $A_3 = 0.8670$, $\alpha^2 = 0.8$.

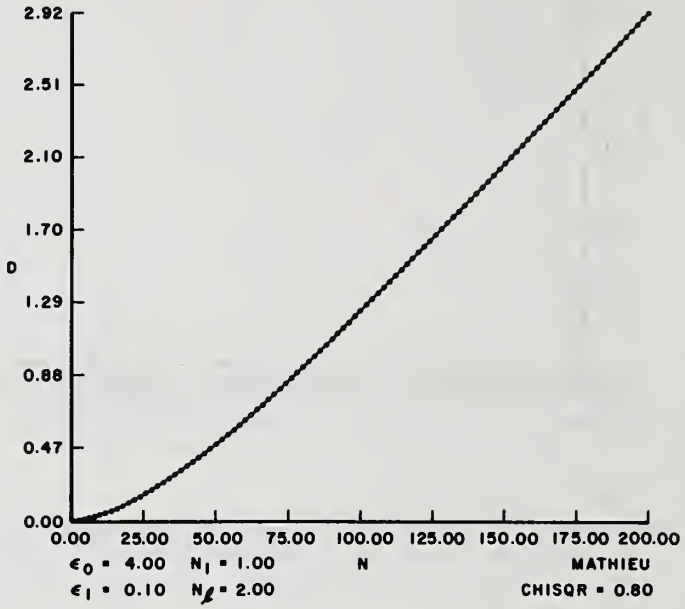

Figure 27. χ^2 fit to analytic predictions of the scaling of optical density with filter length.

3.4 Angular Dependence

All filter characteristics vary with incident angle. It is particularly interesting to see how the variations differ for TM and TE waves. Figures 28 and 29 illustrate a variation in peak height and width as functions of incident angle. The center frequencies for TM and TE waves are the same for all angles. As the angle approaches 45° (approximately Brewster's angle) the TM waves approach complete transmission. The peak reflectance and width both drop before beginning to increase again at higher angles. In contrast, TE wave reflectance is always enhanced by the increasing angle, and the peak height and width both increase. At normal incidence the spectra for TM and TE waves match, but at 20° dissimilarities begin to show between the two cases. All peaks are shifting to the right, and the TE reflectance is growing while the TM reflectance is decreasing. An alternate view of the incident angle effects is given by the dispersion curves. Again the curves match for TE and TM cases at normal incidence. However, at 45° the stop bands on the TE curve have broadened, while those for the TM curve have disappeared.

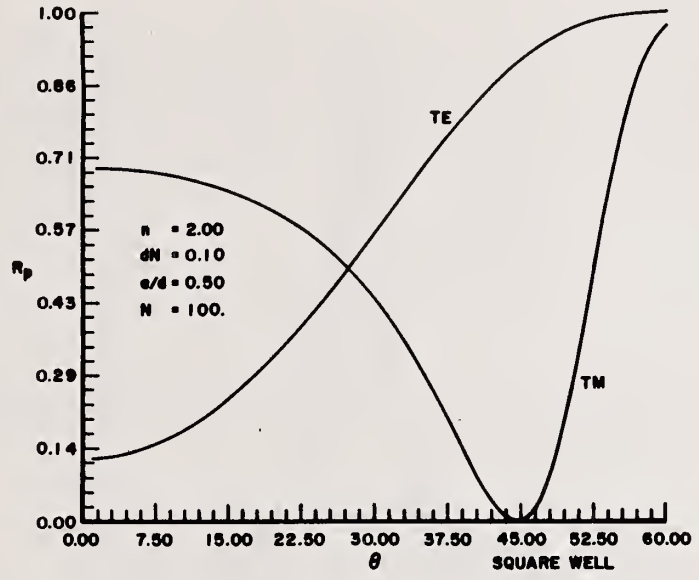

Figure 28. Polarization dependence of peak reflectance versus angle of incidence.

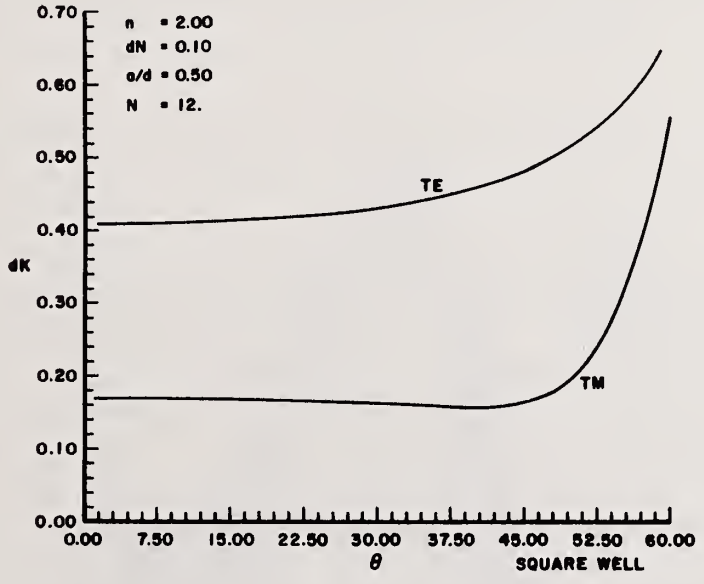

Figure 29. Polarization dependence of a function of incidence angle.

3.5 Sideband Spectra

The sideband data contain useful information about the filter structure. Only the Mathieu case will be treated here, and it should be pointed out that preliminary studies of square well show significant differences from the Mathieu case. If a filter is comprised of N cells, then between any stop bands there will be N-1 side peaks. The conditions for their extreme are

$$\kappa N = n\pi \tag{158}$$

and

$$\kappa N = (n + 1/2)\pi \tag{159}$$

where n is any integer and k is the Block wave number for a particular incident wave number. The reflectance at condition (158) is given by

$$R = \left(\frac{n_1 - n}{n_1 + n_\ell} \right)^2 . \tag{160}$$

These reflectances will be minimal in filters where $n_1 = n_\ell$.

Quantitative expressions for the reflectance at the other condition have yet to be derived, but it is known that the expressions will be a function of ε_1, ε_o and the product of n_1 and n_ℓ. The envelopes traced by reflectances at the extreme are independent of filter length.

Figures 30 and 31 illustrate the independence of the sideband envelopes upon filter length. The cascade plots are taken over a wide range of cell numbers and drawn from the same spectrum.

All of the above discussion applied to filters with only integral numbers of layers. The addition of a top layer that consists of only a fraction of a unit cell often has a profound effect on the filter's performance. This effect has been studied qualitatively in the Mathieu case. For filters with matched indices, the partial layer effect is very small. This is due to the very minor role that the sidebands play in determining the spectrum of a matched index filter. The larger the side peaks are in relation to the main peak, the greater the effect of the partial layer becomes. The physical reason for this is qualitatively simple. As the number of layers in a filter is increased from N to N + 1 the number of sidebands to the left of the first peak and between every two adjacent peaks must change from N - 1 to N. This new peak appears gradually as the filter length is increased continuously from N to N + 1. What happens is that the first main peak begins to shrink and move to the left where, when the new layer is completed, it becomes the additional side peak. Meanwhile, the first side peak to the right of the main peak begins to grow and move to the left until it becomes the new main peak. The same thing happens to the second main peak except that, instead of needing to furnish only one additional side peak, it must provide two--one to make up for the side peak lost to the first main peak, and the other to add the extra side peak corresponding to the addition of a new layer. So the second main peak is replaced twice, the third three times, and so on.

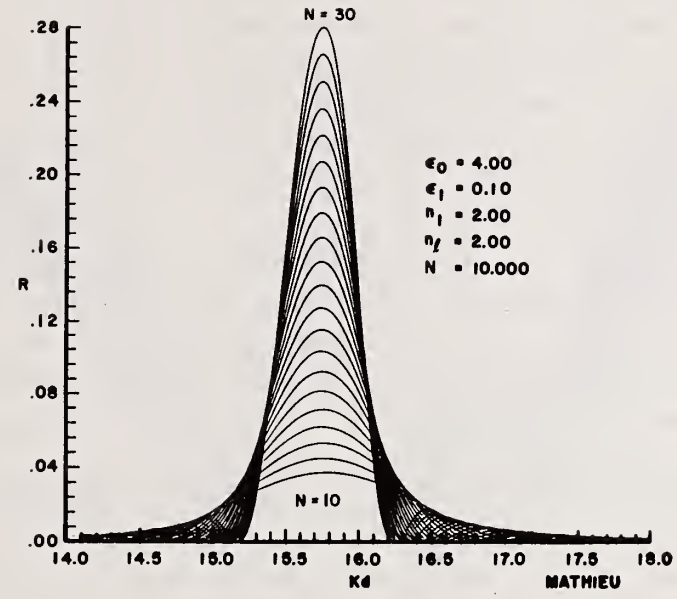

Figure 30. Build up of reflectance with increasing filter length.

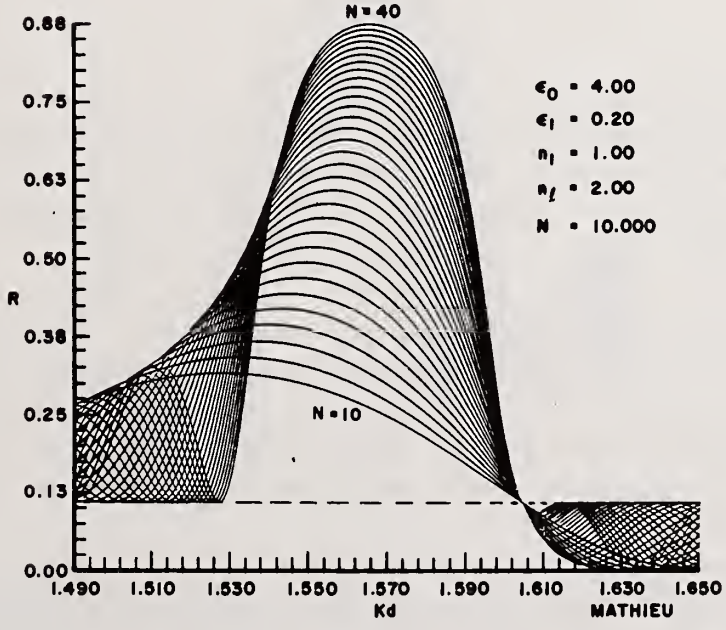

Figure 31. Change in shape of reflectance spectrum as a function of

If the main peak and the side peak to its right (becoming the new main peak) remain distinct throughout the shifting process, there will be a point at which their heights are equal. At this point, rather than a single strong peak, two weaker peaks separated by a dip will occur. In the particular case of $\varepsilon_o = n_\ell$ this dip is most pronounced at a quarter cycle partial layer. At three quarters of a layer with the same bulk parameters, a single peak larger than the ones at either N or N + 1 layers is observed. The particular values for the fractional layer change, but in all unmatched cases the same behavior occurs at some point in the partial cycle.

Depending on the amount of the index discontinuity at the filter surfaces, a large enough N or dielectric modulation will cause the surface layer effect to disappear. Essentially, the contribution from the bulk of the filter to the reflectance is large enough to make the contributions from the index discontinuities insignificant. Figure 32 shows a main peak as the filter changes in length from 30 to 31 layers.

3.6 Complex Dielectrics, Wave Functions, and Incommensurate Lattices

A negative imaginary part in the dielectric constant signifies an absorbing medium. All real materials are at least slightly absorbing. Figure 33 is a spectrum plot that shows the effects of increasing amounts of absorption in the mean dielectric. Across the tops of this reflection spectrum is a transmission curve. In a non-absorbing medium, the sum of reflection and transmission at any wave number would be one, but for an absorbing medium the difference between their sum and one is the amount of light absorbed by the filter. Since the wave number in the filter, k, is given roughly by

$$k \approx \varepsilon_o k_o \tag{161}$$

the rate of oscillation of the wave function scales with k. Note that one feature of deriving the transfer matrix from the solution to the wave equation is that the strength of the electric field as a function of position in the filter is automatically obtained as part of the calculation. This fact is particularly apt for laser hardening applications. Examples of this capability are given in figs. 34 and 35.

The Bragg condition states that maximum reflectance (or least transmittance) will occur when light reflected from the beginning of one layer of the filter is in phase with light reflected from the beginning of the next layer. In fig. 7 the wave function is plotted beneath the potential function--both versus distance. When the light wave incident is below the stop band, the Block wave changes very slowly with respect to the oscillation in the modulation profile.

The propagation of a Block wave belonging to the stop band has a rate of oscillation of about half that of the potential. This means that a wave reflected from the beginning of one layer will be in phase with a wave reflected from the beginning of the next, and the Bragg condition for maximum reflection is satisfied. Above the stop band the Block wave oscillation is much greater than the periodicity in the potential.

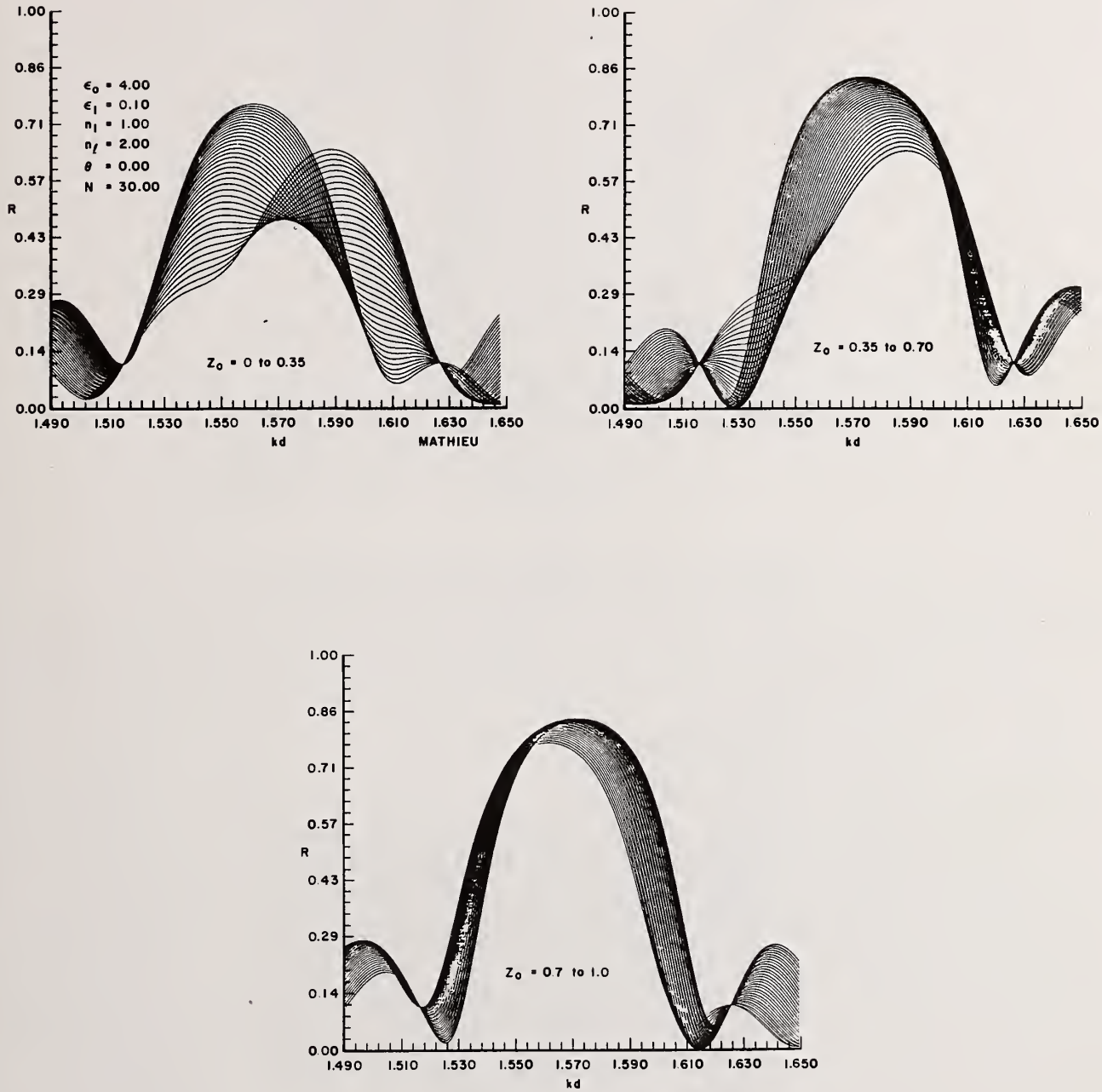

Figure 32a, b, c. Change in shape of reflectance spectrum during the growth of a single layer. The spectrum moves across an envelope determined by the shape of the modulation profile.

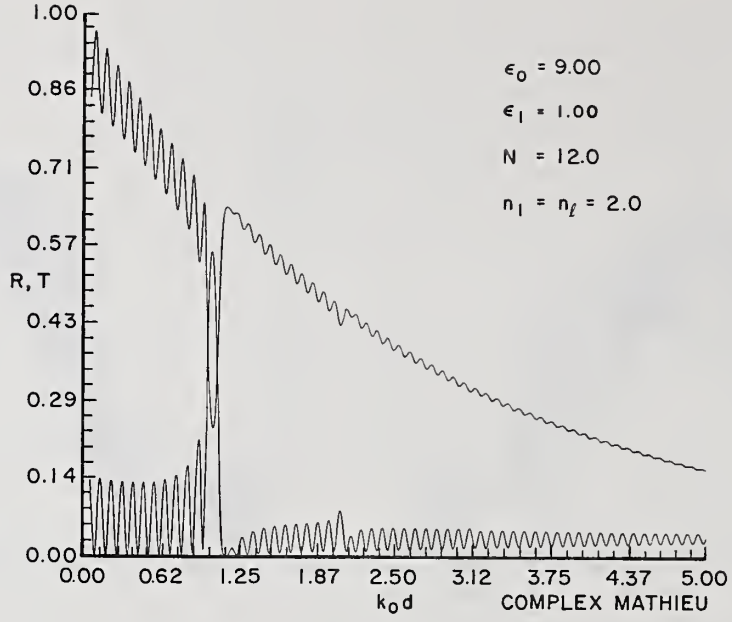

Figure 33. Reflection and transmission spectra for a filter with a complex Dielectric Constant.

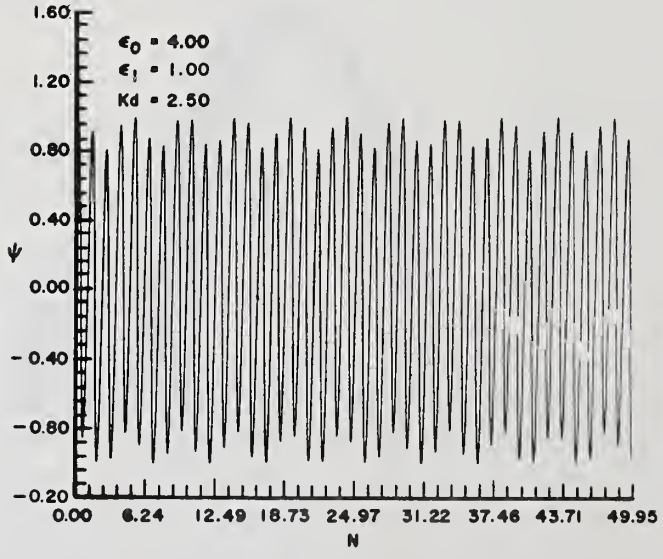

Figure 34. Wave function for sinusoidal profile.

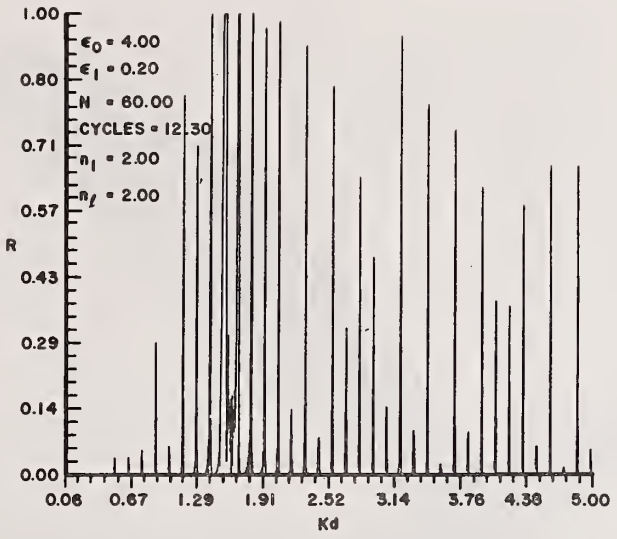

Figure 35. Multiplication of reflectance peaks due to periodic defects in filter profile.

One of the simulations tried was that of a filter with partial layers inserted periodically throughout the filter. The number given by CYCLES in the legend of fig. 36 tells how many periods of dielectric modulation occur before the dielectric is set back to the beginning of a cycle. This length becomes the effective repeat unit for the filter and corresponds to the solid-state case of a unit cell with a molecular formula of A^mB. The number N tells how many of these repeat units comprise the filter. For example, in fig. 35 where N is 60 and CYCLES is 12.3, the filter is equivalent to sixty filters, each 12.3 layers in length, stacked one on top of the other. The resulting spectra are filled with very narrow evenly spaced peaks. The spacing is inversely proportional to the value of CYCLES. When CYCLES is an integer the filter is reduced to a standard Mathieu filter of N x CYCLES layers. Only the characteristic two peaks are visible in this case. With a strong fractional part to CYCLES, extra peaks appear and grow to almost the same height as the original two. The number of ghost peaks between any two ordinary Mathieu stop bands is equal to CYCLES + 1. The relative reflectance at each ghost peak depends on the size of the fractional part of CYCLES.

3.7 Surface Layers

When partial layers are included in the N-dependence of peak reflectance, the reflection versus length curve oscillates as in the case of the peak location. This is especially true of filters with unmatched external indices (see figure 36). The high points on the curve shown occur at three quarters of a partial layer and the low points occur at one quarter of a partial layer.

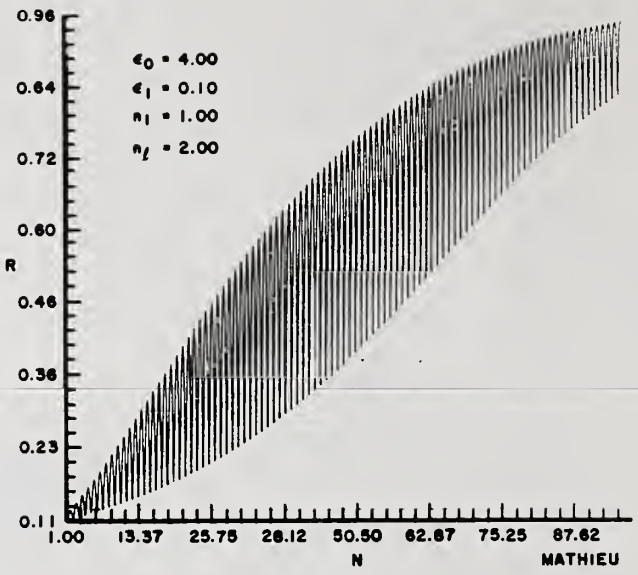

Figure 36. Oscillation in reflectance.

Figure 37 traces the reflectances for a single wave number (the CMT prediction for the peak location) from 1 to 100 cells. This curve is similar to, although not exactly like, that of fig. 36. The differences are greatest for short filters because for these the center frequency varies widely from the CMT prediction. The upper and lower envelopes of this curve in fig. 37 are essentially alike except for a horizontal shift.

Figure 38 shows the effect of a partial layer on the reflectance of the first stop band peaks in the Mathieu spectrum. At each partial layer (horizontal axes of all plots), the program scanned from the upper half height to the lower half height of each peak and identified the point at which the difference in reflectance between the filter with the partial layer and the filter without it was the greatest. This difference (RDIFF) is graphed in fig. 39. For the first peak it is evident from the plot that one such dip occurs. Two dips occurred for the second peak; for the third peak three dips occur.

Figure 40 shows the effect of increasing the modulation depth on the dip that occurs at a quarter partial layer. At low values the dip is very evident, but as modulation depth increases the dip shrinks until finally it disappears. Increasing the modulation also serves to widen the peak. Cascade plots of the spectrum around the stop band for a series of different partial layers show the shift to the left that the peaks on the spectrum undergo as the filters are lengthened. As they shift they trace a definite envelope--one which is defined by modulation depth, the outer indices, and the number of complete cells. When the substrate index (n_ℓ) is matched to the mean

index of the filter, the envelope is nearly symmetric about the line $k_0 = \pi/\sqrt{\varepsilon_0}$. In general, however, symmetry is not always present. Increasing the number of cells only increases the height of the top of the envelope. The bottom is affected differently. For a low number of cells, the base approaches zero, reaching it at N = 20. As cells are added the base of the lower envelope flattens but the middle begins to rise. This behavior is in keeping with a total reflectance that is the product of the reflectance of the partial layer and the reflectance of the completed layers. The greatest effect on the peak is on its height. In this particular case the dip occurs at a quarter of a partial layer and the maximum peak height occurs at three quarters of a layer.

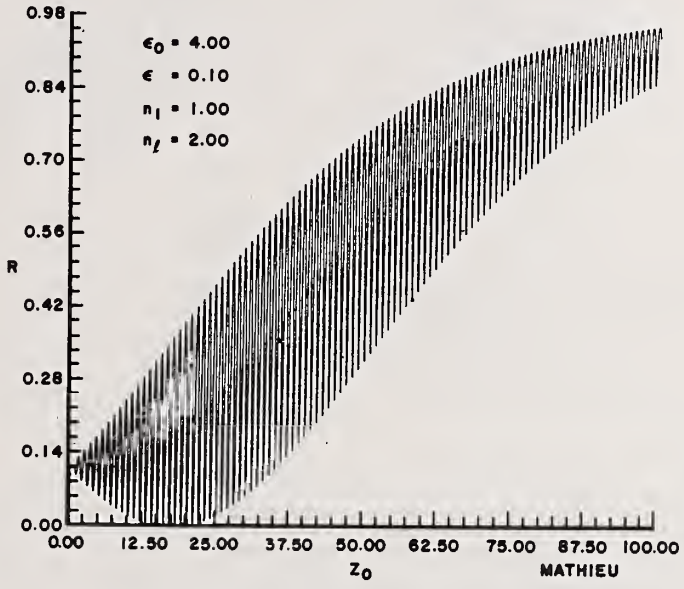

Figure 37. Oscillation in reflectance.

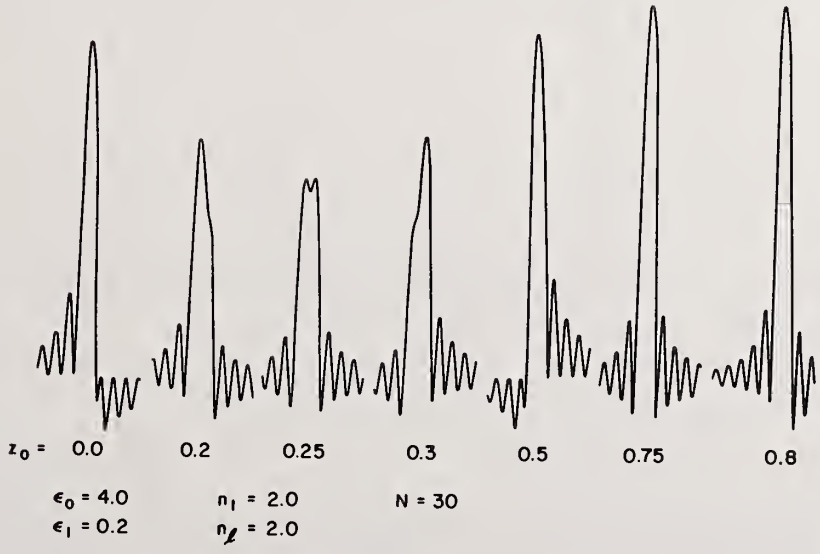

Figure 38. Variation in stop-band shpae during growth of a single layer.

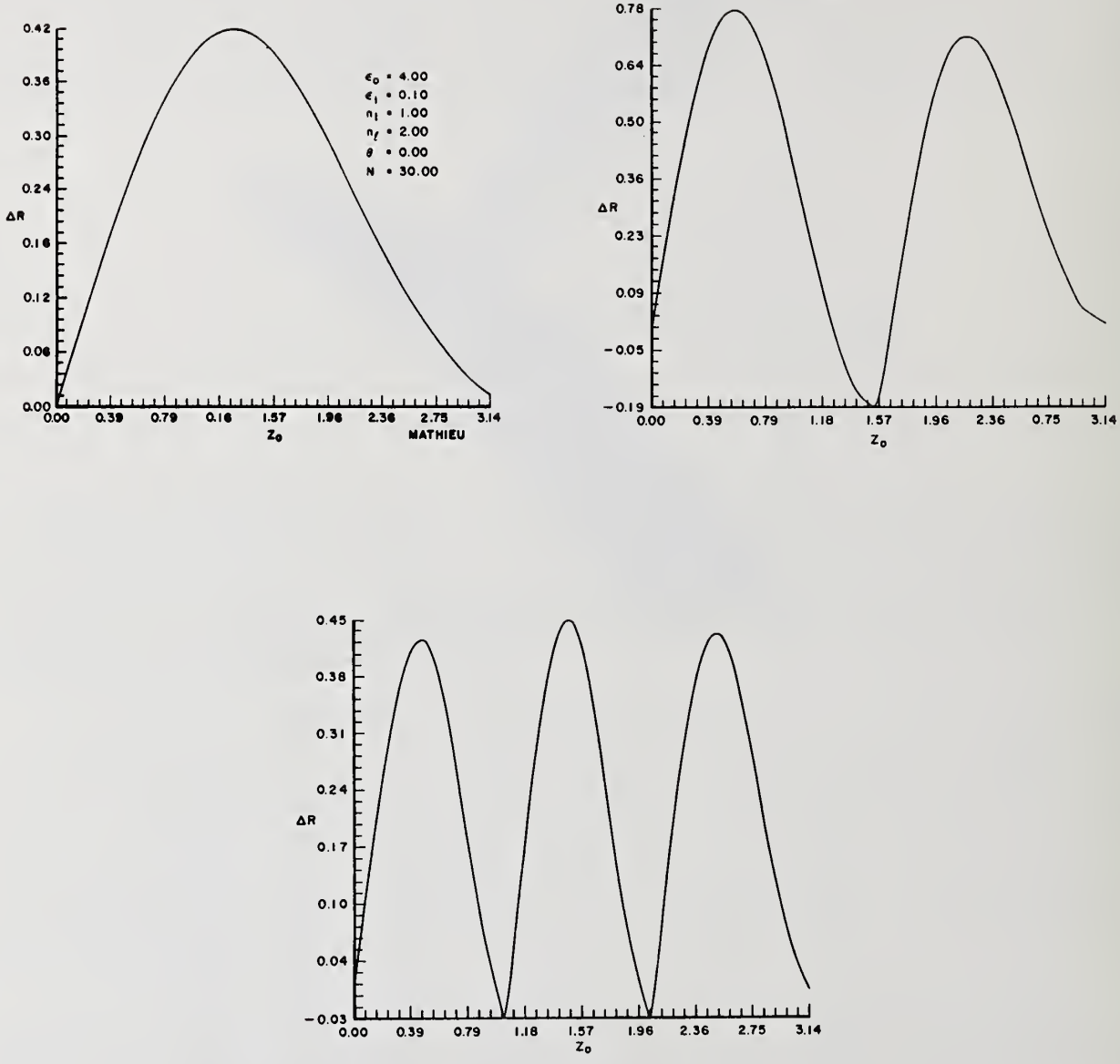

Figure 39a, b, c. Change in reflectance of the first three harmonics of a rugate filter as the partial layer at the surface is incremented from 0 to 1 layer.

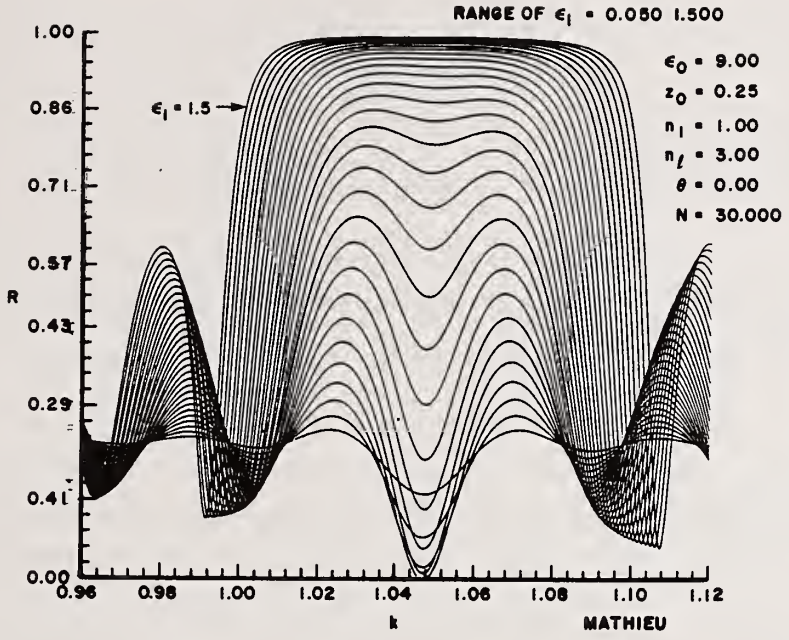

Figure 40. Chance in reflectance for a filter with 30.25 layers as a function of modulation depth.

The partial layer also affects the side bands. Increasing z_0 from 0 to 0.5 lowers the side peaks to the left of the main peak and raises those to the right of the main peak. At 0.5 layers the situation is the reverse of 0 partial layers. From 0.5 to 1 partial layers the side peaks on the left increase, while those on the right decrease until the side peaks appear as they did at 0-partial layers. The side peaks around the second main peak follow the same falling/rising pattern, but they complete it twice in the course of adding one more layer.

4. Conclusions

The main goals of this research were to complete efficient computer programs using the transfer matrix method that would give rapid calculations of wave functions, dispersion curves, and reflection and transmission spectra; to demonstrate the utility of the transfer matrix approach; to develop analytic formulas describing filter behavior; and to investigate the accuracy of Coupled Mode Theory. All of these objectives have been accomplished. Programs were completed to calculate dispersion curves and reflection spectra using transfer matrices for both square well and sinusoidal modulation. The results appear to be accurate to better than one part in 10^5 and spectra can be calculated on a VAX computer at a rate of 200 spectral points per second, regardless of the number of layers in the filter. This speed can probably be doubled by converting to single precision without loss of accuracy. In addition, wave functions and complex dielectric coefficients can be treated in the Mathieu case. A side benefit is that routines were developed to calculate Mathieu functions for both real and complex coefficients. The transfer matrix approach clearly works well. A number of specific conclusions are:

- Stop and pass bands will be formed whenever the susceptibility is periodically modulated. In fact a series of such bands will occur as a function of the wave frequency. The band structure will become more sharply defined as the number of repeat regions, or unit cells, increases, and as the medium approaches absolute periodicity. It is likely that the sharpness of the band edges will be enhanced if the imaginary part of the material susceptance is minimized.

- The centers of successive stop bands occur at wavelengths for which the optical depth of the medium taken over a unit cell distance is an integral number of half wavelengths, i.e., the phase angle is equal to π, or

$$k_o \int_o^d dx\, n(x) = \pi \quad . \tag{162}$$

Thus, the location of the gaps, or stop bands is determined primarily by the dimension of the unit cell, d, and the mean value of the refractive index, $\bar{n}(x)$, rather than the shape of the modulation profile.

- The degree of attenuation of a wave with a frequency within a stop band increases toward the middle of the band. The amount of attenuation is proportional to $\Delta n/n$. If the number of repeat units (unit cells) in the filter is sufficiently large, such a wave will not propagate through the filter at all; it will be totally stopped. The attenuation of the wave is not due to absorption, it is due to reflection, i.e., the stop bands correspond to reflection bands.

- The predictions of Coupled Mode Theory, which assume a semi-infinite filter and small relative modulation depth, hold very well in these limits and are quite good for filters of more than fifty layers and less than ten percent modulation in the dielectric constant. These conditions are both likely to be met in the case of high optical density, narrow bandwidth filters.

- The Fourier-transform prediction that $\Delta k/k_c$ scales linearly with $\Delta n/\bar{n}$ is completely accurate, but there is a nonzero intercept for Δk at Δn equal to zero due to the size effect for finite N.

- The prediction of Coupled-Mode theory that the width of a reflection band is proportional to the modulation depth times the corresponding coefficient for the Fourier-transform of the modulation profile is correct, but again, there is a pedestal, or constant value added to the width which increases as N decreases. The size or finite N value effects are due to the fact that the correct Fourier transform for a filter of finite length must convolve the modulation profile with a rectangle corresponding to the overall thickness of the filter as a whole; theoretical expressions based on a Fourier-transform approximation have implicity assumed that the filters were infinitely long.

- For small modulations, in most cases the widths of stop bands of a given order are roughly proportional to components of the Fourier transform of the modulation profile of similar order.

- The narrowness of the filter linewidth will be limited by random variations in the stoichiometry of the solid solution from which the filter is made.

- The Fourier-transform approximation gives very accurate predictions of k_c for small modulation depths ($\Delta n/\bar{n} < 0.2$), as long as $N > 20$. It is still quite good for N as low as 8, but there is a definite size effect. The true value of k_c is slightly greater than k_o for even numbered modes and slightly less than k_o for odd numbered modes.

- The ratio of k_c/k_o depends on the shape of the modulation profile. This ratio is unity for an a/d ratio of 0.5 but falls below one for both a>>b and a<<b. This effect also depends on N, becoming more pronounced for small N.

- In some cases if a narrow reflection band is needed it will be better to design for the second harmonic with an a/d ratio of 0.5, rather than the fundamental band. Alternately, one may choose a>>b or a<<b.

- The strong shift in the reflection band position with the angle of incidence will limit narrow-band filters to nearly normal incidence. The implication is that very narrow band performance cannot be achieved without stringent controls on stoichiometry and a 3-D design that will open up the acceptance angle of the filter.

- It appears that the only practical means of opening the acceptance angle of a Bragg filter is to increase the filter's mean index or to locate the filter on a curved surface. Simple analytic formulas can be determined for quantities of interest, and the dependence of the spectrum on the shape of the modulation profile can probably also be ascertained. Sinusoidal profiles perform better than step function profiles, but for many applications a square well filter with a/d = 0.5 will perform well.

- Unless performance is desired over many octaves, there is no apparent reason to favor one type of unit length modulation profile (e.g., a step function as a sinusoidal, parabolic, or Gaussian profile) over another. Details of the modulation profile only become significant in the upper level stop, or reflection bands. There may be reasons based on materials for choosing a given type of modulation profile. For example, it may be that impurities will aggregate at discontinuities. However, even if such an aggregation were to occur, it would not affect the amount of absorption in most cases. Some effect might be discernable at stop bands.

- Complex modulation profiles in the medium susceptance will lead to "band splitting"--the formation of new stop bands within what would otherwise be pass bands. Consequently several stop bands can be located at arbitrary frequencies within, say, one octave of the first stop band by appropriate design of the modulation profile. The locations and widths of the various stop bands will be related to the filter parameters in the same manner as for a single stop band. If it is desired to locate stop bands at arbitrary intervals over a multioctave region, then it will probably be necessary to put up with additional "ghost" stop bands.

- The change in the reflectance spectra due to partial surface layers is a complicated subject which shares many features with the problem of surface states in solid-state bond theory and terminal impedance in transmission line theory. This subject should be pursued further as should a continuation of the χ^2 fits already begun, especially in the case of complex dielectric constants.

- We can construct nomograms for design and characterization that engineers may use at a glance, without having to make new computer calculations every time a filter or a design needs to be evaluated.

The author is confident that an analytic description of a filter behavior similar to that discussed in Section 2 can be extended to complex susceptibilities and three-dimensional systems. Similar problems have been treated in three dimensions in band theory, lattice dynamics, and the description of microwave components. Step function modulations are the easiest to analyze because the solutions are in terms of sines and cosines, which are familiar, and can often be manipulated into compact expressions. The analysis of a Rugate filter is much less tractable. However, in many cases of interest, such as sinusoidal modulation, closed form solutions should be obtainable. Indeed, solutions to the Mathieu problem have been known for over half a century.

Commonly, continuously modulated filters are approximated in manufacture by stacking together a large number of very thin layers, with flat index profiles across each layer and sharp discontinuities between layers. Our analysis suggests that the merit of this procedure is at best moot. This practice will indeed give a reasonable approximation of an arbitrary index profile over a limited (one or two octave) frequency range. However, it introduces a very large number of discontinuities. If these discontinuities do, in fact, result in deterioration of the material properties, then these discontinuities are self-defeating. They will also affect the structure of high-order bands. Therefore if the higher-order band structure is important, the use of thin layers will interfere with these upper-level bands.

Note that both the width and the degree of attenuation or reflection in the stop or reflection bands scale as $\Delta n/n$. This creates difficulties if notch filters are desired. It appears that the primary way out of this dilemma is to build a filter with many repeat distances, i.e., a very long filter. It may also be possible to achieve some design freedom by prescribing profiles that have narrow potential wells (regions of large susceptibility) separated by relatively wide distances.

On the basis of this interim survey the author concludes that the choice of optimum filter materials and manufacturing should be dominated by materials and manufacturing questions rather than by filter design criteria. The primary concern should be to minimize intrinsic losses. This can be achieved by selecting materials whose imaginary component of the refractive index, n_i, is small compared to the real component, n_r, and by minimizing local inhomogeneities which will add to losses. The second criteria should be to select a material that is immune to intense levels of signal energy. This implies a low variation of n(x) with temperature, and a high melting or phase transition temperature. Comments on nonlinear susceptibilities are beyond the scope of this paper.

In general, it will be desirable to adjust the widths of the stop or reflection bands and to create multiple stop bands at arbitrary frequencies. This will require tailor-made refraction indices, which are achieved by appropriate solid solutions. If inhomogeneities in the resulting material are to be minimized, the constituents of the solution should be as compatible (mutually soluble) as possible. This suggests similar structures, chemical compositions, and bond lengths.

Acknowledgments

This work was supported by the Air Force Wright Aeronautical Laboratories, Materials Laboratory on Contract Number F33615-82-C-5001. Michael Creed, David Grote, Jeffrey Diller, and Wayne Johnson wrote the computer programs used to obtain the simulated data. The typing was done by Ellen Bordewisch.

References

1. Born, Max, and Wolf, Emil, Principles of Optics, (Pergamon Press, New York, 1965).

2. Yariv, Amnon, and Yeh, Pochi, Optical Waves in Crystals, (John Wiley & Sons, New York, 1984).

3. Becker, Roger J., "Criteria for Selection of Graded Index Filter Materials Based on an Analysis of Wave Propagation in a Periodic Medium," AFWAL-TR-85-4129, January 1986.

4. Loly, P. D. and Bahurmuz, A. A. Physica 100B, p. 29 (1980).

5. Hill, Robert Nyden, and Rosland, Borge Oddvar, Physical Review B, 11 (8) p. 2913 (1975).

6. Brillouin, L., Wave Propagation in Periodic Structures (Dover, New York, 1953).

7. Jacobsson, R., in Progress in Optics, 5, Emil Wolf, ed. (J. Wiley and Sons, New York, 1965).

8. Brekovskikh, L. M., Waves in Layered Media (Academic Press, New York, 1980).

9. Merzbacher, Eugene, Quantum Mechanics (John Wiley & Sons, New York, 1961).

10. Landau, L. D., and Lifshitz, E. M., Mechanics (Pergamon Press, New York, 1966).

11. Lindsay, Robert Bruce, Mechanical Radiation (McGraw-Hill, New York, 1960).

12. Thelen, Alfred, Physics of Thin Films, 5, George Hass & Rudolf E. Thun, ed.(Academic Press New York, p. 47, 1969).

13. Mukherji, D. and Nag, B. R., Solid-State Electronics, 18, p. 1107 (1975).

14. Lindsay, R. B., J. Appl. Physics, 9, p. 612 (1938) 10 p. 680 (1939).

15. Mason, W. P., Bell System Technical Journal, p. 258 (1927).

16. Kronig, R. deL., and Penney, W. G., Proc. Royal Soc. London, A 130 p. 499 (1931).

17. Aerts, E., Physica 26, p. 1047, p. 1057, p. 1063 (1960).

18. Saxon, David S., and Hunter, R. A., Philips Research Reports, 4 (2) p. 81 (1949).

19. Roy, C. L., and Roy, G., Czech J. Phys., B30, p. 941 (1980).

20. Dubrovskii, G. B., and Pogorelskii, Yu V., Sov. Phys., Semicond., 8, (4) p. 530 (1974).

21. Dubrovskii, G. B., and Lepneva, A. A., Sov. Phys., Sol. State, 19 (5) p. 729 (1977).

22. Yeh, Pochi; Yariv, Amnon; and Hong, Chi-Shain, J. Opt. Soc. Am., 67 (4) p. 423 (1977).

23. Morse, Philip M., Phys. Rev. 35, p. 1310 (1930).

24. Abramowitz, Milton, and Stegun, Irene A., Handbook of Mathematical Functions, (Dover Press, New York, 1965).

25. McLachlan, N. W, Theory and Application of Mathieu Functions, (Oxford-Clarendon Press, Oxford, 1951).

26. Slater, John C., Quantum Theory of Molecules and Solids 2, (McGraw Hill, New York, 1965).

27. Smith, R. A., Wave Mechanics of Crystalline Solids, (Chapman and Hall, London, 1963).

28. Davison, S. G., and Levine, J. D., in Solid State Physics 25.

29. Koutecky, Jaroslav, and Davison, Sydney G., Int. J. Quantum Chem., II, p. 73 (1968).

30. Levine, Jules D., and Davison, Sydney G., Phys. Rev., 174, (3) p. 911 (1968).

31. Grimley, T. B., Adv. Catalysis, 12 p. 1 (1960).

32. Collin, Robert E., Field Theory of Guided Waves, (McGraw-Hill, New York, 1960).

33. Brown, Frederick C., The Physics of Solids, (W. A. Benjamin, New York, 1967).

34. Nayfeh, Ali Hasan, Introduction to Perturbation Techniques, (Wiley Interscience, New York, 1981).

APPENDIX A

MATHEMATICAL UNDERPINNINGS OF WAVE PROPAGATION IN PERIODIC MEDIA

In this appendix we derive some of the equations which form a basis for the discussion of Section 2. The fundamental property that facilitates the description of this problem is that the waves obey a second-order equation of motion,

$$\psi'' + f(x)\psi = 0 \quad , \tag{A.1}$$

in which no first derivative term appears. The second property is that the response of the media to the wave is periodic along the path of the wave. No other properties of the system need to be involved in our discussion. Consequently our remarks apply to many fields other than optics, including acoustics, lattice vibrations, transmission line theory, waveguide theory, and the band theory of solids. In paragraph 2, we use

$$f(x) = k_o^2 n^2(x) = k_o^2 \varepsilon(x) = k^2(x) \quad . \tag{A.2}$$

A.1 Form for Transfer Matrix Elements

A second-order differential equation will have two independent solutions for a given set of parameters (e.g., k and ω). Let these be ϕ_1 and ϕ_2. Then, from eq. (A.1),

$$\phi_1\phi_2'' = - f(x)\phi_1\phi_2 \tag{A.3}$$

and

$$\phi_2\phi_1'' = - f(x)\phi_1\phi_2 \quad . \tag{A.4}$$

Subtracting (A.4) from (A.3) we have

$$\phi_1\phi_2'' - \phi_2\phi_1'' = 0 \quad . \tag{A.5}$$

This is a key result, which as we see, stems from the form of (A.1). Now

$$\frac{d}{dx}\{\phi_1\phi_2' - \phi_2\phi_1'\} = \phi_1\phi_2'' + \phi_1'\phi_2' - \phi_2\phi_1'' - \phi_2\phi_1' \quad . \tag{A.6}$$

Consequently, we find

$$\frac{d}{dx}\{\phi_1\phi_2' - \phi_2\phi_1'\} = 0 \quad , \tag{A.7}$$

or

$$\phi_1\phi_2' - \phi_2\phi_1' = \text{constant} \quad . \tag{A.8}$$

The quantity in the l.h.s. of (A.8) is known as the Wronskian for (A.1). The critical point is that the Wronskian is independent of the argument of ϕ_1 and ϕ_2, as long as they are taken at the same point. Note that if we had an equation of the form

$$\psi'' + \gamma(x)\psi' + f(x)\psi = 0 \quad , \tag{A.9}$$

we would obtain the result

$$\phi_1\phi_2' - \phi_2\phi_1' = \exp\left[-\int\gamma(x)dx\right] \quad . \tag{A.10}$$

We would need to use (A.10) instead of (A.8) in regard to the full wave eqs. (43) - (46).

We are now in a position to derive the expressions for the matrix elements eqs. (5) to (9). We begin with a general solution to (A.1), which is a linear combination of the independent solutions ϕ_1 and ϕ_2:

$$\psi = c_1\phi_1 + c_2\phi_2 \quad . \tag{A.11}$$

Differentiation of (A.11) yields

$$\psi' = c_1\phi_1' + c_2\phi_2' \quad . \tag{A.12}$$

We may solve for c_1 and c_2 in (A.11) and (A.12):

$$\psi\phi_2' - \psi'\phi_2 = c_1\underbrace{(\phi_1\phi_2' - \phi_2\phi_1')}_{D} \quad , \tag{A.13}$$

$$\psi'\phi_1 - \psi\phi_1' = c_2\underbrace{(\phi_1\phi_2' - \phi_2'\phi_1')}_{D} \quad . \tag{A.14}$$

Since the c coefficients are the quotients of Wronskians of (A.1), they are indeed constants, by (A.8). We may therefore use the argument at x' for c_1 and c_2 in (A.11):

$$\psi(x) = c_1(x')\phi_1(x) + c_2(x')\phi_2(x) \quad . \tag{A.15}$$

Substituting from (A.13) and (A.14) in (A.15), we find

$$\psi(x) = \frac{1}{D}[\psi(x')\phi_2'(x') - \psi'(\chi)\phi_2(x')]\phi_1(x) + \frac{1}{D}[\psi'(x')\phi_1(x') - \psi(x')\phi_1'(x')]\phi_2(x) \quad . \tag{A.16}$$

We may rearrange the terms in (A.16) to obtain an expression for $\psi(x)$ in terms of $\psi(x')$ and $\psi'(x')$:

$$\psi(x) = \frac{1}{D}\,[\phi_1(x)\phi_2'(x') - \phi_2(x)\phi_1'(x')\psi(x')$$

$$+ \frac{1}{D}\,[\phi_2(x)\phi_1(x') - \phi_1(x)\phi_2(x')]\psi'(x')$$

$$= b_{11}\psi(x') + b_{12}\psi'(x'), \text{ Q.E.D.} \qquad \text{(A.17)}$$

A similar argument will give the expression for the matrix elements b_{21} and b_{22}.

A.2 Dispersion Relation

We now consider a different point of view, in which we express $\psi(x)$ in terms of its value at x', without regard to $\psi'(x')$. We again use (A.11), and write

$$\psi(x) = \lambda(x,x')\psi(x') \qquad \text{(A.18)}$$

Using (A.18), and letting $\psi(x')$ also be of the form (A.11), there will be some matrix A with elements a_{ij}, such that

$$\phi_1(x) = a_{11}\phi_1(x') + a_{12}\phi_2(x') \qquad \text{(A.19)}$$

and

$$\phi_2(x) = a_{21}\phi_1(x') + a_{12}\phi_2(x') \quad . \qquad \text{(A.20)}$$

Equations (A.11) and (A.18)-(A.20) give us

$$\psi(x) = [c_1a_{11} + c_2a_{21}]\,\phi_1(x') + [c_1a_{12} + c_2a_{22}]\phi_2(x') = \lambda[c_1\phi_1(x') + c_2\phi_2(x')] \quad . \qquad \text{(A.21)}$$

From (A.21) we obtain the matrix eigenvalue equation

$$\begin{bmatrix} a_{11} - \lambda & a_{12} \\ a_{21} & a_{22} - \lambda \end{bmatrix} = 0 \quad , \qquad \text{(A.22)}$$

or

$$\lambda^2 - (a_{11} + a_{22})\lambda + \underbrace{(a_{11}a_{22} - a_{12}a_{21})}_{\Delta} = 0 \quad . \qquad \text{(A.23)}$$

We next show that $\Delta = 1$. Note however, that since $\Delta = 1$, we find

$$\lambda^2 - (a_{11} + a_{22})\lambda + 1 = 0 \quad , \tag{A.24}$$

or

$$T_r[A] = \lambda + \lambda^{-1} \quad . \tag{A.25}$$

We now show that $\Delta = 1$. We refer to the (constant) Wronskian D. Using (A.19) and (A.20) we write

$$\begin{aligned} D &= \phi_1(x)\phi_2'(x) - \phi_1'(x)\phi_2(x) \\ &= [a_{11}\phi_1(x') + a_{12}\phi_2(x')]\ [a_{21}\phi_1'(x') + a_{22}\phi_2'(x')] \\ &\quad - [a_{11}\phi_1'(x') + a_{12}\phi_2'(x')]\ [a_{21}\phi_1(x') + a_{22}\phi_2(x')] \quad , \end{aligned} \tag{A.26}$$

or

$$D = (a_{11}a_{22} - a_{12}a_{21})\ [\phi_1(x')\phi_2(x') - \phi_1'(x')\phi_2(x')] \quad . \tag{A.27}$$

i.e.,

$$D = \Delta D \quad . \tag{A.28}$$

Therefore

$$\Delta = 1 \quad . \tag{A.29}$$

The results we have derived have depended on the form (A.1) for the wave equation, and in particular on the consequence (A.8). However, the expression (A.18) is most useful when ψ is periodic in x. This will be the case when f(x) is periodic, as we now show. We may construct a function A(x) such that

$$\psi(x) = A(x)\ e^{ikx} \quad . \tag{A.30}$$

Substituting (A.29) in (A.1) we find

$$A'' + 2ikA' + [f(x) - k^2]\ A = 0 \quad . \tag{A.31}$$

If f(x) is periodic with period d, then from (A.31) A must be also. It is often useful to rewrite (A.30) in another form. We let

$$x - x' = d \quad , \tag{A.32}$$

and obtain

$$\psi = A(x' + nd)\exp [ikx' + iknd] \tag{A.33}$$

$$= A_o(x')\exp [iknd] \quad . \tag{A.34}$$

From (A.33) we see that

$$\lambda = e^{ikd} \tag{A.35}$$

in (A.18). Using (A.35) in (A.25), we have the dispersion relation

$$T_r[A] = 2\cos kd \quad . \tag{A.36}$$

If there is a first derivative in the wave equation, leading to (A.10) instead of (A.8) we would find

$$\exp [\Gamma(x') - \Gamma(x)] \quad , \tag{A.37}$$

where

$$\Gamma = \int_o^x dx\ \gamma(x) \quad . \tag{A.38}$$

Equations (A.11)-(A.23) would otherwise remain unchanged. Equation (A.24) would now become

$$\lambda^2 - (a_{11} + a_{22})\lambda + \exp [\Gamma(x') - \Gamma(x)] = 0 \quad . \tag{A.39}$$

In the case of eqs. (43) and (46) we have $\gamma \frac{d}{dx} \ln \varepsilon$, so that the third term in (A.39) becomes $\varepsilon(x)/\varepsilon(x')$.

Manuscript Received
11-4-87/sar

Damage Thresholds of Antireflection Coatings at 790 nm

Gerald Gallegos, Steve Foltyn, and Jim Boyer

Los Alamos National Laboratory
Los Alamos, NM 87545

Damage thresholds of antireflection coatings on sapphire and alexandrite substrates have recently been measured. Optimization of AR coatings was necessary to improve damage thresholds on alexandrite laser rods, over that observed on the bare material. Eight different coatings supplied by seven different vendors plus uncoated sapphire and alexandrite were tested. Thresholds from 7 J/cm^2 to 80 J/cm^2 were observed. Sapphire was used because it has an index of refraction similar to alexandrite and is more readily available in sizes suitable for testing. An alexandrite laser at a wavelength of 790 nm with a pulse duration of 200 ns at 30 Hz for two seconds was used. The mean spot diameter of the nearly Gaussian beam was 0.380 mm. All of the damage testing in the AR screening survey was done at normal incidence.

Key Words: alexandrite laser; antireflection coatings; damage threshold

1. Introduction

The necessity for optimizing an AR coating for alexandrite rods was due to the low damage threshold, 17 J/cm^2 average, of uncoated alexandrite. It was important to find a coating that would significantly improve the threshold of the laser rods and thus increase system performance.

2. Laser Damage Testing

2.1 Experimental Test Setup

Figure 1 shows the test setup for all of the damage threshold testing of antireflection coatings at 790 nm. Test samples were exposed at normal incidence to a nearly Gaussian alexandrite laser beam with a pulse duration of 200 ns at 30 Hz for 2 seconds.

2.2 Test Samples For Alexandrite Rod Coatings

A total of eight different AR coatings from seven different vendors were tested in the survey. Sapphire substrates were purchased from Adolf Meller Co. and provided by Los Alamos to the participating vendors for coating. The multilayer coatings were of two-layer design with half-wave undercoats of SiO_2. Material combinations included TiO_2/SiO_2 and ZrO_2/SiO_2, Al_2O_3/SiO_2 and Sc_2O_3/SiO_2, Ta_2O_5/SiO_2, and HfO_2/SiO_2. Single-layer ARs of MgF_2 and Na_3AlF_6 were also evaluated, as were uncoated sapphire substrates. A limited number of polished alexandrite samples were available; some were tested as uncoated surfaces and the remainder were included in the TiO_2/SiO_2 coating runs.

2.3 Test Results For Alexandrite Rod Coating Samples

Samples from each vendor were grouped according to coating material and then tested. Thresholds for each coating material were compared from vendor to vendor. The results of these tests are shown in figure 2. Thresholds quoted are by the standard methods used at Los Alamos, which have been previously described [1,2]. The damage threshold is that point at which damage is no longer observed.

3.0 Conclusions

Several material combinations such as ZrO_2/SiO_2, Ta_2O_5/SiO_2, HfO_2/SiO_2, Na_3AlF_6 exhibited uniformly high 790-nm damage thresholds. These coatings will be tried on alexandrite rods to see if they increase the threshold. TiO_2/SiO_2 on sapphire, which showed a marked improvement over uncoated sapphire, showed no improvement on alexandrite. This would indicate that the alexandrite substrate is a limiting factor. Thresholds within coating materials were generally comparable from vendor to vendor. A direction for optimization of an antireflection coating for alexandrite rods has been established.

References

[1] Newnam, B.E.; Foltyn, S.R.; Jolin, L.J.; Carniglia, C.K.; Multiple-shot ultraviolet laser damage resistance of nonquarterwave reflector designs for 248 nm. Nat. Bur. Stand. (U.S.) Spec. Pub. 638; 1983(363-371)

[2] Foltyn, S.R.; Jolin, L.J.; Newnam, B.E.; Progress in ultraviolet damage testing at Los Alamos. Nat. Bur. Stand. (U.S.) Spec. Pub. 669; 1984 (266-273).

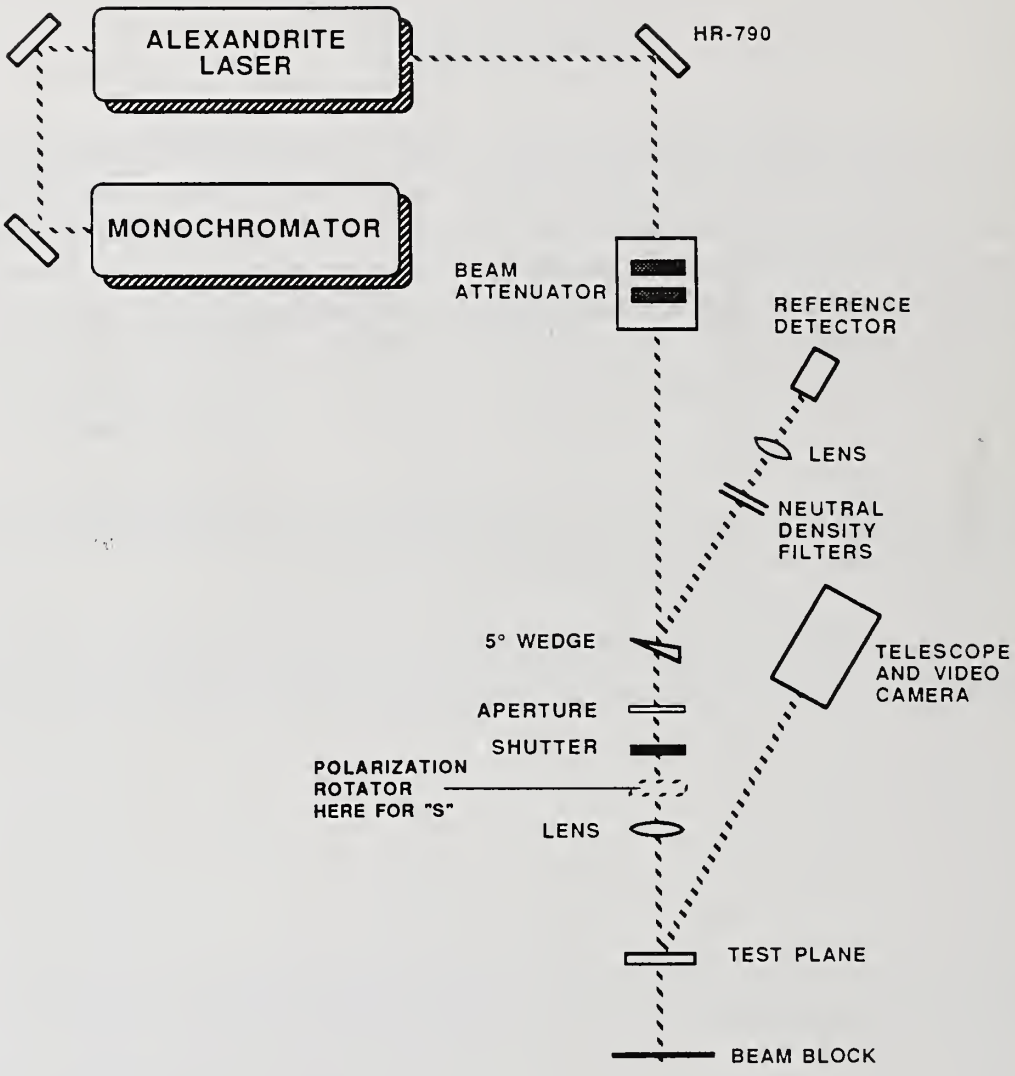

Figure 1. Damage Test Setup

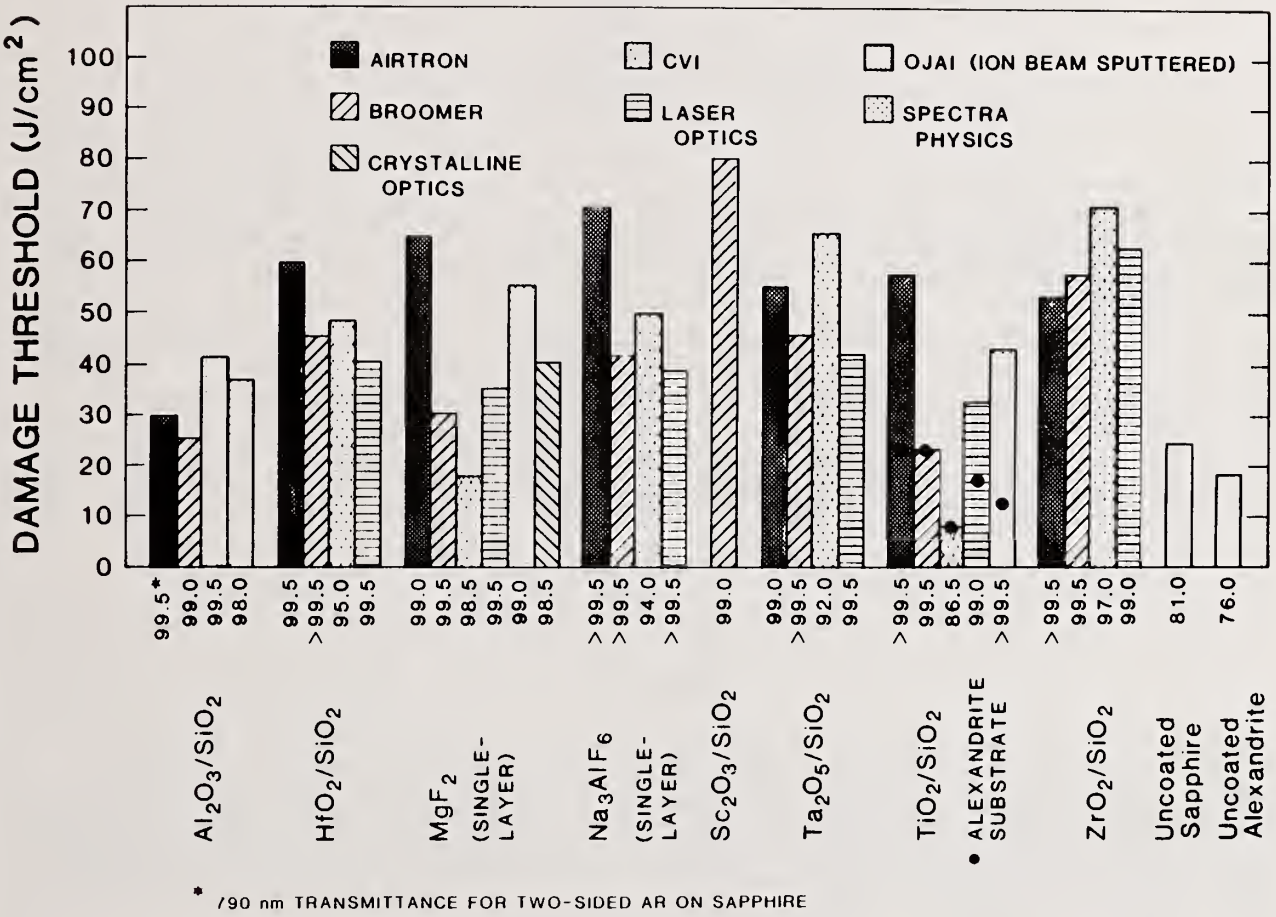

Figure 2. Damage Thresholds of 790 nm Antireflection Coatings on Sapphire Substrates

Manuscript Received
5-13-87

PHOTON INDUCED DESORPTION AND EMISSION FROM THIN FILM DIELECTRIC SURFACES

John A. Kardach[++], Alan F. Stewart, and Arthur H. Guenther
Air Force Weapons Laboratory
Kirtland Air Force Base, New Mexico 87117

and

John K. McIver
Institute for Modern Optics
University of New Mexico
Albuquerque, New Mexico 87131

Results from 1-on-1 and N-on-1 laser induced damage experiments, together with associated charged particle emission from 22 dielectric thin films on fused silica, sapphire, and calcium fluoride substrates are reported. A Q-switched Nd:YAG laser (1.06 microns, 5 nsec (FWHM), 500 microns $1/e^2$ diameter) was used to irradiate the half wave (at 1.06 microns) thin films. The experiments were performed in a UHV vacuum chamber with a base pressure of 10^{-8} Torr, and were computer controlled.

Preliminary analysis indicates that the damage threshold for dielectric thin films increases with the substrates thermal conductivity, even for these very short laser pulses. Laser damage thresholds and charge emission curves are presented and characterized as a function of the incident laser energy density.

[++]To be submitted in part for the fulfillment of the PhD in Physics, Air Force Institute of Technolowy, Wright-Patterson AFB, Ohio.

Key words: fluoride coatings; laser damage; oxide coatings; thin films

INTRODUCTION

An experimental investigation into the correlation between laser induced charge emission and pulsed laser damage in dielectric thin films has been conducted, along with a secondary study of laser damage and the thermal properties of thin film coatings. The possibility of using charge emission as a nondestructive indicator or precursor to laser induced surface damage was investigated. Earlier studies of particle emission from surfaces during laser irradiation (Ref 1,2) had shown that under certain conditions, charge emission occurred below the apparent damage threshold. A "cleaning" phenomena had also been reported whereby repeated irradiation of a surface lead to higher laser damage thresholds (Ref 3,4).

To verify these observations a comprehensive study was performed. The sample matrix consisted of 22 oxide and fluoride coatings deposited using electron beam deposition onto three different types of substrates. These samples were irradiated using a single mode Nd:YAG laser at various power levels above and below the laser damage threshold. The emitted charge was compared with incident power levels.

Our results indicated that each thin film coating material had a different charge emission characteristic. Emission was observed at incident fluence levels below the laser damage threshold, and a "cleaning" of the surface and an accumulation of damage were observed to occur during some of the N-on-1 experiments.

Due to the large sample matrix studied in these experiments, a separate investigation into laser damage and the thermal properties of dielectric thin films was conducted. The influence of the thermal properties of thin film coating materials and substrates have been discussed extensively on a theoretical basis with reasonable good correlation to the available experimental data (Ref 5,6,7). The laser damage data generated in this series of experiments provided information on oxide and fluoride coating materials which have vastly different thermal conductivities and diffusivities in bulk form, and demonstrate a strong dependence of the laser damage threshold on the thermal properties of the substrate.

EXPERIMENTAL

To study the correlation between laser induced charge emission and pulsed laser damage thresholds, a series of experiments were performed. A large sample matrix was prepared and tested using several well established test procedures to determine the damage thresholds of the dielectric thin films. Charge emitted from the irradiated surface was measured for every event. The data were then composed to study the interrelationships between charge emission, laser damage and the chemical and thermal properties of the coating/substrate system.

The experimental arrangement is shown in Figure 1. A Q-switched Nd: YAG laser operating in the TEM_{00} mode was used to irradiate samples with 5 nsec FWHM pulses at 1.06 microns. The laser was focused onto the sample positioned inside an ultra high vacuum (UHV) chamber with a 2m focal length lens, and the Gaussian laser spot size on the sample was nominally 500 microns ($1/e^2$ in intensity diameter).

The energy of each laser pulse was varied using a half waveplate and linear polarizer. A pyroelectric[1] detector was used to determine the energy of each pulse. A beamsplitter provided a low energy reference beam which could be easily monitored during irradiation of samples inside the chamber. The energy detector was calibrated by simultaneously measuring the energy in the main beam path at the target and the energy of the reflected beam at the detector for a series of laser pulses.

A temporal profile was also taken for each laser pulse. The temporal profile was obtained using a vacuum photodiode which had a risetime of < 0.5 nsec. The signal from the vacuum photodiode was recorded by an R7912 digitizer. The signal was analyzed by the computer controller and the Full Width at Half Maximum (FWHM) intensity point was determined and stored. The laser pulse waveform for these experiments was nominally Gaussian with a FWHM of 5.3 ± 1.7 nsec.

Spatial profiles of the laser beam were obtained by using the slit scan method and with a photodiode array detector. The slit scan method consisted of translating a narrow slit aperture across the laser spot at the target plane. A sensitive pyroelectric detector mounted behind the aperture measured the transmitted beam energy. A typical scan consisted of 100 data points across the laser spot, with an average of three pulses at each data point. The laser intensity profile at the target plane was determined in this way to be nominally a Gaussian distribution with a FWHM of 290 ± 35 microns.

Unlike the slit scan method which required hundreds of laser pulses to obtain a profile, a photodiode array[2] detector was used to scan a linear slice of the pulse and recorded a complete spatial profile of a single laser pulse. Since the array detector was unable to withstand the large energy densities at the target plane, it was used at an equivalent focal plane on the optical table. The array detector used has 1024 elements spaced 15 microns apart. Typical temporal and spatial profiles of the laser are shown in Figure 2 (a and b).

Coated substrates were tested inside a UHV chamber. Two samples were loaded into the chamber for each run. A sorption pump and vac-ion triode pump were used to evacuate the UHV chamber which maintained a base pressure of 10^{-8} Torr. The samples were held by a multiaxis manipulator arm and were moved from site to site. The relative position of the beam axis and the charge collection apparatus thus remained unchanged while various sites on each substrate were irradiated.

A charged wire was used to collect any negatively charged particles emitted from the irradiated target surface. The charged wire was shaped in the form of a loop, 1 cm in diameter, and was positioned normally to and approximately 1 cm in front of the target site with the plane of the loop parallel to the target surface. The laser fired through the loop to strike the target site. The wire was biased at positive 1 kV, and was connected to a capacitive voltage divider and a series of amplifiers. The dynamic range of the charge collection system was

---

[1]Laser Precision Model 735/7100

[2]EGA Reticon Model RL1024H

increased by making one channel 100 times less sensitive than the other. Detector linearity was measured and verified over a range of 10^{-14} coul to 10^{-9} coul. Detector saturation occurred at 10^{-8} coul.

The experiment was conducted using two protocols: 1-on-1 testing, meaning irradiation of each target site with a single laser pulse, and N-on-1 testing with each target site irradiated by several laser pulses. The 1-on-1 experiments were designed to measure thin film pulsed laser damage thresholds and to provide charge emission data. The N-on-1 experiments were conducted to study the charge emission phenomena, although damage thresholds could usually be determined from this data as well.

Three types of experiments were performed in the N-on-1 testing: (1) Repeated irradiation of each target site with pulses of the same energy density; (2) Irradiation of a site with a series of pulses of increasing energy density until damage occurred; and (3) Repeated irradiation of the target at a fixed energy density for a number of shots (usually 5 shots), continuing at steadily increasing energy densities. These experimental procedures were developed when it became apparent that the charge emission for most of the samples tested decreased below detector sensitivity after the first couple of laser shots.

The laser was fired at a constant rate of 1 shot every minute. Each sample was partitioned into 170 target sites distributed in a square grid pattern on 2 mm centers. Each 1-on-1 damage threshold measurement involved the irradiation of all 170 test sites, and took about 3-4 hours to complete. The N-on-1 experiments requiring repeated irradiation of target sites often took 8-12 hours to complete.

A long working distance microscope[3] coupled to a video camera was used to observe the sample during each test in order to observe plasma breakdown (sparks) and to note visible damage. Each test site was later examined under a Nomarski microscope to provide a definitive measure of the occurrence of permanent laser induced damage. Damage to the target site was taken as any visible change in the surface, such as pitting, bubbling, holes, discoloration, etc. Figures 3 and 4 show some typical damage morphologies on various types of coatings.

Data was collected and stored using a PDP-11/34 mini computer. The data collected for each shot by the computer included the energy and FWHM of the laser pulse, the laser induced charge emission peak value, whether or not a visual observation of a spark or damage occurred, the position of the target site, and for N-on-1 testing, the number of the shot. After a sample was tested, it was examined under a Nomarski microscope for evidence of laser induced damage.

SAMPLES

There were 22 different dielectric thin film coatings deposited on three different substrates used in this study. These dielectric coating samples were selected to compare the performance of oxide and fluoride coatings of the same metal ion, and to investigate the influence of the substrate thermal properties (i.e. thermal conductivity) on the thin film performance. The thin film coatings and substrates are listed in Table 1.

The dielectric thin film coatings tested in this study were deposited onto substrates supplied by three different vendors. The fused silica substrates were Suprasil I and were fabricated by Zygo. The sapphire substrates were supplied by Insaco, and the calcium fluoride substrates were supplied by Optivac. The sapphire was single crystal with a R-plane orientation. The calcium fluoride was a single crystal with an orientation of [111], and was polished by CVI using a diamond paste and water. These substrates were characterized before and after coating deposition. The results of these tests indicated that these samples represented the state-of-the art in surface fabrication with each of these materials.

The thin film coatings were deposited by the Optical Coating Laboratories, Inc. using electron beam deposition. Three different thicknesses (1/4, 1/2, and 3/4 wave at 1.064 microns) were fabricated under identical conditions, of which only the 1/2 wave thick coatings were damage tested in this study. All samples with coatings of a given dielectric material were deposited at the same time under identical conditions. This insured that the same coating conditions were present for "identical" samples and for coatings on each of the different substrate types.

---

[3]Questar Model QM-1

The samples were stored in a dry nitrogen atmosphere until required for characterization or laser damage testing. Before each test was performed the samples were cleaned using a spin cleaner. The spin cleaner held the sample in a vacuum chuck and dispensed dry nitrogen, spectroscopic grade methanol, dry nitrogen, and then finished with a high speed spin. After cleaning, the sample was examined under a Nomarski microscope for any obvious defects and was then loaded into the vacuum chamber for testing.

SAMPLE CHARACTERIZATION

Extensive characterization of each sample was conducted as a part of this study. Surface roughness measurements of the substrates before coating were performed using an optical heterodyne profilometer at Lawrence Livermore National Laboratory (Ref 8), and surface scattering measurements of a subset of the uncoated and coated samples were made using a variable angle scatterometer at Wright-Patterson AFB (Ref 9). Thin film absorption measurements, X-ray diffraction, and spectroscopic ellipsometry of the thin film coatings were also performed.

The optical heterodyne profilometer at LLNL uses two collinear HeNe beams with slightly different frequencies to illuminate the sample. The test surface is illuminated by two beams of slightly different frequency and the reflected beams are allowed to interfere, so that the phase of the sinusoidal intensity modulation is related to the height difference between the illuminated points on the surface. The instrument is configured so that one of the beams remains focused on a fixed point while the other beam is moved along the surface. In this manner, height variations along the scanned line are measured and the RMS surface roughness can be calculated.

All of the substrates were measured with the profilometer before coatings were deposited. Coated substrates were not measured since a thin film coating causes a phase shift in the reflected light which changes the apparent surface profile. The fused silica substrates used in this study had surface roughness measurements of 3 ± 1 angstroms RMS, the sapphire substrates measured 9 ± 8 angstroms RMS, and the calcium fluoride substrates measured 11 ± 8 angstroms RMS.

Surface scattering measurements were performed using a variable angle scatterometer. The scatterometer measured the bidirectional reflectance distribution function (BRDF) of the sample, scanning an area 3mm by 3mm in the center of a sample with a spatial resolution of 5 microns. The results of the scan were given as an average of the scattered light over the scanned area. The samples tested were measured before and after coating, and the results are given in Table 2.

The thin film absorption measurements were performed using a precision laser calorimeter. Absorption measurements were performed at 3 wavelengths (351 nm, 514 nm, and 1.3 microns) and the results are given in Table 3. X-ray diffraction and spectroscopic ellipsometry studies (Ref 10) were performed to examine the structure of the thin films (if any) on the different substrates.

DATA AND ANALYSIS

The 1-on-1 pulsed laser damage thresholds of the thin film coatings were determined through survivability curves (Ref 11) as shown in Figure 5. Survivability curves show the probability of a coating damaging for a given laser energy density. The energy density for each damage probability was determined by taking an average of all the laser shot energies within a determined energy range. This energy range was usually over a 1 J/cm^2 range, i.e. 2.5 - 3.5 J/cm^2, but the energy range varied depending upon the sample and how the laser output energies were grouped.

The probability of damage at a given energy density was determined by the number of exposures that damaged the thin film coating divided by the total number of exposures within each energy range. The laser damage threshold was calculated by taking a least squares fit to the transition region between the region of no damage (0% probability of damage) to the region where damage always occurred (100% probability). The damage threshold was thus defined as the energy density where the least squares fit intercepted the zero probability of damage point. Table 4 shows the 1-on-1 pulsed laser damage thresholds for the thin films tested.

The damage data revealed a substrate effect on the damage threshold of a thin film. According to Lange et.al. (Ref 5,6), the damage threshold of a thin film coating is effected by the thermal conductivity of the substrate. Lange et.al. determined that the damage threshold of

the coating should increase with the thermal conductivity of the substrate, which was supported by data from this study. However, Lange et. al. showed this to be predicted for 10-50 nsec or longer pulses, and not necessarily observable for short (5 nsec) pulses. Figure 6 shows a plot of some of the damage thresholds against the thermal conductivity of the substrates.

The charge emission data from the 1-on-1 testing showed three distinct patterns, and indicated that the charge emission characteristics of each thin film coating material were different. When the charge emission was plotted against the energy density, the charge emission fell into three distinct patterns as shown in Figure 7: (1) A very distinct curve with little of no scatter in the data; (2) A less distinct pattern with some scatter in the data; and (3) A random pattern with little or no structure at all. Although charge emission was observed below the damage threshold, no distinct indicator or precursor to laser damage was observed. Modeling of the charge emission data is presently being conducted and will be presented at a later date.

The N-on-1 charge emission data was very reproducible. As seen in other studies (Ref 1,2,4), the charge emission in almost all cases decreased below the detectors sensitivity within the first few laser pulses, and no charge emission was then detected until damage occurred (Figure 8). This rapid decline in charge emission seemed to indicate a cleaning effect of the target site. A gradual increase in the charge emission for repeated pulses at the same energy density ending with damage to the surface, indicated an accumulation of damage and is shown in Figure 9.

CONCLUSIONS

Laser induced charge emission has been observed both above and below the damage threshold of the dielectric thin films coatings tested in this study. The charge emission data fell into distinct patterns and indicated that the characteristics of the charge emission depended upon the dielectric thin film. The charge emission showed no distinct indicator or precursor of imminent laser induced surface damage. The charge emission decreased below detector sensitivity when a target site was irradiated repeatedly indicating a cleaning effect, and a gradual increase to indicate accumulation of damage. Single pulse laser damage measurements were examined and presented for 22 oxide and fluoride dielectric thin films on three types of substrates. An increase in the thin film damage threshold was observed for a coating on substrates of a higher thermal conductivity verifying existing theory for very short laser pulses.

REFERENCES

1. Domann, F.E., Becker, M.F., Guenther, A.H., and Stewart, A.F., "Charged Particle Emission Related to Laser Damage," Applied Optics, Vol 25, No 9, pp 1371-1373, 1 May 1986.

2. Siekhaus, W.J., Kinney, J.H., Milam, D., and Chase, L.L. "Electron Emission from Insulator and Semiconductor Surfaces by Multiphoton Excitation Below the Optical Damage Threshold," Appl. Phys. A, Vol 39, pp 163-166 (1986).

3. Allen, Susan, Porteus, J.O., and Faith, W.N., "Infrared Laser-Induced Desorption of H_2O and Hydrocarbons from Optical Surfaces," Appl. Phys. Lett., Vol 41, No 5, pp 416-418, 1 Sept 1982.

4. Becker, M.F., Domann, F.E., Stewart, A.F., and Guenther, A.H., "Charge Emission and Related Precursor Events Associated with Laser Damage," Laser Induced Damage in Optical Materials: 1983, NBS Spec. Pub. 688, eds. H.E. Bennett, A.H. Guenther, D. Milam, and B.E. Newnam, pp. 429-441, 1983.

5. Lange, M.R., McIver, J.K., and Guenther, A.H., "Laser Induced Damage of a Thin Film With an Absorbing Inclusion: Thermal Considerations of Substrates and Absorption Profiles," Laser Induced Damage in Optical Materials: 1983, NBS Spec. Pub. 688, eds. H.E. Bennett, A.H. Guenther, D. Milam, and B.E. Newnam, pp. 448-453, 1983.

6. Lange, M.R., McIver, J.K., and Guenther, A.H., "Laser Damage Threshold Predictions Based on the Effects of Thermal and Optical Properties Employing a Spherical Impurity Model," Laser Induced Damage in Optical Materials: 1983, NBS Spec. Pub. 688, eds. H.E. Bennett, A.H. Guenther, D. Milam, and B.E. Newnam, pp. 454-465, 1983.

7. Lange, M.R., McIver, J.K., and Guenther, A.H., "An Initial Study of: The Inclusion Model for Repetitively Pulsed Laser Damage," Laser Induced Damage in Optical Materials: 1984, NBS Spec. Pub. 727, eds. H.E. Bennett, A.H. Guenther, D. Milam, and B.E. Newnam, pp. 382-393, 1984.

8. Sommargren, G.E. "Optical Heterodyne Profilometer," Applied Optics, Vol 20, No 4, pp 610-618, 15 Feb 1981.

9. Orazio, F.D. Jr., Stowell, W.K., and Silva, R.M. "Instrumentation of a Variable Angle Scatterometer (VAS)," SPIE, Vol 362, pp 165-171.

10. Vedam, K., McMarr, P.J., and Narayan J., "Nondestructive Depth Profiling by Spectroscopic Ellipsometry," Appl. Phys. Lett., Vol 47, pp 339-341, 15 Aug 1985.

11. Foltyn, S.R. "Spotsize Effects in Laser Damage Testing," Laser Induced Damage in Optical Materials: 1982, NBS Spec. Pub. 669, eds. H.E. Bennett, A.H. Guenther, D. Milam, and B.E. Newnam, pp. 368-379, 1982.

TABLE 1: Dielectric Thin Film Coatings and Substrates

DIELECTRIC THIN FILM COATINGS

ThO_2	ThF_4	Al_2O_3	AlF_3
MgO	MgF_2	SiO	LaF_3
Y_2O_3	YF_3	SiO_2	Na_3AlF_6 (Cryolite)
HfO_2	HfF_4	ZrO_2	NaF
Sc_2O_3	ScF_3	TiO_2	ZnS
CeO_2	CeF_3		

SUBSTRATES

Fused Silica (SiO_2)
Sapphire (Al_2O_3)
Calcium Fluoride (CaF_2)

TABLE 2: Variable Angle Scatterometer Measurements

	SiO_2 Substrate		CaF_2 Substrate		Al_2O_3 Substrate	
	Uncoated	Coated	Uncoated	Coated	Uncoated	Coated
THIN FILM	(Parts per Million)					
TiO_2	0.8794	1.9016	3.4652	17.542	0.0749	2.6876
HfO_2	0.3724	4.0874	28.9236	1439.5	1.9146	5.7012
CeO_2	0.4232	18.839	12.0805	759.64	0.1633	22.837
SiO_2	....	....	8.4558	33.7911	6.0399	0.0837
ZrO_2	0.6067	9.6536	....	....	0.8456	7.7232
Al_2O_3	0.2195	1.0702	....	....	0.2551	0.6962
ThO_2	....	139.33	....	....	0.0523	267.40
Sc_2O_3	0.7303	15.186	....	....	....	....
Y_2O_3	0.2833	6.7358	....	....	....	....
ThF_4	....	5.6478	12.3371	46.702	0.3498	8.7880
HfF_4	0.3851	0.9261	....	....	0.0687	0.2125
AlF_3	0.2531	1.5250	....	....	0.0629	1.6365
CeF_3	0.5109	17.961	....	....	0.2213	10.723
ScF_3	0.3829	4.6531				
YF_3	0.4319	153.76				
ZnS	0.5530	1347.8				
NaF	0.2749	71.919				
Na_3AlF_6	0.3130	0.6553				

TABLE 3: THIN FILM ABSORPTANCE MEASUREMENTS
AT 351, 514, AND 1320 nm.

FILM (Half Wave at 1.06 Microns)	A_{351}(%)	A_{514}(%)	A_{1320}(%)
TiO_2	44	0.061	0.0046
MgO	9.2	6	0.21
Sc_2O_3	0.51	0.037	0.0052
Y_2O_3	0.14	0.018	0.0038
HfO_2	0.33	0.037	0.0056
ThO_2	0.92	0.068	0.0015
ZrO_2	1.2	0.066	0.0038
CeO_2	27.1	2	0.0074
SiO	81	24	0.0037
ScF_3	0.25	0.041	0.0026
HfF_4	0.19	0.023	0.0023
LaF_3	0.8	0.31	0.0023
AlF_3	0.16	0.022	0.0074
ZnS	39.5	0.32	0.0078
NaF	33.0	15.0	0.0042
ThF_4	0.13	0.024	0.68
Al_2O_3	0.20	0.034	0.0022
BeO	1.1	0.14	0.0040
AlN	0.64	0.053	....
YF_3	....	....	0.0082
MgF_2	....	....	0.0084
SiO_2 Substrate	0.08	0.019	
BK-7 Substrate	2.0	0.13	

TABLE 4: SINGLE PULSED LASER DAMAGE THRESHOLD MEASUREMENTS

COATINGS	SUBSTRATES Fused Silica (SiO_2)	Calcium Fluoride (CaF_2)	Sapphire (Al_2O_3)
ThO_2	5.5 J/cm^2 (S1311) 5.0 J/cm^2 (S1350)	5.5 J/cm^2 (F5783)	8.7 J/cm^2 (A102)
MgO	4.3 J/cm^2 (S1304) 5.0 J/cm^2 (S1318)	3.2 J/cm^2 (F9858)	11.1 J/cm^2 (A173)
Y_2O_3	8.4 J/cm^2 (S1335)	8.1 J/cm^2 (F8849)	13.8 J/cm^2 (A50)
HfO_2	6.3 J/cm^2 (S1347) 4.9 J/cm^2 (S1359)	4.4 J/cm^2 (F4772)	>15.0 J/cm^2 (A10) 10.7 J/cm^2 (A46)
Sc_2O_3	3.0 J/cm^2 (S1330) 5.6 J/cm^2 (S1365)	6.8 J/cm^2 (F8838)	12.3 J/cm^2 (A137) 12.1 J/cm^2 (A150)
CeO_2	2.3 J/cm^2 (S1345) 2.2 J/cm^2 (S1367)	8.6 J/cm^2 (F5786)	13.7 J/cm^2 (A31) 9.9 J/cm^2 (A116)
Al_2O_3	5.7 J/cm^2 (S1362) 4.1 J/cm^2 (S1441)	6.8 J/cm^2 (F1716) 3.9 J/cm^2 (F6798)	4.4 J/cm^2 (A16) 7.1 J/cm^2 (A139)
SiO	3.9 J/cm^2 (S1300) 2.4 J/cm^2 (S1364)	4.4 J/cm^2 (F5792)	4.7 J/cm^2 (A111) 9.6 J/cm^2 (A119)
SiO_2	14.5 J/cm^2 (S1302) 12.3 J/cm^2 (S1342)	15.6 J/cm^2 (F1703) >17.0 J/cm^2 (F8846)	26.6 J/cm^2 (A115)
ZrO_2	2.0 J/cm^2 (S1368)	6.1 J/cm^2 (F9866)	>12.9 J/cm^2 (A35) 6.9 J/cm^2 (A112)
TiO_2	.....	3.6 J/cm^2 (F7825)	7.3 J/cm^2 (A44) 6.8 J/cm^2 (A66)
ThF_4	8.1 J/cm^2 (S1306) 3.8 J/cm^2 (S1446)	10.8 J/cm^2 (F1705) 7.4 J/cm^2 (F3756)	13.4 J/cm^2 (A5) 8.7 J/cm^2 (A170)
MgF_2	7.4 J/cm^2 (S1316) 6.1 J/cm^2 (S1389)	8.3 J/cm^2 (F2736) 4.3 J/cm^2 (F3750)	27.9 J/cm^2 (A129)
YF_3	11.6 J/cm^2 (S1326) 7.5 J/cm^2 (S1409)	6.5 J/cm^2 (F4770) 8.8 J/cm^2 (F4774)	>27.0 J/cm^2 (A121) 9.2 J/cm^2 (A131)
HfF_4	9.7 J/cm^2 (S1341) 12.3 J/cm^2 (S1397)	14.6 J/cm^2 (F1707)	10.0 J/cm^2 (A41)
ScF_3	11.1 J/cm^2 (S1363) 6.4 J/cm^2 (S1402)	8.7 J/cm^2 (F4760) 10.5 J/cm^2 (F4768)	.....
CeF_3	5.1 J/cm^2 (S1366) 10.0 J/cm^2 (S1405)	8.6 J/cm^2 (F1717) 5.6 J/cm^2 (F6801)	17.2 J/cm^2 (A18) 12.0 J/cm^2 (A138)
AlF_3	19.4 J/cm^2 (S1361)	9.7 J/cm^2 (F1712) 5.4 J/cm^2 (F4767)	19.1 J/cm^2 (A15)
LaF_3	5.8 J/cm^2 (S1319) 8.5 J/cm^2 (S1424)	4.7 J/cm^2 (F7816) 4.7 J/cm^2 (F8837)	27.1 J/cm^2 (A93) 11.3 J/cm^2 (A99)
Na_3AlF_6	8.9 J/cm^2 (S1370) 7.3 J/cm^2 (S1394)	4.9 J/cm^2 (F5784) 3.7 J/cm^2 (F5787)	9.2 J/cm^2 (A90) 11.3 J/cm^2 (A103)

Table 4 (Cont)

NaF	1.7 J/cm^2 (S1373) 1.4 J/cm^2 (S1442)	1.9 J/cm^2 (F1711) 1.8 J/cm^2 (F4766)	4.1 J/cm^2 (A105)
ZnS	1.9 J/cm^2 (S1372)	.....	4.6 J/cm^2 (A154) 5.3 J/cm^2 (A160)

Fused Silica (SiO_2) Substrate	27.7 J/cm^2	(S1434)
Calcium Fluoride (CaF_2) Substrate	13.1 J/cm^2	(F5789)
Sapphire (Al_2O_3) Substrate	9.4 J/cm^2	(A147)

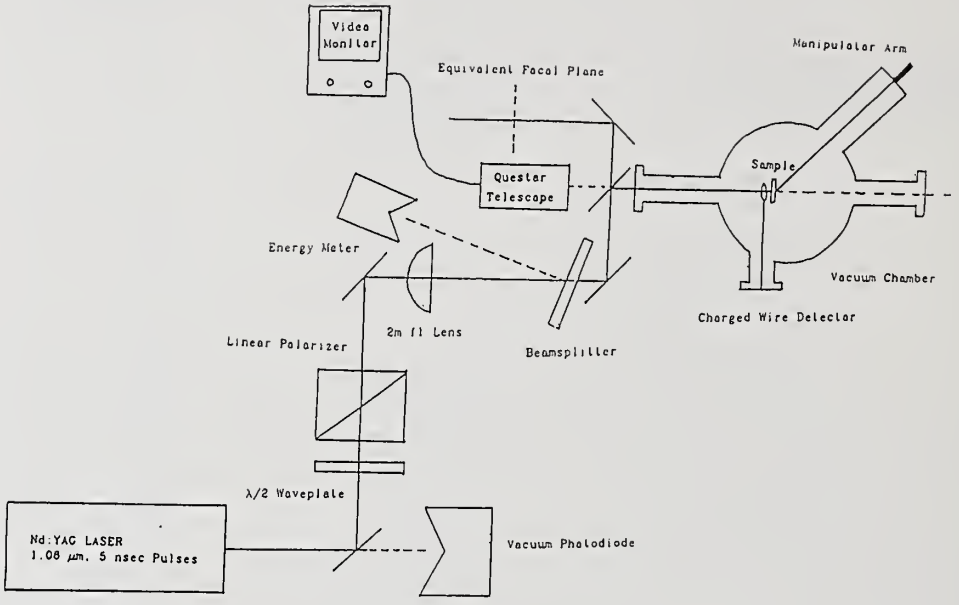

Figure 1. Experimental Arrangement for Studying Laser Induced Charge Emission.

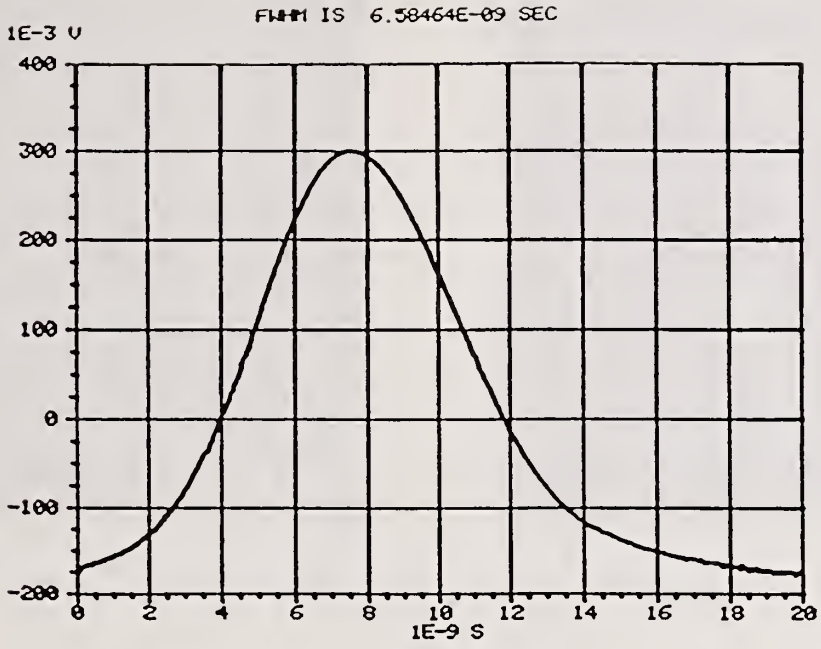

a. Temporal Profile

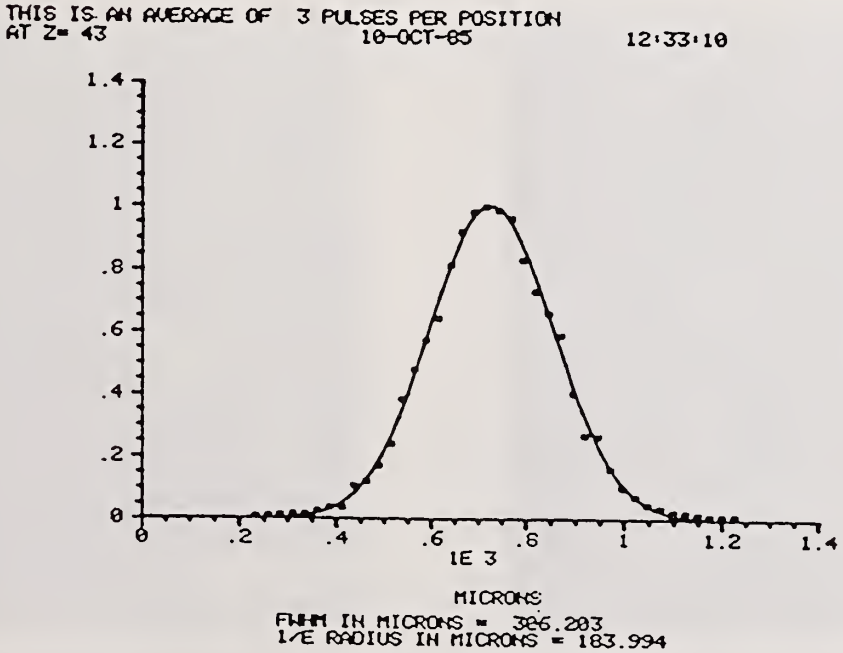

b. Spatial Profile

Figure 2: Temporal and Spatial Profiles of Nd:YAG Laser

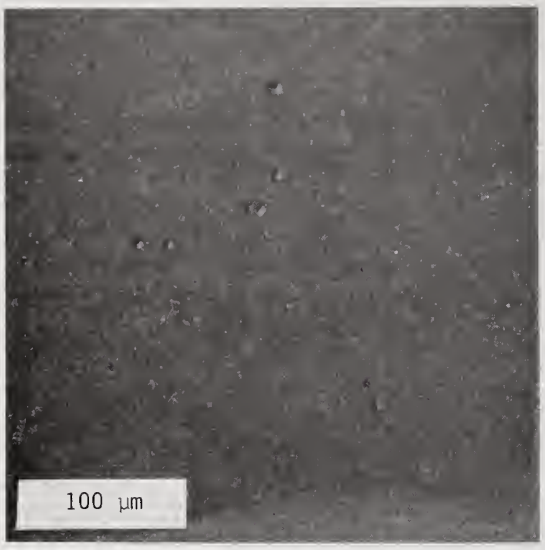

a. HfO_2 (Half Wave) on Sapphire (A10)
Site 23 Mag 20X

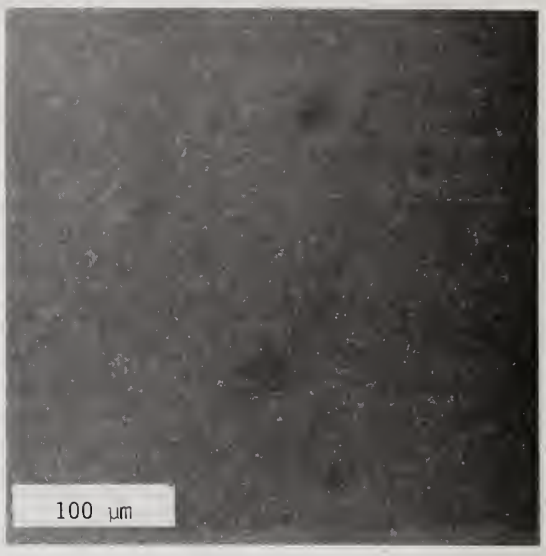

b. HfF_4 (Half Wave) on Sapphire (A41)
Site 112 Mag 20X

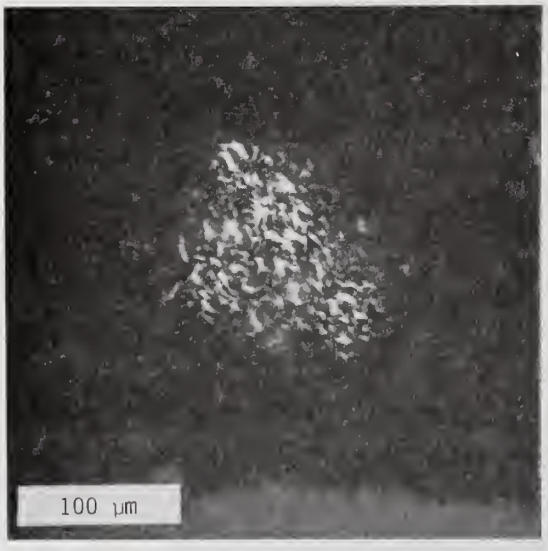

c. YF_3 (Half Wave) on Fused Silica (S1326)
Site 104 Mag 20X

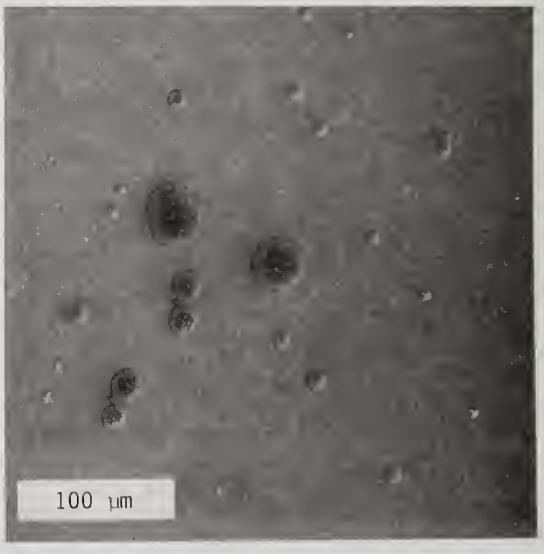

d. Y_2O_3 (Half Wave) on Fused Silica (S1337)
Site 118 Mag 20X

Figure 3. Damage Morphologies of Dielectric Thin Films

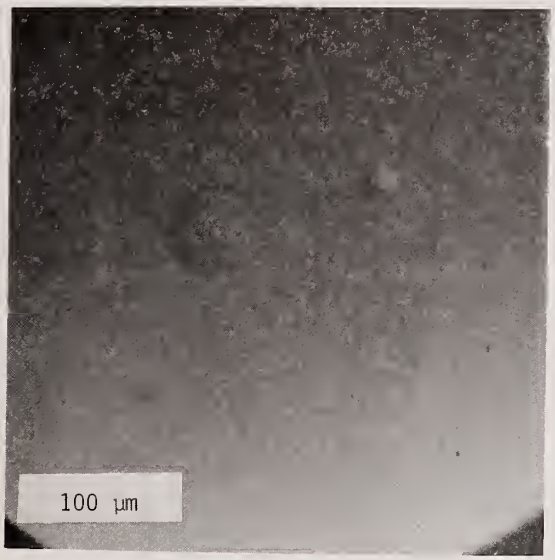

a. CeF_3 (Half Wave) on Calcium Fluoride (F1717)
Site 157 Mag 20X

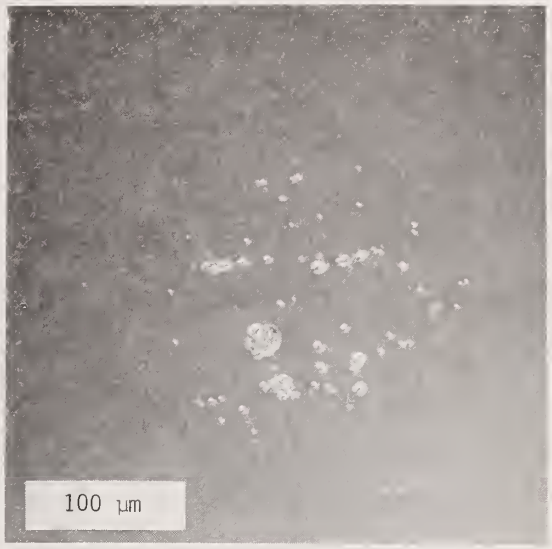

b. CeO_2 (Half Wave) on Calcium Fluoride (F2719)
Site 21 Mag 20X

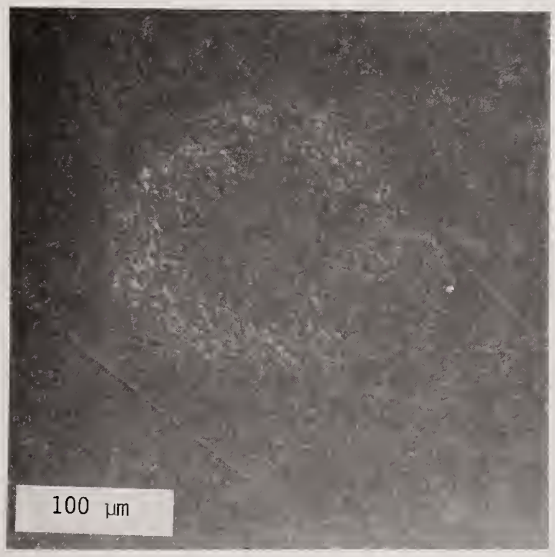

c. Na_3AlF_6 (Half Wave) on Sapphire (A103)
Site 5 Mag 20X

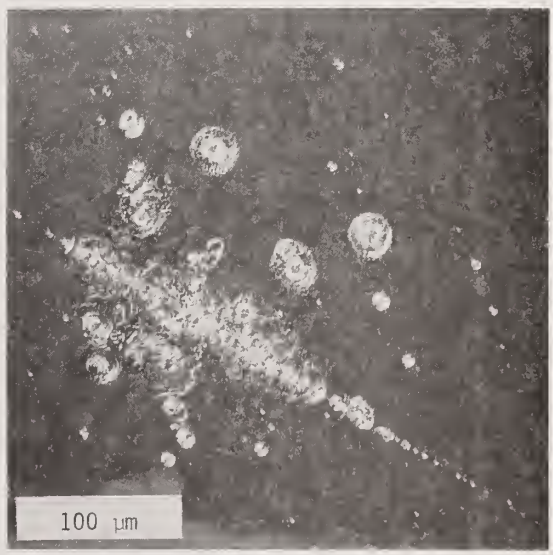

d. ZnS (Half Wave) on Fused Silica (S1372)
Site 40 Mag 20X

Figure 4. Damage Morphologies of Dielectric Thin Films

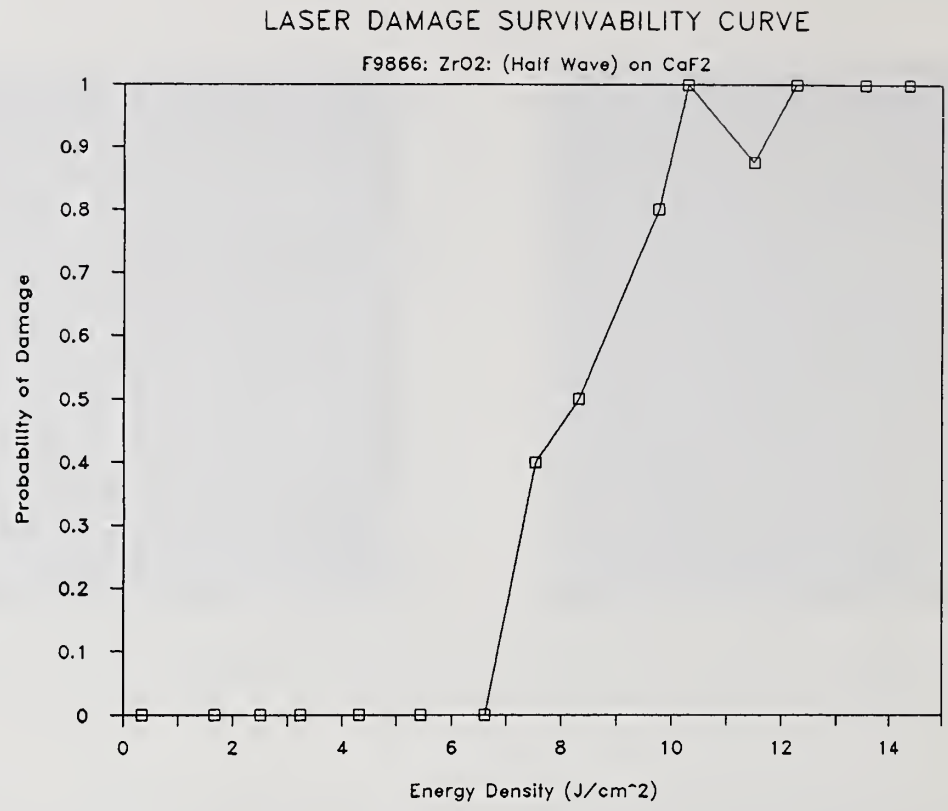

Figure 5. Laser Damage Survivability Curve for ZrO_2 (Half Wave @ 1.06 μm) on CaF_2 with a Damage Threshold of 6.1 J/cm^2.

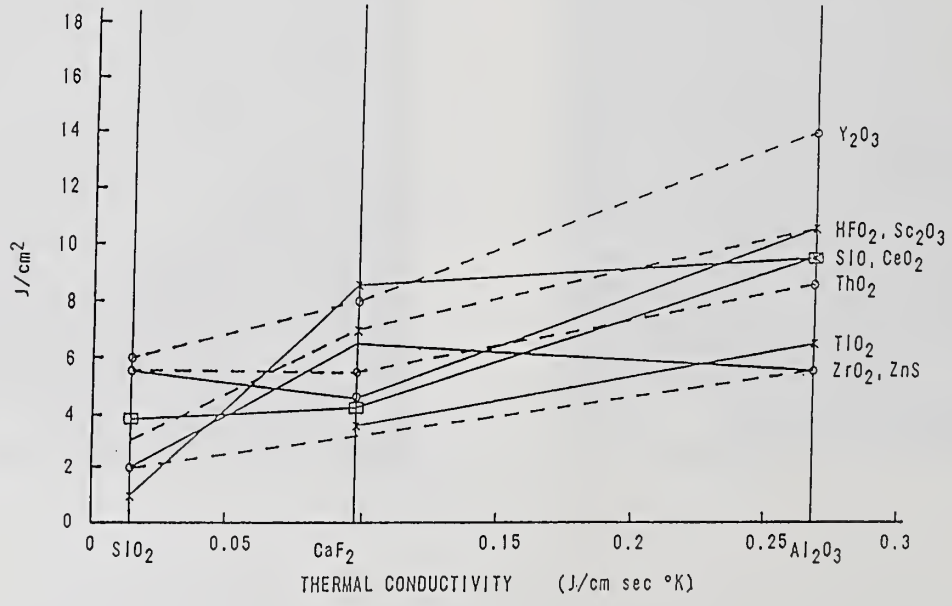

Figure 6. Laser Damage Thresholds of Various Thin Film Dielectric Coatings vs Substrate Thermal Conductivity.

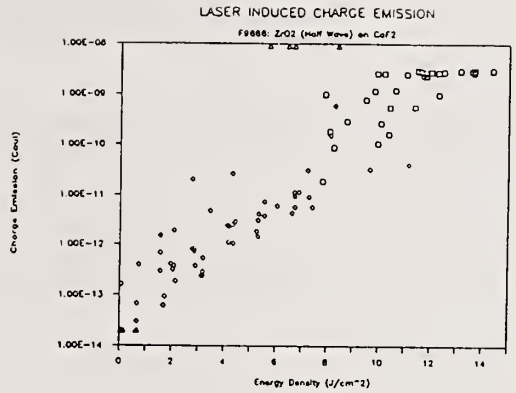

a. Distinct Carge Emission Curve with Little or No Scatter in the Data

◇ UNDAMAGED SITE

□ DAMAGED SITE

Δ OUT OF RANGE-UNDAMAGED SITE

X OUT OF RANGE-DAMAGED SITE

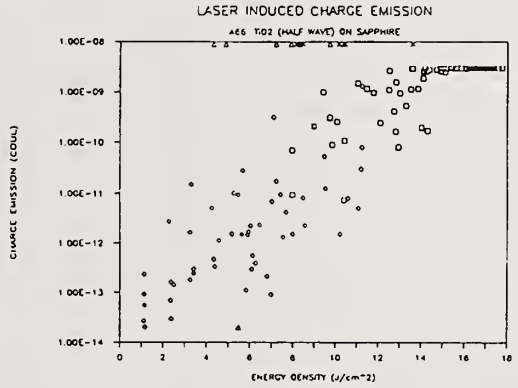

b. Less Distinct Charge Emission Curve with some Scatter in the Data

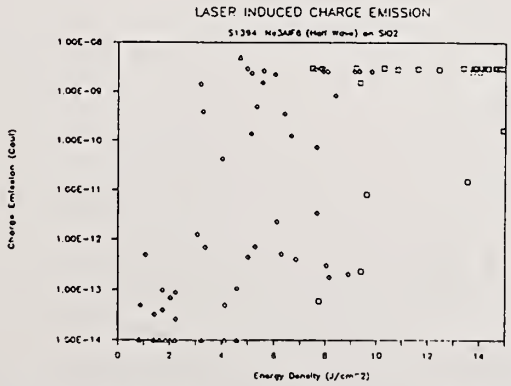

c. A Random Pattern with Little or no structure

Figure 7: Laser Induced Charge Emission Curves

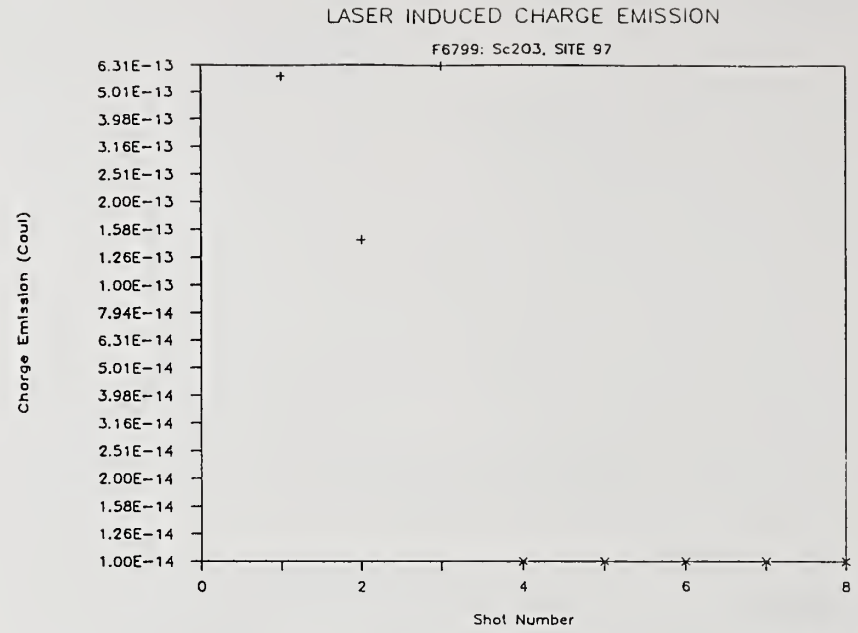

Figure 8: Charge Emission Curve for Sc_2O_3 (Half Wave @ 1.06 μm) on CaF_2. Site was irradiated with 6.0 J/cm^2 pulses, and did not damage.

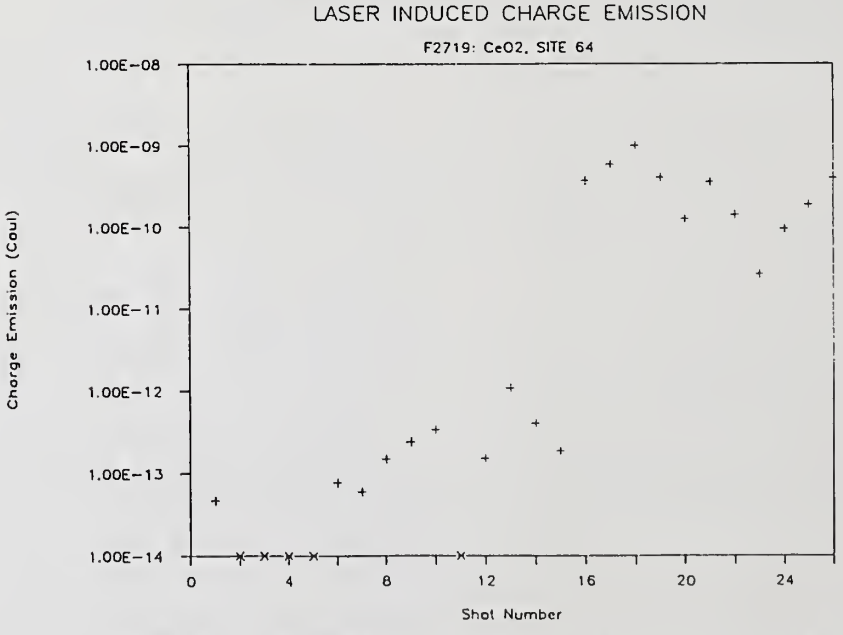

Figure 9: Charge Emission Curve for CeO_2 (Half Wave @ 1.06 μm) on CaF_2. Site was irradiated with 4.7 J/cm^2 pulses, and was damaged.

- Manuscript Not Received -

The Effect of Layer Thickness Errors in the Design of Coatings with Reduced Electric Field Intensity*

Geza L. Keller
Los Alamos National Laboratory
Los Alamos, New Mexico 87545

ABSTRACT

Many papers have been written on the design of laser-damage-resistant high reflectors. Usually, reduction in the peak electric-field intensity in the outermost layers of a multilayer stack is studied.

In this work, the effect of random and systematic errors in the quarter-wave stack below the enhanced layers is investigated. Also, optical monitoring errors in the optimized layers and their relation to the standing-wave electric field through the multilayer stack are discussed.

Key Words: electric field distribution; film thickness error; laser damage; multilayer films.

* Work done under the auspices of the U.S. Department of Energy.

Wavelength dependence of laser-induced sputtering from the (111) surface of BaF_2.

J. Reif, H. Fallgren[a], W.E. Cooke[b], and E. Matthias
Institut für Atom- und Festkörperphysik
Freie Universität Berlin, 1000 Berlin 33
West-Germany

Abstract:

Using blue tunable pulse laser radiation of low fluence, we have investigated laser-induced sputtering from cleaved BaF_2 (111) surfaces under ultrahigh vacuum conditions. Time-correlated with the laser pulses we observed the positive ions Ba^+, Ba^{++}, $(BaF)^+$, and F^+. Practically no negative ions were found. Neutral atomic fluorine (F^O) was desorbed abundantly. A pulse correlation of F^O as well as the relative amount of F^O and F^+ could not be established at this stage. The emission yield of all positive ions as well as of F^O was strongly wavelength dependent and showed a broad resonance around 2.9 eV.

Key words: laser-induced sputtering; ultrahigh vacuum; laser-induced desorption; fluoride optical materials

PACS Number: 7920 D

In this Letter, we report results for wavelength-dependent laser-induced desorption or sputtering from clean ionic surfaces in ultrahigh vacuum at fluences well below the commonly quoted damage threshold. The principal goal of our experiments is to study the electronic structure of ionic surfaces within the band gap and to understand the fundamental mechanism of laser-induced desorption for transparent crystals of optical quality. It has been suggested that laser-induced sputtering involves electronic excitations of localized states[1]. For alkali halides it is assumed[2] that halogen atoms are ejected by the Pooley-Hersh mechanism[3,4], followed by thermal desorption of neutral alkalis[5]. For alkaline-earth halides we expect that the second valence electron can be resonantly excited to form surface excitons, which again may lead to desorption. In that case one would expect a spectral dependence of the laser sputtering yield. The existence of spectral resonances would not only be significant for a detailed understanding of the desorption process, but it would also be of great practical importance. Sputtering using resonant light, for example, could then be carried out at considerably lower intensities thus reducing thermal effects. On the other side, the resistivity of optical materials against radiation damage could be increased by avoiding frequencies near those electronic resonances.

For our experiments we selected BaF_2 as a typical representative of the alkaline-earth fluoride optical materials. To quarantee clean surface conditions the crystal was mounted

and cleaved in ultrahigh vacuum of 3×10^{-8} Pa. The experimental set-up is shown in Fig. 1. At room temperature the easy-cleaved (111) surface of BaF_2 was irradiated by the focused light from a YAG-pumped pulsed tunable dye laser (pulse length $\sim$ 8 ns). For the experiments reported here we used Stilbene 3 covering the spectral range from 410 to 450 nm. Typical interaction spots of 0.5 mm^2 lead to average intensities of about 5×10^7 W/cm^2, which is an order of magnitude less than the macroscopic damage threshold[6]. This figure, however, must be treated with caution, since hot spots in the beam profile and mode beating spikes can locally lead to substantially higher intensities. Also, structural surface defects due to cleaving are expected to locally reduce the quoted damage threshold. The emitted particles were analyzed by a quadrupole mass filter and recorded by a secondary electron multiplier. A gated integrator was used to establish the time correlation between the desorbed particles and the laser pulses. The mass spectrometer could be operated for positive as well as for negative ions and, by means of an additional ion source, for neutrals.

The prevailing result was that the pressure in the vacuum chamber increased significantly whenever the laser radiation reached the crystal. Mass spectrometric analysis showed that this was due to neutral atomic fluorine (F^o) which abundantly desorbed from the irradiated crystal surface. There was no obvious correlation between the desorbed F^o and the laser pulses. However, since fluorine was poorly pumped by our cryo-

pump system we cannot, at this stage, exclude the possibility that a time correlation exists, but it may be suppressed by the fluorine background in the vacuum chamber. The observation of F^o instead of F_2 indicates that we have a non-thermal desorption process[7] triggered by the Pooley-Hersh mechanism. For non-thermal particles, on the other hand, one would expect some time-correlation with the laser pulse[8]. Clearly, this question must be the subject of further investigation, and target temperature, intensity and time-dependence of the F^o yield must be measured before final conclusions can be drawn.

Another dubious point is the emission of neutral barium atoms (Ba^o). For alkali halides the generally accepted picture is that the Pooley-Hersh mechanism leads to a metal-rich surface from which alkali atoms can undergo thermal desorption for sufficiently high target temperatures[2,5]. For thermal particles we expect delay times of the order of milliseconds[8], hence we should have seen Ba^o in between the laser pulses, which was definitely not the case for our laser intensities. We attribute the lack of Ba^o to its low vapor pressure at the target temperature[5]. It may however still be possible that Ba^o appears correlated to the laser pulses. However, in our measurements we could not observe any significant difference in the ion signal, whether the ion source of the mass filter was switched on or off.

The observed strong emission of F^o is in line with the

results of other groups on laser- and electron-stimulated desorption[1,9] of halogens from alkali halides. In our case, however, the question about defect creation must be raised. Two facts should be noted: (1) the investigated BaF_2 crystals were of good optical quality and highly transparent; (2) we used blue radiation (2.8 to 3 eV) and sufficiently low intensities to render unlikely higher order ($n \geq 4$) multiphoton processes which could bridge the band gap. For this reason we hypothesize that most of the energy is absorbed at the surface, and the question is whether there exist surface or impurity states that are responsible for an enhanced absorption. With this in mind we checked the wavelength dependence of the neutral fluorine emission. The result is shown in Fig.2. In part a) below 430 nm a sharp increase of the emission rate above the already present fluorine background is seen which reached saturation at about 420 nm. Clearly, this indicates the onset of an enhanced energy absorption of photons of this wavelength. The saturation is due to insufficient pumping speed for fluorine. Scans b) and c) demonstrate the quenching of the emission. Each scan lasted for about 25 minutes during which the laser pulsed at 10 Hz. As discussed by Kelly[5] for alkali halides, the "bleaching" effect is most likely caused by a metallization of the surface layer with a subsequent change in absorption characteristics. Proof of this assertion can only come from qualitative comparison of the F^o and Ba^o yield which, at the moment, is beyond our experimental capabilities. Another possible explanation of the "bleaching" effect may be the disappearance of impurity states by cleaning off

structural defects caused by cleaving. The results displayed in Fig. 2 can be disputed by arguing that the emission increase occurs close to the culmination of the dye laser intensity. By systematically changing the dye characteristics we have invalidated this objection. Also, the sharp onset of the emission in Fig. 2a is evidence against an intensity effect.

To investigate this wavelength related emission more rigorously, we used a time-gated observation which relates the particle emission to the laser pulses and is therefore indicative of electronic processes. Time correlated to the light pulses we observed the positive ions Ba^+, Ba^{++}, F^+ and $(BaF)^+$. A search for negative ions, in particular neon-like F^-, failed to show any significant signals. The desorption of all positive ions was strongly wavelength dependent and occurred for all ions in the range 415-435 nm. A typical emission yield of Ba^+ as a function of wavelength is shown in Fig. 3. We have recorded many spectra and it is important to note that the detailed structure of the spectra varies from laser scan to laser scan and from site to site. In all cases, however, the gross feature of the wavelength dependence is repeated. Also, the emission yield is strongly site-dependent for a fixed laser intensity. Some spots are dormant and can only be activated by increasing the laser intensity. Others are very active in the beginning but bleach out after exposure to a few thousand laser shots. This site-to-site variation of the emission yield is not surprising in view of the microscopic

damage of the surface after cleaving.

The same wavelength dependence for the emission of neutral fluorine as well as the positive ions suggests that both are triggered by the same electronic excitation. Unfortunately, our present technique did not allow to determine the ratio between the emission rates for neutrals and positive ions. The fact that we observe only positive ions and no F^- points to an efficient charge transfer process similar to that in the Knotek-Feibelman model[10]. However, at this point it is too early to propose any model for the observed emission process and more data on the electronic structure of these type of surfaces are needed to gain a better understanding.

Acknowledgement

This work was in part supported by the Deutsche Forschungsgemeinschaft, Sfb 161. We thank Dr. P.J. West, E. Arndt, and P. Staszak for their assistance in building the apparatus and Dr. H.B. Nielsen for discussions. One of us (W.E.C.) gratefully acknowledges a senior scientist award from the Humboldt Foundation.

References and Footnotes:

a) present address: Chalmers Institute of Technology
S-402 20 Göteborg, Sweden
b) present address: Physics Department, University of
Southern California, Los Angeles, CA 90089-0484

1. A. Schmid, P. Bräunlich, and P.K. Rol, Phys.Rev.Letters 35, 1382 (1975).
2. T. Nakayama and N. Itoh, page 237 in "Desorption Induced by Electronic Transitions, DIET II", edited by W. Brenig and D. Menzel, Springer Series in Surface Sciences 4 (1985).
3. D. Pooley, Proc.Phys.Soc. 87, 245 and 257 (1966).
4. H.N. Hersh, Phys.Rev. 148, 928 (1966).
5. R. Kelly, Surface Sciene 90, 280 (1979)
6. F. Rainer, W.H. Lowdermilk, and D. Milam, NBS Special Publication 669 (1984), page 157.
7. R.W. Dreyfus, R.E. Walkup, and R. Kelly, Radiation Effects, to be published.
8. H. Overeijnder, R.R. Tol, and A.E. de Vries, Surface Science 90, 265 (1979)
9. M. Szymonski and A.E. de Vries, page 216 in "Desorption Induced by Electronic Transitions, DIET I", Editors: N.H. Tolk, M.M. Traum, J.C. Tully, and T.E. Madey, Springer Series in Chemical Physics 24 (1983).
10. M.L. Knotek, Rep.Prog.Phys. 47, 1499 (1984)

Figure Captions:

Fig. 1: Sketch of the experimental set-up. The output intensity of the linearly polarized dye laser light can be varied without changing the beam geometry by use of a Fresnel rhomb combined with an analyzing plan polarizer, and is monitored by a wavelength-independent photo diode. The angle of incidence is about 45^{o}, the light is p-polarized.

Fig. 2: Emission of neutral atomic fluorine from BaF_2 (111) as a function of wavelength. The data in a), b), and c) represent three successive wavelength scans with decreasing wavelength of about 25 min duration each, with 30 min pumping time (laser off) in between to reduce the fluorine pressure.

Fig. 3: Typical emission spectrum of Ba^{+} from a BaF_2 (111) surface time-correlated to the laser pulses.

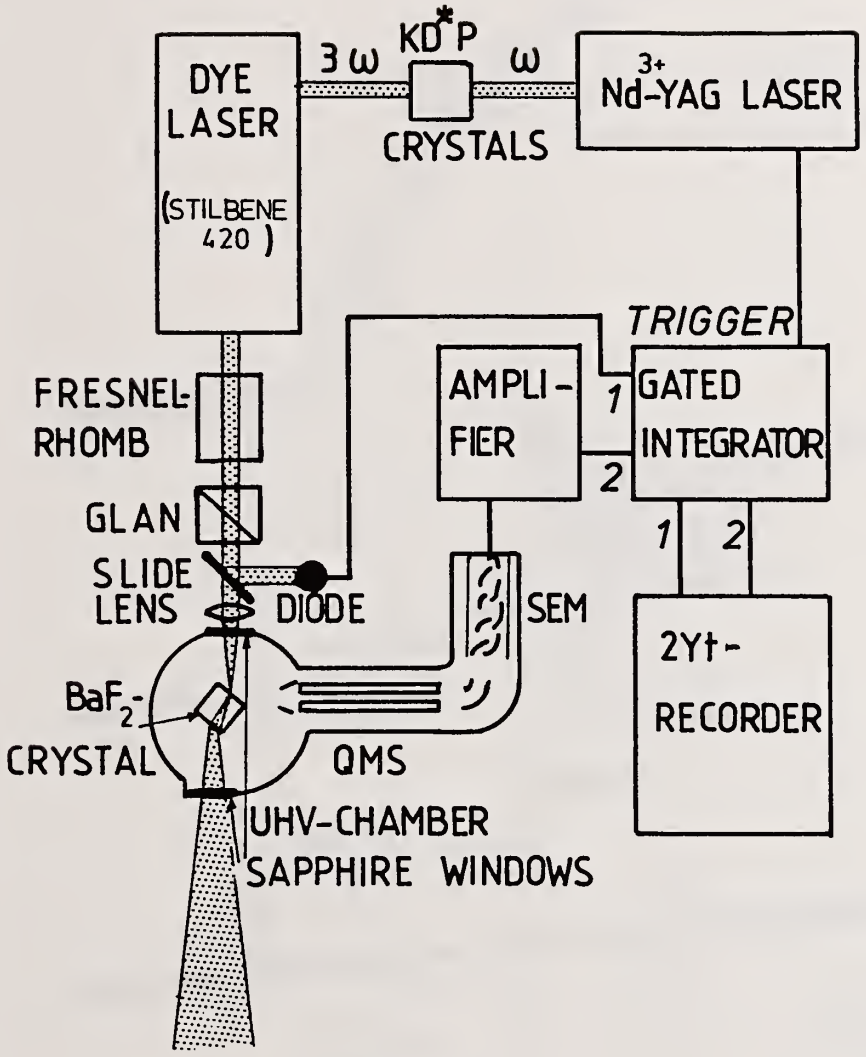
DYE LASER
(STILBENE 420)
3ω
KD*P
CRYSTALS
ω
3+
Nd-YAG LASER
TRIGGER
FRESNEL-RHOMB
GLAN
SLIDE
LENS
DIODE
AMPLI-FIER
1
2
GATED INTEGRATOR
1
2
SEM
2Yt-RECORDER
BaF2-CRYSTAL
QMS
UHV-CHAMBER
SAPPHIRE WINDOWS

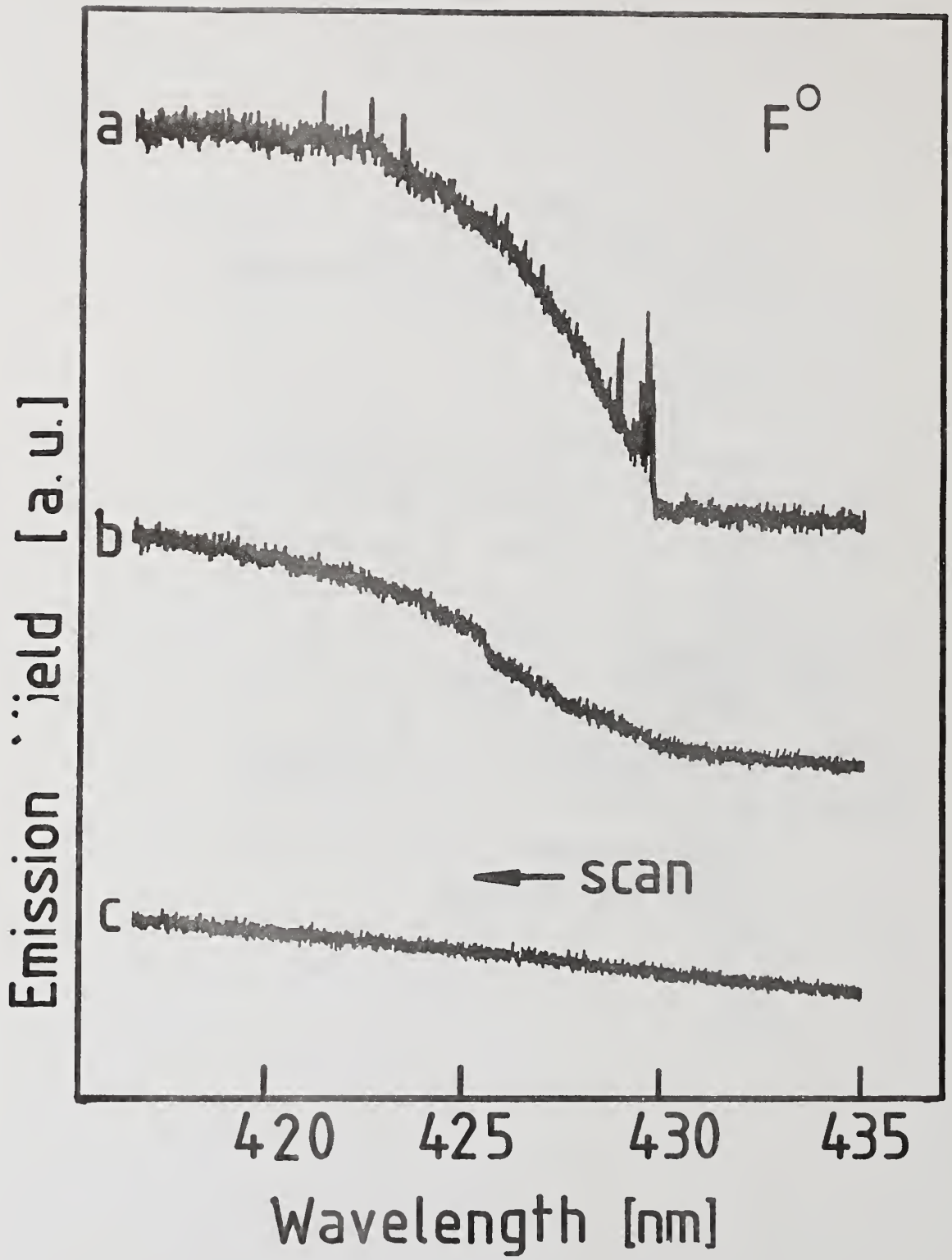
a
F°
b
scan
c
Emission yield [a.u.]
420
425
430
435
Wavelength [nm]

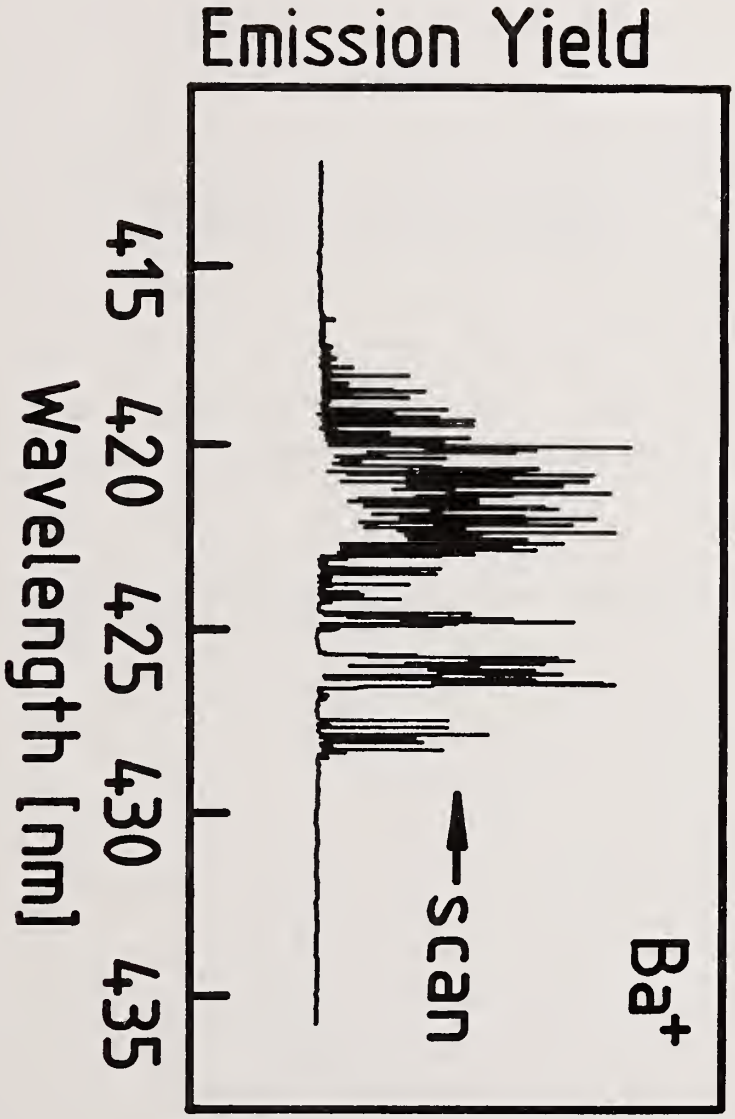
Emission Yield
415
420
425
430
435
Wavelength [nm]
scan
Ba+

Layer-dependent laser sputtering of BaF_2 (111)

J. Reif, H. Fallgren, H.B. Nielsen, and E. Matthias

Institut fur Atom- und Festkorperphysik
Freie Universitat Berlin, 1000 Berlin 33

Abstract

Laser-induced sputtering from the (111) surface of BaF_2 was investigated under ultrahigh vacuum conditions, applying fluences well below the macroscopic damage threshold. Measurement of the wavelength dependent desorption of Ba^+ indicates that Ba^+ is emitted from two chemically different surroundings at the surface. For a fixed wavelength, the emission rate of Ba^+ and F^+ as functions of time show a distinct anticorrelation, confirming the existence of two different chemical states of the surface, and suggesting that the sputtering takes place layer by layer.

Key words: chemical state of film surfaces; laser induced sputtering; ultrahigh vacuum

Laser-induced sputtering or photo-desorption is of great interest both for technological applications[1] and for surface spectroscopy[2]. A prerequisite for surface studies, however, is a detailed understanding of the elementary desorption mechanism. This, in turn, would help improve the control of the sputtering process. It has been suggested that laser-induced sputtering involves electronic excitations on the surface[3,4]. The specific nature of those excitations, of course, varies with material. In an effort to understand the onset of radiation damage on surfaces of transparent optical materials, we are pursuing a program to study the desorption parameters for cleaved ionic surfaces under ultrahigh vacuum conditions and at intensities much below the macroscopic damage treshold[5]. Earlier, we found a striking wavelength dependence of the emission from the (111) surface of BaF_2[6] at low laser intensities. This provides strong support for the assumption that laser-induced sputtering proceeds via electronic excitations on the surface, although the nature of the electronic states involved still remains unidentified.

The purpose of this Letter is twofold. At first we show that the emission rate spectra of Ba^+ exhibit two different energy-dependencies, leading to the conclusion that the emitted Ba^+ ions originate from two chemically different surface environments. Secondly, we present results which can be taken as evidence, that the sputtering yields of Ba^+ and F^+ depend on whether the first surface layer is a barium- or a fluorine layer; i.e., that the surface is ablated layer by layer.

For the experiments we used a pulsed YAG-pumped dye laser which was operated with Stilbene 3 in the blue spectral range. The BaF_2 single crystal was mounted and cleaved in ultrahigh vacuum of about $2x10^{-10}$ Torr. Positive ions emitted from the surface were detected by a quadrupole mass spectrometer. The correlation with the laser pulses was established by processing the signal with a gated integrator. For details of the experimental set-up see Ref. 6.

As reported earlier[6], we observe positive ions emitted from the BaF_2 (111) surface when irradiating it with blue laser light. Evidence for desorption from two chemically different environments is presented in Fig. 1. Successive wavelength scans of the Ba^+ emission from the same spot result in two basically different spectra like the ones shown in Fig. 1a) and b). The spectrum in Fig. 1c) is again similar to the one in a) except energetically somewhat shifted and with a minor contribution reminiscent of spectrum b). It should be remembered that laser-induced sputtering is a destructive process, therefore the surface composition changes and consequently only the general features of the spectra in Fig. 1 are reproducible. In fact, the detailed structure of the emission bands varies from scan to scan and depends on laser intensity and scanning time. Nevertheless, the essence of Fig. 1 is that Ba^+ is emitted from two chemically different surroundings, in one case leading to two energetically separated bands, in the other to one strongly broadened and shifted band in the spectral range from 410 to 450 nm. By

comparison with Fig. 4 we suggest that the spectrum in Fig. 1a) is characteristic for desorption of Ba^+ from a barium-rich layer, while the emission band in Fig. 1b) is attributed to desorption of Ba^+ from a fluorine-rich layer.

For the three most abundant ions the typical time decay of the ion yield is displayed in Fig. 2. The data were obtained with a laser intensity of about $5x10^7$ W/cm^2 and a repetition frequency of 10 Hz. The yields of Ba^+ and $(BaF)^+$ are comparable and about a factor of two stronger than the F^+ emission. The quenching of a spot within a few minutes is typical for the experiments reported here. The reason for this quenching effect is at present not understood and needs further investigation. It could be due to removal of structural defects caused by cleaving, but a possibly non-stoichiometric reconstruction leading to a different electronic structure cannot be ruled out either. It should be noted that sputtering yields as shown in Fig. 2 do not lead to visible macroscopic damage on the surface. Only when the spot is reactivated by applying higher fluences does visible damage occur.

The most conspicuous feature in Fig. 2 is the strong onset of desorption immediately after exposure to laser radiation, which dies out very quickly only to be reactivated a second time for a brief period. This already suggests that we might be peeling off individual layers. What would be expected if such is the case becomes obvious by inspecting Fig. 3 which sketches the sequence of layers along the (111) direction of

BaF_2. Clearly, if the sputtering is sensitive to individual layers, the yields must reflect this F-Ba-F-Ba sequence. To check this we have replotted in Fig. 4 the data of Fig. 2 for Ba^+ and F^+ for direct comparison. We see that the Ba^+ emission starts instantly (dashed lines), while the F^+ emission sets in somewhat delayed after 100 to 150 laser shots. More pronounced is the following anti-correlation between the Ba^+ and F^+ emission. As indicated by the dashed-dotted lines, a maximal yield of F^+ is always accompanied by a minimal yield of Ba^+, and vice versa. We note, that the oscillating yield in Fig. 4 can be viewed as originating from a succession of spectra like the ones in Fig. 1a) to c) when probed at a fixed wavelength. For example, at 429 nm (the dashed line in Fig. 1) spectrum a) would correspond to a high Ba^+ yield, spectrum b) to a low yield, and spectrum c) again to a high yield of Ba^+.

If the assumption that the surface is ablated layer by layer is correct - and we take Fig. 4 as evidence that it is - we see from Fig. 4 that it takes about 500 laser pulses to go through one cycle of the oscillations in the emission rates. This corresponds to an exposure of roughly 4×10^5 photons per emitted atom, and is an indication that the absorption probability is very small, as would be expected for a transparent material.

In summary, we have presented evidence that for layered crystals, such as the fluorite type ionic compounds, resonant laser-induced sputtering at low laser intensities is layer-

sensitive. This opens the prospect of preparing the first surface layer of these crystals at will without affecting the deeper layers to any appreciable extent.

Acknowledgement

We acknowledge helpful discussions with Drs. Chuang and Rhodin. This work was in part supported by the Deutsche Forschungsgemeinschaft, Sfb 161.

Footnotes and References:

a) present address: Chalmers Institute of Technology, S-402 20 Göteborg, Sweden

1. W.W. Duley: Laser Processing and Analysis of Materials. Plenum Press (New York, 1983)
2. M.L. Knotek: Rep.Prog.Phys. 47 (1984) 1499
3. T. Nakayama and N. Itoh, page 237 in "Desorption induced by Electronic Transitions, DIET II", edited by W. Brenig and D. Menzel, Springer Series in Surface Sciences 4 (1985)
4. A. Schmid, P. Bräunlich, and P.K. Rol, Rev.Letters 35, 1382 (1975)
5. F. Rainer, W.H. Lowdermilk, and D. Milam, NBS Special Publication 669 (1984), page 157
6. J. Reif, H. Fallgren, W.E. Cooke, and E. Matthias, to be published

Figure captions

Fig. 1: Emission spectra of Ba^+ from the BaF_2 (111) surface under irradiation with $5x10^7$ W/cm^2. The spectra in a), b), and c) show the yield of successive wavelength scans at the same surface spot.

Fig. 2: Emission yield of positive ions from the BaF_2 (111) surface when irradiated with 2.90 eV radiation of $5x10^7$ W/cm^2 intensity. The laser pulse repetition rate was 10 Hz. The vertical scale is identical in all cases.

Fig. 3: Cross section of the (111) plane of BaF_2.

Fig. 4: Detailed comparison between the emission yields of Ba^+ and F^+, taken from Fig. 2. The dashed-dotted lines indicate number of laser pulses after which the F^+ emission is dominant while the Ba^+ emission is at a minimum.

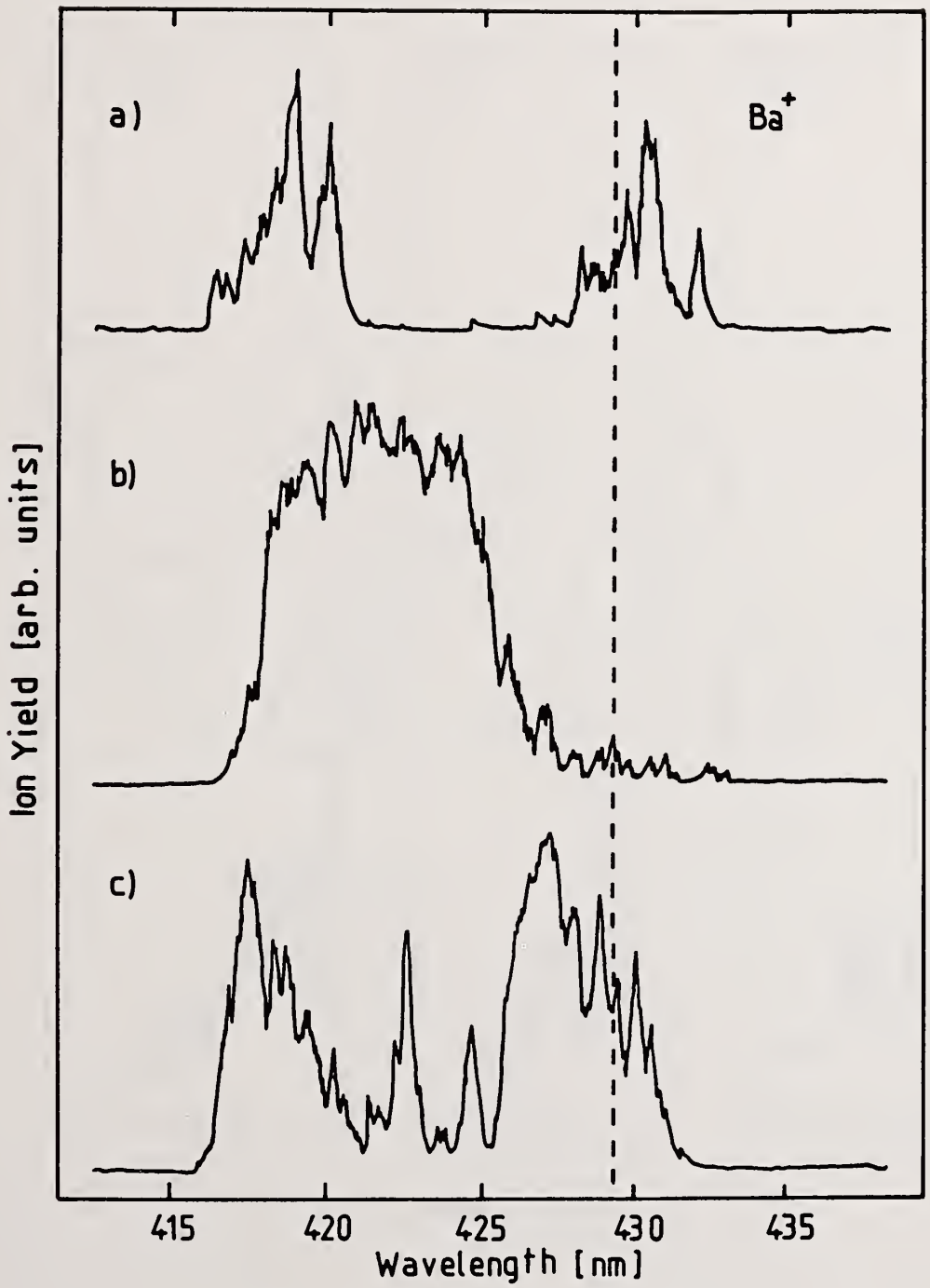
a)
Ba+
b)
c)
Ion Yield [arb. units]
415
420
425
430
435
Wavelength [nm]

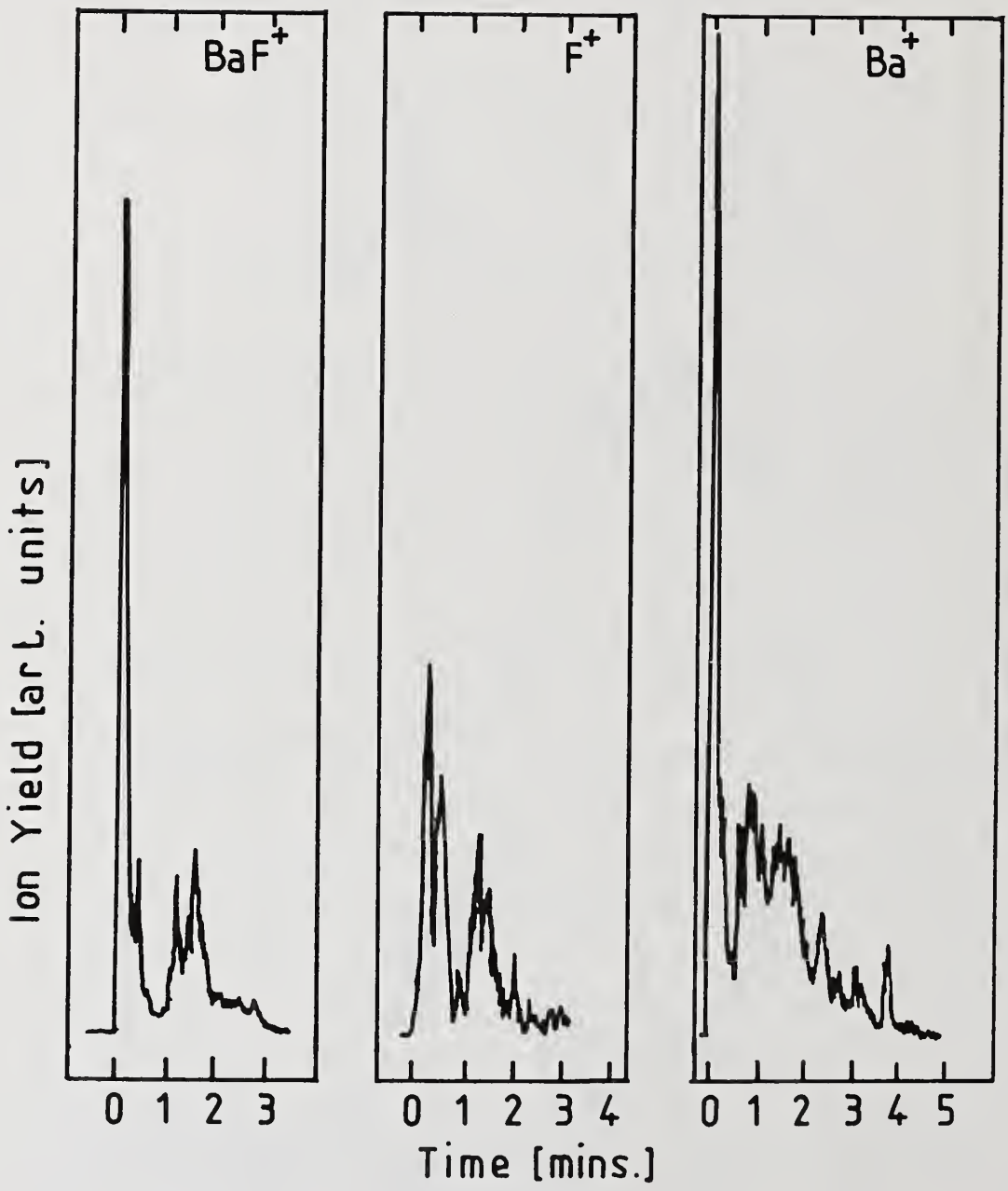
BaF+
F+
Ba+
Ion Yield [arb. units]
0 1 2 3
0 1 2 3 4
0 1 2 3 4 5
Time [mins.]

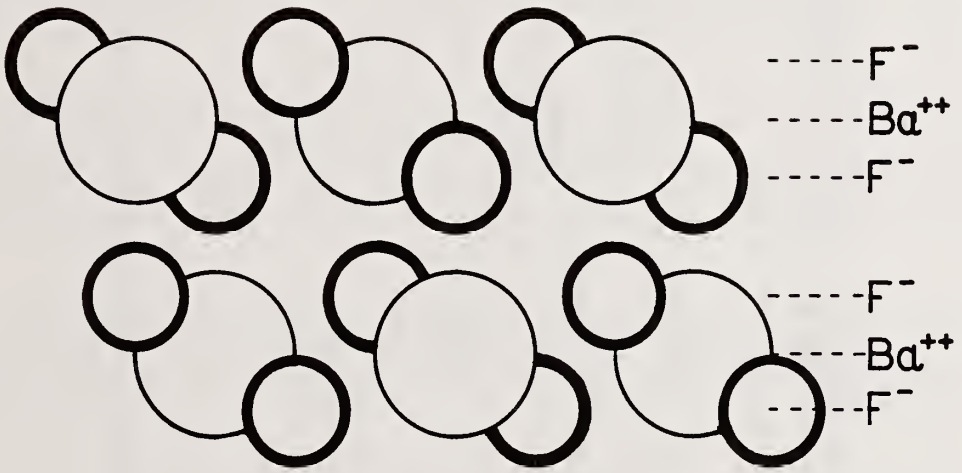
-----F⁻
-----Ba⁺⁺
-----F⁻
-----F⁻
----Ba⁺⁺
----F⁻

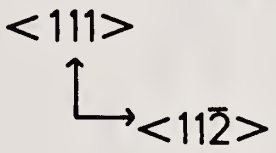
<111>
<11$\bar{2}$>

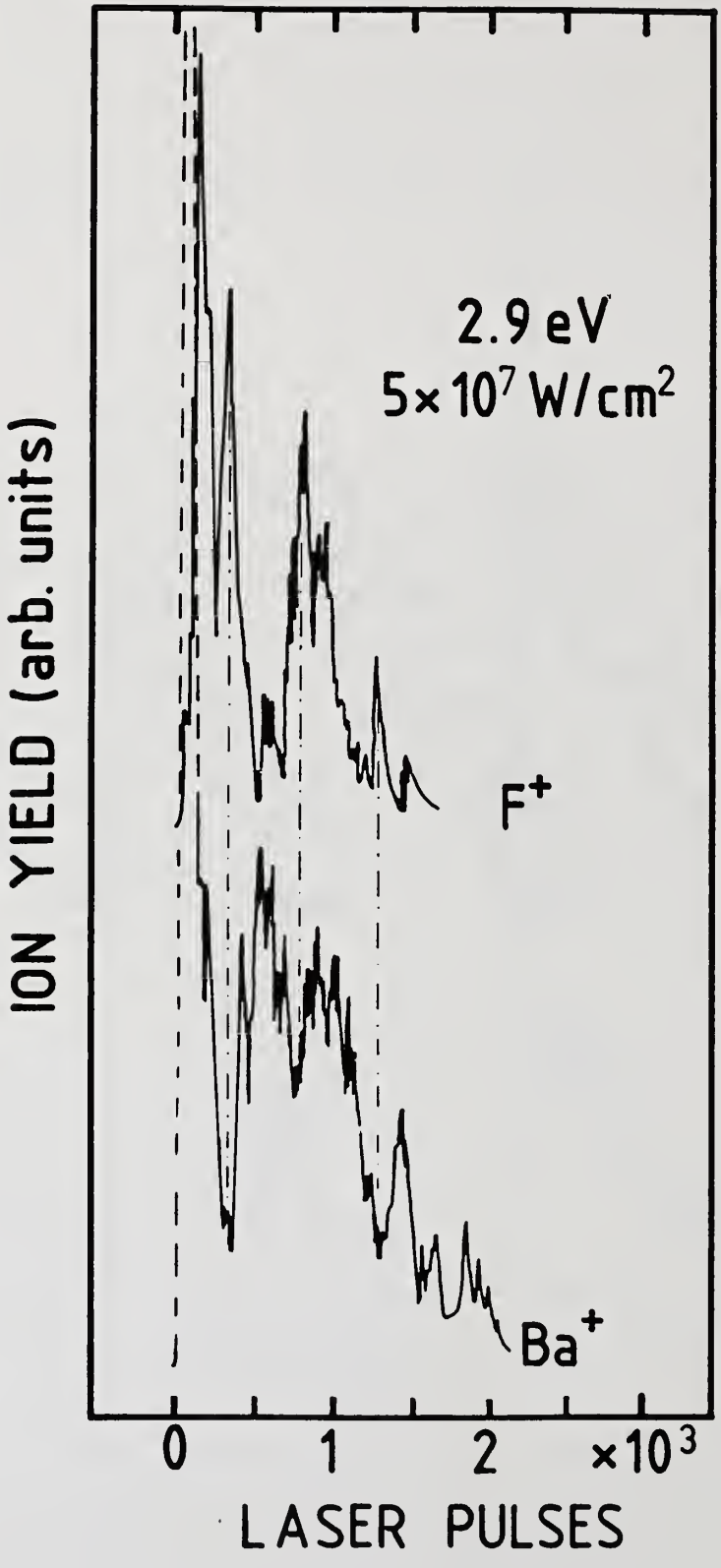
2.9 eV
5×10⁷ W/cm²
F⁺
Ba⁺
ION YIELD (arb. units)
0
1
2
×10³
LASER PULSES

- Manuscript Not Received -

IMPACT OF THERMAL BLOOMING ON LASER DAMAGE MEASUREMENT ACCURACY *

Brian E. Newnam
Los Alamos National Laboratory
Los Alamos, New Mexico 87545

ABSTRACT

The presence of thermal blooming in laser damage experiments conducted in air frequently goes unnoticed. For certain conditions, however, this effect can result in significant errors in determining the magnitude of damage thresholds.

Thermal blooming of a laser beam is a direct result of nonuniform heating of the transmitting medium (air) across the laser beam diameter. The resultant changes in refractive index cause the laser beam to diverge. In a laser damage experiment the test sample is often placed in the focal plane of a positive lens. With thermal blooming, however, the actual focus of the high-intensity laser beam can occur significantly in front of the sample, resulting in overestimates of the damage threshold.

Using the formulation of Skinner[1] for a focused Gaussian beam, we calculate the magnitude of possible errors for damage thresholds of surfaces and thin films measured in air with various wavelengths. Measurements reported by several laboratories fall in the parameter space for which corrections for the effects of thermal blooming are recommended.

Key Words: aerosols; atmospheric absorption; laser damage experiments; thermal blooming; thermal defocussing.

[1] D.R. Skinner, "Thermal Defocusing of Brief Laser Pulses," Opt. Commun. 1, 57 (1969).

* Work performed under the auspices of the U.S. Department of Energy.

Manuscript Received 12-4-87/sar

Characterization of Calcium Fluoride Optical Surfaces

M. Law, J. Bender and C. K. Carniglia

Martin Marietta Astronautics Group, Laser Systems Technology
P.O. Box 9316, International Airport
Albuquerque, NM 87119

A calcium fluoride polishing study has been conducted in an effort to reduce those characteristics which contribute to optical scatter effects. Using both quantitative and qualitative diagnostic techniques, the surface and subsurface characteristics produced by various polishing procedures have been either measured or rank ordered to optimize the polishing process itself. Diagnostic techniques have included bright light illumination, surface profilometry, Nomarski microscopy, total internal reflection microscopy (TIRM), and total integrated scatter (TIS). These techniques have been applied to polished surfaces and to polished surfaces that had been etched with acid. The examination of acid-etched polished surfaces has revealed the presence of subsurface polishing damage which is concealed beneath the polished surface and is undetectable by routine observation.

Key words: acid etching; calcium fluoride; polishing; subsurface damage; surface quality.

1. Introduction

The optical properties of calcium fluoride (CaF_2) make this material a likely candidate for transmissive elements used in some short-wavelength laser systems. With such use, issues of optical scatter and damage threshold become significant. Historically, CaF_2 components have had limited use in less demanding applications, and there has been little impetus for fabricators to perfect processes beyond "standard practice" achievements.

Within the current optical industry, two polishing techniques are in wide use for CaF_2: one employs aluminum oxide powders mixed in water; the other, diamond abrasives, also mixed in water. Both techniques are compatible with pitch polishing procedures which are necessary to achieve high-precision optical surfaces. Work conducted within the Air Force Weapons Laboratory's Developmental Optics Facility (DOF) has shown that, of the two techniques, diamond abrasives consistently provide surfaces of superior optical quality. Parts are usually ground with 5-μm abrasive against a Pyrex tool, prepolished with 1-μm diamond, and then finished with ¼-μm diamond against a fresh pitch lap. Calcium fluoride components as large as 6-in by 6-in have been polished to one-eighth wave peak to valley (visible) accuracy by this technique, and a series of 1¼-in diameter parts from earlier DOF projects was evaluated as having better than a 15-Å RMS surface finish.

Calcium fluoride has a Knoop hardness of between 120 and 158 (fused silica is 461; silicon, 1150) and is comprised of a cubic crystal lattice. Thus, it may prove more susceptible than other materials to the impregnation of polishing slurry constituents. Any investigation should also explore the chemical influences initiated by polishing operations and the effect of these, if any, on the achieved damage threshold of the component.

2. Diagnostic Techniques

Several nondestructive diagnostic techniques were utilized to evaluate surfaces during the polishing process. Visual inspection using high-intensity, bright light illumination, combined with Nomarski microscopy, provides a simple and sensitive means of preliminary inspection of surface and near-surface defects. Taly-Step profilometry is useful for quantifying surface roughness down to about 10-Å peak-to-valley roughness. Total integrated scatter (TIS) measurements of

uncoated surfaces have shown good correlation with visual inspection and Talysurf results. Calculation of actual RMS values is complicated by the unknown interactions of the sample's rear surface.

Total internal reflectance microscopy (TIRM), developed by Temple [1], was investigated as a means of nondestructively identifying subsurface defects not visible by the above methods. This system is illustrated in figure 1. A 100-mW argon laser beam is used to illuminate the underside of the surface of interest at the critical angle required to produce total internal reflection. Defect sites which do not conform to the critical angle become bright scattering sites when viewed through the microscope. The two photos of figure 2 illustrate the advantages of this technique. Photo (a) is a conventional Nomarski photograph typical of a commercially polished surface; a few surface scratches are barely visible. Photo (b) is the same site using TIRM; numerous polishing scratches are obvious.

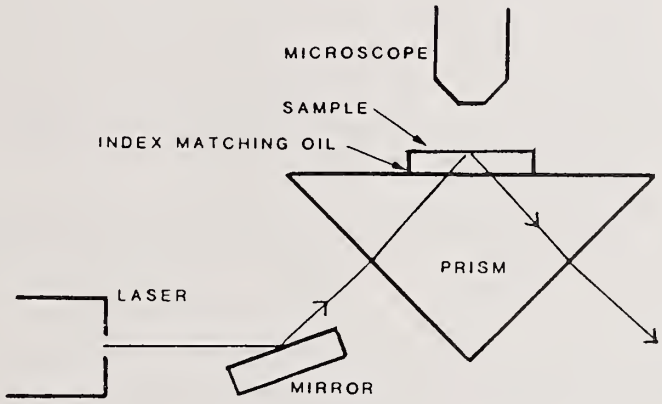

Figure 1. Total Internal Reflection Microscopy.

(a) (b)

Figure 2. Photos of Commercially Polished CaF_2 Surface:
(a) Nomarski, 200X (b) TIRM, 200X

One destructive analytical technique which was carried out as part of this study was acid etching of the surface. Measurement of sample weight loss following etching provides a simple means of comparing etch rates of several acids. A more accurate and sensitive means of determining the amount of CaF_2 removed is by measuring the quantity of dissolved calcium in the etch solution using atomic absorption spectroscopy. Ion-selective electrode analysis allows determination of calcium in-situ, while the sample is still dissolving. Scanning electron microscopy (SEM) is used in conjunction with the aforementioned nondestructive analytical techniques to evaluate the etched surfaces.

3. Subsurface Damage Study

The optical grinding process inflicts a certain amount of damage (e.g., fracturing) at or near the surface. Subsequent polishing operations polish through this damaged region. However, even when the final surface is smooth, there is the possibility that subsurface damage due to the grinding process still remains. It is well known [2] that, during the polishing of glass, a smooth "Beilby" layer is formed, resulting from plastic flow of the surface. This layer has different chemical and physical characteristics than the bulk material. Its thickness, typically 100 to 3000 Å, depends upon polishing pressure, speed and polishing compound [2]. However, below this layer, microdamage can exist within the bulk material. For example, subsurface cracks in LiF ground with alumina have been found to extend to a depth six to seven times the depth of the grinding compound furrows, which were about 4 μm deep [3].

The samples used in the present study were single-crystal, random-oriented CaF_2 discs, 5 cm diameter and 1-cm thick, manufactured by Optovac. The as-received substrates had been polished by Optovac and are henceforth referred to as "commercially polished" parts. Preliminary acid etching experiments with these commercially available, diamond-polished surfaces indicate that below a smooth surface layer is a damaged layer characterized by numerous polishing scratches. Figure 3 shows SEM photos of the relatively featureless, unetched surface (fig. 3a) and the acid-etched surface (fig. 3b) of a 5-cm diameter CaF_2 sample. Numerous polishing sleeks are exposed by the acid etch. Taly-Step results show that the peak-to-peak roughness of the etched surface is approximately four times that of the unetched surface (see fig. 4).

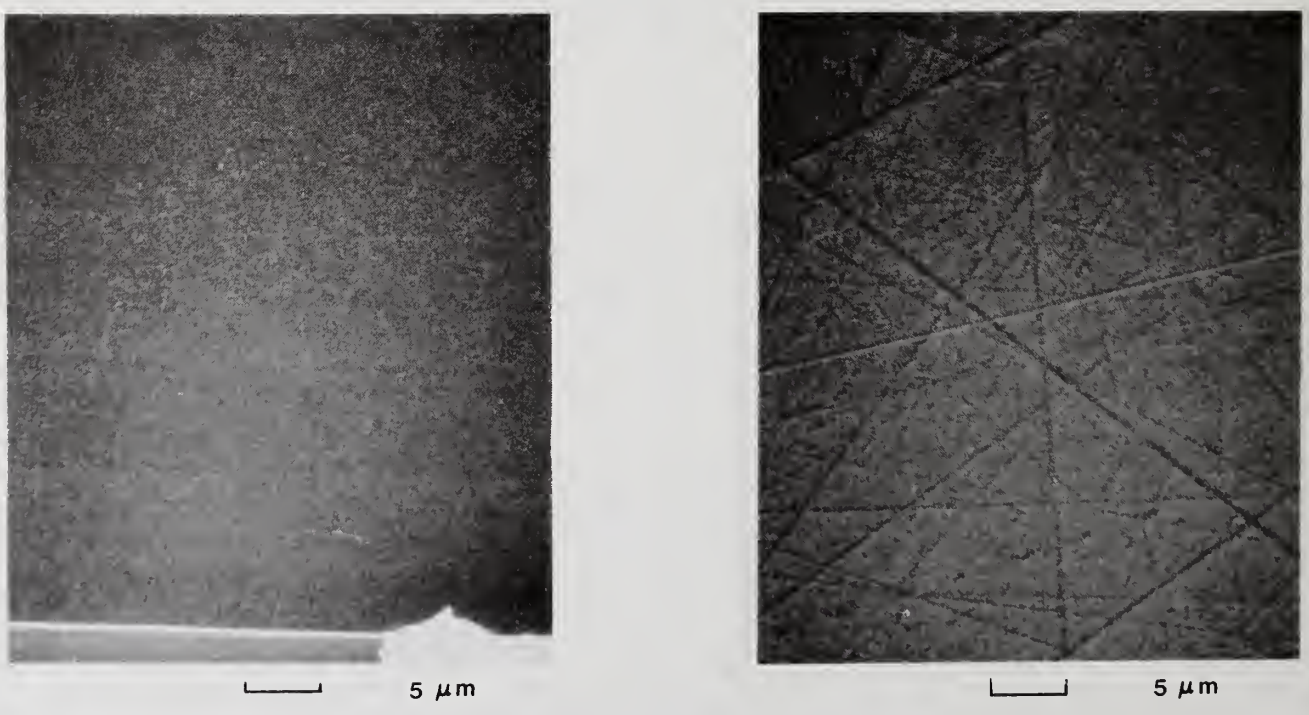

Figure 3. SEM Micrograph of Commercially Polished CaF_2 Surface Before (a) and After (b) Acid Etch.

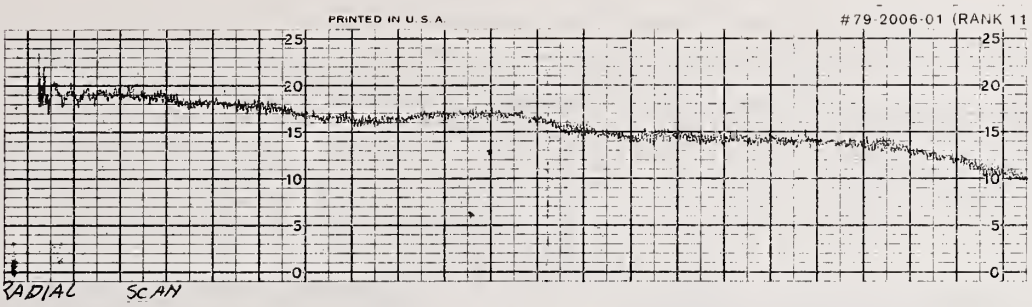

(a)

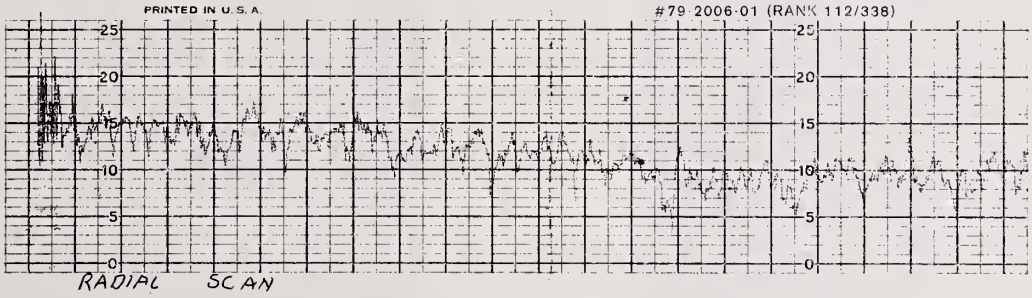

(b)

Figure 4. Taly-Step Profiles of Commercially Polished CaF_2 Surfaces Before (a) and After (b) Acid Etch. (Vertical Scale: 20 Å/Division; Horizontal Scale: 3μm/Division.)

To determine the correlation between polishing time and subsurface damage, four pairs of identically prepared parts were polished for various lengths of time. One surface of each part was fine-ground with 9-μm alumina (Microgrit WCA) and water against a preflattened, Pyrex grinding tool. The parts were then polished against a pitch lap with 0.5-μm polycrystalline diamond powder and deionized water. All polishing operations were conducted with the CaF_2 discs installed on the rotary spindle of a conventional overarm polishing machine. Spindle speed was maintained at 15 rpm, with eccentric speed at 30 rpm. Down-pressure was limited to the weight of the overarm (3.5 lb) to obtain 1.98 lb/in^2 at the surface of the 1½-in diameter polishing lap, which was composed of medium Cycad polishing pitch.

Most of the embedded grinding compound and associated pits are removed during the first eight hours of polishing. Polishing sleeks, visible with bright light inspection, indicate that there is very slow improvement as polishing time increases up to 37 hours (table 1). It should be noted that these sleeks are also visible on the rear, commercially polished surface of each part. Uncoated TIS values as a function of polishing time are shown in figure 5. Although TIS results and visual inspection show only light scratches at 6 or more hours of polishing, TIRM photos show that large numbers of subsurface scratches are still present.

Sample #7 exhibited anomalous behavior. At 22 hours of polishing, the surface showed only a few sleeks. Following an organic solvent clean, many small pits appeared. An additional 15 hours of polishing merely enlarged these pits. As a result, another fully polished sample was prepared, which had a few sleeks but no pitting at 34 hours. At 59 hours, an apparently perfect surface was achieved. TIRM analysis facilities were not available for subsurface examination of this surface.

4. Polishing Parameter Study

A study has been underway of the effects of varying polishing parameters such as polishing abrasives, pitches, speed, pressure, waxes, pH, and various slurry additives.

Table 1. Variation of Surface Quality with Polishing Time

Sample No.	Polish Time (hours)	Bright Light	Nomarski	TIRM	TIS (a)
1	2	gross haze	severe pits (10 μm), embedded grinding compound	gross pits	1260
2					1140
3	4	light haze	moderate pits, scratches (≤ 1 μm)	moderate pits and scratches	100
4		moderate scratches			280
5	6	light scratches	light pits, scratches	gross scratches	66
6					53
7	37	light scratches, many pits	many pull-out pits, scratches	(b)	31
8	37	very few scratches	no features	(b)	9
9	59+	no features	no features	(b)	3

a. TIS measurements - uncoated. Relative units $x10^4$.
b. TIRM analysis unavailable.

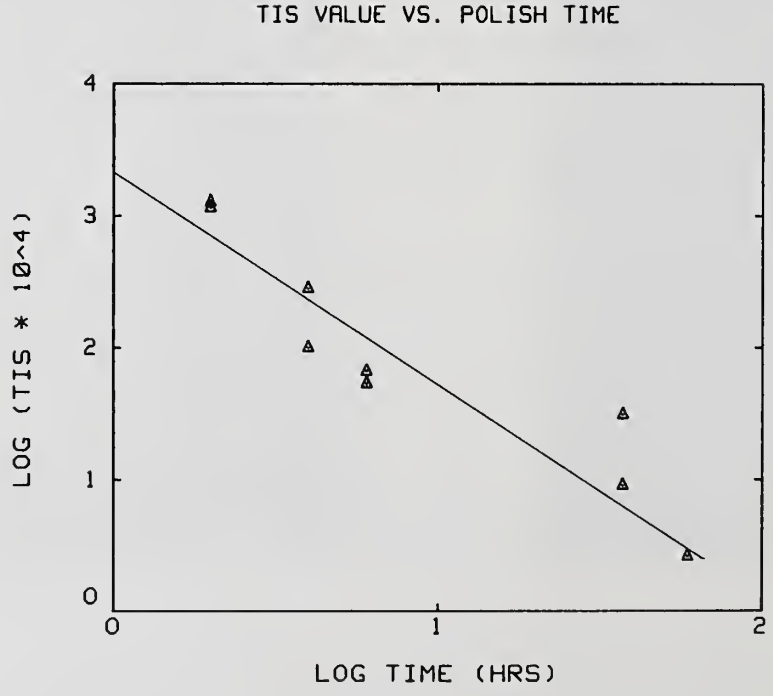

Figure 5. TIS Values as a Function of Polishing Time.

The effect of polishing with monocrystalline, rather than polycrystalline diamond was investigated. The processing time required to obtain a full polish, free of pits, varied from 8 to 37 hours with the polycrystalline diamond. Monocrystalline powders produced surfaces that were only 50 to 60 percent polished at 34 hours, with pits and scratches still visible at 84 hours. The difference in morphology between the powders is illustrated by the SEM micrographs presented in figure 6. The monocrystalline material shows greater size variation and appears more planar. According to the vendor of the powders, the polycrystalline diamond maintains sharp cutting edges as it cleaves, while the monocrystalline diamond tends to round off. This explains the failure of the monocrystalline material to produce a polished surface.

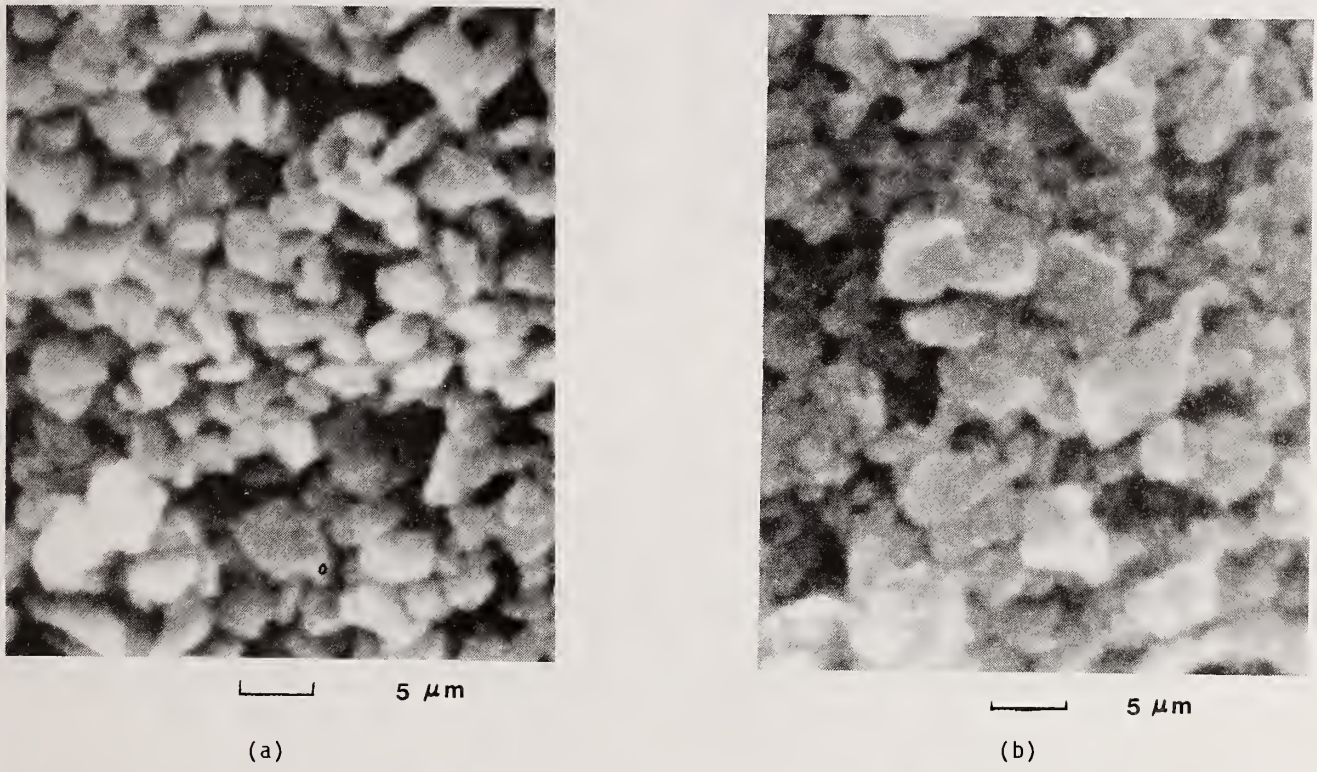

(a) (b)

Figure 6. SEM Micrograph of Diamond Polishing Compounds:
(a) Polycrystalline Diamond (20,000X)
(b) Monocrystalline Diamond (20,000X)

In an effort to reduce sleeks, one pair of samples was polished for 8 hours with 0.5-μm, 8 hours with 0.25-μm and then an additional 36 hours with 0.125-μm polycrystalline diamond. TIRM and visual inspection indicate that the resulting sleeks are finer and less dense than those on the 8-hour, 0.5-μm polished surface.

A pair of samples fully polished with 0.3-μm alumina on bare pitch laps required considerably more effort than visually equivalent surfaces produced with diamond abrasives. The major difficulty was due to a problem often encountered when pitch-polishing CaF_2 with alumina, in that fragments of the crystal are inadvertently pulled from the lattice leaving a pit or void on the optical surface. Continued polishing then abrades the boundary of the void with the result that the apparent diameter grows even larger with persistent effort until, finally, the optical surface is worn away to a level approaching the bottom of the void. Only then does the apparent dimension of the artifact begin to diminish, and it is often at this point that another void is inflicted at some new location on the surface. Common prescriptions for the prevention and cure of "pull-outs" involve thinning the slurry concentration and reducing the pressure at the polishing interface.

Our attempts to reduce these pull-outs have included the use of three types of alumina polishing compounds - 0.1-μm CR agglomerate-free, 0.3-μm CR agglomerate-free and 0.3-μm standard alumina - against Cycad, Gugolz or beeswax laps. The 0.1-μm CR alumina produced a

surface which was only 75% polished after 33 hours, with an additional 27 hours of polishing showing no improvement. Use of this alumina following a 0.3-μm polish also failed to remove pits. Although the 0.3-μm agglomerate-free alumina resulted in lower Taly-Step and TIS values compared with standard alumina, pull-out effects showed little improvement. Taly-Step measurements on the alumina-polished surfaces indicated surface roughness seven to twelve times higher than that obtained on surfaces polished with 0.125-μm diamond (fig. 7). TIRM analysis of an alumina-polished surface, compared to that of a 0.125-μm diamond-polished surface (fig. 8) shows that the alumina surface is covered with numerous scratches and profuse, finite scattering sites. Table 2 summarizes data from the most promising diamond and alumina-polished surfaces.

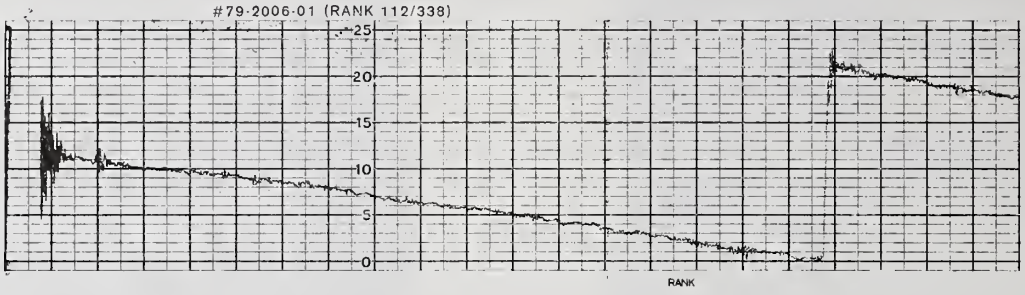

(a)

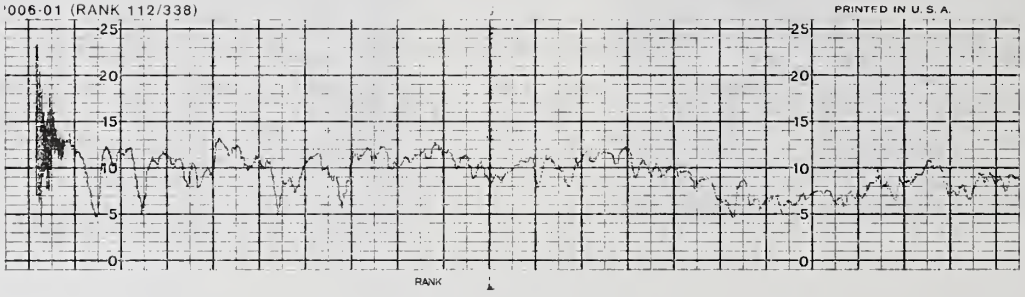

(b)

Figure 7. Taly-Step Profiles of Diamond-Polished (a) and Alumina Polished (b) CaF_2 Surfaces.

Two cerium oxide-based polishing compounds were investigated. Barnesite proved to be an inefficient polishing material, with grinding compound pits still visible after 50 hours of polishing. LRE #85 polished slowly, but more efficiently, with only shallow pits visible at 53 hours. Cerium, however, may be an undesirable surface contaminant because of its absorption at 305 nm.

Rouge (Fe_2O_3) produced a rough, pitted, scratched surface after 19 hours of polishing. Pull-outs also occurred during 25 hours of polishing with zirconium dioxide.

Nitric acid etch tests of commercially polished surfaces and of samples polished with 0.5-μm and 0.125-μm polycrystalline diamond, 0.3-μm standard alumina and LRE #85 show that subsurface scratches begin to appear at a depth of 100 Å and are more clearly defined at about 200 Å. The commercially polished surface shows the most dramatic increase in visual surface sleeks after etching. An additional portion of the surface, about 300 Å, was etched to ensure exposure of a layer further below the smooth layer. The LRE #85 showed the least surface change with etching: the only effect was deepening of existing scratches and exposure of more pits. Although diamond and alumina polish sleeks were visible by bright light after a 100-Å etch, the Taly-Step profile indicated that the surface was only slightly rougher. A significant increase in Taly-Step roughness was found after etching 300 Å. Figure 9 shows the Taly-Step profiles of the 0.125-μm polished surface before etch (a), after a 100-Å etch (b) and after a 500-Å etch (c).

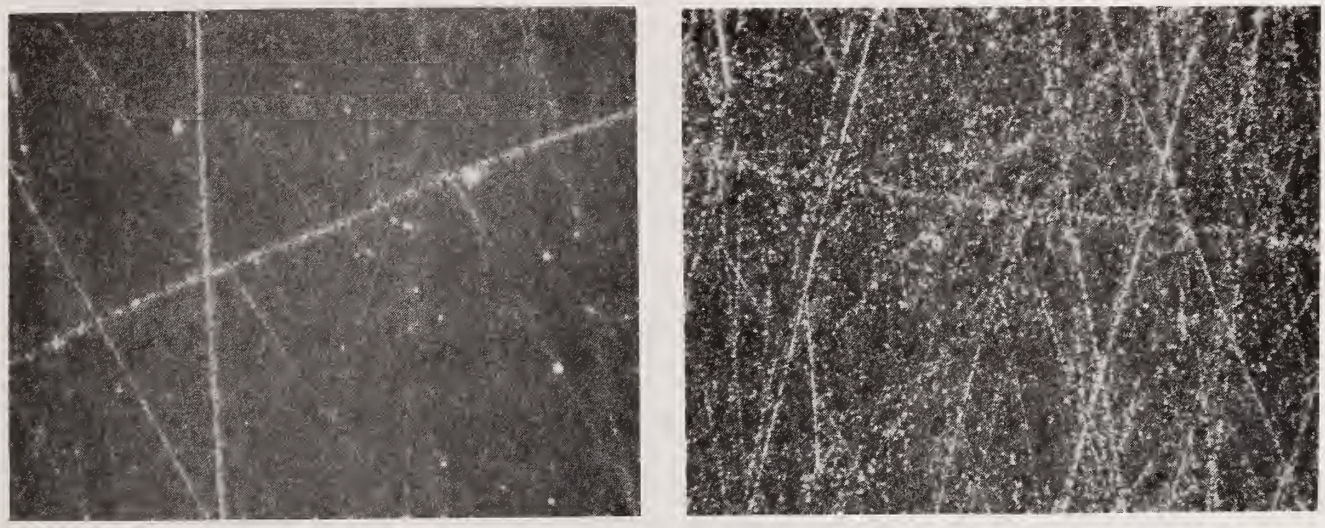

(a) (b)

Figure 8. TIRM Micrographs of Diamond-Polished (a) and Alumina-Polished (b) CaF_2 Surfaces.

Table 2. Variation of Surface Quality with Polishing Material

Polish Used	Abrasive Size (μm)	Polish Time (hours)	Bright Light	Nomarski	TIRM	TIS (a)
Polycrystalline diamond	0.5	59+	no features	no features	(b)	2.6
Polycrystalline diamond (c)	0.5	59+	very few scratches	rare scratch	(b)	5.5
Polycrystalline diamond	0.5 0.25 0.125	8 8 32	none to very faint scratches	no features	gross fine scratches	 5.5 6.1
Polycrystalline diamond	0.5 0.25 0.125	8 8 40	none to very faint scratches	no features	few to moder-- ate scratches	 10.0 12.0
Commercially polished with diamond	--	--	none to very faint scratches	no features	moderate scratches	7.9 8.5
Polycrystalline diamond followed by agglomerate free alumina	0.5 0.3	45 3	gross, fine scratches	light scratches and pull-out pits	(b)	54
Polycrystalline diamond followed by standard alumina	0.5 0.3	47 3	gross, fine scratches and pits	moderate scratches and many pull-out pits	(b)	108
Standard alumina	0.3	122	gross, fine scratches	light scratches and pull-out pits	gross fine, ragged scratches and pits	163 252

a. TIS measurements - uncoated. Relative units $x10^4$.
b. TIRM analysis unavailable.
c. Lap position reversed.

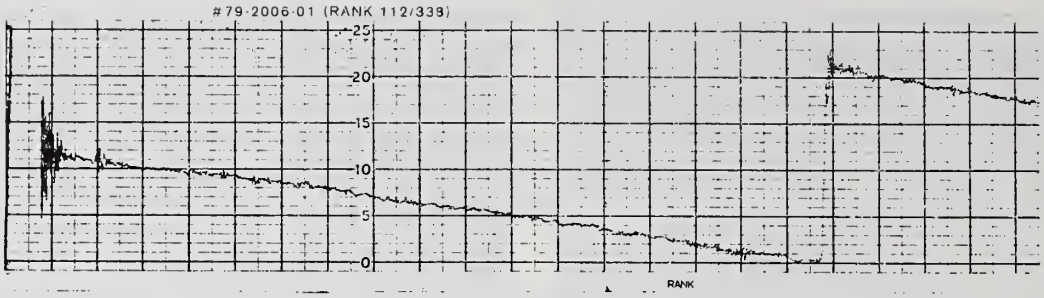

(a)

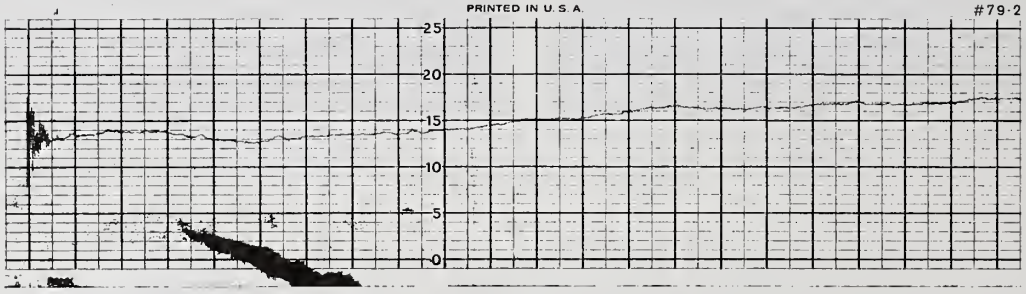

(b)

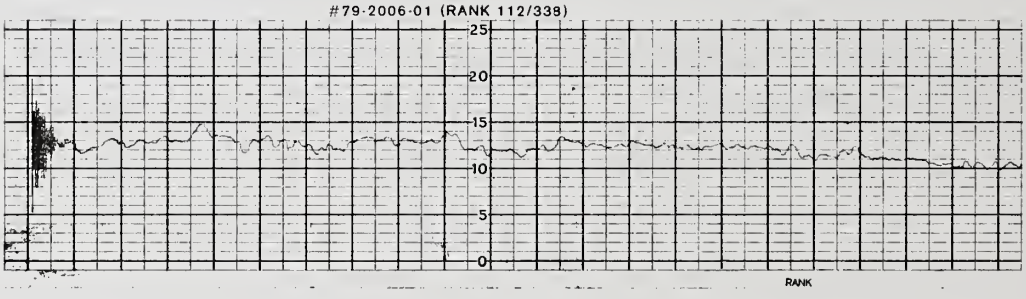

(c)

Figure 9. Taly-Step Profiles of Unetched and Acid-Etched 0.125-μm Diamond-Polished Surfaces. (a) Unetched (b) 100 Å Etch (c) 500 Å Etch

5. Conclusions

TIRM and TIS measurements of uncoated surfaces have proven to be valuable nondestructive aids in evaluating the quality of visually equivalent surfaces.

An acid etch has proven to be a useful tool for revealing subsurface damage. CaF_2, like glass, has a smooth, undamaged layer, less than 200 Å thick, covering subsurface damage. The thickness of this layer varies with the polishing parameters. Cleaning procedures which include acid etching can be expected to downgrade surface quality, depending upon how much of this smooth layer is removed. On the other hand, the use of an acid etch during the polishing process may be useful in reducing subsurface damage.

Polishing with polycrystalline diamond produces the best surface. Alumina polishing of unoriented, single-crystal CaF_2 is complicated by pull-out problems and poor surface quality due to sleeking. Cerium oxide, rouge, zirconium dioxide and monocrystalline diamond produced visually unacceptable surfaces. Further studies, described in the following section, are recommended.

6. Future Work

The next phase of this study will include TIS measurements of coated surfaces before and after etching. The correlation between coated and uncoated TIS results will be determined.

SEM elemental mapping using x-ray fluorescence will be used to determine the presence of residual grinding or polishing compound in the etched surfaces. X-ray fluorescence will also be used to determine composition and impurities in the polishing abrasives. ESCA and laser calorimetry measurements will require preparation of smaller witness samples, if they are to be included as diagnostic techniques.

The CaF_2 parts produced during the subsurface damage study have been submitted for laser damage testing. These parts, which range from intentionally underpolished to the best polish possible, will establish the correlation between degree of surface and subsurface damage and laser damage thresholds.

The study of the effect of other polishing parameters, and use of 111-oriented substrates is presently underway. Laser damage testing will be performed on the best diamond-polished and alumina-polished surfaces produced.

The authors would like to acknowledge the contributions of G. Roberts, MMAG, in polishing the CaF_2 surfaces; G. Petty, Rocketdyne, for the TIS measurements; and W. Kunzler and W. Wasson, AFWL, for the Taly-Step measurements.

This effort was sponsored by the Air Force Weapons Laboratory, Air Force Systems Command, United States Air Force, Kirtland AFB, New Mexico 87117.

7. References

[1] Temple, P.A. Total internal reflection microscopy: a surface inspection technique. Appl. Opt. 20 (15): 2656-2664; 1981 August 15.

[2] Holland, L. The properties of glass surfaces, chapter 1. New York, NY: John Wiley & Sons; 1964. 15-56.

[3] Kumanin, K. G. Generation of optical surfaces, Stoneham, MA: The Focal Press; 1962. 44.

Manuscript Received
4-10-87

An Investigation of Laser Processing of Silica Surfaces

Annetta J. Weber and Alan F. Stewart

Air Force Weapons Laboratory
Kirtland Air Force Base, New Mexico 87117

Gregory J. Exarhos

Battelle Pacific Northwest Laboratories
Richland, Washington 99352

W. Kent Stowell

Avionics Laboratory
Wright-Patterson AFB, OH 45433

An initial set of experiments has been conducted to determine the practicality of laser processing of optical substrates. In contrast to earlier work, a high average power CO_2 laser was used to flood load the entire surface of each test sample. Fused silica substrates were laser polished on both surfaces at power densities ranging from 150 to 350 W/cm^2. During each test sequence sample surface temperatures were recorded using a thermal imaging system.

Extensive pre- and post-test characterization revealed that surface roughness and scattering of bare silica surfaces were reduced while internal stress increased. Laser damage thresholds were found to increase only for certain conditions. Changes in the microstructure were observed. These preliminary experiments have demonstrated that laser processing can dramatically improve the optical properties of fused silica substrates. Optimization of processing parameters will be the subject of future work.

Key words: laser annealing; laser damage; fused silica; optical substrates

1. Introduction

Materials processing is an extremely important application of the laser. Techniques have been developed which extensively modify material surface properties so as to better fit their intended use [1,2]. Dramatic increases in hardening and the formation of alloys and metastable phases on metallic surfaces have been observed in experiments with pulsed and continuous irradiation. Extensive work has dealt with laser annealing of silicon wafers to repair structural damage caused by ion implantation. In addition, lasers have been used to polish the surfaces of fused silica and pyrex for optical applications and produce phase transformations and alloying in thin film structures [3-6].

A preliminary set of experiments designed to determine the practicality of laser processing of optical substrates using a high average power CO_2 laser is described in this paper. In contrast to earlier work in this field, the entire surface of each test sample was flood loaded with a uniform beam intensity distribution. During the irradiation sequence, sample surface temperatures were recorded using a thermal imaging system.

Before and after irradiation, samples were characterized to carefully determine changes in the material properties and optical figure. Analysis methods utilized included total integrated scatter, surface profiling, bidirectional reflectance function distribution measurements, microscopy, interferometry, Raman spectroscopy and laser damage testing.

Our data indicates that laser polishing of fused silica will require extensive additional study. Laser induced damage thresholds measured on laser polished silica surfaces were significantly improved by this treatment confirming earlier work. For moderate irradiation levels, scattering and roughness increased slightly. At higher irradiation levels, silica surface scattering and roughness were dramatically reduced.

2. Experiment

Laser polishing of fused silica has been traditionally performed using lasers producing a few hundred watts, focussing the beam to a small diameter and then either translating the sample across the beam or raster scanning the beam across the sample. In contrast, the continuous wave, 15 kilowatt CO_2 laser system shown in figure 1 was used in these experiments. Multimode operation at 10.6 microns with stable resonator optics results in a uniform circular beam profile. However, annular rings appear in the beam with a 5% modulation depth due to diffraction from the output coupler aperture.

The experimental arrangement used in these experiments is shown in figure 2. Beam power levels were monitored in real time using a sodium chloride beam splitter and a thermopile calorimeter. The system power output during a 10 second run time was stable to within 5%. Throughout these experiments absolute beam power incident on the sample was determined by first test firing the beam into a graphite block calorimeter. Plexiglas burn patterns were used to measure the beam diameter at the sample.

The availability of a multikilowatt laser system with a reasonably uniform beam profile prompted an initial matrix of experiments with the sample held stationary in the beam. Beam power was varied from 150 to 600 W/cm^2 in 50 W/cm^2 increments. The laser run time was fixed at 0.1, 1, 2 and 5 seconds.

Irradiation of stationary samples was found to have a limited feasibility. The interferogram of a sample irradiated for 2 seconds at 300 W/cm^2 appears in figure 3. The annular diffraction rings of the beam in addition to a hot spot in the center have been replicated on the surface of the sample. This initial test matrix did provide a range of intensities and beam dwell times which proved useful in subsequent testing. A total incident energy loading of 400 J/cm^2 and higher was determined to be the range which induced visible surface changes.

Subsequently, samples were translated across the beam in order to average out the effects of beam nonuniformity. As in figure 2, the beam was reflected from a 1 meter focal length mirror towards the sample. The beam diameter used to irradiate fused silica substrates was 70mm in the test plane as determined from Plexiglas burn patterns. The translation stage platform moved at a constant speed of 1.5 cm/sec. Thus the dwell time of the beam at a given point on the sample surface was 4.6 seconds. The substrates were supported by V blocks on the translation stage and the first surface was irradiated. After the samples cooled, both surfaces were cleaned a second time on a spin cleaning system using spectroscopic grade methanol and collodion. The second surface was then irradiated at the same power level.

Five incident intensity levels were used ranging from 150 to 350 W/cm^2 with 50 W/cm^2 intervals. These power levels were selected based on the results of our static tests taking into account the beam dwell time. A set of ranging shots were also taken. Inspection of test samples with a monochromatic light and reference flat revealed that surface figure began to degrade at irradiation levels above 250 W/cm^2. Higher levels were included in the test matrix to bracket the region of interest.

The sample surface temperature during each irradiation was monitored in real time using an infrared camera system [8]. A black body source as used to calibrate this imaging system with an estimated accuracy of 50 C. However, surface temperatures during the experiment frequently exceeded the dynamic range of the camera as indicated by decomposition of the silica at 1850 C. The heating rate above 600 C is nonlinear, as radiative and convective losses come into play. The sample surface during irradiation at high power became white hot and "smoked" as the silica decomposed to SiO. The camera system imaged the SiO coming off the surface of the sample but the temperature exceeded the dynamic range of the camera. The reaction temperature itself could be used as a temperature standard but the onset of the reaction could not be determined reliably. The temperature data recorded in these experiments was thus considered to be uncalibrated.

The fused silica substrates used in this study were conventionally polished Suprasil 1 fused silica. These substrates are 38.6 mm in diameter with a thickness of 9.5 mm. Both surfaces of a set of control samples were characterized using a variable angle scatterometer. While not of exceptional quality with an average BRDF level of 1.33 ± 0.52 ppm/steradian, it was determined that these substrates were of consistent quality with very uniform surfaces. TIS data on representative control samples with aluminum coatings indicated an average RMS surface roughness of 8 ± 2 Angstroms.

3. Analysis and Discussion

Previous investigations of laser polishing of fused silica had led to the observation that irradiated silica surfaces had many peculiar properties. Residual stress following the treatment resulted in extreme fragility of the surface and fracture propagation occured once the surface was disturbed. Unusual structures reminiscent of crystallization were also observed. It was expected that flood loading of the substrate surface as reported in this work would eliminate the problems associated with residual stress. However, structural or chemical changes induced in the silica by the intense heating remained to be studied. To this end, laser processed fused silica substrates were characterized using a number of analytical techniques.

3.1 Surface Quality

After irradiation with the CO_2 laser, fused silica surfaces looked and felt different to the touch. At the higher power levels, dissociation of silica occurred resulting in the deposition of white silicon monoxide on the edges of the samples. These deposits could not be removed by conventional cleaning procedures. At moderate power levels, silica surfaces had a "wet" appearance but also felt "squeaky" clean to the touch. While cleaning these substrates we noted that an o-ring used in a vacuum chuck on the spin cleaner left an indelible mark on the surface after fogging. Dust flashes were observed during irradiation of some of the substrates used in this study but did not leave residual microscopic damage.

Laser irradiated surfaces and control samples were inspected using a high contrast Nomarski microscope. Etching with hydrofluoric acid was used to evaluate residual subsurface damage. In figure 4, a control sample surface is shown before and after etching. Scratches left behind by the polishing process are clearly seen. After etching, the subsurface damage caused by polishing is very apparent. In contrast, figure 5 shows a surface which had been irradiated at 250 W/cm^2. The surface is free of scratches as was seen in the BRDF data but there are occasional cosmetic defects. Dust flashes or the explosion of a subsurface impurity could have resulted in this type of blemish.

Surface figure and transmitted wavefront quality of laser irradiated substrates were determined using a commercial interferometer system. As seen in figure 6, surfaces irradiated at levels above 250 W/cm^2 were severely distorted. At 250 W/cm^2, a few waves of curvature is induced in the surface although the transmitted wavefront quality is still reasonably good.

3.2 Bidirectional Reflectance Distribution Function (BRDF) Analysis

Before and after laser irradition, fused silica substrates were evaluated on the Variable Angle Scatterometer (VAS) at Wright-Patterson AFB. This instrument, which has been described in detail elsewhere [10], has the sensitivity to quantify bare uncoated surfaces. Representative data appears in figures 7 and 8 for the pre- and post-test characterization of a silica substrate irradiated at 250 W/cm^2. Comparison of these plots show that the overall scattering level is reduced by laser processing with the average BRDF level dropping to 6% of its original level. The rotary scans show that polishing sleeks (evidenced by symmetric deviations across the center) have disappeared after processing.

The data obtained on 17 samples using the VAS is summarized in table 2. These figures represent the average scattering level divided by the surface area scanned during the measurement. Before and after irradiation both substrate surfaces were measured at the center of the part using a 3 x 3 mm scan area. Large area scans (2 cm x 2 cm) were also performed in the post test characterization. In general, it is not possible to relate the numerical values of the two types of data because of the area factor involved.

The average values of the data listed in table 2 for first and second surfaces are plotted separately in figure 9. Control samples and the measurements before irradiation ranged from 1 to 2 ppm/Steradian. Irradiation at 150 W/cm^2 resulted in increased scatter at the 5 ppm/Steradian level. At higher power levels, the average surface scattering for front and especially back surfaces decreased to very low levels.

In earlier studies of high quality optical surfaces prepared with minimal residual polishing damage, Stowell observed that thermal cycling to 400 C resulted in a thirty-fold increase in BRDF level. It was determined that thermal cycling caused fracturing extending out of the subsurface damage layer or Beilby layer degrading these surfaces. The substrates used in this study were

conventionally polished with higher initial scattering levels and consequently a more extensive subsurface damage layer. The higher scattering levels measured on surfaces irradiated at 150 W/cm^2 are undoubtedly due to the eruption of this subsurface damage layer during the laser processing. Irradiation at higher power levels causes the fusion of this subsurface damage layer and reduced scattering levels. Laser processing does not, however, completely remove the Beilby layer. This is clearly shown in figure 9 in that first surfaces irradiated always exhibit higher scattering levels due to the additional thermal cycle they experience during treatment of the second surface. The fact that the first surface is handled more and perhaps contaminated may also contribute to the measured BRDF.

3.3 Raman Spectroscopic Analysis

Raman spectroscopy was used at Battelle Pacific Northwest Laboratories to study the structure of CO_2 laser processed fused silica. Very subtle changes were observed in the spectra of fused silica surfaces. A representative spectra for fused silica is shown in figure 10. As in all Raman spectra the observed features correlate to vibrational and rotational transitions in the material. The spectra recorded on laser irradiated fused silica surfaces exhibit subtle band shifts due to internal stress, changes in the Rayleigh scattering background, and the appearance of new features due to the formation of an unusual ring-like structure.

In Raman spectra obtained on laser irradiated fused silica, specific peaks experience band shifts of a few (2-6) cm^{-1}. These shifts correlate to stress induced changes in chemical bonding angles. Data obtained on a silica sample irradiated at 350 W/cm^2 is compared to a control sample in figure 11. These band shifts are easily measurable on this system with a resolution of 0.1 cm^{-1}. In crystalline solid, stress levels could be determined from these band shifts but the calculations are considerably more difficult in the glass phase. Bass and Xiao had predicted a compressive stress layer extending about a millimeter inside the sample surface. This was further confirmed by examination of a cross section of a ample irradiated at 250 W/cm^2 in a polariscope. As shown in figure 12, the stress layer extends 1.5 mm below the surface.

Normalized spectral peak intensities are plotted in figure 13. With the 514 nm laser line and the backscatter collecltion optics used in these experiments, the Rayleigh scattering (as measured at 375 cm^{-1}) experiences a maximum value for surfaces irradiated at 250 W/cm^2. This is a different result from that obtained on the VAS system which seemed to show a minimum scattering level for samples irradiated at this power level. TIS data which, like the 375 cm^{-1} results, should provide a direct measure of the surface does not show a minimum or maximum at 250 W/cm^2. These instruments sample different regions or volumes and hence the data may not be correlatable.

The most interesting feature of the silica spectra is the emergence of a band at 600 cm^{-1} with increasing laser power. The band originates from the formation of planar six member rings (3-SiO) [11,12]. Six member rings form whenever energy is introduced into the silica system whether it results from thermal heating, neutron irradiation or compression. The scattering geometry used in these experiments, $z(xy)\bar{z}$, should preclude observation of the ring band. Apparently, residual strain in the silica scrambles the polarization information carried in the scattered Raman light allowing this mode to be observed.

3.4 Laser Damage Testing

Laser damage testing of laser irradiated fused silica was conducted at Lawrence Livermore by Michael Staggs and at Los Alamos National Laboratory by John Jolin and Billie Mauro. Experimental conditions at the two laboratories were similar. Tests were conducted using commercial 351 nm XeF excimer laser systems operating at approximately 30 pps. The beam diameter used at Los Alamos was 580 microns. The minimum beam diameter used at the highest fluence levels at Livermore was 360 microns. Considering the similarities in equipment and technique, the differences in the data, at first, generated complete confusion.

In contrast to earlier data, which provided an incentive for this study, Los Alamos reported laser damage thresholds of 0 J/cm^2 on fused silica irradiated at 200 and 250 W/cm^2. Testing was conducted only on the first surfaces irradiated with the CO_2 laser.

Testing at Livermore was conducted on only the second surfaces irradiated. Their results showed that the damage threshold measured on the second surfaces of fused silica irradiated at levels of 200 W/cm^2 and above exceeded 20 J/cm^2. A sample irradiated at 150 W/cm^2 damaged at 13 ± 2 J/cm^2.

The results of these laser damage measurements show some correlation to the BRDF data. The low laser damage thresholds measured on the first surfaces irradiated indicate significant degradation of those surfaces as was observed in the BRDF data. However, average scattering levels of these surfaces are still lower (better) than when measured in their pristine condition. A damage threshold of 0 J/cm^2 is much lower than the 8-10 J/cm^2 measured routinely on conventionally polished fused silica. Clearly the thermal cycling of these surfaces has a much more drastic effect on laser damage thresholds than on the other optical properties.

4. Discussion and Conclusion

The data taken in the study has confirmed the results of earlier investigations. Laser treatment of fused silica surfaces can produce beneficial results. Optical figure can be preserved while surface roughness and scattering levels are reduced. Laser damage thresholds can be increased significantly. These changes occur without significant structural modifications at least as determined by Raman spectroscopy. The etching studies seem to indicate that eradication of the subsurface damage layer is responsible for these improvements. This would also confirm an earlier study which demonstrated a correlation between residual polishing damage and low laser damage thresholds [13]. However, it is likely that investigators in that study were never able to generate a completely damage free surface.

During one of our trial runs a crack appeared across the face of the test sample extending about 2 mm into the surface to the bottom of the stress layer. This substrate was used in a second test shot. The crack disappeared. The capacity of laser processing to heal macroscopic fractures was clearly demonstrated. Microscopic fractures resulting from the polishing process must be similarly affected.

Through the proper selection of irradiation levels, laser processing can induce beneficial changes in polished surfaces. Increased laser damage thresholds, reduced scattering and roughness levels have been demonstrated.

The authors gratefully acknowledge the contributions of many notable colleagues: Michael Staggs of LLNL for his relentless and thorough attempts to laser damage our test samples; Steve Foltyn, Billie Mauro and John Jolin of LANL for damage testing; W. Kunzler, W. Wasson, D. O'Shay and C. Miglionico of AFWL for their extensive support at the Weapons Laboratory.

Table 1. Talystep/Talysurf and TIS Data
on Laser Polished Fused Silica

	Profilometer Data		TIS	
	First Surface	Second Surface	First Surface	Second Surface
Control	7	7*	7.8	9.0
150 W/cm^2	7	7-10	12.6	24.7
200 W/cm^2	40	7	12.9	12.5
250 W/cm^2	10	10-15	10.0	16.8
300 W/cm^2	10 400 pk-vy	10 240 pk-vy	22.2	46.9
350 W/cm^2	660 pk-vy	7800 pk-vy	9.5	39.6

* Angstroms RMS roughness.

Table 2. BRDF Data on Laser Polished Fused Silica

	First Surface			Second Surface		
	Before	After	Las*	Before	After	Las*
Control	1.271	1.171	0.676	2.362	1.610	3.050
150 W/cm^2	1.403	5.314	6.788	1.271	11.621	1.214
	1.394	5.001	8.990	3.127	2.650	2.215
	1.776	4.066	4.685	1.672	0.739	2.113
	1.524	4.796	6.81	2.023	5.003	1.847
200 W/cm^2	2.174	0.494	1.402	2.491	0.409	1.069
	2.565	9.587	2.950	1.740	20.708	0.279
	2.114	0.712	0.685	2.431	0.201	1.418
	2.284	(0.603)**	1.679	2.220	(0.305)**	0.922
250 W/cm^2	1.023	1.046	0.665	1.924	0.072	0.112
	---	0.212	0.354	3.242	0.069	0.078
	0.768	1.258	0.663	1.165	0.061	1.505
	0.896	0.839	0.561	2.110	0.068	0.565
300 W/cm^2	1.868	---	48.17	3 182	0.044	22.56
	0.891	0.192	0.367	1.793	9.653	728.1
	3.825	0.167	0.215	2.015	0.069	0.138
	2.194	0.179	0.291	2.330	(0.056)**	250.3
350 W/cm^2	1.630	1.156	1.278	---	0.062	0.209
	1.470	0.119	14.40	2.943	0.064	0.165
	1.550	0.637	7.84		0.063	0.187

* Large Area Scan
** Average of best two values.

List of Figures

Fig. 1) AFWL high power CO_2 laser system.

2) Experimental arrangement.

3) Interferogram of 2 second static test sample at 300 W/cm^2.

4) Fused silica control sample surface as seen under Nomarski microscope before and after etching with hydrofluoric acid.

5) Fused silica substrate surface after processing at 250 W/cm^2 as seen under a Nomarski microscope before and after acid etching.

6) Silica substrate surface figure for various incident power levels.

7) Variable angle scatterometer (VAS) data showing 3 mm x 3 mm area scan and rotary scans taken at center of silica substrate surface prior to processing. Average BRDF level = 1.165 ppm/steradian.

8) VAS data obtained at the same position of the silica substrate surface after processing at 250 W/cm^2. Average BRDF level = 0.061 ppm/steradian.

9) Average VAS scattering levels obtained on silica surfaces after laser processing. Data presented are averaged values for first surfaces "o" and second surfaces "+" processed.

10) Raman spectra obtained on silica reference standard.

11) Raman spectra of control sample compared to a silica surface processed at 350 W/cm^2 showing band shifts due to induced strain.

12) Polariscope photograph of cross sectional view of silica surface irradiated at 250 W/cm^2.

13) Intensities of selected peaks normalized to the 800 cm^{-1} band intensity for various incident power levels.

5. References

[1] See for example:
"Laser and Electron-Beam Solid Interaction and Materials Processing": Gibbons, J.F.; Hess, L.D.; Sigmon, T.W. (editors)
Proceedings of the Materials Research Soc. Ann. Meeting, Boston MA, Nov 1980
"Laser and Electron-Beam Interactions with Solids: Appleton, B.R.; Celler, G.K. (editors)
Proc. of the MRC Soc. Ann. Meeting, Boston MA, Nov 1981
"Laser-Solid Interactions and Transient Thermal Processing of Materials": Narayan, J.; Brown, W.L.; Lemons, R.A. (editors)
Proc. of the MRC Soc. Ann. Meeting, Boston MA, Nov 1982

[2] Gnanamuthu, D.S., Opt. Engr Vol 19,5 pp 783-792 (1980)

[3] Temple, P.A.; Milam, D; Lowdermilk, W.H., Nat. Bur. Stand. (U.S.) Spec. Publ. 568; 1980 pp 229-236.

[4] Temple, P.A.; Soileau, M.J., Nat. Bur. Stand. (U.S.) 620; 1981 pp. 180-188.

[5] Temple, P.A.; Lowdermilk, W.H.; Milam, D., Appl Opt. 21, 3249-3255 (1982).

[6] Xiao, Y.M.; Bass, Michael, Appl. Opt. 22, 2922-2936 (1983)

[7] "A 15kW Electric Discharge Coaxial Laser: Air Force Weapons Laboratory Technical Report 76-115, (August 1976)

[8] Model 525, InFrametrics, Bedford MA 01730

[9] Gallant, D.J.; Stewart, A.F., Nat. Bur. Stand. (U.S.) Spec. Publ. 727, 1984, pp. 272-280.

[10] Orazio, Fred D.; Stowell, W. Kent; Silva, Robert M., Proc. Soc. Phot. Opt. Inst. Eng. 362, 165 (1982).

[11] Garofalini, S.H., J. Chem. Phys. 78, 2069 (1983).

[12] Walrafen, G.E.; Hokmabadi, M.S.; Holmes, N.C.; Nellis, W.J.; Henning, S., J. Chem. Phys. 82, 2472 (1985)

[13] House, R.A.; Bettis, J.R.; Guenther, A.H.; Austin, R., Nat. Bur. Stand. (U.S.) Spec. Publ. 435, 305 (1975).

Figure 1.

EXPERIMENTAL ARRANGEMENT FOR LASER POLISHING/ANNEALING STUDIES

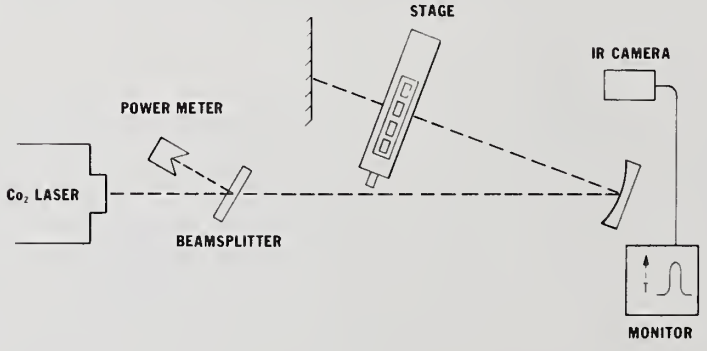

Figure 2.

Figure 3.

Figure 4.

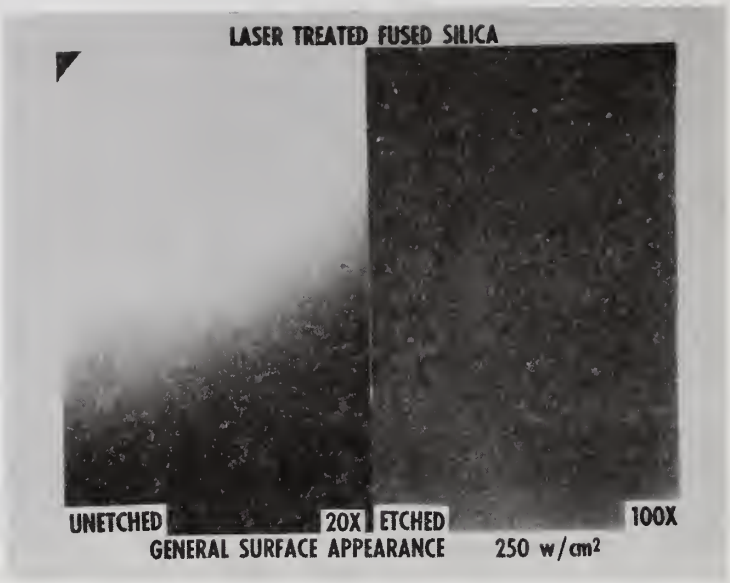

Figure 5.

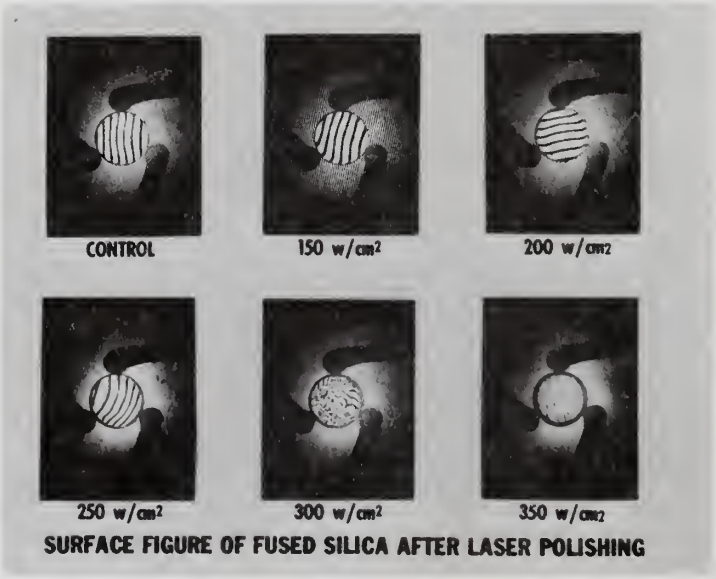

Figure 6.

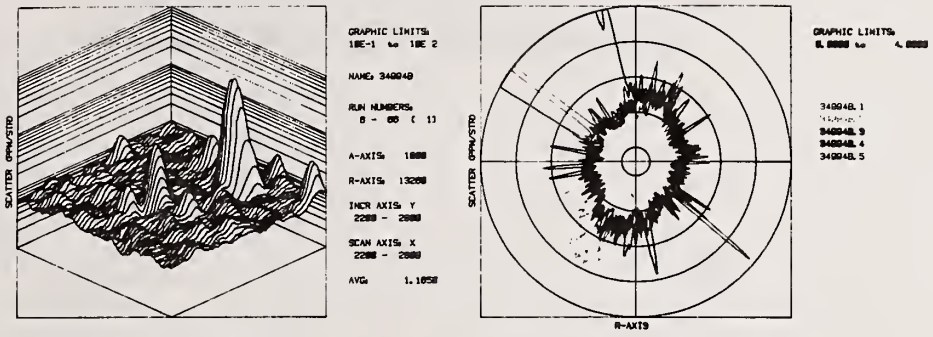

VAS DATA PRIOR TO IRRADIATION

AVG SCATTERING LEVEL = 1.165 PPM/STR

Figure 7.

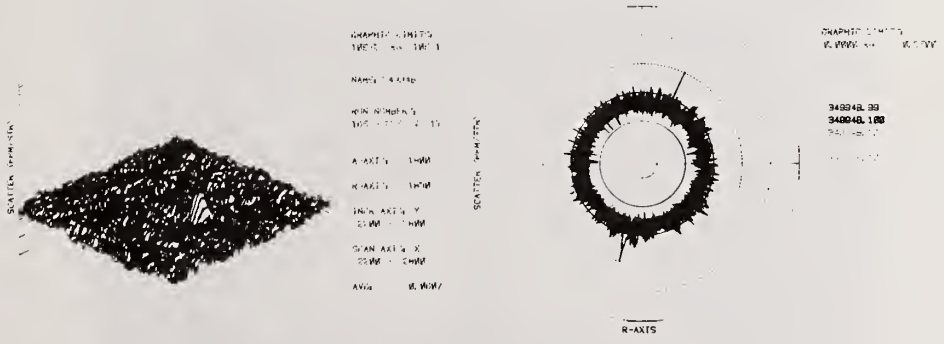

VAS DATA AFTER PROCESSING AT 250 w/cm²

AVG SCATTERING LEVEL = 0.061 PPM/STR

Figure 8.

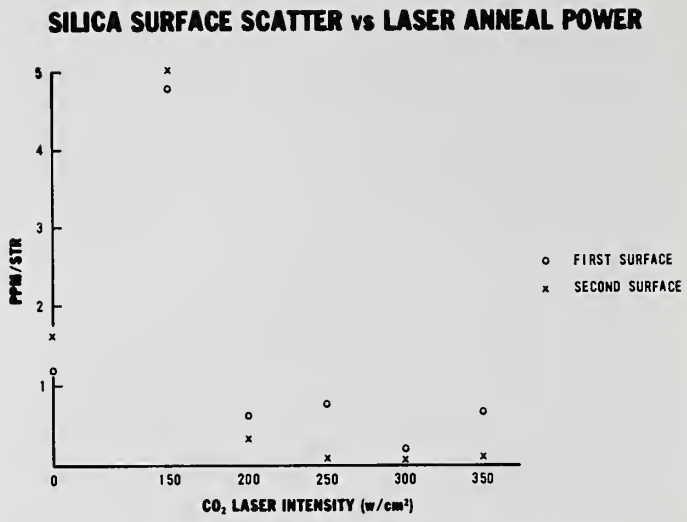

Figure 9.

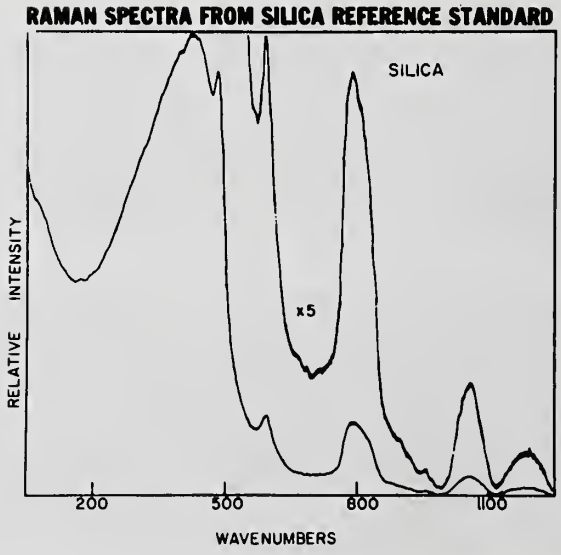

Figure 10.

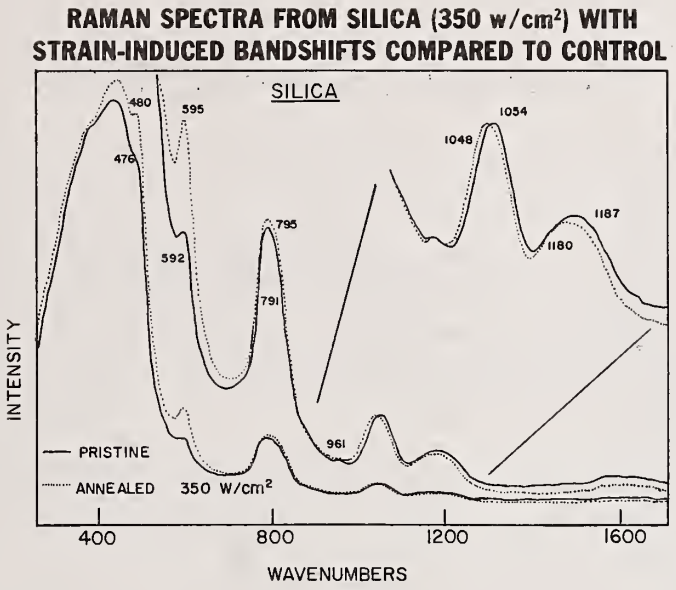

Figure 11.

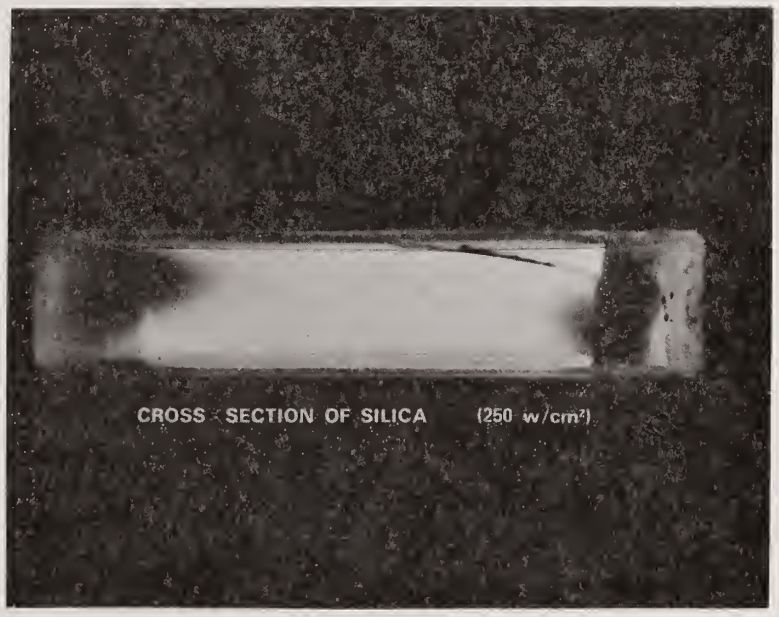

Figure 12.

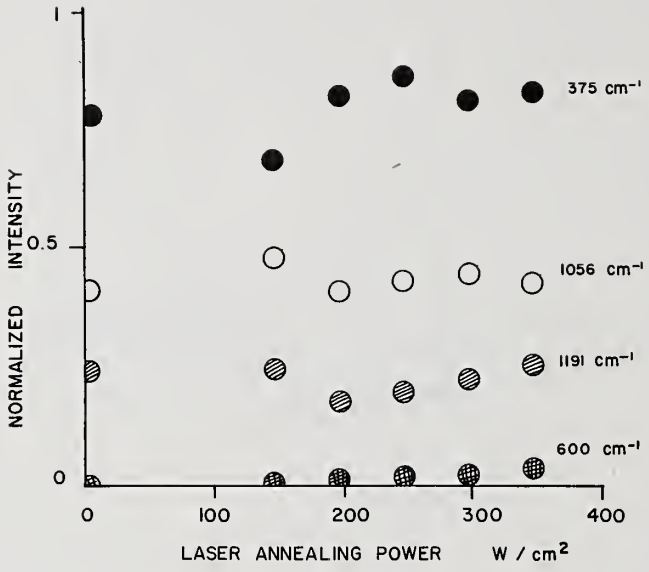
NORMALIZED INTENSITY
1
0.5
0
0
100
200
300
400
LASER ANNEALING POWER W / cm²
375 cm⁻¹
1056 cm⁻¹
1191 cm⁻¹
600 cm⁻¹

Figure 13.

Manuscript Received
3-12-87

SPOT SIZE DEPENDENT LASER MATERIALS INTERACTIONS DUE TO SURFACE ELECTROMAGNETIC WAVES

R. T. Swimm, M. Bass, L. Fathe, J. Z. Lin, and R. Kurtz

Center for Laser Studies
University of Southern California, Los Angeles, Ca 90089-1112

Measurements of the transient reflectivity change due to heating by a surface electromagnetic wave are reported. Initial results are inconclusive with regard to the existence of surface electromagnetic waves. Implications concerning the effects upon the laser-induced damage threshold are discussed.

Key words: laser induced damage threshold; optical absorption; periodic structure; photothermal; reflectivity; ripples; SEW; surface electromagnetic wave.

1. Introduction

The purpose of our reserach is to directly detect the surface electromagetic wave (SEW) that has been postulated [1] to be responsible for the generation of ripples. These ripples are often seen on the surface of materials that have been irradiated and melted by laser light. The detection scheme is to measure the temperature rise induced by the SEW at a point remote from the laser-irradiated site. The motivation of this work is that the SEW may be important in modelling laser damage, but that to our knowledge, no direct detection of the SEW itself in laser damage events has been reported.

The detection method used is a modification of the technique reported by Swimm in another paper in the proceedings. The method is based on the fact that the reflectivity of a surface depends on the temperature of that surface [2]. Consequently, a transient rise in the surface temperature due to heating by the SEW will result in a transient change in the reflectivity. The effect is quite weak, but as will be discussed, we can presently detect a reflectivity change of a about one tenth of a percent, and we expect to attain some additional sensitivity. This capability will allow direct detection of heating by the SEW, rather than having to rely on the morphological remnant ripples for evidence.

2. Experiment

The pump laser consisted of a Molectron MY-32 10 Hz repetition rate Q-switched Nd:YAG laser running in single axial mode, operating at a wavelength of 1.06 μm. The beam from this laser was focused onto a diamond-turned aluminum sample, within a spot diameter of about 200 μm. The pump-beam pulse energy was about 1 mJ incident on the sample, with the pulse length equal to approximately 20 ns. This energy was selected by trial and error to produce ripples. The probe laser was a Spectra Physics model 106-1 10 mW polarized HeNe laser. The pump beam spot diameter was about 200 μm, and the displacement between the centers of the pump probe spots was about 400 μm. The probe spot was displaced relative to the pump spot in a direction parallel to the pump beam polarization.

The basis for operation of the experiment is that during the pump pulse, the postulated surface electromagnetic wave would be radiated along the surface, illuminating a strip of width equal to the pump beam diameter, with reciprocal absorption length as predicted in the paper by Ursu et. al.[1], and oriented to parallel to the pump beam polarization. This surface electromagnetic wave would result in a change in the surface reflectivity, which would be detected using a probe beam. The probe beam samples a remote point away from the pump spot in order that any heating will be due to the postulated surface electromagnetic wave.

The probe beam was collected using a convergent lens, and then passed through a series of filters which included a rejection filter to remove 1.06 μm wavelength scattered light, a narrow-line bandpass filter of 5 nm linewidth to reduce visible emission from the plasma initiated by the pump beam, and finally through a 100 μm diameter spatial filter to remove the residual light from the plasma that was within the bandwidth of the narrow line bandpass filter. This later filter was crucial to the measurement.

The probe beam was detected by a silicon detector, whose output signal was amplified by a PARC model 115 preamplifier with a gain of 100 before being routed to an oscilloscope and a PARC model 162/165 boxcar averager. The sampling duration on the boxcar was set at 5 ns, and delayed by 70 ns relative to the laser pulse. The signal was averaged for about 20 seconds (a total of 200 pulses), and the baseline was also averaged on alternate pulses, also for 20 seconds, resulting in a measurement duration of 40 seconds.

In the process of experimental development, a large signal was observed, due to the surface acoustic wave generated by the pump pulse. This signal resulted from beam deflection due to sample surface deformation as the surface acoustic wave propagated through the probe site, and was seen whenever the pump beam was partially obstructed or apertured. The signal due to the surface acoustic wave was avoided by setting the boxcar aperture delay such that the signal was sampled after the pump pulse ended, but before the surface acoustic wave arrived.

An additional effect that had to be avoided was obstruction of the surface by the buildup of a white powder deposited on the surface in the vicinity of the pump spot during irradiation. The reflected power was compared before and after the 40 second beam exposure to ensure that no significant change in the steady state surface reflectivity occurred.

Following the initial setup work a total of nine sites were irradiated for the reported data. After normalizing the signal to account for pump power variations, the transient relative reflectivity change was determined to be 8×10^{-4}, with a standard deviation of 3×10^{-4}.

3. Discussion

In order to place these results into the proper context, it is necessary to consider the expected signal strength under various experimental conditions. The first step is to assume that the Soviet prediction for the absorption coefficient of the postulated surface electromagnetic wave is correct. Therefore one has [1]

$$\alpha_{diss} = \frac{\pi}{8\lambda} A_0^2 \frac{\kappa}{n}$$

where

$$A_0 = \frac{4n}{n^2 + \kappa^2}$$

where n = refractive index, κ = extinction coefficient, λ = wavelength, and α_{diss} is the dissipative component of the SEW absorption coefficient. Clearly the values of n and κ to be used must be appropriate to the experimental conditions, and in particular they must correspond to the temperature and phase of the irradiated site during the irradiation. Unfortunately, the optical constants of molten metals are not generally available, and so estimates of n and κ are uncertain at best. Scaling room temperature data on the basis of temperature alone is not a reliable method of predicting optical constants for the molten phase. Alternatively, it might be possible to scale according to the electrical conductivity of the room temperature solid, and the molten phase of the same material. This may be accomplished using the following two relations:

$$\alpha_{bulk} = \frac{4\pi}{\lambda} \sqrt{\frac{\mu\sigma}{\nu}}$$

where λ = free space wavelength, μ = relative permeability, ν = frequency of the electromagnetic wave, σ = electrical conductivity, and α_{bulk} = absorption coefficient for an electromagnetic wave propagating through the bulk of the conductor [2]. This expression is subject to the condition

$$\frac{\sigma}{\nu} >> \varepsilon$$

where ε = relative permitivity.

The other expression needed here is [3]:

$$\alpha_{bulk} = \frac{4\pi\kappa}{\lambda}$$

Eliminating the bulk absorption coefficient from these two relations, it follows that

$$\kappa = \sqrt{\frac{\mu\sigma}{\nu}} \text{ if } \frac{\sigma}{\nu} >> \varepsilon$$

The conductivity and the extinction coefficient are strong functions of temperature [4] e.g.,

$$\sigma_{lattice} \propto \frac{1}{T} \text{ (solid phase only)}$$

but the refractive index is a relatively weak function of temperature by comparison.

A rough estimate of α_{diss} for molten aluminum can be made using the fact that [5]

$$\frac{\rho_{\text{molten Al}}}{\rho_{\text{solid Al(20°C)}}} \simeq 7.8$$

where ρ = electrical resistivity = $1/\sigma$. By interpolation of room temperature values of n and κ[6] one finds using the Soviet expression for α_{diss} that for aluminum at a wavelength of 1.06 μm,

$$\alpha_{diss}\Big|_{T = 20°C} \simeq 120 \text{ cm}^{-1} .$$

If this number is scaled using electrical conductivity, then one finds (ignoring temperature dependence of n):

$$\alpha_{diss}\Big|_{\substack{T = 670° \\ \text{Liquid Al}}} \simeq 3 \times 10^3 \text{ cm}^{-1} .$$

From these estimates, one may conclude that the surface electromagnetic wave would propagate only a few microns in the melt region. Thus at wavelengths of m or shorter there will not be significant redistribution of energy outside the laser spot except the for rare case of micron-size spots. It is only at longer wavelengths such as 10μ where energy distribution and resultant spot-size dependence of laser-induced damage threshold can be expected.

Finally, in the context of the present experiment, the surface electromagnetic wave is not expected to have reached the probe site as originally assumed. Therefore the present measurements are inconclusive. However, on the basis of experience gained in this work, we believe that under appropriately chosen operating conditions it should be possible to test the existence of surface electromagnetic waves by their surface heating signature.

4. Summary

The present experiments designed to directly detect the presence of surface electrol-magnetic waves are inconclusive. Surface electromagnetic waves are predicted to propagate only a few microns in molten aluminum at a wavelength of 1 μm, thus precluding significant energy redistribution. Additional experiments to detect surface electromagentic waves by their surface-heating signature are under consideration.

5. References

[1] Ursu, I., Mihailescu, I. N., Prokhorov, A. M., Konov, V. I., and Tokarev, Physica 132c, 395 (1985).

[2] Born, M., and Wolf, E., Principles of Optics, Pergamon Press, 4th ed., sec. 13. 1, p. 614 1970).

[3] Wooten, F., Optical Properties of Solids, Academic Press, 2.7, p. 28 (1970).

[4] Ziman, J. M., Principles of the Theory of Solids, sec. 7.5, p. 221 (1972).

[5] Howard W. Sams and Co., Inc., Reference Data for Radio Engineers, 5th ed., p. 4-21 (1968).

[6] Gray, Dwight, E., Ed., AIP Handbook, 3rd ed., p. 6-125 (1972).

Manuscript Received
10/26/87

Super-Polished Single Crystal Molybdenum Mirror for XUV ∿ X-Ray Radiation

K. Yoshida, K. Takeuchi, Y. Kato, E. Fujiwara and C. Yamanaka

Institute of Laser Engineering, Osaka University
Suita, Osaka 565, Japan

and
K. Yamashita
Faculty of Science, Osaka University
Toyonaka, Osaka 560, Japan

and
K. Kurosawa and W. Sasaki
College of Engineering, University of Osaka Prefecture
Sakai, Osaka 591, Japan

and
K. Uehara
Faculty of Engineering, Tohoku University
Sendai, Miyagi 980, Japan

and
H. Okamoto
Central Research Laboratory, Nippon Mining Co.
Toda, Saitama 335, Japan

High quality single crystal molybdenum (Mo) fabricated by secondary recrystallization method has been polished with a new polishing technique. The super-polished surface of the Mo single crystal has the surface roughness of 3.5Å rms. THis super-polished single crystal Mo has been used for a high power electron-beam pumped argon excimer laser (λ=126nm) as a cavity mirror. Peak output power of more than 3MW has been achieved without any damage on the mirror surface for the first time.

Key words: super-polished single crystal Mo, electron-beam pumped argon excimer laser, surface roughness, laser damage.

1. Introduction

We have been developing electron-beam pumped high power vacuum-ultraviolet (VUV) lasers [1]. The maximum output power of this laser is limited mainly by the laser damage of the cavity mirrors. Aluminium (Al), silicon (Si) and fused silica have been the materials of special interest as the VUV laser mirrors because of their high reflectivities as shown in Table 1. However, these reflectors are damaged by high power VUV laser radiation at the output power of a few MW.

Mo has high reflectivity at VUV wavelength region. So far, Mo has been used for high power CO_2 lasers [2,3] because it has high reflectivity at the infrared, good thermal conductivity and strong mechanical surface hardness. The standard Mo mirrors produced by the sintering method and the electron-beam melting method have many voids and grain boundaries on the surface. Since the

surface roughness of the standard Mo mirrors is larger than 120Å (peak-to-valley value), they are not suitable for VUV lasers due to high scattering loss.

Table 1. Reflectivity of various materials at the wavelength of 126 nm.

Materials	Reflectivity (%)	
	Calculated Value [9]	Measured Value [8]
Al	93	70
Si	66	42
SiO_2	15	15
Mo	29	27

2. Single Crystal Mo

High quality single crystal Mo is considered to be one of the most attractive candidates as the VUV laser mirror because of high melting temperature and lower scattering loss. Strain annealing method [4] or zone melting method [5] have been used for preparing single crystal of refractory metals. However, sizes and shapes of the single crystals produced by these methods are limited. Recently, secondary recrystallization method has been developed [6]. The single crystal Mo metal fabricated by this recrystallization method can have various sizes and shapes such as plates, parabolas and cylinders. Maximum preparing capability at present is 250mm square and 10mm thickness.

3. Surface Evaluation of Super-Polished Single Crystal Mo

It is very important to obtain super-polished surfaces for high power VUV laser mirrors. The surface of the single crystal Mo of 25mm in diameter fabricated by the secondary recrystallization method was lapped and polished by the conventional optical polishing machine. At first, Mo substrate was lapped on the cast iron plate with 10μm Al_2O_3 powder in water. Then the final polishing was done with a specially prepared lapping plate with 0.1μm Al_2O_3 powder in water.

The surface roughness of the Mo mirror was evaluated by two independent measurements. First, it was measured with a Digital Optical Profilometer NCP-1000M (Wyko Corp.) which has a vertical height resolution of 1Å [7]. The measured surface roughness was 3.5Årms as shown in Fig. 1. Second, the surface roughness was measured with the X-ray scattering method. The scattering level α is given by

$$\alpha = \left(\frac{4\pi\sigma\theta}{\lambda} \right)^2 \qquad (1)$$

Where θ is the incident angle, and λ is the X-ray wavelength . In this method, the surface roughness σ is obtained by measuring α. Experimental result of the surface roughness due to the X-ray scattering method for the incident angle of 1° is shown in Fig. 2. The AL-Kα line (λ=8.34Å)

was used for this measurement. The dotted line and the solid line show the angular dependence of the incident and reflected X-ray intensities, respectively. The surface roughness was calculated to be $\sim 3\text{Å}$rms. This value is in good agreement with the result by the Digital Optical Profilometer.

The refectivity of the super-polished single crystal Mo mirror was measured with the synchrotron radiation from the 2.5 GeV electron storage ring at the Photon Factory, National Laboratory for High Energy Physics at Tsukuba, Japan [8]. The radiation from the SOR was monochormatized with a 1m Seya-Namioka monochromator of vertical dispersion type. Reflectance spectra were measured over the photon energies of 10eV to 40eV at an incident angel of 20°. The measured reflectance spectrum is shown by the solid line in Fig. 3. The dashed line in this figure shows the reflectivity measured by Weaver et al. [9] with an electron-beam melted Mo button. As can be seen in Fig. 3, their measurement shows slightly higher reflectivity than our measured value over the whole spectral range. This may be ascribed to the fact they have measured the reflectivity by using a small X-ray beam. It should be noted that the reflectivity of the single crystal Mo mirror is about 27% at the argon (Ar) excimer laser wavelength of 126nm and keeps high value of 20% at the wavelength of 60nm. By these experimental results, we may expect that the super-polished single crystal Mo mirror is useful as the high reflectance mirror for high power VUV lasers.

4. Laser Damage Threshold of Mo Mirror

We have tested Mo mirror as a high reflectance cavity mirror for an electron-beam pumped high power Ar excimer laser [10]. A MgF_2 window having transmittance of 70% at 126nm was used as an output mirror. The experimental setup of the Ar excimer laser and the laser output measurements are shown in Fig. 4. The output energy and the pulse waveform were measured with a pyroelectric joulemeter (Gen-Tec, Model ED-2000) and a fast biplanar phototube (HTV R1328U-04), respectively. The output energy of 21 mJ was obtained without any damage on the Mo mirror surface at the Ar gas pressure of 4 MPa. The pulse width and the peak power were 7 ns and 3 MW, rspectively. In this case, the energy density and the intensity on the mirror surface correspond to 270 mJ/cm^2 and 40 MW/cm^2, respectively. The highest laser energy density limited by the mirror damage with the conventional cavity mirror combination (MgF_2-fused silica mirrors) was 190 mJ/cm^2. It has been thus demonstrated that the Mo mirror has higher damage threshold for high power VUV laser radiation.

In summary, we have developed a super-polished single crystal Mo mirror with the surface roughness of approximately 3Årms. The laser damage threshold of the Mo mirror was found to be higher than 270 mJ/cm^2 at the wavelength of 126 nm. This super-polished single crystal Mo is expected to be also very useful as the grazing incident mirror and the substrate for multilayered coatings for intense XUV and X-ray radiations.

Acknowledgement

The authors thank Prof. S. Sato (University of Tsukuba) for his support to the reflectivity measurement of the Mo mirrors.

References

1. Y. Uehara, W. Sasaki, S. Saito, E. Fujiwara, Y. Kato, M. Yamanaka, K. Tsuchida, and J. Fujita, Opt. Lett. 9, 539 (1984).

2. S. W. Wong, G. Krauss, and J. M. Bennett, Laser Induced Damage in Optical Materials, A. J. Glass and A. H. Guenther, Eds., Natl. Bur. Stand. U. S. Spec. Publ. 435, 132 (1987).

3. Y. Ichikawa, K. Yoshida, Y. Tsunawaki, M. Yamanaka, T. Yamanaka, C. Yamanaka, H. Okamoto, N. Matsusue, and K. Kitajima, Appl. Opt. 26, 3671 (1987).

4. N. K. Chen, R. Maddin, and R. B. Pond, J. Metals 46, 461 (1951).

5. W. R. Witzke, Proc. 1st Symposium on Electron-Beam Melting, Alloyed Research Corp., Watertown, MA, 73 (1959).

6. Y. Hiraoka, T. Fujii, T. Kainuma, M. Okada, and R. Watanabe, Proceeding of a Symposium on Physical Metallurgy and Technology of Molybdenum and Its Alloys, 81 (1985).

7. Wyko Corp. Catalog, "Quantitative Micro-Surface Measurement Systems."

8. S. Sato, Y. Miyahara, T. Koide, T. Shidara, H. Kato, T. Komatsubara, Y. Onuki, K. Naito, H. Fukutani, M. Niwano, A. Fujimori, M. Yanagihara, S. Suzuki, and T. Ishii, J. Magn. Magn. Mater. 52, 190 (1985).

9. J. H. Weaver, D. W. Lynch, and C. G. Olson, Phys. Rev. B 10, 501 (1973).

10. K. Yoshida, K. Takeuchi, Y. Kato, E. Fujiwara, K. Yamashita, K. Kurosawa, W. Sasaki, Y. Uehara, and H. Okamoto, Eighteenth Annual Symposium on Optical Materials for High Power Lasers, Boulder, 65 (1986).

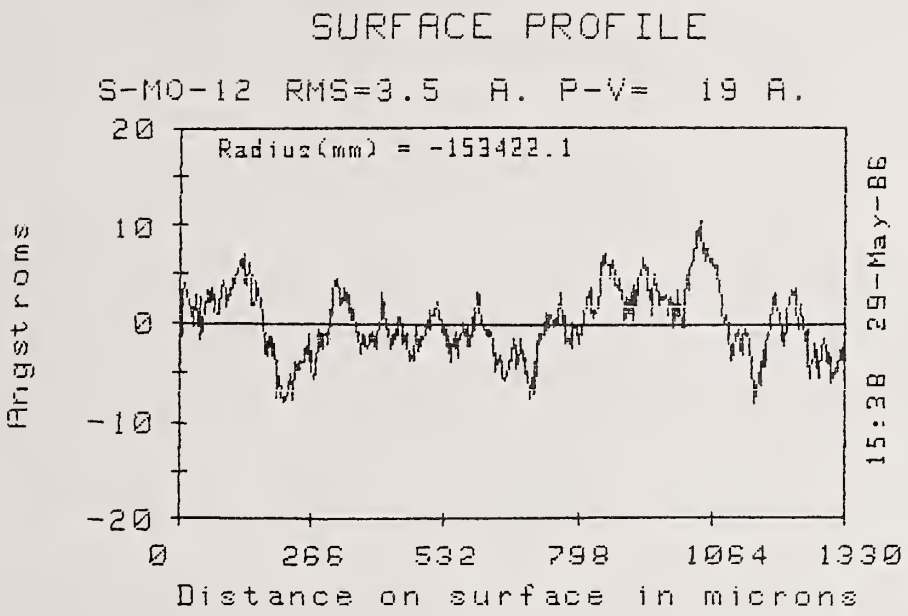

Fig.1 Surface roughness of the super-polished single crystal Mo mirror.

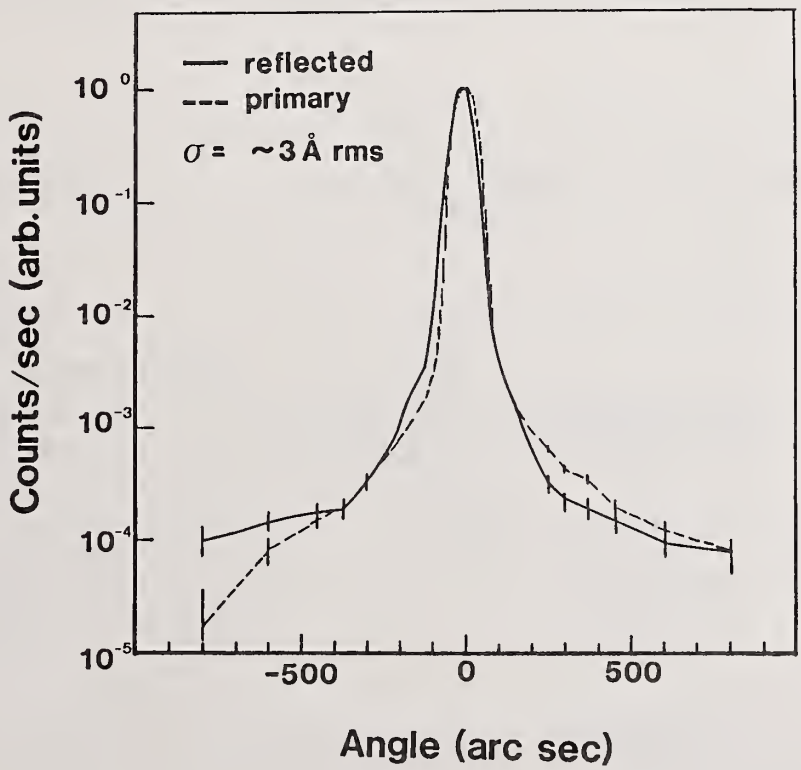

Fig.2 X-ray scattering property of a super-polished single crystal Mo mirror. Number of photon counts us scattering angle measured at the grazing incident angle of 1°. The dotted line and the solid line show the incident and the reflected X-ray intensities, respectively.

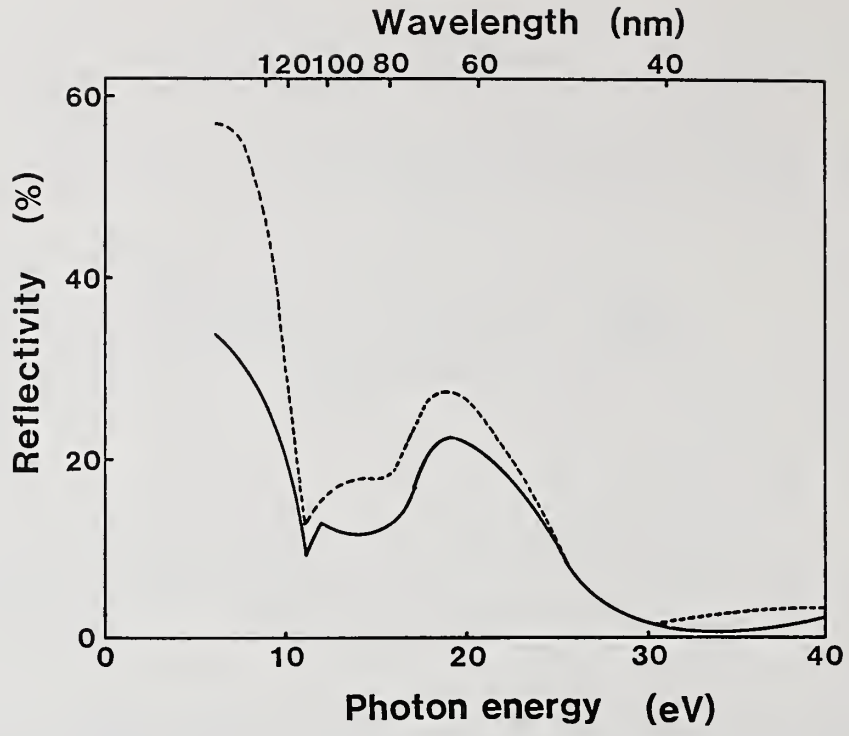

Fig.3 Reflectivity vs photon energy and wavelength for a Mo mirror. The solid line shows the measured reflectivity of the single crystal Mo mirror. The dashed line is the data after Weaver et al. [9].

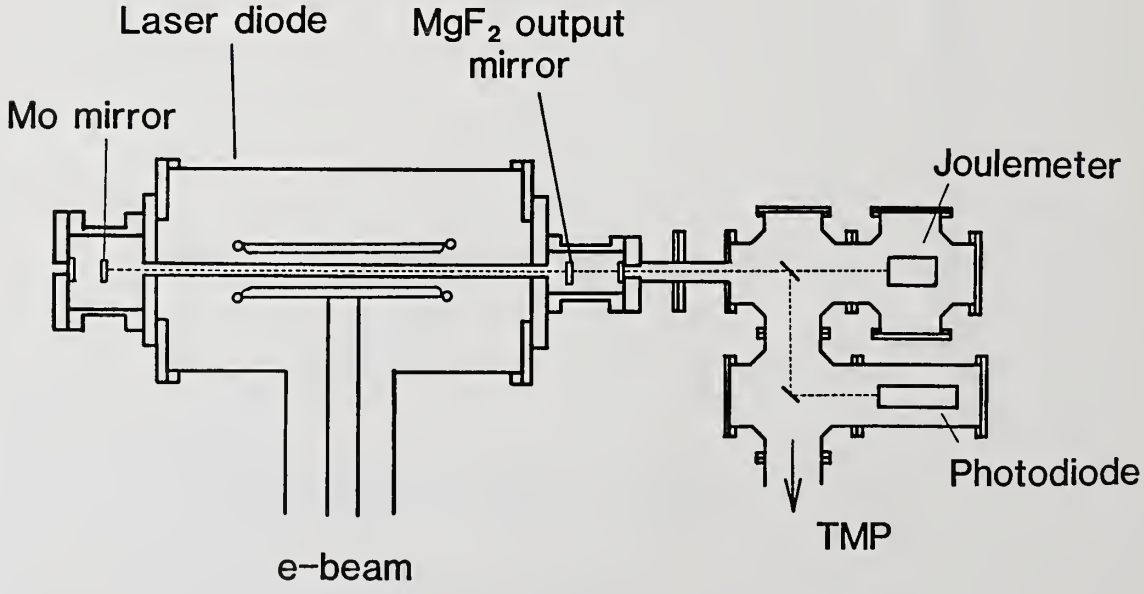

Fig.4 Experimental setup of the argon excimer laser and the laser output measurements.

Manuscript Received
11-6-86

Effect of Diamond Machining on Laser Damage Threshold of Germanium

K. L. Lewis, L. Charlwood, N. G. Chew, A. G. Cullis, O. D. Dosser
and A. Mannion*

Royal Signals and Radar Establishment
Malvern, Worcestershire WR14 3PS, England

A study has been carried out of the various factors influencing the laser damage thresholds of diamond machined Ge components. Planar surfaces were generated using both Pneumo Precision and Bryant Symons machines in both centre turned and fly-cut configurations. Laser damage thresholds were correlated not so much with the surface relief produced by the machining process but with the degree of pitting of the surface caused by excessive cutting rates and the extent of subsurface damage induced by the DM technique. Although limited to germanium optics, the study raises important fundamental issues relevant to other materials.

Key words: diamond machining; germanium; laser damage; surface finish

1. Introduction

The technique of diamond machining has been developed in recent years to provide an alternative means of generating optical surfaces without recourse to abrasive polishing. It has the advantages that it is quick (when properly set up), that it can be automated and that it can produce both planar and curved surfaces, including surfaces with varying degrees of asphericity. It can be applied to a wide range of optical components, both of relatively simple and complex geometries, and has been used to fabricate relatively small components such as polygons for infrared scanners at one end of the scale, to large mirrors for high energy laser applications at the other. An additional important feature of the technique is its freedom from the risk of introducing impurities and particulates.

Studies have been carried out by a number of workers of the application of the technique to a wide range of materials. Initially, interest centred on single point diamond turning (SPDT) of metallic surfaces and the work of Decker and others at NWC China Lake [1] highlighted the degree of attention that had to be paid to such detail as tool rake, machining speed and coolant fluid to allow optimisation of the technique to ensure high laser damage thresholds. Transmission electron microscopy studies [2] suggested that relatively high temperatures were produced at the tool tip, sufficient to induce oxide formation of copper mirrors. Studies have also been carried out of weak ceramic materials such as ZnS and magnesium fluoride [3] and the SPDT technique was shown to be capable of producing cosmetically high grade surfaces without crystallite pull-out. In brittle materials, the production of subsurface damage is of special concern, especially in narrow gap semiconductors such as germanium, where dislocated regions can serve to act as optically absorbing centres. In fact in an earlier study [4] of the deposition of ZnS films on polished germanium substrates, laser damage was initiated at nests of dislocation loops punched into the surface by the action of abrasive particles, rather than in the dense UHV produced ZnS film.

This work is concerned with an assessment of SPDT monocrystalline germanium surfaces and the interrelationship between the degree of subsurface damage and the laser damage threshold of the ensuing component. Since it was considered that the mechanical stiffness of the diamond turning machine was an important factor in controlling the surface finish and extent of subsurface damage, specimens were turned on two separate machines with significantly different design features. It was hoped to establish whether there was any difference in the machines' abilities to produce laser damage resistant surfaces.

2. Experimental

Nine samples of monocrystalline germanium were prepared at Ferranti Astron's diamond machining facility in Dundee. Seven of the samples were machined on two separate lathes, namely a Pneumo Precision MSG 325 and a single-axis Bryant Symons flycutter using standard cutting conditions with fixed tool rake. The fundamental differences between the machines was that the flycutter was driven by hydropneumatic slides and the MSG 325 by a precision lead screw. To simulate identical

---

*Ferranti Astron Limited, Dundee DD2 3TN, Scotland

cutting conditions, the specimens were centre turned off-axis on the MSG 325. Two of the specimens were left as conventionally polished by the vendors. Laser calorimetry was carried out using an 80 Watt laser calorimeter at Ferranti, but showed that all specimens had similar absorption values, dominated by bulk absorption rather than surface characteristics.

Damage thresholds were determined at 10.6 μm using a short cavity TEA laser of pulse length 33 nsec. The beam was focussed using a short focal length lens to give a beam waist of 100 μm $1/e^2$ diameter, measured by pinhole scanning techniques. Ten separate irradiations were carried out at each nominal value of incident energy at separate sites in a well defined matrix pattern. Damage was assessed by reflection microscopy at x400. Damage thresholds were determined from statistical probability plots produced from up to 60 separate irradiations. Results are discussed in terms of the minimum energy at which damage just occurs and the maximum energy at which damage sometimes does not occur.

Subsurface damage was assessed by cross-sectional transmission electron microscopy (XTEM). Cross sections were prepared by diamond saw cutting, epoxy mounting and abrasive thinning to $\simeq$ 100 μm in thickness. Final thinning was carried out by reactive iodine bombardment using iodine ions. Such sample preparation techniques have been demonstrated to give a freedom from extrinsic artefacts (eg ion beam thinning damage) and accurately reflect the true nature of the surface. Cross sections were examined in a JEOL 4000EX electron microscope.

3. Laser Damage Studies and Relation to Surface Finish

Values of laser damage thresholds are listed in Table 1 for a series of seven diamond machined surfaces and are compared with values measured on three conventionally polished surfaces. In general the polished surfaces appear to have slightly higher damage thresholds than the diamond machined. Whilst this may in part be associated with specimen to specimen differences it is apparent for sample 2 (where one surface of the germium disc is diamond machined whilst the other is polished) that polished surfaces appear to be significantly better.

Table 1. Damage Thresholds of Germanium Samples

Sample	LIDT J/cm^2	Machine
1	21.1-28.8	BS
2	8.5-19.5	BS
2a	24.4-25.8	Polished
3	15.8-24.2	PP
4	9.1-10.2	PP
5	8.1-15.8	BS
6	21.0-30.4	PP
7	14.3-23.5	PP
8	24.5-25.7	Polished
9	14.1-26.9	Polished

BS - Bryant Symons
PP - Pneumo Precision

Examination of the damage sites shows an interesting trend. In cases where damage thresholds are low eg sample 5, a high density of pitting is evident where the machining procedure has pulled out material from the surface. This is illustrated in Figures 1 and 2. However the pits do not appear to interact with the laser radiation to give regions of enhanced damage as would have perhaps been expected. This is contrasted to the case shown in Figure 3 where the damage threshold is higher, but where regions of enhanced interaction appear around other artefacts, possibly inclusions or nests of dislocation loops beneath the surface. When damage thresholds are highest, the damage morphology always has the character of that shown in Figure 4, with a smooth walled crater and very little ripple effect produced at the edge of the damage site due to interference effects. The ripple spacing was about 1.4 μm, or $\lambda/2n$.

There appears to be no great difference in the damage thresholds of samples produced on the two machines, showing no advantage in the hydropneumatic ram type even though it may be theoretically stiffer, as compared to the precision lead screw and possible periodic variation in surface profile. Both the Pneumo Precision and Bryant Symons machines are capable of producing both good and bad results. No correlation was found between the magnitude of surface periodic profile (the tooling profile) and laser damage threshold. While the absolute values of damage threshold are low for these particular cases studied in this work, samples of germanium machined under more optimum conditions on the Ferranti Astron MSG 325 have been demonstrated to have damage thresholds as high as 55 J/cm^2 [5].

4. Effects of Subsurface Damage

The effect of subsurface damage was explored by selecting two specimens, one with a high damage threshold (sample 1) and one with a low threshold (sample 5), both produced on the same machine. These were examined by both plan view and cross-sectional transmission electron microscopy. The plan view image of sample 1 as shown in Figure 5 clearly shows the correspondence between the density of dislocation contrast and that of the machining direction. The particular site examined in this case was situated at the periphery of a laser damaged region, and the large triangular features are the edges of the ripple markings delineating the extent of the melt zones as for example in Figure 1. It is notable that the laser induced melting process has completely annealed the surface of the substrate and the resultant material is dislocation-free. The cross-sectional micrographs (Figure 6) clearly reveal the extent to which the work damage induced by the machining process propagates into the substrate. The amount of damage introduced is different for the two selected specimens but takes the form of clusters of dislocation loops and microcracks propagating from the surface. The near surface region has been heavily deformed by the machining process as previously found for copper by Hurt et al [2]. However the basic difference between the two samples examined is that whilst the sample with the highest damage threshold (sample 1) has a reasonably uniform distribution in the density of surface defects, the other specimen, that with the low laser damage threshold is very non-uniform with large microcracked regions appearing at 10-20 μm intervals. These are some 500 nm in length but are extremely narrow and would not be visible from mere surface examination using for example scanning electron microscopy. It is these features, not the gross pitting of Figure 2 which produce regions of high optical absorption and interact with the incident laser radiation. The "good" sample however is clearly not perfect and a significant reduction in the amount of subsurface damage should be possible under more optimal machining conditions.

In comparison the amount of work damage produced in germanium as a result of conventional polishing is significantly lower as shown in Figure 7. This particular specimen was studied in more detail in previous work [4] and has a zinc sulphide anti-reflection coating deposited on its surface. The damage is limited to discrete regions which are made up of small clusters of dislocation loops, which only propagate some 60 Å below the surface.

5. Conclusions

Diamond machining techniques are applicable to the production of high grade optical surfaces in germanium. However unless due care is taken with the control of the machining process, it is possible to form undesirable cosmetic artefacts such as surface pitting as a result of material pull-out. This has a role in determining the laser damage threshold of the finished component. However the dominant factor in determining the damage threshold is the degree of subsurface damage introduced. This can be considerably greater than that produced by conventional optical polishing techniques. The characteristic tooling marks produced by diamond machining appear to have little effect on the damage threshold of germanium at 10.6 μm.

6. References

[1] Decker, D.L., Hurt, H.H., Porteus, J.O. and Grandjean, D.J., Proc. 1983 Boulder Laser Damage Symposium, NBS Spec. Publ. 688, 147 (1985).

[2] Hurt, H.H. and Decker, D.L., Proc. 1983 Boulder Laser Damage Symposium, NBS Spec. Publ. 688, 140 (1985).

[3] Decker, D.L., Grandjean, D.J. and Bennett, J.M., Proc. 1979 Boulder Laser Damage Symposium, NBS Spec. Publ. 568, 199 (1980).

[4] Lewis, K.L., Pitt, A.M., Cullis, A.G., Chew, N.G. and Charlwood, L., Proc. 1985 Boulder Laser Damage Symposium.

[5] Gibson, D.R., MacDonald, C.M. and Wilson, A.D., Proc. 1985 Boulder Laser Damage Symposium.

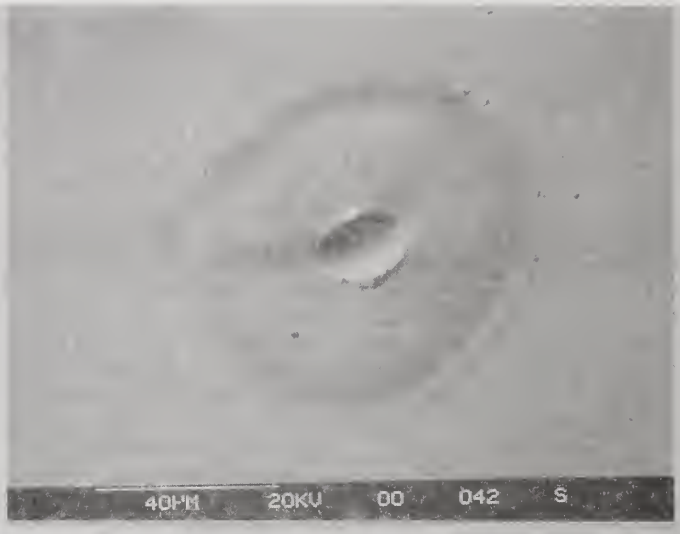

Figure . [illegible] germanium [illegible] surface. [illegible] however highlights the [illegible] with [illegible] pit features. [illegible] of this sample 6.1 J/cm².

[illegible]

Figure 3 Laser Damage Site on SPDT Germanium of moderate surface quality. Regions of enhanced interaction are evident, these may be associated with inclusions or nests of dislocation loops beneath the surface. Damage threshold of this sample was 15.8 J/cm^2.

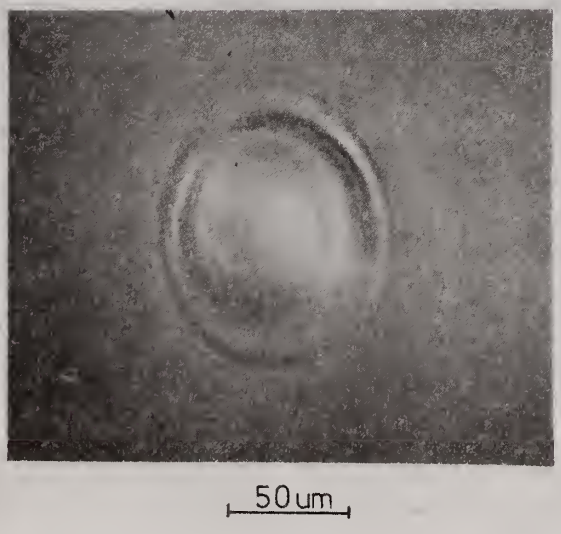

Figure 4 Laser damage site on polished germanium of good surface quality, showing smooth walled morphology of damage crater. Damage threshold of this sample was 24.5 J/cm^2.

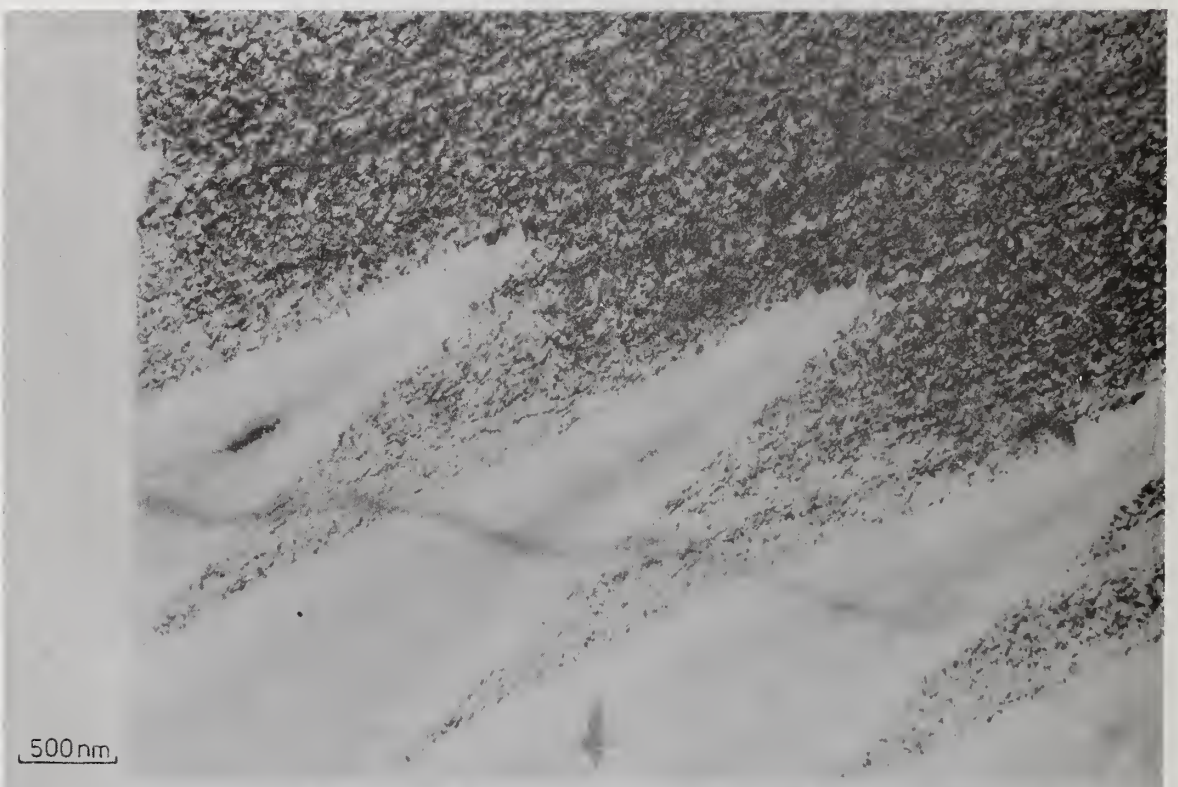
500nm

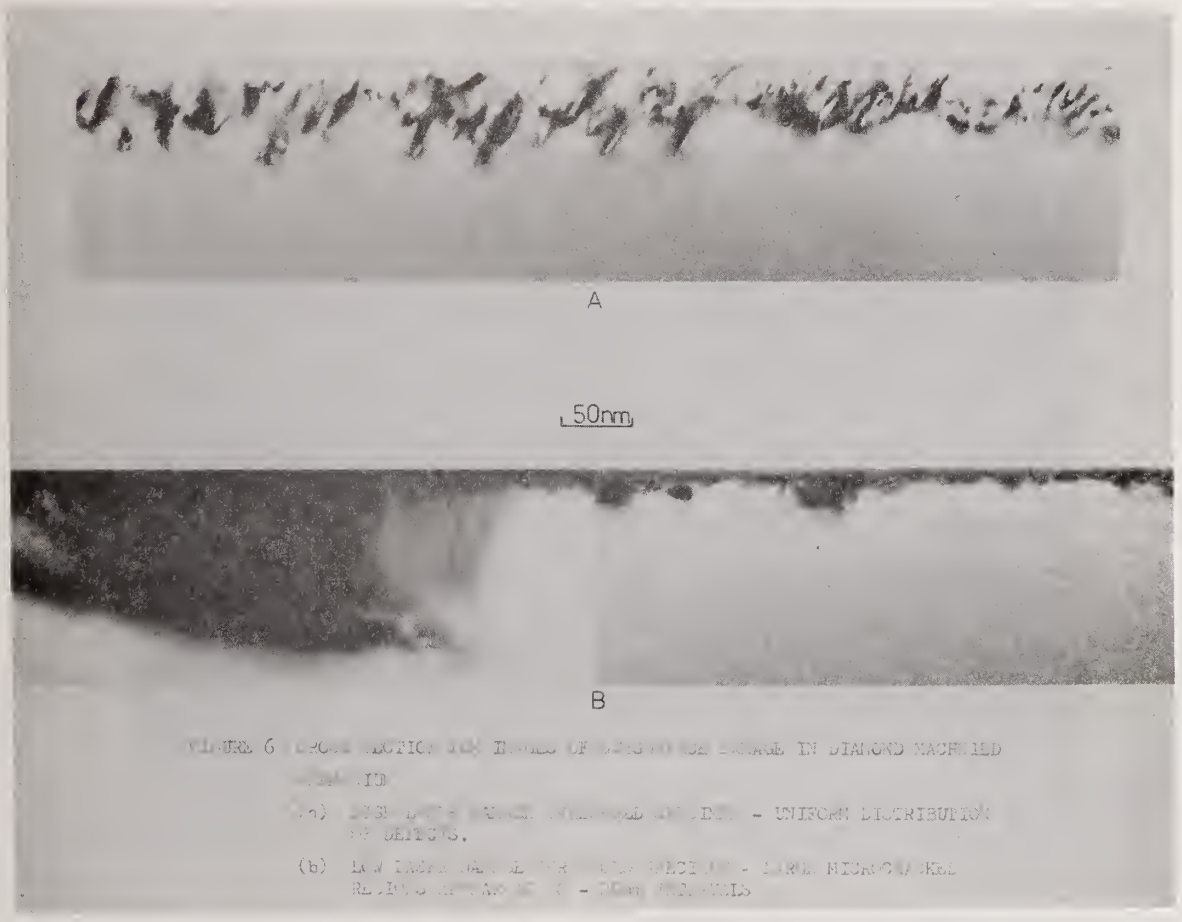

FIGURE 6 CROSS SECTION TEM IMAGES OF SUBSURFACE DAMAGE IN DIAMOND MACHINED
SILICON
(a) LOW DEPTH OF CUT (0.5 nm) - UNIFORM DISTRIBUTION
OF DEFECTS.
(b) HIGH DEPTH OF CUT (50 nm) - LARGE MICROCRACKS
RESULTS IN SURFACE ROUGHNESS (~ 50nm PEAK-TO-VALLEY

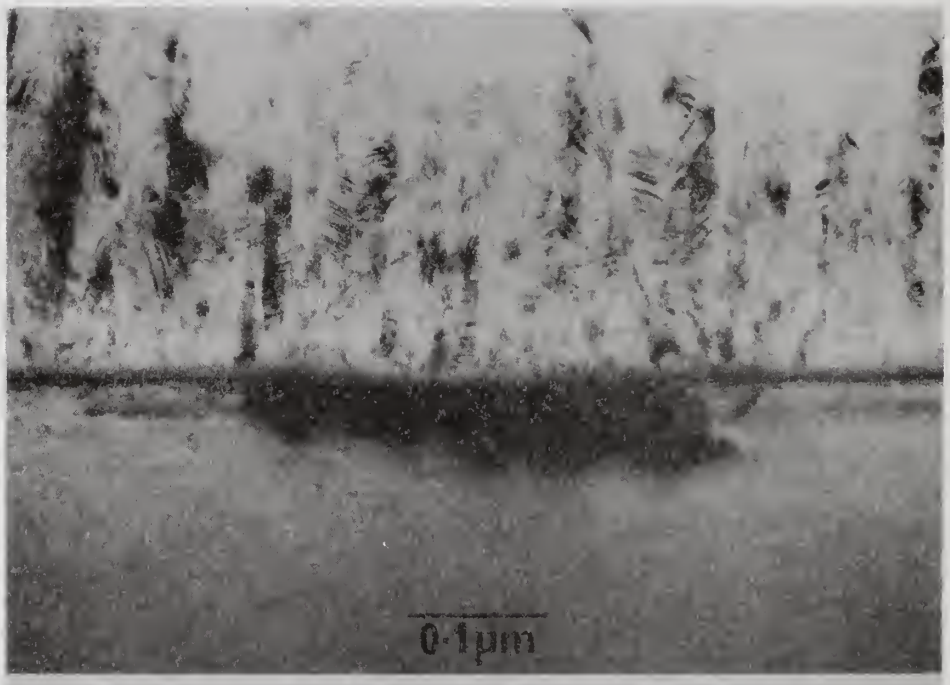

Figure 7 Dislocation loop clusters at surface of [illegible] germanium substrate arising from action of abrasive particles

Manuscript Received
4-16-87

Damage Morphologies and Cumulative Behavior of Laser Damage on Single Crystal Metal Surfaces

Yong Jee, Michael F. Becker, and Rodger M. Walser

The University of Texas at Austin
Center for Materials Science and Engineering and
Department of Electrical and Computer Engineering
Austin, TX 78712-1084

We have observed laser induced damage morphologies and the accumulation dependence of damage on single crystal metal surfaces under Q-switched Nd:YAG laser irradiation (1064 nm, 10 nsec pulses with a 240 μm spot diameter). The samples were chemically-polished copper and electro-polished aluminum of several crystallographic orientations.

Several different damage morphologies have been observed: slip-line formation, ripple patterns, flat-melting, and boiling. Damage probability versus fluence curves and accumulation curves were plotted to investigate damage behavior as it correlates with morphology. Flat-melting damage was observed near the 50% damage fluence on chemically polished copper surfaces, and slip-lines were found near the 50% damage fluence on electropolished aluminum surfaces. Surface defects produced during sample preparation greatly influenced the damage threshold of copper because of its high melting threshold. The influence of surface defects on copper decreased with increasing numbers of laser pulses. Accumulation curves show different damage behavior for crystals of different orientation. Accumulation was the largest on (111) Cu and Al surfaces, and the single shot damage threshold of these surfaces was less than the other crystal orientations for both Cu and Al.

Key Words: damage morphologies; accumulation; copper; aluminum; single crystal metal surfaces

1. Introduction

Laser induced damage on copper and aluminum surfaces has been investigated by a number of research groups. Lee, Koumvakalis and Bass [1,2] explained damage on diamond-turned copper mirrors as a failure triggered by localized surface defects and explained multiple pulse damage as the accumulation of plastic deformation resulting from laser induced thermal stress fields. Figueira and Thomas [3-5] defined the damage criterion as the reflectivity change to 90% peak brightness level on metal surfaces in vacuum and derived the exponential lifetime curve. Marrs, Faith, Dancy, and Porteus [6] observed slip on metal surfaces using 492 nm irradiation. Hurt [7] examined the effect of defects in the laser damage of metal surfaces using 10.6 μm, 100 nsec laser pulses. Our previous report [8] defined laser damage as any permanent change observed under a 200x Nomarski optical microscope and derived a cumulative equation which interpreted the cumulative behavior of laser damage for multiple pulses. Sparks and Loh's thermodynamic model was applied to analyze 1-on-1 damage test data [9]. Musal's model [10] was used to calculate plastic slip deformation thresholds. This model related multiple pulse damage accumulated on metal surfaces to the thermal stress field induced by the laser pulse.

The purpose of the present work is to measure single and multiple pulse damage thresholds, to investigate damage morphologies and damage accumulation, and to determine the damage mechanism on single crystal copper and aluminum surfaces under 1064 nm irradiation. Such wavelengths are more representative of those encountered in free-electron lasers. In the present work, damage is defined as any permanent change observed under a 200x Nomarski optical microscope. Several different polishing methods and crystal orientations are used to study the damage mechanism and several damage probability curves are plotted. We also investigate fluence dependent morphologies near damage threshold for single pulse damage and derive their damage probability behavior by correlating these damage morphologies with the damage probability curves. In multiple pulse damage, we study the accumulation effect by varying the incident number of pulses and plot the accumulation curves. The accumulation curves are plots of log ($F_N \cdot N$) versus log N where F_N is the N-pulse damage threshold fluence and N is the incident number of pulses. From the experimental data, a cumulative equation is derived to explain cumulative behavior of laser damage generated by the storage cycle of laser induced thermal stress-strain.

2. Experimental Procedures

2.1 Sample Preparation

In order to decrease surface defect density, chemically-polished single crystal copper and electro-polished single crystal aluminum samples were prepared. Chemically-polished and electro-polished samples were prepared using the procedure described below. The samples were then placed in the sample holder, blown off with a freon dust chaser, and damage tested.

The sample preparation procedure:

1. Cutting the bulk crystal with a low speed diamond cutter or an electric spark cutter.
2. Hand polishing with SiC (grit 600).
3. Diamond paste (5 μm) cloth polishing.
4. Alumina polishing (0.05 μm).
5. Ultrasonic cleaning in Ultramet solution for 5 min. (only for 1 min. in case of Al).
6. Final polishing.
   a. Chemical-polishing Cu in the following chemical polishing solution with agitation. Nitric acid (HNO_3) 20%; Phosphoric acid (H_3PO_4) 55%; Acetic acid (CH_3COOH) 25%; time = 20-30 min.
   b. Electro-polishing Al in the following electrolytic polishing solution. Ethanol (95% CH_3CH_2OH) 80%; Water (H_2O) 14%; Perchloric acid ($HCLO_4$) 6%; time = 20 sec. Voltage = 50-70 volt.
7. Rinse Al sample with running water for 30 sec.
8. Rinse Al sample with distilled water for 10 sec. The copper sample was rinsed with methanol for 30 sec.
9. Dry with warm air by using a dryer for 30 min.

Prepared sample surfaces were checked with electron channeling patterns (ECP) and by an X-ray diffractometer. Chemically-polished and electro-polished surfaces exhibited good single crystal quality for either the ECP or X-ray diffractometer.

2.2 Damage Testing

The laser source used in these experiments was an electro-optic Q-switched Nd:YAG laser with a 10 nsec pulse width and energy fluctuations of less than 2%. The experimental setup and other procedures were the same as in reference [8].

During damage testing, samples were placed at the actual focal plane of a 50 cm focal length lens. The beam spatial profile was measured with the knife-edge scanning method [11] at the beginning and at the end of each session. Spot sizes, W_o, are given as $1/e^2$ radii, or as diameter, $w_d = 2W_o$. Corresponding peak-on-axis beam fluences are calculated using $F = 2E/\pi W_o^2$ where E is the pulse energy.

3. Single Shot Damage

3.1 Copper

Damage probability curves were drawn using the same method as in the previous report [8]. A straight line fit to the data near threshold was used to determine 50% damage probabilities and damage onsets. An example is shown in figure 1 for a chemically-polished (110) copper surface tested with a 163 μm beam spot size. The 1-on-1 50% threshold is 10.8 J/cm^2, and the damage onset is 9.8 J/cm^2. We observed consistent damage morphologies over various regions of the damage probability curve. These observed morphologies show surface-cleaning, slip-line formation, ripples, flat-melting, and boiling. Surface defects sometimes hampered the observation of these morphologies.

Surface-cleaning and slip-lines are observed simultaneously on copper surfaces. The micrograph of figure 2.a shows surface-cleaning and tiny slip-lines, for testing at 10.0 J/cm^2, where the beam spot diameter is 326 μm (w_d) for a 10 nsec pulse width. The surface-cleaning diameter is about 80 μm, which is 0.25 times the beam spot diameter ($0.25w_d$). Another surface-cleaning region, observed in the micrograph of figure 2.c, was tested at 10.8 J/cm^2. Its surface-cleaning diameter is about 85 μm ($0.26w_d$).

The diameters measured from the micrographs of figure 2.a and c can be used to predict the surface-cleaning onset. The peak-on-axis fluence F_D at which the damage feature is initiated is related to the damage diameter x_D by [12,13]

$$F_D = F_{peak} \exp(-2x_D^2/w_d^2) \qquad (1)$$

where F_{peak} is the incident peak-on-axis fluence, and w_d is the incident beam spot diameter ($1/e^2$ of the intensity). We have assumed that the incident beam spatial profile is Gaussian. By measuring the damage diameter x_D, we can compute its onset fluence. For x_D = 80 μm ($0.25w_d$) and F_{peak} = 10.0 J/cm^2, as shown in the micrograph of figure 2.a, the surface-cleaning onset is 8.8 J/cm^2.

We could also see tiny slip-lines on the micrographs of figure 2, but these slip-lines are visible only when surface-cleaning is also present. Otherwise, slip-lines are not detectable with a Nomarski optical microscope or a scanning electron microscope on copper surfaces. Based on this observation, we conclude that surface-cleaning and slip-lines are initiated simultaneously on copper surfaces, and the damage threshold for slip-line formation may be represented by the surface-cleaning threshold on copper surfaces.

In the development of fluence-dependent morphology, the second stage is ripple patterns. Ripple patterns are observed in the micrographs of figure 2.c and d. Figure 2.b seems to show the onset of the ripple pattern. As the incident fluence increases, the diameter of the ripple pattern increases as follows: 22 μm ($0.067w_d$) at 10.6 J/cm^2 (figure 2.b), 36 μm ($0.11w_d$) at 10.8 J/cm^2 (figure 2.c), 48 μm ($0.15w_d$) at 10.9 J/cm^2 (figure 2.d), 61 μm ($0.19\ w_d$) at 11.4 J/cm^2 (figure 2.e), and 69 μm ($0.21w_d$) at 12.0 J/cm^2 (figure 2.g). Using these data and eq (1), we predict the ripple formation onset fluence is 10.5 J/cm^2, which is higher than the surface-cleaning and visible slip-line formation onset.

The ripple direction is perpendicular to the incident optical electric field. For some localized ripple patterns near defects, the localized ripple directions may be slightly different. The ripple spacing (see figure 2.d) is approximately 1.07 μm, which is close to the free space wavelength of the incident light. All these observations are consistent with the Young et al. theory of ripple formation [14].

The third morphology observed is flat-melting. The micrograph of figure 2.e, tested at 11.4 J/cm^2, shows a flat-melting region of 30 μm ($0.09w_d$) in diameter. In the micrograph of figure 2.g, tested at 12 J/cm^2, the flat-melting diameter is 52 μm ($0.16w_d$). From these data and eq (1), the flat-melting onset is calculated to be 11.3 J/cm^2.

The final damage stage of fluence-dependent morphology development is boiling. This stage can be easily recognized by its irregular shape and large cratering as shown in micrographs of figure 2.g and h. This boiling damage occurs simultaneously with a light flash or spark. The boiling morphology is always accompanied by annular regions showing flat-melting, ripples, and a large area of slip-lines in the surrounding material. The boiling damage appears to be nucleated on surface defects that were either preexisting or laser-induced. The micrograph of figure 2.f shows that small boiling damage pits seem to be nucleated heterogeneously on local surface defects. The boiling diameter increases from about 18 μm ($0.06w_d$; figure 2.g) to 120 μm ($0.37w_d$; figure 2.h) with the incident fluence. Using these data and eq (1), the boiling damage onset is found to be 12.7 J/cm^2.

The effect of surface defects always exists in the interaction of laser beams with materials. Their influence on laser damage is usually identified by a small boiled pit shape as shown in figure 2.f. In the case of copper, the influence of surface defects is great because of its high melting damage threshold. Surface defects such as pits, grooves, and slight surface height differences may decrease the damage threshold of the material. These surface defects increase the range from minimum damage fluence to maximum nondamage fluence. Thus the influence of surface defects appears in increasing the slope of the damage probability curve.

A detailed investigation of the damage features using a Nomarski optical microscope, indicates that the damage morphologies are correlated to the damage probability curve. Figure 3 is the same drawing as figure 1 with additional marks indicating the onset fluences for each damage morphology. Surface-cleaning and visible slip-lines (marked with "slip") are formed above 8.8 J/cm^2. Ripple patterns (marked with "ripple") are produced above 10.5 J/cm^2. Flat-melting damage (marked with "flat-melt") is present at 11.3 J/cm^2, and boiling damage (marked with "boiling") starts at 12.7 J/cm^2. This curve shows that as the incident fluence increases, damage probability increases, and several different damage morphologies develop in succession.

3.2 Aluminum

The damage probability curves of aluminum surfaces show a steeper slope than those of copper surfaces, as shown in figure 4. Low surface defect density and the low damage threshold seem to contribute to this steeper slope. The steep slope indicates that the overlapped interval between the highest nondamaged fluence and the lowest damaged fluence is small. Figure 4 shows the damage probability curve of a well-prepared electro-polished (111) aluminum surface. In this case, the 50% damage threshold is 0.93 J/cm^2, and the damage onset is 0.88 J/cm^2.

Aluminum surfaces show the same trend as copper surfaces in the development of fluence-dependent morphologies but at much lower fluences. Slip-lines are observed first, then ripple patterns, flat-melting, and boiling, successively. Slip-lines are highly visible on aluminum surfaces, but not on copper surfaces. However, surface-cleaning and flat-melting cannot be observed as easily on aluminum. There is no evidence of surface-cleaning on electro-polished aluminum surfaces. Since the very thin aluminum oxide layer (Al_2O_3) formed after polishing prevents further growth of the oxide layer, we may not detect the surface cleaning on aluminum surfaces.

Each of the micrographs in figure 5 shows slip-lines. Micrographs of figure 5.a and b reveal only slip-lines produced for a single shot test. Close observation of the Nomarski optical micrographs shows that the slip-lines form terraces which are stepped downward as the beam axis is approached [15]. In addition, the slip-lines are directed along favorable crystallographic orientations. For example, the angle 53° instead of 60° between two slip directions in figure 5.f indicates that the sample orientation is tilted slightly from a (111) surface. The micrographs of figure 5 show the increase of slip region diameter as the incident fluence increases from 135 μm ($0.56w_d$) at 1.2 J/cm^2 (figure 5.a) to 850 μm ($3.54w_d$) at 16.8 J/cm^2 (figure 5.f). We cannot precisely determine the slip-line formation onset, because we cannot measure the exact boundaries of the slip region due to the visibility limit of the Nomarski optical microscope. If we use the data of the micrograph of figure 5.a and eq (1), the visible slip-line onset is approximately 0.6 J/cm^2.

The micrograph of figure 5.c shows ripple patterns 35 μm in diameter ($0.15w_d$) within the slip-line region. The diameter of the ripple patterns increases with incident fluence as follows: 55 μm ($0.23w_d$) at 2.6 J/cm^2 (figure 5.d) and 95 μm ($0.4w_d$) at 3.4 J/cm^2 (figure 5.e). Using eq (1) and the above ripple diameters, the ripple formation onset is 2.30 J/cm^2.

Flat-melting is present, but not easily observed in the micrograph of figure 5.e tested at 3.4 J/cm^2. This photo also shows boiling nucleated on surface defects. The boiled area is 35 μm in diameter ($0.15\ w_d$) and is surrounded by flat-melting, ripples, and slip-lines. This micrograph indicates that on aluminum, slip-lines develop first, and then ripple, flat-melting, and boiling occur in succession as the incident fluence increases. Using eq(1) and measurements of flat-melting and boiling diameters, we determine the flat-melting and boiling damage onsets to be 2.99 J/cm^2 and 3.32 J/cm^2, respectively.

Each observed damage morphology onset is plotted on the damage probability curve in figure 4. In the case of low surface defect density, the damage threshold of aluminum surfaces seems to be marked only by visible slip-line formation which is produced by the thermal stress field induced by the laser beam.

3.3 Crystal Orientation Effects

In these experiments, the various crystallographic orientations of copper and aluminum surfaces were used to investigate the effect of crystallographic orientation on laser-induced damage. For the chemically-polished copper surfaces, the 50% single shot damage threshold of (111) surfaces is 9.16 J/cm^2, that of (100) surfaces is 9.18 J/cm^2, and that of (110) surface is 10.8 J/cm^2. This same ordering of damage thresholds was observed for single-point diamond-machined surfaces of the same material [8]. On aluminum surfaces, the single shot damage threshold of (111) surfaces is 0.93 J/cm^2, that of (110) is 1.81 J/cm^2, and a (100) aluminum surface was not measured. The lowest single shot damage thresholds are found on (111) surfaces for

both copper and aluminum. This is in agreement with the results of references [15-17]. The difference in the damage threshold of different crystal orientations can be explained by the fact that slip occurs more easily on the (111) surface planes of face-centered cubic (FCC) structures resulting in the least resistance to shear stress.

3.4 Discussion of the Single Shot Damage Morphologies

Surface-cleaning was observed on chemically-polished copper surfaces with a Nomarski optical microscope as shown in the micrographs of figure 2.a and c. The optical absorptance change and/or the surface height change caused by the heterogeneous surface material removal [18] may be the explanation for the surface-cleaning phenomenon. This surface-cleaning phenomenon may be easily monitored by detecting charge emission [19,20], which shows that the surface emits charge prior to damage and that the charge emission threshold is about one tenth of the single shot damage threshold.

One possible explanation for surface-cleaning is that heterogeneous surface materials, such as an oxide layer, introduced during or after sample preparation may be at least partially removed by the laser beam. On copper surfaces, this oxide layer (CuO or Cu_2O) grows continuously as time passes. But on aluminum surfaces, once the aluminum oxide layer (Al_2O_3) is protectively formed, there is no further growth of the surface oxide layer. These heterogeneous surface materials, may have a lower damage threshold than the substrate [19,21], and be melted or evaporated before the substrate is damaged. This removal of the heterogeneous surface materials changes the surface height and the surface optical quality. The surface height change can be recognized by the contrast change at the boundary as shown in the micrographs of figure 2.a and c.

Slip-line formation suggests that the interaction of metal surfaces with laser pulses near the damage threshold is thermomechanical in nature. Figure 5.f shows obvious slip-lines on aluminum surfaces. When the incident laser fluence is sufficiently intense, the absorbed energy is transformed to a thermal stress field which generates plastic slip-lines on the surface [10]. These plastic slip-lines are produced along favorable crystallographic orientations.

The free surface displacement, u, can be predicted by integrating eq (8) of reference [10]. The induced thermal stress amplitude follows the surface temperature rise (dT) according to eq (6) of reference [10]

$$\sigma = -E\alpha dT/(1-\nu) \tag{2}$$

where ν is Poisson's ratio, E is Young's modulus, and α is the thermal expansion coefficient. At the plastic yield point ($|\sigma| = Y$), the surface temperature rise, for a spatially uniform and rectangular pulse shape, is expressed by $dT = (1-\nu)Y/E\alpha$, where Y is yield stress of the material. The normal surface displacement is obtained by using above equations and by assuming a thermal diffusion depth $d = 2(K_d t_p)^{1/2}$ for thermal diffusivity K_d and the pulse width t_p,

$$u = (1 + \nu)Yd/E = 2(1 + \nu)Y(K_d t_p)^{1/2}/E \tag{3}$$

The computed plastic yield onsets are 0.09 J/cm^2 for aluminum and 0.6 J/cm^2 for copper. Corresponding surface displacements are calculated to be approximately 1.3 nm on high quality aluminum mirror surfaces and 1.4 nm on high quality copper mirror surfaces. If we convert these displacement values to displacement per incident J/cm^2, then the plastic displacement rate is 13.7 nm-cm^2/J on aluminum surfaces and 2.1 nm-cm^2/J on copper surfaces. Using this rate for the electro-polished aluminum surfaces, the predicted free surface displacement will be approximately 8.2 nm at the visible slip threshold of 0.6 J/cm^2, and for copper surfaces it will be 18.5 nm at the visible slip threshold fluence of 8.8 J/cm^2. The considerable difference between the theoretical and measured slip thresholds appears consistent with the expected vertical detectivity threshold in Nomarski microscopy. In other words, the threshold for visibility and for subsequent damage due to plastic deformation might be larger than the threshold for the initiation of plastic deformation, i.e. 10-20 nm versus 1-2 nm, respectively. Surface deformation above the slip damage threshold is distinguished by an increase in absorptance sufficient to lead to catastrophic surface damage or to microscopically visible surface roughening. As we shall describe later, this cyclic thermomechanical effect can also lead to the accumulation observed in N-on-1 damage.

The Nomarski micrograph of figure 2.d shows ripple patterns. Ripple patterns are generally formed by the constructive interference of the scattered surface waves and the incident wave [14]. If the laser pulse energy is sufficiently strong, but slightly less than the melting threshold, the surface layer can be locally melted by the constructive interference pattern. It appears more likely in this case that the surface is uniformly melted where ripples form. The mechanism appears to involve the slip lines which appear before and adjacent to the ripples. The strongly scattered surface waves from the slip lines interfering with the incident wave could produce the observed morphology [12,22,23]. Although the ripple direction is generally perpendicular to the incident electric field [24], the ripple pattern direction on metal surfaces may be influenced by the direction of the slip-lines produced during the initial part of the laser pulse.

The fourth damage stage is flat-melting, which is distinguishable from the ripple patterns. The typical flat-melting damage morphology looks melted in the center, surrounded by ripples and slip-lines. If the absorbed energy increases the surface temperature above the melting point, the surface may be melted locally for a very short time, and then resolidified. Surface tension and evaporation dynamics will affect the localized melting and resolidification of the surface, and in this case, the surface remains relatively flat [3].

When the incident laser fluence is increased above the boiling threshold, material begins to be ejected from the surface simultaneously with a light flash or spark [1,2]. Because the sudden temperature increase in the small volume generates a high pressure wave, or shock wave [25], material can be boiled, vaporized, and ejected with high kinetic energy. Material will be ejected from the surface and some will accumulate on the surrounding area. The size of the boiled area and the quantity of ejected material increases with incident laser energy, and eventually liquid droplets are ejected from the surface, leaving a large crater behind. Intense plasmas are produced during this catastrophic failure, the surface optical scattering is greatly increased, and the surface reflectance is greatly reduced. Boiling damage appears to be heterogeneously nucleated on either preexisting or laser induced surface defects, as shown in the micrographs of figure 2.f and 5.e.

Surface defects can have various aspects; pits, craters, holes, grooves, scratches, pores, embedded holes, heterogeneous surface layers, and surface irregularities. These surface defects have hampered the complete study of laser damage behavior in terms of intrinsic or extrinsic material properties. As pointed out by Bloembergen [26], complex dielectric constants and optical coefficients are increased at these surface defects. Thereby, the damage behavior and measurement of damage thresholds can be easily misinterpreted by the change of the optical properties caused by these surface defects. The influence of surface defects is significant when the laser fluence is high and the testing pulse number is low. In the case of copper, the influence of surface defects is great because of its high melting threshold. However, the influence of defects is much less on aluminum surfaces because of its lower melting threshold.

If the incident laser fluence is higher than the boiling damage threshold, all fluence dependent damage morphologies can be observed simultaneously as shown in figure 2.g. The simple damage morphologies diagram drawn in figure 6 summarizes this single shot fluence dependent damage behavior. As the incident laser energy increases, surface-cleaning and slip-lines are formed, and ripple patterns, flat-melting, and boiling damage are generated in succession. In the case of copper surfaces, the observation of slip-lines is difficult because of the small slip displacement per unit incident fluence, but ripple and flat-melting areas are easily observed. On aluminum surfaces, slip-lines are easily seen because the slip displacement is large per unit incident fluence, but the flat-melting area is not easily discerned.

3.5 **Comparison to Theoretical Calculations**

The measured melting damage threshold agrees relatively closely with the theoretical values; both of which are shown in Table 1. The theoretical melt threshold on copper surfaces is 11.9 J/cm^2, and the ripple formation onset fluence, which indicates the experimental melt threshold of metal surfaces, is 10.5 J/cm^2. On aluminum surfaces, the theoretical melt threshold is 1.95 J/cm^2 and the experimental onset fluence of ripple formation is 2.3 J/cm^2. The theoretical thresholds were calculated, as shown in [27], by assuming one dimensional heat transport.

There is a big difference between the theoretical and experimental slip thresholds. The theoretical slip threshold on copper surfaces is 0.66 J/cm^2, and the measured slip threshold is 8.8 J/cm^2 on chemically-polished surfaces. The visible slip threshold is nearly thirteen times the theoretical value. In the case of aluminum surfaces, the theoretical slip threshold is 0.09 J/cm^2 [27], and the measured value on electropolished aluminum surfaces 0.6 J/cm^2 is

seven times greater. As discussed previously, this discrepancy may be due to the low visibility of very small slip displacements.

A mere 9% increase in laser fluence is needed in the theoretical calculation to take the copper surface temperature from melting to boiling [29], whereas a 38% increase in laser fluence is required to raise the surface aluminum temperature from melting to boiling. Experimentally, this increase in laser fluence was found to be 21% in copper and 44% in aluminum in reasonable agreement with the theory.

Table 1. Comparison of theoretical and experimental damage fluences (J/cm^2)

	Copper F_{peak}		Aluminum F_{peak}	
	Theory	Experiment	Theory	Experiment
Slip-lines	0.66	8.8	0.09	0.60
Ripples	11.9	10.5	1.95	2.30
Flat-melting	11.9	11.3	1.95	2.99
Boiling	13.0	12.7	2.70	3.32

(Single Shot test at 10 nsec with a 240 μm ($1/e^2$) beam diameter)

4. Multipulse Damage

4.1 Accumulation Curves

We have repeatedly tested samples at different pulse numbers, drawn damage probability curves similar to that in figure 1, and put the 50% damage threshold data obtained from these curves onto the damage fluence curve, as shown for copper surfaces in figure 7. These damage fluence curves indicate that the damage threshold decreases as the pulse number increases. The error bars indicate the standard error of estimation for the 50% damage fluence, which is much smaller than the difference between minimum damaging fluence and maximum nondamaging fluence.

If we redraw the damage fluence curve in another way, we can get a damage accumulation curve. This accumulation curve is used to examine the effect of cumulative laser action on metal surfaces. The y-axis is the log of the product of the N-pulse damage threshold, F_N, and the incident pulse number, N, [$\log(F_N \cdot N)$]; and the x-axis is the log of the pulse number, [log N]. The plot, figure 8, shows straight lines for the various chemically-polished copper surfaces from this linear segment of the damage accumulation curve, we can derive the following cumulative equation [8]:

$$F_N = F_1 N^{S-1} \tag{4}$$

where F_1 is single shot damage threshold, and S is the slope of accumulation curve. We have examined the slope of the accumulation curve for different crystallographic orientations. The curves have slopes of S = 0.95 for a (100) surface, S = 0.92 for a (110), and S = 0.85 for a (111). The average value of the slope for (110) copper surfaces is 0.92 whether the surface was prepared by single-point diamond-machining or by chemically-polishing. As N increases, the N-pulse damage thresholds of (111) surfaces decrease more rapidly than those of (100) surfaces. This rapid decrease on (111) surfaces indicates that the magnitude of plastic slip deformation per unit pulse number is greater than for the other surfaces. This experimental result is in agreement with the fact that the slip system for (111) surfaces has the least resistance to shear stress along its slip direction [17]. This large plastic slip deformation, accumulated on the surfaces under repeated irradiation, increases the surface roughness and is followed by the increase of absorbed laser energy. The large magnitude of damage accumulation appears as a small slope on the accumulation curves. When the curve has a slope of 0.95, it indicates that there is a small accumulation of plastic deformation and no great change in additional energy to damage the surface with decreasing N. A slope of one means that the damage threshold does not change at all with increasing pulse number and that there is no accumulation effect.

As will be shown in the next section, the slope of the accumulation curve is inversely proportional to the amplitude of the plastic deformation storage and proportional to the resistance to plastic deformation, which is dependent on the crystal orientation. This low resistance of (111) surfaces in FCC crystals to laser induced damage is in agreement with metallurgical test results [15,17]. Thus, crystallographic orientation affects the amplitude of the storage cycle of plastic slip deformation in multiple pulse damage. This aspect will be developed further in the next section.

4.2 Discussion of the Cumulative Behavior

Mechanical fatigue damage of metals shows similar behavior to that of laser accumulation. In this section, we relate laser induced cyclic stress to material parameters derived from mechanical fatigue testing. The thermal stress amplitude, σ, induced by laser beam is proportional to the surface temperature change as given in eq (2). Temperature change, dT, below melting point is proportional to the incident laser fluence, F, [9] and is given by

$$dT = \frac{2A}{(\pi K C t_p)^{\frac{1}{2}}} F \tag{5}$$

for a spatially uniform and rectangular pulse of width t_p, where K is thermal conductivity, C is specific heat capacity of the metal, and A is the average optical absorptance. From eqs (2) and (5), we see that the induced stress amplitude is directly proportional to the incident laser fluence. When the induced stress amplitude is larger than the plastic yield point, plastic strain is produced and manifested as plastic slip deformation at the metal surface. Under repeated irradiation, this plastic strain accumulates and surface roughness increases.

Similar phenomena are observed in the bulk mechanical fatigue damage of metals [28,29]. For example, some useful analogies may be drawn to the present case. The stress amplitude of fatigue damage is expressed by [28]

$$\sigma = \sigma_f N^b \tag{6}$$

where σ is the stress amplitude, σ_f is the fatigue-strength coefficient for a single cycle and b is the fatigue-strength exponent. This stress-life equation can be compared with the cumulative eq (4) for laser damage. Since the thermal stress induced by laser beam is proportional to the incident laser fluence, we find that

$$b = S - 1 \tag{7}$$

and σ_f is given by

$$\sigma_f = \frac{2AE\alpha F_1}{(1-\nu)(\pi K C t_p)^{\frac{1}{2}}} \tag{8}$$

In addition, similar behavior was observed by Coffin [30] and Manson [31] for plastic strain where they formulated the plastic strain-life equation

$$\varepsilon_p = \varepsilon_f N^C \tag{9}$$

where ε_f is fatigue-ductility coefficient for one cycle (2.18 for Cu and 0.43 for Al [32]) and c is the fatigue-ductility exponent. From eqs (6) and (9), the stress-strain equation in fatigue damage is given by

$$\sigma = \sigma_f(\varepsilon_p/\varepsilon_f)^n \tag{10}$$

where n = b/c is the cyclic strain-hardening exponent. This equation defines the hysteresis behavior observed in fatigue damage.

Through the relationship between fatigue properties of the materials and cyclic stress-strain properties, and by following energy arguments shown by Morrow [29], the cyclic strain-hardening exponent n, fatigue-strength exponent b, and fatigue-ductility exponent c are related in the following manner:

$$b = -n/(1 + 5n), \tag{11}$$

$$c = -1/(1 + 5n), \tag{12}$$

$$n = b/c \tag{13}$$

The typical range of b is between -0.05 and -0.12, that of c between -0.5 and -0.7, and that of n between 0.1 and 0.2 [28]. These relations hold for many metals. From eqs (7) and (11)-(13), we can express the fatigue parameters, c and n, in terms of the slope S of accumulation curve as follows,

$$n = (1 - S)/(5S - 4), \tag{14}$$

$$c = 4 - 5S \tag{15}$$

When solved for S, equation (14) shows that the value of S should be within the range of $0.8 < S < 1$ to represent proper thermal stress-strain behavior. Equation (15) shows that the fatigue-ductility exponent, c, is negative indicating that the magnitude of the induced plastic strain decreases with the increase of pulse number, as expressed in eq (9). These relationships connect the cumulative behavior of laser induced damage to the fatigue damage properties. If we use S = 0.92, obtained as the typical value for copper, we can obtain b = -0.08, n = 0.133, and c = -0.6. These coefficients are in agreement with the results in fatigue tests for metals [28].

From the area of the hysteresis loops shown in figure 9 and given by eq (10), we can determine the cumulative plastic strain energy stored by each pulse. The plastic strain energy per pulse for a given stress and strain is given by [31]

$$dW = \sigma\ \varepsilon_p - \int_0^{2\sigma} \varepsilon_p\, d\sigma = 2\sigma\ \varepsilon_p\ (1-n)/(1+n) \tag{16}$$

The total plastic strain energy is obtained by substituting eqs (6) and (9) into (16) and multiplying by N to obtain,

$$W = dW\ N = 2[(1-n)/(1+n)]\sigma_f\varepsilon_f N^{b+c+1} \tag{17}$$

These plastic strain energy accumulation equations can be expressed in terms of the slope S of the experimental accumulation curves as

$$dW = 2[(6S - 5)/(4S - 3)]\sigma_f\varepsilon_f N^{3-4S} \tag{18}$$

and

$$W = 2[(6S - 5)/(4S - 3)]\sigma_f\varepsilon_f N^{4(1-S)} \tag{19}$$

When S is less than one, the total plastic strain energy always increases with the increase of pulse number, and the plastic strain energy per pulse decreases. For the case of S = 0.92, $W = 1.53\sigma_f\varepsilon_f N^{0.32}$ and $dW = 1.53\sigma_f\varepsilon_f N^{-0.68}$, showing $N^{1/3}$ and $N^{-2/3}$ behavior, respectively. From this correlation between accumulation of laser damage and fatigue damage, we can predict the storage cycle of thermal stress-strain energy induced by laser beam on metal surfaces.

5. **Conclusions**

Laser induced damage of single crystal copper and aluminum metal surfaces at 1064 nm has been studied for single and multi-pulse behavior. Damage probability curves have been correlated with damage morphologies to investigate the 1-on-1 damage mechanism. Accumulation curves and a cumulative equation have been derived to analyze multiple-pulse damage.

Several different damage morphologies were observed; surface cleaning, slip lines, ripples, flat-melting, and boiling. As the incident energy fluence increased, surface-cleaning and slip-lines were formed first, then ripple patterns, flat-melting, and boiling damage were generated successively. The morphology observed at 50% damage probability was flat-melting on copper surfaces and visible slip line formation on electro-polished aluminum surfaces. From this observation, we found that in some cases where the plastic slip threshold was extremely low, plastic deformation damage was dominant at N = 1. On copper surfaces, the slope of the damage probability curve was moderate whereas on electro-polished aluminum surfaces, the slope was steep. Experimental melting and boiling damage thresholds showed good agreement with the theoretical values. However, there was a large difference between the theoretical and experimental slip onsets. We have shown how this great difference between the theoretical and the visible slip onsets may arise from the limit of visible detectivity for a Nomarski optical microscope and the very small slip displacement at the theoretical slip threshold.

Accumulation curves for copper surfaces had only one straight line whose average slope was 0.92. The slope was indicative of the amplitude of the storage cycle of plastic slip deformation. This accumulation effect can be summarized by a cumulative equation for damage, $F_N = F_{th}N^{S-1}$, which can be related to the storage cycle of thermal stress-strain energy induced by laser pulse. From the relation of the slope S to mechanical fatigue damage of metals, we found that the induced plastic strain amplitude and the total plastic strain energy required to damage decreased with the increase of the slope, S. And thus the pulse number required to damage increased for increasing S.

Investigation of the effect of crystallographic orientation on laser damage showed that (111) surfaces had lower single shot damage threshold for both copper and aluminum than the other crystal orientations studied. In multiple pulse damage, (111) surfaces produce larger plastic deformation in the storage cycle of stress-strain than (110) surfaces which are in turn larger than (100) surfaces.

The experimental results in this study suggest the following damage mechanism. In single shot damage, various damage morphologies nucleate at increasing threshold fluences on polished single crystal metal surfaces. In multiple pulse damage, plastic slip deformation accumulates on metal surfaces under repeated irradiation, following the energy storage cycle of thermally induced circuits of the stress-strain hysteresis loops.

This research was supported by the DoD Joint Services Electronics Program under research contract AFOSR F49620-82-C-0033 and the Texas Advanced Technology Research Program.

6. **References:**

[1] C.S. Lee, N. Koumvakalis, and M. Bass, "Spot-Size Dependence of Laser-Induced Damage to Diamond Turned Cu Mirrors," Appl. Phys. Lett., vol. 41(7), 625, 1982.

[2] N. Koumvakalis, C.S. Lee, and M. Bass, "Single and Multiple Pulse Catastrophic Damage in Cu and Ag Diamond Turned Mirrors at 10.6, 1.06 and 0.532 μm" Laser Induced Damage in Optical Materials: 1982, Nat. Bur. Stand. (US) Spec. Publ. 669, 186, 1984.

[3] S.J. Thomas, R.F. Harrison, and J.F. Figueira, "Observation of the Morphology of Laser-Induced Damage in Copper Mirrors," Appl. Phys. Lett., 40(3), 200, 1982.

[4] J.F. Figueira, S.J. Thomas, and R.F. Harrison, "Damage Thresholds at Metal Surfaces for Short Pulse IR Lasers," IEEE, J. Quantum Electron., vol. QE-18(9), 1381, 1982.

[5] J.F. Figueira, S.J. Thomas, and R.F. Harrison, "Damage Thresholds to Metal Mirrors by Short-Pulse CO_2 Laser Radiation," Laser Induced Damage in Optical Materials: 1981, Nat. Bur. Stand. (US) Spec. Publ. 638, 229, 1983.

[6] C.D. Marrs, W.N. Faith, J.H. Dancy, and J.O. Porteus, "Pulsed Laser-Induced Damage of Metals at 492 nm," Appl. Opt., vol. 21(22), 4063, 1982.

[7] H.H. Hurt, "The Effect of Defects on the Laser Damage Performance of Metal Mirror Surfaces," Laser Induced Damage in Optical Materials: 1984, Nat. Bur. Stand. (US) Spec. Publ. 996, 66, 1986.

[8] Yong Jee, M.F. Becker, and R.M. Walser, "N-on-1 Damage Testing of Single Crystal Metal Surfaces at 1.06 μm," 17th Symposium on Optical Materials for High Power Lasers, Oct. 1985.

[9] M. Sparks and E. Loh, Jr., "Temperature Dependence of Absorptance in Laser Damage of Metallic Mirrors: I. Melting," J. Opt. Soc. Am., vol. 69(6), 847, 1979.

[10] H.M. Musal, Jr., "Thermomechanical Stress Degradation of Metal Surfaces under Pulsed Laser Irradiation," Laser Induced Damage in Optical Materials: 1979, Nat. Bur. Stand. (US) Spec. Publ. 568, 159, 1980.

[11] D.C. Cohen, B. Little, and F.S. Lueche, "Techniques for Measuring 1 μm Diam. Gaussian Beams," Appl. Opt., vol. 23(4), 637, 1984.

[12] A.L. Smirl, I.W. Boyd, T.F. Boggess, S.C. Moss, and H.M. van Driel, "Structural Changes Produced in Silicon by Intense 1-μm ps Pulse," J. Appl. Phy., 60(3), 1169, 1986.

[13] J.M. Liu, "Simple Technique for Measurements of Pulsed Gaussian-Beam Spot Sizes," Opt. Let., vol. 7(5), 196, 1982.

[14] J.F. Young, J.S. Preston, H.M. van Driel, and J.E. Sipe, "Laser-Induced Periodic Surface Structure," Phys. Rev. B27, 1155, 1983.

[15] J.O. Porteus, M.J. Soileau, and C.W. Fountain, "Slip Banding in Al Single Crystals Produced by 10.6 μm Laser Pulses," Appl. Phys. Lett., 29(3), 156, 1976.

[16] F. Haessner, W. Seitz, "Laser-Induced Dislocation Structures in Copper Single Crystals," J. Mat. Sci., 6, p 16-18, 1971.

[17] D. Hull, Introduction to dislocations, 2nd ed., Pergamon Press, Oxford, 1975, p 15-28.

[18] R.P. McConnell, K.D. Jamison, F.B. Dunning, and G.K. Walters, "Laser Annealing of Ni(001)," J. Vac. Sci. Technol., A1(4), 1852, 1983.

[19] M.F. Becker, F.D. Domann, A.F. Stewart, and A.H. Guenther, "Charge Emission and Related Precursor Events Associated with Laser Damage," Laser Induced Damage in Optical Materials: 1983, Nat. Bur. Stand. (US) Spec. Publ. 688, 429, 1985.

[20] F.E. Domann, M.F. Becker, A.H. Guenther, and A.F. Stewart, "Charged Particle Emission Related to Laser Damage," Appl. Opt., vol. 25(9), 1371, 1986.

[21] J.O. Porteus, D.L. Decker, J.L. Jernigan, W.N. Faith, and M. Bass, "Evaluation of Metal Mirrors for High Power Applications by Multithreshold Damage Analysis," IEEE J. Quantum Electron., vol. QE-14(10), 776, 1978.

[22] A.E. Siegman and P.M. Fauchet, "Stimulated Wood's Anomalies on Laser-Illuminated Surfaces," IEEE, J. Quantum Electron., vol. QE-22(8), 1384, 1986.

[23] P.A. Temple and M.J. Soileau, "Polarization Charge Model for Laser-Induced Ripple Patterns in Dielectric Materials," IEEE, J. Quantum Electron., vol. QE-17(10), 2067, 1981.

[24] P.M. Fauchet and A.E. Siegman, "Surface Ripples on Silicon and Gallium Arsenide under Picosecond Laser Illumination," Appl. Phys. Lett., vol. 40, 824-826, 1982.

[25] J.F. Ready, Effects of High-Power Laser Radiation, Academic Press, New York, 1971, 95-123.

[26] N. Bloembergen, "Role of Cracks, Pores, and Absorbing Inclusions on Laser Induced Damage Threshold at Surfaces of Transparent Dielectrics," Appl. Opt., vol. 12(4), 661, 1973.

[27] Yong Jee, Ph.D. dissertation, Electrical and Computer Engineering, The University of Texas at Austin, 1987.

[28] M.R. Mitchell, "Fundamental of Modern Fatigue Analysis for Design," Fatigue and Microstructure, p. 385-437, ASM, 1979.

[29] J.D. Morrow, "Cyclic Plastic Strain Energy and Fatigue of Metals," ASTM STP 378, International Friction Damping, and Cyclic Plasticity, ASTM, 1965, p 45-87.

[30] L.F. Coffin, Jr. and J.F. Tavernelli, "The Cyclic Straining and Fatigue of Metals," Transactions, Metallurgical Soc., Am. Institute Mining, Metallurgical, and Petroleum Engrs., vol. 215, 794-806, Oct., 1959.

[31] S.S. Manson, "Fatigue: A Complex Subject - Some Simple Approximations," Experimental Mechanics, 193-226, July, 1965.

[32] P. Lukas, M. Klesnil, and J. Polak, "High Cycle Fatigue Life of Metals," Mat. Sci. Eng., 15, 1974, p 239-245.

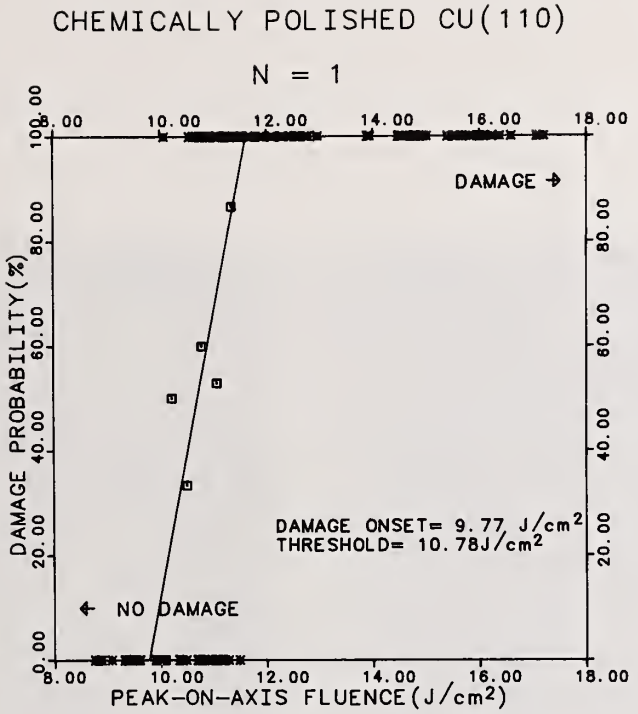

Figure 1. Damage probability curve for chemically-polished (110) copper surfaces for N = 1, 10 ns pulses. The x's represent single sites and the squares represent probabilities in the damage-nondamage overlap region.

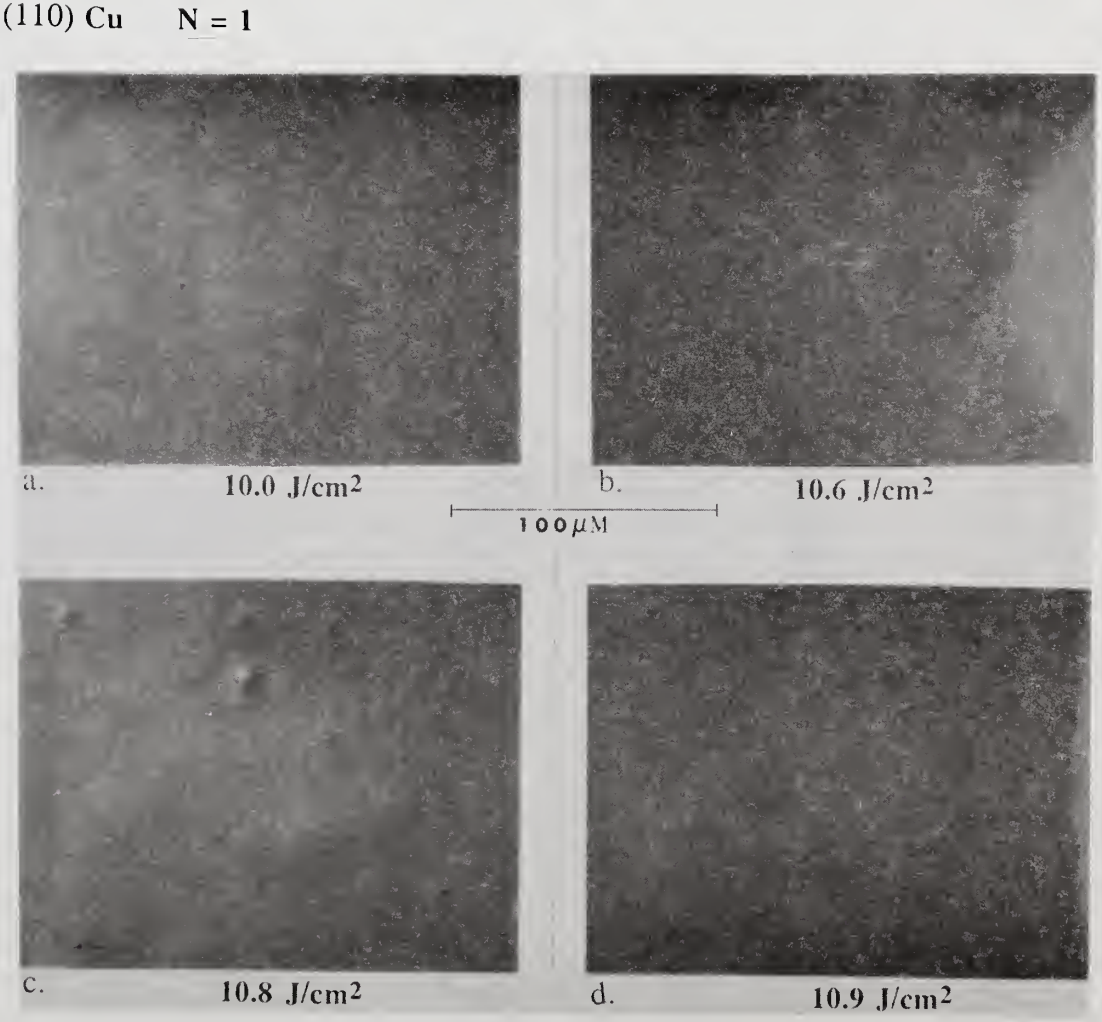

Figure 2. Nomarski micrographs of the single shot damage morphologies observed with increasing incident laser fluence on chemically-polished (110) copper surfaces. a) Surface-cleaning and tiny slip lines at 10.0 J/cm^2. b) The onset of the ripple pattern at 10.6 J/cm^2. c) Surface-cleaning and ripple pattern formation at 10.8 J/cm^2. d) Ripple pattern formation at 10.9 J/cm^2.

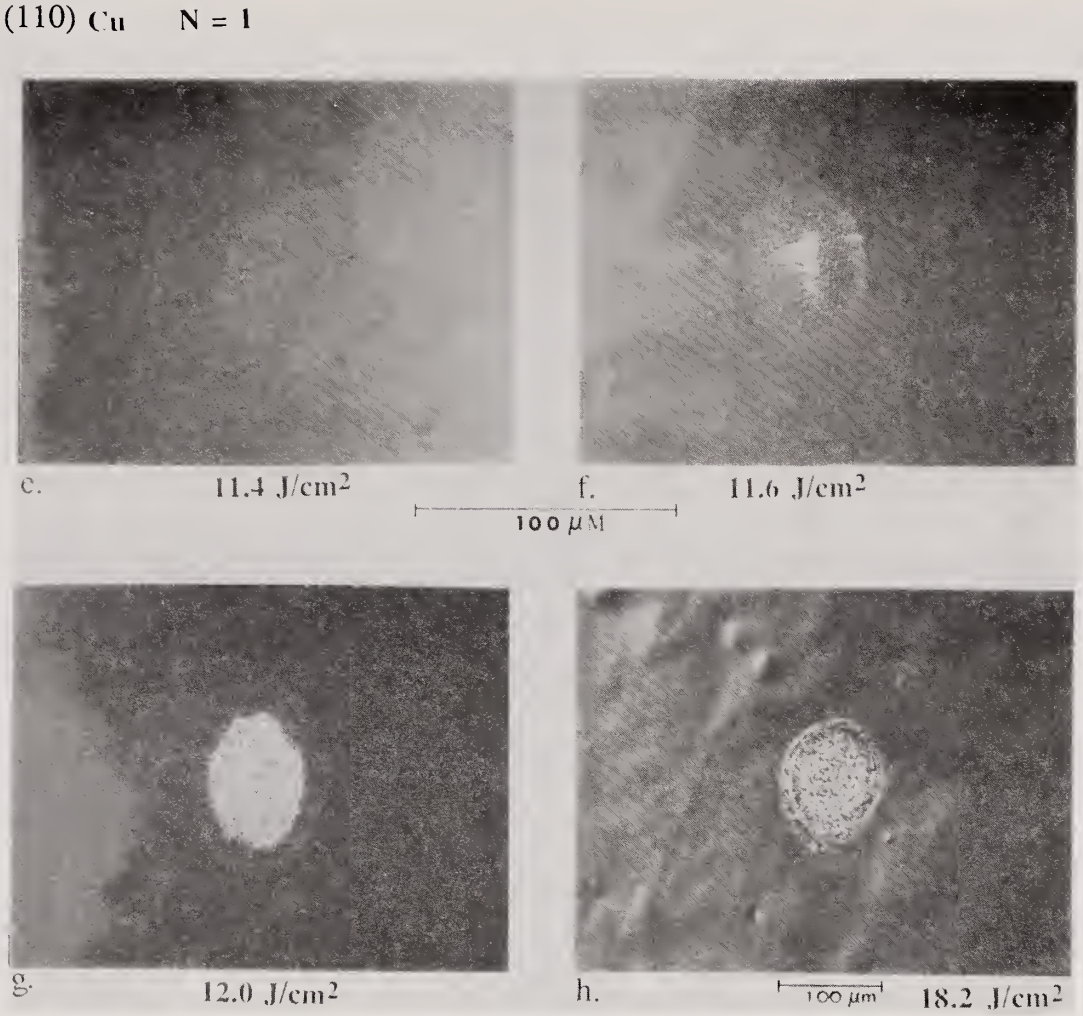

Figure 2. (Part 2) Nomarski micrographs of the single shot damage morphologies observed with increasing incident laser fluence on chemically-polished (110) copper surfaces. e) Flat-melting in the center area at 11.4 J/cm^2. f) The onset of boiling damage at 11.6 J/cm^2. g) Typical boiling damage morphology at 12.0 J/cm^2. h) Boiling damage at a higher fluence, 18.2 J/cm^2.

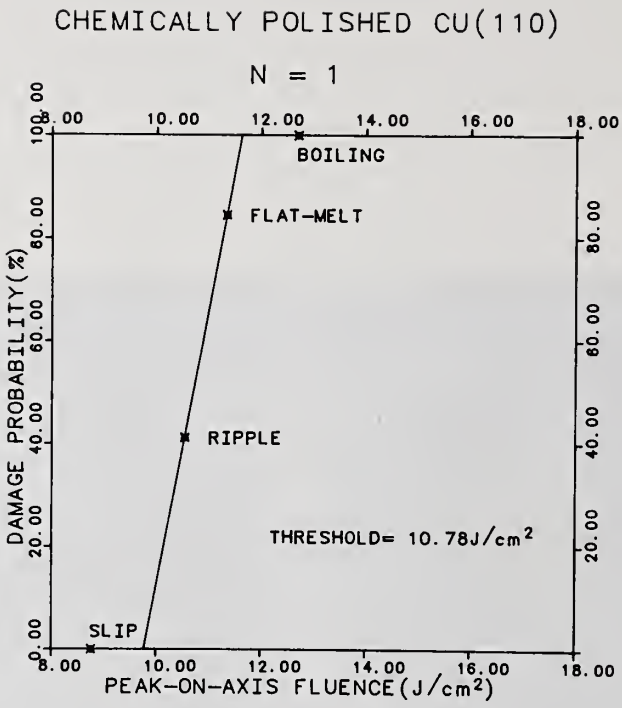

Figure 3. In this damage probability curve, the damage morphologies observed in Figure 2 are correlated with the damage probability curve of Figure 1. Labels indicate the onset fluence for each damage morphology.

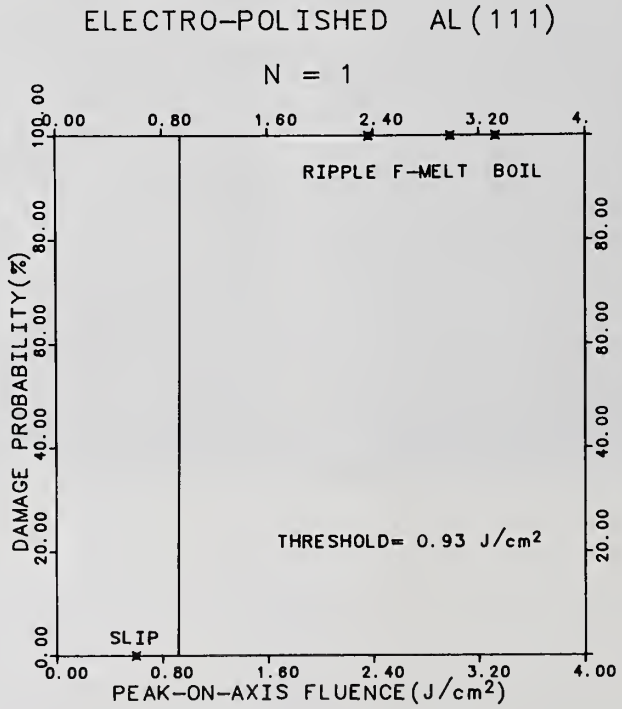

Figure 4. Damage probability curve of electro-polished (111) aluminum surfaces. Labels indicate the onset fluence of each morphology. The data points used to create the curve are omitted for clarity.

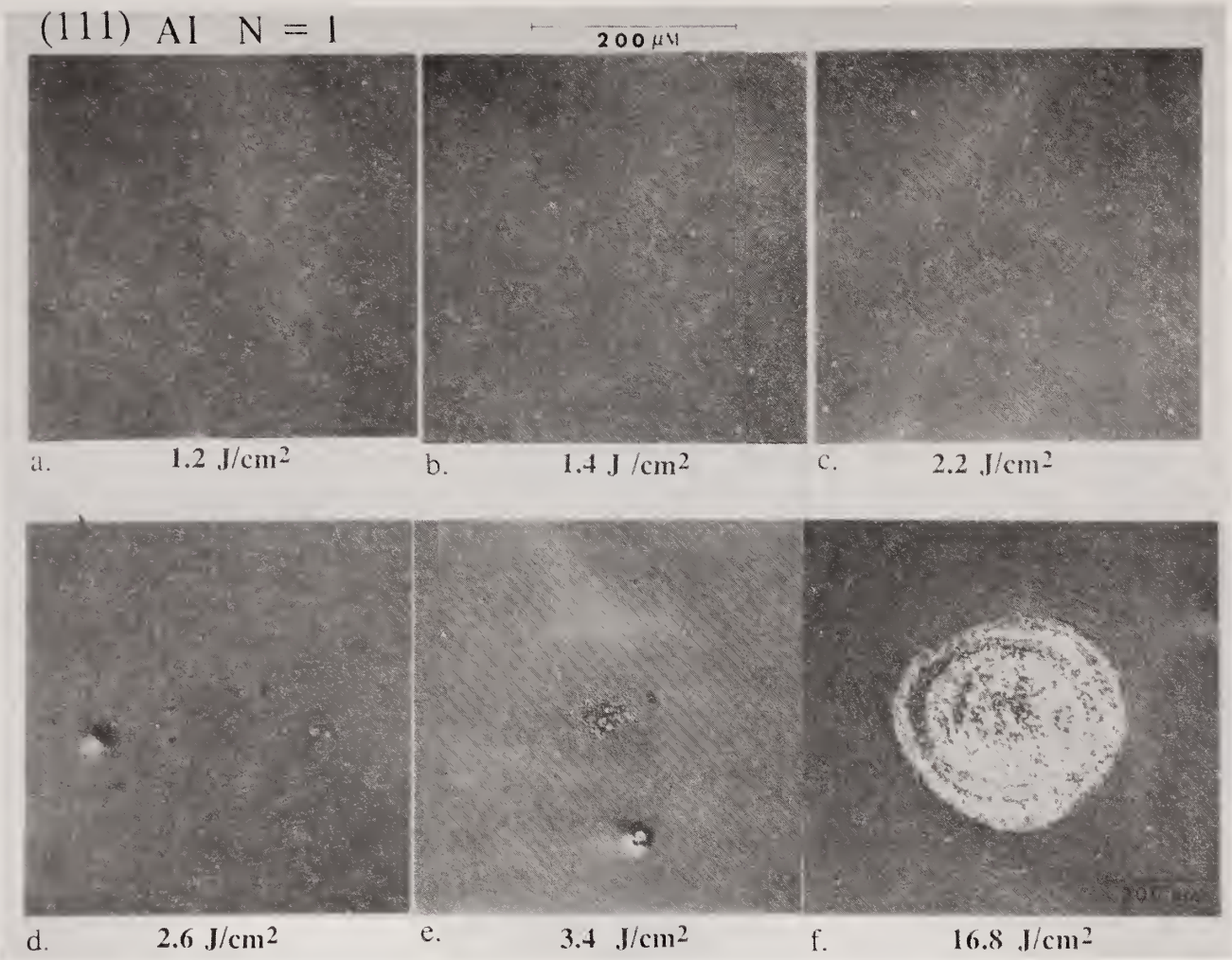

Figure 5. Nomarski micrographs of the single shot damage morphologies observed with increasing incident laser fluence on electro-polished (111) aluminum surfaces. a) Slip line formation at 1.2 J/cm^2. b) Slip line formation at 1.4 J/cm^2. c) Slip line formation at 2.2 J/cm^2. d) Ripple pattern formation at 2.5 J/cm^2. e) Boiling damage in the center area at 3.4 J/cm^2. f) A large boiling damage area and slip lines at 16.8 J/cm^2.

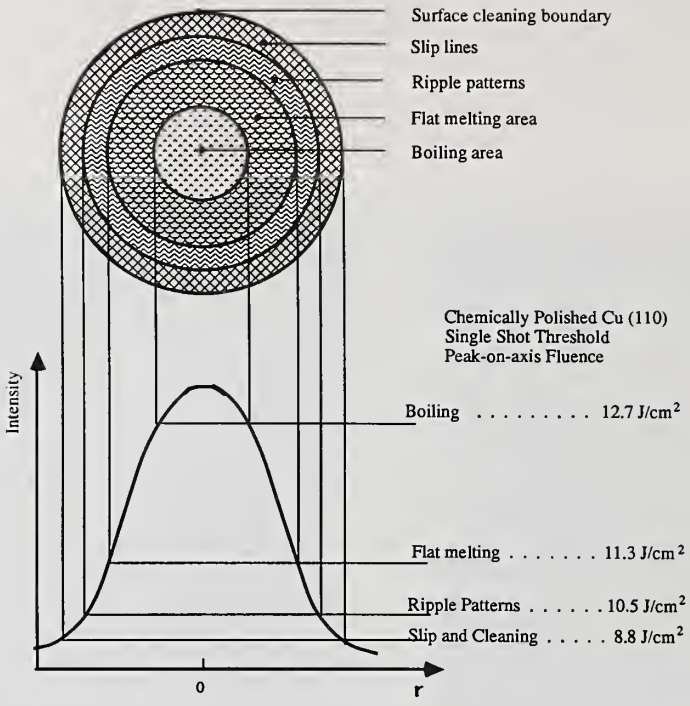

Figure 6. The single pulse damage morphologies are summarized in this diagram. As the incident laser energy fluence increases, surface-cleaning and slip-lines, ripple patterns, flat-melting, and boiling damage are generated in succession. The onset fluences for these damage morphologies are given for chemically-polished (110) copper surfaces.

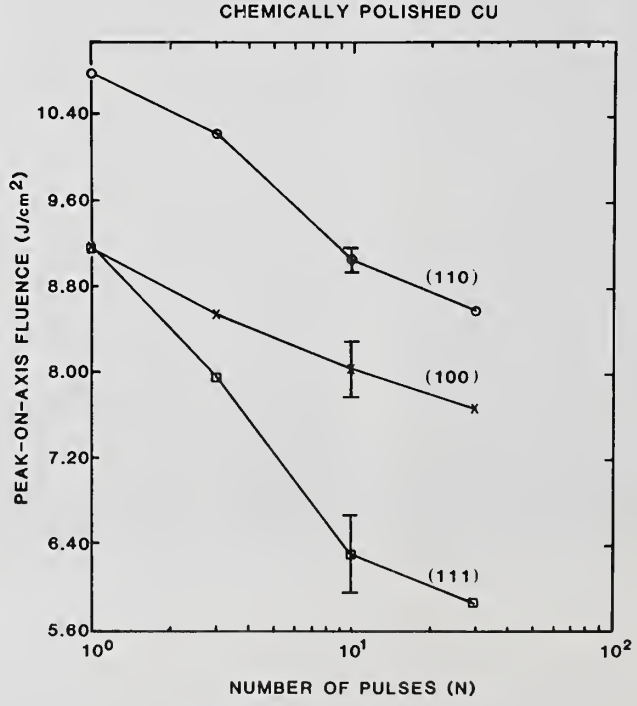

Figure 7. Damage fluence versus pulse number curves for the different crystallographic orientations of chemically-polished copper surfaces.

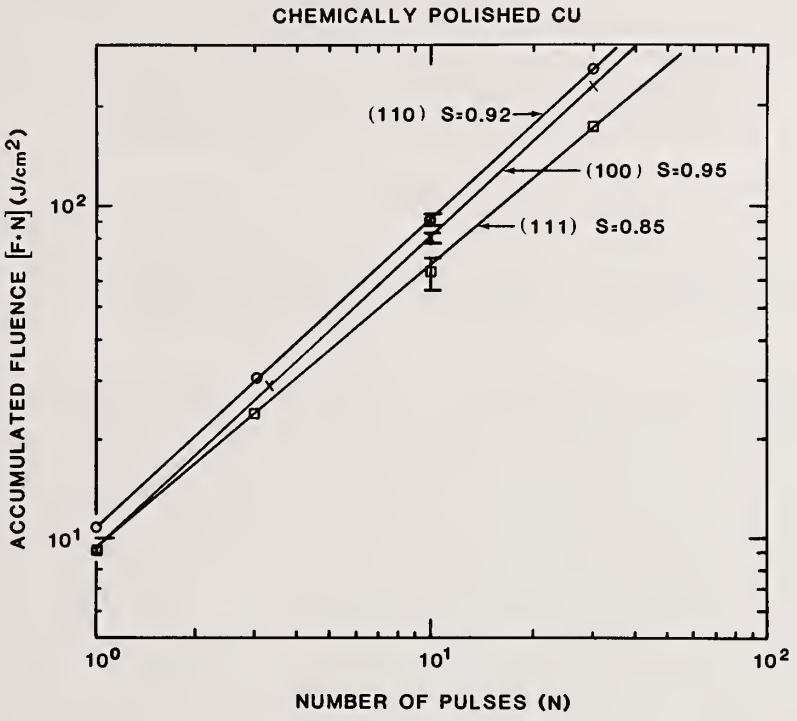

Figure 8. Accumulation curves replotted from Figure 7.

Manuscript Received
11-20-86

SCATTERING DISTRIBUTION FROM MULTILAYER MIRRORS - THEORETICAL RESEARCH OF A DESIGN FOR MINIMUM LOSSES

C. AMRA

Laboratoire d'Optique des Surfaces et des Couches Minces (Associé au C.N.R.S.- U.A. 1120)
Ecole Nationale Supérieure de Physique de Marseille
Domaine Universitaire de St Jérôme - 13397 Marseille Cedex 13 - France

The vector theory of light scattering from slightly rough surfaces allows a prediction in the whole space of the scattering distribution from a high-reflecting multilayer coating. A comparison with experimental results concerning classical quarterwave multidielectric coatings enables us to point out the influence of the initial substrate roughness and that of the fine microstructure of the materials used for the coating. Some results are presented for two materials (TiO_2, SiO_2), and we specify the consequences of the microstructure "grain size" for each one.

In order to reduce scattering losses, it is interesting to know if it is possible to use non-quarterwave multilayer stacks. A theoretical search for solutions leads us to study the consequences of a protective layer deposited on a classical mirror. The influence of the optical thickness of this layer is first studied. Then we examine the case where the top layers of the stack are non-quarterwave layers, so that the electric field associated with the stationary wave is reduced. We can show that, in some particular cases, the total integrated scattering is perceptibly reduced. Nevertheless, this result is only obtained when the roughnesses of the successive interfaces are not correlated. From an experimental point of view, it is not obvious that we can meet this condition whatever the spatial frequency of the defects, and this leads us to study the effect of the cross-correlation coefficient between interfaces.

Key Words: absorption; anti-scattering; cross-correlation functions; microstructure; multilayer mirror; roughness; scattering.

1. Introduction

At the present time, numerous studies are developed to improve the resistance of laser mirrors to high flux. We know that the damage threshold is largely connected with the absorption properties of the materials used to realize the multilayer coatings, together with the impurities and structure inhomogeneities of these materials |1|, |2|, |3|. Improving flux-resisting can be obtained by a lower absorption in some particular layers of the stack, and some authors |4|, |5| have already shown how the use of non-quarterwave layers in a multidielectric mirror allows absorption to be reduced in appreciable proportions.

Added to this intrinsic absorption which is connected with extinction coefficients of materials, there are also scattering losses that are due to surface and volume irregularities in the stack |6|. We are interested here in scattering from interface roughnesses in a multidielectric mirror, with the commonly admitted assumption that it is preponderant over scattering from volume irregularities |7|,|8|.

First, we will briefly present the theory we use |9| to interpret our experimental scattering curves, and for which we have shown |10| the equivalence with Elson's theory |11|. Concerning the apparatus used to measure the spatial distribution of scattered light in the whole space, a detailed description is given elsewhere |12|.

Starting from a carefully done comparison between theory and experiment, we determine the key parameters responsible for scattering in the case of a high reflecting multidielectric mirror. The origin of roughness and its associated cross-correlation coefficients are discussed, and we point out the influence of substrate defects and of material microstructure.

We then show how the methods used to reduce absorption |4| can equally be

applied to limit scattering under particular conditions related to the cross-correlation coefficients between the stack interfaces.

Finally, we try to generalize the "antiscattering effect" observed in the case of a single layer |13| to the case of a multidielectric mirror, that is to say that we modify the design of the coating in order to obtain destructive interferences between the scattered waves.

2. Scattering from a classical quarterwave multidielectric mirror

To the scale of a fraction of nanometer, surfaces and interfaces of a multidielectric stack are not perfectly flat, but must be considered as the result of the superposition of an infinite number of gratings. It has been shown that the effect of these roughnesses (quadratic mean heights of the interface defects) can be taken into account by introducing surface currents |9|, |11| on each of the interfaces.

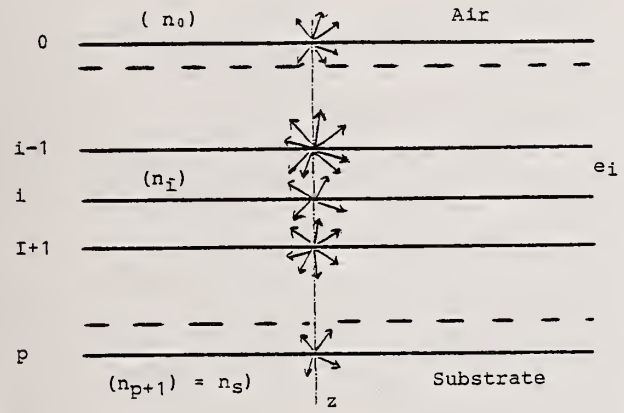

Figure 1: In the case of a multilayer stack, each rough interface is a source of scattered light.

Thus, when a multilayer mirror is illuminated by a monochromatic light, the electric field created in the stack excites the existing dipoles, and each rough interface becomes a source of scattering (fig. 1). The scattered intensity that can be measured at infinity in a particular direction (θ, ϕ) of the space then results from interference phenomena between these various scattering sources. The vector theory of Bousquet |9| gives for this scattered intensity the following expression:

$$I(\theta,\phi) = \sum_{i=1}^{p} |a_i|^2 \gamma_{ii} + \sum_{i \neq j} a_i \bar{a}_j \gamma_{ij} \qquad (1)$$

where p is the number of layers of the stack, and θ and ϕ characterize the scattering direction in the external medium (air) (fig. 2).

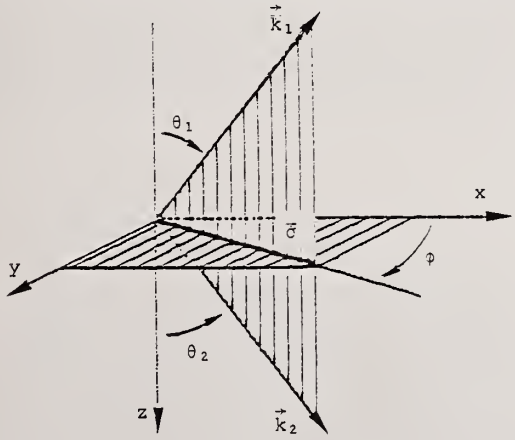

Figure 2: Definition of the scattered wave. (x,y) is the mean plan of the rough interface. θ_1 and θ_2 are the scattering angles on either side of the interface, in the polar scattering plane ϕ.

The a_i coefficients are called "ideal" coefficients because they do not depend on the statistical properties of the rough interfaces, but only on the indices and thicknesses of the layers, and on the illumination and observation conditions (wavelength, incidence and polarization). The roughness spectrum γ_{ii} contains all the information related to the defects of interface i; it is the Fourier transform of the autocorrelation function of the defects of this interface. Concerning the terms γ_{ij}, they measure a degree of similitude between interfaces (i) and (j) and take into account the coherence between the waves emitted by these interfaces.

For more precision, we can say that this coherence depends on the scattering

direction, and therefore on the spatial frequency which is concerned. Thus we can see that interpreting an experimental scattering curve is an extremely difficult problem, because the number of involved parameters is very high (5p+4 parameters for a stack of p layers if we approximate each spectrum with the help of two analytical functions |12|,|14|.

In the case of a classical quarterwave multidielectric mirror, this problem is slightly simplified by the fact that only two interfaces are responsible for practically all the scattering |15|.

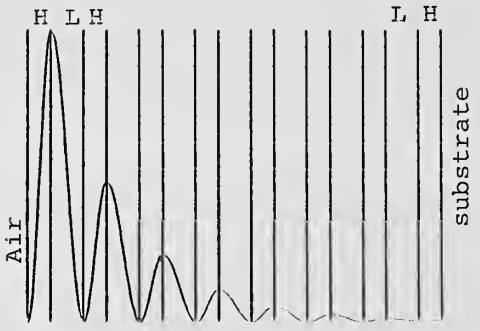

Figure 3: Distribution of the electric field intensity in a quarterwave multidielectric mirror.

Indeed, as shown in figure 3, the electric field exhibits significant maxima only on the first two odd interfaces. Since the ideal coefficients a_i in expression (1) are proportional to the excitating field, we can expect that scattering originates almost solely from the roughness irregularities of these two interfaces. Our numerical computing programs enabled us to verify that these two first odd interfaces were responsible for nearly 80% of the whole scattering whatever the cross-correlation laws between the various interfaces of the stack.

On figure 4, we have plotted a mean plane section of a scattering distribution measured on a mirror of 15 quarterwave SiO_2/TiO_2 layers illuminated by a He-Ne laser (λ = 0.6 nm). Though there are only two scattering interfaces, the problem of determining the parameters (roughnesses and cross-correlation coefficients) remains critical because it is not possible to separate the effects related to each of these two interfaces. We do not yet try to approximate this experimental curve with the help of our numerical computing programs because, as the whole scattering varies with a factor of two for two extreme values of the cross-correlation coefficient (0 and 1), we would find very different roughnesses according to the considered law. The following study will now permit us to remove this ambiguity.

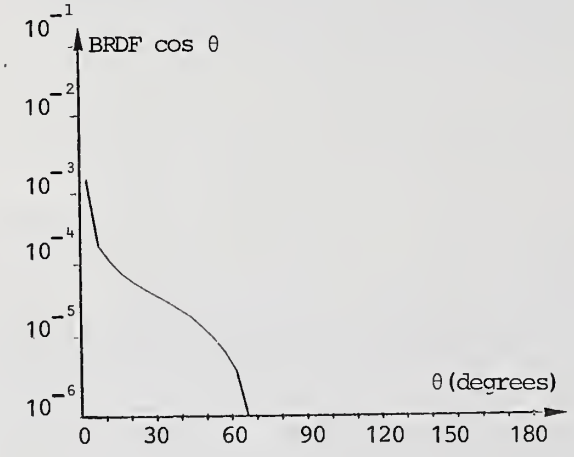

Figure 4: Mean plane section of an angular scattering curve measured from a 15 quarterwave TiO_2/SiO_2 layer mirror at wavelength λ = 0.6 nm (normal incidence). BRDF cos θ characterizes the scattered intensity per unit solid angle and per unit incident flux. The angular field (0° → 90°) corresponds to the half space of the specular reflection direction.

3. Comparison between theory and experiment for classical quarterwave multidielectric mirrors

It is obvious that the main difficulty in interpreting a scattering curve consists in separately determining the various parameters (roughnesses and cross-correlation laws) involved in scattering calculation |16|. Besides, these parameters are not really independent, because the cross-correlation laws depend on the origin of roughness. Indeed, roughness can be due to reproduction of the substrate defects by the evaporated layers, or to the size grain |13| which characterizes the material fine microstructure |17|. In the first case, we obtain a cross-correlation coefficient which is close to unity, while in the second one, the interfaces are not correlated *a priori*. This problem is not simple because the two phenomena may also coexist in different spatial frequency domains.

We demonstrate here that a good technique to investigate these parameters consists in covering the multidielectric stack with a thin opaque aluminum layer

(fig.5), that permits to eliminate scattering from all interfaces other than the top one, and thus to characterize this air-metal interface. For this, we have shown |17| that it was possible to control the evaporation conditions of aluminum in such a way that the metallic layer exactly reproduces the defects of the substrate, with an accuracy of a tenth of a nanometer in the whole range of measurable spatial frequencies.

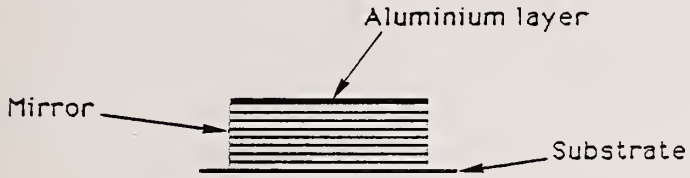

Figure 5: Deposition of a thin opaque aluminum layer on a multilayer mirror.

Then we can deduce that a roughness obtained from measurements of the scattered flux on the aluminized mirror is the same as the roughness of the top interface of the non aluminized mirror.

This technique of deposition of a thin metallic layer allows us to study the influence of the substrate defects on the roughness of the top interface of a mirror. For this purpose, we have produced two classical quarterwave multidielectric mirrors (TiO_2/SiO_2) with 15 layers, on two absorbing substrates of very different qualities, the roughnesses of which had been previously determined |12|. Results are given in Table 1.

	Sample	Top interface
δ_e, L_e	0.5 nm; 3000 nm	0.8 nm; 2500 nm
δ_g, L_g	< 0.5 nm	1.1 nm; 200 nm
δ_e, L_e	3 nm; 2000 nm	2.8 nm; 2000 nm
δ_g, L_g	0.5 nm; 180 nm	1 nm; 200 nm

Table 1: Influence of the substrate defects on the top interface roughness of a mirror. δ_e,L_e characterize roughness and correlation length for large period defects (scattering of small angles), while δ_g,L_g are related to short period defects |17|.

Concerning large period defects, we find for the top interface a roughness which is nearly the same as that of the bare substrate, both for the superpolished substrate and for the substrate of lower quality. This emphasizes the fact that high quality substrates must be used to obtain mirrors with very low scattering losses.

For short period defects, the roughness of the external interface is the same for the two mirrors, whatever the quality of the substrate. It is probably a residual roughness that is due to the grain size which characterizes the material microstructure, according that we have found for TiO_2 residual roughness a value of the same order of magnitude |13|.

Thus we can see that roughness originates from two different phenomena. It is now possible to investigate the cross-correlation laws between the mirror interfaces; on figure 6, we have plotted the experimental and theoretical angular scattering curves for the mirror produced on the superpolished substrate (Table 1). As for the calculated curves, we have supposed that all roughnesses were

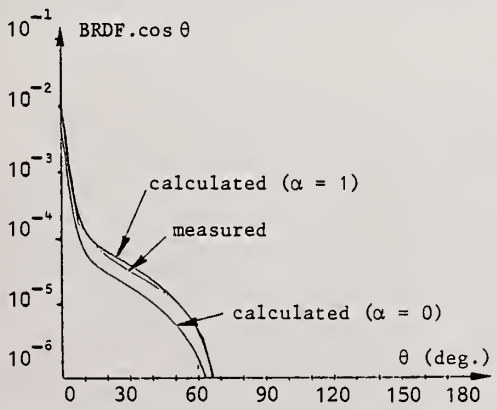

Figure 6: Comparison between theory and experiment in the case of a 15 TiO_2/SiO_2 layer mirror produced on an absorbing substrate, for two extreme values of the cross-correlation coefficients α. The value α = 1 leads to very good approximation of the experimental curve.

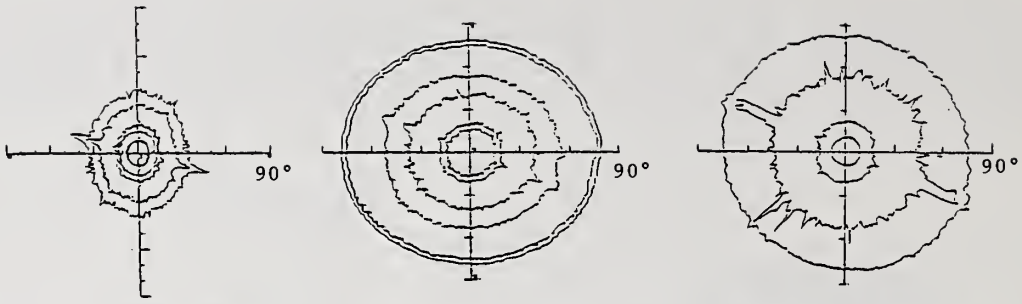

Figure 7: Anisotropy curves |9| of a substrate before coating, after coating (15 layers), and after deposition of aluminum on the coating.

identical to that of the mirror top interface (it is better to choose the roughness of the external interface rather than that of the substrate, since we have shown that, in the case of a mirror, the main part of scattering was due to the first two odd interfaces (fig.3), which are closer to the external interface than to the substrate). The excellent agreement we obtain between theory and experiment in the case where the cross-correlation coefficients are close to unity shows that the interface large period defects, which are responsible for most of the scattering, are perfectly correlated for this mirror.

Such a value for the cross-correlation coefficients is in good agreement with that obtained by Elson in |16|, where the top interface roughness was determined by means of a Talystep.

Finally, figure 7 shows that the substrate anisotropy is not modified even after deposition of fifteen layers.

4. Search for a design with minimal losses

An ideal solution to limit scattering obviously consists in an improvement of layer deposition techniques in order to obtain the finest microstructure for materials and interfaces as plane as possible. Scattering measurements are a precise mean for characterizing this microstructure and this roughness |13|.

But we can also look for the possibility of altering the multilayer design to obtain minimal scattering losses. For that, two solutions are possible |10|:

- the first solution consists in altering the distribution of the electric field, which is the source of scattering. Indeed, we can reduce the magnitude of the electric field at the classical mirror interfaces by addition of non-quarterwave layers on this mirror. This method has already been developed |4|,|5| to reduce absorption in some particular layers of the stack and to possibly increase the "damage" threshold.
- the second solution consists in trying to generalize the anti-scattering effect observed in the case of a single layer |13| to the case of a multidielectric mirror, that is in modifying the multilayer design in order to obtain destructive interferences between the scattered waves.

4.1. Reduction of the electric field at interfaces

Fig. 8 gives the configuration chosen to reduce the electric field at the mirror interfaces. On a classical quarterwave mirror M with reflectance R, two layers with phase thickness θ and ϕ are added so that we obtain a mirror M' with reflectance R'. The phase thickness θ of the first added layer (fig. 8a) is calculated in order to assign a condition such as $E_1 = aE_3$ ($a \leq 1$) between the fields at interfaces (1) and (3). This condition is only interesting in the case where the final value E_3 of the field in the new mirror M' (M' = M + 2 layers) is lower than the value of the maximal field in the classical mirror M taken separately. We can show that this is obtained if the reflectance of mirror M' is greater than that of mirror M, and for this reason we calculate the phase thickness ϕ of the second added layer (fig. 8b) in such a manner as to obtain maximal reflectance for mirror M'.

The values of θ and ϕ are given below; the analytical calculations are not

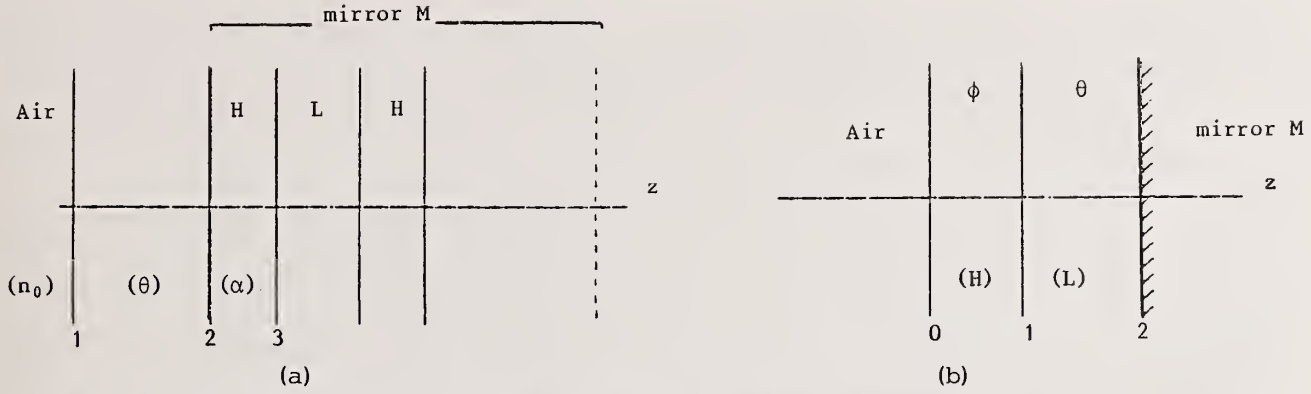

Figure 8: Addition of non-quarterwave layers on a classical mirror:
(a) - addition of a first layer to reduce the electric field at interfaces;
(b) - addition of a second layer to increase reflectance.

presented, since they are partly given in |4|, in the case where parameter a is given a value of 1. More complete calculations will be found in |10|.

$$\text{tg } 2\phi = \frac{r_1(f_1^2 - 1)\sin 2\theta}{f_1(1 + r_1^2) + r_1(1 + f_1^2)\cos 2\theta} \qquad \cos 2\theta = \frac{a^2 B - (1 + r_1^2)(1 + f_1)^2}{2r_1 (1 + f_1)^2}$$

with: $B = (1 + f_1 r_1)^2 + (r_1 + f_1)^2 + 2(1 + f_1 r_1)(r_1 + f_1)\cos 2\alpha$

and: $r_1 = \frac{r_M + r_{id}}{1 + r_M r_{id}}$, $r_{id} = \frac{n_L - n_0}{n_L + n_0}$, $f_1 = \frac{n_H - n_L}{n_H + n_L}$, $r_M = -\sqrt{R}$

where n_0, n_H and n_L are respectively the indices of the incident medium, of the high index and low index materials. In the case where a = 1, we obtain:

$$\cos 2\theta = \frac{1}{r_1(1 + f_1)^2}\{ -f_1(r_1 - 1)^2 + (1 + f_1 r_1)(f_1 + r_1)\cos 2\alpha \}$$

The term α represents the phase thickness of the top layer of the classical mirror, where its value is π/2. It is obvious that we can add as pairs of layers as we want, which requires a computing iteration, justifying thus the presence of this term ($\alpha \neq \pi/2$ after the first iteration; in other words, α is the initial value of φ).

Fig. 9 shows the field distribution in the case of a four layer addition. For two reasons, the values of θ and φ are chosen such as: $\pi/2 \leq \theta \leq \pi$ and $0 \leq \phi \leq \pi/2$. First, the maximum of the field has to be situated in the low index material |4|; secondly, it is necessary to obtain an amplitude reflection coefficient which is a negative number (zeroing the electric field on the first interface), so that supplementary scattering

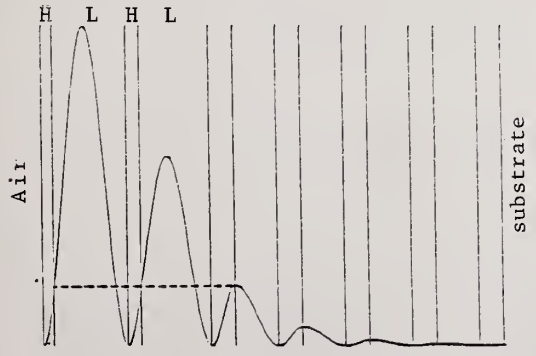

Figure 9: Distribution of the electric field in the case of a four layer addition, with:
$\pi/2 \leq \theta \leq \pi$ *and* $0 \leq \phi \leq \pi/2$, *and* $a = 1$.

interface would not be added (moreover, in this case, we would obtain R' < R).

Concerning the mirror damage mechanisms, and with the assumption that the damage threshold is correlated with the high value of the electric field at interfaces, the gain F relative to this threshold can be written as: $F = (1 - R)/(1 - R')$. Table 2 gives the value of this gain as a function of the number of added layers, in the case where a = 1.

	R	SI	F
mirror M (p = 9)	0.988	0.75	
M + one pair of layers (p=11)	0.993	1.4	1.7
M + 2 pairs of layers(p=13)	0.995	1.6	2.4

Table 2: Variation of the gain F with the number of added layers. F can be defined as the ratio between the maximal intensity of the interface electric field in the classical mirror M and that of the modified mirror M'. SI characterizes the value of the maximal field intensity in the volume of the stack.

Concerning now the value of the total integrated scattering, it is not obvious that it will be reduced, because scattering also depends on the relative influence of the admittances on the two sides of the scattering interface (it concerns the probability for a scattered photon to get out of the stack). We must use our numerical computation programs which give the results of Table 3, and then lead to the following conclusion: in the case of uncorrelated interfaces scattering decreases as the number of added layers increases. Whatever the polarization state of the incident light, the gain is about 30% with a pair of layers; with two pairs of layers, it is near 45%. Let us recall that the optical thicknesses of these layers were calculated to obtain a reflectance higher than that of the initial mirror.

	Uncorrelated case		Correlated case	
	Pol. S	Pol. P	Pol. S	Pol. P
classical mirror M (p = 9)	967 ppm	1042 ppm	1866 ppm	2107 ppm
M + one pair (p = 11)	672 ppm	750 ppm	1882 ppm	2185 ppm
M + 2 pairs (p = 13)	527 ppm	599 ppm	1927 ppm	2280 ppm

Table 3: Variation of the total integrated scattering with the number of added layers, for two polarization states of the incident light, and for two extreme values of the cross-correlation coefficient α. In the case α = 0, scattering is perceptibly reduced. (1 ppm = 10^{-6})

On the other hand, in the case of perfectly correlated interfaces, the shift of the electric field does not allow scattering to be reduced. Scattering slightly increases with the number of added layers, which is a limit to this method.

From an experimental point of view, we can wonder if it is possible to obtain uncorrelated interfaces. In the case of a mirror (see previous section), we showed that the substrate defects were reproduced over the whole stack, which occurs for large period defects. Then, eliminating large period defects (that is using substrates with roughnesses as slight as possible in this spatial frequency range) and controlling the evaporation conditions to obtain the finest microstructure, would possibly lead to uncorrelated interfaces.

We can note that we have used for the parameter a a value which is equal to unity; we will see later if it is possible to find an optimal value for this parameter, from a scattering point of view.

4. 2. Attempt to generalize anti-scattering effect

Until now, we have only given our attention to the means for reducing the source of scattered flux, without taking into account interference phenomena that occur between all the scattered waves. In the case of a single layer |13|, we have shown that it was possible to create destructive interferences between the waves scattered from the two interfaces of the layer, in order to reduce or even to annul

the whole scattering. Is it then possible, in the case of a multilayer mirror, to choose the layer indices or to modify the mirror design, in order to obtain analogous effects?

In a first approach, we tried to answer this question. Let us remark that interferences can only be obtained in the case where interfaces are correlated, which case we will consider here.

The first result we have achieved |10| is that the waves scattered from the various interfaces of a quarterwave multidielectric mirror (with an amplitude reflection coefficient $r < 0$) are all in phase on the top interface of the stack. Interferences are thus constructive and the whole scattering will increase as the cross-correlation coefficients are close to unity.

We have equally shown that adding an absentee half-wave layer slightly increases the whole scattering. This is not surprising, for two reasons: on the one hand, the half-wave layer does not modify the distribution of the electric field in the multilayer stack, nor thus the magnitude of the scattering sources. On the other hand, this layer is equally absent for the waves scattered in the neighborhood of the specular direction, which are responsible for the main part of the scattered flux.

Starting now from a mirror with an amplitude reflection coefficient $r > 0$ (fig. 10), it is possible to obtain destructive interferences. The waves emitted by interfaces 0 and 2 are in phase cancellation and give rise to annulment of scattering if their roughness ratio is given by:

$$\frac{\delta_0}{\delta_2} = \left(\frac{n_L}{n_H}\right)^2 \frac{n_H^2 - n_L^2}{n_L^2 - n_0^2}$$

Figure 10: Case of a mirror with a positive amplitude reflection coefficient.

Unfortunately, and contrary to the preceding mirror ($r < 0$), these two interfaces are responsible for only a small amount (20%) of scattering. We have equally considered the case where several half-wave layers are added on the mirror, in order to create new scattering interfaces, without obtaining any really interesting result.

Finally, let us specify that these results can be used for studying cross-correlation laws: in the uncorrelated case, the mirror with $r > 0$ has a total integrated scattering seven times higher than that of the mirror with $r < 0$ ($n_H = 2.26$ and $n_L = 1.47$) while the scattering of these mirrors are nearly the same in the case of a perfect correlation.

5. Conclusion

Scattering losses are very complex to investigate, since it is difficult to have a separate access to roughnesses and to cross-correlation laws existing between multilayer stack interfaces. We have shown that the technique of deposition of a thin opaque aluminum layer constituted an excellent method to determine these parameters. It permitted us to show that the material microstructure and the substrate quality were both responsible for the roughnesses of the various stack interfaces.

The search for a filter design leading to minimal scattering losses is not a problem easy to solve, because the solutions depend on the considered cross-correlation laws. In the case of uncorrelated interfaces, adding non-quarterwave layers on a classical mirror allows an important reduction of scattering together with an increase in reflectance. This method is all the more interesting as it equally permits to reduce absorption in some particular layers of the stack and thus to improve the resistance to intense flux. Optimizing some parameters will be the subject of a further study.

Concerning the generalization of the anti-scattering effect to the case of a multilayer mirror, it does not seem possible *a priori*. Nevertheless, it can present more interest for studying cross-correlation laws.

References

1 A.J. Glass and A.H. Guenther, Laser induced damage in optical materials: 8th ASTM Symposium, Applied Optics, 16,(5), 1214-1231, (1977)

2 Thomas W. Walker, Arthur H. Guenther, Fellow, IEEE, and Philip E. Nielsen, Pulsed Laser - Induced Damage to Thin Film Optical Coatings - Part I: Experimental, IEEE Journal of Quantum Electronics, vol. QE 17, n° 10 (1981)

3 Arthur H. Guenther, Thomas W. Humpherys, Physical aspects of laser - induced damage of optical coatings, Proceedings of SPIE, Thin Film Technologies, 401, 247-256, (1983)

4 Joseph H. Apfel, Optical coating design with reduced electric field intensity, Applied Optics, 16, (7), 1880-1885, (1977)

5 C. K. Carniglia and Joseph H. Apfel, Maximum reflectance of multilayer dielectric mirrors in the presence of slight absorption, J. Opt. Soc. Am., 70, (5), 523-534, (1980)

6 H.E. Bennett and D.K. Burge, Simple expressions for predicting the effect of volume and interface absorption and of scattering in high-reflectance or antireflectance multilayer coatings, J. Opt. Soc. Am., 70, (3), 268-276, (1980)

7 H.E. Bennett, and J.O. Porteus, Relation between surface roughness and specular reflectance at Normal Incidence, J. Opt. Soc. Am., 51, 123, (1961)

8 J. Ebert, H. Pannhorst, H. Küster and H. Welling, Scatter losses of broadband interference coatings, Applied Optics, 18, 818-822, (1979)

9 P. Bousquet, F. Flory, and P. Roche, Scattering from Multilayer Thin Films: Theory and experiment, J. Opt. Soc. Am., 71, 1115, (1981)

10 C. Amra, Développement et comparaison de deux théories vectorielles de la diffusion de la lumière par des surfaces peu rugueuses. Application à l'étude des surfaces et des empilements de couches., Thèse de Doctorat d'Etat, Université d'Aix - Marseille III, 1986

11 J.M. Elson, Angle-resolved light scattering from composite optical surfaces, Proc. Soc. Photo.Opt.Instrum. E, 240, 296-305, (1980)

12 P. Roche and E. Pelletier, Characterizations of optical surfaces by measurement of scattering distribution, Applied Optics, 23, (20), 3561-3566, (1984)

13 C. Amra, G. Albrand and P. Roche, Theory and application of antiscattering single layers: antiscattering antireflection coatings, Applied Optics, 25,(16), 2695-2702, (1986)

14 J.M. Elson, J.P. Rahn and J.M. Bennett, Relationship of the total integrated scattering from multilayer-coated optics to angle of incidence, polarization, correlation length, and roughness cross-correlation properties, Applied Optics, 22, (20), (1983)

15 J. Garcin, Diffusion de la lumière: étude expérimentale et représentation théorique des rugosités des interfaces de filtres multidiélectriques., Thèse de Docteur-Ingénieur, Université d'Aix-Marseille III, 1982

16 J.M. Elson, J.P. Rahn and J.M. Bennett, Light scattering from multilayer optics: comparison of theory and experiment, Applied Optics, 19, (5), 669-679, (1980)

17 P. Roche, C. Amra, E. Pelletier, Measurement of scattering distribution for characterization of the roughness of coated or uncoated substrates.,Third Int. Symposium on Optical and Optoelectronic Applied Sciences and Engineering, Innsbruck 14-18 April 1986, To be published in SPIE Proceedings.

Manuscript Received
2-12-88

Initiation of Laser Induced Damage by Small Metallic Particles

W. Becker*, J. K. McIver*, and A. H. Guenther**

*Center for Advanced Studies, and Dept. of Physics and Astronomy
University of New Mexico, Albuquerque, NM 87131 and
**Air Force Weapons Laboratory, Kirtland Air Force Base, NM 87117

Laser induced damage in a dielectric material is triggered by the presence of a sufficient number of electrons in the conduction band. When these are accelerated by the laser field with phonon assistance, they can lead to an electron avalanche and, in turn, may initiate permanent detectable damage. We have investigated the precondition of the electron avalanche model, i.e. the initial creation of electrons in the conduction band. We assume the presence of small metallic inclusions ($r \sim 10$ to $100\mathring{A}$) in the dielectric which we model by infinitely deep one-dimensional square well potentials. The dynamics of such a model are known to be chaotic if the laser field exceeds a certain threshold value. Under these conditions an electron can gain enough energy to bridge the gap between the valence band and the conduction band. The present model yields threshold fields associated with intensities of the order of $10^{10} W/cm^2$. Unfortunately, the dependence on the wavelength is complicated, however, a threshold value exists for that wavelength above which no damage occurs no matter how strong the field is.

Key words: laser induced damage, metallic particles, chaos

The process of absorption that leads to laser induced damage to dielectrics is usually perceived as proceeding in two steps. In the first step, the laser field brings an electron (in fact, several electrons, but comparatively few) into the otherwise empty conduction band of the dielectric. In the second step, the laser field assisted by phonons accelerates the electron from the bottom to the top of the conduction band. If the gap between the conduction and the valence band is small enough the electron may then fall back down to the bottom of the conduction band and in this process lift a second electron to the bottom of the conduction band. This process may then rapidly lead to an electron avalanche and, in turn, to observable damage of the material. Neither step is fully understood. It is, however, the first one that is considered as the foremost problem, that is to identify a process which is able to generate quickly a sufficient number of electrons in the conduction band in order to begin the avalanche. It is this specific problem that we will address in this paper.

The mechanism that is nearest at hand, namely to bridge the gap between the valence band and the conduction band solely by multiphoton absorption, has been shown to fail in providing enough electrons during the pulse length of the laser field, for the moderate field strengths at which damage is known to occur [1]. There is now fairly general agreement that electrons in the conduction band are not created uniformly throughout the dielectric. One possible mechanism relies on the presence of isolated, small metallic inclusions having a diameter of 20 to 200 Å. However, this assumption by itself does not solve the problem either. On the contrary, various previous investigations [2] have yielded wildly conflicting results with respect to both the detailed mechanism that allows electrons inside the metallic inclusion to gain enough energy from the laser field as well as the orders of magnitude and scaling laws that govern the process. There is not even agreement about whether the process is classical or quantum mechanical in nature.

We assume that the nature of the metallic inclusion is such that the conduction band of the metal provides access to the empty conduction band of the dielectric. The electrons in the inclusions may then be modeled as independent electrons in an infinitely deep square well potential, the simplest version being one-dimensional. The problem then boils down to the question of whether or not an electron can gain from the laser field an energy corresponding at least to the difference between the bottom of the conduction band and the top of

the valence band. In the absence of phonon assistance an affirmative answer is by no means obvious. On the contrary, it appears to be unlikely. To investigate this question we will adopt a classical description.

In the absence of the reflecting walls of the potential, the electron energy in the laser field, E_{field}, oscillates about a value that is shifted versus its energy E_{free} outside the field only by the small $\vec{A}^2$ term ($\vec{A} = \vec{A}(t)$ being the vector potential of the laser field), i.e. the average satisfies

$$\langle E_{\text{field}} \rangle = E_{\text{free}} + \frac{e^2 \langle \vec{A}^2 \rangle}{2mc^2}. \tag{1}$$

The $\vec{A}^2$ term is much too small to account for the necessary energy gain. The presence of the walls changes the situation inasmuch as the electron may now be accelerated over several periods of the laser field if it happens to collide with the walls at about the time when the laser field goes through zero. For a one-dimensional square well potential of diameter 2a, a necessary condition for this to occur is that the electron's round trip time $T(= 4a/v$ with v denoting its velocity) equal an odd integer number of periods $\tau(= 2\pi/\omega$ with ω the frequency of the laser field), viz.

$$T = (2n+1)\tau \quad (n = 0, 1, 2 \ldots) \tag{2}$$

This will be referred to as the resonance condition. Here it has been assumed that the laser field is weak enough for the electron's round trip time T or velocity v to be essentially constant. If the electron experiences a significant acceleration this is, of course, not the case and the electron will soon be off resonance. A rough estimate then suggests that again the electron energy gain is too limited to play the desired role. The same conclusion is borne out by a quantum mechanical calculation based on first order perturbation theory.

It has turned out, however, that the preceding conclusion is not totally justified. This arises from the recent observation [3] that the classical motion in the one-dimensional square well potential is chaotic so that individual electron trajectories may exhibit significant energy gain once the laser field exceeds a certain threshold value. Let us first summarize these results and then apply them to the problem of interest. The Hamiltonian governing the motion of the electron in the absence of the laser field is

$$H_0 = \frac{p^2}{2m} + b(\theta(x-a) + \theta(-x-a)) \tag{3}$$

where $b \to \infty$ and $\theta(x) = 0$ for $x < 0$ and 1 for $x > 0$. A typical trajectory (with the initial conditions $x(0) = -a$, $v(0) = v = \sqrt{2E_0/m}$) is

$$x(t) = (-)^{i+1}(2n+1)a + (-)^i vt, \quad \left(\frac{2ia}{v} \le t \le \frac{2(i+1)a}{v}\right). \tag{4}$$

We can introduce action and angle variables I and ϑ by a canonical transformation

$$I = \frac{1}{2\pi}\oint p\,dx = \frac{2a}{\pi}\sqrt{2mE_0}, \tag{5}$$

where $H = E_0 = \text{const}$, and

$$\vartheta = \sqrt{\frac{2E_0}{m}}\,\frac{\pi t}{2a}, \tag{6}$$

so that

$$H_0 = \frac{\pi^2 I^2}{8ma^2} \tag{7}$$

In the presence of the laser field the Hamiltonian is

$$H = H_0 + e\epsilon x \, sin\omega t, \tag{8}$$

or, after the canonical transformation (5), (6) has been performed,

$$H = \frac{\pi^2 I^2}{8ma^2} - \frac{4e\epsilon a}{\pi^2} \sum_{n=-\infty}^{\infty} \frac{1}{(2n+1)^2} \sin[(2n+1)\vartheta - \omega t]. \tag{9}$$

In transforming the interaction term, $x(t)$ has been expressed in terms of the angle variable ϑ and expanded in a Fourier series. The interaction term is seen to be resonant if

$$(2n+1)\frac{d\vartheta}{dt} = (2n+1)\frac{\pi}{2a}\sqrt{\frac{2E_0}{m}} = \omega, \tag{10}$$

which agrees with the previously derived resonance condition (2).

If the electron starts with a velocity near one of the resonant values given by Eq. (10) (or Eq. (2)) for a particular n and such that it is reflected off the wall at a time when the field goes through zero, it will gain energy for several periods of the field. However, as long as the field strength is below some threshold value (to be determined below), the electron will sooner or later get out of phase and will never reach the energy corresponding to the next highest resonance numbered by $n-1$. This is a consequence of the Kolmogorov-Arnold-Moser (KAM) theorem [4] which says that within some neighborhood of $\epsilon = 0$ the different resonance zones numbered by the integer n are separated by invariant tori in phase space called KAM-surfaces. These surfaces in three-dimensional phase space (x, p, and t) are made up of particle trajectories. Hence, they cannot be intersected by any other trajectories and, consequently, provide insurmountable barriers between different resonance zones. The KAM-surfaces between adjacent resonance zones are destroyed when the field increases. For some value of the field the last KAM-surface between the resonance zones numbered by n and $n-1$ has been destroyed. In the present case this can be shown to imply that all KAM-surfaces in between resonance zones numbered by integers higher than n have already been destroyed earlier. The particle is then free to diffuse in phase space from a velocity of zero up to the $(n-1)$st resonance zone. The motion in this part of phase space is chaotic.

It is not difficult to understand the phenomenon outlined above in a semiquantitative way. The particle trajectories generated by the Hamiltonian (8) are ($i = 0, 1, 2, \ldots$)

$$x^{(i)}(t) = -\frac{e\epsilon}{m\omega^2}(\sin\omega t - \sin\omega t_i) + (v_i + \frac{e\epsilon}{m\omega}\cos\omega t_i)(t - t_i) - (-)^i a, \tag{11}$$

$$v^{(i)}(t) = -\frac{e\epsilon}{m\omega}(\cos\omega t - \cos\omega t_i) + v_i, \tag{12}$$

for $t_{i+1} \geq t \geq t_i$. Here $v_i = v^{(i)}(t_i)$ and the particle starts at time $t = t_0$ at the left wall, i.e., $x^{(0)}(t_0) = -a$. The time t_{i+1} at which the electron bounces off the wall has to be determined from the trigonometric equation

$$2a(-)^i = -\frac{e\epsilon}{m\omega^2}(\sin\omega t_{i+1} - \sin\omega t_i) + (v_i + \frac{e\epsilon}{m\omega}\cos\omega t_i)(t_{i+1} - t_i), \tag{13}$$

in terms of t_i and v_i. Then

$$v_{i+1} = -v_i(t_{i+1}) = -v_i + \frac{e\epsilon}{m\omega}(\cos\omega t_{i+1} - \cos\omega t_i). \tag{14}$$

Suppose the particle starts at time $t_0 = 0$ from the left wall such that it is at the center of the n-th resonance zone, i.e. when it reaches the right wall it has traveled through exactly $2n+1$ half periods of the field. Further, suppose that during this first half round trip it has been accelerated so much that on the way back it travels through exactly $2n-1$ half periods of the field. If this is the case the particle has worked its way from the n-th to the $(n-1)$st resonance zone. From Eqs. (13) and (14) we get the conditions

$$2a = (v_0 + \frac{e\epsilon}{m\omega})\frac{(2n+1)\pi}{\omega},$$

$$-2a = (v_i - \frac{e\epsilon}{m\omega})\frac{(2n-1)\pi}{\omega},$$

$$v_1 = -v_0 - \frac{2e\epsilon}{m\omega},$$

$$v_2 = -v_1 + \frac{2e\epsilon}{m\omega},$$

with the solution

$$v_0 \equiv v_{0,n} = \frac{4a\omega}{\pi}\frac{3(n-1)}{4n^2-1}, \tag{15}$$

$$\frac{e\epsilon}{am\omega^2} = \frac{2}{\pi(4n^2-1)} \equiv \frac{e\epsilon_n}{am\omega^2}, \tag{16}$$

$$v_2 \equiv v_{2,n} = \frac{4a\omega}{\pi}\frac{3n-1}{4n^2-1}. \tag{17}$$

Equation (16) constitutes a very crude estimate of the field strength ϵ_n which is necessary to cause breakdown between the n-th and $(n-1)$st resonance zone. The actual field strength which is required for this purpose will turn out to be significantly lower. However, Eq.(16) gives the correct order of magnitude and scaling laws. It also shows that

$$\epsilon_n > \epsilon_m \quad \text{for} \quad m > n, \tag{18}$$

i.e. if breakdown has occurred between the n-th and $(n-1)$st zone it has already occurred between all zones with $m > n$. One may also note the order of magnitude agreement between v_0 as given by Eq. (15) and Eq. (10) (the latter giving $v_0 = (4a\omega/\pi)(1/2(2n+1))$). Of course, the present simple model must not be overextended. For example, since $v_{2,n} \neq v_{0,n-1}$, it seems to preclude motion of the particle over more than one zone. This is, in fact, perfectly well possible owing to the chaotic character of the motion once the KAM-surfaces have been destroyed.

A more accurate estimate of the breakdown field strength ϵ_n is provided by the so-called overlap criterion [6]. In the present case of the square well potential, an apparently exact estimate can be obtained by renormalization group methods [7]. From Ref. 7 it can be deduced that the field strength ϵ_n for which breakdown between the n-th and $(n-1)$st resonance zone sets in is given by

$$\frac{e\epsilon_n}{am\omega^2} = \frac{X_n^2}{(2n+1)^2}, \tag{19}$$

where $X_1 \cong 0.54$, $X_2 \cong 0.46$, $X_3 \cong 0.44$, $X_4 \cong 0.42$ and $\lim_{n\to\infty} X_n \cong 0.34$. For $n = 1$ and $n = 2$ these values agree with numerical experiments [3] within the accuracy of the latter. The fields ϵ_n determined from Eq. (19) are lower than those obtained from Eq. (16) by a factor of about five.

In order to compare these results with available experimental data we first have to choose some energy E_c given by the bottom of the conduction band which the electron is to reach. If this energy E_c is situated in the n-th resonance zone the laser field must be strong enough so that the n-th zone has become accessible, i.e. the laser field strength ϵ must exceed ϵ_{n+1}. For the determination of the breakdown field ϵ_{n+1} the initial electron energy is unimportant (as long as it is not already in the same zone to begin with), i.e. the Fermi energy of the dielectric plays no role at this stage. As a rough estimate we may assume, guided by Eq. (10), that the n-th resonance zone extends over all electron energies E_0 which are bounded according to

$$\frac{1}{2(n+1)} \leq \frac{\pi}{2a\omega}\sqrt{\frac{2E_0}{m}} \leq \frac{1}{2n}. \tag{20}$$

For $n = 0$, the upper limit is infinity. Equation (20) can be rewritten

$$n \leq \frac{a}{\lambda} 10^3 \left(E_0[eV]\right)^{-\frac{1}{2}} \leq n+1, \tag{21}$$

with $\lambda = 2\pi c/\omega$ the laser wavelength. For example, for $a = 100\mathring{A}$, $\lambda = 1.06\mu m$, and $E_c = 8eV$, the third zone must be accessible ($n = 3$), and from Eq. (19) the required field is $E_4 = 3.9 \times 10^6 V/cm$. A more convenient form of Eq. (19) is

$$\epsilon_n[\text{Volt/cm}] = 2 \times 10^7 \frac{a[\mathring{A}]}{\lambda[\mu m]^2} \frac{X_n^2}{(2n+1)^2} \tag{22}$$

The corresponding average intensity is

$$S_n[W/cm^2] = c\epsilon_0 \epsilon_n^2 \langle \cos^2 \omega t \rangle = 5.3 \times 10^{11} \frac{a^2[\mathring{A}]}{\lambda^4[\mu m]} \frac{X_n^4}{(2n+1)^4} \tag{23}$$

which for the given example yields $S_4 = 2. \times 10^{10} W/cm^2$.

The dependence of the breakdown field on its parameters E_c, a, and λ is quite complicated because first the applicable resonance zone has to be determined from Eq. (21) before Eqs. (22) or (23) can be used to evaluate the respective breakdown field or intensity. The discreteness of the number designating the resonance zone gives rise to discontinuities in the breakdown field. In Fig. 1 the breakdown intensity is plotted for $a = 100\mathring{A}$ and $E_c = 8eV$ as a function of λ for $1.3 > \lambda > 0.4$. For $\lambda = 1.3$, E_c is situated in the second resonance zone, while for $\lambda = 0.4$ it has moved down to the eight zone. The plot is dominated by the discontinuities which occur when E_c as a function of λ moves from one zone to the next. For increasing n(decreasing λ) the zone changes occur more and more rapidly. For $n \gg 1$ we may then neglect the difference

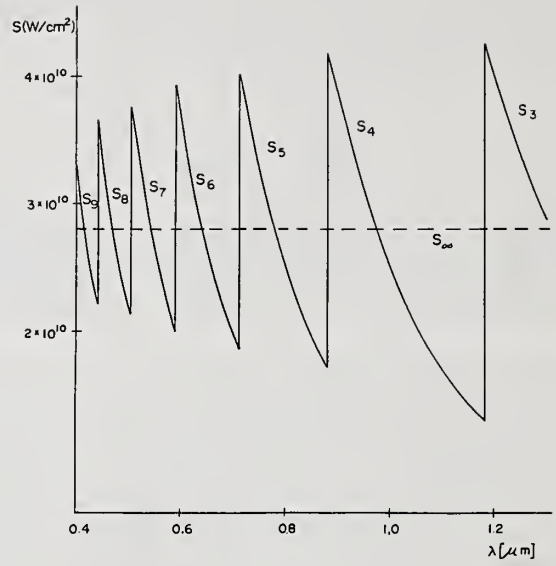

Figure 1. The intensity $S[W/cm^2]$ at which the bottom of the conduction band (assumed at $E_c = 8eV$) becomes accessible by stochastic diffusion in phase space, is plotted versus the wavelength $\lambda[\mu m]$ of the laser field for $0.4 < \lambda < 1.3$. The diameter of the one-dimensional metallic inclusion is $a = 100\mathring{A}$. The designation S_n of a segment of the curve means that the $(n-1)$'st resonance has become accessible.

between n and $n+1$ and use Eq. (21) to eliminate n from Eqs. (22) and (23). This yields the short wavelength limit

$$S_\infty\,[W/cm^2] = \lim_{n\to\infty} S_n = 4.4 \times 10^{12}\,\frac{E_0^2[eV]}{a^2[\mathring{A}]}. \tag{24}$$

which is independent of λ. In obtaining Eq. (24) the value of X_∞ has been used. The values of the breakdown intensity as a function of λ are spread around S_∞ with the fluctuations decreasing with decreasing λ. For increasing wavelength λ the energy E_c finally comes to be situated in the zeroth zone $n = 0$, and it would appear from Eq. (23) that now $S = S_1 \sim \lambda^{-4}$ for $\lambda \to \infty$, i.e. the breakdown field would become arbitrarily small. This is certainly not the case, in fact, the opposite is likely to happen. This is strongly suggested by the semiquantitative argument given above (starting with Eqs. (11) and (12)) in order to explain the existence of breakdown. Breakdown is possible since the electron on its way from left to right may travel through exactly $(2n+1)$ half periods of the field and, if the latter is strong enough, may be accelerated so much that on its way back from right to left it now travels through exactly $(2n-1)$ half periods so that again it experiences a net acceleration. Obviously, this mechanism only works up to $n = 0$. After that, there is no way the electron can remain on resonance for many periods and indefinitely increase its energy. Hence it appears that the zeroth zone, for energies sufficiently far above the resonance $n = 0$, i.e. for

$$E_0 > \frac{m}{2}\left(\frac{2a\omega}{\pi}\right)^2 \tag{25}$$

from Eq. (10), will always remain deterministic no matter how strong the applied laser field is. Thus Eq. (25) implies the existence of a cutoff wavelength λ_c such that for

$$\lambda \tilde{>} \lambda_c = 2a\sqrt{\frac{2mc^2}{E_0}} = 2 \times 10^3\, a\,(E_0[eV])^{-\frac{1}{2}} \tag{26}$$

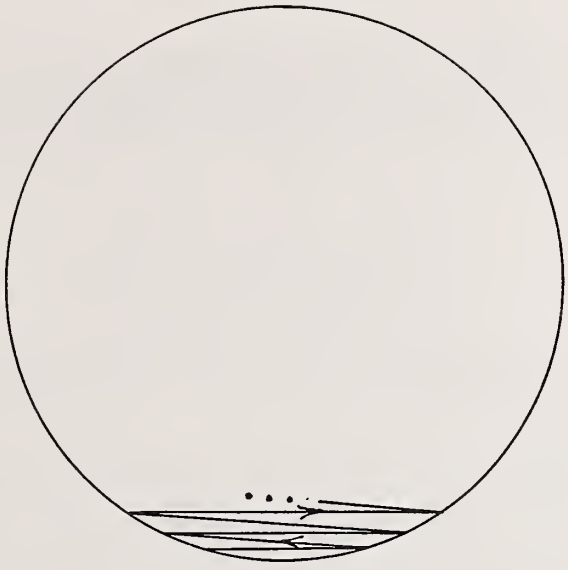

Figure 2. A possible trajectory for a cylindrical inclusion in the case of diffuse reflection.

even an arbitrarily strong field will never succeed in lifting an electron into the conduction band. For the situation discussed above ($a = 100\mathring{A}$, $E = 8eV$) we have $\lambda_c = 7.1\mu m$. This must be considered as an order of magnitude estimate only; the exact value could only be determined by numerical calculation.

There is no *a priori* justification in identifying the breakdown fields evaluated above with the experimentally observed damage thresholds. However, in principle, the former should provide lower limits for the latter. Our present results are not in agreement with experimental data [7] in two respects: first, the experimental damage thresholds at $\lambda = 1.06\mu m$ are of the order of a few $10^9 W/cm^2$. Our results rather than providing lower limits are about one order of magnitude larger. Second, the data uniformly exhibit a decrease of the damage threshold with decreasing wavelength that is at least linear. In contrast, our model on the average does not show any frequency dependence (as long as the wavelength stays below the cutoff wavelength λ_c, Eq. (26)). The sawtooth shape of the curve giving the breakdown intensity S as a function of λ in Fig. 1 does allow for a decrease of S for particular values of $\lambda(\lambda = 1.06m, 0.53m, 0.26m)$, but, of course, it allows equally well for increases which have not been observed in a single case.

The feature of our model that one is most likely to fault for its deficiencies is its one-dimensionality. There are good reasons to believe that a more realistic model in two or three dimensions will significantly lower the breakdown intensity; in particular, there are two reasons: first, in the case of a two or three-dimensional inclusion it is possible for the electron to remain in resonance with the field over many round trips, because for certain orbits the round trip distance effectively increases with increasing energy. This may easily be envisioned for a two-dimensional inclusion with a circular cross section if allowance is made for diffuse reflections at the boundaries of the inclusion so that the segments of the electron orbit stay parallel to each other (cp. Fig. 2). Secondly, and, possibly, equivalently, it is known that in two and more dimensions the KAM-surfaces lose their confining quality, i.e. there is, in principle, no well defined breakdown intensity any more [4] and diffusion in phase space (called Arnold diffusion) to higher energies can occur for arbitrarily low field strengths. In general, one might worry whether a quantum mechanical treatment which is ultimately necessary will not deprive those exceptional classical trajectories, that gain a far above average amount of energy, of their significance. Recent investigations [8] show that this is not the case and that classical results are essentially unaltered in quantum mechanics.

A similar one-dimensional model has been applied to the ionization of hydrogen atoms in highly eccentric Rydberg states [9] by microwave fields. The model was able to describe the experiments quite well but overestimated the field required for ionization by a factor of about two [10] even though the considered states

are really almost one-dimensional in nature. This overestimate of the breakdown field may be a general shortcoming of any one-dimensional model.

The very existence of a breakdown field strength does not yet imply that the process occurs fast enough to generate an electron avalanche. Since for fields exceeding the breakdown field the motion of the electron in phase space is stochastic, one may try to obtain an estimate of the time it takes the electron to diffuse from the n-th resonance zone to the $(n-1)$st in analogy to the theory of Brownian motion. The diffusion constant is [10,12]

$$D(I) = \lim_{t\to\infty} \frac{1}{2t} \int_0^t dt' dt'' \langle \dot{I}(t') \dot{I}(t'') \rangle, \tag{27}$$

where $\dot{I}(t) \equiv dI/dt$ is evaluated along the particle orbit in action-angle space and the average is taken over an ensemble of initial angles $\vartheta(0)$. Diffusion from the n-th to the $(n-1)$st resonance zone is then governed by the characteristic time

$$\tau_{dn} = \frac{(I_{n-1} - I_n)^2}{2D(I_n)}. \tag{28}$$

We have evaluated the diffusion constant (27) along the lines followed in Ref. 9. The procedure involves two approximations, viz. a lowest order approximation to the solution $I(t)$ of the equations of motion and an average over frequency of the resulting expression for $D(I)$. Neither approximation appears very trustworthy, in particular for the uppermost resonance zones (low n). In view of that, it is not surprising that the resulting diffusion time

$$\tau_{d,n} = \frac{2(2n+1)^3}{\pi^2 (2n-1)^2 X_n^4} T \sim \frac{4n}{\pi^2} X_n^{-4} T \sim 16nT, \tag{29}$$

with T the period of the laser field comes out to be implausibly short.

This work was supported in part by Los Alamos National Laboratory, and the Air Force Weapons Laboratory.

References

[1] V. Nathan and A. H. Guenther, J. Opt. Soc. Amer. B**2** (1985) 294.
[2] L. P. Gorkov and G. M. Eliashberg, Sov. Phys. JETP **21** (1965) 940; A. S. Epifanov, Sov. Phys. JETP **40** (1974) 987; S. I. Zakharov, Sov. Phys. JETP **41** (1975) 1085; E. A. Manykin, P. P. Poluektov, and Yu. G. Rubezhnyi, Sov. Phys. JETP **43** (1976) 1105; A. A. Lushnikov, V. V. Maksimenko, and A. Ya. Simonov, Sov. Phys. Solid State **20** (1978) 292; A. G. Malshukov, Sov. Phys. JETP **58** (1983) 409; E. I. Babadzhan, V. V. Kosachev, Y. N. Lokhov, and M. I. Ryazanov, Fiz. i. Khim. Obr. Met. **17** (1983) 12.
[3] W. A. Lin and L. E. Reichl, Physica D **19** (1986) 145.
[4] See e.g., A. J. Lichtenberg and M. A. Lieberman, Regular and Stochastic Motion, (Springer, NY, 1982).
[5] B. V. Chirikov, Phys. Rep. **52** (1979) 263.
[6] D. F. Escande and F. Doveil, J. Stat. Phys. **26** (1981) 257.
[7] T. W. Walker, A. H. Guenther, and P. E. Nielsen, IEEE J. Quant. Electron. QE-17 (1981) 2041.
[8] L. E. Reichl and W. A. Lin, Phys. Rev. A**33** (1986) 3598.
[9] R. V. Jensen, Phys. Rev. A**30** (1984) 386; R. V. Jensen, Chaotic Behavior in Quantum Systems, ed. by G. Casati, NATO ASI Series B, Vol. 120 (Plenum, NY), p. 171; K. A. H. van Leeuwen et al., Phys. Rev. Lett. **55** (1985) 2231.
[10] R. V. Jensen, Phys. Rev. Lett. **54** (1985) 2057.
[11] G. M. Zaslavskii and N. N. Filonenko, Sov. Phys. JETP **25** (1968) 851.

Manuscript Received
3-8-88

Some Comments On: Temperature Dependent Effects In Laser Induced Damage

M. R. Lange[#*], J. K. McIver

University of New Mexico
Albuquerque, New Mexico 87131

A. H. Guenther
Air Force Weapons Laboratory
Kirtland AFB, New Mexico 87117

Abstract

The temperature dependence of various processes can be extremely important in laser induced damage mechanisms. This has been well known since study in this field began. The ways in which temperature plays a role are both varied and many. However, one must be careful not to attribute too much of the responsibility for damage to temperature effects alone. Its specific roles must be carefully characterized and quantified.

On more than one occasion, there have been suggestions of temperature dependent absorption as an important pulsed laser damage mechanism in dielectrics. Similarly, there have been a collection of works supporting theories which do not significantly involve temperature. A comparison of both macroscopic and microscopic scales indicate that, in general, damage must consist of a natural series of evolutionary events that generally involve both temperature independent effects combined with those that are temperature dependent. The series of events that dominate in any process leading to damage depends critically upon the structure and state of the material involved and the photon energy that is incident, to name but the two most obvious. Thus, they must be tediously reconstructed for each given interaction, though certain cases, e.g., classes of material, may be generalized to some extent.

Recent works by the present authors have suggested the level of absorption involved in damage of certain optical films. Subsequently, some of the mechanisms for absorption were assumed and analyzed. In the present work some perspective is placed upon the role temperature plays in the steps leading up to damage.

Key words: laser induced damage, temperature dependence, thin films, optical materials

In partial fulfillment of requirements for his PhD as the University of New Mexico
* Currently at Litton Laser Systems, Orlando, Florida

1. Introduction

A fundamental process for the evolution Of laser induced damage in at least some coating materials has been theorized previously.[1] This work, though purely theoretical, was based upon principles that are feasible and energetically likely to occur. The primary assumption involved was that traditional optical coatings must exhibit priorities of a material that is far from ideal in structure. Many microscopic studies of optical coatings support this premise.

Many details and effects were neglected in the [1] study. The concentration of the work was on demonstrating feasibility. Certain processes were chosen over others due to the scales involved. That does not mean that other physical processes not considered do not contribute.

A theoretical study by Komolov [2] supports the concept that temperature dependent absorption dominates the damage process in certain optical coatings. It is felt that sufficient arguments have been presented [1] to support the fact that this cannot be true in general. Each case of laser induced damage in optical coatings is unique due to the enormous variation in material properties between the various coating materials. Many complicated processes occur in a logical and natural sequence. Thus, each case most be carefully constructed according to the energetically likely series of events that could occur.

The present work concentrates on a certain class of processes that are believed to be, in general, secondary processes. They, however, may be quite important to the damage evolution in many materials. The class of processes concentrated on here ate those that depend upon temperature. The purpose of this expose is to attempt to outline temperature dependent roles in the typical optical coating damage in order to help classify coatings and damage processes more thoroughly.

2. Theory

Theoretically, temperature dependence exhibits itself through several mechanisms. The first and most obvious is through the electron distribution. Increased temperature means increased phonon activity and an increase in electrons promoted to the conduction band, from either a shallow state or a valence band.

The second mechanism for temperature dependence is the band gap. The band gap invariably decreases with increased temperature.

A third effect of temperature is its affect on the material parameters. That is, the thermal diffusion, electron diffusion, electron recombination, etc.

One final role that temperature has is the secondary role that it plays in primary processes, such as avalanche ionization. Here, the temperature, as above, exhibits itself via electron phonon collisions. The high energy phonons assist in increasing the energy of the electrons in the conduction band. This role is considered of secondary importance since it requires a quantitative adjustment of the dominant processes. It is very important, however, for quantitative calculations and may even be required to explain the initiation of avalanche ionization.

The appropriate approach to the problem of intense field interactions with a solid is to study the distributions of electrons and phonons. For optical frequencies, the primary interaction of the field is with electrons. The behavior of the electron distribution is described by eq (1) [3]

$$\frac{d}{dt} f(\vec{r},\vec{k},t) = \frac{\partial f}{\partial t} + \frac{-e}{h} (\vec{E} + \vec{V} \times \vec{B}) \quad \vec{V}_{\vec{k}} f + \frac{1}{h} \vec{V}_{\vec{k}} E(\vec{k}) \quad \vec{V}_{\vec{r}} f = \left.\frac{\partial f}{\partial t}\right|_{\text{coll}}$$

$$\left.\frac{\partial f}{\partial t}\right|_{\text{coll}} = W_{e\vec{q}} (\vec{k} + \vec{q} \rightarrow \vec{k}) + W_{a-\vec{q}} (\vec{k} + \vec{q} \rightarrow \vec{k}) - W_{a\vec{q}} (\vec{k} \rightarrow \vec{k} + \vec{q}) - W_{e-\vec{q}} (\vec{k} \rightarrow \vec{k} + \vec{q})$$

The second term on the right-hand side expresses explicitly the field interaction term. This is the initial driving term of the electron distribution. The far right-hand side term is the electron-phonon interaction term. This term is expressed in terms of transition rates in eq (2).

Collisions provide the driving and damping terms for the phonon distribution. Equation (3) represents the behavior of the phonons.

$$\frac{dg}{dt} = \frac{\partial g}{\partial t} + \vec{r} \quad \vec{V} \rightarrow g = \left.\frac{\partial g}{\partial t}\right|_{\text{coll}}$$

$$\left.\frac{\partial g}{\partial t}\right|_{\text{coll}} = W_{e\vec{g}} (\vec{k} + \vec{q} \rightarrow \vec{k}) - W_{a\vec{q}} (\vec{k} \rightarrow \vec{k} + \vec{q})$$

The simultaneous solution of these two equations, (1) and (3), provides a description of the behavior of electrons and phonons in an optically driven solid. Although this is the correct approach to such problems, the coupled equations cannot be solved in general. In fact, the initial and boundary conditions are seldom known. Furthermore, the structure of the materials is not always well known.

This approach is not even attempted in the current effort. This presentation may be considered, at best, an attempt to define the constraints of the problem.

The energy and momentum transfer process from the laser field to the solid is extremely complicated. Photons are absorbed through both direct and indirect (involving phonons) transitions of electrons in an array of processes. The excited electrons subsequently interact with phonons and holes in an equally large number of ways. Descriptions of these interactions may be found in such references as.[3]

In the limit of an equilibrium condition, a simple model may be used. This model is the simplist solution to eq (1) and is probably not valid for situations of interest. It is, however, very useful for lending insight into the problem. The extent of its validity for applications to laser-induced damage is not completely understood.

The model of interest is the electron distribution in an equilibrium condition in ideal solids. In this case, the density of electrons in the conduction band, n_e, is given by:

$$n_e = \frac{8(\pi k_B T)^{3/2}}{h^3\sqrt{2}} m_n^{*3/4} m_p^{*3/4} e^{-E_g/2kT}$$

Where k_B is the Boltzman constrant, E_g is the band gap, m_n^* and m_p^* are the effective electron and hole masses and h is Planck's constant. This quantity is directly proportional to the free carrier absorption coefficient predicted by the Drude model

$$\alpha = \frac{\mu 4\pi\ e^2 \tau_k n_e}{C n_r m_N^* (1 + \omega^2\ \tau_K^2)}$$

where μ is the magnetic permeability, τ_k is the momentum exchange (collision) time, ω is the incident field frequency, n_r is the real part of the index of refraction, and n_e is the electron density.

Komolov [2] finds experimentally that

$$\alpha(T) = \alpha_I + \alpha_0 e^{-u/T}$$

where α_I is some initial anomalous absorption in the coating. For TiO_2 at optical frequencies he finds that

$$\epsilon\ (T) = (80 \rightarrow 180) + (4.\text{x}10^{7} \rightarrow 10^{8})\ e^{-(21{,}000 \rightarrow 17{,}600)/T}\ (\text{cm}^{-1}).$$

Since the band gap is at about 3eV (corresponding to 2kT) this yields a value of $T \simeq u \simeq 1.8\text{x}10^2$. With a melting temperature of 2133 K this yields a maximum value at melting of $\alpha(T) = 180 + 10^8 \exp(-17{,}600/2133) = 2.6\text{x}10^4$. Although this is nearly on the order of the required absorption ($\sim 10^5$), [5] it requires reaching the melting temperature to achieve this

This example is used as a scaling baseline and is not intended to imply that these simple relations hold in the region near melting. The value of $\alpha_0 = 10^8$ is alao about two orders of magnitude greater than theory predicts. However, the temperature dependence of the band gap will contribute to this process.

The band gap variation may be included as $E_g = E_{g0} - \gamma Tk$ where a relatively large value of 7 from literature is 8.[6] To be liberal, the value of $\gamma = 10$ is chosen. Thus $E_g = 3eV - 10\ (0.86x10^{-4})\ (2133) = 1.17$ at melting, so that $\alpha(T) = 1.7x10^5$ cm^{-1}. Under these liberal Conditions, clear that temperature dependence can be important. However, for this temperature dependent absorption to dominate requires an impurity with a significant absorption to initiate the process.[2]

Absorption centers in common oxide coating materials (MgO, SiO_2, Al_2O_3) are well known by those who study color centers.[7] It is also likely that many impurity transitions are within range of the conduction band in oxides. Thus if absorption centers of some sort initiate absorption in a film such as TiO_2, then temperature dependent absorption may contribute via a spread by an absorption wave. This is an alternative to an avalanche ionization process. It is, however, likely that if conditions are appropriate for an avalanche, it will dominate. It does not, in theory, demand as significant an initial absorption as that required to initiate a thermal instability involved in temperature dependent absorption. Furthermore, temperature dependent absorption may apply to only a select range of materials with small band gap.[2]

For example, if a typical fluoride film (e.g. CaF_2) is considered, it can be found that $\alpha \simeq (10^2 + 10^8 \exp(-5.8x10^4/1775)$ cm^{-1} $= (10^2 + 8.35x10^{-7})$ cm^{-1}, where $\alpha_I = 10^2$ cm^{-1} is the assumed initiating absorption. If the temperature dependence of the band gap is included $E_g = 10eV - 10(0.86x10^{-4})\ (1775)\ ^{eV} = 8.5\ ^{eV}$, $\alpha = (10^2 + 8.1x10^{-5})$ cm^{-1}. This is still an insignificant absorption at the melting temperature. In addition, it would require a very large absorption to achieve a temperature near melting.

Thus, the only possible primary dependence on temperature for this case would be in the assist of the ionization of shallow trap centers and impurities. Since photoionization of certain resonant trap centers occurs on a scale of 10^{-11} seconds [1] it is not likely that ionization of these is thermal. If temperature dependence does play a part in the absorption in large band gap coatings, it is more likely that its contribution is in the assistance of impact ionization and photon absorption.[8] Another way to look at this is to realize that for high intensity optical frequency interaction the electron temperature leads the phonon temperature. That is, the field interacts solely with electrons which impart their energy to phonons. It is less likely that electrons impart their energy to phonons and equilibrate with other phonons which ionize valence or impurity bound electrons than it is that electrons are directly ionized. Trap centers, by their nature, have larger electron cross sections

lattice ions. Any significant density of both trap centers and excited carriers necessitates impact ionization. Furthermore, simple computations (eq 5) show that an optical field (~ 500 nm) at damage intensities (~ 1-2 GW/cm^2 for fluorides) can generate one half to three eV electrons in 10^{-10} seconds (depending upon the collisional frequency). These energies are sufficient to ionize many trap centers (~ 1 to 3 ev) along with some impurities.[9] In this same time period even the most strongly absorbing ($\alpha = 10^5$ cm^{-1}) regions could increase at best a couple of tens of degrees K in temperature. If a strongly absorbing region such as this exists, there is no need for a temperature dependent increase to produce damage.

$$\frac{d\epsilon}{dt} = |E|^2 \frac{e^2 \tau_k}{m^*(1 + \omega^2{}_k \tau^2)}$$

(ϵ = Energy of an Electron, $|E|$ = Electric Field Strength)

The temperature dependence of the material parameters may also be expressed theoretically. The thermal conductivity $k = \frac{1}{3} \sum_i c_i v_i \ell_i$, where i denotes the type of carrier, c is the contribution of carriers to the specific heat, v is the carrier velocity and t is its mean free path. At low temperatures $k \tilde{\propto} T^{3-n}$ where n = 0, 1, 2, or 3, due to the phonon frequency dependence of ℓ and c.[10] It generally has a positive slope at lower temperatures. At high temperatures k(T) is primarily governed by the temperature dependence of ℓ (i.e. $\ell \tilde{\propto} 1/T$).

With the outstanding exceptions of SiO_2, HfO_2 and ZrO_2, most of the optical materials of interest [11] are on the down slope of the conduc-tivity curve at room temperature and above, with usually similar slopes.[9] HfO_2 and ZrO_2 are approximately independent of temperature and SiO_2 is clearly positive ($\tilde{\propto} T^{1/2}$). Since the rate at which the heat is conducted away by the surrounding film is important [5], a relative comparison between materials is useful. In problems of interest, significant conduction takes place. It is felt that a relative measure of this rate may be estimated from the room temperature conductivity. This is particularly true for materials where the behavior of the conductivity with temperature is similar. It may be questioned as to whether materials which behave differently (SiO_2, HfO_2, ZrO_2) may be compared by this criterion.

The electron diffusivity is given theoretically by $D_e = \mu k_B T/e$, where the electron mobility $\mu = e\tau/m^*$.[4] The collision time τ can be a complicated function of temperature because it depends upon the energy of both the electrons and the phonons. Electron diffusivity, as thermal diffusivity, is a difficult quantity to determine for thin films. This quantity is used primarily to determine the rate of spread of the electron density. An order of magnitude value based upon theoretical considerations may suffice for most calculations. Its dependence on temperature is not important for most damage processes. This is true also of the other secondary effect rate constants.

3. Scaling Behavior

The importance of the above comments may be partially quantified. The appropriate approach to such problems is to compare relative scales associated with the various processes.

Previous work [1] has shown that in some cases the damage threshold of certain optical coatings may be scaled as

$$E_D \ (J/cm^2) \propto \int_o^{Tm} dT \rho c_v \delta_{eff}$$

Here, T is temperature, ρ is density, C_v is specific heat and δ_{eff} is the effective length over which energy is deposited about some absorbing center,

$$\delta_{eff} = \left[\frac{X_1}{\left[\alpha^{-1} + \delta_T\right]} + \frac{X_2}{\left[\alpha^{-1} + \delta_e + \delta_T\right]} \right]^{-1}$$

where X_1 is the fraction of laser energy deposited directly into the lattice, X_2 is the fraction of energy that diffuses before being deposited and δ_T and δ_e are the effective lengths for phonons and electrons. The behavior of the damage threshold may be vastly altered depending upon which diffusion length dominates.

For example, if $\delta_T >> \delta_e$, α^{-1}

$$E_D \propto \int_o^{Tm} dT \sqrt{\rho C_v \kappa \ t_p} \quad \left[\frac{X_1}{\left[1 + \frac{\alpha^{-1}}{\delta_T}\right]} + \frac{X_2}{\left[1 + \frac{\alpha^{-1}}{\delta_T} + \frac{ue}{\delta_T}\right]} \right]$$

where the term in brackets becomes an insignificant constant and t_p is the laser pulsed length. If, on the other hand, α^{-1}, the length over which laser absorption occurs locally, is such that $\alpha^{-1} >> \delta_{e,T}\delta$, then

$$E_D \propto \int_o^{Tm} dT \ \rho C_v \alpha^{-1} \quad \left[\frac{X_1}{\left[1 + \alpha\delta_T\right]} + \frac{X_2}{\left[1 + \alpha\delta_e + \alpha\delta_T\right]} \right]^{-1}$$

Similarly if δ_e dominates we find its corresponding relationship

$$E_D \propto \int_o^{Tm} dT \rho C_v \sqrt{\tau_p \tau K_B T/m^*} \quad \left[\frac{X_1}{\left[\frac{\alpha^{-1}}{\delta e} + \frac{\delta T}{\delta e}\right]} + \frac{X_2}{\left[\frac{\alpha^{-1}}{\delta e} + \frac{\delta T}{\delta e} + 1\right]} \right]^{-1}$$

This little exercise should serve to demonstrate some of the basic scales involved in laser induced damage. Comparison of these scales determines the relative importance of the material properties involved including those which depend upon and relate to temperature.

These expressions need to be modified for short laser pulses. Short pulses refers to durations small compared to the material response times (for example picosecond pulses). In general, the role that temperature dependence plays in the material properties does not appear that important to the process of an electron density generation that seems to be required for optical damage. The temperature effect is a quantitative correction. The behavior of the thermal conductivity can affect the quantitative determination of damage threshold. However, due to the difficulty of a quantitative determination of the dominant absorption process, a qualitative (relative) measure of conductivities is adequate. This is particularly true if the temperature dependence is similar for various materials. The outstanding exception of the similar behavior of conductivities is that of SiO_2. Its behavior may, in part, contribute to its anomalously high damage threshold with respect to other oxide coatings.

The temperature dependence in avalanche ionization may be overlooked as well. Avalanche ionization in optical thin films is a secondary process. The initial absorbing center would dominate the initiation of damage and an avalanche would simply provide a mechanism for the growth of an absorbing region. The basic temperature affect on avalanche ionization is to assist in promoting electrons to higher energies by collisions with more and higher energy phonons.

The basic conclusion of this study is that the primary role that temperature plays in laser induced damage to certain optical dielectric coatings is in the damage itself. The steps leading to damage caused by localized intense heating are weakly dependent upon the temperature. This conclusion results from a simplistic comparison of the scales involved. Temperature dependence in absorption can play a part in the absorption of optical radiation in small band gap oxide coatings if avalanche ionization does not dominate. However, it is probably a secondary effect which results in the growth of pre-existing absorption center regions. Temperature dependent absorption cannot play any significant role for absorption in larger gap coatings.

This study cannot be considered a rigorous investigation. Such a study is not possible for optical coatings. The theory of thermal processes in optical coatings are not yet understood. This study was conducted as a necessary and integral part of the study of the process of laser induced damage in optical coatings. It is a required step in isolating the constraints necessary to attempt the solution of the appropriate problem, eq (1) and (3). Each topic mentioned above constitutes in itself an entire field of study. Out purpose is not to advance the understanding of any of the topics, but more to place perspective on their roles in laser induced damage.

5. References

[1] Lange, M.R.; McIver, J.K.; Guenther, A.H. Anomalous absorption in optical coatings, Laser Induced Damage in Optical Materials. NBS Spec. Publ. (to be published).

[2] Komolov, V.L. Optical breakdown produced by intense light in thin films having spatially varying absorption. Sov. Phys. Tech. Phys. 27, 311 p (1982).

[3] Madelung, O. Introduction to Solid State Theory, Springer Verlag (1978).

[4] Deam, W.R. McGraw Hill (1965).

[5] Lange, M.R.; McIver, J.K.; Guenther, A.H. Laser induced damage in optical coatings: fluorides and oxides. Thin Solid Films 125, 143-155 p (1985).

[6] Popov, S.P.; Fedorov, G.M. Influence of narrowing of energy gap width of the velocity of ionization waves in transparent dielectrics. Sov phys. Tech. Phys. 28, 494 (1983).

[7] Schulman, J.H.; Compton, W.P. Color Centers in Solids. Pergamon Press, (M963).

[8] Sparks, M.; Duthler, C.J. Theoretical studies of high power ultraviolet and infrared materials. Fifth Tech. Rep. Xomics, Corp. Contract DAHC15-73-C 0127 (1975).

[9] Sparks, M.; Duthler, C.J. Theoretical studies of high power ultraviolet and infrared materials. 9-10 Tech. Rep. Xonics Corp. Contract DHHC15-73-C 0127 (1977).

[10] Tonloukain, Y.S. Thermo Physical Properties of Matter. Plenum Press, (1970).

[11] Walker, T.W.; Guenther, A.H.; Neilson, P. Pulsed laser induced damage to thin film optical coatings, Part I and II. IEEE J. Quant. Electron, QE-17, 2041 (1981).

- Manuscript Not Received -

LASER INDUCED DAMAGE THRESHOLD DERIVED FROM CHAOTIC ELECTRON DYNAMICS

W. Becker and J. K. McIver
Center for Advanced Studies
Department of Physics and Astronomy
University of New Mexico
Albuquerque, NM 87131

and

A. H. Guenther
Air Force Weapons Laboratory
Kirtland Air Force Base, NM 87117

ABSTRACT

An important stage in the laser induced damage of a dielectric material is a mechanism-initiated triggering by the presence of sufficient electrons in the conduction band. When these electrons are subsequently accelerated by the laser field under photon assistance, they can lead to an electron avalanche, and, in turn, may initiate visible damage.

We have investigated the precondition or presetting of the electron model, i.e. the initial creation of electrons in the conduction band. We assume the presence of small metallic inclusions ($r \sim 10$ to 100 Å) in the dielectric which we model by infinitely deep one-dimensional square well potentials. The dynamics of this model are known to be chaotic if the laser field exceeds a certain threshold value. Under these conditions the electrons can gain enough energy to bridge the gap between the valence band and the conduction band.

The model yields threshold fields of the order of 10^{10} W/cm^2. However, the dependence on the wave length is complicated.

Manuscript Received
8-24-87

The Mechanism of Prebreakdown Nonlinear Energy Deposition from Intense Photon Fields at 532 nm in NaCl

S. C. Jones, X. A. Shen, and P. F. Braunlich
Department of Physics, Washington State University
Pullman, WA 99164-2814

Paul Kelly
Division of Physics, National Research Council
Ottawa, Ontario, K1A 0R6, Canada

A. S. Epifanov
General Physics Institute, Academy of Sciences
117942 Moscow, USSR

We present direct experimental evidence that significant amounts of energy can be deposited in NaCl by short laser pulses of 532 nm wavelength without electron avalanche formation. The mechanism is four-photon free carrier generation and free carrier absorption with contributions by self-trapped holes. We also report the first reliable measurements of four-photon absorption cross sections in any wide-gap ionic solid.

Key Words: alkali halide; avalanche ionization; four-photon absorption; free electron heating; polaron heating; prebreakdown absorption; primary defects; purity; self-focusing.

1. Introduction

Two fundamentally different models of laser induced damage of optical materials exist: shortcomings of the classical avalanche model led to the development of the so-called multiphoton-polaron model. In addition to the difference in free carrier generation processes, subsequent absorption by the carriers, and their energy transfer to the lattice are also substantially different.

Data presented by Manenkov [1], representing the temperature dependence of laser damage threshold in high threshold alkali halides of four-photon bandgap at 532 nm, did not f it the expectations of the avalanche model (for $h\nu << E_g$). This led to a reanalysis of the avalanche mechanism for "large" quanta ($3 \leq E_g/h\nu \leq 5$, where E_g is the bandgap and $h\nu$ the photon energy) [2], but contributions to damage by four photon absorption was also speculated.

Historically, model validity has been based on damage threshold predictions compared with threshold measurements. However, direct correspondence between theoretical (calculated melting temperature, critical free electron density) and experimental (light scattering, residual strain, filament formation) damage criteria has not been established, weakening the connection between theory and experiment and making damage threshold measurements a poor indicator of postulated microscopic processes. Further, damage models for pure, perfect (intrinsic) materials are probably off the mark for comparison with incompletely characterized, real materials containing impurities and defects, so it is small wonder that theoretical-experimental agreement is not particularly good.

A better indicator of the energy deposition mechanisms would be to measure the absorption of laser light by the material before it is damaged. This not only is more directly related to the fundamental processes but also avoids the difficulties associated with the incomplete connection between theoretical and experimental damage thresholds.

Using the photoacoustic technique we find that the *primary* excitation process for energy deposition from 532 nm, 80 ps pulses into NaCl is four-photon absorption and that focal point temperature increases exceeding 300 K are induced without indications of damage or impact ionization avalanche. However, model calculations show that most energy is transferred from the laser pulse to the lattice through *secondary* processes of free carrier or defect absorption, enabled by the primary four-photon event.

The initial goal of this research was to measure the four-photon absorption cross section:
$\sigma^{(4)} \approx 5 \times 10^{-113}$ cm^8 sec^3 is indicated, where the rate of valence to conduction band transitions is given by

$$\frac{dn_c}{dt} = N\sigma^{(4)}F^4. \qquad (1)$$

Here n_c is the conduction band carrier density, N the density of absorbing species (Cl^- in this case), and F is the photon flux in photons/cm^2sec. However, since the photoacoustic method registers all absorptions, the value of $\sigma^{(4)}$ must be revised downward after considering secondary processes of free carrier and defect absorption. Two treatments of lattice heating resulting from the interaction of free carriers with laser light, polaron absorption [3] and that calculated by Epifanov [4], satisfactorily account for the experimental results but with different values of $\sigma^{(4)}$. The correct model is undecidable via the photoacoustic technique without an independent measurement of the four-photon cross section. We have also compared the data with calculations of the large quanta avalanche theory and find no agreement for nondamaging pulses. Our results pertain to ultrapure NaCl samples that were processed in a reactive (HCl) atmosphere, to reduce OH^- contamination. These were the most purified samples we could obtain.

2. The Photoacoustic Technique for Measuring Absorbed Energy

Previous photoacoustic measurements of nonlinear absorption in solids include two-photon absorption by Van Stryland and Woodall [5], and three photon absorption by Van Stryland et al. [6]. Horn et al. reported calibrated measurements of energy deposition by three-photon absorption in TlBr and TlBrCl (KRS-6) [7].

The thermal acoustic source generated by the nonlinear absorption of a tightly focused laser pulse in a nominally transparent material is much more localized than the usual (unfocused or cylindrical) source considered in photoacoustic theory. In our experiments the laser pulse is focused to a radius, w_o, of 10 μm or less, near the midplane of a slab of single crystal NaCl of approximate dimensions 5 x 10 x 30 mm^3, with the entrance and exit faces being the 5 x 30 surfaces. The focal point is on the plane bisecting the 5 x 30 surface at the midpoint of the beam path through the crystal. The crystal is bonded to a fused silica plate, of truncated elliptical shape, on which a PZT transducer is affixed (fig. 1). The separation of sample and transducer allows discrimination of signal from scattered light and the elliptical shape provides some focusing of acoustic waves on the transducer. This complicated arrangement makes impractical solving for the pressure wave at the transducer. However, it is sufficient to show that one can have equivalent acoustic sources under 266 and 532 nm illumination, making the boundary conditions and waveform irrelevant, and that a valid calibration can be obtained [8]. In this regard, we ignore the crystalline nature of the sample and assume it to be isotropic and consider generation of longitudinal waves only. Thus, the problem reduces to that of solving for the pressure wave in an infinite isotropic medium for a given source.

We have derived in detail the expression for the pressure wave induced by the nonlinear absorption of a single, sharply focused laser pulse as sensed by an acoustic transducer of resonant angular frequency ω [8]. Both thermal and electrostrictive source terms were considered in a multipole expansion of a Green's function analysis. We found that, for our experimental geometry (fig. 1) and focal conditions, the thermally generated (by absorption) wave was completely dominated by the monopole term, with vanishing dipole and negligible quadrupole contributions. The lowest nonvanishing electrostrictive contribution was the quadrupole term at 10^{-8} of the thermal monopole for a given pulse of Gaussian shape in cross section and time.

If the intensity of the pulse is given by

$$I(\bar{r},t) = \frac{E(1 - R)\exp\{-r^2/w_o^2(1 + z^2/z_o^2)\}\ \exp\{-t^2/\tau^2\}}{\pi^{3/2}w_o^2\tau(1 + z^2/z_o^2)}, \qquad (2)$$

where the photon flux is F=I/hν, r the radius in cylindrical coordinates from the pulse propagation axis, z the distance from the focal plane along the axis, w_o the 1/e intensity radius on the focal plane, z_o the confocal parameter ($z_o = 2\pi w_o^2 n/\lambda$), E the pulse energy, τ the pulse half- width at 1/e intensity, R is the reflectivity of the crystal entrance face, then the rate of energy absorption per unit volume, by four-photon absorption only, is

$$\partial u(\bar{r},t)/\partial t = 4h\nu\sigma^{(4)}NF^4(\bar{r},t).$$

The total absorbed energy is

$$U = 2\sqrt{\pi}\ h\nu\sigma^{(4)} N\tau\left[E(1-R)/\pi^{3/2} w_o^2 \tau h\nu\right]^4 V, \qquad (3)$$

where the interaction volume V is given by

$$V = \int d^3r \left\{ \frac{\exp\left[-r^2/w_o^2(1 + z^2/z_o^2)\right]}{1 + z^2/z_o^2} \right\}^4$$

$$\approx 3\pi^2 w_o^2 z_o/32 \qquad \text{if} \qquad z_o/d < 1/5\,, \qquad (4)$$

and d is the thickness of the crystal in the direction of beam propagation.

The measurements are of acoustic signal, S, versus absorbed energy, U, or incident energy, E. However, the acoustic pressure, and thus the signal, is a linear function of U such that at a fixed frequency ω, the signal S obeys $S \propto U$. Since $U \propto E^4$ for a four-photon absorption process, four-photon absorption is indicated by a slope of 4 on a plot of log(S) vs log (E), as in figure 2.

The acoustic system is calibrated to yield absolute values of absorbed energy U for signal level S. When this is accomplished, the upper limit on $\sigma^{(4)}$ (where we are here neglecting secondary absorption processes) is given by

$$\sigma^{(4)}_{upper} = \frac{8\pi^3 w_o^4 \tau^3 (h\nu)^3 \lambda}{3\sqrt{\pi}\ Nn\left[(1-R)E\right]^4} U, \qquad (5)$$

and the temperature increase at the geometrical focal point is

$$\Delta T_o = U/\rho c V = (16\lambda/3\pi^3 \rho c w_o^4 n)U, \qquad (6)$$

where we have used eqs (3) and (4) to obtain these expressions (ρ is the mass density and c the specific heat).

The system is calibrated by measuring the signal generated by absolute energy absorbed by a two-photon process at 266 nm, easily obtained by attenuation measurements. The 266 nm pulse is sharply focused to produce the necessary geometrical requirements of the interaction volume, i.e., monopole dominated, and then the energy absorbed under 532 nm excitation is obtained from the calibration U(S).

The absorbed energy measurements are always valid, but the inferred temperature rise, ΔT_o, depends on the energy distribution. If the S vs E measurement verifies four-photon absorption is occurring, then eq 6 is valid. (Heat diffusion is negligible for $\tau \approx 80$ psec [8]).

3. Experiment

3.1. Experimental Details and Preliminary Findings

The laser system consists of a Quantronix model 116 Nd:YAG, both Q-switched and mode-locked, a mode-locked pulse selector and a double-pass Nd:YAG amplifier. The output is a single mode-locked pulse with energies up to 20 millijoules at 1.06 μm. The IR pulse passes through a passive attenuator before frequency doubling in KD*P, where 532 nm pulses of energy up to several millijoules are produced, having temporal parameter $\tau \approx 80$ psec (see eq (2)). The 266 nm pulses are produced in a temperature tuned KD*P crystal.

The temporal parameter is obtained by the zero-background second harmonic generation autocorrelation technique. The beam focal radius, w_o, is obtained by scanning a slit across the input plane of the focusing lens and using diffraction-limited formulas for the focusing of Gaussian beams. This is justified for the large effective f/numbers we use [8]. Absolute incident pulse energies are determined by a calibrated pyroelectric joulemeter. Signals from the 175 kHz acoustic transducers and pulse energy detectors are recorded by a Data Precision 6000 transient digitizer. Because of the highly nonlinear nature of the laser pulse-crystal interaction, signal averaging would lead to loss of information and, therefore data points correspond to single shots.

Figure 2 shows an early effort at verifying the measurability of four-photon absorption in NaCl by the photoacoustic method. This result was not easily reproducible in a random collection of NaCl samples from both Harshaw Chemical Co. and University of Utah Crystal Growth Laboratory, i.e., bulk damage occurred before signal attributable to four-photon absorption was detected. The variation of damage threshold within a group of samples, with a few having exceedingly high breakdown thresholds, is not an unknown occurrence, as Manenkov [1] observed this several years ago. The nature of the interaction and the limited sensitivity of the acoustic detection system makes necessary the use of high threshold crystals in order to detect prebreakdown energy absorption. This led to efforts to obtain samples of the highest available purity, to find if the irreproducibility was associated with contamination.

We found that only ultrapure reactive-atmosphere processed NaCl crystals (obtained from the Crystal Growth Laboratory at the University of Utah) had sufficiently high damage thresholds for consistent measurements of prebreakdown energy deposition. This material contains alkali and alkaline earth impurities (notably K, Li, Ba, Rb, Sr, and Mg) at a 0.1 to 5 ppm (parts per million) level together with other metallic impurities (Al, Fe, Cu, Ni, Tl, and Zn) at less than 0.01 ppm [9]. Processing the starting material in an HCl atmosphere reduces the normally present OH^- concentrations of a few ppm by one or two orders of magnitude.

The presence of OH^- has some implications for acoustic signal vs absorbed energy calibrations [10,11]. First, buildup of F-centers due to x-ray exposure (producing electron-hole pairs) is initially proportional to OH^- concentration, implying that multiple laser shots on one site could lead to efficient production of stable defects in the interaction volume. Secondly, an OH^- associated emission of yellow-green fluorescence peaks with excitation at 260 nm. Thus, OH^- contaminated NaCl will be a linear absorber of the calibration light source, leading to error in the calibration. In [10] it is also noted that the OH^- concentration of thin sections varies according to the position in the boule from where it came. A dramatic verification of the first of these effects due to OH^- was obtained by exposing two wafers of ultrapure NaCl, one processed in the HCl atmosphere, to approximately two megarads of gamma radiation from a ^{60}Co source. The reactive atmosphere processed sample remained clear, while the unprocessed ultrapure sample turned amber in color (implying F center creation) and, additionally, was riddled with black specks in the bulk.

Measurements yielding a nonlinear index (the slope of a log-log plot) of four were obtained over a dozen times in crystals with damage thresholds ranging from 400 to over 500 GW/cm^2 (uncorrected for self-focusing). Crystals with higher thresholds had nonlinear indices closer to four; the range was from 3.55 ± 0.15 to 3.95 ± 0.4 (see fig. 3).

3.2. Calibrated Results

The calibration procedure was carried out on three different samples of reactive atmosphere processed ultrapure NaCl, two cut from one boule, the third from a second boule. In all cases, the polarization of the incident 532 nm laser pulse was parallel to the [110] crystal direction with propagation along the [100] axis.

Crystal No. 1

The first calibration was performed on a 4 mm thick wafer cut from the middle of the first boule. This sample was chosen purposely to see if a wafer from the middle of the boule was clean enough to yield prebreakdown data. That the crystal quality is critical is indicated by our observation that a sample from the bottom of the boule did not yield a signal attributable to four-photon absorption before damage.

The data for this calibration are the lower set of eight points in figure 4. The upper limit of the four-photon absorption cross section obtained from the data set is $\sigma_{max}^{(4)} = (5.7 \pm 2.5) \times 10^{-113}\ cm^8\ sec^3$. The relevant parameters are listed in table 1, as is the peak intensity of the highest pre-damage pulse.

This set of eight points was obtained on a single site in the crystal. The number was limited to avoid possible buildup of lattice defects (F-centers) which are created as a result of electron-hole pair generation. The set was terminated when damage was detected, with points attributed to damage not included. Our damage criteria are a) scattering of laser light at approximately 90° to the optic axis from focal region coupled with b) a very large acoustic signal inconsistent with that generated by a pulse of similar energy before damage. The simultaneous observation of a) and b) signaled bulk damage. A further qualitative check is distortion of the transmitted beam profile, usually similar to a

Table. 1. Parameters of Energy Deposition Calibration and Results

Sample	w_o (cm)	τ (psec)	V(cm^3) 532 nm	V(cm^3) 266 nm	d (cm)	I_{max} (GW/cm^2)	$\sigma_{max}^{(4)}$ (cm^8 sec^3)
1	6.32x10-4	81	2.7x10-8	2.6x10-8	1	335	(5.7 ± 2.5) x 10-113
2	3.9x10-4	86.7	4.0x10-9	4.8x10-9	0.46	590	(4.3 ± 2.4) x 10-113
3	8.4x10-4	83	8.4x10-8	9.7x10-8	1	182	(2.75 ± 1) x 10^{-112}

f, lens focal length; w_o, spot radius (1/e intensity); τ, pulse temporal parameter; V, interaction volume; d, path length; I_{max}, maximum peak intensity of nondamaging pulse in data set; $\sigma_{max}^{(4)}$, upper limit of four-photon absorption cross section obtained from this data set. The 266 nm interaction volume V is given by $V = 2\pi^2 w_o^4 n \tan^{-1}(d/2z_o)/\lambda$, where n, w_o, z_o, and λ refer to that appropriate for the UV wavelength.

pinhole diffraction pattern, when the interaction volume is damaged. Damage at this level is not detected by visual inspection, in contrast to the visible damage track or filament usually taken as indication of catastrophic damage in most breakdown threshold measurements [12,13].

Crystal No. 2

This sample was the second wafer from the top of the first boule (the very top wafer is unsuitable due to the growth characteristics). With this sample we tried a shorter focal length lens to obtain data at a higher peak intensity, since the damage threshold is expected to increase for smaller focal volumes. These data are the higher set of points in figure 4. We present them together with those from sample No. 1 as a composite plot in order to show the consistency for two different samples from the same boule, even under different focal conditions. The slope of the line in the double-logarithmic plot is 3.82 ± 0.11.

The data are a collection of 27 shots over eight sites in a small matrix (approximately 3 mm x 3 mm). The high intensities necessary to obtain signal (the apparatus is sensitive to absorbed energy, and we have a very small interaction volume in this data set) required this strategy. Pulses obviously producing damage were deleted from the data set.

The upper limit of $\sigma_{max}^{(4)} = 4.3 \times 10^{-113}$ cm^8 sec^3 is satisfactorily consistent with the result from sample No. 1.

There is one point in this data set for which we are confident that we have measured a very high temperature rise without damaging the crystal. This point is $\Delta T_o = 324°C$ at $I_{peak} = 550$ GW/cm^2. Subsequent pulses of lower intensity on this site were entirely consistent with the data set and exhibited no evidence of damage.

Crystal No. 3

The third sample is the second wafer from the top of the second boule. The data are presented in figure 5. They occur for lower intensities than for sample Nos. 1 and 2, and we have a smaller slope of approximately 3.3 on the double logarithmic plot. The pulse of highest energy without damaging the crystal had peak intensity of only 182 GW/cm^2. The slope is indicative of the presence of a lower order process. We include the value of $\sigma_{max}^{(4)}$ obtained from these data to demonstrate the variation of results one might expect from using a variety of crystals. The upper limit for the four-photon absorption cross section obtained from these data is $\sigma_{max}^{(4)} = (2.75 \pm 1.0) \times 10^{-112}$ $cm^8 sec^3$. The difference in interaction volumes (see table 1) does not explain the inconsistency in $\sigma_{max}^{(4)}$ obtained from samples 1 and 3, since those of samples 1 and 2 were even more different but yielded consistent results. We thus attribute the discrepancy of $\sigma_{max}^{(4)}$ in crystal 3 compared to samples 1 and 2 to the fact that they originate from different boules and, thus, from different starting material. Just like Manenkov[1], we put our trust in the data of samples 1 and 2 because they exhibited higher threshold and agree well. Of the samples from the two boules, we believe the data from the first most nearly exhibit intrinsic (to pure NaCl) phenomena.

The uncertainties reported in table 1 are the results of a mean-square error analysis of eq (5). Measurement error in the pulse energy, E(≈10%), and the beam waist, w_0 (≈5%), make the largest contributions to the uncertainty of $\sigma^{(4)}$.

The temperatures in figures 4 and 5 have uncertainties of approximately 20%, with the most significant error being in the measurement of w_0.

3.3. Beam Deformation

Our predamage absorption measurements indicate that self-focusing is not significantly occurring, at least according to the simplified theory employed by Smith et al. to obtain the nonlinear refractive index of transparent dielectrics from damage threshold measurements [13,14]. The highly nonlinear dependence of the intensity at the focal plane expected from self-focusing is entirely inconsistent with our results for the photoacoustic signal as a function of incident energy or intensity. According to simple self-focusing theory, the nonlinearity of the power dependence of the intensity [$I \propto P/(1 - P/P_c)$, where P_c is the critical power of self-focusing] would cause a photoacoustic signal versus power dependence much stronger than fourth order for $P \leq P_c$. This is clearly not observed even at the highest fluxes shown in figures 2-5. On the other hand, beam defocusing caused by free-electron contributions to the refractive index would reduce the fourth-power dependence. These observations corroborate the conclusions of Soileau et al. [15], who have shown that for tightly focused ($w_0 < 10$ μm) 532 nm pulses of subnanosecond duration in NaCl, self-focusing does not measurably occur for intensities up to the damage threshold. We therefore do not "correct" our results for self-focusing, but do list all the relevant parameters (table 1) so that it may be done, if desired.

4. Multiphoton Absorption, Avalanche, and Lattice Heating Calculations

The total interaction between the laser photons and crystal is not merely multiphoton electron-hole (e-h) pair generation. Additionally, conduction-band electrons absorb energy from the photon field, as do certain so-called primary defects which are created as a result of e-h pair generation. For this reason, the four-photon absorption cross sections obtained from the data in the previous section are overestimated. Since we are only interested in *intrinsic* material we do not attempt to model effects due to impurities.

We have performed model calculations to simulate the data in figure 4, considering single-photon absorption by V_K- and F- centers, and self-trapped excitons (intrinsic defects created as a result of e-h pair generation) together with two different treatments of lattice heating by free carrier absorption. The polaron model of Schmid, Braunlich, and Kelly [3], and the electron to lattice energy transfer mechanism derived by Epifanov et al. [2] in their "large-quanta" avalanche theory of laser-induced breakdown (hereafter referred to as the free electron heating mechanism as opposed to the polaron heating mechanism). We show that the essential demonstration of the primary event of four-photon absorption; i.e., a nonlinear index of approximately 4 for absorbed energy vs incident pulse energy, is not masked by free carrier and defect absorption. For completeness we also consider the avalanche mechanism of e-h pair generation, both in the absence of four-photon carrier generation with an assumed starting density of conduction electrons, and four-photon assisted.

The details of the microscopic processes and the kinetic equations used to calculate the defect formation, etc., are too lengthy to reproduce here. The kinetic equations are similar to those in the paper by Brost et al. [16], concerning three-photon absorption in KI. The details of the present calculation are available in [8]. Here we discuss those aspects of greatest importance.

The rate of increase of carriers in the conduction band due to four-photon absorption is given by eq (1). The avalanche e-h pair generation term is the usual $dn_c/dt = \gamma n_c$ (where γ is the avalanche coefficient). Using the large quanta avalanche theory (in the notation of Gorshkov et al. [2]) for the case of 532 nm photons interacting with conduction electrons in NaCl ($h\nu = 2.33$ eV, $E_g \cong 8.6$ eV), the avalanche coefficient is given by $\gamma = Q(1)\gamma_0$, where for a four-photon bandgap $\gamma_0 \approx (4^6/4!)(q\delta)^5$ and Q(1) is the rate constant at which electrons lose energy via acoustical phonon scattering: $Q(1) \approx 5 \times 10^{13} \text{sec}^{-1}$, which is approximately one-tenth of the electron-phonon collision frequency [17]. The dimensionless product $q\delta$ is given by $q\delta \approx a(T/T_0)E^2$, which arises from the solution of the diffusion equation. E is the electric field maximum amplitude, T is the lattice temperature, $T_0 = 300$ K, and a is a coefficient equal to $e^2kT_0/6m^2v_s^2(2\pi\nu)^2E_g \approx 5 \times 10^{-6}$ (cm/V)^2, where e and m are the charge and mass of the electron, k is Boltzmann's constant, and v_s is the longitudinal sound velocity. In terms of intensity, E^2 (in V^2/cm^2) $= 240\pi$ I (W/cm^2)/n, where n is the index of refraction. In terms of flux, F = I/hν, this reduces to

$$\gamma \approx 5 \times 10^{13}\gamma_o \text{sec}^{-1} \approx 1.5 \times 10^{-62}\left[a(T/T_o)F/n\right]^5 (\text{sec}^{-1}), \quad (7)$$

and

$$3 \times 10^{-17} \leq a \leq 1 \times 10^{-15} \text{ (in units of cm}^2/\text{V}^2\text{)}$$

for NaCl. The large range for a in NaCl arises from uncertainties in the effective mass of electrons and collision frequencies, and leads to an enormous uncertainty in γ, demonstrating the difficulties encountered in modeling the interaction of laser photons with wide gap materials.

Lattice heating due to the electron-phonon scattering implicit in the avalanche generation of free carriers can be reduced to the form [2,8]

$$\rho c(dT/dt) \approx (mkT/2\pi)^{1/2} (eE/2m\pi v)^3 n_c/l_{ac} v_s,$$

where l_{ac} is the mean free path of an electron between collisions with acoustic phonons. Again we have a rather wide latitude in this heating term due to uncertainties in the effective mass of the carriers, m, and the mean free path l_{ac}. Since both of these parameters are functions of the electron energy, some intermediate value must be assumed. The effective mass of a low energy carrier may be as low as 0.5 m_e (m_e = free electron mass). We assume a value of $m \approx 0.75\ m_e$. The electron mean free path is estimated by $l_{ac} \sim v\tau_{coll}$, where v is the electron velocity ($v = \sqrt{2\varepsilon/m}$) and τ_{coll} is the reciprocal collision frequency. The average energy of the free carriers under pre-damage conditions is probably considerably less than $E_g/2$ (approximately 4.3 eV for NaCl). We assume $\varepsilon \approx 2$ eV and $\tau_{coll} \sim 1/(6 \times 10^{14}\ \text{sec}^{-1})$ and obtain $l_{ac} \sim 10^{-7}$ cm. With these values the lattice heating relation is

$$\rho c(dT/dt) \approx 8.3 \times 10^{-29} E^3 T^{1/2} n_c \text{ (Joules/cm}^3 \text{ sec)}, \quad (8)$$

where E is in V/cm. Of course, this value is highly uncertain; the nature of the uncertainties will be discussed below in relation to the calculated results.

For computation of heating with an avalanche-only carrier generation mechanism, a number of electrons must be initially present in the conduction band, supposedly arising from shallow electron traps imposed by impurities. In the literature, it is commonly held that the avalanche builds from initial carrier density of 10^{11} - 10^{13} cm^{-3} [4], but due to the rapid carrier buildup once the avalanche rate γ gets large during a laser pulse, the calculations are not very sensitive to variations in this parameter.

The case where free carriers are considered to be polarons is discussed in detail in [3]. The single photon absorption cross section for polarons in NaCl is $\sigma_p \approx 5.5 \times 10^{-19} \text{cm}^2$ at 532 nm, for temperatures from 300 to 600 K. This value is obtained from the acoustic phonon scattering mechanism, which has been shown to be the most effective when free carrier velocities are not "slow" [3,17].

The responses of alkali halides following electron-hole pair creation, and their possible relation to laser-induced damage, has been discussed in [16]. The rate equations in this work were derived primarily for the purpose of calculating the effects of primary defect absorption on self-trapped exciton (STE) luminescence yield. Here we particularize the model equations to NaCl for our experimental conditions. Our goal is to model energy deposition and lattice heating at high temperatures (where STE luminescence is quenched), and production of permanent defects (F centers).

The processes modeled by the rate equations are depicted in figure 6. The details are available in [8]. The primary defect contributions to lattice heating arise from the energy dissipated as a result of their formation and their photon absorption characteristics.

Thermal diffusion, as well as diffusion of primary defects and free carriers, have been shown to be negligible for our short laser pulses [8]. Thus, using the model equations, we are justified in calculating the temperature increase at the focal point of the laser beam as a function of peak photon flux.

We calculate the focal point temperature increase, ΔT_o, vs peak laser flux, F_p, for essentially three different models. These are

1) multiphoton-polaron-defect heating
2) multiphoton-assisted avalanche heating
3) unassisted avalanche heating.

Model 1) has a variation wherein we exchange free electron and polaron heating terms. In Model 2), multi-photon free carrier generation provides starting electrons for the avalanche, and in Model 3) we assume a starting electron density n_{co}.

4.1. Principal Findings

Our aim was to computer-simulate the intrinsic behavior of NaCl, that is, to reproduce the experimental results shown in figure 4 by varying $\sigma^{(4)}$ in the various models described above. We achieved this only for models where four-photon absorption was the sole mechanism for e-h pair generation (see figure 7). Due to the approximate nature of most model parameters, a "best fit" was not sought in the calculations, but rather a reasonable one satisfactorily accounting for the data. Implicit in the principal results are the defect concentrations and the individual contributions to the temperature increase, obtained from the model equations. The results for each model are summarized as follows:

1. a) Multiphoton-polaron-defect model

The approximation to the data for this model is represented by the solid line in figure 7, obtained with $\sigma^{(4)} = 2 \times 10^{-113}$ cm^{8}sec^3. This indicates that (in this model) direct e-h recombination contributes significantly to the heating, since this value of $\sigma^{(4)}$ is quite close to that obtained experimentally by assuming all heating arises from recombination ($\sigma^{(4)} \approx 5 \times 10^{-113}$ cm^{8}sec^3). The slope of the solid line is approximately 3.7, showing that, even though other mechanisms contribute to the heating, four-photon absorption is the primary interaction of the overall process and that a photoacoustic demonstration of four-photon absorption is valid. In this model, only hole absorption, direct e-h recombination and polaron absorption contribute to heating, with other species contributing much less. We consider this in more detail below.

1. b) Multiphoton-free electron-defect model

When the free electron heating expression is substituted for the polaron heating term, we obtain the dashed line in figure 7 with $\sigma^{(4)} \approx 1.5 \times 10^{-114}$ cm^{8}sec^3 to yield a reasonable fit. The slope of this line is 3.93, again indicating four-photon absorption is the primary process of the overall interaction, although clearly in this case direct e-h recombination plays a minor role in heating and the free electron heating mechanism is much more efficient than polaron heating. This is reflected by the much smaller value of $\sigma^{(4)}$ needed to approximate the data, which implies fewer conduction band carriers are needed to heat the sample.

2. Multiphoton-Assisted Avalanche with Free Electron Heating Model

No value of the parameter a (see eq (7)) in the range $3 \times 10^{-17} \leq a \leq 1 \times 10^{-15}$ could account for the experimental data. Either a had to be so small that avalanche multiplication was negligible or, if a was large enough to contribute at all, it was explosive as the nearly vertical line in figure 7 indicates for the avalanche only mechanism.

3. Avalanche e-h Generation-Free Electron Heating Model

The model with avalanche carrier generation as the only mechanism for valence electron excitation is represented by the broken, nearly vertical line in figure 7, with $a = 3 \times 10^{-16}$ and a starting carrier density of $n_{co} \approx 7 \times 10^{10}$ cm^{-3}, chosen to match the highest temperature point. This line demonstrates the general behavior of the avalanche model. Varying a only displaces the line horizontally (to lower flux for larger a and vice versa). Slightly less steep lines may be obtained for a near the low end of its range but only for $n_{co} \geq 10^{17}$ cm^{-3}, for which the crystal would no longer be transparent anyway. Thus we conclude that the avalanche mechanism (as we have used it) plays no role in carrier generation up to the temperatures we have obtained. However, it is clear that it would be nearly impossible to measure pre-damage energy deposition if it were due to avalanche generation. Since temperatures we measured do not reach the melting point (a damage criterion), we cannot conclude with certainty that avalanche formation does not occur or play a role in laser damage at higher fluxes in this case.

It is clear why the avalanche mechanism is often invoked to explain the threshold aspect of extrinsic laser damage. The line in figure 7 representing the avalanche model demonstrates the perceived aspect of negligible absorption below threshold and explosive heating at or above threshold.

4.2. Detailed Model Results

Here we present the details of the temperature increase at a typical point in the data set, $\Delta T \cong 217°C$ and $F_p = 1.34 \times 10^{30}$ photons/cm^2 sec, for both the polaron and free electron heating models with four-photon e-h pair generation.

In the polaron-defect model (model 1a), heating is dominated by hole absorption, followed by direct e-h recombination and finally polaron absorption, and in the free electron-defect model, heating is completely dominated by the free electron heating term.

We summarize the results in the following paragraphs and figures. We shall refer to model 1a) as the polaron model and 1b) as the free electron model. The four-photon cross sections used were $\sigma^{(4)} = 2 \times 10^{-113}$ cm^{8}sec^3 in model 1a) and $\sigma^{(4)} = 1.5 \times 10^{-114}$ cm^{8}sec^3 in model 1b). The temperatures are expressed in Kelvin and the starting temperature is 293 K.

In figure 8, the solid curve represents the total temperature increase in the polaron model and the dashed curve the free electron model. The total increase is 215 K and 218 K, respectively, achieved with a pulse of peak flux $F_p = 1.3 \times 10^{30}$ photons/cm^2 sec. These temperatures do not agree exactly for we have not tried to obtain precise results due to the inexact nature of the model parameters. There is only slight variation in the heating rate for the two models.

Polaron and hole absorption and e-h recombination account for approximately 208 K of the 215 K total temperature increase in the polaron model. Ignored in the recombination is the 0.7 eV difference between the e-h pair creation energy (4hv = 9.3 eV) and the band gap of 8.6 eV, which the electrons dissipate while relaxing to the bottom of the conduction band. This term accounts for most of the difference between the total temperature increase and that of the three dominant terms.

The free electron contribution to the total temperature increase in model 1b) is 204K of the total rise of 218 K. Clearly, as we have used it, the free electron model predicts very efficient heating of the lattice through electron-phonon scattering. The carrier and defect densities calculated in this model are much smaller than in the polaron model, reflecting on the much smaller value of $\sigma^{(4)}$ in this model to account for the experimental data. The temperature deficit was mostly accounted for by hole absorption. The heating rate (first derivative of the curves in figure 8) peaks with the photon flux for both models, but the rate function is much narrower than the laser pulse, so that instantaneous conversion of electromagnetic to thermal energy implicit in the photoacoustic discussion are justified. A maximum of 3×10^{12} K/sec is calculated for the modeled pulse.

Figure 9 represents the conduction carrier densities, n_c, as functions of time for the polaron model (solid curve) and free electron model (dashed curve). The maximum concentrations are $n_{cmax} \approx 3 \times 10^{18}$ cm^{-3} and 8.5×10^{17} cm^{-3}, respectively. Since this laser pulse represents a nondamaging one, it is apparent that merely achieving a carrier density of $n_c \approx 10^{18}$ cm^{-3} does not account for damage.

Detailed results indicate that neither self-trapped excitons or F centers contribute to lattice heating for either model. This holds even if one assumes an initial F center concentration of 10^{15} cm^{-3}, at which the crystal would be significantly colored. Thus, we can conclude that the measured temperature in multiple-shot-on-one-site experiments should not be influenced by F center buildup.

5. Summary

The photoacoustic technique used to obtain the experimental data clearly demonstrates the occurrence of fourth-order nonlinear absorption for nondamaging laser pulses, but does not yield an exact numerical value for the four-photon cross section $\sigma^{(4)}$, due to the nature of the photoacoustic response to total absorbed energy. The secondary absorption processes by free carriers and primary lattice defects have been shown to contribute significantly to energy absorption and subsequent material heating, but uncertainties in the requisite parameters preclude a definitive statement of their individual importance. But we conclude, based on our interpretation of the experimental results, that the four-photon cross section must lie in the range 1×10^{-114} cm^{8}sec$^3 \leq \sigma^{(4)} \leq 20 \times 10^{-114}$ cm^{8}sec^3.

We believe that the temperature increases calculated from the calibrated absorbed energy data definitely prove that significant lattice heating occurs for nondamaging laser pulses without formation of an electron avalanche. As we have documented, the damage mechanism active in NaCl at 532 nm had not been unequivocally assigned to be either avalanche or multiphoton based on damage threshold measurements. This experimental verification of significant energy deposition due primarily to four-photon absorption is the most important result of this work. However, it does not prove one mechanism or the other is responsible for laser induced damage in NaCl at this wavelength, for we could not obtain data for which the calculated temperature increase was very near the melting point of 800°C.

From our experience it is clear that further theoretical investigations should rely on data obtained only from the purest sample material available to test damage models. Use of inferior materials will only introduce more confusion than already exists in the field.

Deciding whether the polaron or free electron heating model is more appropriate must be the subject of further experimentation.

6. References

[1] A. A. Manenkov, Nat. Bur. Stand. (U.S.) Spec. Publ. 509; 1977. 455-464.

[2] B. G. Gorshkov, A. S. Epifanov, and A. A. Manenkov, Sov. Phys. JETP 49, 309 (1977).

[3] A. Schmid, P. Kelly, and P. Braunlich, Nat. Bur. Stand. (U.S.) Spec. Publ. 509; 1977. 465-472.

[4] A. S. Epifanov, Sov. Phys. JETP 40, 897 (1975).

[5] E. W. VanStryland and M. A. Woodall, Nat. Bur. Stand. (U.S.) Spec. Publ. 620; 1981. 50-57.

[6] E. W. VanStryland, M. A. Woodall, W. E. Williams, and M. J. Soileau, Nat. Bur. Stand. (U.S.) Spec. Publ. 638; 1983. 589-600.

[7] P. Horn, P. Braunlich, and A. Schmid, J. Opt. Soc. Am. B2, 1095 (1985).

[8] Scott C. Jones, Ph.D. Dissertation, Washington State University (1986).

[9] Matthew Delong, University of Utah Crystal Growth Laboratory, Salt Lake City, Utah (Private Communication, 1985).

[10] H. W. Etzel and D. A. Patterson, Phys. Rev. 112, 1112 (1958).

[11] J. Rolfe, Phys. Rev. Lett. 1, 56 (1958).

[12] W. L. Smith, Opt. Eng. 17, 489 (1978).

[13] W. L. Smith, J. H. Bechtel, and N. Bloembergen, Phys. Rev. B12, 706 (1975).

[14] W. L. Smith, J. H. Bechtel, and N. Bloembergen, Phys. Rev. B15, 4039 (1977).

[15] M. J. Soileau, W. E. Williams, and E. W. VanStryland, Nat. Bur. Stand. (U.S.) Spec. Publ. 660; 1984. 387-405.

[16] G. Brost, P. Braunlich, and P. Kelly, Phys. Rev. B30, 4675 (1984).

[17] M. Sparks, D. L. Mills, R. Warren, T. Holstein, A. A. Maradudin, L. J. Sham, E. Loh, and D. F. King, Phys. Rev. B24, 3519 (1981).

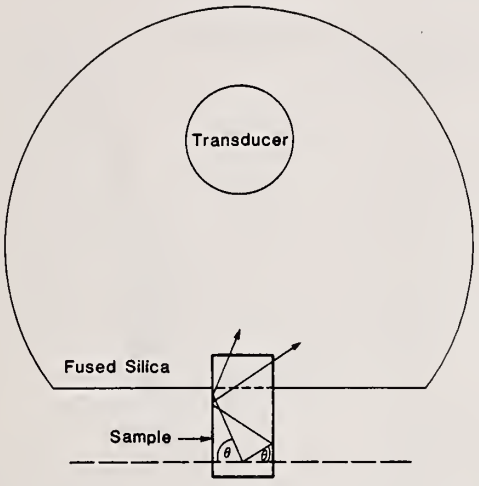

Figure 1. Acoustic detection system. The transducer is mounted at one focus of the truncated silica ellipse and the sample is mounted so that the other focus lies within it. The arrows indicate the propagation direction of acoustic wavelets leaving the interaction volume at angles (θ) relative to the beam axis.

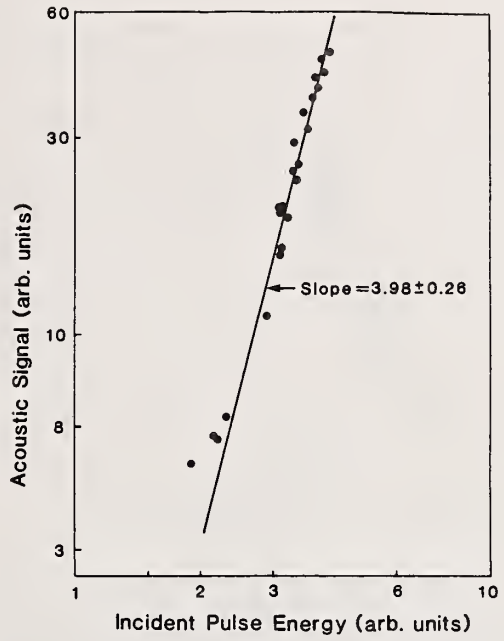

Figure 2. Double logarithmic plot of acoustic signal vs laser pulse energy in NaCl at 532 nm. The slope of 4 demonstrates the four-photon nature of the absorption.

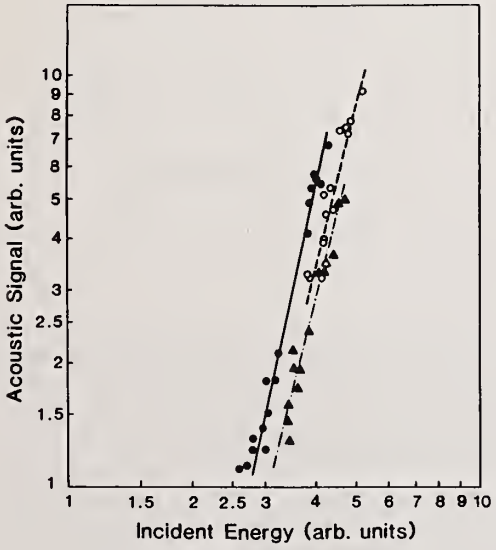

Figure 3. Double-logarithmic plot of acoustic signal vs incident pulse energy, verifying the existence of measurable four-photon absorption. The slopes and highest nondamaging intensities are: ●, 3.55 ± 0.15 and 420 GW/cm^2; ○, 3.95 ± 0.4 and 500 GW/cm^2; ▲, 3.87 ± 0.25 and 445 GW/cm^2.

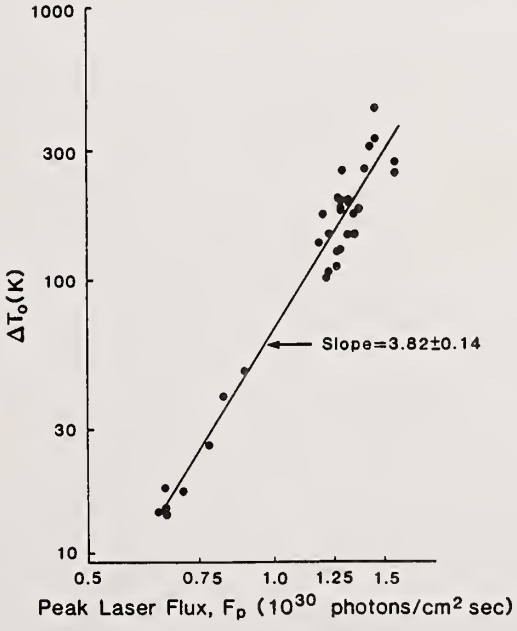

Figure 4. Composite double-logarithmic plot of calculated temperature increase at focal point vs incident energy of 532 nm pulses for sample numbers 1 and 2. Sample no. 1 data (lower 8 points) indicate an upper limit on $\sigma^{(4)}$ of $(5.7 \pm 2.5) \times 10^{-113}$ cm^{8}sec^3. The upper set of points, obtained from sample no. 2, yield an upper limit of $\sigma^{(4)} = (4.3 \pm 2.4) \times 10^{-113}$ cm^{8}sec^3.

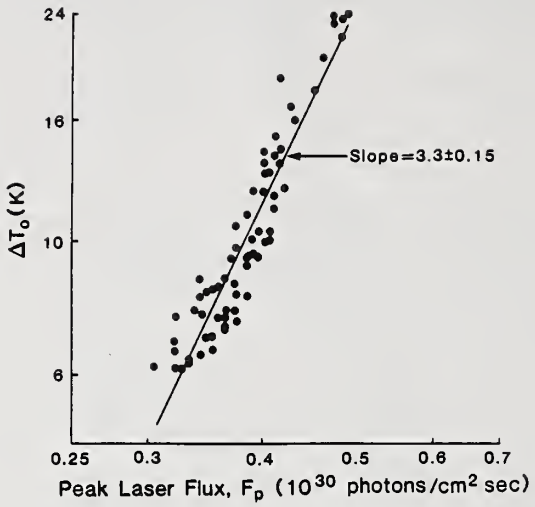

Figure 5. Double-logarithmic plot of calculated temperature increase at focal point vs incident 532 nm pulse energy for sample no. 3. The smaller slope (3.3 ± 0.15) and larger indicated cross section [$\sigma^{(4)}$ = (2.75 ± 1.0) x 10^{-112} cm^8sec^3] compared with sample nos. 1 and 2 imply impurities may be playing a more important role in the absorption process.

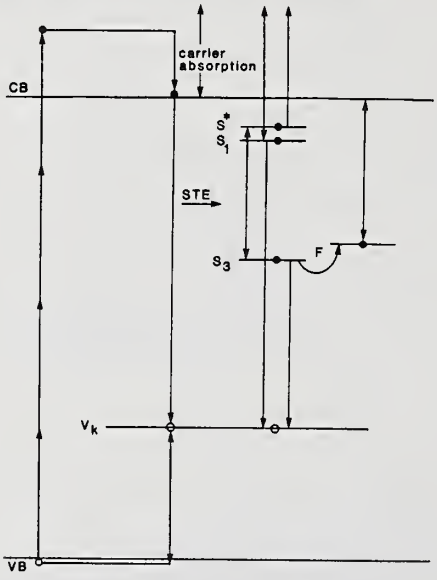

Figure 6. Level diagram and transitions incorporated in model equations. Four-photon-generated free carriers and holes are trapped to form self-trapped excitons (STEs) and V_K centers. Holes can be released by single photon absorption, as can electrons in the S_1 and S* STE states. Electrons in S_3 can be excited to S* by single photon absorption. All downward electron transitions are nonradiative in model calculations. Free carriers can also absorb electromagnetic energy. At high temperature, F centers are formed through the S_3 STE state.

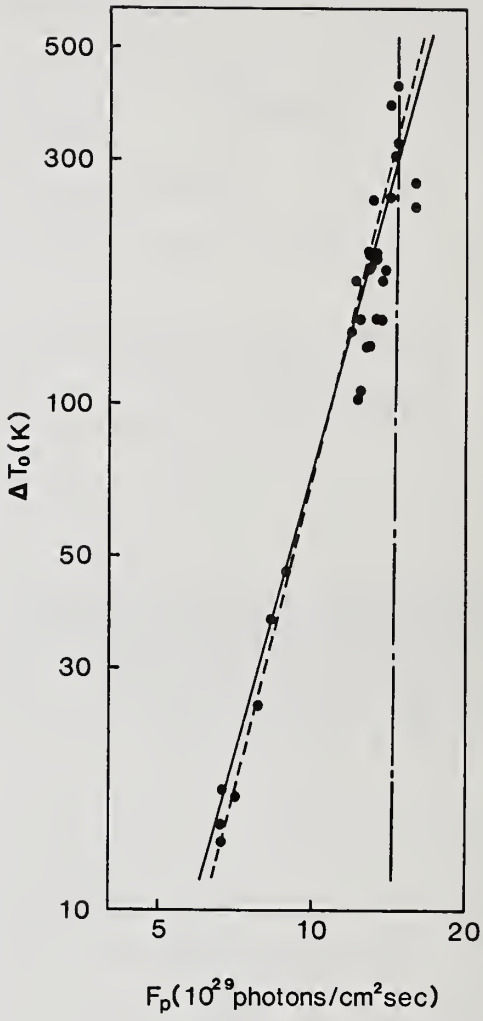

Figure 7. Model calculations superimposed on data of sample nos. 1 and 2 (Fig. 4). The solid line is that calculated with the four-photon-polaron model, using $\sigma^{(4)} = 2 \times 10^{-113}$ cm^8sec^3; the slope is ≈ 3.7. The dashed line is that obtained with the four-photon-free electron model, using $\sigma^{(4)} = 1.5 \times 10^{-114}$ cm^8sec^3; the slope is 3.93. The broken line was obtained with the avalanche-free electron model, using $a = 3 \times 10^{-16}$ and initial carrier density $n_{co} \approx 7 \times 10^{10}$ cm^{-3}.

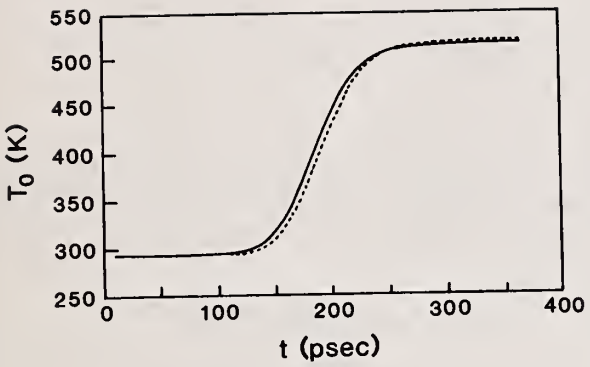

Figure 8. Focal point temperature, T_0, vs time calculated for a pulse with $F_p = 1.34 \times 10^{30}$ photons/cm^{2}sec. Solid line; multiphoton-polaron model (model 1a)) using $\sigma^{(4)} = 2 \times 10^{-113}$ cm^{8}sec^3. Dashed line; multiphoton-free electron model (model 1b)), $\sigma^{(4)} = 1.5 \times 10^{-114}$ cm^{8}sec^3. Laser pulse "begins" at $t = 0$ with $\tau = 85$ psec.

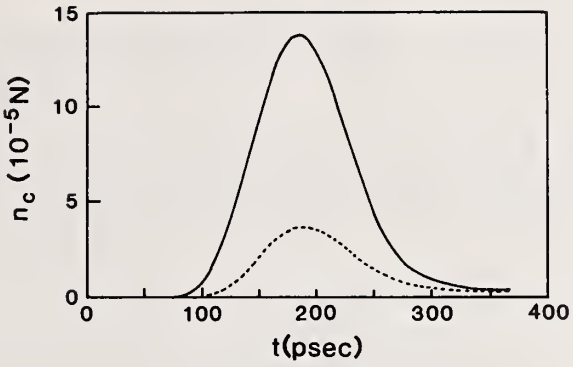

Figure 9. Free carrier density, in terms of the density of active atoms, $N = 2.2 \times 10^{22}$ cm^{-3}. Many more carriers are generated in the polaron model (solid line) than in the free electron model (dashed line).

Manuscript Received
6-10-87

An Anomalous Absorption Model to Account for Accumulation in N-on-1 Damage in Si and GaAs

N.R. Shetty*, M.F. Becker, and R.M. Walser

The University of Texas at Austin
Center for Materials Science and Engineering and
Electrical and Computer Engineering Department
Austin, Texas 78712-1084

*Fullbright Fellow from Karnataka Regional Engineering College, India

In this work we have investigated a model for anomalous optical absorption and laser damage in Si and GaAs. The model determines the increase in charge density in the vicinity of small, compared to the optical wavelength, clusters of defects in the material. The aim is to determine if increases in defect density in these regions can account for the experimentally observed decrease in damage threshold or accumulation. We found that 10% to 20% reductions in damage threshold could be accounted for by this model, but that this is only sufficient to account for some of the experimental observations.

Keywords: N-on-1 damage; silicon; gallium arsenide; modelling laser damage

1. Introduction

Accumulation in laser damage has been observed in many materials. In this theoretical investigation we concentrate on modelling the laser damage and accumulation behavior of Si and GaAs at a laser wavelength of 1064 nm. Much N-on-1 laser damage data is available at this wavelength, and experimental observations have indicated laser damage threshold reductions from 10% to as much as 50% as N is increased [1-3]. Speculations on the causes of accumulation in these semiconducting materials has centered on pre-existing and laser induced defects of as yet unspecified types [4]. However, no direct evidence for their existence has been presented to date.

We have undertaken this work in order to achieve a better understanding of the energy transfer mechanisms during the laser irradiation of Si and GaAs. We have investigated an anomalous model for absorption in an effort to see how the evolution of charge density in the vicinity of defects much smaller than the optical wavelength can produce sufficiently large and dense plasmas as to lead eventually local melting and damage. Avalanche ionization is included in this model as a means to achieve such densities. In addition, we investigated the effect of the density of defects on damage threshold in an attempt to link the defect density at the start of a laser pulse with the damage threshold observed in the presence of accumulation. Significant motivation for this task was provided by the work by Lange, McIver, and Guenther [5] on the modelling of the charge evolution from defects in laser damage of wide band-gap insulators and thin film materials.

2. The Model

The underlying assumption of the model is the existence of a spherical region, of radius r_0, in the semiconductor which contains a higher density of ionizable defects than the surrounding material. When the laser pulse is incident, the spherical defect region becomes the center of a growing region of charge. Carrier generation by single photon, multi-photon, and impact ionization should be considered in addition to the usual diffusion and recombination terms. The model is described pictorially in figure 1. Accumulation will be investigated by determining what change in the defect spheres, increase in defect density N_D for example, will result in the damage threshold decrease observed in accumulation. The result will determine if such changes in the defect clusters is a possible or probable explanation for accumulation.

Since we are dealing with unspecified ionizable defects and with electron impact ionization, we will model electron dynamics only. The classical equation of electron diffusion can be written as

$$\frac{\partial n}{\partial t} = 1/r \frac{\partial^2}{\partial r^2} (rD_e n) + g(n,T,|E|) - (n-n_i)\gamma(n,T) \qquad (1)$$

where D_e is the electron diffusivity, $|E|$ the optical electric field strength, g is the electron generation rate, n the electron density, n_i the initial electron density, and γ is the electron decay rate. The general solution to the above equation may be obtained by an integral transform technique [6] and can be written as

$$n(r,t) = \frac{2}{\pi r} \int_0^\infty d\beta \sin(\beta r) e^{-(D_e\beta^2 + \gamma)t} \int_0^t dt' \int_0^\infty r'dr' \sin(\beta r') g(r',t') \exp[(D_e\beta^2 + \gamma)t'] \qquad (2)$$

These integrals may be simplified for three cases of interest: inside the defect cluster without impact ionization, outside the defect cluster without impact inization, and in any region with impact ionization present if an initial electron density is assumed.

For the first case, $r \leq r_0$, generation is assumed only in the spherical defect cluster region. The generation term becomes

$$g(r',t') = f(t')\,[\Theta(r') - \Theta(r'-r_0)] \qquad (3)$$

where $\Theta(r)$ are unit step functions and f(t') is given by

$$f(t') = \left[\frac{\eta_Q \alpha_1 I(1-R)}{h\nu} + \frac{\beta I^2 (1-R)^2}{2h\nu}\right] \Theta(t') \qquad (4)$$

Both single and two photon excitations are considered, where I is the incident laser intensity, α_1 is the one photon absorption coefficient with quantum efficiency η_Q, β is the two photon absorption coefficient, R is the reflection coefficient at the material surface, and $h\nu$ is the photon energy. The simplified solution to the diffusion equation becomes

$$n(r,t) = \frac{2f(t_p)r_0^3}{\pi r D_e} \int_0^\infty \frac{dx \sin x \frac{r}{r_0} (\sin x - x\cos x)(1-\exp[D_e x^2/r_0^2 + \gamma)t])}{x^2(x^2 + r_0^2\gamma/D_e)} \qquad (5)$$

where the remaining integral will be evaluated numerically.

In the second case, for $r > r_o$, the generation term becomes a delta function in the form

$$g(r',t') = \frac{\delta(r')f(t')V_a}{4\pi r'^2} \tag{6}$$

where V_a is the characteristic volume of absorption, $V_a = 4\pi r_o^{3/3}$, and $f(t')$ is still given by (4). Substituting eq (6) into (2) we get

$$n(r,t) = \int_0^t \frac{dt' V_a f(t')}{8(\pi D_e(t-t'))^{3/2}} \exp\left[\frac{-r^2}{4D_e(t-t')}\right] \exp\left[-\gamma(t-t')\right] \tag{7}$$

As before, the remaining integral will be evaluated numerically.

In the third case, we assume that generation is augmented by avalanche ionization. For a case where the charge density is already more than 10^{10} cm^{-3}, one and two photon excitations are dominated by impact ionization. The generation rate may then be written as

$$g(r,t') = f(t')\exp[-p^2(t')r'^2] \tag{8}$$

where $f(t') = n_i\ \alpha_a \exp(\alpha_a t')$ is the ionization rate term with α_a being the intensity dependent avalanche coefficient and n_i the initial electron density. The second term in eq (7) represents the diffusive spread of the electron source and $p(t')$ is given by

$$p(t') = \frac{1}{\sqrt{D_e t'}} \tag{9}$$

Substitution of (8) and (9) into (2) yields the solution for this case

$$n(r,t) = \frac{1}{8} \int_0^t \frac{dt'\ f(t')(D_e t')^{3/2}}{(D_e((t-t') + \frac{1}{4D_e p^2}))} \exp[-\gamma(t-t')] \exp\left[\frac{-r^2}{4(D_e(t-t') + \frac{1}{4D_e p^2})}\right] \tag{10}$$

which will be solved numerically. Equation (8) represents a means by which to generate carriers at an exponential rate dependent on the optical intensity or electric field strength. This process will be terminated at some point due to processes such as the dynamic Burnstein effect, the ionization of a large fraction of the available atoms, or catastrophic damage.

3. The Solutions

In the next section, we will examine the solutions for the three cases given above. Subsequently, the regime of early charge build-up in the absence of avalanche ionization will be combined with the regime where charge density increases to damaging levels by avalanche ionization in order to realize a comprehensive model. First, values for constants such as absorption coefficients in the defect clusters will be determined.

The cases to be examined are for Si and GaAs irradiated at 1064 nm, above and below bandgap photons respectively. In both cases, the defects are assumed to be one photon ionizable and having an initial density of 10^{17} cm^{-3}. The stimulated transition rate for these transitions is given by

$$W_{ik} = \frac{Ig(\nu)e^2 f_{ik}\pi}{mch\nu\ n} \tag{11}$$

where $g(\nu)$ is the normalized line shape function, f_{ik} is the oscillator strength and assumed to be one, and n is the refractive index. At line center, the lineshape function is given by $g(0) = \frac{1}{\Delta\nu}$, where $\Delta\nu$ is the FWHM linewidth for the defect absorption. We shall estimate these values to be 2.2×10^{13} Hz and 3.2×10^{13} Hz respectively for Si and GaAs, based on measurements of impurity behavior [7]. A value for α_1 for the impurity region can be determined using eq (11) and the following

$$\frac{(1-R)\eta_Q \alpha_1 I}{h\nu} = W_{ik} N_d \tag{12}$$

where η_Q is the quantum efficiency and is taken as one, and N_D is the initial defect density. The values for α_1 are found to be 25 cm^{-1} and 17 cm^{-1} respectively for Si and GaAs. These numbers are reasonable since typical values of α_1 for common samples of these materials are 10 cm^{-1} and 1 cm^{-1} respectively. Thus, the defect clusters have absorption constants somewhat greater than that of their typical host material. Two photon absorption is considered only for GaAs and a two photon absorption constant of 0.05 cm/MW is used [8].

Recombination rates are treated differently for cases where carrier density is low or high. For cases without avalanche ionization where carrier densities will be less than 10^{17} cm^{-3}, Auger recombination is negligible, and the effects of standard recombination are negligible with respect to diffusion. In the case of avalanche ionization and higher carrier densities, Auger recombination only will be considered. Auger constants for Si and GaAs are 4×10^{-31} cm^6/s and 10^{-31} cm^6/s respectively [9]. For carrier densities of 10^{20} cm^{-3}, the carrier relaxation rates, γ, become 4×10^9 s^{-1} and 10^9 s^{-1} respectively. Parameter values covering this range are shown in the following numerical simulations. Other constants used in the simulation are given in the table insert of figure 2.

Typical results for the growth of electron density inside a defect cluster using eq (5) are shown in figure 2, and results outside a defect cluster using eq (7) in figures 3 and 4. In all cases, steady state is reached in 10-20 ps. Further, the assumption that carrier decay may be neglected is shown to be justified since decay rates up to 10^9 to 10^{10} s^{-1} do not affect the result. Steady state values obtained from these calculations will be used later as initial carrier concentrations for avalanche ionization build-up.

In the presence of avalanche ionization, eq (9) is used to model the charge density. As discussed previously, the generation terms in this case are dominated by the avalanche term and only it is retained. As higher electron densities are reached, Auger recombination cannot be neglected. For the solutions modeled in this section, a range of decay rates between 10^9 s^{-1} and 10^{11} s^{-1} is shown. Although, the model does not include the variation of Auger decay rate with electron density, only small errors result from this approximation. This is seen most clearly in the typical results shown in figures 5 and 6 for Si and GaAs respectively. In these cases, the initial charge density was 10^{10} cm^{-3} and other constants as shown in figure 2. These examples were chosen since the values of the avalanche ionization coefficient, 10^9 s^{-1} and 5×10^9 s^{-1} are in the range we will later determine is appropriate for these semiconductor materials. The rapid

increase of carrier density due to avalanche ionization is immediately apparent, and the strong sensitivity of this rate to changes in $_a$ and laser intensity is also clear.

4. Accumulation Behavior

A model combining the initial build-up of charge from one and two photon absorption followed by avalanche ionization over a growing volume should be able to model the initial evolution of the laser damage process in these materials. Once the plasma density reaches about 10^{20} cm^{-3} in a region approaching a wavelength in size, thermal heating can rapidly proceed to melting and damage. For the purposes of this model, damage will be defined as having occurred when the carrier density reaches 10^{20} cm^{-3}, and pulse shapes will be taken as rectangular. In all the cases shown here, the charge density is monitored near the center of the initial defect cluster at r = 20 nm (r_o is 100 nm in all cases).

First, initial carrier densities are determined using eq (5) and taking the near-steady-state value reached at 10 ps as the initial value for avalanche ionization. As a starting point, we know Si and GaAs damage at several J/cm^2 for 10 ns pulses at 1064 nm. This is equivalent to intensities of a few tenths of GW/cm^2. Initial carrier densities for both materials for this intensity range are shown in figure 7. The nonlinear behavior of GaAs is not surprising since two photon as well as one photon absorption are present. Estimating avalanche ionization rates at optical frequencies for these materials is a serious problem. We have used DC values of ionization coefficient and drift velocity as a starting point as these have been widely measured as a function of electric field [10]. The ionization rate is simply the product of the ionization coefficient and the drift velocity. The approach taken was to adjust the DC field values for Si to fit the data point of damage at 0.3 GW/cm^2 for a 10 ns pulse. This resulted in the value of α_a being decreased by 1/6. A plot of the DC and corrected avalanche rates for Si is shown in figure 8. The adjustment constant can probably be justified by assuming a lower efficiency for impact ionization as frequency increases [11-12]. The case of GaAs is not as simple. GaAs is observed to damage by local melt pits; a behavior associated with local imperfections. A damage threshold higher than the measured value of 3 J/cm^2 or 0.3 GW/cm^2 for 10 ns pulses may be justified. In fact, if the DC avalanche rates for GaAs are corrected downward by the same 1/6 factor as used for Si, a damage threshold of 5 J/cm^2 or 0.5 GW/cm^2 is predicted by the model. The DC and corrected values for avalanche ionization rates in GaAs are shown in figure 9. Values obtained from these graphs are used in subsequent modelling.

The central question in this work is whether accumulation can be accounted for by an increase in the defect density in the initial spherical regions. To determine this, the model was exercised in reverse. The threshold intensity was lowered by percentages between 0% and 20% and new values of n_i and N_D were determined. The new value of defect density would have been created by previous pulses and would account for the threshold reduction observed in accumulation. The results for such reverse modelling are shown in figure 10 where F_N/F_1 is the ratio of the N-th pulse damage threshold fluence to the single pulse damage fluence. As can be seen from the figure, the increase in N_D is not sufficient to account for large amounts of accumulation as initial defect densities and charge densities near 10^{20} cm^{-3} do not seem reasonable. At best a 20% decrease in threshold for Si and a 10% decrease for GaAs can be accounted for in this way. Experimentally observed values range from 15% to 20% for well prepared Si samples and commonly up to 50% for GaAs.

A final check on the performance of the model was performed. That was to predict the dependence of damage threshold on laser pulse length. This behavior has been experimentally determined for pulse lengths ranging from picoseconds to milliseconds. However, several approximations in our model will fail if the pulse length becomes either much longer or much shorter than the nanosecond range assumed. We used the same starting values and avalanche ionization rates as the previous solutions, and fit the damage thresholds to 3 J/cm^2 and 5 J/cm^2 for Si and GaAs respectively for 10 ns pulses. The results are shown in figure 11. The general trend is excellent and the power law dependence is also in the range shown for experiments. The experiments generally show exponents around 0.5 or less with a tendency toward lower values for shorter pulses and larger values for longer pulses [13]. The model is quite close to predicting the pulse width dependence of damage thresholds for this range of pulse lengths.

5. Conclusions

In this work we have developed an anomalous defect absorption model for laser damage in semiconductors and applied it to multi-pulse damage of Si and GaAs. Spherical regions of about 100 nm radius with higher defect density than the bulk material were assumed to be the starting point for charge growth. Initial charge density was generated by one and two photon absorption in the spherical regions and spread by diffusion. This initial charge density was used as the

source of charge for impact ionization in the strong optical electric fields. Damage was assumed to be inevitable when the charge density exceeded 10^{20} cm^{-3} by the end of the rectangular shaped laser pulse. Based on reasonable adjustments to the avalanche ionization rates for DC fields, damage thresholds in Si and GaAs could be predicted correctly for 10 ns pulses at 1064 nm.

Accumulation was investigated by determining how much of an increase in the initial defect density was required to produce reductions of the damage threshold similar to those observed in N-on-1 damage experiments. Only about a 20% decrease for Si and a 10% decrease in threshold for GaAs could be predicted by the model. This is satisfactory agreement for good quality Si samples which do not show more than a 20% threshold decrease due to accumulation. However, experiments with GaAs have typically shown decreases of up to 50% and morphologies dominated by local defects. The model is clearly unsuccessful for GaAs and a more complex defect accumulation model is required. As a test of the general effectiveness of the model, predictions of the pulselength dependence of damage thresholds were found to be in good agreement with measurements in the ps to ns range for which the model assumptions are valid.

This research was supported by the Texas Advanced Technology Research Program. The authors would like to thank Daniel Ho and Rodolfo Reveles for their expert assistance with the numerical modelling.

6. References

[1] Y.K. Jhee, M.F. Becker, and R.M. Walser, "Charge Emission and Precursor Accumulation in the Multiple-Pulse Damage Regime of Silicon," J. Opt. Soc. Am. part B 2, 1626 (1985)

[2] A.L. Huang, M.F. Becker, and R.M. Walser, "Laser Induced Damage and Ion Emission of GaAs at 1.06 Microns," Appl. Opt. 25, 3864 (1986)

[3] D.K. Sardar, M.F. Becker, and R.M. Walser, "Auger Analysis of Elemental Depth Profiles Correlated with Multipulse Laser Damage of GaAs Surfaces," Topical Meeting on Optics in Adverse Environments, Optical Society of America, Washington, D.C. 1987

[4] J. Platenak, M.F. Becker, and R.M. Walser, "Temperature Effects on Laser Induced Damage and Accumulation in Silicon," 18th ASTM Laser Damage Symposium, NBS Special Publication, Boulder, CO, 1986

[5] M.R. Lange, J.K. McIver, and A.H. Guenther, "Anomalous Absorption in Optical Coatings," 17th ASTM Laser Damage Symposium, NBS Special Publication, Boulder, CO, 1985

[6] M.R. Lange, J.K. McIver, and A.H. Guenther, "Pulsed Laser Damage in thin film Coatings: Fluorides and Oxides," Thin Solid Films 125, 143 (1985)

[7] J.I. Pankov, Optical Processes in Semiconductors, Prentice-Hall, New Jersey, 1971

[8] E.W. Van Stryland, M.A. Woodall, H. Vanherzeele, and M.J. Soileau, "Energy Band-GAp Dependence of Two-Photon Absorption," Opt. Lett. 10, 490 (1985)

[9] J.R. Meyer, M.R. Kruer, and F.J. Bartoli, "Optical Heating in Semiconductors: Laser Damage in Ge, Si, InSb, and GaAs," J. Appl. Phys. 51, 5513 (1980)

[10] S.M. Sze, Physics of Semiconductor Devices, Wiley, New York, 1969

[11] A.S. Epifanov, "Avalanche Ionization Induced in Solid Transparent Dielectrics by Strong Laser Pulses," Sov. Phys. JETP 40, 897 (1975)

[12] M. Sparks, "Current Status of Electron-Avalanche-Breakdown Theories," 7th ASTM Laser Damage Symposium, NBS Special Publication #435, Boulder, CO, 1975

[13] A.L. Smirl, T.F. Boggess, I.W. Boyd, S.C. Moss, K. Bohnert, and K. Mansour, "Application of Nonlinear Optical Properties and Melt Dynamics of Crystalline Silicon to Optical Limiting of 1 Micrometer Picosecond Radiation," Optical Engineering 25, 157 (1986)

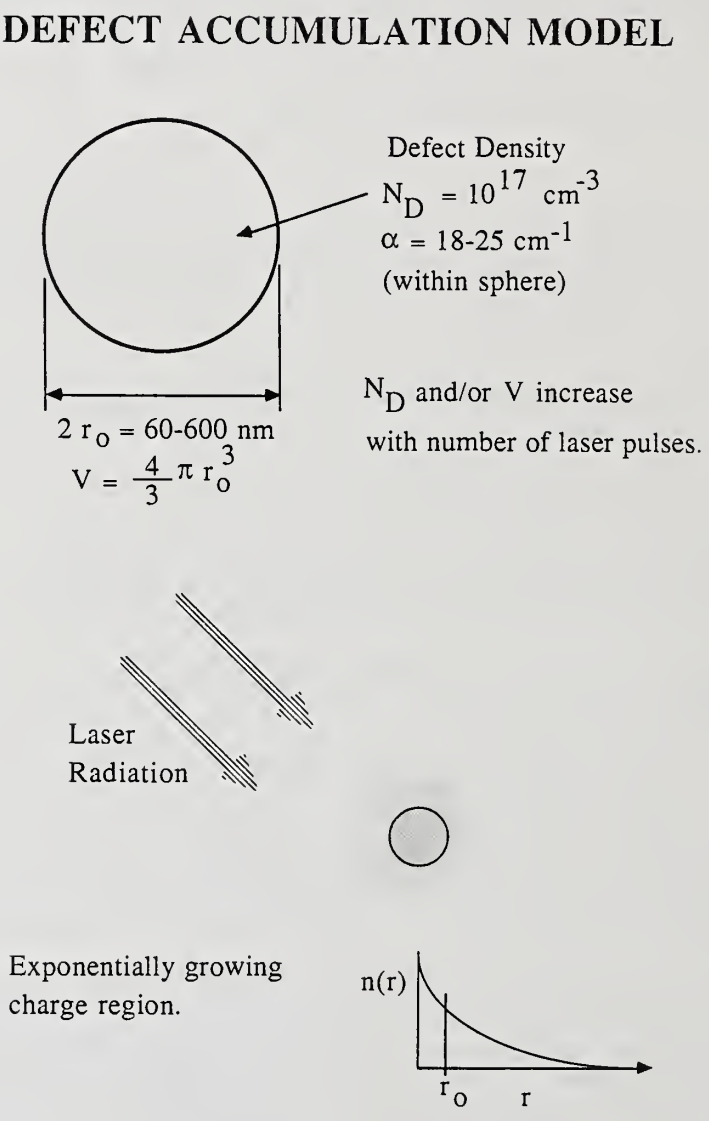

Figure 1. Schematic description of the model. Above, the small spherical defect region before laser irradiation. Below, in the presence of avalanche ionization, the defect sphere becomes the center of an exponentially growing region of free charge.

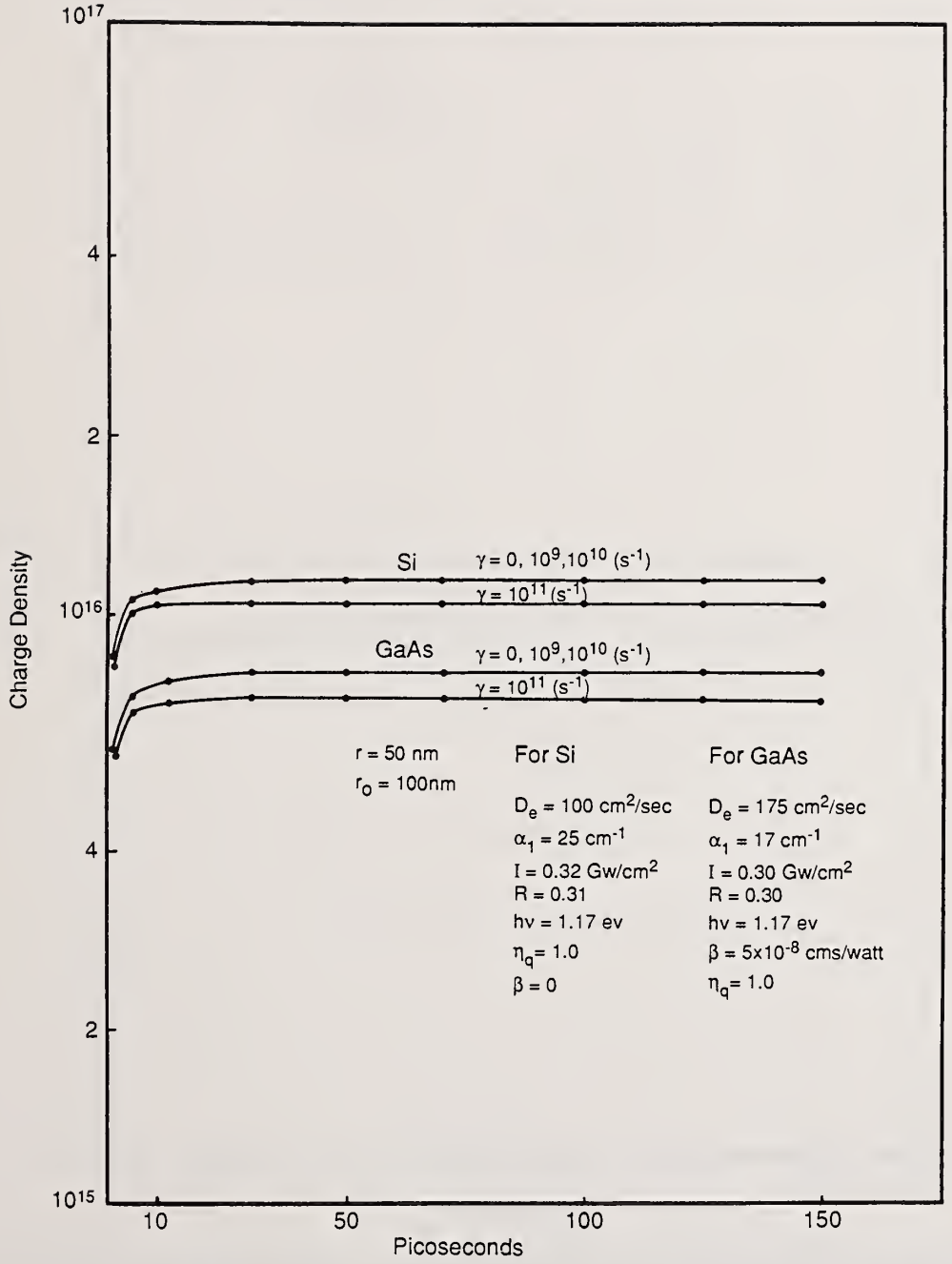

Figure 2. The growth of electron density at a radius of 50 nm within a 100 nm radius absorbing region in Si and GaAs for various decay rates and listed parameters.

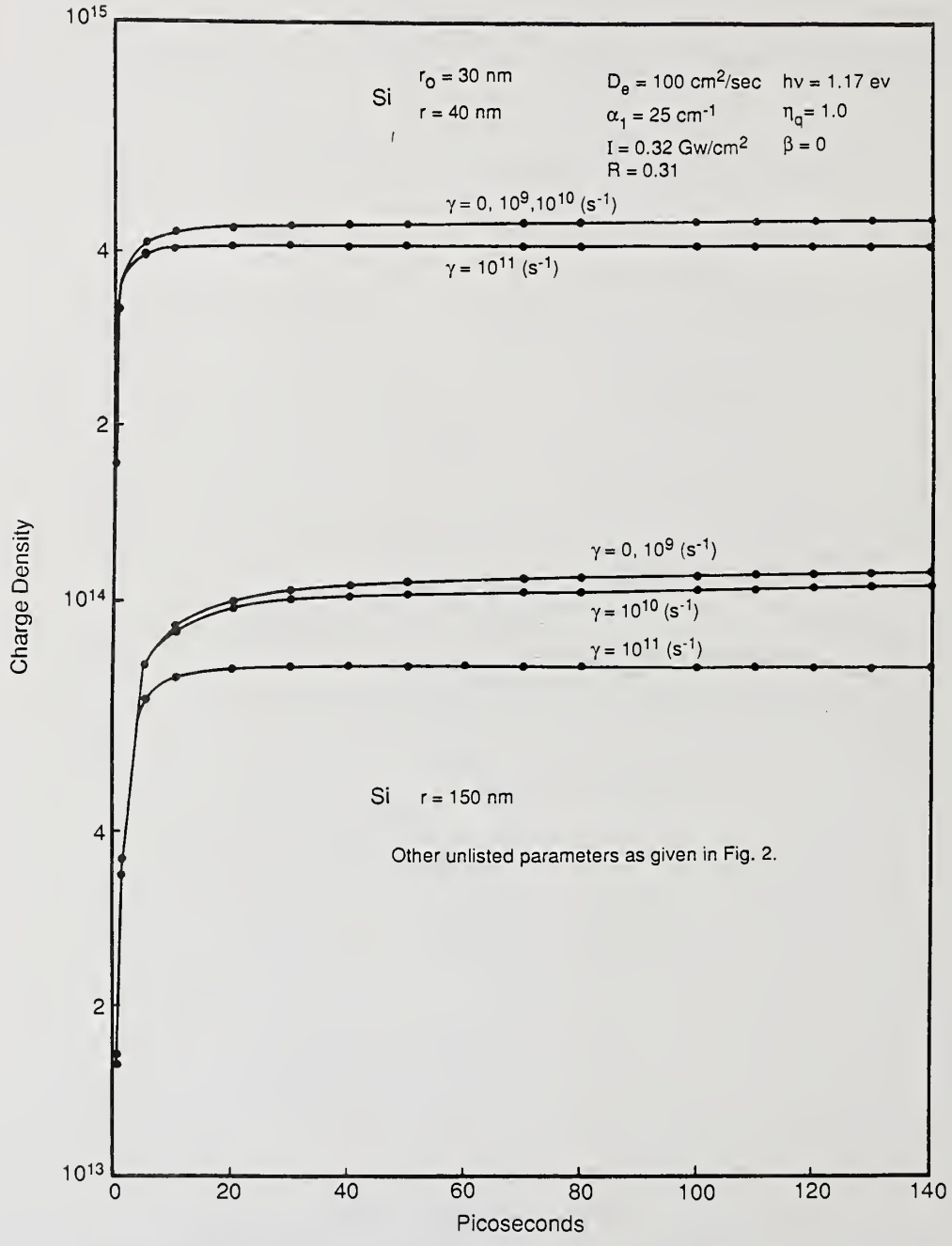

Figure 3. The growth of electron density at radii of 40 nm and 150 nm outside a 30 nm radius absorbing region in Si for various decay rates and listed parameters.

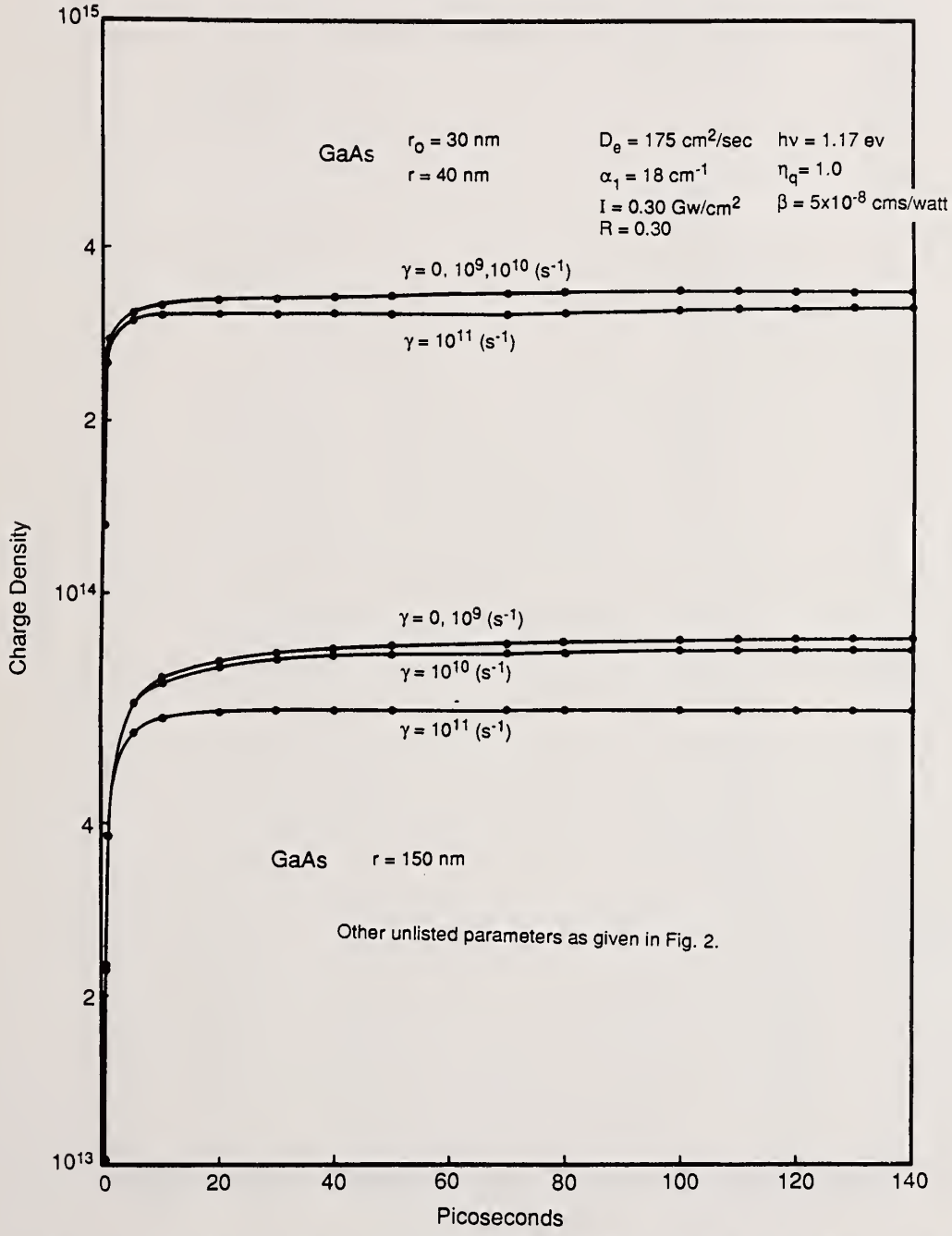

Figure 4. The growth of electron density at radii of 40 nm and 150 nm outside a 30 nm radius absorbing region in GaAs for various decay rates and listed parameters.

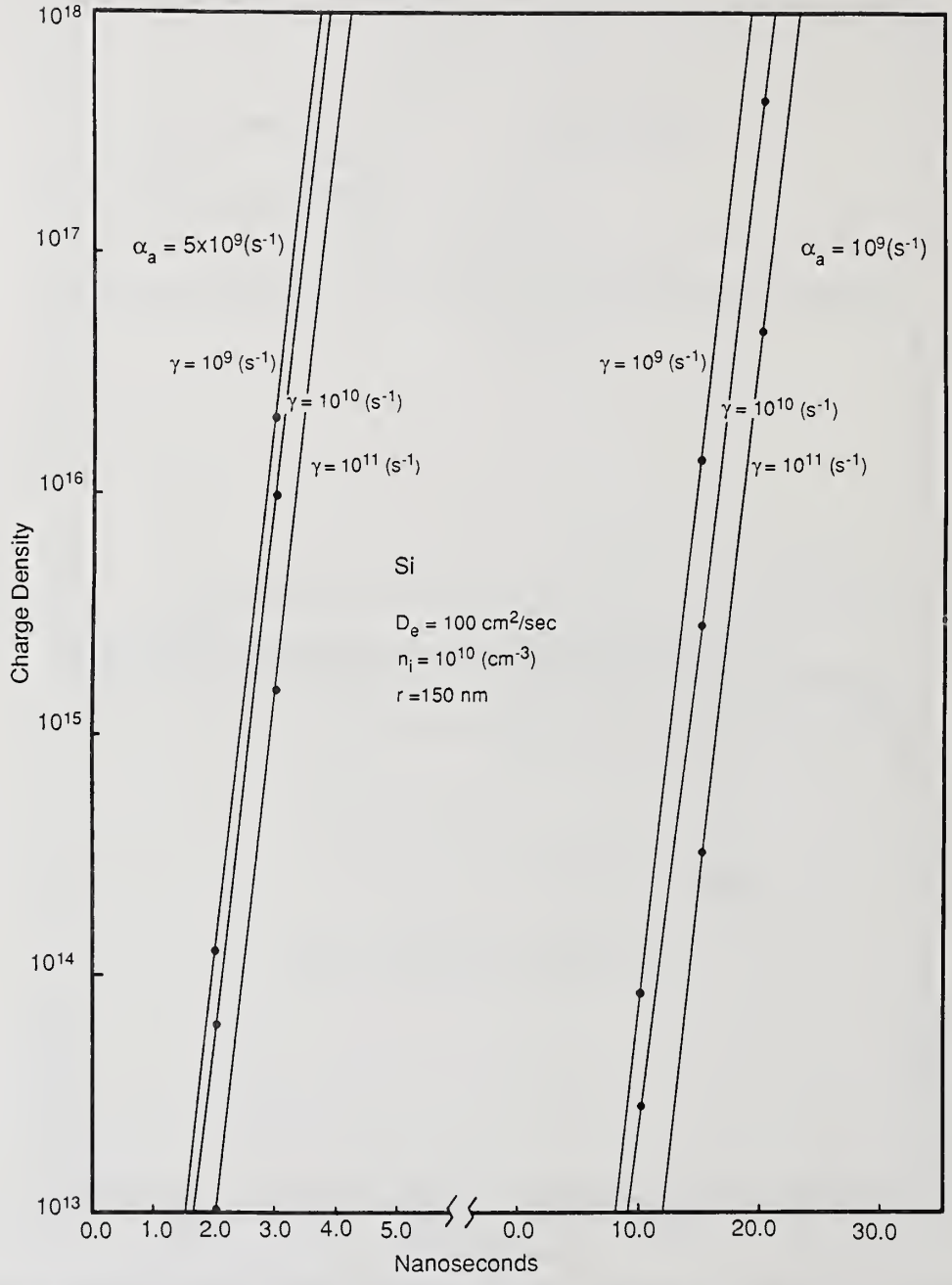

Figure 5. The growth of electron density at a radius 150 nm in Si by avalanche ionization for various ionization and decay rates.

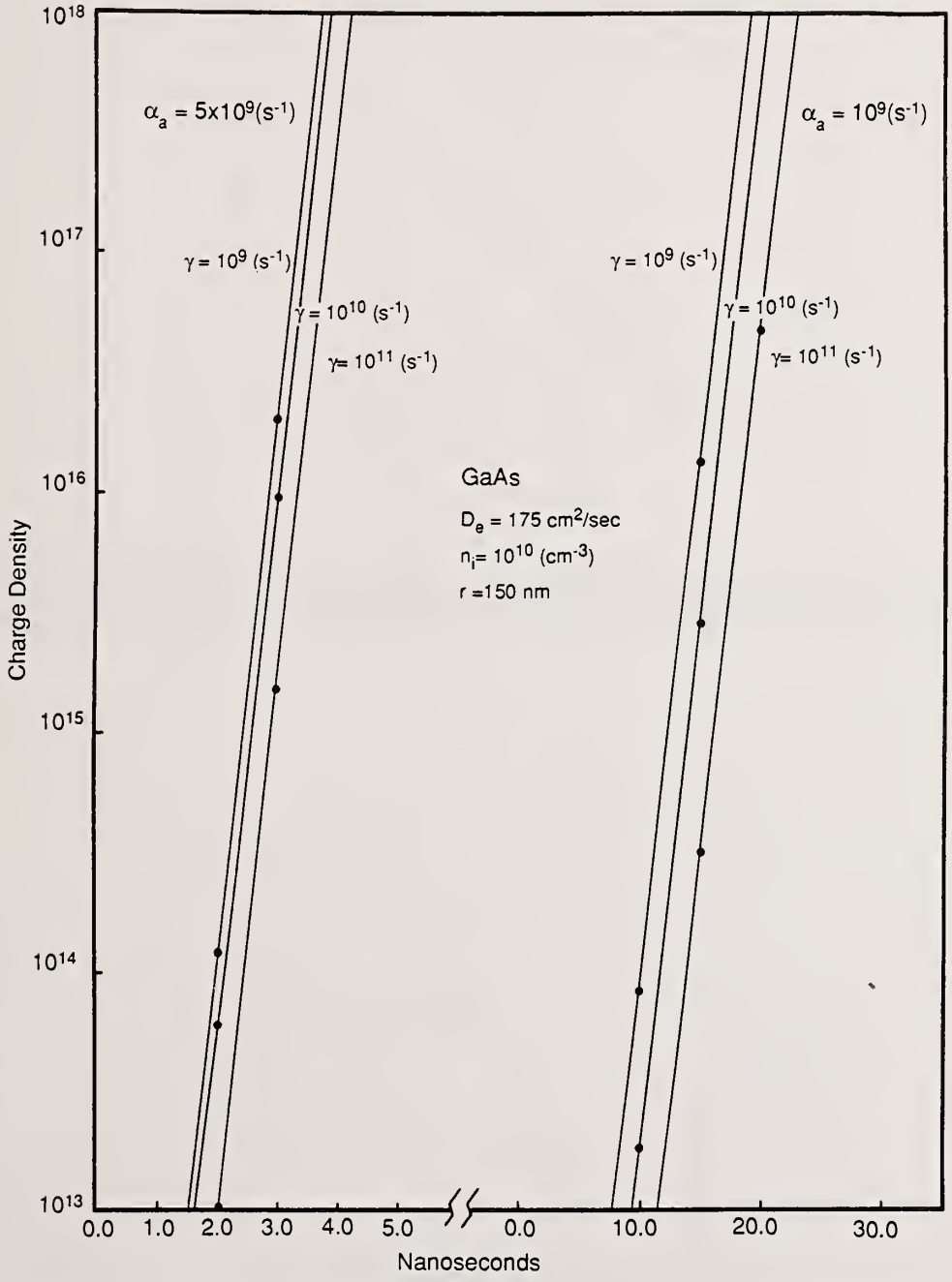

Figure 6. The growth of electron density at a radius 150 nm in GaAs by avalanche ionization for various ionization and decay rates.

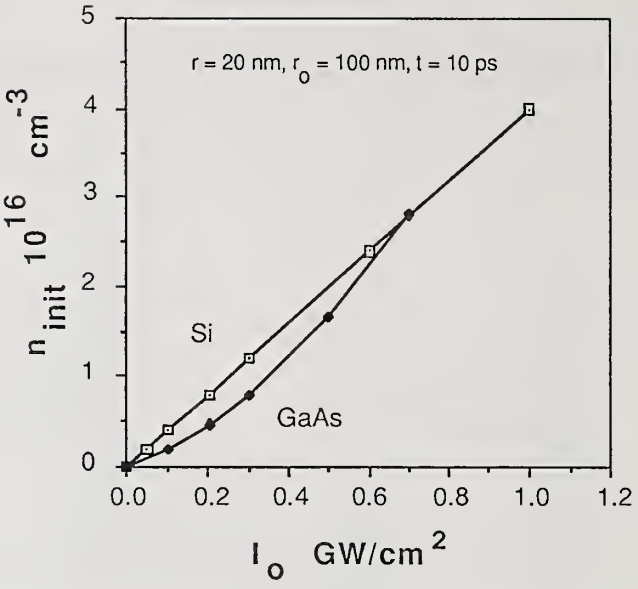

Figure 7. Initial electron density versus intensity at a radius of 20 nm inside a 100 nm radius absorbing region of $N_D = 10^{17}$ cm^{-3} for Si and GaAs. The time is taken as 10 ps when carrier densities are reaching steady-state values.

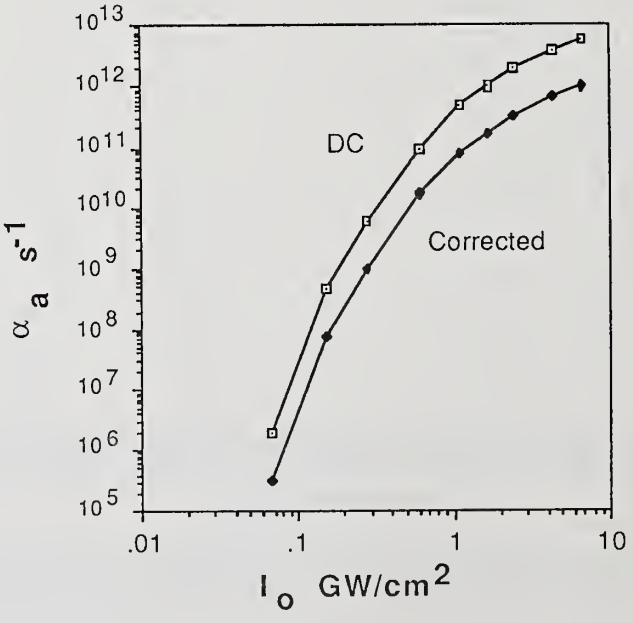

Figure 8. Avalanche ionization rate for Si versus incident laser intensity. The DC curve is computed directly from DC ionization rates for the corresponding optical electric field strength. The correction is described in the text.

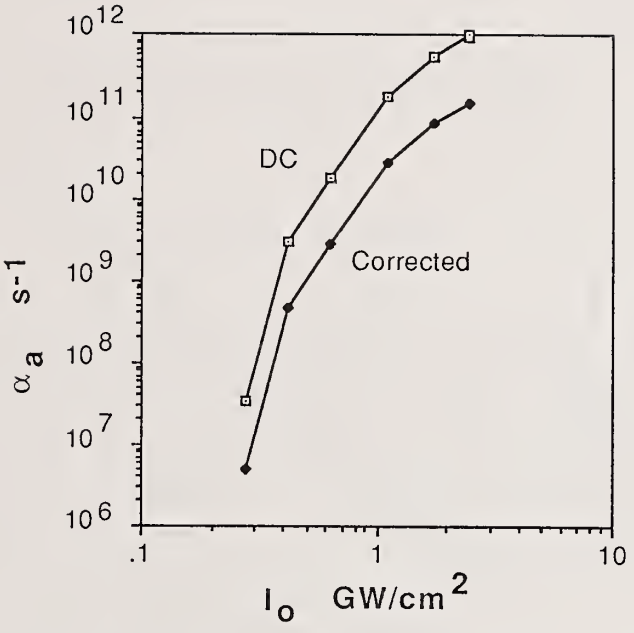

Figure 9. Avalanche ionization rate for GaAs versus incident laser intensity. The DC curve is computed directly from DC ionization rates for the corresponding optical electric field strength. The correction is described in the text.

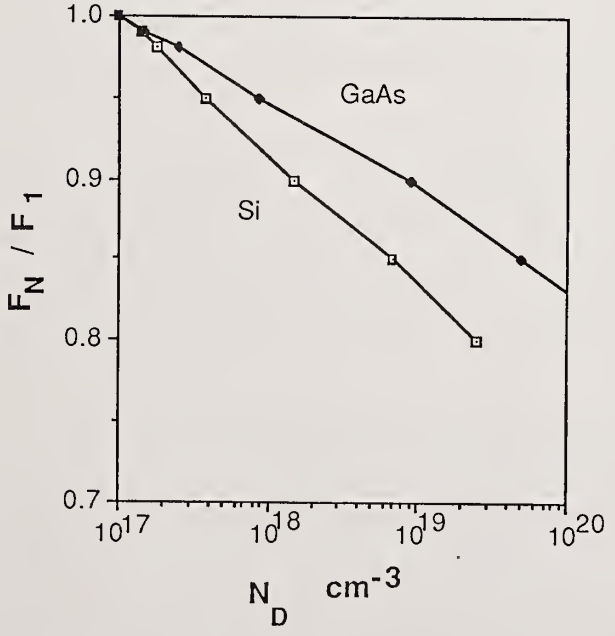

Figure 10. Prediction of accumulation by the model for Si and GaAs. Fractional reduction in damage threshold is plotted against the initial density of defects in the spherical cluster.

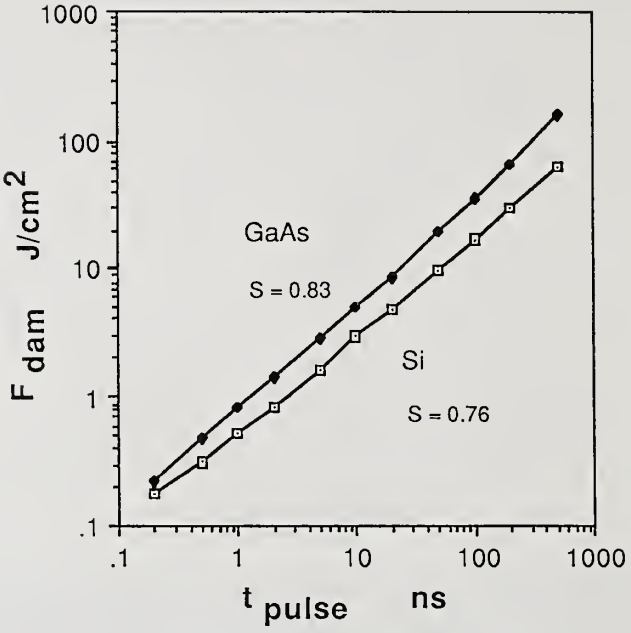

Figure 11. Prediction of damage thresholds for Si and GaAs versus pulse length. S gives the approximate power law dependence of each curve.

Manuscript Received
12-29-86

A model for probing small absorption changes during Multiple Pulse Laser-Induced Damage

D. Kitriotis

Physics Department
University of Arkansas
Fayetteville, AR 72701

A sensitive technique for the detection of temperature changes in the bulk of a transparent material due to absorption of any laser beam is the thermal-lensing technique. So far to our knowledge the thermal-lensing models will yield zero signal, if one probes the temperature changes in the space where the laser beam focuses. We developed a model that uses a low power c.w. laser to detect the absorption changes in the focal volume of a Q-switched laser beam. The change in the absorption from pulse to pulse will be detected as a change in the far field intensity profile of the c.w. beam; taking in account the aberrant nature of the induced thermal-lens, an expression for the above profile is given; the far field fractional axial intensity is derived without any high order terms elimination, which allows for an accurate and sensitive measurement of the absorption coefficient for one and n-photon absorption processes.

Key words: thermal-lensing; temperature change; Q-switched laser; c.w. laser; fractional axial intensity; absorption coefficient

1. Indroduction

The multiple pulse damage of optical materials is not well understood; optical experiments have failed to detect absorption changes at the wavelength of the pump Q-switched laser beam prior to the optical breakdown [1], which occurs during one pulse and after a certain number of pulses depending on the pump fluence, wavelength and pulse duration [1-3]. Induced absorption by multiple pulse irradiation at 532 nm has been reported in [4], and it was measured by a thermal-lensing technique. It is clear from that work that the induced absorption has a peak in the uv region, and that it is due to induced structural defects with electronic levels close to the valence band, as their metastability and resistance to photobleaching indicates. Prior to the optical breakdown no visible coloration has been reported yet; it is not a surprise that attenuation of the beam is not observed, as the induced changes can be linearly transparent to the pump wavelenth.

Any absorbed energy, partially when metastable states are created, is transfered to the lattice by phonons. In this paper we present a technique and its mathematical formulation for the detection and measurement of an induced absorption and the resulted heat. The absorbed energy will produce local heating; due to the radial dependence of the pump intensity, a radially dependent temperature distribution is created around the propagation axis of the beam, which in turn produces a refractive index change. This turns the medium into a lens for any collinear incident probe beam. As the lens develops, a change in the far field profile of the probe beam is observed, which permits the thermooptic properties of the absorbing medium to be studied. The thermal-lensing induced by c.w. lasers is examined in [5-6].

A model suitable for Q-switched lasers was described in [7] and it was applied in [4]. In that model the sample was at a distance from the coincident focal planes of the pump and probe beams, and an optimum distance was required for the maximum signal, that would decrease rapidly otherwise. In our experimentation we found it was difficult to obtain coincident focal planes and achieve the optimum distance too; it is also desirable for bulk studies the sample to be inside the focal volume of the pump beam, in order to avoid an early surface damage. We overcome these difficulties by decoupling the two focal planes; without any elimination of high order terms we derive an accurate and simple expression for the signal of a detector with linear response to the c.w. laser light, and we took in account the aberrant nature of the medium. The signal increases as the distance between the focal plane of the probe beam and sample increases, and its minimum is not zero.

2. Optical components of the thermal-lens experiment

The optical components of the thermal-lensing experiment are shown in figure 1. The intensity

profile of the Q-switched laser is considered to be the Gaussian of the fundamental mode; the temporal profile is left unspecified; the intensity of the pump beam is given below.

$$I(r,t)= \frac{P(t)}{w_p^2}\exp(-2r^2/w_p^2) \tag{1}$$

where P(t) describes the time dependence of the pulse and includes the normalization constant; w_p is the waist of the beam, r the radial distance from the optical axis, and t stands for time. The sample is positioned symmetrically in the focal volume of the pump beam; for an optimum cylidrical symmetry the length of the sample l_o should be smaller than the Raleigh Range of the pump laser, that is equal to $n_o \pi w_p^2 2/\lambda$, where w_p is the minimum beam waist, λ the pump wavelength, and n_o the refractive index of the sample. The probe beam, any stabilized low power c.w. laser in the fundamental mode, has a minimum waist w_o at a distance z' from the front surface of the sample; w_o and z' can be adjusted by the focal length of the thin lens A and its distance from the c.w. resonator and thin lens D, that adjusts the minimum waist of the pump beam [11]. The thin lens 1 will prevent strong divergence of the probe beam; its distance from the detector is choosen to be equal to its focal length; in doing so a lot of high order terms in the expression of the far field profile of the probe beam cancell out. The case of a thick sample and minimum waists of few microns is discussed in part 5. A review of the theory of the Gaussian beams is given in [8], which notation we follow too.

3. The change in temperature

For n-photon absorption the energy flow into a unit volume of the sample per unit of time at a distance r from the optical axis, o.a., is

$$Q(r,t)= \frac{1}{J}\, bI(r,t)^n \tag{2}$$

where J is equal to 4.184 joules/cal, and b is the n-photon absorption coefficient; we set the quantum fluerescence q equal to zero; otherwise eq (2) is to multiplied by 1-q. For a Q-switched laser the pulse duration is much smaller than the involved relaxation time of the heat conduction, so the delivery of the heat to the sample is practically instantaneous at t=0, given by

$$Q(r)= \frac{1}{J}\, bI(r)^n P \tag{3}$$

$$P= \int_o^\infty P(t)^n dt$$

The width of the sample can be taken as infinite, and for the intensity of the pump beam is practically zero at distances r larger than $2w_p$ and the values of the thermal diffusivity of the optical materials are small we can consider the boundaries at r=∞ to be at constant temperature. The Green's function for the above heat problem can be deduced from [9], and it is given below.

$$G(r,t;r',t'=0)= \frac{1}{l_o 4\pi K}\exp(-(r^2+r'^2)/4dt)\; I_o(rr'/2Dt) \tag{4}$$

where I_o is a modified Bessel function, K the thermal conductivity, D the thermal diffusivity equal to K/pc, p is the density, and c the specific heat capacity of the sample. The change in temperature and the result of the involved integration is [10],

$$\Delta T=2\pi l_o \int_o^\infty Q(r')G(r,t;r')r'dr'$$

$$\Delta T= \frac{bPn}{Jpcw_p^2(1+2nt/t_c)}\exp\left(-\frac{r^2}{w^2}\,\frac{2n}{1+2nt/t_c}\right) \tag{5}$$

$$t_c= w_p^2/4D \qquad , \qquad w_t= w_p/\sqrt{2n} \tag{5.1}$$

where t_c is the relaxation time, and w_t is the width of the induced thermal lens. For pulse repe-

tetion periods much larger than t_c, that is of the order of a ms, we can neglect the effect of the residual heat due to previous pulses. There is strong dependence of the ΔT peak value, the diffusion rate of the heat, and the thermal-lens width on the number n of the n-photon absorption process; it is shown explicitly in figure 2.

4. The thermal lens and its ray transfer matrix

The refractive index of the sample for the involved temperature changes and values of (dn/dT) can be expressed as

$$n(r,t)=n_o+\frac{dn}{dT}\Delta T \tag{6}$$

where n_o is the refractive index at the room temperature and the probe beam wavelength. The waist of the probe beam w_{12} inside the sample is arranged to be at least smaller than the half width of the thermal lens, and z' and l_o such that there is no large divergence inside the sample; $w_t>2w_{12}$ is a satisfactory condition for the approximation of ΔT by the first two terms of its expansion around r=0. In any case the far field axial intensity of the probe beam is determined mainly by the optical rays close to the o.a. Expanding ΔT and keeping only the first two terms we have

$$n(r,t)=(n_o+\frac{dn}{dT}\frac{bP}{Jpcw_p^{2n}}\frac{1}{1+2nt/t_c})-\frac{1}{2}(\frac{dn}{dT}\frac{bP4n^2}{Jpcw^{2n+2}}\frac{1}{(1=2nt/t_c)}2\ r^2) \tag{7}$$

$$\text{or}\quad n(r,t)=n_1+\frac{1}{2}n_2r^2 \tag{7.1}$$

For a sample of length l_o and a refractive index given by an equation as in eq (7.1) its ray transfer matrix is given in [8]. It is shown in [11] that if we take in account the two interfaces in the front and back surface of the sample, as well as the condition $n_2<<n_1$ then the ray transfer matrix from plane 1 to plane 2 is

$$\begin{vmatrix} 1 & 0 \\ -n_2n_ol_o & 1 \end{vmatrix}$$

The refractive index of the air was set equal to 1; otherwise n_o is to be divided by that value. The above matrix is equivalent to the matrix of a perfect thin lens with a focal length equal to

$$\frac{1}{f_{ot}}=n_ol_o\frac{dn}{dT}\frac{bP4n^2}{Jpcw^{2n+2}}\frac{1}{(1+2nt/t_c)^2} \tag{8}$$

$$\frac{1}{f_o}=n_ol_o\frac{dn}{dT}\frac{bP4n^2}{Jpcw^{2n+2}} \tag{8.1}$$

The medium close to the o.a. is converted by the pump pulse to a thin lens with a focal length equal to f_o at t=0, and equal to infinity at a time much larger than t_c, or before the next pulse arrives, figure 3; the lens is converging for positive dn/dT.

5. The transformation of the probe beam

The c.w. probe beam is considered to be in the fundamental mode; the time independent electric field is [8]

$$E(z,r)=\frac{C}{w}\exp(-i(r^2k/2q'))\exp(-i(kz-\Phi)) \tag{9}$$

$$\frac{1}{q'}=\frac{1}{R}-\frac{i\lambda}{\pi w^2} \tag{9.1}$$

where R is the curvature of the wavefront, k the wavevector, and λ is the wavelength in the medium.

The part of the electric field that depends on q' is transformed according to the ABCD law. Taking the distance between the thin lens 1 and the detector plane to be equal to f_1 the waist of the probe beam at z_4 is [11]

$$\frac{\pi^2 w_o^2 w_4^2}{\lambda^2} = f_1^2\left(\frac{z_o^2}{f_{ot}^2} + \left(1 - \frac{z'}{f_{ot}}\right)^2\right) \tag{10}$$

$$z_o = \frac{\pi w_o^2}{\lambda} \tag{10.1}$$

where w_o is the minimum waist of the probe beam , and w_4 is its waist at the location of the detector; eq (10) was derived without any elimination of terms; it is easy to verify that at the limit $t=\infty$ it is identical to what we would get for the transformation due to matrix of the displaceent from plane 0 to plane 4 without the thermal-lens. For the reason that we kept only the first two terms of the expansion of ΔT, the q' is not described by w_4 at points far from the o.a., $r>w_4$. for points close to the o.a. w_4 does describe the q' accurately, so the axial intensity at z_4 can be considered proportional to the inverse of the square of w_4.

The plane wave part of eq (9) $\exp(-i(kz-\Phi))$ is also affected by the thermal-lens. At points close to the o.a. the phase speed is larger than for those far from the o.a.; the plane wave emerges slightly distorted with a phase

$$kz' + kl_o n(0,t) + kl_o \frac{dn}{dT}\Delta T \tag{11}$$

The change in the optical path is smaller than a wavelength, so we can expand the second term; the plane wave is then given by

$$\exp(-ikz'') - \exp(-ikz'').ikl_o \frac{dn}{dT}\Delta T \tag{12}$$

where $z''=z'-kl_o n(0,t)$.
The above equation describes an ideal plane wave, the first term, and a perturbation which is due to the action of the thermal-lens. The transformation by the displacement R of the first term is given by $\exp(-ikz'')\exp(-ikR)$, where R is the distance between plane 2 and 4. For the transformation of the second term we utilize the diffraction integral; for $R \gg w_t$ and w_4 the Fraunhofer integral is adequate enough; the integral is given below.

$$\int_o^\infty r'dr' J_o(krr'/R)(1/R)\exp(-ikR)\{-ikl_o \frac{dn}{dT}\Delta T \exp(-ikz'')\}$$

where $J_o(krr'/R)$ is the Bessel function (of the first kind) of order zero; r' and r are the radial distances at z_2 and z_4; using eq (5) in the integral above we have after the integration for the total plane wave field at z_4

$$\exp(-ik(z''+R))\{1 - ikl_o \frac{dn}{dT}(1/R)\frac{bP}{4Jpcw^{2n-2}} \exp\{-(\frac{kr}{R})^2 \frac{w_p^2}{4(2n)}(1+2nt/t_c)\}\} \tag{13}$$

It is clear that at the limit $t=\infty$ the plane wave is reduced to $\exp(-ik(z''+R))$, as it was expected.

The intensity profile at z_4 is

$$I(r,t) = \frac{C}{w_4^2}\{1 + (kl_o \frac{dn}{dT}(1/R)\frac{bP}{4Jpcw^{2n-2}})^2 \exp(-(\frac{kr}{R})^2 \frac{w_p^2}{2(2n)}(1+2nt/t_c))\} \tag{14}$$

$$C = C'\exp(-2r^2/w_4^2) \tag{14.1}$$

where C' is a normalization constant.
The above equations describe a Gaussian beam with a small perturbation, which also has a maximum at r=0. At the limit t=∞, or in the case that b=0, the beam is a perfect Gaussian with a waist w_{40}.

$$I(r) = C'\exp(-2r^2/w_{40}^2)$$

$$w_{40}^2 = \lambda^2 f_1^2/\pi^2 w_o^2$$

where w_o is the min waist of the probe beam at z_0.
As an induced absorption starts to develop, the far field intensity of the probe beam will deviate from the Gaussian profile, and the maximum distortion will be at time t=0. The maximum fractional axial intensity at z_4 is

$$\Delta S = \frac{I(r=0,t=0)-I(r=0,t=\infty)}{I(r=0,t=0)} = \frac{(z_o^2/f_o^2 + (1-z'/f_o)^2)}{1+(kl_o\frac{dn}{dT}(1/R)\frac{bP}{4Jpcw_p^{2n-2}})^2} \tag{15}$$

where z_o is given by eq (10.1) and f_o by eq (8.1).
ΔS can be measured with a linear response detector with a pinhole in front of it. It is possible to determine the n-photon absorption process from the dynamical behavior of the thermal-lensing signal, ΔS, figure 4; the signal drops to half of its maximum value at $t=(.21/n)t_c$. A short computer program may determine b from eq (15) by best fit of trial values. For weak signals the denominator may be neglected and the nominator to be reduced to $2z'/f_o$; the sensitivity can be increased by increasing z', up to the point that w_{12} remains smaller than $w_t/2$.

For very thick samples and only few microns minimum waists of the pupm beam, as effective length for the thermal-lens we consider the Raleigh range $2\pi w_p^2/\lambda_p$, where anyway the optical breakdown is observed. The n_o must be omitted in eq (8.1), and very small minimum waists for the probe beam are necessary in order eq (10) that determines the value of the signal to be valid. In any case a change in the absorption can still be detected and measured with a rather good accuracy, as eq (15) is mainly determined by the paraxial rays.

6. Conclusions

We presented a technique and its mathematical formulation for the detection and measurement of weak absorptions during multiple pulse induced damage. The described model is free of scattering and reflection effects, and it probes the bulk directly; it is easy to be set up, and it has the advantage of probing the sample from pulse to pulse. The mathematical formulation with a carefull design of the thermal-lensing experiment will allow for a sensitive and accurate measurement of the absorption coefficient. It is applicable in the pump power region where there is no electrostriction and the high frequency Kerr effect [13].

7. References

[1] Merkle, L.; Koumvakalis, N.; Bass, M. J. Appl. Physics. 55(3): 772-775; 1984.

[2] Kitriotis, D.; Merkle, L.; Dodson, A. Proc. of the Seventeeth Symp. on Opt. Mater. for High Power Lasers; to be published by Nat. Bur. Stand. (U.S.).

[3] Kitriotis, D.; Merkle, L. Proc. of the Eighteenth Symp. on Opt. Mater. for High Power Lasers (this volume).

[4] White, W.T.; Henesian, M.A.; Weber, M.J. J. Opt. Soc. Am. 2(9): 1402-1408; 1985.

[5] Hu, C.; Whinnery, J.R. Appl. Opt. 12(1): 72-79; 1973.

[6] Sheldon, S.J.; Knight, L.V.; Thorne, J.M. Appl. Opt. 21(9): 1663-1669; 1982.

[7] Twarowski, A.J.; Klinger, D.S. Chemical Physics 20: 253-258; 1977.

[8] Kogelnic, H.; Li, T. IEEE Proc. 54: 1312-1329; 1966

[9] Garslaw, H.S.; Jaeger, J.C. Operational Methods in Mathematics. London; Oxford University Press; 1941. 106 p.

[10] Watson, G.N. Theory of Bessel Functions. 2nd Edition. London; Cambridge University Press; 1944. 393 p.

[11] Kitriotis, D. Ph. D. dissertation, Un. of Arkansas; Spring 1987; unpublished.

[12] Gradshteyn, I.S.; Ryzhic, I.M. Table of Integrals, Series, and Products. New York; Academic Press; 1980. 717 p.

[13] Akhmanov, S.A.; Sukhorukov, A.P.; Khokhlov, R.V. Sov. Phys. Usp. 10: 609-612; 1968.

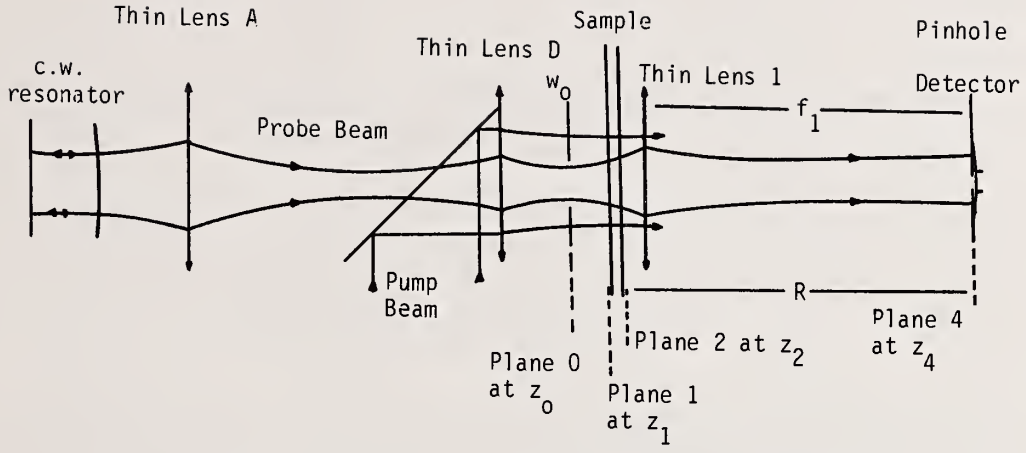

Figure 1. Optical configuration for the analysis of the thermal-lensing experiment.

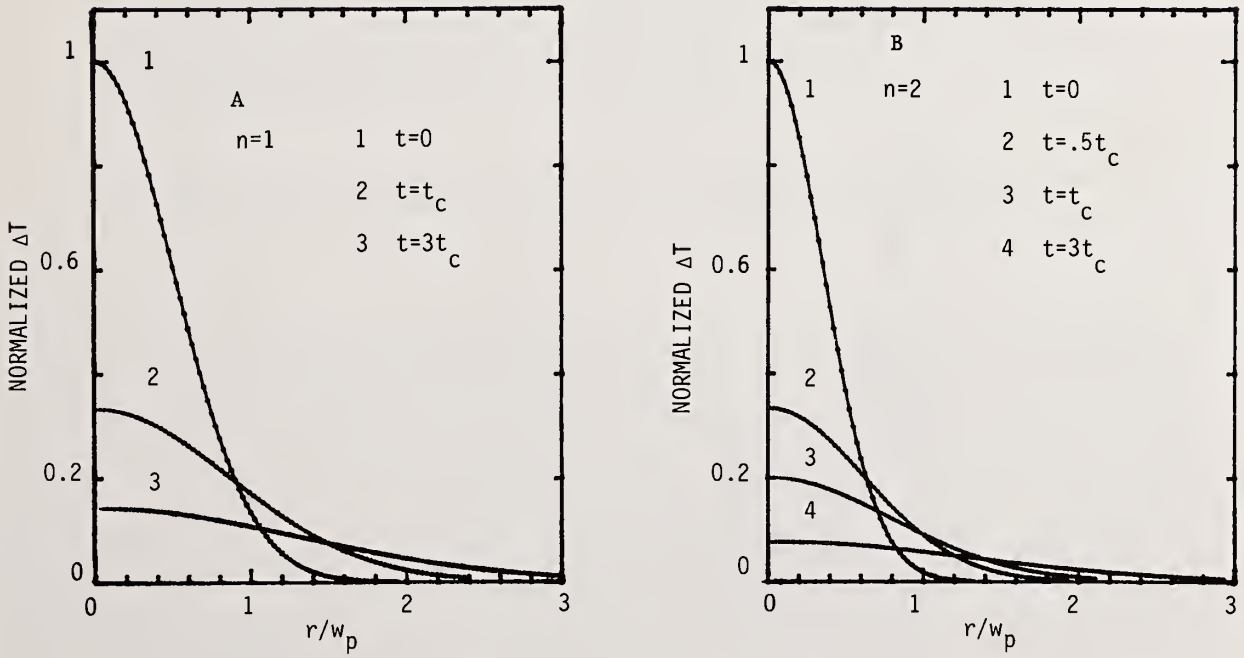

Figure 2. The temperature inside the sample at various times for 1-photon, A, and 2-photon absorption, B, processes.

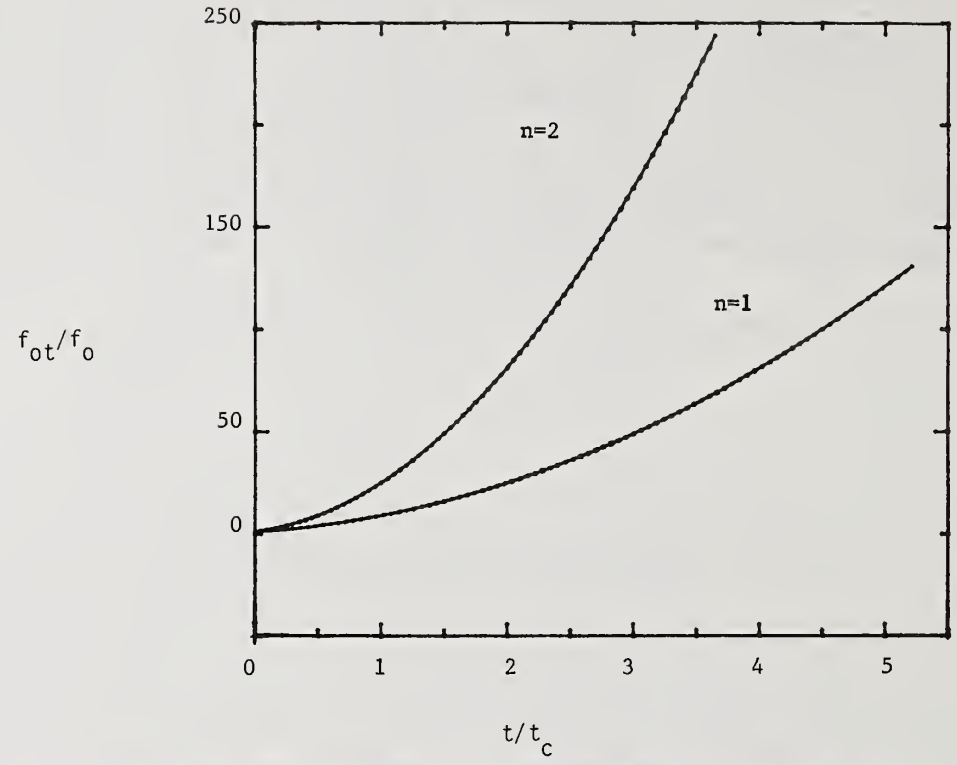

Figure 3. The focal length of the thermal lens as a function of time for 1 and 2 photon absorption processes: at t=0 is equal to f_o, eq (8.1).

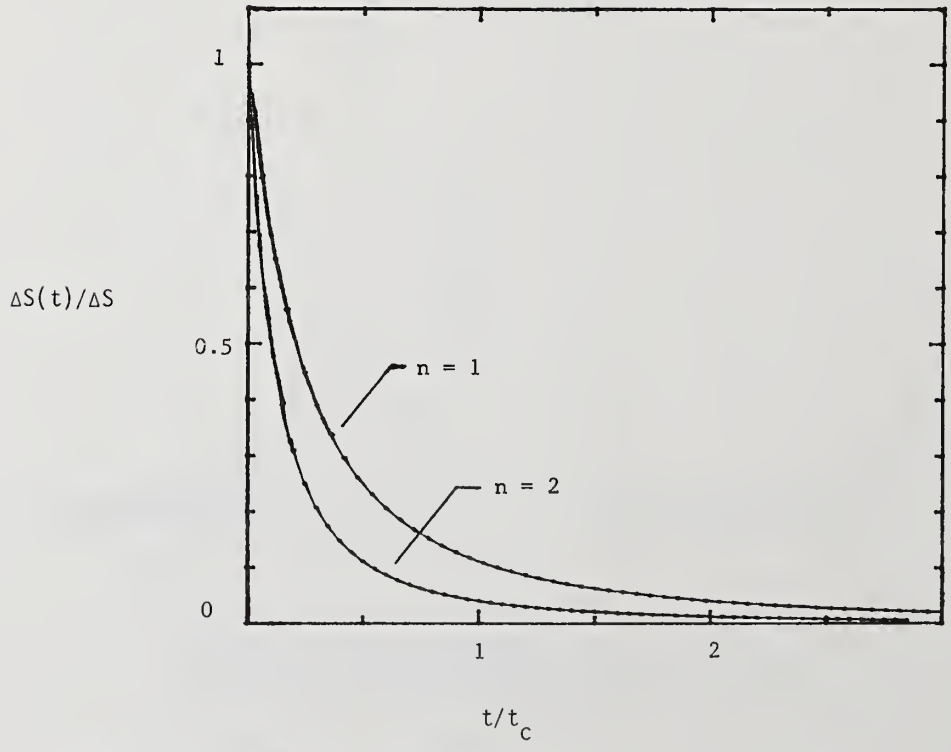

Figure 4. The thermal-lens normalized signal for 1 and 2 photon absorption processes.

Manuscript Received 10-19-87/sar

Nonlinear Absorption Initiated Avalanche Breakdown In Dielectric ZrO_2

N. Mansour, E. Canto, M.J. Soileau and E.W. Van Stryland

Center for Research in Electro-Optics and Lasers (CREOL)
University of Central Florida
Orlando, Florida 32816

We report direct measurements of nonlinear transmission in dielectric ZrO_2 prior to the observation of catastrophic damage for nsec laser pulses at 532 nm. The tested cubic zirconia (ZrO_2) specimens are stabilized with yttria (Y_2O_3) having concentrations of 9.4%, 12%, 15%, 18%, and 21%. Transmission measurements were performed for a broad range of pulsewidths from 40 psec to 18 nsec (FWHM) at 532 nm. Our results indicate that the nonlinearity prior to breakdown is mainly attributed to the formation of material defects (color centers) by two-photon absorption (2PA) at high irradiance. These induced color centers appear to be long-lived (the order of hours) but can be bleached by repeated irradiation with relatively low irradiance 532 nm pulses. The accumulated effects of color center absorption during the 2PA measurements makes extraction of the two-photon absorption coefficient difficult. However, the smallest value for the 2PA coefficient (~0.04 cm/GW) was measured in the ZrO_2 sample stabilized with 9.4% Y_2O_3 for the shortest pulsewidth (40 psec) with which the measurements were performed. The observed nonlinear transmission prior to breakdown is consistent with the interpretation that damage in this material is due to 2PA induced avalanche breakdown.

Key words: color centers; cubic zirconia; damage; 532 nm; nonlinear absorption; nsec pulses; psec pulses; two-photon absorption.

1. Introduction

The contributions of multiphoton absorption to the process of avalanche ionization breakdown in wide-gap dielectric materials has been the subject of considerable discussion in the literature [1 - 3]. In recent work [4 - 8], observations of frequency and spot size dependences of dielectric breakdown has remained a source of controversy to the theory of avalanche ionization. This led various researchers to speculate that bulk laser-induced damage is due to avalanche ionization initiated by multiphoton absorption. However, a detailed quantitative description of the generation of the initial conduction band electrons and the dynamics of the damage process is not yet available. A major obstacle to the development of a detailed description of the breakdown phenomena has been the inability of researchers to measure the onset of nonlinear absorption (e.g., multiphoton absorption) which initiates the avalanche process.

This work presents measurements of pre-breakdown studies in dielectric ZrO_2 at 532 nm. The results provide detailed experimental information on the material defects induced by two-photon absorption prior to optical breakdown.

2. Experiment

The experimental apparatus is described in greater detail elsewhere [9,10]. For the nanosecond pulses, the laser source was an actively Q-switched Nd:YAG laser system operating at 1064 nm. Single pulses of measured Gaussian spatial profile were produced by the oscillator and amplified by a single pass through the amplifier. A KD*P crystal was used with the Nd:YAG laser to produce pulses at 532 nm. Residual 1064 nm radiation was eliminated by reflection off three dichroic mirrors. The temporal pulsewidth was approximately 18 nsec (FWHM) at 532 nm. The width of each pulse was monitored by a PIN photodiode detector and fast Tektronix storage oscilloscope (Model 7834). For the picosecond study, we used an actively/passively mode-locked Nd:YAG laser which produces pulses of duration ranging from 40 to 150 psec (FWHM) at 1064 nm. The temporal pulsewidth was varied by selecting etalon output couplers of various thicknesses. Single pulses with Gaussian spatial and temporal profiles were switched out of the mode-locked pulse train and amplified. The width of each pulse was measured using the procedure described in reference [6].

In the case of damage threshold measurements for nanosecond pulses, a 40 mm focal length "best form" lens was used to focus the laser light into the bulk of the material. The spatial beam spot size (of the unfocused beam) was determined by pinhole scans. The calculated focal spot size was 3.5 μm (HW $1/e^2$ M in irradiance). The lens used for the nonlinear transmission measurements for picosecond pulses was a f=750 mm "best form" lens which provided a nominal focused spot size of 170 μm (HW $1/e^2$ M in irradiance). Both lenses were designed to minimize spherical aberrations and to provide diffraction-limited performance. For the nonlinear transmission measurements the actual focused spot sizes were obtained by scanning the spatial profile in both the horizontal and vertical dimentions with a 5 μm diameter pinhole placed in the plane of the samples. A rotating half-wave plate/polarizer combination was used to vary the irradiance on the sample. The energy incident on samples was continuously monitored by a sensitive photodiode peak-and-hold detector, and was calibrated with respect to a Gentec (ED-100) pyroelectric energy meter.

3. Results and Discussion

Table 1 summarizes the results of measurements of the multiple shot (or n-on-1) laser-induced damage thresholds for yttria stabilized cubic zirconia. The ZrO_2 samples having Y_2O_3 concentrations of 9.4%, 12%, 15%, 18%, and 21% were studied for linearly polarized light at 532 nm. For all data listed in table 1, we used 18 nsec (FWHM) laser pulses and a calculated 3.5 μm focused spot size (HW $1/e^2$ M in irradiance). Each site irradiated many times with irradiance level below threshold and the incident irradiance continuously increased until damage occured (fig. 1). The onset of damage was determined by both monitoring the transmitted beam and observing increased scattering of coaxial HeNe laser light. The values given for the electric field are rms fields corresponding to the peak-on-axis irradiance. As indicated in the table of data, the breakdown field remains unchanged (to within ± 5%) for Y_2O_3 concentrations ranging from 9.4 to 21%.

Figure 1 represents the results of transmission measurements prior to laser-induced damage for cubic zirconia stabilized with 18% Y_2O_3 at 532 nm for 18 nsec (FWHM) laser pulses. As indicated in the plot, there is a pronounced change in transmission of the sample (about 15%) prior to the occurrence of catastrophic damage. The observed nonlinear transmission is more clearly seen when the same data is plotted as inverse transmission versus the incident irradiance (fig. 2). This nonlinearity was observed for all ZrO_2 samples tested, and the smallest change of transmission prior to damage (about 10%) was measured for the ZrO_2 sample having 9.4% yttria concentration. Although the damage threshold were found to be independent of Y_2O_3 concentration, the detected nonlinear transmission prior to breakdown appears to be related to the percentage of stabilizer (Y_2O_3). Self-focusing does not play an important role in these measurements, since the breakdown power for the samples (table 1) are

about three orders of magnitude smaller than the critical power for self-focusing. The detailed analysis of self-focusing is given in references 11 and 12.

Figure 3 shows the linear transmission spectrum for the 18% Y_2O_3 sample for a wavelength range of 0.2 to 2.5 μm. Similar spectra were obtained for all the tested Yttria stabilized cubic Zirconia samples. The UV cutoff frequency of this material is about .33 μm. This suggests that two-photon absorption plays an important role in the observed nonlinear transmission prior to damage.

To reiterate, figure 2 shows a plot of inverse transmission (1/T) versus irradiance at 532 nm for 18 nsec (FWHM) pulses incident on ZrO_2 stabilized with 18% Y_2O_3. The data is plotted in this manner to investigate whether or not two-photon absorption (2PA) is the responsible mechanism for the nonlinearity prior to breakdown in this material. In fact, our results (fig. 2) look like the nonlinear transmission that we would expect to get for two-photon absorption [13]. We found similar behavior by performing the transmission measurement at 532 nm for picosecond pulses ranging from 40 to 95 psec (FWHM). If we assume that the nonlinearity is due to 2PA, then the slope of (1/T) curve would give the 2PA coefficient [14, 15]. Table 2 contains the calculated values of the 2PA coefficient under this assumption using nanosecond and picosecond pulses. The assumed 2PA coefficient are summarized in table 2 for five samples studied at four different pulse widths from 40 psec to 18 nsec (FWHM). By looking at results of any one of the samples, the extracted values for the 2PA coefficient grows with increasing pulsewidth. However, the 2PA coefficient *is not pulse-width dependent*. Therefore, the nonlinearity is not simply 2PA. The complexity associated with the nonlinear processes are more clearly elucidated in the paragraphs to follow.

Figure 4a shows the plot of inverse transmission as a function of incident irradiance for 40 psec laser pulses at 532 nm. The experiment was performed at low irradiance and the irradiance was increased up to 20 GW/cm^2. The entire measurement was conducted at the same spot of the sample. We repeated the experiment without changing the position of the sample (fig. 4b). The conclusions drawn from the repeated experiment are:
(1) The transmissions of the sample at low irradiance is significantly decreased, indicating that material induced defects (color centers) are created by the prior irradiation at high irradiance (~20 GW/cm^2).
(2) Note that the induced material defects are removed by irradiating the sample at low irradiance levels.
(3) At higher irradiance the transmission decreases as before, and defects are again produced.

The presence of the color centers was directly monitored by transmission measurements. Figure 5 represents the plot of transmission as a function of number of shots with a constant irradiance level of 1 GW/cm^2 on the same irradiated spot (irradiated with high intensity of 20 GW/cm^2). By irradiating the sample, the transmission starts to increase, which implies that the induced defects are being removed. After some number of shots, the transmission is constant and equal to its value prior to the high intensity irradiation. We repeated this experiment at different repetition rates from 1 hz to 10 hz. This curve (fig. 5) remained unchanged, indicating that the removal of the defects depends only on the total integrated fluence or total number of the shots. At room temperature, the lifetime of these defects is long, and the samples recover their original transmission in a few hours (~2 hours).

The observed pulsewidth dependence of the transmission is strongly influenced by the induced defects. However, the accumulated contributions of the induced defects to the nonlinear absorption is significantly decreased using shorter pulses (table 2). At a pulsewidth of 40 psec, the value extracted for nonlinear absorption is at its smallest value of 0.04 cm/GW. This sets an upper limit on the magnitude of the 2PA coefficient.

4. Summary

Multiple shot laser-induced breakdown was studied at 532 nm for nanosecond laser pulses in yttria stabilized cubic zirconia. Samples having concentrations of 9.4%, 12%, 15%, 18% and 21% were investigated. We found that increasing the percentage of Y_2O_3 to stabilize the zirconia does not decrease the breakdown threshold. The breakdown fields are unchanged (to within ±5%) for Y_2O_3 concentrations ranging from 9.4 to 21%. Pronounced nonlinear transmission was measured prior to the occurence of damage in the ZrO_2 specimens at 532 nm. Transmission measurements were performed using a broad range of pulsewidths from 40 psec to 18 nsec at 532 nm. The observed pulsewidth dependence to the transmission is due to material defects (color centers) induced by two-photon absorption. The induced defects are generated by irradiating the ZrO_2 samples at high intensity levels and are long-lived (on the order of hours) but can be removed by repeated irradiation at low irradiance levels.

5. References

[1] Braunlich, P.; Schmid, A.; Kelly, P. "Contributions of Multiphoton absorption to laser-induced intrinsic damage in NaCl". Appl. Phys. Lett. 26 (4): 150-153; 1975

[2] Schmid, A.; Kelly, P.; Braunlich, P "Optical breakdown in alkali halides." Phys. Rev. B 16 (10): 4569-4582; 1977.

[3] Gorshkov, B.G.; Epifanov, A.S.; Manenkov, A.A. "The relative role of impact and multiphoton ionization mechanisms in laser induced damage of transparent dielectrics." Natl. Bur. Stand. (U.S.) Spec. Pub. 541; 299-302; 1978.

[4] Soileau, M.J.; William, W.E.; Van Stryland, E.W.; Boggess, T.F.; Smirl, A.L. "Picosecond damage studies at 0.5 and 1μm." Opt. Eng. 22(4):424-430; 1983

[5] Soileau, M.J.; Williams, W.E.; Van Stryland, E.W.; Boggess, T.F.; Smirl, A.L. "Temporal dependence of laser-induced breakdown in NaCl." Natl. Bur. Stand. (U.S.) Spec. Pub. 669; 387-405; 1982.

[6] Van Stryland, E.W.; Soileau, M.J.; Smirl, A.L.; Williams, W.E. "Pulsewidth and Focal Volume dependence of laser-induced breakdown." Phys. Rev. B 23(5): 2144-2151; 1981.

[7] Soileau, M.J. "Frequency and focal volume dependence of laser-induced breakdown in wide band gap insulators." Ph.D. Dissertation; University of Southern California; 1979.

[8] Gorshkov, B.G.; Danileiko, Yu.K.; Epifanov, A.S.; Lobachev, V.A.; Manenkov, A.A. "Laser induced breakdown of alkali-halide crystals." Sov. Phys. JETP 45 (3): 612-618; 1977.

[9] Soileau, M.J.; Mansour, N.; Canto, E.; Griscom, D.L. "Effects of radiation induced defects on laser-induced breakdown in SiO_2" Natl. Bur. Stand. (U.S.) Spec. Pub.; 1985.

[10] Mansour, N.; Guha, S.; Soileau, M.J. "Laser-induced damage in doped and undoped fluorozirconate glass." Natl. Bur. Stand. (U.S.) Spec. Pub; 1985.

[11] Mansour, N.; Soileau, M.J.; Van Stryland, E.W. "Picosecond damage in Y_2O_3 stabilized cubic zirconia." Natl. Bur. Stand. (U.S.) Spec. Pub. 727; 31-38; 1984.

[12] Guha, S.; Mansour, N.' Soileau, M.J. "Direct N_2 measurement in yttria stabilized cubic zirconia." Natl Bur. Stand. (U.S.) Spec. Pub. 727; 31-38; 1984.

[13] Van Stryland, E.W.; Woodal, M.A.; Williams, W.E.; Soileau, M.J. "Two and three-photon absorption in semiconductors with subsequent absorption by photogenerated carriers." Natl. Bur. Stand. (U.S.) Spec. Pub. 638; 589-600; 1981.

[14] Liu, P.; Smith, W.L.; Lotem, H.; Bechtel, J.H.' Bloembergen, N. "Absolute two-photon absorption coefficients at 355 and 266 nm." Phys. Rev. B 17(12): 4620-4631; 1978.

[15] Boggess, T.F.; Bohnert, K.M.; Mansour, K.; Moss, S.C.; Boyd, I.W.; Smirl, A.L. "Simultaneous measurement of two-photon coefficient and free-carrier cross section above the bandgap of crystalline silicon." IEEE, J.Q.E. QE-22 (2): 360-368; 1986.

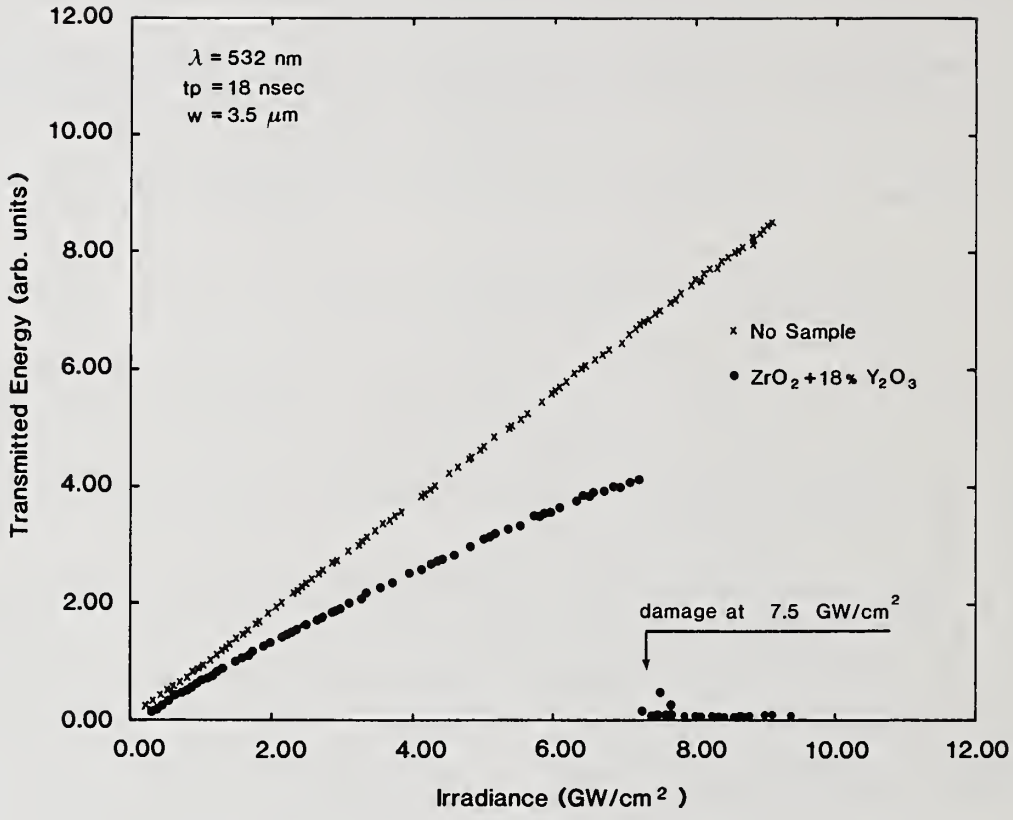

Figure 1. Transmission as a function of incident irradiance in ZrO_2 for 18 nsec (FWHM) pulses at 532 nm. Note that there is a significant change in transmission prior to laser-induced damage.

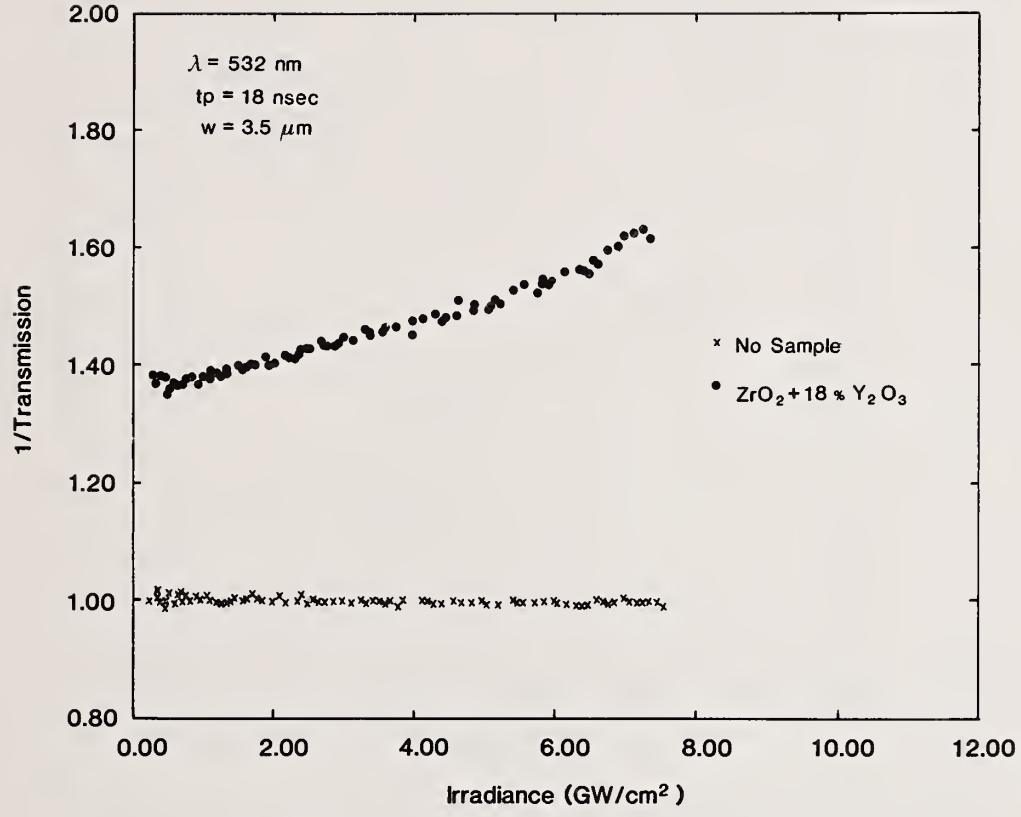

Figure 2. Inverse transmission as a function of incident irradiance for nsec pulses at 532 nm.

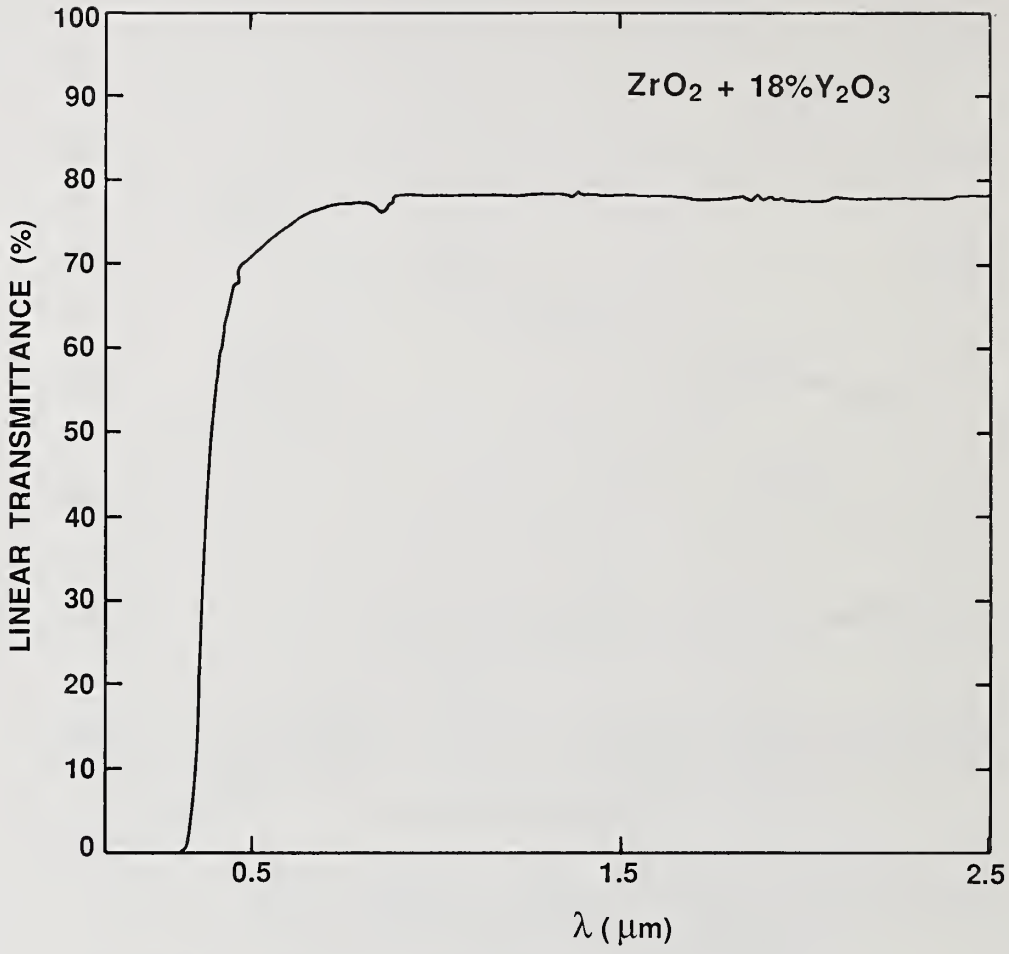

Figure 3. Linear transmission spectra for cubic zirconia stabilized with 18% Y_2O_3 for wavelength range of 0.2 to 2.5 μm.

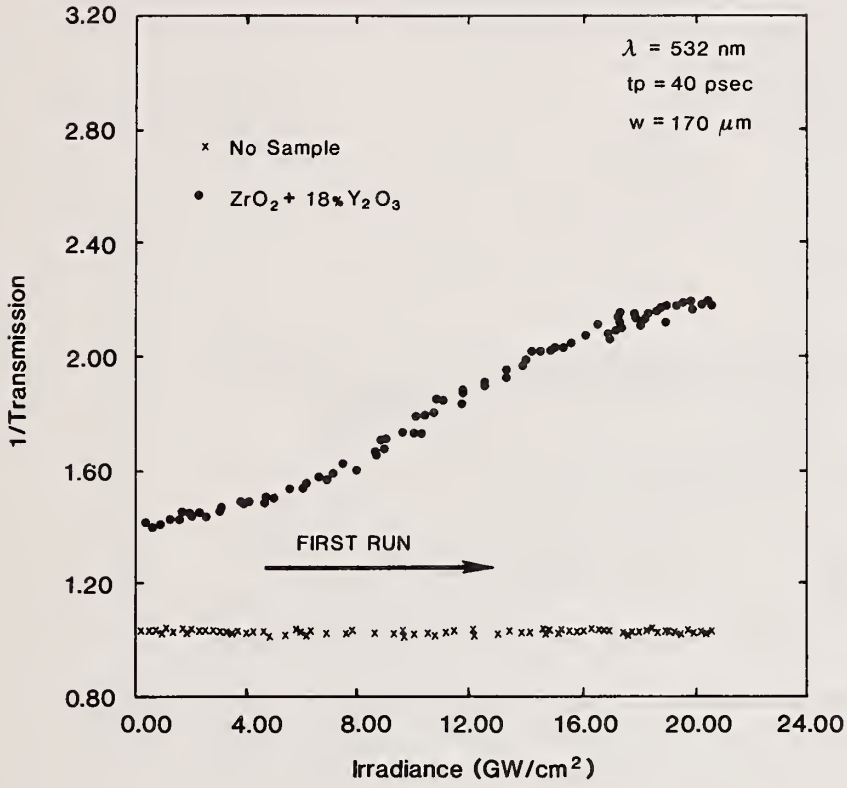

Figure 4a. Inverse transmission as a function of incident irradiance for psec pulses at 532 nm.

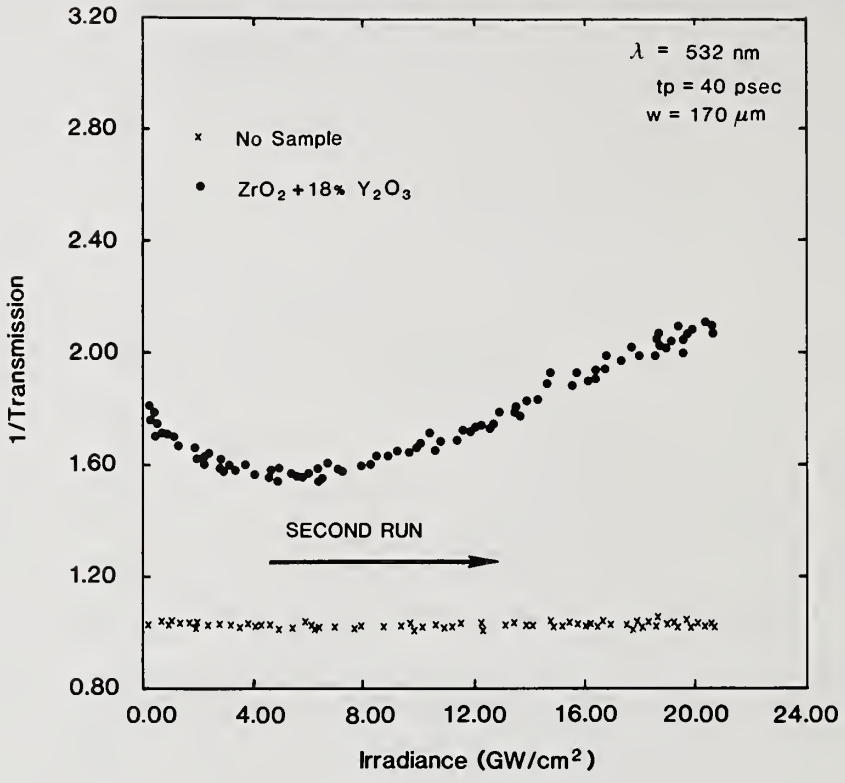

Figure 4b. Repeated inverse transmission measurements at same position on the sample on which the measurements were taken in Figure 4a.

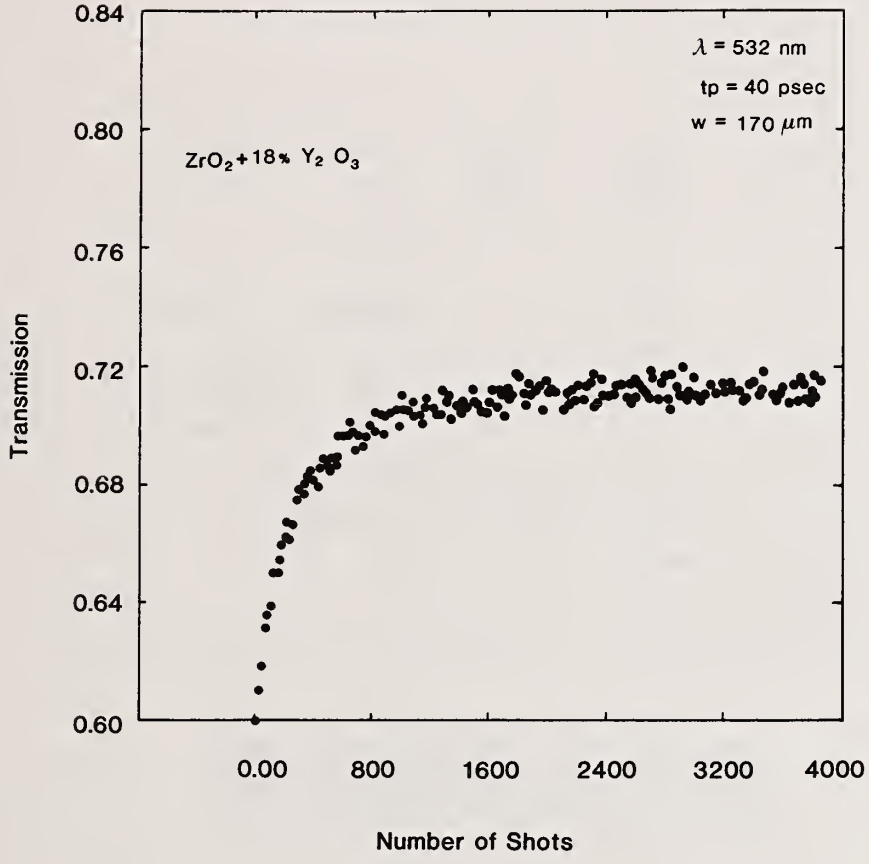

Figure 5. Monitoring the change in transmission of the pre-irradiated ZrO_2 sample as function of number of shots at constant irradiance level of 1 GW/cm² for 40 psec (FWHM) pulses at 532 nm.

Y_2O_3 Concentration	I_B GW/cm^2	E_B MV/cm	P_B kw	F_B J/cm^2
9.4%	8.1	1.2	1.6	160
12%	7.9	1.2	1.6	160
15%	8.1	1.2	1.6	160
18%	7.4	1.1	1.4	140
21%	6.7	1.1	1.3	130

I_B=breakdown irradiance (peak on-axis irradiance)

E_B=breakdown field

P_B=breakdown power

F_B=breakdown fluence

Table 1. Multiple shot laser-induced damage thresholds of ZrO_2 stabilized with Y_2O_3 for 18 nsec (FWHM) pulses at 532 nm.

	40 psec ↓	65 psec ↓	95 psec ↓	18 nsec ↓
Sample	s cm/GW	s cm/GW	s cm/GW	s cm/GW
ZrO_2+9.4%Y_2O_3	0.04	0.08	0.15	0.85
ZrO_2+12% Y_2O_3	0.06	0.08	0.13	0.68
ZrO_2+15% Y_2O_3	0.08	0.10	0.14	0.93
ZrO_2+18% Y_2O_3	0.06	0.13	0.23	1.10
ZrO_2+21% Y_2O_3	0.06	0.11	0.16	0.79

$s = (\text{slope})\ (2\sqrt{2}\ /\ \ell\ )$, where ℓ is the sample thickness.

Table 2. Extracted values for slope of inverse transmission curves for broad range of pulsewidths from 40 psec to 18 nsec (FWHM) at 532 nm.

Manuscript Received
12-22-86

An Investigation of the Possibility that Laser-Induced Color Centers are Responsible for Multiple Pulse Damage

Dimitrios Kitriotis and Larry D. Merkle

Physics Department
University of Arkansas
Fayetteville, AR 72701

The mechanisms responsible for multiple pulse laser damage in transparent solids are still not understood. Recent reports related to laser generation of point defects in fused silica and BK-7 glass raise the possibility that such defect generation is the cause of multiple pulse damage. The difference in defect generation between high-OH and low-OH fused silica offers a means to test this possibility.

We have compared multiple pulse damage properties of "wet" and "dry" fused silica at 1064 nm and 532 nm. Nearly identical behaviors are observed for the two materials. In addition we have studied laser damage in BK-7 X-irradiated to produce color centers. The presence of these centers lowers the damage threshold only modestly. We conclude that optical generation of color centers is not the primary mechanism in multiple pulse damage in these materials.

Key words: BK-7; bulk damage; color centers; fused silica; multiple pulse damage ; x-rays

1. Introduction

In recent years the phenomenon of multiple pulse laser-induced damage has attracted the interest of many scientists. In some materials the damage of the sample after many pulses at intensities too low to induce damage in a single pulse has been traced to the laser-induced growth of absorbing inclusions. [1,2] In other cases changes induced prior to catastrophic damage have been inferred from the damage behavior but have eluded direct observation. [3-7]

The indirect evidence as to the mechanism of multiple pulse damage in silicate glasses, in particular, may be summarized as follows. The distribution of damage events against the number of pulses needed to obtain damage has been taken as evidence that gradual changes in the material do occur [6], as has the observation of a pulse repetition frequency dependence in certain cases. [5,7] Calculations suggest the phenomenon is not simply due to gradual heating. The lack of increased Rayleigh scattering or increased absorption at the laser wavelength in fused silica during irradiation indicates that these changes are very subtle [6] and the dependence on pulse repetition frequency indicates that at least some of the changes are transient. In addition, multiple pulse "thresholds" appear to be reduced by a larger factor compared with single pulse thresholds as the laser irradiation wavelength becomes shorter, [5,7] perhaps indicative of multiphoton excitation of electrons to the conduction band. One mechanism which could produce these characteristics is laser-induced point defect formation, providing states in the band gap to promote electron excitation to the conduction band on subsequent pulses.

Recent studies of fused silica lend credence to this possible role of point defects (color centers) in multiple pulse damage. In the 1985 Boulder Damage Symposium Soileau, et al., reported that the presence of E' centers [8] induced in fused silica by neutron bombardment reduces the single pulse damage threshold significantly at 532 nm but not at 1064 nm. [9] It was suggested that two photon absorption by these centers provides a lower order means of free carrier production, promoting damage. Stathis and Kastner have recently reported the production of E' and other defect centers in fused silica under irradiation by modest intensity ultraviolet laser light. [10,11] (Of interest in the present study, this defect generation was found to be far more efficient in low-OH fused silica than in the high-OH variety.) The possibility therefore exists that multiphoton generation of these centers using high intensity (near damage threshold) light at longer wavelengths may produce E' centers which eventually reach sufficient concentration to lower the damage threshold significantly: multiple pulse damage.

The borosilicate glass BK-7 is another material in which point defect generation may be important to multiple pulse damage. White, et al., have observed color center generation in this glass

by 532 nm light at fluences very comparable to those which cause laser-induced damage. [12,13] These centers give rise to optical absorption over a broad spectral range, including significant absorption at 532 nm. Thus, if the presence of new excitation channels due to color centers lowers the damage threshold in BK-7 as it does in fused silica the formation of these centers may explain multiple pulse damage in this glass.

In the study reported here the importance of point defect generation in the multiple pulse damage process has been investigated in fused silica and BK-7. The 1064 nm and 532 nm damage properties of "wet" and "dry" fused silica were compared, since defect generation is more likely in the latter. The damage resistance of BK-7 was studied as a function of x-irradiation dose, since it was found that x-irradiation induced coloration similar to that reported by White, et al. [12]

In section two of this paper the experimental techniques are briefly described. The third section reports the results of the fused silica study, the fourth the results of the experiments on BK-7. In the fifth section the results are discussed and conclusions drawn.

2. Experimental

Multiple pulse damage studies have been carried out using the apparatus described previously. [13] Pulses from a Quanta Ray DCR-1 Q-switched Nd:YAG laser with a 10 Hz pulse repetition frequency were directed through a spatial filter to produce an approximately Gaussian spatial profile. The beam was then focused tightly into the sample (focal spot radius typically several microns) to assure bulk damage. In this work "damage" is taken to have occurred when sample cracking occurs, accompanied by a visible spark, increased optical scattering and attenuation of the laser beam. Both the fundamental laser output at 1064 nm and the frequency doubled beam have been employed.

The laser used operates in multiple axial modes, resulting in a complex and nonreproducible temporal pulse profile. For this reason data are presented in terms of fluence rather than peak irradiance, and emphasis is placed on comparisons of damage properties between different materials rather than on absolute values of damaging fluences. Care must be taken in the interpretation of wavelength dependence, as the frequency doubling process accentuates the high intensity spikes in the waveform.

To test the effect of point defects on laser-induced damage in BK-7, samples were irradiated by unfiltered Mo radiation from a Philips x-ray machine operated at 50 kV and 15 mA. Irradiation times of three, six and eleven hours were used. The absorption spectrum following x-irradiation was found to be very similar to that reported by White, et al., [12] so that we assume the color centers generated by x-rays to be similar to those induced by intense 532 nm laser light.

The x-ray penetration depth in BK-7 was found to be only about two millimeters, so that the defect density varied with depth in the sample. A collimated beam of lamp light near 532 nm was used to probe the optical absorption along a direction transverse to the direction of x-ray propagation. Together with a spectrophotometric measurement of attenuation along the x-ray direction this permitted an estimate of the 532 nm absorption coefficient as a function of depth in the sample, yielding a relative measure of defect concentration at the location of laser damage. These data also permitted correction of laser fluence for the effect of attenuation, which was particularly significant at 532 nm.

Samples used in this study were BK-7, a borosilicate glass produced by Schott, and two grades of synthetic fused silica produced by Corning. One was ultraviolet grade Corning 7940, a material with about 1000 ppm molecular concentration of OH but otherwise extremely pure, the other being infrared grade Corning fused silica with only a few parts per million of OH. All three materials have been studied by many workers, and are regarded to be highly pure and homogeneous glasses.

3. Fused silica results

Damage data for experiments on "wet" fused silica with 1064 nm irradiation are presented in figure 1. Each point represents an experiment in which catastrophic damage occurred in the number of pulses indicated on the ordinate due to irradiation with pulses of average on-axis fluence given by the abscissa. Note that the single pulse damage "threshold," defined as the average of the lowest fluence at which single pulse damage ever occurred and the highest fluence at which single pulse damage ever failed to occur, is about 3900 j/cm^2. A similarly defined threshold for damage within one thousand pulses is 1850 j/cm^2 for this sample. Table 1 summarizes the damage data on both types of fused silica under 1064 nm and 532 nm irradiation. The modest difference in 1064 nm single pulse thresholds between the two materials is consistent with that observed by other workers. [14,15] On the whole, however, the damage resistance is nearly identical for wet and dry fused silica. As will be discussed in section 5, this suggests that the progressive generation of

Table 1. Comparison of damage to "wet" fused silica (Corning UV grade) and "dry" fused silica (Corning IR grade). F_N for N = 1 or 1000 is the threshold fluence for damage within N pulses.

Wavelength (nm)	Focal Spot Radius (e^{-2}) (μm)	Material	F_1 (on axis) (j/cm^2)	F_{1000} (on axis) (j/cm^2)
1064	7.5 ± .25	"wet"	3900	1850
		"dry"	3600	1850
532	8 ± .5	"wet"	255	110
		"dry"	255	110

point defects by intense laser light is not responsible for the damage of fused silica by repeated pulses of light too weak to induce damage on the first pulse.

To assess the influence of the complex temporal profile of the laser pulses on these results, two features should be noted. The scatter in the pulse number versus fluence data is not significantly worse than that found in the multiple pulse damage data on Corning 7940 using a single mode laser. [6,7] Thus, the irreproducible wave form used in this study does not prevent the determination of relative thresholds. The single pulse thresholds found in this study are comparable to those found in the single mode laser study at 1064 nm, but are lower at 532 nm by an order of magnitude. This effect appears to be consistent with the presence in the wave form of short-duration spikes (due to beating among modes) which do not dominate the damage process at 1064 nm but are much more important after frequency doubling. This point is discussed at greater length in another paper in these proceedings. [16] Thus, although it is possible to compare single pulse with multiple pulse damage fluences within a data set and to compare samples damaged at the same wavelength, the laser used in this study does not permit study of wavelength dependence or direct comparisons of thresholds with single mode laser studies.

4. BK-7 results

Single and multiple pulse damage studies at 1064 nm and 532 nm have been undertaken on BK-7 glass with and without x-irradiation, to investigate the influence of x-ray-induced point defects on the damage properties. The 532 nm damage data on the unirradiated sample and after six hours of irradiation are presented in Figure 3. The fluences for the irradiated material have been corrected for attenuation due to the color center absorption. Note that the single pulse threshold is lower by about 15% in the irradiated material, but that the two samples' damage resistance becomes much more similar at lower fluence. The damage data at 1064 nm as well as 532 nm are summarized in Table 2. The presence of color centers has virtually no effect on the 1064 nm damage properties, the small difference in single pulse thresholds being within the scatter in the data. Sufficiently heavy irradiation does reduce the thresholds at 532 nm, primarily near the single pulse limit.

This reduction in 532 nm damage threshold is presumably related to the color center absorption at that wavelength, which provides a new channel for energy deposition and may also permit excitation of electrons to the conduction band by two single photon transitions instead of the otherwise required two photon absorption. Since it is known that 532 nm laser irradiation produces defects with similar absorption the question arises as to whether the generation of such defects can lower the damage threshold sufficiently to explain multiple pulse damage.

White, et al., found that the laser generation of color centers saturates due to photobleaching at a concentration roughly proportional to the pulse fluence. [12] Indeed, at fluences comparable to those needed in the present work to induce damage after several thousand pulses they observed an absorption coefficient at 532 nm of about 0.08 cm^{-1}. The 532 nm absorption coefficient at the focal plane of the damaging laser in the sample irradiated for six hours in this study is approximately 1.6 cm^{-1}. Thus the observed 15% drop in damage threshold was apparently induced by a defect concentration an order of magnitude higher than that which can be induced by the laser. Indeed, since the laser beam encountered a defect concentration higher than the value dictated by the balance between nonlinear generation and photobleaching, it is probable that bleaching occurred

Table 2. Comparison of damage to BK-7 with and without x-irradiation. The fluences in irradiated samples have been corrected for attenuation between the sample face and focal plane.

Wavelength (nm)	Focal Spot Radius (e^{-2}) (μm)	Irradiation Time (hours)	F_1 (on axis) (j/cm^2)	F_{1000} (on axis) (j/cm^2)
1064	7.5 ± .25	unirradiated	3000	1400
		11	2850	1400
532	12.5 ± .25	unirradiated	43	20
		3	43	20
		6	36	19

during multiple pulse irradiation. This may explain the tendency of the unirradiated and irradiated damage curves to approach each other in the many pulse damage regime. It is evident that the relatively low concentration of defects generated by the laser can account for only a small part of the reduction in threshold induced by multiple pulse laser irradiation.

5. Discussion and conclusions

Both tests of the influence of point defects on laser-induced damage indicate that the multiple pulse damage phenomenon is not primarily due to laser generation of such centers. Indeed, there is qualitative similarity between the situations in the two materials.

In fused silica it is known that E' centers can reduce the 532 nm damage threshold considerably, [9] and that laser generation of the relevant centers using a photon energy approximately twice that of 532 nm light is much more efficient in "dry" than in "wet" fused silica. [10,11] Thus, the lack of difference in multiple pulse damage behavior between these two types of SiO_2 indicates that even in the low-OH material and even at damaging intensities two-photon laser generation of these centers does not create a sufficient density to significantly affect damage.

In the case of BK-7 the present study shows that sufficiently large concentrations of point defects lower the damage threshold, at least at 532 nm. (The actual concentration is difficult to estimate without knowledge of oscillator strengths and of a strong ultraviolet absorption band the wing of which is evident in our absorption data.) Since the x-ray induced visible absorption is much stronger than that expected due to laser generation, it is again the case that laser generation of defects is too weak to explain multiple pulse damage.

It is interesting that a concentration of defects large enough to give rise to considerable optical absorption has so little effect on laser damage in BK-7. Linear absorption due to an absorption coefficient of 1.6 cm^{-1} deposits less than 3.6×10^{-5} j from a 1.0×10^{-4} j incident pulse in a volume of about 7×10^{-7} cm^3. This results in about a 24 C^o temperature rise, but due to thermal diffusion between pulses this does not result in significant long term heating. Linear absorption, however, may permit two single-photon transitions to excite electrons to the conduction band, in which free carrier absorption contributes to the damage process. It may be that two-photon absorption across the band gap is a more important process due to the high joint density of states. The 1064 nm damage data also make it clear that stepwise excitation has little influence on the damage process at this wavelength. This lack of importance of color centers to the damage process may be a common state of affairs. Color centers have also been calculated to play only a minor role in alkali halide damage. [17] Indeed, the insensitivity of the 1064 nm damage thresholds to color centers in BK-7 suggests that the effect of E' centers on the damage in fused silica may be more complex than the stepwise excitation process suggested by Soileau, et al. [9]

In conclusion, it is often assumed that the multiple pulse damage phenomenon is due to the laser-induced generation or growth of states capable of providing starting electrons for electron avalanche in a subsequent pulse. Although one of the more plausible mechanisms by which this process may occur is point defect generation, the present study shows that this mechanism is not, in fact, responsible for multiple pulse damage in the materials studied.

The authors are grateful to the Research Corporation for support of this work, and to Ralph Perkins of Corning Glass Works for donation of the samples of infrared grade fused silica.

6. References

[1] O'Connell, Robert M.; Deaton, Terrence F.; Saito, Theodore T. Appl. Opt. 23(5); 682-688; 1984.

[2] Wu, S.-T.; Bass, M.; Stone, J.P. Nat. Bur. Stand. (U.S.) Spec. Publ. 638; 152-159; 1981.

[3] Jhee, Y.K.; Becker, M.F.; Walser, R.M. J. Opt. Soc. Am. B2(10); 1626-1633; 1985.

[4] Wood, R.M.; Sharma, S.K.; Waite, P. Nat. Bur. Stand. (U.S.) Spec. Publ. 669; 44-49; 1982.

[5] Balitskas, S.K.; Maldutis, E.K. Sov. J. Quantum Electron. 11(4); 541-543; 1981.

[6] Merkle, Larry D.; Bass, Michael; Swimm, Randall T. Nat Bur. Stand. (U.S.) Spec. Publ. 669; 50-59; 1982.

[7] Merkle, Larry D.; Koumvakalis, N.; Bass, M. J. Appl. Phys. 55(3); 772-775; 1984.

[8] Griscom, David L. J. Non-Cryst. Sol. 73; 51-77; 1985.

[9] Soileau, M.J.; Mansour, Nastaran; Canto, Edesly; Griscom, D.L. Proc. of Seventeenth Symp. on Opt. Mater. for High Power Lasers; to be published by Nat. Bur. Stand. (U.S.).

[10] Stathis, J.H.; Kastner, M.A. Phil. Mag. B49(4); 357-362; 1984.

[11] Stathis, J.H.; Kastner, M.A. Phys. Rev. B29(12); 7079-7081; 1984.

[12] White III, W.T.; Henesian, M.A.; Weber, M.J. J. Opt. Soc. Am. B2(9); 1402-1408; 1985.

[13] Kitriotis, D.; Merkle, L.D.; Dodson, A. Proc. of Seventeenth Symp. on Opt. Mater. for High Power Lasers; to be published by Nat. Bur. Stand. (U.S.).

[14] Soileau, M.J.; Bass, M. IEEE J. Quantum Electron. 16(8); 814; 1980.

[15] Soileau, M.J.; Williams, William E.; Van Stryland, Eric W.; Boggess, Thomas F.; Smirl, Arthur L. Opt. Eng. 22(4); 424-430; 1983.

[16] Merkle, Larry D.; Bandyopadhyay, Pradip K. Proc. of Eighteenth Symp. on Opt. Mater. for High Power Lasers (this volume).

[17] Braunlich, P.; Schmid, A.; Kelly, Paul. Appl. Phys. Lett. 26(4); 150-153; 1975.

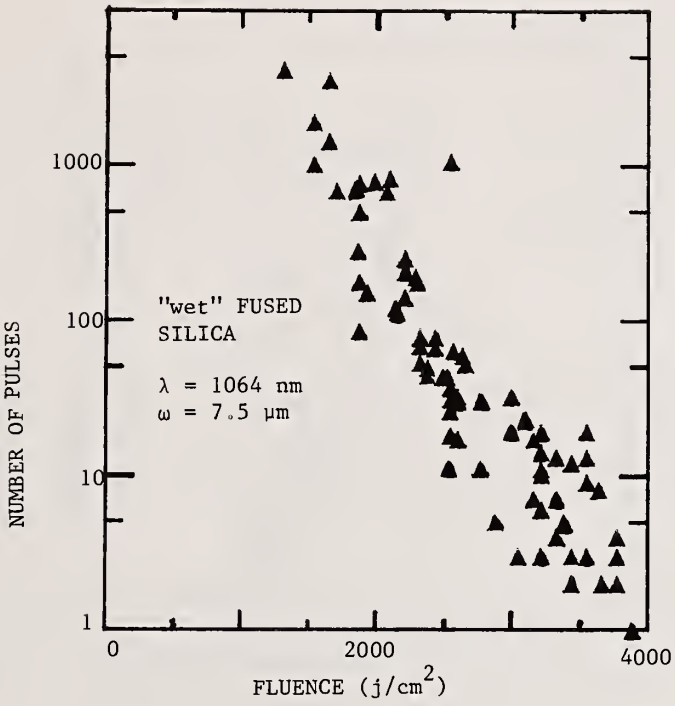

Figure 1. Damage data on high-OH UV grade Corning fused silica under 1064 nm laser irradiation. Triangles indicate experiments in which damage occurred in the indicated number of pulses.

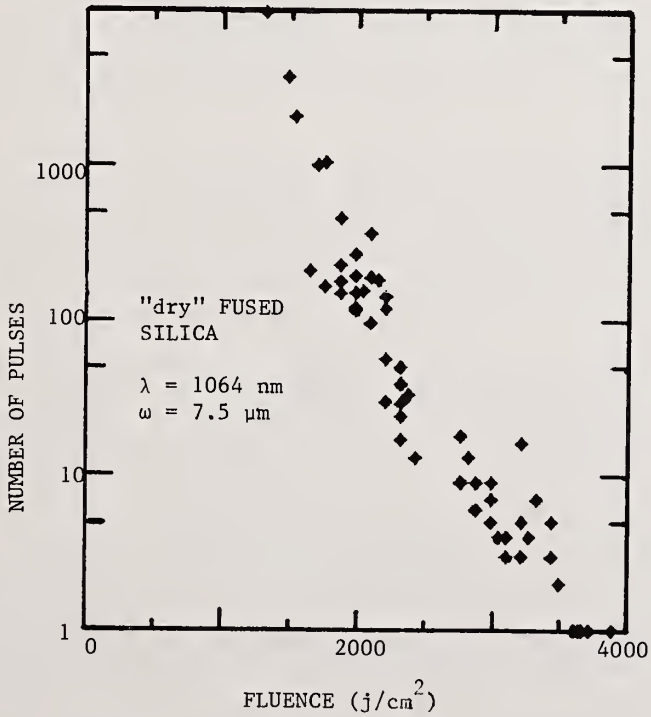

Figure 2. Damage data on low-OH IR grade Corning fused silica under 1064 nm laser irradiation. The diamonds have the same meaning as the triangles of figure 1.

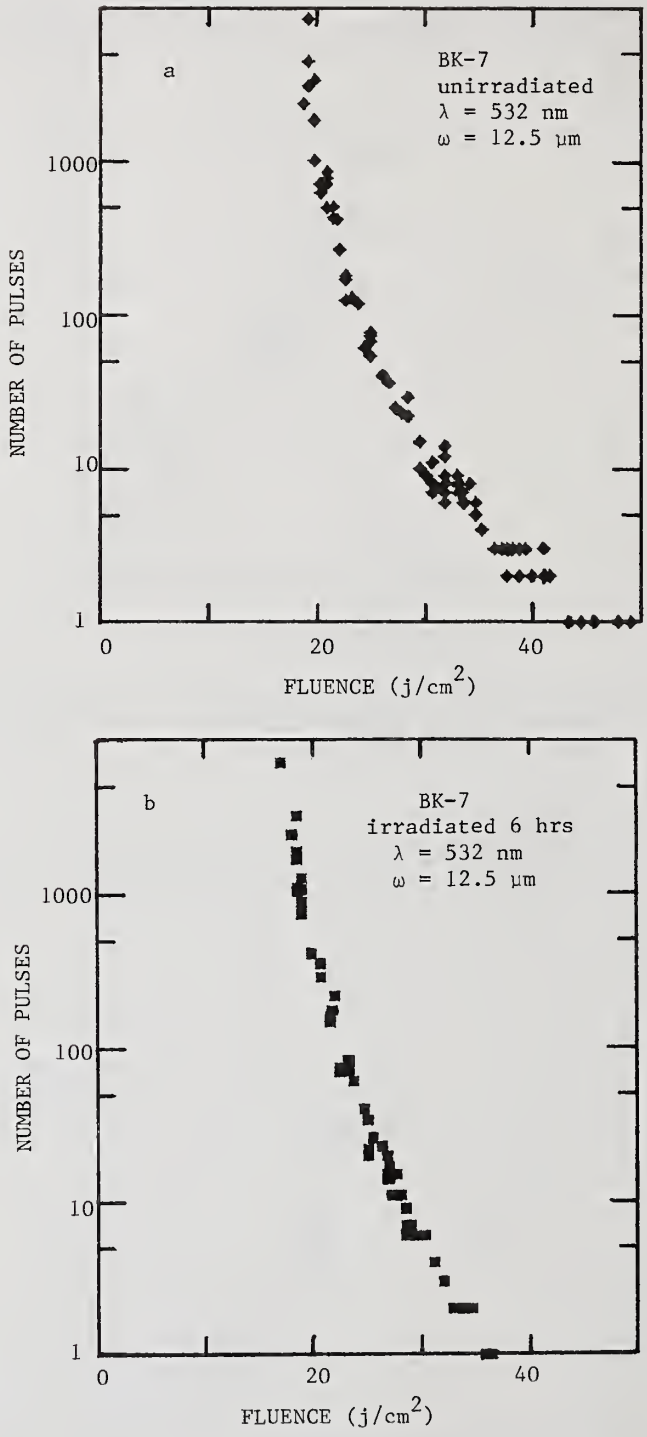

Figure 3. Damage data on BK-7 under 532 nm laser irradition. a: sample not irradiated by x-rays; b: sample x-irradiated for six hours. The symbols have the same meanings as in figures 1 and 2.

Manuscript Received
12-22-86

Influence of Impurities and Defects on 1064 nm and 532 nm Damage in Quartz

Larry D. Merkle and Pradip K. Bandyopadhyay*

Physics Department
University of Arkansas
Fayetteville, AR 72701

It is axiomatic that even low concentrations of defects or impurities can control the damage behavior of transparent solids. Following the observation, reported in the 1985 Symposium, of strikingly different damage properties in two apparently similar samples of crystalline quartz, a study of several grades of quartz has been made to determine the influence of impurities and structural defects on their damage resistance. Data were taken at 1064 nm and 532 nm using a Q-switched YAG laser.

It has been found that considerable differences in single and multiple pulse damage "thresholds" exist among quartz samples of varying quality. These variations do not correlate with the concentrations of the most common impurities, Al and OH, but they appear to correlate with the density of coarsely spaced defects such as inclusions or etch channels (dislocations). These results tend to rule out damage mechanisms involving point-like defects, emphasizing instead the importance of larger impurities, even if submicroscopic.

Key words: aluminum; bulk damage; impurity; inclusion; multiple pulse damage; quartz

1. Introduction

It is widely regarded that impurities and defects are important to the laser-induced damage properties of even the purest transparent solids. In high quality materials, however, it may be difficult to identify the most important impurities or the mechanism by which they promote damage. Such knowledge is important both for the scientific understanding of damage and to guide the development of improved optical materials.

In the 1985 Symposium the observation of quite different bulk damage properties in two apparently similar samples of crystalline quartz was reported. [1] The single and multiple pulse 532 nm damage thresholds were found to be considerably higher and the uncertainty in the damage threshold far greater in the sample of nominally lower quality. Further, the concentrations of the best-known impurities in artificially grown (cultured) quartz, Al and OH, were found to be nearly identical in the two samples. The study reported here was undertaken to investigate the cause of this surprisingly large variation in damage properties in quartz.

Quartz is an appropriate material for the investigation of impurity influence on damage for reasons beyond the puzzling nature of the data summarized above. It is a widely used optical material whose damage properties are thus of some practical importance. In addition, the most common impurities and defects in quartz have been studied extensively, maximizing the probability that their role in laser damage can be understood. [2-4]

The most common impurities and defects in cultured quartz are as follows. Aluminum impurities with nearby alkali ions as charge compensators are common, and when the alkali is replaced by a trapped hole optical absorption in the visible range results. [5] Hydroxyl ions are also present, as apparently are inclusions of water. [6] The other common impurity is iron, which is also thought to take the form of inclusions. The most important structural defects are bundles of dislocations filled with impurity ions, often referred to as etch channels. [4]

The remainder of this paper will describe investigations of the laser-induced bulk damage properties of several quartz samples of varying purity. In the second section the experiments are

*permanent address: Physics Department, Hendrix College, Conway, AR 72032.

briefly described and in the third section the results are presented. Finally the implications of the data are discussed, permitting conclusions to be drawn as to the probable cause for the variation in damage properties among the samples.

2. Experimental

The apparatus and procedure for the laser-induced damage experiments were described in the 1985 Symposium, [1] and only a brief summary is given here. The fundamental and frequency doubled outputs of a Quanta Ray DCR-1 Q-switched Nd:YAG laser were used. The laser operated at a pulse repetition frequency of 10 Hz, and after spatial filtering the beam was focused into the bulk of the sample to a nearly Gaussian focal spot. The laser operated in multiple longitudinal modes, resulting in complicated and irreproducible pulse waveforms with average durations of 16 nsec at 1064 nm and 10 nsec at 532 nm. Due to the complex waveform all data are presented in terms of on-axis fluence rather than irradiance and comparisons of relative thresholds are emphasized over absolute values. As will be discussed in the final section, the waveform also requires that care be taken in the interpretation of wavelength dependence.

In this study catastrophic damage is regarded to have occurred on a given pulse if that pulse results in a sudden reduction of transmission, an increase in light scatter, a flash of light indicative of high temperature, and the development of cracks in the focal region.

Some of the major impurities and defects in quartz can be detected and their concentrations estimated. The aluminum concentration was determined from electron spin resonance measurements performed by Larry Halliburton of Oklahoma State University. Infrared absorption measurements near 3500 cm^{-1} were made to infer the ultrasonic Q-value, the inverse of which is roughly indicative of the OH concentration. [7] Surfaces etched by ammonium bifluoride were examined to estimate the density of pits indicative of "etch channels" and other defects. [4]

The properties of the quartz samples studied are summarized in table 1. The first sample listed was grown by Alton Armington of Hanscom Air Force Base and is a product of a growth technique which minimizes the concentration of etch channels. [8] As can be seen from the table, it is also very low in aluminum and OH content. The other samples are commercially produced cultured quartz of varying purity. The density of surface pits produced by the ammonium bifluoride etch was found to vary widely from place to place on each sample so that these data give only a rough estimate of the average density of etchable defects. Microscopic inspection of representative regions of each sample indicate that there are very few visible inclusions: from zero to thirty per cubic centimeter. Of course, inclusions much smaller than a wavelength of visible light are not detectable by this means. All samples were cut and polished such that laser light propagated along the z-axis. The direction of linear polarization did not affect the damage properties.

Table 1. Quartz sample properties. All samples were cut from z-growth material except sample TX.

Sample Label and Source	Aluminum concentration (ppm atomic)	Ultrasonic Q value	Density of surface pits (cm^{-2})
HA, Hanscom AFB	0.2	3.2×10^6	not measured
SP, Sawyer Research Products (premium Q)	6.7	1.8×10^6	$2 - 6 \times 10^5$
TE, Thermo Dynamics (electronic grade)	4.4	1.6×10^6	$1 - 6 \times 10^5$
TP, Thermo Dynamics (premium Q)	3.7	1.5×10^6	$1 - 7 \times 10^5$
TX, Thermo Dynamics (premium Q, x-growth)	26.3	1.7×10^6	$1 - 4 \times 10^5$
TZ, Thermo Dynamics (same bar as TX, z-growth)	3.5	2.0×10^6	$2 - 5 \times 10^5$

3. Results

Data from the damage of two of the samples at 1064 nm are presented in figures 1 and 2. Each symbol represents an experiment in which catastrophic damage of the irradiated site was observed after the indicated number of pulses or in which irradiation was terminated after 5000 pulses without damage. The abscissa indicates the average on-axis fluence of the irradiating pulses. Note that damage was produced within a given number of pulses at significantly lower fluences in sample TZ than in sample HA. It is also clear that there is considerable scatter in the data, particularly in the few-pulse region of the TX data. This scatter is not primarily due to the irreproducible pulse waveform of the irradiating laser, as the data for damage of fused silica and BK-7 glass using the same laser are cleaner. [9] Rather, it is indicative of sample inhomogeneity. Figures 3 and 4 present damage data due to 532 nm irradiation of the same samples. Note that sample HA still typically requires higher fluences to damage within a given number of pulses, but that at this wavelength the data for HA exhibit even more scatter than those for TZ.

The damage data for all samples are summarized in Table 2. The fluences required to induce damage are characterized by the single pulse threshold, F_1, and the thousand pulse threshold, F_{1000}. Each threshold is defined as the average of the lowest fluence at which the sample ever damaged within the stated number of pulses and the highest fluence at which it ever survived that number of pulses undamaged. The columns labelled "Spread in F_1" give the fluence range in which single pulse damage only sometimes occurred, indicative of the scatter in the data. Figure 5 is a photomicrograph of a damage site induced in sample SP by 532 nm irradiation. The large region of cracks and apparent melting which extends along the beam "upstream" from approximately the focal plane is typical of all damage sites. The small bubbles "downstream" from the focal plane are representative of a considerable fraction of 532 nm damage sites and a small fraction of the 1064 nm sites. The fraction of all damaged sites exhibiting this bubble morphology is tabulated for each sample in table 2.

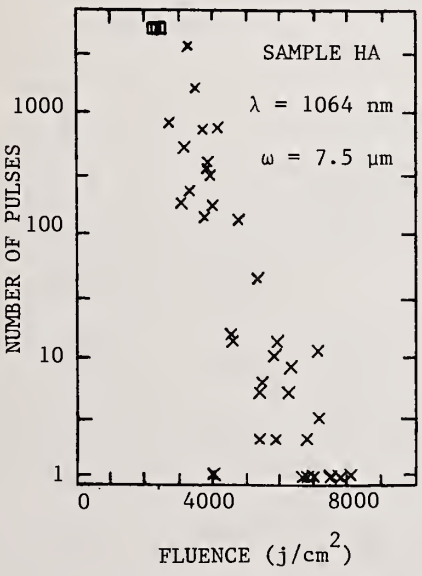

Figure 1. Damage data on sample HA irradiated at 1064 nm. Crosses indicate experiments in which damage occurred in the indicated number of pulses. Open squares indicate experiments terminated after 5000 pulses without damage.

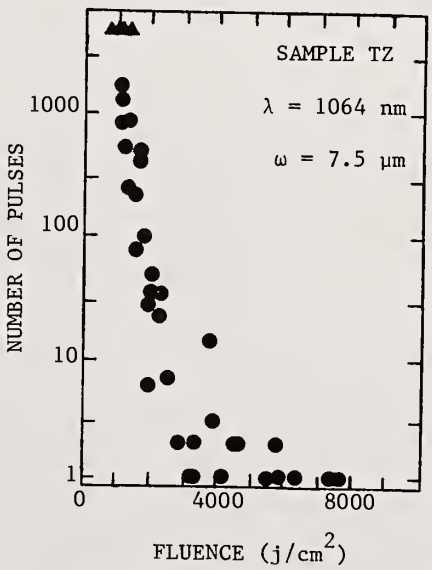

Figure 2. Damage data on sample TZ irradiated at 1064 nm. Filled circles indicate experiments in which damage occurred in the indicated number of pulses. Filled triangles indicate experiments terminated after 5000 pulses without damage.

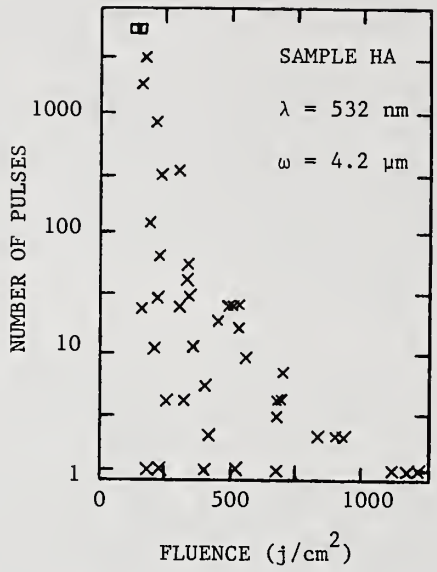

Figure 3. Damage data on sample HA irradiated at 532 nm. The symbols have the same meanings as in Figure 1.

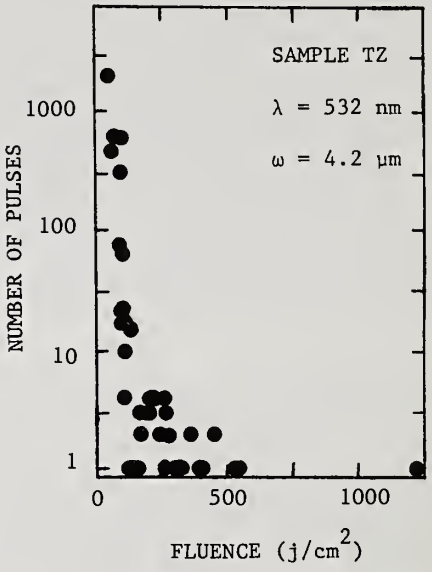

Figure 4. Damage data on sample TZ irradiated at 532 nm. The symbols have the same meanings as in Figure 2.

Table 2. Summary of damage properties.

Sample	Damage at 1064 nm (ω_{1/e^2} = 7.5 μm)				Damage at 532 nm (ω_{1/e^2} = 4.2 μm)			
	F_1 (j/cm^2)	Spread in F_1	F_{1000} (j/cm^2)	Fraction of sites with "bubble" morphology	F_1 (j/cm^2)	Spread in F_1	F_{1000} (j/cm^2)	Fraction of sites with "bubble" morphology
HA	5,700 (7,000)[a]	±26% (±4%)[a]	3,300	0	560	±65%	180	0.20
SP	5,500	±5%	2,500	0.20	290	±15%	90	0.60
TE	5,200	±15%	2,500	0	575	±64%	235	0.10
TP	6,800	±25%	2,500	0.15	235	±6%	90	0.50
TX	---	---	---	---	325	±21%	125	0.30
TZ	4,400	±31%	1,400	0.20	290	±54%	65	0.60

[a]These values were obtained excluding the single-pulse damage event at 4,200 j/cm^2, evident in figure 1, giving values more representative of the bulk of the HA data.

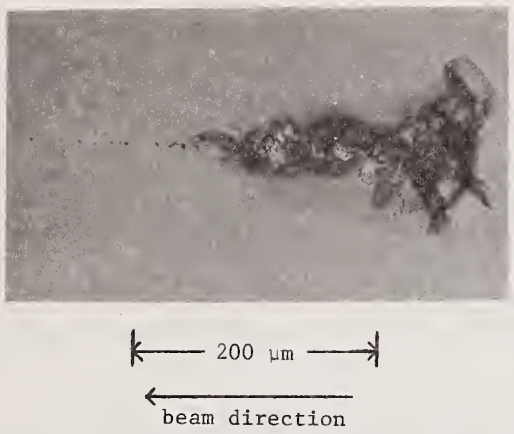

Figure 5. Photomicrograph of a site in sample SP damaged by 532 nm irradiation.

A comparison of tables 1 and 2 permits the making of inferences about the importance of different impurities to laser damage properties. Although the Hanscom sample, with the lowest aluminum concentration, has damage thresholds among the highest, the thresholds of the other samples exhibit no correlation with aluminum content. Similarly the Q value (and thus the OH content) fails to correlate with damage thresholds. However, there do appear to be correlations between the frequency of occurrence of bubbles in the damage morphology and the damage scatter and thresholds. In particular, in the 1064 nm data there is a tendency for samples exhibiting a relatively high incidence of bubble morphology to exhibit large scatter in the damage data (large spread in F_1). At 532 nm, interestingly, exactly the opposite tendency is evident: high bubble frequency correlates with small spread in the data. At 532 nm there is also a clear correlation between low probability of bubble morphology and high damage thresholds (F_1 and F_{1000}). A similar, though weaker, correlation exists in the 1064 nm data. The interpretation of these trends will be discussed in Section 4.

4. Discussion

One striking feature of the data not yet addressed is the strong wavelength dependence of the damage thresholds. The fluences required for damage at 1064 nm are comparable to those reported by Merkle, et al., in a study employing a single mode YAG laser. [10] However, the thresholds observed at 532 nm are lower by an order of magnitude than those observed in that work. The difference must be due to the non-smooth waveform employed in the present work. The bandwidth of the DCR-1 laser permits beats as short as 100 psec, much too short to be resolved with equipment available in this laboratory.

Without specific knowledge of the waveform a detailed understanding of its influence on the wavelength dependence is not possible, but a plausible explanation may be outlined as follows. Assume the fundamental laser pulse can be modeled as a relatively smooth 16 nsec pulse containing most of the energy with one or more peaks superimposed with several times higher amplitude but durations perhaps one percent of that total duration. The fluence in each short-duration peak is too small to control the damage in light of the often-cited square root dependence of threshold fluence on pulse duration. However, the quadratic irradiance dependence of frequency doubling results in a 532 nm pulse in which the tallest short-duration peak contains a considerable fraction of the total pulse energy. Again assuming a square root of pulse duration threshold dependence, reasonable ratios of short-duration peak height to long-duration smooth pulse height can be found for which the spike-dominated 532 nm pulse reaches damage threshold at a fluence nearly an order of magnitude lower than that required by a smooth pulse without short-duration spikes.

Since the above argument is necessarily speculative it is important to consider other possible causes for the strong wavelength dependence. The most likely is catastrophic self-focusing, which can cause such a dependence if the limiting radius set by the opposition of n_2 and plasma defocusing is larger than the linear optics spot size at 1064 nm but smaller at 532 nm. [11] However, available estimates of n_2 for both the nanosecond and picosecond time scales are sufficiently small to suggest that the limiting radius should remain larger than the linear optics spot size at both wavelengths in this work. [12,13] Thus self-focusing is not expected to be important.

Addressing the correlations between damage thresholds and sample properties, it is evident

that aluminum and hydroxyl ions play little role, if any, in the damage process. Rather, it is proposed that coarsely spaced defects, probably submicroscopic inclusions or dislocation bundles, initiate laser damage. In this model the bubbles often observed in the damage morphology represent defect sites at which damage has initiated but could not grow due to the lower fluence available away from the focal plane. Dislocation bundles (etch channels) and inclusions are suggested as damage initiators in part because they are known to be common in quartz. Interestingly, too, the density of initiation sites implied by the frequency of occurrence and average spacing of damage bubbles at 532 nm is comparable to the density of defects revealed by etching. This damage initiator density is far lower than the aluminum concentration in even the purest sample. For objects of such low concentration to control damage when higher concentrations of point defects such as aluminum (or color centers in related materials [9]) do not, it is probable that they are large enough objects to result in significant local energy deposition, again suggesting inclusions or other many-atom structures.

If the damage initiators are much smaller than one micron their failure to appear under a microscope prior to damage is to be expected, as is the higher probability of bubble damage morphology at 532 nm than at 1064 nm. The latter follows simply due to the stronger coupling of light to an object as the wavelength approaches the object's size.

Initiation of damage at coarsely spaced defects can explain the various correlations noted between bubble morphology occurrence and damage scatter and thresholds. At 1064 nm the light interacts weakly with the defects, so that in the samples with small defect concentration damage rarely initiates on such a defect. The results are high damage thresholds, small scatter in the data and few sites with damage bubbles. In samples with high defect concentration a significant fraction of experiments do result in damage initiation on a defect, lowering the thresholds and increasing data scatter and bubble occurrence. At 532 nm the interaction of light with defects is so strong that even in the purest samples damage fairly often initiates on a defect. This produces large data scatter (the sample appears less homogeneous) and a significant probability of bubble morphology. In high defect concentration samples the 532 nm light is almost certain to find a defect in the focal spot with which to interact, so that damage thresholds are driven down and the frequency of bubble morphology becomes high. If the probability of finding a damage initiating defect in the high-fluence portion of the beam becomes sufficiently near unity the scatter in the damage data may actually decrease, consistent with the most surprising correlation in the data.

In conclusion, the data reported here suggest that point defects such as Al and OH centers do not weaken the damage resistance of quartz in the concentrations found in these samples. However, some type of defect present in much lower concentrations does indeed result in reduced single and multiple pulse thresholds. It is argued that these defects are many-atom objects such as etch channels or submicroscopic inclusions. The resultant severely inhomogeneous damage resistance at 532 nm of even the extremely pure and structurally near-perfect Hanscom material provides a sobering example of the importance of defects to the optical properties of even the best quartz.

The authors wish to thank Dimitrios Kitriotis for his experimental help, Aaron Murray of Thermo Dynamics and Alton Armington of Hanscom Air Force Base for the donation of samples, and Larry Halliburton of Oklahoma State University for samples and electron spin resonance measurements. This work was funded by a grant from the Research Corporation.

5. References

[1] Kitriotis, D.; Merkle, L.D.; Dodson, A. Proc. of Seventeenth Symp. on Opt. Mater. for High Power Lasers; to be published by Nat. Bur. Stand. (U.S.).

[2] Halliburton, L.E. Cryst. Latt. Def. and Amorph. Mat. 12; 163-190; 1985.

[3] Jani, M.G.; Halliburton, L.E. J. Appl. Phys. 56(4); 942-946; 1984.

[4] Vig, John R.; LeBus, John W.; Filler, Raymond L. Proc. of Thirty-first Ann. Symp. on Freq. Control; 131-143; 1977.

[5] Koumvakalis, N. J. Appl. Phys. 51(10); 5528-5532; 1980.

[6] Larkin, John. Hanscom Air Force Base, Cambridge, MA; private communication.

[7] Sawyer, Baldwin. IEEE Trans. Sonics and Ultrasonics SU-19(1); 41-44; 1972.

[8] Armington, Alton F.; Larkin, John J. J. Crystal Growth 71; 799-802; 1985.

[9] Kitriotis, Dimitrios; Merkle, Larry D. Proc. of Eighteenth Symp. on Opt. Mater. for High Power Lasers (this volume).

[10] Merkle, Larry D.; Koumvakalis, N.; Bass, M. J. Appl. Phys. 55(3); 772-775; 1984.

[11] Van Stryland, E. W.; Soileau, M. J.; Smirl, Arthur L.; Williams, William E. Phys. Rev. B 23(5); 2144-2151; 1981.

[12] Soileau, M.J.; Ph.D. Dissertation; University of Southern California; 1979.

[13] Feldman, Albert; Horowitz, Dean; Waxler, Roy M. IEEE J. Quantum Electron. QE-9(11); 1054-1061; 1973.

Manuscript Received
12-4-86

Model Comparisons With Glancing Incidence Measurements of Overcoated Metal Mirrors

W.D. Kimura
Spectra Technology, Inc.
Bellevue, Washington 98004-1495

F.J. Woodberry
Rockwell International Science Center
Thousand Oaks, California 91360

and

L.F. DeSandre
Naval Weapons Center
China Lake, California 93555-6001

The absorptance characteristics of metal mirrors, with thin dielectric overcoats on their surface, have been measured at angles of incidence from 0 to 89°, for both s and p-polarizations. The mirrors tested are silver overcoated with ThF_4, and aluminum overcoated with MgF_2. To understand the experimental results requires the use of models incorporating thin film theory. Estimations of parameters, such as film thickness, can be made by varying parameters within the model until the best fit with the experimental data is obtained. This paper presents the results of model comparisons with the glancing incidence data. In addition, thin film designs for overcoated mirrors with enhanced reflectivity at glancing incidence are discussed.

Key words: thin film model; glancing incidence; overcoat; optimum mirror design; silver; aluminum; ThF_4; MgF_2.

1. Introduction

Glancing or grazing incidence mirrors are critical components in some laser system designs. For example, a proposed [1] free electron laser for generation of XUV or soft x-rays uses a ring resonator comprised of many mirrors adjusted to operate at glancing incidence. Although bare metal mirrors are logical choices for glancing incidence applications, some preferred metals, such as silver and aluminum, have problems with tarnishing. It has been shown [2] that the absorptance, caused by the tarnish, tends to be worse at glancing incidence than at normal incidence. One way to prevent the tarnishing is to apply a protective dielectric overcoat on the metal surface. However, there has been little work done to understand how an overcoated metal mirror behaves at high angles of incidence.

A photoacoustic calorimetry system [3] has been developed at Spectra Technology, Inc. (STI) and has been successfully used to measure the absorptance characteristics of bare metal mirrors from 0 to 89° [4]. The system has also been used to measure the glancing incidence absorptance characteristics of overcoated metal mirrors. The results for two mirrors, MgF_2 on aluminum and ThF_4 on silver, are discussed in this paper.

While simple Fresnel theory for bare metals [5] cannot be used to predict the absorptance behavior of overcoated mirrors, the theory of thin films on surfaces is well established [6], and computer codes are available to accurately predict the optical characteristics of films on metal surfaces. This paper discusses the application of thin film theory to interpret the glancing incidence experimental data. In addition, examples are given of model predictions for thin films designed to not only overcoat the metal surface, but at the same time enhance the reflectivity at a high angle of incidence for a given polarization.

2. Review of Thin Film Theory

As mentioned earlier, there has been a great deal of work in the area of optical thin films; Macleod's [6] book is a classic reference. Hence, the description in this paper shall be restricted to the codes and basic equations used in this work.

Figure 1 is a cross section of a single layer film on a substrate. The index of refraction n_2 is assumed to equal 1 (air). The film is assumed to be non-absorbing (i.e., the extinction coefficient, k, is zero) and has a thickness d with an index n_1. This is a reasonable assumption for most films at the visible and IR wavelengths examined during this program. The absorbing substrate has a complex index of refraction given by n - ik. The Fresnel reflectance and transmittance coefficients [5] at each of the boundaries are designated by r_n and t_n, n = 1, 2, respectively. For a single layer, non-absorbing film on an absorbing substrate, the reflectance as a function of angle of incidence is given by [7],

$$R = \frac{r_2 + r_1 \exp(-2i\delta_1)}{1 + r_1 r_2 \exp(-2i\delta_1)} \qquad [1]$$

where $\delta_1 = (2\pi n_1 d\cos\phi)/\lambda$ is the phase thickness at angle ϕ within the film.

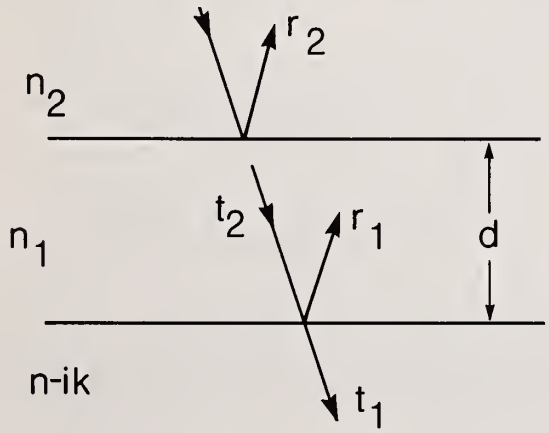

Figure 1. Schematic cross section of a non-absorbing thin film on an absorbing substrate. See text for explanation.

Equation 1 is valid only for a single layer, non-dispersive film. More complex films can be analyzed using the characteristic matrix formalism. The elements of the matrix are solutions to the wave equation, which satisfy the conditions of continuity of the tangential components of the electric and magnetic fields across the plane film boundaries. Sophisticated computer models have been developed, which are capable of analyzing multi-layer films, dispersive (absorbing) films, films with gradients, and so on. However, for the data presented in this paper, the simple expression given by Eq. (1), reveals much about the characteristics of the mirrors tested. Hence, all the theoretical curves displayed in this paper are based upon Eq. (1).

3. Comparisons of Experiment With Theory

The glancing incidence absorptance measurement system has been described in detail elsewhere [3]. It uses photoacoustic calorimetry to detect the laser energy absorbed on the mirror surface as a function of the incidence angle. Absolute absorptance is determined using a laser energy ratiometer. The uncertainty of the absolute absorptance measurement is ≈±20%; error bars on the data, given in this paper, represent the reproducibility of the photoacoustic measurements and not the variance in the absolute value of the absorptance.

Figure 2 shows the measured absorptance characteristics of an aluminum mirror with a MgF_2 overcoat. The laser wavelength for all the work discussed in this paper is 0.5145 μm (argon ion laser). Figure 2(a) is for s-polarization (perpendicular to the plane of incidence); Figure 2(b) is for p-polarization (parallel to the plane of incidence). The solid curves in Figure 2 are the Fresnel equation predictions for a bare metal surface, using the values of n (0.819) and k (6.26) given by Shiles, *et al.* [8]. Not surprising, the bare metal theoretical curves are very poor at predicting the absorptance characteristics of the overcoated aluminum mirror.

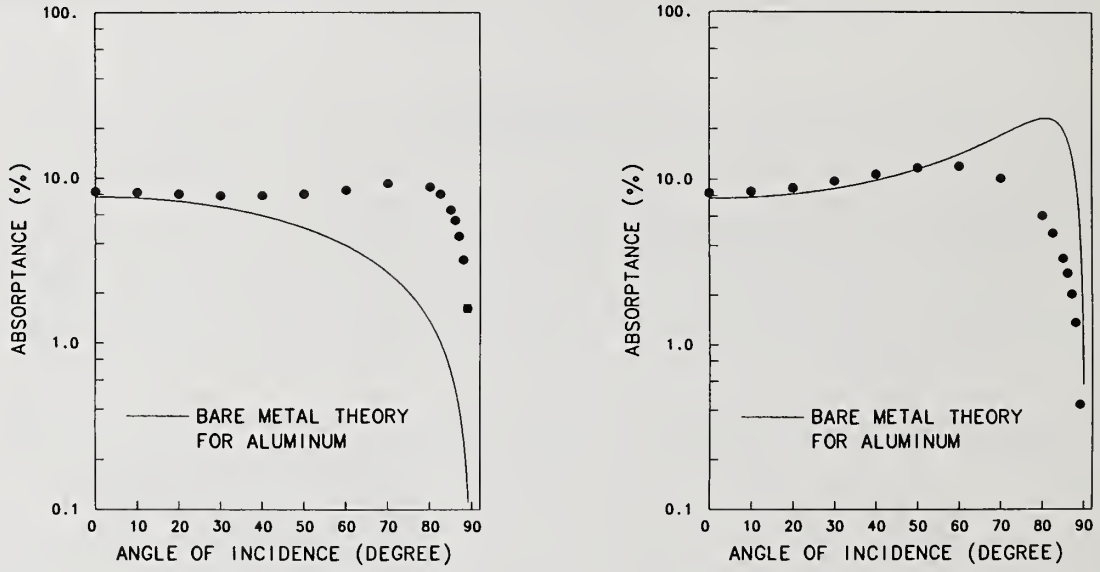

Figure 2. Measured absorptance characteristics of a MgF_2 overcoated aluminum mirror at 0.5145 μm. (a) is for s-polarization; (b) is for p-polarization. The solid curve is the Fresnel theory prediction for a bare metal surface using the values of n and k given by Shiles, *et al.* [8].

Figure 3 shows that the agreement between the data and theory is much better when using a thin film model. In this case, the computer code varied the thickness of the MgF_2 coating (n = 1.38 [6]), until the best fit with the data was obtained at a thickness of 1489 angstroms.

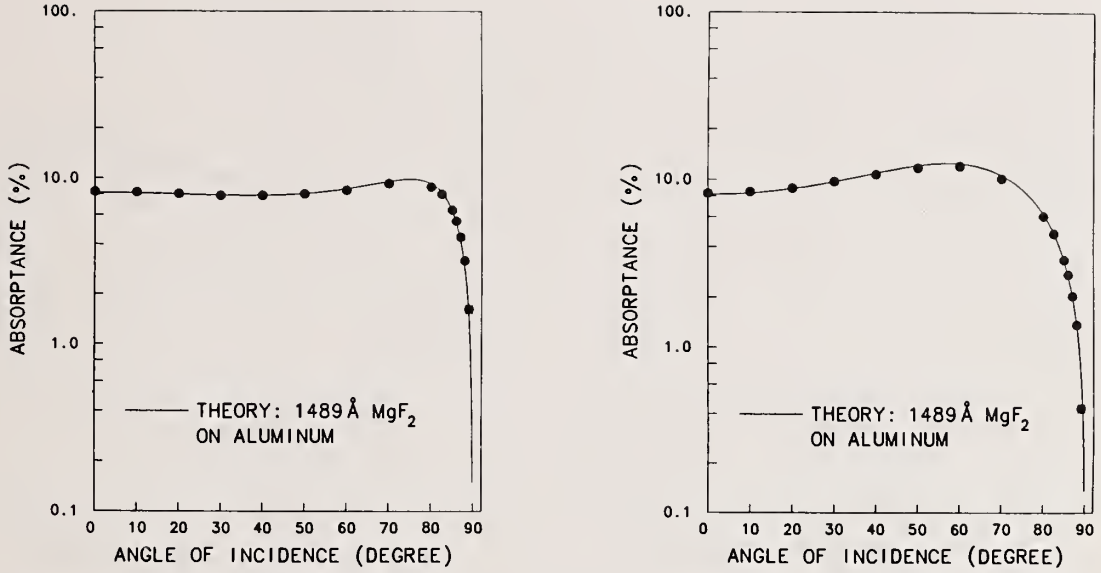

Figure 3. Optimum fit of thin film model with experimental data. The data is the same as given in Fig. 2. (a) is for s-polarization; (b) is for p-polarization. The solid curve is the prediction assuming a MgF_2 thickness of 1489 angstroms.

The experimental data for silver overcoated with ThF_4 is plotted in Figure 4, along with the Fresnel equation predictions for a bare metal surface using the values of n (0.245) and k (3.25) given by Hagemann, *et al.* [9]. Although, the bare metal predictions are closer in agreement in this case than for the overcoated aluminum mirror, there are still significant differences evident. Applying the thin film code again, optimum fit is obtained if a ThF_4 (n = 1.53 [6]) thickness of 1557 angstroms is assumed; this is shown in Figure 5.

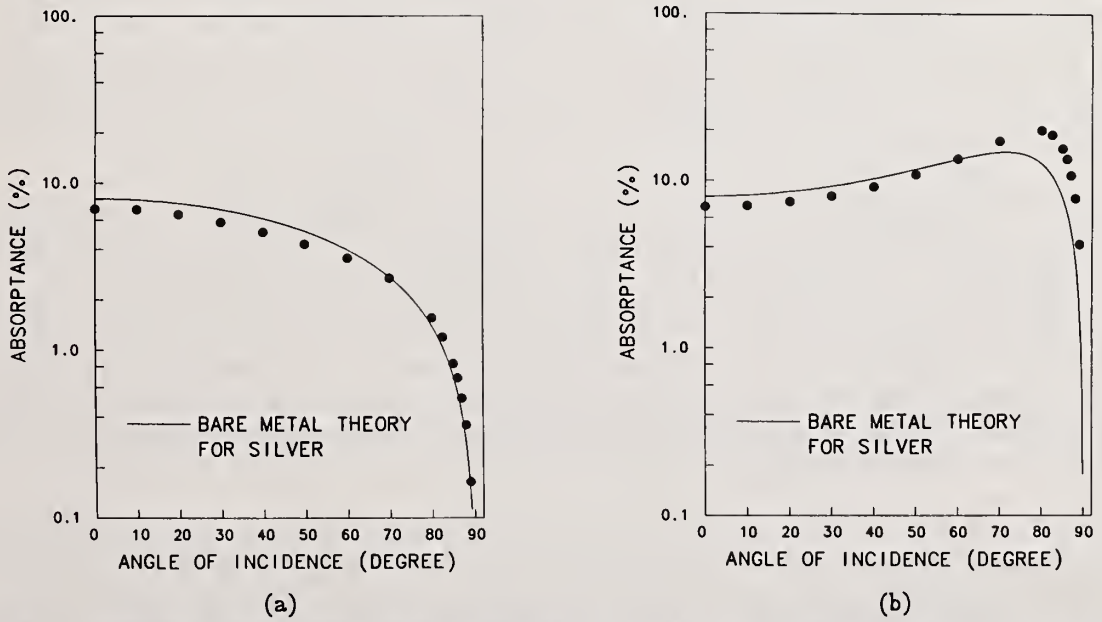

Figure 4. Measured absorptance characteristics of a ThF_4 overcoated silver mirror at 0.5145 μm. (a) is for s-polarization; (b) is for p-polarization. The solid curve is the Fresnel theory prediction for a bare metal surface using the values of n and k given by Hagemann, *et al.* [9].

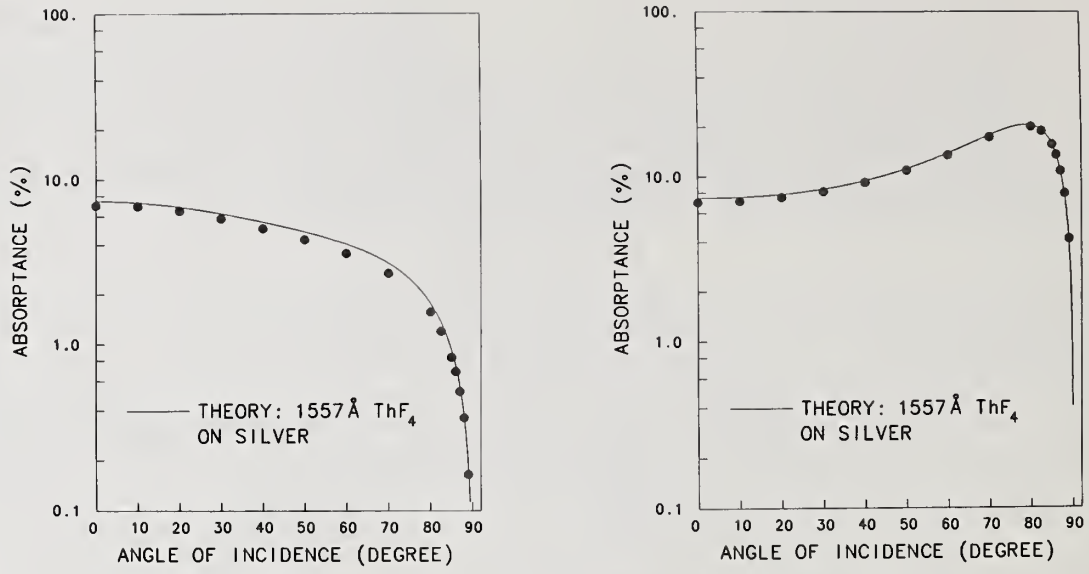

Figure 5. Optimum fit of thin film model with experimental data. The data is the same as given in Fig. 4. (a) is for s-polarization; (b) is for p-polarization. The solid curve is the prediction assuming a ThF_4 thickness of 1557 angstroms.

4. Discussion

Agreement between the thin film model and the experimental data is very good. The fact the agreement remains good over the full range of incidence angles and for both polarizations is a strong indication that the solution determined by the model (i.e., the film thickness for optimum fit) is a unique one. The actual thicknesses of the films on these mirrors is currently being measured by independent means.

Given the ability to predict accurately the absorptance (or reflectance) properties of overcoated mirrors at glancing incidence, it is interesting to ask the question: what film thickness will minimize the absorptance (and thereby maximize the reflectance) of an overcoated mirror at a specified polarization and high angle of incidence? From the data shown in the previous section, it is clear that arbitrarily choosing a film thickness can result in adversely affecting the absorptance of the mirror at high angles of incidence.

To answer this question, the MgF_2 film thickness on the aluminum mirror is systematically varied in the model until the minimum absorptance is predicted. The results for minimizing the s-polarization at 85° are shown in Figure 6. The model predicts an optimum thickness of 2571 angstroms MgF_2; for comparison the theoretical curve for bare metal (i.e., 0 angstroms MgF_2) is also plotted. At angles greater than roughly 70°, the thin film absorptance curve is very similar to the bare metal curve and, therefore, its absorptance at 85° is essentially as low as a bare metal. There is, however, a penalty associated with the film. The absorptance at normal incidence is higher than for a bare metal, and the p-polarization absorptance at glancing incidence has increased over nearly all angles.

Figure 7 shows the theoretical results for a MgF_2 film on aluminum designed to minimize the p-polarization absorptance at 85°. At a film thickness of 1080 angstroms, the p-polarization absorptance curve no longer displays a Brewster angle effect at high angles of incidence, but instead has a curve shape similar to that for s-polarized light on bare metal. Although the p-polarization absorptance has become smaller at high angles of incidence, it is not as small as the s-polarization absorptance of a bare metal. Note, in Figure 7(a), that the s-polarization absorptance now increases dramatically with angle.

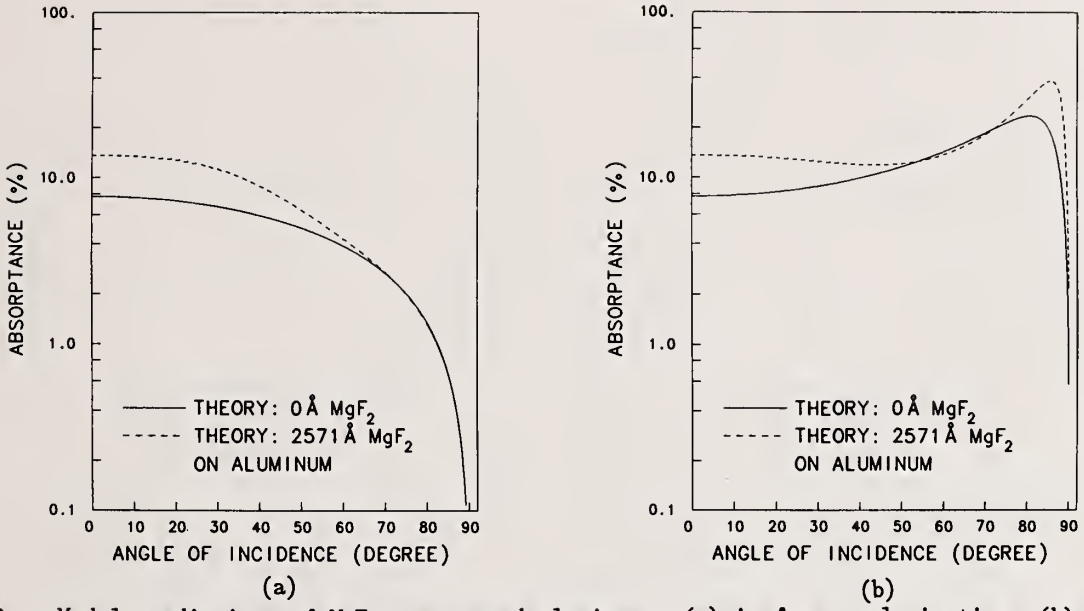

Figure 6. Model predictions of MgF_2 overcoated aluminum. (a) is for s-polarization; (b) is for p-polarization. The solid curve is the prediction for a bare metal surface; the dashed curves for a film thickness designed to minimize the s-polarization absorptance at 85°

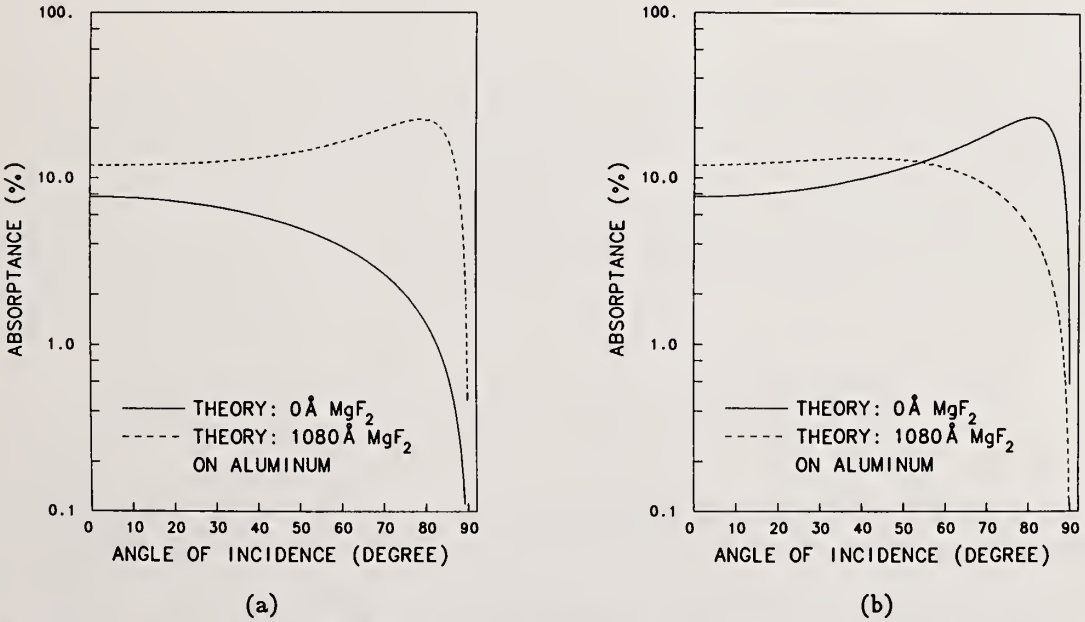

Figure 7. Model predictions of MgF_2 overcoated aluminum. (a) is for s-polarization; (b) is for p-polarization. The solid curve is the prediction for a bare metal surface; the dashed curves for a film thickness designed to minimize the p-polarization absorptance at 85°.

Figures 8 and 9 show the results of similar efforts to determine the thicknesses of ThF_4 films on silver, which minimize the absorptance at 85° for s and p-polarization, respectively. In Figure 8(a), with 2007 angstroms ThF_4, the absorptance of the s-polarization is actually slightly less than it is for a bare metal.

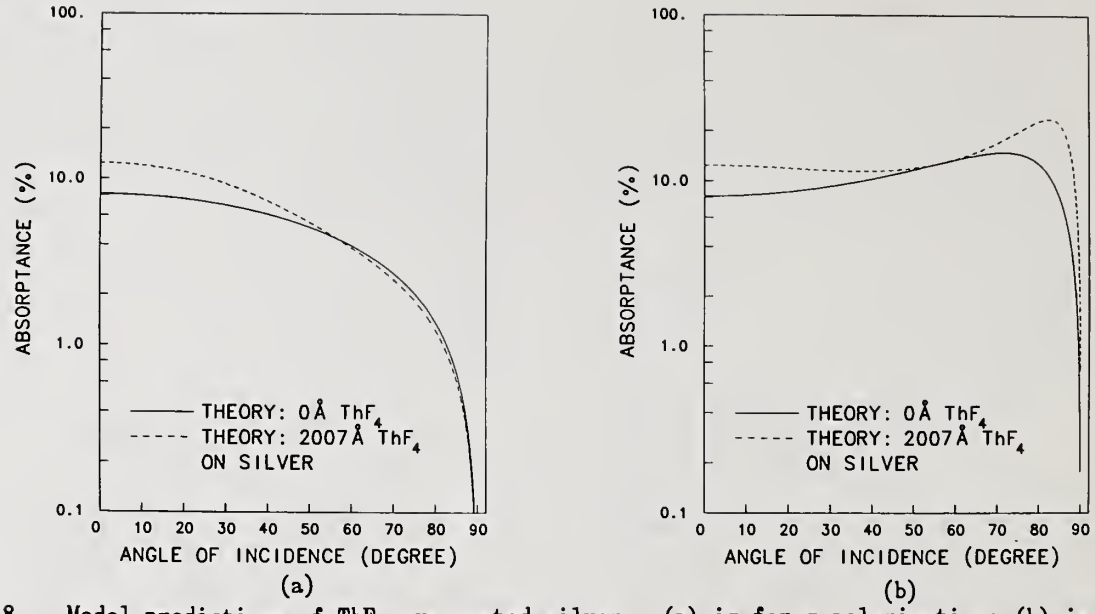

Figure 8. Model predictions of ThF_4 overcoated silver. (a) is for s-polarization; (b) is for p-polarization. The solid curve is the prediction for a bare metal surface; the dashed curves for a film thickness designed to minimize the s-polarization absorptance at 85°.

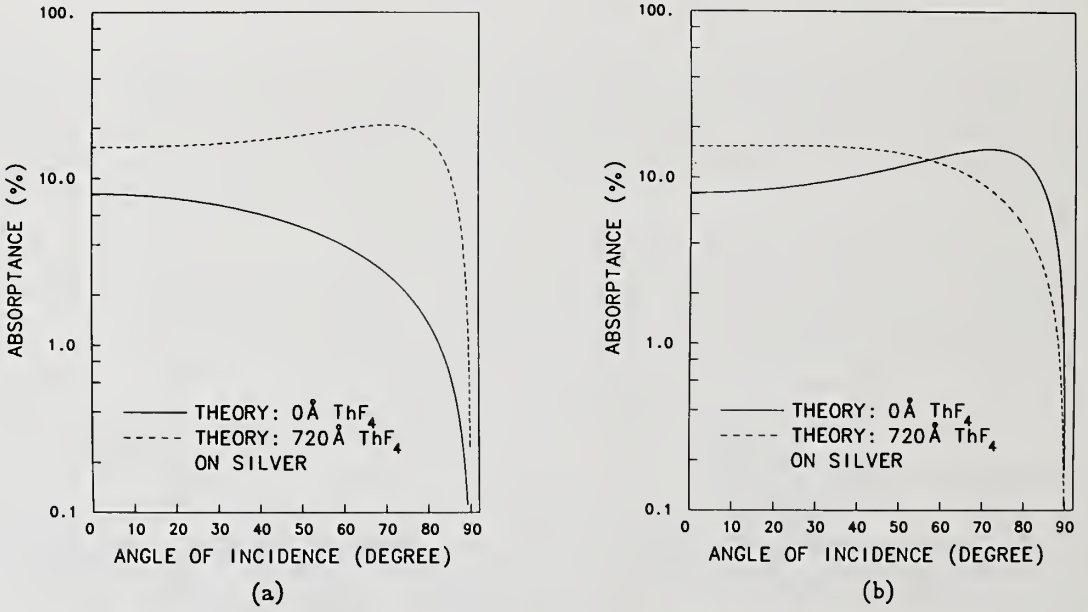

Figure 9. Model predictions of ThF_4 overcoated silver. (a) is for s-polarization; (b) is for p-polarization. The solid curve is the prediction for a bare metal surface; the dashed curves for a film thickness designed to minimize the p-polarization absorptance at 85°.

It is apparent when comparing Figures 6 and 7, and Figures 8 and 9, that the absorptance characteristics tend to change with film thickness in opposing manners for each polarization. This implies there exists a film thickness which causes both polarization components to display a similar angular dependence. Indeed, this is demonstrated in Figure 10, which shows that a 550 angstrom ThF_4 film on silver causes both polarizations to have nearly identical absorptance behavior. Such a film thickness may be important when high reflectivity at both polarizations is needed at high angles of incidence.

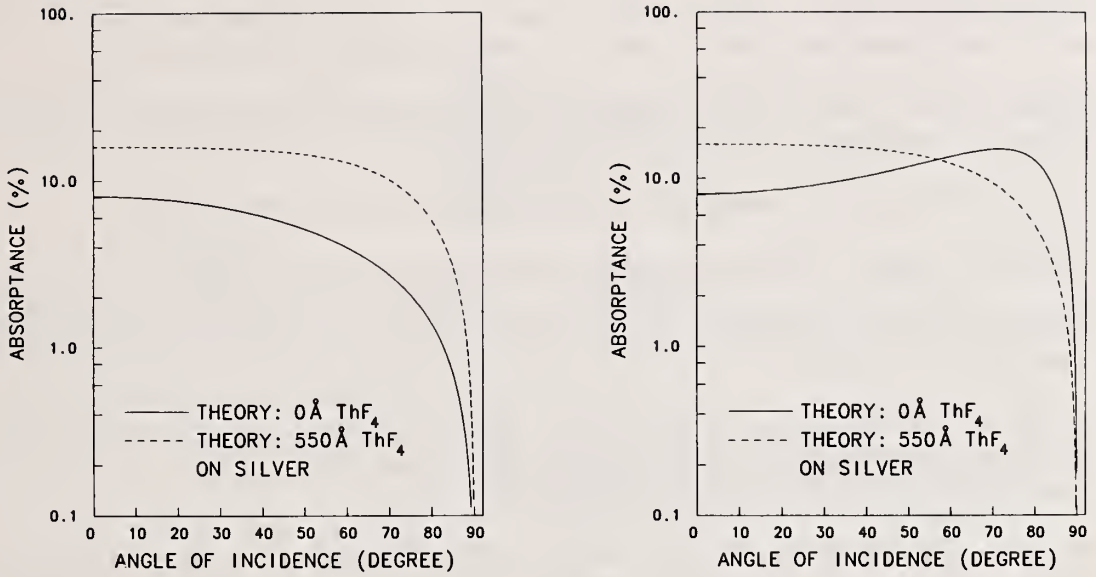

Figure 10. Model predictions of ThF_4 overcoated silver. (a) is for s-polarization; (b) is for p-polarization. The solid curve is the prediction for a bare metal surface; the dashed curves for a film thickness designed to make the absorptance characteristics similar for both polarizations.

5. Conclusion

Thin film models provide an accurate means of interpreting the glancing incidence measurements of dielectric overcoated mirrors. They can also be used to predict the best film thickness to apply, in order to optimize a desired characteristic of the mirror at a high angle of incidence. This is important because of the need to apply overcoats on bare metal mirrors, such as silver, to prevent tarnishing. It may be also possible to design films that yield reflectivities at glancing incidence higher than is obtainable with a bare metal. Further study is needed to determine whether this can be obtained with a single layer dielectric on metal or would require multi-layer dielectric coatings.

---

6. Acknowledgments

The authors wish to thank D.H. Ford for his assistance during the glancing incidence measurements of the mirrors. This work was sponsored by the Department of Energy, Contract No. DE-AC06-83ER40128.

7. References

[1] Newnam, Brian E. Multifacet - all metal reflector design for soft x-ray and XUV free electron resonators. 17th Annual Symposium on Optical Materials for High Power Lasers, Boulder, CO, October 28-30, 1985.

[2] Kimura, Wayne D. Comparison of bare silver and bare silver on copper mirrors. Optical Society of America Workshop on Optical Fabrication and Testing, Seattle, WA, October 21-23, 1986, paper no. IV-WB8.

[3] Kimura, Wayne D.; Ford, Dennis H. Photoacoustic calorimetry system for glancing incidence mirror absorptance measurements. Rev. Sci. Instrum. 57(11): 2754-2762; 1986.

[4] Kimura, Wayne D.; Ford, Dennis H. Absorptance measurements of metal mirrors at glancing incidence. Appl. Optics. 25(20): 3740-3750; 1986.

[5] Born, Max; Wolf, Emil. Principles of optics: Pergamon Press; 1975. 628-630.

[6] Macleod, H. Angus. Thin-film optical filters: American Elsevier; 1969.

[7] Heavens, O.S. Optical constants of thin films, in Physics of thin films, vol. 2: Academic; 1964. 203.

[8] Shiles, E.; Sasaki, Taizo; Inokuti, Mitio,; Smith, D.Y. Self-consistency and sum-rule tests in the Kramers-Kronig analysis of optical data: application to aluminum. Phys. Rev. B. 22(4): 1612-1628; 1980.

[9] Hagemann, H.J.; Gudat, W.; Kunz, C. Optical constants from the far infrared to the x-ray region: Mg, Al, Cu, Ag, Au, Bi, C, and Al_2O_3. J. Opt. Soc. Am. 65(6): 742-744; 1975.

1986

Boulder Damage Symposium

Closing Remarks

A. H. Guenther

It certainly appears that the Symposium is alive and prospering. We had about 190 participants this year. Besides the presentations we have heard and seen, the most important ingredients of this event are you the participants. I was most glad to see the considerable interaction that took place during the course of the meeting. This year, perhaps more than any other year, there were more requests for papers and discussions going on in the hall. I hope this is not an indication of the one major problem we still have and that is that people want to get the information now rather than wait for the proceedings to come out. In that regard, I would like to show you what we do to people when they don't get their manuscripts in by publication time. We, in fact, do publish the paper and we put up on the top of the manuscript, "manuscript not received", title, author, abstract and discussion, all inside this very wide very black border. We are prepared to do it again this year. We have all the papers for 1984 and as I said we got promises from everybody who was here concerning the delinquent papers for 1985. They say they will all be with us before this calendar year is out and we are essentially almost finished with our reviews so we hope to have that to the publishers early in the next calendar year.

There are some observations that I would like to make about this particular year's meeting. Most of you who do know the history of the conference realize that it started out as a mini-symposium of the laser section of the American Society of Testing and Materials. The ASTM is a standards setting organization. We were going to have this meeting for a year and maybe two at the most, and by then we would have solved all the problems; we would have standards, and off we would go and we would know all about laser induced damage. That was eighteen years ago and it was interesting for me to note that somebody got up here on the stage today and said he sent the same samples to two places for testing, two of the premiere testing places, and one came back with 0 joules per square centimeter and the other came back with 30-40 joules per square centimeter. I think that observation says that we still have a way to go, but that way to go may be the fact that we still have not agreed on definitions, test protocols, how we can record our particular data, data analysis procedures and other aspects of this subject, or, for that matter, even what damage is. The lesson we can take from the standards community is that it is, in fact, generally done by consensus; by people in the field. In the ASTM there are people who are not only vendors or buyers but people from within the Government, particularly the National Bureau of Standards, who are, I wouldn't say exactly innocent bystanders, but are supposed to be objective participants to interact with this group to, in fact, help in standardizing test protocols so that, in fact, the tests and the procedures are material sensitive and not test or operator

sensitive. I hope, as a result of some work that we started a few years ago on Round Robins, that this may trumpet, at least to our community, a need to carry this on and continue this work to develop a standard damage procedure or a reporting mechanism so that we can enhance the communication in this field of obvious importance.

Another item heard at this meeting was somewhat of a renaissance in the discussion of chemical polishing. For years we heard the discussion, "get the dirt out, get the dirt off the surfaces" and we heard something about laser annealing. There is no question that what we are hearing today, however, is not only just the application of those techniques to make improvements in the cleanliness of surfaces and samples, but by doing it in such a manner that you don't destroy the optical quality such as the topography of those samples, that we are, in fact, strengthening the surfaces. When it comes to thin films, there was a lot of discussion of thermal conductivity and I suspect there will be a lot more in the future. There was a question asked today about "Is it thermal conductivity or diffusivity that you are interested in?", and the answer came back that "You really are interested in the product of the density and the specific heat and the thermal conductivity." I agree with those comments but I would like to point out that the density cannot vary very much including packing fraction considerations, which for most film materials that we are talking about, are like 10-20%, unless you are dealing with something like sol-gels, or what have you. The specific heat is something that is really a composition-dependant property of the material while the thermal conductivity, which seems to be varying all over the map is structure-dependent. This is the property over which we have the most control and opportunities, I may add, for improvement.

Last year I gave a talk back east and I made the comment that at this meeting I heard someone talk about thermal conductivities of a specific material and one person said that it was a factor of 5 lower than the bulk, yet another paper reported a factor of 50 or 60 below and someone just recently had said it may be as much as 600. I make the observation that I did not know which one was right. Well, someone in the audience pointed out that they may all be right and that, in fact, is true because the thermal conductivity structure dependent is, therefore, very process-dependent. I think as we proceed further with these thermal modeling calculations, in an attempt to understand the failure mechanisms, I think we are going to have to go more into what we have been alluding to all these years, and that is a correlation of process with structure. That is why I personally feel that techniques like spectroscopic ellipsometry may be a useful, nondestructive test that will allow us to find something out about the film structure simply and inexpensively. It still also means that we have to take the same films and have the thermal conductivities measured by a variety of techniques or the diffusivity so that we can, in fact, have some confidence in the numbers that are being presented.

Those are just some comments that I have for this meeting. We would like to thank all for your participation. We would further like to thank the National Bureau of Standards again for acting as our host. As you know, we have selected a date for next year; October 26-28, 1987. As of now, those are the dates. There is a possibility that those dates may change by one or two days, but we are pretty sure it is going to be that week. That will be the week before Halloween and that will be in preparation for our big 20th in 1988. We will start to think about what we'll do and if anybody has some suggestions or ideas, I am sure all of the conference co-chairmen, Hal Bennett, Dave Milam, Brian Newnam and myself would be most receptive of your inputs and if there is any way we can improve this meeting, please let us know because we are flexible. Last, but not least, we would like to acknowledge the following most important individuals whose support before, during, and after this Symposium have helped make it the success that is was: Ms. Susie Rivera, Ms. Patricia Whited, Ms. Edit Haakinson, Ms. Sharon Chesnut and Ms. Ann Mannos.

Thanks again for coming. Have a safe trip home! See you next year.

BOULDER DAMAGE SYMPOSIUM
Attendees
November 3-5, 1986

Joseph Abate
Hampshire Instruments, Inc.
P.O. Box 10159
250 East River Road
Rochester, NY 14610
(716) 482-4070

M. A. Acharekar
Litton Laser Systems
P.O. Box 7300
Orlando, FL 32854-7300
(305) 295-4010

S.M.Jayed Akhtar
Institute fuer Quantenoptik
Universitat Hannover
Welfengarten 1
D-3000 Hannover 1
WEST GERMANY
0511/ 762-4265

Claude Amra
University of Marseilles
ENSP
Domaine Universitaire St. Jerome
13397 Marseilles
FRANCE
(33) 91 68 25 0 6

Joseph H. Apfel
Optical Coating Laboratory, Inc.
2789 Northpoint Parkway
Santa Rosa, CA 95401
(707) 525-7184

Jonathan W. Arenberg
Hughes Aircraft Co.
P. O. Box 902
Bldg. E1 M/SD126
El Segundo, CA 90245
(213) 616-3090

Michael F. Becker
University of Texas at Austin
Electrial Engineering Department
133 Engineering Science Building
Austin, TX 78712
(512) 471-3628

Roger J. Becker
Univ. of Dayton Res. Institute
Dayton, OH 45469-0001
(513) 229-3964

Jerome G. Beery
Los Alamos National Laboratory
MS D429
Los Alamos, NM 87545
(505) 667-1499

Steven C. Bender
Los Alamos National Laboratory
P.O. Box 1663, MS E523
Los Alamos, NM 87545
(505) 667-4941

Harold E. Bennett
Michelson Labs
Naval Weapons Center, Code 38101
China Lake, CA 93555
(619) 939-1440

V. Warren Biricik
Northrop Research & Tech. Center
One Research Park
Palos Verdes Peninsula, CA 90274
(213) 544-5306

Norman L. Boling
Deposition Sciences, Inc.
386 Tesconi Court
Santa Rosa, CA 95401
(707) 579-2008

James Boyer
Los Alamos National Laboratory
CLS-5 MS J566
P.O. Box 1663
Los Alamos, NM 87545
(505) 667-6448

Peter Braunlich
Physics Dept.
Washington State Univ.
Pullman, WA 99164
(509) 335-4946

Ernie Braunschweig
R & D Associates
2301-F Yale Boulevard, SE
Albuquerque, MN 87106
(505) 842-8911

Morris Braunstein
MRB Instrument Co.
4746 H La Villa Marina
Marina del Rey, CA 90292
)213) 823-3815

John H. Campbell
Lawrence Livermore National Lab
P.O. Box 5508, L-482
Livermore, CA 94550
(415) 422-6497

Ian H. Campbell
Princeton University
Dept. of Electrical Engineering
Engineering Quadrangle
Princeton, NJ 08544
(609) 452-3710

Charles K. Carniglia
Martin Marietta Aerospace
P.O. Box 9316
International Airport
Albuquerque, NM 87119
(505) 844-1064

Susan D. Carson
BDM Corporation
1801 Randolph Road, S.E.
Albuquerque, NM 87106
(505) 848-5696

Lloyd L. Chase
Lawrence Livermore National Lab
P.O. Box 5508, L-490
Livermore, CA 94550
(415) 422-6151

Steve Chelli
McDonnell Douglas Astronautics Co.
P.O. Box 516
St. Louis, MO 63166
(314) 234-6428

Sharon K. Chesnut
Naval Weapons Center
Code 381
China Lake, CA 93555
(619) 939-2470

Charles S. Cockrum
Rocky Mountain Instruments
1501 So. Sunset
Longmont, CO 80501
(303) 449-6652

Bob Cooper
Aerospace Corp.
Mail Stop M2/241
P.O. Box 92957
Los Angeles, CA 90009-2957
(213) 336-7314

Alain Culoma
ETCA
16 bis Avenue Prieur de la Coted'Or
94114 Arcueil Cedex
FRANCE
16 1 42.31.92.71.

A. W. Czanderna
Solar Energy Research Institute
1617 Cole Blvd.
Golden, CO 80401
(303) 231-1240

Barbara A. Darnell
Ragged Hill Road
West Brookfield, MA 01585

Eric Daugy
Laboratoires de Marcoussis
91460 Marcoussis
FRANCE
19.33.1.64 49 14 36

Michael Daum
Naval Air Development Center
Code 5011
Warminister, PA 18974
(215) 441-3760

William J. Davis
Itek Optical Systems Division
10 Maguire Road
Lexington, MA 02173
(617) 276-2233

Donald L. Decker
Code 3816
Naval Weapons Center
China Lake, CA 93555
(619) 939-3247

Marilyn J. Dodge
National Bureau of Standards
A331 - Technology Bldg.
Gaithersburg, MD 20899
(301) 921-3625

Fred Domann
AFWL/CCN
Kirtland ARB, NM 87117-6008
(505) 844-7368

David Doryland
USAF
AFWL/ARBD
Kirtland AFB, MN 87117-6008
(505) 844-1776

Fred W.Doss
Spectra Physics
Optics Division
1250 W. Middlefield Road
Mountain View, CA 94039
(415) 961-2550

Marc Drumez
DRET
26 Boulevard Victor
75015 Paris
FRANCE
(1) 45 52 6803

Dr. Johannes Ebert
Laseroptik GmbH
Gneisenaustrasse 14
3008 Garbsen 8
WEST GERMANY
05131 / 2188

David F. Edwards
Lawrence Livermore National La
L-332
Livermore, CA 94550
(415) 422-0747

David Emmony
Dept. of Physics
University of Technology
Loughborough Leicestershire LE11 3TU
UNITED KINGDOM
(509) 223306

Gary C. Escher
AT&T Bell Laboratories
Room 2A-209
600 Mountain Ave.
Murray Hill, NJ 07974
(201) 582-3631

Gregory J. Exarhos
Pacific Northwest Laboratory
P.O. Box 999
Richland, WA 99352
(509) 375-2440

Albert Feldman
National Bureau of Standards
A329 Materials Bldg.
Gaithersburg, MD 200899
(301) 921-2817

Kim F. Ferris
Pacific Northwest Laboratory
P.O. Box 999
Richland, WA 99352
(509) 375-3754

Stephen R. Foltyn
Los Alamos National Laboratory
MS-J 566, CHM-5
P.O. Box 1663
Los Alamos, NM 87545
(505) 667-1123

Jerome B. Franck
Naval Weapons Center
Code 3817
China Lake, CA 93552
(619) 939-2470

Mark E. Frink
Hughes Aircraft Co.
P.O. Box 902, E1/E142
El Segundo, CA 90245
(213) 616-3126

David J. Gallant
Rockwell International
Rocketdyne Division
P.O. Box 5670
Kirtland AFB, NM 87185
(505) 844-2065

Gerald Gallegos
Los Alamos National Laboratory
CLS-5, MS J566
P.O. Box 1663
Los Alamos, NM 87545
505) 667-7748

Diane George
Lawrence Livermore National Lab
P.O. Box 5508, L-490
Livermore, CA 94550

Dennis H. Gill
Los Alamos National Labs.
Chemistry Division, J563
P.O. Box 1663
Los Alamos, NM 87545
(505) 667-8680

Ray Gonzales
Lawrence Livermore National Lab
P.O. Box 5508, L-490
Livermore, CA 94550
(415) 422-6059

George A. Graves
University of Dayton
RM 165 Kettering Labs.
300 College Park
Dayton, OH 45469
(513) 229-4415

David K. Greenlaw
Honeywell Inc.
Systems & Research Center
3660 Technology Drive
Minneapolis, MN 55440
(612) 782-7750

Arthur H. Guenther
AFWL/CCN
Kirtland AFB, NM 87117
(505) 844-9856

Jaques Guerain
Matra Technology, Inc.
5300 Stevens Creek Blvd. #420
San Jose, CA 95129
(408) 243-7170

Koichi Hara
Hoya Corporation
572 Miyazawa-Cho Akishima-Shi
Tokyo
JAPAN
0425-41-3131

F. B. Harrison
Los Alamos National Laboratory
Los Alamos, NM 87544
(505) 665-0104

Sammy Henderson
Coherent Technologies, Inc.
3300 Mitchell Lane, Suite 330
Boulder, CO 80306
(303) 449-8736

Toshiyuki Hirose
Showa Optical Co.
3-5-3 Shinmachi
Setagaya-ku
Tokyo
JAPAN

William T. Goosey, Jr.
D/177 Special Fabrication
Eastman Kodak Company
901 Elmgrove Rd.
Rochester, NY 14650
(716) 253-6044

Michael R. Greenberg
Spectra-Physics, Inc.
Optical Products Division
MS 4-30
1250 West Middlefield Road
Mountain View, CA 94042
(415) 961-2550 Ext. 3032

Mark J. Guardalben
Lab. for Laser Energetics
University of Rochester
250 East River Road
Rochester, NY 14623
(716) 275-5101

Karl H. Guenther
Center for Applied Optics
Univ. of Alabama in Huntsville
Huntsville, AL 35899
(205) 895-6442

Sandra R. Gyetvay
The Aerospace Corporation
P.O. Box 92957
Los Angeles, CA 90009
(213) 336-8239

N. W. Harris
MIT Lincoln Laboratories
P.O. Box 73
Lexington, MA 01873
(617) 803-5500

Chiemi Hata
Hoya Corporation
572 Miyazawa-Cho
Akishima-Shi
Tokyo 196
JAPAN
0425-41-3131

Edward A. Hildum
Lawrence Livermore National Lab
P.O. Box 5508, L-490
Livermore, CA 94550
(415) 423-3987

Lowell M. Hobrock
Hughes Aircraft Company
2000 E. El Segundo Blvd.
P.O. Box 902
El Segundo, CA 90245
(213) 616-9620

Lonnie Holder
McDonnell Douglas Astronautics Co.
MS-E804/101A/2/230
P.O. Box 516
St. Louis, MO 63166
(314) 234-8436

Samuel J. Holmes
Northrop Research & Tech. Center
One Research Park
Palos Verdes Peninsula, CA 90274
(213) 544-5314

Alan K. Hopkins
AFWAL/Materials Lab.
Wright-Patterson AFB, OH 45459

Jaques Huyghe
Matra Technology
5300 Stevens Creek Blvd. #420
San Jose, CA 95129
(408) 243-7170

Takashi Inazumi
Hoya Corporation
572 Miyazawa-cho
Akishima-shi
Tokyo
JAPAN
(0425) 41-3131

Tetsuro Izumitani
Hoya Corporation
572 Miyazawa-cho
Akishima-shi
Tokyo 196
JAPAN
(0425) 41-3131

Stephen D. Jacobs
Laboratory for Laser Energetics
University of Rochester
250 East River Road
Rochester, NY 14623
(716) 275-4837

Yong Jee
University of Texas at Austin
E-104 Colorado Apts.
2501 Lake Austin Blvd.
Austin, TX 78703
(512) 471-4735

Linda F. Johnson
Naval Weapons Center
Physics Division, Code 3818
China Lake, CA 93555
(619) 939-1422

George T. Johnston
Optical Coating Laboratory, Inc.
2789 Northpoint Parkway
Santa Rosa, CA 95401-7397
(707) 525-7148

John A. Kardach
U.S. Air Force
AFWL/ARBF
Kirtland AFB, NM 87117-6008
(505) 844-0166

Geza L. Keller
Los Alamos National Laboratory
M/S E523
P.O. Box 1663
Los Alamos, NM 87545
(505) 667-1537

Wayne D. Kimura
Spectra Technology
2755 Northup Way
Bellevue, WA 98004-1495
(206) 827-0460

C. William King
Harshaw/Filtrol
6801 Cochran Road
Solon, OH 44139
(216) 248-7400

Claude A Klein
Raytheon Company
131 Spring St.
Lexington, MA 02173
(617) 860-3069

Jurgen Kolbe
University Hannover
Institut fur Quantenoptik
Welfengarten 1
D-3000 Hannover 1
WEST-GERMANY
0511-762-4894

William A. Koldewyn
Scientech, Inc.
5649 Arapahoe
Boulder, CO 80303
(303) 444-1361

G. Edward Kuhl
W. Schafer Associates, Inc.
5100 Springfield Pike
Suite 311
Dayton, OH 45431-1231
(513) 253-9572

Russell Kurtz
TMS
8455 Naylor Ave.
Los Angeles, CA 90045
(213) 641-9625

Nisso Lagnado
Hughes Santa Barbara Res. Center
75 Coromar Drive
Goleta, CA 93117
(805) 562-2615

Ramin Lalezari
PMS Electro Optics
1855 S. 57th Ct.
Boulder, CO 80301
(303) 443-7100

Michael R. Lange
Litton Laser Systems
4415-B Hawkins NE
Albuquerque, NM 87109
(505) 345-9094

Marilyn Law
Martin Marietta Aerospace
P.O. Box 9316
International Airport
Albuquerque, NM 87119
(505) 844-1064

Thomas A. Leonard
Analytic Decisions Inc.
5100-211 Springfield Pike
Dayton, OH 45431
(513) 258-1192

Daniel H. Leslie
W.J. Schafer Associates
1901 N. Fort Myer Drive
Arlington, VA 22209
703) 558-7900

Paul W. Levy
Brookhaven National Laboratory
Bldg. 480
Upton, NY 11973
(516) 282-3820

Keith L. Lewis
Royal Signals & Radar
Establishment
St. Andrews Rd.
Malvern, Worcs. WR14 3PS
UNITED KINGDOM
(06845) 2733 Ext 3062

Eric Lobenstine
University of Rochester
Laboratory for Laser Energetics
250 East River Road
Rochester, NY 14623
(716) 275-5101

I. J. Lowe
Airtron Litton
200 E. Hanover Ave.
Morris Plains, NJ 07950
(201) 539-5500 Ext. 701

Michael Lunt
Technical Optics Ltd.
Second Avenue,
Onchan, Isle of Man
UNITED KINGDOM 0624 4443
44 624 74443

Richard Lyon
Lawrence Livermore National Lab
P.O. Box 5508, L-490
Livermore, CA 94550

Autrey Mannion
Ferranti Astron
Kinnoull St.
Dundee
SCOTLAND
0382 38391

Nastaran Mansour
North Texas State University
Physics Dept., Box 77
Denton, TX 76203
(817) 565-3312

C. Denton Marrs
Naval Weapons Center
Code 3817
China Lake, CA 93555
(619) 939-2470

Diane J. Martin
USAF
AFWL/ARAD
Kirtland AFB, NM 87117-6008
(505) 844-1776

Carl S. Masser
Northrop Research & Tech. Center
One Research park
Palos Verdes Peninsula, CA 90274
(213) 544-5306

Fred McClung
Hughes Aircraft Co.
1600 Randolph Ct.
Albuquerque, NM 87106
(505) 768-6118

David E. McCready
Martin Marietta Aerospace
P.O. Box 9316
International Airport
Albuquerque, NM 87119
(505) 844-1064

Michael McGuirk
Perkin-Elmer
761 Main Avenue
Norwalk, CT 06856-420
(203) 834-4921

John K. McIver
Univ. of New Mexico
Dept. Physics & Astronomy
Albuquerque, NM 87131
(505) 277-8484

Theodore S. McMinn
McDonnell Douglas Corporation
P.O. Box 516
Bldg. 106, Level 2
MS/8
St. Louis, MO 63166
(314) 234-4321

James F. McNally
United States Air Force
Department of Physics
U.S. Air Force Academy
Colorado Springs, CO 80840
(303) 472-2240

John R. McNeil
University of New Mexico
Electrical Engineering Dept.
Albuquerque, NM 87131
(505) 277-5626

Jean Francois Mengue
Commissariat a L'Energie Atomique
CEL-V
B.P. 27
94190 Villeneuve Saint Georges
FRANCE

Larry D. Merkle
University of Arkansas
Physics Department
Fayetteville, AR 72701
(501) 575-6425

David Milam
Lawrence Livermore
National Laboratory
PO Box 5508, L-490
Livermore, CA 94550
(415) 422-5499

Mark B. Moran
Naval Weapons Center
Code 3817
China Lake, CA 93555
(619) 939-3247

David Mordaunt
Hughes Aircraft Company
P. O. Box 902, E1/B129
El Segundo, CA 90245
(213) 616-5422

Jacques Mouchart
Laboratories de Marcoussis
CR-CGE Route de Nozay
91460 Marcoussis
FRANCE

Ross E. Muenchausen
Los Alamos National Laboratory
CHM-2 MS G738
Los Alamos, NM 87545
(505) 667-9306

Ian T. Muirmeap
OCLI Optical Coatings
Central Way
Hillend Inpst. Est.
Dunfermline, Fife
SCOTLAND
(0383) 823631

George Nado
Texas Instruments
13500 N. Central Exp.
Mail Stop 3196
Dallas, TX 75266
(214) 480-6412

Ontario H. Nestor
Harshaw Chemical Company
6801 Cochran Road
Solon, OH 44122
(216) 248-7400

Brian E. Newnam
Los Alamos National Laboratory
MS-J564
Los Alamos, NM 87545
(505) 667-7979

Davis B. Nichols
Boeing Aerospace Co.
Mail Stop 8H-18
PO Box 3999
Seattle, WA 98124
(206) 773-8938

Nicholas S. Nogar
Los Alamos National Labs.
CHM2 G-738
Los Alamos, NM 87545
(505) 667-9305

C. J. Norman
MOD(PE)AWRE
Bldg. C-15
Aldermaston, Reading
Berkshire
UNITED KINGDOM
07356-4111 Ext 7877

Joni M. Nuernberger
Naval Weapons Center
Code 3817
China Lake, CA 93555
(619) 939-2470

Robert M. O'Connell
Univ. of Missouri - Columbia
Elect. Engineering Dept.
College of Engineering
Columbia, MO 65201
(314) 882-8373

Yoshiaki Okamoto
Okamoto Optics Work, Inc.
8-34 Haramachi, Isogoku
Yokohama 235
JAPAN
(045) 752-2233

Takayuki Okamoto
Okamoto Optics Work, Inc.
8-34 Haramachi, Isogo-Ku
Yokohama 235
JAPAN

Richard S. Owens
Spiricon Inc.
2600 No. Main
Logan, UT 84321
(801) 753-3729

James R. Palmer
COMCARO, Inc.
208 E. Radar
Ridgecrest, CA 93555
(619) 375-8487

Roger A. Paquin
Perkin-Elmer Corporation
Optical Group Research
100 Wooster Heights Road
Danbury, CT 06810-7589
(203) 797-6130

Emile Pelletier
University of Marseilles
ENSP
Domaine Universitaire St. Jerome
13397 Marseilles
FRANCE
(33) 91 68 25 0 6

Jeff Persoff
Hughes Aircraft Co.
P.O. Box 902
MS EO/E55/G223
El Segundo, CA 90245
(213) 616-6859

John R. Platenack
Texas Instruments
8650 Southwestern Blvd. #2828
Dallas, TX 75206
(214) 692-7220

James O. Porteus
Naval Weapons Center
Code 3817
China Lake, CA 93555
(619) 939-3247

Howard T. Powell
Lawrence Livermore National Lab
P.O. Box 5508, L-490
Livermore, CA 94550
(415) 422-6149

Lawrence R. Pratt
Los Alamos National Laboratory
MS G738
Chemistry Division
Los Alamos, NM 87545
(505) 667-8624

Rod K. Quinn
Los Alamos National Laboratory
P.O. Box 1663/CLS-DO
MS - J563
Los Alamos, NM 87545
(505) 667-6250

Frank Rainer
Lawerence Livermore
National Laboratory
P. O. Box 5508, L-490
Livermore, CA 94550
(415) 423-4376

Tilak Raj
Martin Marietta Denver Aerospace
P.O. Box 9316
International Airport
Albuquerque, NM 87119
(505) 844-1064

John Ranson
Pilkington P.E.
Glascoed Road
St. Asaph
Clwyd - LL170LL
Wales
UNITED KINGDOM
0745-583301

J. Reif
Freie Universitat Berlin
Institut fur Atom & Festkorperphysik
Arnimallee 14
1000 Berlin 33
WEST GERMANY
+44.30.8382157

Clifford E. Rhoades, Jr.
Lawrence Livermore National Lab
P.O. Box 808, L-298
Livermore, CA 94550

Detlev Ristau
Universitat Hannover
Welfengarten 1
3000-Hannover 1
GERMANY
0511/762-4265

Theresa M. Roberts
USAF/RADC
RADC/ESMO
Hanscom AFB, MA 01731-5000
(617) 377-3693

Steve Robinson
Colorado State University
Physics Dept.
Ft. Collins, CO 80523
(303) 491-7809

Carlos Roundy
Spiricon, Inc.
2600 N. Main
Logan, UT 84321
(801) 753-3729

Steven J. Salazar
Los Alamos National Laboratory
P.O. Box 1663
MS J566
Los Alamos, NM 87545
(505) 667-6448/9222

Aaron Sanders
724.02
National Bureau of Standards
325 Broadway
Boulder, CO 80303
(303) 497-5341

Virgil E. Sanders
Los Alamos National Laboratory
CLS-5 MS J566
P.O. Box 1663
Los Alamos, NM 87545
(505) 667-6448

Paul Schall
JAYCOR
2811 Wilshire Blvd.
Suite 690
Santa Monica, CA 90403
(213) 829-0584

Terry Schemmel
Hughes Santa Barbara Res. Center
75 Coromar Drive
Goleta, CA 93117
(805) 562-2789

Marion L. Scott
Los Alamos National Laboratory
P.O. Box 1663, MS E549
Albuquerque, NM 87545
(505) 667-7557

Ian Seddon
Optical Coating Laboratory, Inc.
2789 Northpoint Parkway
Santa Rosa, CA 95407-7397
(707) 525-7667

David W. Seegmiller
W.J. Schafer Associates, Inc.
2000 Randolph Road
Suite 205
Albuquerque, NM 87106
(505) 242-9992

Steven C. Seitel
Montana Laser Optics, Inc.
P.O. Box 4151
Bozeman, MT 559772-4151
(406) 586-5100

Skip Shepherd
Newark AFB
Newark, OH
(614) 522-7695

W. Dan Shirkey
Eastman Kodak Company
901 Elmgrove Road
Rochester, NY 14650
(716) 235-2338

Dennis R. Sigler
Burleigh Northwest Optical
Burleigh Park
Fishers, NY 14453
(716) 925-9350

Mary F. Singleton
Lawrence Livermore National Lab
P.O. Box 5508, L-490
Livermore, CA 94550
(415) 422-6649

James R. Sites
Physics Department
Colorado State University
Fort Collins, CO 80523
(303) 491-5850

James G. Sliney, Jr.
Rockwell International
Rocketdyne Division
MS-FA-03
6633 Canoga Ave.
Canoga Park, CA 91304
((818) 700-4900

Jerry J. Smith
Naval Weapons Center
Code 381
China Lake, CA 93555
(619) 939-1401

LaRell K. Smith
US Air Force
EOARD
Box 14
FPO NY 09510
AV 235-4505

M. J. Soileau
North Texas State University
Dept. of Physics
CAQE
Denton, TX 76203
(817) 565-3263

James L. Stanford
Naval Weapons Center
Code 3818
China Lake, CA 93555-6001
(619) 939-1418

Alan F. Stewart
Air Force Weapons Lab.
AFWL/ARBE
Kirtland AFB, NM 87117-6008
(505) 844-7368

W. Kent Stowell
AFWAL/AADO-2
Wright-Patterson AFB, OH 45433
(513) 255-5147

Randall T. Swimm
U.S.C., Center for Laser Studies
University Park, DRB 17
Los Angeles, CA 90089-1112
(213) 743-4370

Michael Tarasevich
Singer
1225 McBride Ave.
Little Falls, NJ 07470
(201) 785-2623

Frederick D. Tart
W. J. Schafer Associates, Inc.
2000 Randolph Road
Suite 205
Albuquerque, NM 87106
(505) 242-9992

Ian Thomas
Lawrence Livermore National Lab
P.O. Box 5808, L-483
Livermaore, CA 94550
(415) 423-3896

Dennis Thompson
Eastman Kodak Company
121 Lincoln Avenue
Rochester, NY 14650
(716) 253-2684

Yoshi Toratani
Hoya Optics, Inc.
3400 Edison Way
Fremont, CA 94538
(415) 490-1880

Michael Treadaway
JAYCOR
P.O. Box 85154
San Diego, CA 92138
(619) 453-6580

Trudy Tuttle Hart
Optical Coating Laboratory, Inc.
2789 Northpoint Parkway
Santa Rosa, CA 95407-7397
(707) 525-7192

K. Vedam
Pennsylvania State University
Materials Research Laboratory
University Park, PA 16802
(814) 865-1146

Gerard Villela
Laboratories de Marcoussis
91460 Marcoussis
FRANCE
33164491000

Steve J. Walker
Naval Weapons Center
Code 3817
China Lake, CA 93555
(619) 939-2470

Carolyn Weinzapfel
Lawrence Livermore National Lab.
P.O. Box 5508, L-490
Livermore, CA 94550

Patricia L. White
Air Force Weapons Laboratory
ARBD - Optical Components
Kirtland AFB, NM 87117-6008
(505) 844-1776

Keith Wier
Scientech Inc.
5649 Arapahoe
Boulder, CO 80303
(303) 444-1361

John G. Wilder
Lawrence Livermore National Lab
P.O. Box 5508, L-483
Livermore, CA 94550
(415) 423-3896

Dan Wildt
W.J. Schafer Associates
20501 Ventura Blvd.
Suite 270
Woodland Hills, CA 91364
(818) 704-1455

Gregg Wilensky
RDA
4640 Admiralty Way
Marina del Rey, CA 90295
(213) 822-1715

Ron Willey
OPTO Mechanik, Inc.
P.O. Box 640
Melbourne, FL 32902
(305) 724-2017

Scott R. Wilson
1630 Grand Ave.
N.E. No.6
Albuquerque, NM 87106

G. Richard Wirtenson
Lawrence Livermore National Lab
P.O. Box 5508, L-491
Livermore, CA 94550
(415) 422-1332

C. Robert Wolfe
Lawrence Livermore National Lab
P.O. Box 808, L-489
Livermore, CA 94550
(415) 422-3516

Kunio Yoshida
Institute of Laser Engineering
Osaka University
2-6 Yamada-oka
Suita Osaka, 565
JAPAN
(06) 877-5111

Thomas G. Zocco
Los Alamos National Laboratory
P.O. Box 1663, MS G730
Los Alamos, NM 87545
(505) 667-4481

Richard Zoborowski
OCLI
2789 Northpoint Parkway
Dept. 428-1
Santa Rosa, CA 95407-7397
(707) 525-7709

☆ U.S. GOVERNMENT PRINTING OFFICE: 1988— 2 2 0 - 9 6 5 / 9 0 1 4 1

NBS-114A (REV. 2-8C)

U.S. DEPT. OF COMM. BIBLIOGRAPHIC DATA SHEET (See instructions)	1. PUBLICATION OR REPORT NO. NIST/SP-752	2. Performing Organ. Report No.	3. Publication Date September 1988

4. TITLE AND SUBTITLE

Laser Induced Damage in Optical Materials: 1986

5. AUTHOR(S) Editors: Harold E. Bennett (NWC), Arthur H. Guenther (AFWL), David Milam (LLNL), and Brian E. Newnam (LANL)

6. PERFORMING ORGANIZATION (If joint or other than NBS, see instructions)

NATIONAL BUREAU OF STANDARDS
U.S. DEPARTMENT OF COMMERCE
GAITHERSBURG, MD 20899

7. Contract/Grant No.

8. Type of Report & Period Covered
Final

9. SPONSORING ORGANIZATION NAME AND COMPLETE ADDRESS (Street, City, State, ZIP)

National Bureau of Standards
American Society for Testing and Materials
Office of Naval Research
Department of Energy
Defense Advanced Research Project Agency
Air Force Office of Scientific Research

10. SUPPLEMENTARY NOTES

Library of Congress Catalog Card Number: 88-600571

[ ] Document describes a computer program; SF-185, FIPS Software Summary, is attached.

11. ABSTRACT (A 200-word or less factual summary of most significant information. If document includes a significant bibliography or literature survey, mention it here)

The Eighteenth Annual Symposium on Optical Materials for High Power Lasers (Boulder Damage Symposium) was held at the National Bureau of Standards in Boulder, Colorado, November 3-5, 1986. The Symposium was held under the auspices of ASTM Committee F-1, Subcommittee on Laser Standards, with the joint sponsorship of NBS, the Defense Advanced Research Project Agency, the Department of Energy, the Office of Naval Research, and the Air Force Office of Scientific Research. Approximately 200 scientists attended the Symposium, including representatives from the United States, the United Kingdom, Japan, France, and the Federal Republic of Germany. The Symposium was divided into sessions concerning Materials and Measurements Mirrors and Surfaces, Thin Films, and Fundamental Mechanisms. As in previous years, the emphasis of the papers presented at the Symposium was directed toward new frontiers and new developments. Particular emphasis was given to materials for high power apparatus. The wavelength range of the prime interest was from 10.6 μm to the uv region. Highlights include surface characterization, thin film-substrate boundaries, and advances in fundamental laser-matter threshold interactions and mechanisms. Harold E. Bennett of the Naval Weapons Center, Arthur H. Guenther of the Air Force Weapons Laboratory, David Milam of the Lawrence Livermore National Laboratory, and Brian E. Newnam of the Los Alamos National Laboratory were co-chairmen of the Symposium. The Nineteenth Annual Symposium is scheduled for October 26-28, 1987 at the National Bureau of Standards, Boulder, Colorado.

12. KEY WORDS (Six to twelve entries; alphabetical order; capitalize only proper names; and separate key words by semicolons)

Laser damage; laser interaction; optical components; optical fabrication; optical materials and properties; thin film coatings

13. AVAILABILITY

[X] Unlimited

[ ] For Official Distribution. Do Not Release to NTIS

[X] Order From Superintendent of Documents, U.S. Government Printing Office, Washington, D.C. 20402.

[X] Order From National Technical Information Service (NTIS), Springfield, VA. 22161

14. NO. OF PRINTED PAGES
724

15. Price

U.S. Department of Commerce
National Institute of Standards and Technology
(formerly National Bureau of Standards)
Gaithersburg, MD 20899

Official Business
Penalty for Private Use $300